AFRL-RX-WP-TM-2010-4263

JOINT AOARD/AFRL/LLNL WORKSHOP ON THE NUCLEATION OF PHASE TRANSFORMATIONS IN METALLIC SOLIDS

University of North Texas

MAY 2010
Final Report

Approved for public release; distribution unlimited.

See additional restrictions described on inside pages

STINFO COPY

AIR FORCE RESEARCH LABORATORY
MATERIALS AND MANUFACTURING DIRECTORATE
WRIGHT-PATTERSON AIR FORCE BASE, OH 45433-7750
AIR FORCE MATERIEL COMMAND
UNITED STATES AIR FORCE

NOTICE AND SIGNATURE PAGE

Using Government drawings, specifications, or other data included in this document for any purpose other than Government procurement does not in any way obligate the U.S. Government. The fact that the Government formulated or supplied the drawings, specifications, or other data does not license the holder or any other person or corporation; or convey any rights or permission to manufacture, use, or sell any patented invention that may relate to them.

This report was cleared for public release by the USAF 88th Air Base Wing (88 ABW) Public Affairs Office (PAO) and is available to the general public, including foreign nationals. Copies may be obtained from the Defense Technical Information Center (DTIC) (http://www.dtic.mil).

AFRL-RX-WP-TM-2010-4263 HAS BEEN REVIEWED AND IS APPROVED FOR PUBLICATION IN ACCORDANCE WITH THE ASSIGNED DISTRIBUTION STATEMENT.

*//Signature//

JAIMIE TILEY, Project Engineer
Metals Branch
Metals, Ceramics & NDE Division

//Signature//

PAUL RET, Chief
Metals Branch
Metals, Ceramics & NDE Division

//Signature//

ROBERT MARSHALL, Deputy Chief
Metals, Ceramics & NDE Division
Materials & Manufacturing Directorate

This report is published in the interest of scientific and technical information exchange, and its publication does not constitute the Government's approval or disapproval of its ideas or findings.

*Disseminated copies will show "//Signature//" stamped or typed above the signature blocks.

REPORT DOCUMENTATION PAGE

Form Approved
OMB No. 0704-0188

The public reporting burden for this collection of information is estimated to average 1 hour per response, including the time for reviewing instructions, searching existing data sources, gathering and maintaining the data needed, and completing and reviewing the collection of information. Send comments regarding this burden estimate or any other aspect of this collection of information, including suggestions for reducing this burden, to Department of Defense, Washington Headquarters Services, Directorate for Information Operations and Reports (0704-0188), 1215 Jefferson Davis Highway, Suite 1204, Arlington, VA 22202-4302. Respondents should be aware that notwithstanding any other provision of law, no person shall be subject to any penalty for failing to comply with a collection of information if it does not display a currently valid OMB control number. **PLEASE DO NOT RETURN YOUR FORM TO THE ABOVE ADDRESS**.

1. REPORT DATE *(DD-MM-YY)*	2. REPORT TYPE	3. DATES COVERED *(From - To)*
May 2010	Technical Memo	18 September 2008 – 30 April 2010

4. TITLE AND SUBTITLE
JOINT AOARD/AFRL/LLNL WORKSHOP ON THE NUCLEATION OF PHASE TRANSFORMATIONS IN METALLIC SOLIDS

5a. CONTRACT NUMBER
FA8650-08-C-5226

5b. GRANT NUMBER

5c. PROGRAM ELEMENT NUMBER
62102F

6. AUTHOR(S)

5d. PROJECT NUMBER
4349

5e. TASK NUMBER
20

5f. WORK UNIT NUMBER
LM114100

7. PERFORMING ORGANIZATION NAME(S) AND ADDRESS(ES)
University of North Texas
1147 Union Circle
Denton, TX 76203

8. PERFORMING ORGANIZATION REPORT NUMBER

9. SPONSORING/MONITORING AGENCY NAME(S) AND ADDRESS(ES)
Air Force Research Laboratory
Materials and Manufacturing Directorate
Wright-Patterson Air Force Base, OH 45433-7750
Air Force Materiel Command
United States Air Force

10. SPONSORING/MONITORING AGENCY ACRONYM(S)
AFRL/RXLM

11. SPONSORING/MONITORING AGENCY REPORT NUMBER(S)
AFRL-RX-WP-TM-2010-4263

12. DISTRIBUTION/AVAILABILITY STATEMENT
Approved for public release; distribution unlimited.

13. SUPPLEMENTARY NOTES
Document contains color. This is the best quality available of the presentations assembled from the conference (pagination is not continuous across the document).

PAO Case Number: 88ABW 2010-3948; Clearance Date: 22 July 2010.

14. ABSTRACT
A workshop on the Nucleation of Phase Transformations in Metallic Solids was held in Maui, Hawaii on May 2-7, 2010. The meeting was sponsored by the Asian Office of Aerospace Research and Development (AOARD), the Air Force Research Laboratory (AFRL), the Air Force Office of Scientific Research (AFOSR), and the Lawrence Livermore National Laboratory (LLNL). Representatives attended from the United States, Australia, Singapore, India, and France. The focus of the workshop was to develop research tasks aimed at improving current capabilities in the areas of experimentation, modeling and characterization as they apply to the nucleation of solid phase transformations. The overall objectives of the workshop were to bring together a diverse group of researchers to establish the state of the art in experimenting, characterizing and modeling. Specifics items addressed included (1) what advances are needed in the atomistic/computational modeling area to significantly impact the science? (2) what tools and techniques are required to characterize the formation of nucleants and the local chemical and energy environment? and (3) what opportunities exist for combining advance characterization techniques with experimental validation of nucleation models. The results are provided within this document, including the presentation materials from participants.

15. SUBJECT TERMS
advanced characterization, nucleation

16. SECURITY CLASSIFICATION OF:			17. LIMITATION OF ABSTRACT:	18. NUMBER OF PAGES	19a. NAME OF RESPONSIBLE PERSON (Monitor)
a. REPORT	b. ABSTRACT	c. THIS PAGE			Jaimie Tiley
Unclassified	Unclassified	Unclassified	SAR	1108	19b. TELEPHONE NUMBER *(Include Area Code)* N/A

Standard Form 298 (Rev. 8-98)
Prescribed by ANSI Std. Z39-18

Table of Contents

Summary	1
Findings	1
Presented Experimental and Theory Topics	2
Presented Modeling Topics	2
Presented Characterization Topics	3
Participants	4
Acknowledgments	4
Appendix A: List of Participants	5
Appendix B: Presentation Materials	6

Joint AOARD/AFRL/LLNL Workshop on the Nucleation of Phase Transformations in Metallic Solids

Summary

A workshop on the Nucleation of Phase Transformations in Metallic Solids was held in Maui, Hawaii on May 2-7, 2010. The meeting was sponsored by the Asian Office of Aerospace Research and Development (AOARD), the Air Force Research Laboratory (AFRL), the Air Force Office of Scientific Research (AFOSR), and the Lawrence Livermore National Laboratory (LLNL). Representatives attended from the United States, Australia, Singapore, India, and France. The focus of the workshop was to develop research tasks aimed at improving current capabilities in the areas of experimentation, modeling and characterization as they apply to the nucleation of solid phase transformations. The overall objectives of the workshop were to bring together a diverse group of researchers to establish the state of the art in experimenting, characterizing and modeling. Specifics items addressed included (1) what advances are needed in the atomistic/computational modeling area to significantly impact the science? (2) what tools and techniques are required to characterize the formation of nucleants and the local chemical and energy environment? and (3) what opportunities exist for combining advance characterization techniques with experimental validation of nucleation models?

Findings

The following points were made by the participants during discussions:

1. ***Experimentation and Theory.*** Classical theory has provided tremendous insight into the nucleation process although it has been difficult to experimentally verify specific elemental composition changes, vacancies, and energies associated with nucleant and embryo formation. The use of composition wave functions, understanding of shear, consideration of dynamic nucleation events from atom clustering, knowledge of electronic structures, and spinoidal decomposition events may provide added insight into nucleation. There is a need for improved thermodynamic data, diffusivities, and interfacial energies as well as requirements for statistical analysis of rare events.

2. ***Modeling.*** The modeling discussions centered on the use of phase field approaches that utilize nudged elastic band methods, Langevin noise terms and/or use of monte carlo simulations. There is a need for accurate energy surface representations in addition to better thermodynamic and surface energy terms. The use of these techniques provides nucleation parameters that are very difficult to measure directly. Researchers also identified the need for new techniques for atomistic descriptions of multi-component systems, identifying the transition states, and the need for understanding the interactions between defects and nucleation events.

3. ***Advanced Characterization Techniques.*** Advances with atom probe tomography provides atomic level compositions, critical for evaluation of embryos and nucleants. However efficiency problems with the techniques still present serious issues and should be resolved. Dynamic and hi-resolution transmission electron microscopy techniques have also advanced to the art of

providing structural and chemical information at the atomic level. Although there are issues related to surface and thin film considerations, in situ experiments utilizing these techniques may provide vital information on embryo and nucleant precursors that are critical for model verification.

Presented Experimental and Theory Topics

Experts in the field of experimentation and theory of nucleation presented 4 topics, including 3 plenary speeches. In addition, four sessions were designed to address specific nucleation theory and experimental concerns. The sessions were titled (1) Heterogenieties, (2) Nucleation as a Rare Event, and (3) Experimental Advances.

Dr. Jim Belak (Lawrence Livermore National Laboratory) presented the first Plenary Speech, providing an overview of the field from the first work by Kolmogorov, Johnson. Mehl and Avrami to the work by Cahn, Russel, up to the recent work of today. He was followed by Professor John Perepezko (University of Wisconsin) who gave a plenary presentation on the analysis and modeling of nucleation controlled reactions. Secretary Srikumar Banerjee, PhD, (Government of India) gave a plenary presentation on the structural evolution during nucleation processes. The final plenary presentation was provided by Dr. Alan Ardell (National Science Foundation) on the nucleation and coarsening in normal and inverse Ni-Al alloys. In the Heterogenieties session chaired by Dr. Belak, Dr. Brian Reed (Lawrence Livermore National Laboratory) presented material on grain boundary engineered materials as correlated networks, and the implications of large-scale twin nucleation**.** Professor Gary Shiflet (University of Virginia) gave a presentation on the control of embryo formation and critical nucleus properties. He discussed the possibilities of developing and applying knowledge of electronic structures and atomic interactions into the modeling of the nucleation process. Professor Julia Hammer (University of Hawaii) combined classical theory and advanced characterization in her presentation on the nucleation of crystals in magma. She discussed the use of high temperature, high pressure furnaces to experimentally validate nucleation models of glass that forms deep beneath the surface in volcanoes.

Presented Modeling Topics

Leaders in the field of modeling presented current problems and successes that have been achieved at the different length scales. There were three classes of modeling: (1) atomistic studies, (2) research at the meso scale, and (3) continuum scale modeling.

Professor Wolfgang Windl (The Ohio State University) presented a briefing on lessons learned from the world of semiconductors. His presentation was followed by Professor Jeff Rickman (Lehigh University) who discussed the kinetics and microstructure associated with heterogenous nucleation and growth. Dr. Alphonse Finel (ONERA, France) provided a briefing on the coarse grain derivation of the phase field equations. Dr. Blas Uberuaga (Los Alamos National Laboratory) discussed the use of accelerated dynamics methods. Professor Srini Srivillipurtha (University of North Texas) followed with a presentation on first principles simulation of beta to omega transformations in titanium alloys. His talk was supported in part by experimental work conducted by Professors Hamish Fraser (The Ohio State University) and Rajarshi Banerjee

(University of North Texas), also in attendance. During the discussion period, Professor Srivillipurtha discussed the need for new approaches to address atomistic modeling of multi-component systems. Professor Yunzhi Wang (The Ohio State University) provided a discussion on the effect of local stress on nucleation and variant selection during solid state transformation with symmetry reductions. His use of the phase field approach was heavily discussed during several of the presentations. Professor Qiang Du (Penn State University) also presented a discussion on the use of phase field, focusing on the prediction of critical nucleus morphologies in solids. His work was followed by a briefing by Dr. Chen Shen (General Electric, USA) on the use of phase field techniques. Professor Greg Olson (Northwestern University) and Dr. Fan Zhang (Computherm Inc.) gave presentations on their meso-scale models. Professor Olson discussed the use of multiscale integration in the study of nucleation engineering. He presented numerous examples where multi-scale modeling had effectively captured the nucleation and growth of phase transformations. Dr. Zhang discussed the use of thermodynamic modeling of multi-component systems and the integration of the modeling into kinetic simulations. She discussed the current challenges facing the use of thermodynamic models in simulations of nucleation events, especially in commercial alloys where specific data on three and four component energy interactions are limited. Dr. S. Ranganathan (National Metallurgical Laboratory, India) spoke about the thermodynamic modeling of the early stages of solid state precipitation in alloy systems. Dr. Dan Miracle (AFRL) presented on the nucleation mechanisms for aluminum crystals in amorphous aluminum alloys.

Presented Characterization Topics

Leaders in the field of advanced characterization presented 11 topics. The major discussions concerned the use of transmission electron microscopes and/or atom probe tomography.

Dr. Thomas LaGrange (Lawrence Livermore National Laboratory) gave a presentation on the quantification of crystallization kinetics using nanosecond time resolved electron microscopy. His talk was followed by Dr. Daniel Orlikowski (Lawrence Livermore National Laboratory) who presented a briefing on high pressure considerations and the use of the dynamic anvil cell. Dr. Barry Muddle (Monash University, Australia) presented material on the heterogenous nucleation of plate shaped transformation products. His characterization techniques employed the high resolution transmission electron microscope. Professor Rajarshi Banerjee (University of North Texas) also used advanced TEM techniques in his presentation on the early stages of nucleation and growth of omega precipitates within the beta matrix of titanium alloys. His work provided the experimental validation for the modeling work presented by Professor Srivillipurtha. Dr. Mike Miller (Oak Ridge National Laboratory) followed with a presentation on the advances in atom probe tomography for nucleation studies. His discussion included an overview of the limitations associated with the techniques. Dr. Babu Viswanathan (UES, AFRL) presented a briefing on the gamma/gamma prime phase transformation in nickel alloys, including the issues with characterizing fine scale precipitates. Professor Dipankar Banerjee (IISC, India) provided a presentation on the alpha and beta transformations in titanium alloys, including the nucleation of alpha during thermal processing. Professor Jian Feng Nie (Monash University, Australia) presented on shape strain and its accommodation during the precipitation of precipitate plates. He relied heavily on the use of hi-resolution TEM techniques as well. Professor Raju

Ramanujan (Nanyang Technological University, Singapore) presented material on the nucleation of soft magnetic nanomaterials. He highlighted the impact of different elements on the nucleation rate and growth rate of particles. He also suggested the use of a hot stage TEM to further study the concepts. The final presentation was provided by Professor Hamish Fraser (The Ohio State University) on the use of new characterization techniques. His talk emphasized the need to apply different characterization techniques to validate techniques and offset limitations associated with different approaches. One example was the use of image corrected high resolution TEM systems along with atom probe tomography techniques to determine structural information.

Participants

The workshop was attended by 37 people, including speakers from academia, government laboratories, and industry. The audience was predominantly from the US, although six attendees traveled under the Window on Science program sponsored by AOARD.

Academic Institution Representation. The audience included representatives from 10 academic institutions: Monash University, Nanyang Technological University, India Institute of Science, University of Virginia, Northwestern University, The Ohio State University, University of North Texas, Penn State University, University of Hawaii, and Lehigh University.

Government Laboratory Representation. Seven government laboratories or agencies were represented: Air Force Research Laboratory, Air Force Office of Scientific Research, Asian Office of Aerospace Research and Development, Los Alamos National Laboratory, Lawrence Livermore National Laboratory, Oak Ridge National Laboratory, and the National Science Foundation. In addition the Secretary of Nuclear Energy for India attended (Atomic Energy Commission), and the Deputy Director of the National Metallurgical Laboratory, India, attended.

Industrial Representation. Representatives of 3 private sector entities were also represented: Questek, Computherm, and General Electric Global Research.

International Representation. Five nations were represented in the audience: Singapore, India, France, Australia, and the United States.

Acknowledgments

Funding for this workshop was provided by Air Force Research Laboratory and the Asian Office of Aerospace Research and Development. The workshop was also supported by the Lawrence Livermore National Laboratory. Administrative and logistic support was provided by the Maui Economic Development Company under a contract with the Air Force Research Laboratory.

Appendix A

List of Participants

Jim Belak*	Lawrence Livermore National Laboratory
John Perepezko	University of Wisconsin
Srikumar Banerjee	Atomic Energy Comission, India
Alan Ardell	National Science Foundation
Barry Muddle *	Monash University, Australia
Wolfgang Windl	Ohio State University
Jeff Rickman	Lehigh University
Alphonse Finel	ONERA, France
Blas Uberuaga	Los Alamos National Laboratory
Jeff Simmons*	Air Force Research Laboratory
Jay Tiley*	Air Force Research Laboratory
Greg Olson	Northwestern University
Dipankar Banerjee	India Institute of Science, India
Fan Zhang	Computherm Inc.
Dan Miracle	Air Force Research Laboratory
Long-Qing Chen*	Penn State University
Chen Shen	General Electric Global Research
Jian-Feng Nie	Monash University, Australia
S. Ranganathan	National Metallurgical Laboratory, India
Julia Hammer	University of Hawaii
Hamish Fraser*	Ohio State University
Rajarshi Banerjee*	University of North Texas
Ken Gorretta	Asian Office of Aerospace Research and Development
Yunzhi Wang*	Ohio State University
Laura Cooney	Air Force Office of Scientific Research
Thomas LaGrange	Lawrence Livermore National Laboratory
Daniel Orlikowski	Lawrence Livermore National Laboratory
Brian Reed	Lawrence Livermore National Laboratory
Srini Srivillipurtha	University of North Texas
Mike Miller	Oak Ridge National Laboratory
Babu Viswanathan*	Air Force Research Laboratory
Raju Ramanujan	Nanyang Technological University, Singapore
Gary Shiflet	University of Virginia
Qiang Du	Penn State University
Traci Haerr	Air Force Research Laboratory
Sandy Ryan	Maui Economic Development Board Inc.
Leilani Bulosan	Maui Economic Development Board Inc.

* workshop organizer

Appendix B

Presentation Materials

Nucleation and Coarsening in Normal and Inverse Ni-Al Alloys

Alan J. Ardell

Program Director
Metals and Metallic Nanostructures Program
Division of Materials Research
National Science Foundation
Arlington, VA 22201

AFOSR/AFRL/LLNL Workshop, May 2-7 2010
Maui, HI

Outline

- Brief review of the classical theory of homogeneous nucleation

- The nucleation of γ' (Ni_3Al) precipitates in normal Ni-Al alloys and γ (Ni-Al solid-solution) precipitates in "inverse" Ni-Al alloys offer the best prospects ever of investigating homogeneous nucleation during precipitation from solid solution---Why and How!!!

  - ❖ The Ni-rich region of the Ni-Al phase diagram;

  - ❖ How data on coarsening of precipitates in normal and inverse Ni-Al alloys can be used to provide values of parameters that are important in the process of nucleation;

  - ❖ Observations that suggest the efficacy of studying nucleation in inverse alloys, and experimental advantages that can be used to inform nucleation studies;

  - ❖ Observations that highlight the obstacles to studying nucleation in normal alloys and what can be done to overcome them;

- Presentation of data that might be useful in studies of nucleation in Ni-Al alloys…elastic constants, lattice mismatch

- Musings about diffuse γ/γ' interfaces---might these muddy the waters?

Classical Theory of Nucleation---Energetics

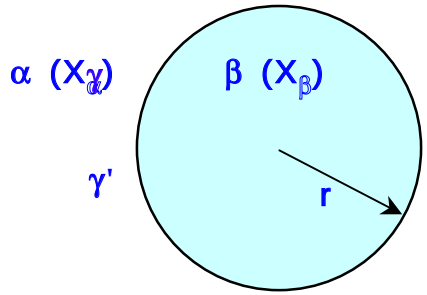

X_β = atom fraction B in β

X_α = atom fraction B in α

Total change in free energy on formation of a nucleus of radius r is

$$\Delta G = \frac{4\pi r^3}{3}\Delta G_v + 4\pi r^2\sigma$$

ΔG_v is the difference in the Gibbs free energy/vol of the α and β phases ($\Delta G_v < 0$);

Elastic energy/vol (>0) for coherent precipitates can contribute, but it is usually very small compared to ΔG_v

σ is the energy/area of the α - β interface ($\sigma > 0$)

ΔG has a maximum value of ΔG* at a critical value of r*, as shown in the diagram below:

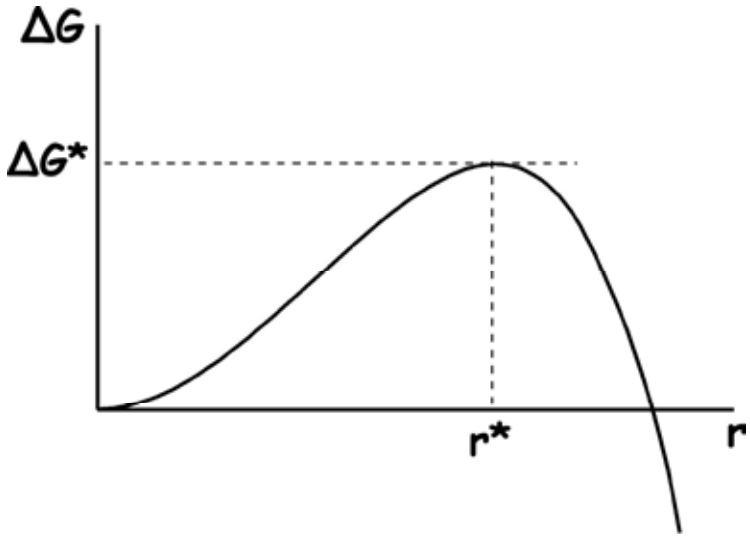

$$r^* = \frac{-2\sigma}{\Delta G_v}$$

$$\Delta G^* = \frac{16\pi\sigma^3}{3(\Delta G_v)^2}$$

Interfacial energy opposes the formation of the nucleus, giving rise to an energy barrier, ΔG*, that must be overcome before the nucleus can be considered stable. Nuclei with radii r > r* are always able to grow with a reduction in energy of the system.

It is sometimes more useful to express the change in free energy in terms of n, the number of B atoms in the nucleus:

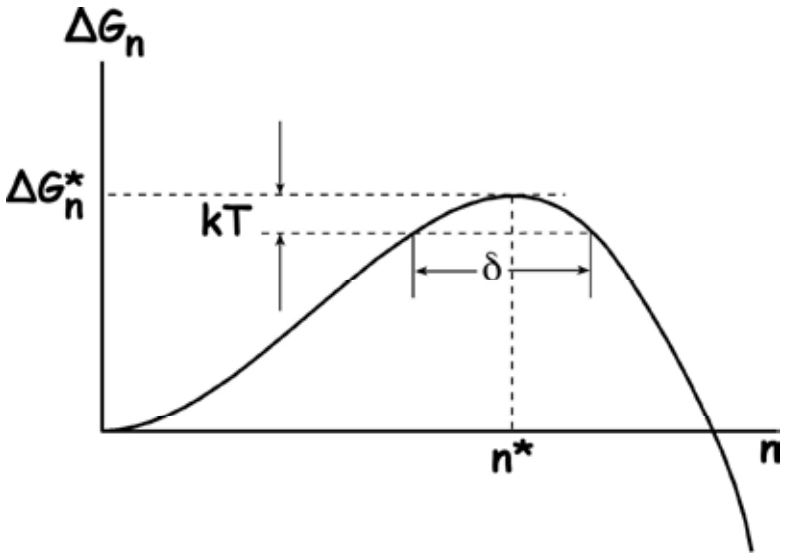

The variation of ΔG in the vicinity of n^* (or r^*) is relatively small over the range of energy $\Delta G^* - kT$. Nuclei with sizes $n^* \pm \delta/2$ are considered to "random walk" over the energy barrier until they reach a size $n^* + \delta/2$, beyond which the probability that they become subcritical is essentially zero.

It is possible to derive partial differential equation that describes the concentration of nuclei of size n, C_n, at any time t. This equation does not have a formal solution. The Classical Theory assumes a solution of the form

$$J^* = J_s \exp(-t/\tau)$$

J_s is the STEADY STATE NUCLEATION RATE

$$J_s = \beta^* C^o_{n^*} Z$$

β^* is the rate at which B atoms attach themselves to a nucleus of critical size

$$\beta^* = \frac{4\pi (r^*)^2 X_o}{a^4} D_B$$

X_o is the initial concentration of B in α

D_B is diffusion coefficient of B in α

a is the jump distance

$C^{o}_{n^*}$ is the concentration of nuclei containing n^* B atoms

$$C^{o}_{n^*} = X_o N_o \exp(-\Delta G_{n^*} / kT)$$

N_o is number of atomic sites/vol

Z is the Zeldovich non-equilibrium factor. It takes into account the fact that there is a finite probability that a nucleus can become subcritical until it contains more than $n^* + \delta/2$ B atoms and depends on the curvature of the ΔG vs. n curve at $n = n^*$

$$Z = \left[\frac{-1}{2\pi kT} \left(\frac{\partial^2 \Delta G_n}{\partial n^2} \right)_{n^*} \right]^{1/2}$$

The incubation time, τ, is

$$\tau = \frac{\delta^2}{2\beta^*} = \frac{2}{\pi Z^2 \beta^*}$$

$$\delta = \left\{ \frac{-8kT}{\left(\partial^2 \Delta G_n / \partial n^2 \right)_{n=n^*}} \right\}^{1/2} = \frac{2}{Z\sqrt{\pi}}$$

Any attempt to validate the classical theory of nucleation necessarily involves measurements of J_s and τ, preferably as functions of T and X_o, both of which govern the supersaturation of the solid solution.

This in turn involves measurements of the number of precipitates/vol, Nv, vs aging time t, with the expectation that only stable precipitates with $n > n^*$ will be detectable.

The expected behavior is shown below:

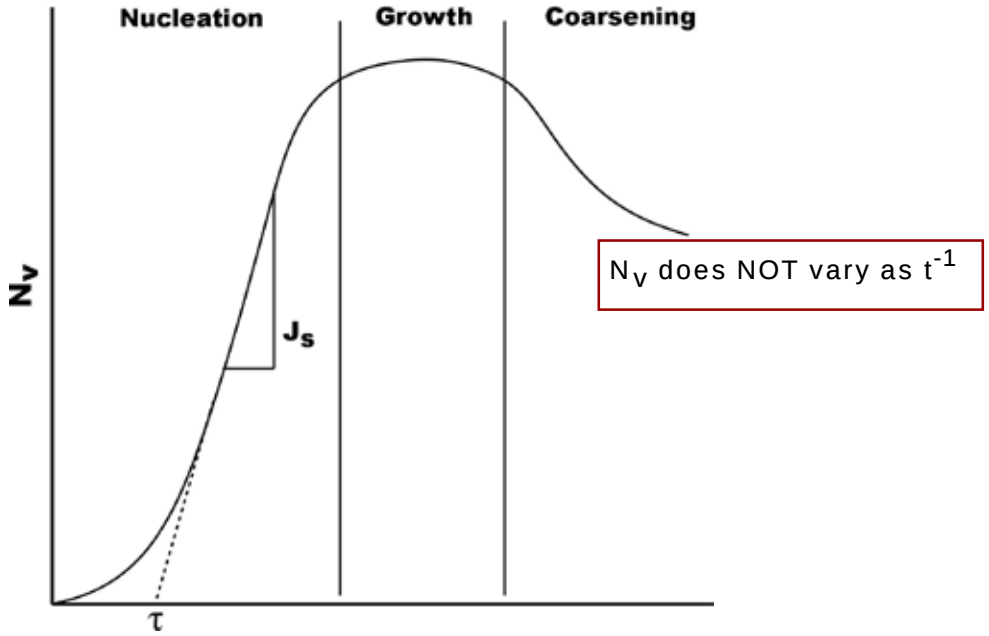

To compare experiment and theory there is a lot we need to know, with many necessary precautions.

The CRUCIAL parameters are σ, ΔG_V and D_B

In Ni-Al alloys σ and D_B can be estimated with reasonable accuracy from data on coarsening, but ΔG_V is tricky.

Free Energy Diagram for Nucleation of an A-B alloy, initial composition X_o

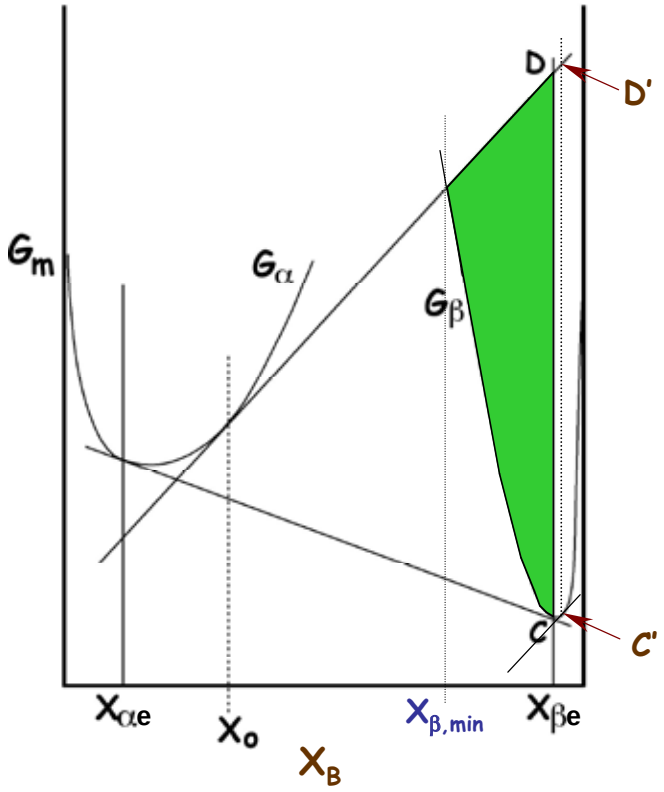

The distance -DC = ΔG_m = free energy/mol β for nucleation of a β-phase nucleus of equilibrium composition, $X_{\beta e}$.

The distance -D'C' = $\Delta G_{m,max}$ is the maximum value of the driving force for nucleation. But it is for a β-phase nucleus of composition $X_\beta > X_{\beta e}$.

For any β-phase composition > $X_{\beta,min}$ there exists a positive driving force for nucleation (i.e. $\Delta G_m < 0$). This region is represented in green for nucleus compositions up to $X_{\beta e}$.

$G_v = G_m/V_m$; V_m is the partial molar volume of B

Estimating ΔG_v requires knowledge of the Gibbs free energy of mixing of the α and β phases, and is sensitive to the curvatures of the free energy functions

If both phases are ideal solutions

$$\Delta G_v = -\frac{kT}{V_m}\left\{X_{\beta e}\ln\frac{X_o}{X_{\alpha e}} + \left(1-X_{\beta e}\right)\ln\left(\frac{1-X_o}{1-X_{\alpha e}}\right)\right\}$$

This equation is a very good approximation when α and β are both terminal solid solutions with limited solubility

So…What's the big deal? Why is classical nucleation theory so difficult to verify, and why are we talking about it amost 75 years after Becker and Doring published their paper in 1935[†]:

[†]R. Becker and W. Doring, ANNALEN DER PHYSIK, 24 (1935) 719-752.

The reason is that, at least for precipitation from solid solution, accurate measurements of steady-state nucleation rates and incubation times are DIFFICULT

One important factor is that diffusion is strongly affected by Quenched-in Vacancies, even when every effort is made to minimize their influence!

Some results that illustrate this follow

Alloys quenched directly from solution treatment temperature, 870 °C, to the aging temperature.

fcc Co precipitates are fully coherent, lattice mismatch = -1.7%

Cu-1% Co

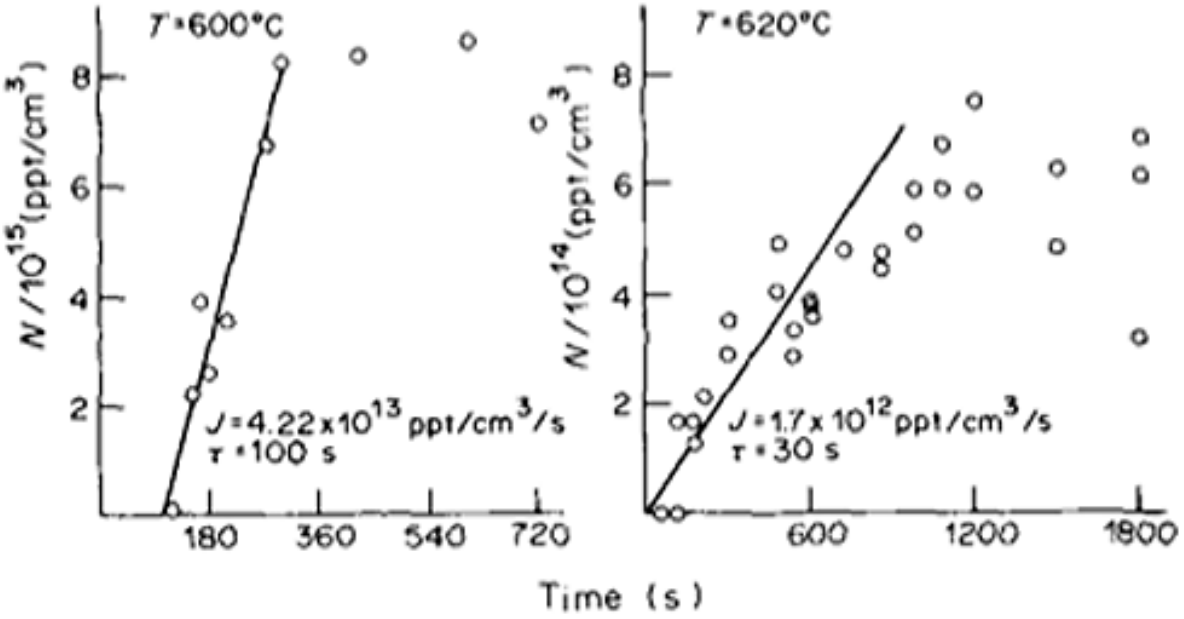

The equilibrium volume fraction is ~0.01

The maximum value of N_v is ~$10^{21}/m^3$

F.K. LeGoues and H.I. Aaronson, Acta Metall. 32 (1984) 1855

Steady-state Nucleation Rates

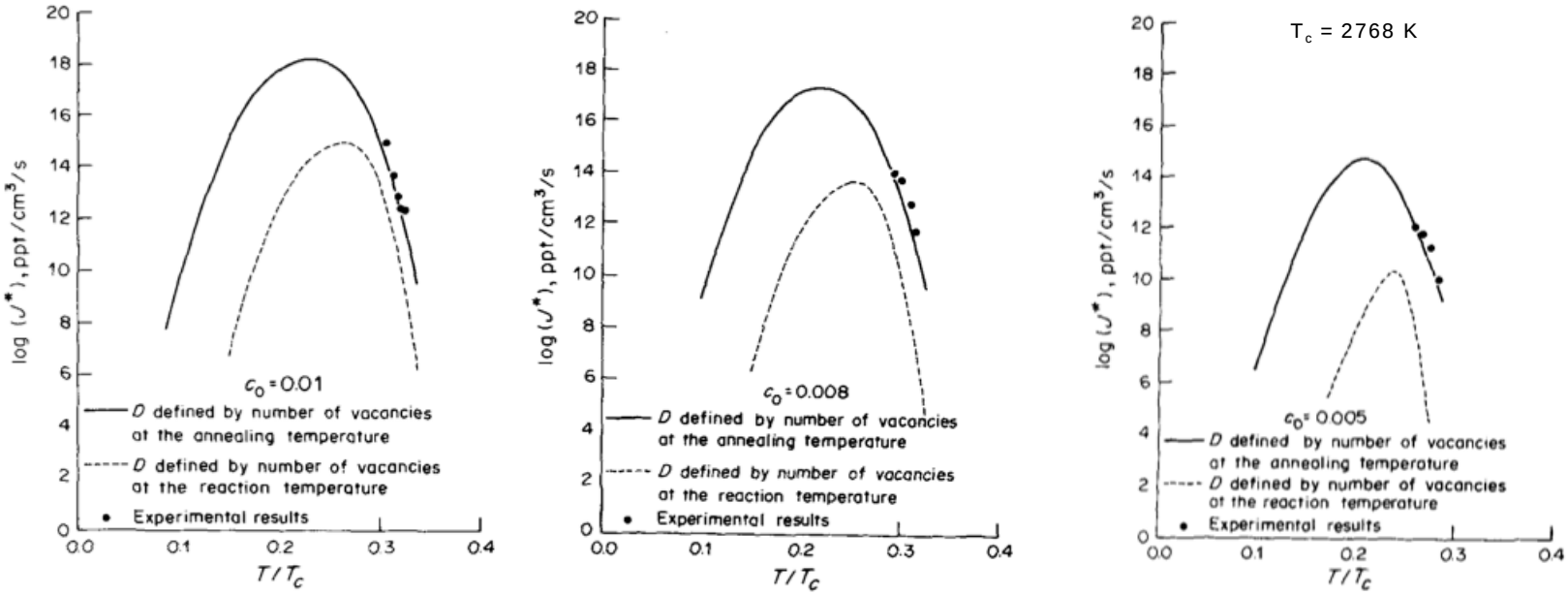

There is reasonably good agreement with theory assuming diffusion of Co at the solution-treatment temperature

F.K. LeGoues and H.I. Aaronson, Acta Metall. 32 (1984) 1855

Incubation Times

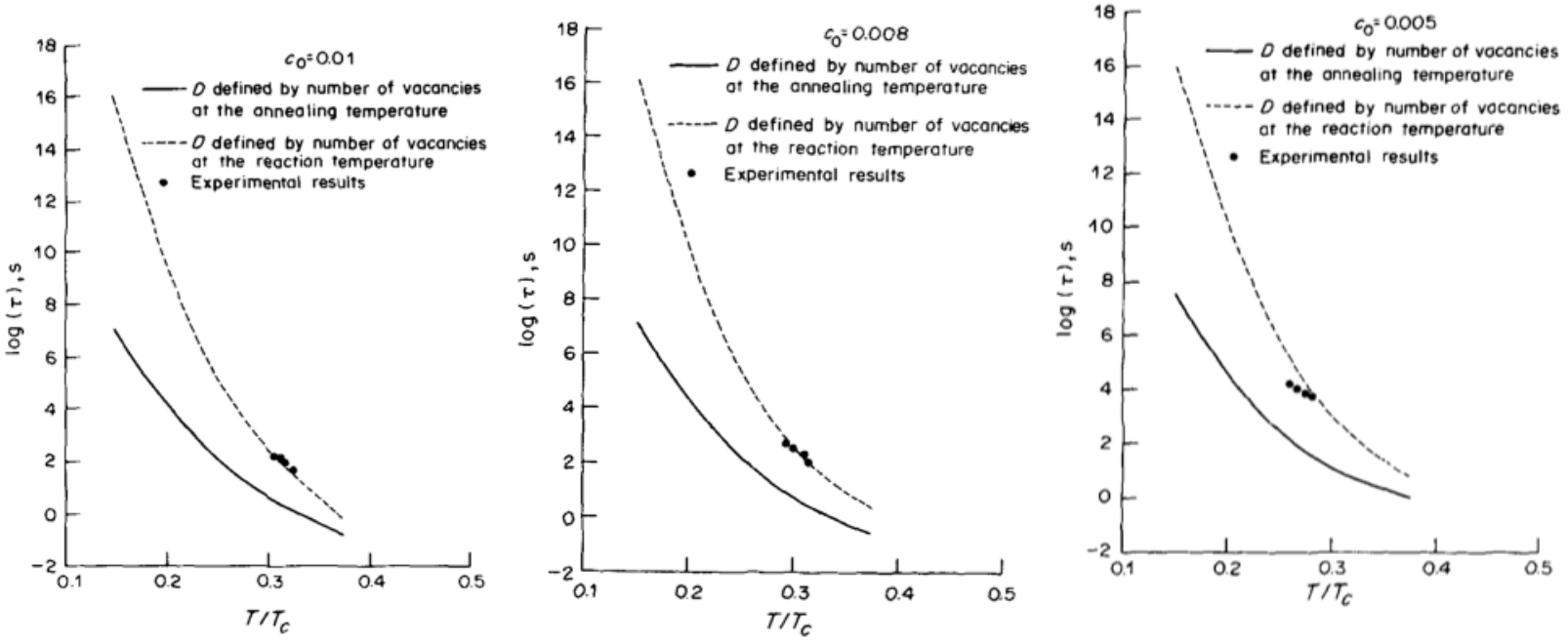

Here there is reasonably good agreement with theory assuming diffusion of Co at the aging temperature

F.K. LeGoues and H.I. Aaronson, Acta Metall. 32 (1984) 1855

Strain energy was included in the previous comparisons with theory. Here it is ignored.

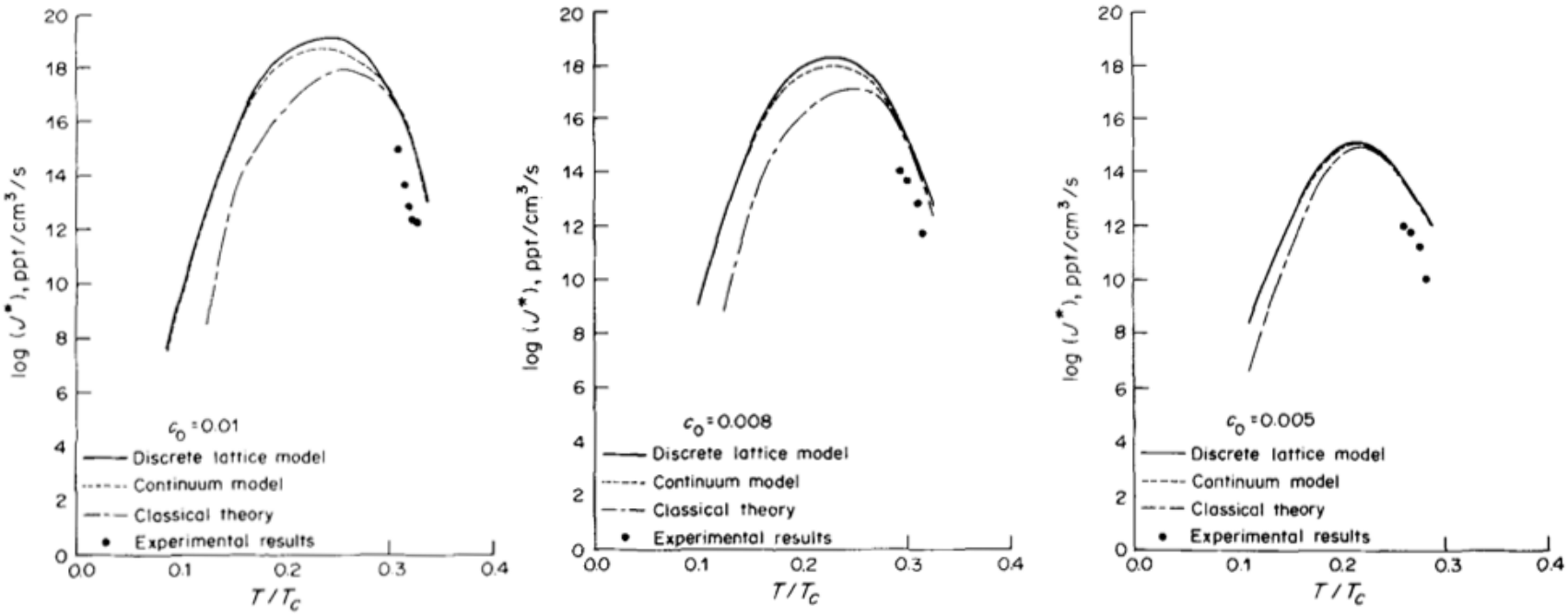

F.K. LeGoues and H.I. Aaronson, Acta Metall. 32 (1984) 1855

Crucial role of excess vacancies on nucleation in Al -5.9% Zn-2.9% Mg alloys

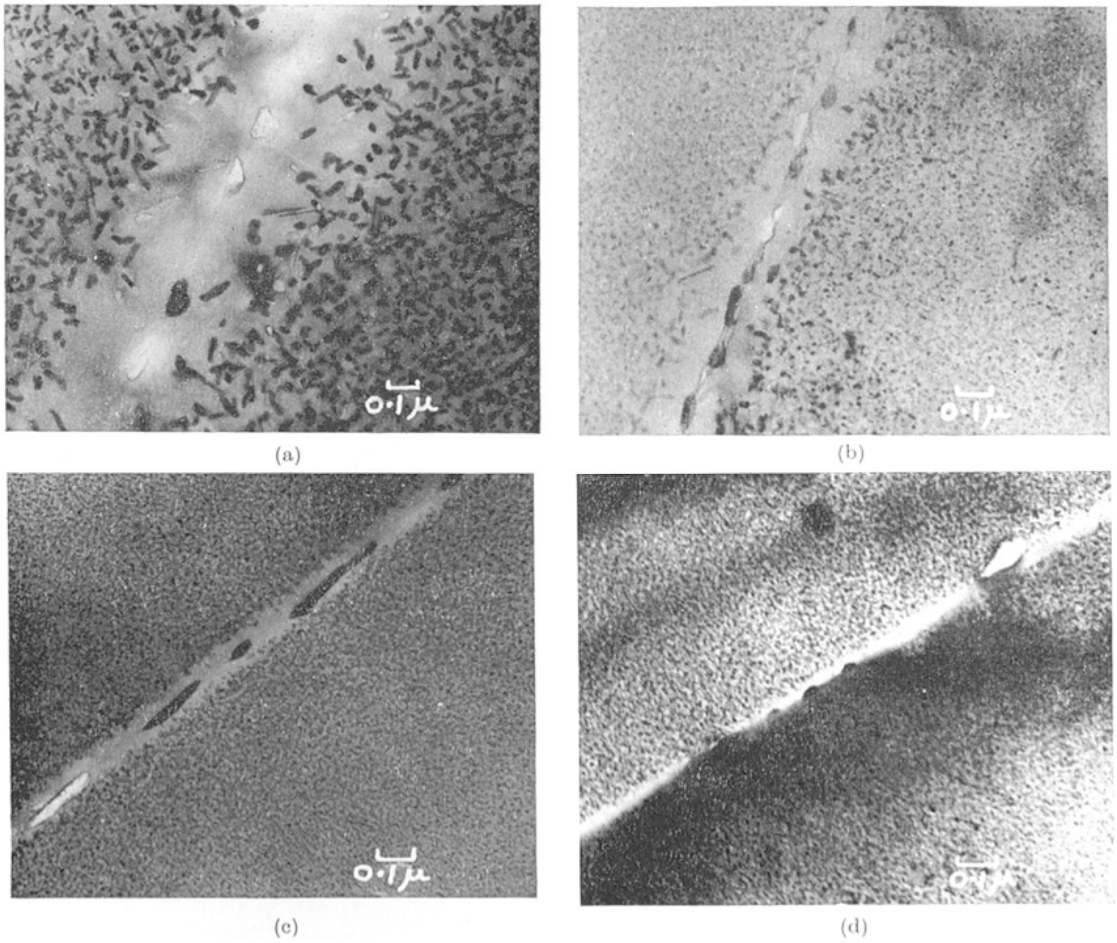

Ternary alloy solution-treated and quenched into boiling water, below the GP zone solvus and held for (a) 0.1 min; (b) 1 min; (c) 15 min; (d) 60 min

The alloy is then aged for 3 hr at 180 °C, ABOVE the GP zone solvus, but where η' is stable, producing these microstructures

GP zones coarsen at 100 °C, aided by quenched-in vacancies, and serve as nuclei for η' at 180 °C. Depletion of excess vacancies at the GB is responsible for the width of the PFZ

G.W. Lorimer and R.B. Nicholson, Acta Metall. 14 (1966) 1009

Despite a heroic effort by LeGoues and Aaronson to test the classical theory, uncertainty remains. Depending on how you look at the results, the disagreement is as much as several orders of magnitude. The role of excess vacancies in the evolution of precipitate microstructures in Al alloys is crucial.

Can we possibly do better in testing the nucleation of precipitates in Ni-Al alloys, avoiding the problems that plague these studies in other alloys?

I think so!

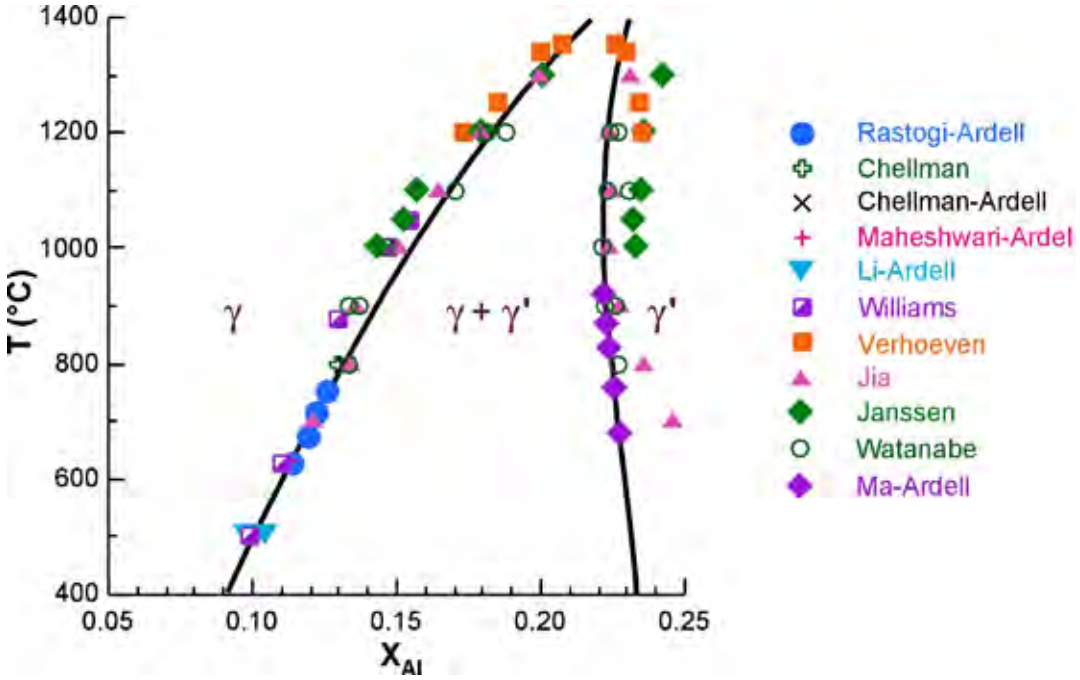

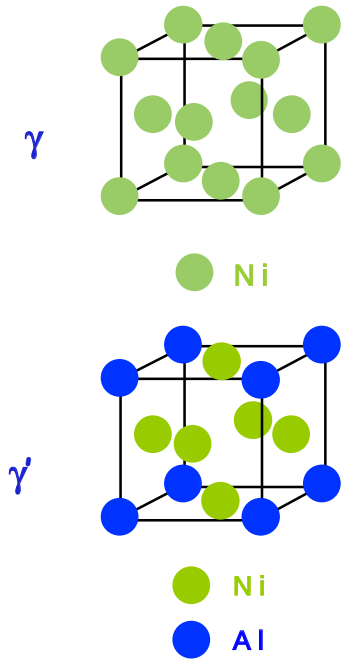

Nearly all the data in the world on the Ni-Ni_3Al phase diagram

How do the kinetics of precipitation of γ in γ' compare with those of γ' in γ?

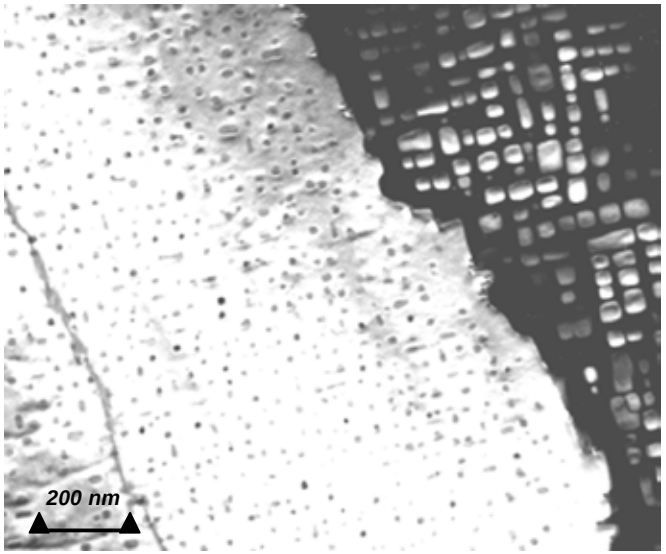

Precipitation observed in a dendritic region of an alloy containing 22.25 at.% Al. The specimen was aged for 48 h at 700 °C. The kinetics are much faster in normal alloys. One contributing factor is much slower diffusion in the ordered Ni_3Al matrix in the inverse alloy. Other factors could also be important (the free energy functions for example).

Jaykumar Joshi, 2000

INVERSE ALLOYS

Ni_3Al is the matrix phase, Ni-Al is the precipitate phase

Typical aging experiment for an "inverse" Ni-Al alloy

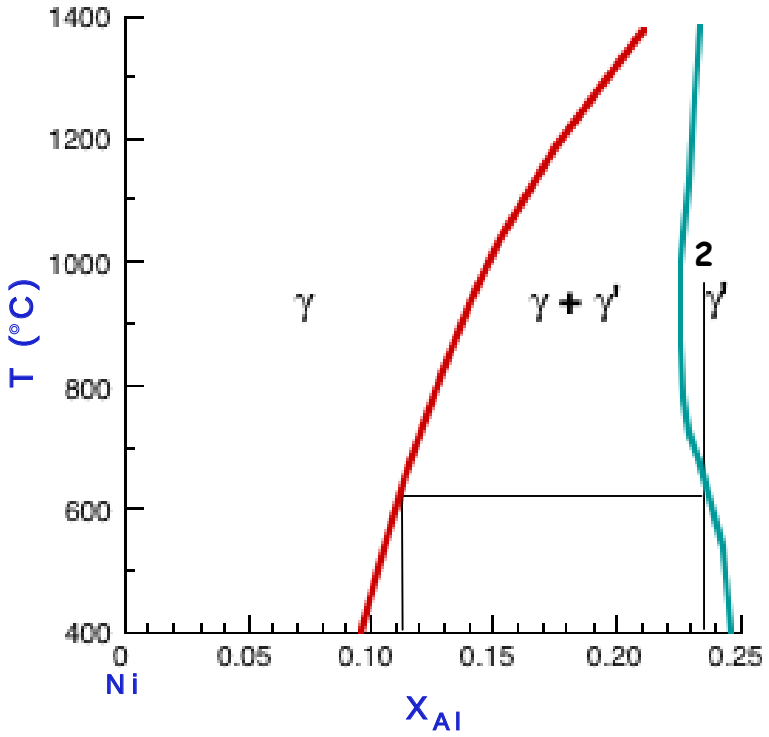

Results on coarsening of γ precipitates in "inverse" Ni-Al alloys

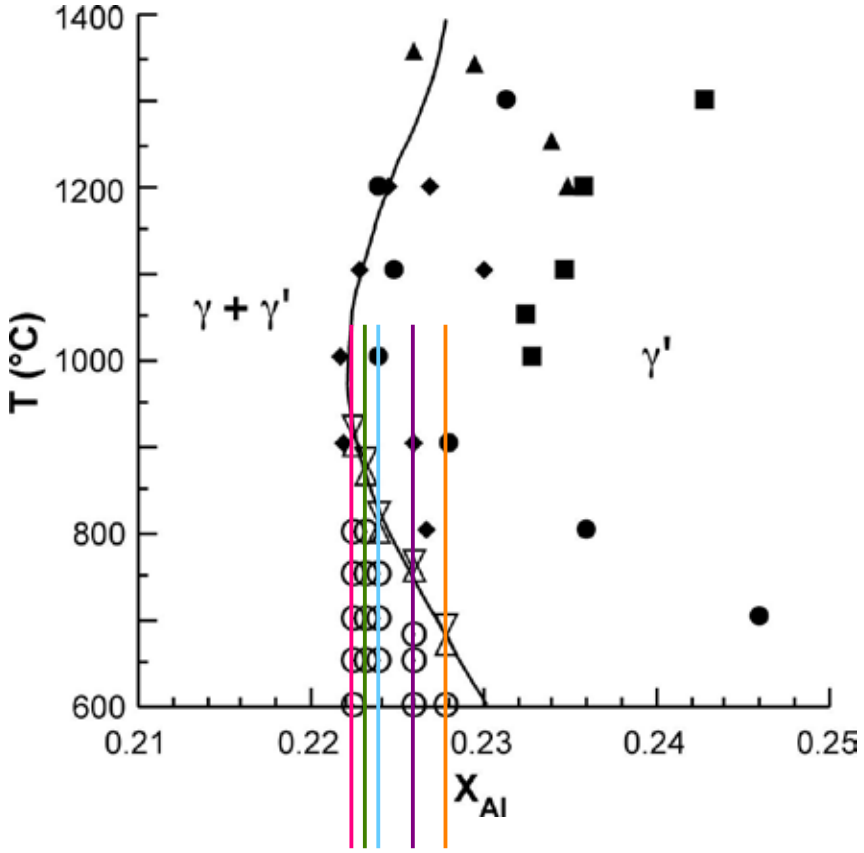

Y. Ma and A.J. Ardell, Zeit. für Metallkunde 94 (2003) 972.

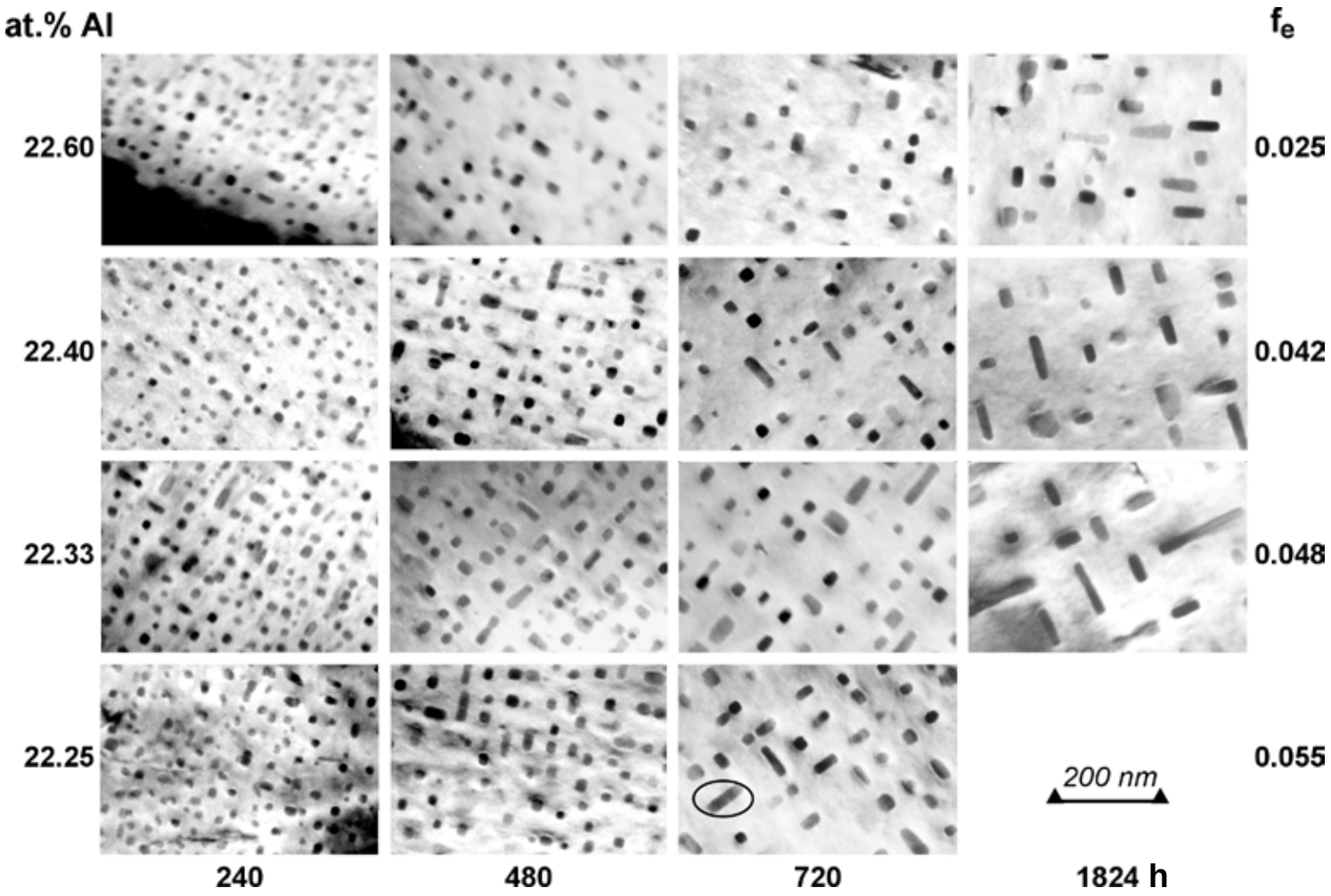

Y. Ma and A.J. Ardell, Acta Mater 55 (2007) 4419

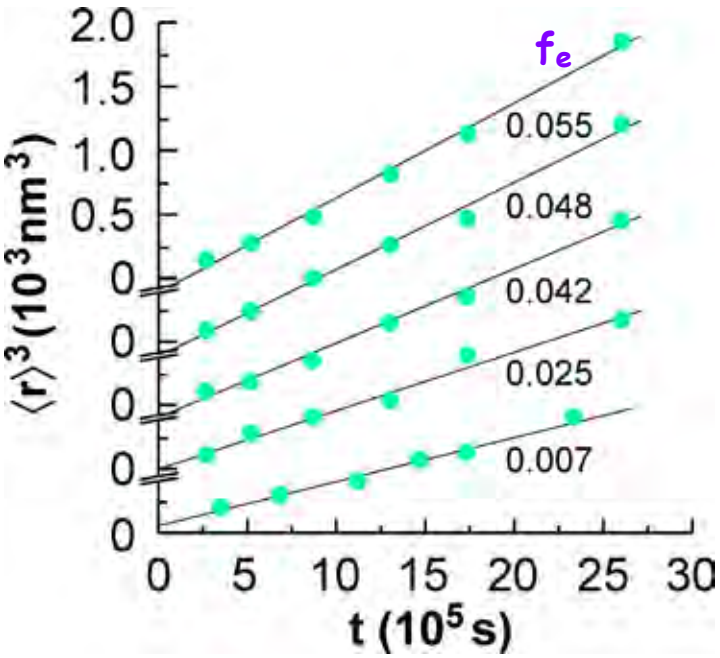

Data on the kinetics of coarsening at 650 °C. The slopes of the curves provide values of $k(f_e)$, which clearly increases with increasing f_e.

Y. Ma and A.J. Ardell, Scripta Mater. 52 (2005) 1335

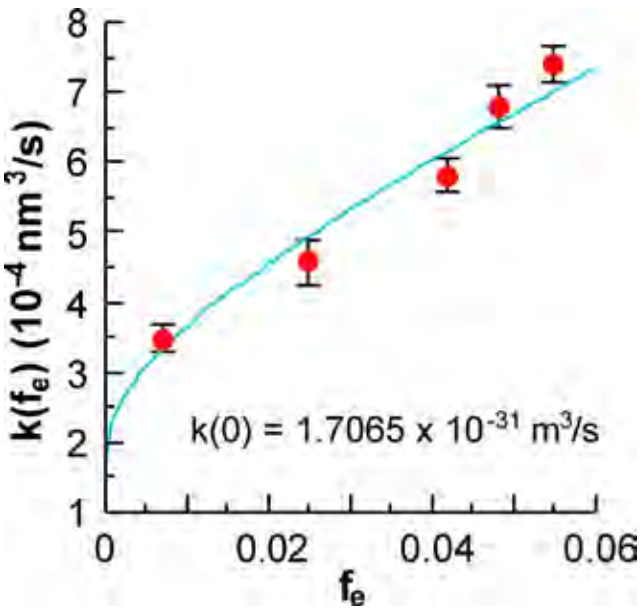

$$k_{(0)} = \frac{8\tilde{D}\, v_{Al}\, \sigma}{9\, G''_{m\gamma}\, \Delta X_e^2}$$

The data on $k(f_e)$ for the 5 inverse alloys aged at 650 °C were fit to the MLSW theory, yielding $k(0) = 1.7065 \pm 0.0917 \times 10^{-31}$ m^{-3}/s. As can be seen, the agreement between the MLSW theory and experiment is quite good.

Y. Ma and A.J. Ardell, Scripta Mater. 52 (2005) 1335

To calculate $\tilde{D}$ we need to know G''_m. For this we used the thermodynamic model of T. Ikeda et al.

$$G''_{m\gamma'} = \frac{4RT}{X_{Al}\left(1 - X_{Al}\right)}\Phi$$

$$\Phi = X_{Al}X_{Ni}\left\{24\frac{E}{RT} + \frac{X_{Al}X_{Ni} - \frac{3S^2}{16} - \frac{S}{2}\left(X_{Ni} - X_{Al} - \frac{S}{2}\right)\left(\frac{3}{8}\frac{\partial S}{\partial X_{Al}} - 1\right)}{\left(X_{Ni} - \frac{3S}{4}\right)\left(X_{Al} - \frac{S}{4}\right)\left(X_{Ni} + \frac{S}{4}\right)\left(X_{Al} + \frac{3S}{4}\right)}\right\}$$

$$\frac{\left(X_{Ni} - \frac{3S}{4}\right)\left(X_{Al} - \frac{S}{4}\right)}{\left(X_{Ni} + \frac{S}{4}\right)\left(X_{Al} + \frac{3S}{4}\right)} = \exp\left(-8\frac{ES}{RT}\right)$$

$$\frac{\partial S}{\partial X_{Al}} = \frac{S\left(X_{Ni} - X_{Al} - \frac{S}{2}\right)}{X_{Al}X_{Ni} - \frac{3S^2}{16} - 8\frac{E}{RT}\left(X_{Ni} - \frac{3S}{4}\right)\left(X_{Al} - \frac{S}{4}\right)\left(X_{Ni} + \frac{S}{4}\right)\left(X_{Al} + \frac{3S}{4}\right)}$$

S is the long-range-order parameter and E is the ordering energy

T. Ikeda, H. Numakura and M. Koiwa, Acta Mater 46 (1998) pp. 6605

Chemical Diffusion Coefficients calculated from data on coarsening of γ in inverse Ni-Al alloys using σ = 8.3 mJ/m^2 + thermodynamic model of Ikeda et al. (filled symbols) & extrapolation (Y. Ma, Ph.D. thesis) of high-temperature thermodynamic data on activities of Hilpert et al. (open symbols)

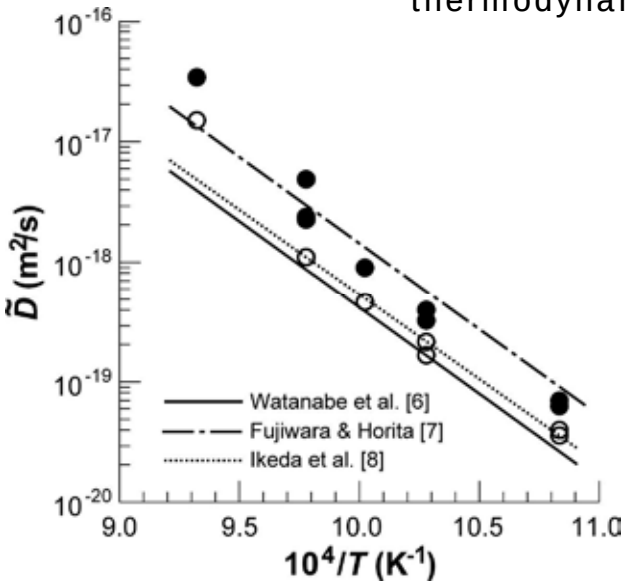

Lines---extrapolation of high-temperature data on diffusion, 23 and 24 % Al

Y. Ma and A.J. Ardell, *Mater. Sci. Engr.* **A516** (2009) 259

PSDs in inverse Ni-Al alloys

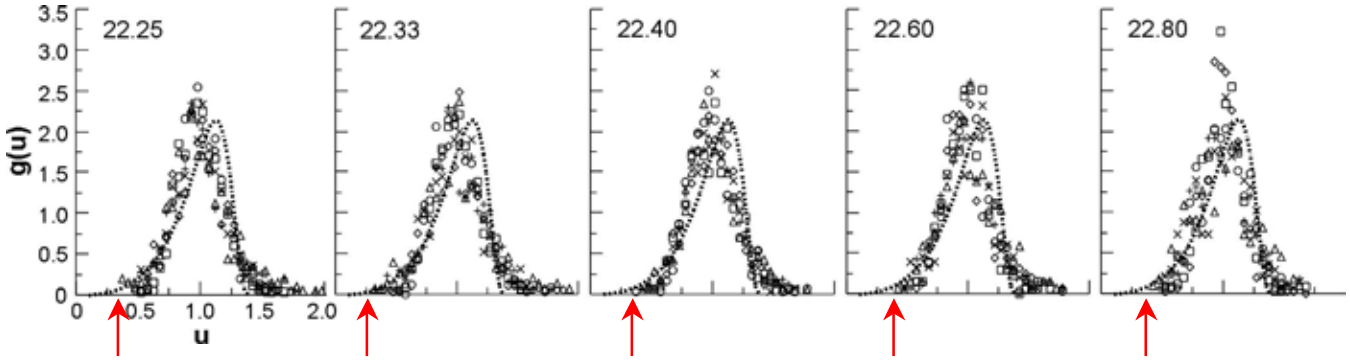

Particles with radii < 0.4 r are not observed, even though they should be visible

Estimate of minimum visible particle size, r_{min}, from Structure-Factor contrast:

$$r_{min} = \frac{|\Delta I / I|}{4\pi\left|\xi_{gp}^{-1} - \xi_{gm}^{-1}\right|}$$

$\Delta I/I$ = contrast = 0.1;

ξ_{gm} extinction distance for a {100} superlattice reflection in Ni_3Al at 100 kV = 385 nm;

ξ_{gp} extinction distance for a {100} reflection in Ni-Al at 100 kV = ∞ nm;

$r_{min} \approx 3.1$ nm

Conclusion: the missing particles in the PSDs are not missing because they are too small to be seen

Y. Ma and A.J. Ardell, Scripta Mater. 52 (2005) 1335

Reasons why experiment on nucleation in inverse alloys are likely to succeed

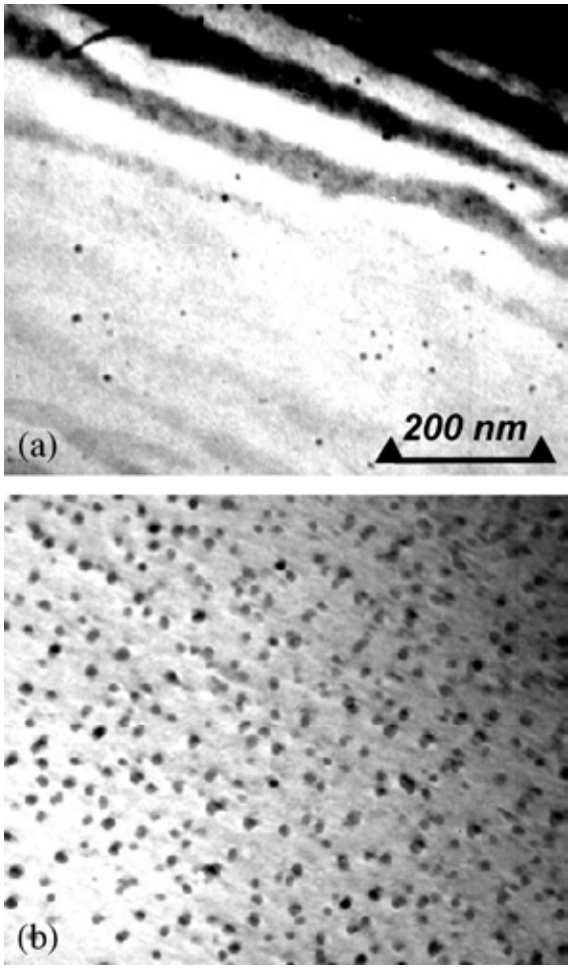

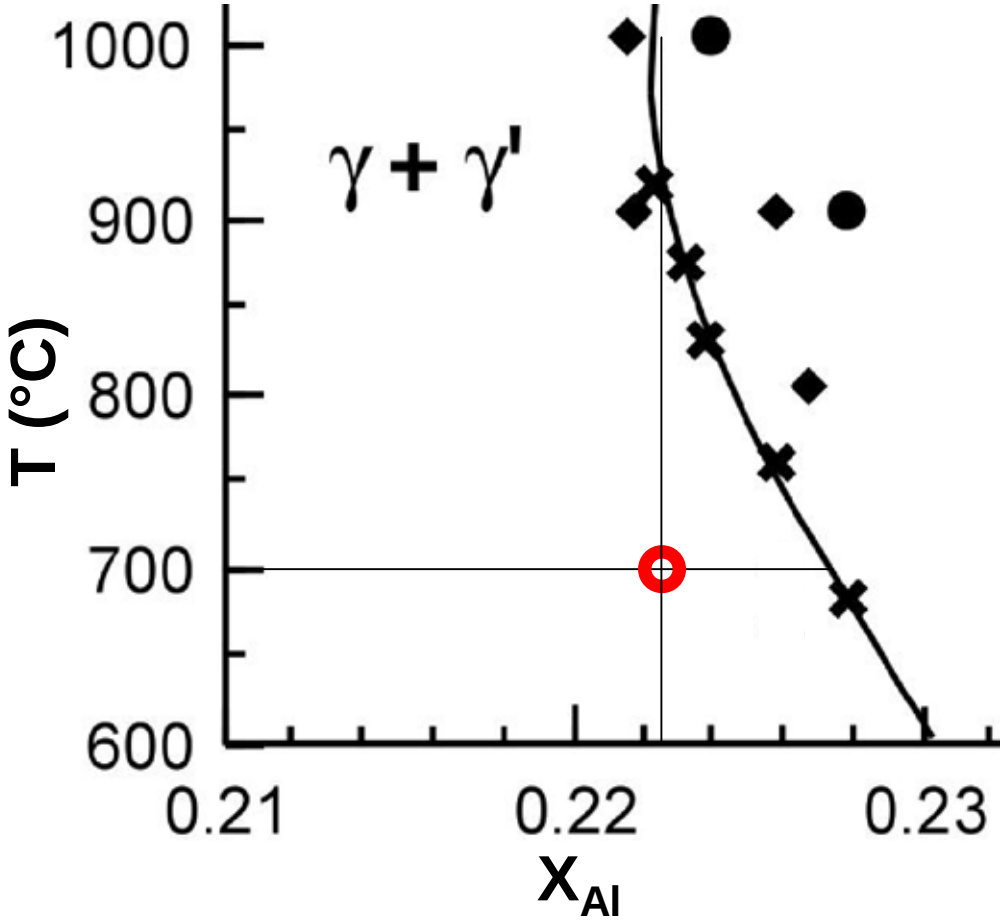

Ni-22.25 at.% Al alloy solution treated at 1000 °C, quenched and aged at 700 °C for (a) 8 h and (b) 24 h.

Even though the undercooling is large ($\Delta T > 100$ °C), nucleation is slow!

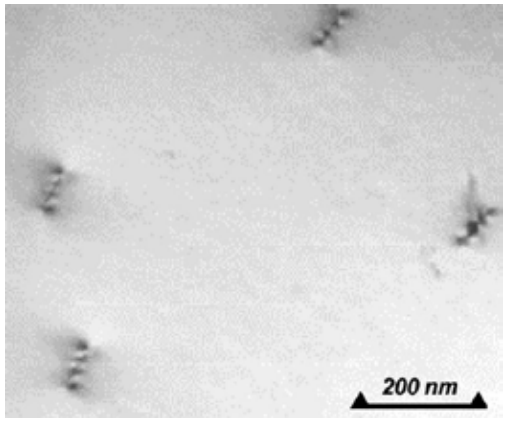

700 °C for 120 h. Only dislocations are visible in the image.

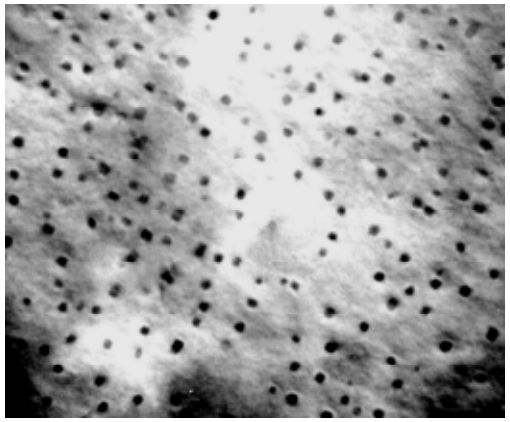

650 °C for 96 h + 730 °C for 1.5 h. Many γ precipitates visible at a small undercooling (~25 to 30 °C)

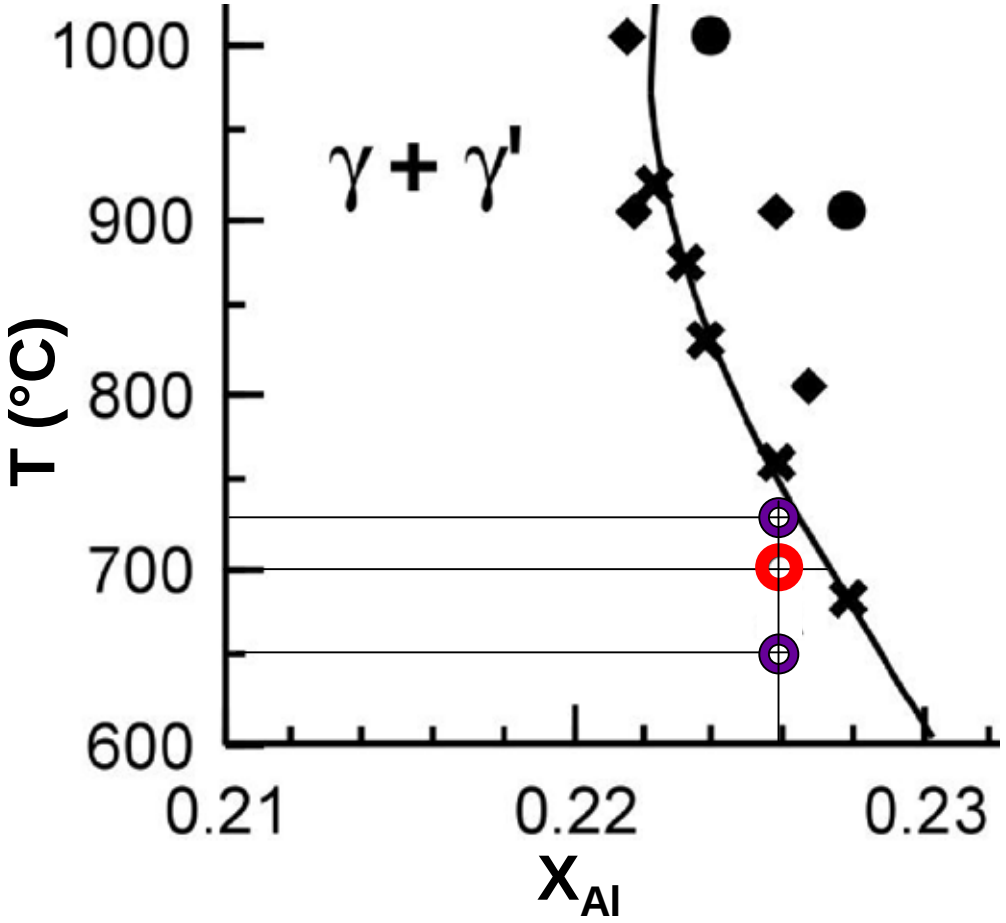

These results suggest that the incubation time for an alloy containing 22.6 % Al aged exceeds 120 h at 700 °C, but is less than 96 h at 650 °C.

These observations suggest that an investigation of nucleation kinetics in inverse Ni-Al alloys have a very good chance of being successful: f_e is small, incubation times are long, significant concentrations of excess vacancies are avoidable and except for the thermodynamics the physical parameters are reasonably well known.

Assuming that the γ' phase is an ideal solution, I obtain r* = 4.83 and 17.40 nm for the 22.25 and 22.60 % Al alloys aged at 700 °C. These are undoubtedly inaccurate, but suggest that stable nuclei should be readily visible in the TEM by either structure-factor or stain-field contrast

Is there any chance of investigating nucleation in normal Ni-Al alloys?

This was attempted years ago by Kirkwood and co-workers, Wagner & Kampmann and Xiao & Haasen without quantitative success, because nucleation of γ' is typically extremely rapid, occuring during quenching from the solution treatment temperature

It is advantageous to keep f_e small in the hope that N_v will be roughly equal to the values in the experiments of LeGoues and Aaronson ($10^{21}/m^3$). This helps minimize the issue of overlapping diffusion fields during nucleation.

Seidman and co-workers have measured N_v vs. t during the early stages of decomposition of ternary Ni-Cr-Al alloys using APT, f_e ranging from 0.10 to 0.16, N_v as large as $10^{24}/m^3$. Measured nucleation rates are 2 to almost 3 orders of magnitude slower than predicted by theory, but the physical parameters are not well constrained as they are in the binary alloy system.

An Illustration of the effect of small compositional non-uniformity on a γ' dispersion at small undercoolings

Ni-11.78 % Al aged at 630 °C for 273.5 h

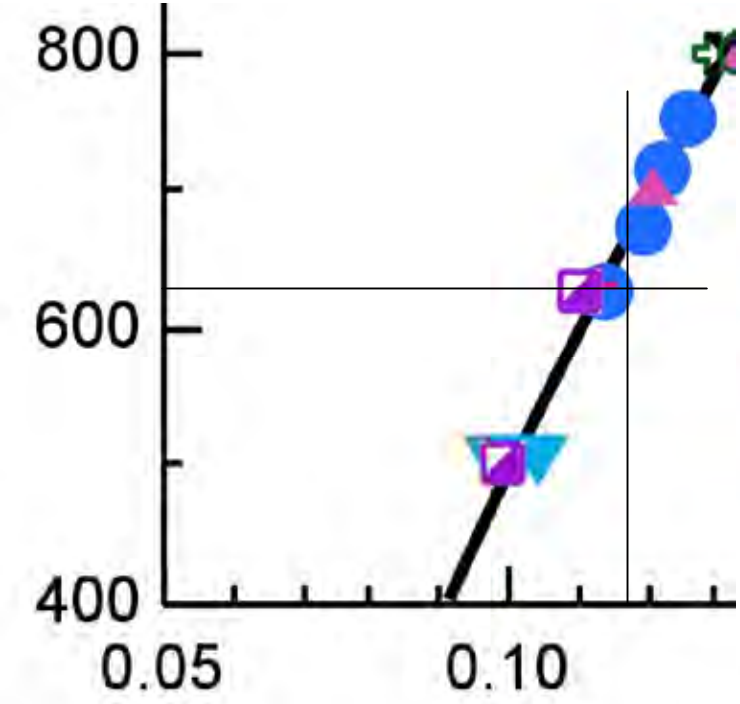

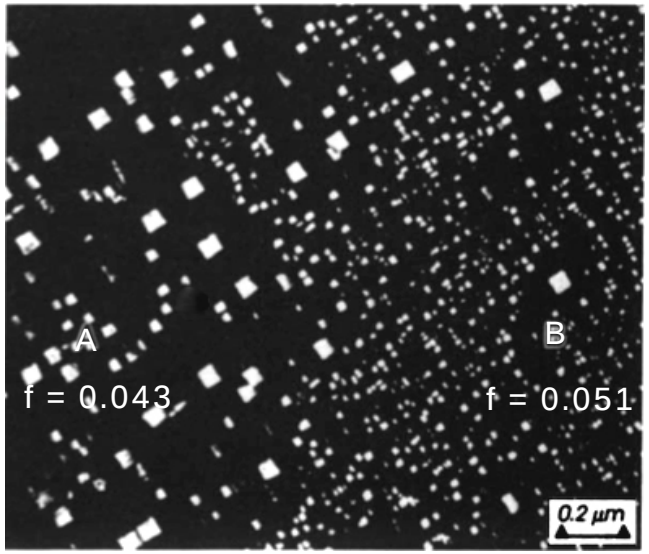

The γ' precipitates are much larger in the part of the specimen with the smaller volume fraction as a consequence of the anomalous dependence of coarsening kinetics on f: Region A is slightly depleted in Al while Region B is slightly enriched

A. Maheshwari and A.J. Ardell, *Scripta Metall. Mater.* **27** (1992) 943

Can we devise a heat treatment that eliminates compositional inhomogeneities in the starting alloy, suitable for investigations of nucleation of γ' precipitates?

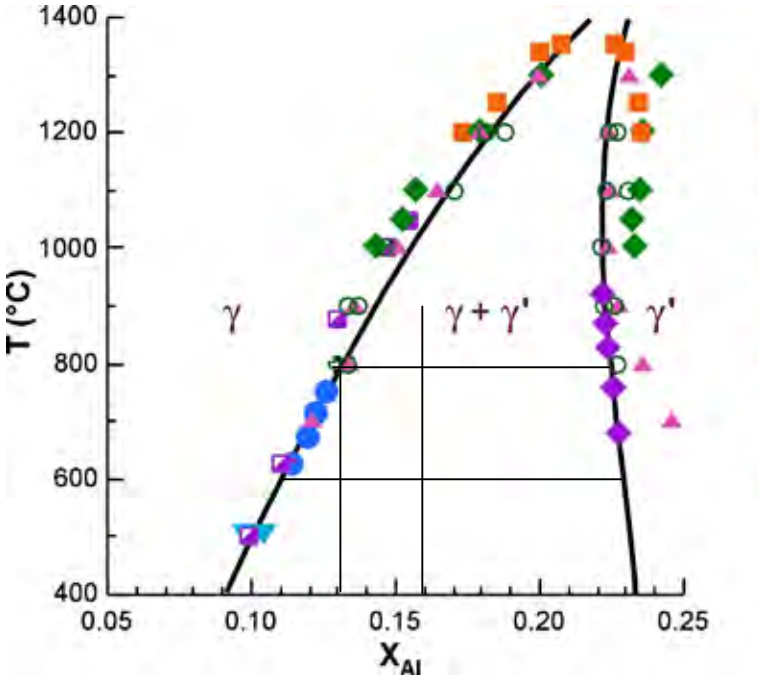

Yes...We can first age a concentrated alloy (~16% Al) at a high temperature (~800 °C), producing a homogeneous matrix of γ with a concentration of 13.16% Al

then re-age this same alloy at a lower temperature (~600 °C) to produce a relatively large volume fraction of γ' (~0.17)

This aging sequence produces a bimodal distribution of γ', not unlike the bimodal and trimodal distributions found in commercial superalloys

Ni-15.91 %Al aged first for 16.67 h at 800 °C, followed by aging at 600 °C for the times indicated

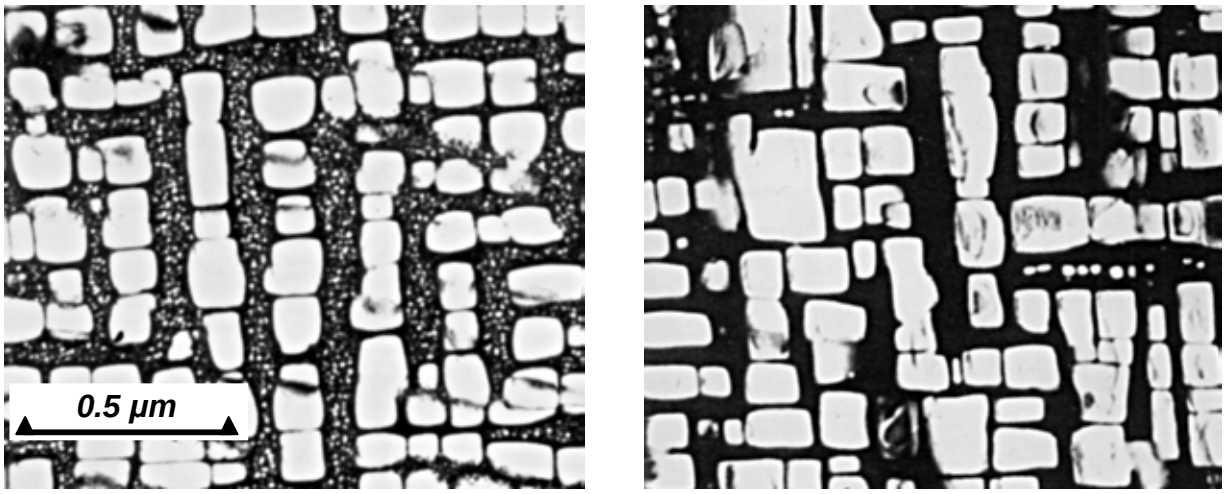

24 h 288 h

D.J. Chellman and A.J. Ardell, in *Materials Architecture*, Proc. 10th Risø International Symposium on Metallurgy and Materials Science, Roskilde, Denmark, 1989, p. 295.

The small Class II precipitates coarsen as if the large Class I precipitates were not there, until only very few of them remain. The Class I precipitates grow by consuming the Class II precipitates, not by coarsening in the conventional sense

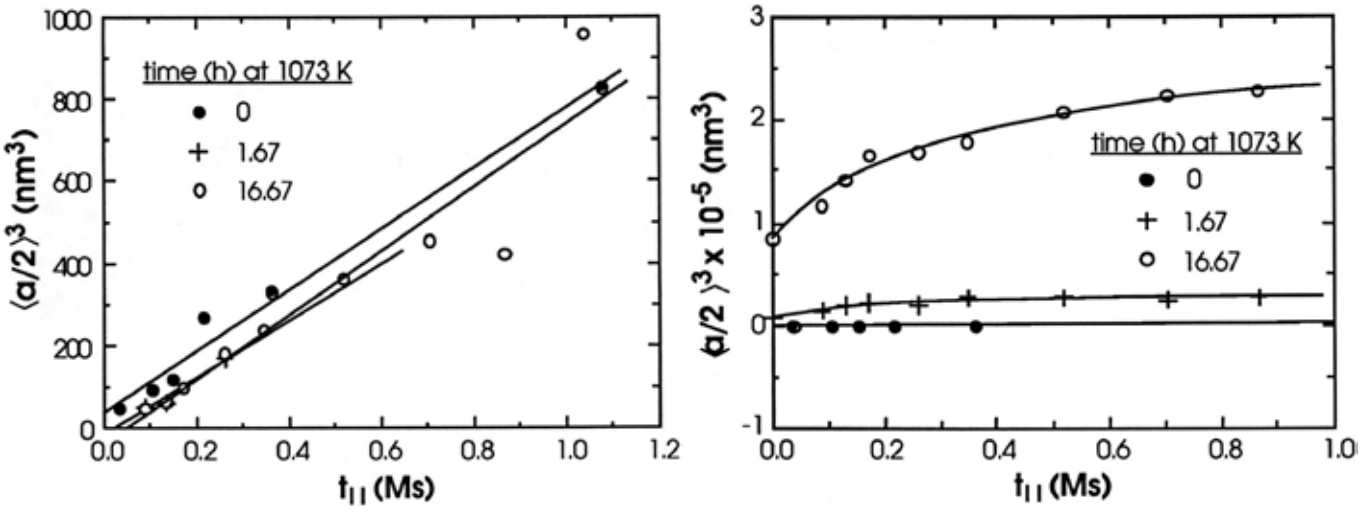

D.J. Chellman and A.J. Ardell, in *Materials Architecture*, Proc. 10th Risø International Symposium on Metallurgy and Materials Science, Roskilde, Denmark, 1989, p. 295.

We can also use the same idea to produce very small volume fractions of γ', comparable to the volume fractions in the dispersions of Co precipitates in Cu-Co alloys

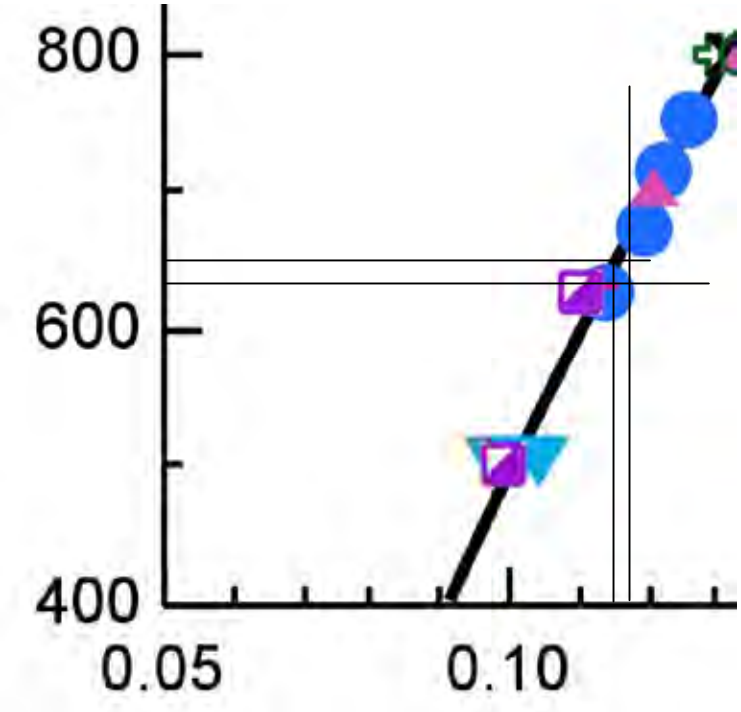

The alloy containing 11.78 % Al is now first aged at 648 ± 2 °C for 120 h.

It is then re-aged at 630 °C for various times.

The microstructure (f_e = 0.0332) after aging for 120 h is

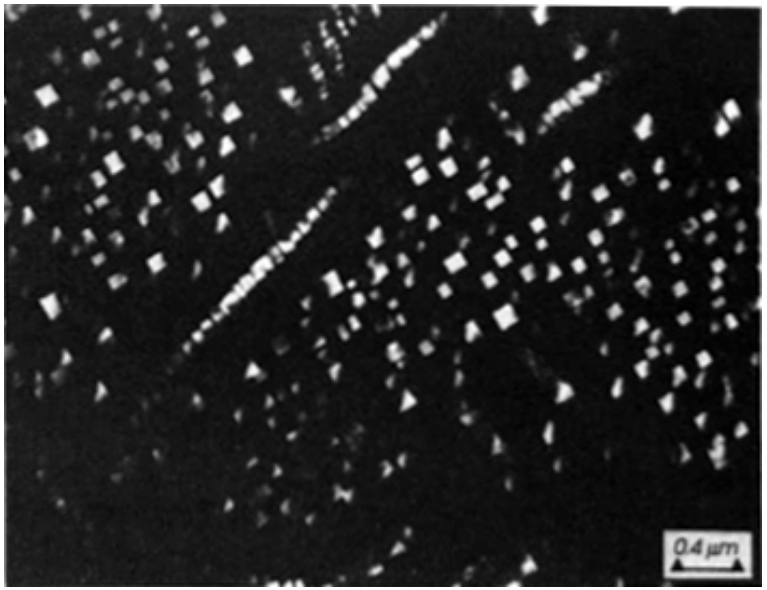

Results of experiments on coarsening at small f_e

Specimens containing 11.66, 11.70 and 11.78 % Al were PRE-AGED a few degrees below the best estimate of the solvus temperature for each alloy for 120 to 160 h, then aged for various times at 630 °C

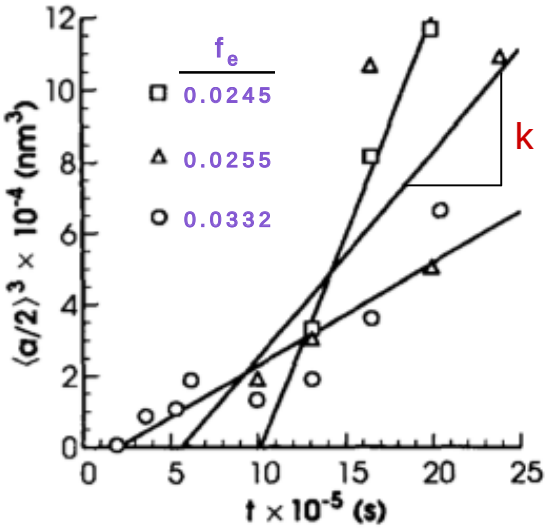

The rate constant DECREASES as f_e increases. It is exactly the opposite of the behavior in inverse alloys. In this sense the coarsening behavior is ANOMALOUS

A. Maheshwari and A.J. Ardell, Acta Metall. Mater. 40 (1992) 2661

Coarsening in pre-aged alloys is anomalous, but the success of the aging sequence in removing compositional fluctuations bodes well for possible investigations of homogeneous nucleation of γ' precipitates in Ni-Al alloys, which has proved heretofore impossible. The possibility of a successful investigation of nucleation is at least feasible.

Inverse alloys are not immune from compositional non-uniformity, as shown below, but they can also be heat-treated to minimize this problem

Different regions of 22.4 % Al alloy aged at 650 °C for 240 h plus 800 °C for 6 h

Summary

- The nucleation of γ' (Ni_3Al) precipitates in normal Ni-Al alloys and γ (Ni-Al solid-solution) precipitates in "inverse" Ni-Al alloys offer the best prospects ever of investigating homogeneous nucleation during precipitation from solid solution

  - ❖ Pre-aging treatments can be used to eliminate compositional variations in the parent matrix phase;
  - ❖ Pre-aged normal and inverse alloys can aged at small undercoolings to produce small volume fractions of precipitates, thereby minimizing the influence of excess vacancies on diffusion;
  - ❖ The important parameters needed to compare steady-state nucleation rates and incubation times, namely interfacial free energy and chemical diffusion coefficients, are known within reasonable limits for both normal and inverse alloys;
  - ❖ The Gibbs free energies of mixing of both phases is perhaps not known with the same certainty, but this is always an issue;

- Just In case data on elastic constants and lattice mismatch might be useful in studies of nucleation in Ni-Al alloys…

There are now well-constrained estimates of the following quantities as well, just in case they are needed:

The "Equilibrium" Elastic Constants for Binary Ni-Al Alloys from 800 to 1200 K

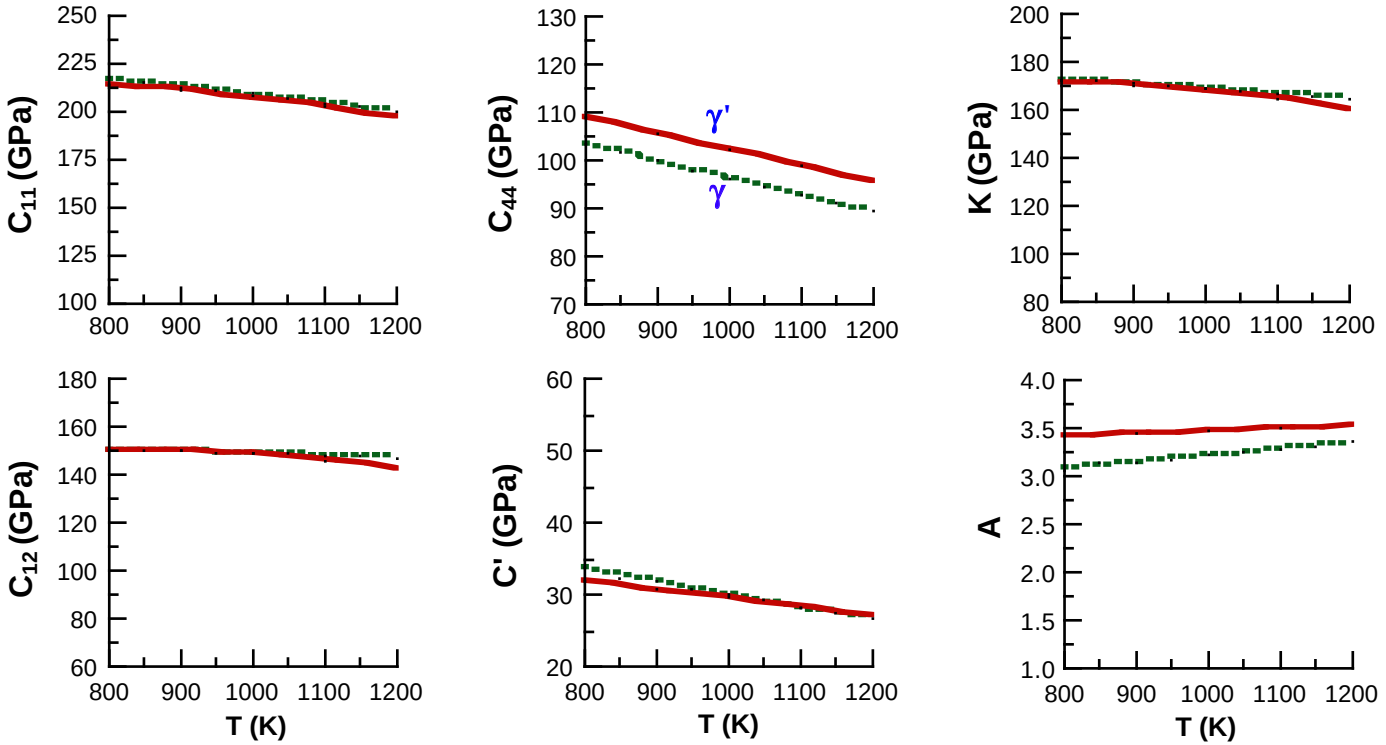

Ni-Al Data: S.V. Prikhodko, J.D. Carnes, D.G. Isaak and A.J. Ardell, *Scripta Mater.* 38 (1997) 67; S.V. Prikhodko, J. D. Carnes, D. G. Isaak, H. Yang and A. J. Ardell,, *Metall. Mater. Trans. A* 30A (1999) 2403

Temperature dependence of the equilibrium lattice mismatch in 4 binary Ni-X alloys

$$\varepsilon = \frac{a_{\gamma'} - a_{\gamma}}{a_{\gamma}}$$

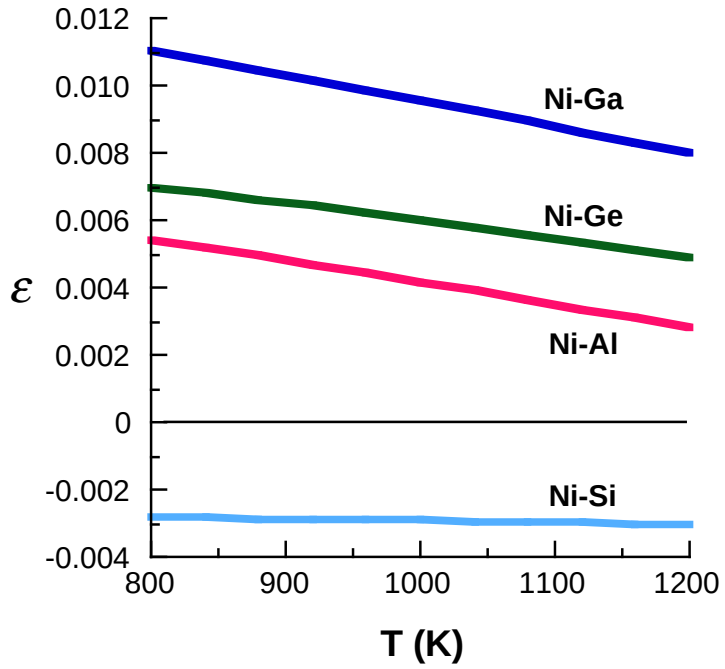

Ferromagnetic Curie temperature as a function of Al concentration in Ni-Al solid solutions

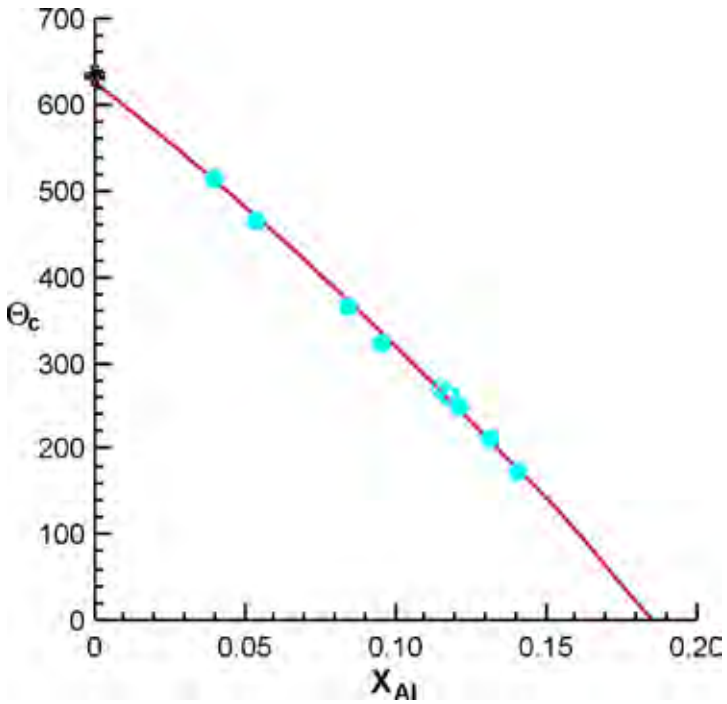

In principle, this offers the prospect of measuring the Al content of γ nuclei

A.J. Ardell, *Acta Metall.* **16** (1968) 511

- Musings about diffuse γ/γ' interfaces---might these muddy the waters?

Results of Monte Carlo computer simulation experiments on planar γ/γ' interfaces

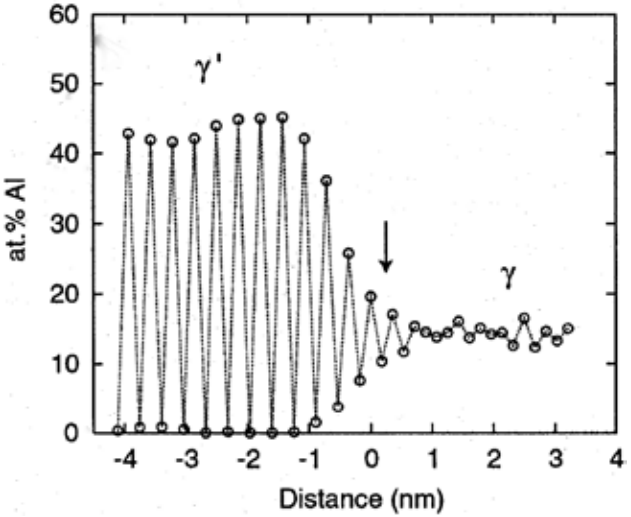

Y. Mishin, Acta Mater. 52 (2004) 1451

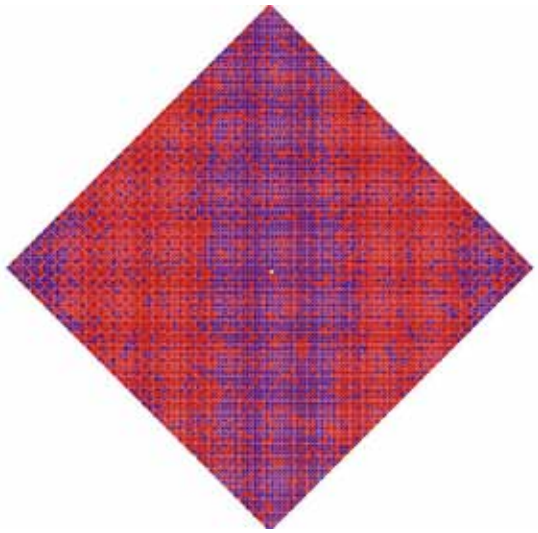

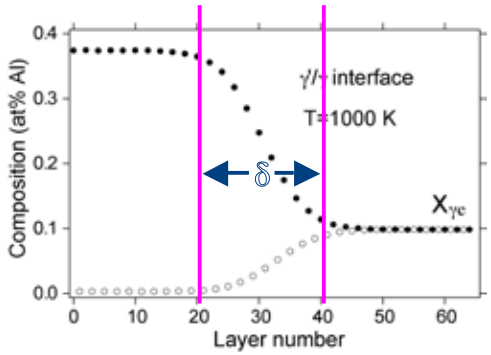

A.J. Ardell and V. Ozolins, Nature Mater. 4 (2005) 309

Composition profiles across γ/γ' interfaces in a ternary Ni-Cr-Al alloy measured using APT

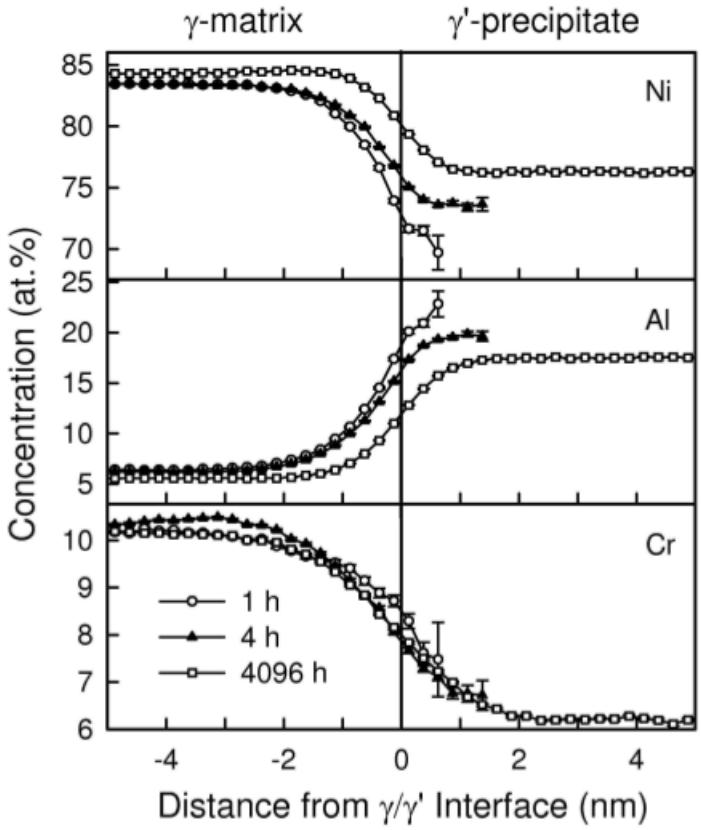

C. Booth-Morrison, Y. Zhou, R.D. Noebe and D.N. Seidman, *Philos. Mag.* (2009)

Long-range-order profile across a γ/γ′ interfaces in René 88 measured using HRTEM

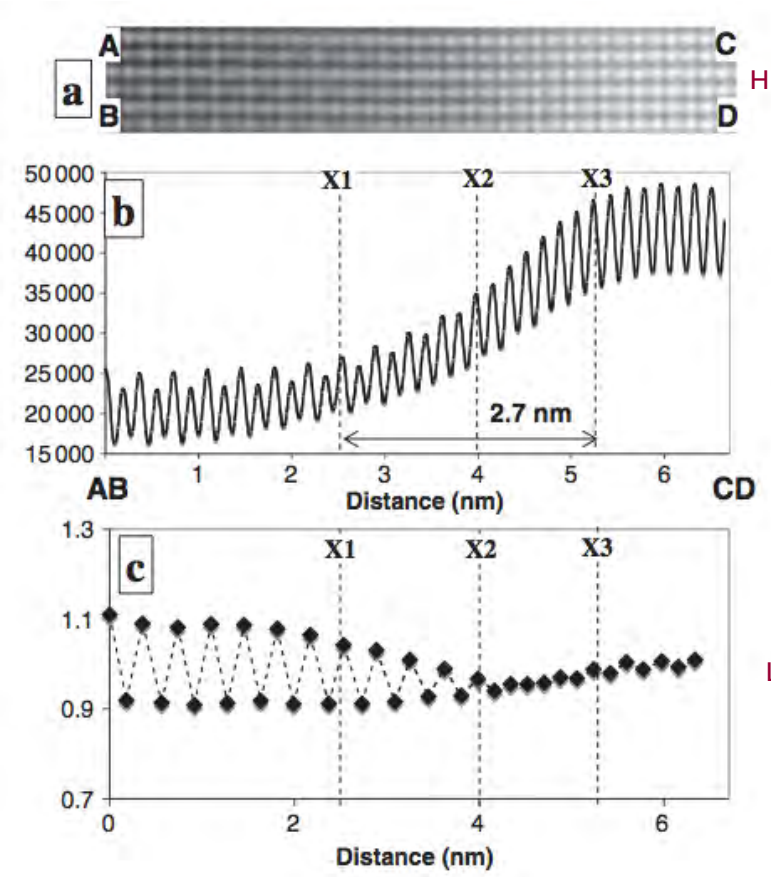

R. Srinivasan, R. Banerjee, J.Y. Hwang, G.B. Viswanathan, J. Tiley, D.M. Dimiduk and H.L. Fraser, PRL 102 (2009) 086101

γ/γ' interfaces must become sharper the smaller the particle, e.g. as the critical radius is approached. γ' particles a few unit cells in size should have sharp interfaces to be regarded as particles of a new phase

Thanks for putting up with me!

ALPHA/BETA TITANIUM ALLOYS REVISITED

Adam Pilchak, *Air Force Research Laboratory, Materials and Manufacturing Directorate, Wright Patterson Air Force Base, OH 45433, USA
adam.pilchak@wpafb.af.mil

Dipankar Banerjee, Department of Materials Engineering, Indian Institute of Science, Bangalore 5601012, India.
dbanerjee@materials.iisc.ernet.in

Jim Williams, Department of Materials Science and Engineering, The Ohio State University, Columbus, OH-43210, USA
williams.1726@osu.edu

Joint AFRL/AOARD/LLNL Workshop on Nucleation during Solid-Solid Phase Transformations in Metallic Systems: Current Understanding and Future Directions
Maui, Hawaii May 2 - 7, 2010

PHASE DIAGRAM

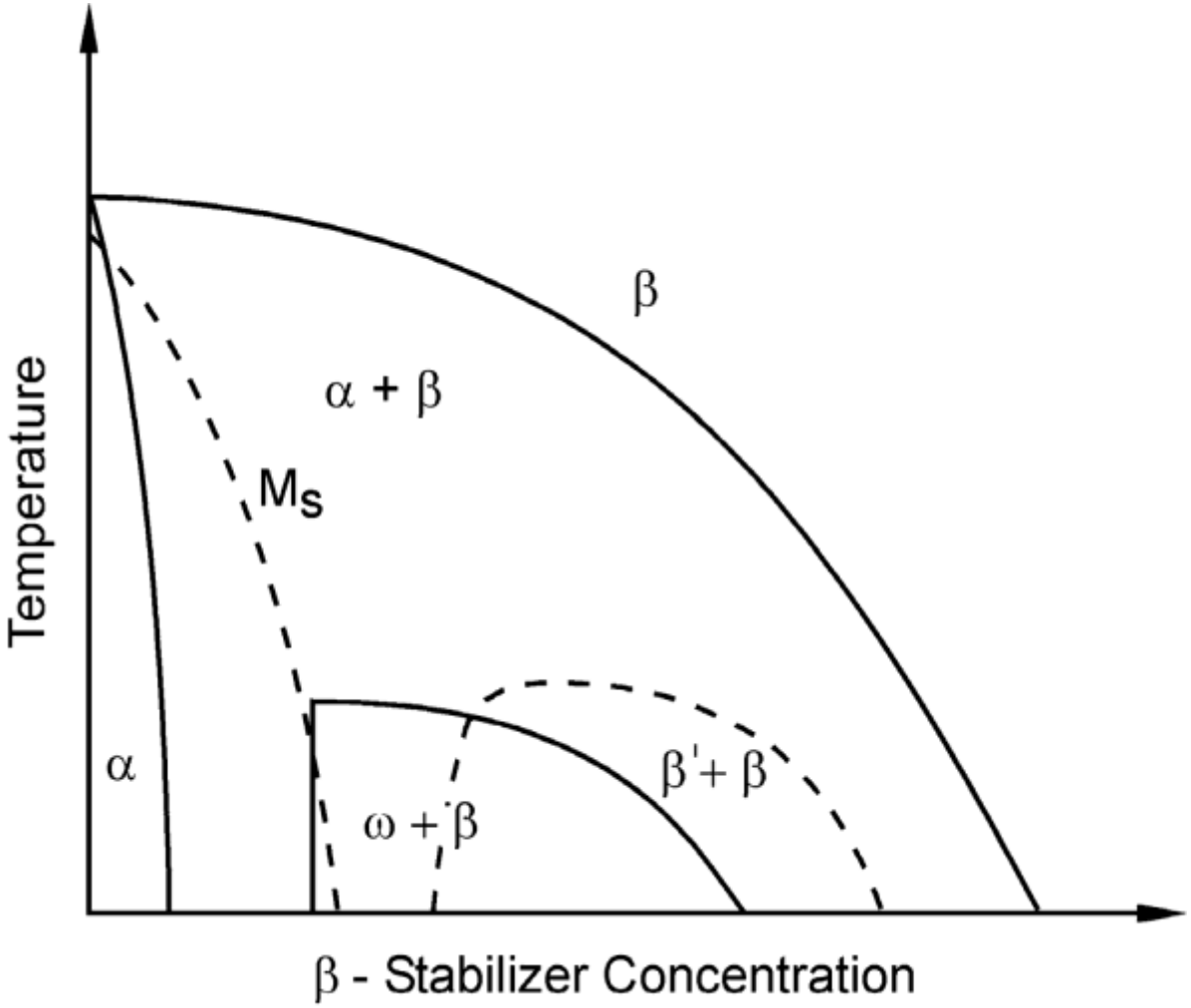

- **A simple phase diagram underlies all useable titanium alloy structure**
- **inclusion free, two phase structures at different length scales ranging from the nanometric to the micrometer scale**

STRUCTURE

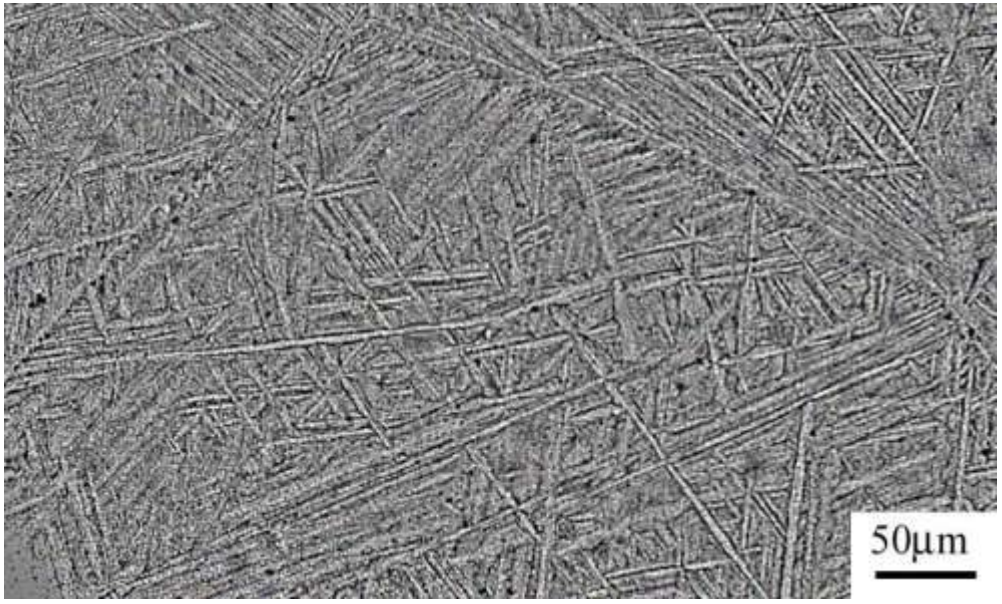

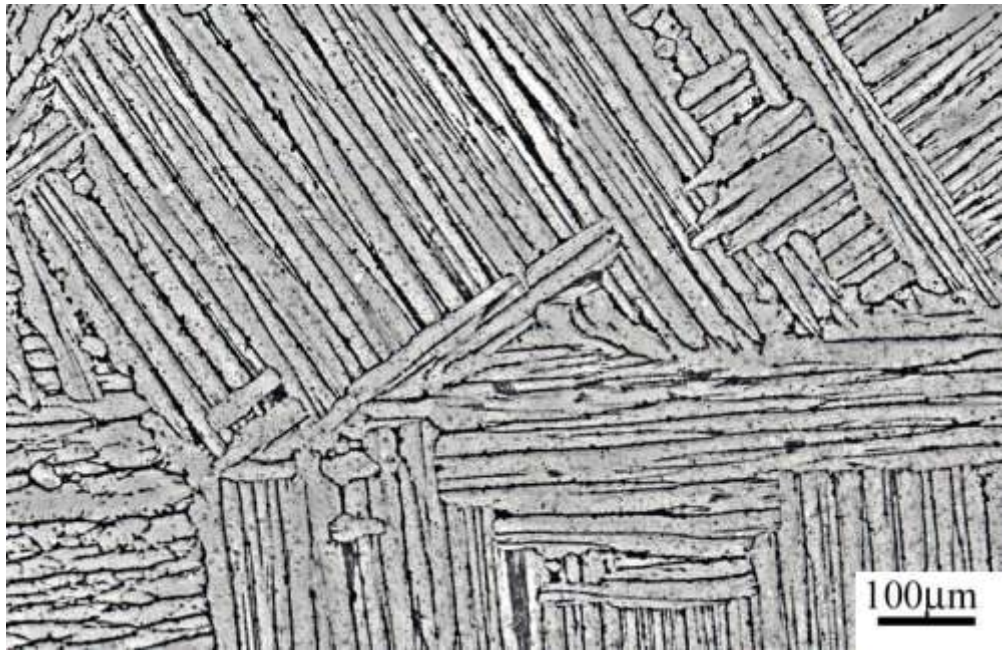

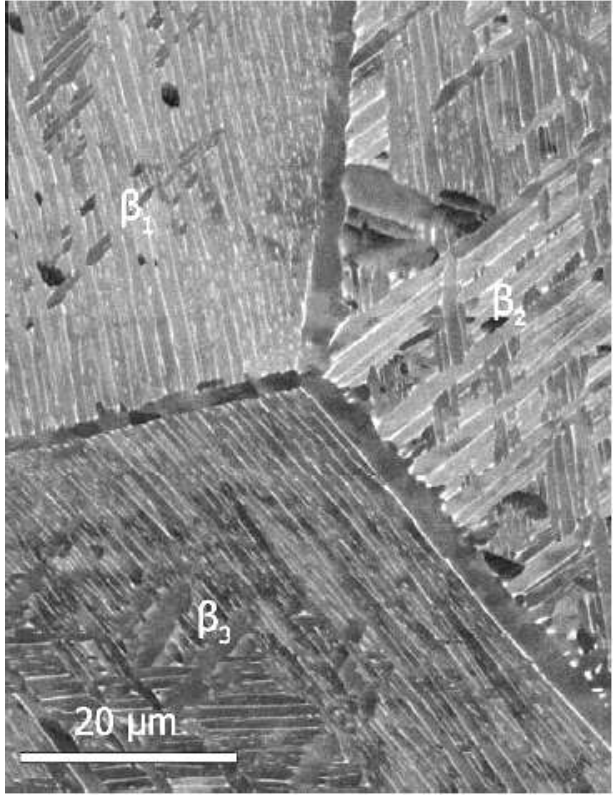

- **The starting cast/beta cooled structure is dominated by alpha morphologies determined by interface and strain energies between the two phases –the burgers relationship**

- **Grain boundary and alpha and related sideplates emanating from it can dominate the structure under some conditions**

THE BURGERS RELATIONSHIP

[0001]//[1-10] [1-210]//[111] [10-10]//[112]$_{-21-10}$

12 variants of alpha from the beta to alpha transition

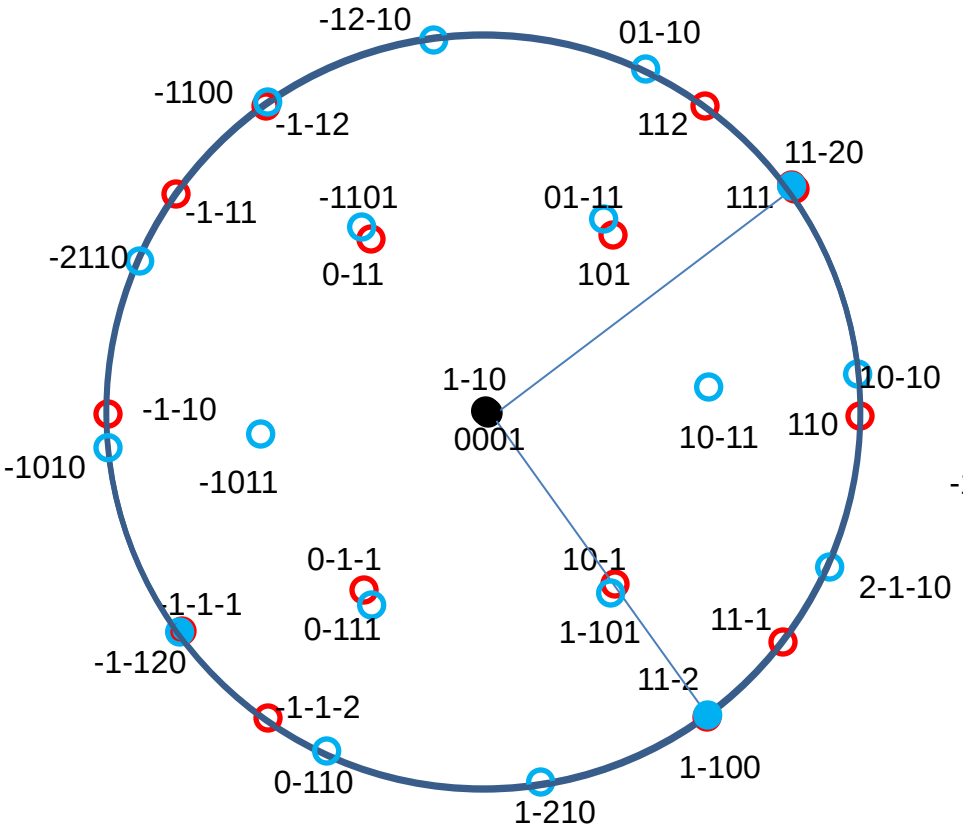

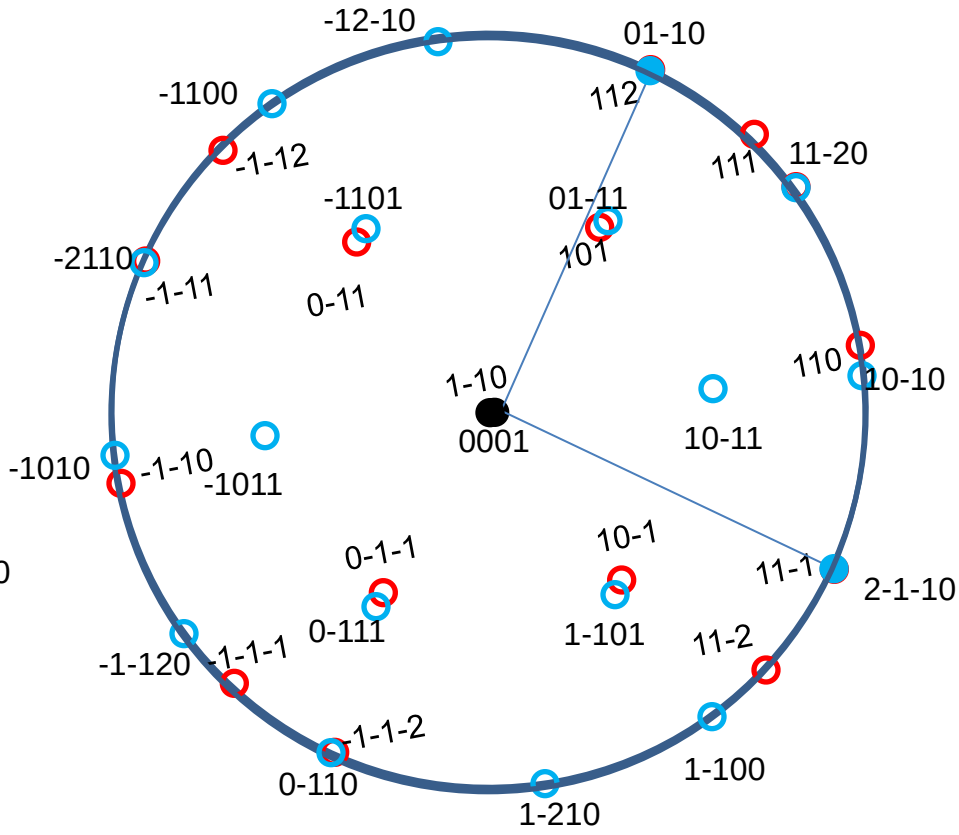

THE BURGERS RELATIONSHIP
Morphology and Interfaces

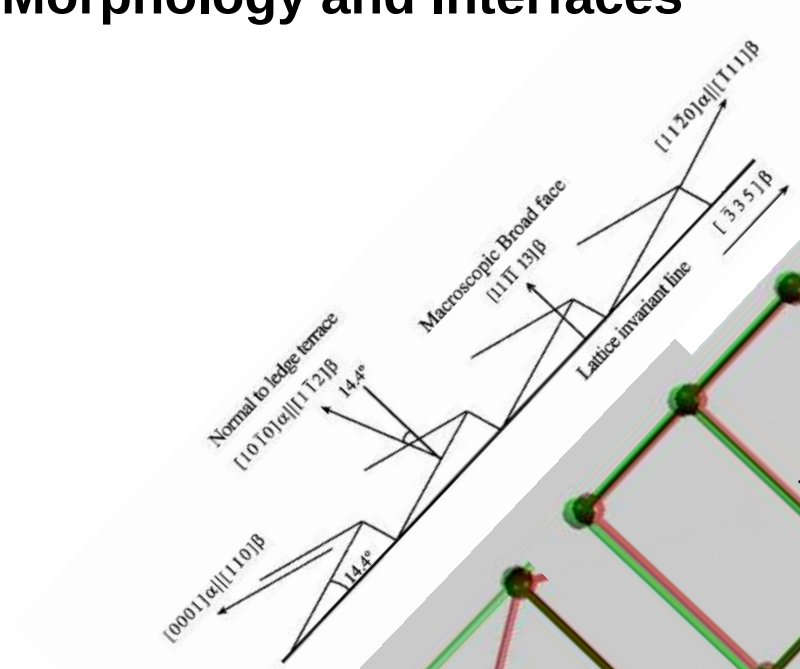

[0001] // [1-10]
-1.53%

[1-210] // [1-11]
-3.65%

[10-10] // [112]
4.84%

broad face

edge

side face

[10-10] // [112]
4.84%

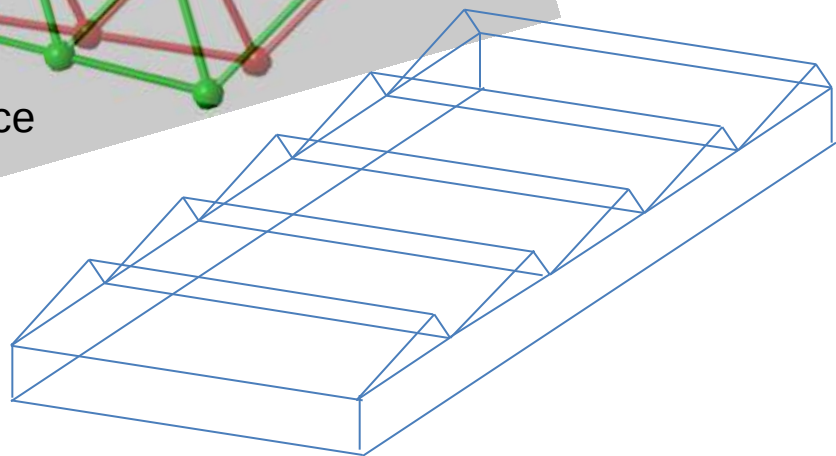

Furuhara, Howe and Aaronson, Acta Met, 1991

Furuhara, Ogawa and Maki . Phil Mag Letters, 1995

RECRYSTALLISATION AND STRUCTURE

thermomechanical processing controls distribution and morphology of the two phases

The equiaxed alpha morphology is assumed to have lost the burgers relationship with beta

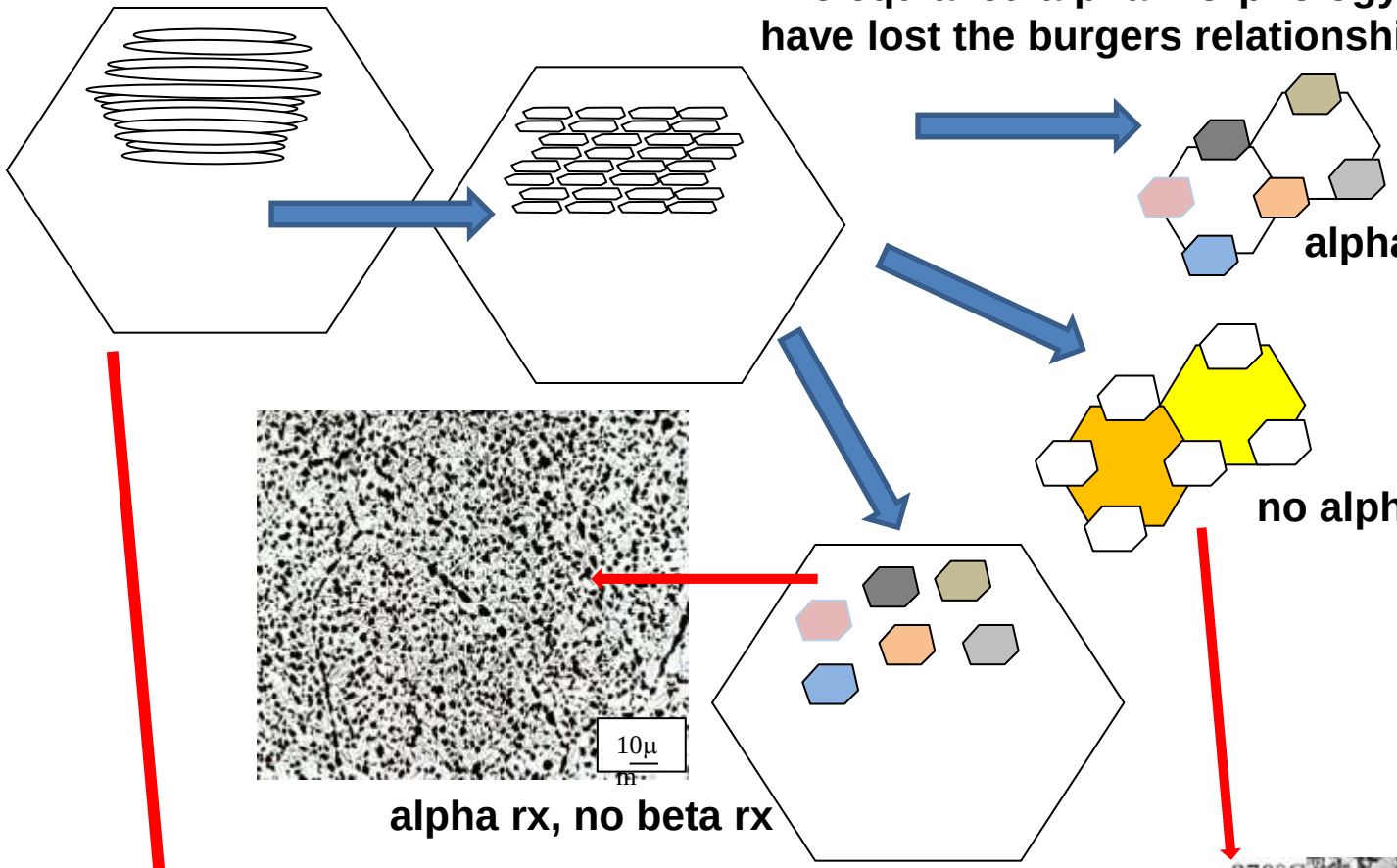

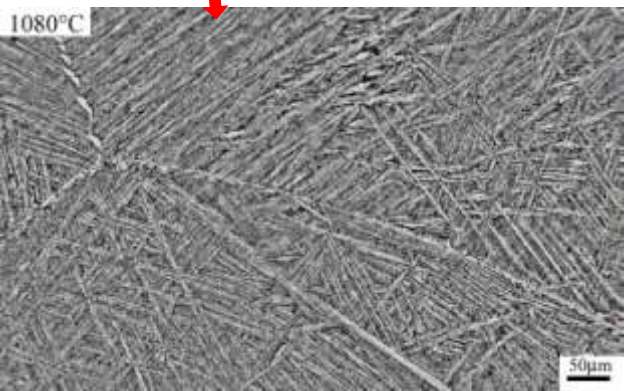

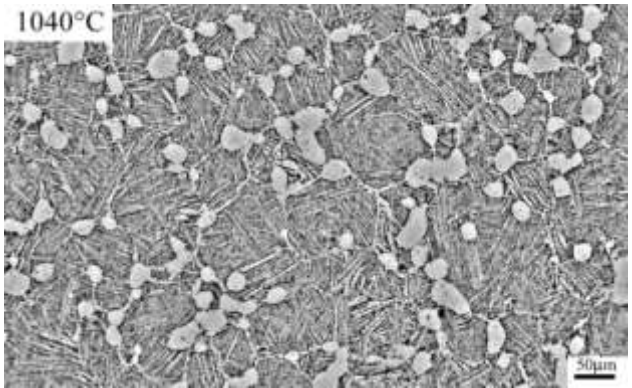

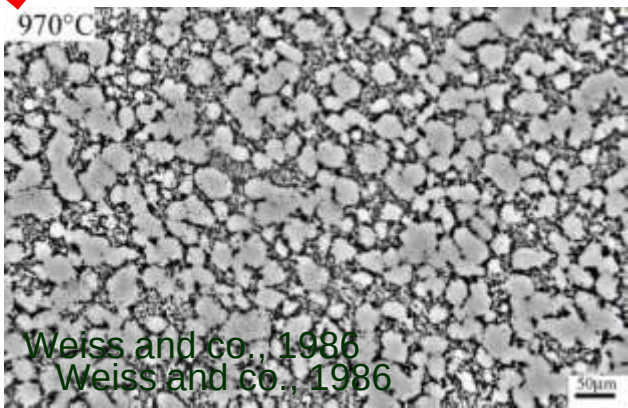

Weiss and co., 1986

Weiss and co., 1986

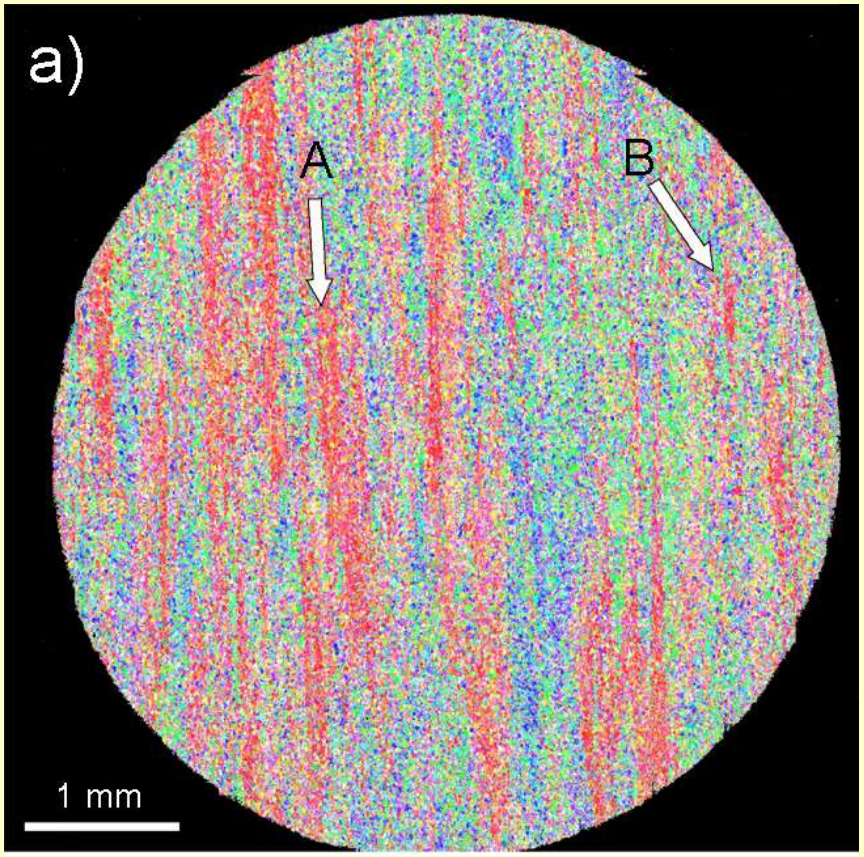

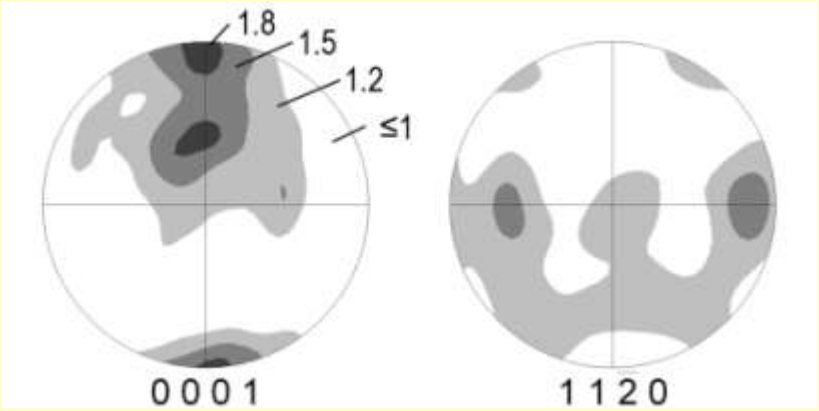

Bands of microtexture are often evident in thermomechanically processed titanium alloys

Texture of the entire cross-section of a fatigue specimen would reveal weak texture, less than 2x random.

MICROTEXTURE

DWELL FATIGUE CRACK ORIGINS

Courtesy: Amit Bhattacharjee, OSU and DMRL

OIM on layer 3 after removing 59 μm from layer 1

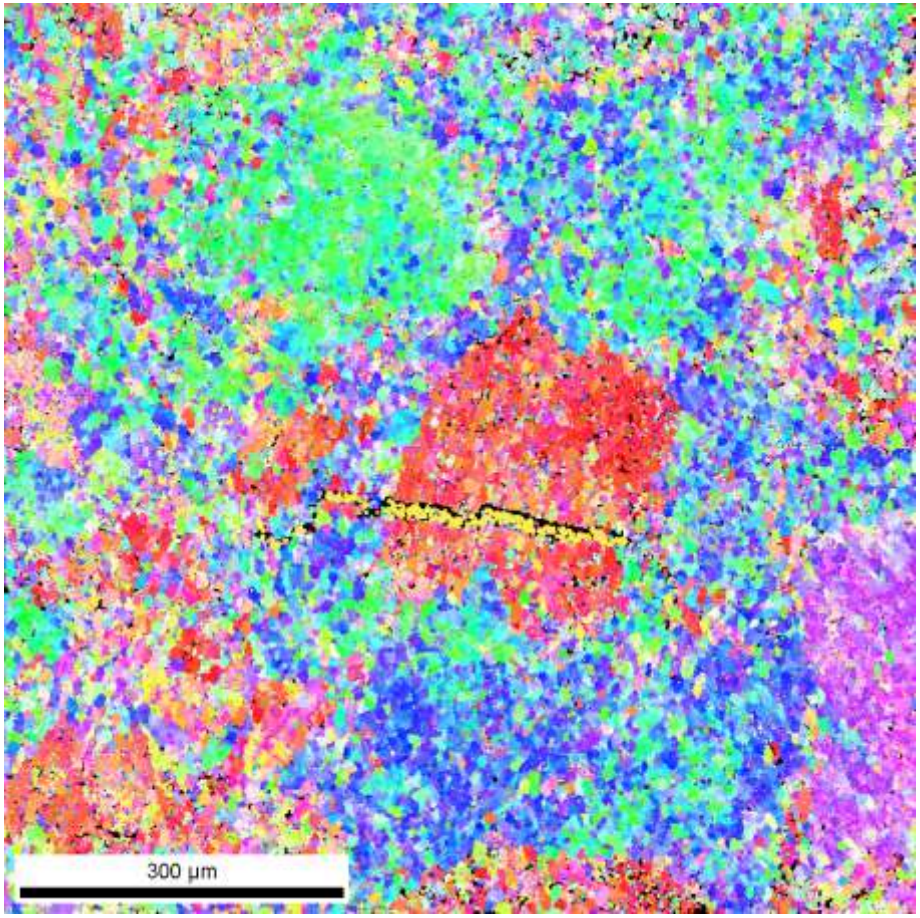

OIM on layer 2 (163 μm) from top surface- Another dwell tested specimen

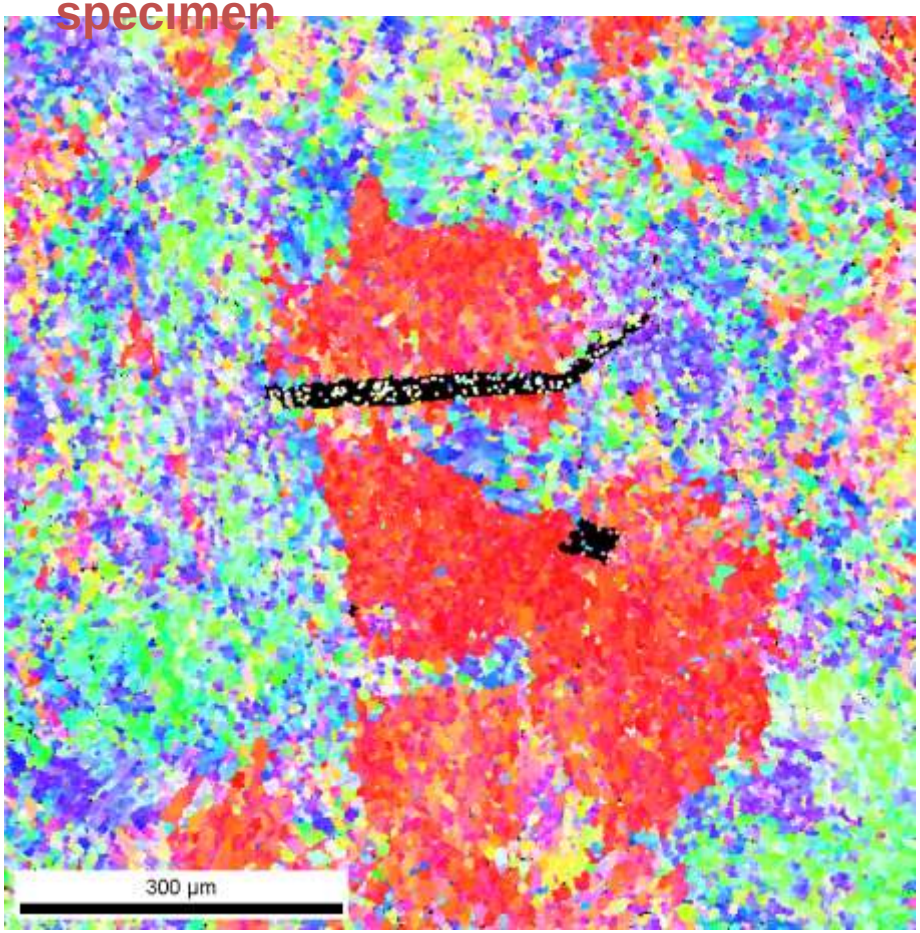

DWELL FATIGUE LIFE DEBIT IN TI-6242

At room temperature!

Courtesy: Amit Bhattacharjee, OSU and DMRL

Material	Load Ratio	σ_{max}/σ_{YS}	Dwell Time (minutes)	Plastic Strain –to-Failure (ε^{pl}_f)	Nf (Cycles to failure)	Dwell Life Debit
Ladish P1 (Low microT)	0	0.954	2 0	3.0 % 0.6 %	8803 51235	6
Ladish P1 (Low microT)	0	0.954	2 0	2.8 % 1.5 %	11946 47906	4
Ladish P2 (High microT)	0	0.955	2 0	3.8 % 2.0 %	1303 22991	18
Ladish P2 (High microT)	0	0.915	2 0	2.3 % 1.0 %	3074 45843	15
Ladish P3 (β forged)	0	0.957	2 0	3.2 % 0.5%	10846 30020	3
Ladish P3 (β forged)	0	0.957	2 0			
Retired Impeller (α/β forged)	0	0.933	2 0			
Retired Impeller (α/β forged)	0	0.933	2 0			

STRUCTURE

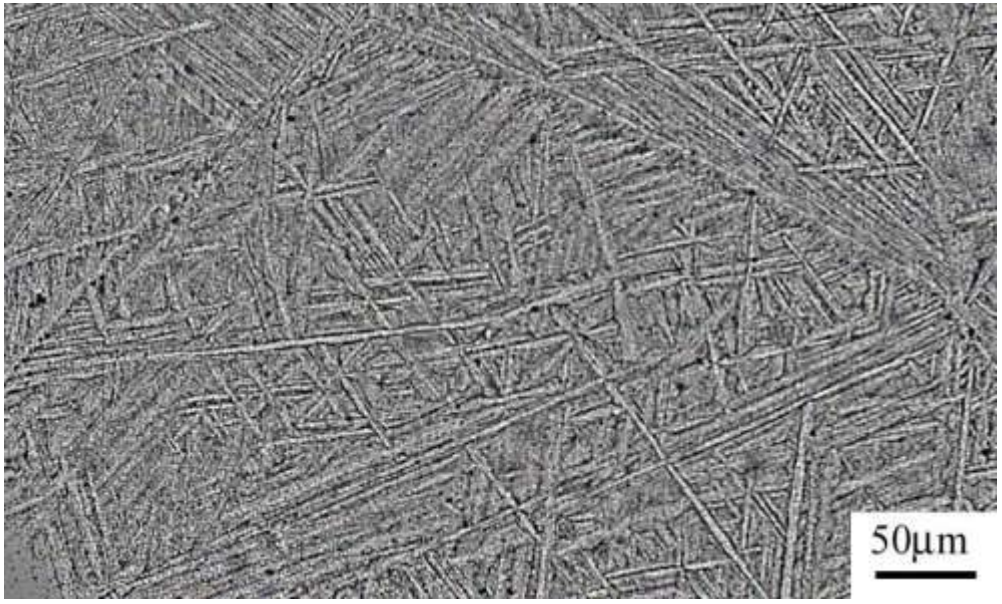

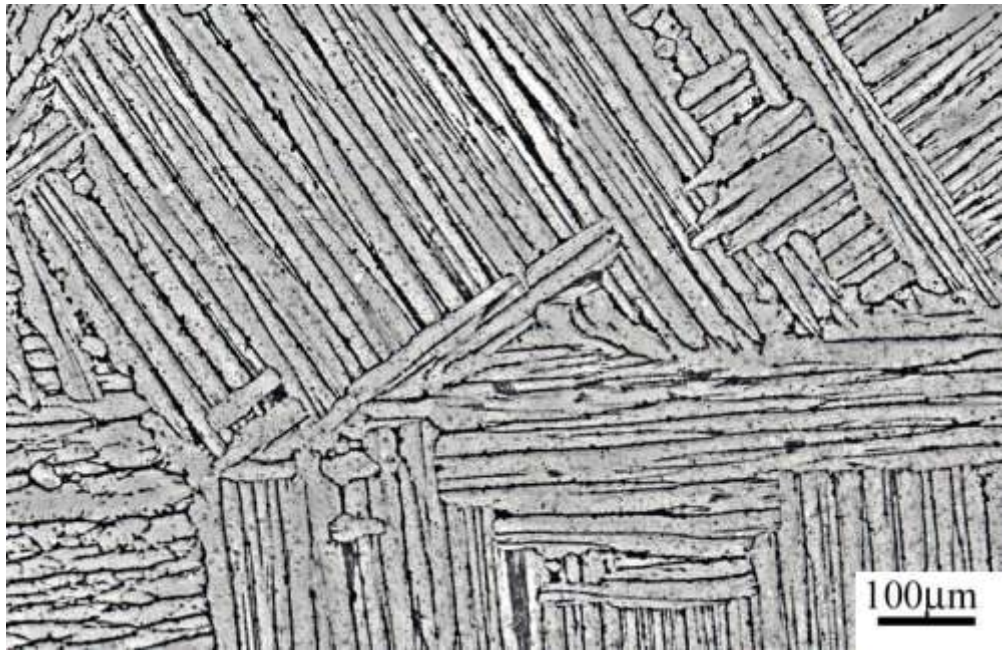

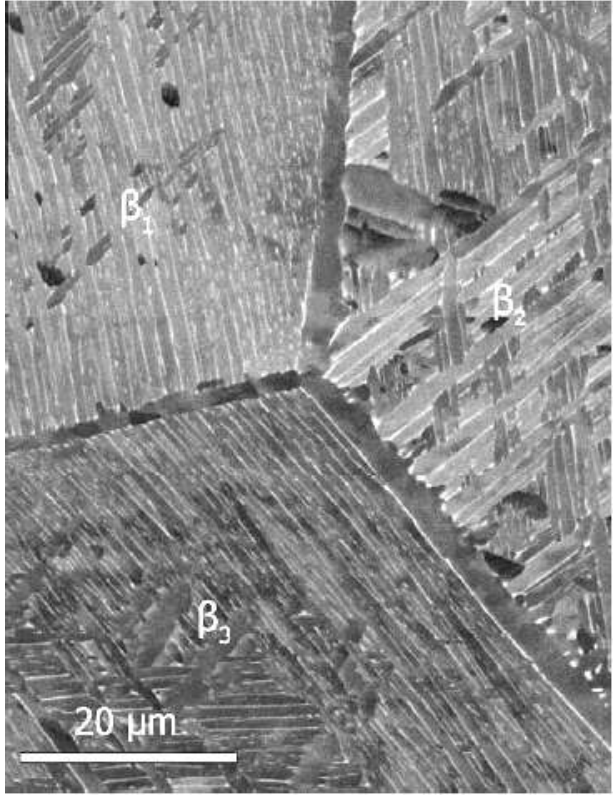

- **The starting cast/beta cooled structure is dominated by alpha morphologies determined by interface and strain energies between the two phases –the burgers relationship**

- **Grain boundary and alpha and related sideplates emanating from it can dominate the structure under some conditions**

GRAIN BOUNDARY NUCLEATION: A BRIEF HISTORY

Winterbottom, Acta Met, 1967
The equilibrium nucleus shape at a grain boundary

Lee and Aaronson , Acta Met 1975

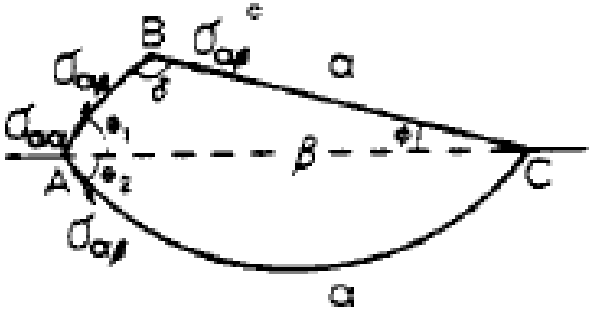

Luo and Weatherly, Acta Met 1989

fcc-bcc in the Ni-Cr system

Preferred nucleation at boundaries where habit plane in one grain is close to boundary plane

Growth into neighboring irrationally oriented grain

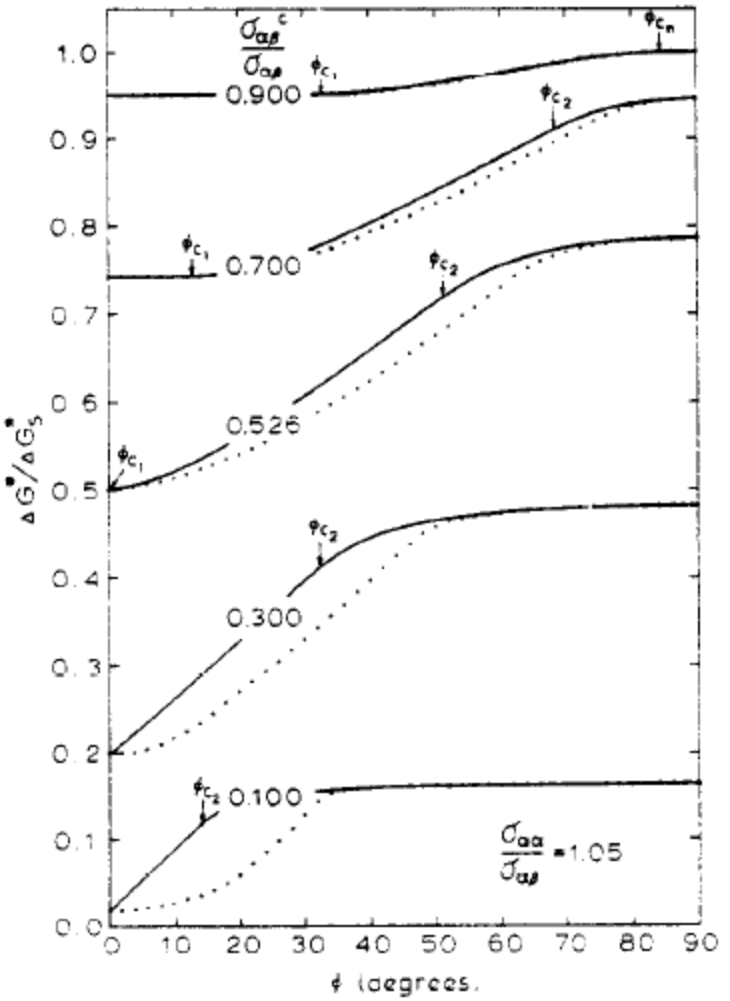

FIG. 9. Variation of $\Delta G^*/\Delta G_v^*$ with ϕ, where ΔG_v^* is the the critical free energy of formation for an unfaceted grain boundary allotriomorph ($\sigma_{\alpha\alpha}/\sigma_{\alpha\beta} = 1.05$).

GRAIN BOUNDARY ALPHA: A BRIEF HISTORY

Furuhara, Tagaki, Watanabe and Maki, Met Trans 1996

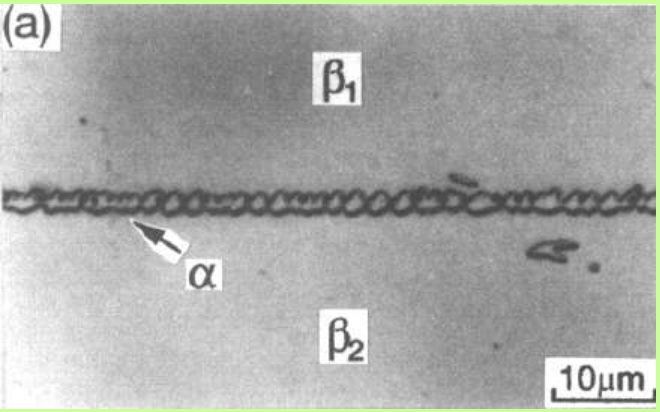

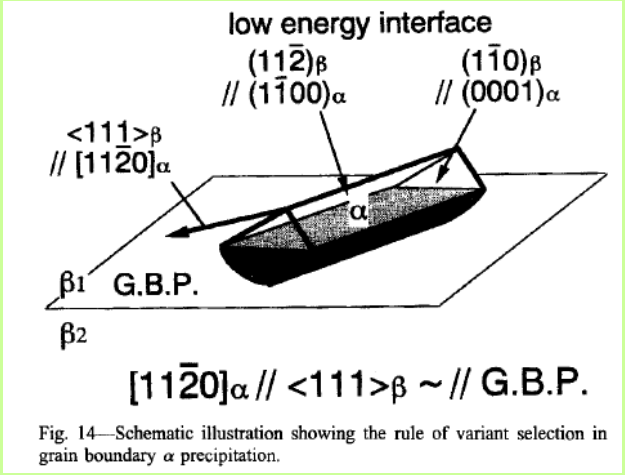

Fig. 14—Schematic illustration showing the rule of variant selection in grain boundary α precipitation.

Variant selection rules:

Burgers OR with one of the two grains

Close packed directions in gb plane
Low misorientation from Burgers OR in neighbouring grain

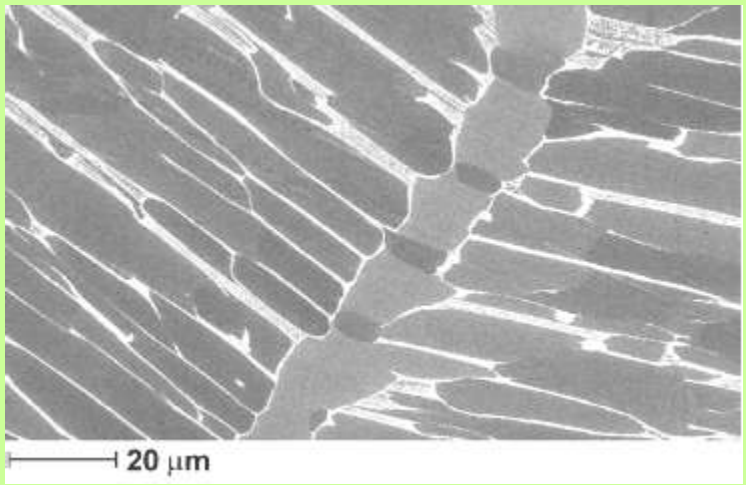

If adjacent beta grains share a common (110) pole, then those (2)variants with (0001) parallel to this (110) are selected

Bhattacharya, Viswanathan, Denkenberger, Furrer, and Fraser, Acta Materiala, 2003

R. Banerjee *, D. Bhattacharyya, P.C. Collins, G.B. Viswanathan, H.L. Fraser Acta Materialia 52 (2004) 377–385

Stanford and Bate, Acta Materiala, 2004

Bhattacharya, Viswanathan and Fraser, Acta Materiala, 2007

GRAIN BOUNDARY ALPHA and INTRAGRANULAR ALPHA

Greater detail in the variant selection process to understand specific choices among the 24 variants

EBSD for better statistics, 3d information including grain boundary normal

The variant selection process when the habit plane/close packed direction parallel to gb plane condition is not on offer ?

What happens at triple points ?

Why do colony structures (of parallely oriented variants) form ?

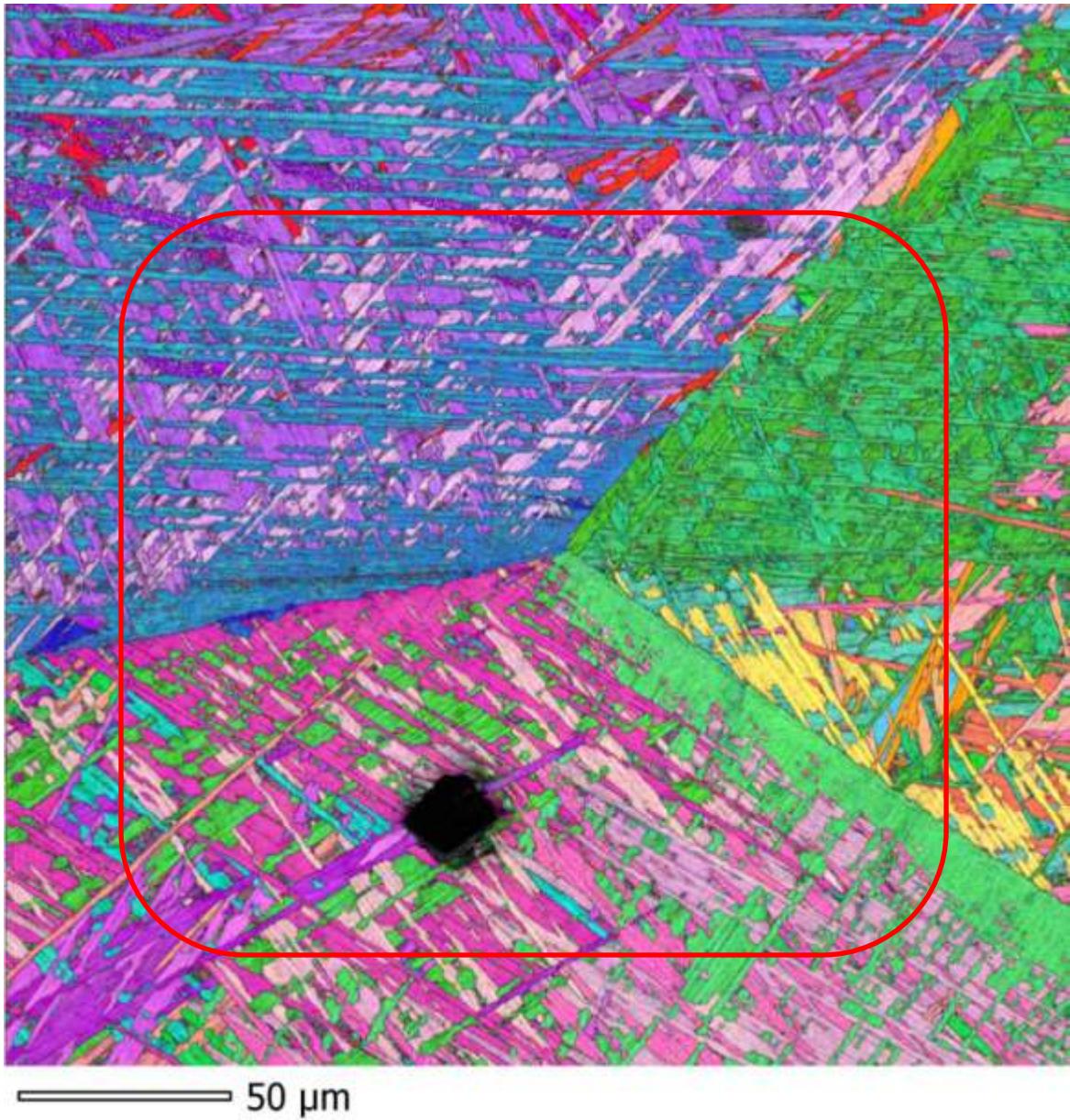

THE IDEAL GRAIN BOUNDARY ALPHA

THE IDEAL GRAIN BOUNDARY ALPHA
Terrace (10-10)//(112), or macroscopic habit plane parallel to boundary plane?

TP1 β1								
<111>		<110>		<112>		<335>		BF
111	85.40	1-10	88.00	11-2	5.70	335	80.20	10.3
1-1-1	65.60	101	76.20	-1-21	28.70	3-5-3	79.50	
-1-1-1	85.40	01-1	28.40	2-1-1	62.10	533	78.80	
111	85.40	10-1	32.40	-12-1	58.10	353	77.90	
1-11	61.90	011	78.20	-2-11	31.00	-53-3	76.00	
-111	65.60	01-1	28.40	-2-1-1	76.60	5-3-3	63.00	
1-11	61.90	10-1	32.40	121	75.40	-35-3	58.76	
-111	65.60	110	50.20	-11-2	49.80	3-3-5	55.80	
1-11	61.90	110	50.20	-112	52.80	-33-5	52.70	
-1-11	15.20	011	78.20	-21-1	80.90	-5-33	26.40	
-1-11	15.20	101	76.20	-121	84.40	-3-53	24.40	
-1-11	15.20	1-10	88.00	112	75.20	-3-35	3.30	

TP1 β2								
<111>		<110>		<112>		<335>		BF
-1-11	73.90	1-10	87.90	112	16.50	-3-35	88.30	3.7
-111	70.70	01-1	86.10	-2-1-1	19.90	5-3-3	85.10	
1-11	67.10	10-1	88.20	121	23.10	-35-3	81.50	
-1-11	73.90	101	31.90	-121	63.40	-3-53	67.60	
-1-11	73.90	011	35.70	-21-1	59.30	-5-33	66.70	
1-1-1	70.70	101	31.90	-1-21	65.70	3-5-3	65.00	
-111	70.70	110	38.70	-11-2	58.00	3-3-5	63.20	
1-11	67.10	011	35.70	-2-11	64.40	-53-3	61.00	
1-11	67.10	110	38.70	-112	60.80	-33-5	60.10	
111	4.70	10-1	88.20	-12-1	86.60	353	18.10	
-1-1-1	4.70	01-1	86.10	2-1-1	89.90	533	15.00	
111	4.70	1-10	87.90	11-2	86.70	335	11.60	

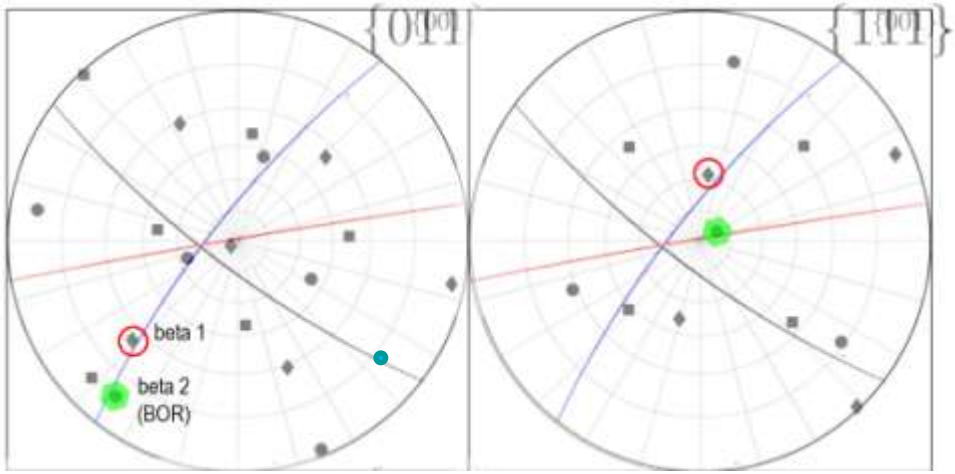

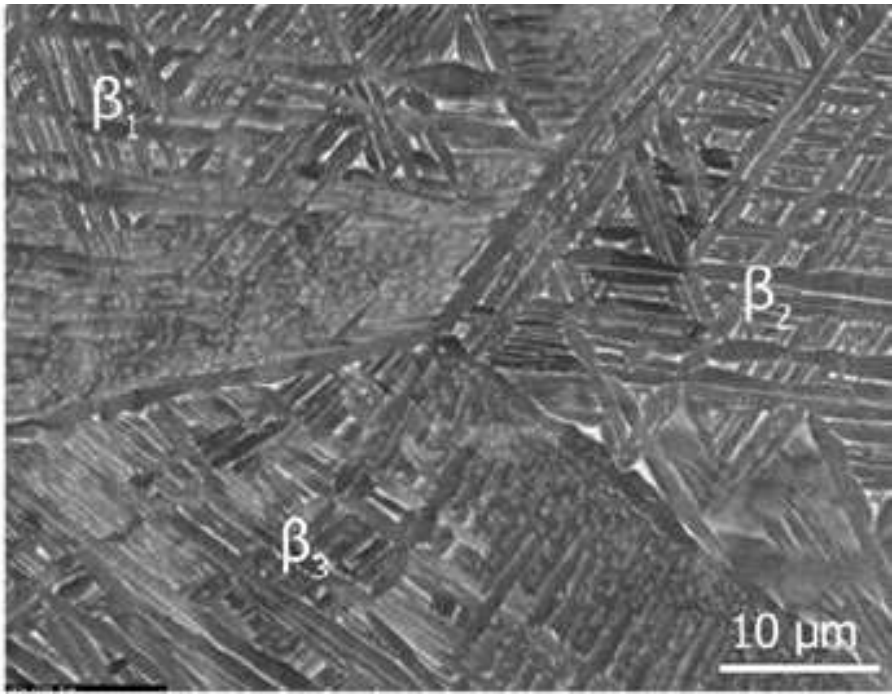

THE IDEAL GRAIN BOUNDARY ALPHA

The observed variant has the lattice invariant line and macroscopic habit plane in the gb plane

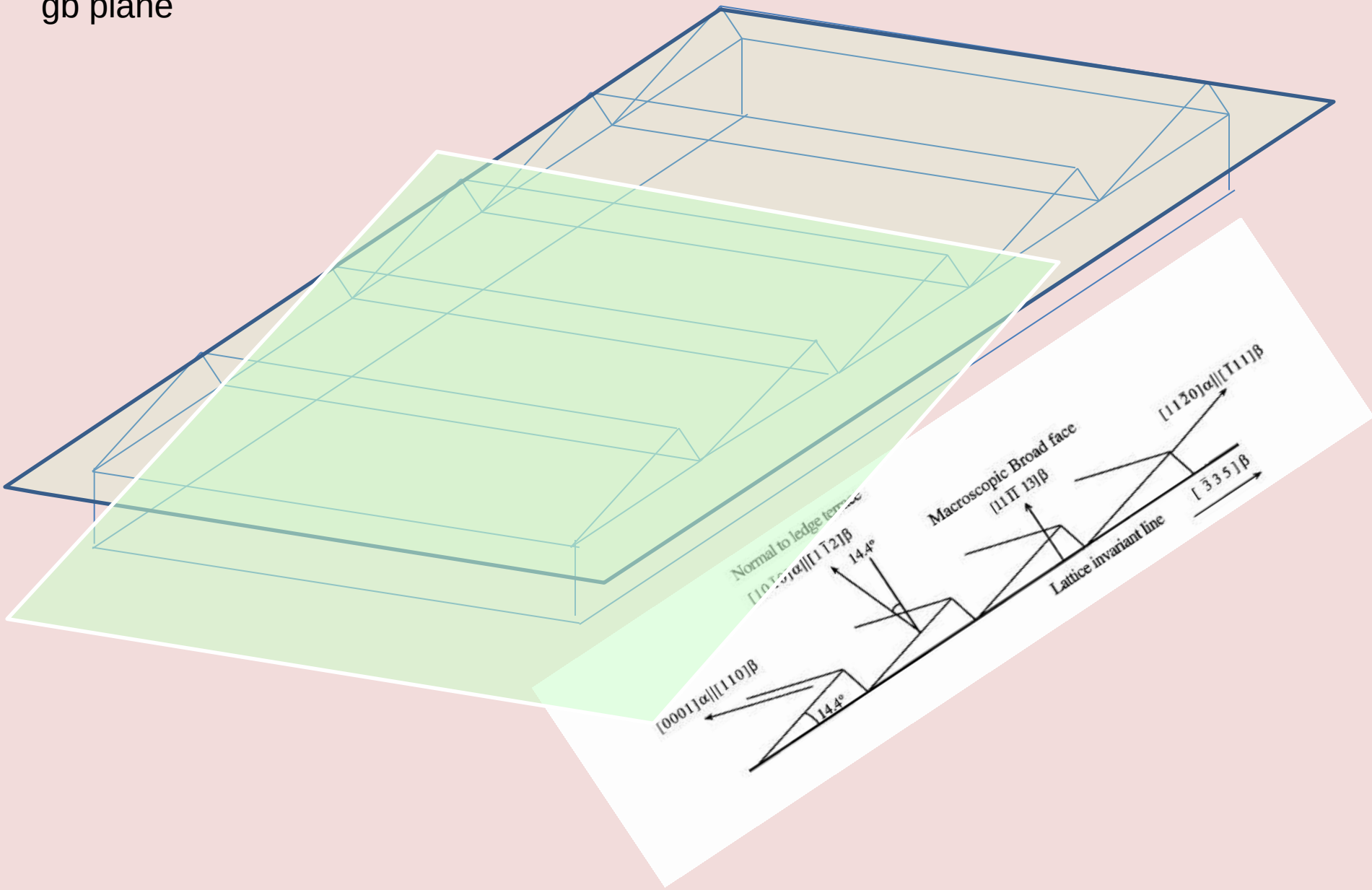

SPECIAL BOUNDARIES

TP2/BETA1								
111		110		112		335		BROAD FACE
-1-11	31 5	101	61	-121	89.8	-3-53	34.5	77.5
1-1-1	73 3	101	61	-1-21	36.7	3-5-3	85.5	31.9
111	47 3	10-1	45.7	-12-1	83.2	353	46.6	86.9
1-11	83 5	10-1	45.7	121	47.2	-35-3	86.6	46.7
1-11	83 5	110	20.4	-112	74.6	-33-5	87.5	73.4
-111	73 3	110	20.4	-11-2	88.9	3-3-5	74.1	84.8
-1-11	31 5	1-10	75.8	112	65.3	-3-35	43.8	51.9
111	47 3	1-10	75.8	11-2	48.4	335	60.6	35.7
1-11	83 5	011	76.2	-2-11	19.2	-53-3	69.8	27.6
-1-11	31 5	011	76.2	-21-1	65	-5-33	21.45	78.7
-1-1-1	47 3	01-1	63.1	2-1-1	57	533	37.6	69
-111	73 3	01-1	63.1	-2-1-1	34.8	5-3-3	61.1	43.6

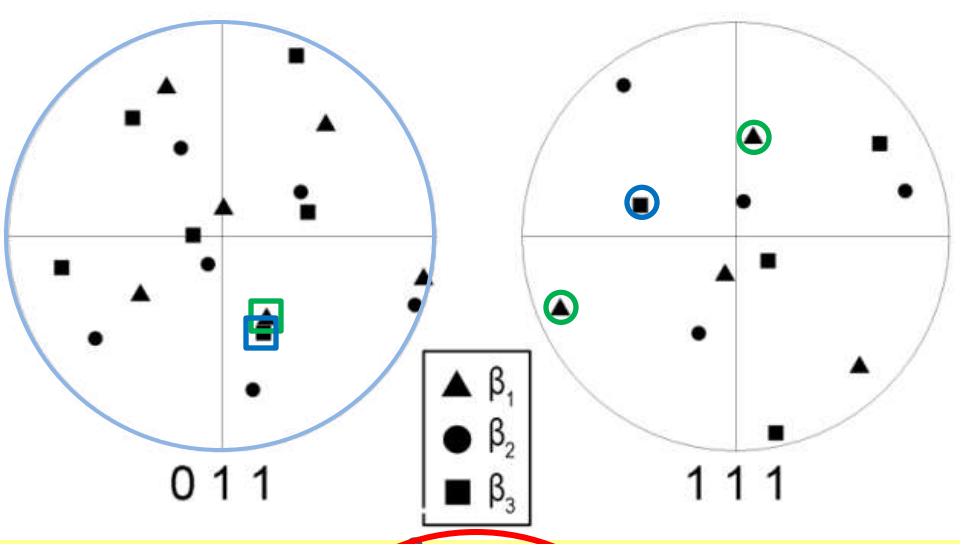

TP2/BETA3									
111		110		112		335		BROAD FACE	
-1-11	73 9	101	39.8	-121	57.1	-3-53	66 2	62.8	
1-1-1	65.1	101	39.8	-1-21	63.8	3-5-3	58 9	71.1	
111	12.7	10-1	84.9	-12-1	87.2	353	16 9	78.8	
1-11	73 8	10-1	84.9	121	20.6	-35-3	87 9	12.6	Near ideal
1-11	73 8	110	39.9	-112	57	-33-5	66.1	62.8	
-111	65.1	110	39.9	-11-2	63.6	3-3-5	58 8	71	actual
-1-11	73 9	1-10	85	112	20.5	-3-35	88	12.5	
111	12.7	1-10	85	11-2	87	335	16 8	78.8	
1-11	73 8	011	31.3	-2-11	66.9	-53-3	68 5	71.9	
-1-11	73 9	011	31.3	-21-1	66.9	-5-33	68.6	71.8	
-1-1-1	12.7	01-1	89.9	2-1-1	84.2	533	23.1	70.1	
-111	65.1	01-1	89.9	-2-1-1	27.6	5-3-3	79 2	15.7	

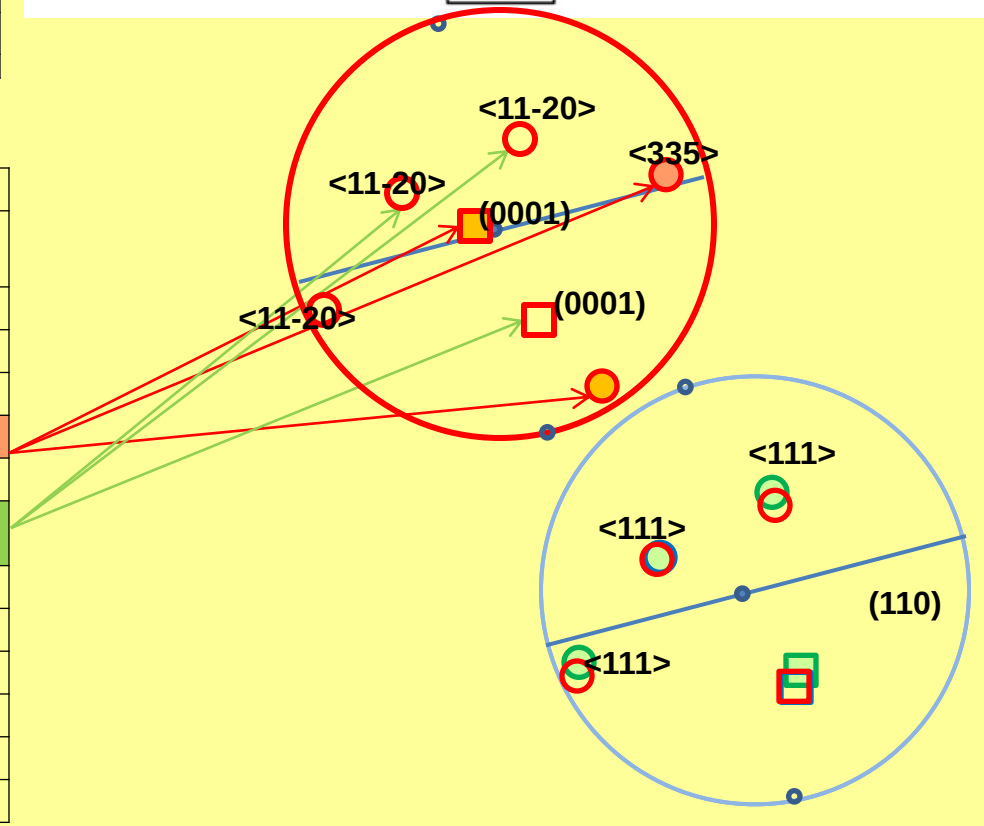

SPECIAL BOUNDARIES: the chosen variant is Burgers oriented to both grains, in preference to a near ideal variant

THE RANDOM BOUNDARY

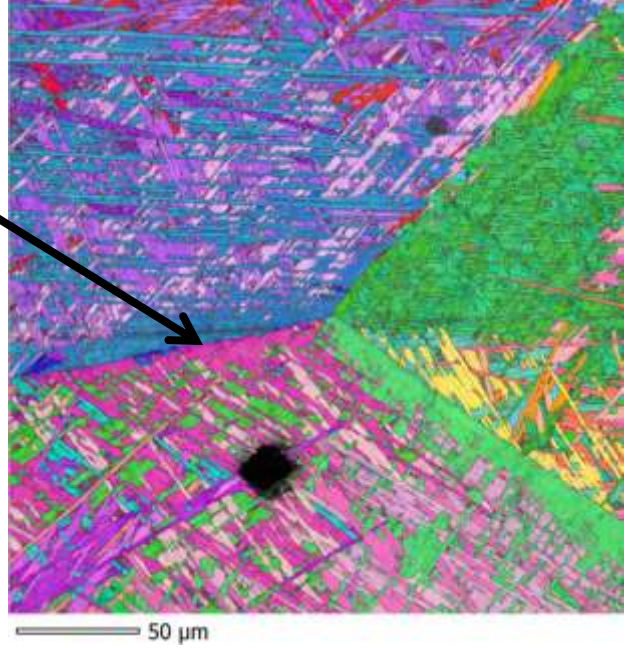

TP1 beta1								
<111>		<110>		<112>		<335>		BF
1-1-1	53.8	101	63.5	-1-21	47.7	3-5-3	66.20	28.76
111	61	10-1	29.5	-12-1	85	353	63.40	36.03
-111	53.8	01-1	68.9	-2-1-1	43.7	5-3-3	41.30	36.98
1-11	75.9	10-1	29.5	121	64.7	-35-3	82.60	49.34
-1-1-1	61	01-1	68.9	2-1-1	37.1	533	48.10	54.30
1-11	75.9	110	36.3	-112	57.3	-33-5	84.20	56.44
-1-11	33.8	011	86.3	-21-1	56.5	-5-33	19.50	58.09
-1-11	33.8	101	63.5	-121	70.6	-3-53	43.70	61.64
1-11	75.9	011	86.3	-2-11	14.6	-53-3	61.50	65.16
111	119	1-10	59.3	11-2	44.7	335	73.00	70.88
-1-11	33.8	1-10	59.3	112	77.3	-3-35	41.40	78.18
-111	53.8	110	36.3	-11-2	92.8	3-3-5	56.00	78.76

TP1 beta3								
<111>		<110>		<112>		<335>		BF
-1-11	62.1	101	48.00	-121	54.8	-3-53	72.00	40.6
-111	64.5	110	33.50	-11-2	69.9	3-3-5	70.70	43.59
1-11	64.5	110	83.20	-112	26.5	-33-5	50.20	47.52
1-11	48.5	011	56.60	-2-11	59.5	-53-3	59.00	48.92
111	48.5	1-10	80.50	11-2	43.1	335	34.60	50.18
111	45.6	10-1	56.60	-12-1	62.9	353	55.60	52.03
-1-1-1	62.1	01-1	33.50	2-1-1	73.1	533	67.60	57.14
-111	64.5	01-1	44.30	-2-1-1	56.6	5-3-3	73.70	59.49
-1-11	45.6	1-10	48.00	112	75.6	-3-35	52.00	63.86
1-1-1	62.1	101	80.50	-1-21	29.8	3-5-3	48.00	65.45
-1-11	48.5	011	44.30	-21-1	77.1	-5-33	54.10	66.51
1-11	45.6	10-1	83.20	121	45.2	-35-3	31.40	67.64

The chosen variant neither has the nearest habit plane to the boundary, nor the growth direction in the boundary

The chosen variant is oriented to thebeta1 grain but has no relationship to beta2
No relationship to the variants at the other grain boundaries

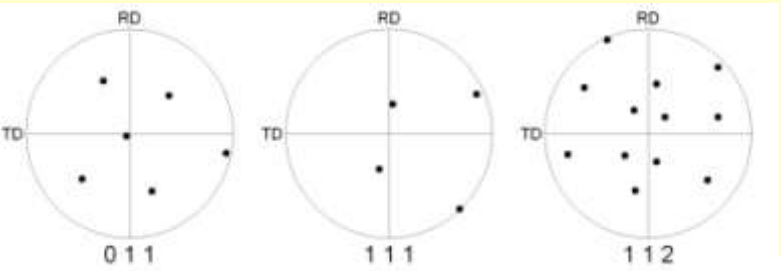

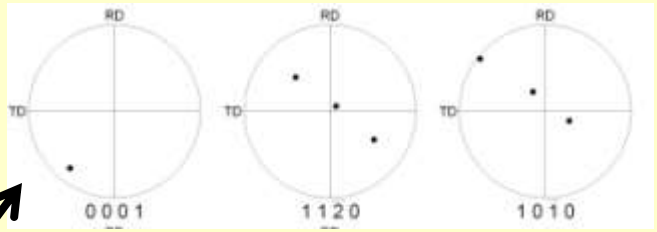

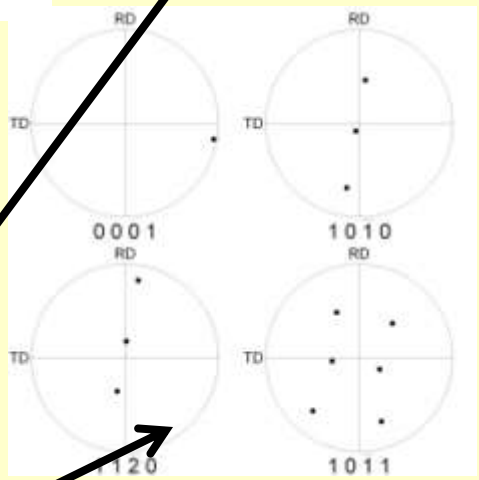

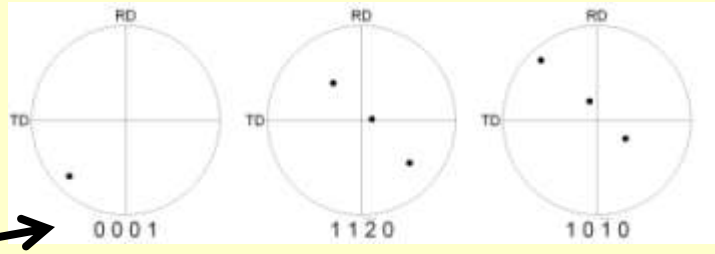

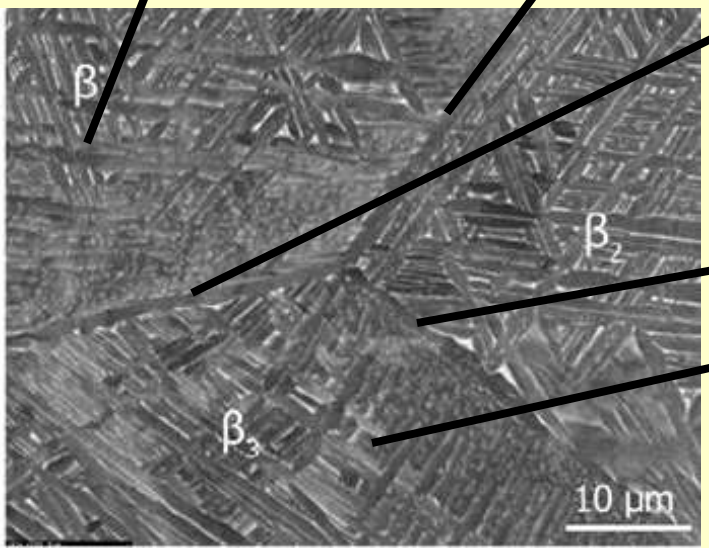

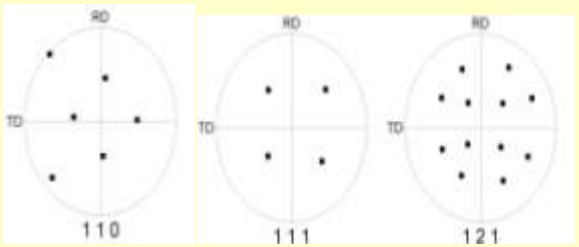

WIDMANSTATTEN ALPHA SIDEPLATES AND DISCONTINUOUS PRECIPITATION

GRAIN BOUNDARY ALPHA AND SIDEPLATE GROWTH AT SPECIAL BOUNDARIES

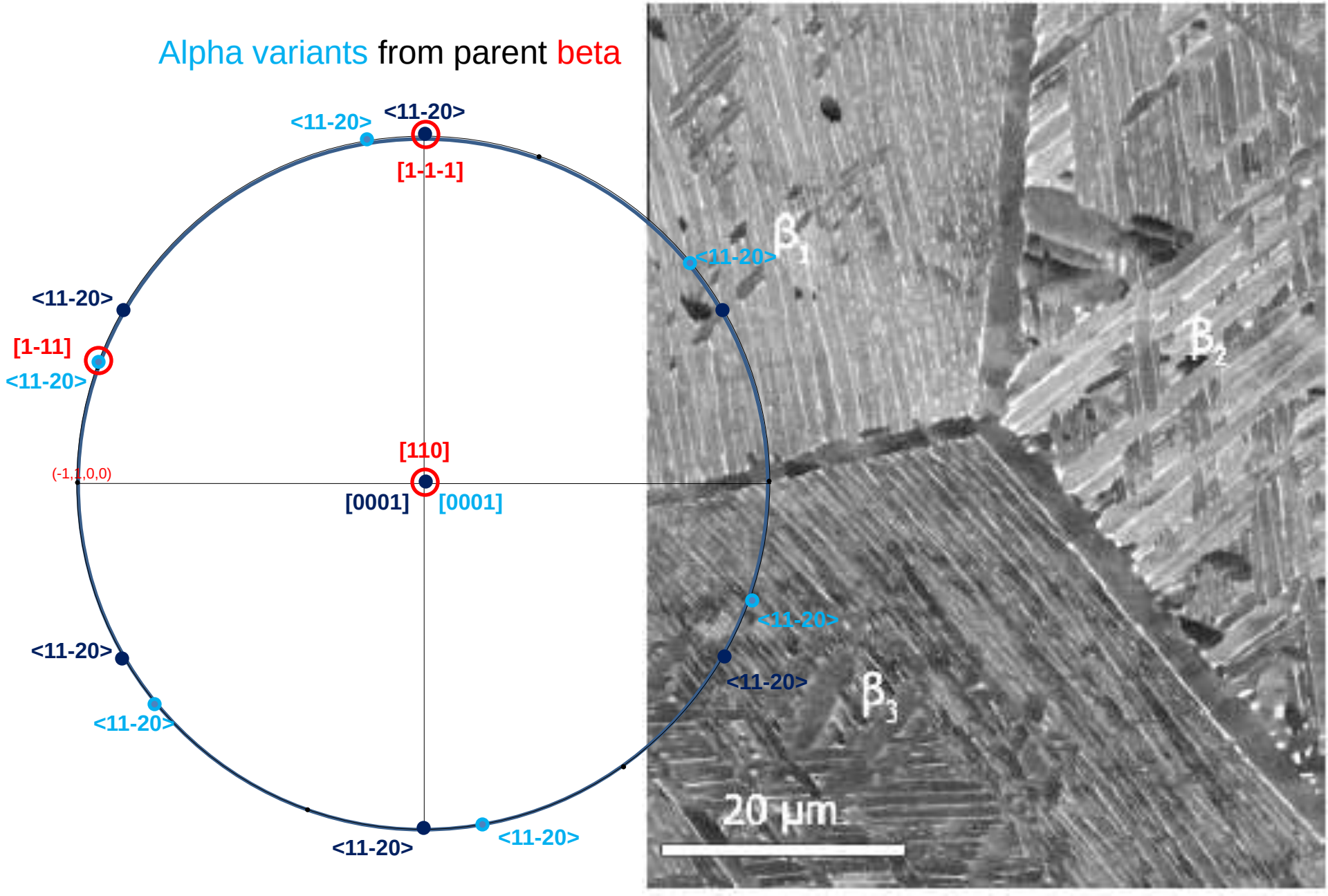

INTRAGRANULAR STRUCTURE

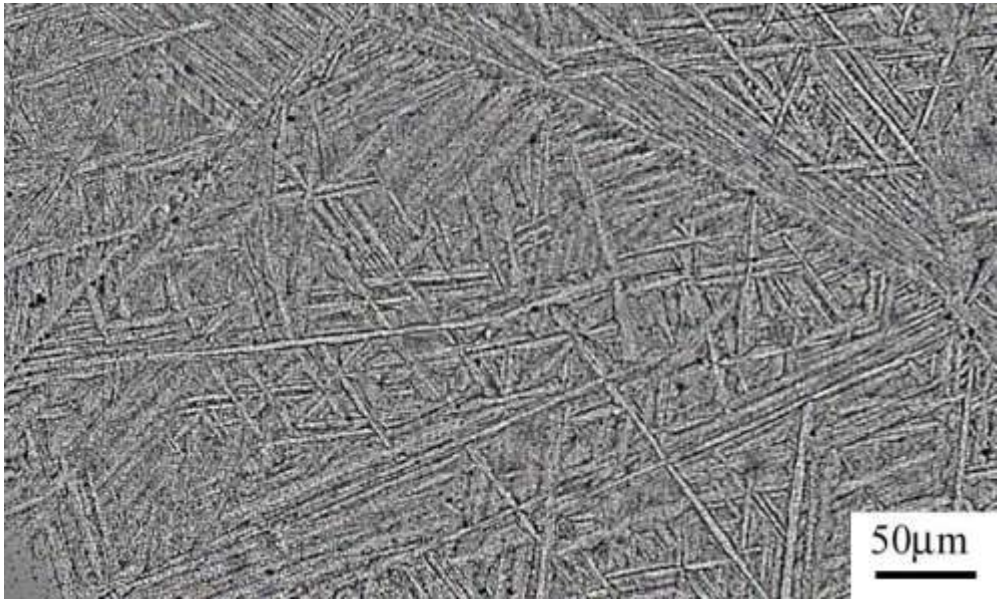

S.C. Wang M. Aindow M.J. Starink
Acta Materialia (2003)

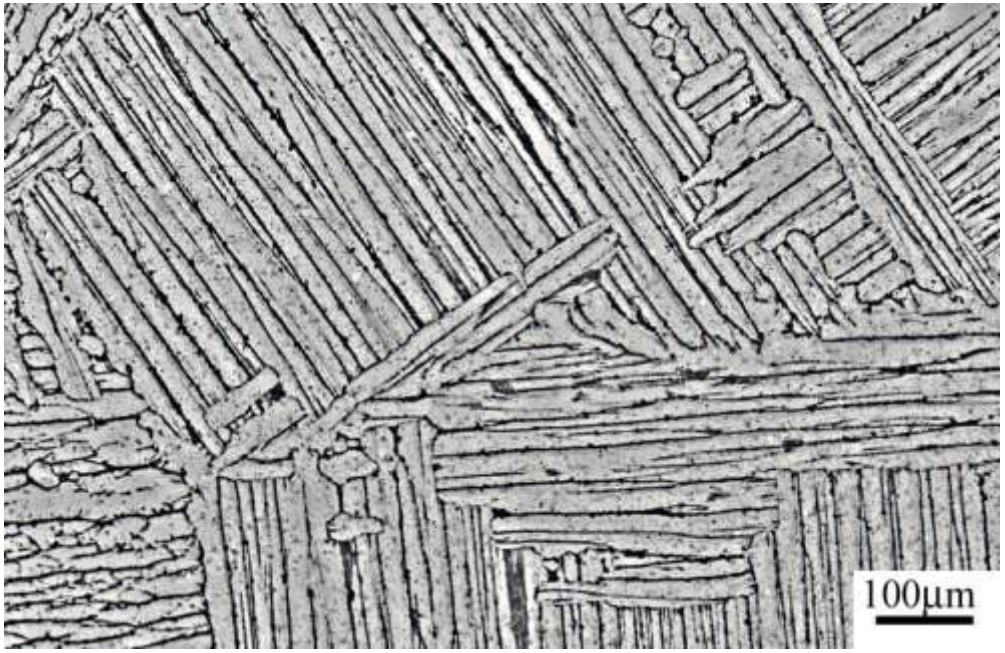

- **self -accommodation structures?**

144 combinations of two variants

220 combinations of three variants

495 combinations of 4 variants

- **the colony structure dominates at low undercooling and high growth rate conditions**

COLONY STRUCTURES

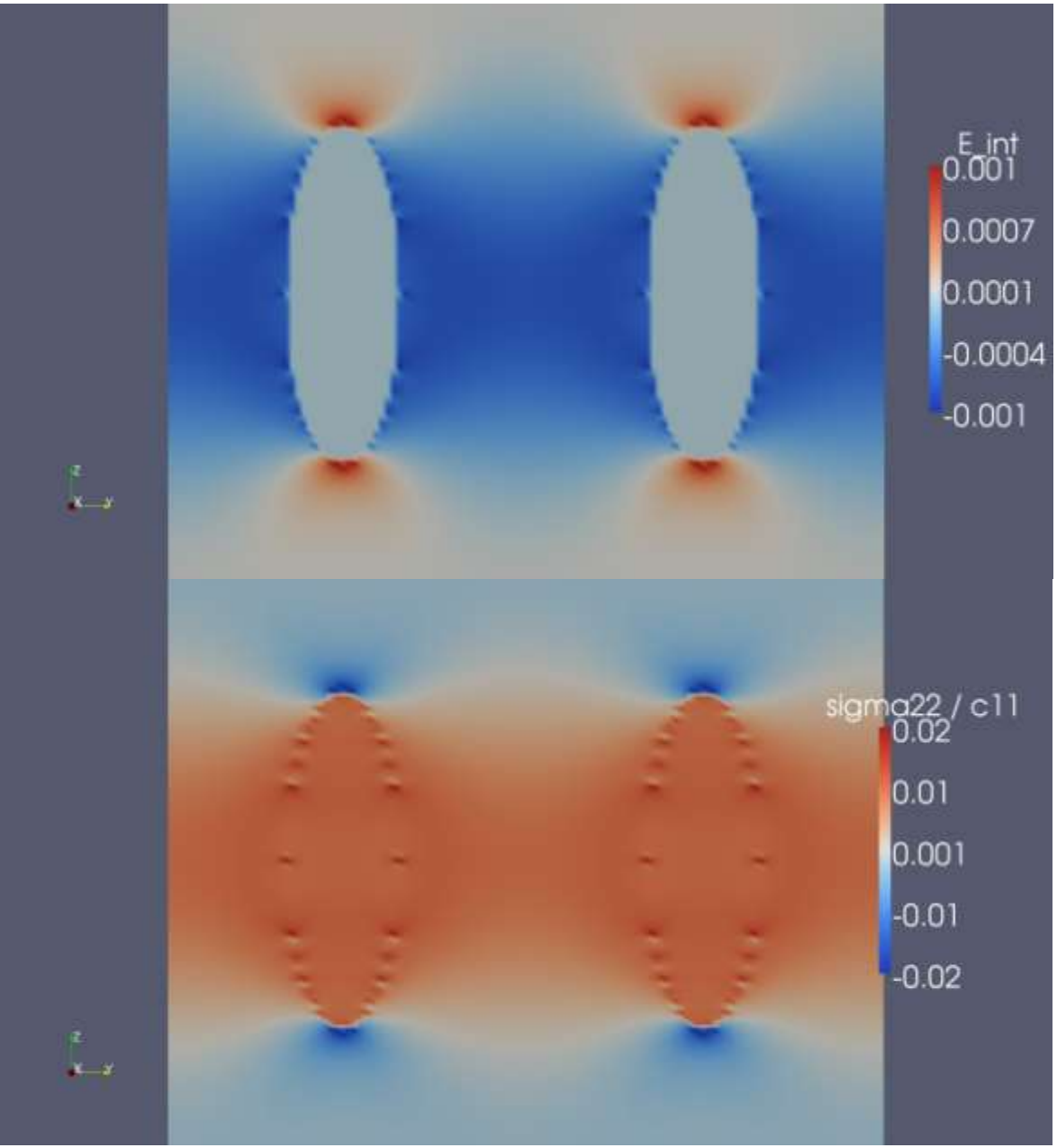

Does the colony structure originate from elastic interactions?

C. Shen, J.P. Simmons, and Y. Wang ,2006

Focus: grain boundary nucleation

Is the grain boundary alpha structure(observed variants) nucleation dominated or growth dominated
we can devise critical experiments to test this
then determine the variant selection process under different conditions
identify the configuration at earliest stages of gb alpha formation

Can you predict variant selection at grain boundaries?
Do we have a statistical data base?
What is the structure of the nucleus: coherent or semicoherent?
Do elastic stresses play a role?
Can we understand stress relaxation at grain boundaries?
How accurately do we need to know relevant surface energies, especially grain boundary energy as a function of grain boundary orientation?

What is the origin of the colony structure at low undercooling and high growth rate conditions?
elastic stresses alone?
coupling of stresses and diffusion fields?

RECRYSTALLISATION AND STRUCTURE

thermomechanical processing controls distribution and morphology of the two phases

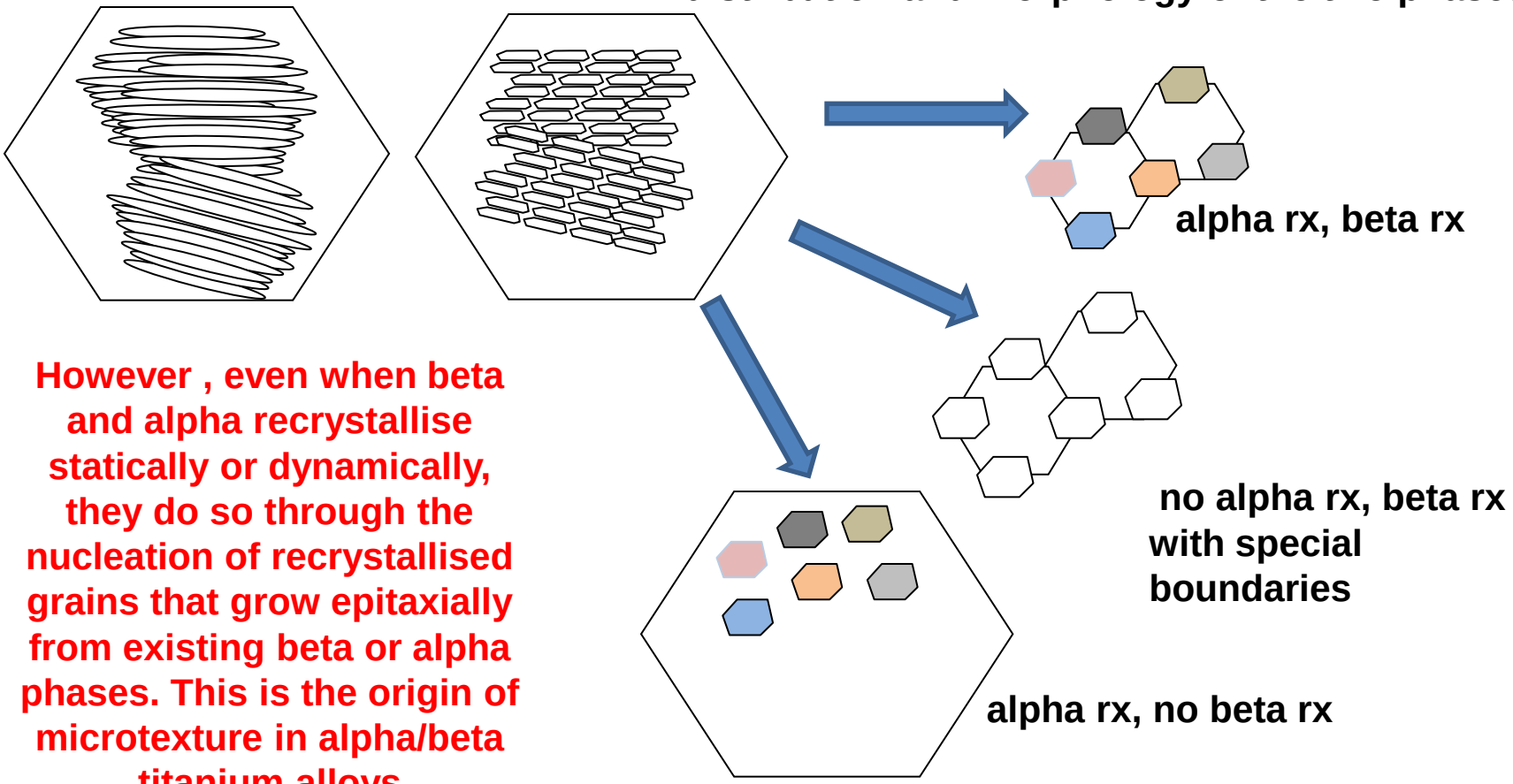

However , even when beta and alpha recrystallise statically or dynamically, they do so through the nucleation of recrystallised grains that grow epitaxially from existing beta or alpha phases. This is the origin of microtexture in alpha/beta titanium alloys

Strategies to eliminate microtexture:

- **Control colony size prior to processing (section thickness effects)**
- **Large superplastic deformation (extensive grain rotation)**
- **Friction stir processing of surfaces (extensive shear and rotation)**

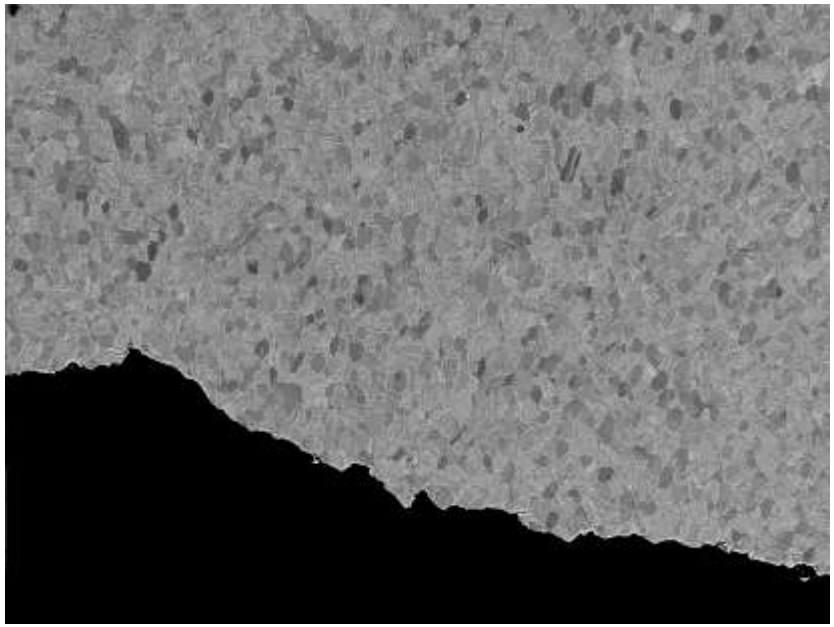

MICROTEXTURE IN EQUIAQXED ALPHA STRUCTURES

Pilchak and Banerjee, OSU

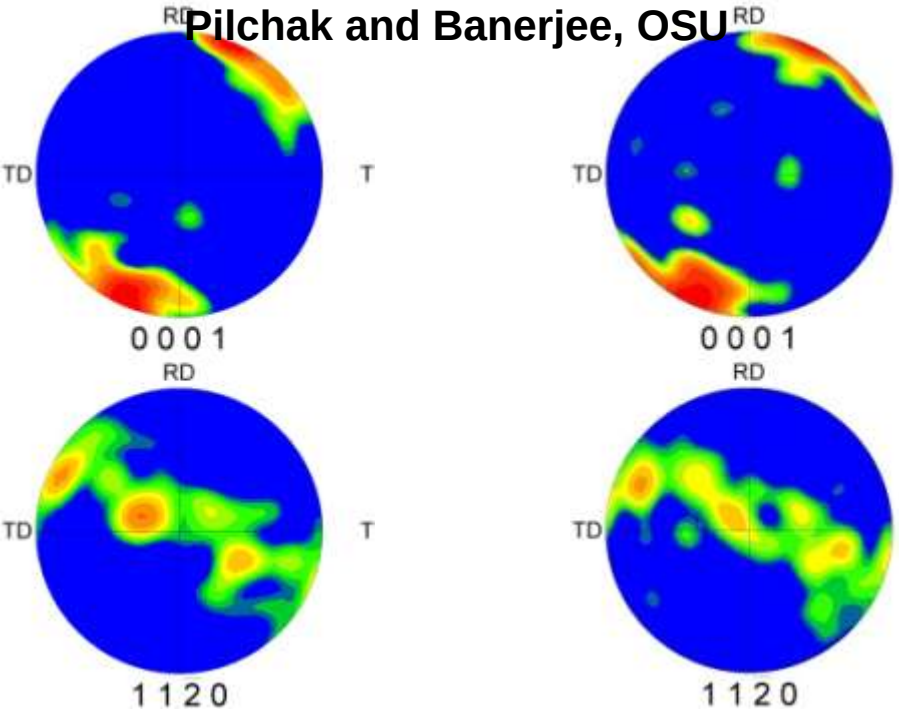

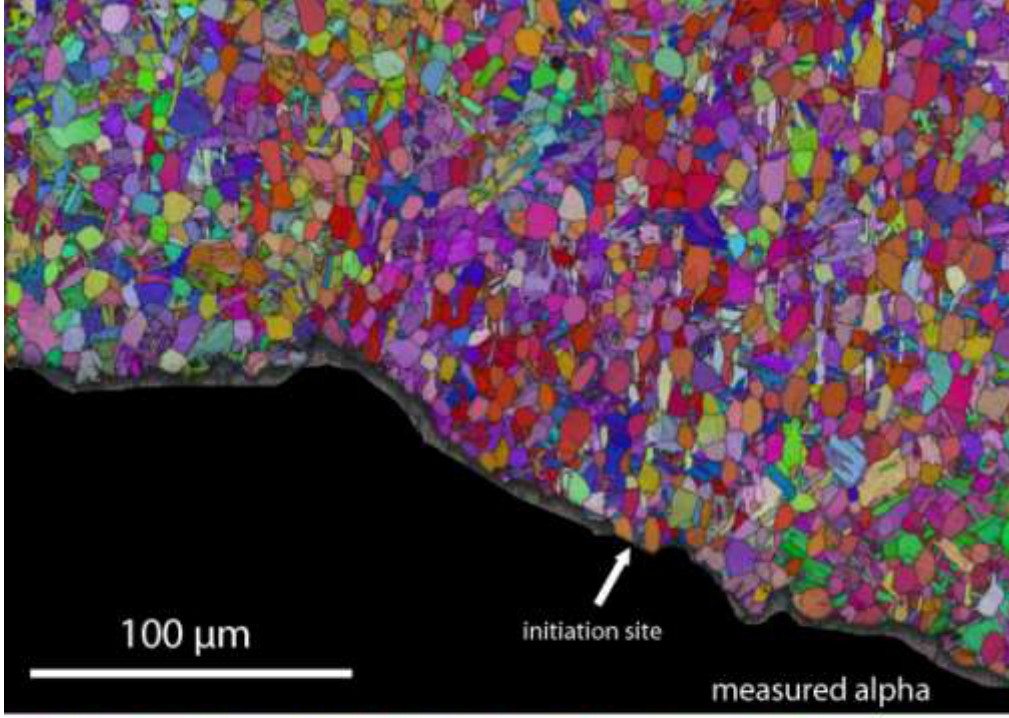

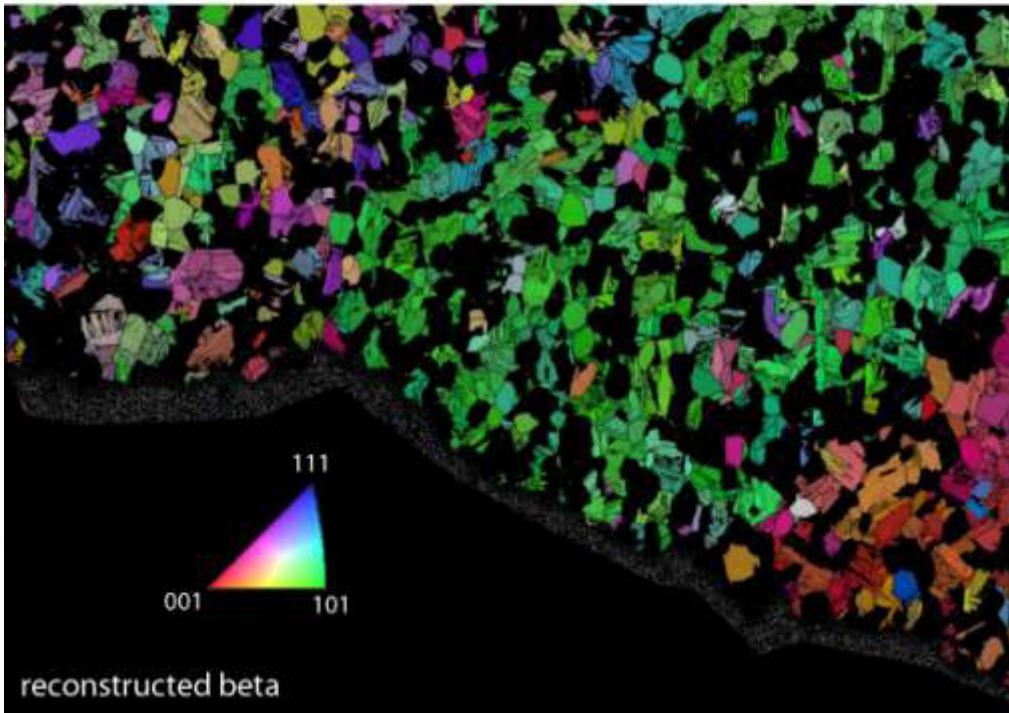

PROCESSING AND STRUCTURE
the initiation of ‘recrystallisation’

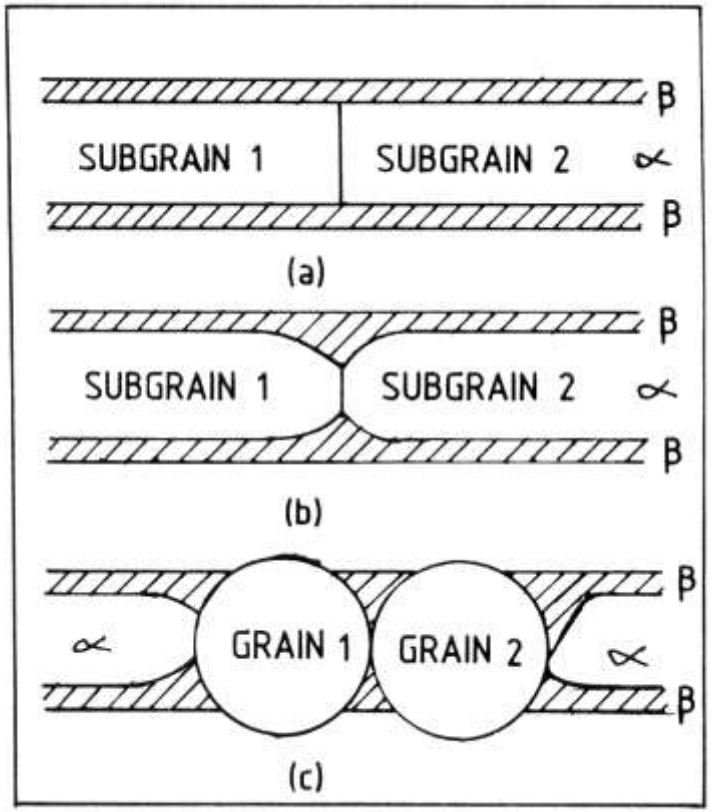

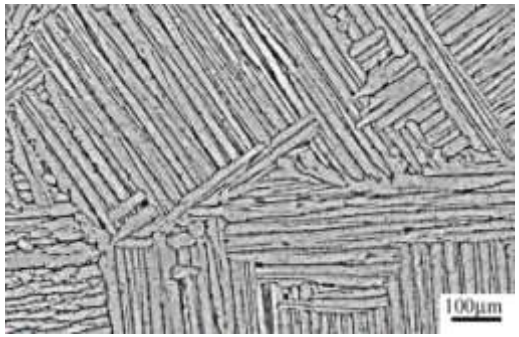

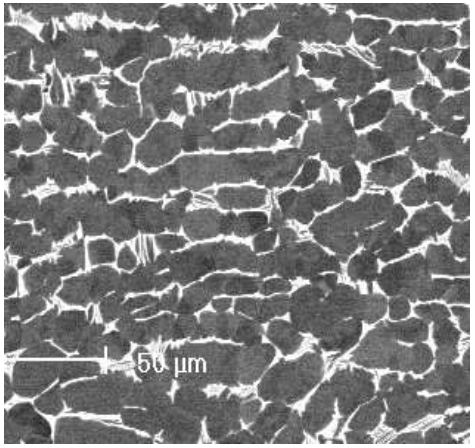

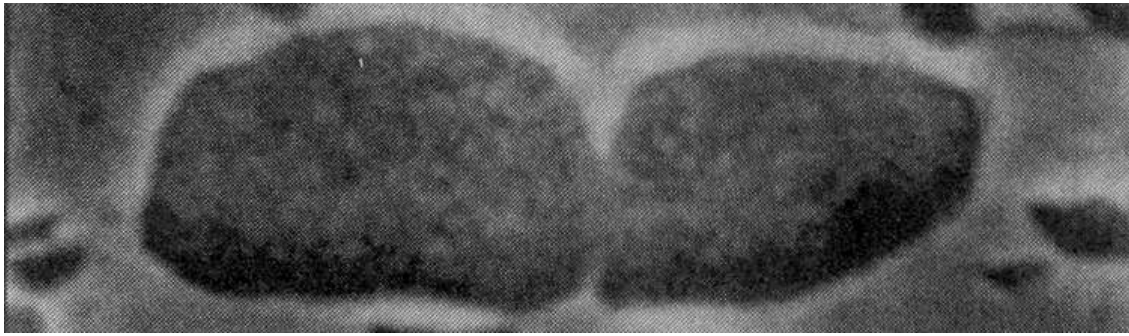

Weiss and co., 1986

subgrain formation in alpha, beta percolation

BETA RECRYSTALLISATION

The {110} poles of the beta grains are often clustered together and the relative rotation about these poles is about 60°

This happens when beta grains nucleate from parent alpha with the burgers relationship

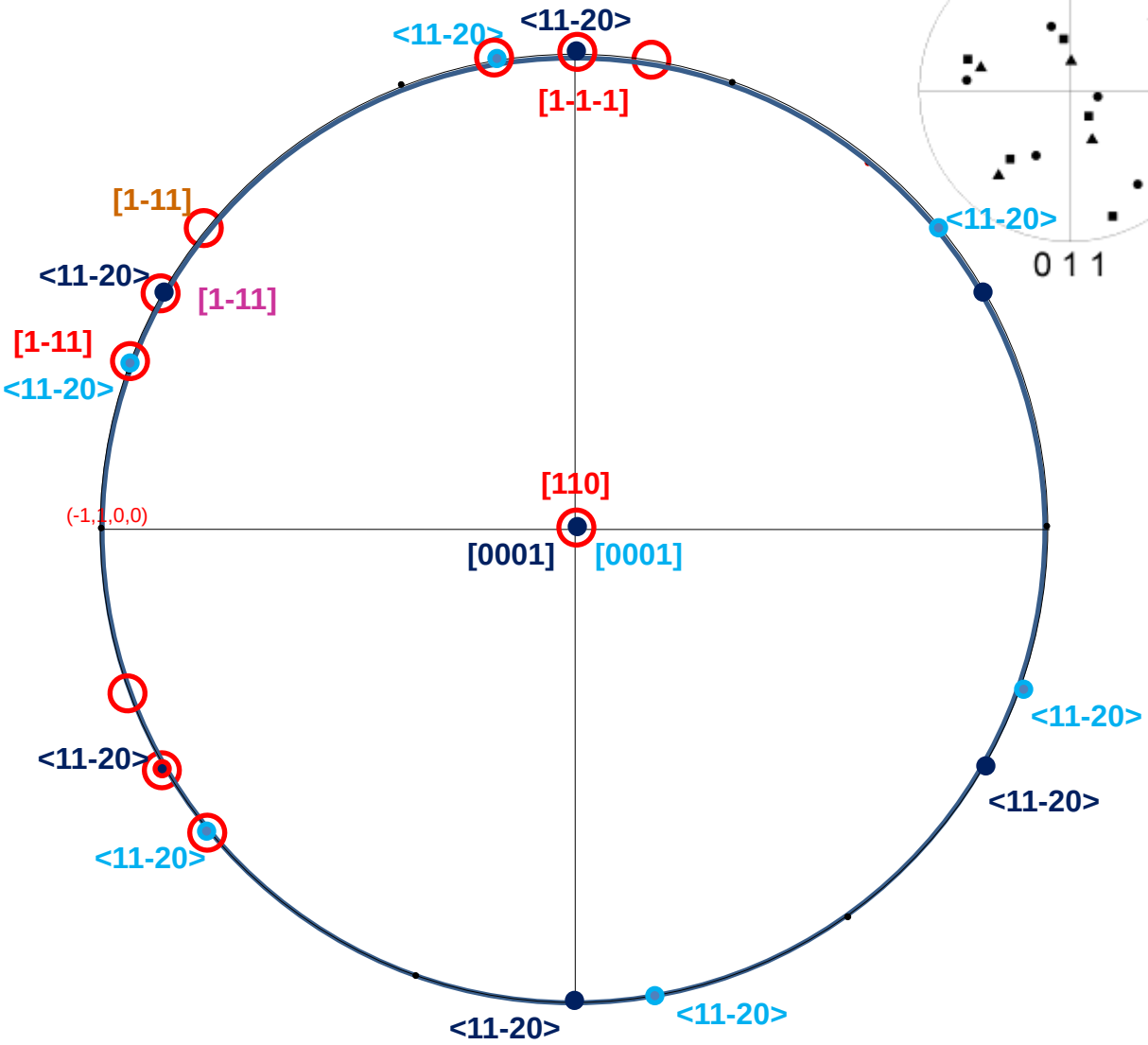

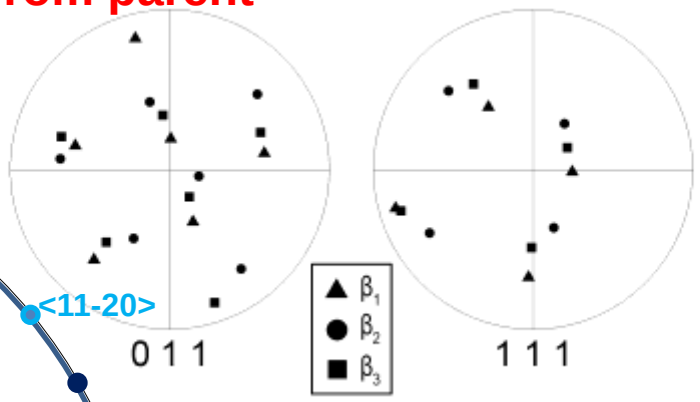

The nucleation of recrystallisation in multiphase materials?

Early Stages of Nucleation and Growth of ω Precipitates within the β Matrix of Titanium Alloys

Rajarshi Banerjee

Center for Advanced Research and Technology
Department of Materials Science and Engineering
University of North Texas
Denton, Texas, U.S.A.

UNT
UNIVERSITY OF
NORTH TEXAS
Discover the power of ideas

Acknowledgements

S. Nag, A. Devaraj, and S. Srivilliputhur
University of North Texas
Denton, Texas, U.S.A.

S. Rajagopalan and H. L. Fraser*
Ohio State University
Columbus, Ohio, U.S.A.
**Now at Exxon Mobil*

Financial support for this work has been provided by the National Science Foundation and the Air Force Research Laboratory

Phase Transformation in β Titanium Alloys

β phase instabilities:

$\beta \rightarrow \beta + \omega$

$\beta_{hom} \rightarrow \beta' + \beta$

$\beta \rightarrow \beta + \alpha$

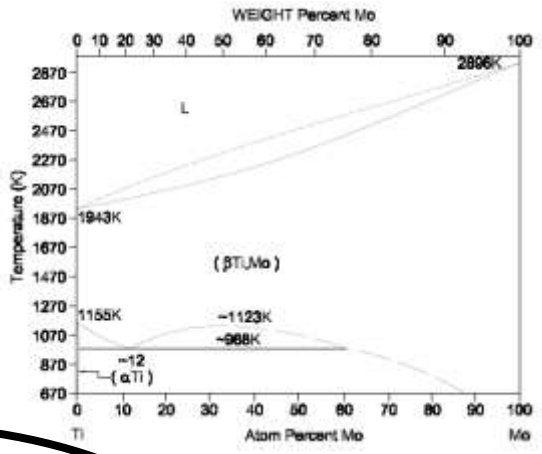

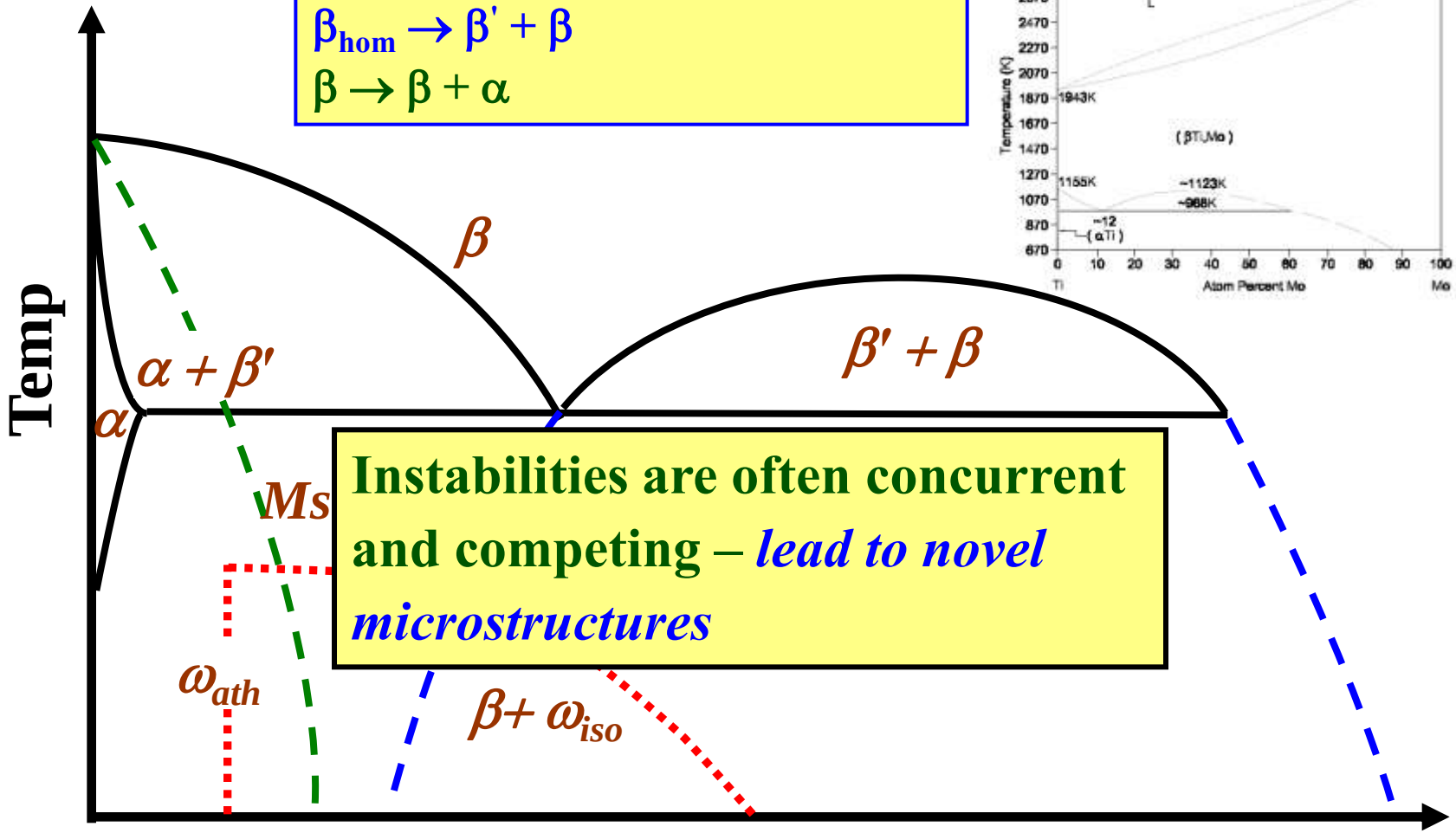

Instabilities are often concurrent and competing – *lead to novel microstructures*

Nucleation and Growth of ω and α in β matrix

Two types of sites for nucleation of α:

- ***Inter-granular at β grain boundaries***
- ***Intra-granular sites***

Intra-granular heterogeneous nucleation sites within β grains:

- **Instabilities within the β matrix – *compositional and structural***
- **Uniformly distributed ω precipitates**
- **Phase separation leading to β + β' – compositional partitioning**

Alloy systems:

- **Commercial system TIMETAL 5553: Ti-5Al-5Mo-5V-3Cr-0.5Fe (all wt%, Ti-5553) or Ti-9Al-2.5Mo-5V-3Cr-0.5Fe (at%) - nominal alloy composition**
- **Ti-18wt%Mo (or Ti-9at%Mo)**

Ti-5553 Quenching from Above T_β

$\beta \rightarrow \beta + \omega$ (Precipitation of the ω phase)

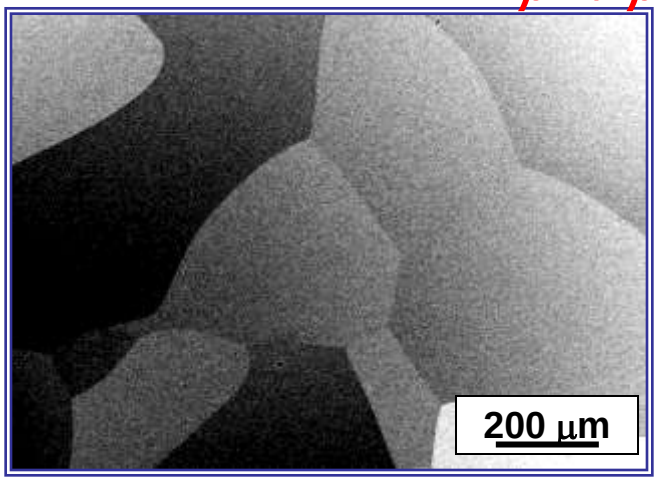

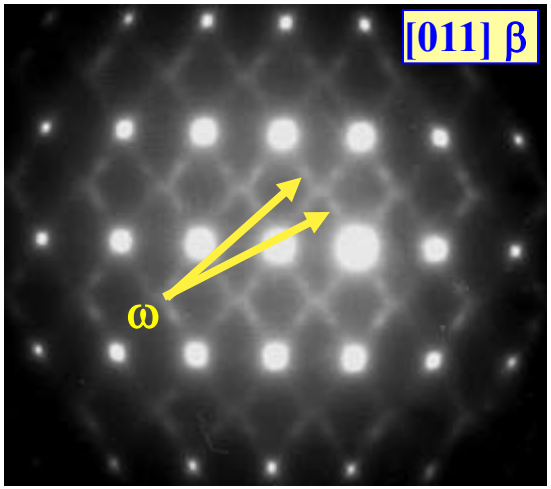

SAD [011] β + ω reflections at 1/3{112} positions

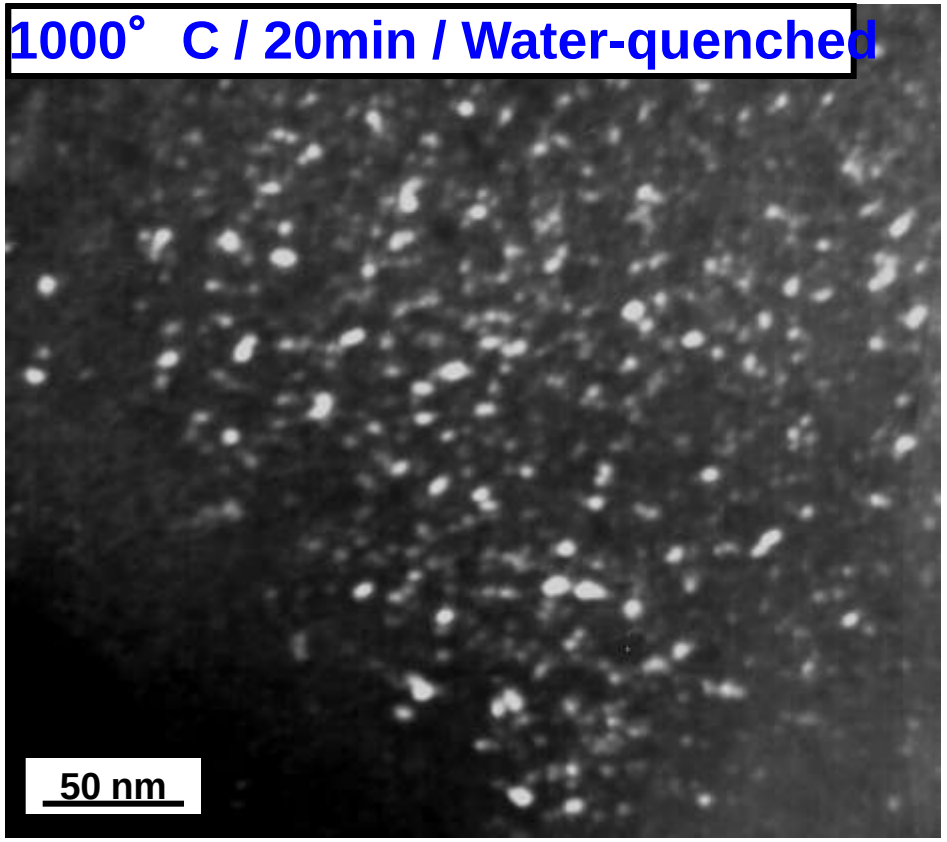

Dark Field TEM micrograph

Athermal ω phase in as-quenched condition

Ti-5553 Nucleation site for α – ω precipitates

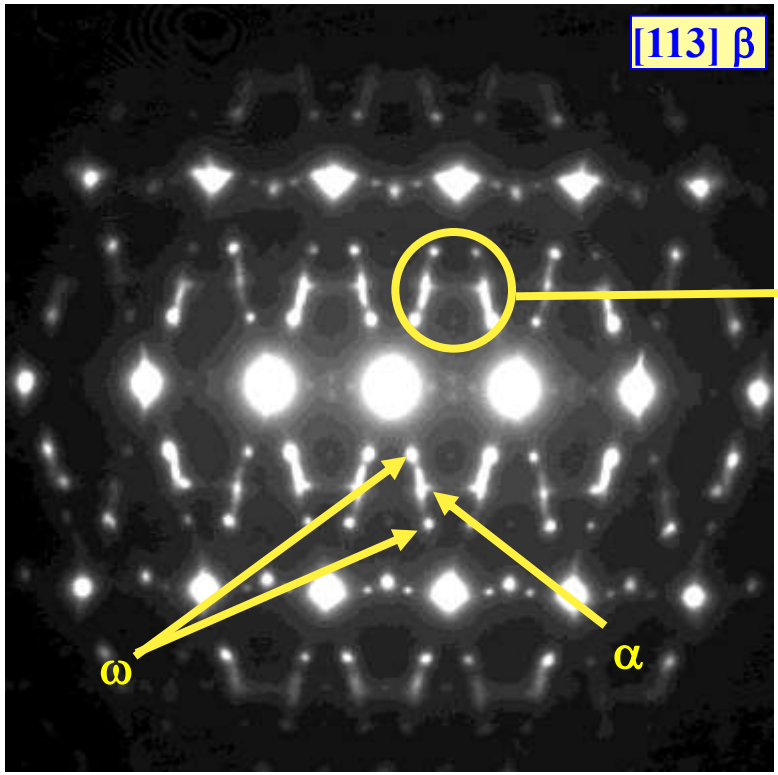

SAD [113] β + ω reflections at 1/3{112} positions + α reflections at 1/2{112} positions

Dark-field TEM image from ω + α reflections

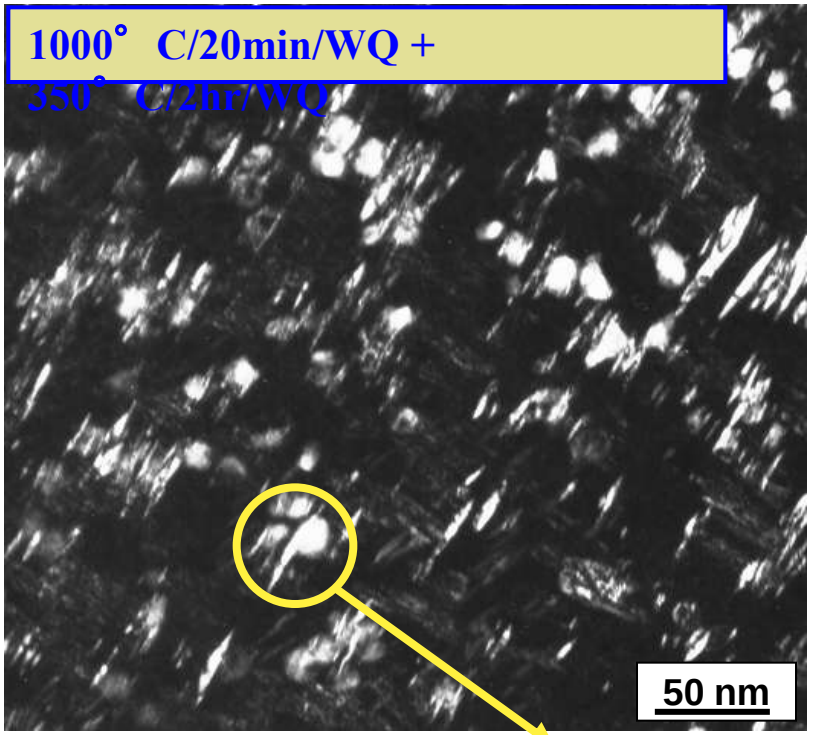

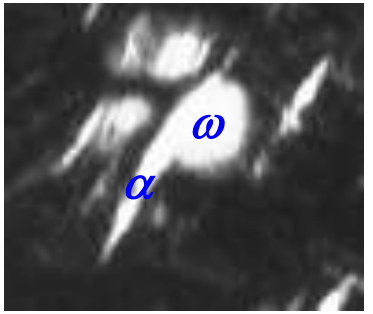

α lath nucleating on ω precipitate

Nag, Banerjee, Srinivasan, Harper, and, Fraser, *Acta Mater.* (2009)

Annealing at 400° C for 2 hours - TEM

Ageing at 400° C / 2 hours

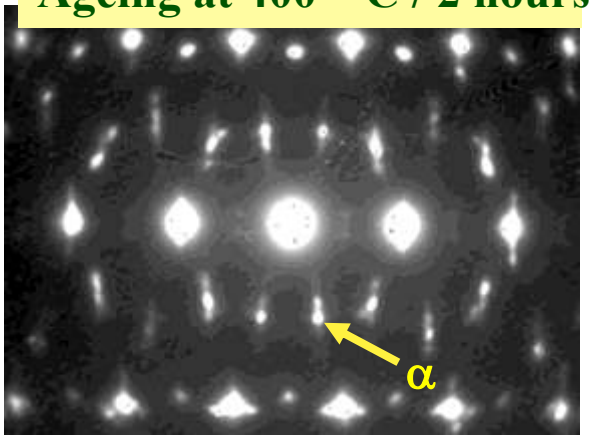

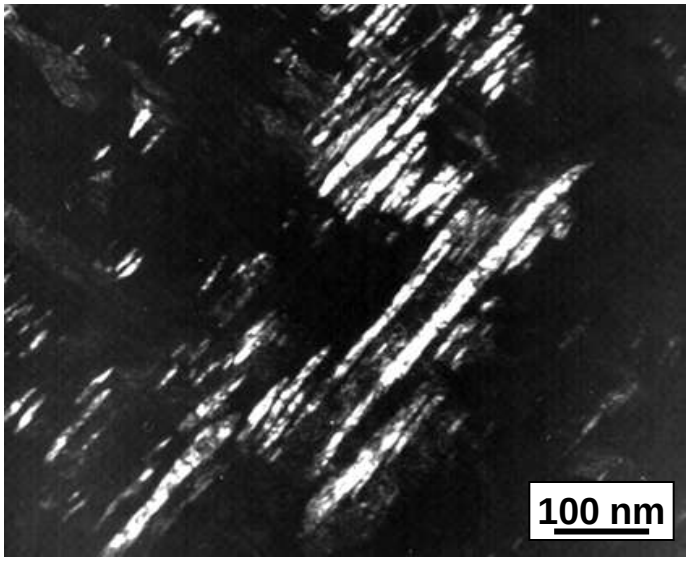

Dissolution of ω precipitates

Coarsening of α precipitates

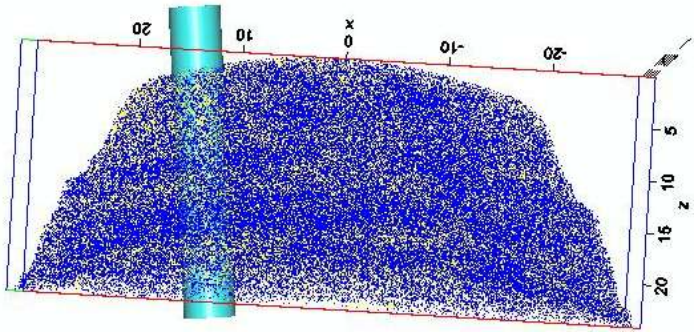

3D reconstruction of Al - blue, V - red, Cr - yellow atoms

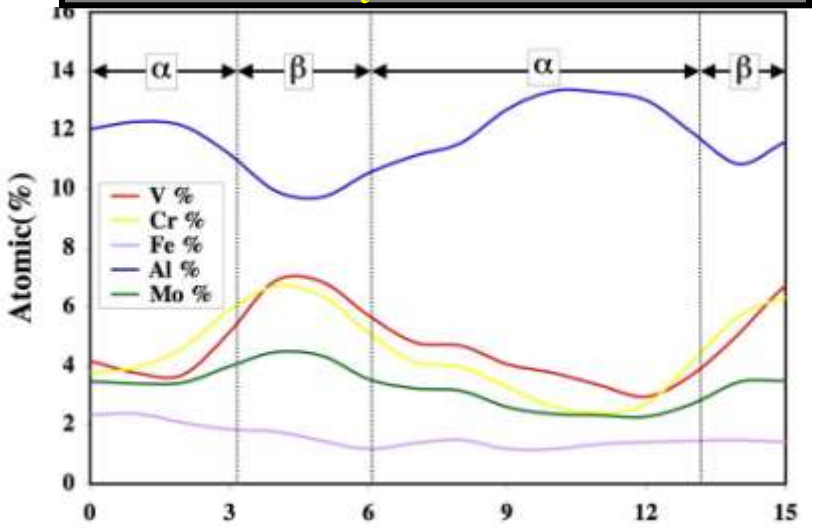

Small Al enrichment in α precipitate -
Al = 13.5 at% (avg. = 11 at%)

Far from equilibrium composition

Nag, Banerjee, Srinivasan, Harper, and, Fraser, *Acta Mater.* (2009)

HRTEM of α-platelets in 400° C/2 hrs annealed Ti-5553

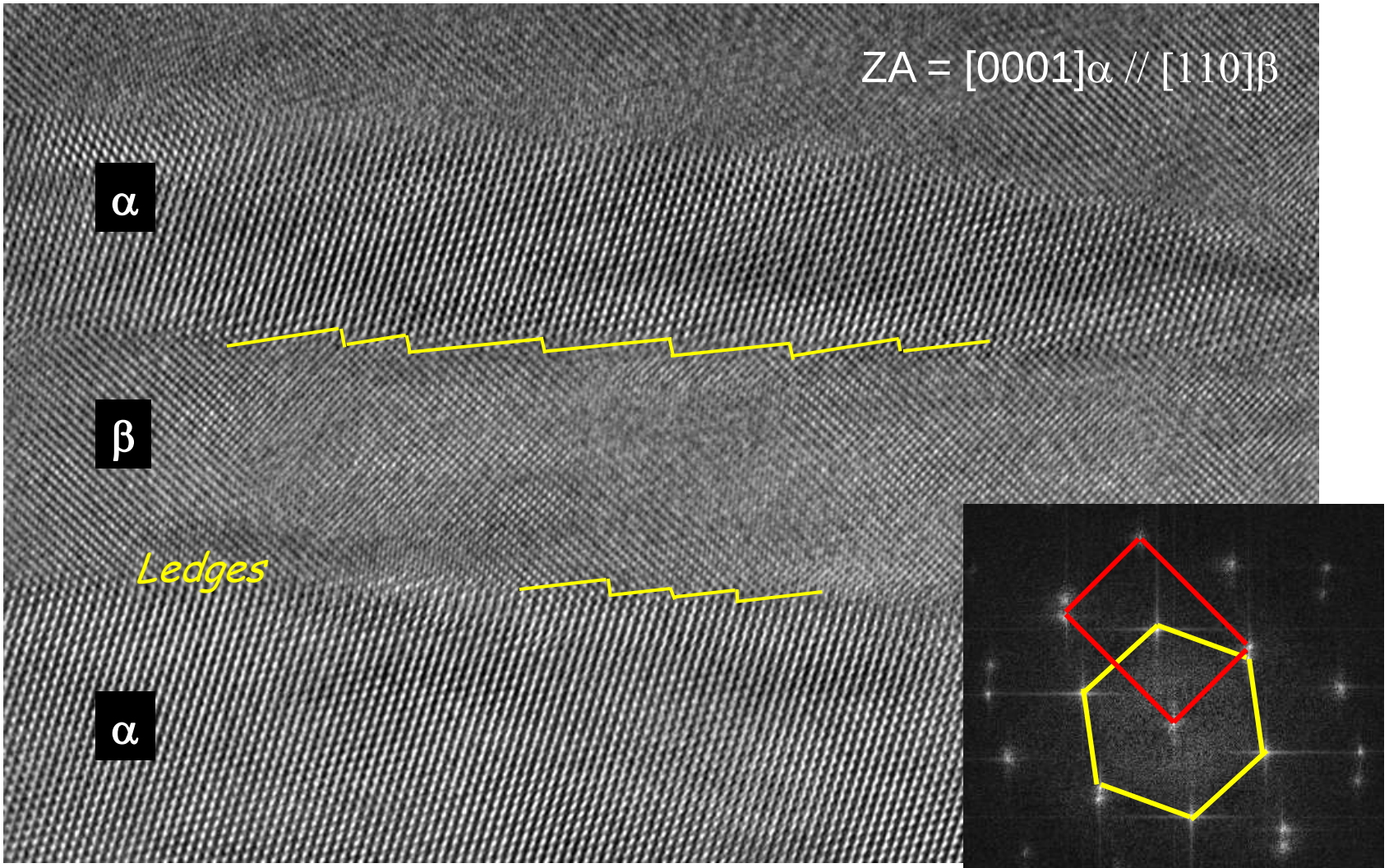

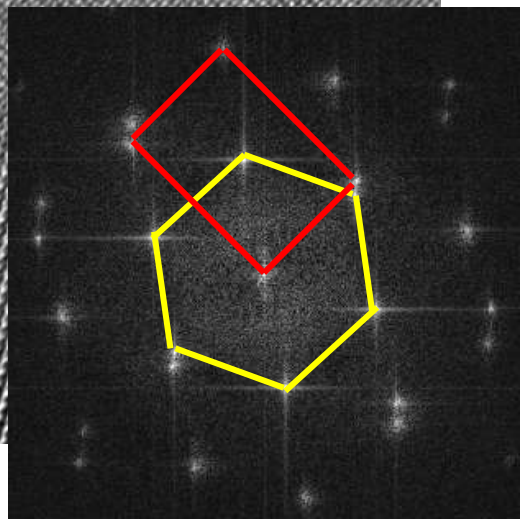

Burgers OR
(0001)α // (110)β
[11–20]α // [1–11]β

Clear evidence of ledges at the α/β interfaces

Nag, Banerjee, Srinivasan, Harper, and, Fraser, *Acta Mater.* (2009)

Nucleation and Growth of ω in β matrix

- **Early stages of formation of athermal ω precipitates when quenched from above β - transus temperatures**
  - ***Formation of ω nuclei - structural collapse of {111} β planes***
  - ***Compositional partitioning***

- **Isothermal growth of ω precipitates during aging post quenching**
  - ***3D morphology of ω precipitates***
  - ***Compositional partitioning between β and ω during isothermal growth***

Alloy system studied:
Model alloy Ti-18Mo (wt%) or Ti-9Mo (at%) - binary alloy

Goal: Better understanding of β–ω transformation by coupling advanced microscopy techniques:
Aberration-corrected high-resolution HAADF-STEM – TITAN
3D atom probe - LEAP (nanoscale compositional analyses)

ω (hexagonal) Precipitation in β (bcc) Phase of Titanium

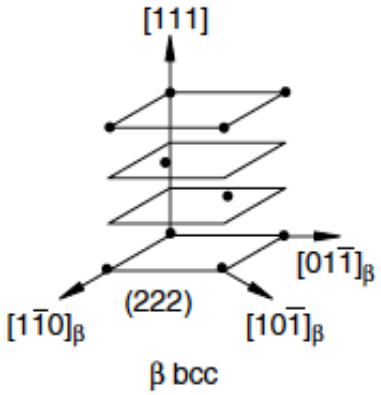

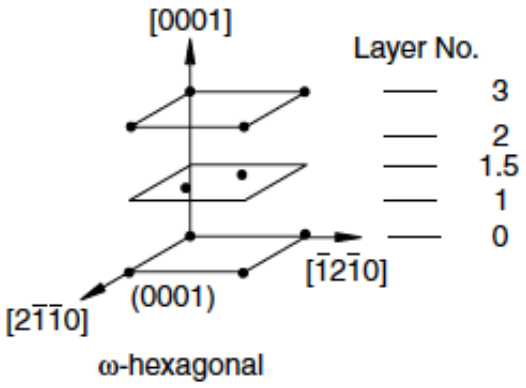

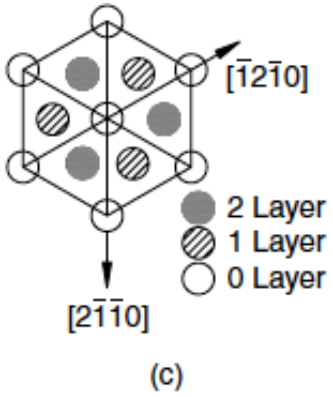

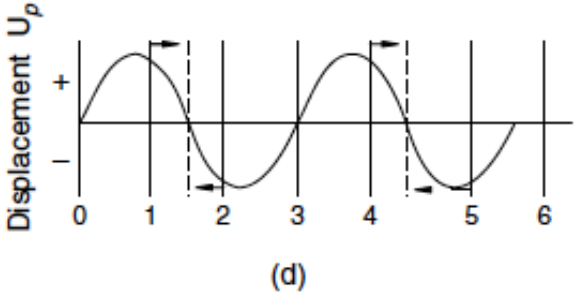

{111} planes of bcc β Stacked as *abcabca*…

0th and 3rd planes are undisplaced

1st and 2nd planes collapse into one plane

J. C. Williams, D. de Fontaine, and, N. E. Paton, Metall. Trans. A, 4, 2701 (1973)
D. de Fontaine, N. E. Paton, and, J. C. Williams, Acta Metall., 19, 1153 (1971)

Ti-9Mo (β solutionized + water quenched)

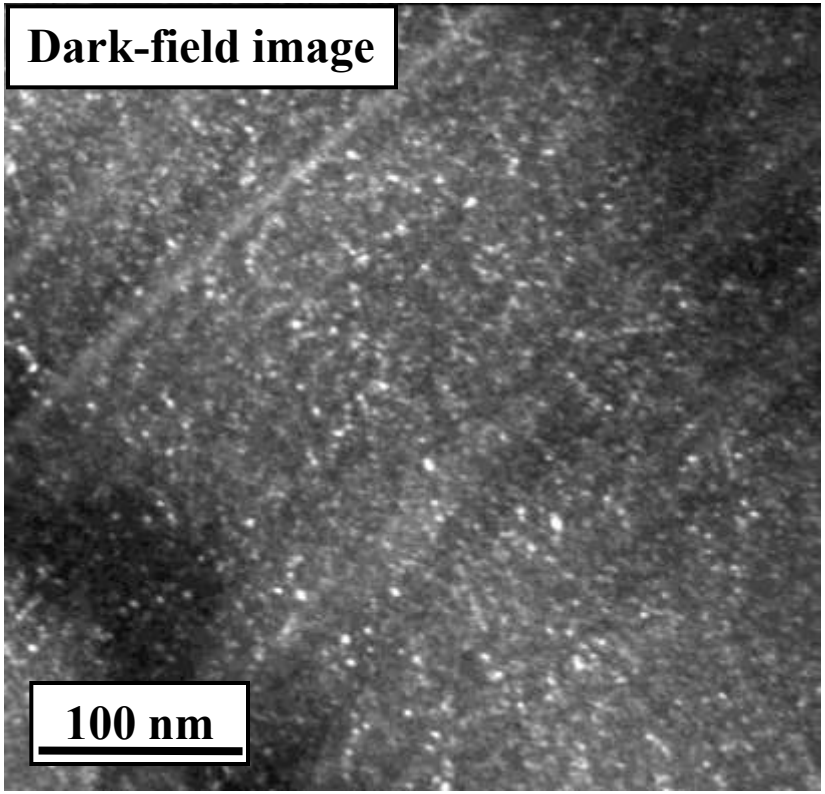

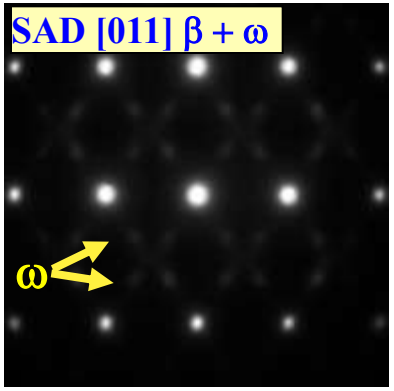

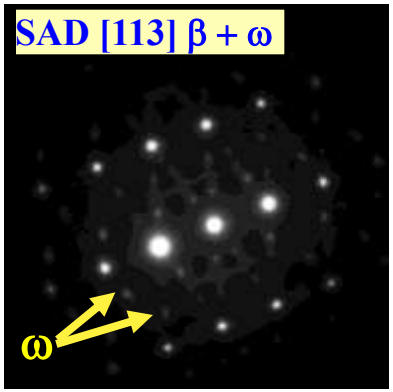

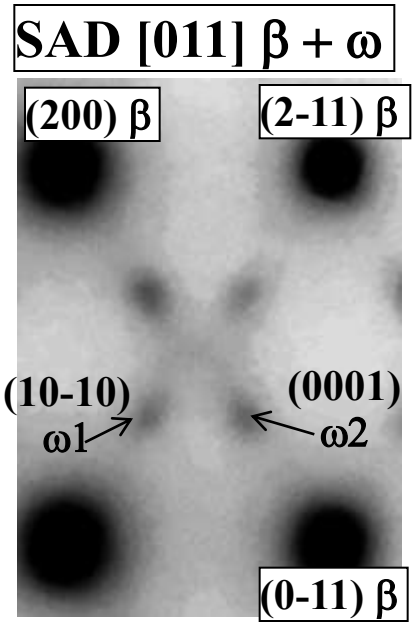

- Nanometer scale homogeneously distributed athermal ω preciptates
- Diffraction patterns - *Intensity maxima developing at 1/3 and 2/3 {112}β locations* – early stages of formation of ω preciptates

HRTEM of Ti-18Mo (β-soln. + water-quenched)

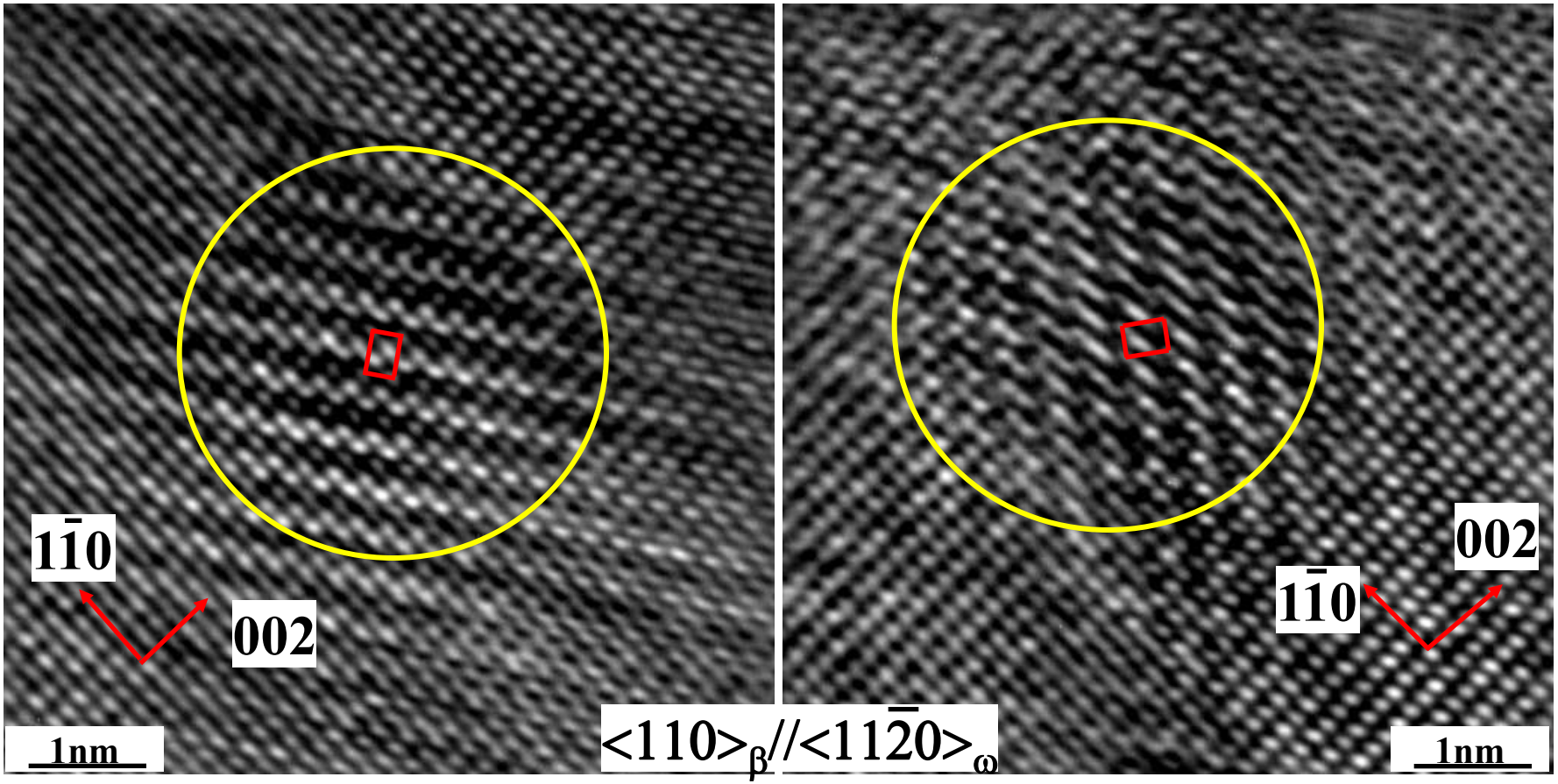

- HRTEM images - early stages of formation of ω precipitates
- Change in structure between β matrix and ω precipitates is clearly visible

HAADF-HRSTEM of Ti-9Mo (water-quenched)

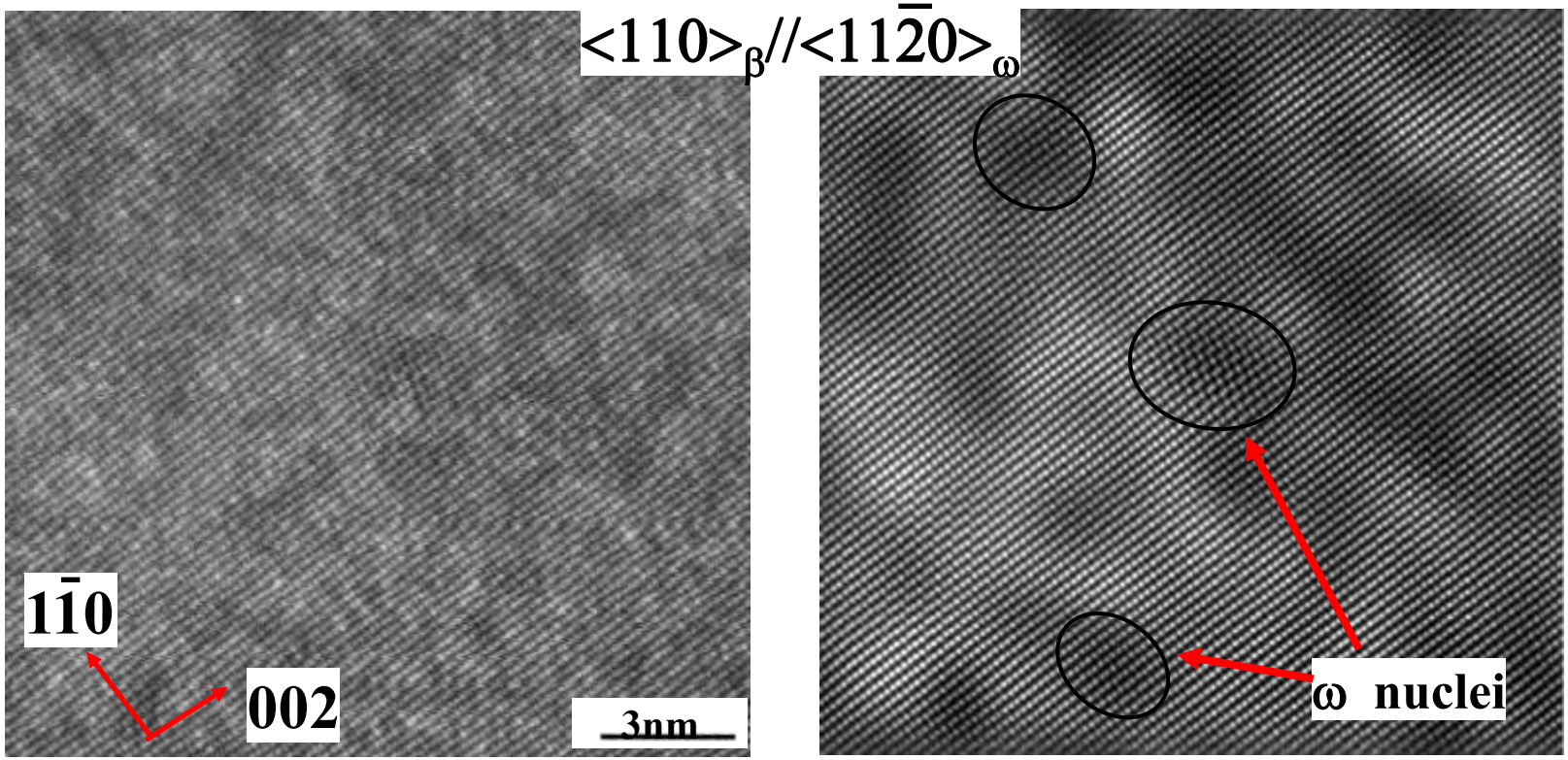

- Aberration-corrected HAADF-HRSTEM images - **early stages of formation of ω nuclei**
- Darker contrast in HAADF image corresponding to ω nuclei - **Diffusional partitioning of Mo? – *independent analysis using 3D atom probe required***
- **Displacement of atomic columns visible**

HAADF-HRSTEM of Ti-9Mo (water-quenched)

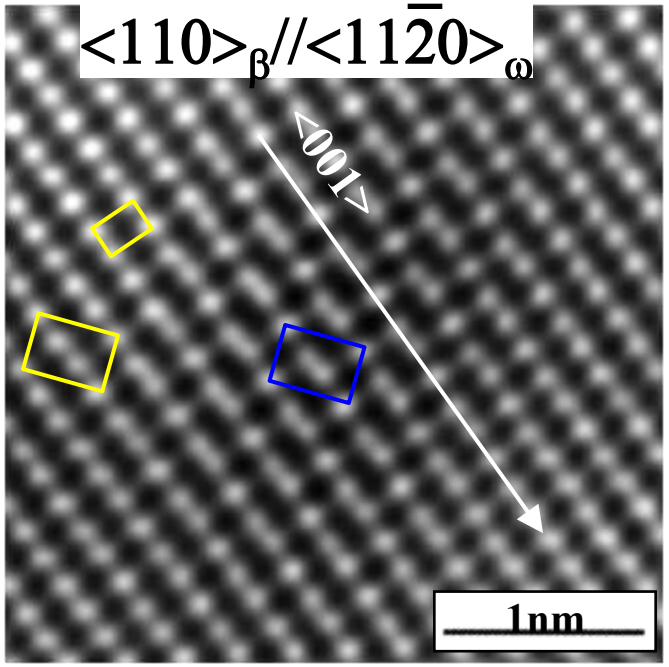

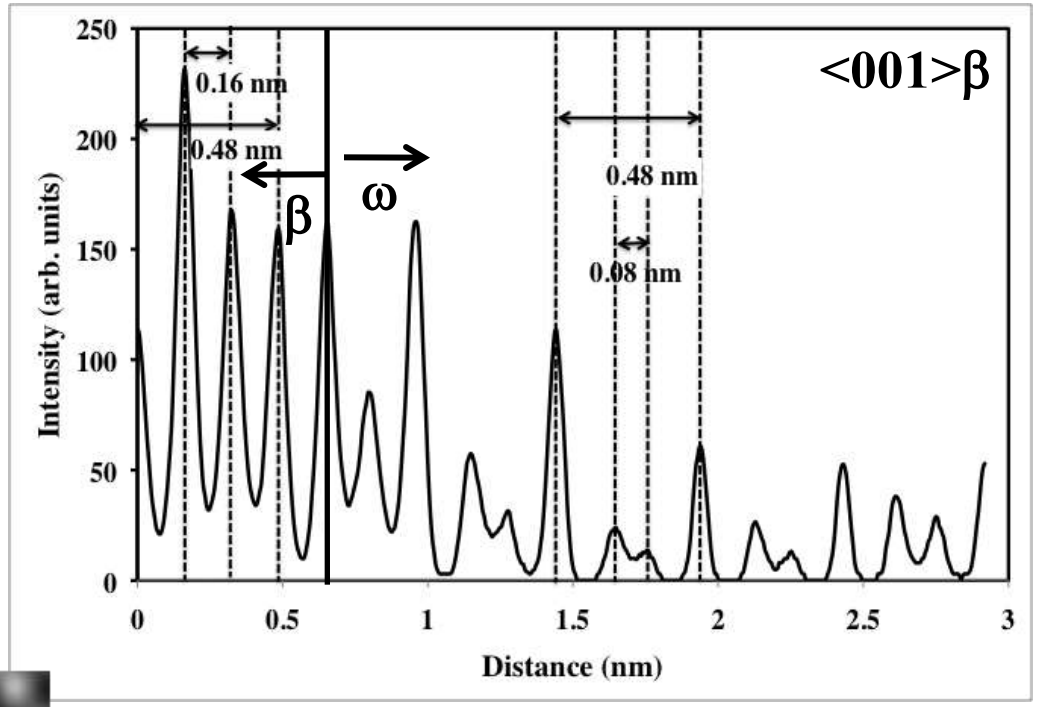

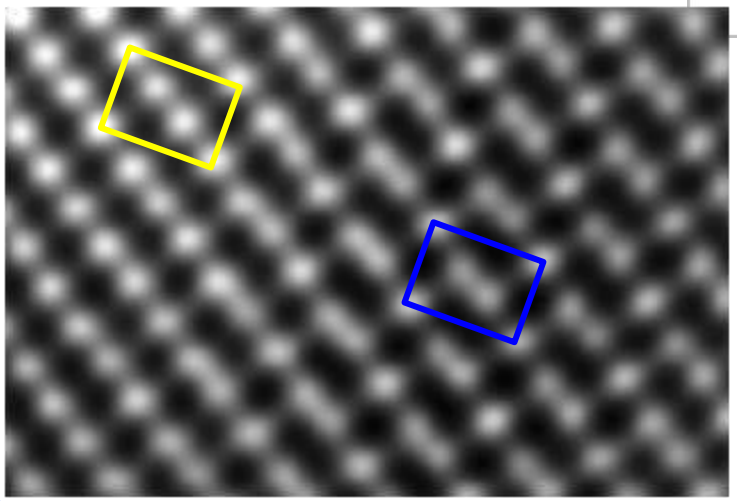

Partial collapse of β planes within ω nucleus

Quantifying the Displacement of {111} β Planes

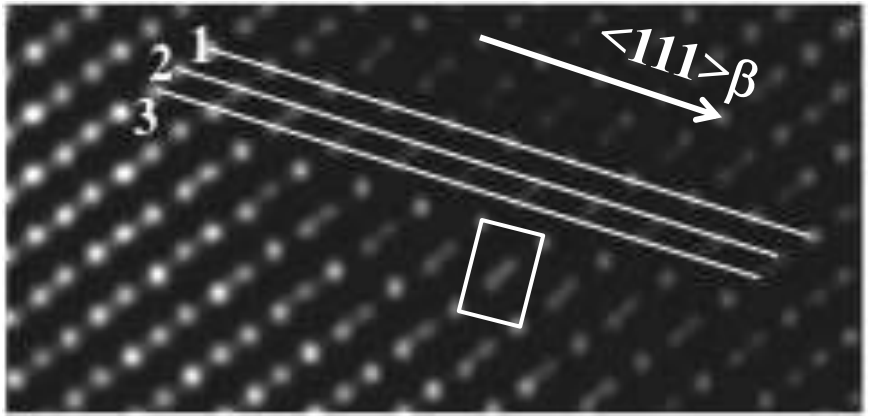

Partial collapse of {111} β planes within ω nuclei – *still not complete collapse*

Complete collapse corresponds to displacement of the {111} planes by $0.5d_{222}$

Maximum displacement observed = $0.2d_{222}$

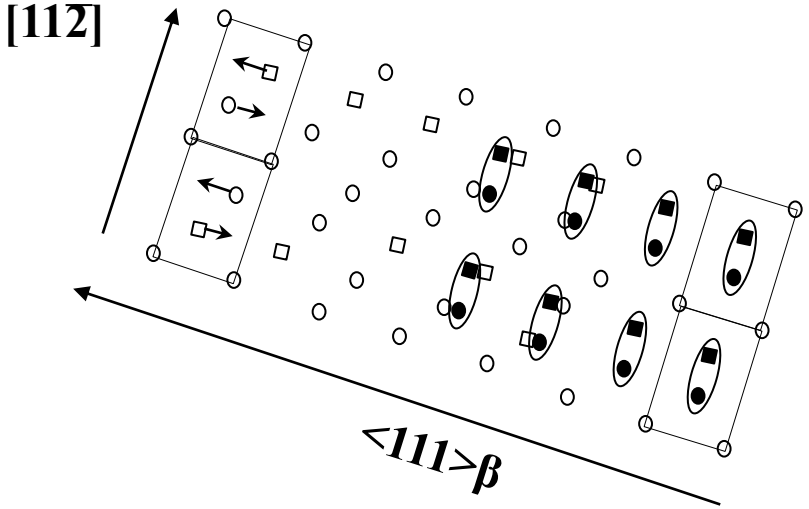

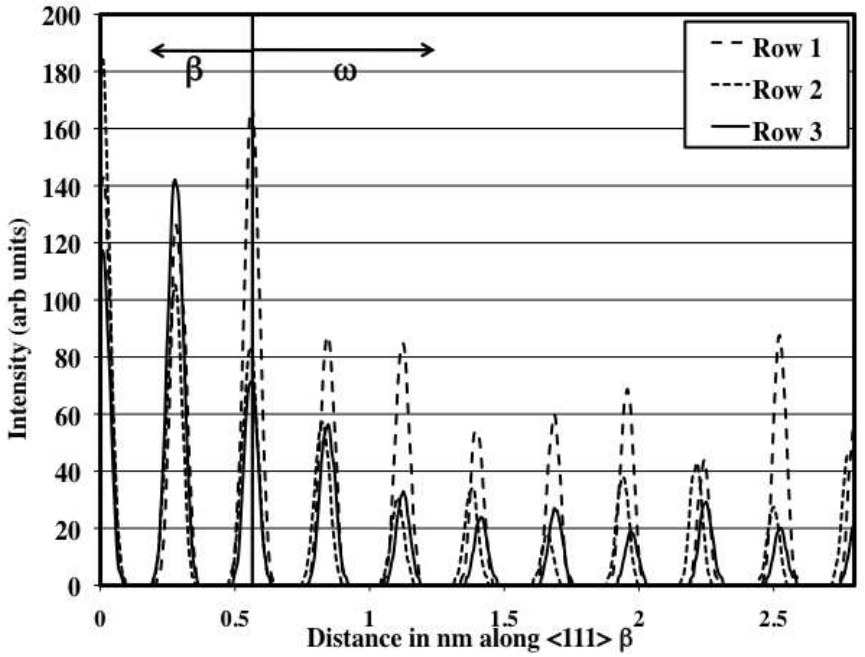

Peak Number	4	5	6	7	8	9	10
Fraction of d_{222}	0.12	0.14	0.17	0.17	0.14	0.20	0.14

3D atom probe: Ti-9Mo (β solutionized + water quenched)

Overall Composition:

Ti = 91.22at%, Mo = 8.78at%

Ti = 92% isosurface (blue)

Mo = 8% isosurface (red)

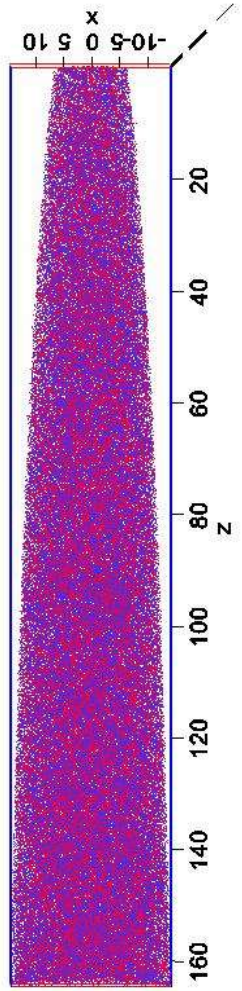

- **Some compositional partitioning of Ti and Mo based on iso-concentration surfaces**
- ***Statistical relevance needs to be determined***

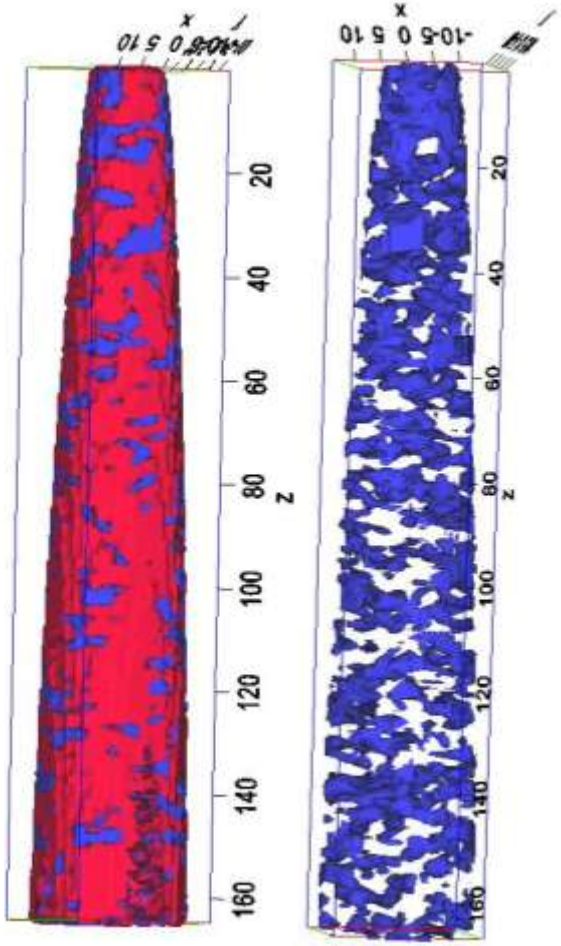

3D atom probe: Composition fluctuations in Ti-9Mo

Overall Composition:

Ti = 91.22at%, Mo = 8.78at%

- **Compositional fluctuations in Mo content**

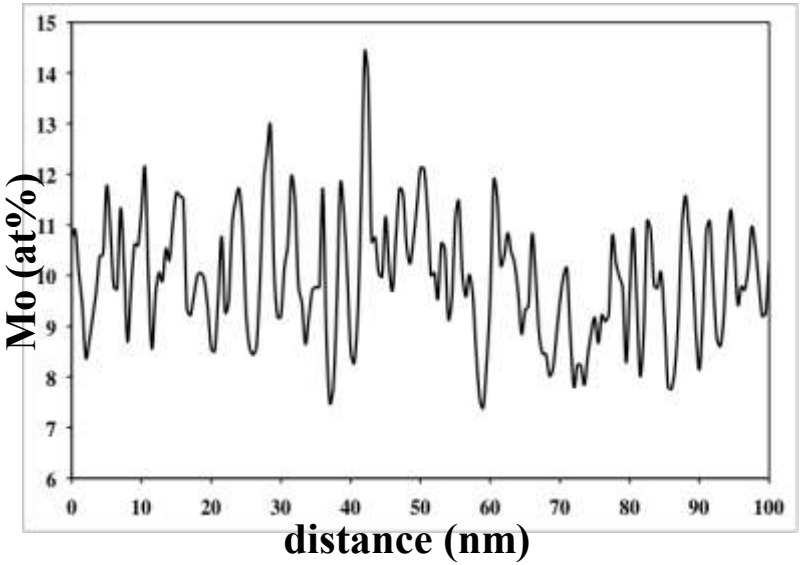

Statistical relevance – *Frequency distribution plot for 100 atom bins of Ti*

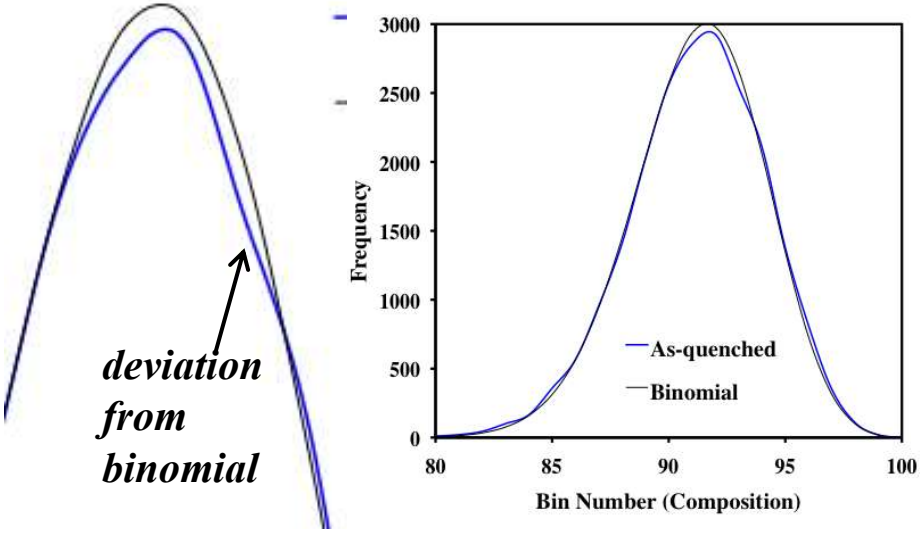

Iso-surface Ti = 93% (blue)

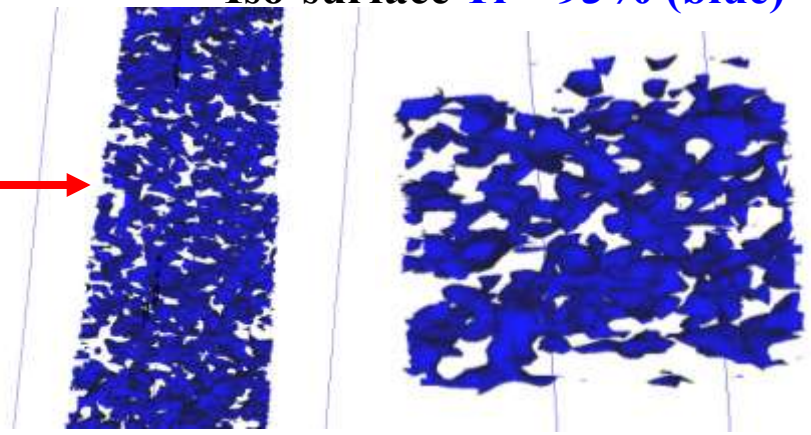

Interconnected network of marginally Ti-rich regions

Phase separation in β matrix prior to ω nucleation?

Ti-9Mo β solutionized + WQ - RDF function

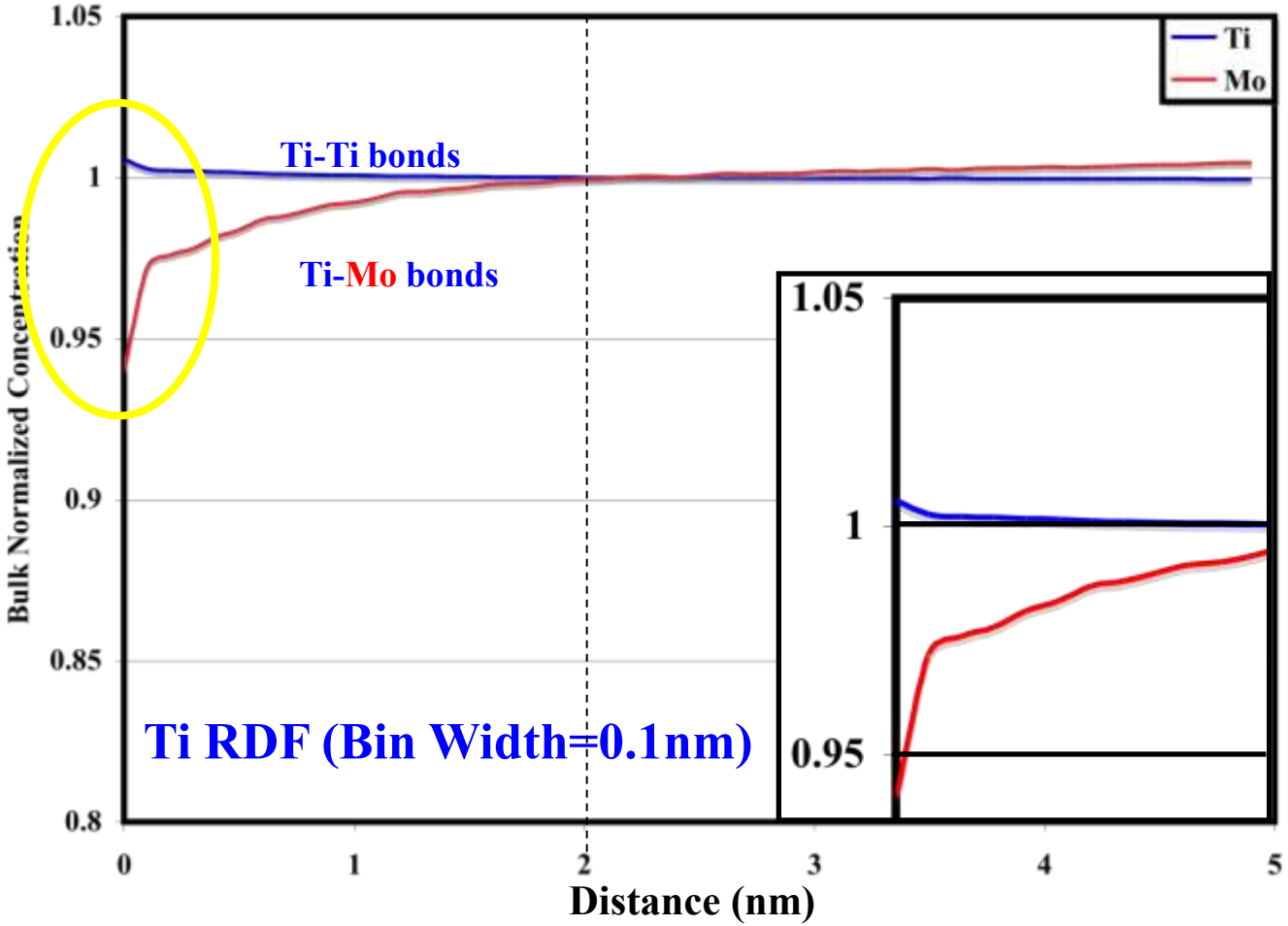

Ti- Ti bonds favored over Ti-Mo bonds -> Clustering tendency

Average alloy composition: Ti-8.8at%Mo

Phase separation into ~Ti-6at%Mo and ~Ti-9at%Mo regions

Ti-9Mo (β soln. + WQ + 475° C/30 mins)

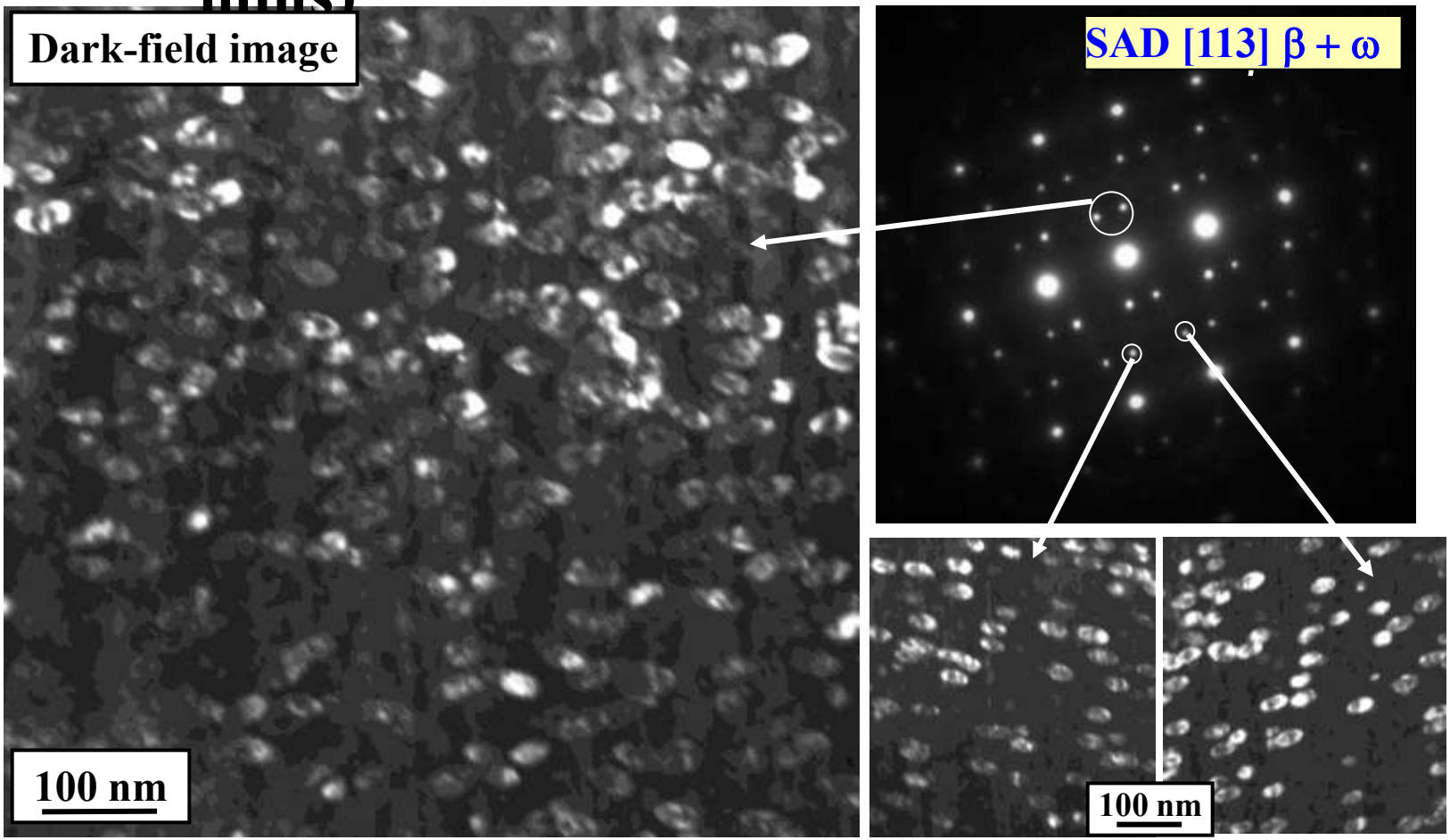

- Growth and coarsening of ω precipitates as compared with as-quenched
- *Sharper intensity maxima at 1/3 and 2/3 {112}β – structurally well developed ω precipitates*

Ti-9Mo (β soln. + WQ + 475° C/30 mins)

HRTEM images of ω/β interfaces

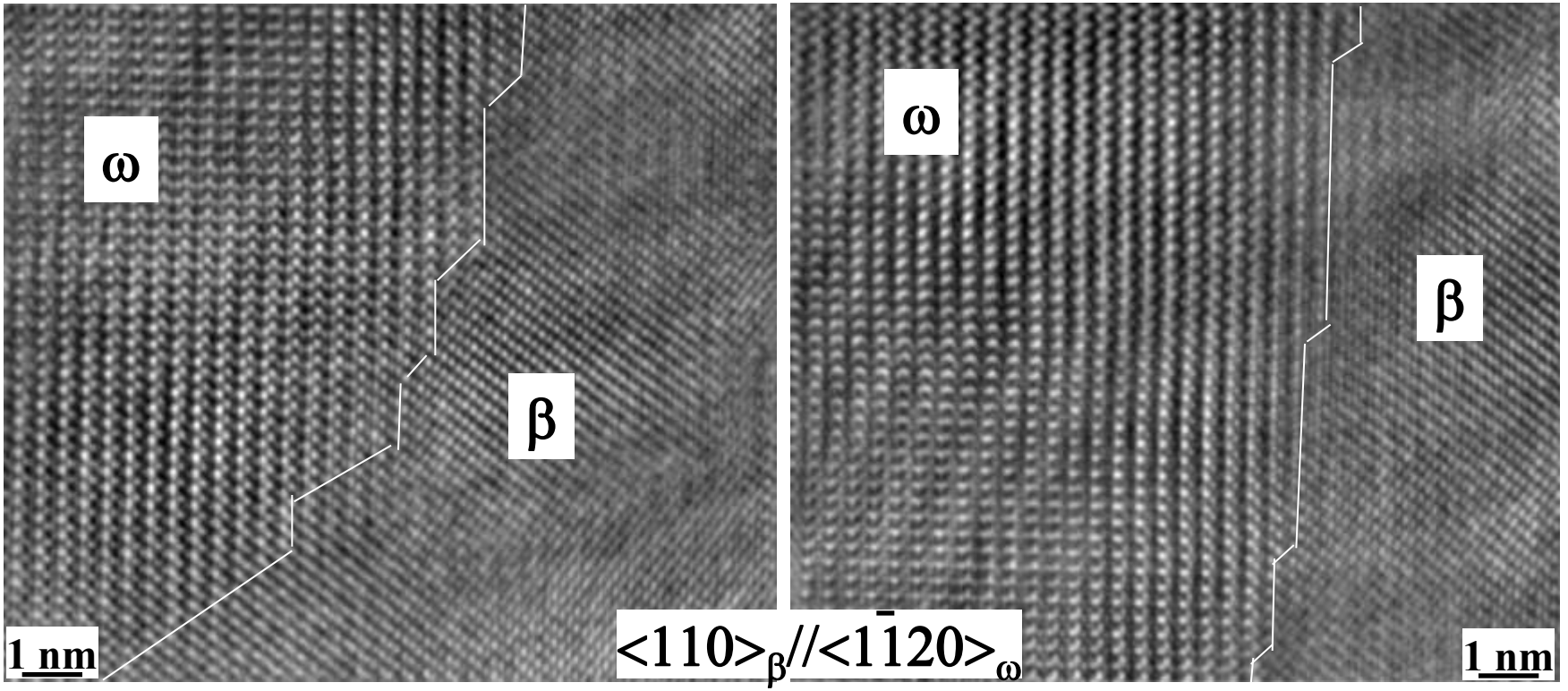

- Ledges present at ω/β interfaces
- *Displacive component involved in the isothermal β➔ω transformation*

HRTEM of Ti-9Mo (β soln. + WQ + 475° C/30 mins)

Ti-18Mo (β soln./quenched/475° C-30mins)

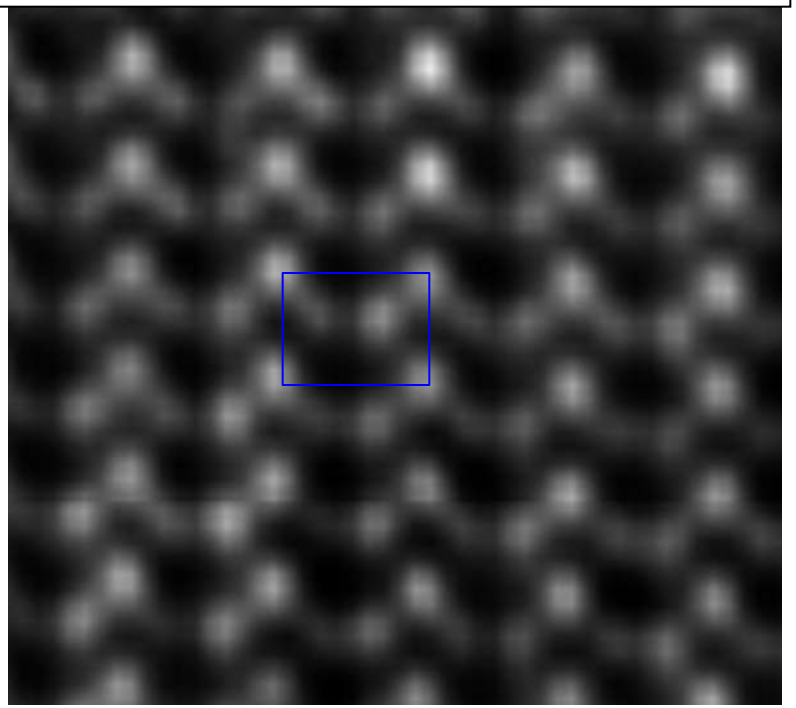

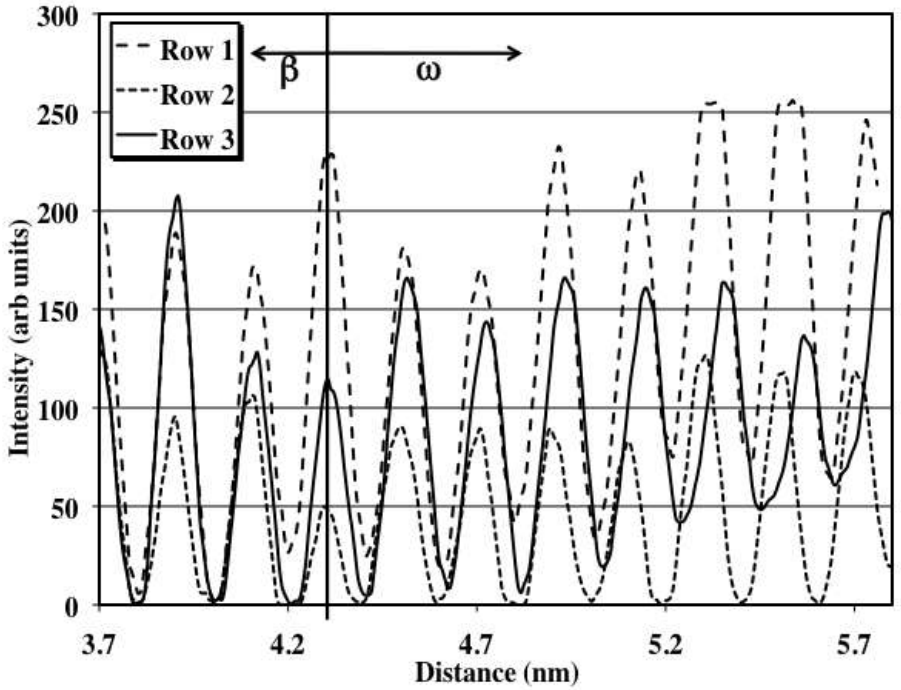

Peak number	24	25	26	27	28
Fraction of d_{222}	0.27	0.31	0.35	0.35	0.5

Full collapse of β planes within ω –
fully developed ω structure

3D atom probe: Ti-9Mo β soln. + WQ + 475° C/30mins

Overall Composition:

Ti = 90.52at%, Mo = 9.48at%

- ***ω – precipitates depleted in Mo***
- ***3D morphology of ω precipitates can be determined***

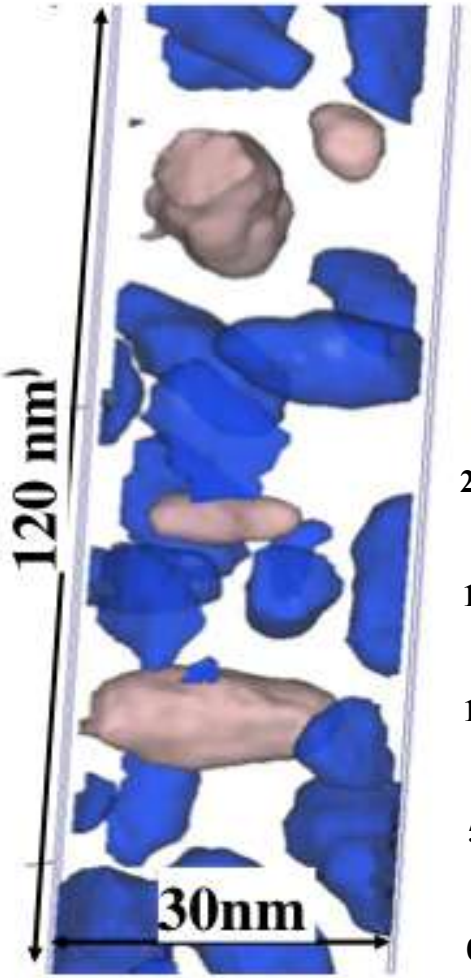

Ti = 92% isosurface (blue)

Mo ions (red)

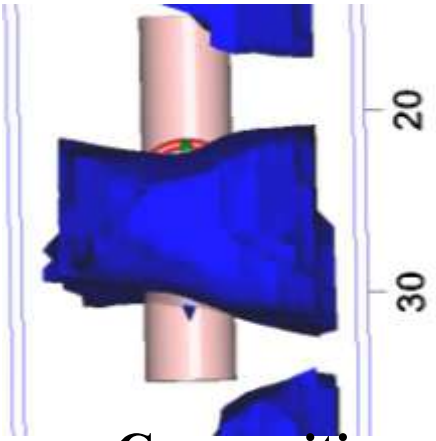

Omega Composition:

Ti = 95.4at%, Mo = 5at%

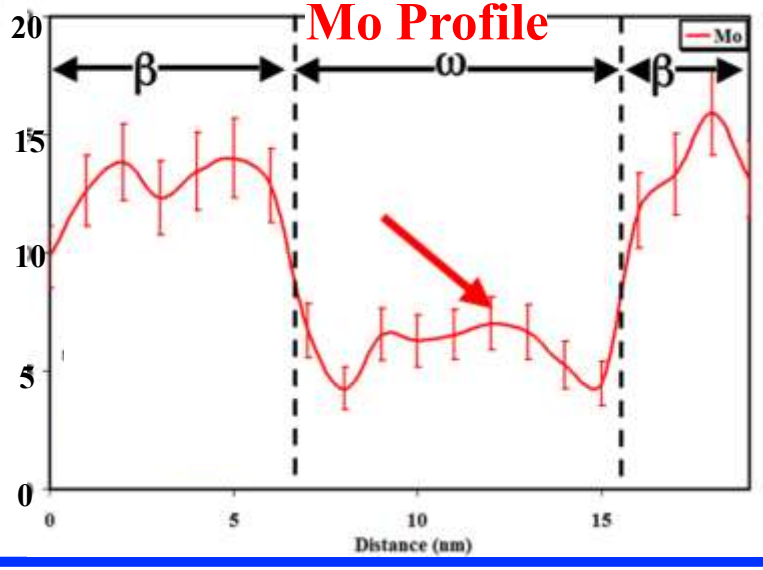

A. Devaraj et.al., Scripta Materialia,61, 701-704 (2009).

Summary

- **Mechanism of β→ω transformation not completely understood**
- **β solutionized and quenched Ti-18Mo exhibits fine scale ω embryos**
  - **Different stages of the collapse of {111} β planes – *aberration corrected HAADF-STEM***
  - **Clear evidence of Ti-Ti clustering from 3D atom probe – *3D atom probe***
  - ***Phase separation in β matrix prior to ω formation?***
- **Subsequent annealing at 475° C/30mins**
  - **well-developed ω precipitates – complete collapse of {111} β planes**
  - **Substantial partitioning of Mo between β and ω**

What do we learn from experiments?

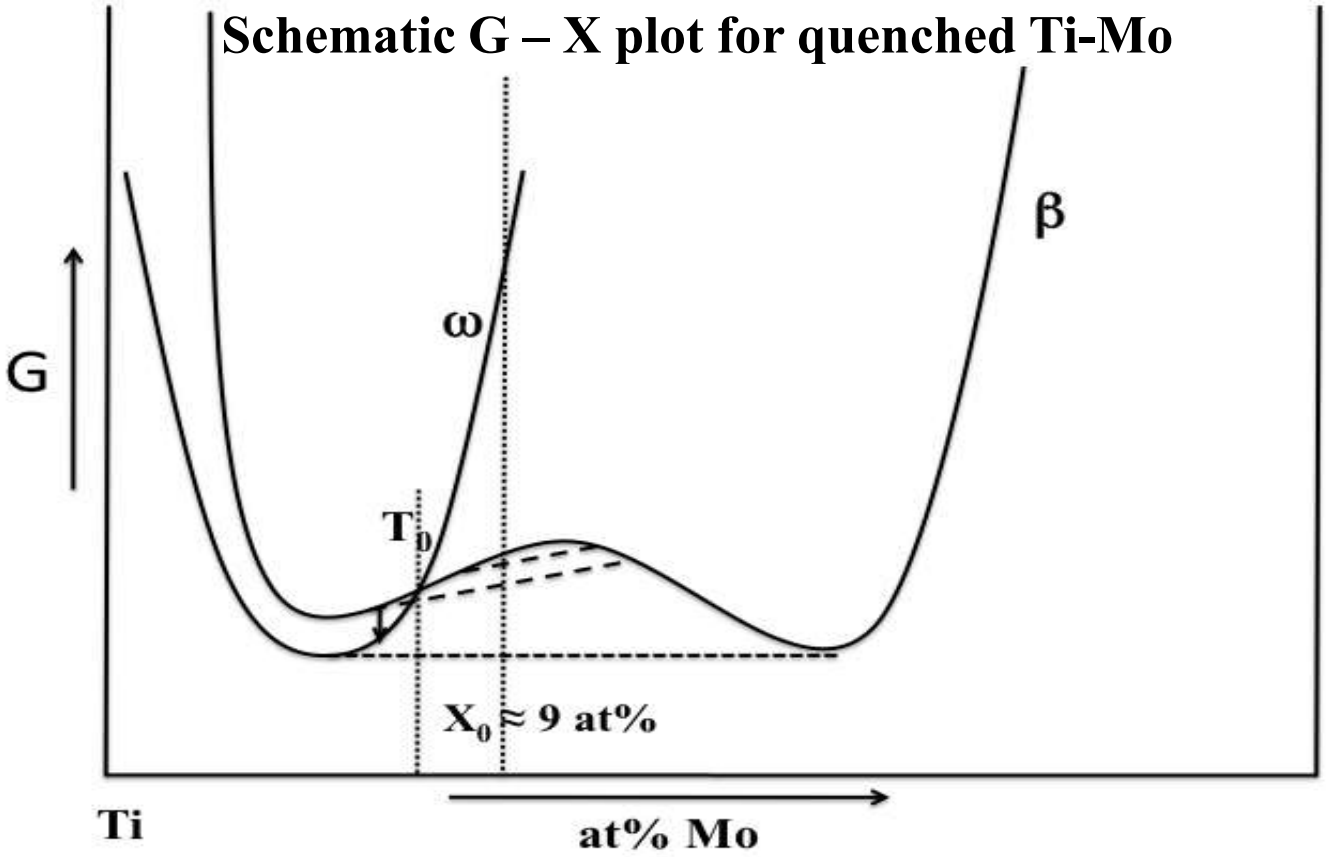

- Phase separation in β matrix required for ω formation in Ti-9at%Mo
- *Mo-depleted pockets with compositions < T_0 undergo displacive collapse to form ω nuclei*
- **Is the displacive collapse complete within ω nuclei?**

Schematic G – η plots for Ti-Mo

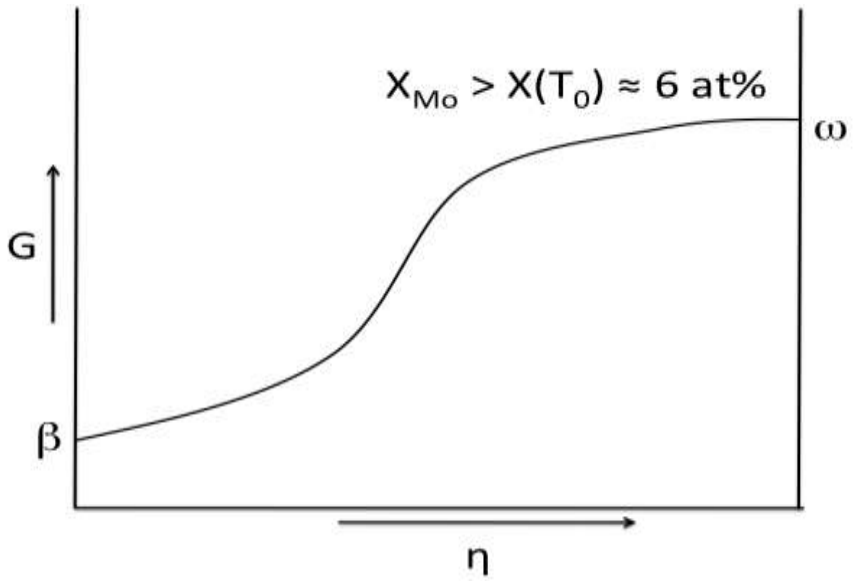

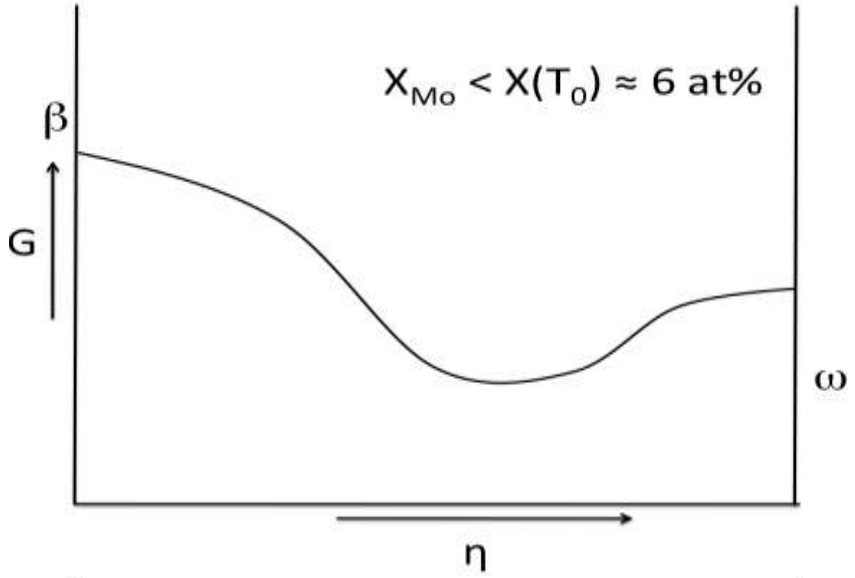

- ***Mo-depleted pockets with compositions < T_0 undergo displacive collapse to form ω nuclei***
- **Extent of displacive collapse can be incomplete within ω nuclei – *composition dependent amplitude of phonon wave*?**

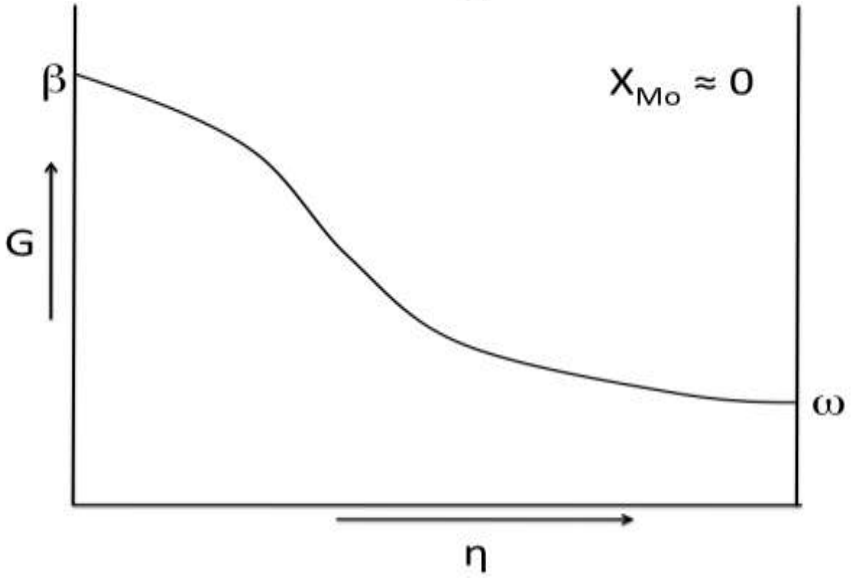

Questions

- **Is phase separation in β matrix mandatory for ω formation in Ti-18Mo (or Ti-9at%Mo)?**
- **Though ω forms via a displacive collapse of {111} β planes, *why is the collapse arrested (partial collapse) in quenched ω embryos***
  - **Is the extent of collapse dependent on the composition of the ω pocket? Why?**
- **Is there a mixed-mode displacive-diffusional transformation involved in the formation of isothermal ω precipitates?**
- ***We use first-principles calculations using the Vienna Ab Initio Simulation Package (VASP) coupled with the Nudged Elastic Band (NEB) transition path technique to investigate the β to ω transformation in Ti-Mo system***

Ti-5553 Summary of ω-assisted α nucleation

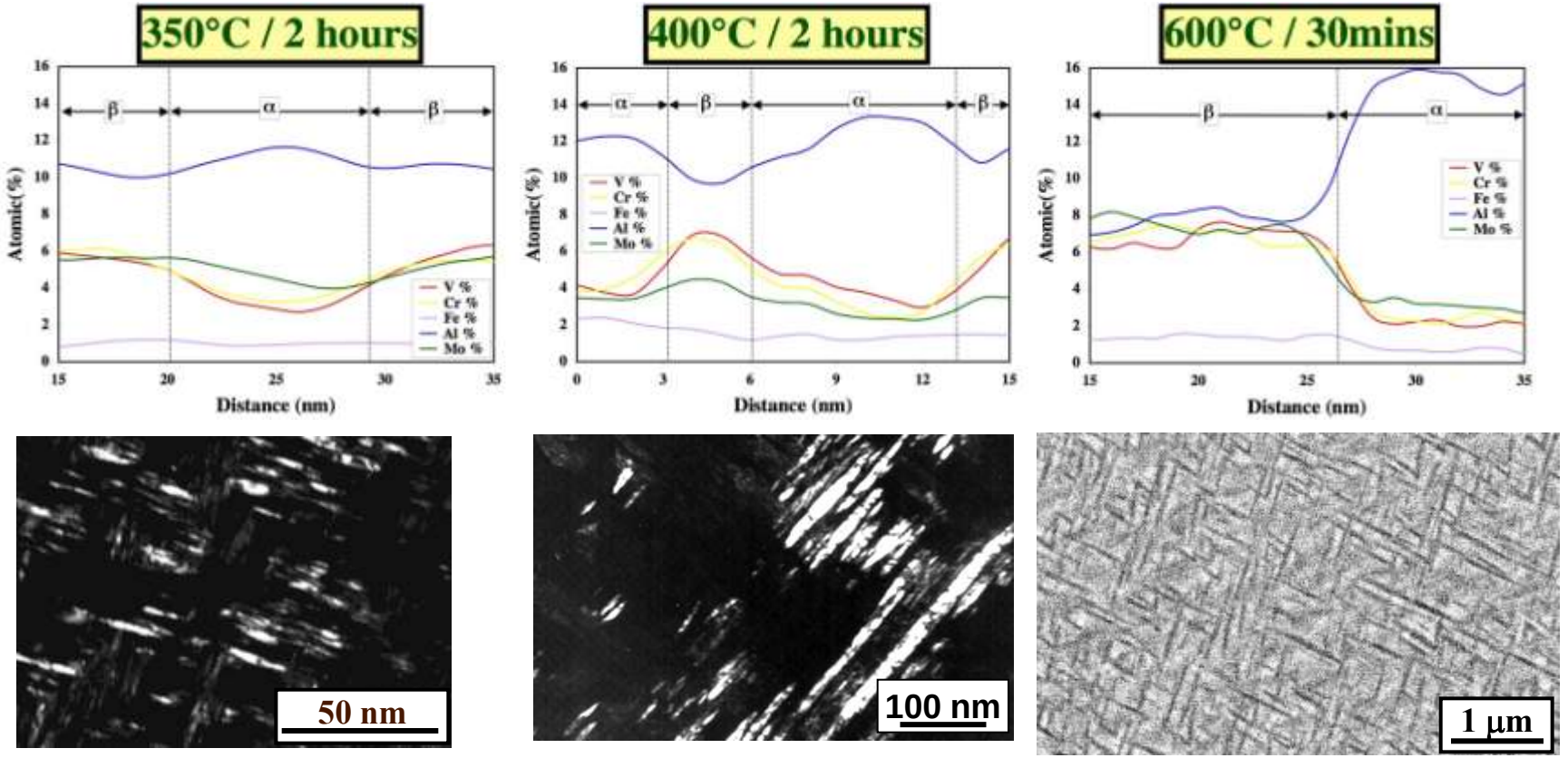

- Nucleation of α precipitates appears to be assisted by ω precipitates
- Nucleation of α precipitates at composition far-from equilibrium - *minimal partitioning of alloying additions between α and β phases*
- Structurally well-defined α platelets exhibiting *hcp* crystal structure formed in the early stages - *ledges at the α/β interface*

Nag, Banerjee, Srinivasan, Harper, and, Fraser, *Acta Mater.* (2009)

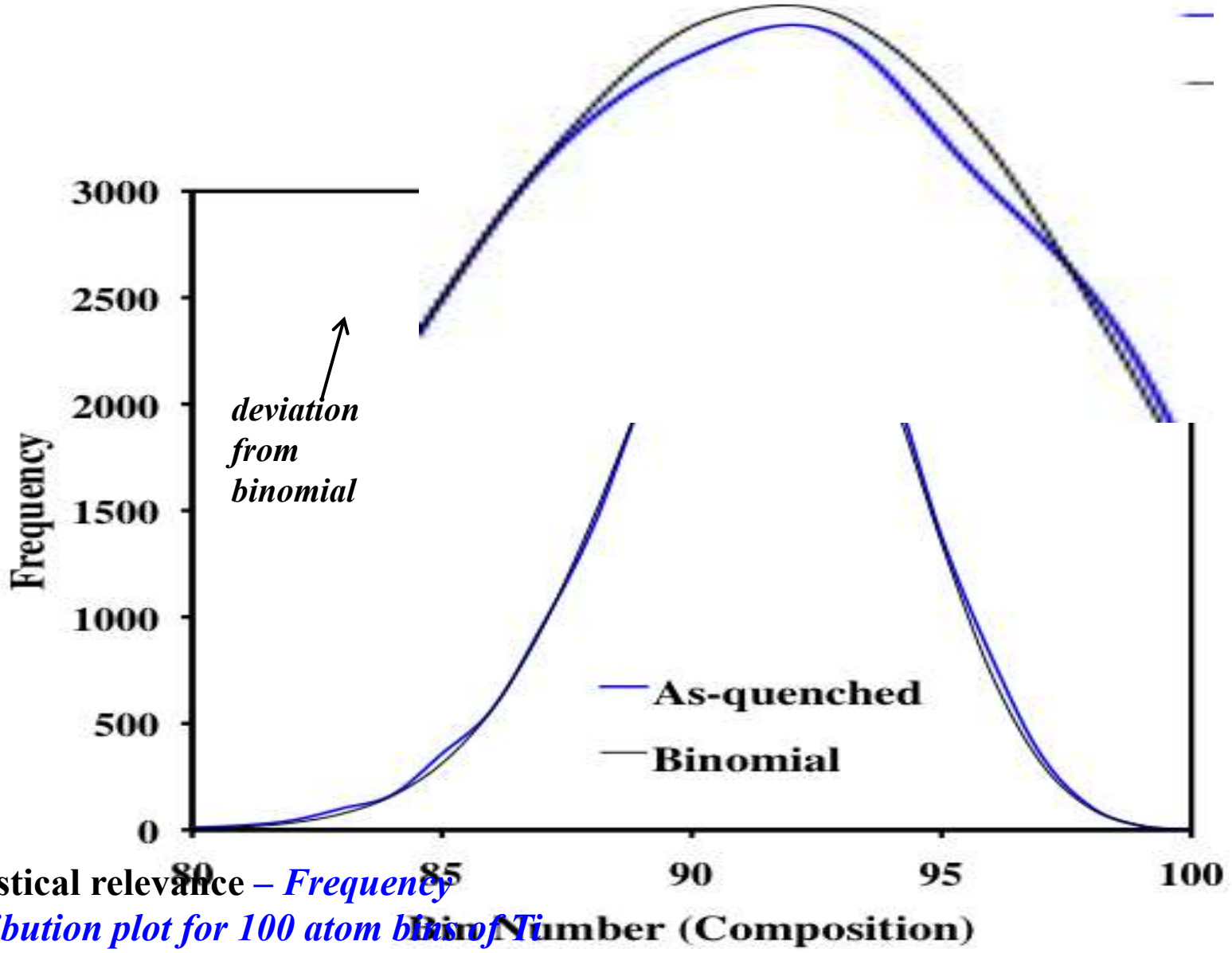

Statistical relevance – ***Frequency distribution plot for 100 atom bins of Ti***

Structural Evolution in the Process of Nucleation

Srikumar Banerjee

Department of Atomic Energy, India

Pacific Rim Workshop on Nucleation

May 2-7, 2010

What is Nucleation

- Creation of an assembly of atoms which **'represent'** the product phase

All symmetry elements of the product appear ⟹ At least one unit cell

"Structural Evolution in the Nucleation Process"

means

Probing the embryonic structures appearing during the evolutionary process ahead of nucleation

Outline

- How fluctuations in the earlier stage lead to the formation of nuclei ?
  - Chemical Ordering
  - Magnetic Ordering
  - Displacement Ordering
  - Mixed mode-displacement + chemical ordering

- Nucleation mediated by defects

Ordering – Chemical, ferromagnetic, ferroelectric

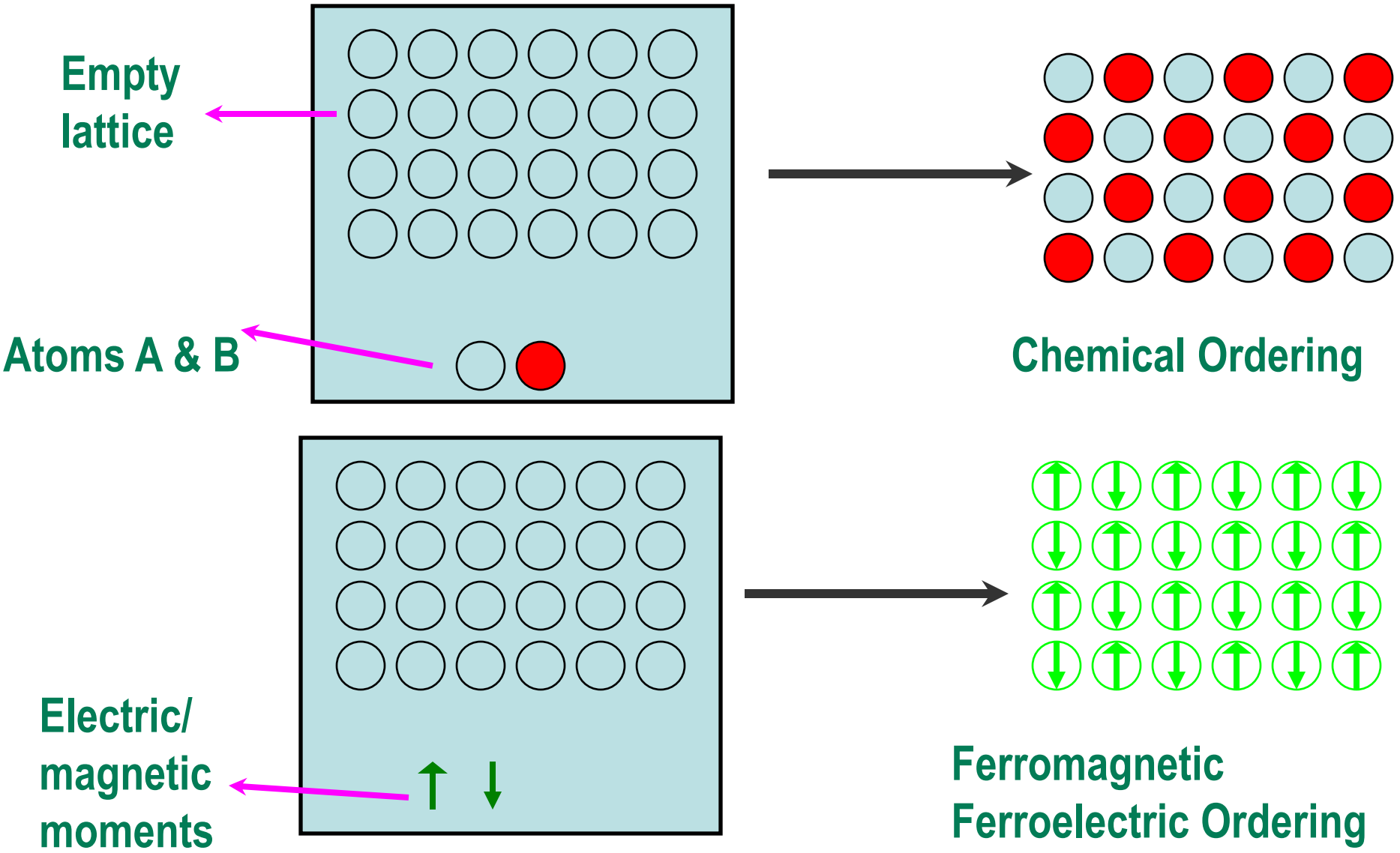

Ordering & Clustering Processes

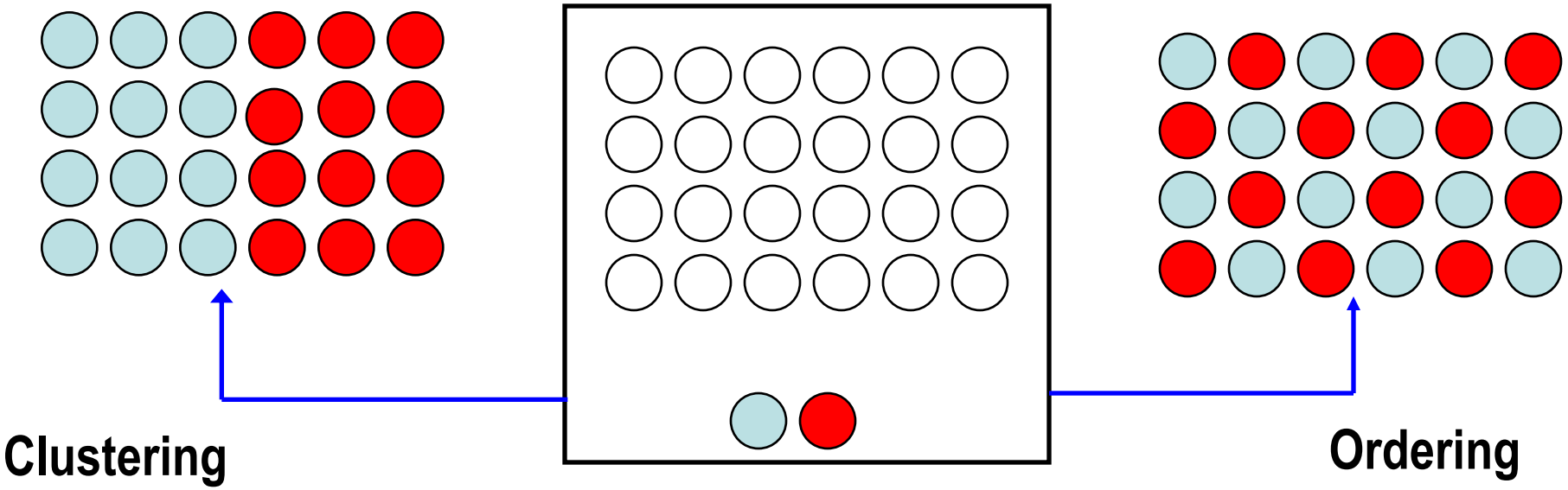

Disordered

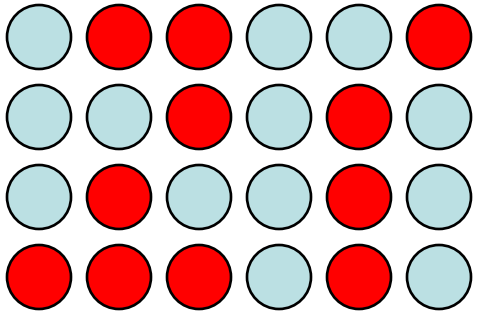

Ordering & Clustering tendencies are dictated by sign & magnitude of pair & multisite interaction potentials (J's)

Evolution of Ordering: Discrete Mode (Nucleation & Growth)

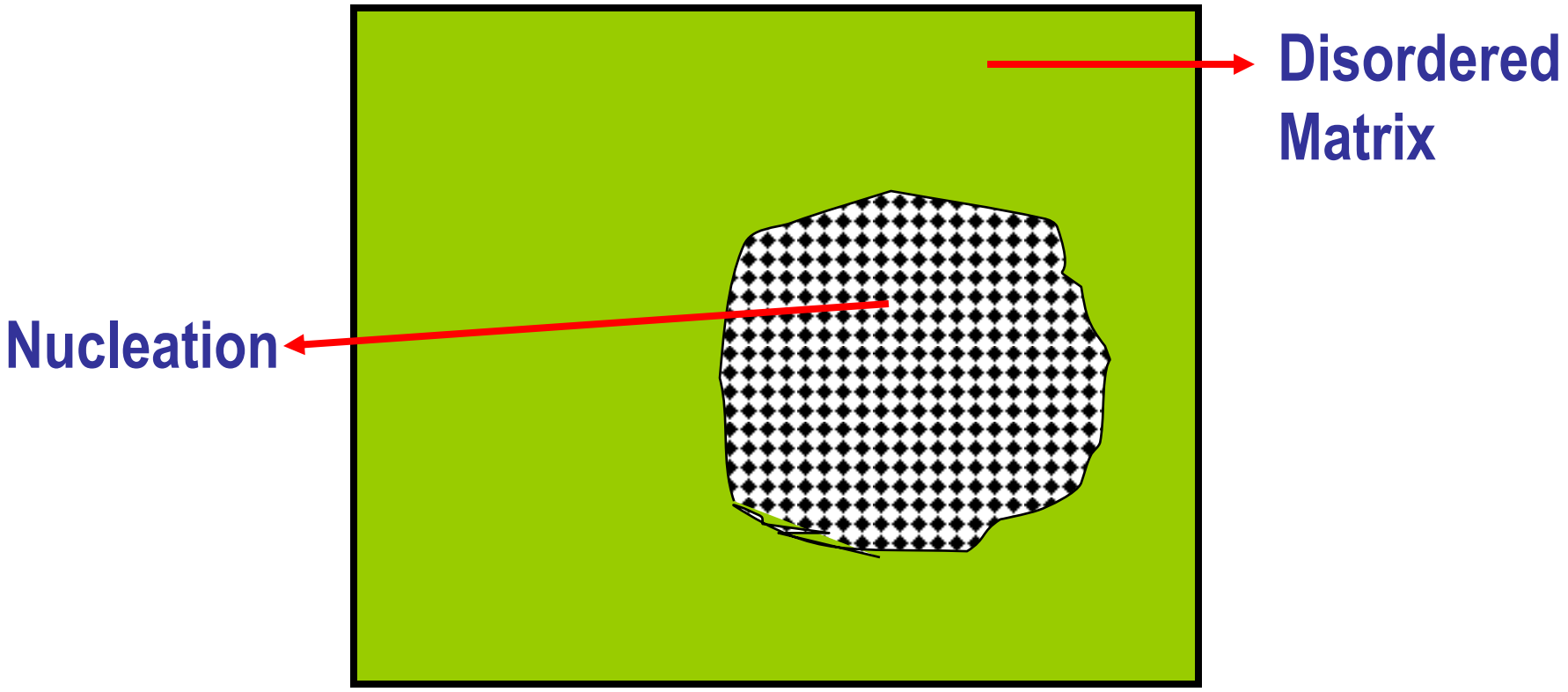

Continuous Ordering – Amplification of concentration wave

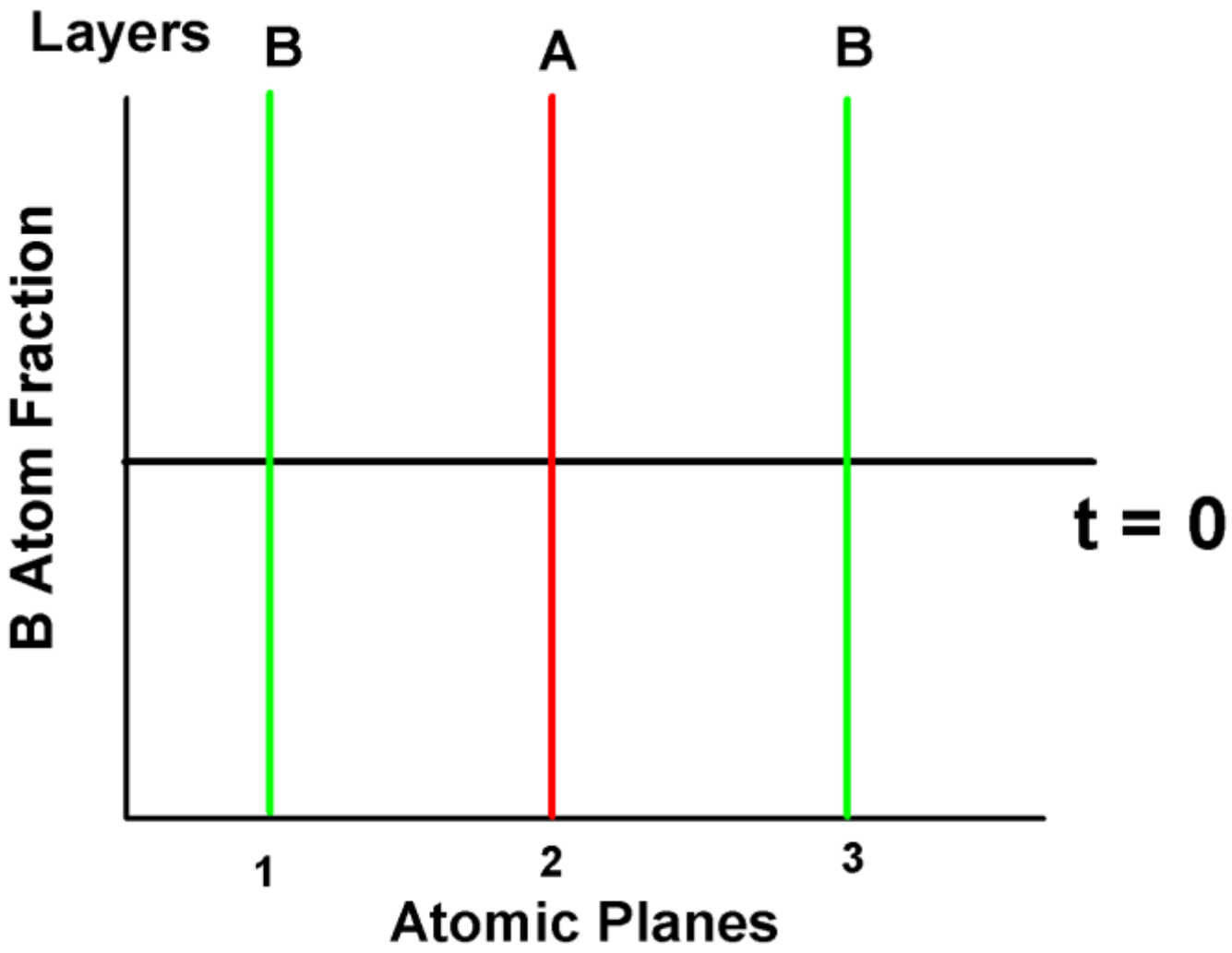

Continuous Ordering – Amplification of concentration wave

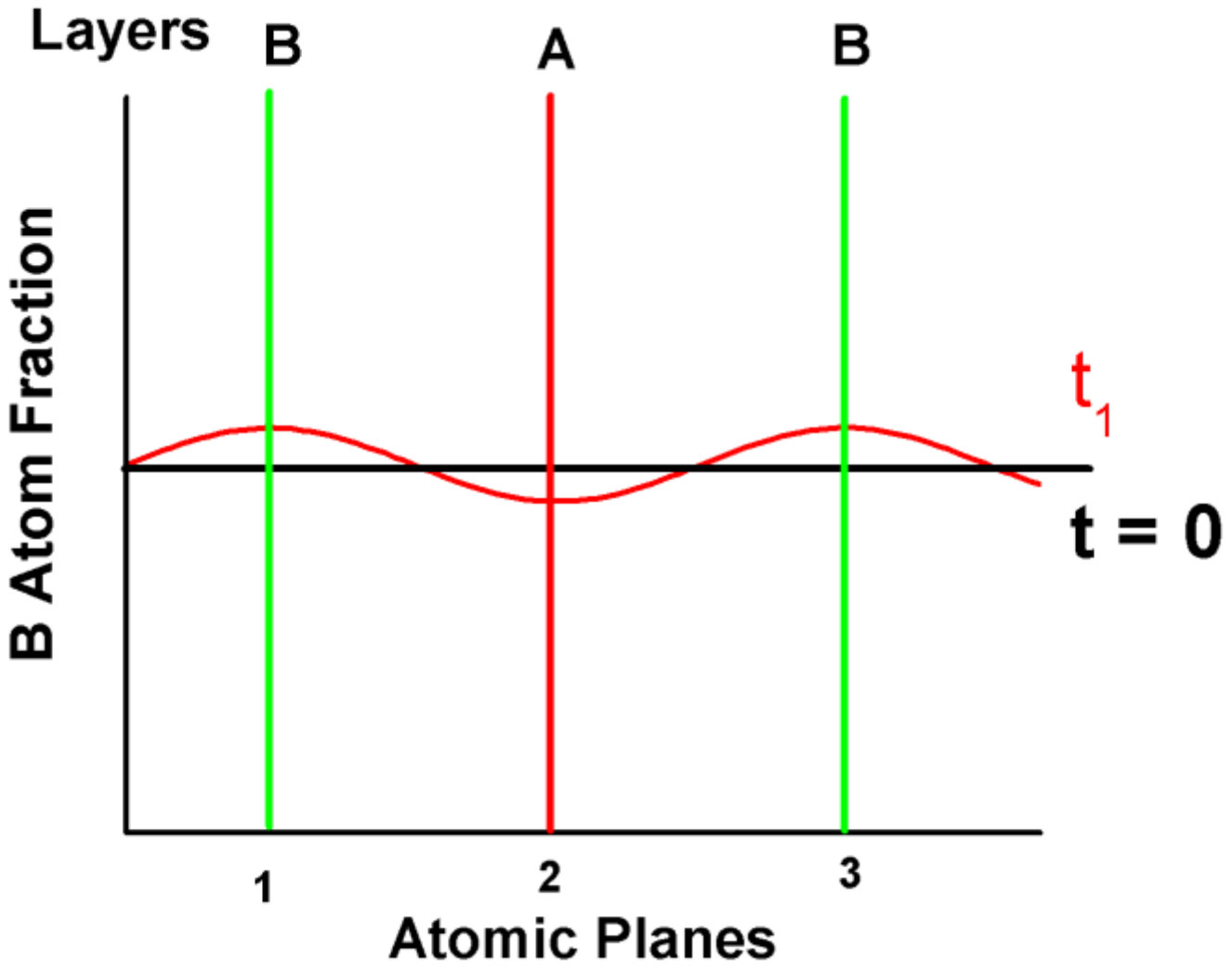

Continuous Ordering – Amplification of concentration wave

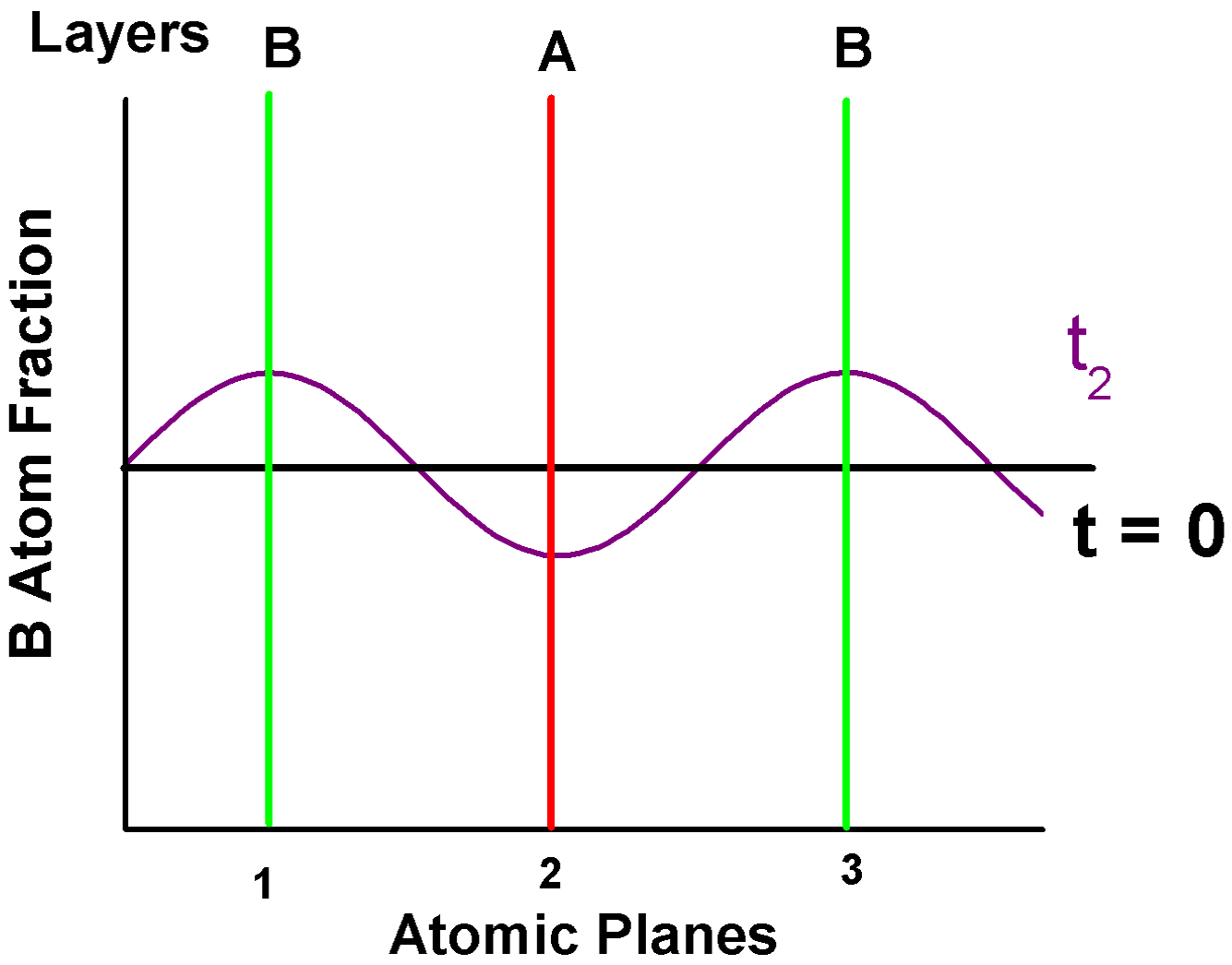

Continuous Ordering – Amplification of concentration wave

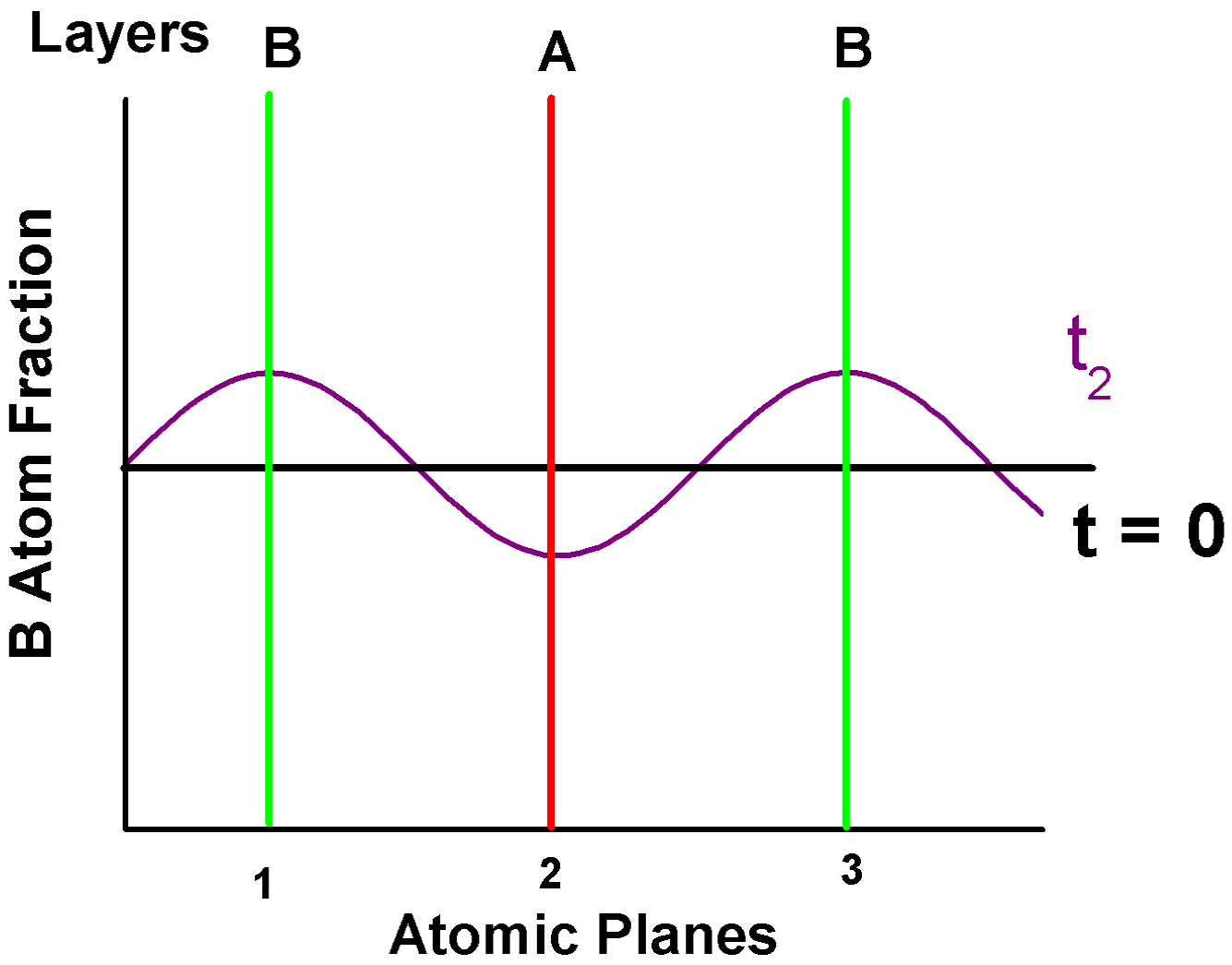

Continuous Ordering – Amplification of concentration wave

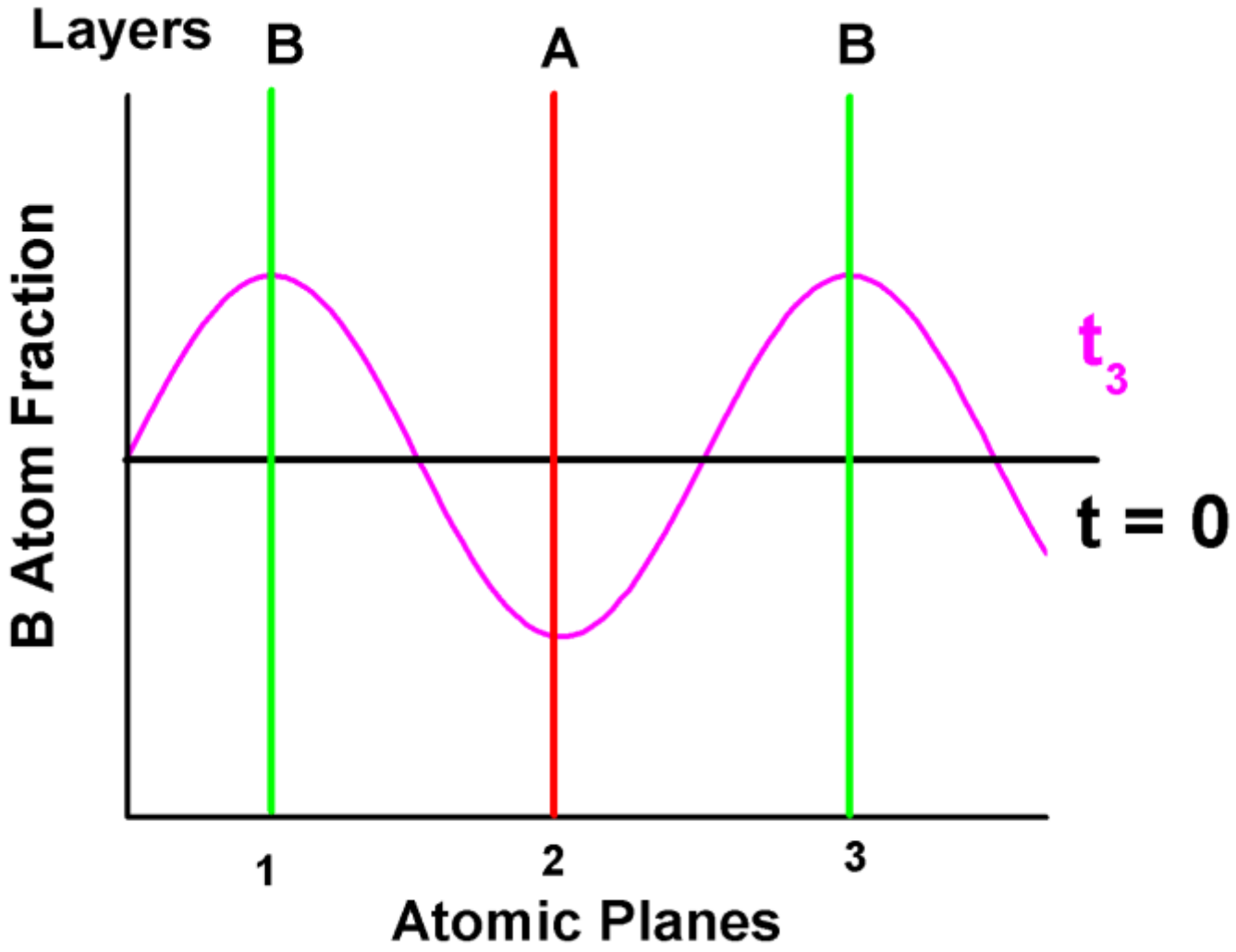

Continuous Ordering – Amplification of concentration wave

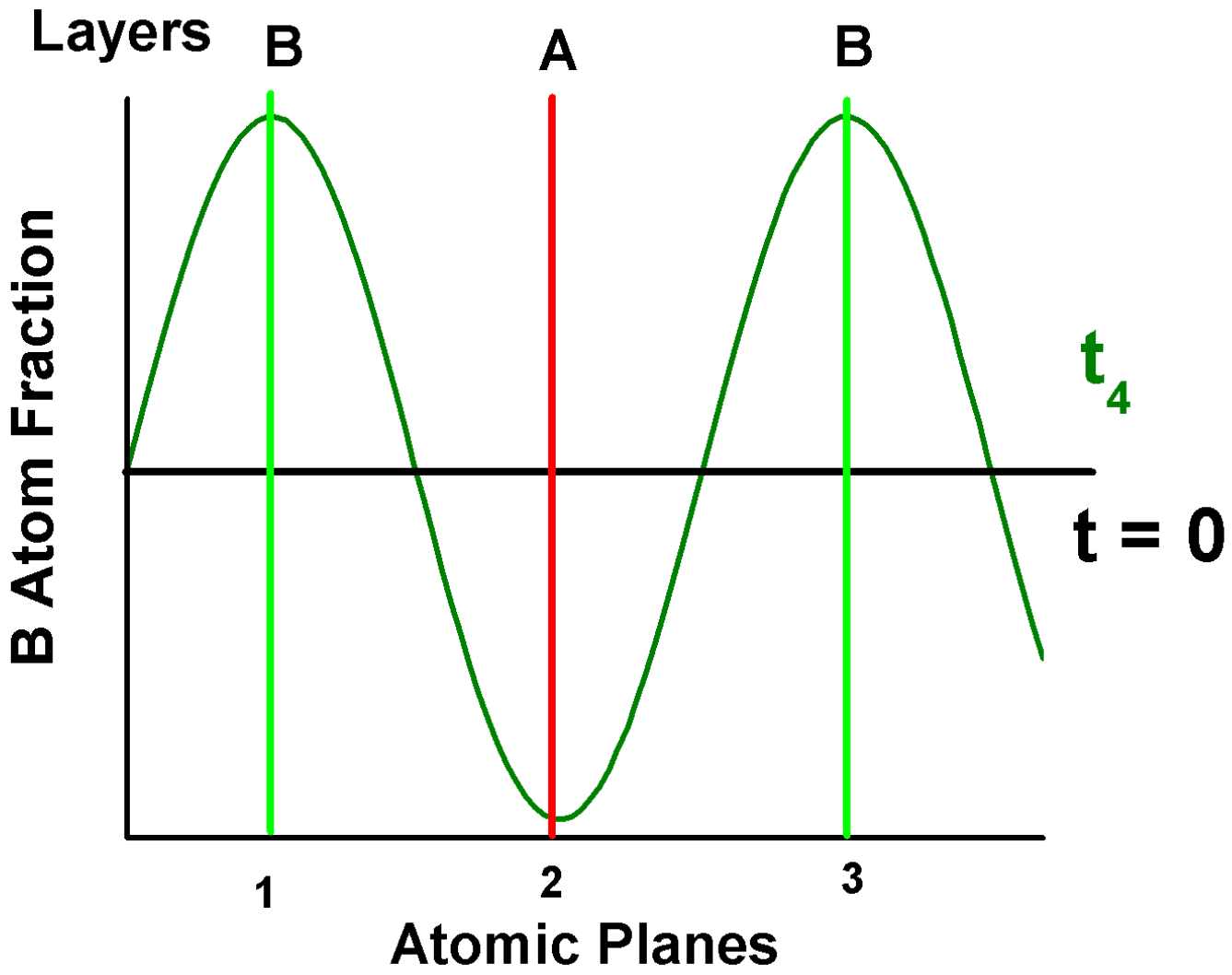

Continuous Ordering – Amplification of concentration wave

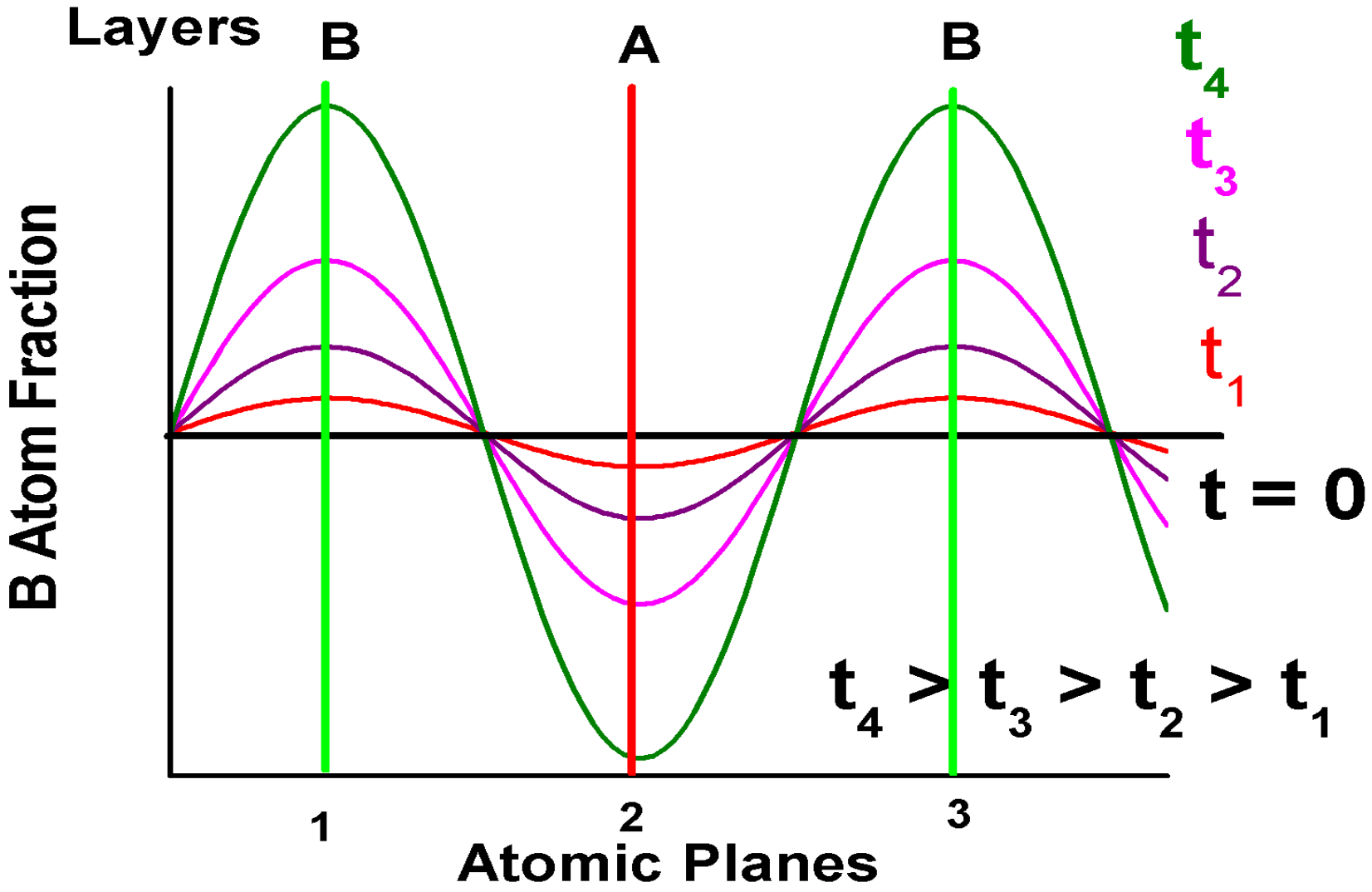

Continuous vis-à-vis Discrete Transformations

- Fluctuations – large in extent – small in degree

classical example – continuous decomposition of a solid solution through

– SPINODAL DECOMPOSITION

- Fluctuations – small in extent – large in degree

– NUCLEATION & GROWTH

GIBB'S Criterion

Originally proposed for unmixing of fluids

If $\partial^2 G/\partial^2 c < 0$: No thermodynamic barrier for continuous phase separation

First & second order transitions: Landau Plots

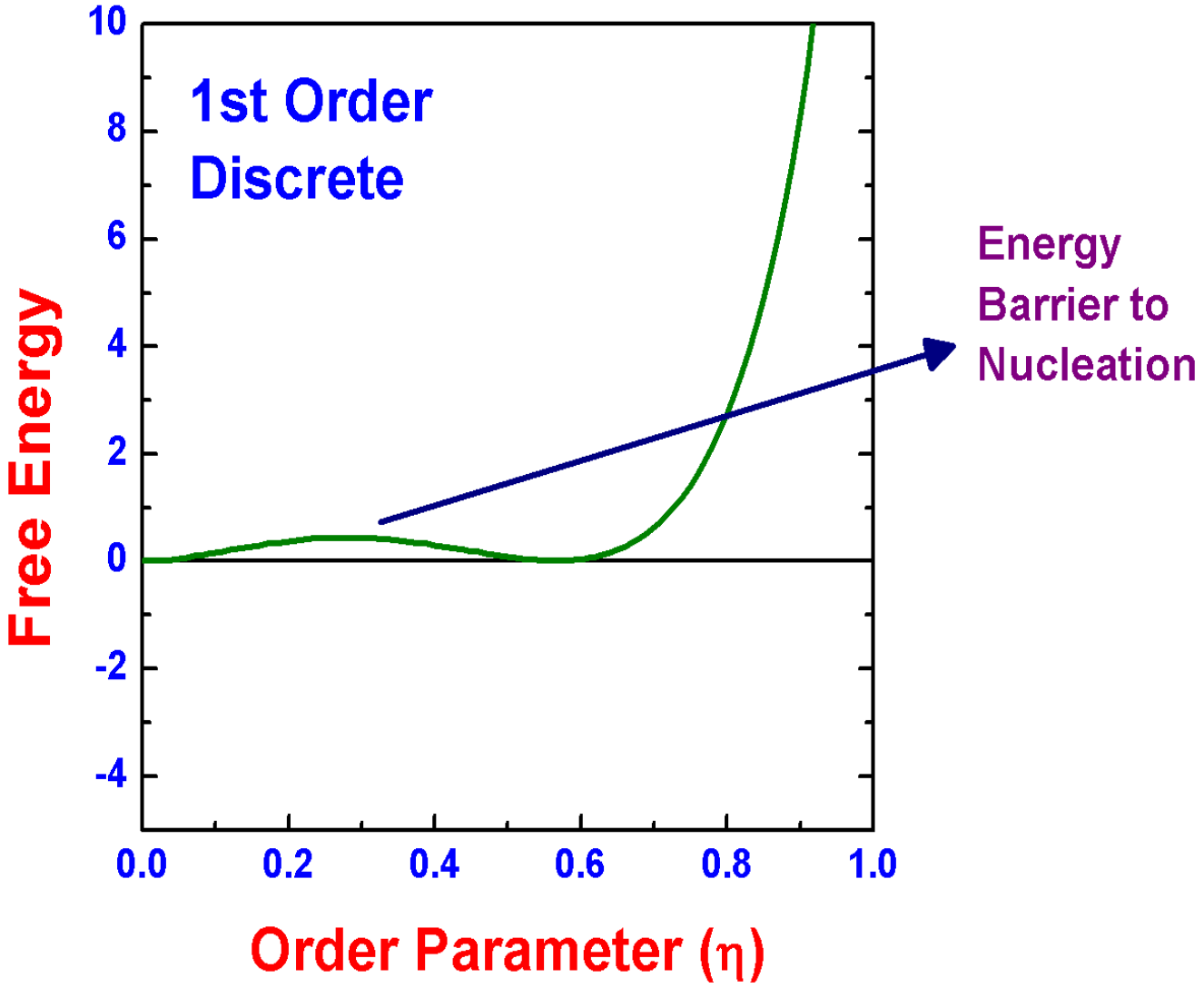

First & second order transitions: Landau Plots

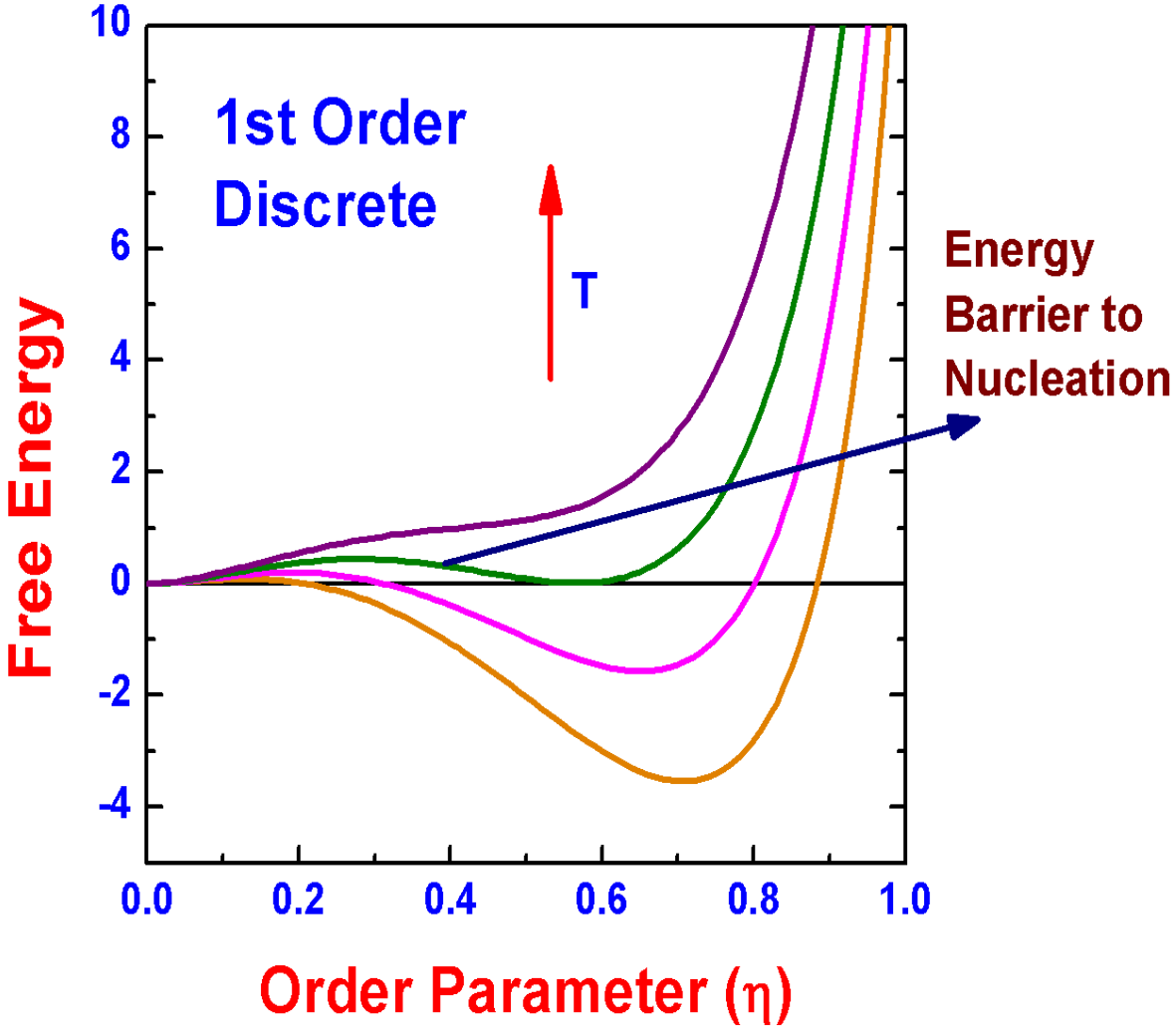

First & second order transitions: Landau Plots

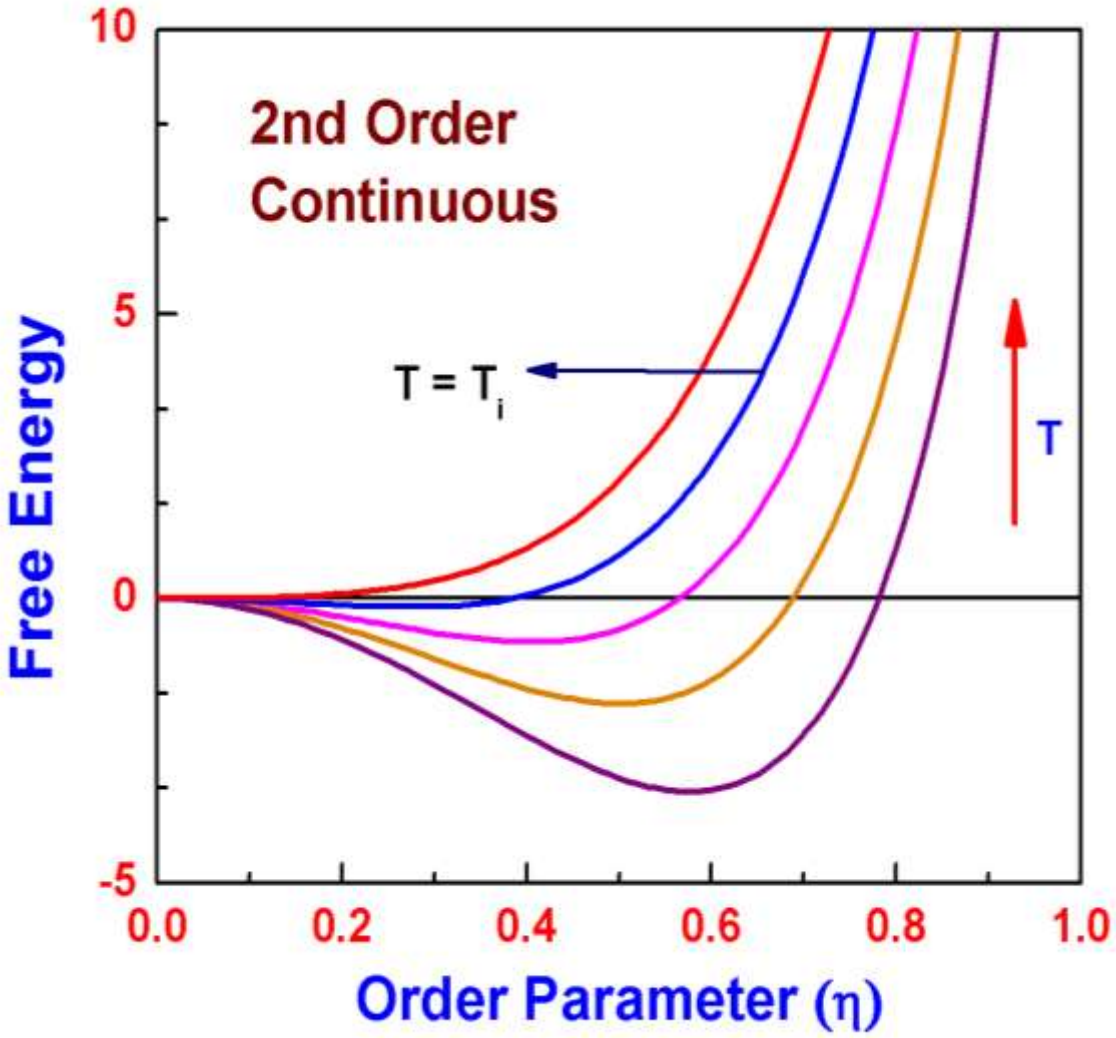

Special-Point Ordering

A wide range of phenomena related to order–disorder and magnetic transitions can be explained using the symmetry properties of the pair potentials (Vij).

Landau Theory of Continuous Phase Transitions

- The symmetry, **H**, of the ordered phase should be a subset of symmetry, **G**, of the disordered phase (**H** $\subset$ **G**)
- The ordering wave vector must be located at the **special points** of the Brillouin zone of the disordered phase, where symmetry elements intersect at a point.
- It must not be possible to find combinations of three members of the **star*** of the ordering wave vector satisfying rule II which will sum (vectorially) to a reciprocal lattice vector (No 3rd order invariant)

Special points are the points in the Brillouin zone where $\nabla V(k) = 0$
For simple structures: two symmetry elements intersect at these points

*The star associated with a vector **k** is a set of vectors obtained by applying all the Rotation or rotation-inversions on **k**.

Special Points, Stars and Ground State Structures

For bcc structure

k-vector Star	Members	Brillouin Zone Points	Ordering Structure
$\langle 000 \rangle$	$[000]$	Γ	
$\langle 100 \rangle$	$[100]$	H	$B2$
$\langle \frac{1}{2}\frac{1}{2}\frac{1}{2} \rangle$	$\left[\frac{1}{2}\frac{1}{2}\frac{1}{2}\right]$ $\left[\overline{\frac{1}{2}\frac{1}{2}\frac{1}{2}}\right]$	P	$B32$
$\langle \frac{1}{2}\frac{1}{2}0 \rangle$	$\left[\frac{1}{2}\frac{1}{2}0\right]$ $\left[\frac{1}{2}0\frac{1}{2}\right]$ $\left[0\frac{1}{2}\frac{1}{2}\right]$		
	$\left[\frac{1}{2}\overline{\frac{1}{2}}0\right]$ $\left[\frac{1}{2}0\overline{\frac{1}{2}}\right]$ $\left[0\frac{1}{2}\overline{\frac{1}{2}}\right]$	N	AB

For fcc structure

k-vector Star	Members	Brillouin Zone Points	Ordering Structure
$\langle 000 \rangle$	$[000]$	Γ	
$\langle 100 \rangle$	$[100]$ $[010]$ $[001]$	X	$L1_2$, $L1_0$
$\langle 1\frac{1}{2}0 \rangle$	$\left[1\frac{1}{2}0\right]$ $\left[\frac{1}{2}01\right]$ $\left[01\frac{1}{2}\right]$	W	A_2B_2
	$\left[\overline{1}\overline{\frac{1}{2}}0\right]$ $\left[\overline{\frac{1}{2}}0\overline{1}\right]$ $\left[0\overline{1}\overline{\frac{1}{2}}0\right]$		
$\langle \frac{1}{2}\frac{1}{2}\frac{1}{2} \rangle$	$\left[\frac{1}{2}\frac{1}{2}\frac{1}{2}\right]$ $\left[\overline{\frac{1}{2}\frac{1}{2}\frac{1}{2}}\right]$	L	$L1_1$
	$\left[\overline{\frac{1}{2}}\frac{1}{2}\overline{\frac{1}{2}}\right]$ $\left[\overline{\frac{1}{2}}\overline{\frac{1}{2}}\frac{1}{2}\right]$		

Free Energy of Ordering

The configurational free energy, in the simple mean-field theory, can be expanded in a Taylor series about the homogeneous state:

$$\Delta F = F_M - F_o = \frac{N}{2}\sum_h F''(h)\left|X(h)\right|^2 +$$

$$\frac{N}{3!} f_o''' \sum_{h,h',h''} X(h)X(h')X(h'')\delta(h+h'+h'';g) +$$

$$\frac{N}{4!} f_o'''' \sum_{h,h',h'',h'''} X(h)X(h')X(h'')X(h''')\times\delta(h+h'+h''+h''';g)$$

$X(h)$: Fourier transform of concentration deviation from the mean value, C_o.
V(h) : Fourier transform of pair interaction function, V(r).
g :reciprocal lattice translational vector,.

$$F''(h) = 2V(h) + \tau / q_o$$

As amplification rate α(*h*) of a Fourier Component *h* is proportional to F”(*h*), is expected to mimic the V(*h*) function at relatively lower temperatures

Amplification Rates for Clustering and Ordering Instabilities

Amplification rate α(h) vs. a/λ for a system inside the spinodal.

The λ_c is the critical wavelength and λ_m is the one receiving the maximum amplification

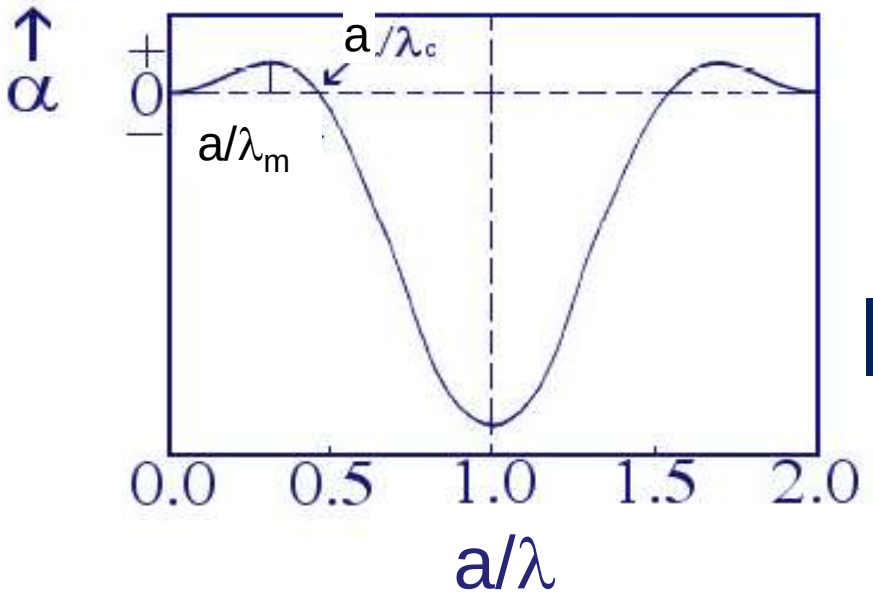

Spinodal clustering

Amplification rate α(h) vs. a/λ for a Ordering system below the critical temperature

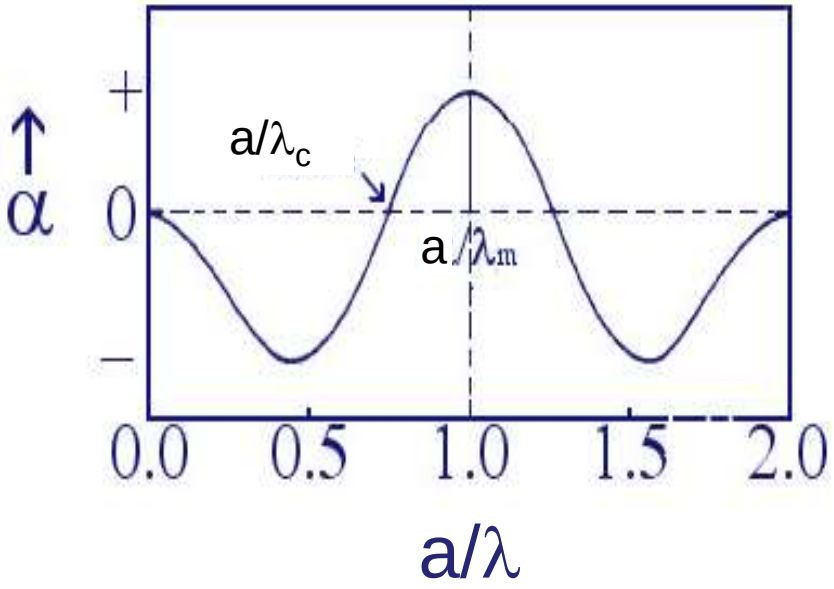

Spinodal ordering

HE Cook, D de Fontaine and JE Hilliard, Acta metal. Vol. 17, 765 (1969).

Lattice Wave Descriptions of Homogeneous Transformations

Nature of Wave	Long Wavelength	Short Wavelength
Replacive	Spinodal Clustering	Spinodal Ordering
Displacive	Martensitic	Omega
Electric	Ferroelectric	Antiferroelectric
Magnetic	Ferromagnetic	Antiferromagnetic

Competing Superlattices in Ni-Mo Alloys

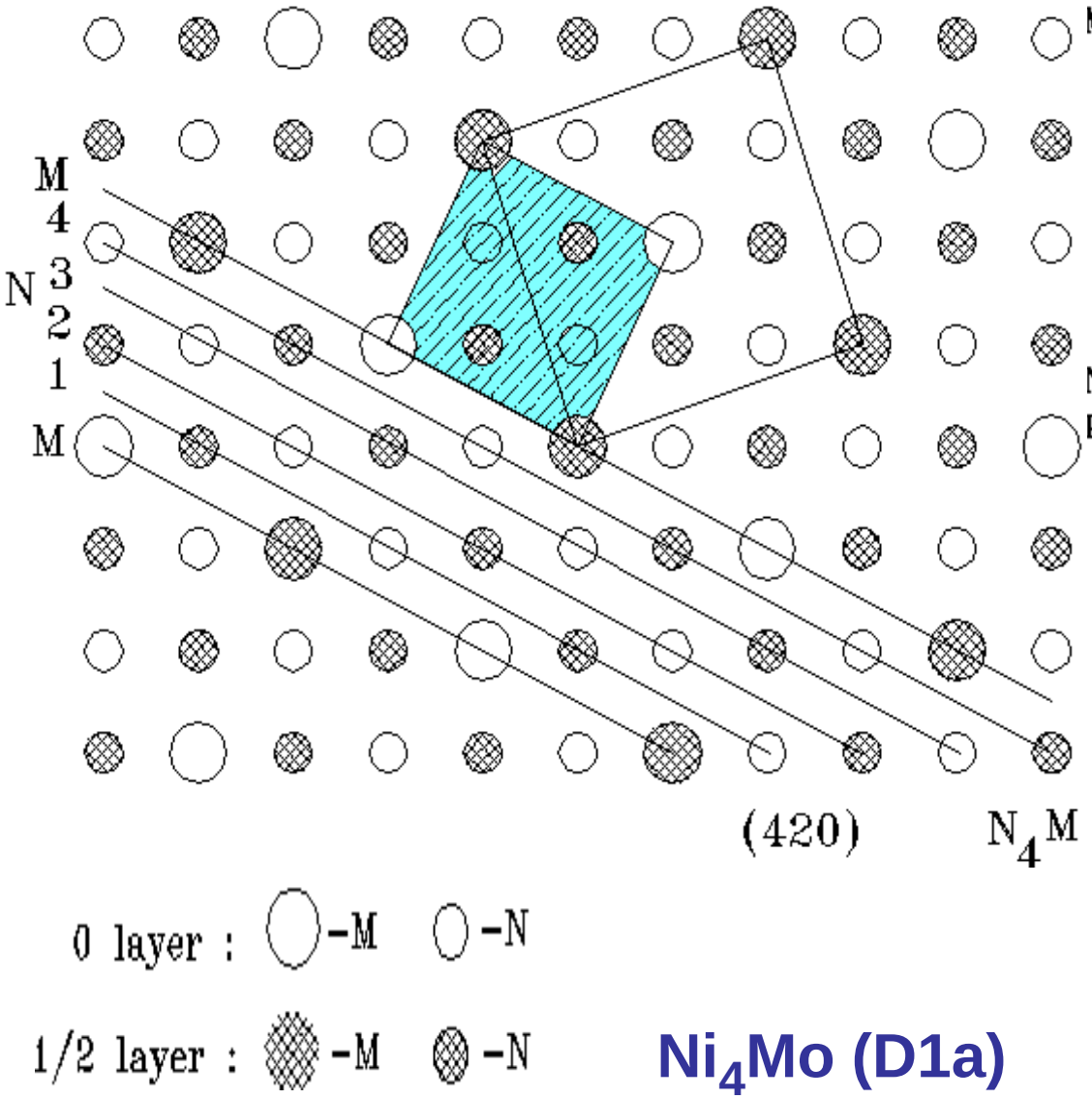

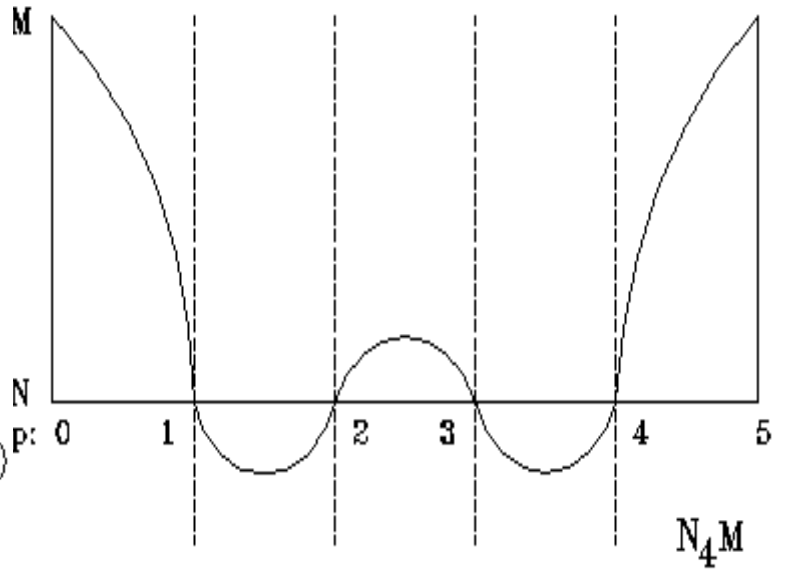

k=1/5 <420>

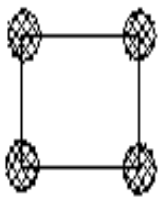

- Unit Cell

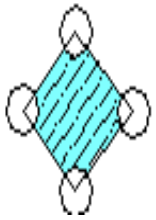

- Tile

Ni_4Mo (D1a)

Competing Superlattices in Ni-Mo Alloys

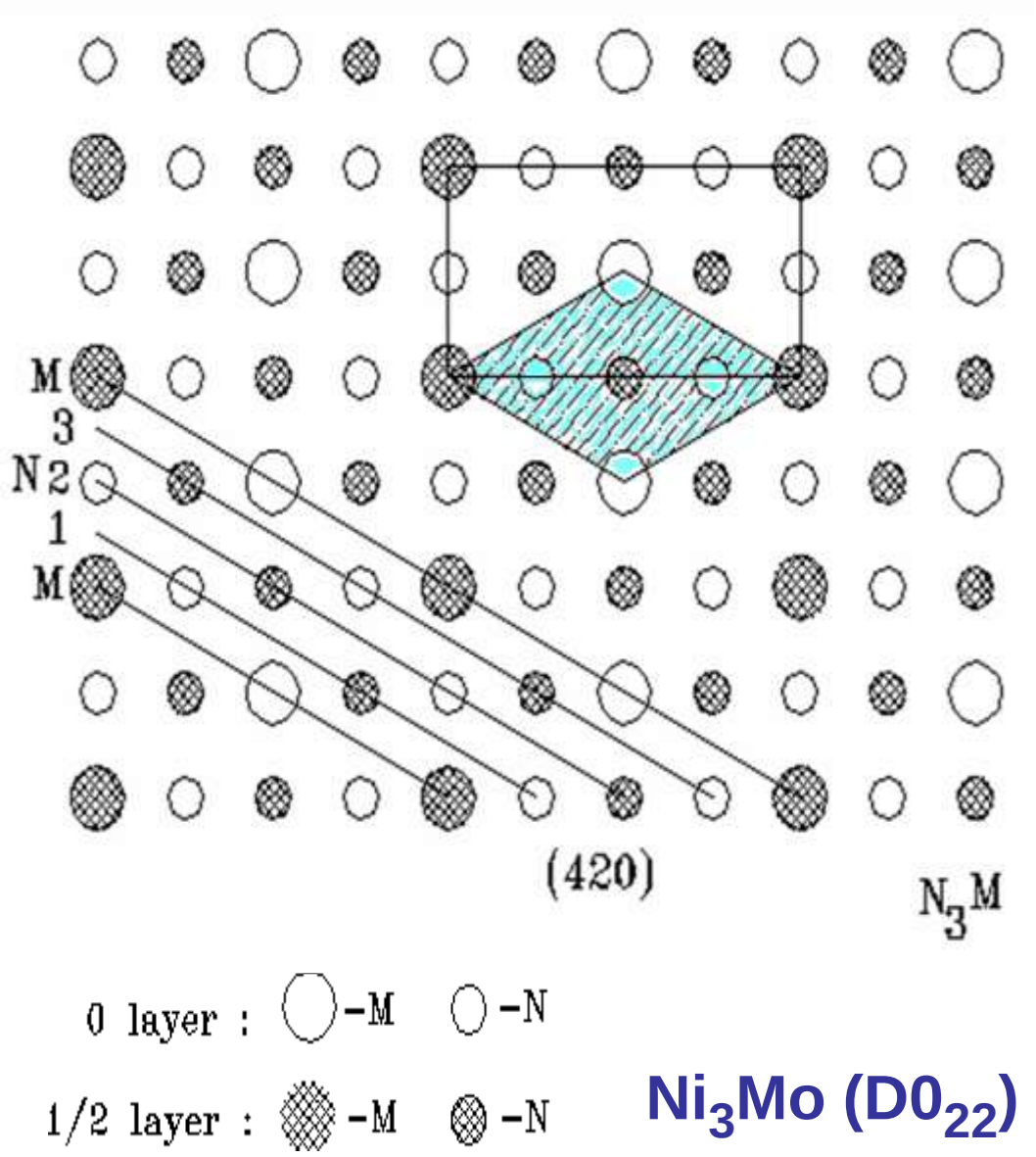

Ni_3Mo ($D0_{22}$)

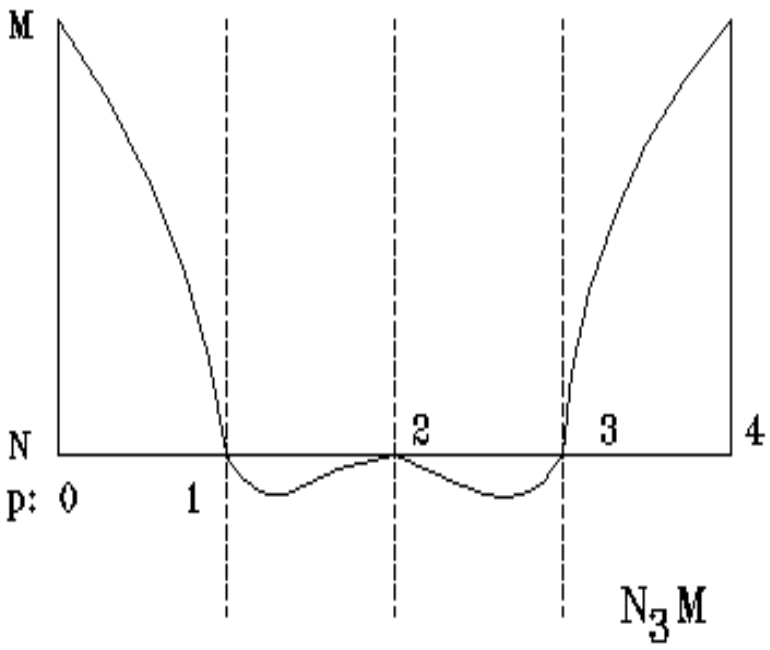

k=1/4 <420>

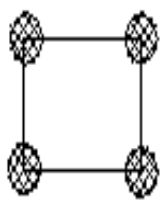

- Unit Cell

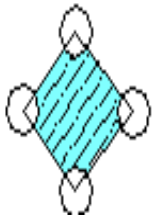

- Tile

Competing Superlattices in Ni-Mo Alloys

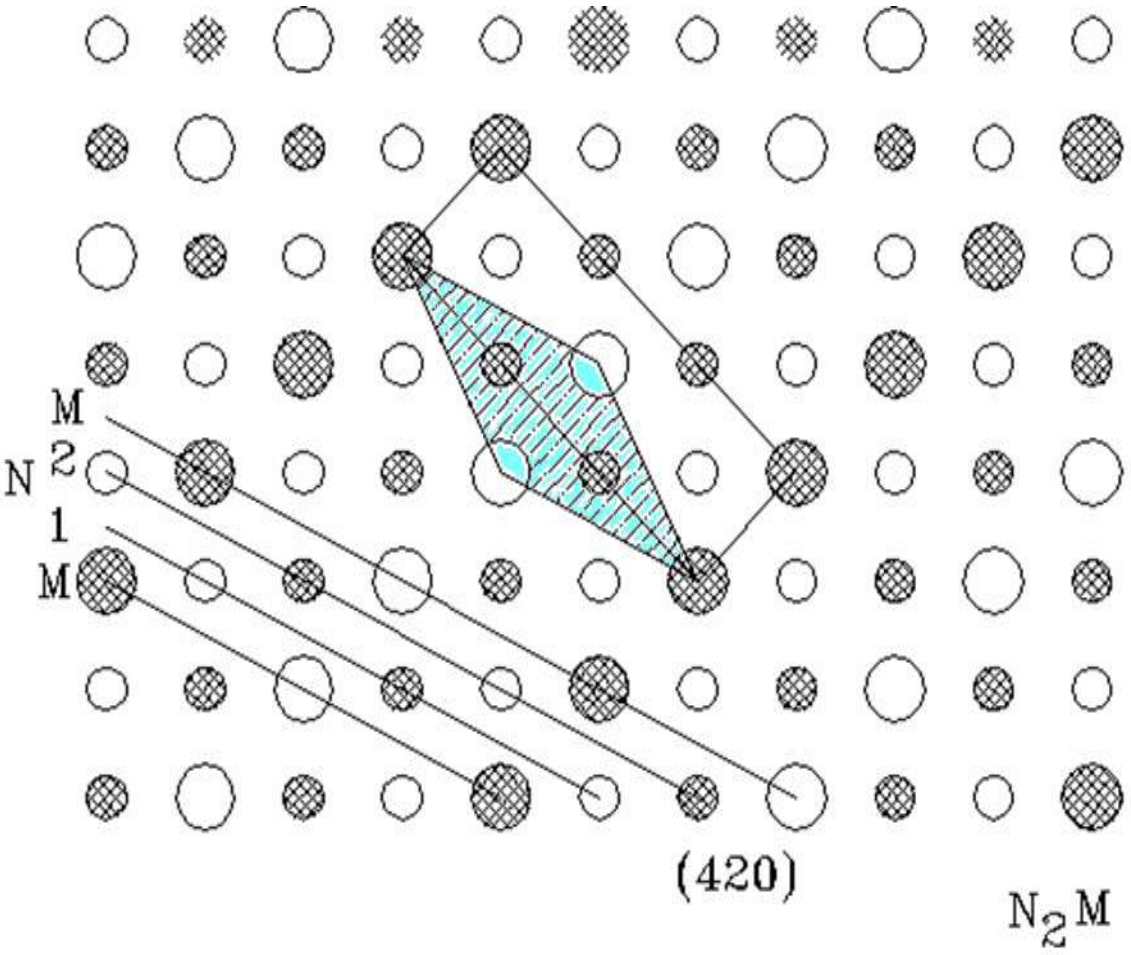

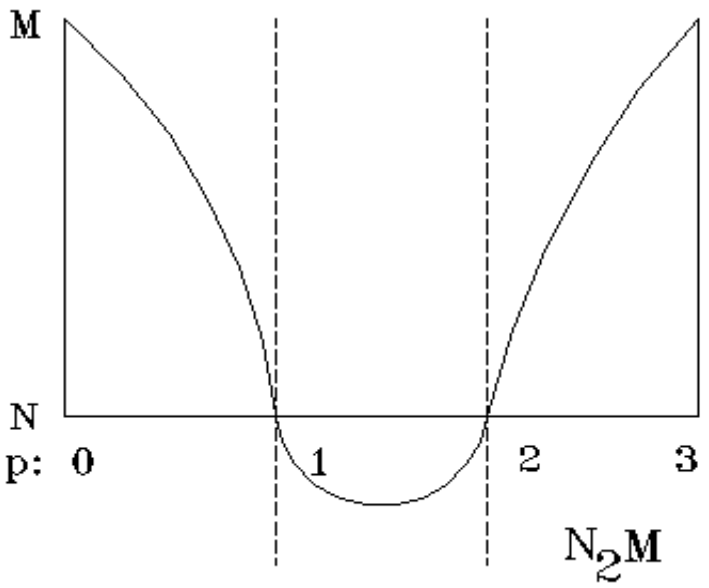

k=1/3 <420>

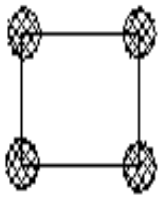

- Unit Cell

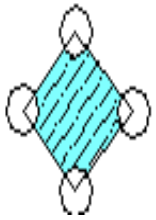

- Tile

0 layer : -M -N

1/2 layer : -M -N

Ni_2Mo (Pt_2Mo)

Competing Superlattices in Ni-Mo Alloys

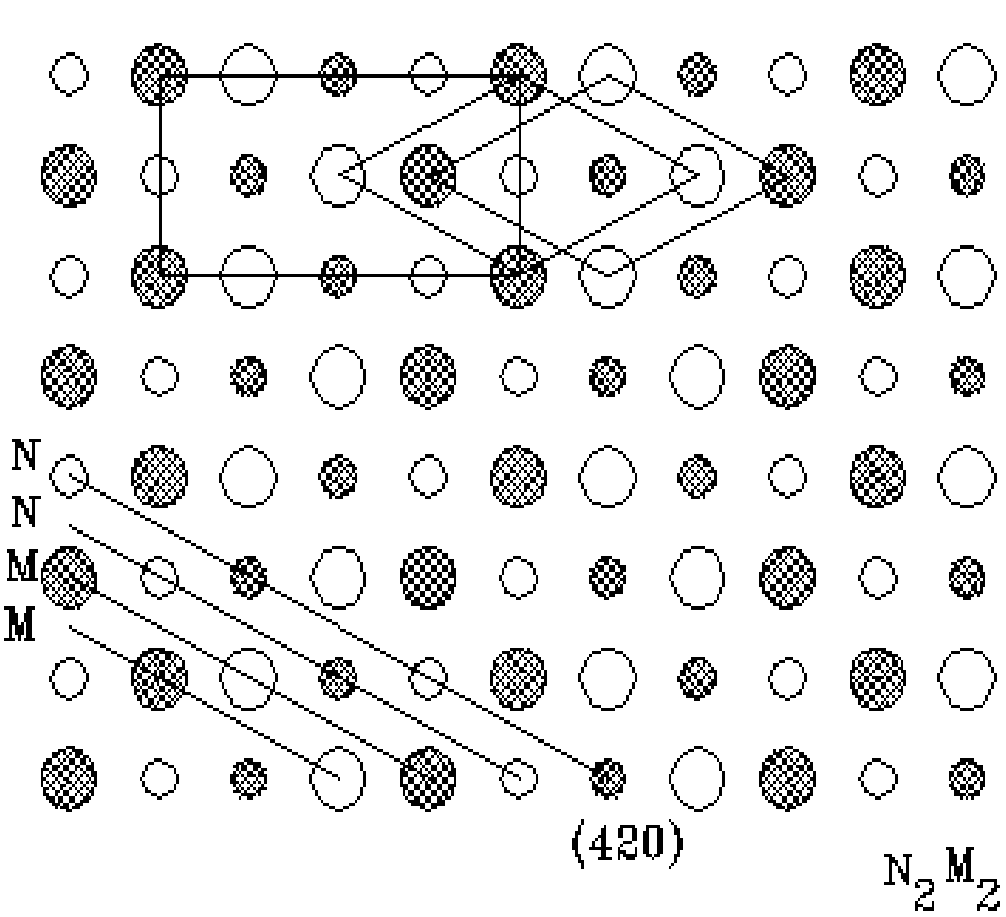

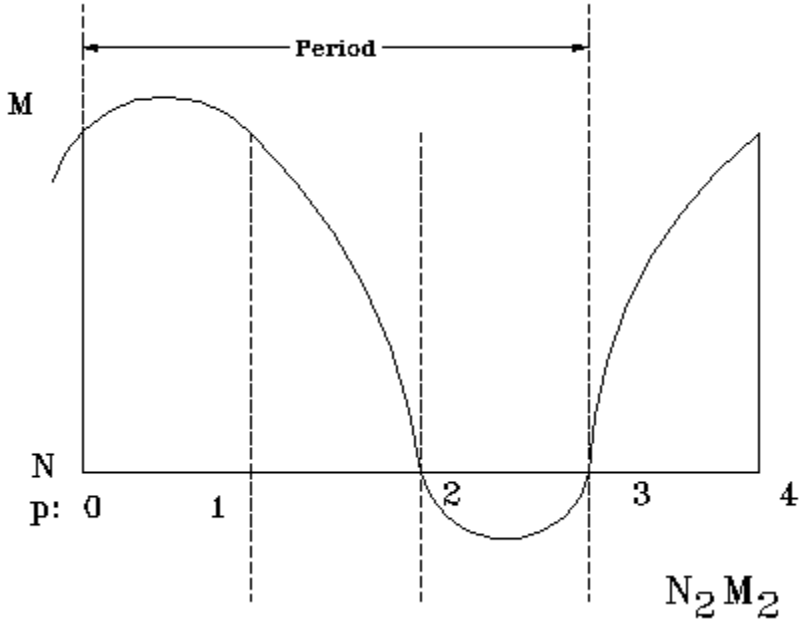

k = <1 ½ 0>

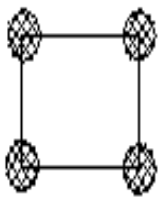

- Unit Cell

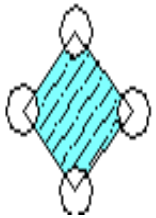

- Tile

0 layer : -M -N

1/2 layer : -M -N

Ni_2Mo_2

Structural Description of <1 ½ 0> Ordering

- Microdomain model
  - Isostructural microdomains
  - Multiple microdomains
- Subunit cell structure
- Concentration wave
- Concentration wave packets

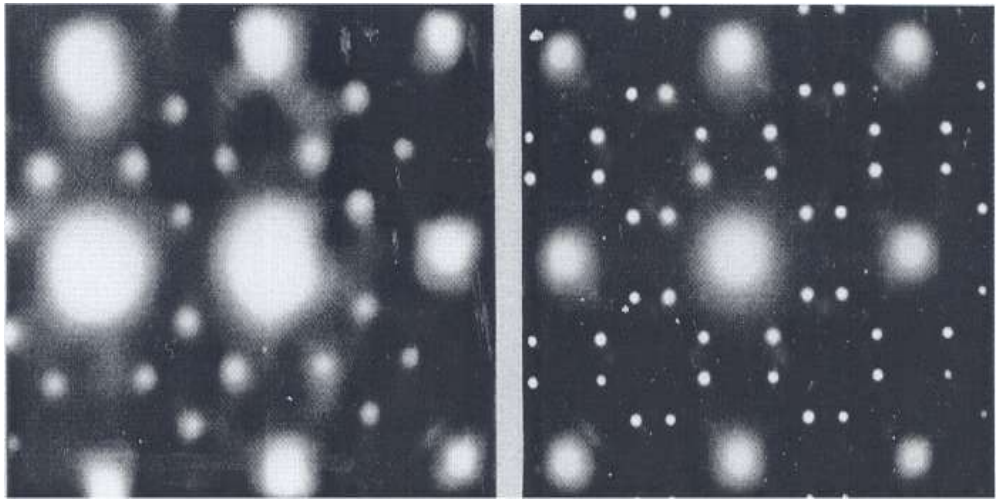

<1 ½ 0> 1/5 <420>

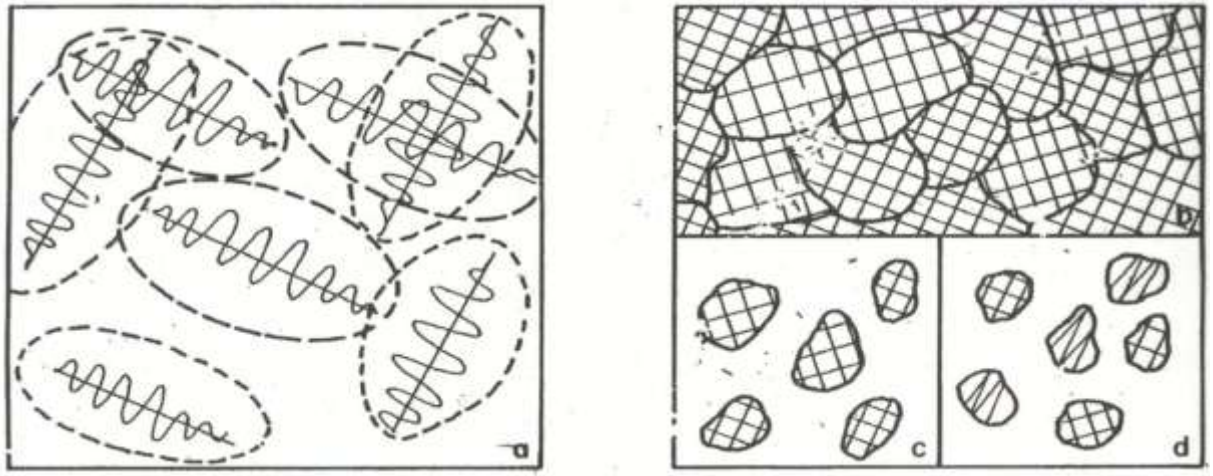

Concentration wave packets Microdomains

Evolution of Order in Ni_4Mo under Electron Irradiation

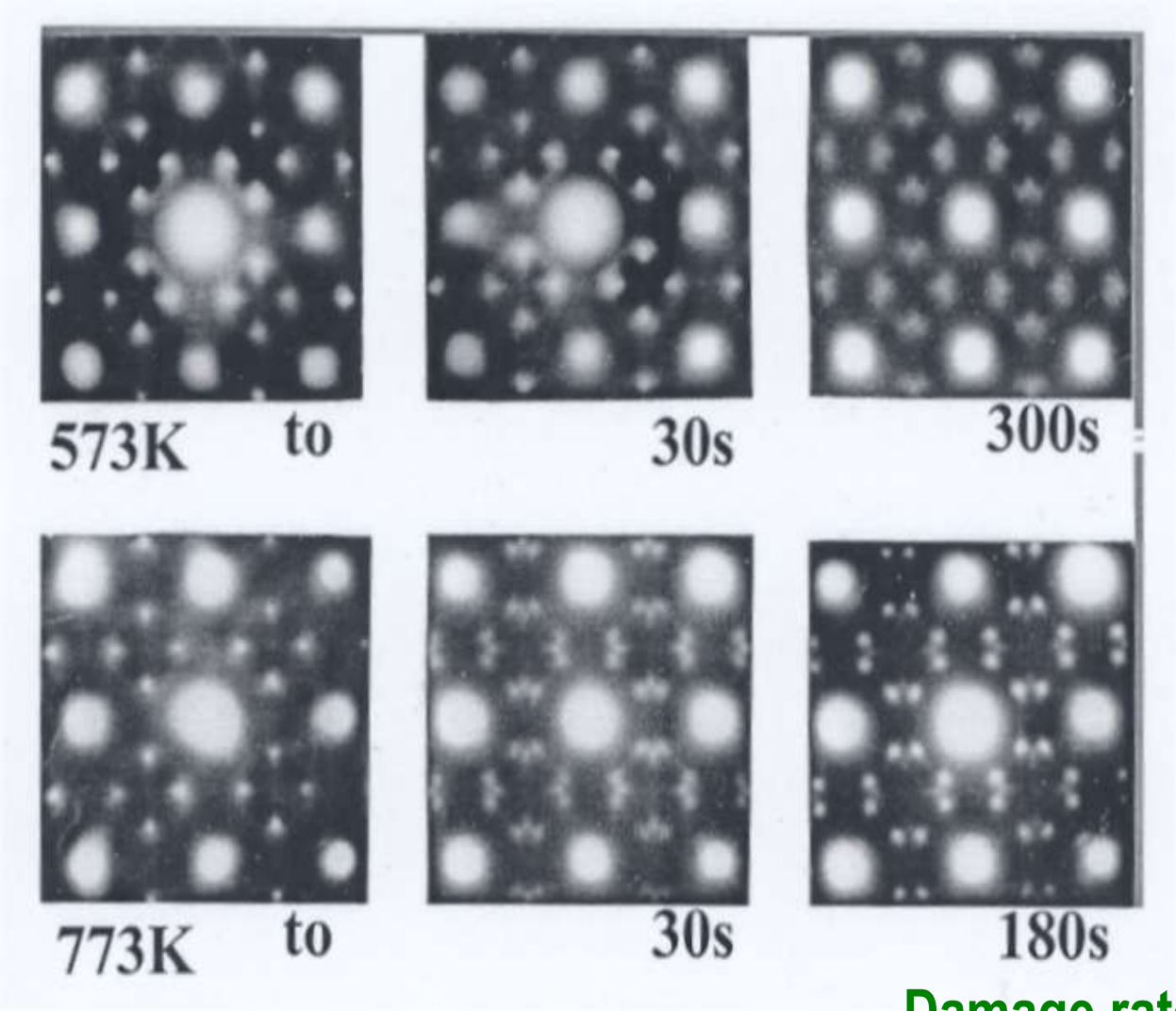

Damage rate: 10^{-3} dpa/s

<1 ½ 0> & 1/5 <420> diffraction spots remain linked During evolutionary stages

S Banerjee, K Urban, M. Wilkens
Acta Met., 32 (1984) 299

Evolution of Order in Ni_3Mo under Electron Irradiation

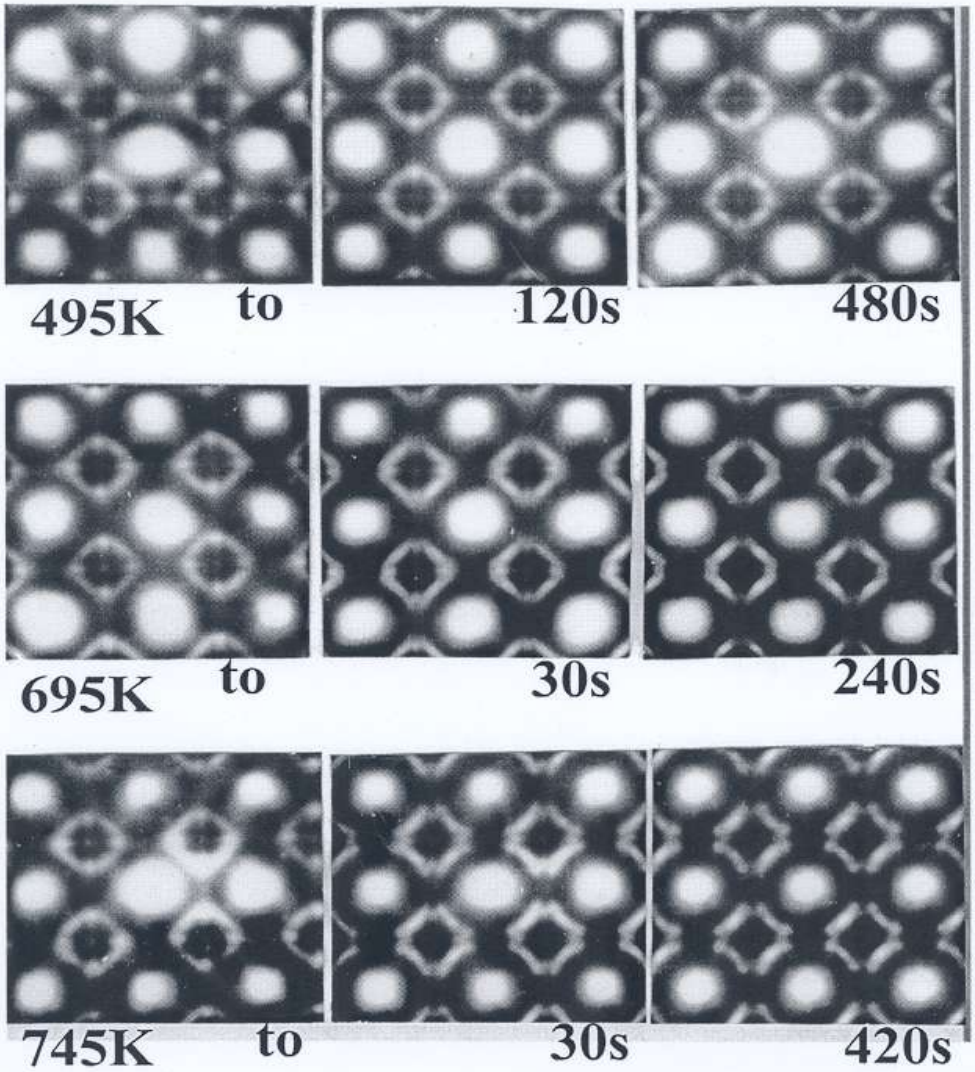

Diffuse intensity links superlattice reflections associated with
<1 ½ 0> (N_2M_2),
1/5 <420> (N_4M) &
1/3 <420> (N_2M) ordering

Damage rate: 10^{-3} dpa/s

S. Banerjee, U.D. Kulkarni, K. Urban, Acta Met., 37 (1989) 35

Superimposition of <1 ½ 0> Concentration Waves

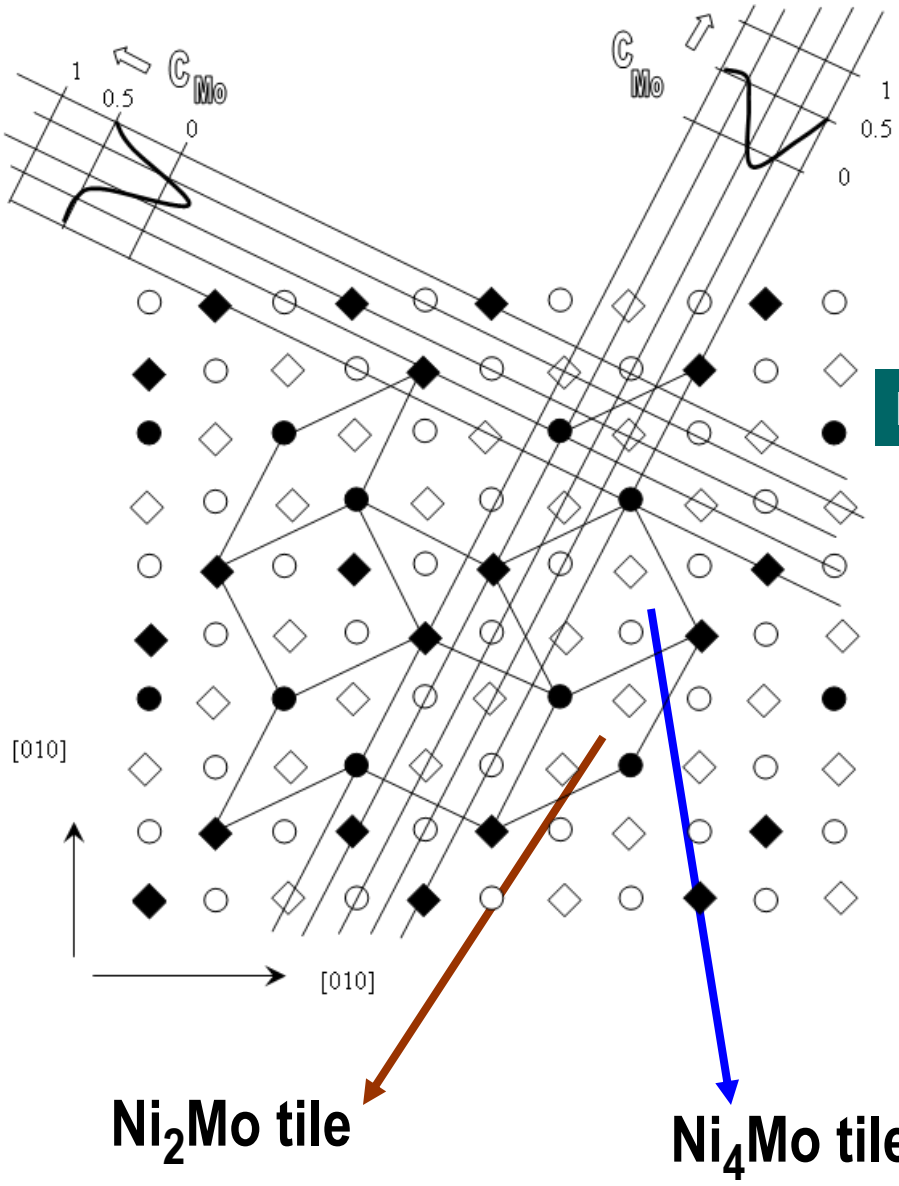

η=0.7

Phase locking

Random clusters

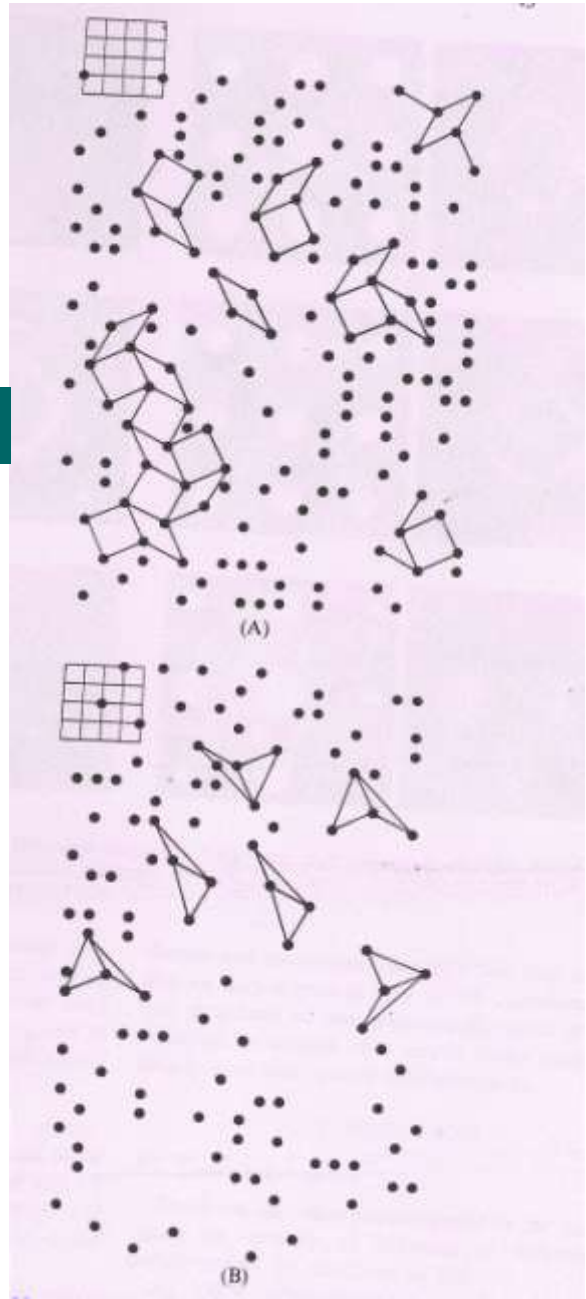

U.D. Kulkarni, S. Banerjee, Acta Met, 36 (1988) 413

DPs Showing Evolutionary Stages of Ordering in Ni_3Mo

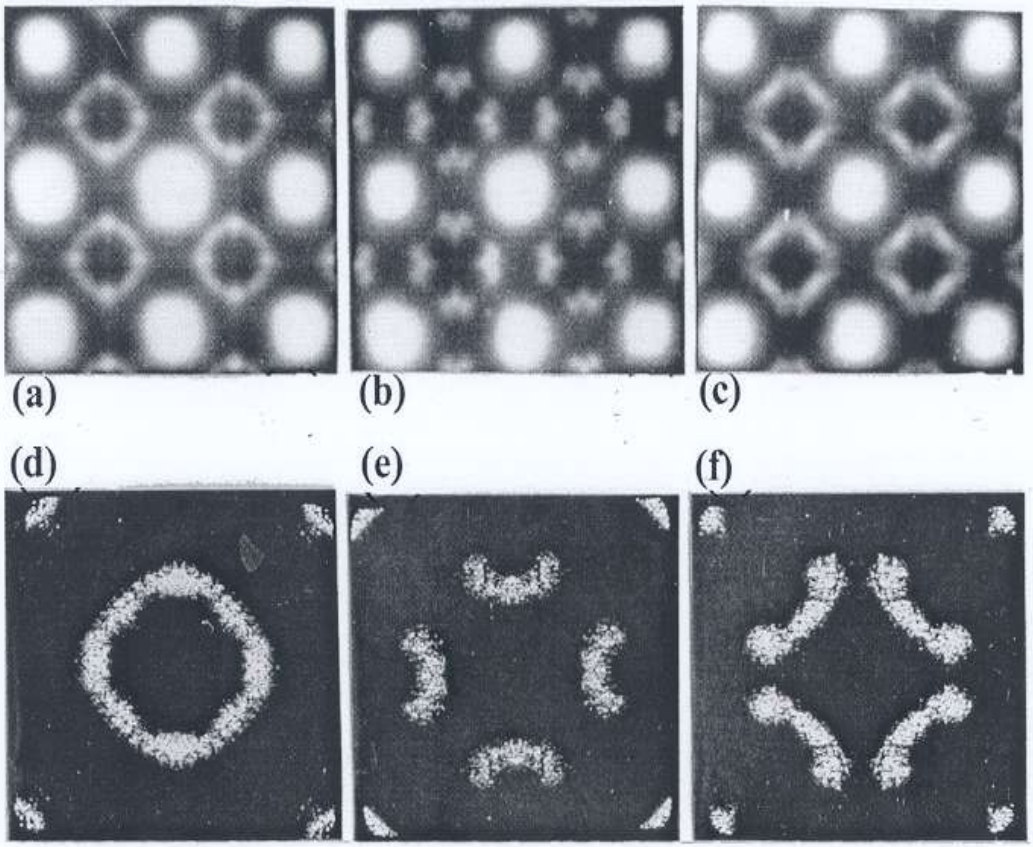

Experimental

Simulated

Simulated pattern	# of clusters	Ratio
d	N_2M_2 (16), Pt_2Mo (16), Pt_2Mo (4)	1:1:4
e	N_2M_2 (16), D1a (16), D1a (4)	1:1:4
f	D1a (16), Pt_2Mo (16), D1a (4), Pt_2Mo (4)	1:2:2:4

S. Banerjee, U.D. Kulkarni, K. Urban, Acta Met., 37 (1989) 35

Coexistence of N_4M and N_2M tiles in $Ni_{10}Mo_4Cr$

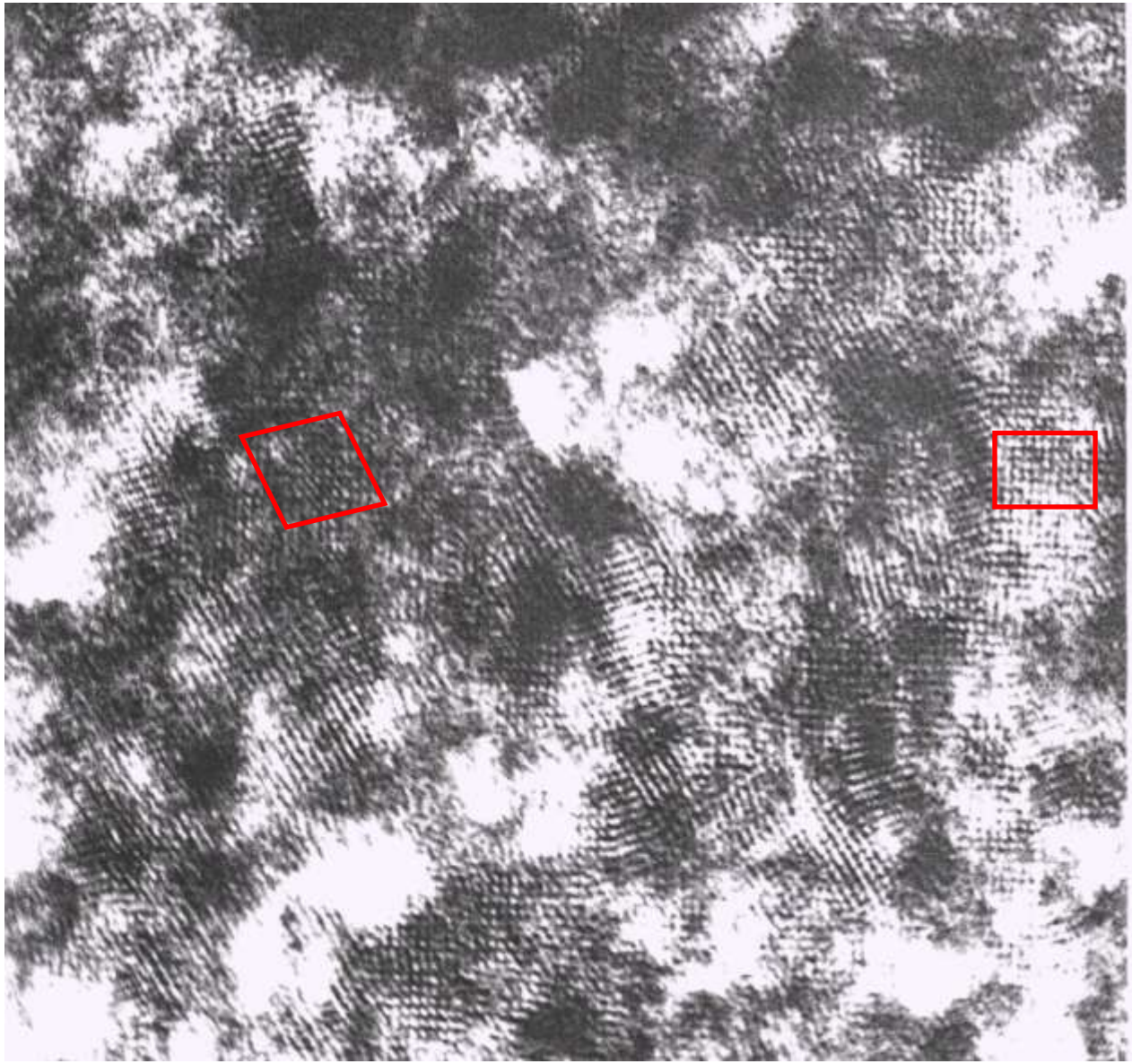

A Arya, G.K. Dey
V. Vasudevan
S. Banerjee
Acta Mater., 50
(2002) 3301

Coexistence of Competing Superlattices in Ternary $Ni_{10}Mo_4Cr$

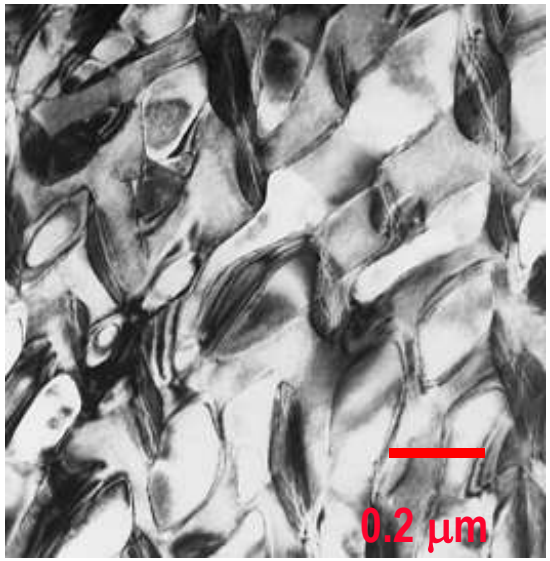

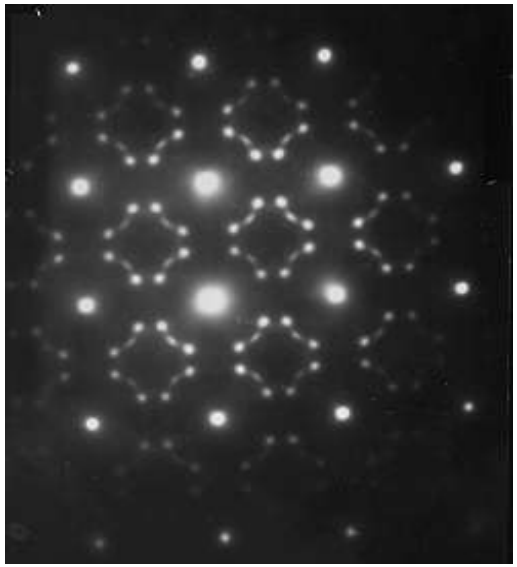

$Ni_4(Mo,Cr)$ & $Ni_2(Mo,Cr)$ domains

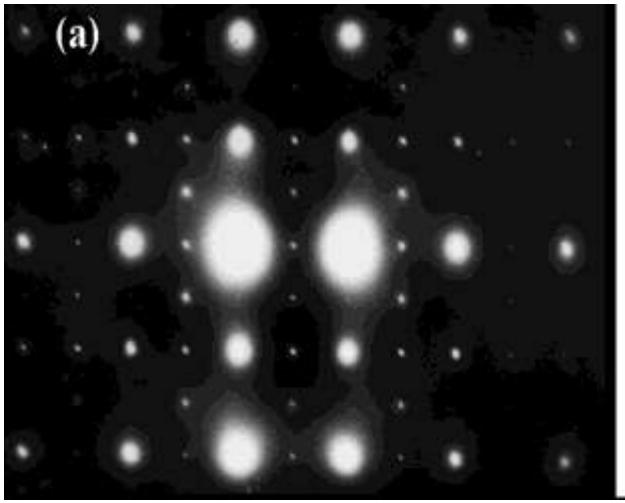

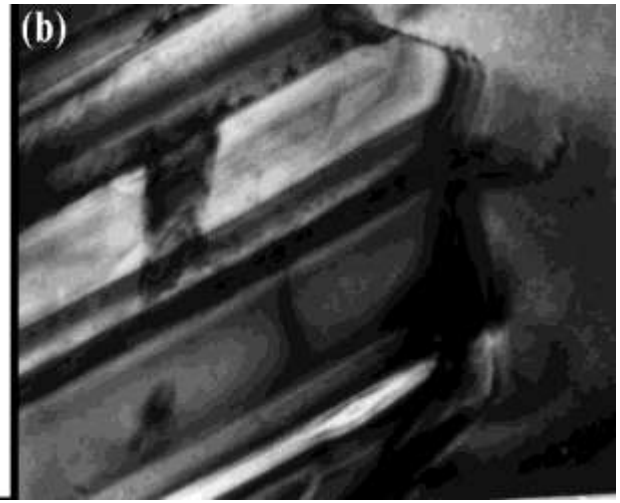

DO_{22} Plates Forming at T≈873 K

A Arya, G.K. Dey, V. Vasudevan, S. Banerjee, Acta Mater., 50 (2002) 3301

Coherent Arrangement of Superlattice Tiles

Tiles

Ni_4Mo

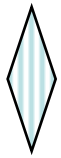

Ni_2Mo

Ni_3Mo

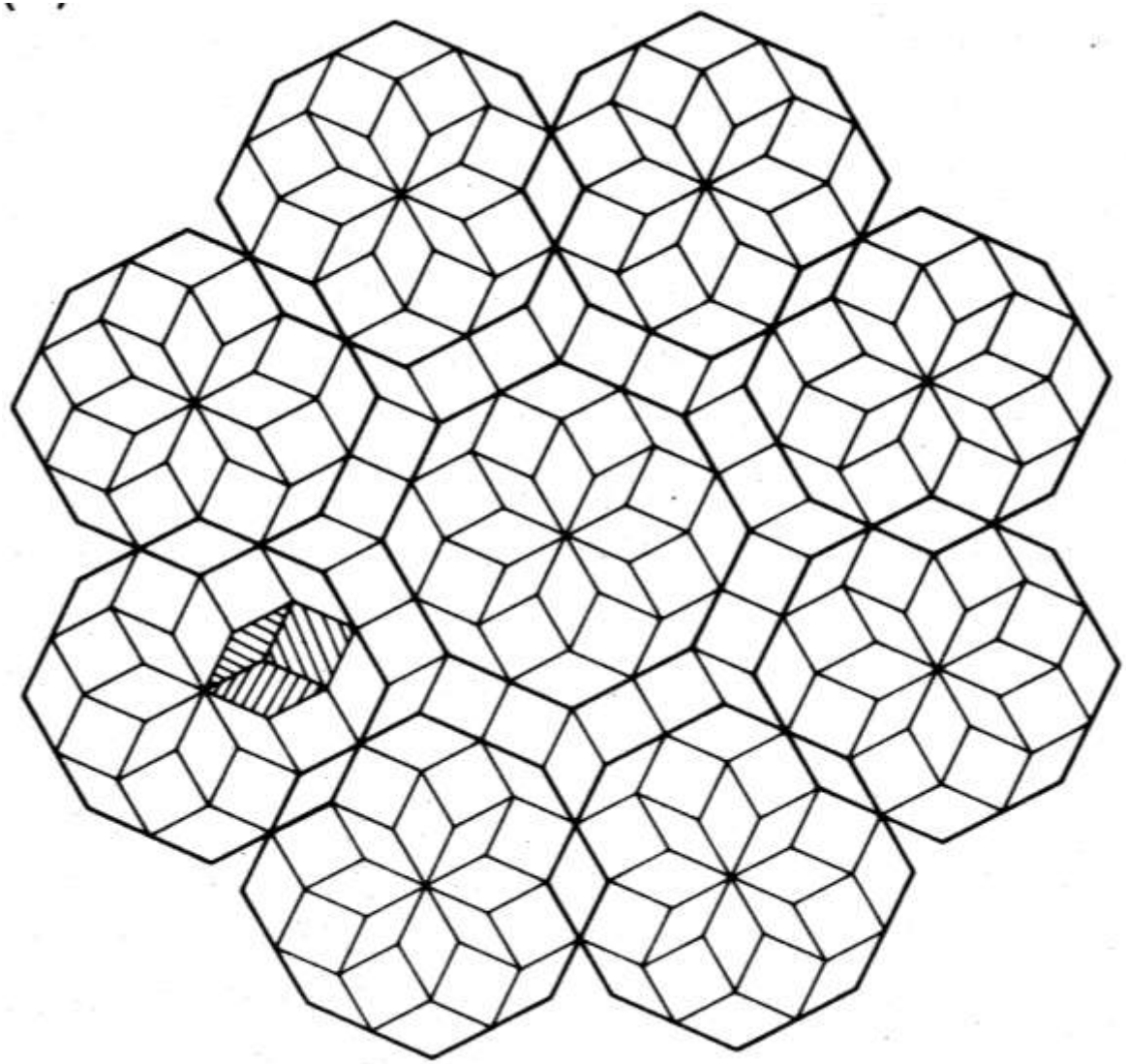

First-Principles Approach to Order-Disorder Transformations

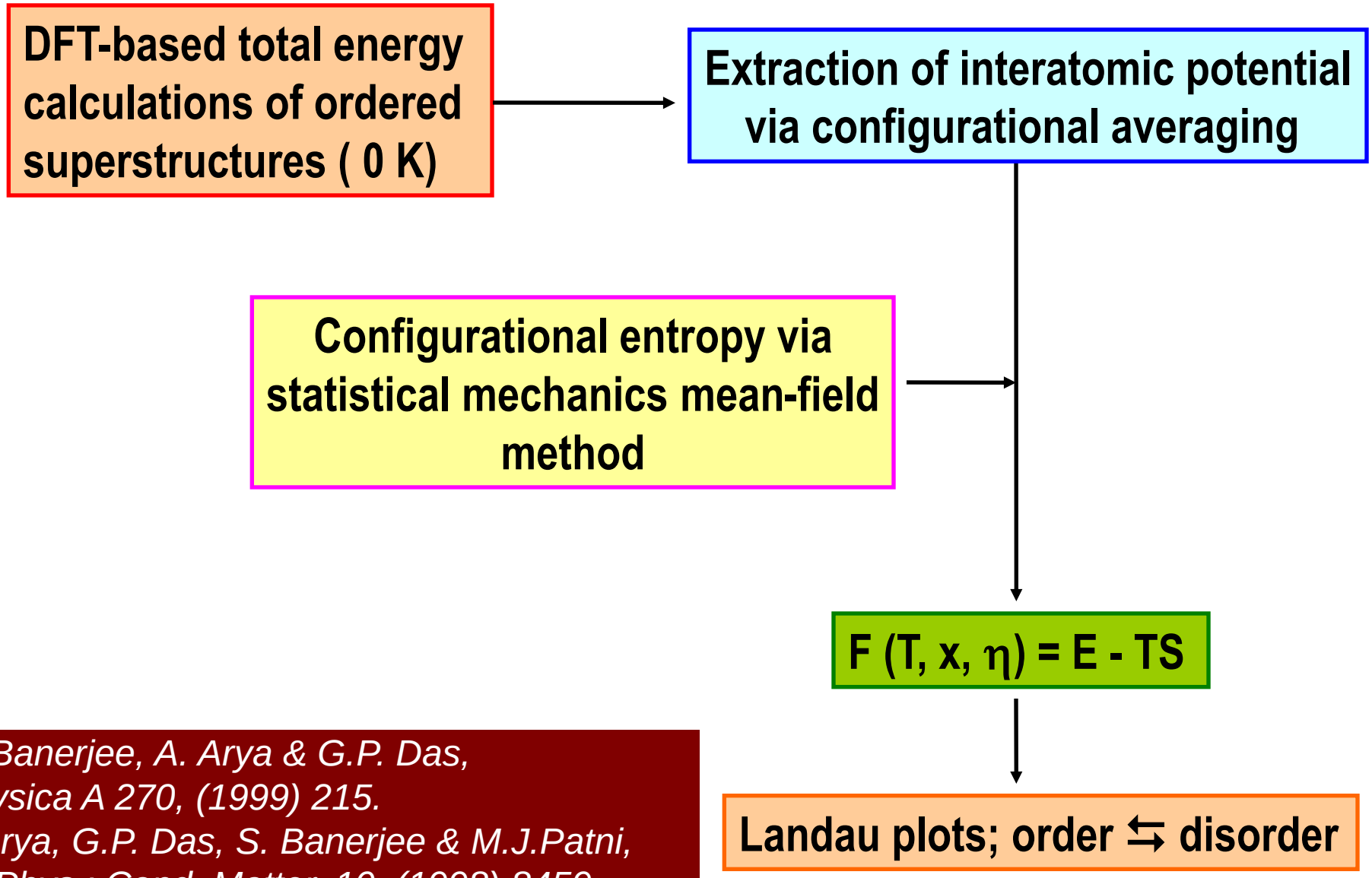

S. Banerjee, A. Arya & G.P. Das, Physica A 270, (1999) 215.
A Arya, G.P. Das, S. Banerjee & M.J.Patni, J. Phys.: Cond. Matter, 10, (1998) 8459.

Formation Energies of fcc-based Superstructures of Ni-Mo System Under NN & NNN Approximation Using DFT-LDA based TB-LMTO Method

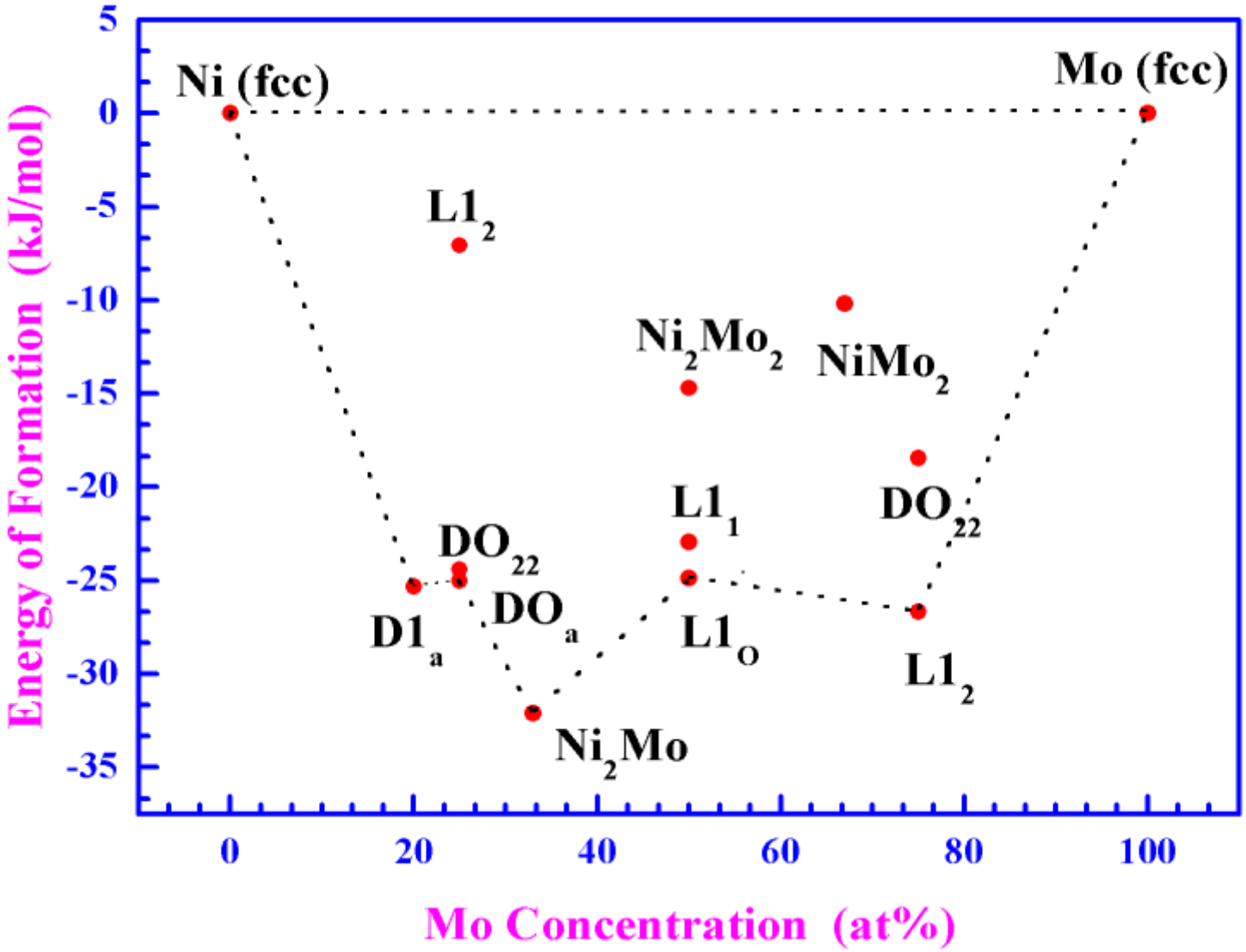

Equilibrium Structures

Ni_4Mo (D1a),
Ni_3Mo (D0a)
Ni_2Mo,
NiMo ($L1_0$)
NiMo3 ($L1_2$)

Landau Plots: <1 ½ 0> vs. 1/5 <420> ordering

1/5 <420> ordering

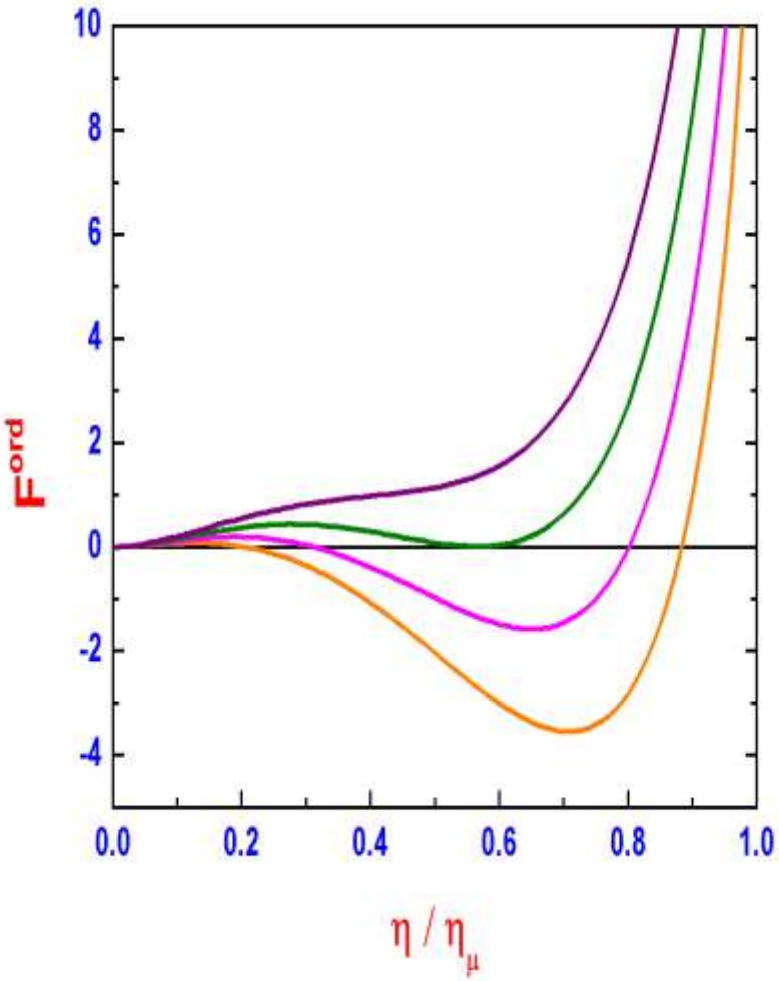

<1 ½ 0> ordering

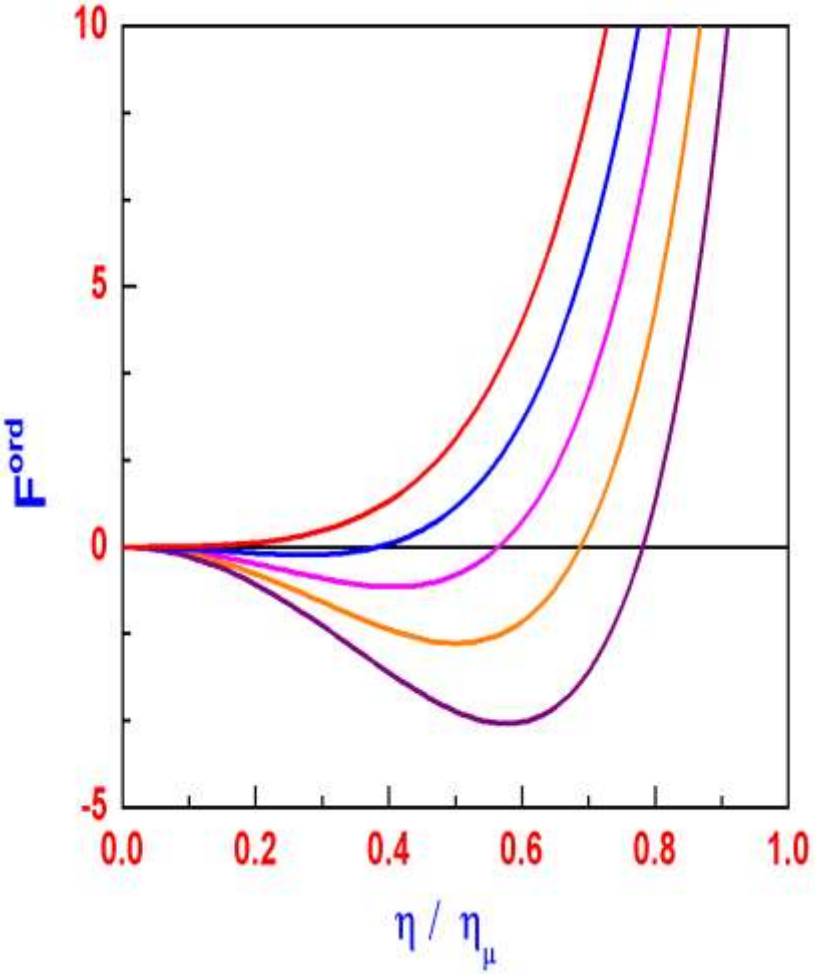

A Arya, S. Banerjee, G.P. Das, I. Dasgupta, T. Saha-Dasgupta & A. Mookerjee, Acta Mater. 49, 3575 (2001).

<1 ½ 0> & 1/5 <420> Ordering Competencies

T = 800 K

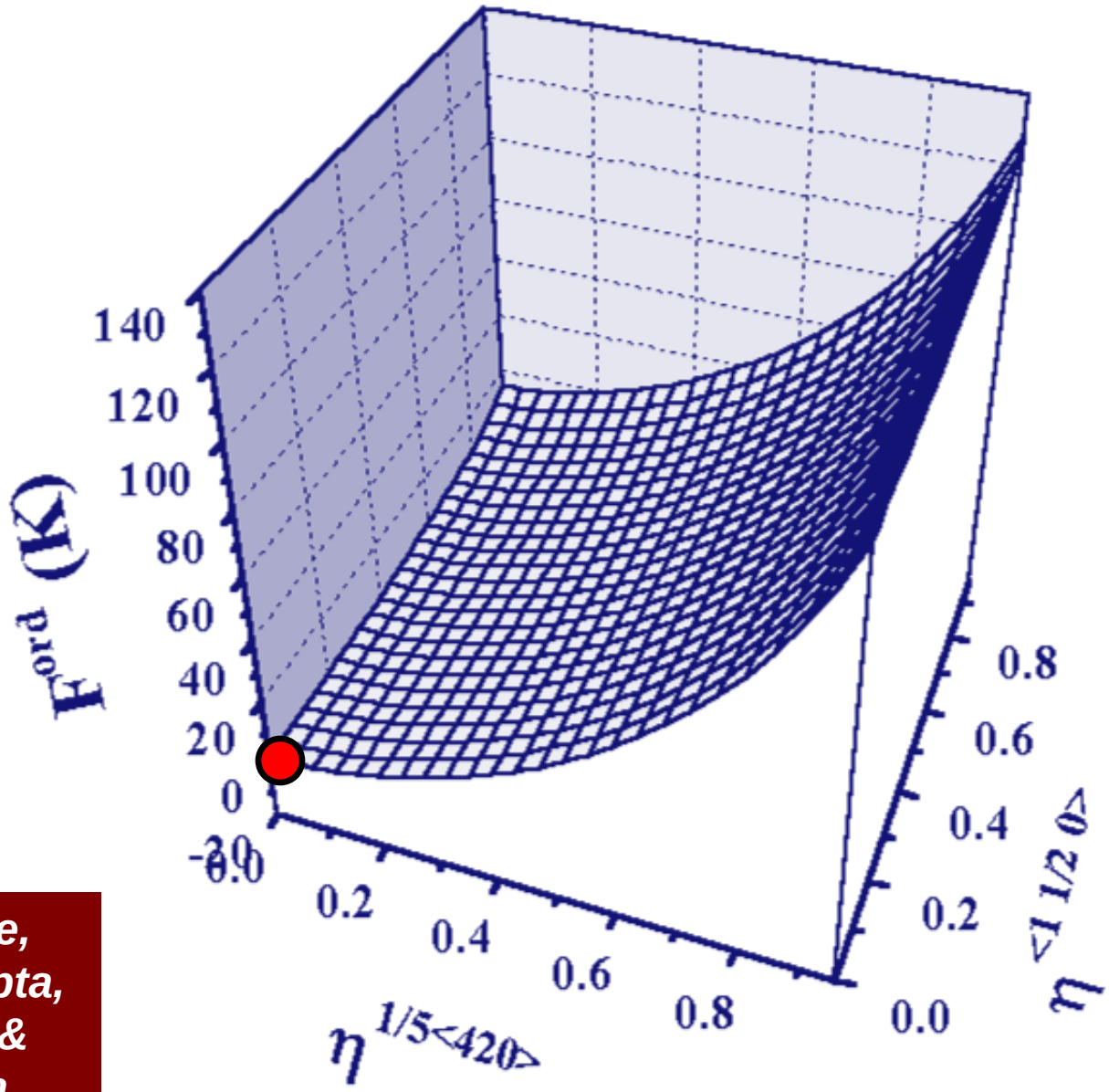

A Arya, S. Banerjee, G.P. Das, I. Dasgupta, T. Saha-Dasgupta & A. Mookerjee, Acta Mater. 49, 3575 (2001).

<1 ½ 0> & 1/5 <420> Ordering Competencies

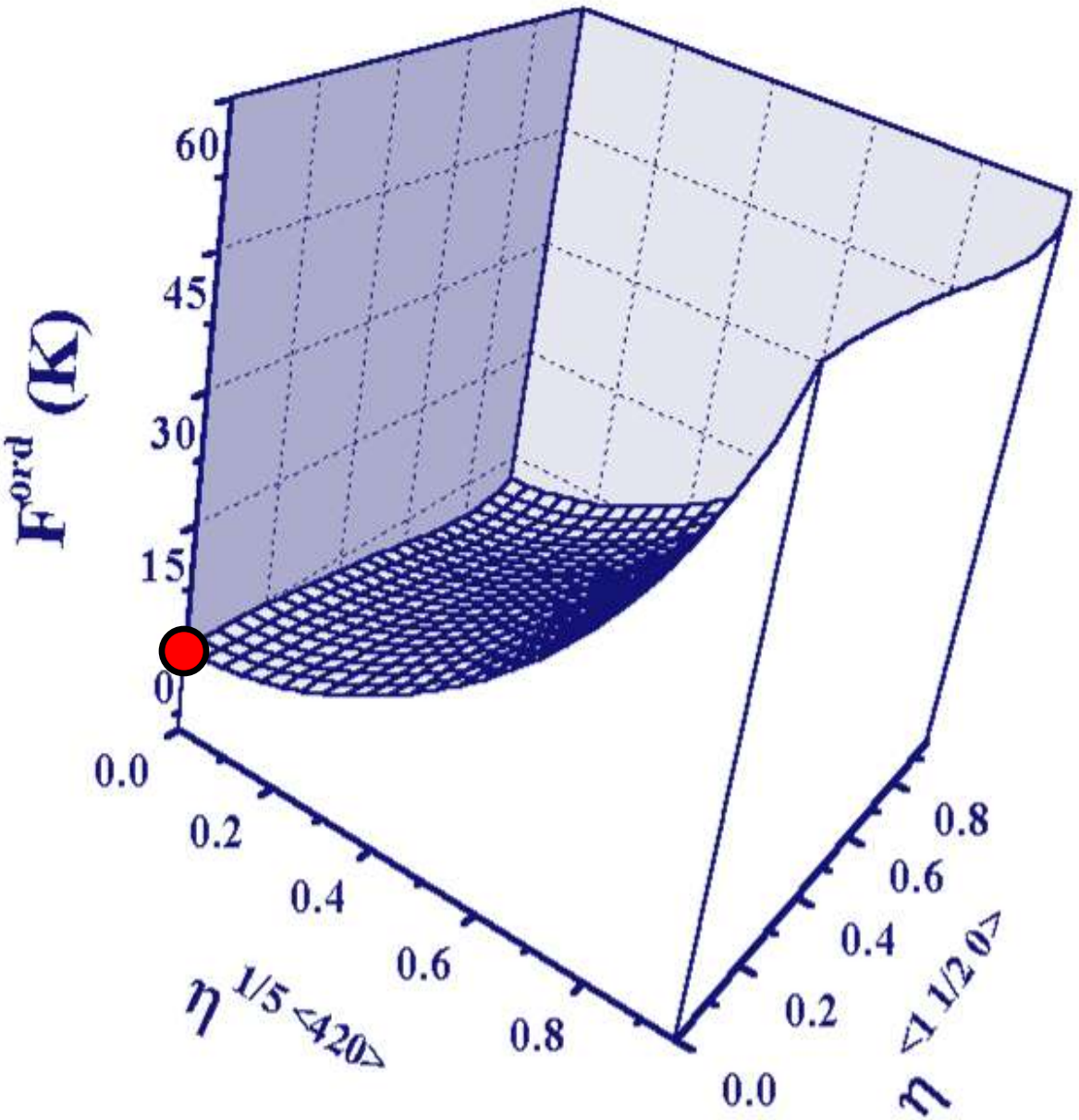

<1 ½ 0> & 1/5 <420> Ordering Competencies

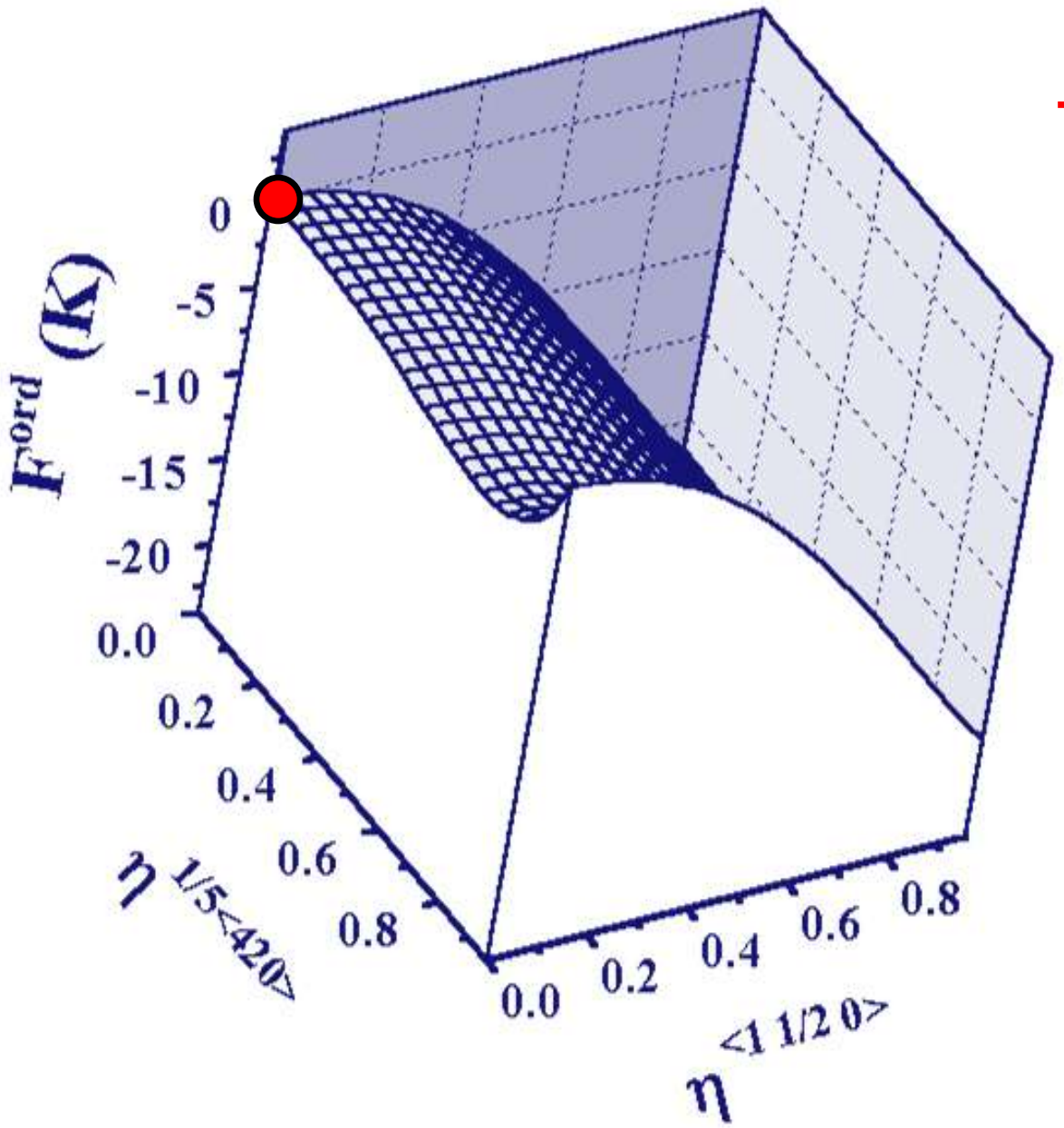

<1 ½ 0> & 1/5 <420> Ordering Competencies

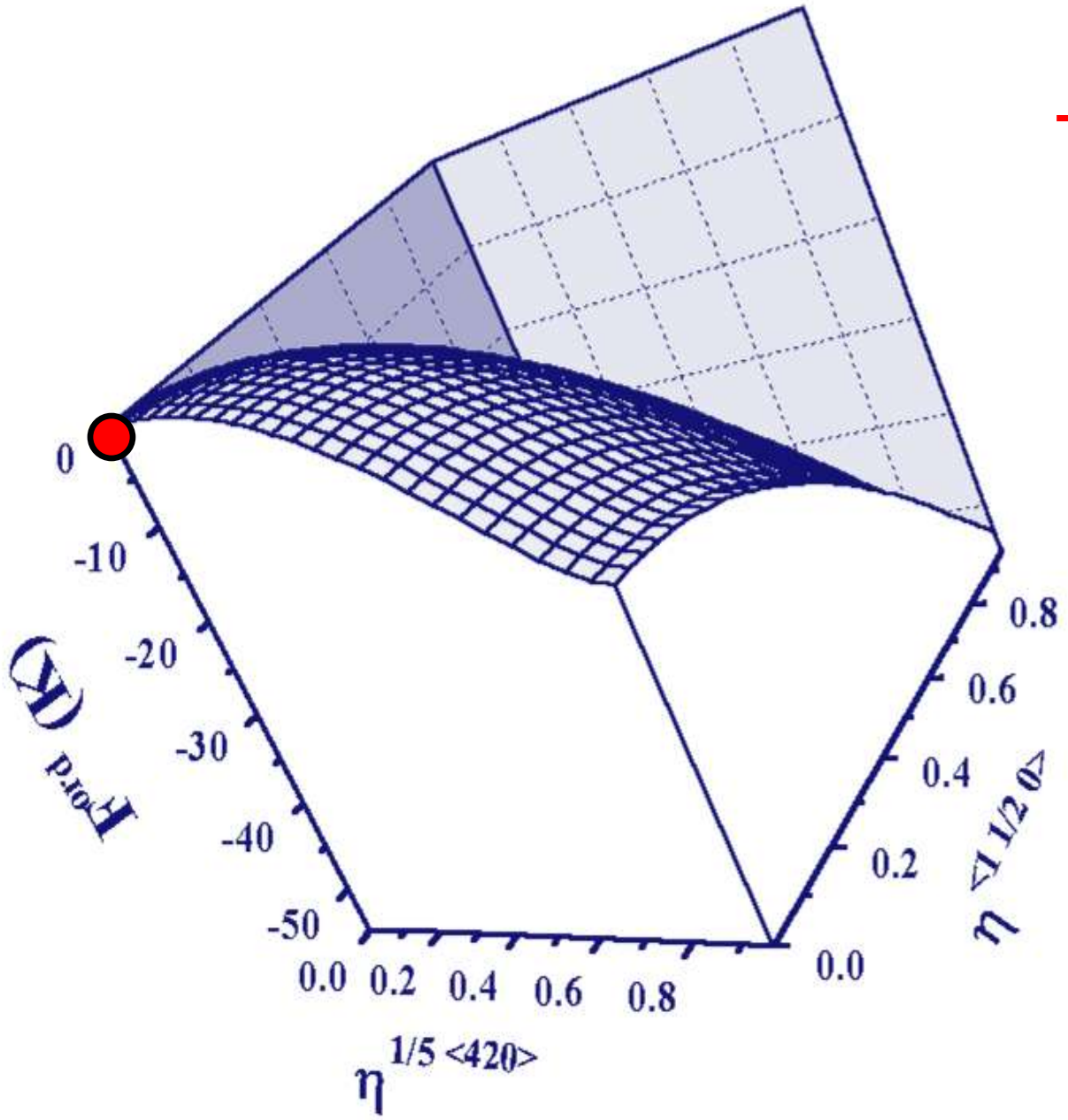

Monte Carlo Simulation: V(k) Maps for v_i, i = 1, 10

3D ensemble size of 128x128x32 points

Random selection of atom pair & calculation of energy change for a possible exchange based on pair interaction energies, v_i, i = 1, 10

Computed diffraction patterns (CDPs) are a FFT spectrum of atom positions in the ensemble for compariosn with experimentally obtained SAEDPs

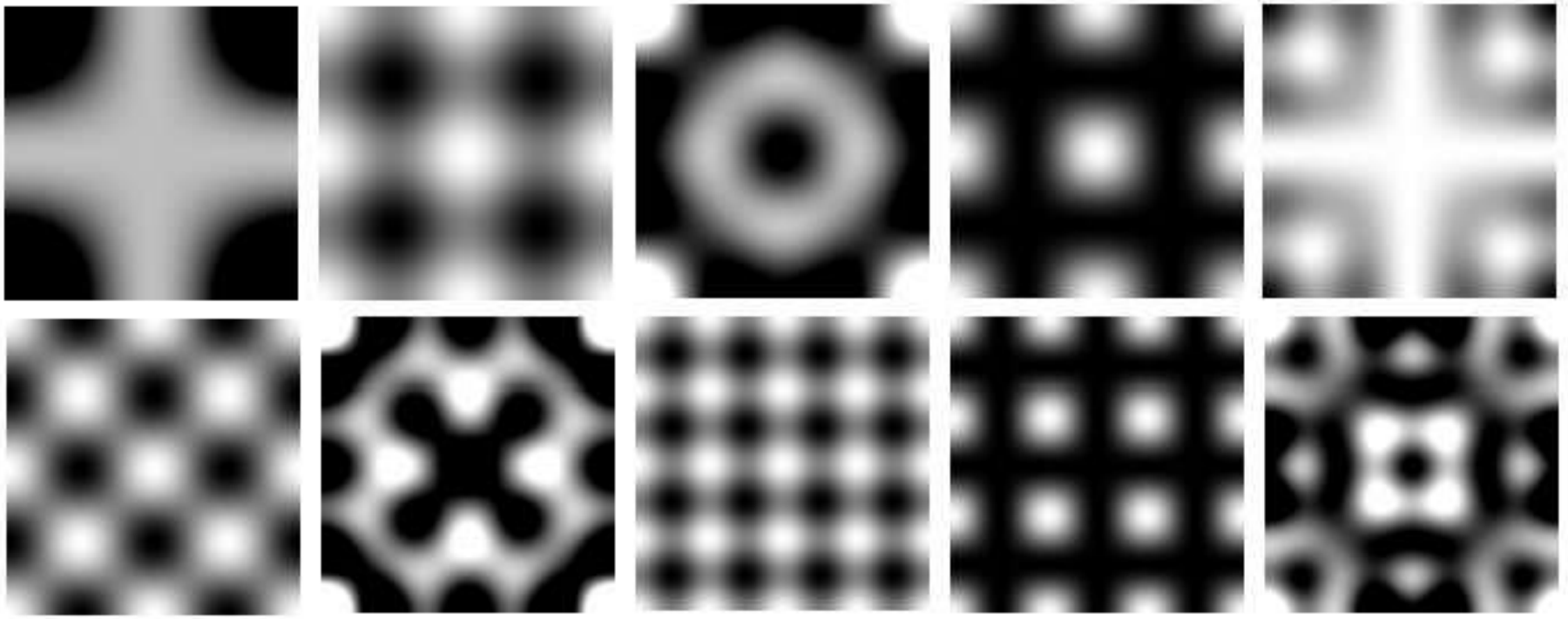

Monte Carlo Simulation of Ordering in Ni_4Mo Alloy

$Ni_{80}Mo_{20}$ Alloy

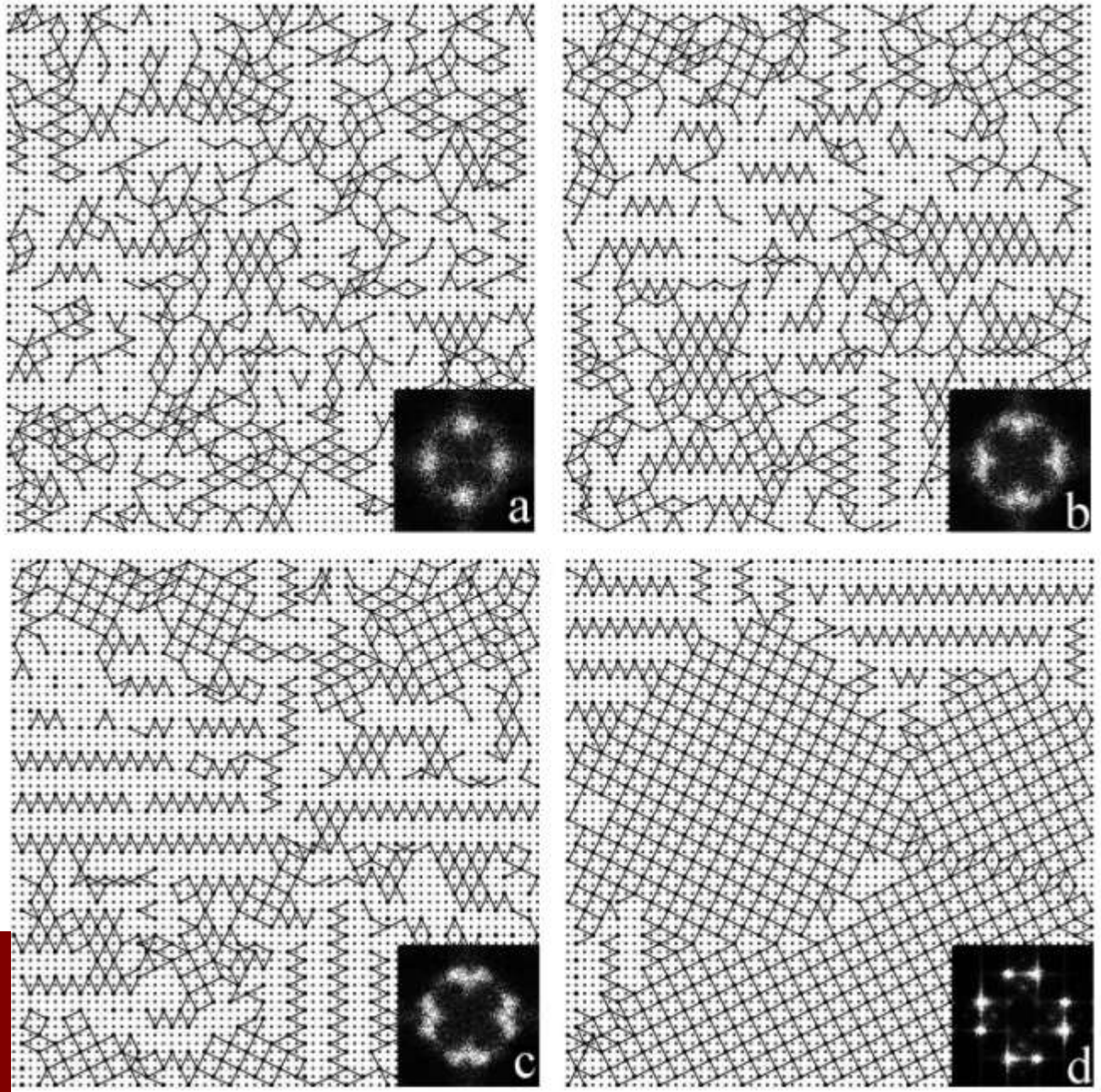

U D Kulkarni,
Acta Mater. Vol. 52,
2721 (2004).

V(k) Maps & Early Stage CDPs

V(k) Maps

Computed Diff Patterns

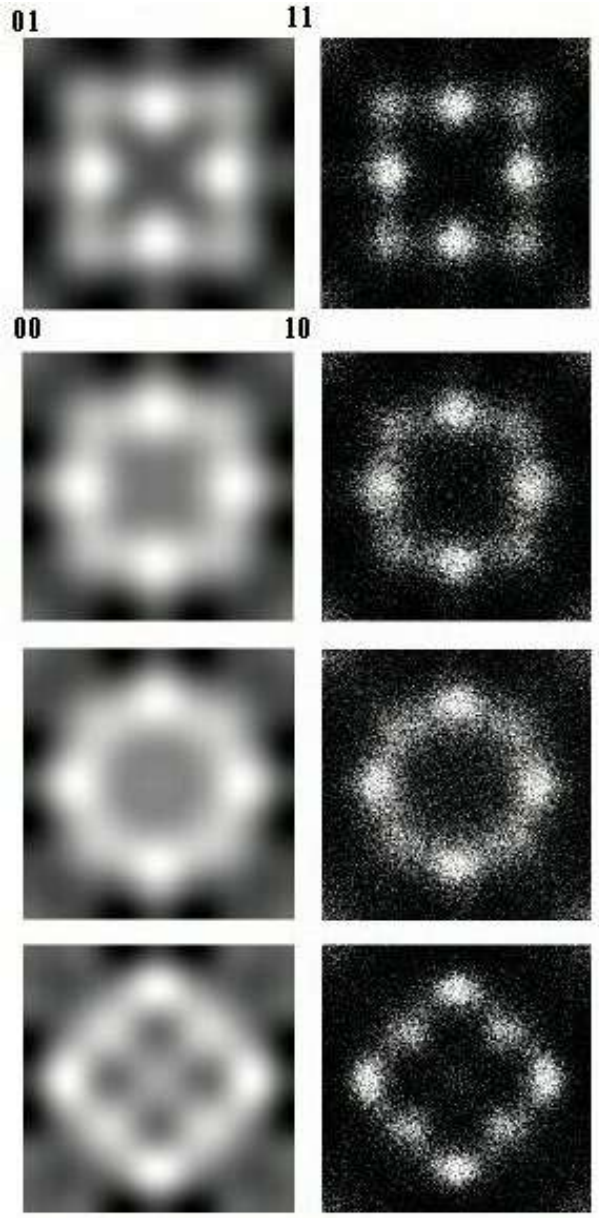

Ni_3Mo ($D0_{22}$)

High +ve

Ni_4Mo ($D1_a$)

moderate

Ni_2Mo

Zero

N_3M

High -ve

APB energies

Interference of Concentration Waves Leading to the Formation of Nuclei

- Very early stage of the transformation is dictated by the second derivatives of free energy w.r.t. order parameter.
- Formation of localized clusters can be a consequence of superimposition of concentration waves. The resulting embryo can be viewed as the transformation nucleus. Superimposition of waves leads to a positive third order coefficients in LL, the condition necessary for ordering of the first kind.
- Phase locking causes localization of the nucleation event
- The final structure is determined by the deepest well in the free energy space.

Analogy with Magnetic Ordering

Analogy with Magnetic Ordering

Naturally Occurring Layered Compounds:
$Ca_{2.5-x}La_xSr_{0.5}GaMn_2O_8$

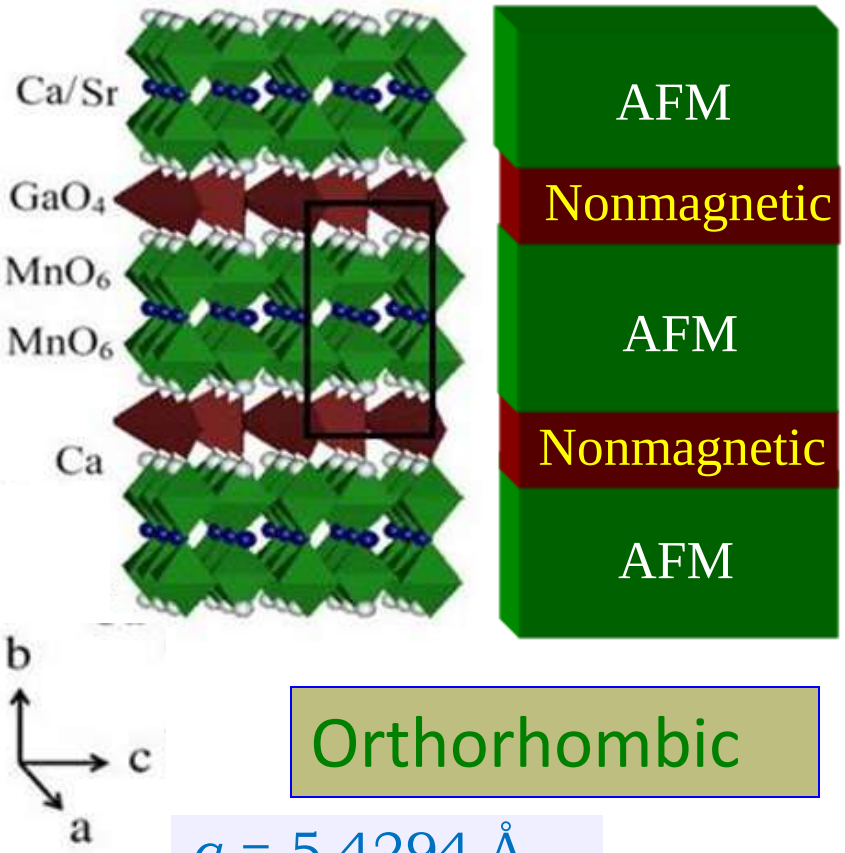

Orthorhombic

a = 5.4294 Å
b = 11.3722 Å
c = 5.2983 Å

"Locking" of 2D & 3D short-range Antiferromagnetic Ordering over extended temperature range

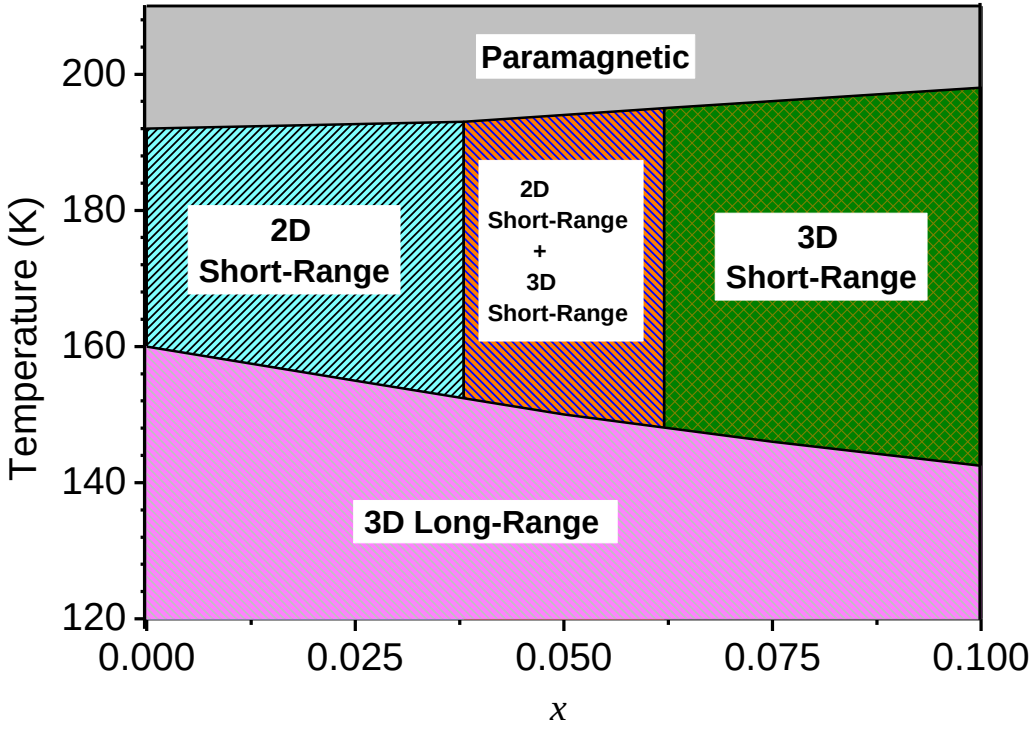

S. M. Yusuf *et al.*, Phys. Rev. B 74, 184409 (2006)
A. K. Bera, S. M. Yusuf, J. Appl. Phys. 107, 013911 (2010)

Evaluation of Antiferromagnetic Correlations with Temperature

Temperature Evolution of Neutron Diffraction Patterns

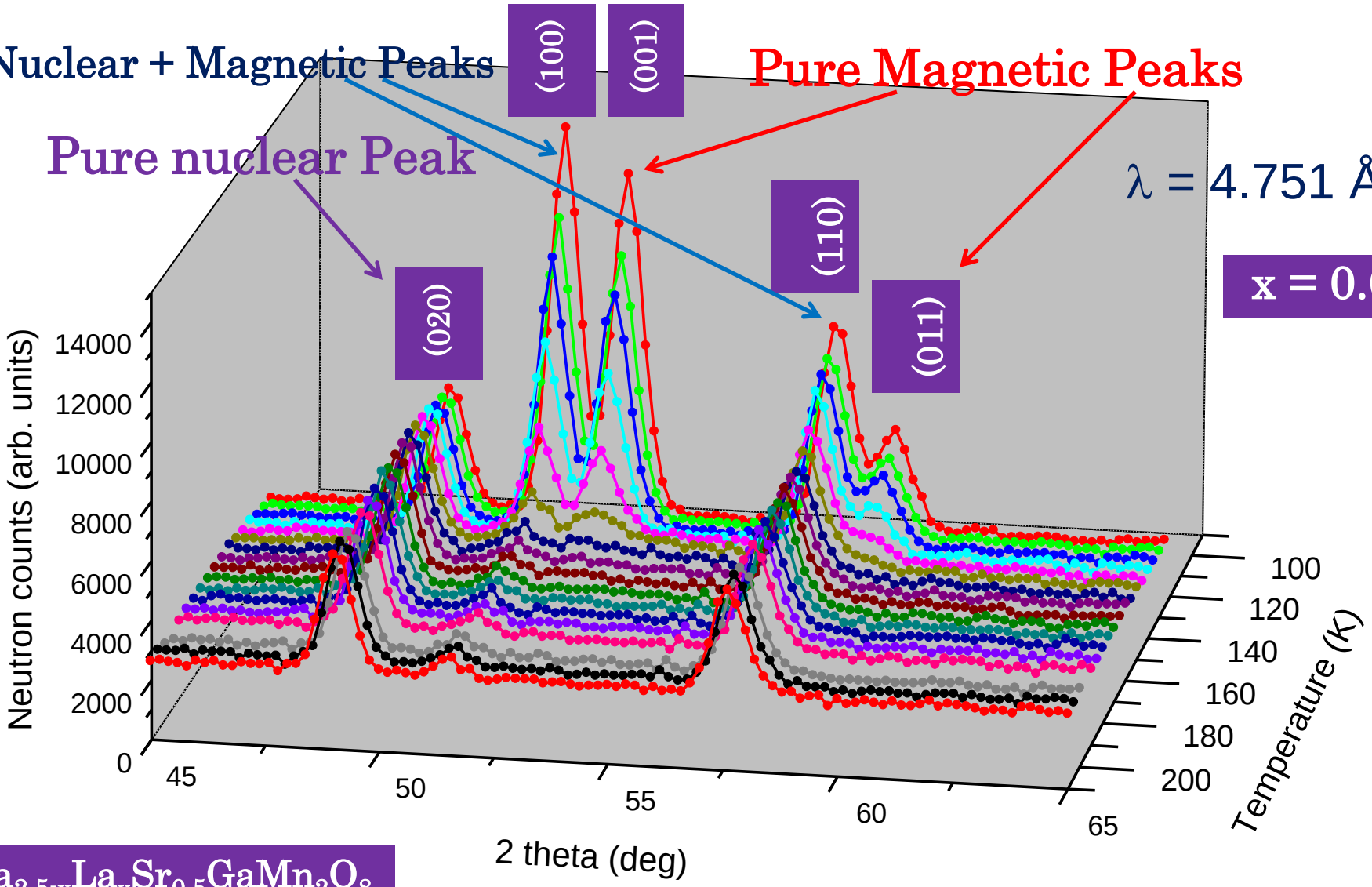

$Ca_{2.5-x}La_xSr_{0.5}GaMn_2O_8$

Naturally Occurring Layered Compounds: $Ca_{2.5-x}La_xSr_{0.5}GaMn_2O_8$

Neutron Powder Diffraction Study

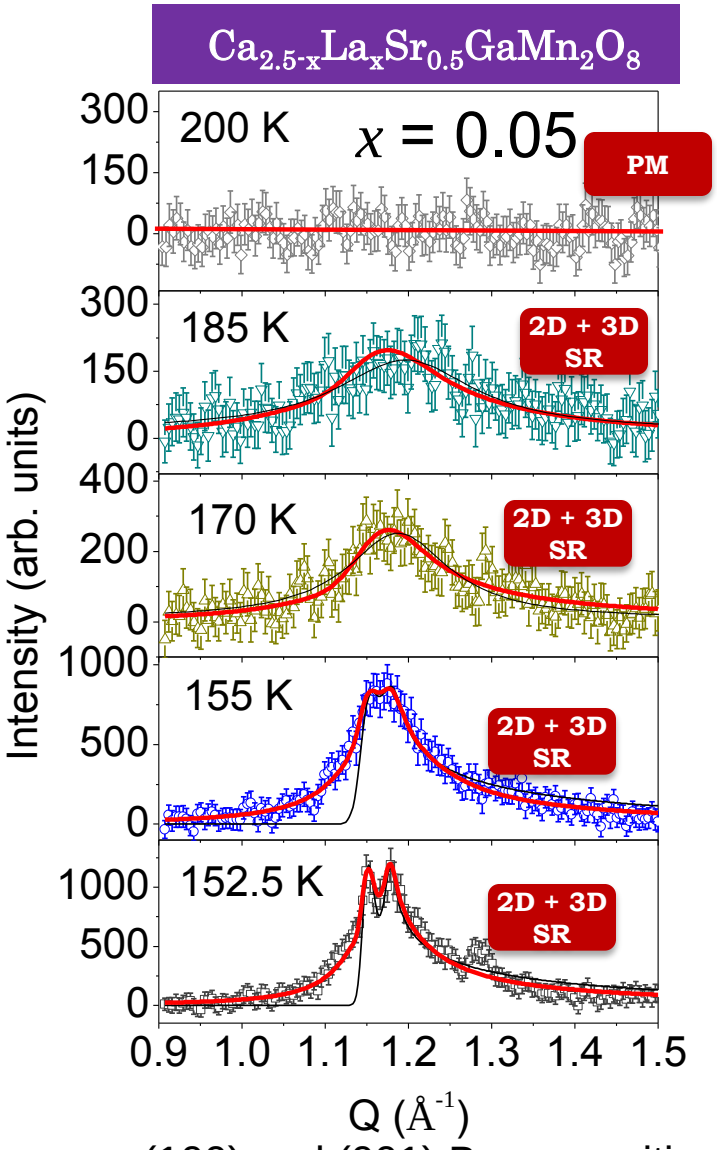

(100) and (001) Bragg position

Nuclear Scattering at 210 K is Subtracted out

x = 0.05

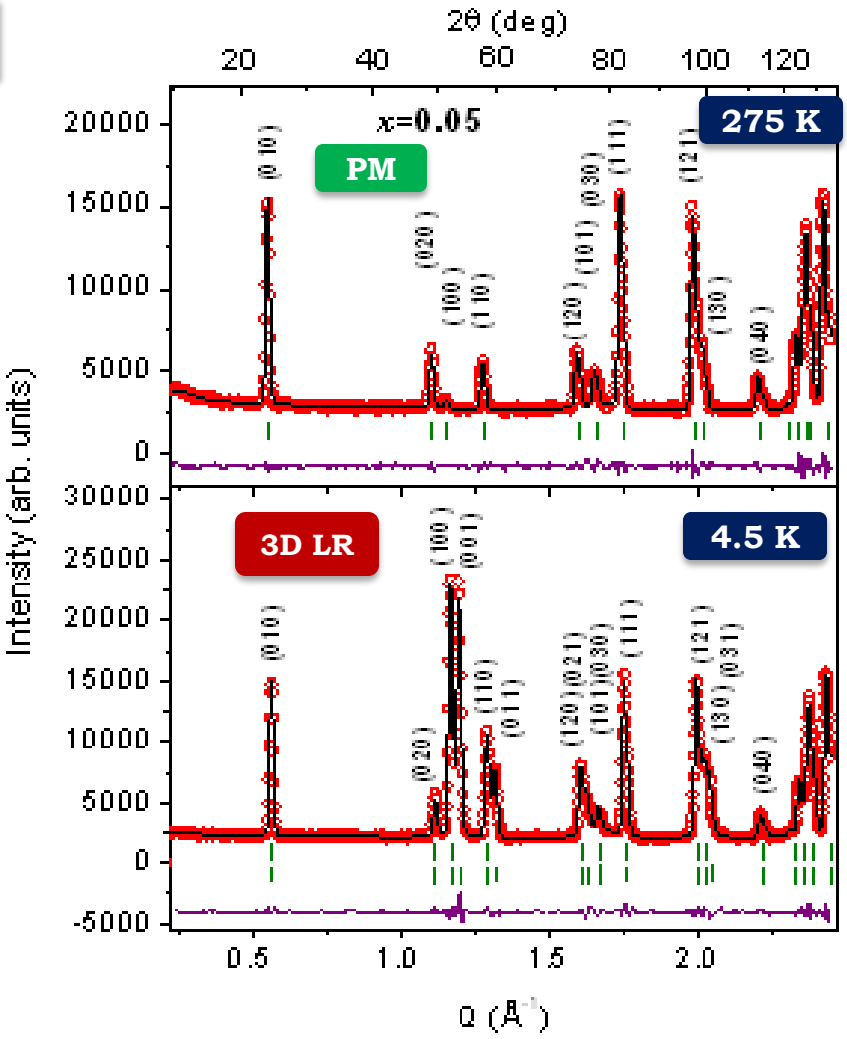

2D: Warren Function

3D: Lorentzian Function

$Ca_{2.45}La_{0.05}Sr_{0.5}GaMn_2O_8$

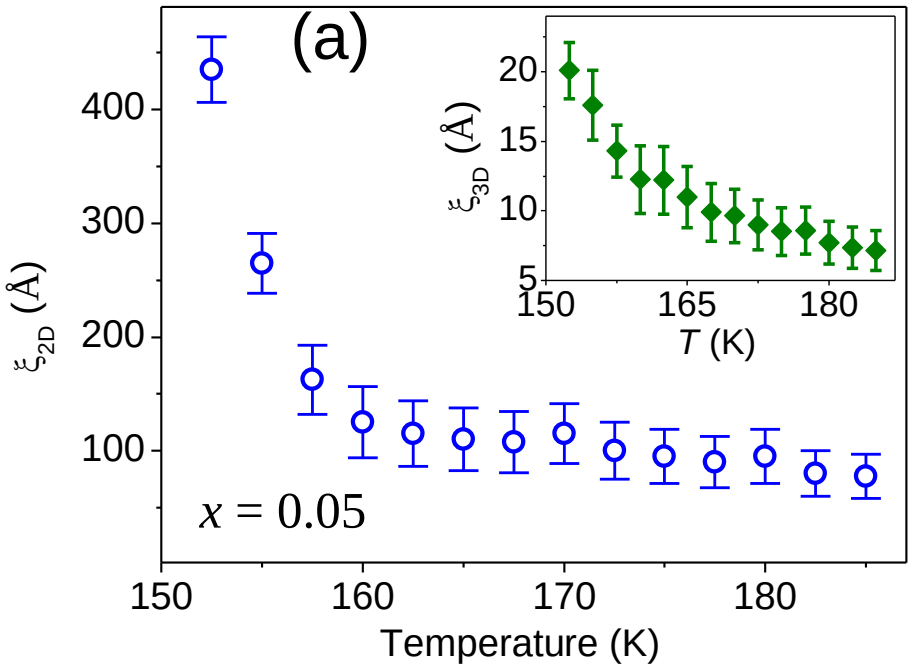

T > 200

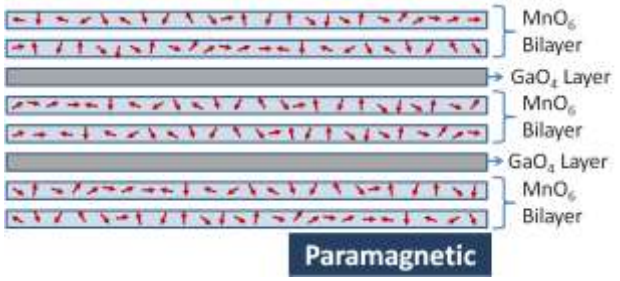

190-200

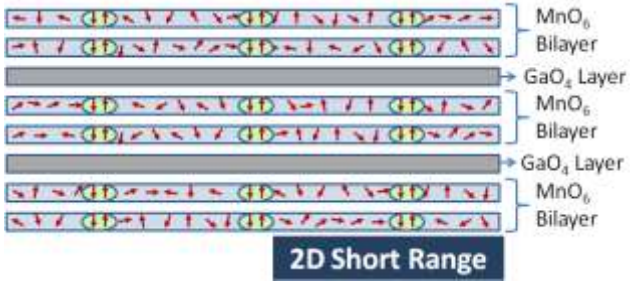

165-190

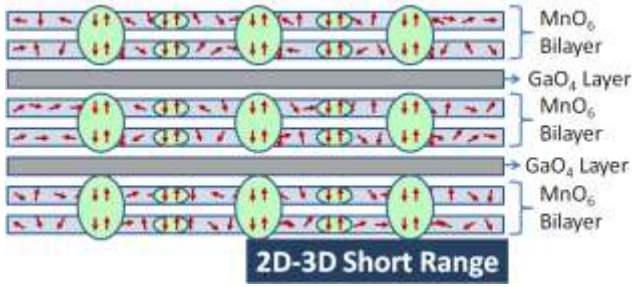

155-165

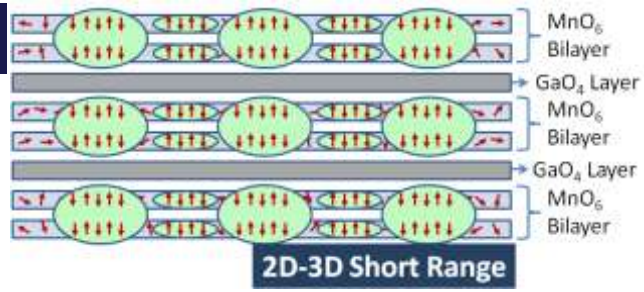

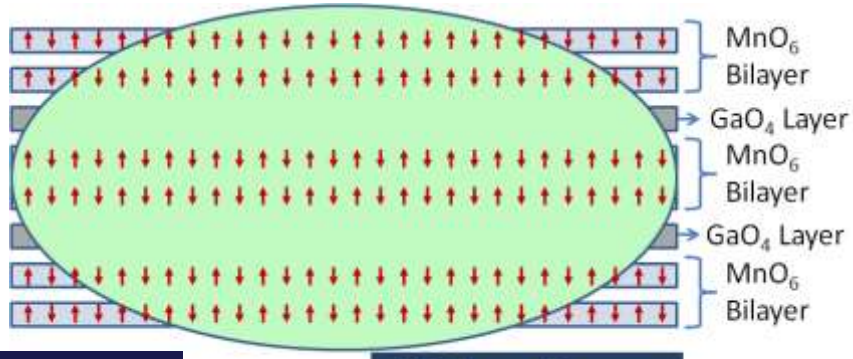

T < 155 K

$(La_{1-x}Dy_x)_{0.7}Ca_{0.3}MnO_3$ CMR Perovskites

Growth of Spin-Spin correlation length (ξ)
(Measured by small angle neutron scattering)

$X = 0.347$

$(La_{1-x}Dy_x)_{0.7}Ca_{0.3}MnO_3$

Temperature dependence of ξ

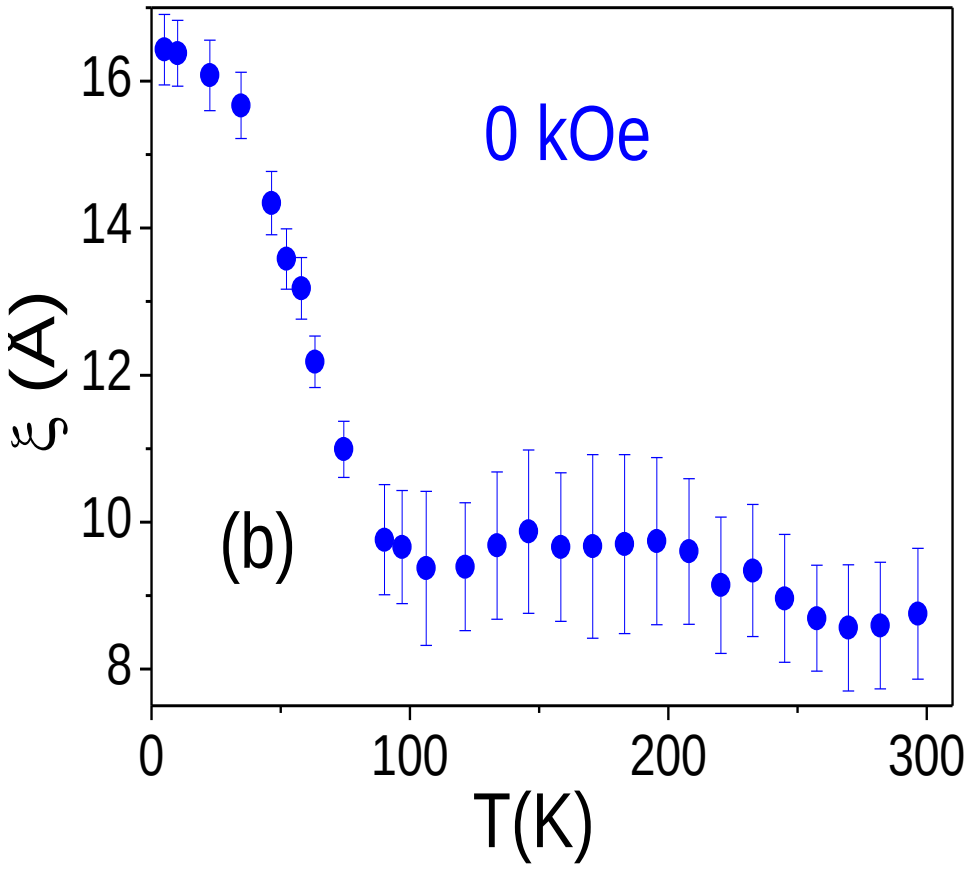

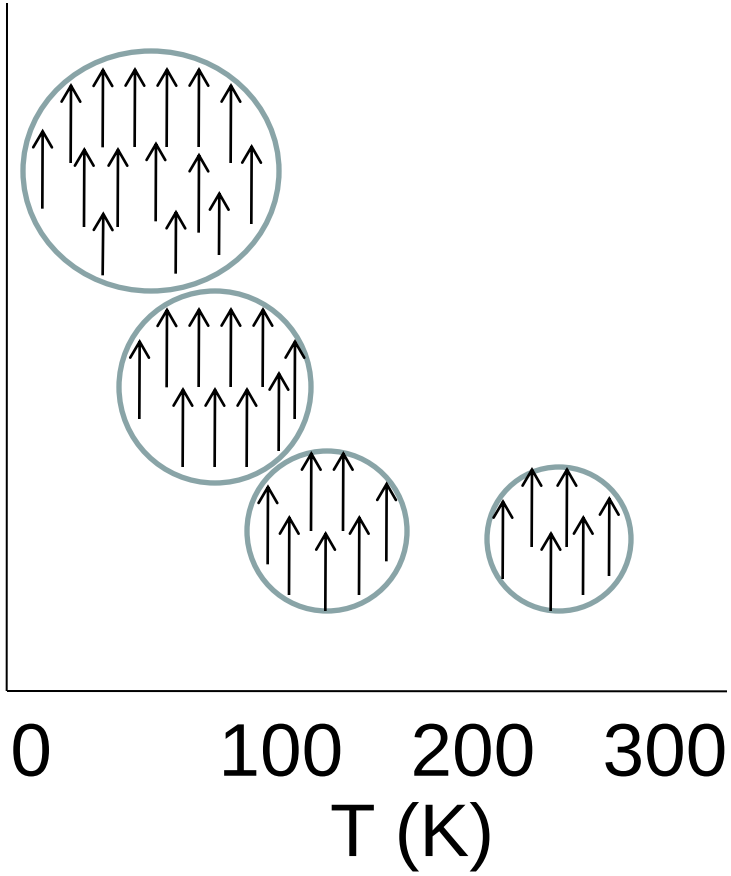

$(La_{1-x}Dy_x)_{0.7}Ca_{0.3}MnO_3$ CMR Perovskites : Neutron Diffraction study under Magnetic field

Growth of Spin-clusters under Field

$(La_{1-x}Dy_x)_{0.7}Ca_{0.3}MnO_3$

Appearance of Ferromagnetic Bragg Intensity

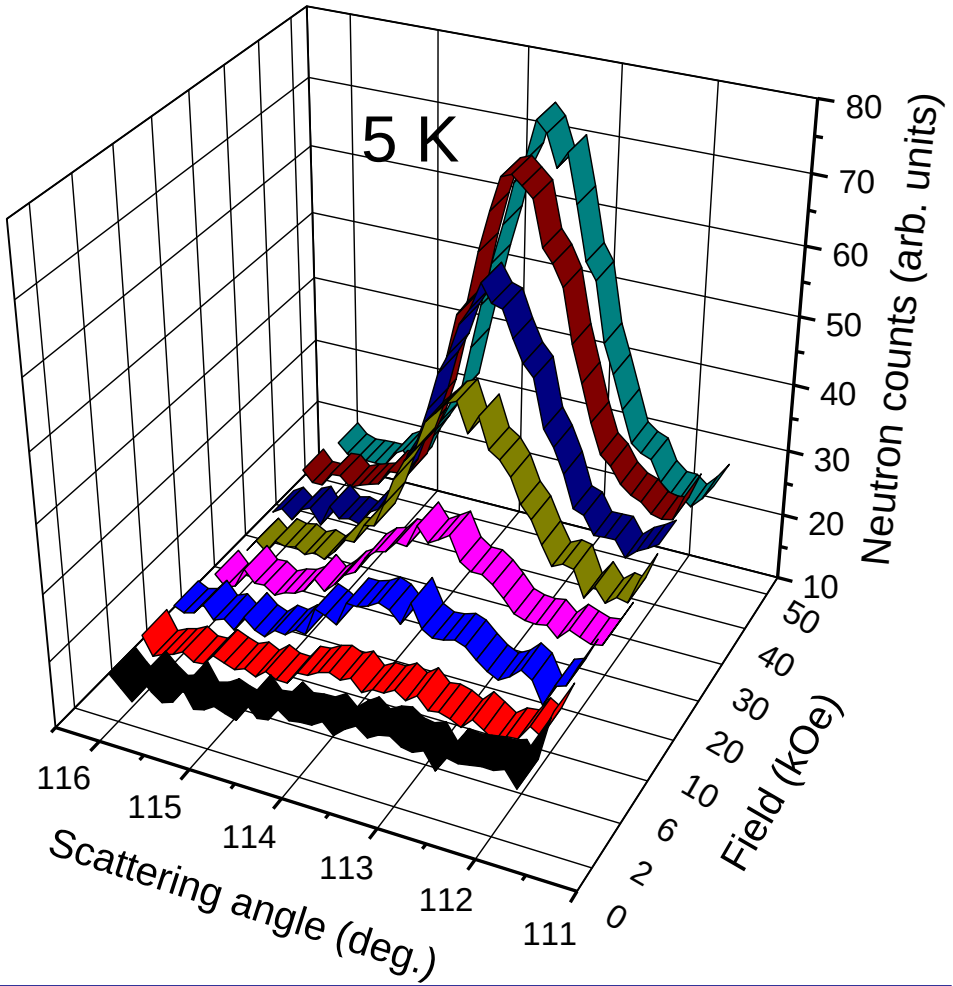

S. M. Yusuf, *et al.* Phys. Rev B 68, 104421 (2003)
J. Magn Magn Mater 272-276, 1288 (2004)
S. M. Yusuf *et al.* Phys. Rev. B (2006)

$X = 0.347$

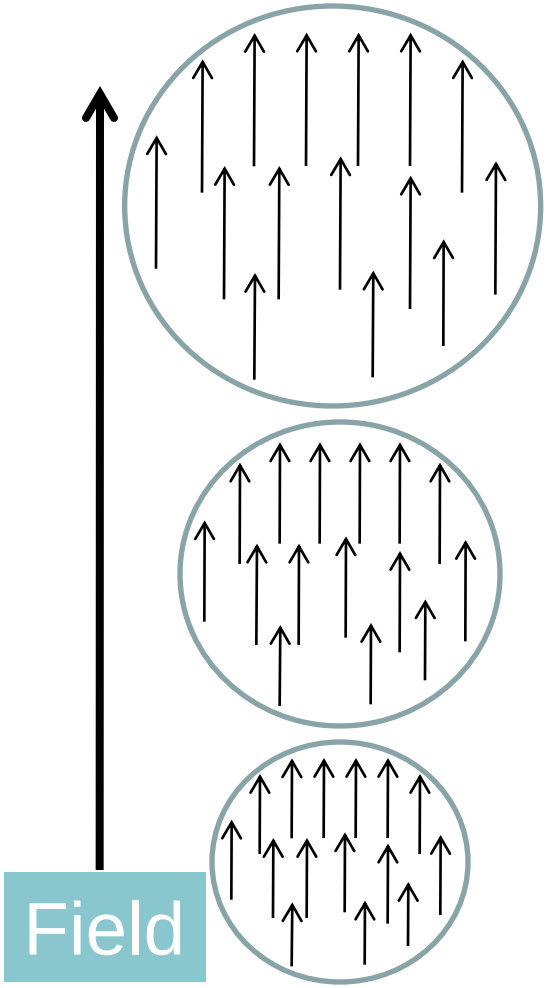

Spin Clusters to Long-range Ferromagnet

Coupling of Chemical phase separation and magnetic ordering

Coupling between the magnetic and chemical ordering lead to the formation of different degree of two dimensional and three dimensional ordering.

Free energy vs composition plot for a temperature below the bicritical point.

The paramagnetic $A2_p$ phase separates into two phase: one rich in magnetic component (A2) and the other lean (B2).

The former orders into Antiferromagnetic and the later remains paramagnetic

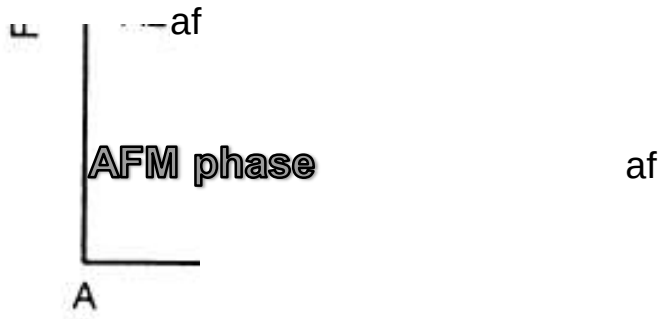

Displacive Ordering

Displacive Ordering: β→ ω Phase Transformation

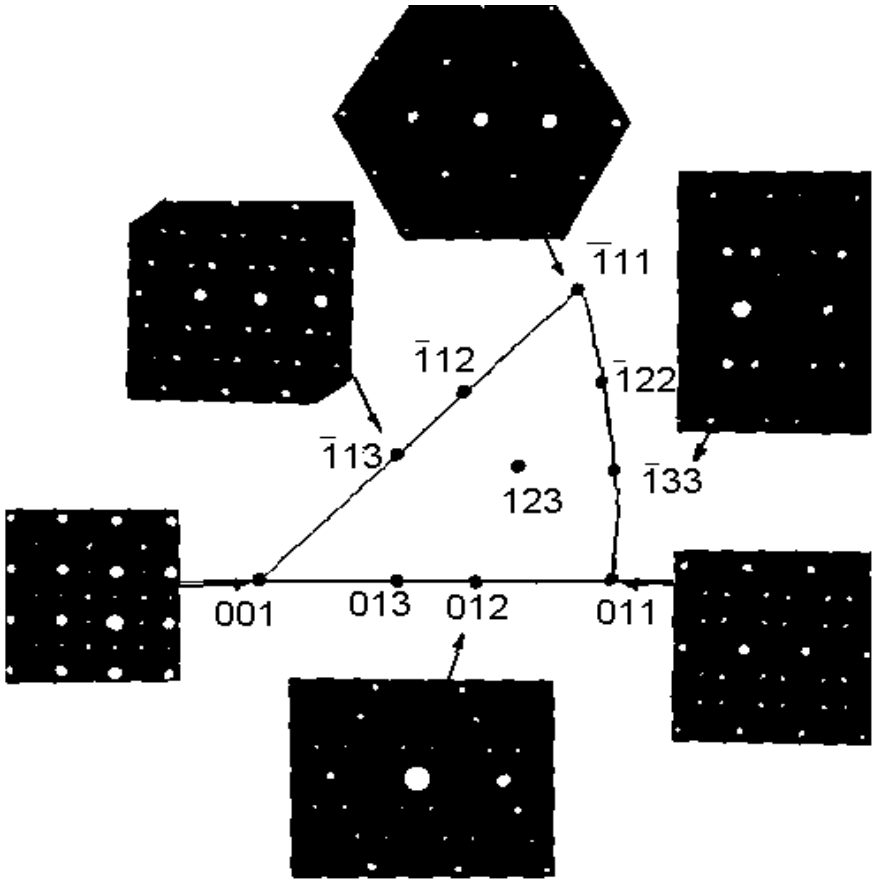

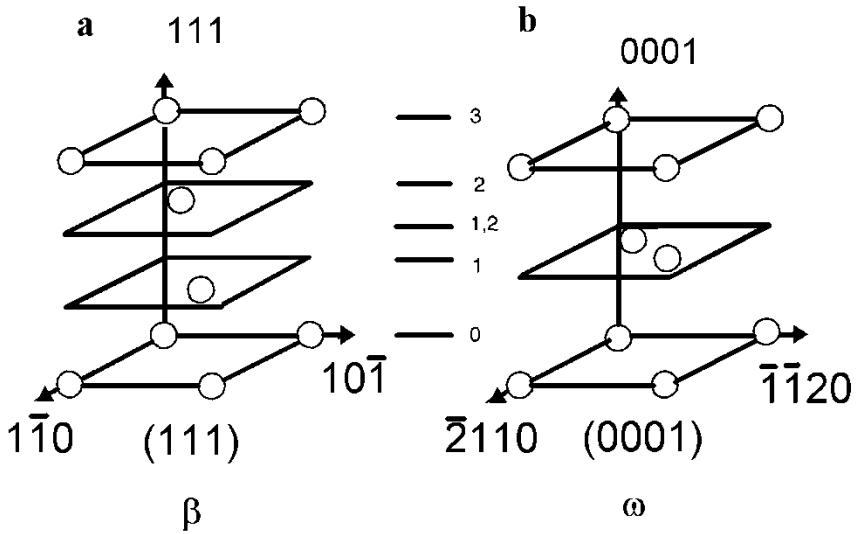

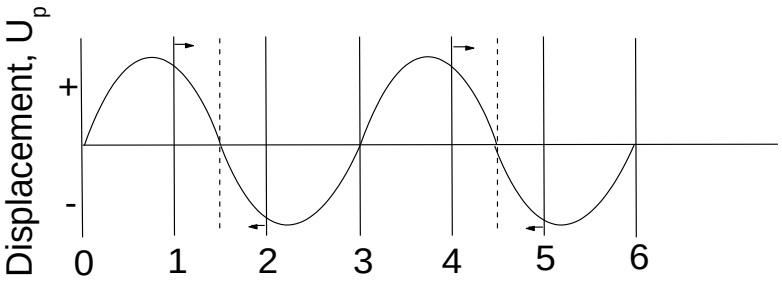

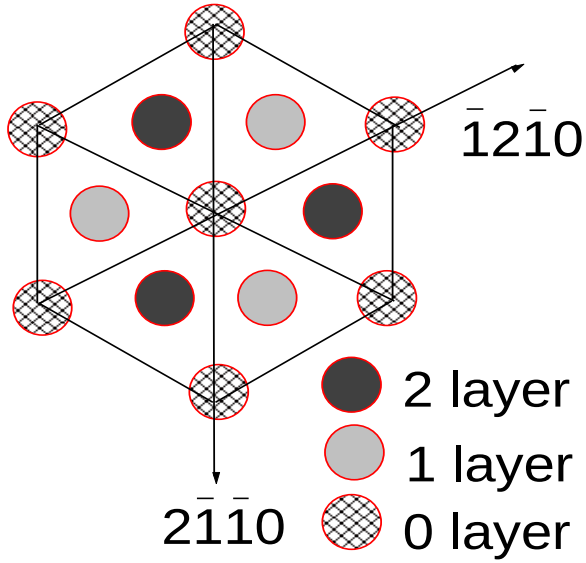

Omega Transformation

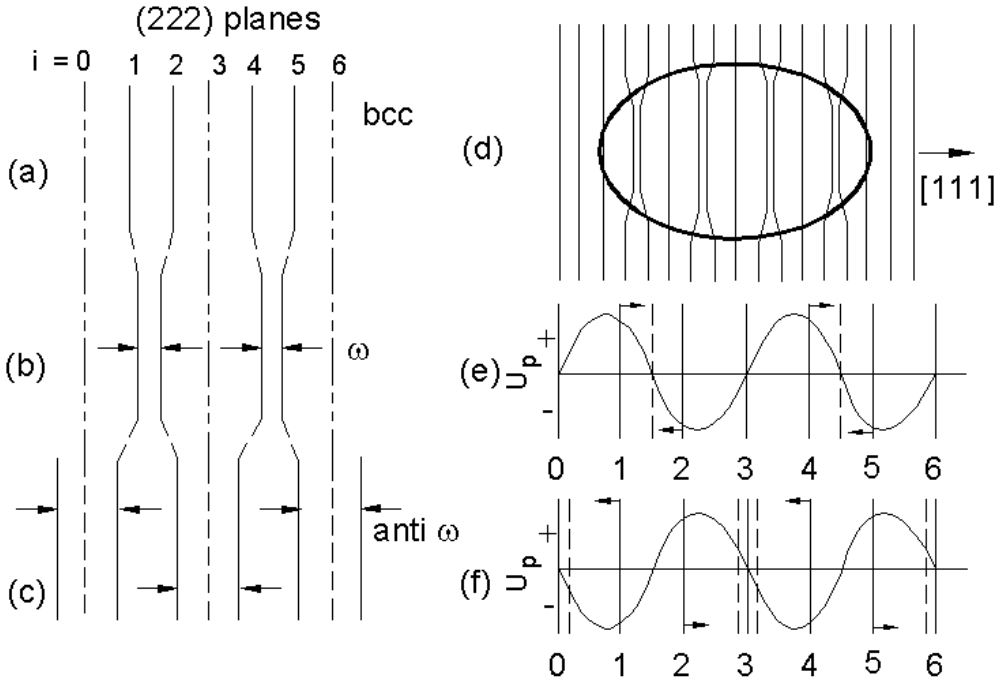

Longitudinal Displacement Waves

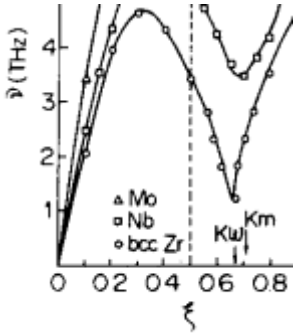

Landau plots explaining
Dual phase β + ω structure

HREM Image of Aged Zr-20Nb Alloy

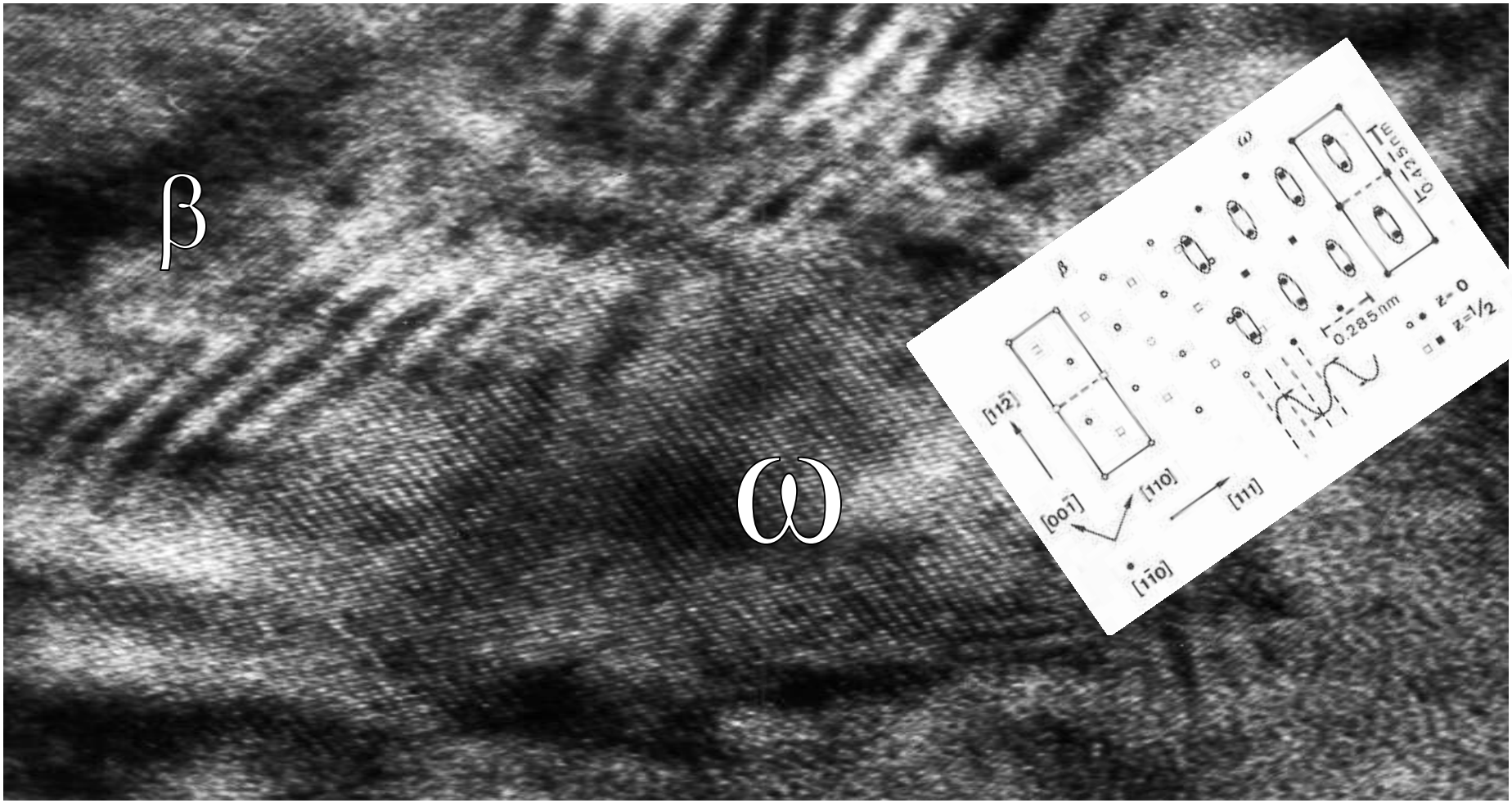

G.K. Dey, R. Tewari, S. Banerjee, G. Jyoti, S.C. Gupta, K.D. Joshi, S.K. Sikka, Acta Materialia, 52, (2004),

Diffuse ω Patterns

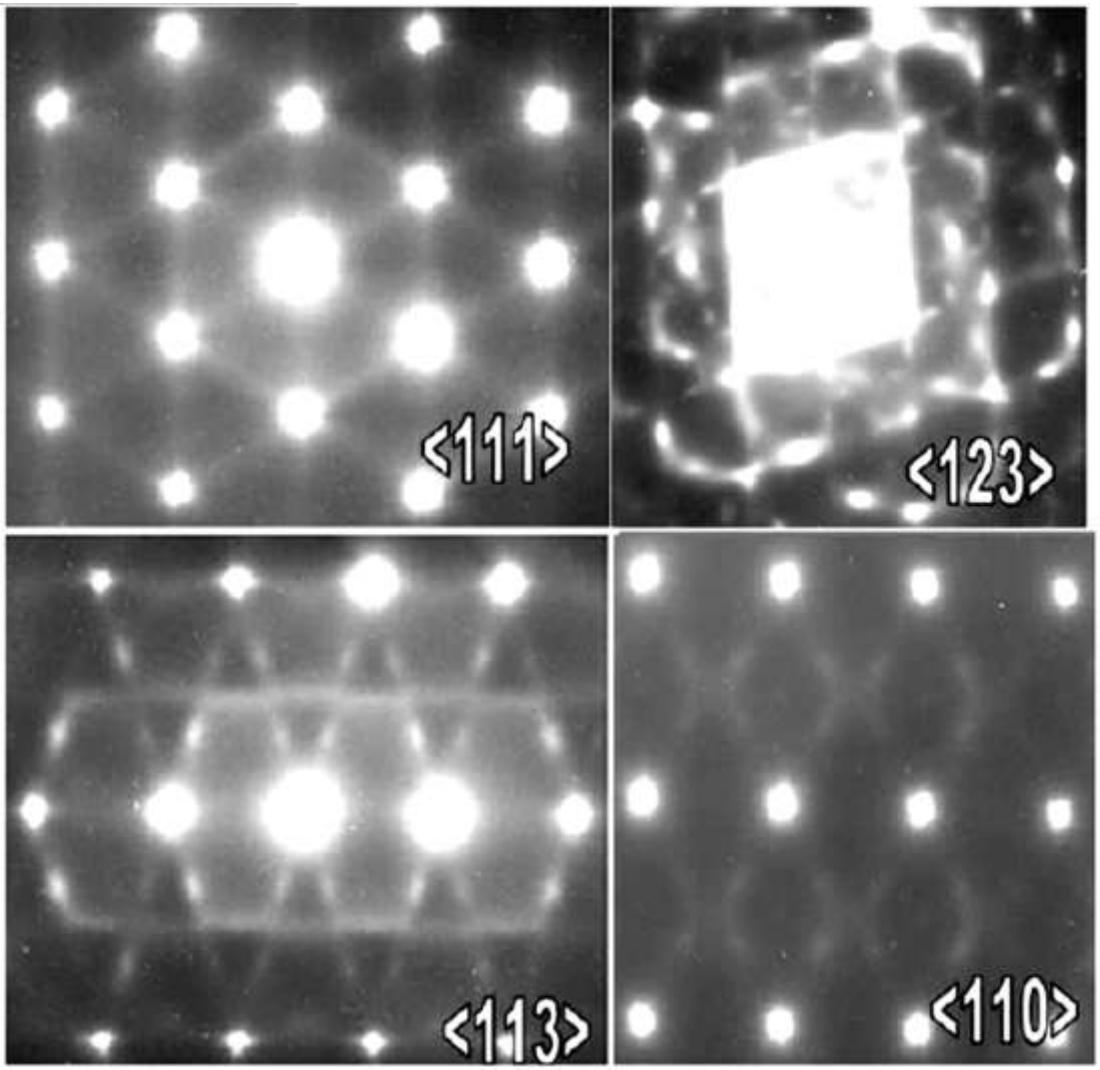

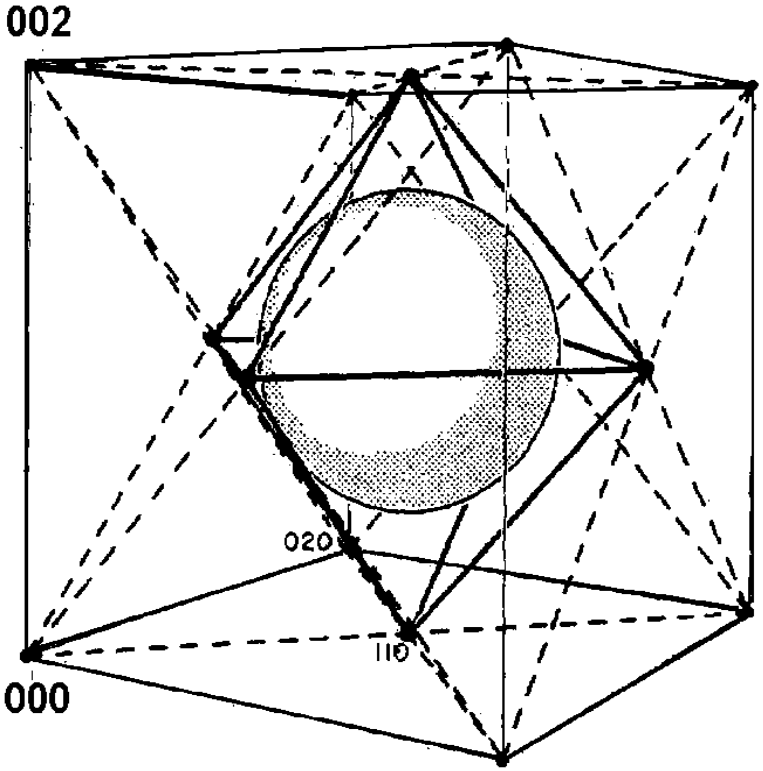

Diffuse ω Patterns

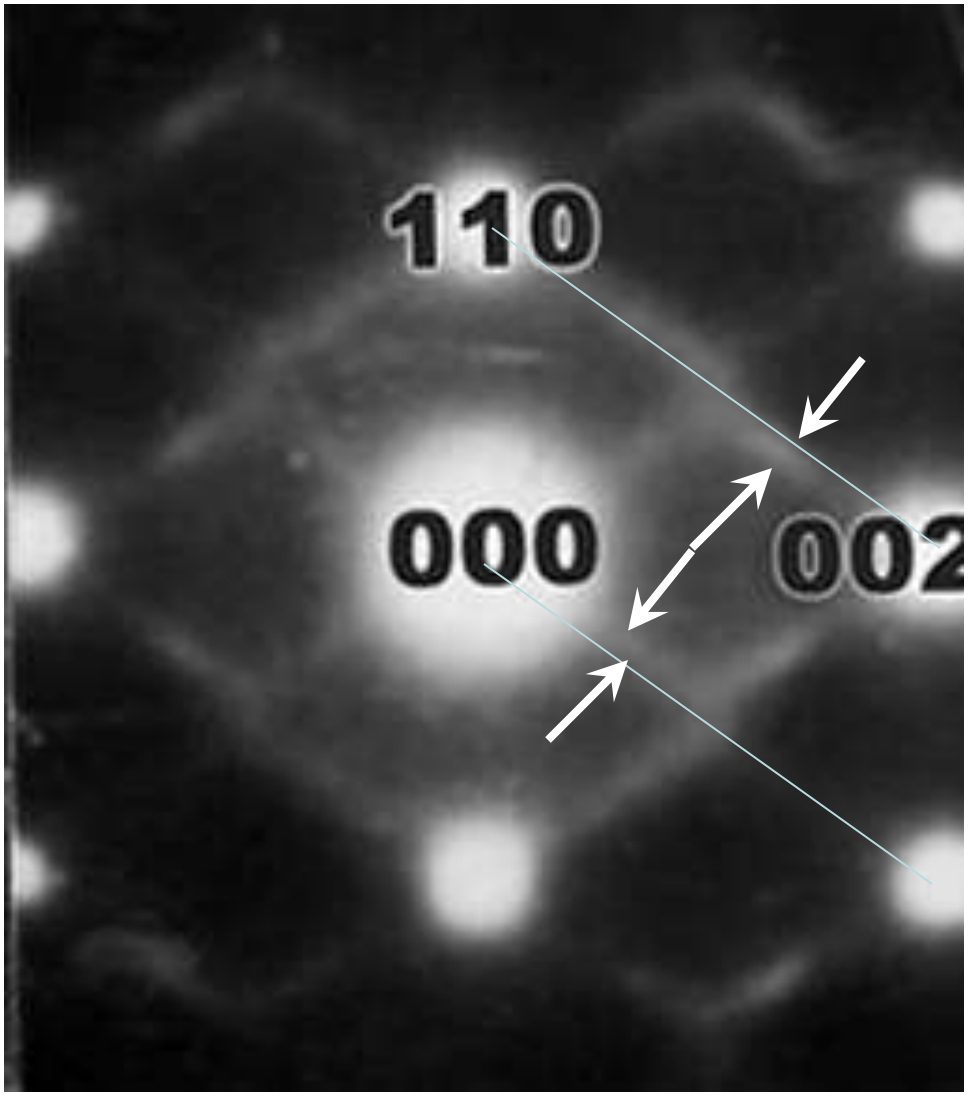

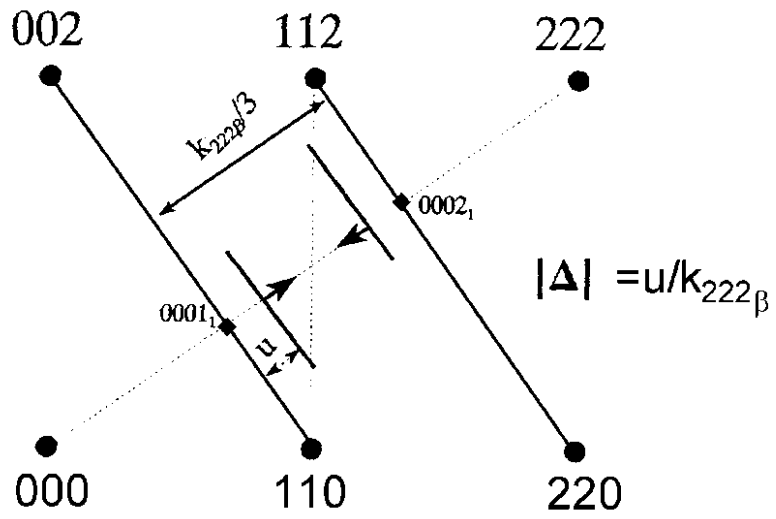

$$|\Delta| = \frac{R_{0001_R} - \frac{1}{3} R_{222_\beta}}{\frac{1}{6} R_{222_\beta}}$$

Embryonic ω

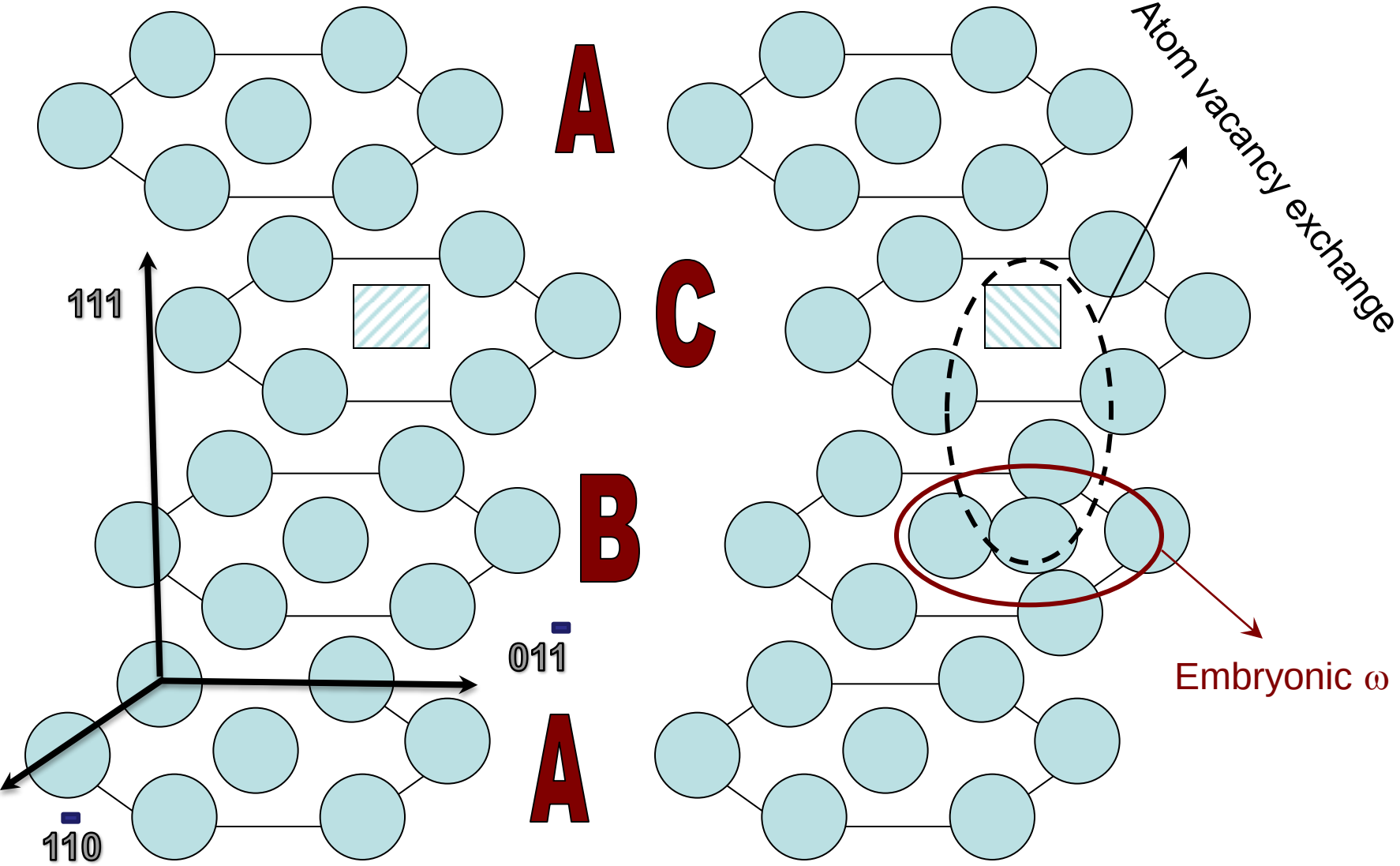

Embryonic ω

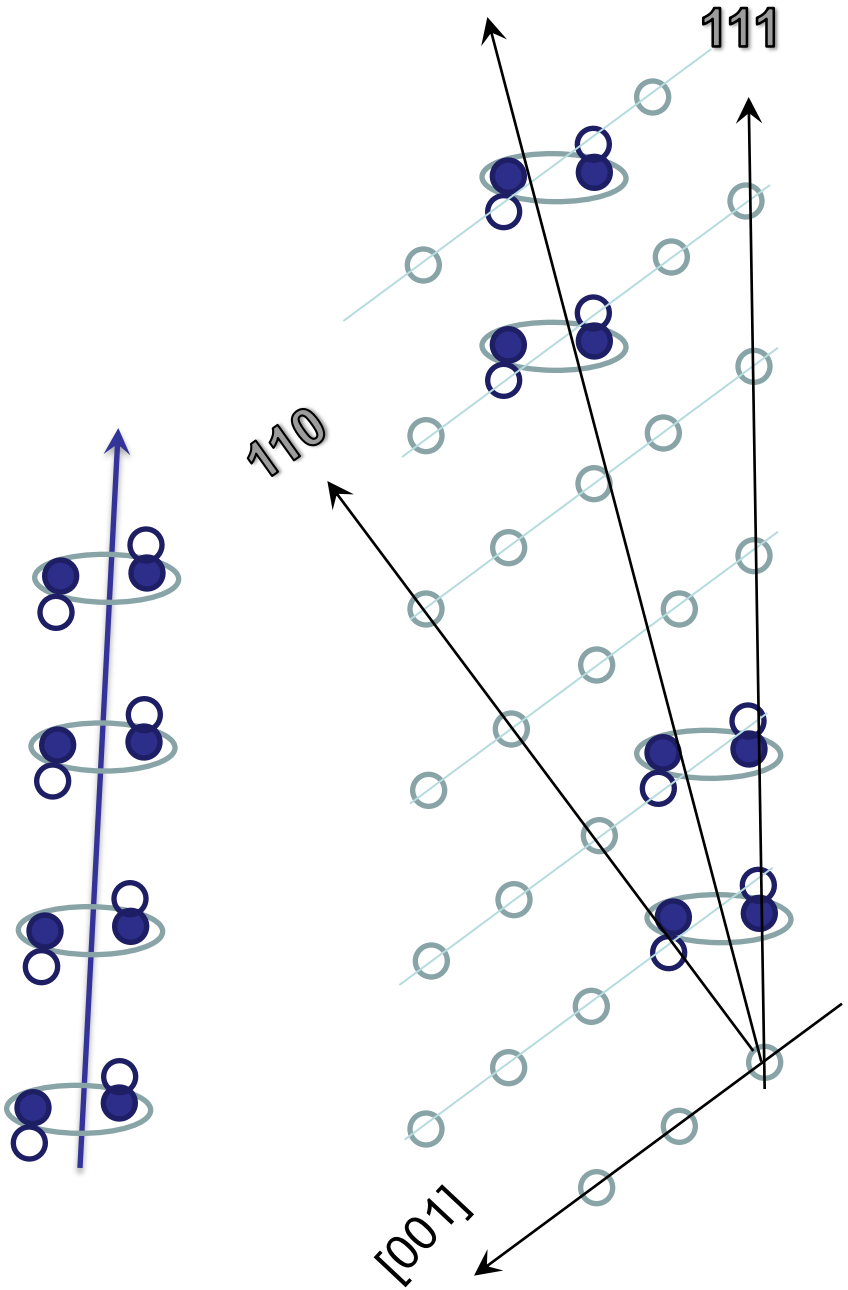

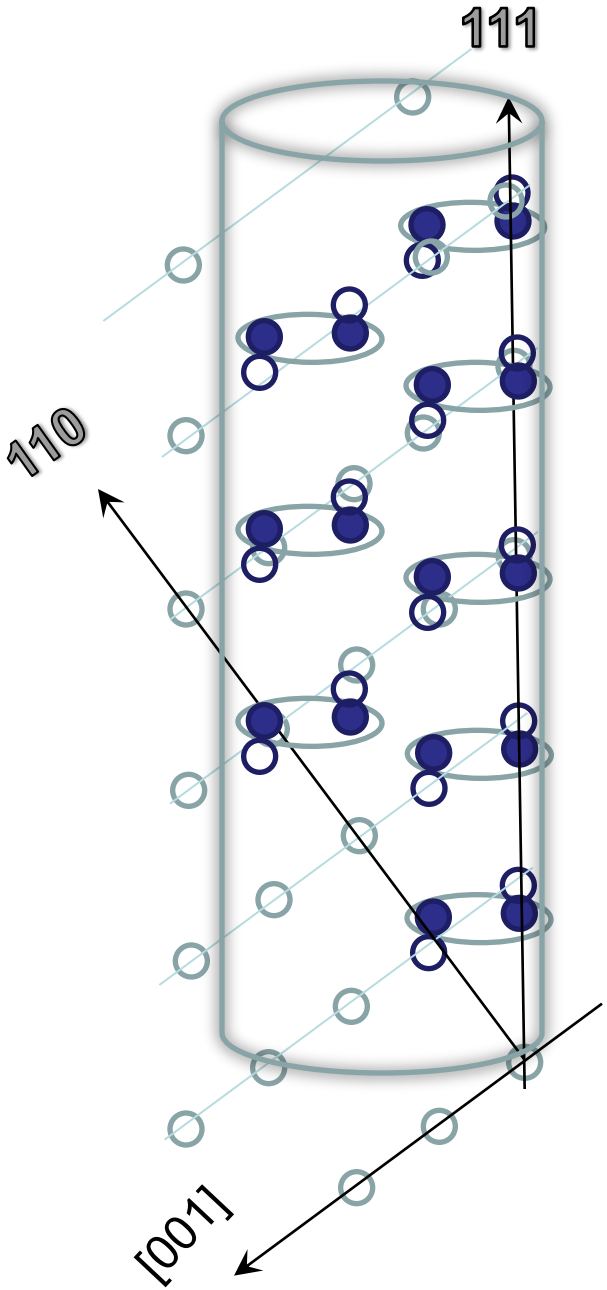

HREM of Diffuse ω

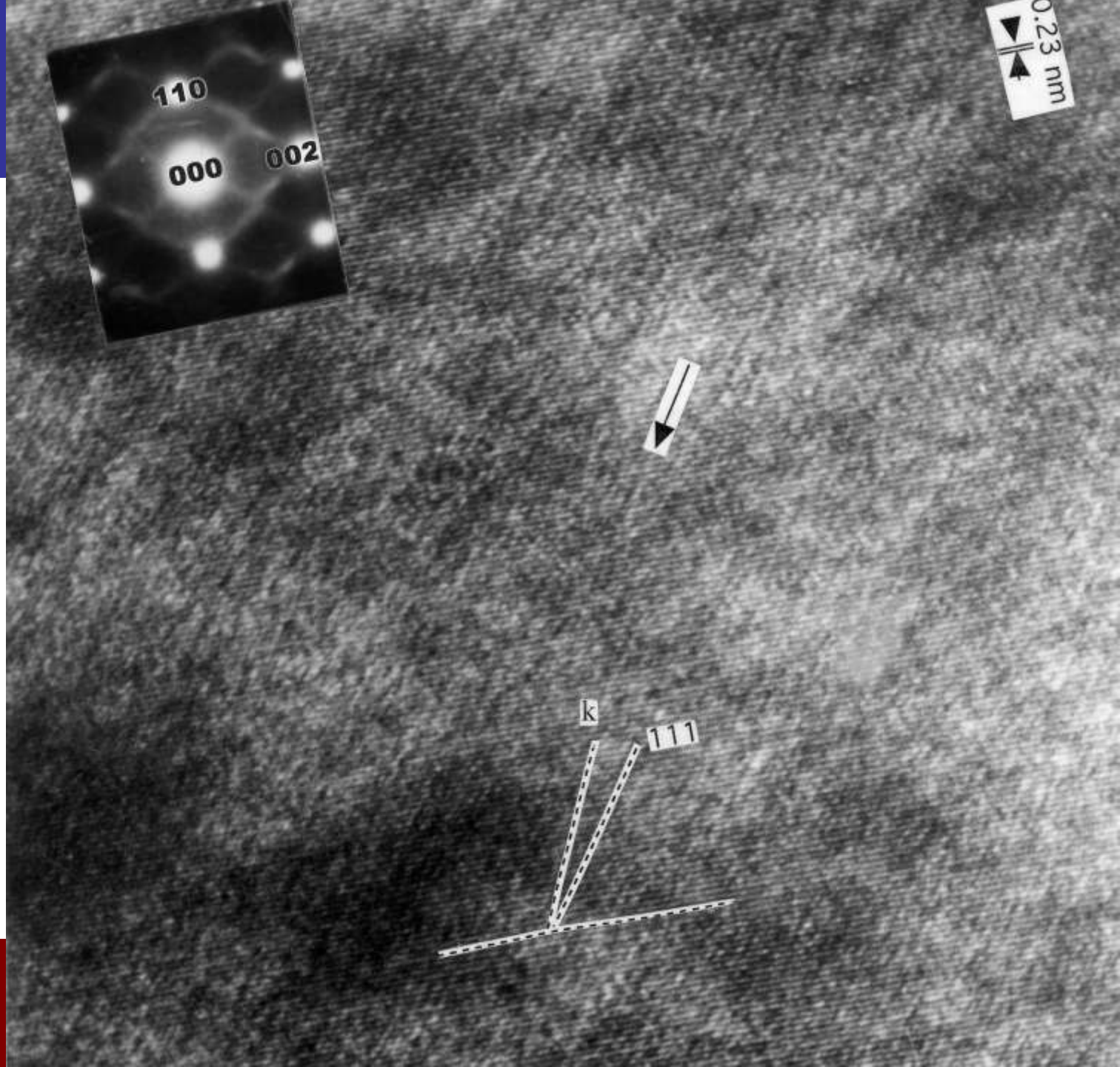

G.K. Dey, et al., Acta Materialia, 52, (2004),

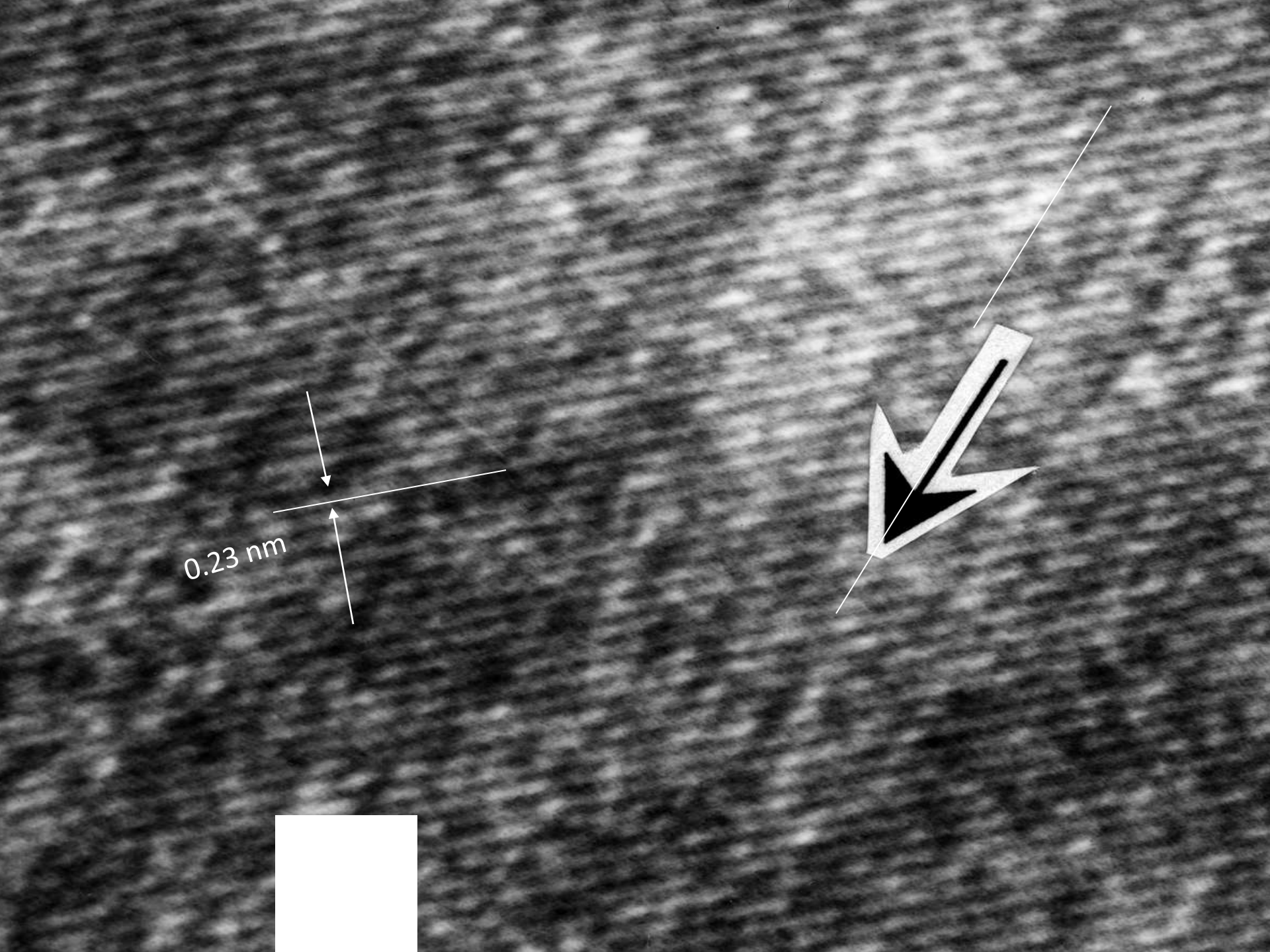
0.23 nm

Irradiation Induced ω Formation

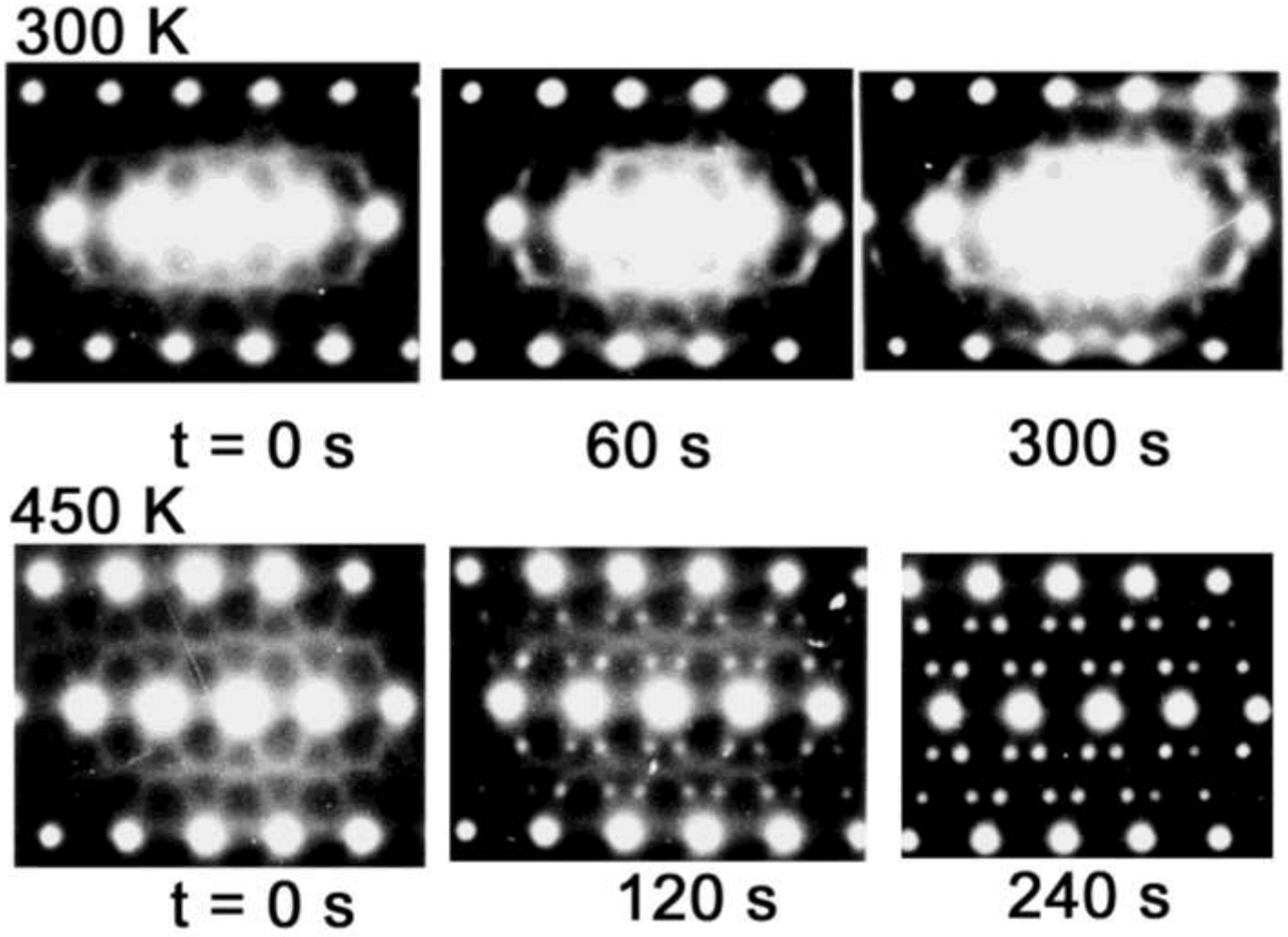

Zr-20Nb , 1 MeV

2Mev

15 Seconds **60 Seconds** **120 Seconds** **480 Seconds**

473K

30 Seconds **120 Seconds** **480 Seconds** **600 Seconds**

573K

Deviation Parameter Estimation

Thermal

irradiation

1 MeV

2 MeV

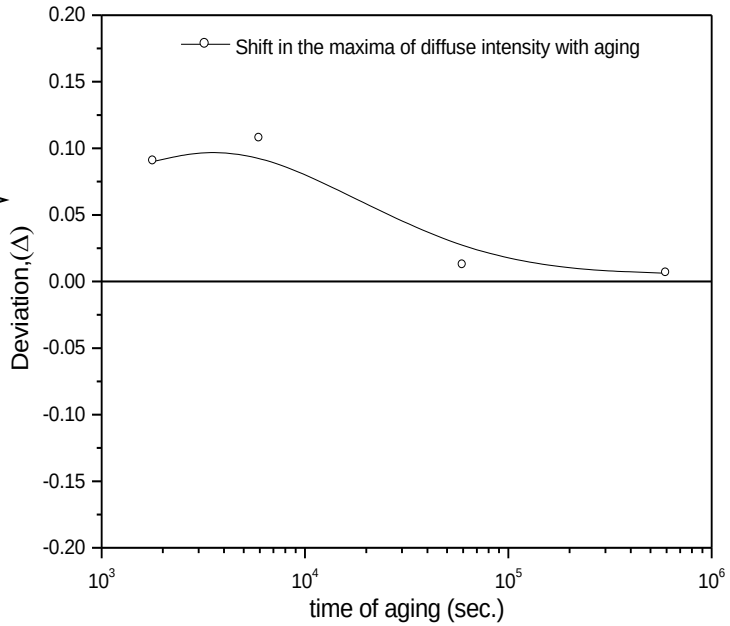

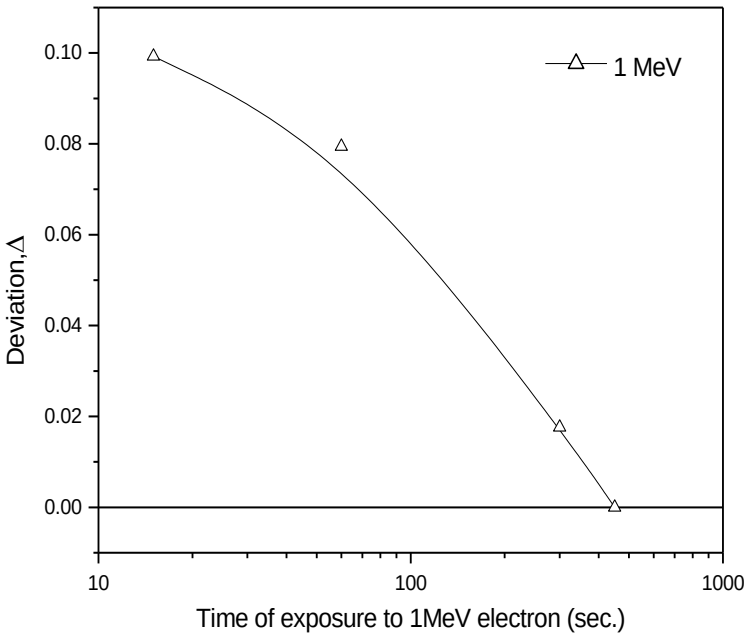

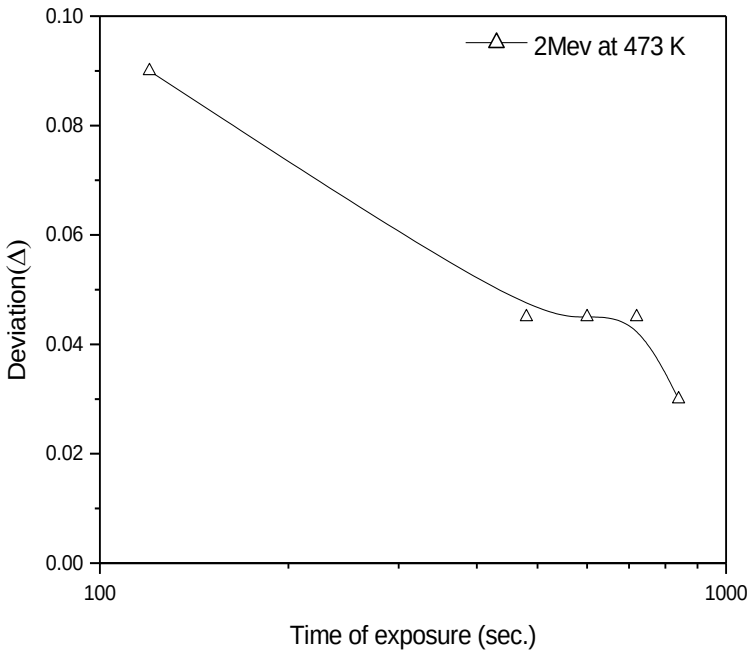

Comparison of Deviation Parameter in Irradiation and Thermal ω

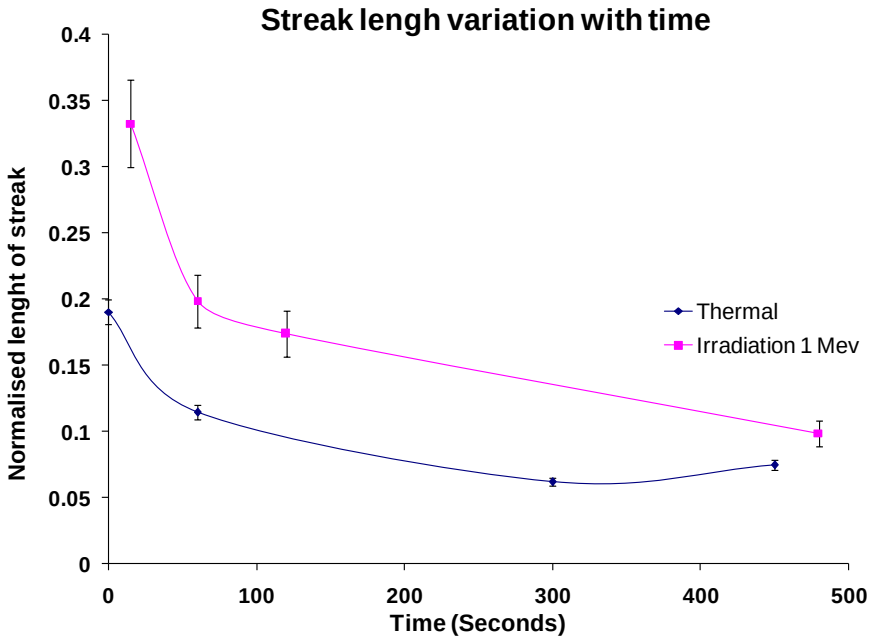

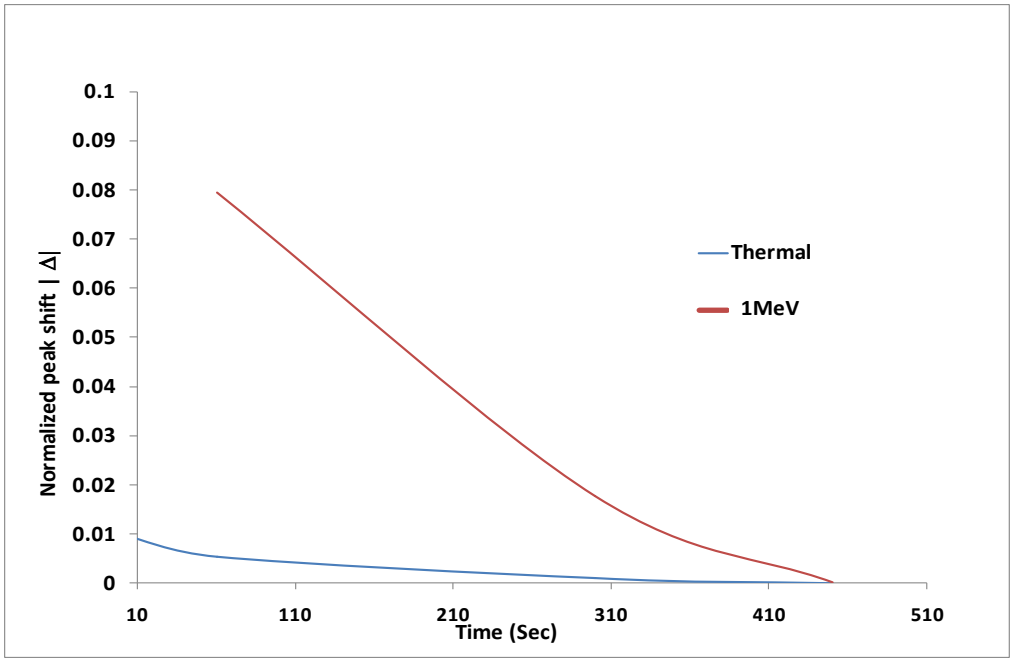

Both streak length and scatter in it are more pronounced in irradiation

Deviation is more pronounced in case of irradiation indicating more fraction of higher ω structural units

Stacking of ω

$n_{av} = 3x\omega(3) + 5x\omega(5) + 7x\omega(7) \ldots\ldots$

$|\Delta| = 1\text{-}3/n_{av}$

$$|\Delta| = \frac{R_{0001_R} - \frac{1}{3} R_{222_\beta}}{\frac{1}{6} R_{222_\beta}}$$

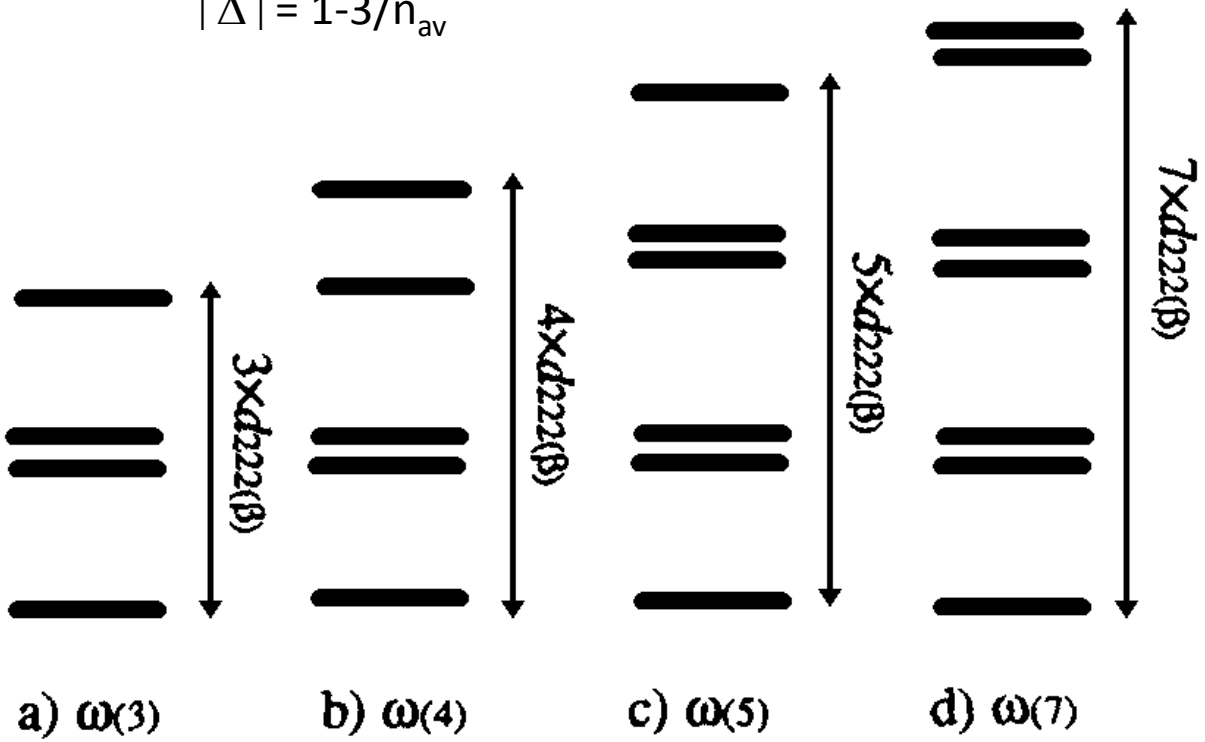

Sinkler and Luzzi Acta Mater.

(a)

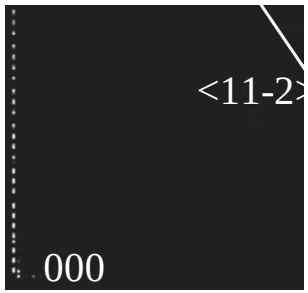

(b)

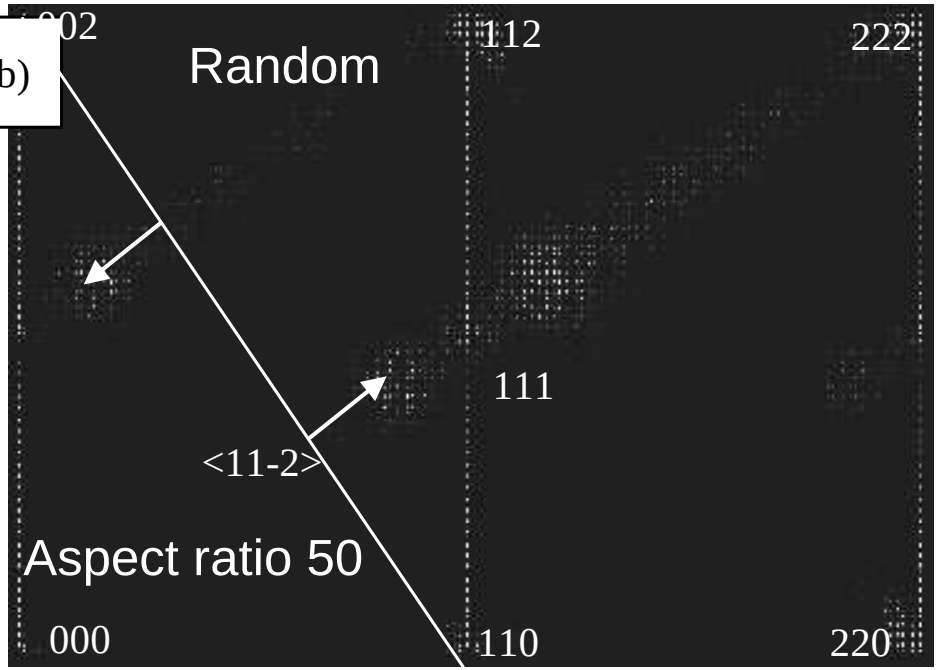

Coupling Between Displacive and Concentration Ordering: Ordered ω Phases

Ordered ω Structures - $B8_2$ and $D8_8$

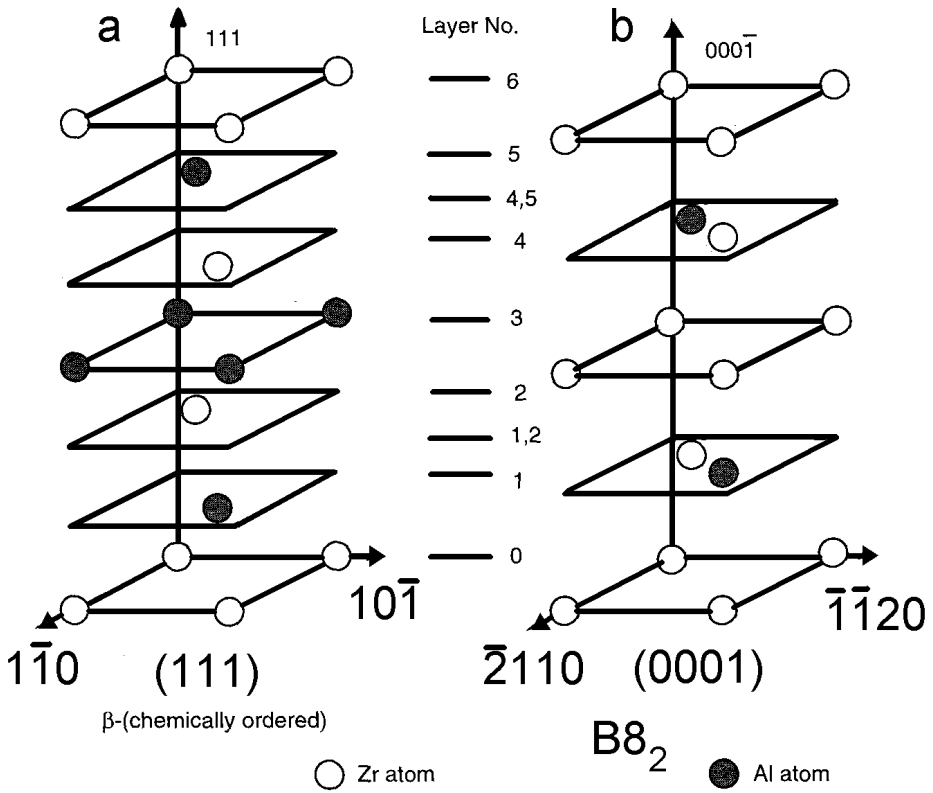

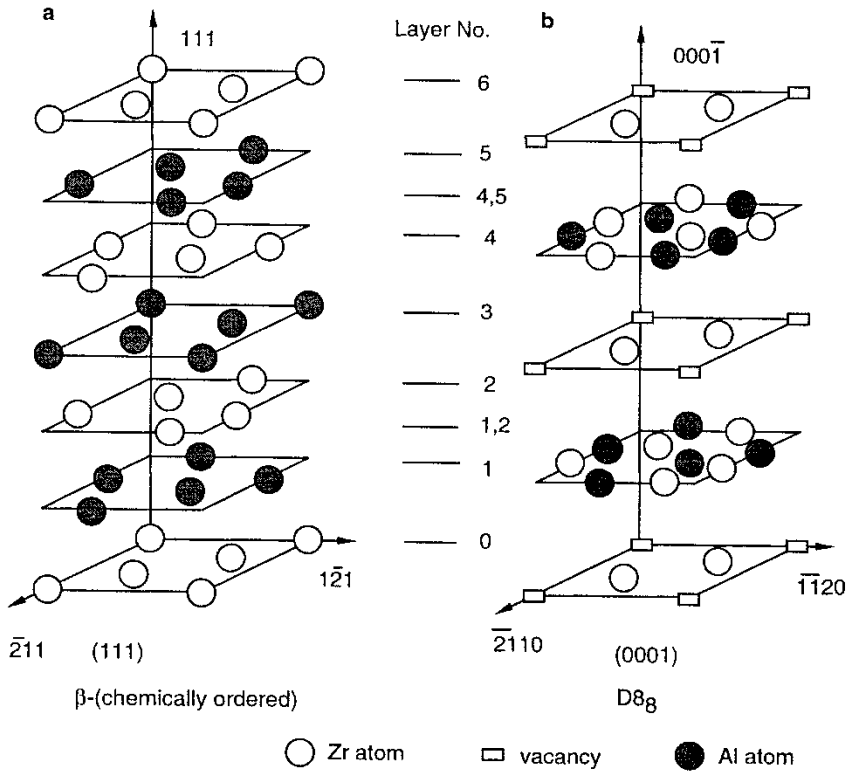

Superposition of waves:

$$U_p = A_d \mathrm{Sin} K_d x_p$$ Displacement

$$C_p = \frac{1}{3} + \frac{1}{6} A_c \sum_{n=1}^{5} [\cos \frac{2n\pi}{6}(p-1) + \cos \frac{2n\pi}{6}(5-p)]$$ Solute Concentration

$$Cv = \frac{1}{3} + \frac{2}{3} A_v \cos \frac{2\pi}{3} l$$ Vacancy Concentration

Tewari et al.,Mater. Sci. Engg. A, (2001)

Spinodally Decomposed Microstructure in Zr_3Al-Nb Alloys

<100 > Concentration modulation

-Solute lean regions transform into α

–Solute rich regions transform to $B8_2$ (ordered ω)

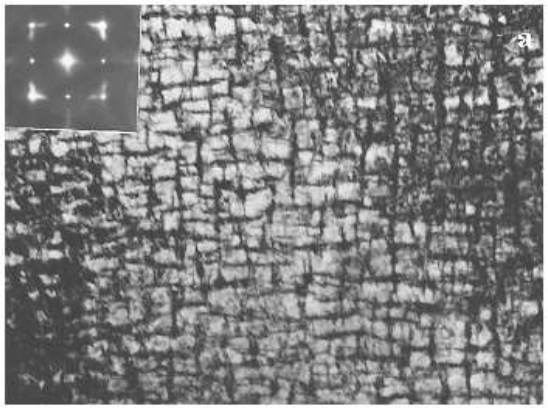

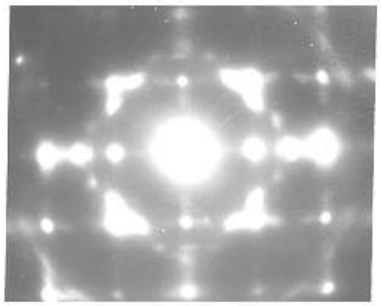

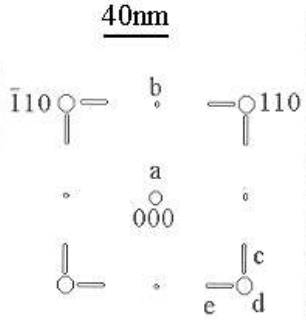

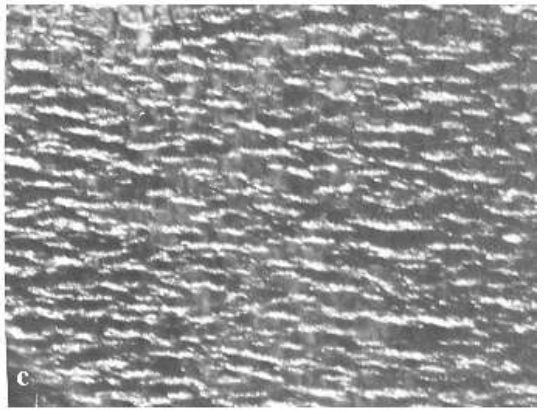

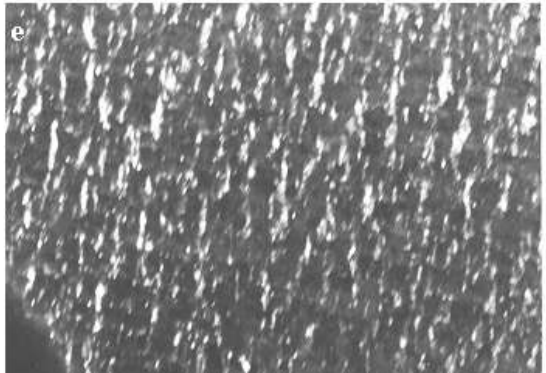

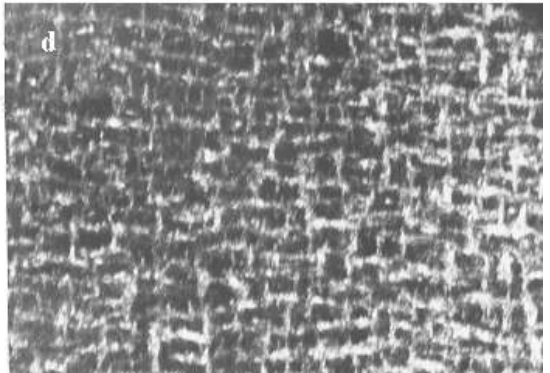

Ordered Omega Phases in Zr – Al – Nb

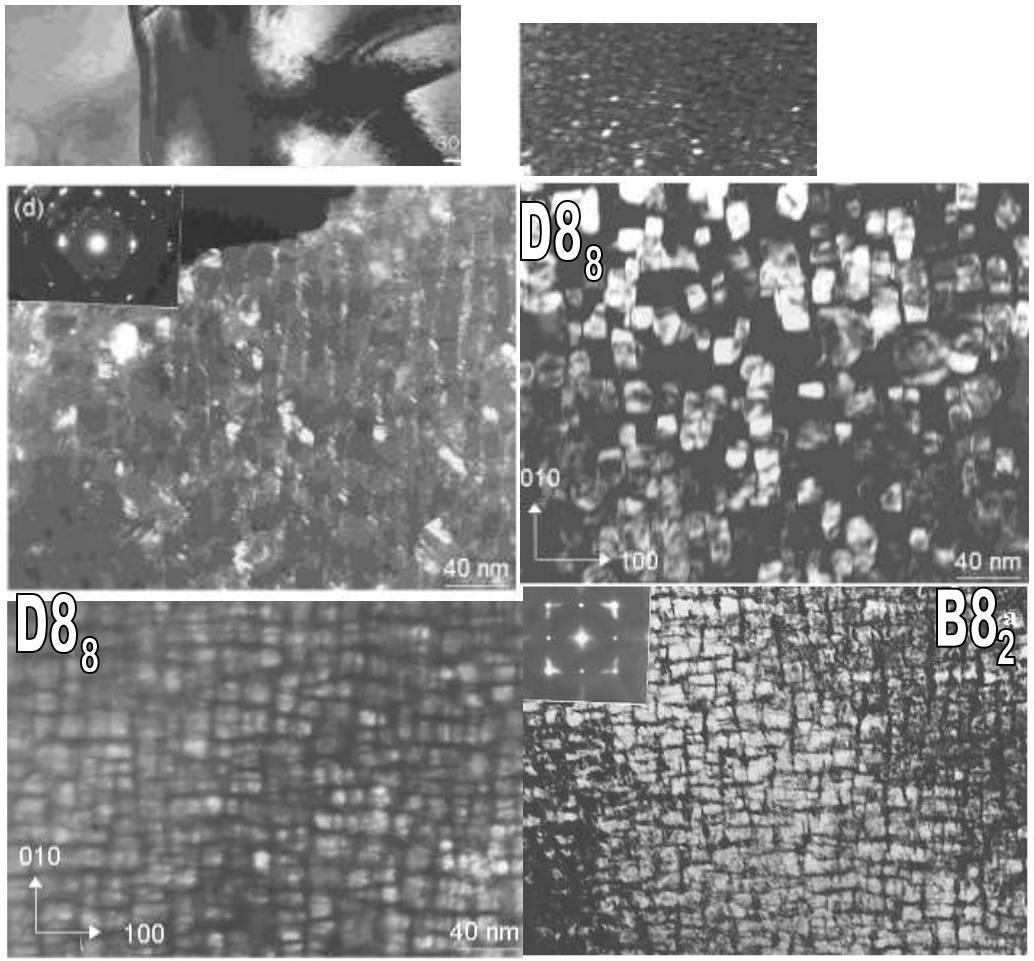

Rapid solidification

↓ ~ 10^5 K/s

Liquid

↓

Partitionless Solidification (β)

↓

Spinodal Decomposition

(Chemical Fluctuation)

Solute rich region	Solute lean region
↓	↓
β-stabilized / partially stabilized	ω Collapse + Ordering
	↓
	$D8_8$ Phase (derivative of ω)

Tewari et al. Acta Mat.(1999)

Atomic Correspondence of the β and $D8_8$ Phases

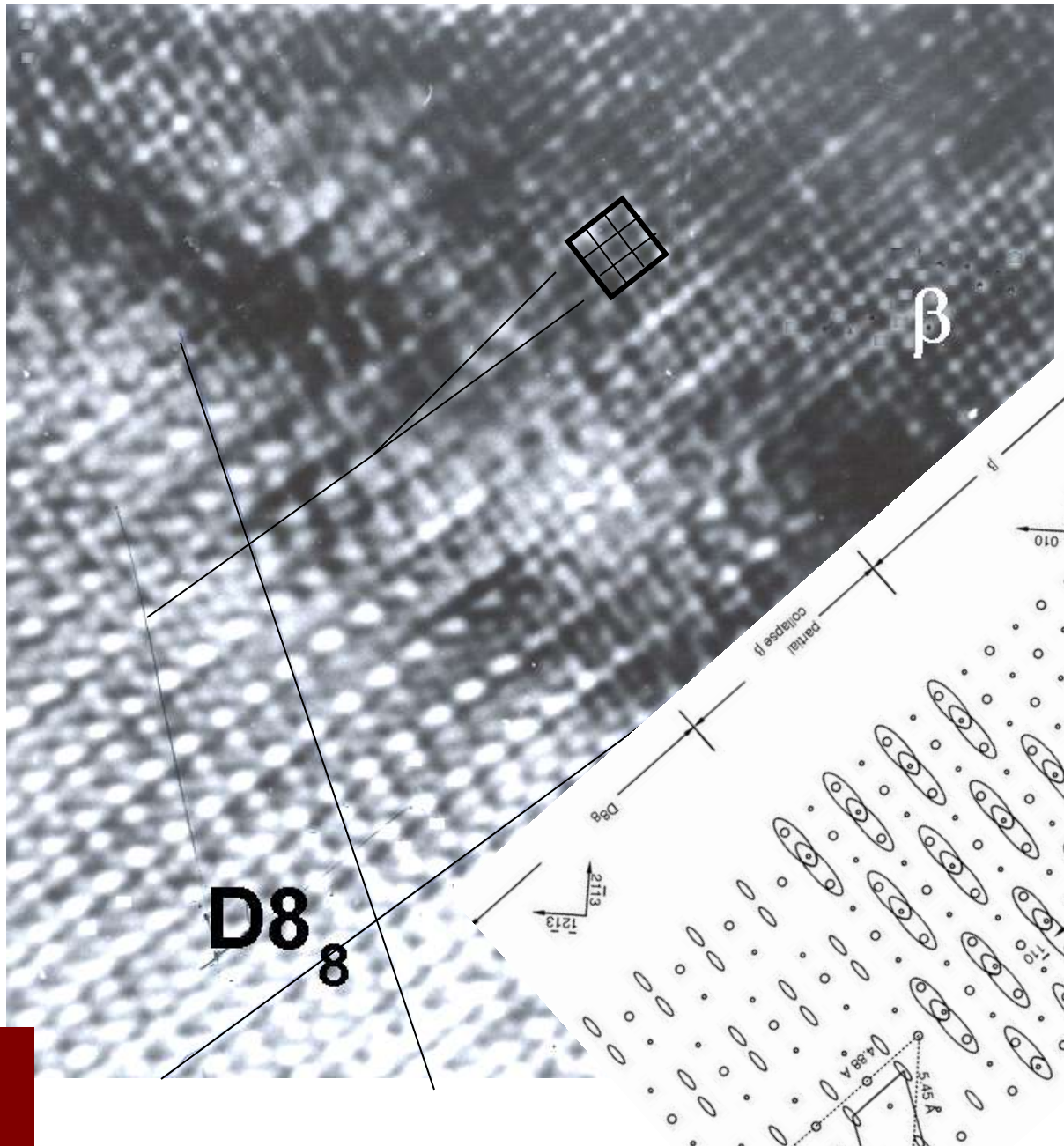

Tewari et al. Acta Mat. (1999)

Symmetry Tree

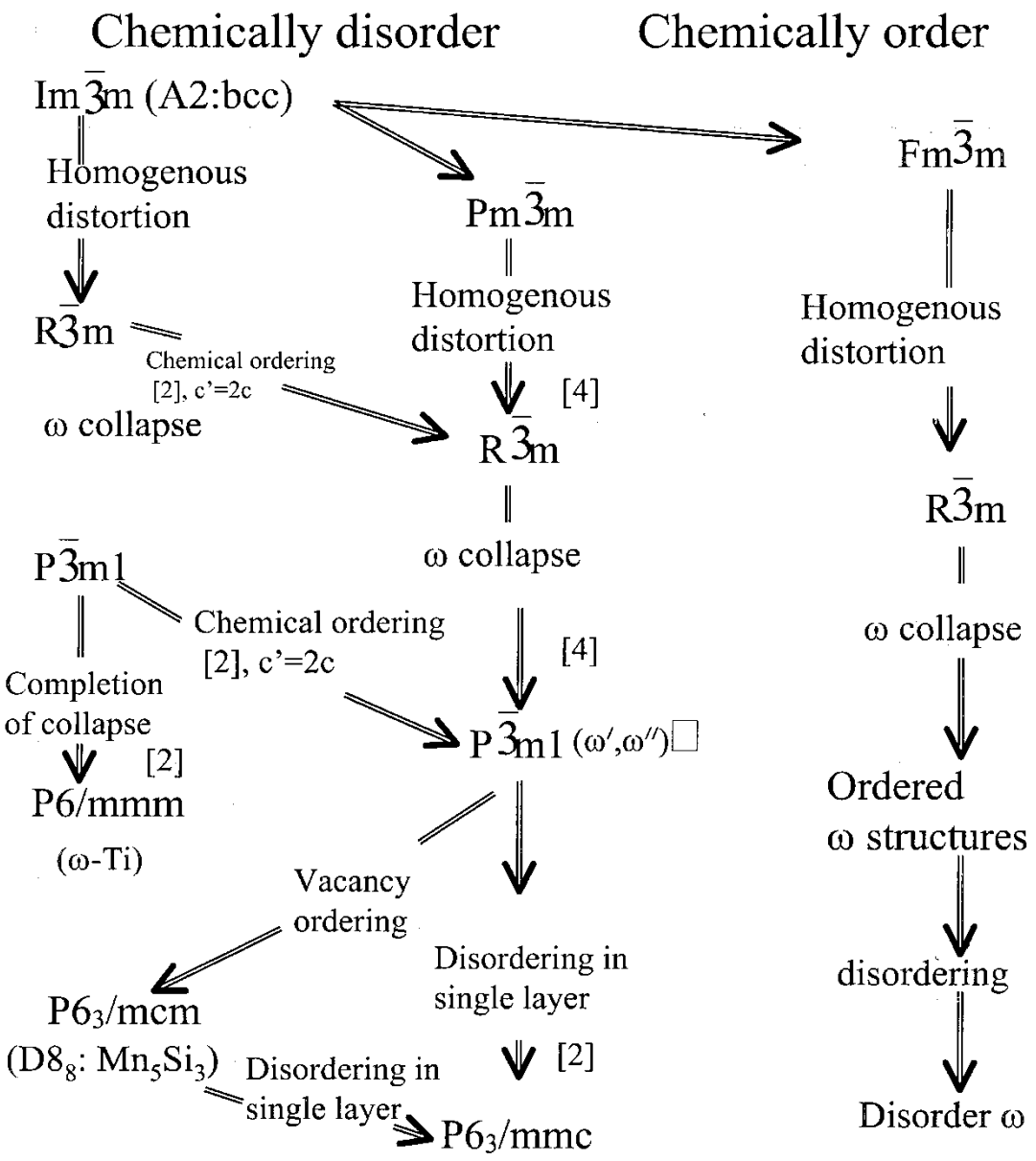

Tewari et al.
Acta Mat(1999)

Nucleation mediated by defects

Nucleation in a Complex Metallic Alloy- AlPdFe

C_2 phase (FCC) of Al-Pd-Fe has large lattice parameter of 15.52Å and number of atoms per unit cell is 250.

Exhibits plasticity through dislocation motion

Energy of such dislocations will be very high as $E \propto |b|^2$

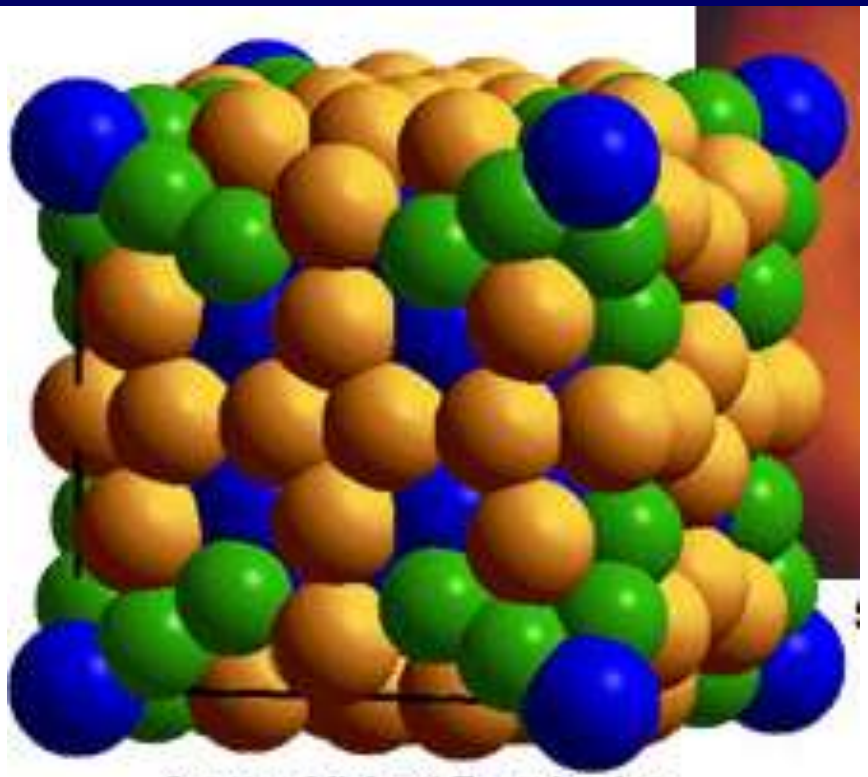

Source: Michael Feuerbacher

Source: CMA website

Dislocations are stabilized by nucleation of a defect phase

Novel Defects in Al-Pd-Fe Complex Alloy

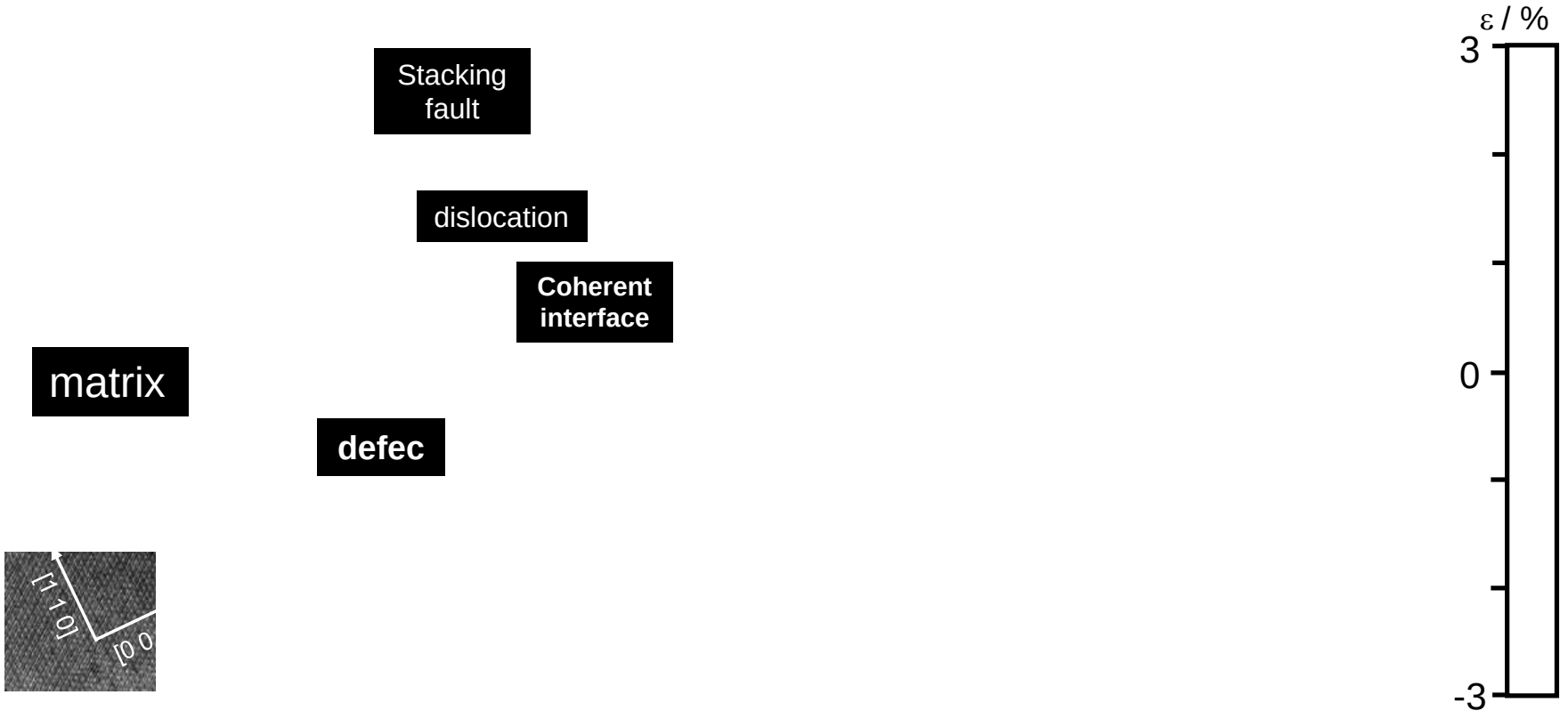

Dislocation showed the presence of nano sized defect phase in the matrix on compressive stress field of dislocation
Self energy of the dislocation is substantially reduced by the nucleation of the defect phase

Possible Mechanism of fcc to bcc Transformation

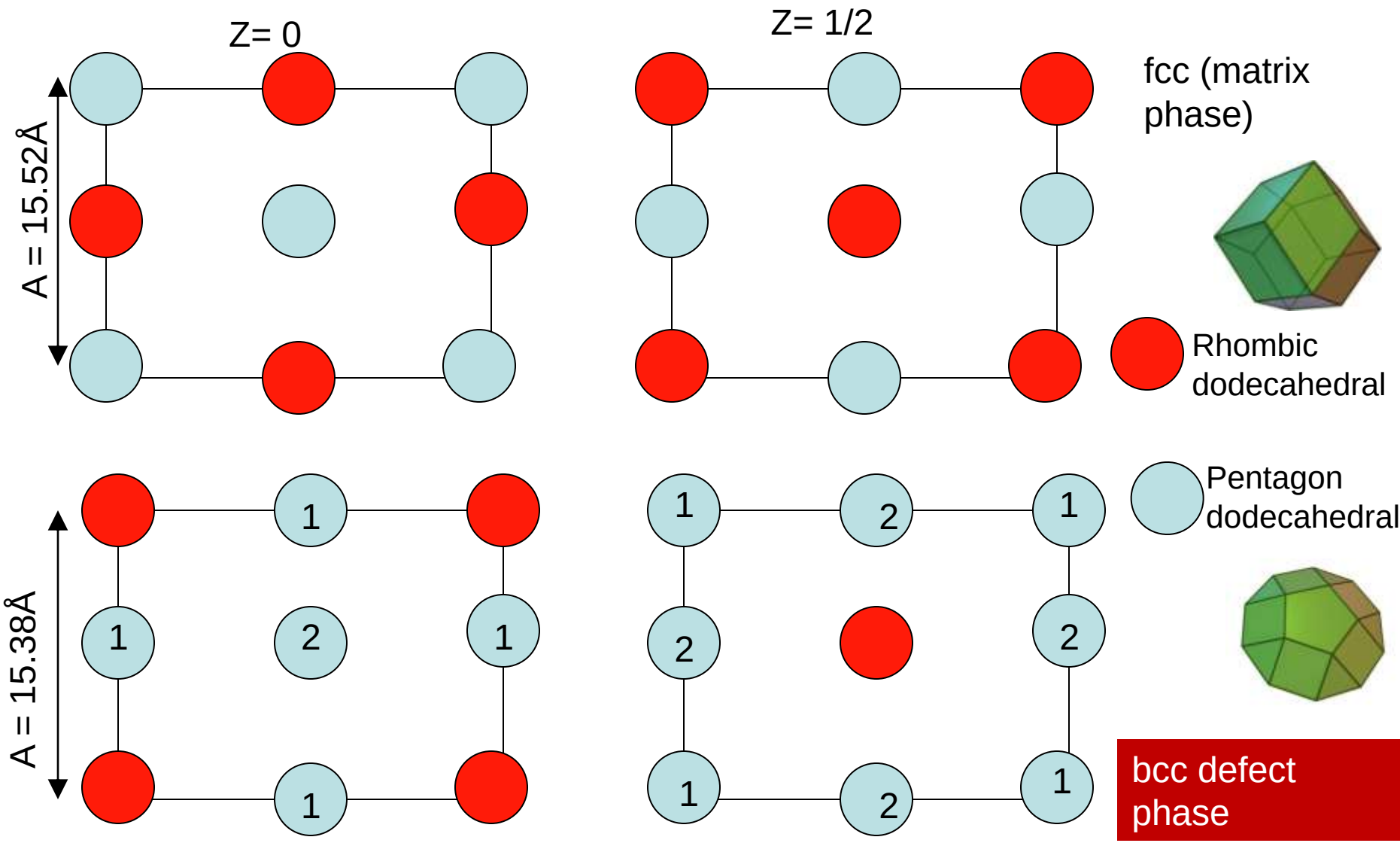

It can be seen that minor flip flop of structural motifs converts the fcc to bcc with a net drop of 1% lattice parameter.

Micro-mechanical Model of the bcc Defect as Infinite Elliptical Cylinder Running Along the Core of the Dislocation

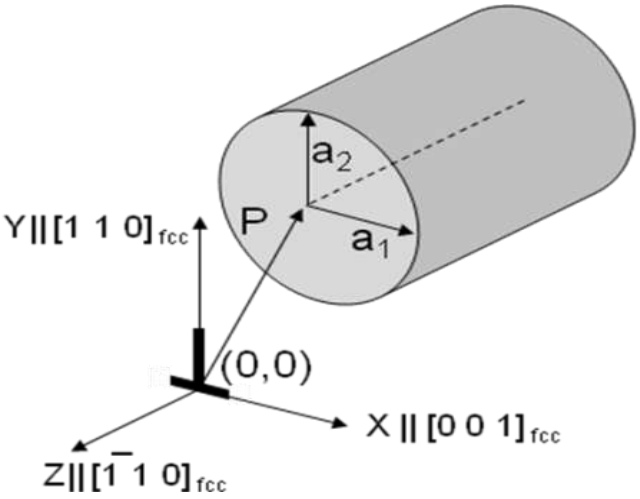

σ_{ij}^{o} stress due to dislocation at any given point

ε_{ij}^{p} constrained stress at the point due to defect,

σ_{ij} eigen strain of the defect

ε_{ij}^{*} equivalent eigen strain

Driving Force for bcc defect formation, elastic interaction energy, given by

$$W_1 = -\frac{1}{2}\int_{\Omega}\sigma_{ij}^{o}\varepsilon_{ij}^{*}dD - \frac{1}{2}\int_{\Omega}\sigma_{ij}\varepsilon_{ij}^{p}dD - \int_{\Omega}\sigma_{ij}^{o}\varepsilon_{ij}^{p}dD$$

Simulation of Defect Induced Strain

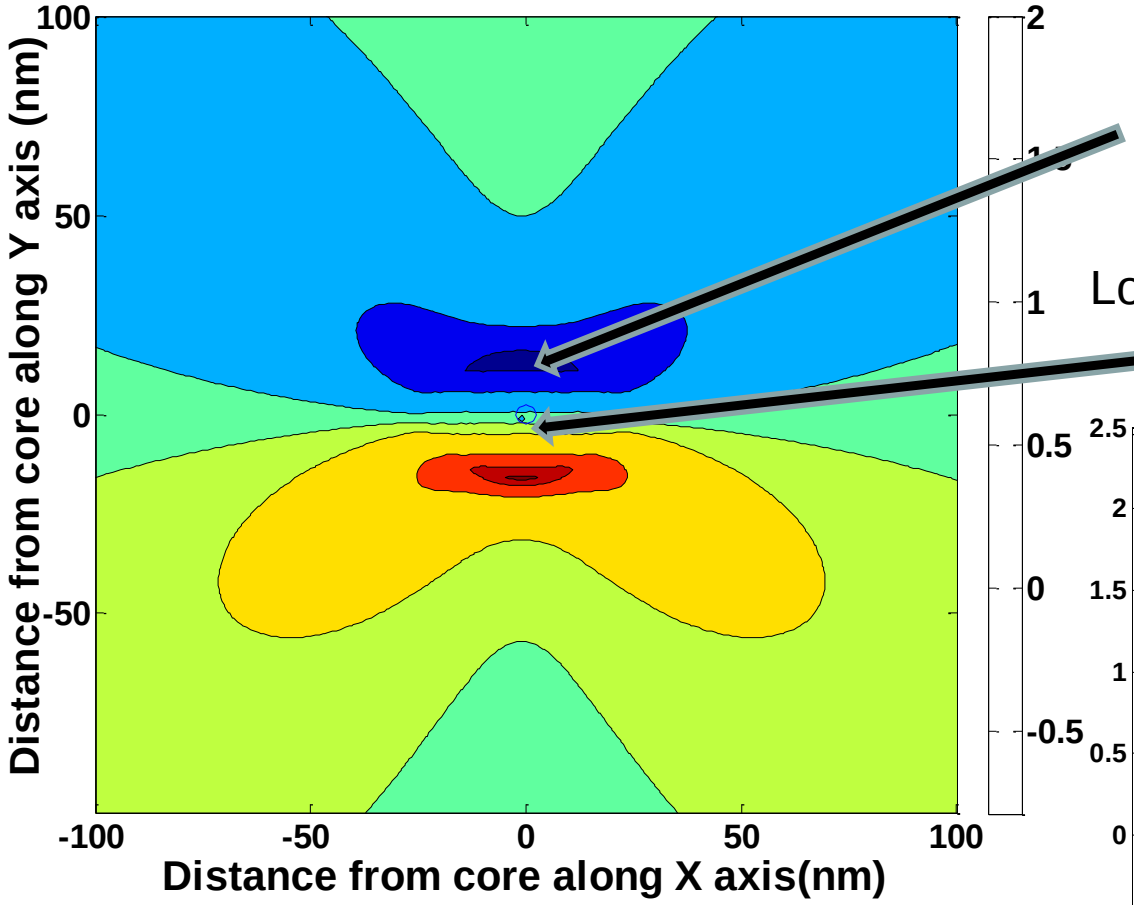

Predicted position of defect

Location of dislocation core

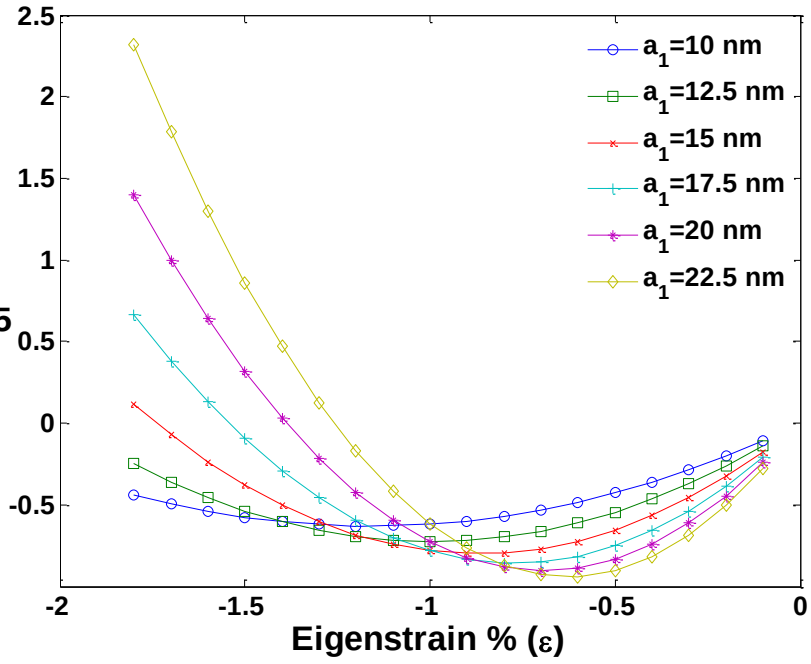

It could be shown that such defect nucleation could indeed reduce over energy of dislocation substantially

The predicted size and strain of the defect phase are close to experimental values

Summary

Homogeneous fluctuations in concentration, displacement and spin correlation mark the early stage of several transformations.

Interference of waves of different types results in localization of a transformation process

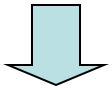

Cluster/motif mimicking partial symmetry elements of product are created.

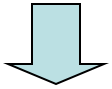

Spatial correlations of such clusters allow establishment of all symmetry elements of the product: **Nucleation sets in**

Incommensurate Structures & Lock-in Transitions

- If critical star does not correspond to a special point or critical wave vectors are not commensurate with vectors of the reciprocal lattice – LL rules fail

- If any incommensurate wave vector, **k'**, is not very different from commensurate wave vector, $\mathbf{k}_c$, one may obtain third & higher order terms in Landau functional with the possibility that sum of several vectors of the relevant star is equal to a vector of reciprocal lattice.

- This yields additional terms in Landau Functional called '**Umklapp'** terms.

- It may so happen that quadratic term favors the incommensurate state; while the quartic term favors the commensurate state. Below Tc, the latter terms dominate & one may expect an incommensurate-commensurate transition; where phase φ in the functional gets locked-in at that point.

- This is a **lock-in transition** driven by Umklapp terms in Landau functional.

- These may be treated by Soliton Theory

Lawrence Livermore National Laboratory

Coupling of Atomistic and Meso-scale Phase-field Modeling of Rapid Solidification

James Belak, Patrice Turchi, Milo Dorr, David Richards, Jean-luc Fattebert, Daniel Orlikowski, Michael Wickett, and Fred Streitz

Lawrence Livermore National Laboratory

AFRL/AOARD/LLNL Workshop on Nucleation

May 2-7, 2010, Maui, HI, USA

"Art (simulation) is the lie that helps us see the truth." -Picasso

Lawrence Livermore National Laboratory, P. O. Box 808, Livermore, CA 94551

This work performed under the auspices of the U.S. Department of Energy by Lawrence Livermore National Laboratory under Contract DE-AC52-07NA27344

All roads lead to Tamman

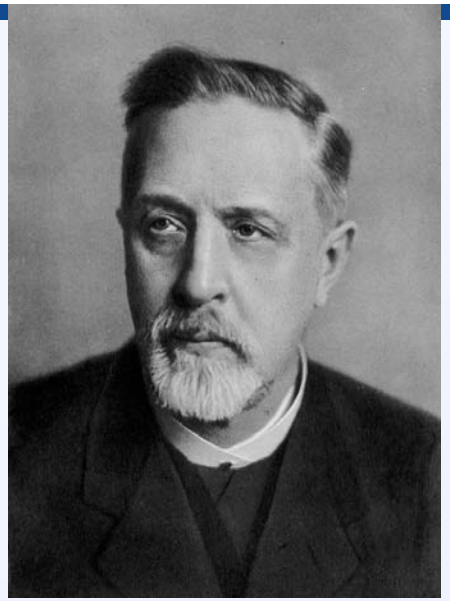

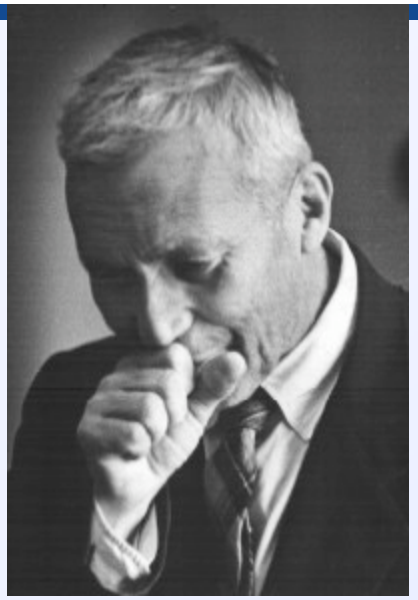

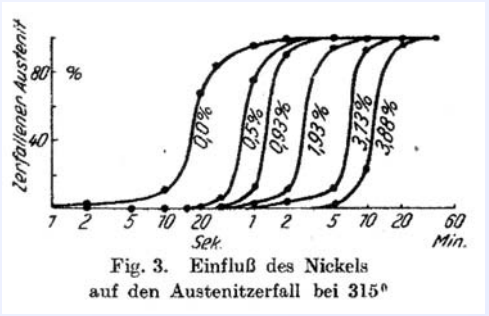

Fig. 3. Einfluß des Nickels auf den Austenitzerfall bei 315°

$$f_2 = 1 - exp\left[-\frac{A}{4} J_d v_{int} (t - t_0)^4\right]$$

G. Tammann, Z. Andrg. Chemie 214 (1933) 407, "The States of Aggregation," by Gustav Tammann, Translated by Robert Mehl (Van Nostrand 1925), KJMA: Kolmogorov (1937), Johnson-Mehl (1939), Avrami (1941)

Quotes

"... in general it seems to me that it is through particular problems which can be subjected to experimental verification or compared with natural phenomena that most advances are made." - G.I. Taylor

"Nothing can be learned as to the physical world save by observation and experiment, or by mathematical deductions from data so obtained."
- P.G. Tait

"Crystals are like people---it's the defects in them that make them interesting." - F.C. Frank

"Art (simulation) is the lie that helps us see the truth." - Picasso

Focus: Pressure-driven Solidification of Metals

Explicitly model the details of the solidification process

- Extend highly successful molecular dynamics (MD) results to longer times and larger lengths
- Determine structure and stability of metals under dynamic loading conditions
- Identify relevant time scales (from ps to μs) for solidification
- Locate non-equilibrium phase boundaries
- Describe rate and path dependence of approach to final structure

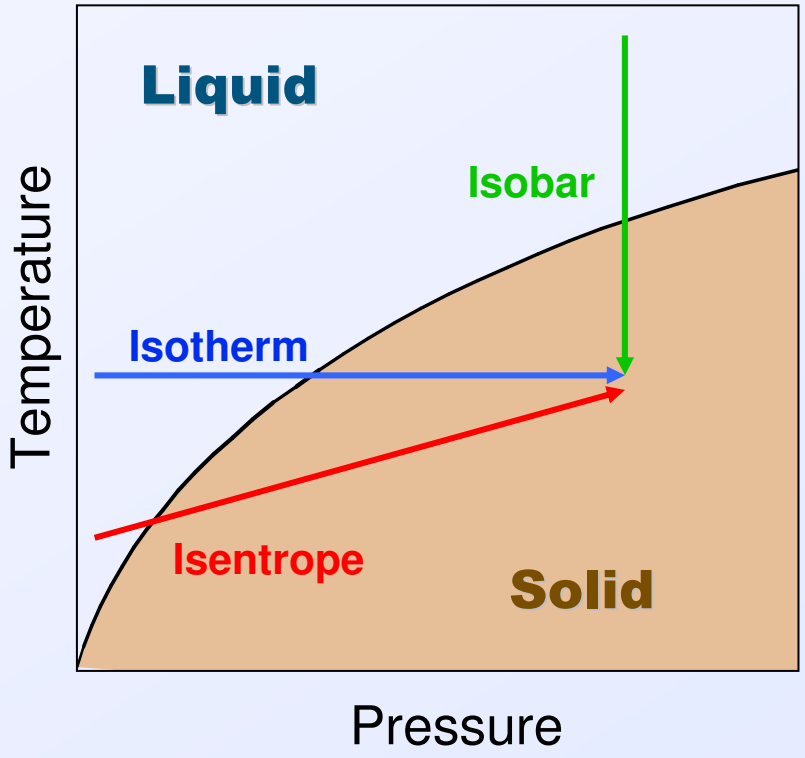

- Corroborate details with experiments where possible
- Condense results into phenomenological models which can be incorporated into hydrocodes

Molecular Dynamics (MD) are now large enough to model the initiation of realistic microstructure

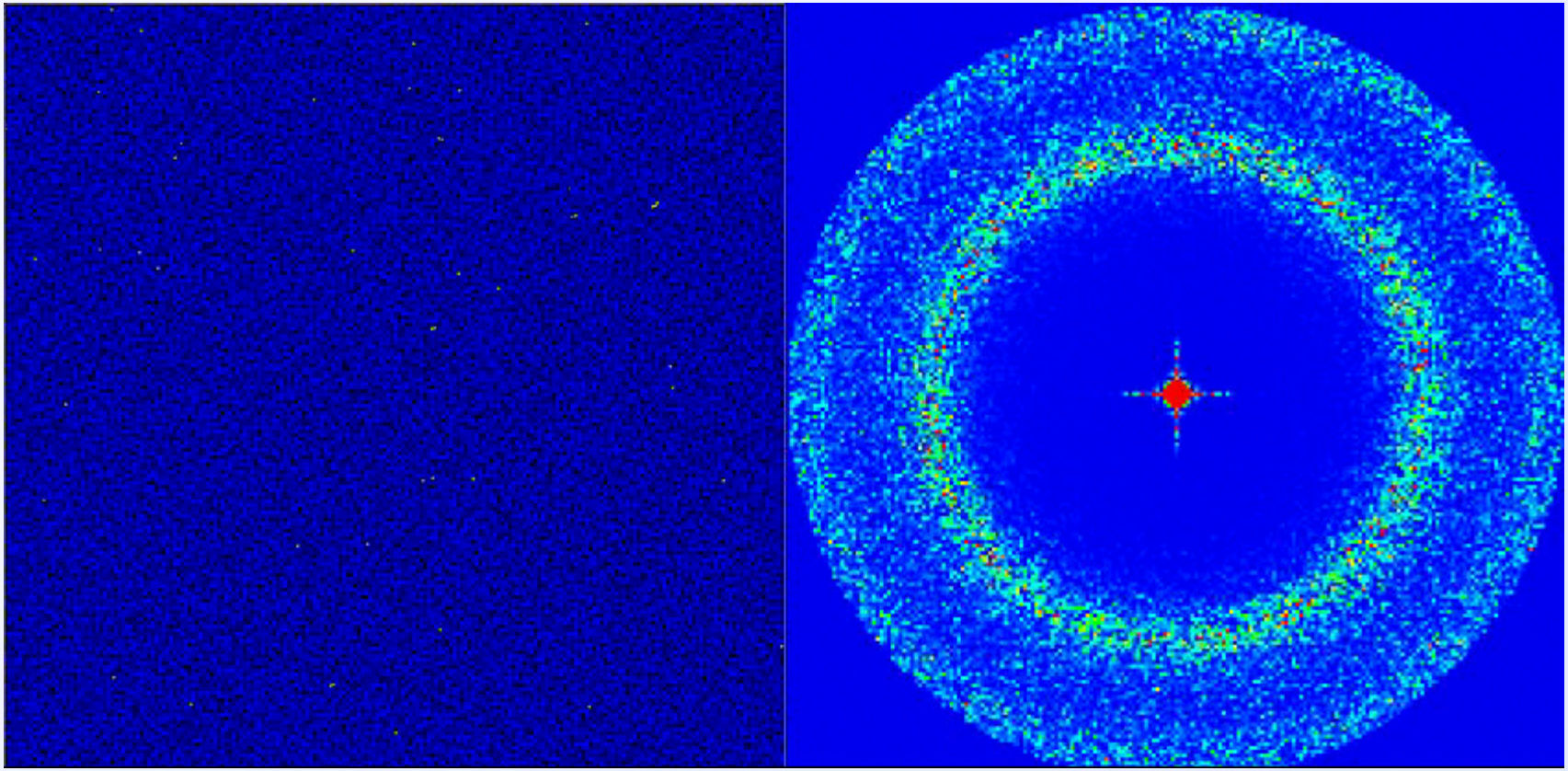

Simulations suggest novel in situ x-ray scattering experiments using emerging sources such as LCLS

Streitz *et al.* Phys. Rev. Lett. 2006

Quantification of local order from the atom positions

- **Utilize locally averaged combinations of spherical harmonics**
- **For L = 6, local structure described by a 13 component vector q_l.**
- **Dot product defined to measure correlation between atomic sites. Q_6 defined by summing these over neighbors.**
- **Truly a local quantity - assigned atom by atom**

2*l*+1 components of vector $\vec{q}_l(i)$ given by:

$$q_{lm}(i) = \left\langle Y_{lm}(\hat{r}_{ij}) \right\rangle_{N_i}$$

Define dot product:

$$\vec{q}_l(i) \cdot \vec{q}_l(j) \equiv \sum_{m=-l}^{l} q_{lm}(i)\, q_{lm}^*(j)$$

Then

$$Q_l(i) = \frac{\left\langle \vec{q}_l(i) \cdot \vec{q}_l(j) \right\rangle_{N_i}}{\vec{q}_l(i) \cdot \vec{q}_l(i)}$$

Steinhardt *et al.* PRB **28,** 784, 1983

ten Wolde *et al.* PRL **75,** 2714,1995

Distribution of Local Order Parameter: Q_6

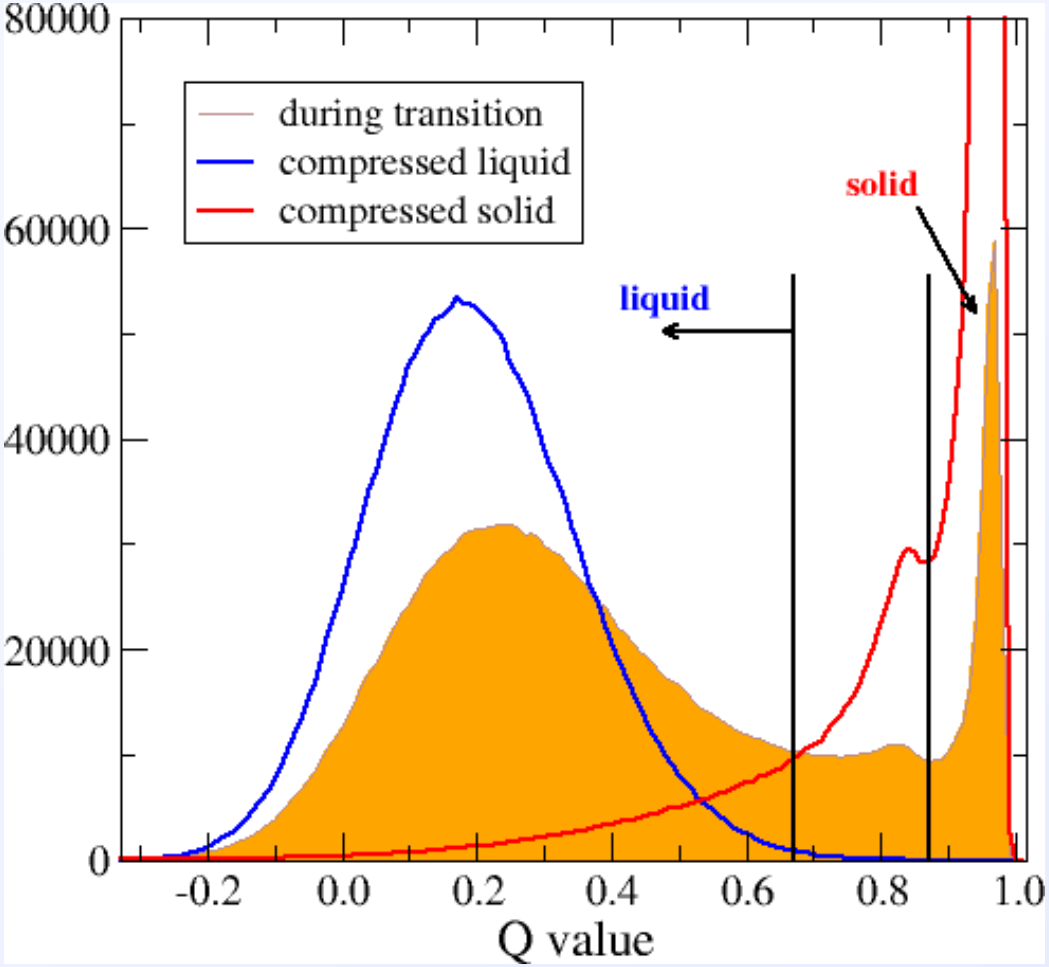

- L=6 allows excellent discrimination between the liquid and solid.
- Identifies mixed phase region
- Does not discriminate between crystal phases
- Define liquid for Q < 0.67
- Define solid for Q > 0.87
- Define interface for 0.67 < Q < 0.87

The time-scale for nucleation is fast

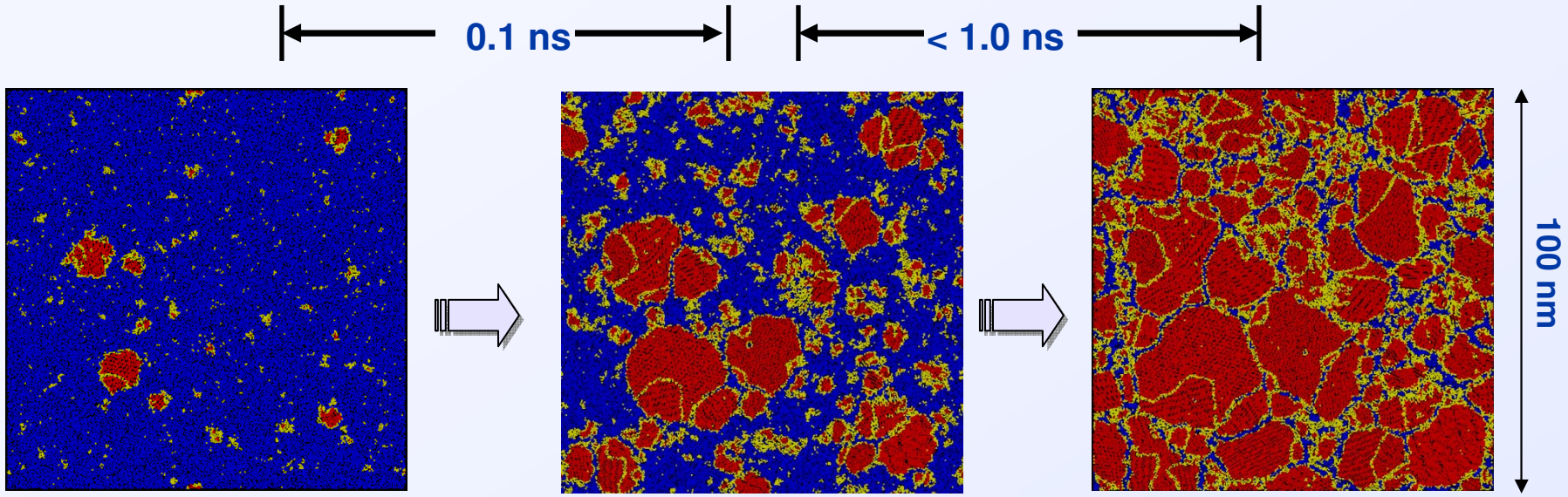

Nucleation:

Solid Grains surrounded by Liquid

Grain Growth: Mixed Liquid and Solid

Coarsening: Incipient Microstructure

Molecular dynamics simulations provide initial structure for continuum phase evolution model

MD will not get us to the hydrodynamic time of interest

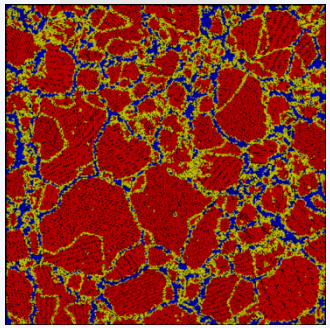

MD Simulation

Nucleation:
Poisson
Distribution

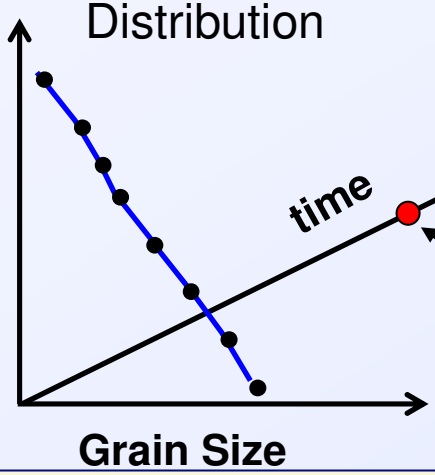

Late Time:
Log-Normal
Distribution

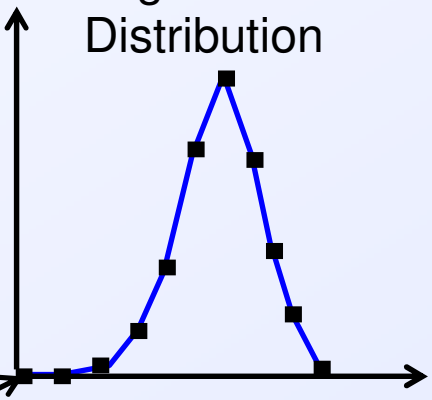

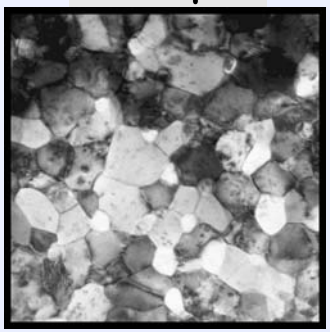

Recovery
Experiment

intermediate time
- **unknown kinetics**
- **unknown microstructure**
- **unknown material behavior**

Phase Field Modeling (PFM) will get us to the hydrodynamic time of interest

What is Phase Field modeling? - PFM

$|\vec{\phi}(r,t)| = liquid$

$|\vec{\phi}(r,t)| = solid$

$\vec{\phi}(r,t) = green$

$\vec{\phi}(r,t) = pink$

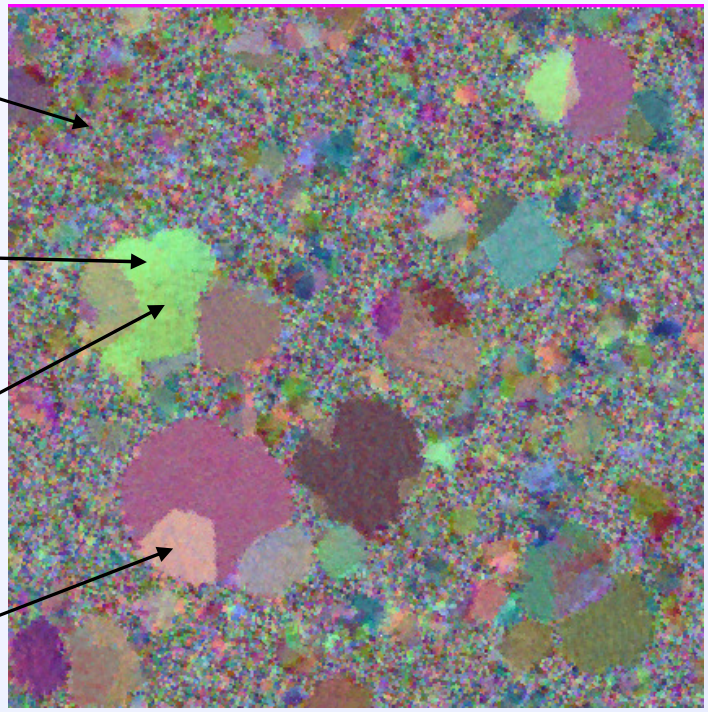

- **Each color represents a different value of the phase field $\vec{\phi}$ (solid orientation)**
- **Free energy describes how colors interact and evolve**
- **Accuracy depends on fidelity of physics in the equations**

Thermodynamic representation of phase (or "color") everywhere

Evolution Equations

$$F(P,T) = \int dx \left\{ \left|\nabla \vec{\phi}\right|^2 + f(\vec{\phi},P,T) + \ldots \right\}$$

$$\frac{\partial \vec{\phi}}{\partial t} = -\Gamma \frac{\delta F}{\delta \vec{\phi}} + noise$$

We propagate the phase order parameter using the molecular dynamics

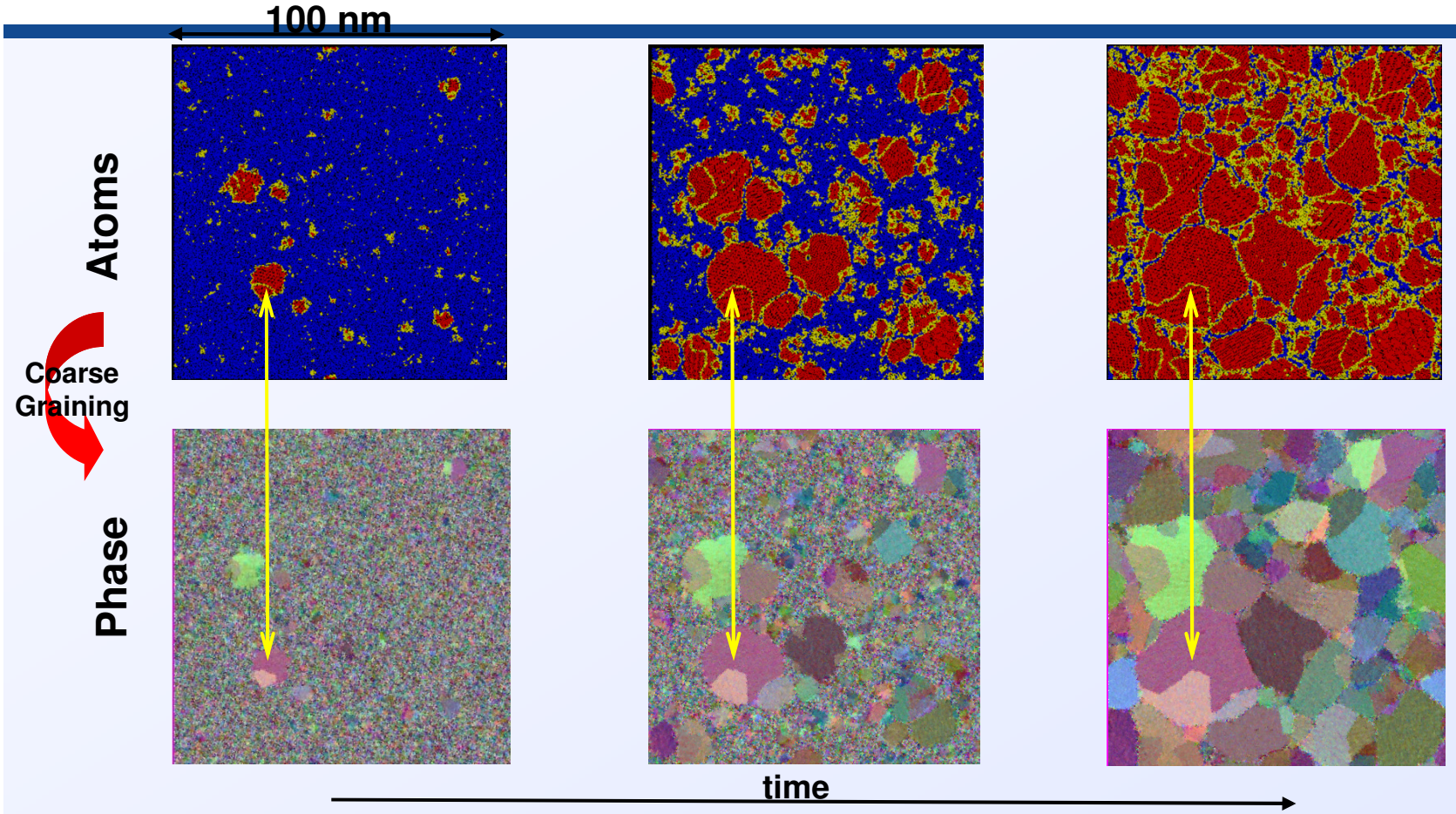

Validate micro-physics within Phase Field Model with MD simulations that overlap in time and space

What is Phase Field modeling? Basic Equations

Phase Field modeling is time-dependent Ginzburg-Landau theory

Solid Liquid

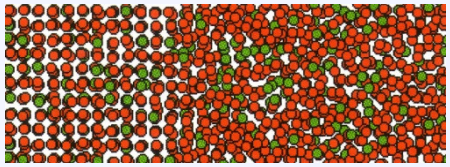

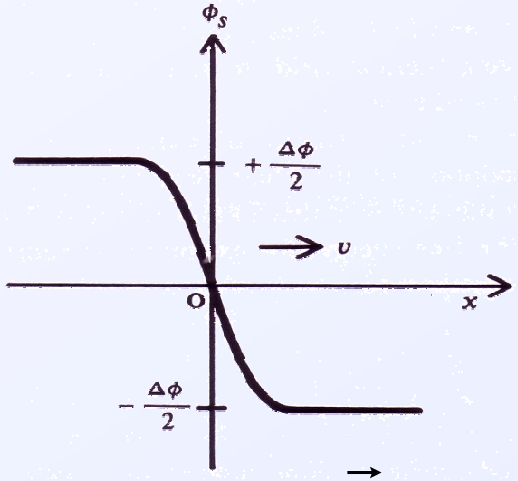

Order Parameter $\vec{\phi}(r,t)$

$$F(\phi) = \int dx[\frac{1}{2}|\nabla\phi|^2 + f(\phi,P,T) + f_{GB}(\nabla\theta) + f_{el}]$$

Total Free Energy of multi-phase material

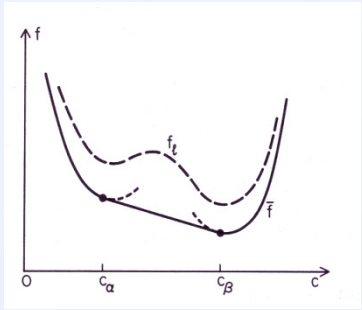

Local Free Energy Density $f(\phi) \approx \phi(1-\phi)(1+\phi)$

$$\frac{\partial\phi}{\partial t} = -\Gamma(-\nabla^2)^a \frac{\delta F}{\delta\phi} + noise$$

Kinetic Equation with Thermal Noise

What does a crystallographic-aware phase-field model of polycrystal solidification look like?

Pusztai et al., have proposed a 3D quaternion-based phase-field model

- Represents crystal orientation with quaternion order parameter
- Quaternions are widely used to analyze crystallography of polycrystal interfaces
- Quaternion algebra is fast, efficient, avoids singularities, …

Free Energy

$$F = \int \left[\frac{\varepsilon_\phi^2}{2} |\nabla \phi|^2 + f(\phi, c, T) + HT[1 - p(\phi)] \left(\sum_i (\nabla q_i)^2 \right)^{1/2} \right] d^3 r$$

Evolution

$$\frac{\partial q_i}{\partial t} = -M_q \frac{\delta F}{\delta q_i} + \zeta_i = M_q \left[\nabla \cdot \left(D \frac{\nabla q_i}{|\nabla q_i|} \right) - 2\lambda q_i \right] + \zeta_i$$

Where q_i is the quaternion order parameter, M_q is the associated mobility and ζ is the fluctuation in q.

We have implemented the Pusztai model in our 3D AMR code

- Enhance energy functional to represent energetics of grain boundaries
- Crystal symmetry aware quaternion mathematics
- Extend energy functional to include elasticity and alloy concentration

Refs: T. Pusztai, G. Bortel, and L. Granasy, “Phase field theory of polycrystalline solidification in three dimensions,” Europhys. Lett, 71 (2005) 131-137; R. Kobayoshi and J.A Warren, “Modeling the formation and dynamics of polycrystals in 3D,” Physica A 356 (2005) 127-132.

Quaternions are used extensively to represent rotations, e.g. in computer graphics (games)

Complex numbers have the form, a + ib, and multiplying by $e^{i\theta}$ produces rotation by an angle θ in the complex plane

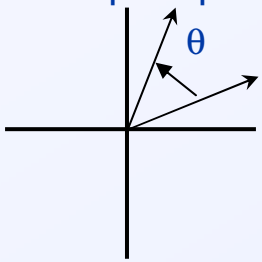

Quaternions have the form, a + ib +jc +kd, where $i^2=j^2=k^2=ijk=-1$. A rotation about the unit vector $\hat{n}$ by an angle θ can be computed using the unit quaternion:

$$(s,v) = (\cos(\frac{\theta}{2}), \hat{n}\sin(\frac{\theta}{2}))$$

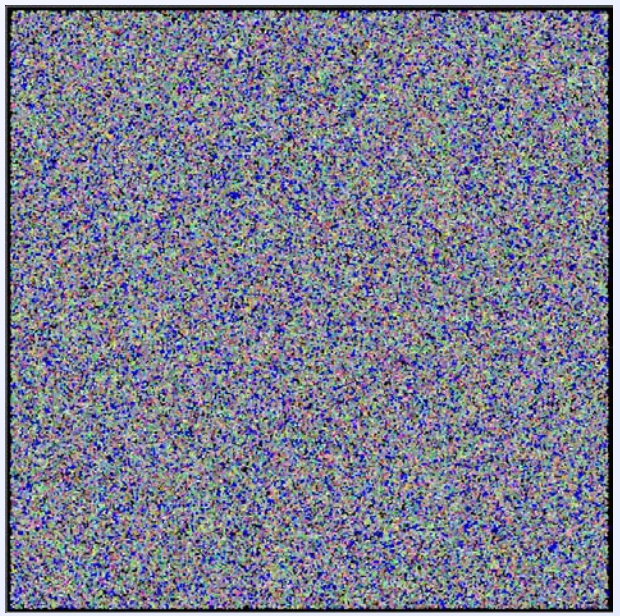

We assign to each atom a quaternion that best represents the local value of the Q6 order parameter with the smallest rotation from a reference unit cell.

The associated quaternion enables quick calculation of the rotation between two misoriented grains (c.f. Reed et.al Acta Cryst. (2004) A60, 263-277)

Model Problem: Single Spherical Grain (2D with scalar order-parameter)

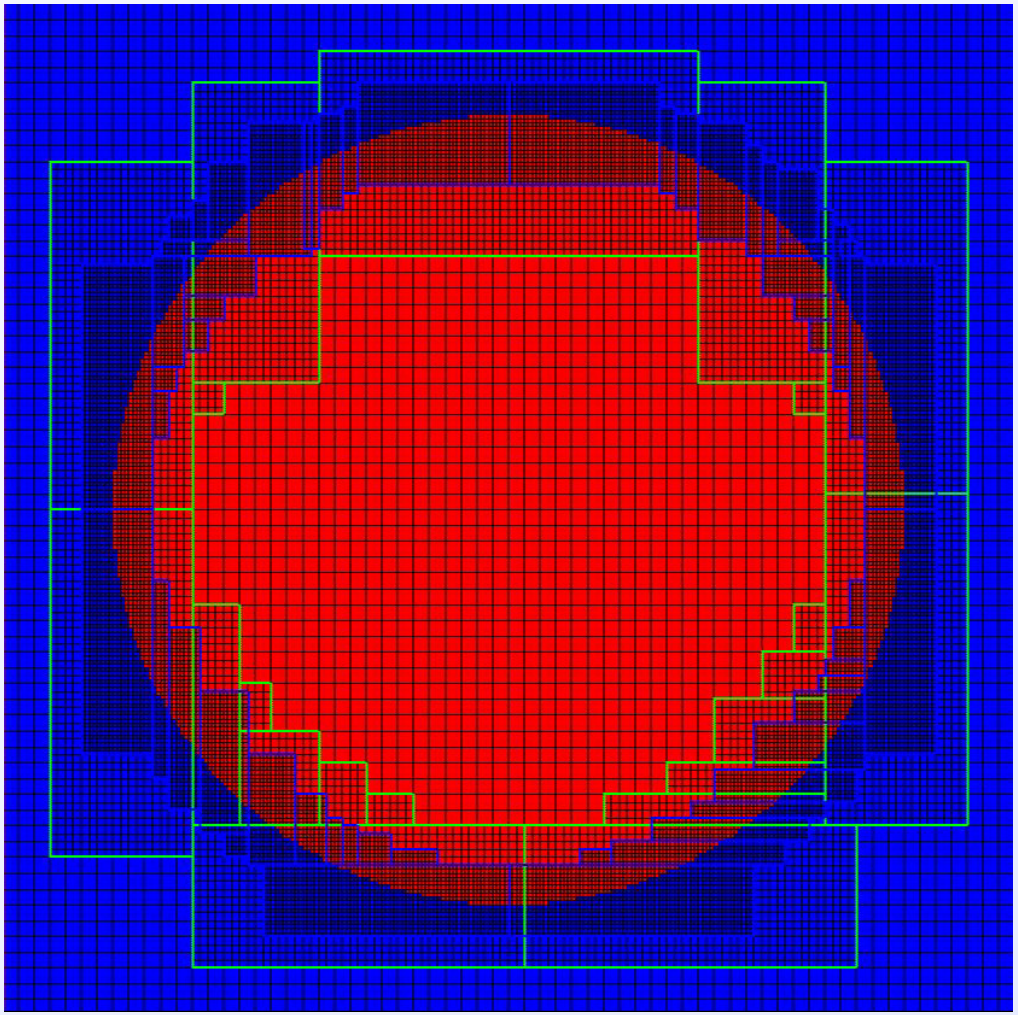

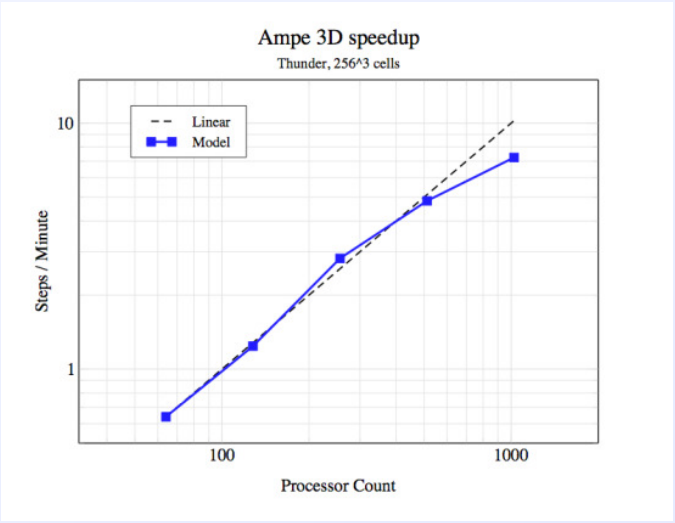

We obtain strong scalability to thousands of processors by leveraging LLNL's investment in parallel computing (e.g. SAMRAI)

Representation of MD Data onto the AMR Grid Hierarchy - 2D example

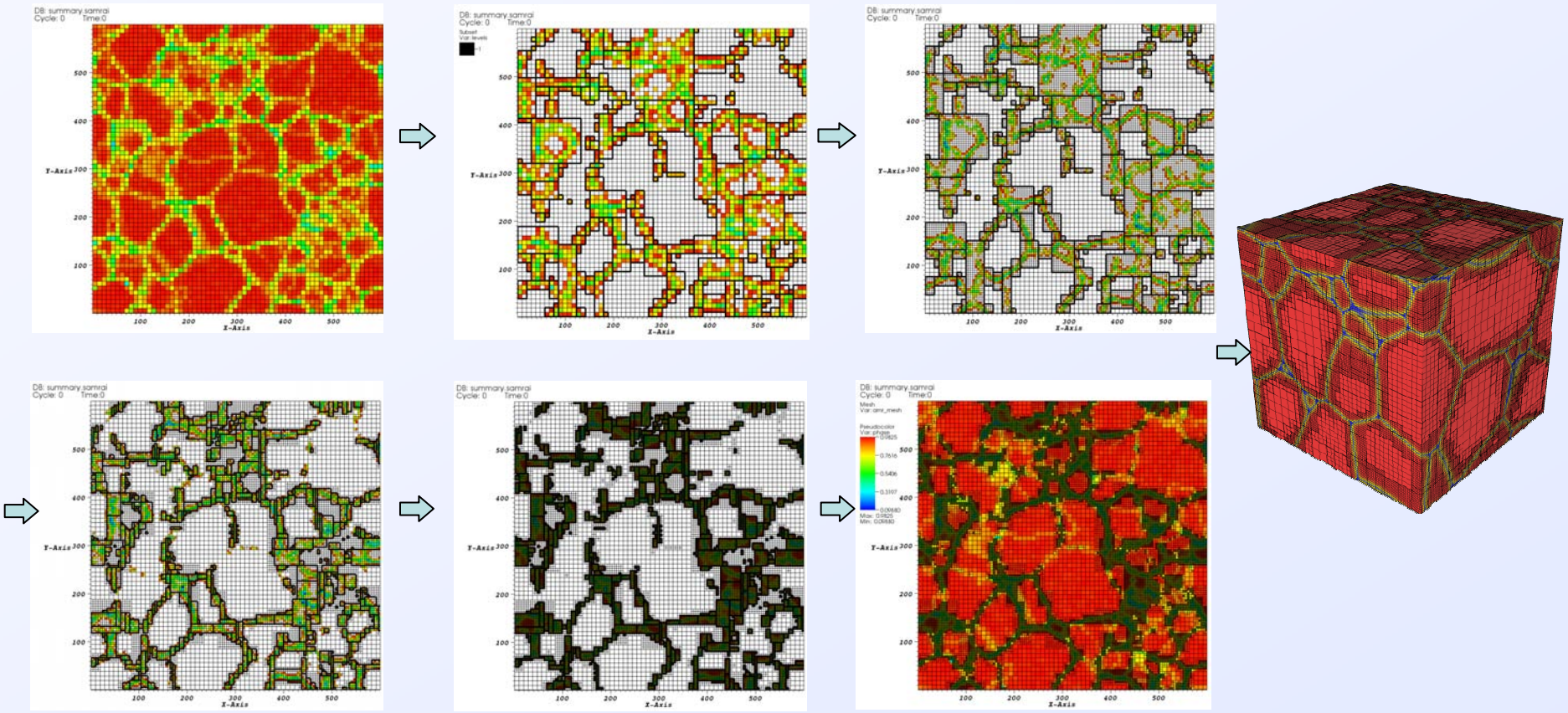

MD nucleated microstructure onto the micro-second hydro time-scale with the crystallographic quaternion model

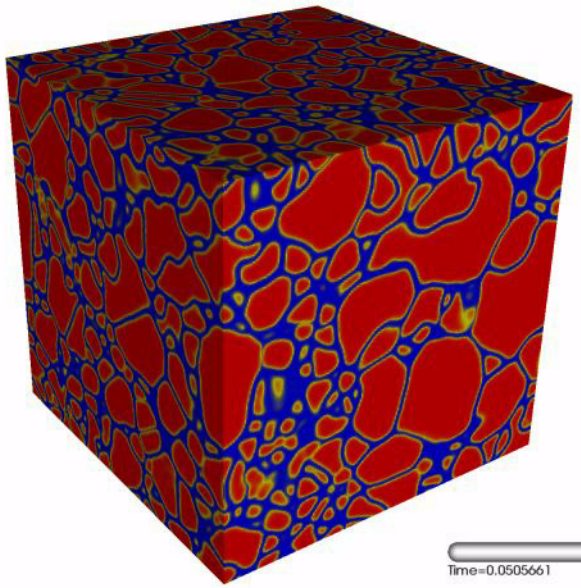

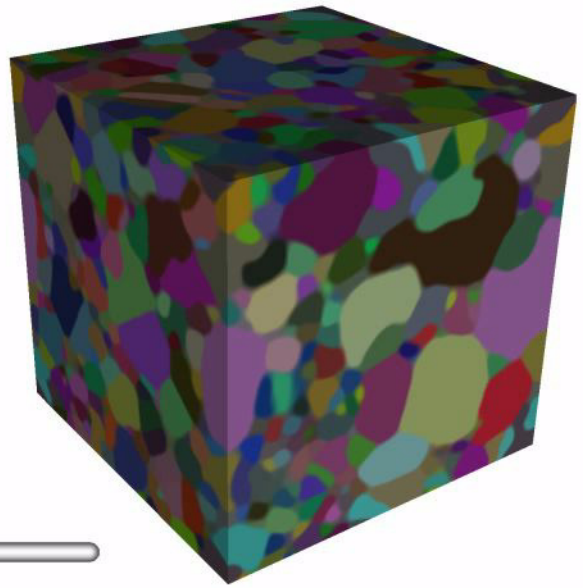

Phase Order Parameter

Quaternion Order Parameter

Growth of large grains
Blue: MD nucleation
Red: Phase-field evolution

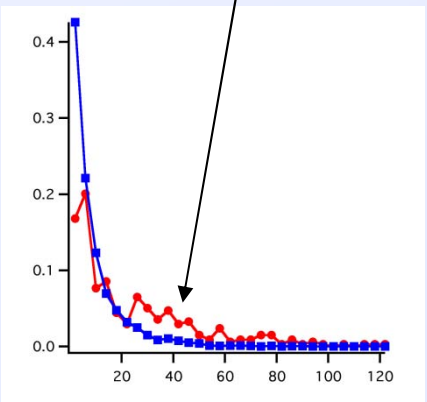

While significant grain coarsening has occurred on the microsecond scale, the microstructure is far from log-normal

Focus: Pressure-driven Solidification of Metals

Explicitly model the details of the solidification process

- Extend highly successful molecular dynamics (MD) results to longer times and larger lengths
- Determine structure and stability of metals under dynamic loading conditions
- Identify relevant time scales (from ps to μs) for solidification
- Locate non-equilibrium phase boundaries
- Describe rate and path dependence of approach to final structure

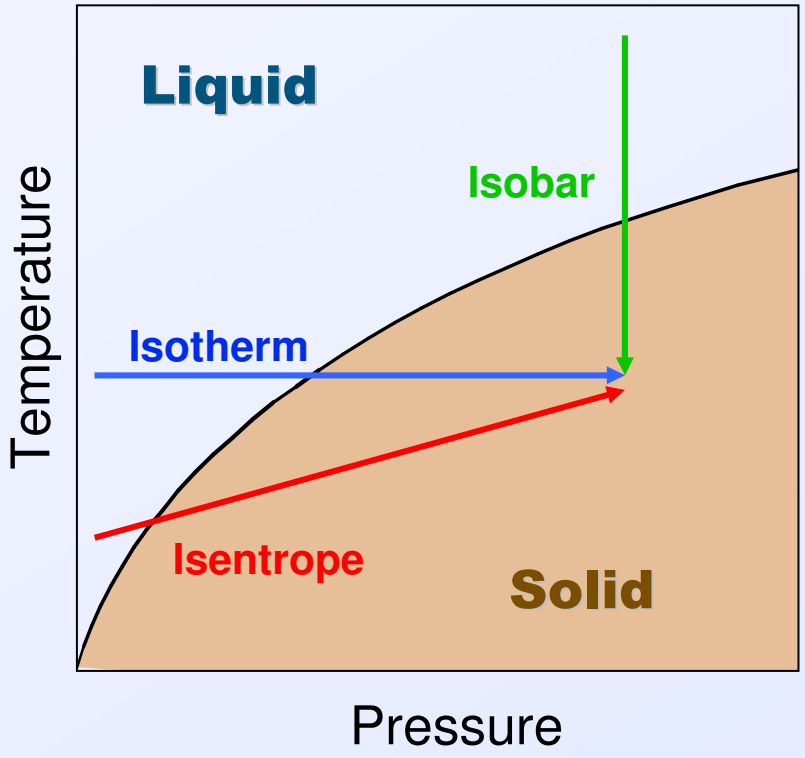

- Corroborate details with experiments where possible
- Condense results into phenomenological models which can be incorporated into hydrocodes

Becker-Doring-Volmer (Gibbs-Thomson)

$$\Delta G = \gamma 4\pi R^2 - \Delta G_v \frac{4}{3}\pi R^3$$

$$\frac{\partial \Delta G}{\partial R} = \gamma 8\pi R - \Delta G_v 4\pi R^2 = 0$$

$$R_c = \frac{2\gamma}{\Delta G_v} = \frac{2\gamma}{\Delta S_f (T_m - T)}$$

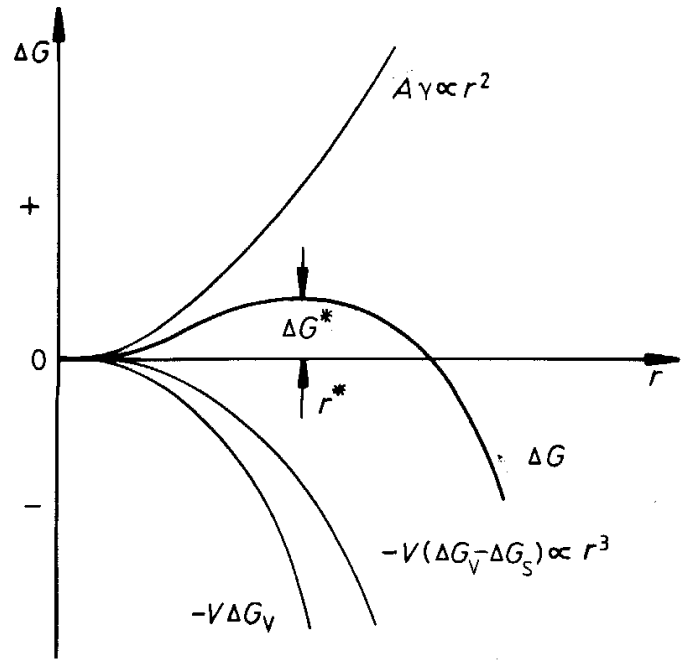

Fig. 5.2 The variation of ΔG with r for a homogeneous nucleus. There is an activation energy barrier ΔG^*.

Molecular Dynamics simulation of nucleant evolution

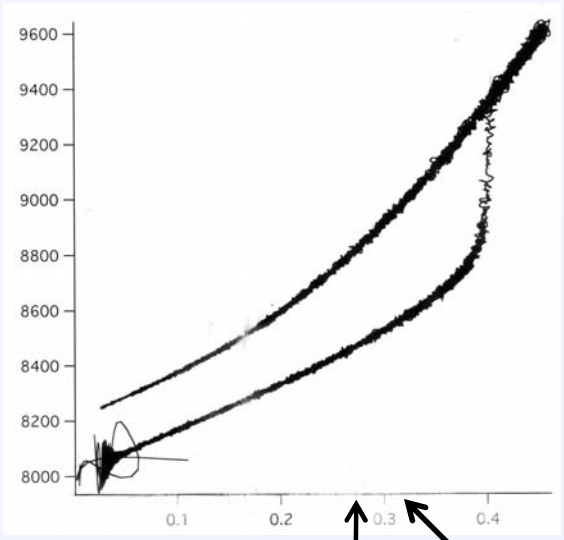

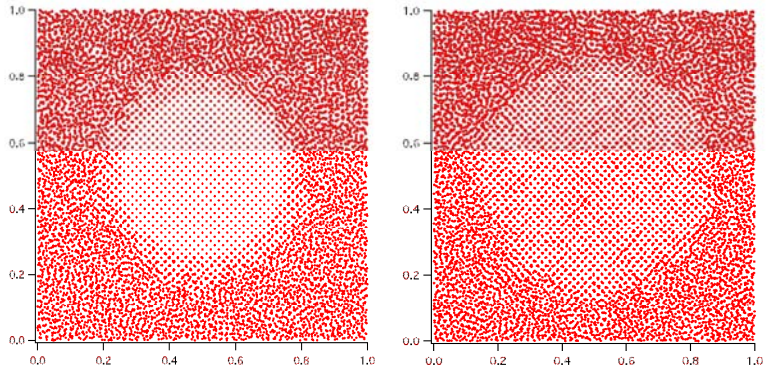

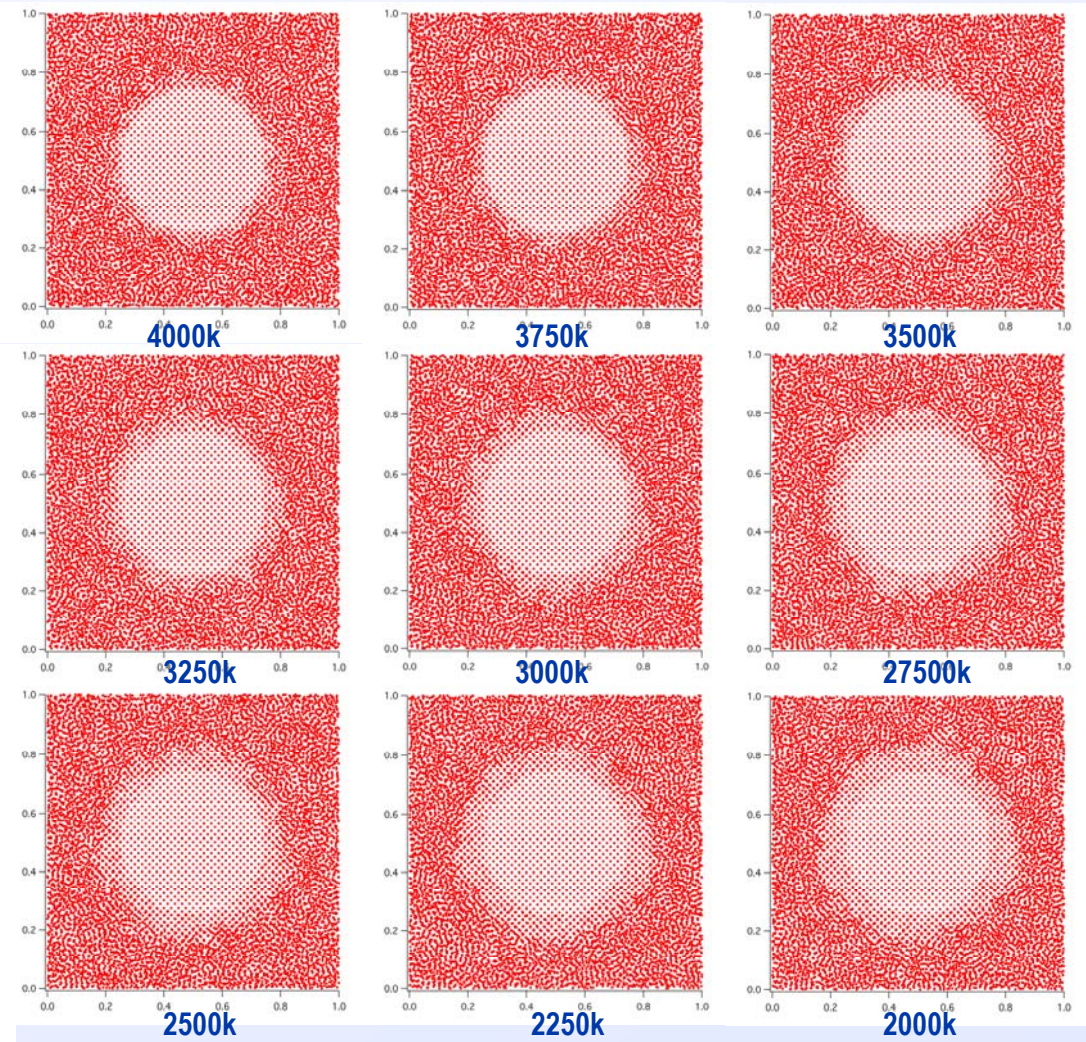

Growth Kinetics obeys a “C” curve

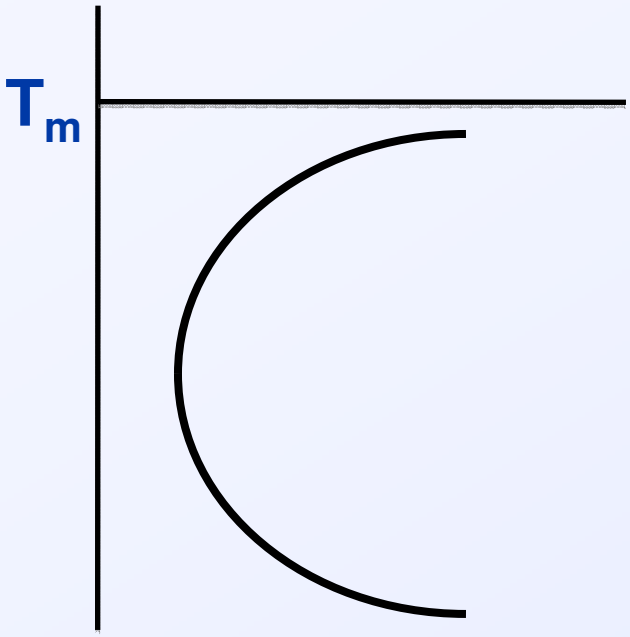

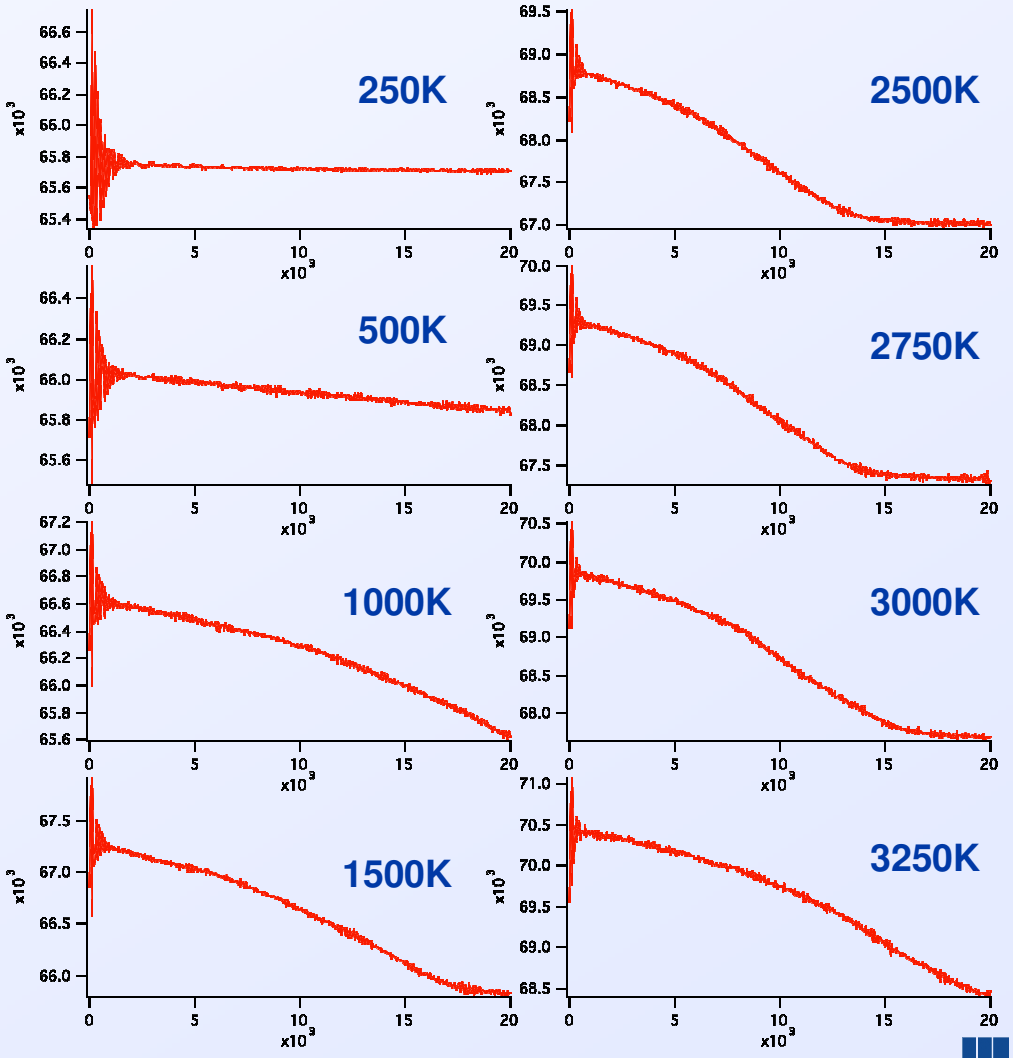

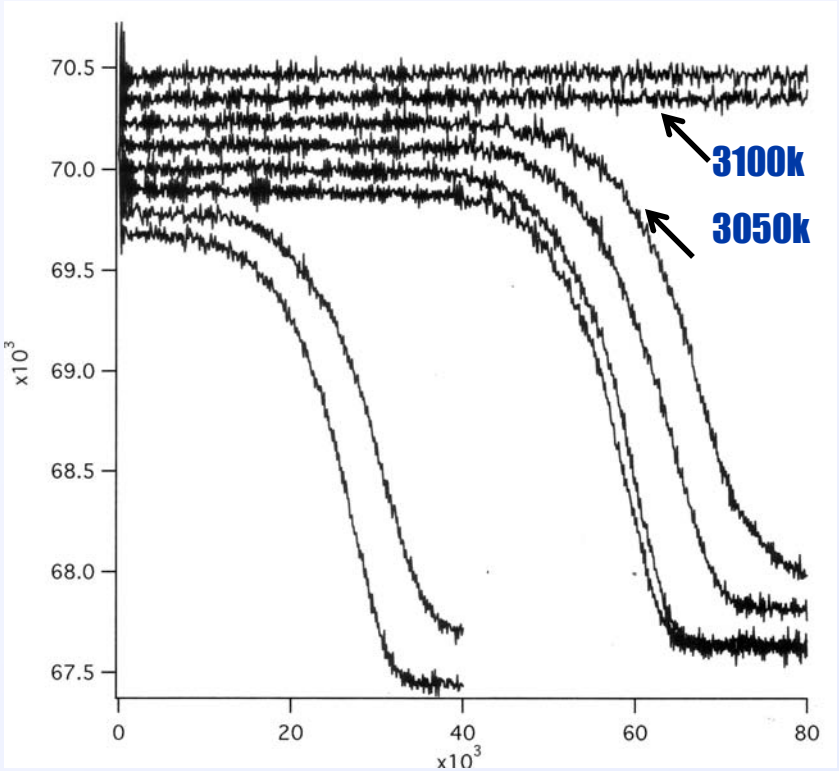

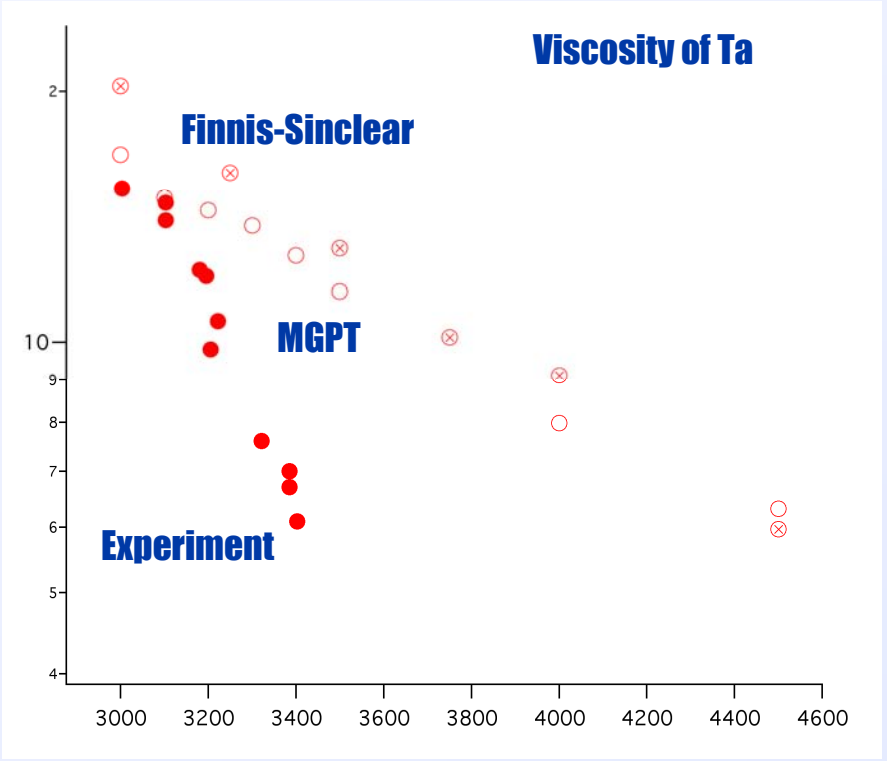

"Lag-time" for nucleant->nucleus

R_nucleant ~ 1nm

How do we know MD with an empirical potential gets the "kinetics" anywhere right?

$$R_c \approx \frac{2\gamma_{sl}}{\Delta S_f (T_m - T)}$$

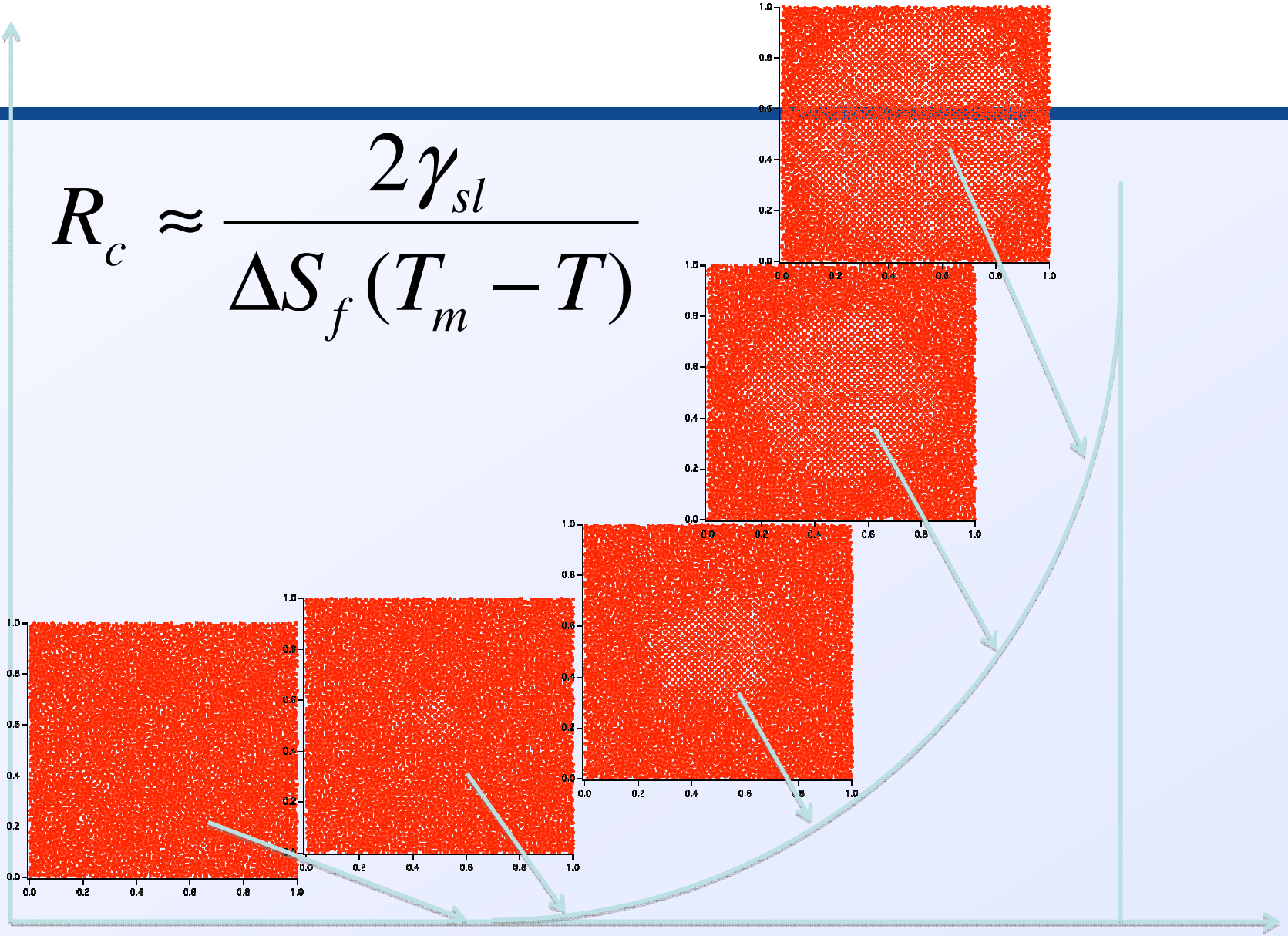

In Situ Kinetics

- Material “State”
- Kinetics = Change of “State”
  - Phase (Strain): Observable = Diffraction
  - Strength (Defects/Dislocations): Observable = Diffuse Scattering
  - Damage (Voids/Porosity): Observable = Imaging/Tomography + Small-Angle Scattering

Molecular dynamics (MD) simulations are used to model *Nucleation (homogeneous and beyond)*

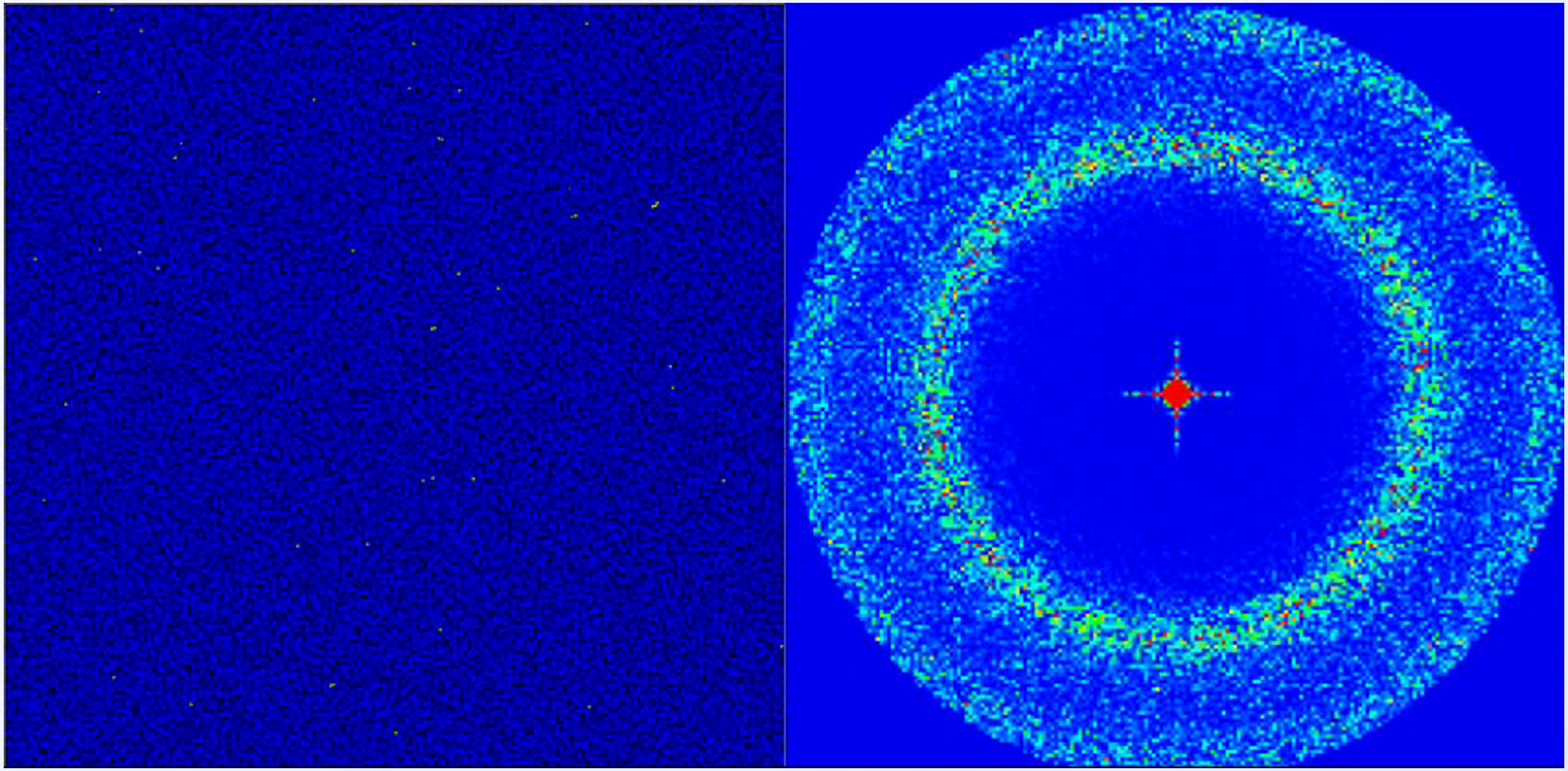

Simulations suggest novel in situ x-ray scattering experiments using emerging sources

Streitz *et al.* Phys. Rev. Lett. 2006

What is spallation fracture?

HE Shock

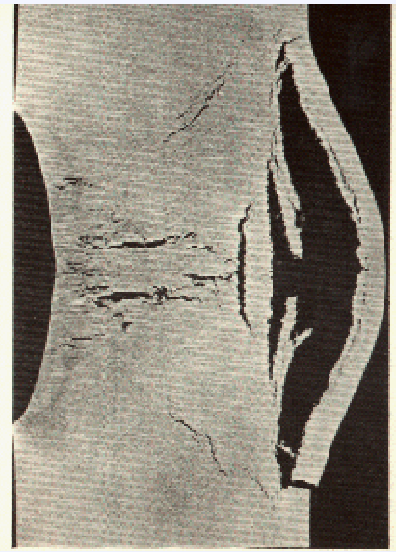

Free Surface

Rinehart and Pearson, "Behavior of Metals Under Impulsive Loads," 1954

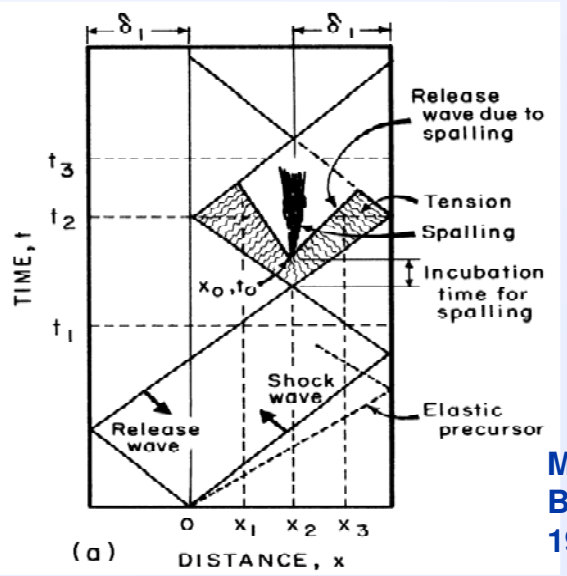

Meyers, "Dynamic Behavior of Materials," 1994, Barbee, 1972

Gas Gun Impact Experiment

Spallation fracture is an internal rupture process when strong shock waves interact in solids. The dynamic fracture of ductile metals occurs through the nucleation, growth and linking of microscopic voids.

NDE: Synchrotron-based 3D X-ray Tomography

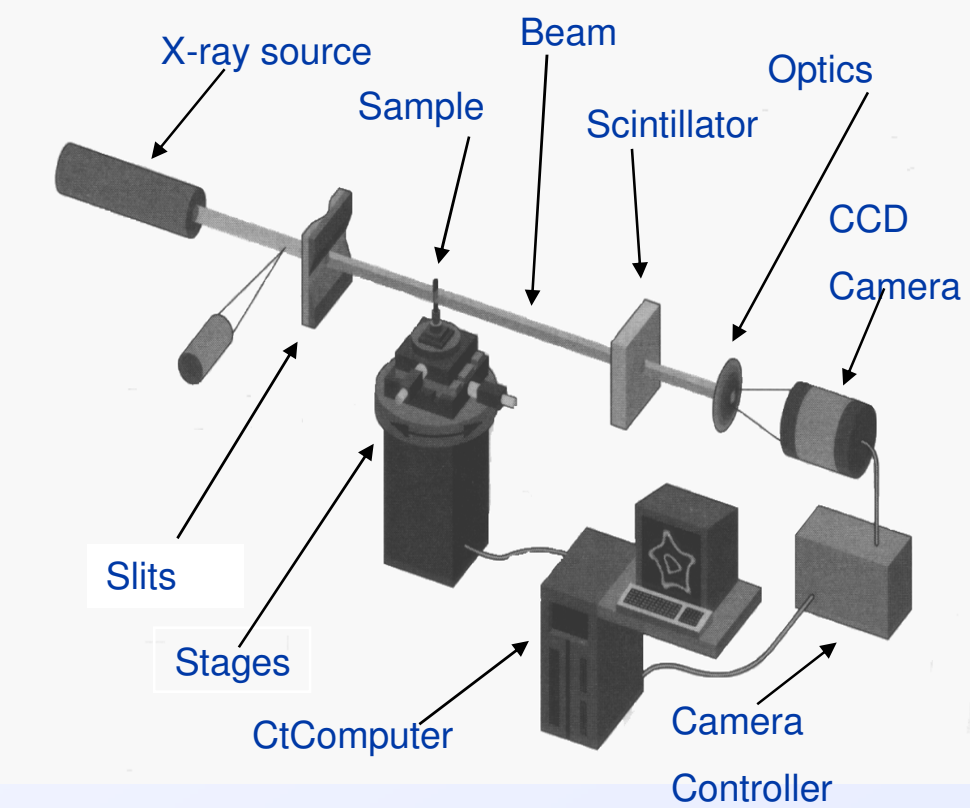

Al995 [110], 3mm core

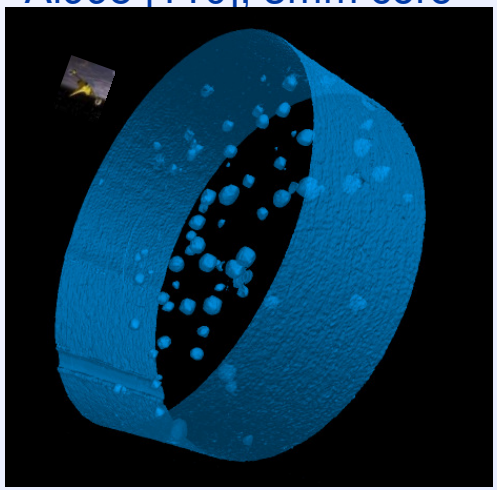

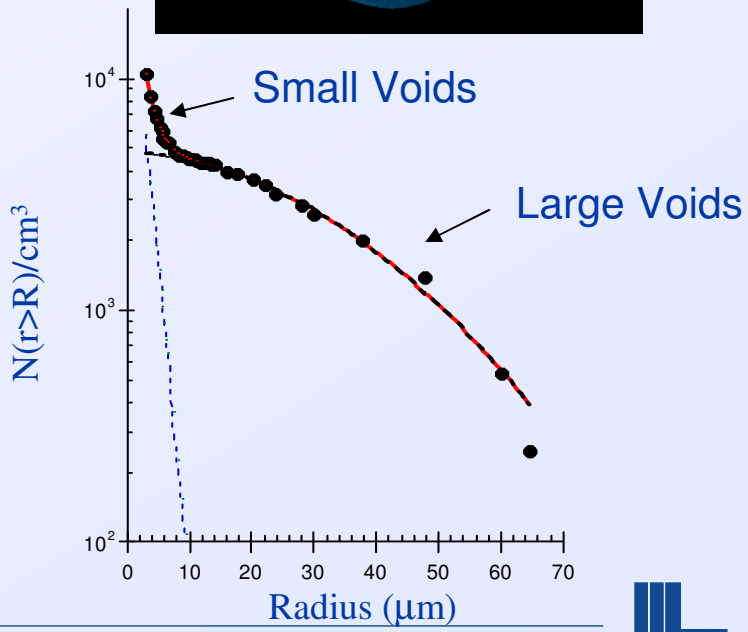

Rotate sample through 720 orientations and measure attenuation of X-ray beam

The region surrounding the voids shows increased hardness (strength)

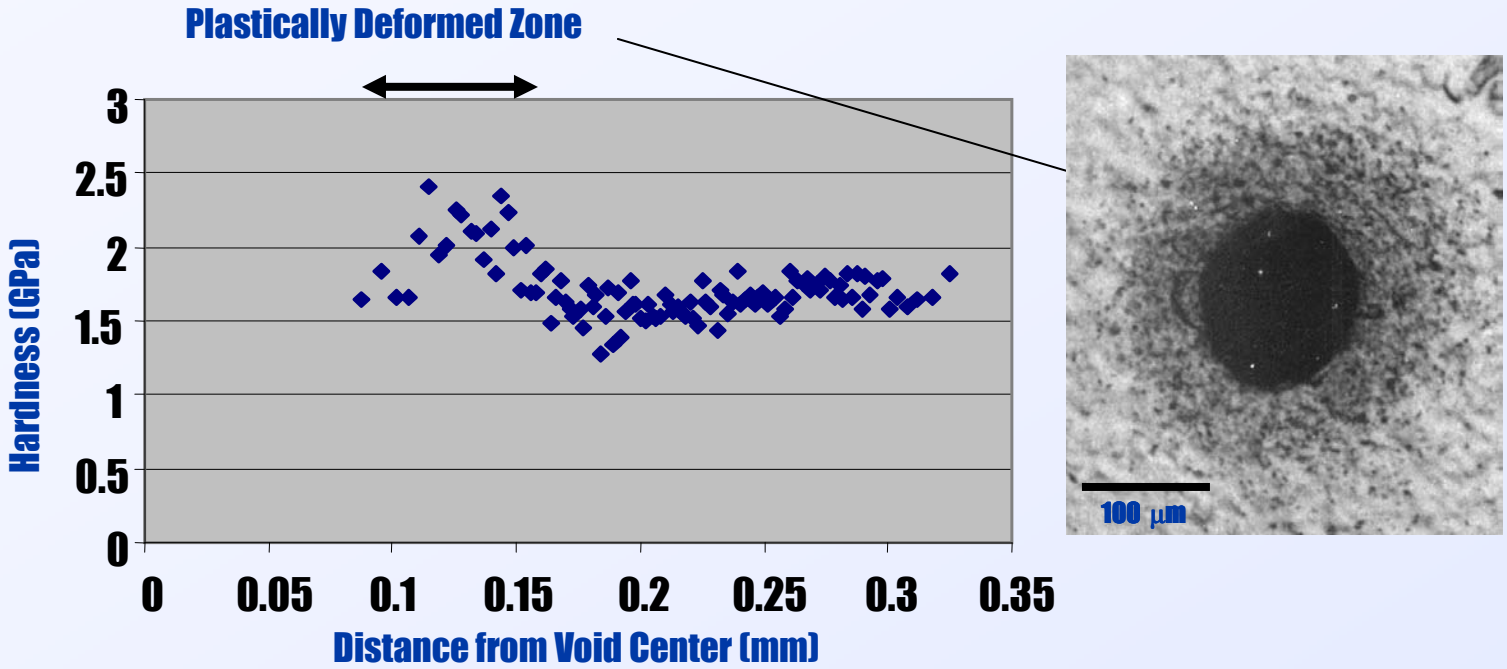

The enhanced hardness (strength) in the metal surrounding the voids suggests a plastic zone with higher dislocation content.

The microbeam-Laue diffraction in single x-tal Al with voids reveals several distinct zones located at different depth

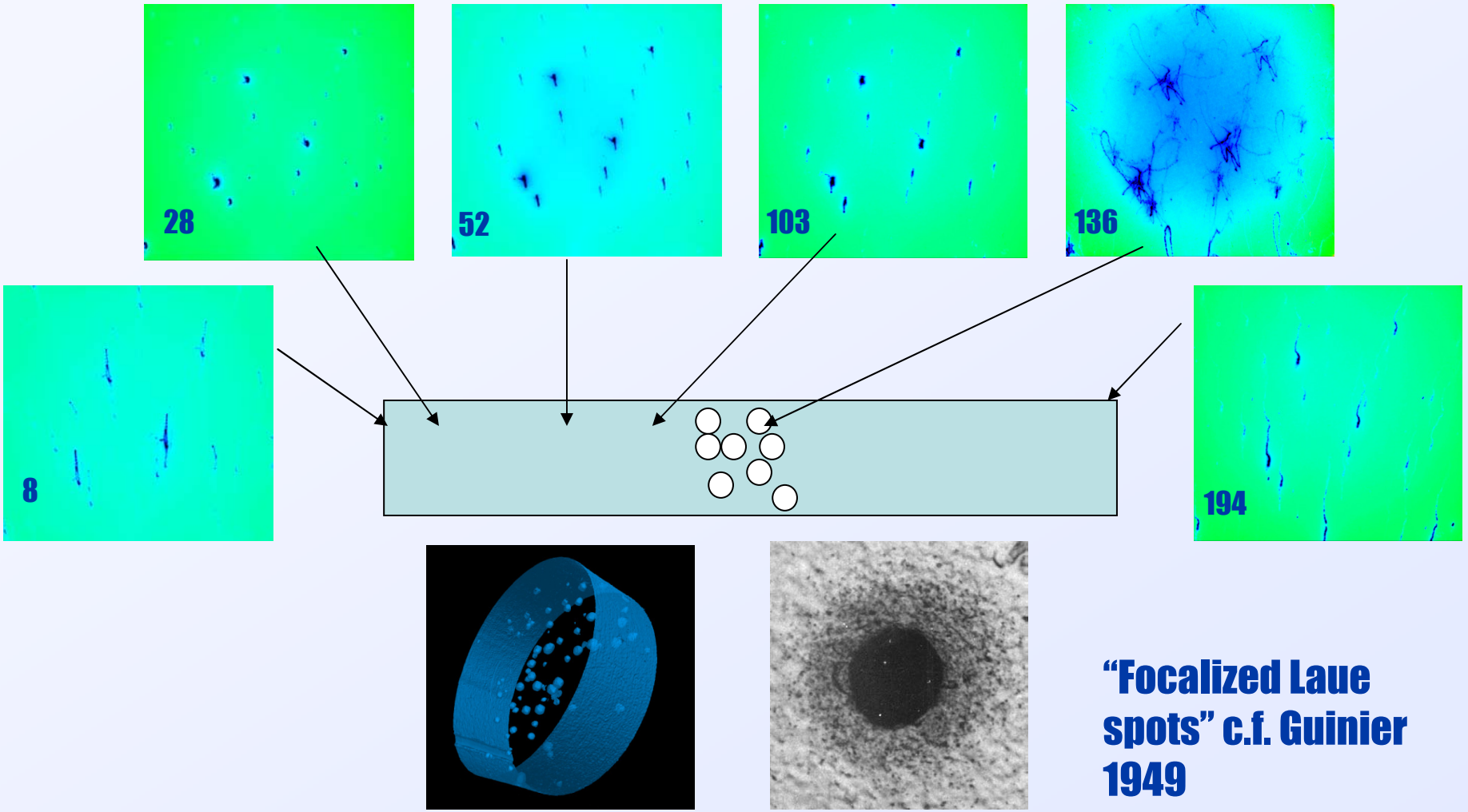

"Focalized Laue spots" c.f. Guinier 1949

Barabash et al. Int J. Plasticity, 2009

Small angle x-ray scattering (SAXS) directly measures sub-micron void distribution

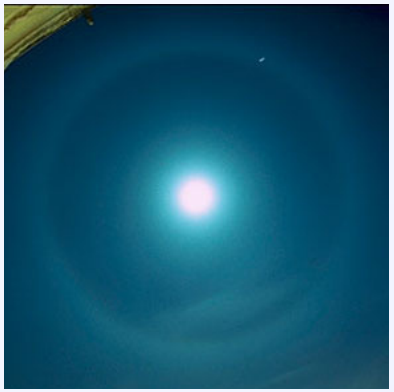

Moon Halo

Experimental void structure (greater than micron) from 3D x-ray tomography (Kinney and Belak, at ALS)

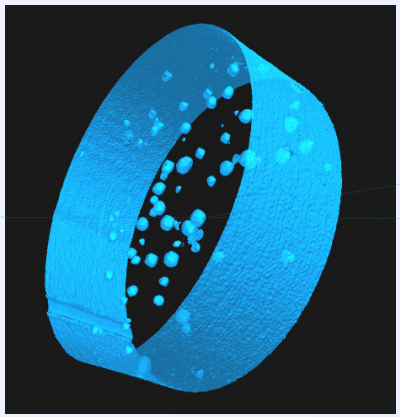

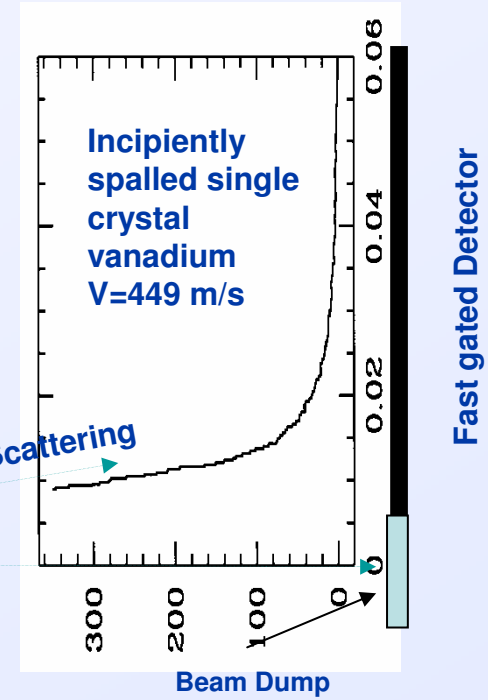

Monochromatic and Collimated X-ray pulse

HESAXS with 80keV at APS and 0.5mm sample

$\Theta \sim \lambda / d$

$q = 4 \pi \sin(\theta) / \lambda$

Experimental sub-micron void structure from small-angle scattering (with Ilavsky at APS)

Analysis of SAXS/SANS data yields information on particle size, spacing and morphology

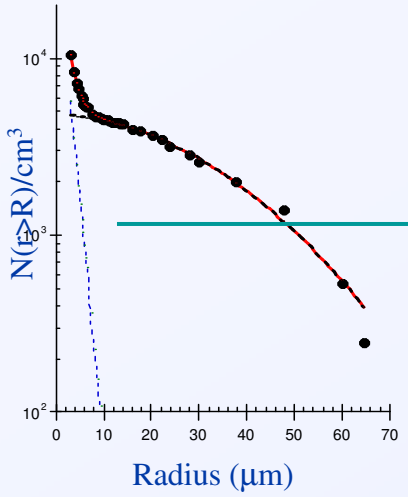

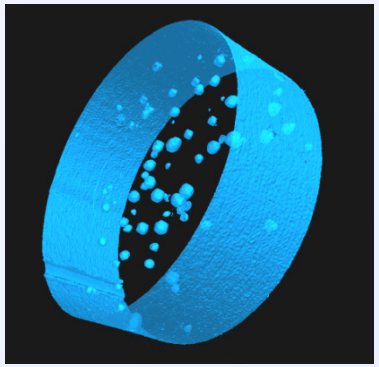

q^{-5} probably due to the diffuse spall interface

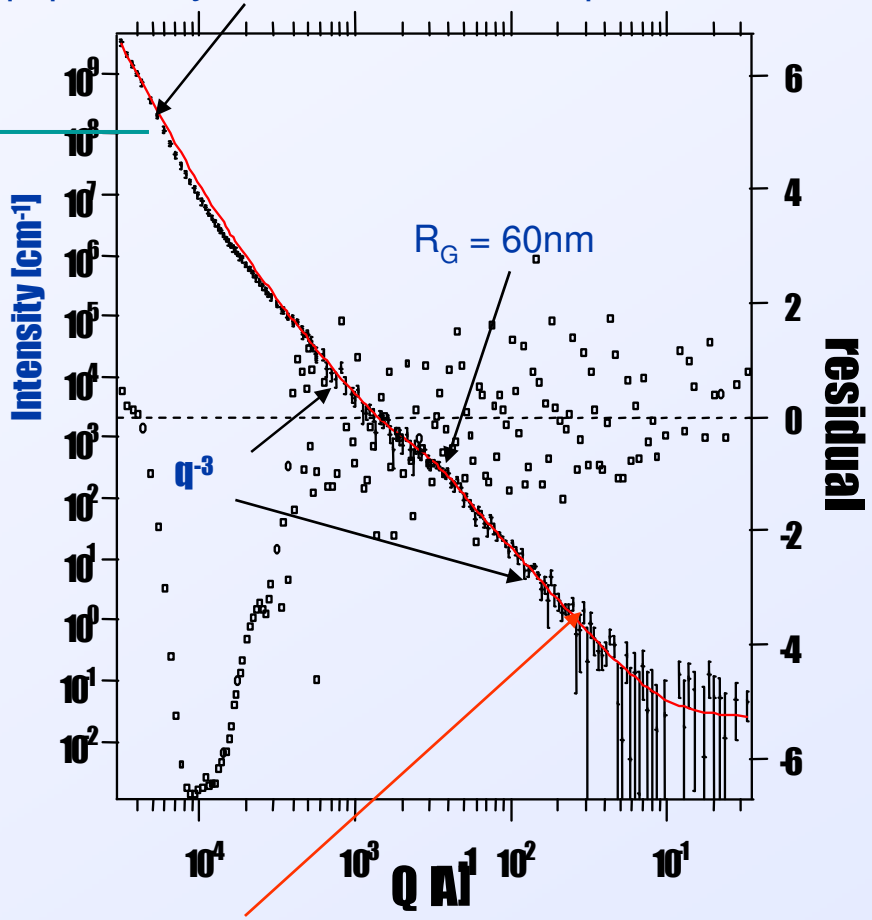

Unified Fit (Beaucage, Ilavsky)

Extracting the void distribution from the scattering data requires "fitting" the experiment. We have overlapping tomography and scattering data!

Scattering and tomography together results in a void size distribution spanning 4-5 orders of magnitude in scale!!

Conclusions: *Questions*

- What is a nucleant?
- How does it become a nucleus? (lag time)
- How do we NDE characterize the initial nucleant, their potencies, their transition into a nucleus, and the kinetics in situ and non-destructively?
- How does the picture change (if at all) when thermodynamics are changed? (stress/pressure)
- Can we “calculate” the nucleation curve “ab initio”?

Coarse Graining for Time

Timescales

Deterministic part

timestep Δt

Stochastic part

timestep ***dt***

$$\frac{\partial c}{\partial t} = \underbrace{M \nabla^2 \left[f_c - \alpha \nabla^2 c \right]}_{\text{slowly varying}} + \underbrace{\xi}_{\text{rapidly varying}}$$

Strategy

Deterministic part

integrate as usual with timestep Δt

Stochastic part

replace with stochastic term with timestep Δt

integrate as usual with timestep Δt

Sufficiently Large Fluctuation Approximation

"Large Enough" Approx.

Large enough to cause a nucleation event

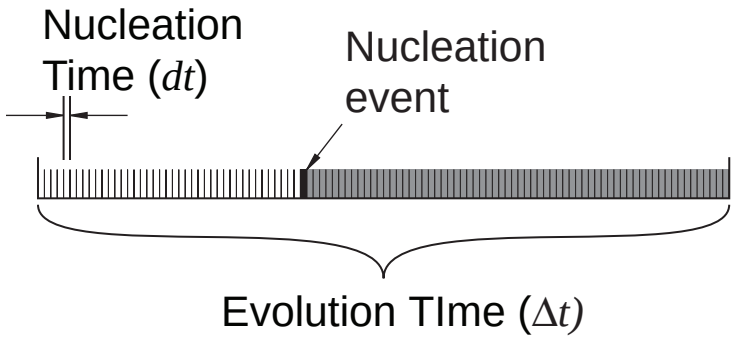

Pr(nucleation) = 1 - Pr(0 nuclei form)

$1 - \lambda^0/0!\, e^{-\lambda}$ *(Poisson statistics)*

$$p_{nucl} = 1 - e^{-J^* \Delta t}$$

Nucleation

Used as an input

"heaviside" function — *Simmons, et al., 1999*

classical nucleation theory — *Wang, et al., 2009*

Success

Wen, et al., 2002

Dynamic interplay between nucleation and growth kinetics

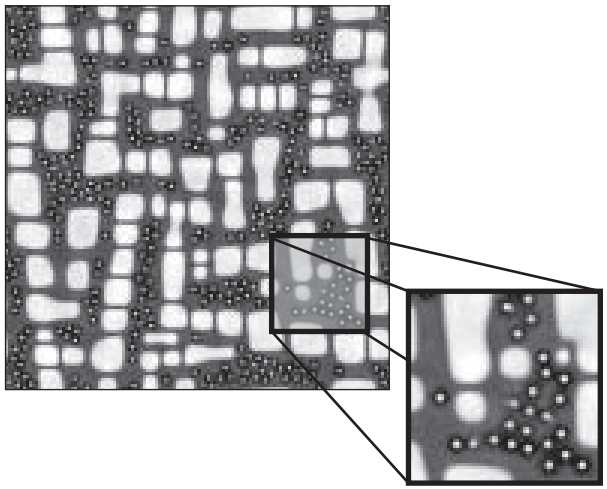

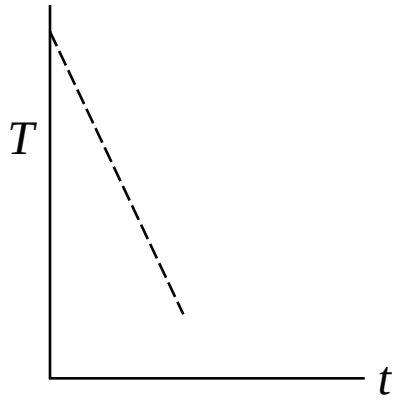

Langevin Noise

$$\frac{\partial c}{\partial t} = \underbrace{M \nabla^2 \left| f_c - \alpha \nabla^2 c \right|}_{\text{slowly varying}} + \underbrace{\xi}_{\text{rapidly varying}}$$

Convolve Small Flucutations

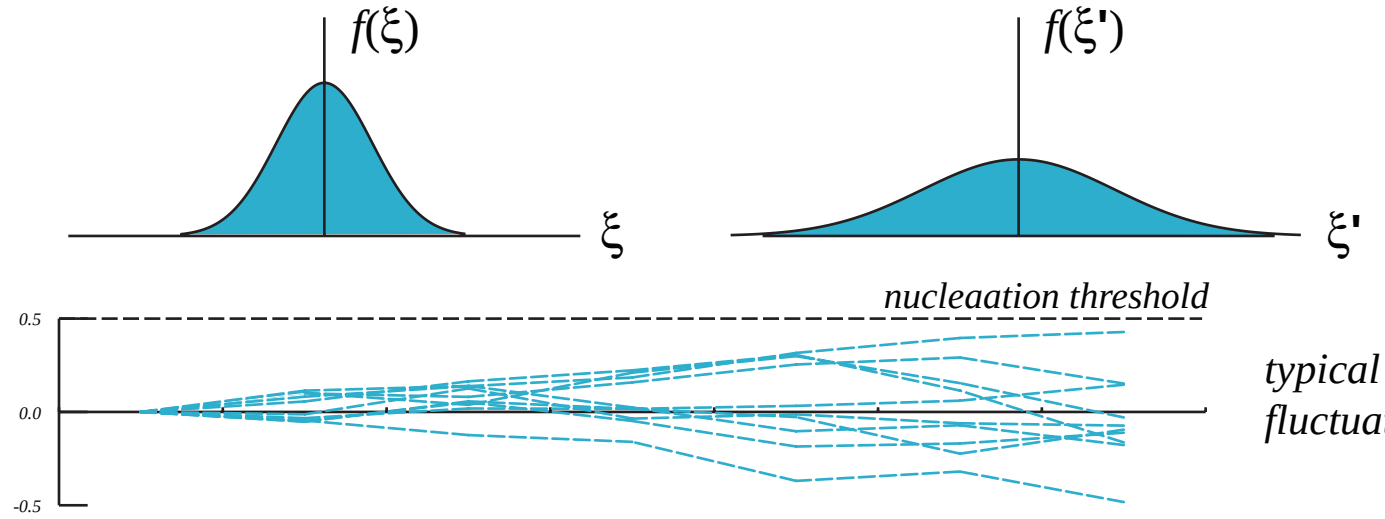

Scale up fluctuations to match growth time

Convolve n small ξ fluctuations to give ξ' fluctuations

*ξ' ~ **Gaussian distributed**, irrespective of distribution of ξ*

*typical fluctuations: **nucleation starts when √n gets large enough***

Bleading Edge

Nucleation can be caused by very rare event

***outlier**: convergence to Gaussian will wash out*

Coarse grain to preserve rare largest fluctuation

Extreme Value Theory

Extreme Values

Probability that ξ is as large as β

Cumulative distribution function

$$F(\xi) = \int_{-\infty}^{\xi} f(\eta) d\eta$$

1 fluctuation: $F(\xi)$
2 fluctuations ala β: $F^2(\xi)$
...
n fluctuations ala β: $F^n(\xi)$

Example

Exponential distribution

$$f(\xi) = e^{-\xi}$$

$$F(\xi) = 1 - e^{-\xi}$$

$$F^n(\xi) = (1 - e^{-\xi})^n$$

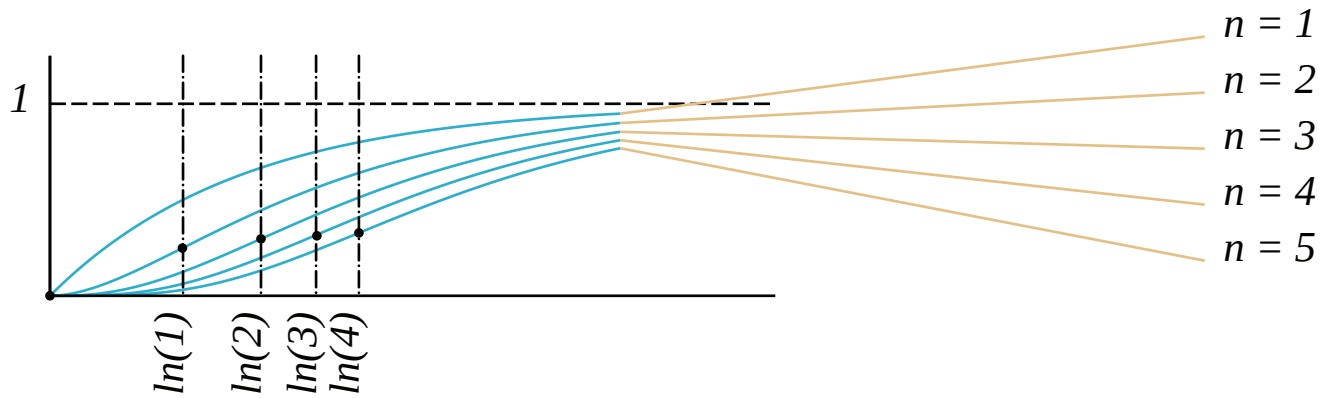

$F^n(\xi - \ln(n))$ maintains position of the inflection point

Asymptotic Form

$$F^n(\xi) \sim \exp(-\exp(-\xi + \ln(n)))$$

$$\boxed{F^n(\xi) \sim \exp(-\exp(-1/b_n(\xi - a_n)) }$$

Gumbel distribution

Fisher-Tippett Theorem (1928)

Space of initial distributions of ξ

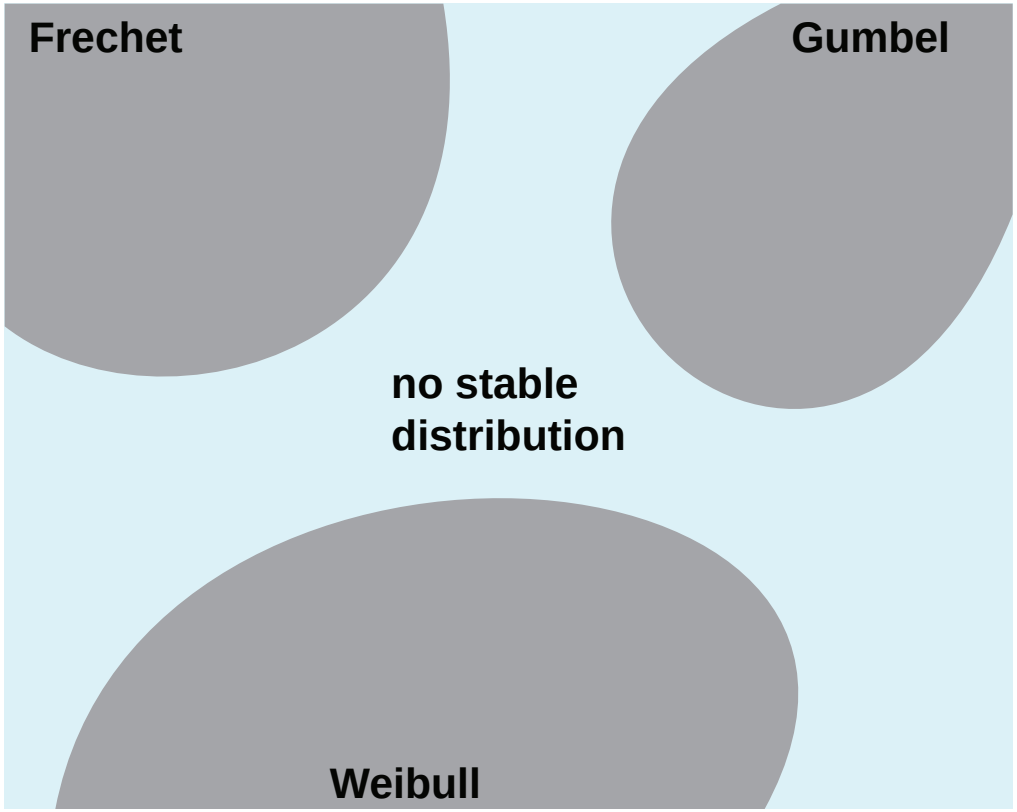

Frechet

$$\lim_{t\to\infty} (1 - F(t\,\xi)\,)/(1 - F(t)\,) = e^{-\gamma}$$

$$Pr(\xi_{max} < \beta) = e^{-e^{-1/b_n}(\beta^{-\gamma})}$$

Gumbel

$$\lim_{t\to\infty} (1 - F(t + \xi\, r(t))\,)/(1 - F(t)\,) = e^{-\xi}$$

$$Pr(\xi_{max} < \beta) = e^{-e^{-1/b_n}(\beta - a_n)}$$

Weibull

$$\lim_{t\to\infty} (1 - F(t\,\xi)\,)/(1 - F(t)\,) = e^{-\gamma}$$

x has a maximum possible value

...

$$Pr(\xi_{max} < \beta) = e^{-e^{-1/b_n}((-\beta)^{\gamma})}$$

Stable Distributions

Only 3 limiting distributions

*determined by **tails of ξ distribution***

***invertable:** random numbers can be generated directly*

use this as Langevin noise

UnstableRegion

Time dependent distribution

Phase Field Simulation of Critical Nuclei Morphology in Solid State Transformations

Qiang Du

Department of Mathematics, Penn State University

With Lei Zhang, Long-Qing Chen

Joint ARL/AOARD/LLNL Workshop on Nucleation During Solid-Solid Phase transformations, Maui, 2010

Nucleation

Nucleation: a process where clusters of atoms form via fluctuations in a meta-stable phase with those beyond certain critical threshold grow.

Significance: predicting nucleation rate and its dependence on composition and temperature is an interesting and challenging problem in materials sciences, given the complex energy landscape in high dimension and the unstable nature of saddle/transition points.

Phase field/diffuse interface critical nuclei morphology

Outline

1. Problem/Objective
2. Approach/Algorithms
3. Examples
   - Single nonconserved order parameter
   - Single conserved order parameter
   - Two order parameters
4. Observation/Conclusion

I. Problem/Objective

The importance of the problem and the challenging computational nature motivated our recent studies:

- **to build rigorous mathematical foundation to the models of nucleation;**
- **to develop algorithms needed in the computational study of nucleation in solid state transformations;**
- **to develop methods and codes for the computation of the critical nucleus shape/size and nucleation rate.**

II. Approach: Critical nuclei morphology via the large deviation principle

- **Large Deviation Principle: for a Langevin system, the most probable transition path between local energy wells, in the zero fluctuation limit and without any time limitation, is the minimum energy path (MEP) connecting the equilibria.**

- **The lowest energy barrier is given by the largest energy difference reached on the MEP**

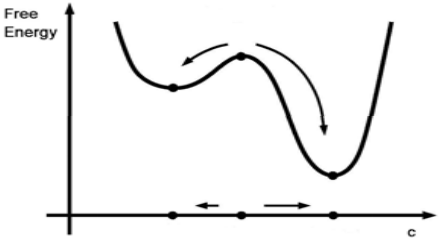

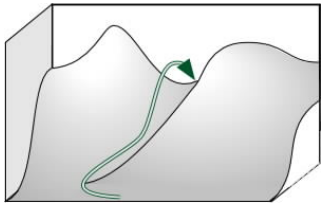

- **Points on the MEP with the highest energy: saddle points (unstable critical point) with a minimax property**

II. Approach: diffuse interface/phase field

- **We work with the diffuse interface/phase field framework.**

- **We develop/implement suitable algorithms (minimax method/constrained string method) to gather information on the saddle point and minimum energy path (transition pathway) which helps to determine the nucleation rate and the critical nuclei profiles**

- **We incorporate the gathered information into phase field simulations of the nucleation and growth processes**

II. Approach: Phase Field and Nucleation

In existing phase field simulations, nucleation mostly are treated either via Monte Carlo or classical theory

Classical theory: nucleus shares the same thermodynamic properties as the equilibrium with assumed shape *a priori* .

Non-classical: Cahn-Hilliard, diffuse interface

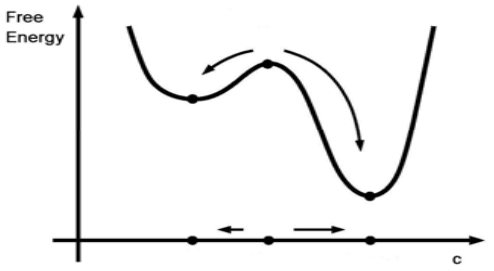

Free energy

$$\int_{\Omega} \left(\frac{\epsilon}{2} |\nabla \phi|^2 + \frac{1}{4\epsilon} (\phi^2 - 1)^2 + \lambda (3\phi - \phi^3) \right) dx$$

λ: driving force ε: interfacial width Ω unit periodic cell

II. Approach: Cahn-Hilliard theory

Nonclassical theory of Cahn-Hilliard considers bulk and interfacial energy contributions but not the contribution due to the anisotropic elasticity energy

$$\int_\Omega \left(\frac{\epsilon}{2} |\nabla \phi|^2 + \frac{1}{4\epsilon} (\phi^2 - 1)^2 + \lambda (3\phi - \phi^3) \right) dx$$

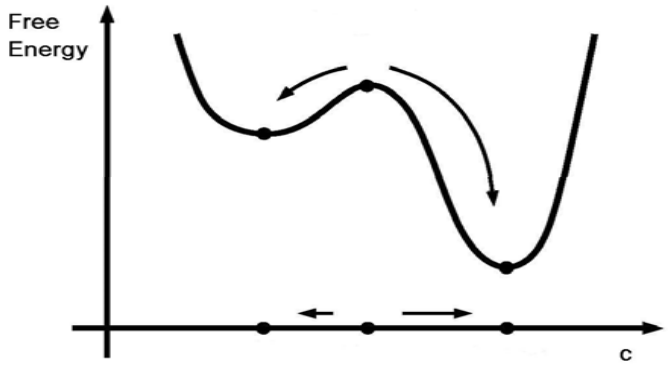

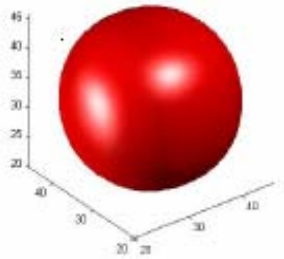

Profile of critical nuclei,

consistent with classical theory in the thin interface limit

II. Approach: Energy and Nucleation

Solid state phase transformations:

Energy contribution: bulk + interfacial + elastic

$$\int_\Omega \left(\frac{\epsilon}{2} |\nabla \phi|^2 + \frac{1}{4\epsilon} (\phi^2 - 1)^2 + \lambda (3\phi - \phi^3) \right) dx + E_e$$

Misfit Elastic Energy:
via Khachaturyan's micro-elasticity theory

$$\frac{\beta}{2} \int_{\widehat{\Omega}} \frac{dk}{(2\pi)^d} B(n_k) |\widehat{\eta}(k) - \widehat{\eta}_0(k)|^2$$

III. Examples: first, a proof of concept

- A single order parameter: isotropic/anisotropic elastic energy
- Elastic energy $\frac{\beta}{2}\int_{\widehat{\Omega}} \frac{dk}{(2\pi)^d} B(n_k)|\hat{\eta}(k) - \hat{\eta}_0(k)|^2$

$$B(n) = 3(c_{11}+2c_{12})\epsilon_0^2 - (c_{11}+2c_{12})^2\epsilon_0^2 \cdot \frac{1+2\zeta s(n)+3\zeta^2 n_1^2 n_2^2 n_3^2}{c_{11}+\zeta(c_{11}+c_{12})s(n)+\zeta^2(c_{11}+2c_{12}+c_{44})n_1^2 n_2^2 n_3^2}$$

$\zeta = (c_{11}-c_{12}-2c_{44})/c_{44}$ elastic anisotropic factor

$s(n) = n_1^2 n_2^2 + n_1^2 n_3^2 + n_2^2 n_3^2$

ϵ_0 lattice mismatch, Ω **periodic cell** $\widehat{\Omega}$ reciprocal domain

II. Approach: energy functionals for diffuse/sharp interface

$$E_\epsilon(\eta) = \int_\Omega [\frac{\epsilon}{2}|\nabla\eta|^2 + \frac{1}{4\epsilon}(\eta^2-1)^2 + \frac{\lambda}{2}(3\eta-\eta^3)]dx + \frac{\beta}{2}\int_{\hat{\Omega}} \frac{dk}{(2\pi)^d} B(n_k)|\hat{\eta}(k) - \hat{\eta}_0(k)|^2$$

Sharp interface limit: $\varepsilon \longrightarrow 0$

$$E_0(v) = \int_\Omega (\frac{\sqrt{2}}{3}|\nabla v| + \lambda v) + \frac{\beta}{2}\int_{\hat{\Omega}} B(n)|\hat{v}(k) - \hat{\eta}_0(k)|^2$$

if $v \in BV(\Omega, \{\pm 1\})$, and $E_0(v) = \infty$ otherwise.

Zhang-Chen-D. 2007

II. Approach: saddle point of diffuse interface energy

$$E_\epsilon(\eta) = \int_\Omega [\frac{\epsilon}{2}|\nabla\eta|^2 + \frac{1}{4\epsilon}(\eta^2-1)^2 + \frac{\lambda}{2}(3\eta-\eta^3)]dx$$
$$+\frac{\beta}{2}\int_{\widehat{\Omega}} \frac{dk}{(2\pi)^d} B(n_k)|\hat{\eta}(k) - \hat{\eta}_0(k)|^2$$

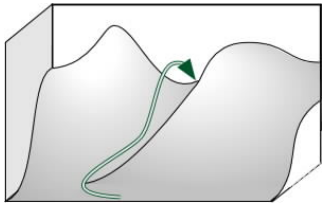

With periodic boundary condition:

a) the energy satisfies the Palais-Smale condition;

b) for small ε, there is a nontrivial saddle point connecting two trivial local minima

Zhang-Chen-Du 2008 J. Sci. Comp., Barrett lecture special issue

II. Approach: numerical method

Most of our algorithms for computing MEP/Saddle point are based on:

Minimax method : classical calculus of variation.
Rabinowitz 1986; Choi, 1993; Lin, 1997; Zhou, 2001

String method: more recently developed
W. E, W. Ren and E. Vanden-Eijnden, 2002

With suitable modifications (for conserved variables) and high order, adaptive implementation

III. Example: first, a proof of concept

- A single order parameter describing structural difference with an anisotropic elastic energy

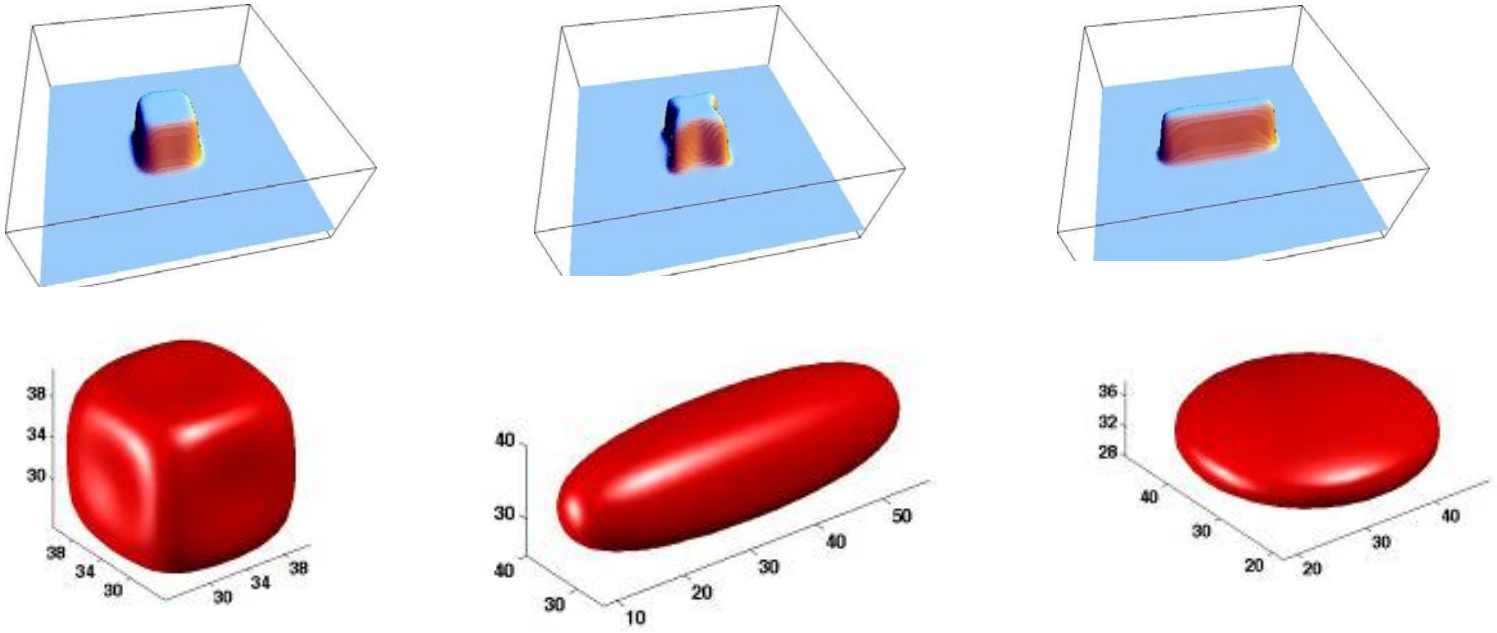

Critical nuclei with increasing elastic energy contributions (Zhang, Chen, Du, PRL, 2007, Acta Mater., 2008)

III. Example: effect of anisotropic elasticity – 2d

Zhang-Chen-Du PRL 2007

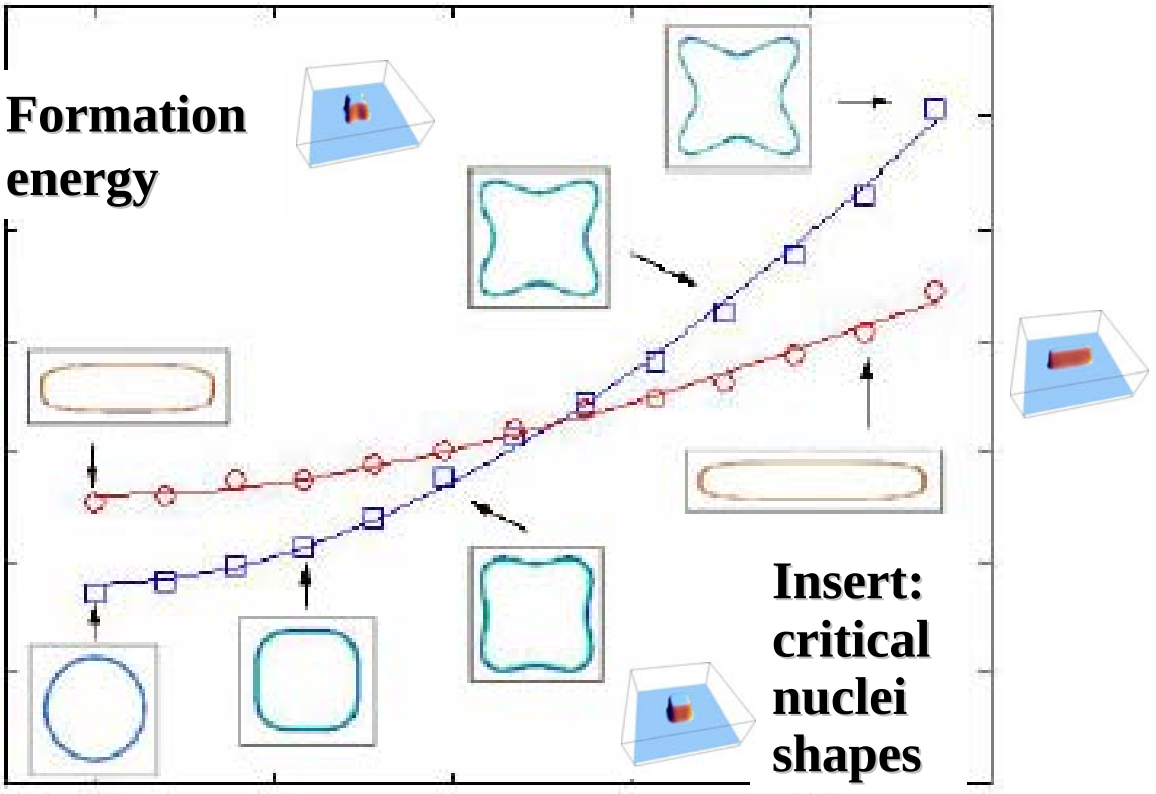

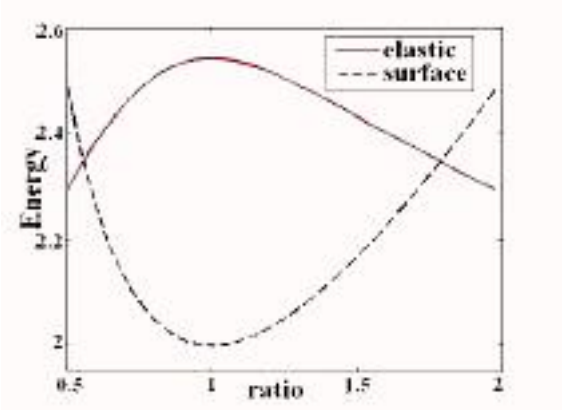

Elastic energy contribution (changing β)

III. Example: simulations of 3D critical nuclei

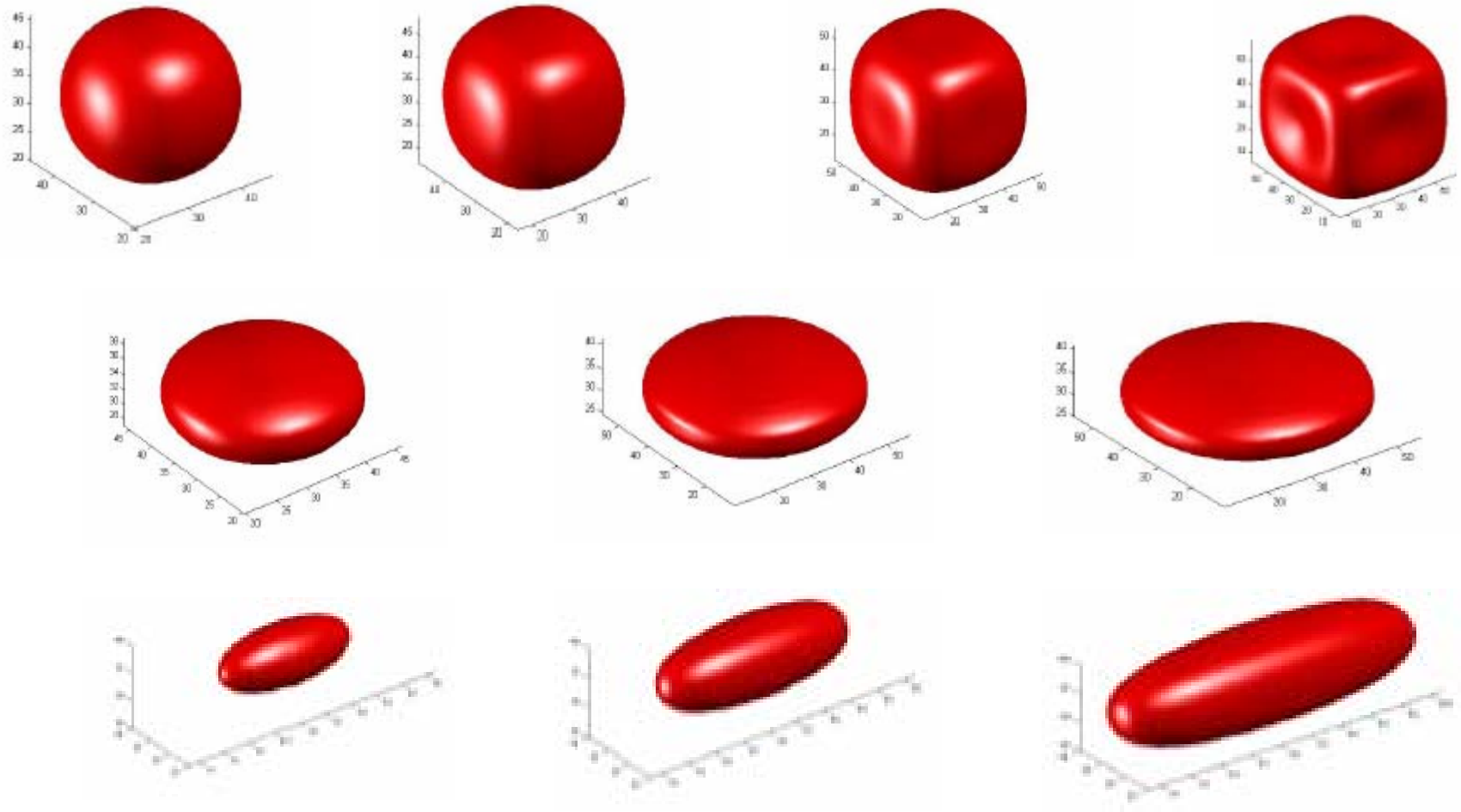

Saddle point branches with varying elastic energy contribution

III. Example: most probable 3D nuclei morphology

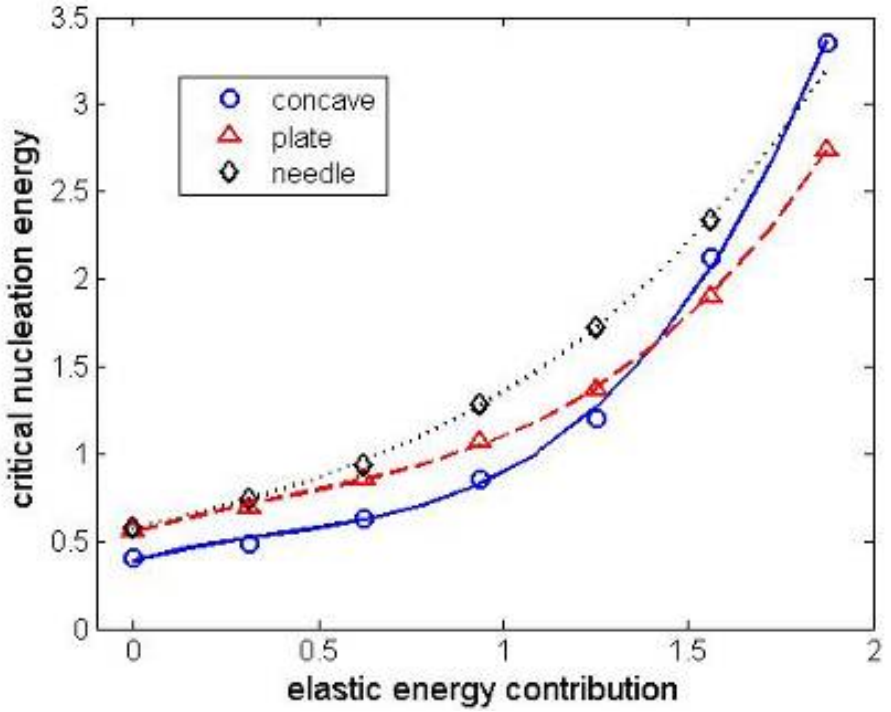

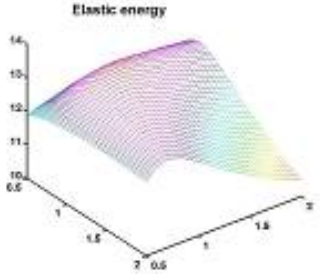

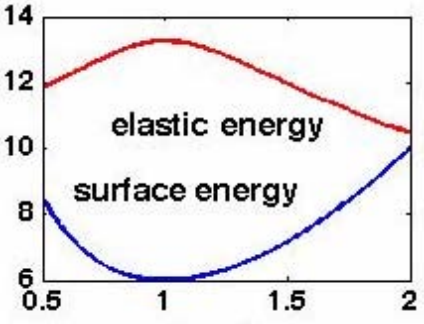

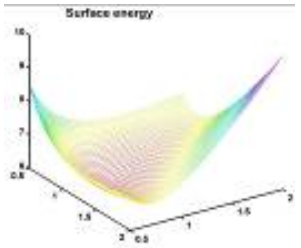

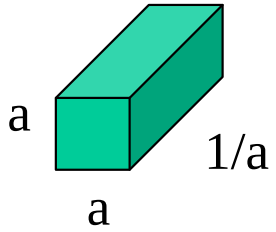

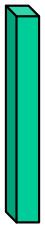

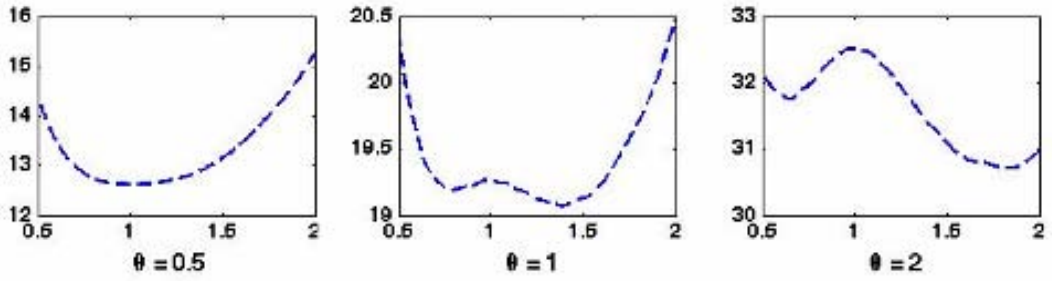

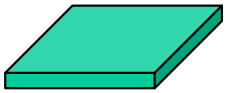

Free energy with various elastic energy contribution

III. Example: critical nucleus in the conserved field

- **Composition profile: c(x)**
- **Total free energy increase:**

$$E_{total}(c) = \int_{\Omega} [f^{c}(c) + \frac{\alpha}{2} |\nabla c(x)|^{2}] dx + \beta \cdot E^{elastic}$$

where $f^{c}(c) = f(c) - f(c_0) - \frac{\partial f(c)}{\partial c}|_{c=c_0}$

and $f(c) = \frac{1}{4}(c^2 - 1)^2$

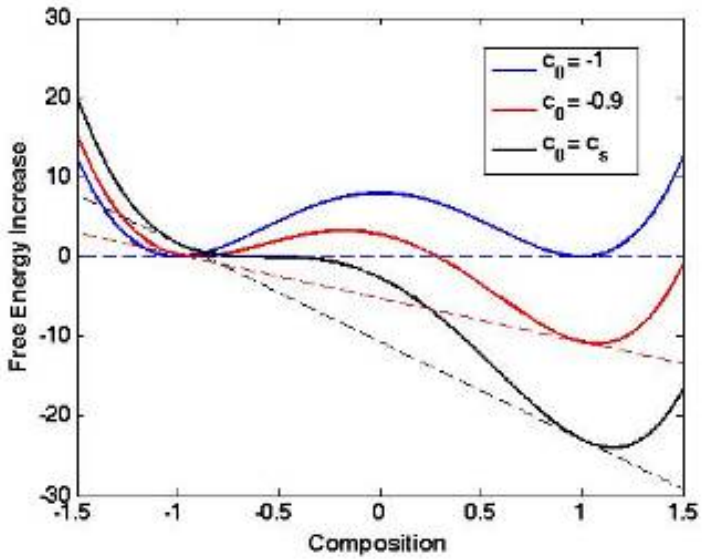

- **The volume constraint is** $\int [c(x) - c_0] dx = 0$
- **MEP gets modified when one or more constraints are imposed**

III. Example: an illustration of constrained MEP

- **3-D potential energy** $E(x,y,z) = (1-x^2)^2 + y^2 + 2z^2$

  with the constraint $x^2 + y^2 + z^2 - 1 = 0$

- **Containing the two energy wells of E:** $(\pm 1,0,0)$

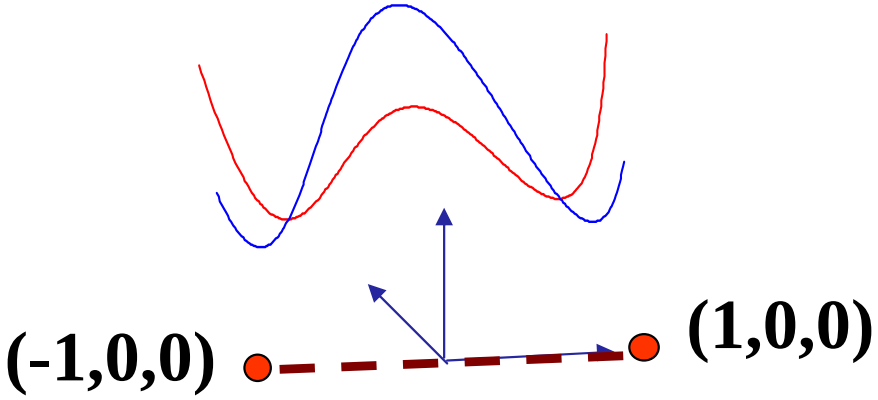

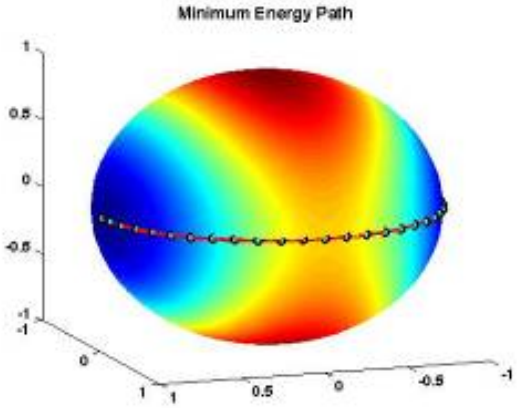

MEP without constraint and constrained MEP

- **We developed a constrained string method via augmented Lagrange multipliers to compute MEP**

III. Example: nucleation with a single conserved field

- **Critical nucleus, equilibrium solution, and MEP**

$(1) c_0 = -0.95$

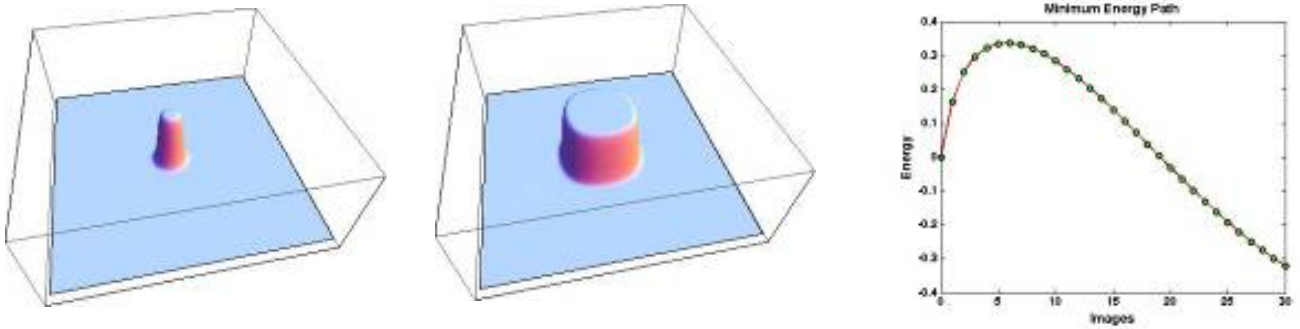

$(2) c_0 = -0.85$

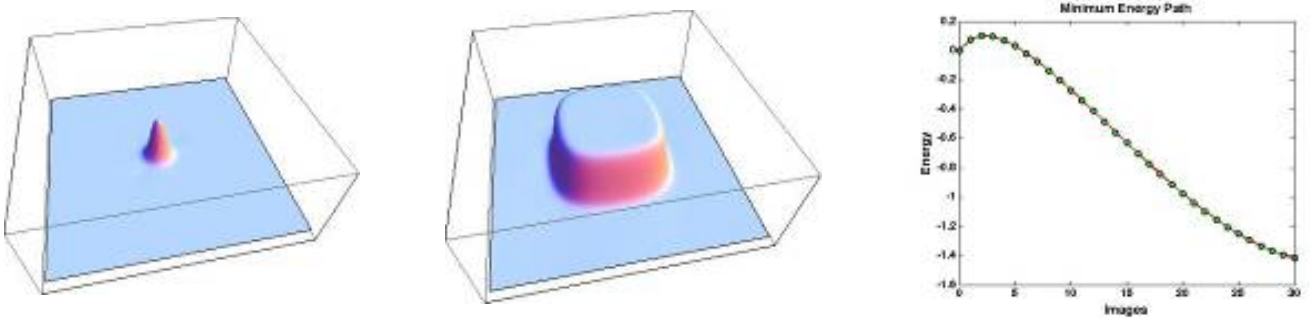

Zhang, Chen, Du, Comm. Comp. Phys., 2010

III.Example: effect of elastic energy

- **MEP with increasing elastic energy in conserved field**

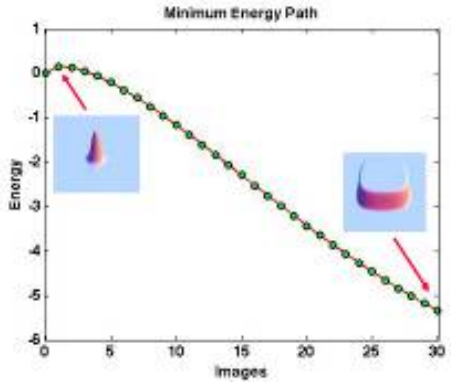

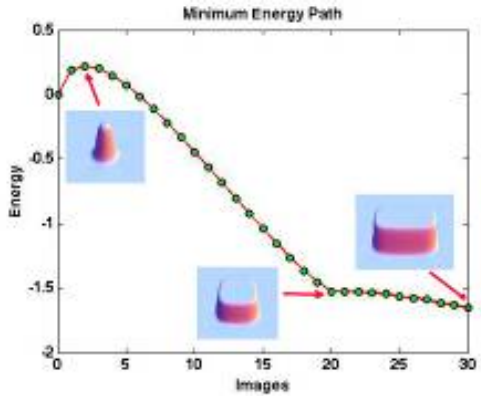

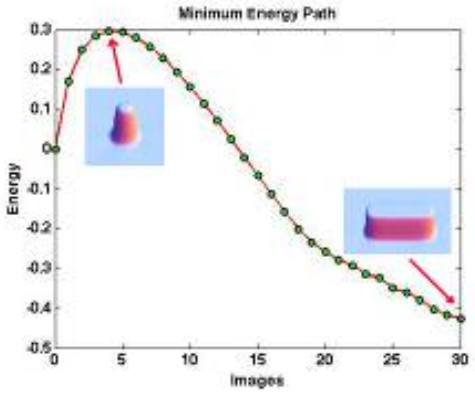

Critical nuclei morphology can be very different from that of the equilibrium!

- **Compare with critical nuclei in the non-conserved field**

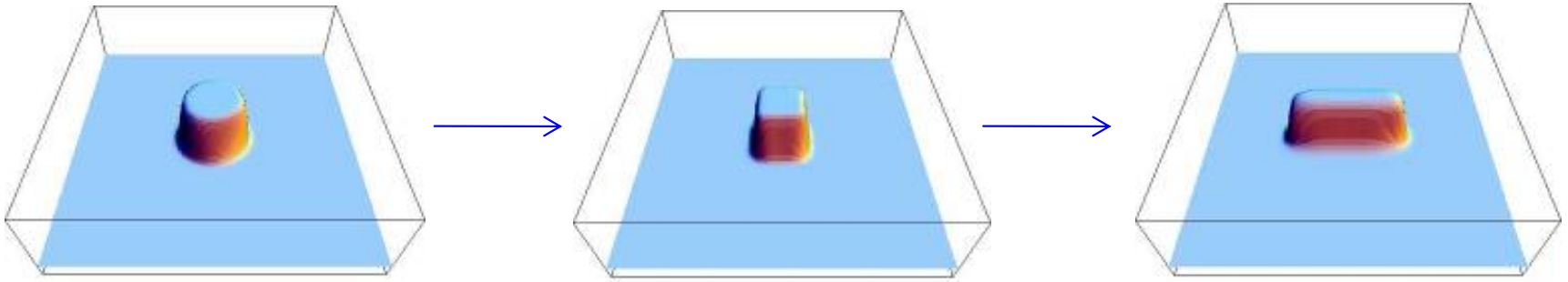

III. Example: nucleation involving multiple order parameters

- **Extensions to more complicated systems, in particular, those with multiple order parameter fields**

  - **A case of two non-conserved phase field order parameters representing different orientation variants**

  - **A case of a conserved field (composition) with a non-conserved field (order parameter):**

    θ' precipitates in Al-Cu alloys

    γ' precipitates in Ni-Al alloys

III.Example: two non-conserved order parameters

Type 1: Critical nucleus

Type I: Equilibrium state

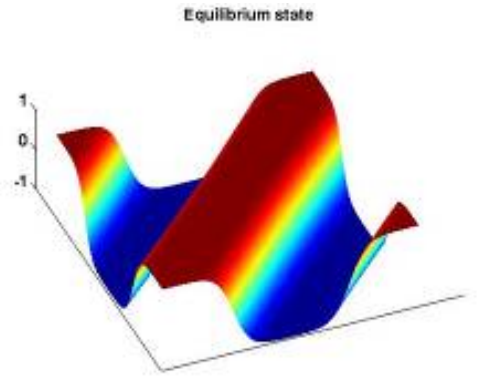

One type of critical nuclei

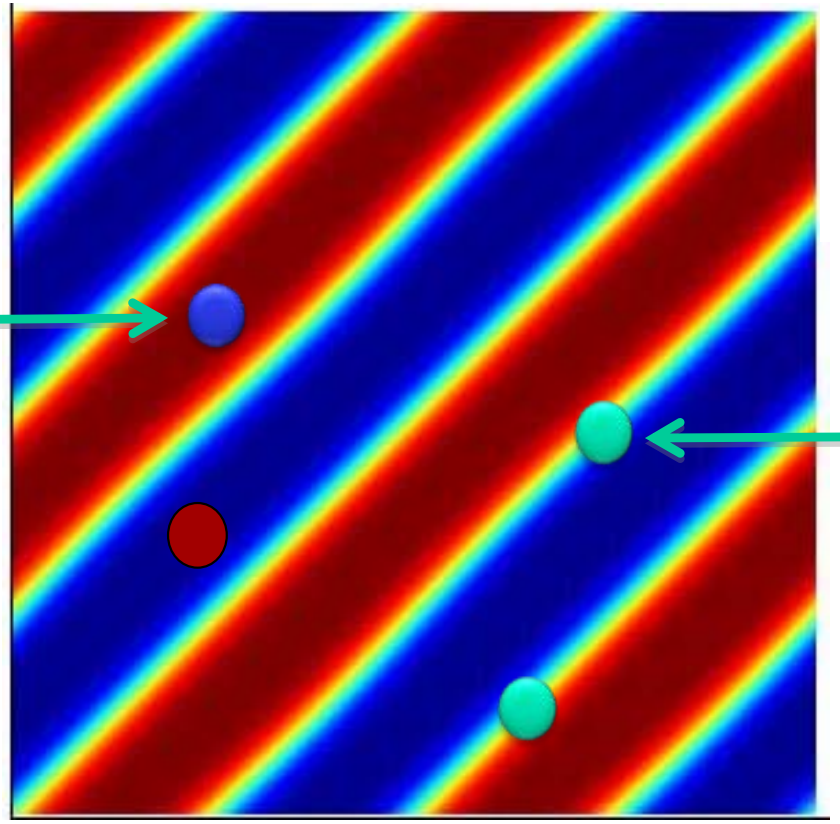

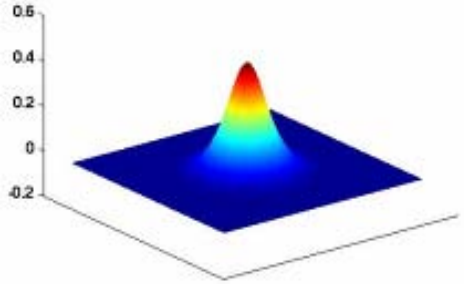

Another type of critical nuclei

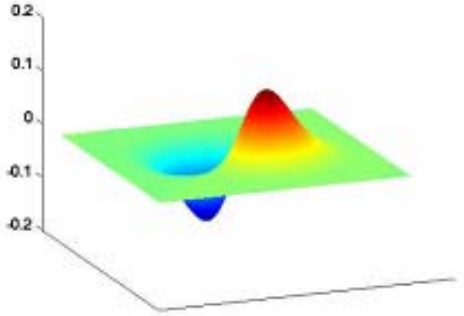

III.Example: two non-conserved order parameters

- **Type II: Equilibrium state**

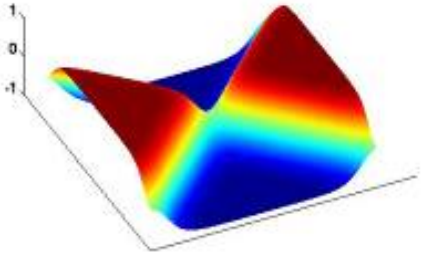

First type of critical nuclei

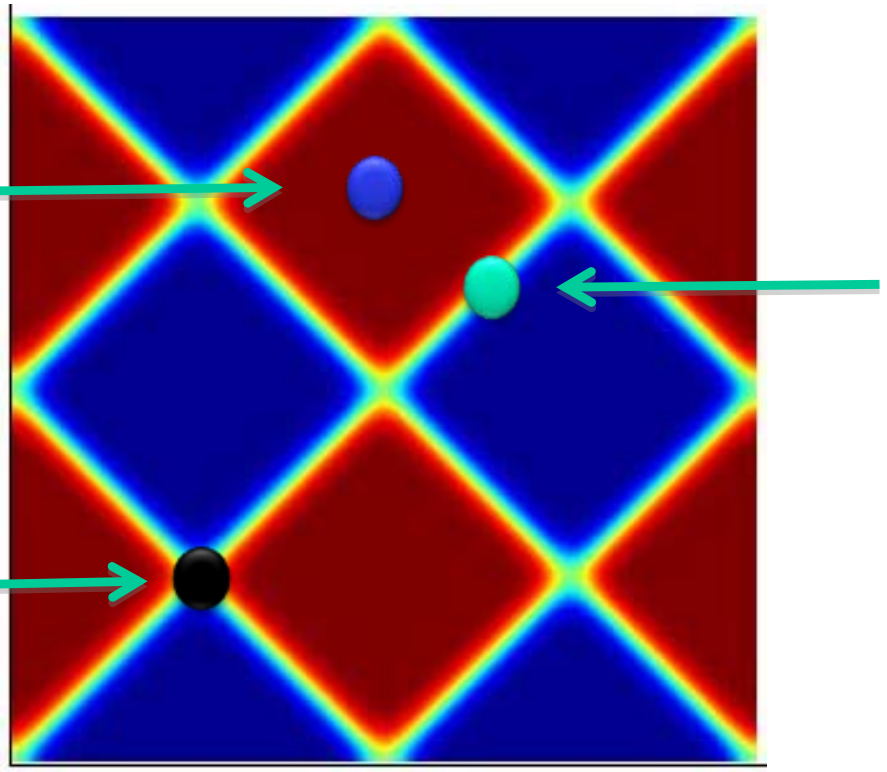

Second type of critical nuclei

Third type of critical nuclei

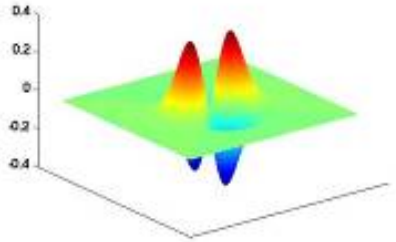

III.Example: One conserved + one nonconserved

Applications are now considered for Ni-Al and Al-Cu alloys involving both conserved and nonconserved fields

Example (in progress): θ' precipitates in Al-Cu alloy, with data from L.Q. Chen/T.W. Heo

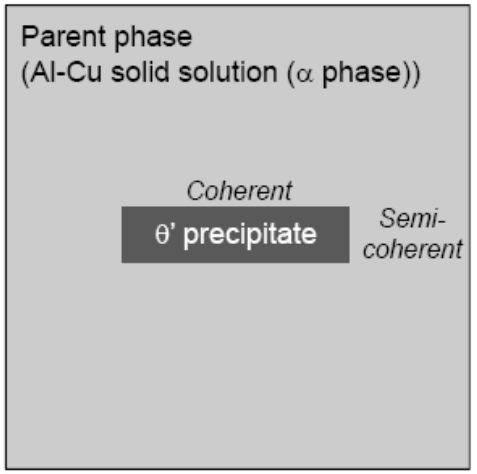

θ' precipitate

$\eta = 1$ (or -1)

$c = c_{eq,\theta'}$

Parent phase (Al solid solution)

→ $\eta = 0$

$c = c_{eq,matrix}$

III.Example: integrating dynamic phase field simulations with diffuse-interface nuclei computation

Solving dynamic Allen Cahn equations, using a classical nulceation event sampling (Simmons 2000), but with nucleation via diffuse interface nuclei computation

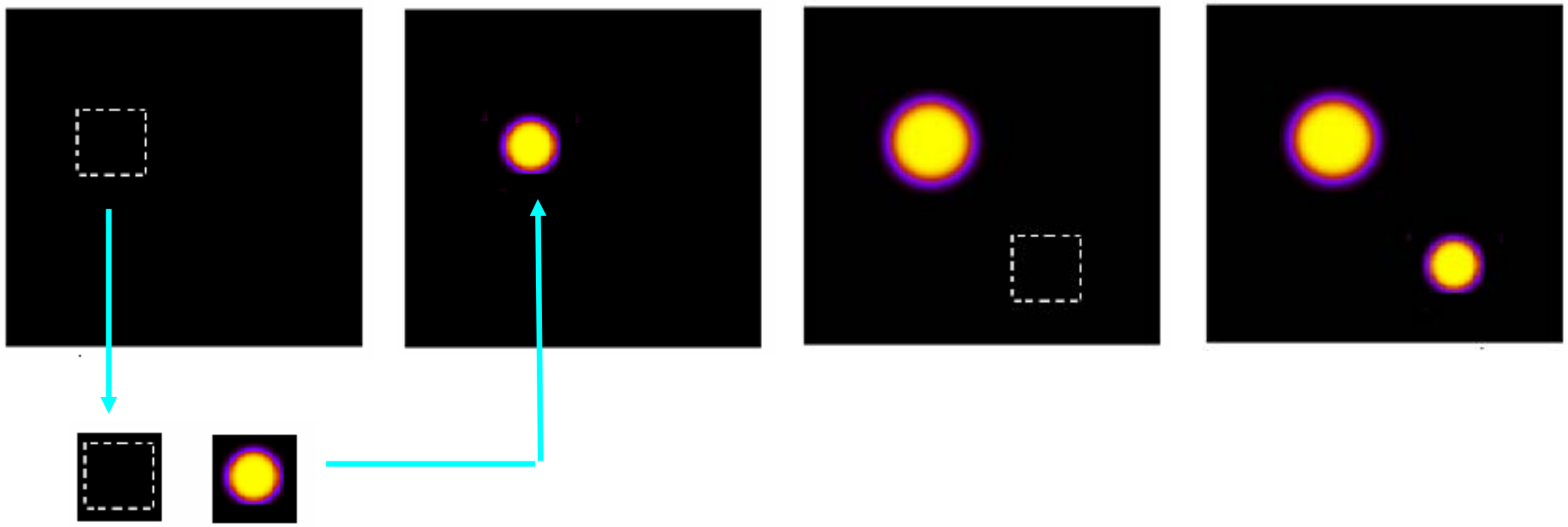

Heo, Zhang, Du, Chen, 2010 Scripta Mat.

III.Example: integrating dynamic phase field simulations with diffuse-interface nuclei computation

The growth of a single nucleus via Allen-Cahn

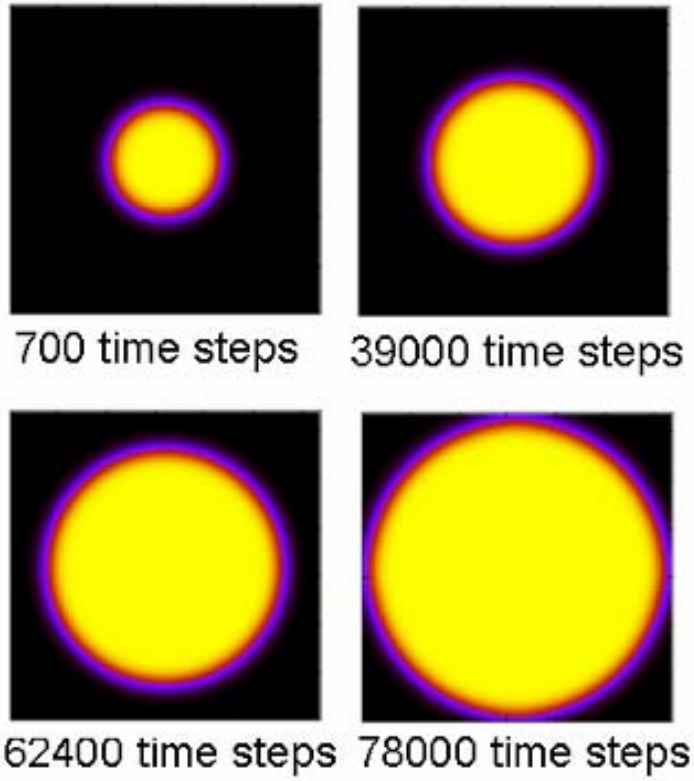

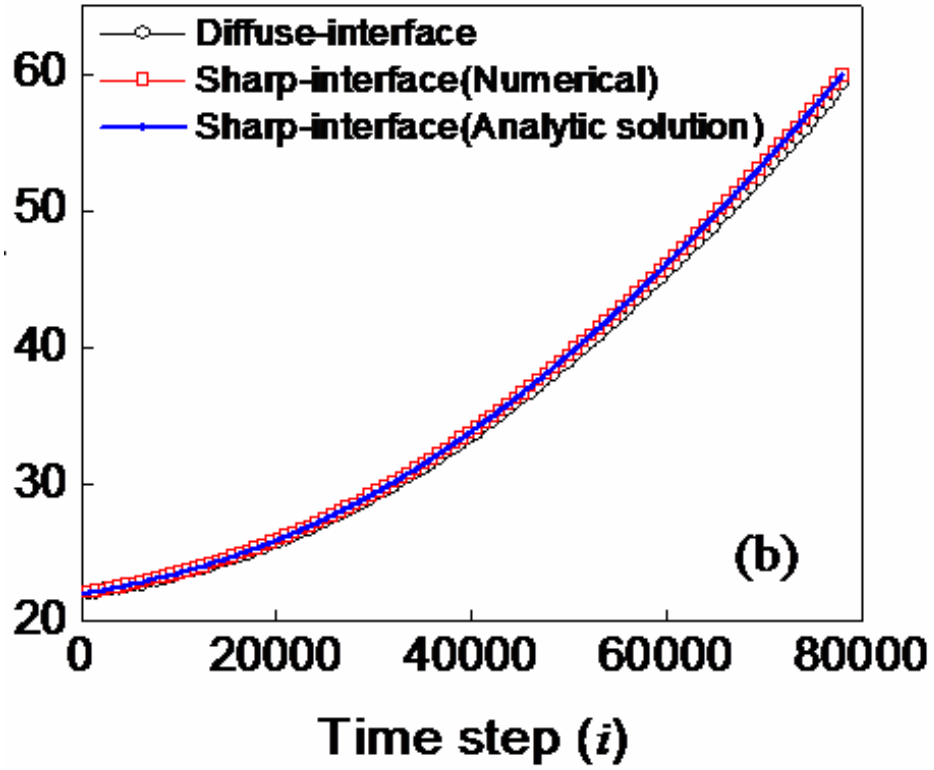

III.Example: phase field simulations with diffuse-interface nuclei and classical nucleation theory

Comparison with the phase transformation kinetics using the classical nucleation and normal growth theory and the Kolmogorov-Johnson-Mehl-Avrami equation

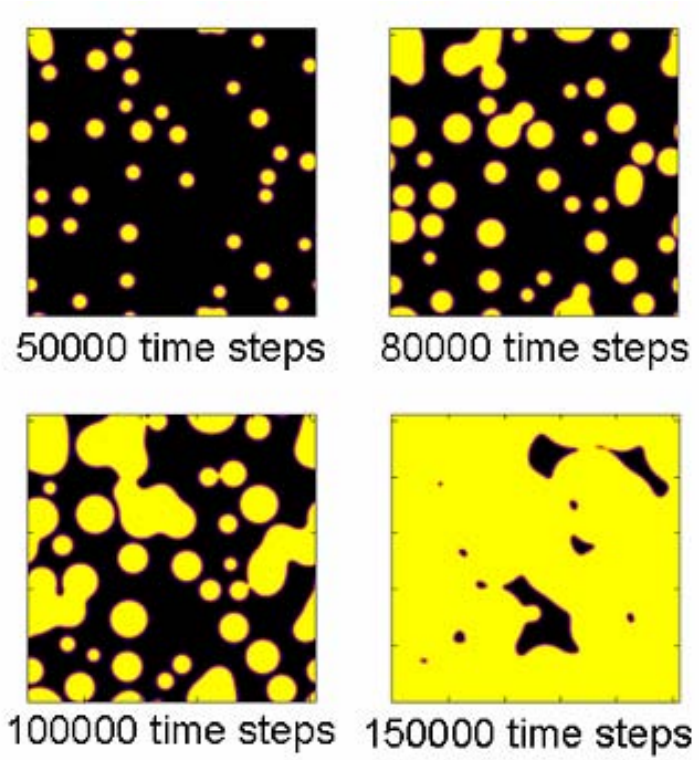

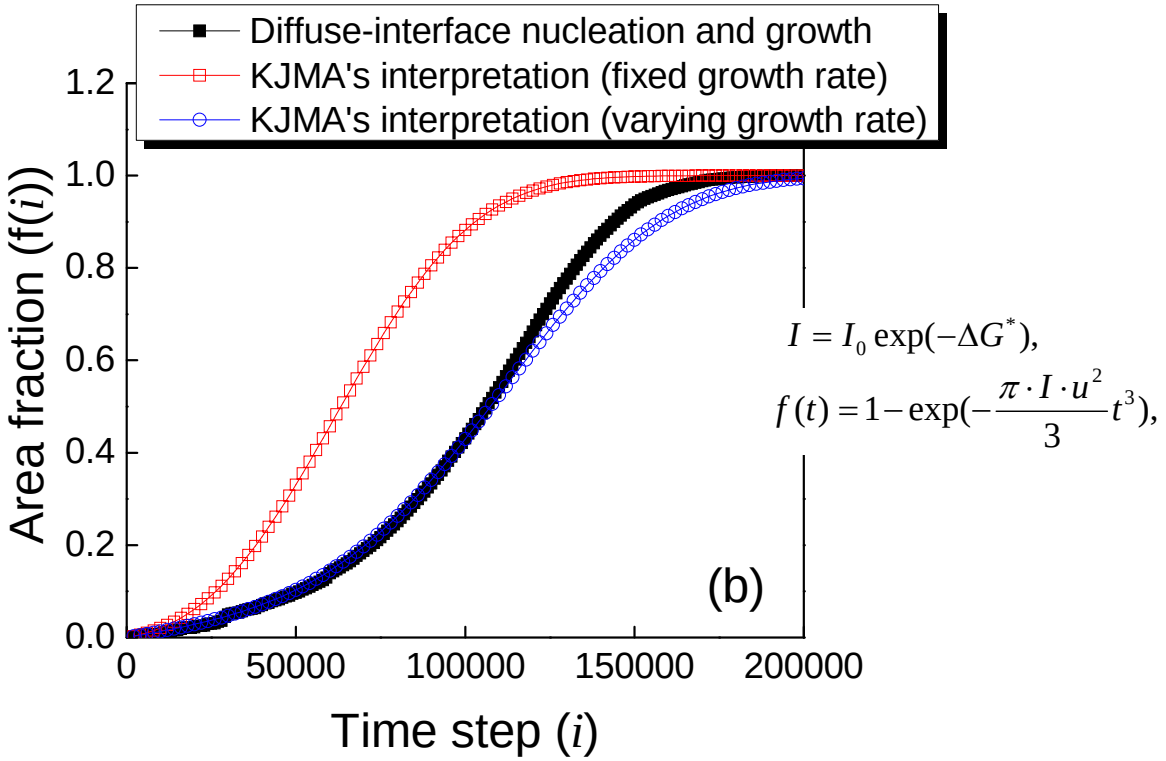

IV. Observation/Conclusion: phase field/diffuse interface

- **Phase field type methods are insensitive to topological changes (advantage/deficiency?**

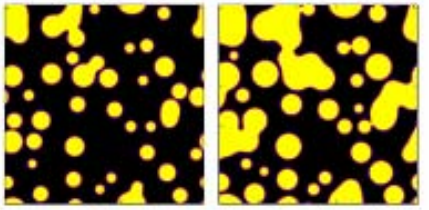

- **How about the detection/control of topology of the implicitly defined surfaces? (or for collecting statistics)**
- **Formulae were developed to detect /control topology change in shape transformation via Euler number**
- **Providing interesting statistics of large scale simulations and connecting geometry with topology: the key is to effectively estimate curvatures in the diffuse interface framework**

Du -Liu-Wang SIAM Appl Math 2005

IV. Observation: Euler-Poincare index in Phase Field

- In 3d:

$$\chi = \frac{1}{4\pi(b-a)} \int_{\Omega_a^b} |\nabla\phi|^{-1} \Lambda(M) d\Omega$$

$$M = c(\nabla^2\phi - (\nabla|\nabla\phi|^2 \cdot \nabla\phi)|\nabla\phi|^{-4}\nabla_i\phi\nabla_j\phi)$$

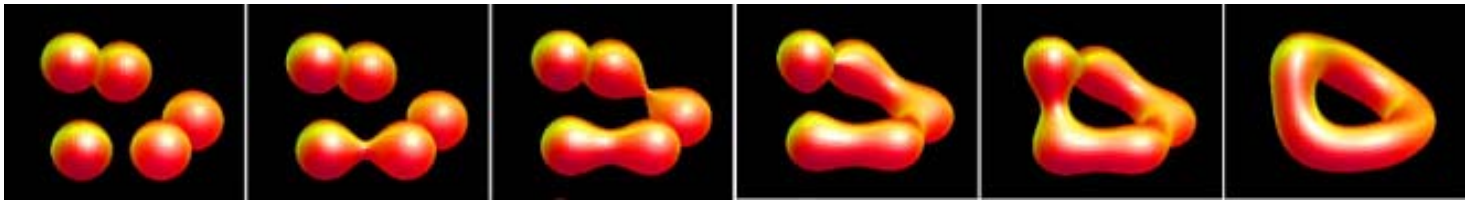

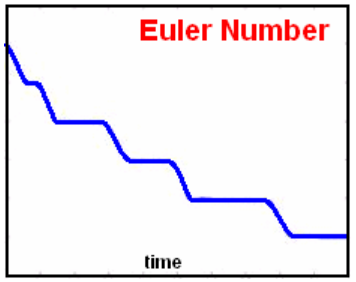

- In 2d:

$$\chi = \frac{1}{2\pi(b-a)} \int_{\Omega_a^b} F d\Omega$$

$$F = c(\nabla^2\phi + (\nabla|\nabla\phi|^2 \cdot \nabla)|\nabla\phi|^{-2}/2$$

Phase-field Based Euler number!

Simplified versions possible
Du–Liu-Ryham-Wang *2007 CMS*

IV Conclusion

Goals: rigorous mathematical description and robust algorithms and codes for nucleation in solid-state transformation.

Progress: methods to compute diffuse-interface critical nuclei; some stand-alone codes for single order parameter already available; demonstration of integration with phase field dynamic simulations.

Collaborators: L. Zhang, L.-Q. Chen, T.W. Heo

Thanks: support from NSF-ITR (2002-2007), NSF-IUCRC CCMD

A coarse grained derivation of the Phase Field equations

A. Finel

Q. Bronchart , Y. Le Bouar,

Laboratoire d'Etudes des Microstructures
ONERA-CNRS, Chatillon

Why Phase Field modeling (1) ?

→ Mesoscopic modeling:

- large scale simulation (μm^3)
- easy to incorporate elastic effects
- extended to dislocation dynamics (plasticity), fracture, voids ...
- polycrystals, grain boundaries...

Microstructures in γ/γ'

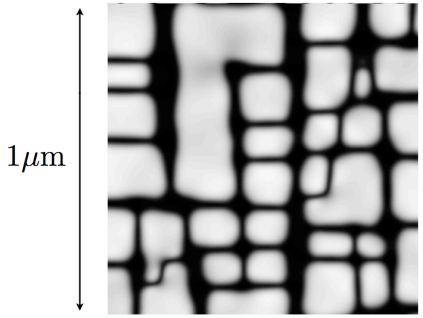

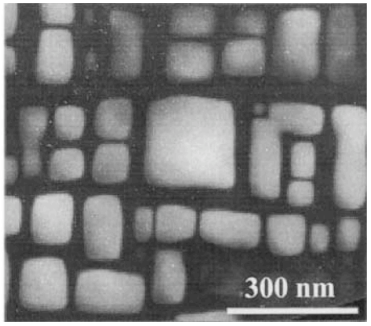

Sequiera et al, Scripta Met. Mat., 30(1994)

Formation and ageing of bimodale microstructures in γ/γ'

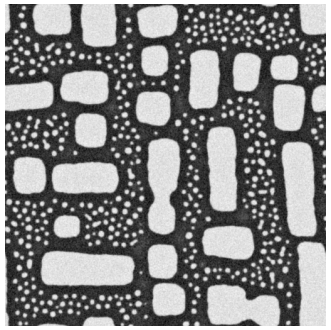

Boussinot et al. ,
Acta Mat (2009)

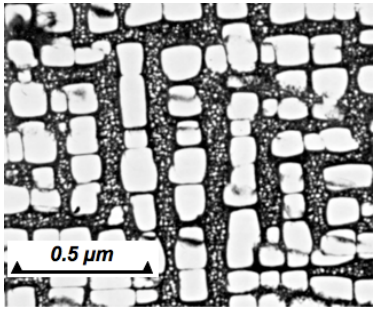

from Chellman et al. (1989)

Directional coarsening under external stress (rafting): phase field + viscoplasticity

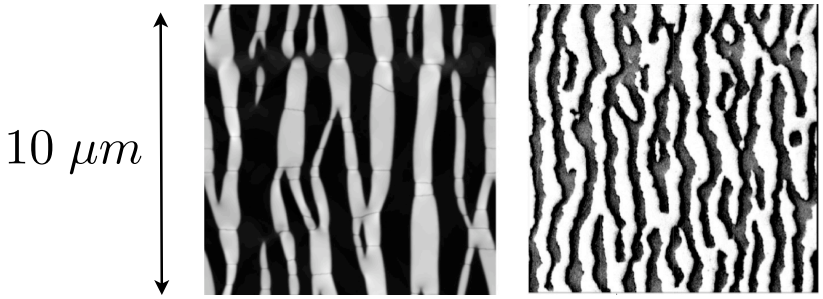

Phase Field + viscoplasticity
Gaubert et al., Phil. Mag. (2010)

Caron et al. (2002)

Why Phase Field modeling (2) ?

→ Mesoscopic modeling:

- large scale simulation (μm^3)
- easy to incorporate elastic effects
- extended to dislocation dynamics (plasticity), fracture, voids ...
- polycrystals, grain boundaries...

Ex : Shape memory alloys: the martensitic transition

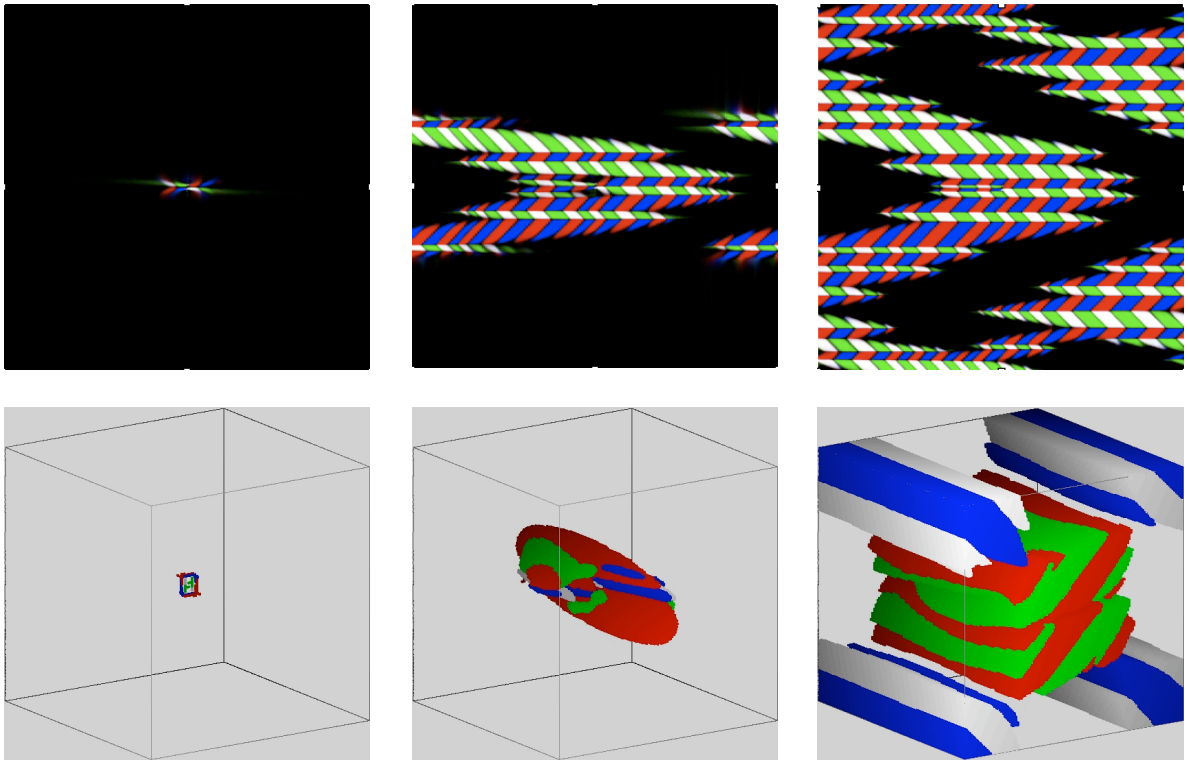

→ Phase Field simulation in Ti-Ni:

- heterogeneous precipitation of R phase along a screw dislocation
- elastic accomodation
- thermoelastic equilibrium

Questions

→ Transitions driven by fluctuations : nucleation

- how well can the Phase Field method reproduce nucleation ?

- how to intruduce fluctuations in a consistent way ?

- what is the meaning of a local free energy density ?

- which fluctuations are already incorporated into this free energy density ?

Q. Bronchart, Y. Le Bouar, and A. Finel, Phys. Rev. Lett., vol.100 (2008) 015702

Introduction (1)

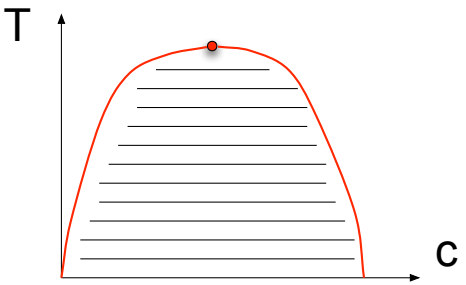

→ basics of the Phase Field method:

- consider a simple miscibility gap:
- "good" order parameter: concentration field: $c(r,t)$

- free energy: (Ginzburg-Landau)

$$F_{tot}(\{c(r,t)\}) = \int d_3r \;\; f_{homo}[c(r,t)] + \frac{\lambda}{2} \; ||\nabla \; c(r,t)||^2$$

- kinetics: (Cahn-Hilliard-Cook)

$$\frac{\partial \, c(r,t)}{\partial \, t} = \nabla M(c) \nabla \; \frac{\delta F_{tot}}{\delta \; c(r,t)} + \eta(r,t)$$

$$\lim_{t \to \infty} P(\{c(r),t\}) = P_{eq}(\{c(r)\}) \sim \exp(-\frac{F_{tot}(\{c(r)\})}{kT})$$

Fluctuation-dissipation theorem

$$< \eta(r,t) \; \eta(r',t') >= -2 \; kT \; \nabla M(c) \nabla \delta(r-r') \; \delta(t-t')$$

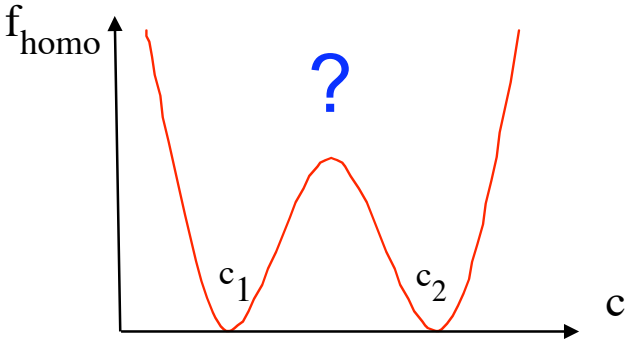

→ $f_{homo}(c) = ? \quad \lambda = ?$

$M(c) = ?$

Introduction (2)

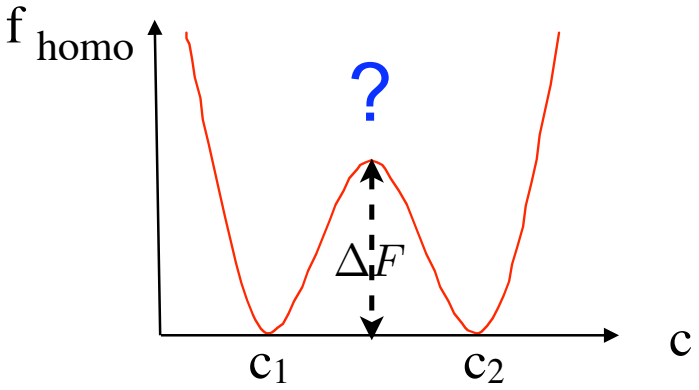

$\rightarrow \quad f_{homo}(c) = ? \quad \lambda = ?$

$\rightarrow$ phenomenological expansion (Landau free energy) and theory with no fluctuations :

fitted on phase diagram, interface energy :

$$f_{homo}(c) = \Delta F \, \frac{(c-c_1)^2 \, (c-c_2)^2}{[\,(c_2-c_1)\,/\,2\,]^4}$$

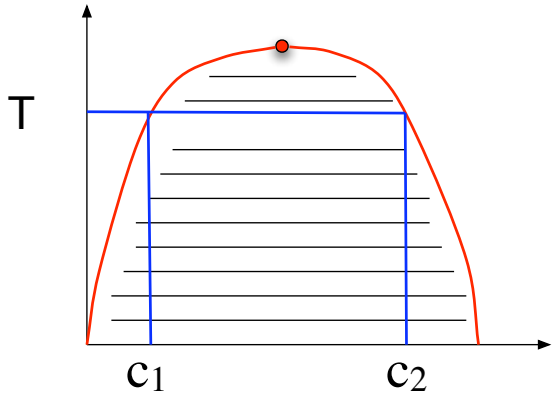

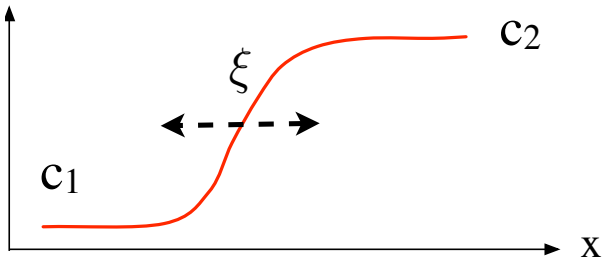

$$\text{interface energy :} \quad \sigma = \frac{2\sqrt{2}}{3} \, (c_2 - c_1) \, \sqrt{\lambda \, \Delta F}$$

$$\text{interface thickness :} \quad \xi = \frac{\sqrt{2}}{4} \, (c_2 - c_1) \, \sqrt{\frac{\lambda}{\Delta F}}$$

but $\xi_{exp} \simeq 1nm$!!

$\lambda \quad \nearrow \quad \Delta F \quad \searrow$

$\sigma \quad = \quad$ cte

Introduction (3)

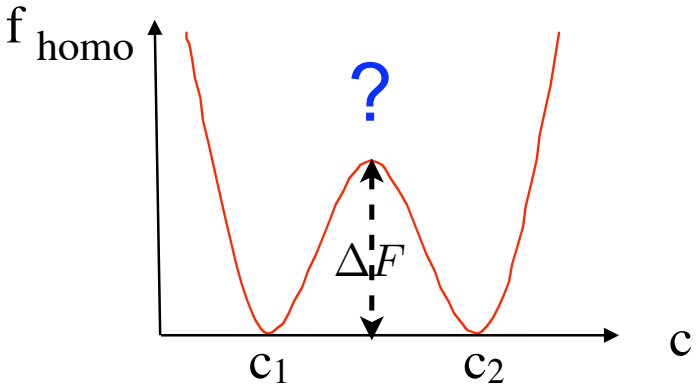

→ $f_{homo}(c) = ?$ $\lambda = ?$

→ time scale for nucleation:
interplay noise / nucleation barrier
(depends on metastable free energies)

→ phenomenological expansion (Landau free energy) → status of metastable regime ?

→ use of thermo. database in the Calphad spirit (ThermoCalc) → status of metastable regime ?

→ atomistic model (Ising type) + Mean Field + small *q* expansion → status of the fluctuations ?

→ Questions:

1. Status of the metastable free energies ?

2. Critical analysis of the Phase Field equations: mobilities, noise ?

→ need a coherent formulation that "solves" simultaneously 1 and 2

Phase Field method: how to get the basic equation (1)

→ Starting point: Microscopic master equation

- atomic configuration: $\mathcal{C} = (....p_i.....p_j.....)$ $\qquad p_i = 0$ or 1 if A or B on site i

- kinetic model: direct exchange between A and B on 1st neighbor sites

$$\frac{\partial P(\mathcal{C})}{\partial t} = -\sum_{i,j}^{*} W(\mathcal{C} \rightarrow \mathcal{C}^{ij}) P(\mathcal{C}) + \sum_{i,j}^{*} W(\mathcal{C}^{ij} \rightarrow) P(\mathcal{C}^{ij})$$

- transition probability:

local mechanism:

direct exchange through saddle point (G. Martin, Phys. Rev. B, 1990)

$$W(\mathcal{C} \rightarrow \mathcal{C}^{ij}) = \theta \ \exp -\beta(2E_{saddle} - h_i^A(\mathcal{C}) - h_j^B(\mathcal{C}))\ \delta(p_i)\delta(p_j - 1)$$

$h_i^A(\mathcal{C})$: interaction energy between site i and the other sites if i is occupied by atom A

if pair interactions only: $h_i^A(\mathcal{C}) = \sum_j V_{ij}^{AA} p_j + V_{ij}^{AB}(1 - p_j)$

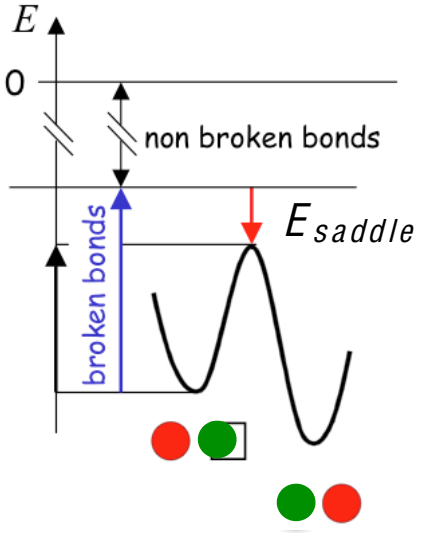

Phase Field method: how to get the basic equation (2)

→ Mesoscopic scale :

cell of volume d ^{3}

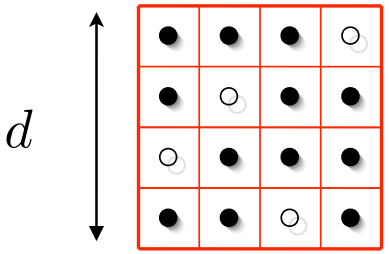

$$N_d = \frac{d^3}{a^3}$$

mesoscopic ← $c_n = \frac{1}{N_d} \sum_{i \in n} p_i$ → microscopic

- average out microscopic fluctuations of wavelength < d
- keep mesoscopic fluctuations of wavelength > d

$$\widetilde{\mathcal{C}} = (...c_n....c_m...) \qquad P(\widetilde{\mathcal{C}}) = \mathrm{Tr}_{\mathcal{C}/\widetilde{\mathcal{C}}}\, P(\mathcal{C})$$

→ Mesoscopic master equation:

$$\frac{\partial P(\widetilde{\mathcal{C}})}{\partial t} = \mathrm{Tr}_{\mathcal{C}/\widetilde{\mathcal{C}}}\, \frac{\partial P(\mathcal{C})}{\partial t}$$

Phase Field method: how to get the basic equation (3)

→ need simplification:

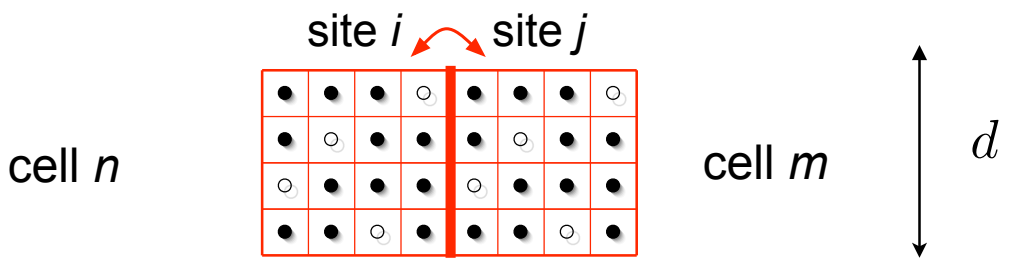

1) "quasi-static" approximation: Markov process (time scale available $\tau \gtrsim d^2/D$)

microscopic fast ← $\mathcal{C}$ in quasi-equilibrium with $\widetilde{\mathcal{C}}$ → mesoscopic slow

$$P(\mathcal{C}) \simeq P(\widetilde{\mathcal{C}}) \frac{\exp -\beta H(\mathcal{C})}{\mathrm{Tr}_{\mathcal{C}/\widetilde{\mathcal{C}}} \exp -\beta H(\mathcal{C})}$$

mesoscopic averaging:

$$< X(\mathcal{C}) >_{\mathcal{C}/\widetilde{\mathcal{C}}} = \frac{\mathrm{Tr}_{\mathcal{C}/\widetilde{\mathcal{C}}} \; X(\mathcal{C}) \; \exp -\beta H(\mathcal{C})}{\mathrm{Tr}_{\mathcal{C}/\widetilde{\mathcal{C}}} \exp -\beta H(\mathcal{C})}$$

2) small fluctuations between cells: *if cells large enough*

$$< ...f(i \in n)...f(j \in m... >_{\mathcal{C}/\widetilde{\mathcal{C}}} \sim < ...f(i \in n)... >_{\mathcal{C}/\widetilde{\mathcal{C}}} < ...f(j \in m... >_{\mathcal{C}/\widetilde{\mathcal{C}}}$$

Phase Field method: how to get the basic equation (4)

→ Master equation becomes:

$$\frac{\partial P(\tilde{\mathcal{C}})}{\partial t} = -N_d \, \frac{a}{d} \; \theta \; e^{-2\beta E_{col}} \sum_{n,m}^{*} e^{\frac{\beta}{2}(g_n^A(\tilde{\mathcal{C}})+g_n^B(\tilde{\mathcal{C}})+g_m^A(\tilde{\mathcal{C}})+g_m^B(\tilde{\mathcal{C}}))} \; e^{\frac{\beta}{2}\frac{a}{d}(\mu_m(\tilde{\mathcal{C}})-\mu_n(\tilde{\mathcal{C}}))} \; P(\tilde{\mathcal{C}}) + \; (\text{gain term})$$

mobilities — driving force

chemical potentials of *A* and *B* in cell *n* :

$$g_n^A(\widetilde{\mathcal{C}}) = \frac{1}{N_d} \sum_{i \in n} kT \; \ln < \; \delta(p_i(\mathcal{C})) \; \exp \beta h_i^A(\mathcal{C}) >_{\mathcal{C}/\widetilde{\mathcal{C}}}$$

$$g_n^B(\widetilde{\mathcal{C}}) = \frac{1}{N_d} \sum_{i \in n} kT \; \ln < \; \delta(p_j(\mathcal{C}) - 1) \; \exp \beta h_j^B(\mathcal{C}) >_{\mathcal{C}/\widetilde{\mathcal{C}}}$$

"alloy chemical potential" :

$$\mu_n(\widetilde{\mathcal{C}}) = g_n^B(\widetilde{\mathcal{C}}) - g_n^A(\widetilde{\mathcal{C}})$$

→ look for the equivalent dynamical equation on C (evolution of a single system)

- Kramers-Moyal expansion to 2nd order in a/d to get a Fokker-Planck equation

- Itô calculus to get the equivalent Langevin equation

Phase Field method: how to get the basic equation (5)

→ Results:

$$\frac{\partial c_n}{\partial t} = \frac{a^2}{d^2}\,\frac{\theta}{kT}\,\sum_m^{(n)} l_{nm}(\widetilde{\mathcal{C}})\,(\mu_m(\widetilde{\mathcal{C}}) - \mu_n(\widetilde{\mathcal{C}})) \;+\; \xi_n(t)$$

- mobilities:

$$l_{mn}(\widetilde{\mathcal{C}}) = \exp(-2\beta E_{saddle})\exp\frac{\beta}{2}(g_n^A(\widetilde{\mathcal{C}}) + g_n^B(\widetilde{\mathcal{C}}) + g_m^A(\widetilde{\mathcal{C}}) + g_m^B(\widetilde{\mathcal{C}}))$$

- alloy chemical potential:

$$\mu_n(\widetilde{\mathcal{C}}) = g_n^B(\widetilde{\mathcal{C}}) - g_n^A(\widetilde{\mathcal{C}})$$

- gaussian noise:

$$\begin{aligned}
< \xi_n(t) > &= 0 \\
< \xi_n(t)\,\xi_m(t') > &= 2\theta\,\frac{a^2}{d^2}\,\frac{1}{N}\,g_{nm}(\widetilde{\mathcal{C}})\,\delta(t-t') \\
g_{nn}(\widetilde{\mathcal{C}}) &= \sum_m^{(n)} l_{nm}(\widetilde{\mathcal{C}}) \\
g_{nm}(\widetilde{\mathcal{C}}) &= -\;\; l_{nm}(\widetilde{\mathcal{C}}) \quad \text{if } n \text{ and } m \text{ are } 1^{st} \text{ neighbors}
\end{aligned}$$

→ Cahn-Hilliard type equation, but with :

- multiplicative Langevin noise
- cell-size dependant quantities: mobility, chem. potentials, amplitude of noise term

Phase Field method: how to get the basic equation (5)

→ Results:

$$\frac{\partial c_n}{\partial t} = \frac{a^2}{d^2}\,\frac{\theta}{kT}\,\sum_m^{(n)} l_{nm}(\widetilde{\mathcal{C}})\,(\mu_m(\widetilde{\mathcal{C}}) - \mu_n(\widetilde{\mathcal{C}})) \;+\; \xi_n(t)$$

- mobilities:

$$l_{mn}(\widetilde{\mathcal{C}}) = \exp(-2\beta E_{saddle})\exp\frac{\beta}{2}(g_n^A(\widetilde{\mathcal{C}}) + g_n^B(\widetilde{\mathcal{C}}) + g_m^A(\widetilde{\mathcal{C}}) + g_m^B(\widetilde{\mathcal{C}}))$$

- alloy chemical potential:

$$\mu_n(\widetilde{\mathcal{C}}) = g_n^B(\widetilde{\mathcal{C}}) - g_n^A(\widetilde{\mathcal{C}})$$

- gaussian noise:

$$\begin{aligned}
< \xi_n(t) > &= 0 \\
< \xi_n(t)\,\xi_m(t') > &= 2\theta\,\frac{a^2}{d^2}\,\frac{1}{N}\,g_{nm}(\widetilde{\mathcal{C}})\,\delta(t-t') \\
g_{nn}(\widetilde{\mathcal{C}}) &= \sum_m^{(n)} l_{nm}(\widetilde{\mathcal{C}}) \\
g_{nm}(\widetilde{\mathcal{C}}) &= -\;\; l_{nm}(\widetilde{\mathcal{C}}) \quad \text{if } n \text{ and } m \text{ are } 1^{st} \text{ neighbors}
\end{aligned}$$

→ Cahn-Hilliard type equation, but with :

- multiplicative Langevin noise
- cell-size dependant quantities: mobility, chem. potentials, amplitude of noise term

How to compute the chemical potentials ? (1)

(*i.e. Ginzburg-Landau free energy*)

→ Chemical potentials $g_n^A(\widetilde{\mathcal{C}})$ and $g_n^B(\widetilde{\mathcal{C}})$ are function of all the cell concentrations c_n :

$$g_n^A(\widetilde{\mathcal{C}}) = g_{homo}^A(c_n) + H^A(c_n)||\hat{\nabla} c_n||^2 + K^A(c_n)\hat{\nabla}^2 c_n + ...$$

→ $g_n^A(\widetilde{\mathcal{C}})$ and $g_n^B(\widetilde{\mathcal{C}})$ enter into the mobilities and in the alloy chemical potential :

$$l_{mn}(\widetilde{\mathcal{C}}) = \exp(-2\beta E_{saddle}) \exp \frac{\beta}{2}(g_n^A(\widetilde{\mathcal{C}}) + g_n^B(\widetilde{\mathcal{C}}) + g_m^A(\widetilde{\mathcal{C}}) + g_m^B(\widetilde{\mathcal{C}}))$$

$$\mu_n(\widetilde{\mathcal{C}}) = g_n^B(\widetilde{\mathcal{C}}) - g_n^A(\widetilde{\mathcal{C}})$$

→ If cells large enough : inhomo. components can be neglected in mobilities, but are crucial in the alloy chem. potential

- for the mobilities:

$$g_n^A(\widetilde{\mathcal{C}}) \simeq g_{homo}^A(c_n)$$

- for the alloys chemical potential:

$$\mu_n(\widetilde{\mathcal{C}}) \simeq g_{homo}^B(c_n) - g_{homo}^A(c_n) + H(c_n)||\hat{\nabla} c_n||^2 + K(c_n)\hat{\nabla}^2 c_n +$$

How to compute the chemical potentials ? (2)

(*i.e. Ginzburg-Landau free energy*)

→ Numerical procedure for homogeneous chemical potentials $g_n^A(\widetilde{\mathcal{C}})$ and $g_n^B(\widetilde{\mathcal{C}})$

Widom-like insertion method by Monte Carlo on a single cell

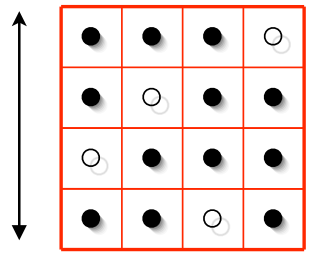

→ Numerical procedure for the inhomogeneous component of $\mu_n(\widetilde{\mathcal{C}})$

we expect $$F_{tot}(\widetilde{\mathcal{C}}) = N_d \sum_n \{f^d_{homo}(c_n) + \frac{1}{2}\lambda^d(c_n)||\hat{\nabla}c_n||^2\}$$ with $$\mu_n(\widetilde{\mathcal{C}}) = \frac{1}{N_d}\frac{dF_{tot}(\widetilde{\mathcal{C}})}{dc_n},$$

thus : $$\mu^d_n(\widetilde{\mathcal{C}}) = \mu^d_{homo}(c_n) - \lambda^d(c_n)\hat{\nabla}^2 c_n + \frac{1}{2}\frac{\partial\lambda^d(c_n)}{\partial c_n}||\hat{\nabla}c_n||^2$$

→ Procedure for $\lambda^d(c_n)$: gaussian fluctuations between cells

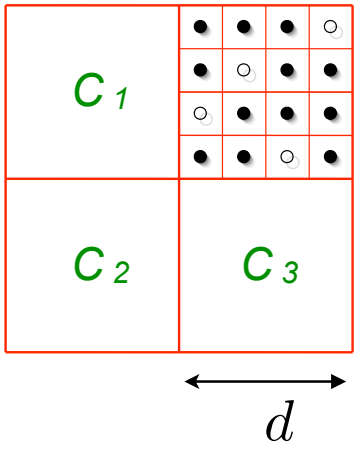

How to compute the chemical potentials ? (3)

ex : simple cubic lattice

→ Simple cubic lattice, 1st neighbor interactions J1

$$H = \frac{1}{2} \sum_{n,m} \sigma_n \, \sigma_m \qquad \sigma_n = +/-1 \qquad T_c \sim 4.51 J_1$$

→ chemical potential : homogeneous part $\mu^d_{homo}(c)$ by Monte Carlo on a single cell + fit

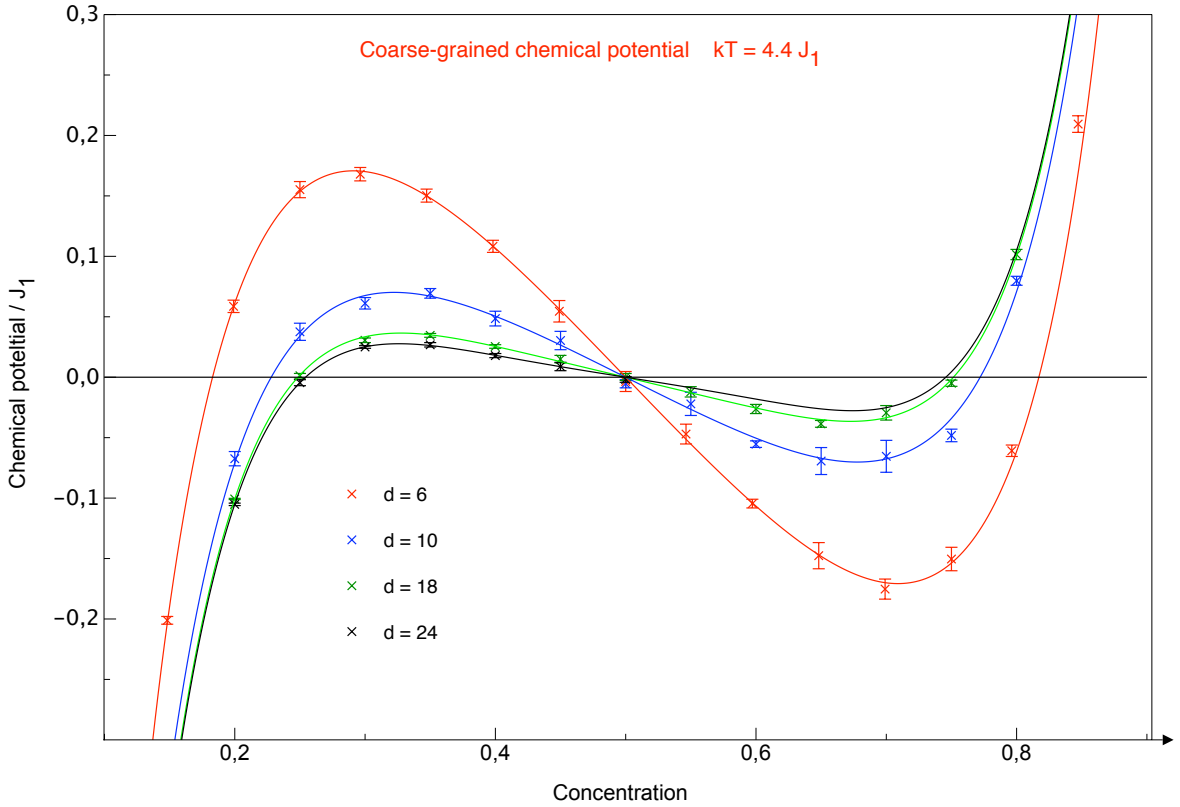

$$\mu_d(c) = 2pJ_1(2c-1) + Ac(1-c)(c-0.5)\{1 + B(c-0.5)^2\} \; + kT \; \ln \frac{c}{1-c}$$

Free energies as a function of the coarse graining size

ex : simple cubic lattice

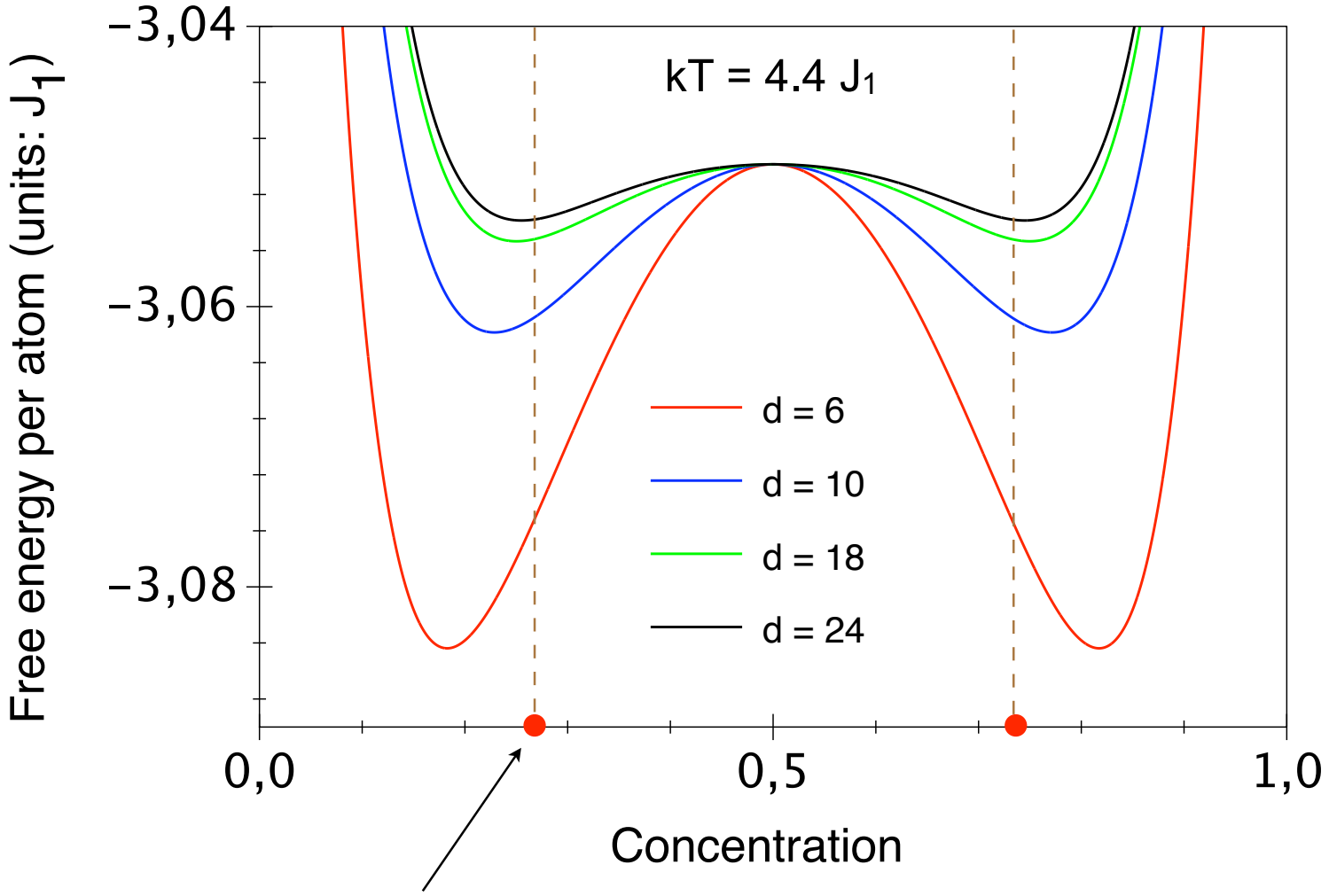

c_0 = 0.273...

phase diagram for infinite system

Free energies as a function of the coarse graining size

ex : simple cubic lattice

→ by-product: spinodal as a function of the coarse graining size....

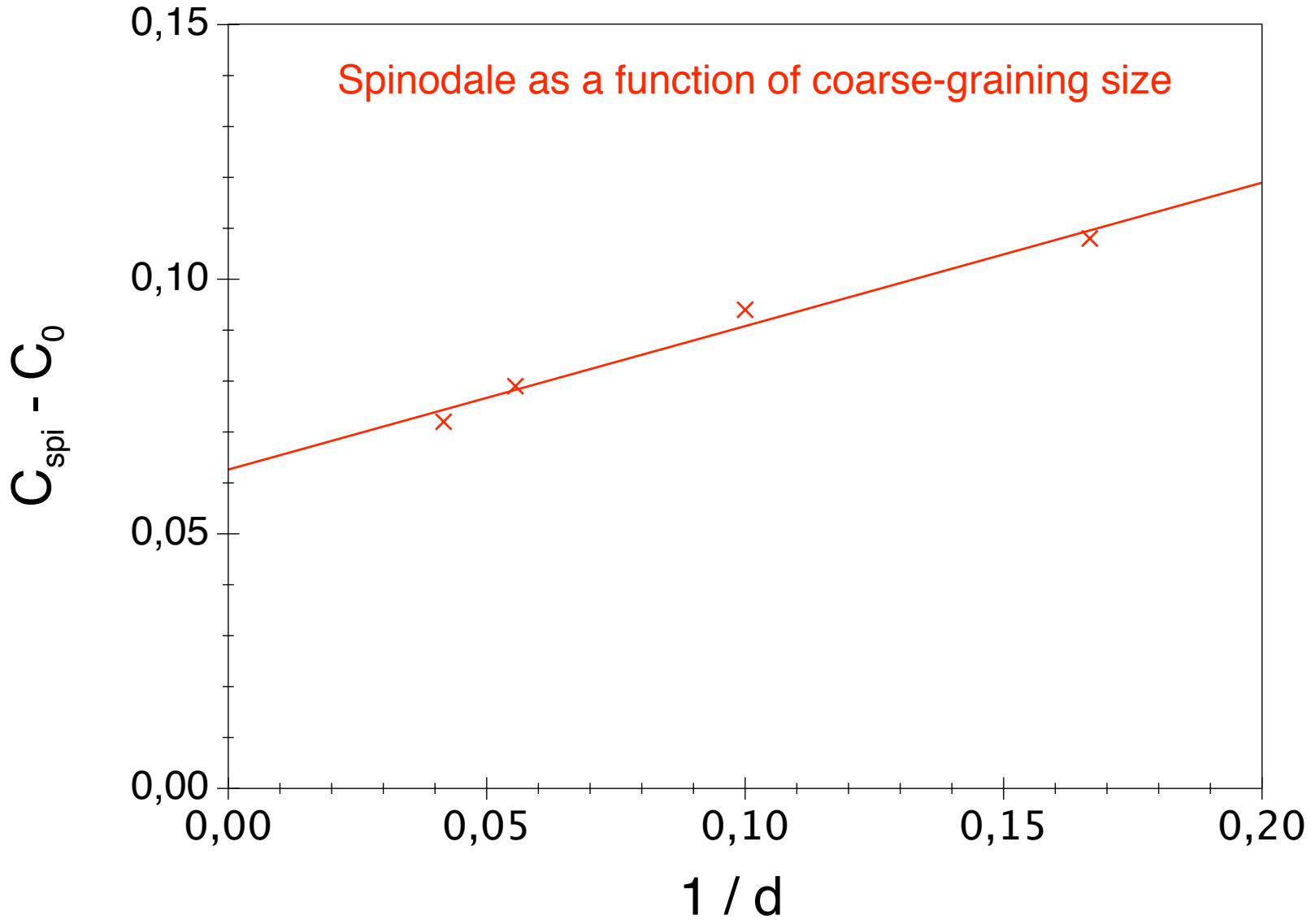

How to compute the stiffness coefficient ?

ex: simple cubic lattice

→ Next: stiffness coefficient $\lambda^d(c_n)$

$$\mu_n^d(\widetilde{\mathcal{C}}) = \mu_{homo}^d(c_n) - \lambda^d(c_n)\hat{\nabla}^2 c_n + \frac{1}{2}\frac{\partial \lambda^d(c_n)}{\partial c_n}||\hat{\nabla} c_n||^2$$

→ $\lambda^d(c_n)$ governs (in part) fluctuations between cells

→ Monte Carlo analysis of gaussian fluctuations between cells:

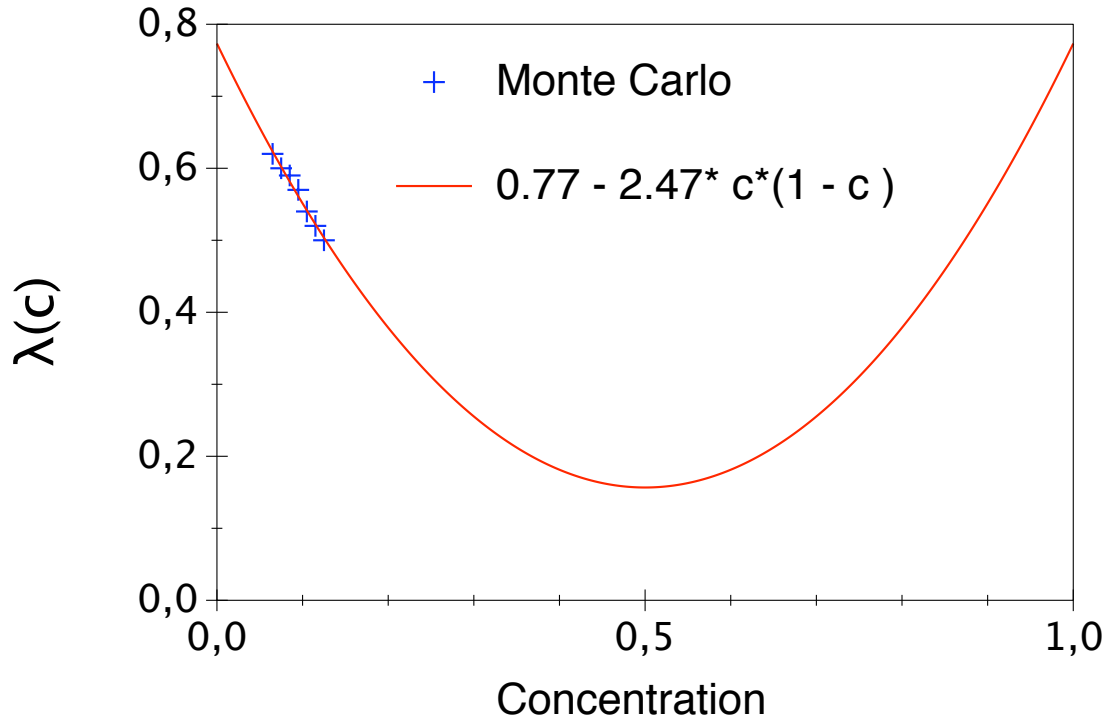

$$\lambda^d(\bar{c}) = A + B\ \bar{c}(1-\bar{c})$$

Precipitation: from nucleation and growth to coalescence (1)

→ coarse-grained free energy (chemical potential) from Monte Carlo (d = 8) and kT = 4 J1:

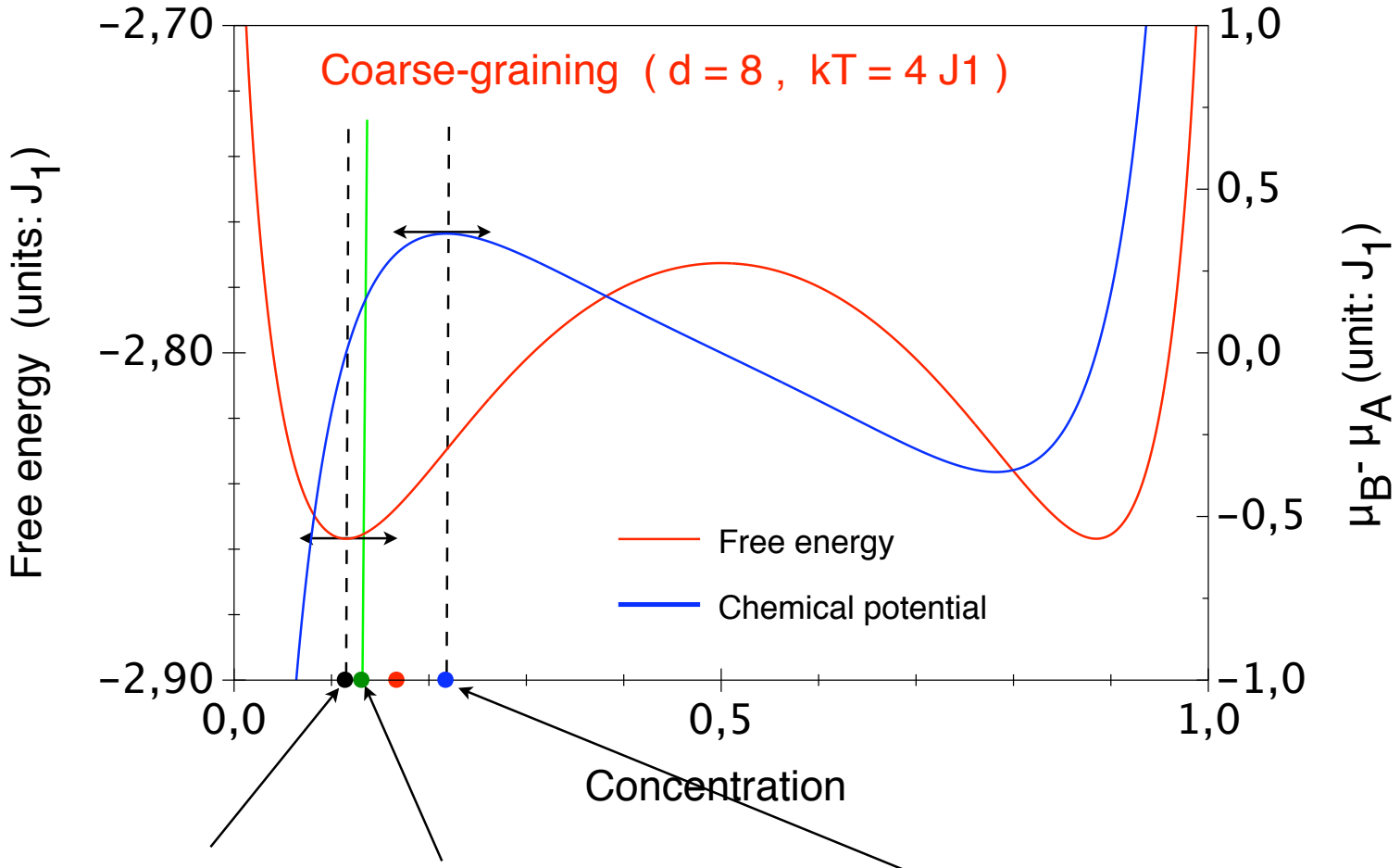

coarse-grained free energy minimum: c_1 = 0.115...

Solubility limit: c_0 = 0.125...
$c_0 > c_1$ because of fluctuations..... !!!!!

Spinodale: c_{spi} = 0.218....

● → precipitation for c = 0.17 ($c_0 < c < c_s$): nucleation and growth mechanism....

Precipitation: from nucleation and growth to coalescence (2)

→ Simulation box 64 x 64 x 64 kT = 4 J1:

Precipitation: from nucleation and growth to coalescence (3)

→ Simulation box 64 x 64 x 64 kT = 4 J1:

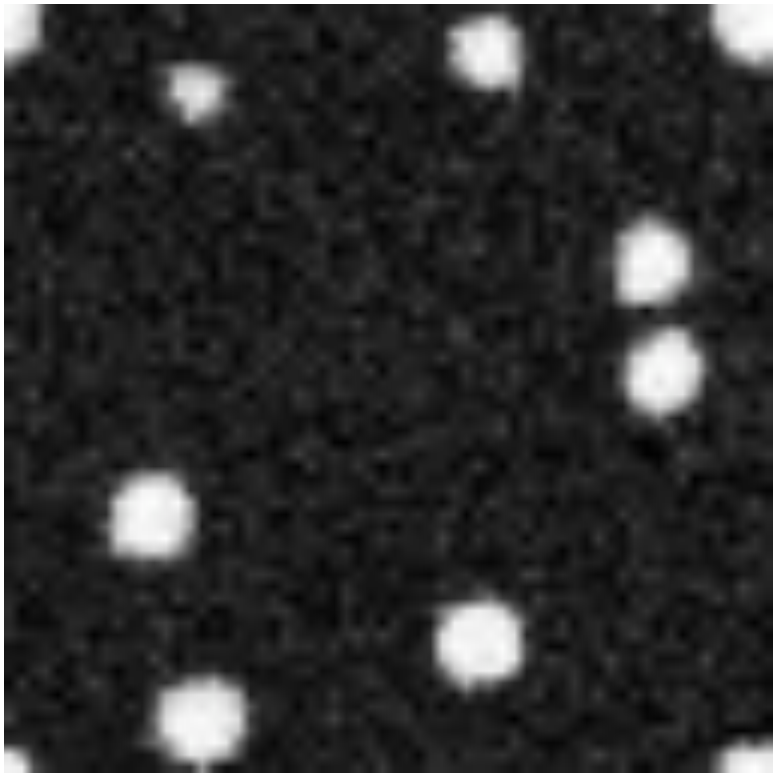

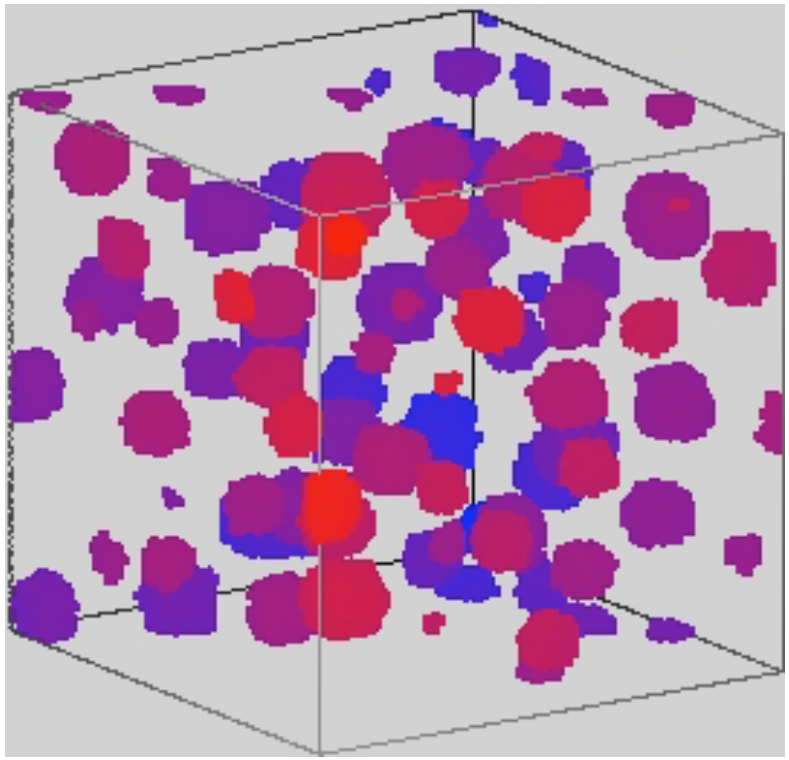

Precipitation: from nucleation and growth to coalescence (4)

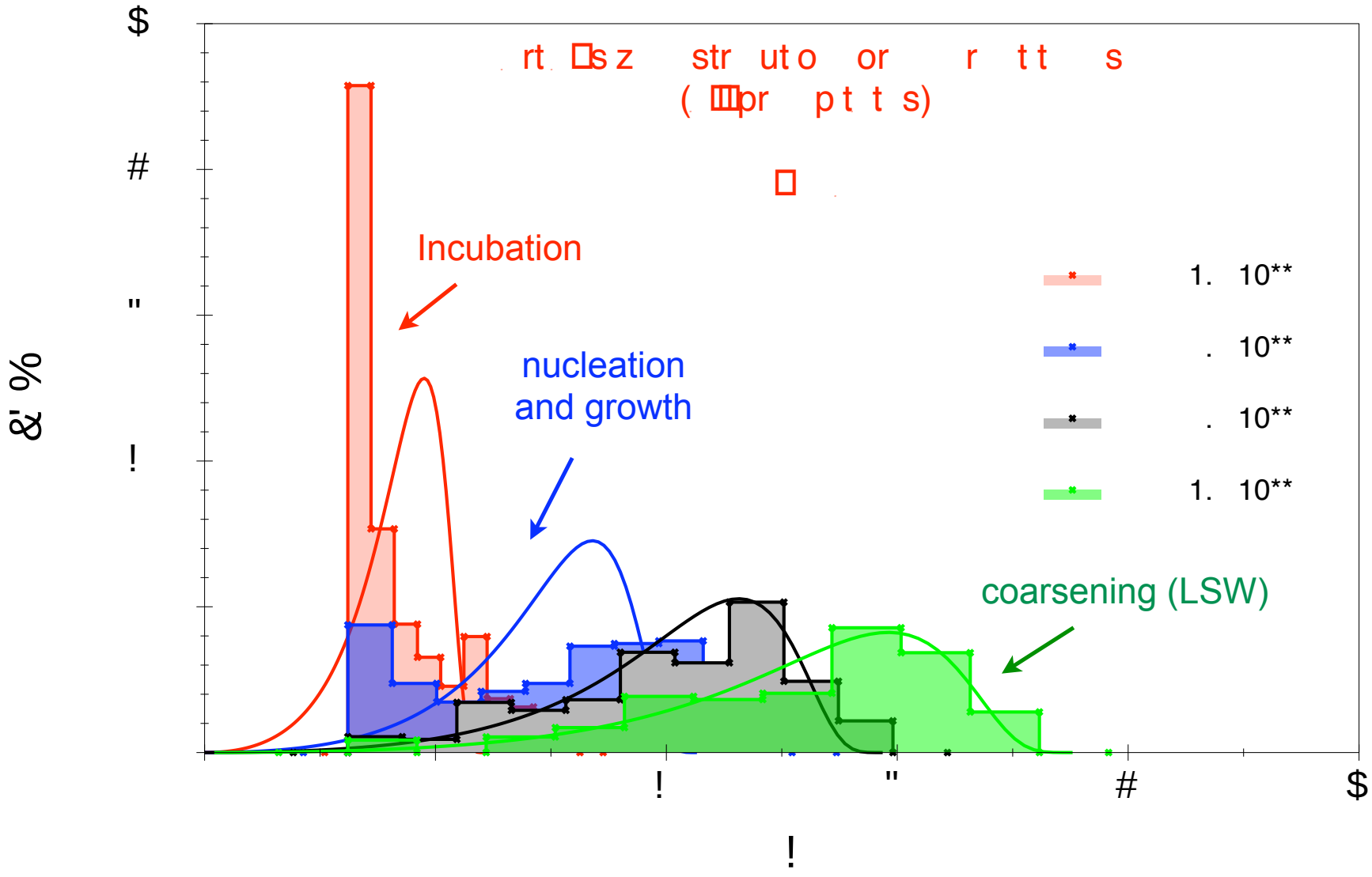

→ Critical radius : $R_c \sim 1\ d$

Precipitation: from nucleation and growth to coalescence (5)

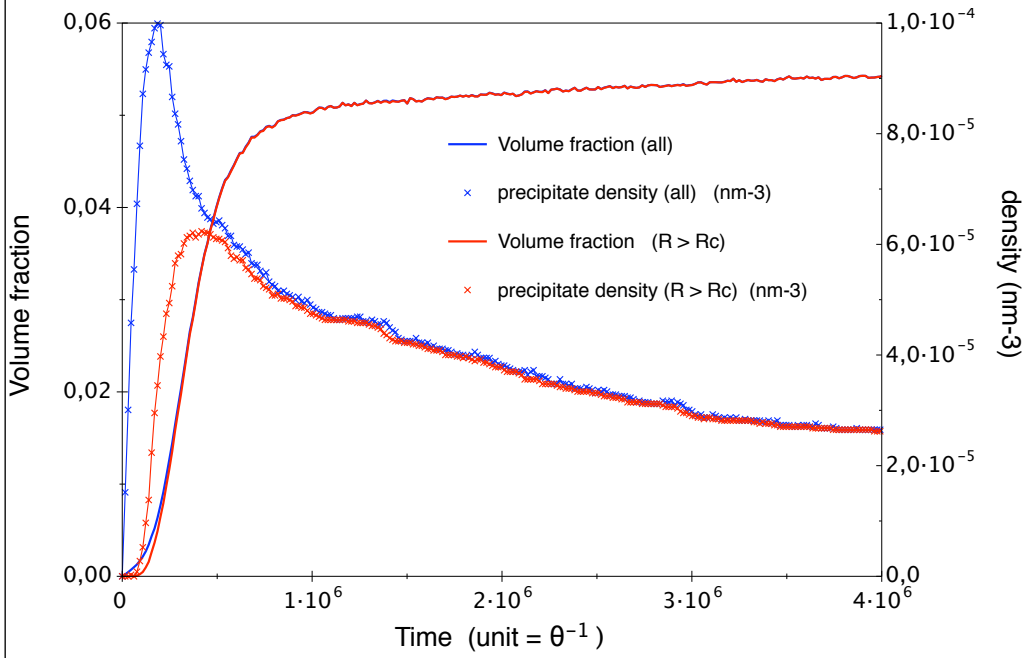

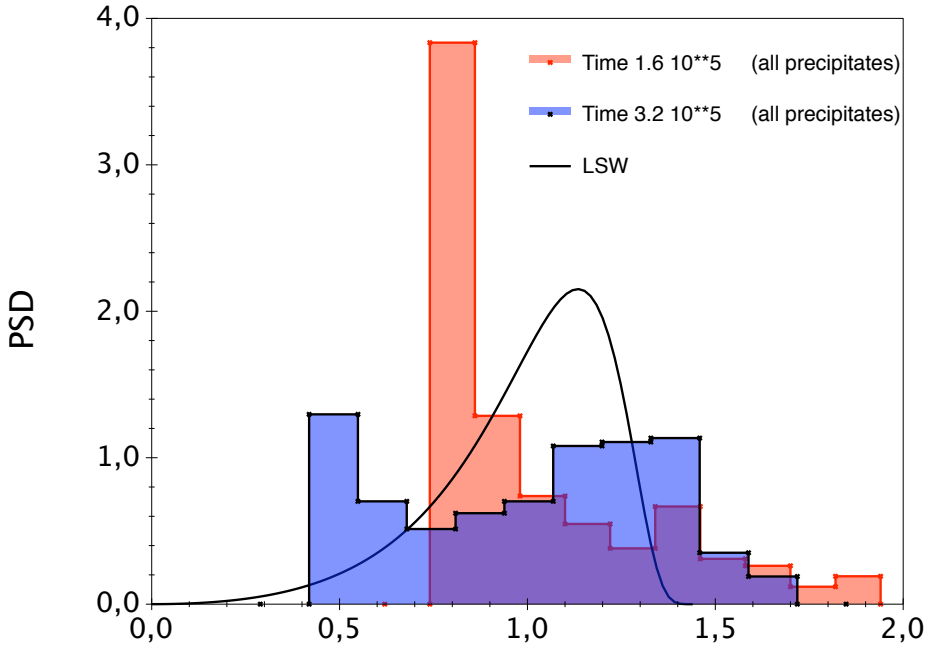

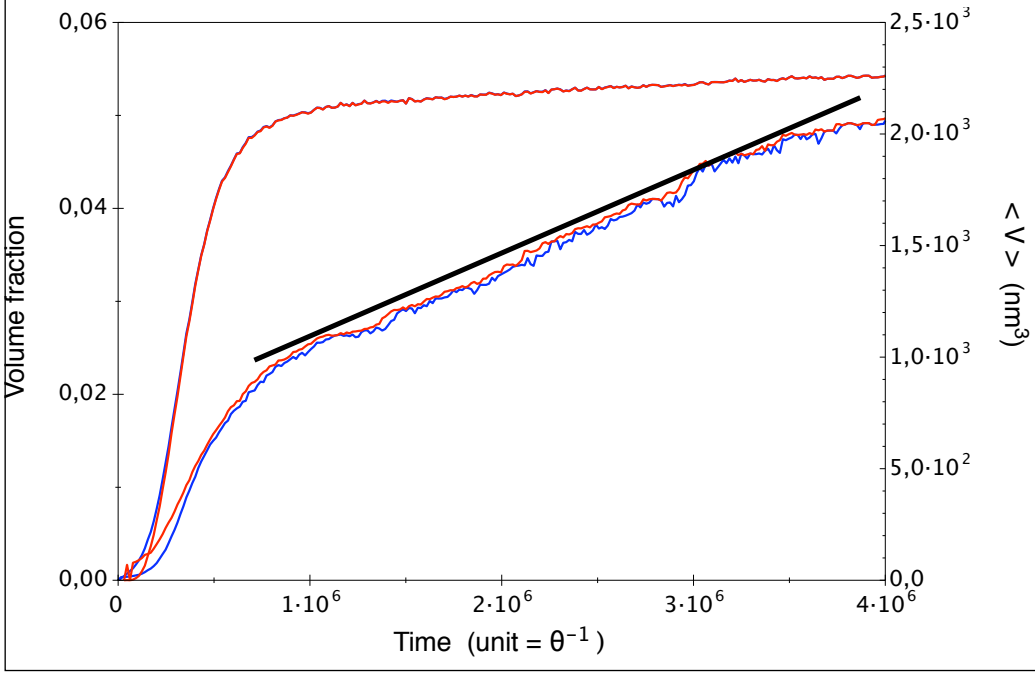

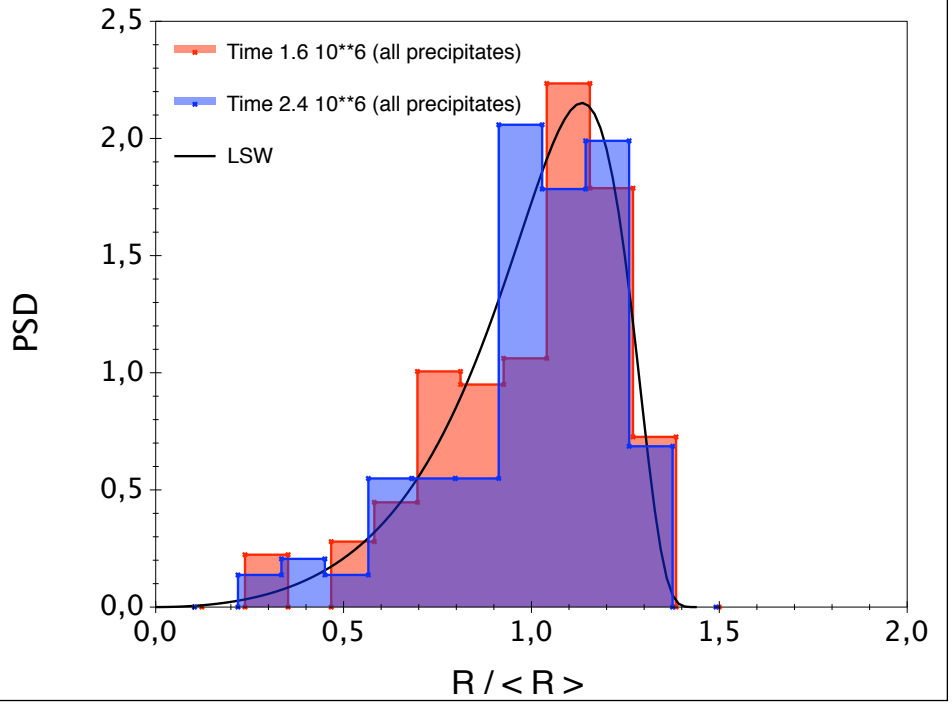

On the influence of the coarse-graining size

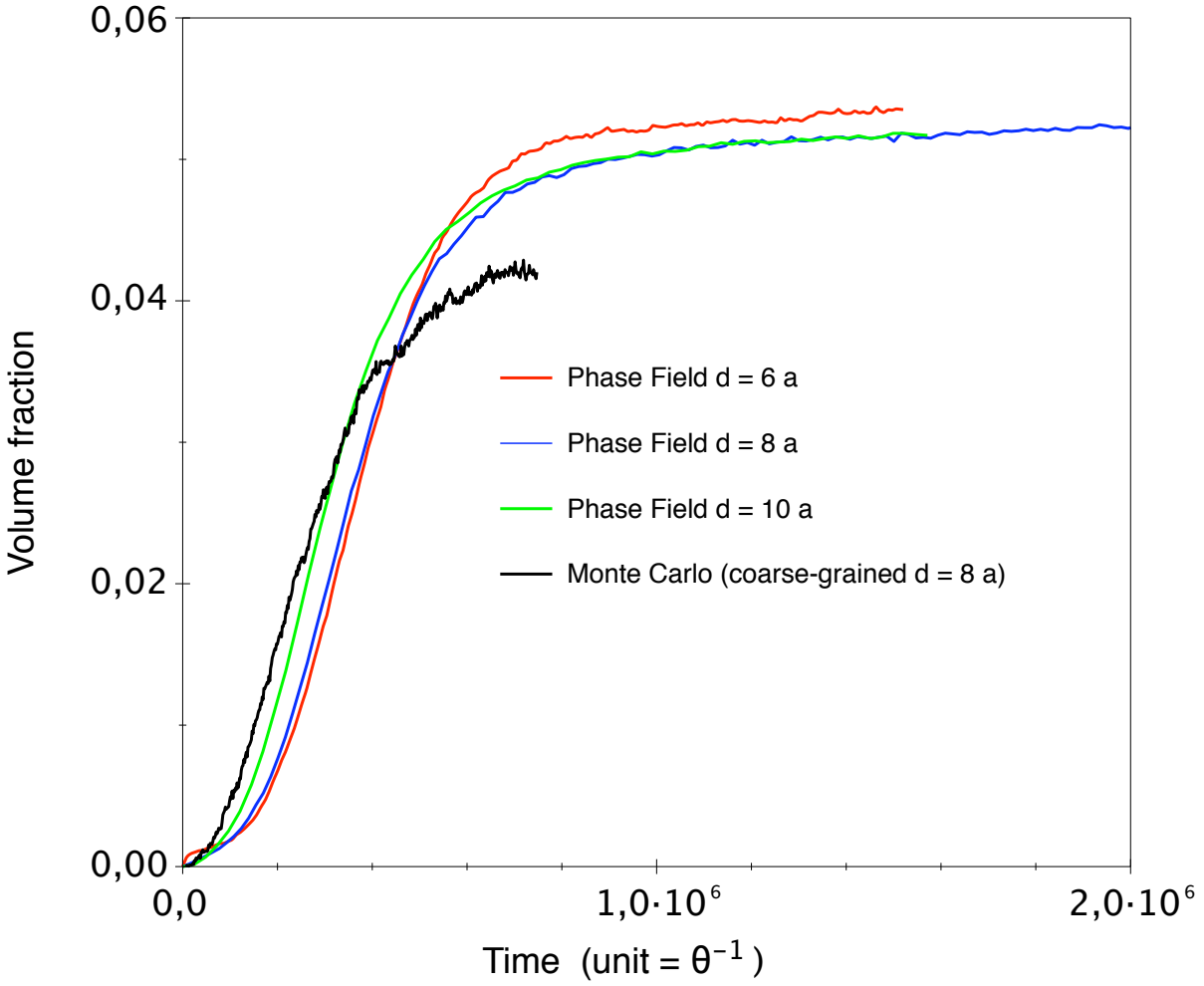

Comparison with classical nucleation theory

→ Incubation time as a function of sursaturation $(c - c_0)$

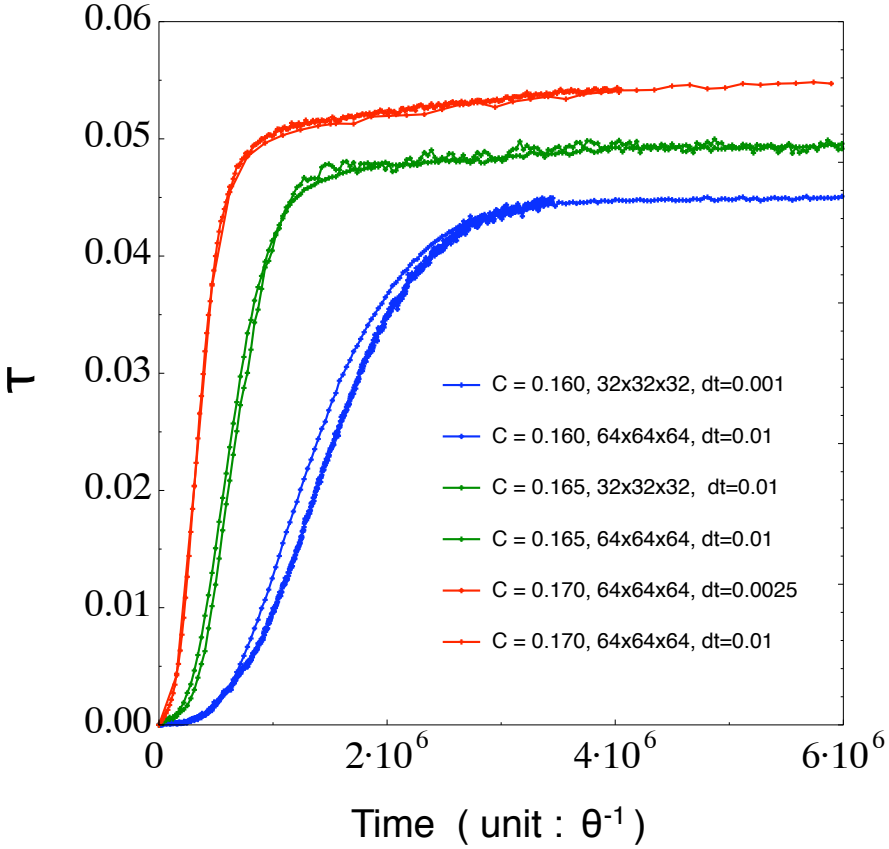

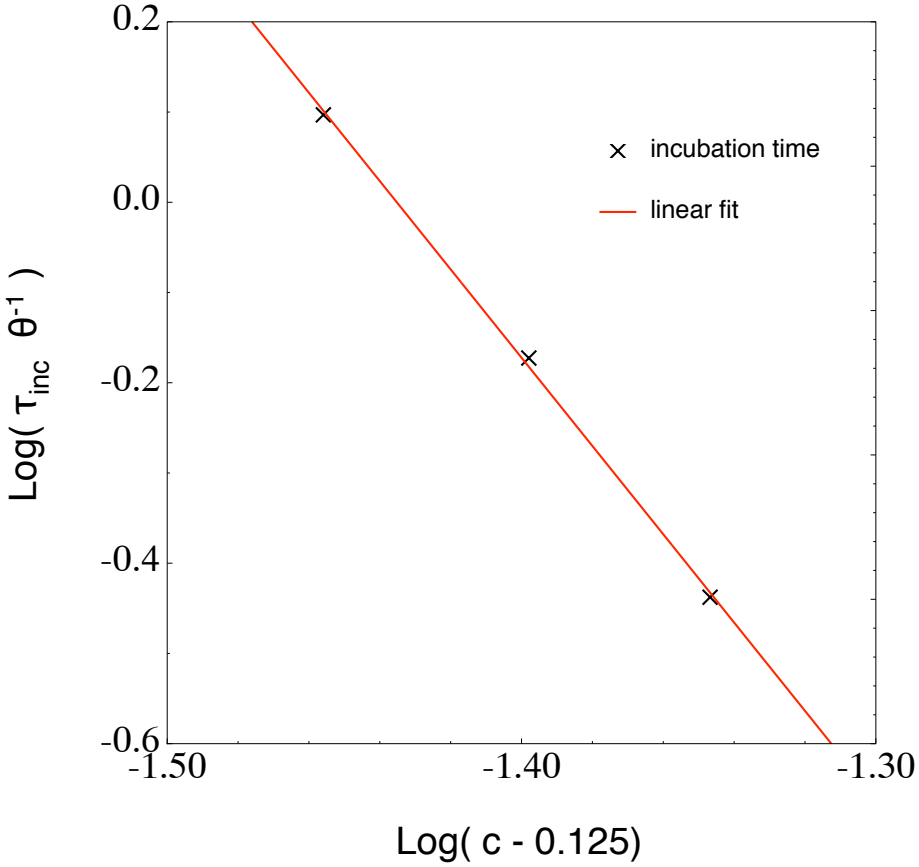

$$\tau \sim (c - c_0)^{-\alpha} \qquad \alpha \simeq 4.8 \pm 0.1 \qquad CNT : \alpha = 4$$

Conclusion

→ “exact” procedure:

- the Phase Field as a coarse-graining procedure
- a stochastic equation with a “simple” noise term (fluctuation theorem)
- Mobility M(c) and noise correlations depend on coarse-graining size and on local concentration
- “stiffness” constant $\lambda^d(c)$ depend on coarse-graining size and on local concentration
- no arbitrary parameters !!!
- reproduces equilibrium fluctuations as well as precipitation
- no need for an extra nucleation flux

→ needed if:

- nucleation and growth mechanism (activated processes)
- if complete time scale needed

Cool New Stuff with Experiments

A. Genç, S. Rajagopalan, [#]G. Thompson, [@]R. Banerjee,*
[**]J. Ringnalda, [$$]D. McComb, [##]C. Dwyer
and Hamish L Fraser

Center for the Accelerated Maturation of Materials
Department of Materials Science and Engineering
The Ohio State University
Columbus, OH

**Now at Intel Inc., Hillsboro, OR*
[#]Now at University of Alabama (Tuscaloosa)
[@]Now at University of North Texas
[**]Now at FEI Company
[$$]Imperial College, London
[##]Monash University, Clayton, Vic, Australia

Jay's Fun Workshop 2010
Ka'anapali, Maui

Thanks to Jay and other organizers
and research sponsors

THE OHIO STATE UNIVERSITY

CAMM

Integrated Computational Materials Science & Engineering

Integrated Computational Materials Science and Engineering

- *The art and practice of predicting materials' behavior and properties*
- *A discipline changing activity*
  - *e.g., 2009 Gordon Research Conference on Physical Metallurgy (topic: ICSME)*
    - *From 65 attendees at the last Phys. Met. Conference (GRC threatened to terminate conference) to an attendance maximized (160) for the current one*
    - *60 graduate students*
    - *2nd highest funding of all GRCs (only medical GRC higher!!)*

Demonstrates tremendous level of interest and points the way forward

Cool New Stuff with Experiments

- *Topics:*
- *Integration modeling with experiments*
- *Useful recent characterization techniques*
- *Limitations with experimental techniques*
  - *sample preparation*
  - *compositional analysis*
- *What are we (OSU/CAMM) doing?*

Aim: To develop research tools for the accelerated insertion of new materials and optimization of existing ones.

Method: This is done by developing and integrating computational modeling and simulation with advanced materials characterization

- *Integration between modelers and materials characterization folks*
- *Multiscale modeling – integration over length and time scales*
- *Integration from ab-initio to industrial practice*

Modeling of Phase Transformations (side-plates in α/β-Ti alloys)

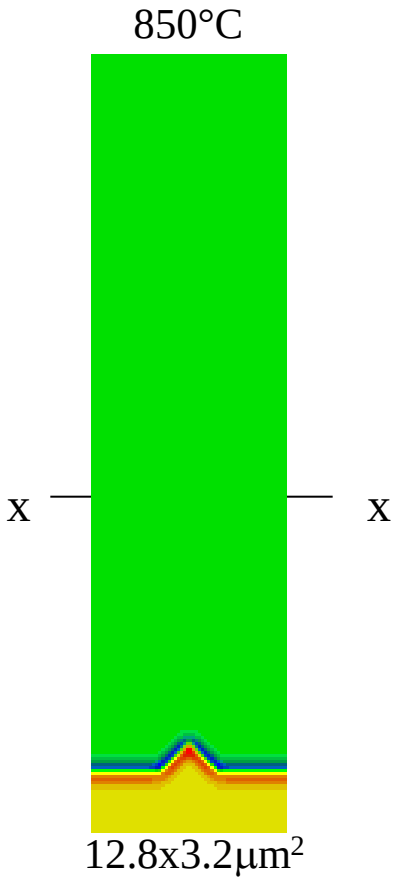

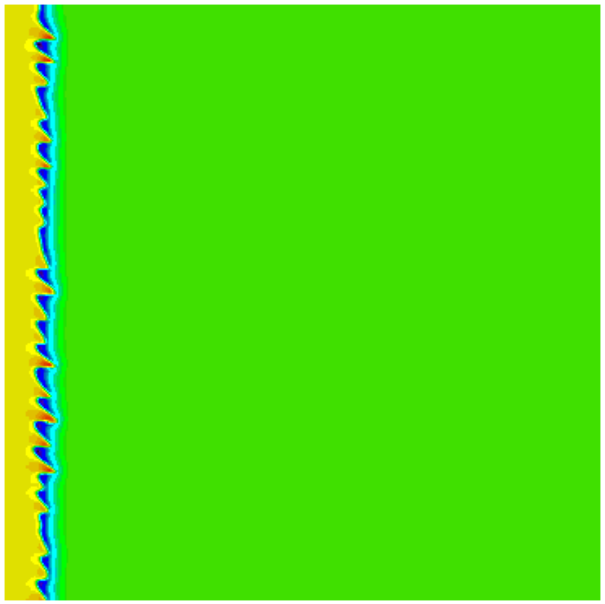

Length of plate

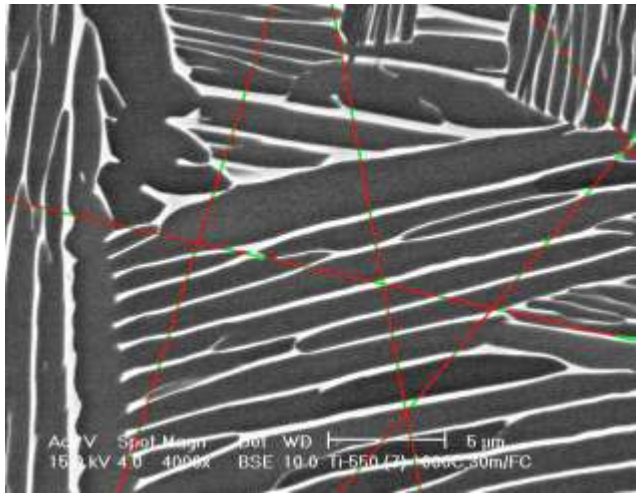

Width of plate

x-x

Linear lengthening and parabolic thickening kinetics, and tip radius and tip velocity from simulations all match analytical solutions.

α/β-Ti alloys – Side-plates vs. Basketweave Structure

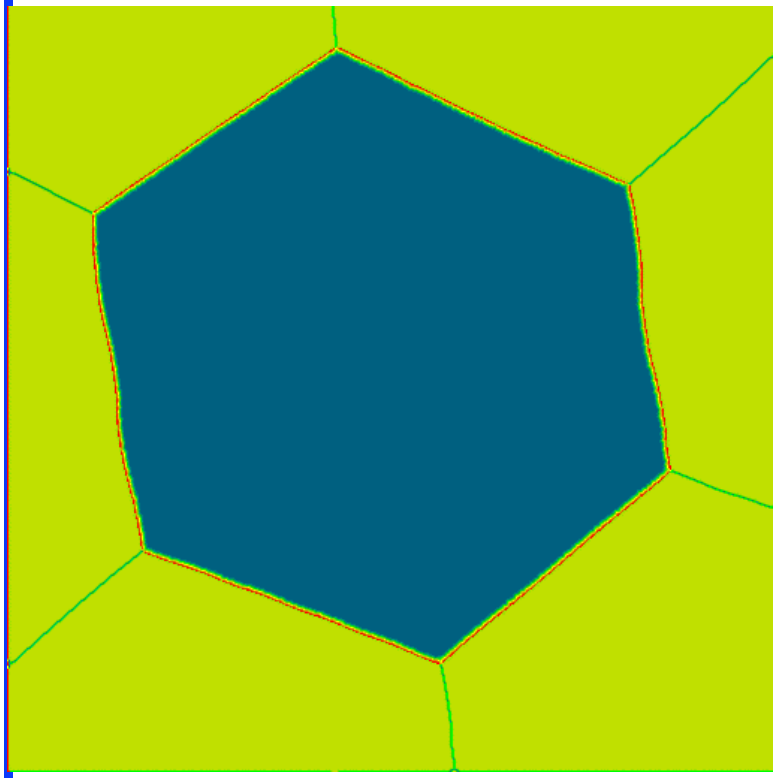

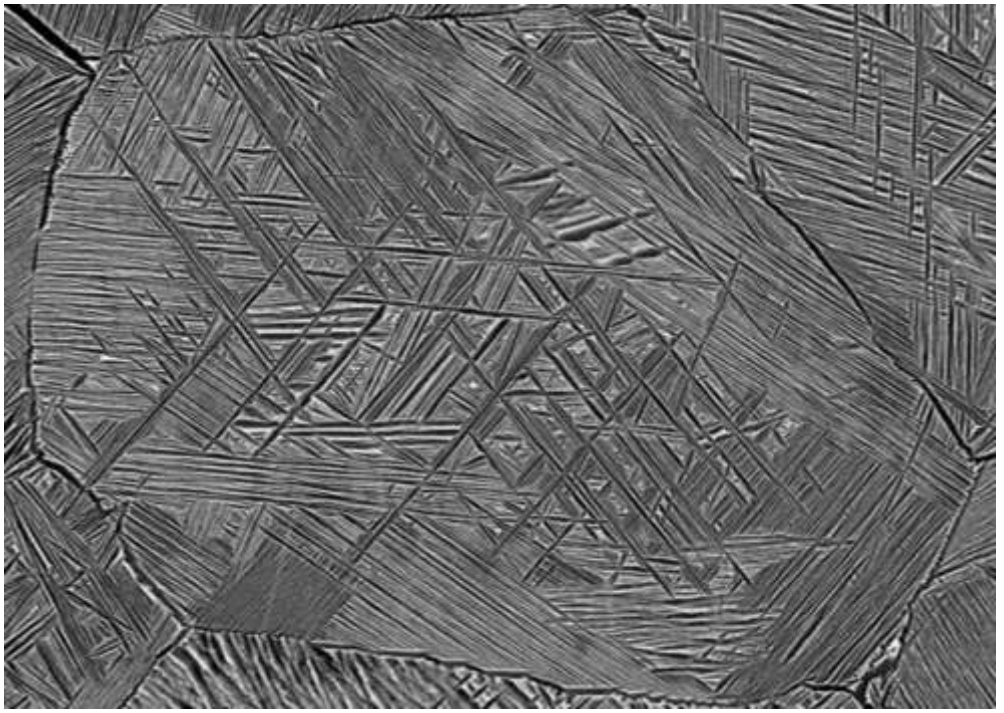

Needed in both cases: details of nucleation mechanisms, variant selection, etc.

Cool New Stuff with Experiments

- *Topics:*
- *Integration modeling with experiments*
- ***Useful recent characterization techniques***
- *Limitations with experimental techniques*
  - *sample preparation*
  - *compositional analysis*
- *What are we (OSU/CAMM) doing?*

3D information

- *Why do we need 3D information ?*
  - *Superposition*
  - *Projection*

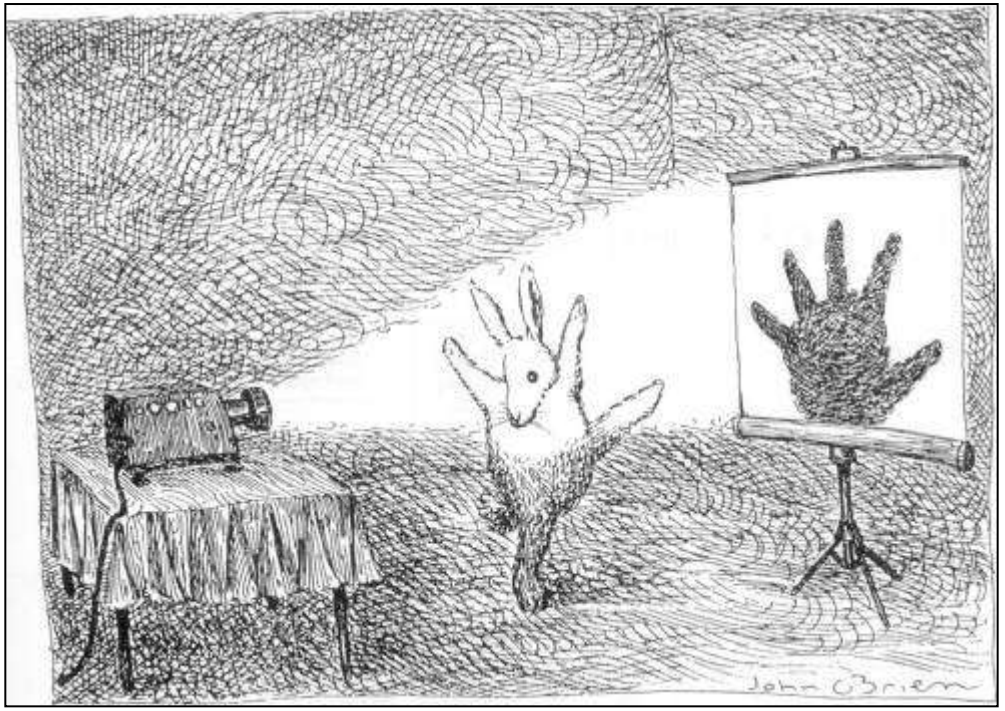

Drawing by John O'Brien, The New Yorker Magazine (1991)

3D Characterization Tools

Solute distributions
β phase separation

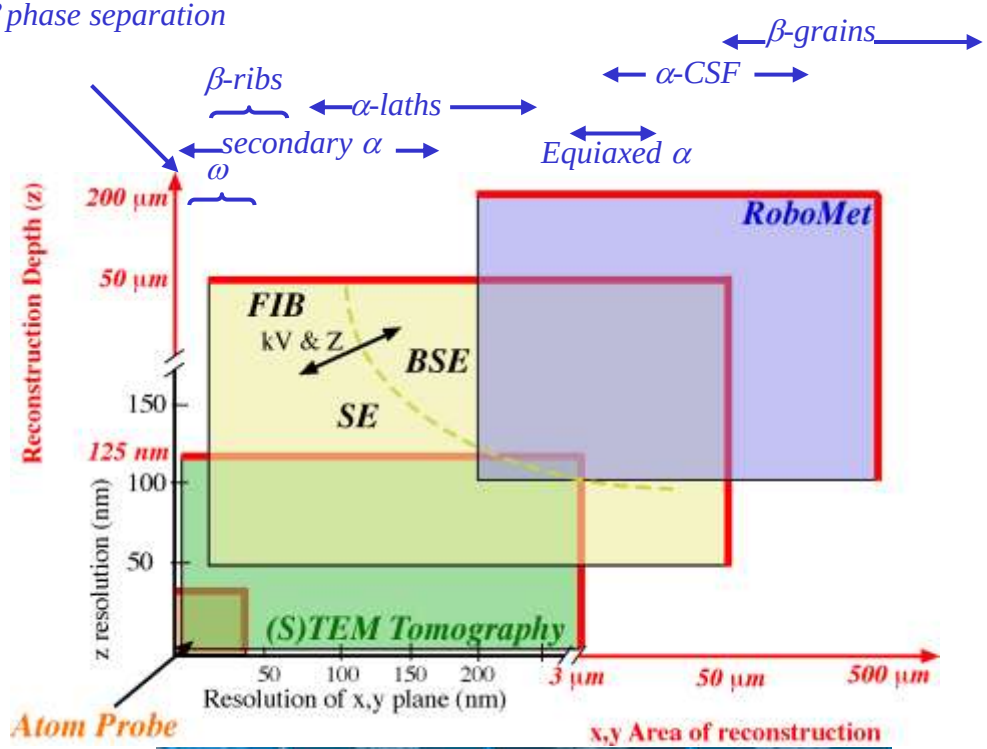

Robo.Met-3D™

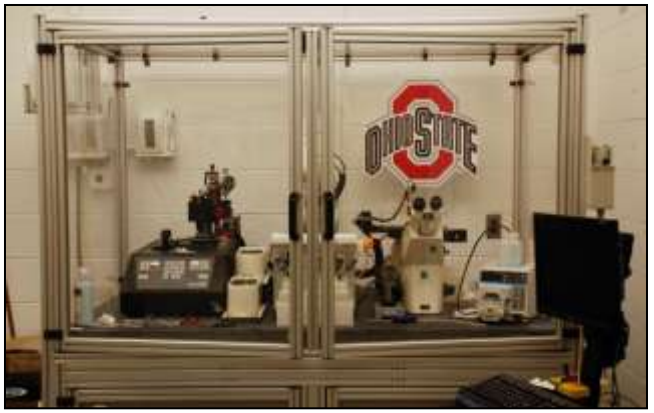

DualBeam (FIB/SEM)™

THE OHIO STATE UNIVERSITY

CAMM

Raw Robo.Met-3D™ Data Set

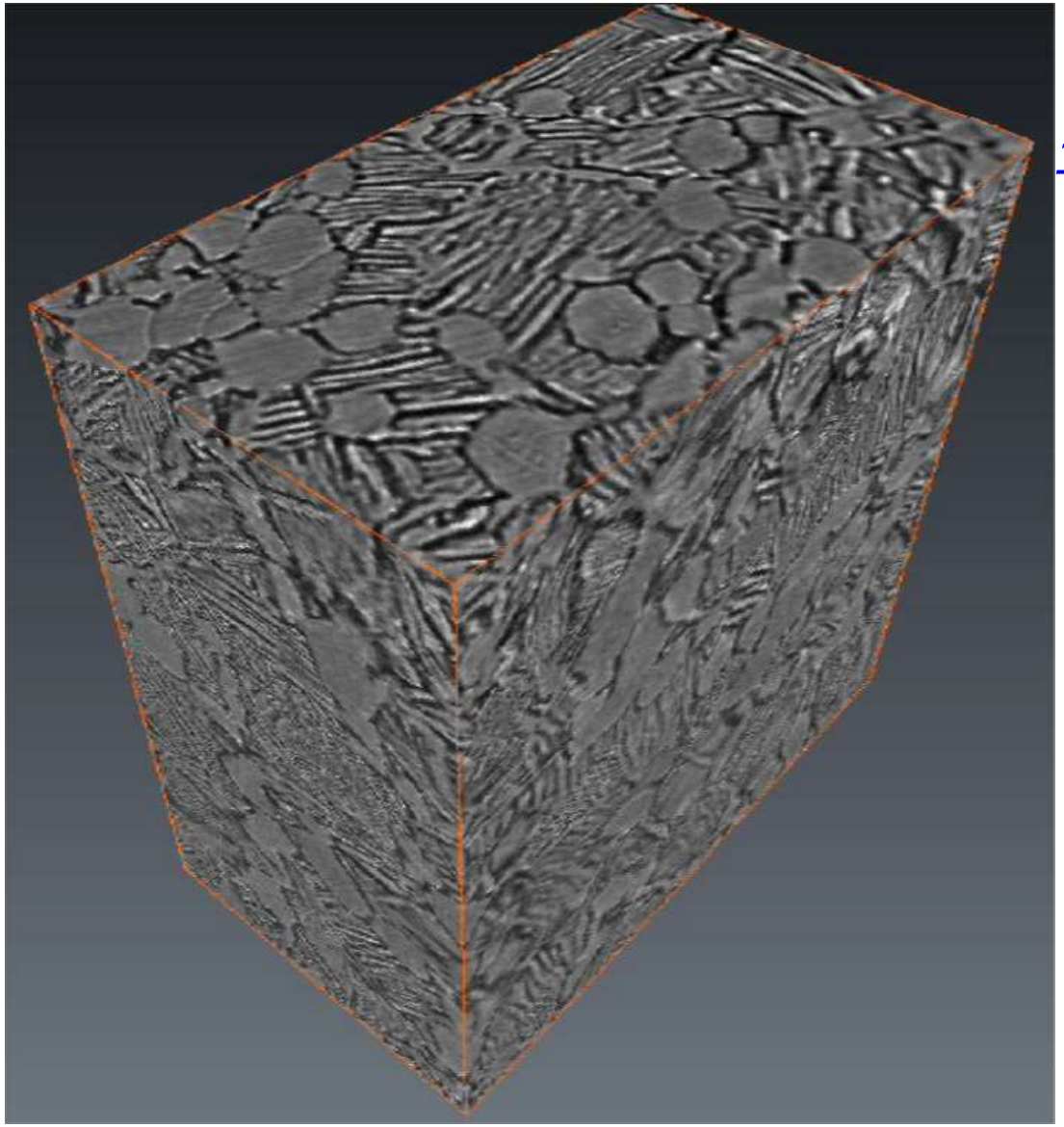

120 μm x 90 μm x 120 μm

THE OHIO STATE UNIVERSITY

CAMM

Ti – 6246 Grain Boundary α Interrogation

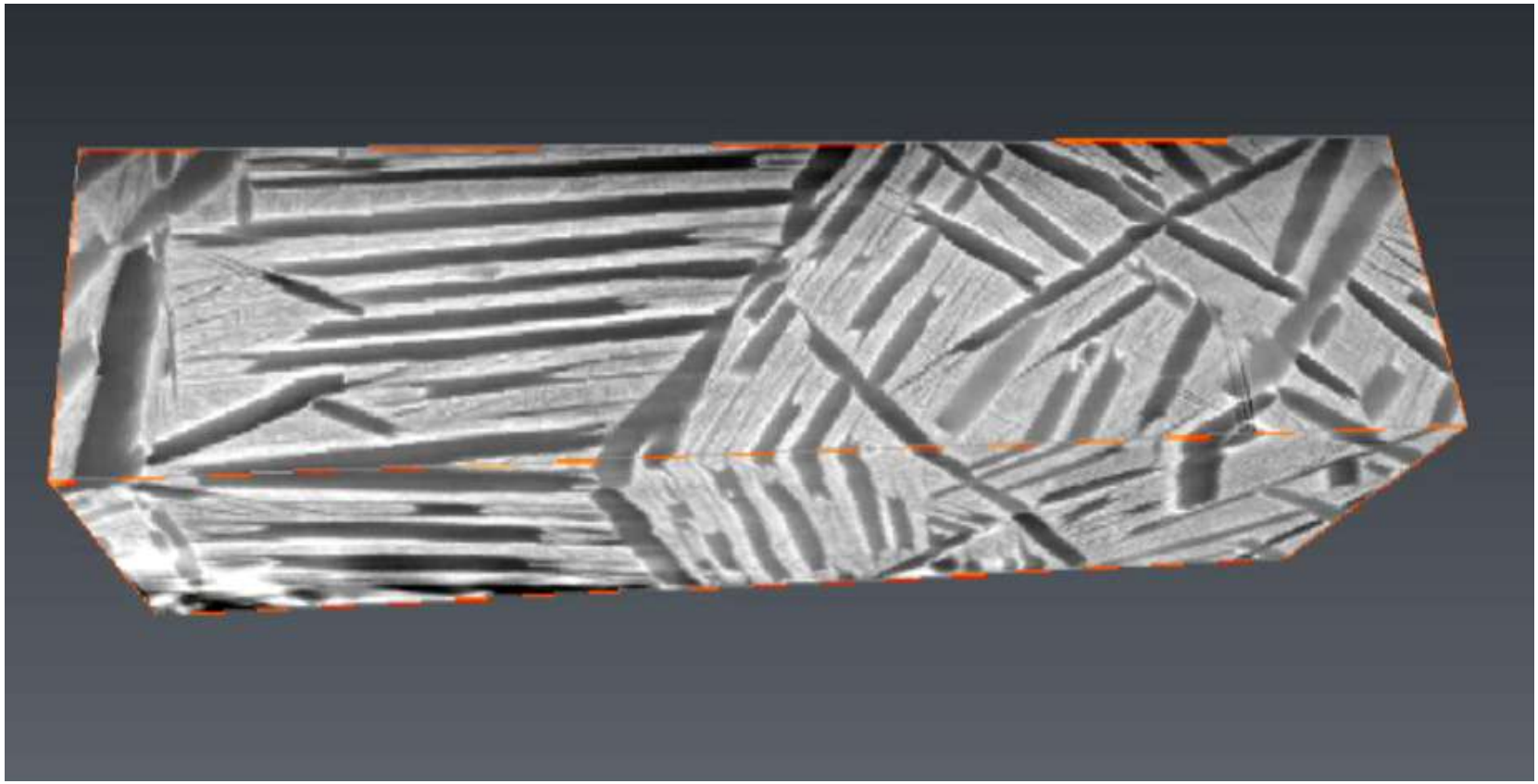

300, ~50 nm slices taken through a 40 μm x 20 μmx 15 μm volume

Ti – 6246 Grain Boundary α Interrogation

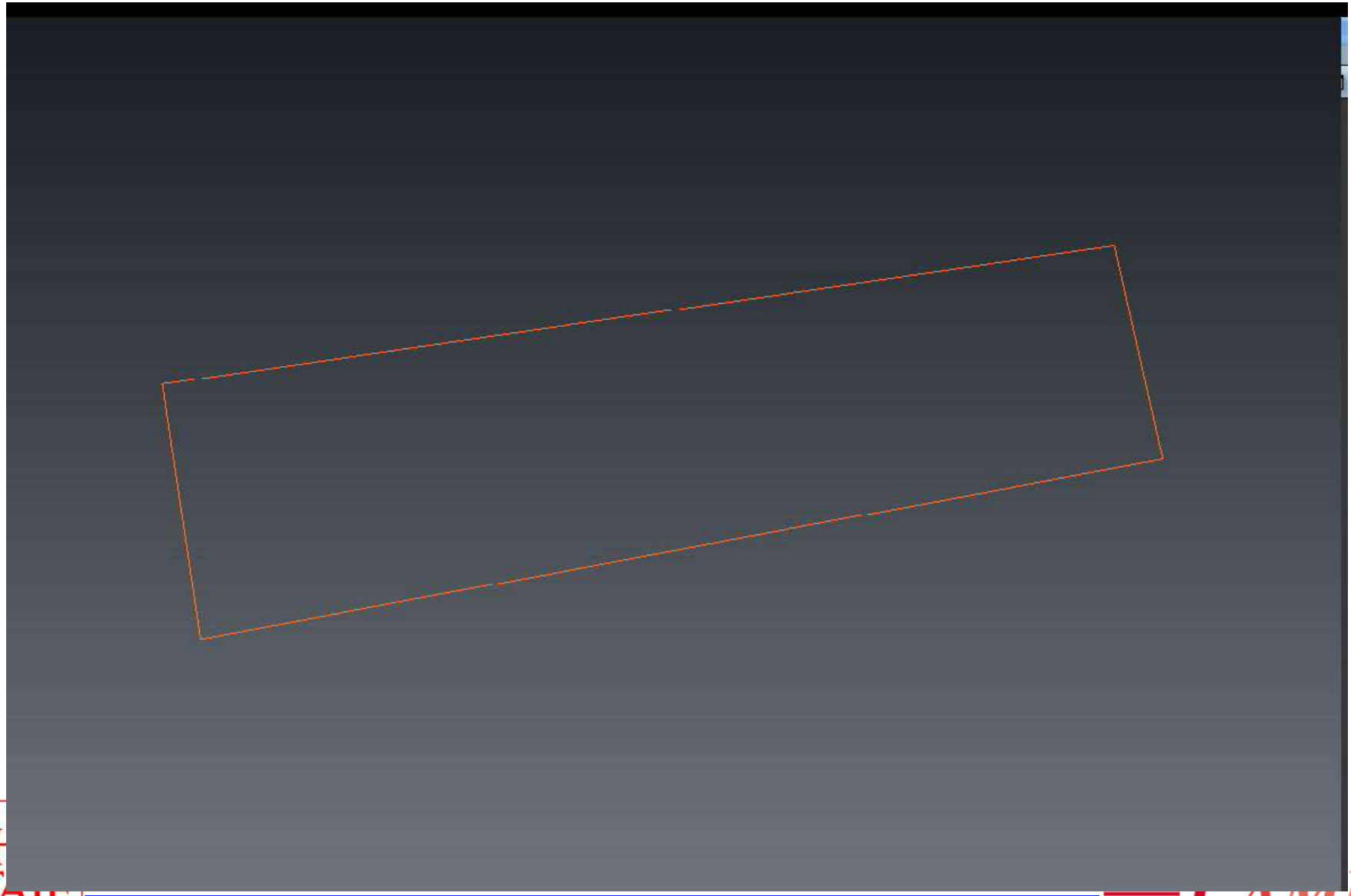

Promise of Aberration-Corrected Electron Microscopy

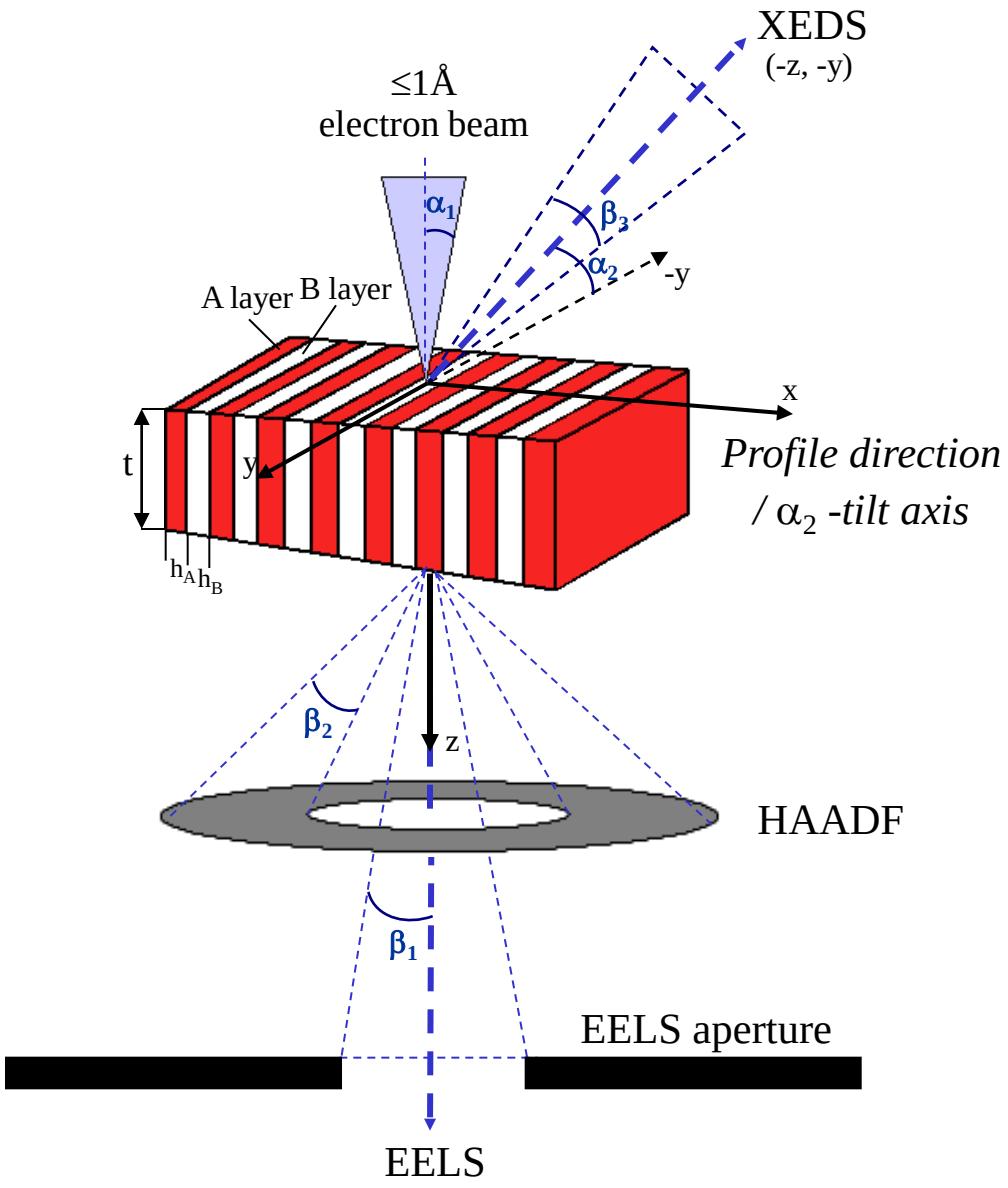

α_1: 18-25mrad

α_2: 20° (+10° tilt)

β_1 : 20mrad

β_2 : 46-325mrad

β_3 : 0.18sr

Spatial Resolution Improvements using Aberration-Corrected Electron Microscopy

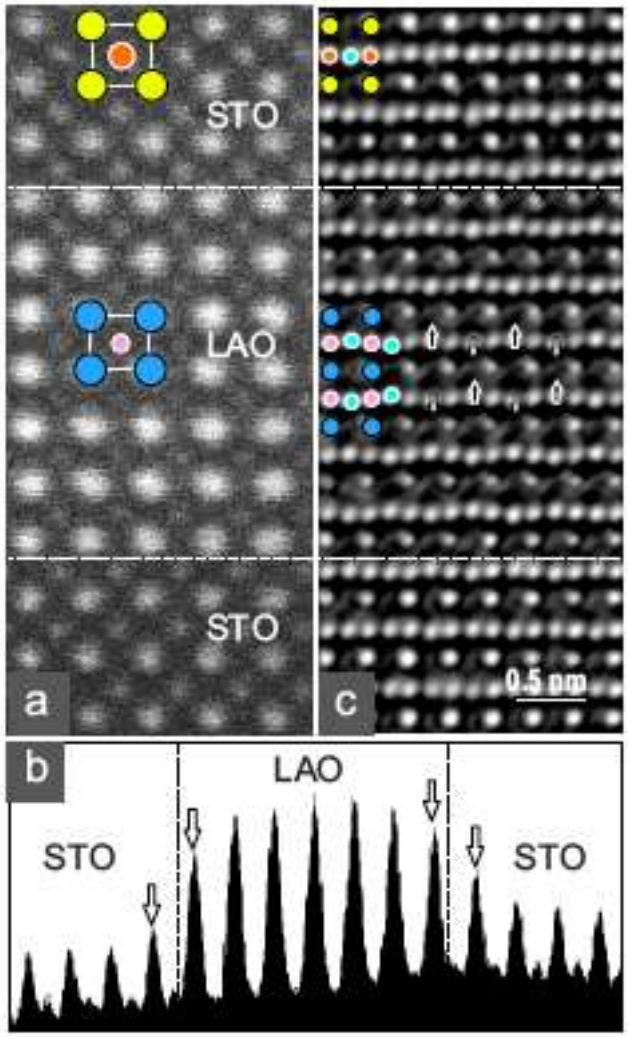

PHYSICAL REVIEW B 79, 081405(R) (2009)

Oxygen octahedron reconstruction in the $SrTiO_3/LaAlO_3$ heterointerfaces investigated using aberration-corrected ultrahigh-resolution transmission electron microscopy

C. L. Jia,[1,*] S. B. Mi,[1] M. Faley,[1] U. Poppe,[1] J. Schubert,[2] and K. Urban[1]

[1]*Institute of Solid State Research and Ernst Ruska Centre for Microscopy and Spectroscopy with Electrons, Forschungszentrum Jülich, D-52425 Jülich, Germany*

[2]*Institute of Bio- and Nanosystems and Centre of Nanoelectronic Systems for Information Technology, Forschungszentrum Jülich, D-52425 Jülich, Germany*

- ***Measurement of atom (column) location to within a few picometers precision***
- ***To image in this manner (NCSI) requires thin foils of thickness ≈ 4nm***
- ***What is the effect of foil thickness on relaxations?***
- ***Need for computational assistance to interpret correct result***

Ti-L near-edge : monochromated STEM-EELS

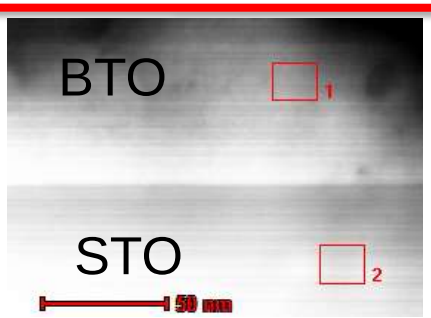

Imaging: filtered (800 V), Mono excitation 0.3
50 μm C2 aperture, no C3 aperture, no C1 slit
Analysis: GIF ap. 2.5mm, CL 36.7mm
Dispersion 0.05 eV/pixel
GIF energy resolution: 0.2 eV
Acquisition time: 10 seconds

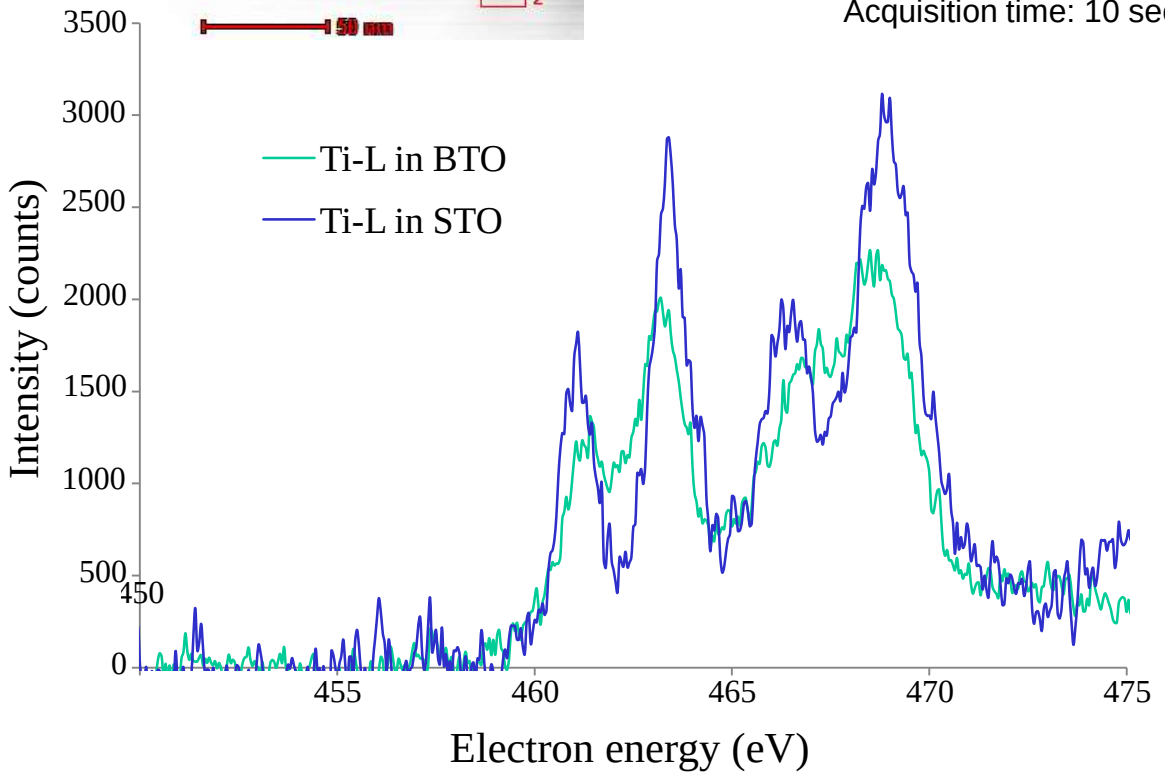

But, not possible to perform spatially resolved monochromated EELS in our system:
- need more signal – the high brightness gun

THE OHIO STATE UNIVERSITY

CAMM

Comparison of monochromated vs. non-monochromated EELS

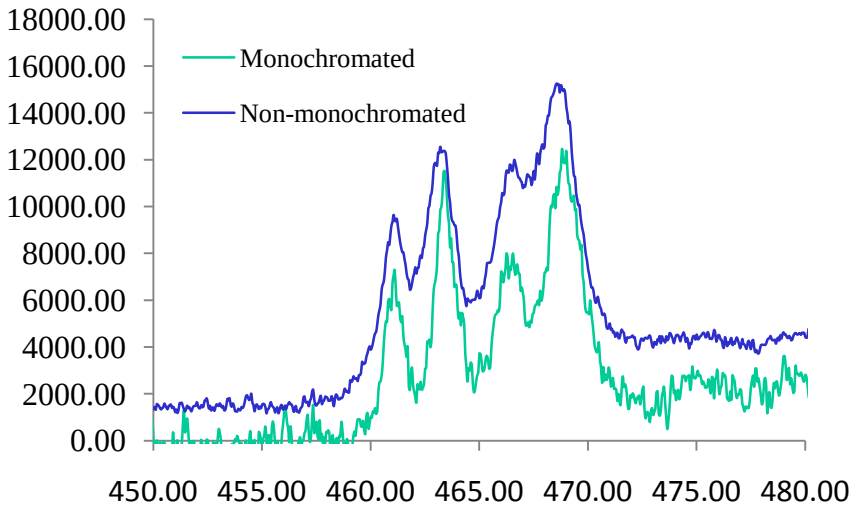

Ti-L in STO

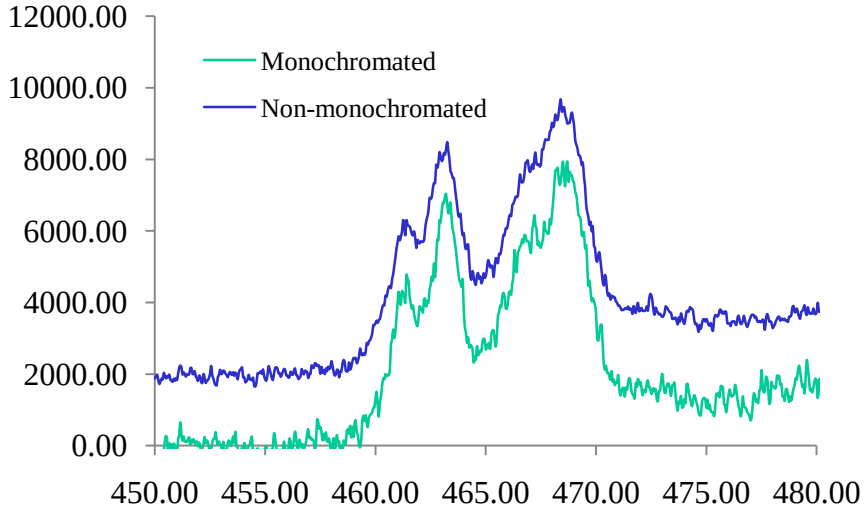

Ti-L in BTO

- ***Need for computational assistance to interpret correct result, i.e., electronic structure***

THE OHIO STATE UNIVERSITY

CAMM

Cool New Stuff with Experiments

- *Topics:*
- *Integration modeling with experiments*
- *Useful recent characterization techniques*
- *Limitations with experimental techniques*
  - *sample preparation*
  - *compositional analysis*
- *What are we (OSU/CAMM) doing?*

Low Energy Ar Milling

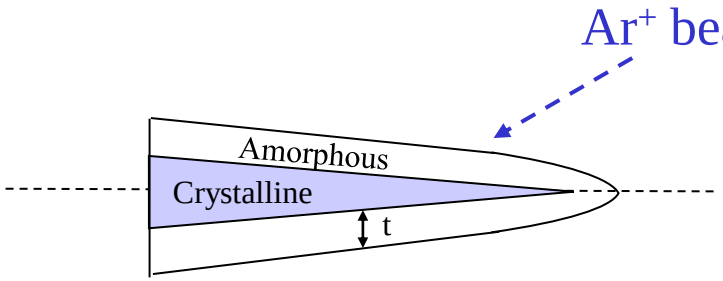

cross-section of TEM foil

Fischione 1040 NanoMill

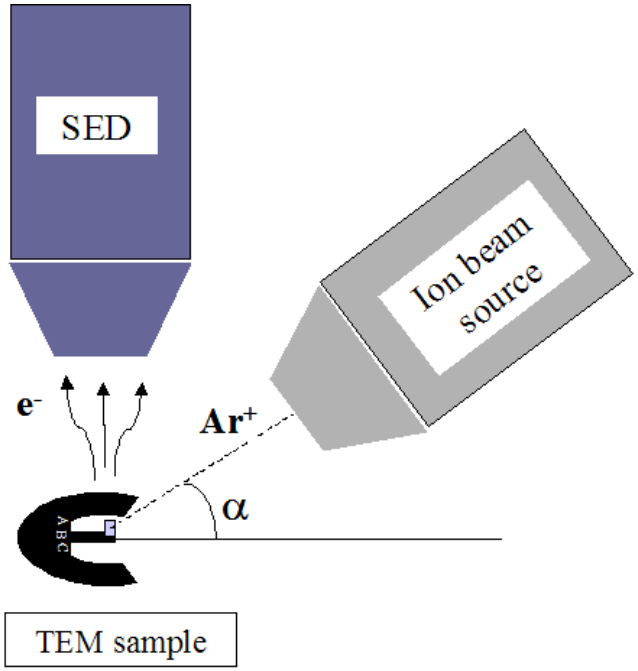

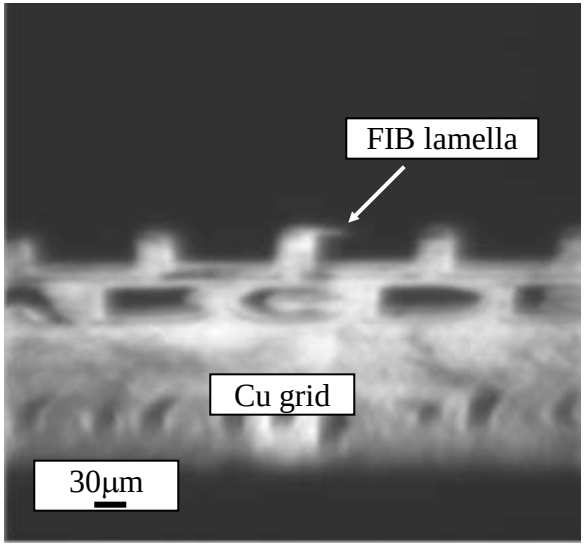

500V Ar Ion Image of FIB lamella at 15° beam incidence angle

Focused Ar beam source : 10-12µm beam size

Low energy : **2000-50V**

Low angle: 0° to +30°/-10°

THE OHIO STATE UNIVERSITY

CAMM

Conventional ion mill damage in Ni-based superalloy (Renè 88DT)

HRTEM imaging

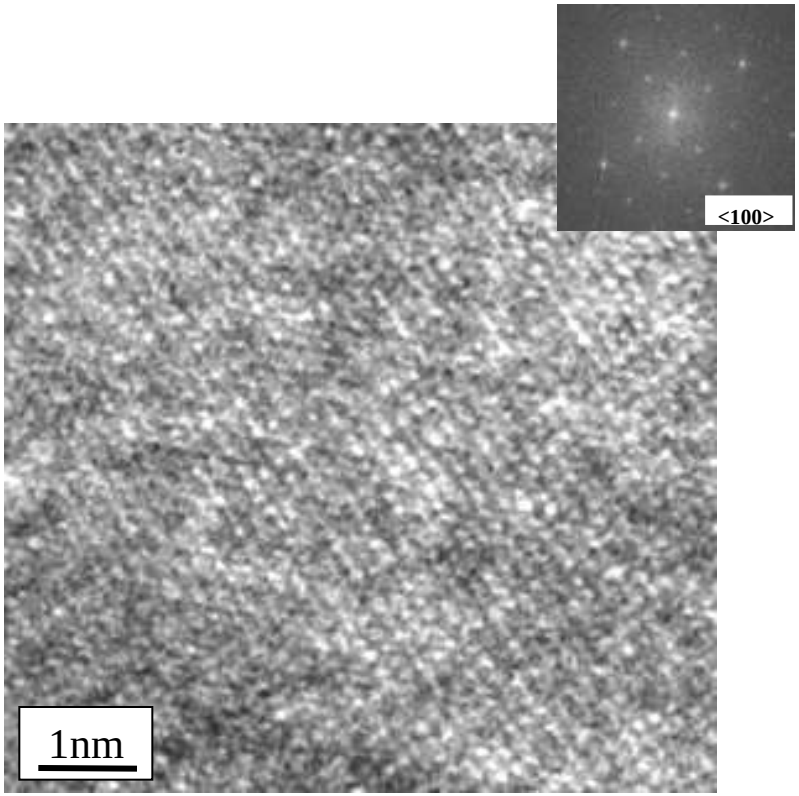

5kV Ar milling

+15º/-10º

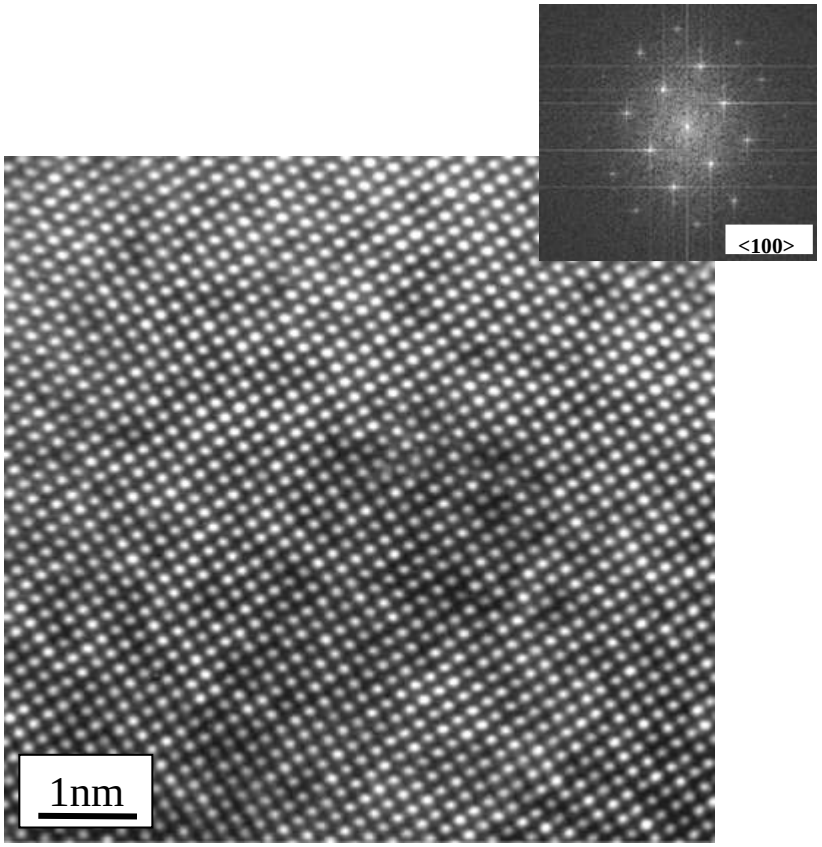

500V Low energy Ar ion milling

Phenomenological Correlation between depth of amorphous damage and atomic displacements

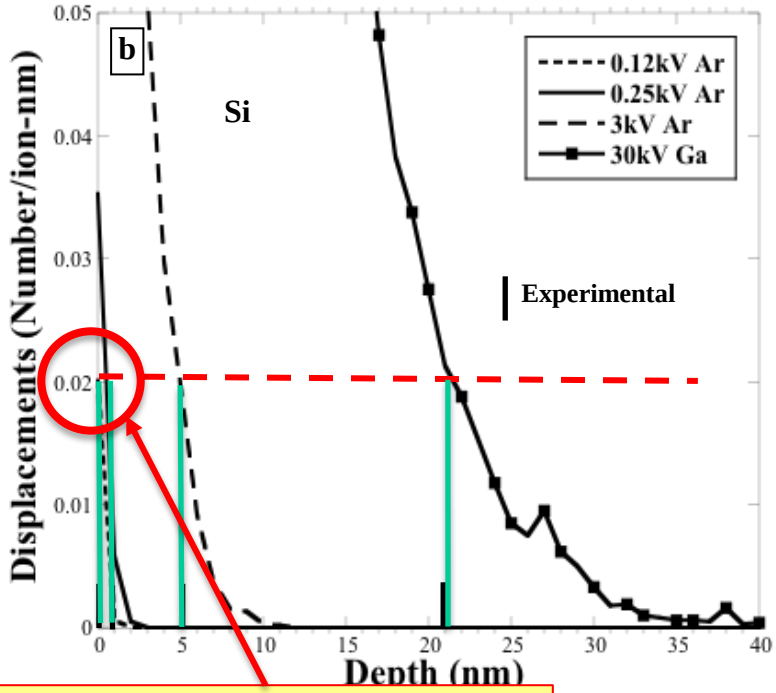

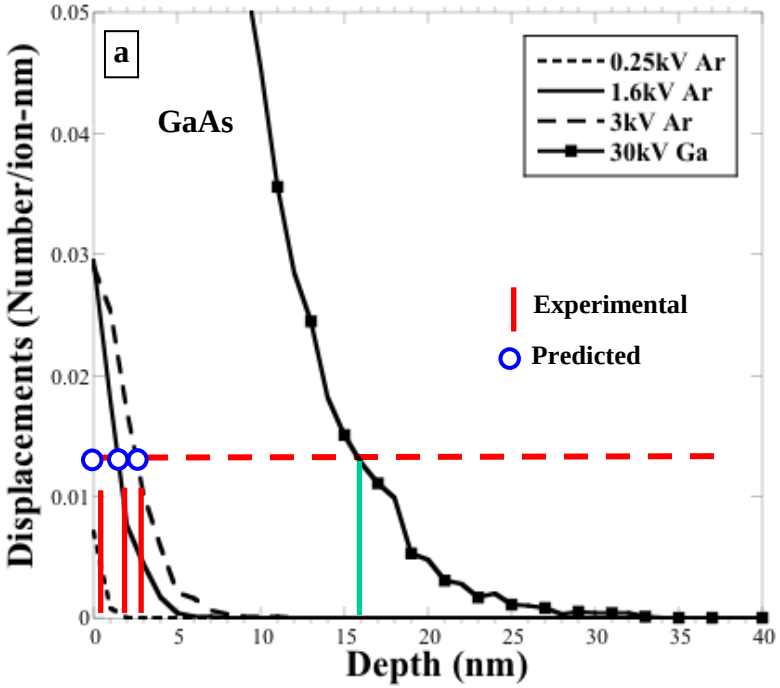

Critical dose for formation of amorphous layer

Phenomenological Correlations – our results for Ge

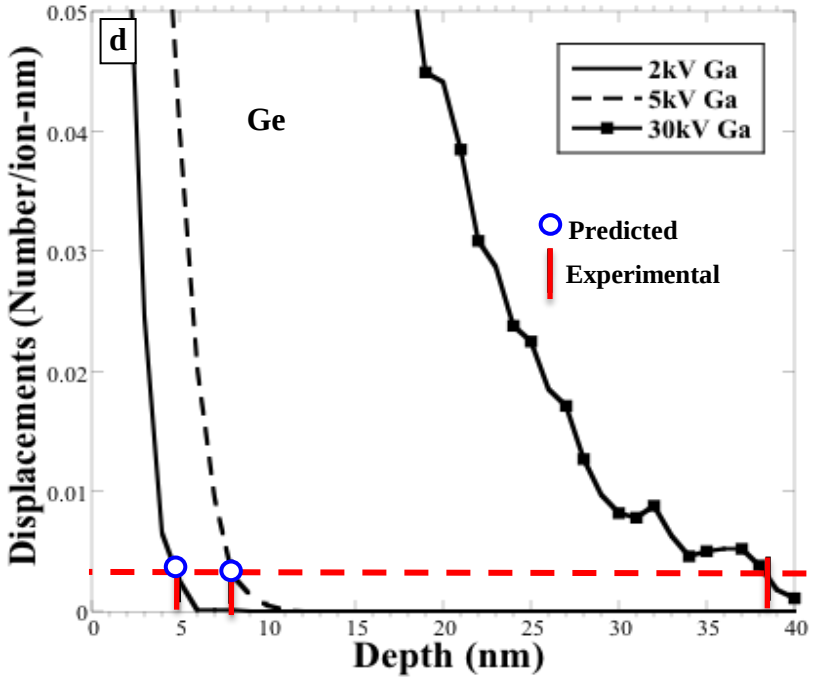

Tells us about removing the amorphous damage but the secondary defects may still be present

Cool New Stuff with Experiments

- *Topics:*
- *Integration modeling with experiments*
- *Useful recent characterization techniques*
- ***Limitations with experimental techniques***
  - *sample preparation*
  - ***compositional analysis***
- *What are we (OSU/CAMM) doing?*

XEDS – Spatial Resolution and Quantification

From Chris Kiely

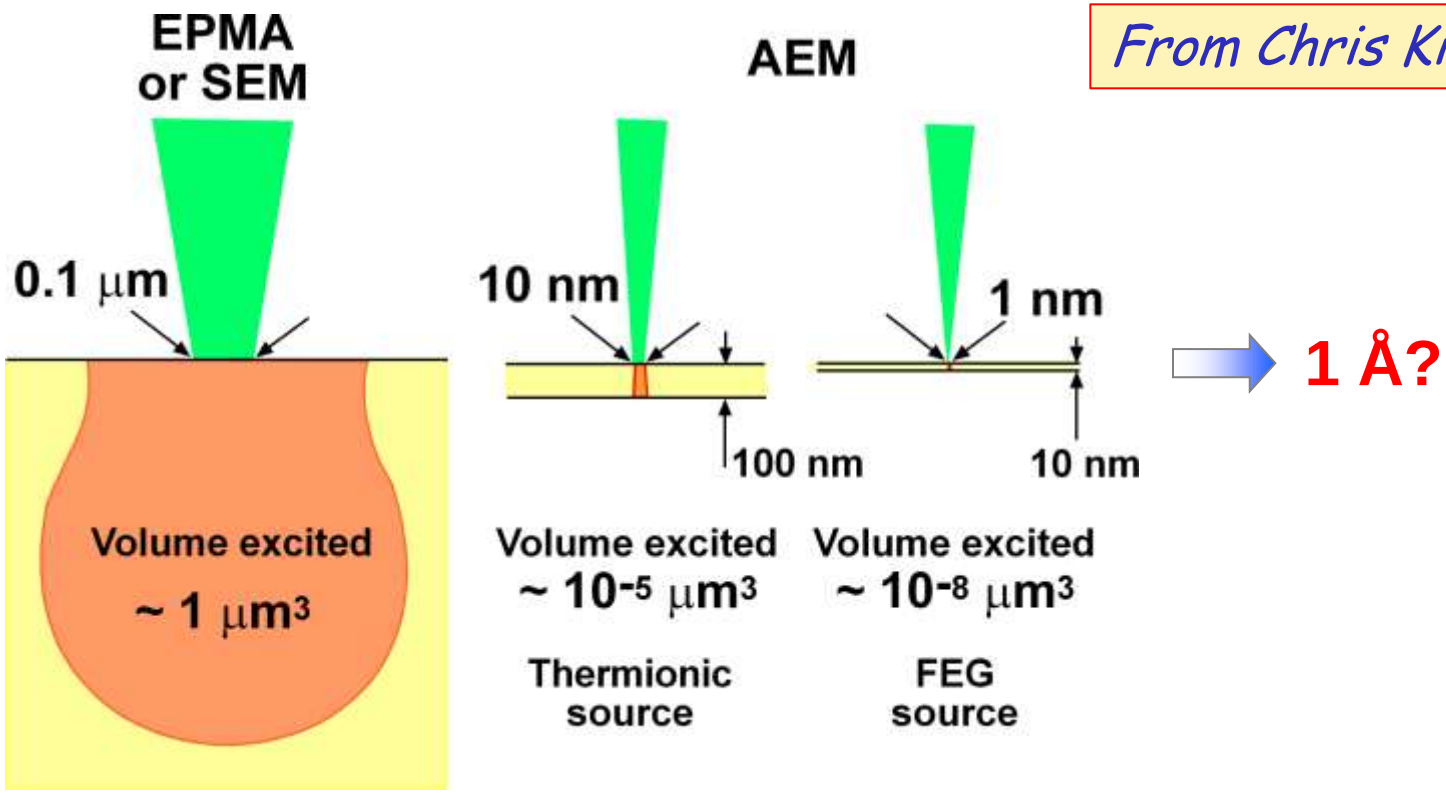

Spatial resolution ↑ → Analytical sensitivity ↓

Improving STEM-XEDS Maps

- Increase dwell time of probe (more X-rays collected)
- Increase current (more X-rays generated)
- Multivariate statistical analysis (MSA) of spectrum images

The Detection of Minor Alloying Elements:

Au-Pd/C

From Chris Kiely

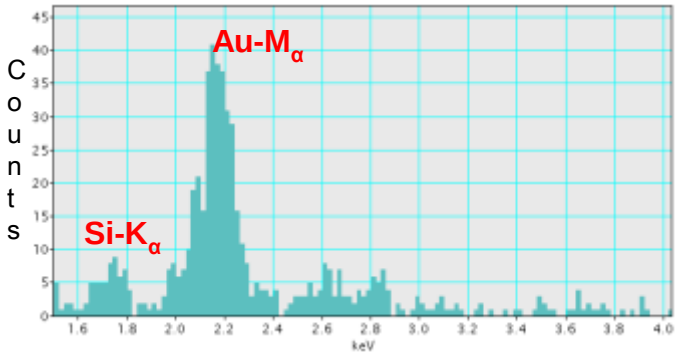

As Acquired

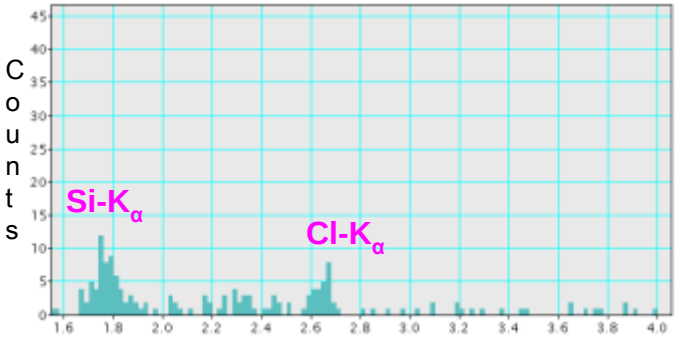

On Carbon Support

On Metal Particle

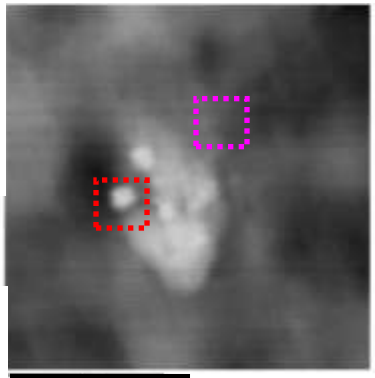

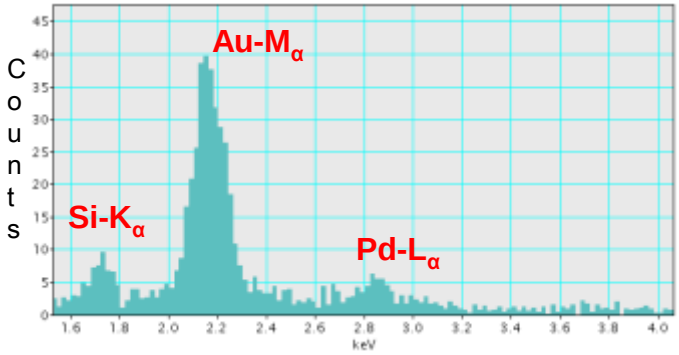

After MSA

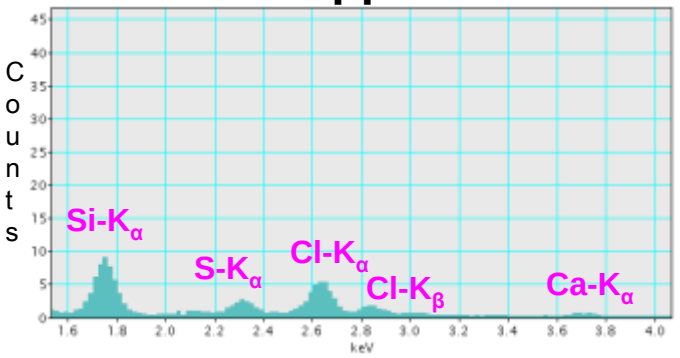

95at.%Au-5at.%Pd : 1% total metal loading

THE OHIO STATE UNIVERSITY

CAMM

“Bulk Samples”: Phase stability/ Ti/Nb multilayers

bcc Ti / *bcc* Nb

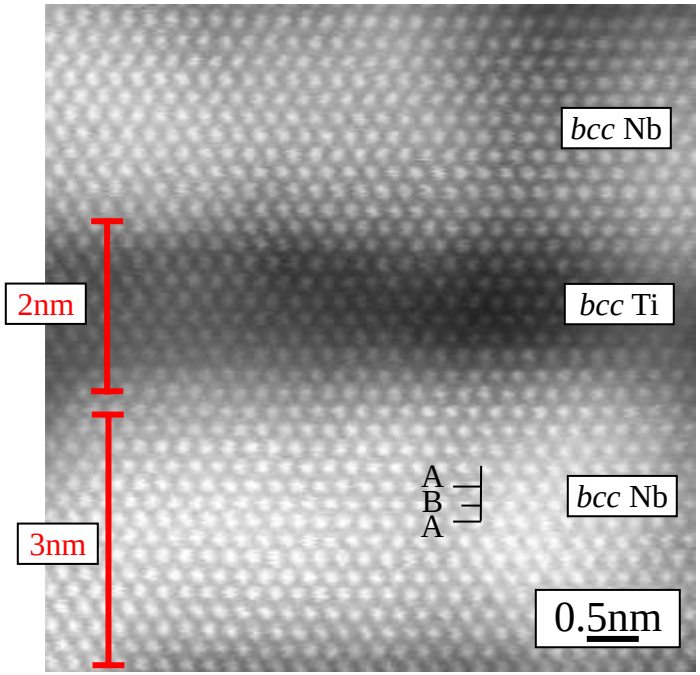

Layer thickness : 2nm Ti / 3.2nm Nb

Question: How compositionally sharp are the interfaces?
Answer: Need compositional analysis at the nanometer scale

Analysis of nanoscale multilayers

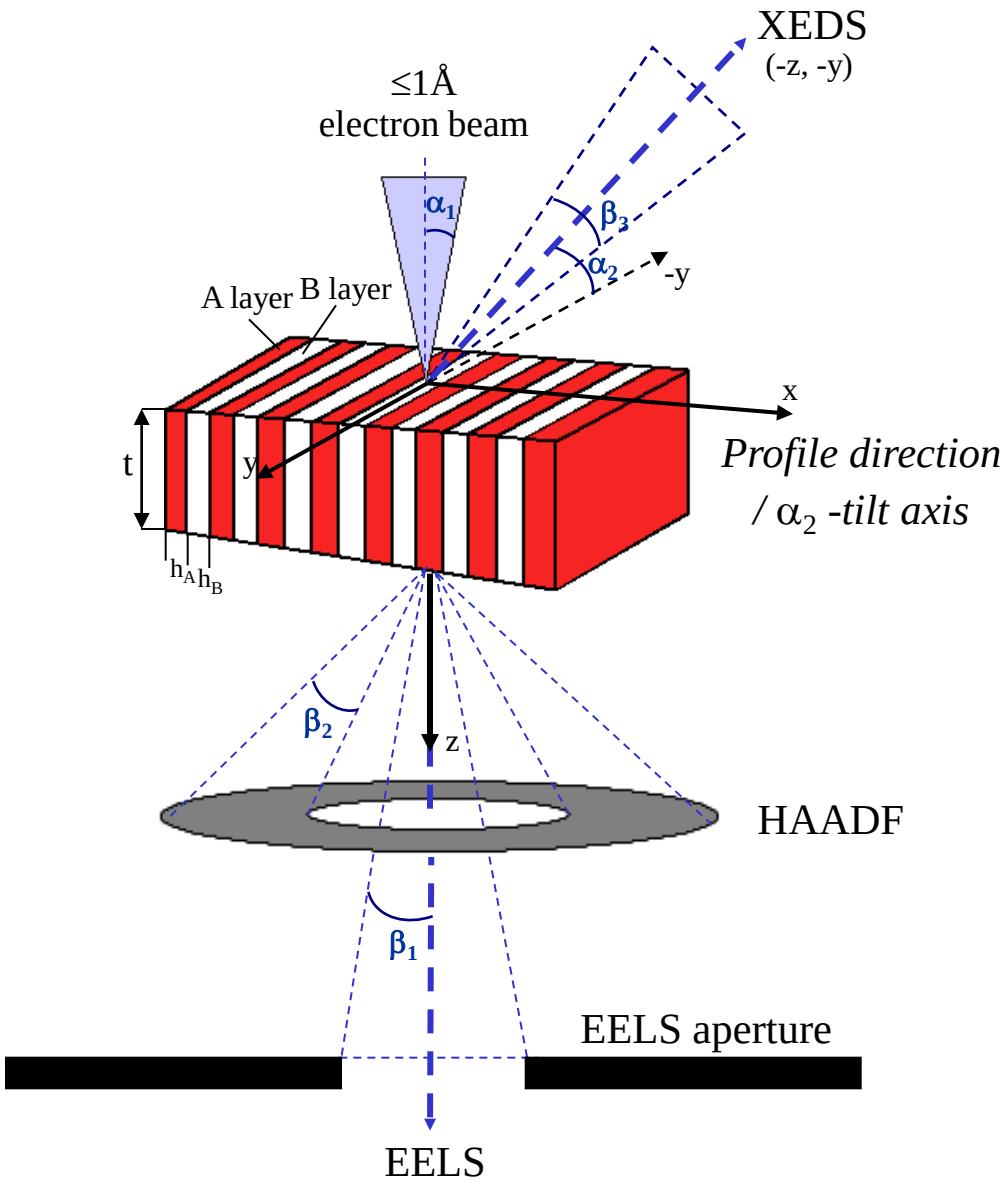

α_1: 18-25mrad

α_2: 20° (+10° tilt)

β_1: 20mrad

β_2: 46-325mrad

β_3: 0.18sr

Ti/Nb Multilayers

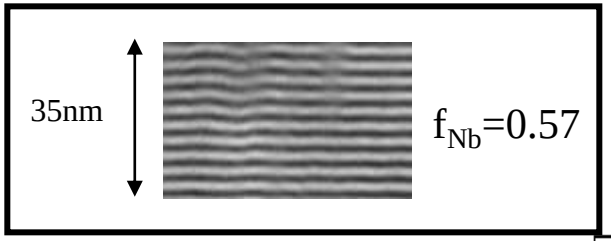

f_{Nb}=0.57

bcc Ti / *bcc* Nb

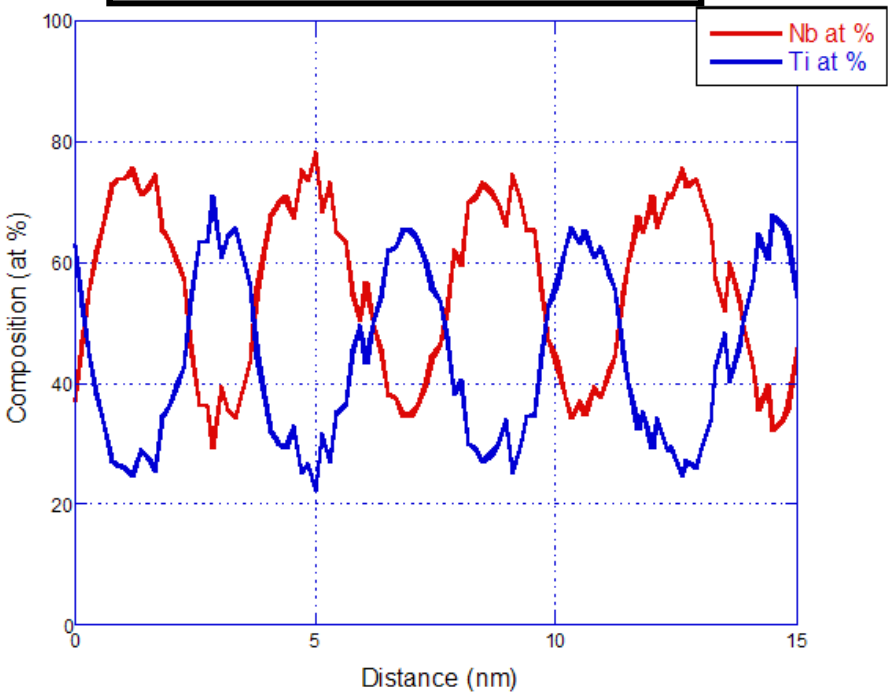

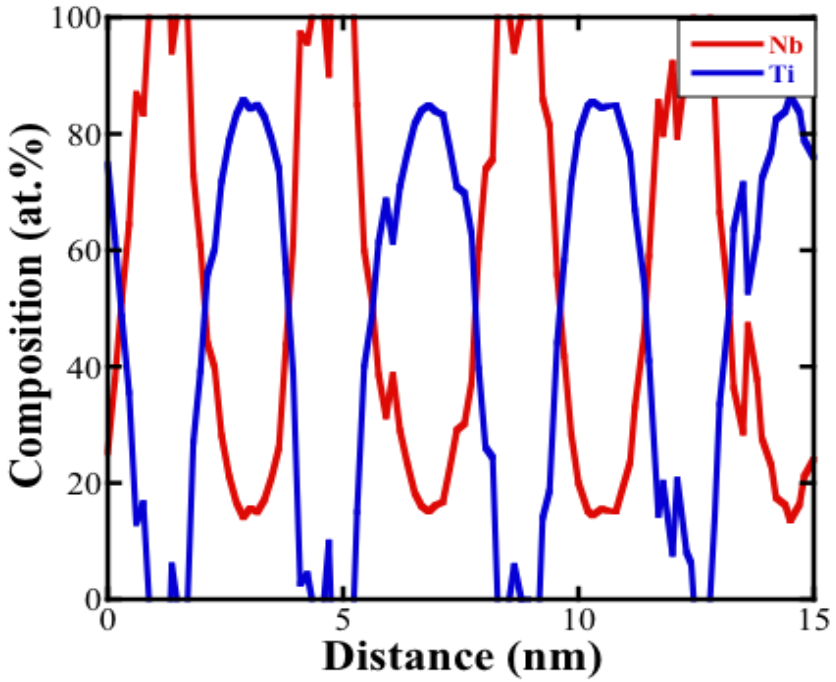

XEDS

EELS

Layer thickness : 1.8nm Ti / 1.7nm Nb

THE OHIO STATE UNIVERSITY

CAMM

Use of Tomographical Atom Probe to determine intermixing in Ti/Nb Multilayers

Nb has significantly intermixed into Ti

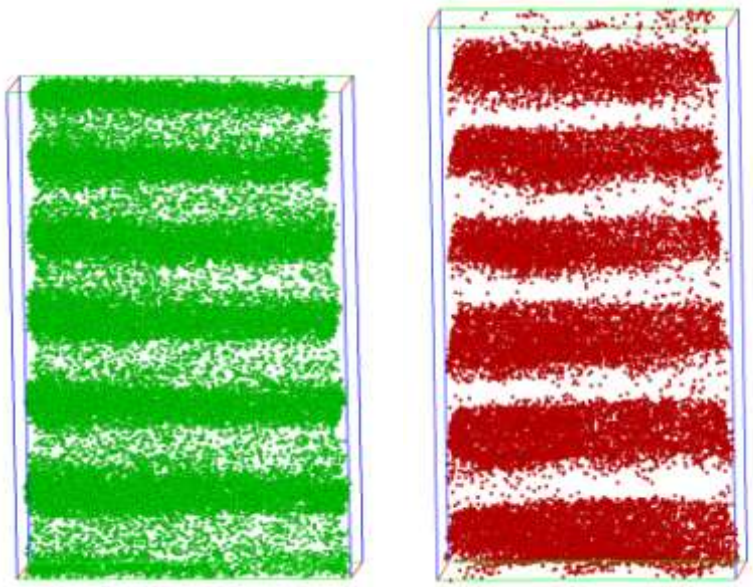

Nb Ti

Atom Probe composition profile

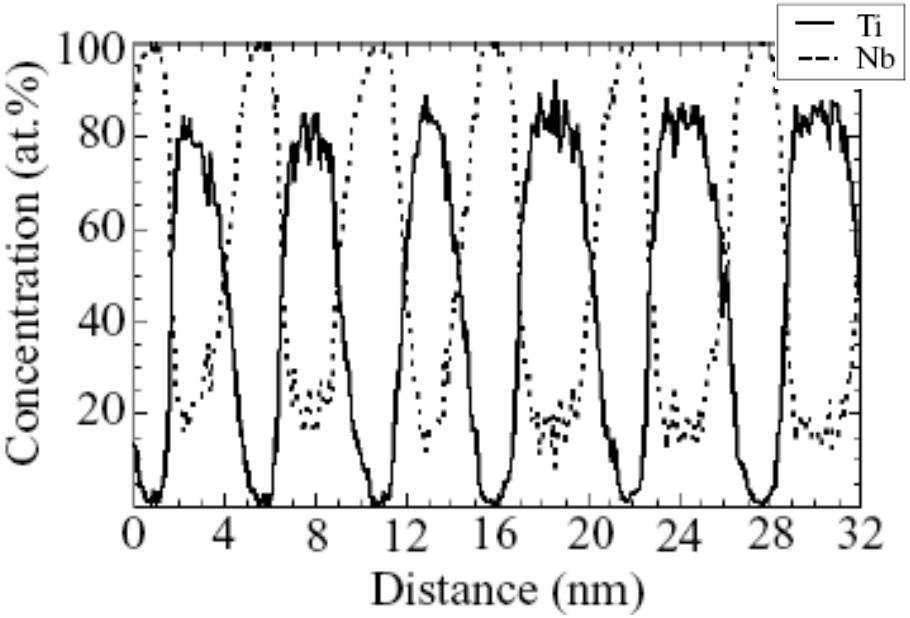

Layer thickness : 2nm Ti / 3nm Nb

bcc/bcc

Probe Corrected Titan: STEM/EELS Ananlysis of Ti/Nb Multilayers

STEM EELS composition profile

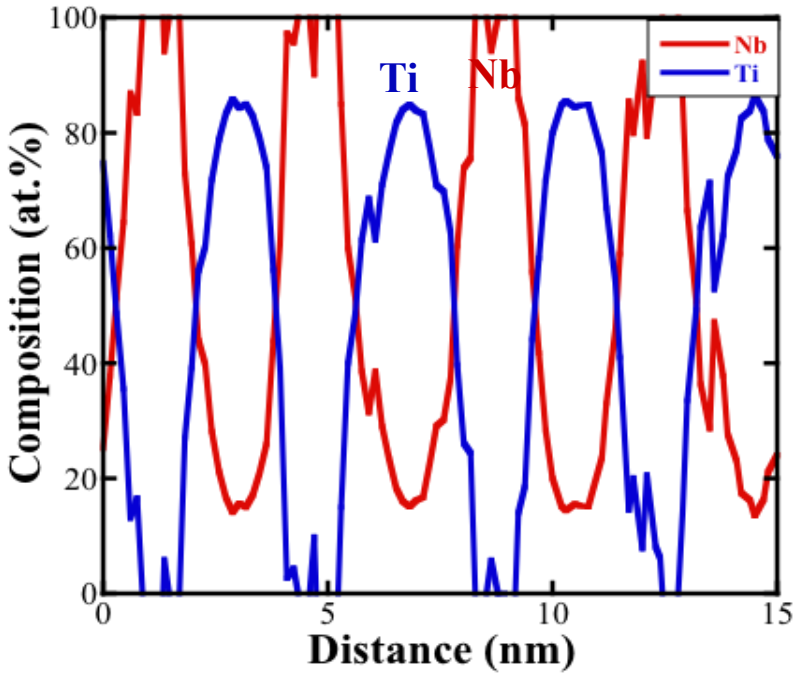

Layer thickness : 1.6nm Ti / 2.1nm Nb

bcc/bcc

Atom Probe composition profile

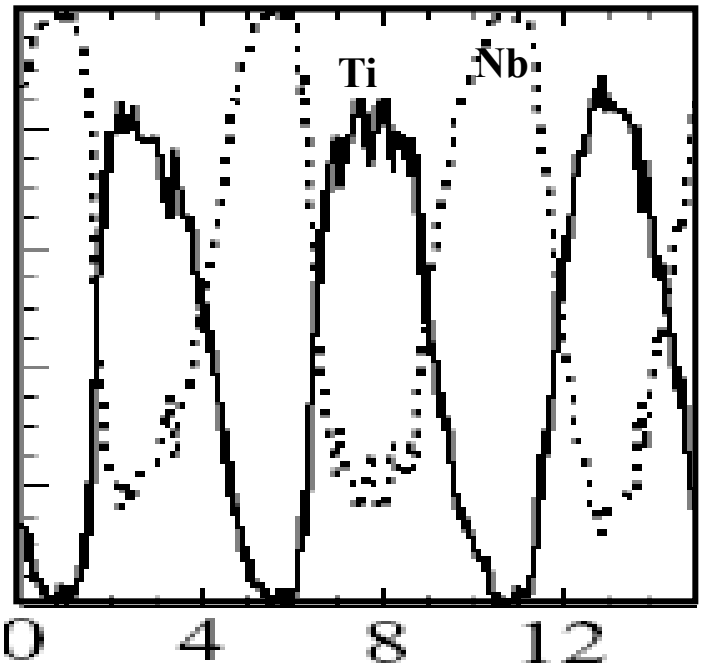

Layer thickness : 2.2nm Ti / 3.3nm Nb

bcc/bcc

THE OHIO STATE UNIVERSITY

CAMM

Beam Broadening

Beam broadening

EELS

$$b \sim \beta t$$

(EELS collection angle, β = 20mrad and specimen thickness, t = nm)

XEDS

b ~ Monte Carlo simulation (MC)

$$b = 7.21x10^5 \frac{Z}{E_o}\left(\frac{\rho}{A}\right)^{1/2} t^{3/2}$$

Single scattering (SS) approach

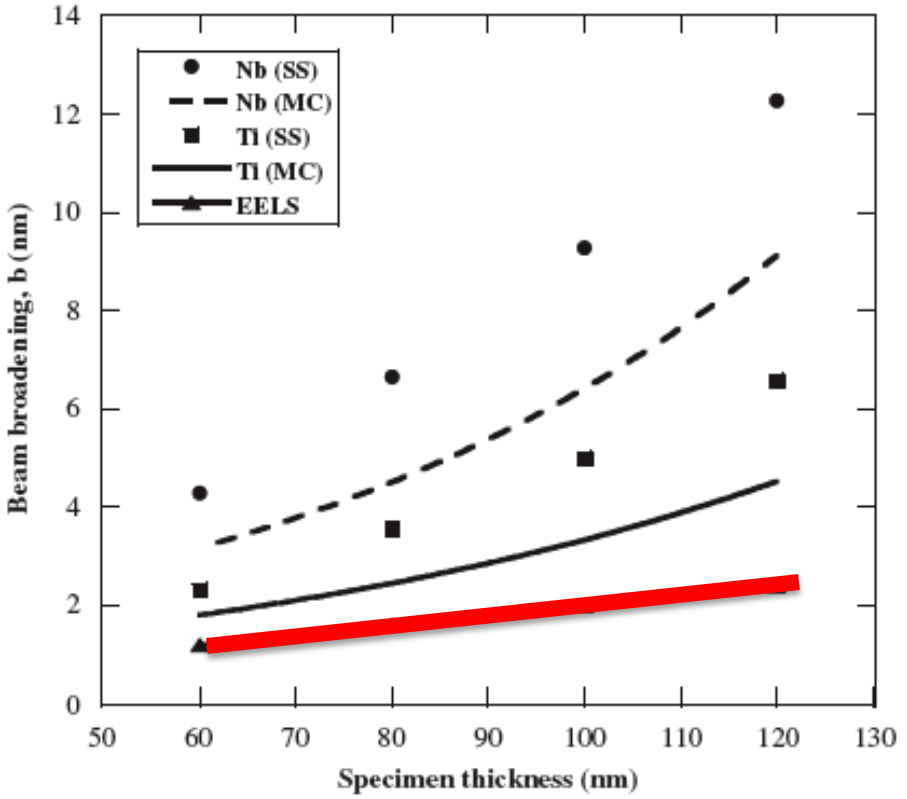

Fig. 4. The plot of beam broadening, *b* (nm) vs. TEM specimen thickness, *t* (nm) in Nb and Ti (SS = single scattering, MC = Monte Carlo).

Limits to High Spatial Resolution of EDS and EELS in an Aberration-Corrected (S)TEM

- *Topics:*
- *Sample preparation*
- *Composition from EELS & EDS (not spatially resolved)*
- ***Spatially resolved EELS – not monochromated***
- *Spatially resolved EELS - monochromated*

Spectrum Image

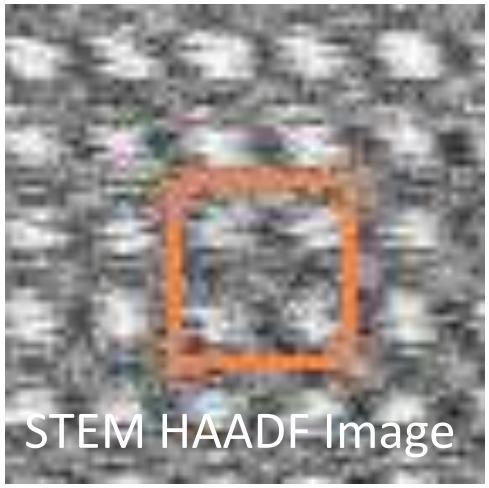

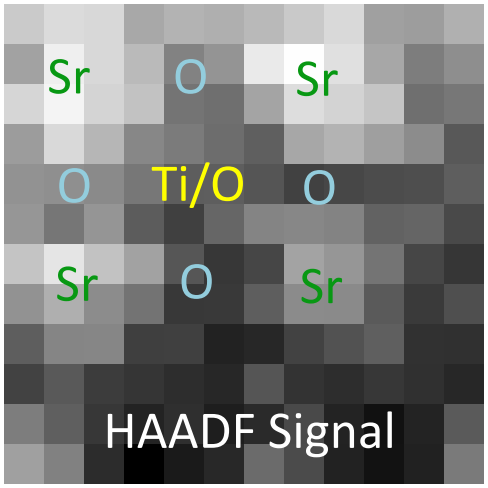

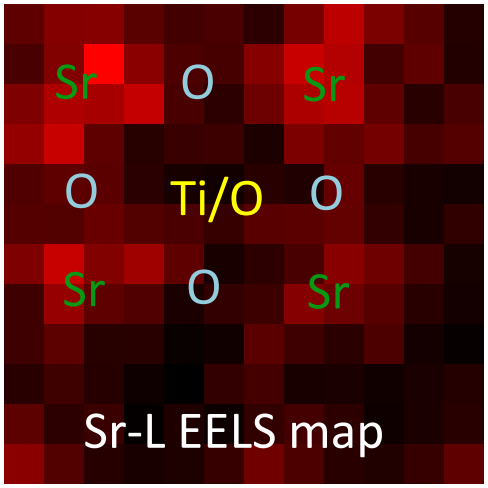

EELS profile on Sr-Ti/O-Sr

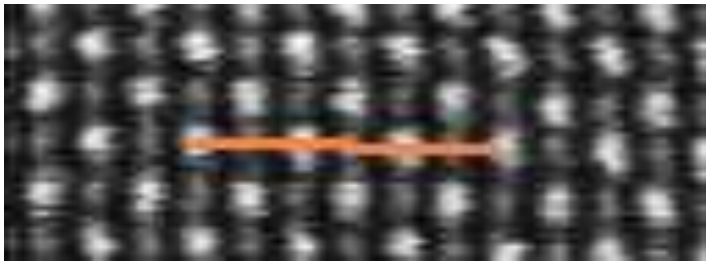

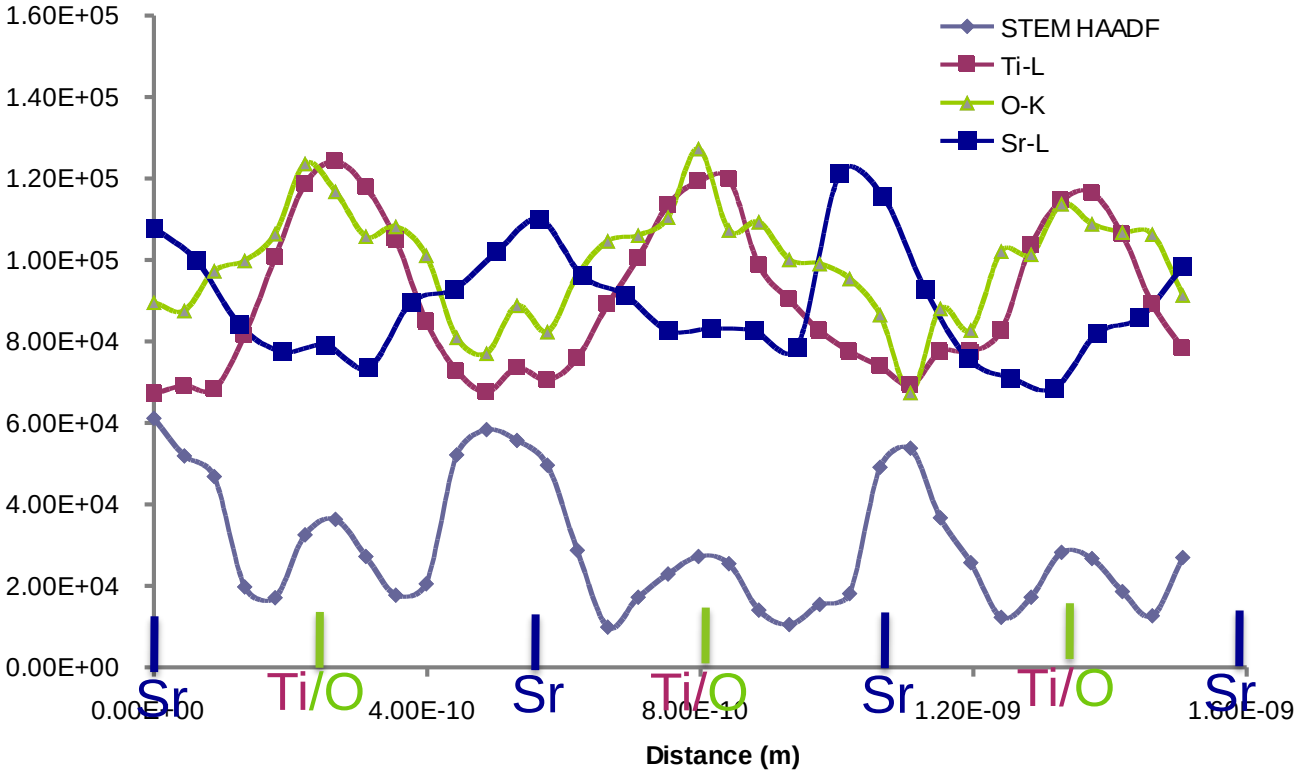

Accelerating Voltage: 300kV

THE OHIO STATE UNIVERSITY

CAMM

EELS profile on Ti/O-O-Ti/O

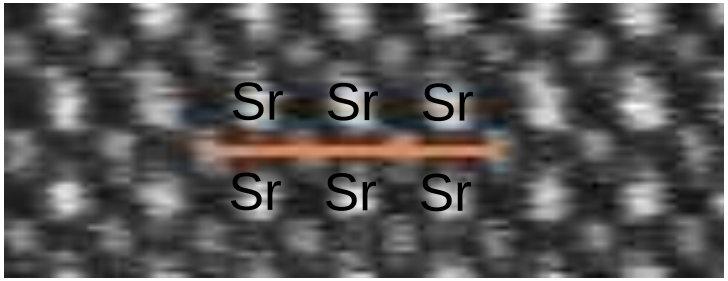

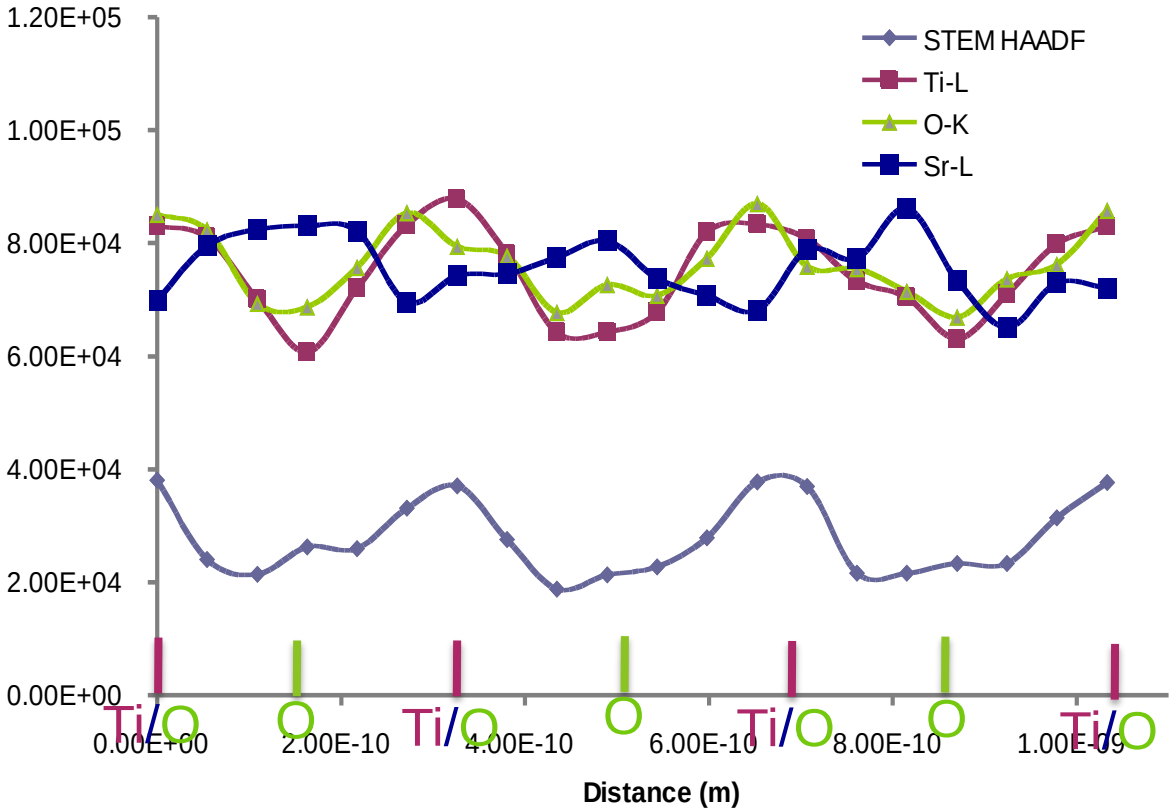

Accelerating Voltage: 300kV

THE OHIO STATE UNIVERSITY

CAMM

Possible Causes and Remedies

Possible causes:

- ***Electron tails***

C2:50μm C3: 2000 μm

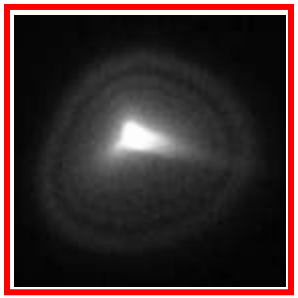

C2:150μm C3: 30μm

25% electron beam intensity in skirt

Probe corrected up to 18mrad

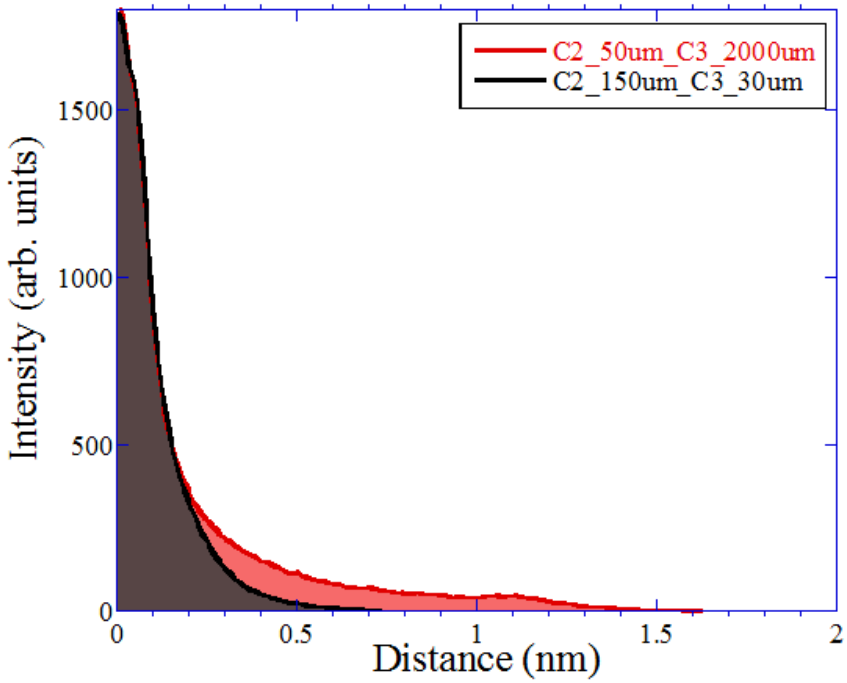

Possible Causes and Remedies

Possible causes:

- *Electron tails*
- *Beam broadening*
- *Column jumping*
  - *Christian Dwyer*
    - *transverse momentum for highly convergent probe*

C. Dwyer and J. Etheridge, Ultramicroscopy 96 (2003) 343

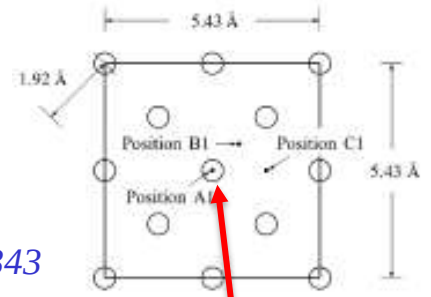

Probe on column A1

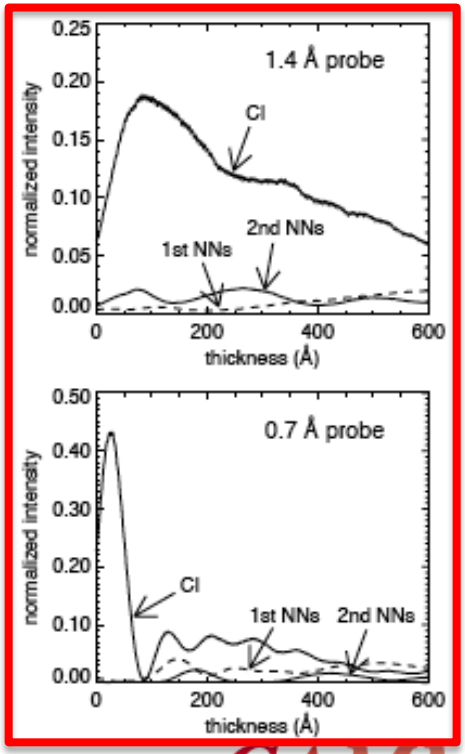

THE OHIO STATE UNIVERSITY

CAMM

Calculated O-K Edge (EELS) profile on Ti/O-O-Ti/O Columns

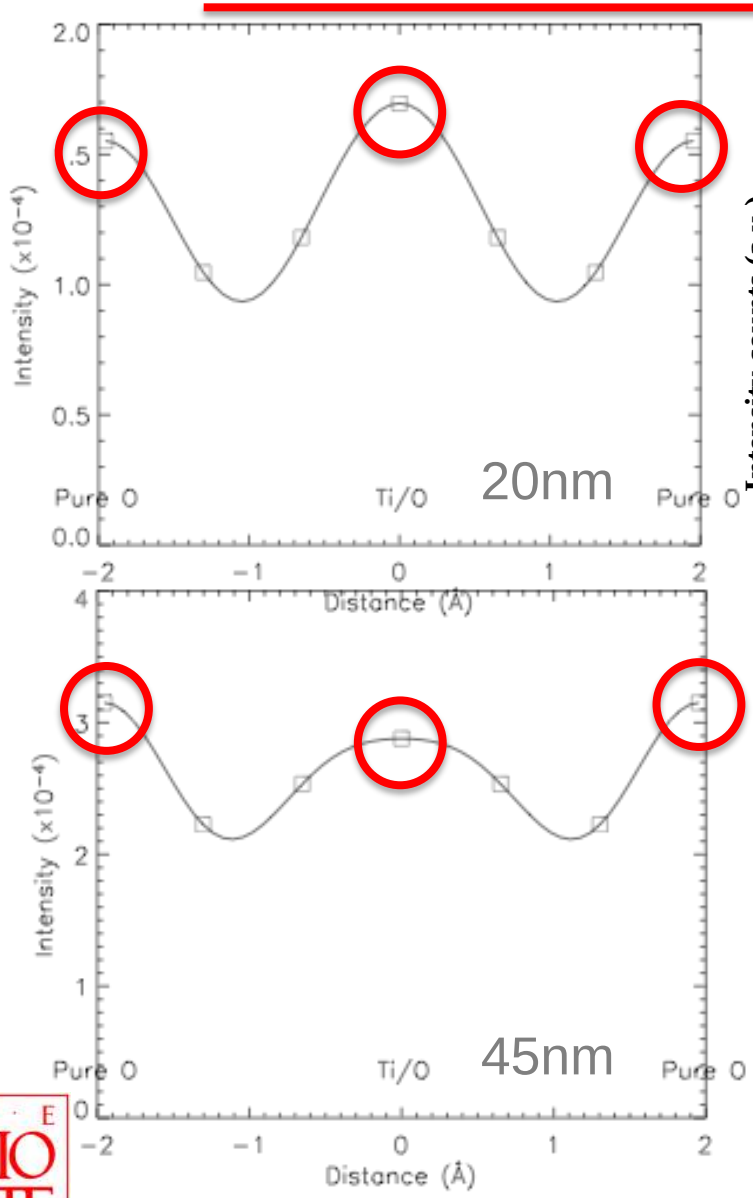

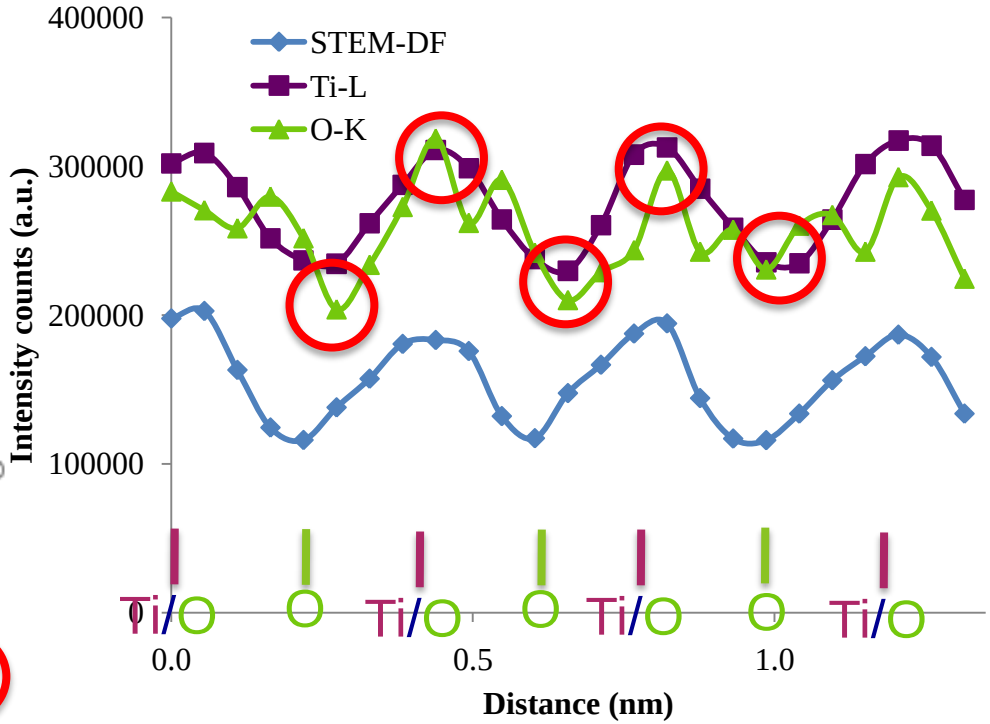

Calculations by Christian Dwyer

- frozen phonon multislice calculation with 8 phonon configurations
- E_0 = 300 keV
- alpha = 17 mrad
- beta = 35 mrad
- no lens aberrations were included
- energy window = 0 to 40 eV above O-K threshold

THE OHIO STATE UNIVERSITY

CAMM

Possible Causes and Remedies

Possible causes:

- *Electron tails*
- *Beam broadening*
- *Column jumping*
  - *Christian Dwyer*
    - *transverse momentum for highly convergent probe*
- *Sample is changing*
  - *Radiation damage*

Possible remedies:

- *Use thinner foils*
- *Use lower accelerating voltages*

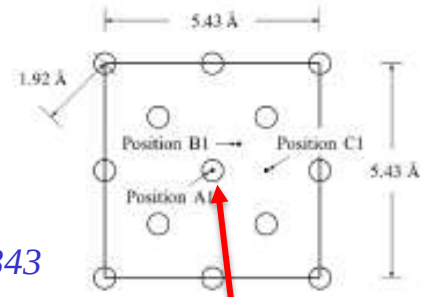

C. Dwyer and J. Etheridge, Ultramicroscopy 96 (2003) 343

Probe on column A1

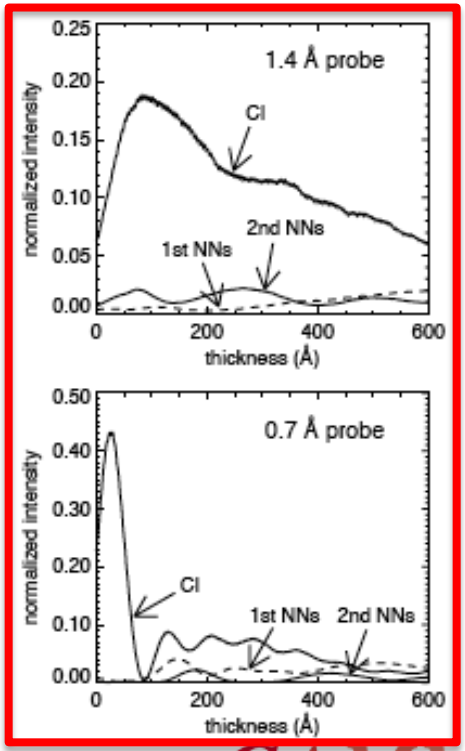

THE OHIO STATE UNIVERSITY

CAMM

Using thin foils of STO to improve spatial resolution

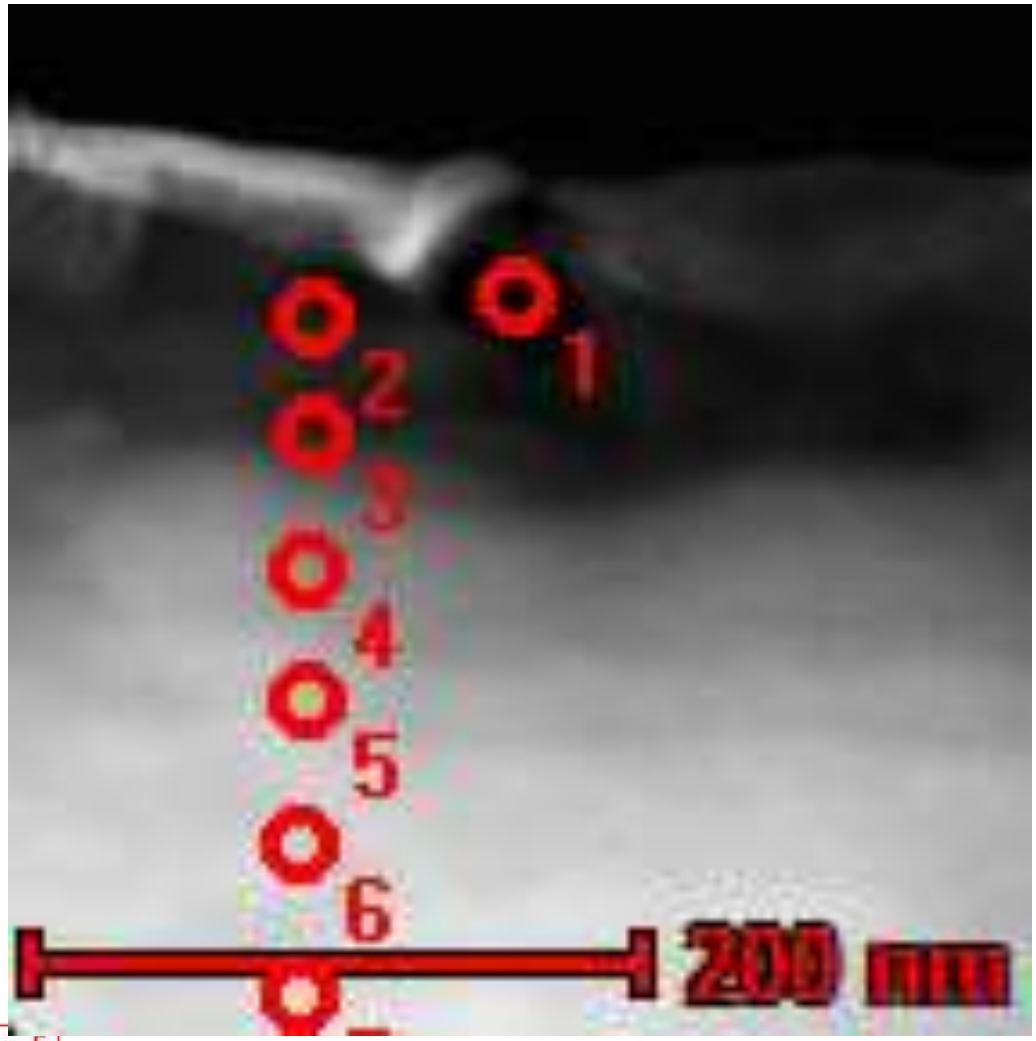

Point 1: 0.03λ
Point 2: 0.21λ
Point 3: 0.14λ
Point 4: 0.20λ
Point 5: 0.24λ
Point 6: 0.22λ
Point 7: 0.26λ

Near Point 1 (thinnest region)

Before

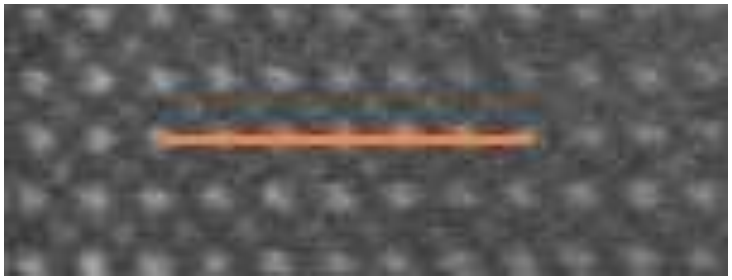

After

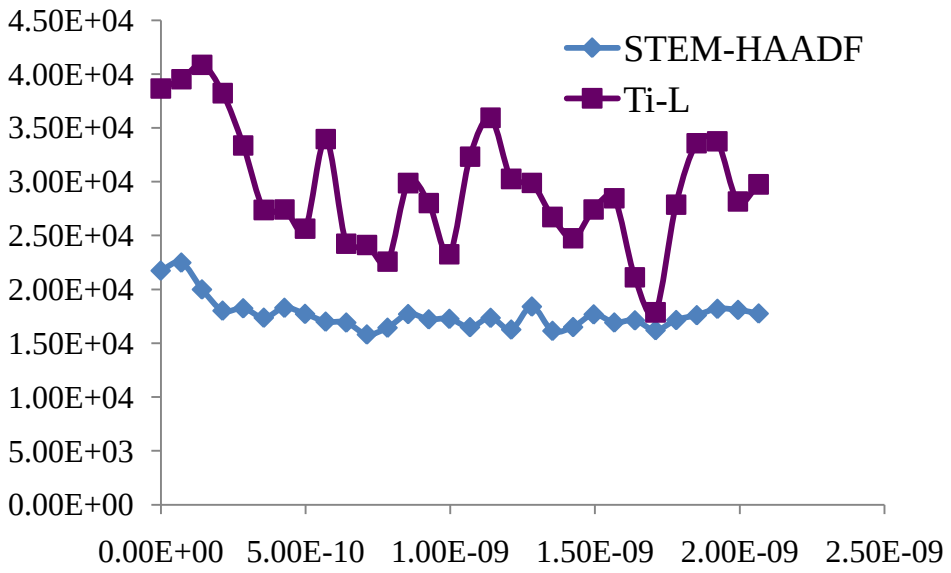

Accelerating Voltage: 300kV

THE OHIO STATE UNIVERSITY

CAMM

Near Point 4

Before

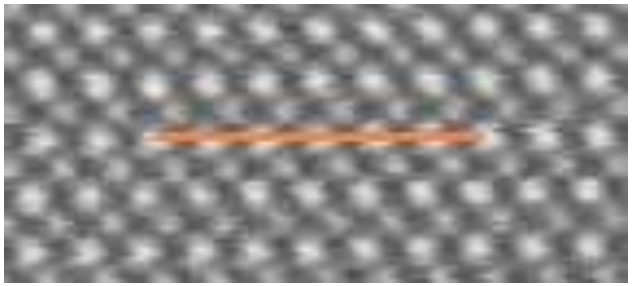

After

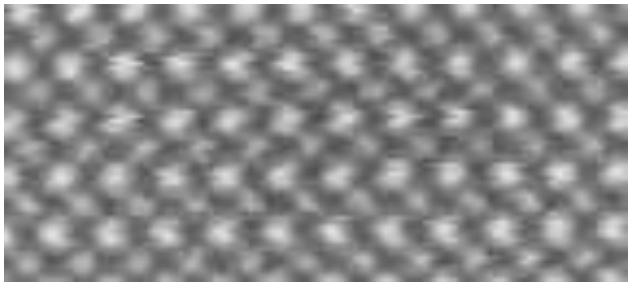

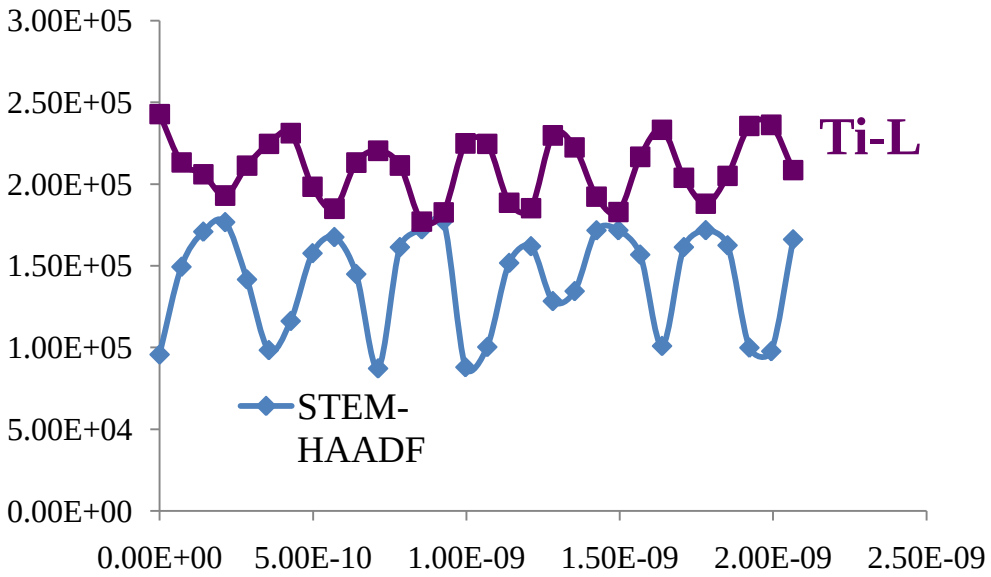

Accelerating Voltage: 300kV

Possible Causes and Remedies – Radiation Damage

Displacement damage:

Direction	Threshold Displacement Energy (eV)		
	Oxygen	Strontium	Titanium
<001>	30	35	115
<110>	60	70	90

Thomas, Marks and Begg, Nucl. Instr. & Methods in Physics Research B, 254, 2007, 211

Maximum Energy Transferred (Windl):

Element	Accelerating Voltage	
	80kV	300kV
O	12eV	53eV
Ti	4eV	18eV
Sr	2eV	10eV

Obvious experiment: repeat measurements at 80kV

STO – lattice image at 80 kV

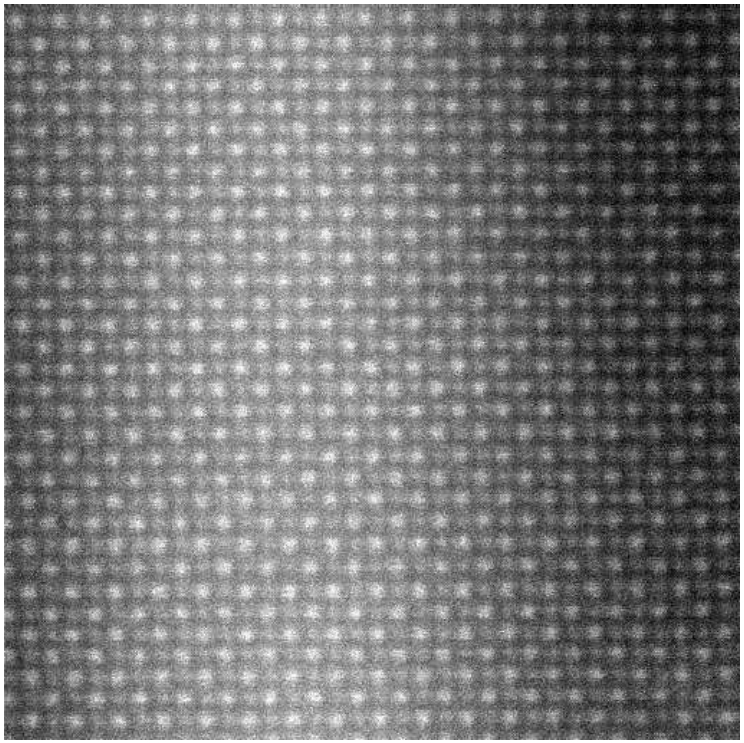

Acquisition conditions (imaging and analysis):

Camera length: 7.2 mm
GIF aperture: 2.5 mm
Conv. semi-angle: 23.9 mrad
Collection semi-angle: ~ 125 mrad
Spot size: 9
C2 Aperture: 70 mm

Mode: non-monochromated
Probe current: 40 pA

Acquisition time: 300 ms/pixel (line profiles)
30 ms/pixel (maps)

Ti/O-O-Ti/O columns

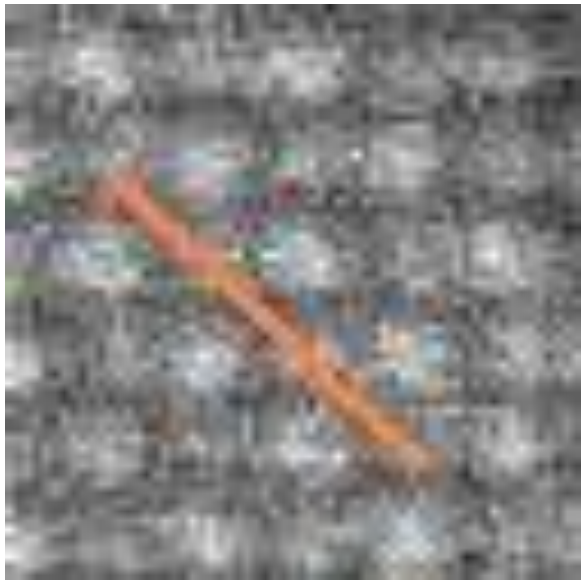

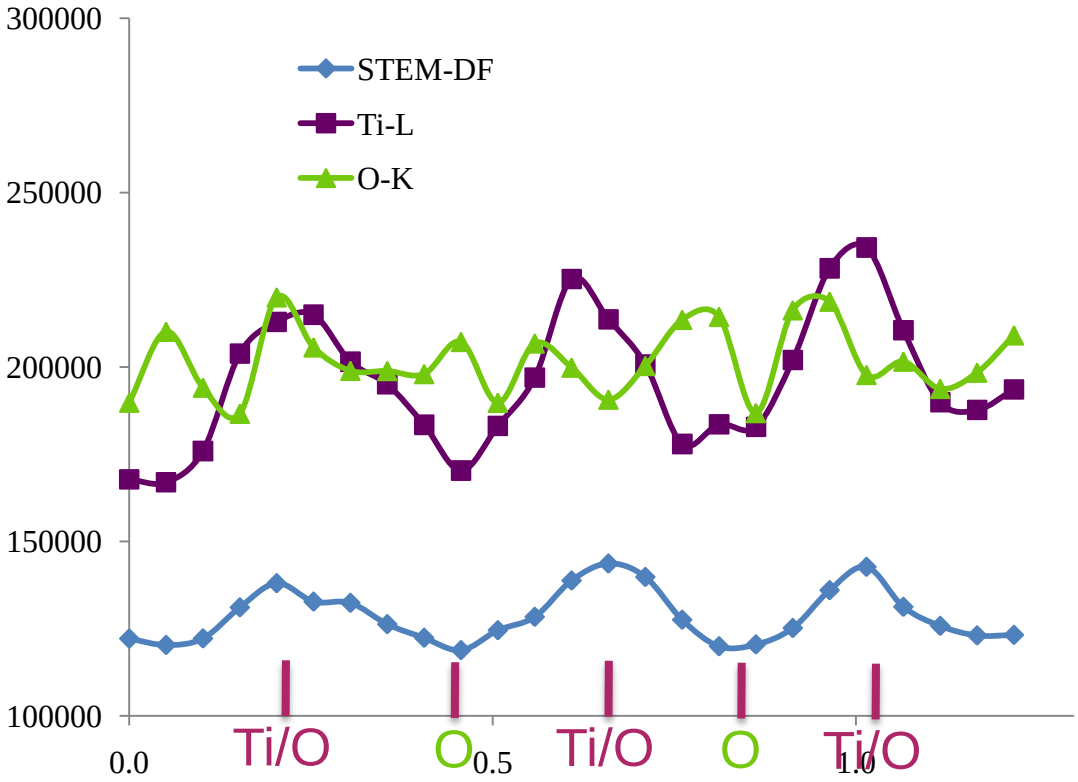

Accelerating Voltage: 80kV

THE OHIO STATE UNIVERSITY

CAMM

Cool New Stuff with Experiments

- *Topics:*
- *Integration modeling with experiments*
- *Useful recent characterization techniques*
- *Limitations with experimental techniques*
  - *sample preparation*
  - *compositional analysis*
- ***What are we (OSU/CAMM) doing?***

Our Efforts aimed at Improving (ST)EM Imaging & Analysis

Features:

- Chromatic-aberration corrected STEM
- Lower voltage to reduce damage
- Make foil and observe in STEM in same microscope
- Accelerated and automated analysis
- Foil thickness measurement – supplied to modeling backup

The FEI Magellan SEM, which is the basis of the Helios NG, the proposed acquisition.

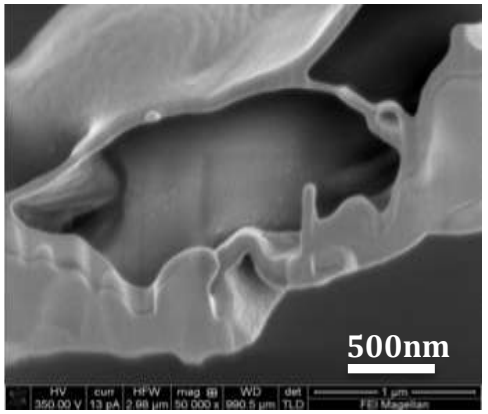

A thin section of pig skin prepared at room temperature by use of a dual-beam FIB imaged (as-FIB'd) in an FEI Magellan, with an accelerating voltage of 350V.

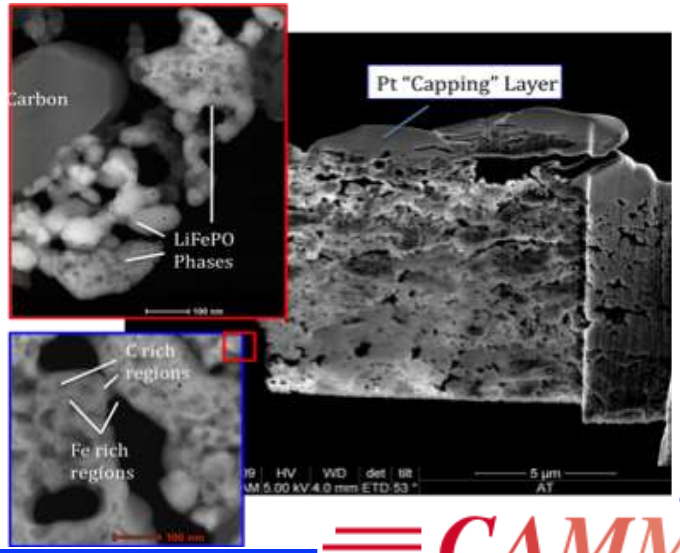

STEM images of an FIB extracted cross-section of a LiFePO cathode from a commercial Li ion battery showing the ability of technique to prepare thin-foils of this delicate, highly porous, multi-scale structure of these cathode materials.

THE OHIO STATE UNIVERSITY

CAMM

Our Efforts at Novel Approaches to Improving Laser-assisted Atom Probe Analysis

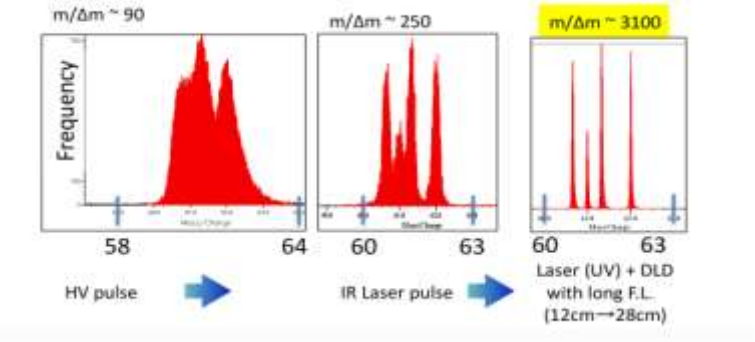

Dramatic improvement in mass spectrum (mass to charge ratio versus number) of W with a decrease in λ, and by use of an improved PSD).

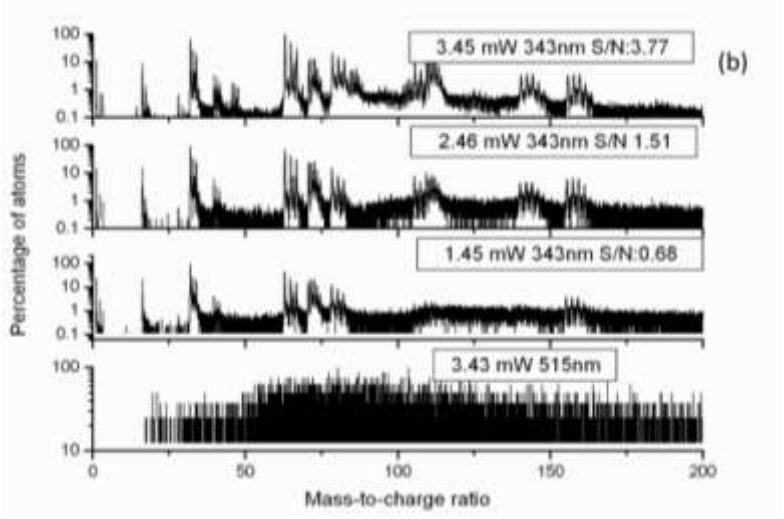

Similar improvement in mass spectrum of ZnO with a decrease in λ

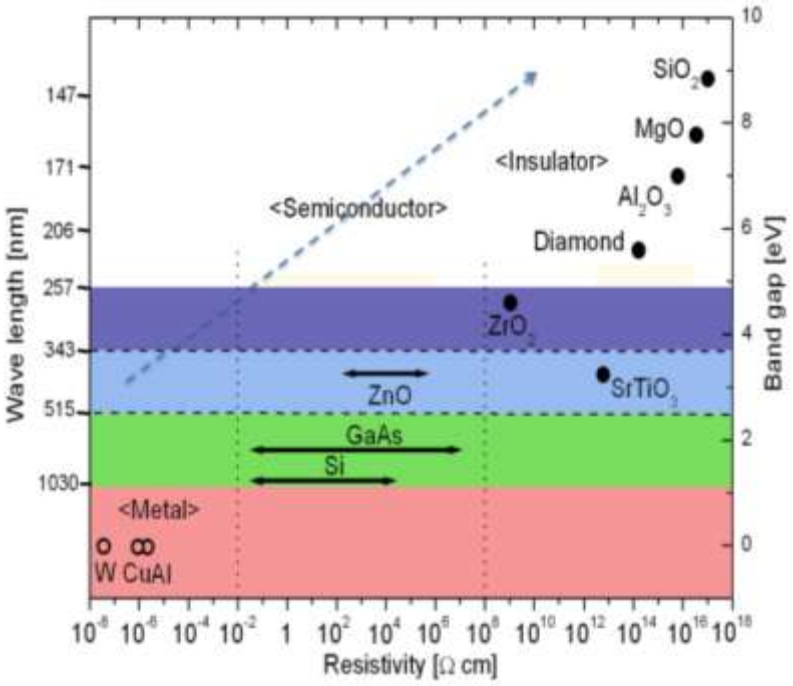

Correlation of laser wavelengths used for different materials and corresponding band gap energies with their electrical resistivities

Question: Have we reached the maximum mass resolution with UV lasers or not?

THE OHIO STATE UNIVERSITY

CAMM

Cool New Stuff with Experiments

Importance of Coupling of Efforts between Computational folks (unimaginative) and Experimentalists (creative):

- *Provision of accurate and physically relevant mechanistic data*
- *Computational assistance in interpreting experimental data*
- *Validation of predictions – at scale!!*

Analysis of nanoscale multilayers / Ti/Nb multilayers

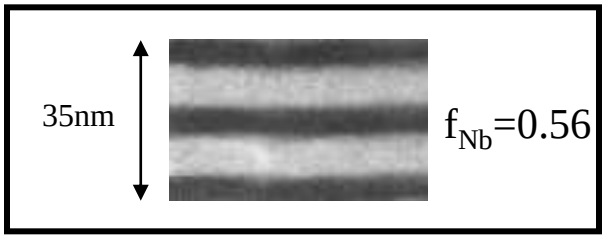

hcp Ti / *bcc* Nb

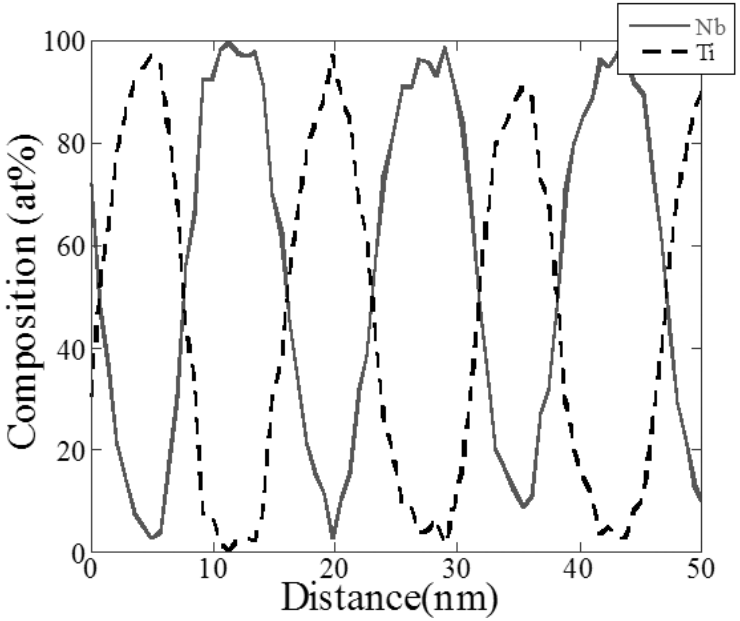

XEDS

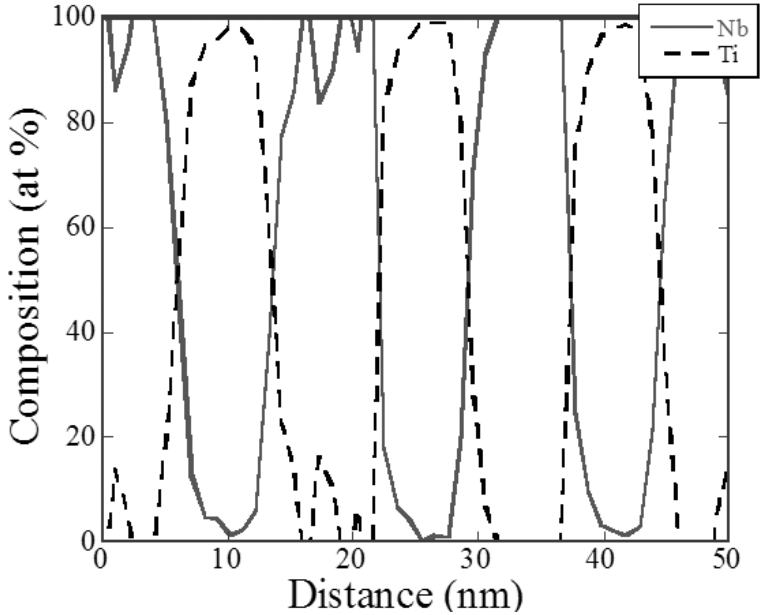

EELS

Layer thickness : 7nm Ti / 9nm Nb

EELS profile on Sr-O-Sr

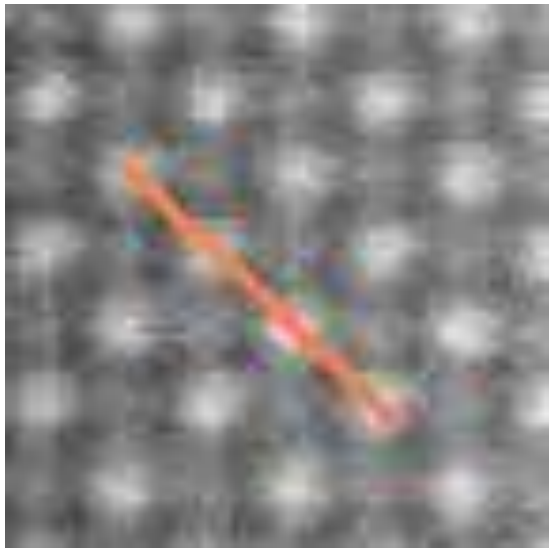

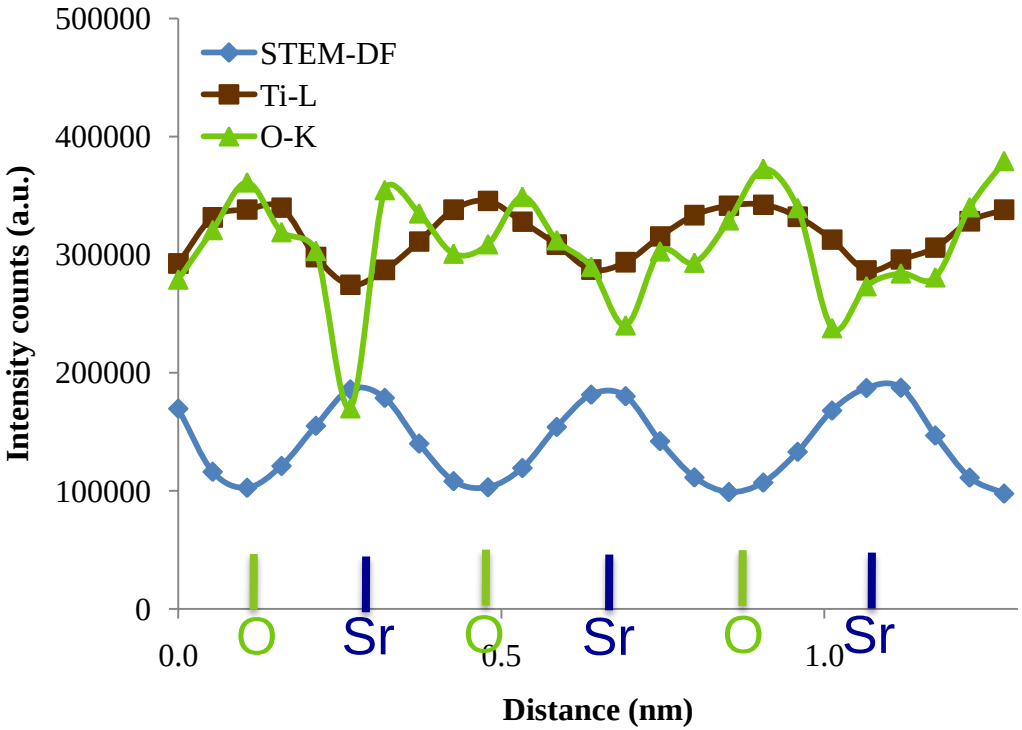

Accelerating Voltage: 200kV

THE OHIO STATE UNIVERSITY

CAMM

EELS profile on Ti/O-O-Ti/O

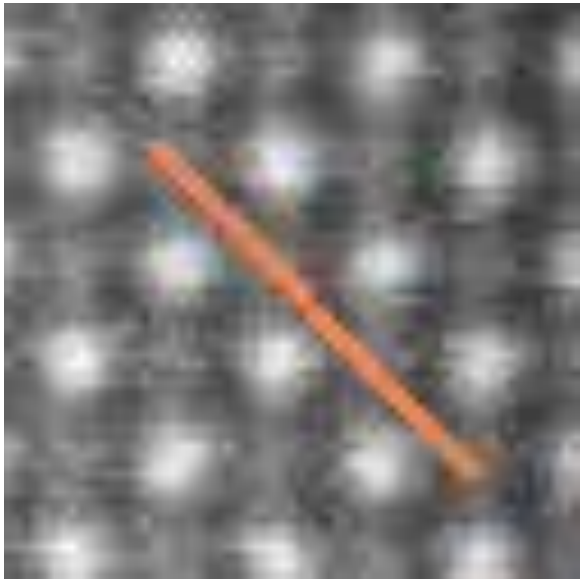

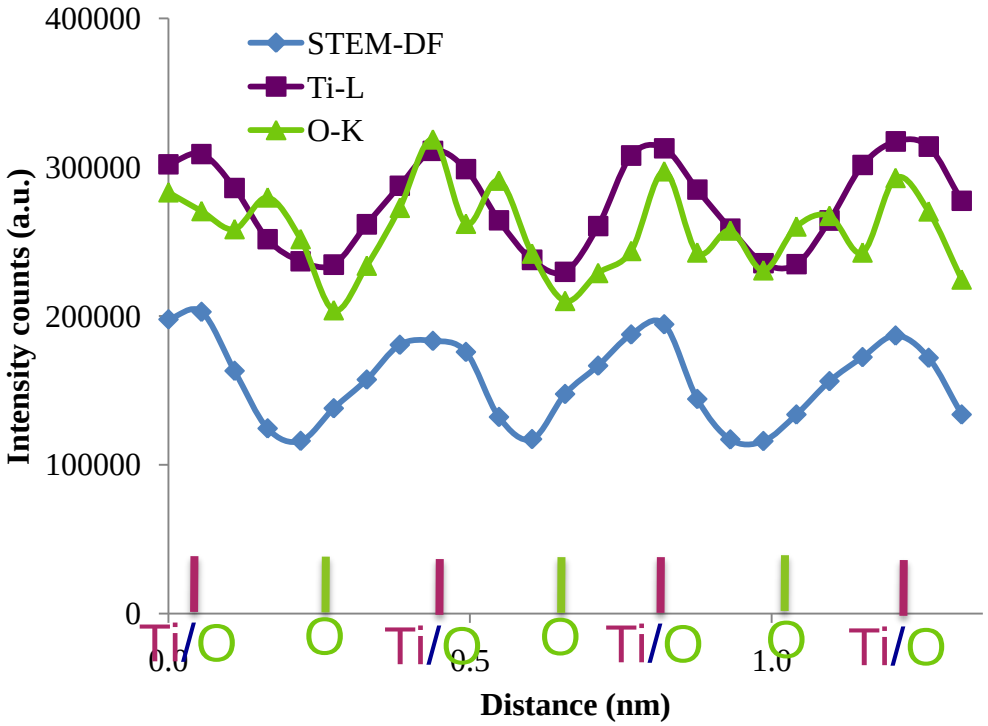

Accelerating Voltage: 200kV

THE OHIO STATE UNIVERSITY
CAMM

OSU Studies: Spectrum Image

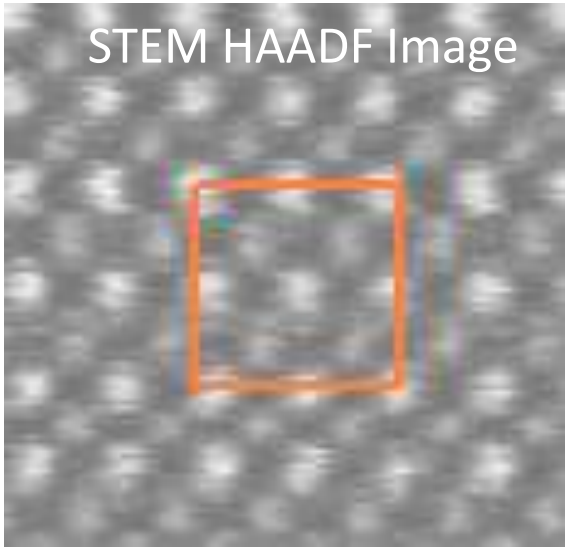

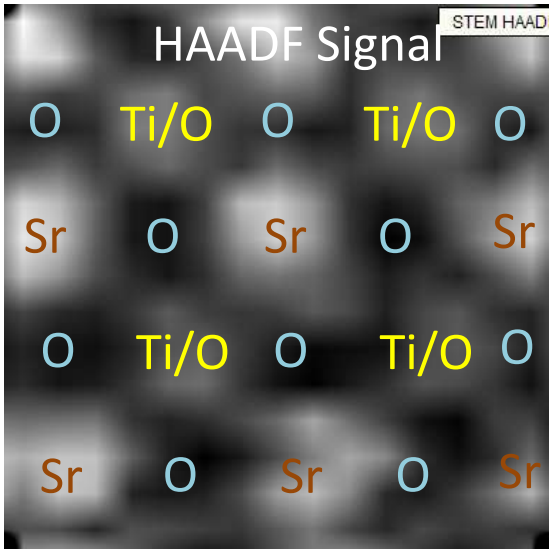

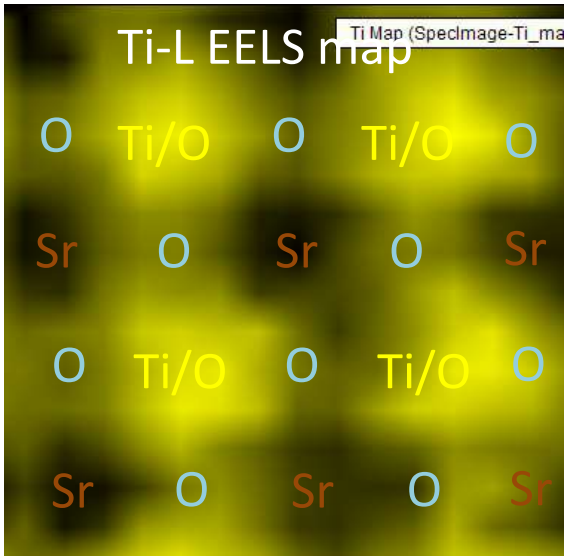

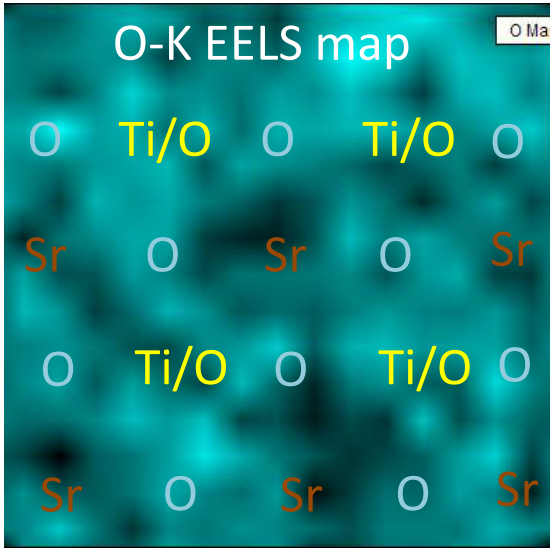

THE OHIO STATE UNIVERSITY

CAMM

Quantitative Analysis

Calculation

The relation between the concentration and characteristic X-ray intensity is given by;

$$C = \left\{ \frac{1}{K\left(\frac{\sigma\omega a\varepsilon}{A}\right)} \right\} \left(\frac{I}{t}\right)$$

Thin film criterion;

$$\frac{C_A}{C_B} = \frac{A_A(\sigma\omega a\varepsilon)_B}{A_B(\sigma\omega a\varepsilon)_A}\left(\frac{I_A}{I_B}\right)$$

$$\frac{C_A}{C_B} = k_{AB}\left(\frac{I_A}{I_B}\right)$$

Cliff-Lorimer factor;

$$k_{AB} = \frac{(\sigma\omega a\varepsilon / A)_B}{(\sigma\omega a\varepsilon / A)_A}$$

Experiment

The concentration is given by;

$$C = \frac{n}{V}$$

Atom ratio;

$$R = \frac{n_A / V_A}{n_B / V_B}$$

Atom ratio, R_s assuming specimen thickness is constant and where h is layer width;

$$R_S = \left(\frac{h_A}{h_B}\right)\frac{n_A / V_A}{n_B / V_B}$$

Experimental Cliff-Lorimer factor;

$$k_{AB} = \left\{ \frac{I_A^{Total} / I_B^{Total}}{R_s} \right\}$$

Quantitative analysis

XEDS

$$\frac{C_A}{C_B} = k_{AB}\left(\frac{I_A}{I_B}\right)$$

EELS

$$\frac{N_A}{N_B} = \frac{I_A(\beta\Delta)\sigma_B(\beta\Delta)}{I_B(\beta\Delta)\sigma_A(\beta\Delta)}$$

Partial cross-sections for EELS were measured using an experimental spectrum in Gatan DM software

XEDS

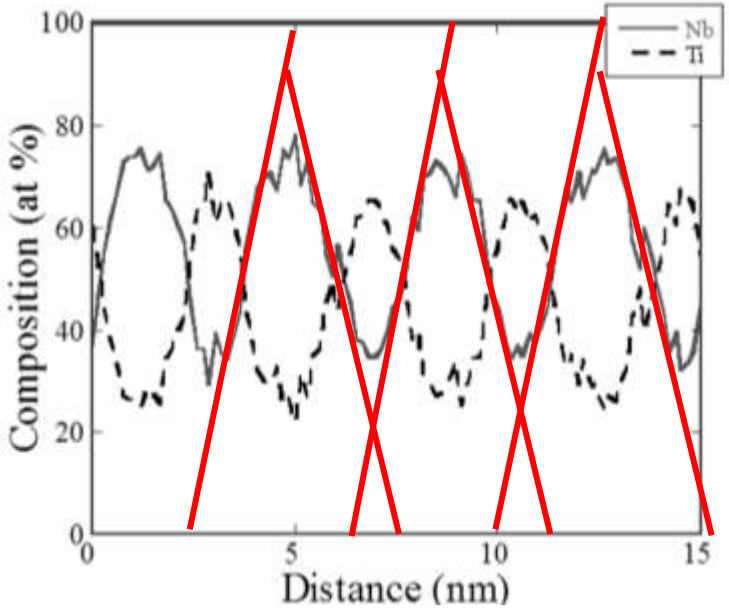

Atom probe

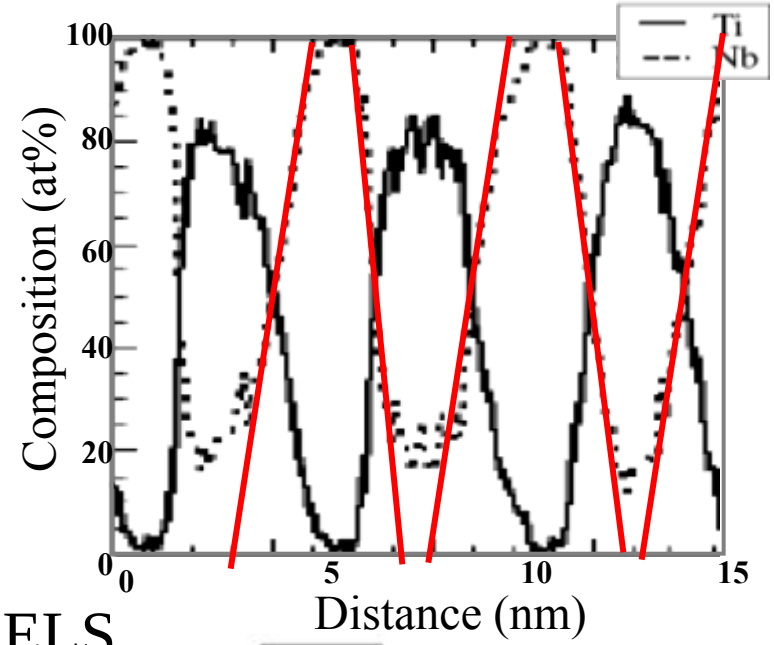

EELS

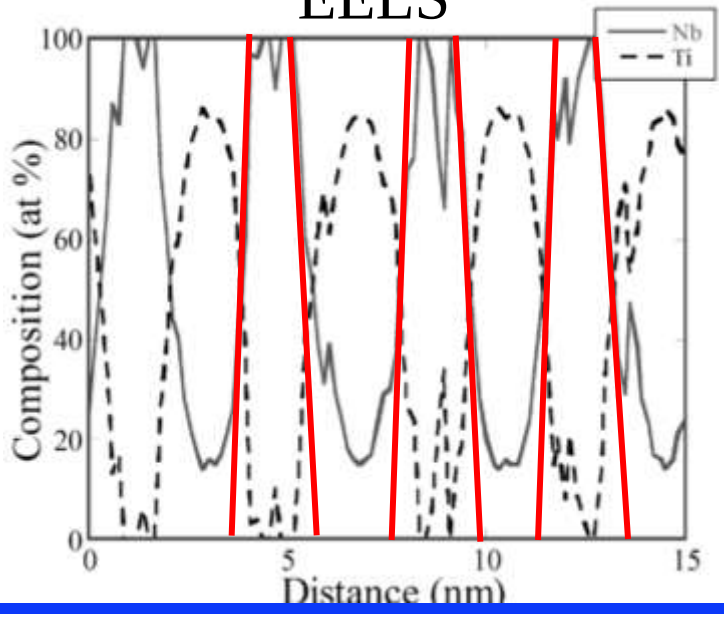

THE OHIO STATE UNIVERSITY

CAMM

Knowledge of Sample?

Sr deficient: phase separation – oxygen vacancies

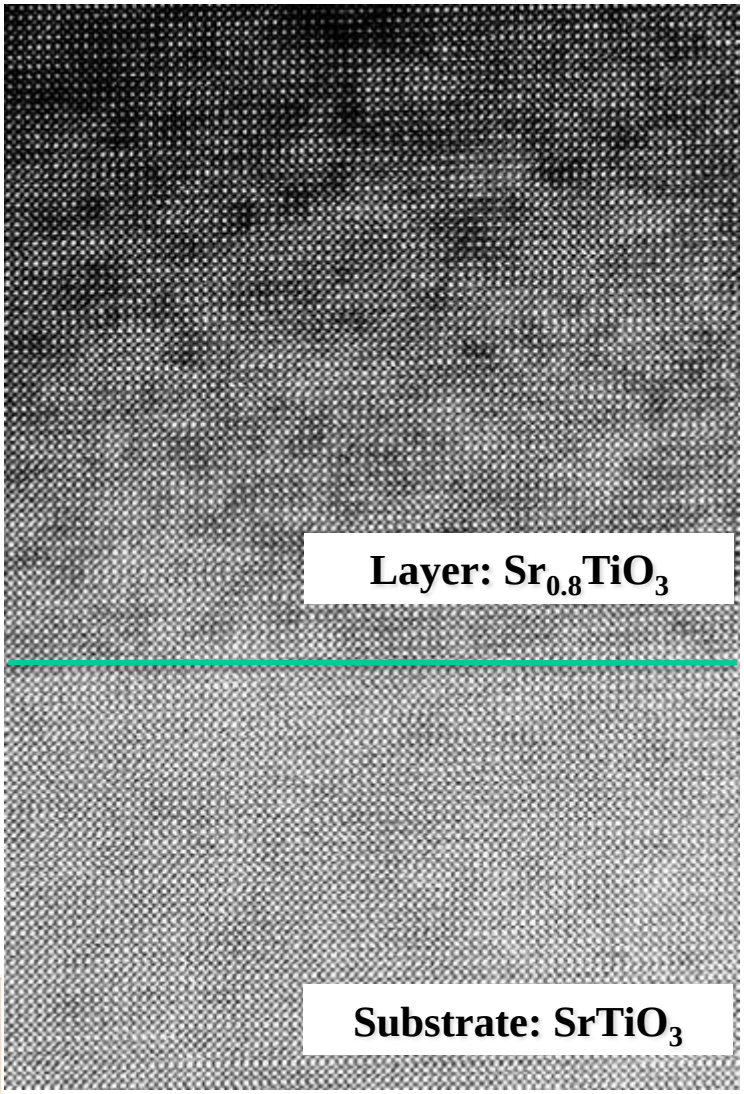

Do the STO layers adjust composition because of the constraints of the interface with BTO?

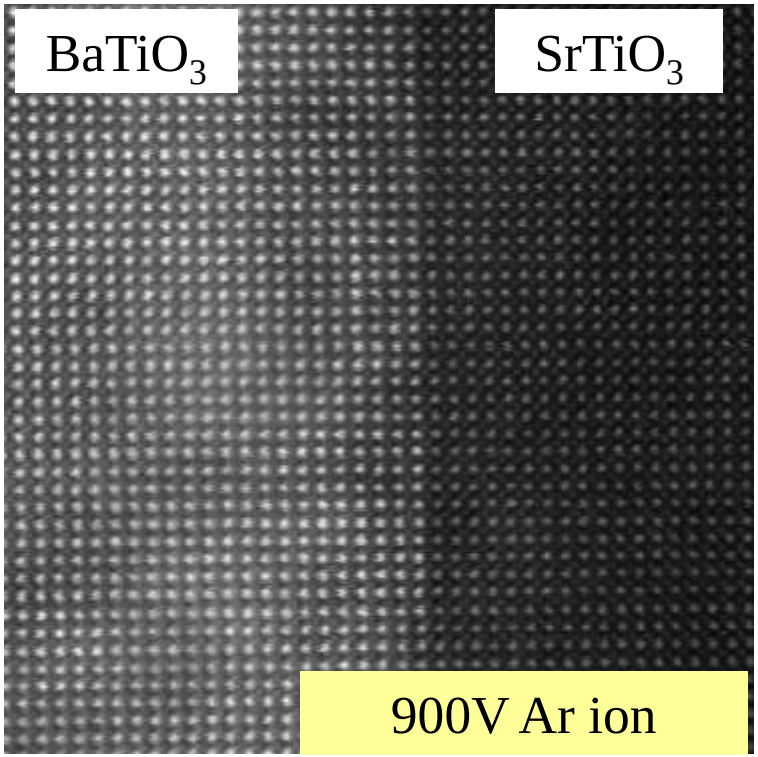

THE OHIO STATE UNIVERSITY

CAMM

Experimental study of crystal nucleation in magma

Julia E Hammer
Dept. Geology and Geophysics
School of Ocean and Earth Science and Technology
University of Hawaii
http://www.soest.hawaii.edu/GG/FACULTY/JHAMMER/

Carrie Brugger, *University of Hawaii*
Tom Sharp, *Arizona State University*
Malcolm Rutherford, *Brown University*

NSF EAR-Geochemistry and Petrology CAREER program
NASA- Mars Fundamental Research Program

Joint AFRL/AOARD/LLNL Workshop on Nucleation During Solid-Solid Phase Transformations in Metallic Systems: Current Understanding and Future Directions

Maui, Hawaii May 2 - 7, 2010

photo: USGS

pahoehoe
a'a

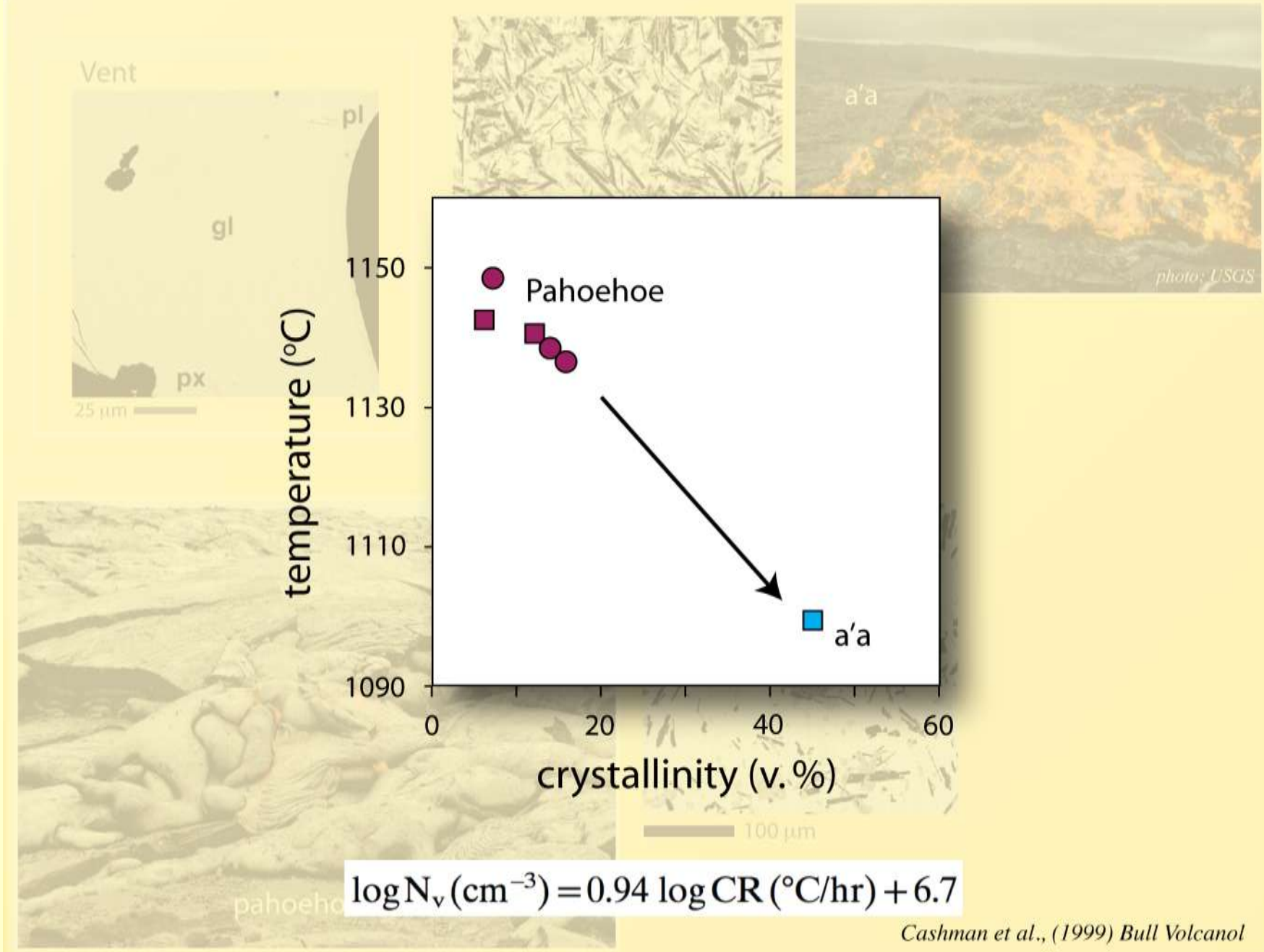

$$\log N_v\,(\mathrm{cm}^{-3}) = 0.94 \log \mathrm{CR}\,(^{\circ}\mathrm{C/hr}) + 6.7$$

Cashman et al., (1999) Bull Volcanol

Merapi
andesite

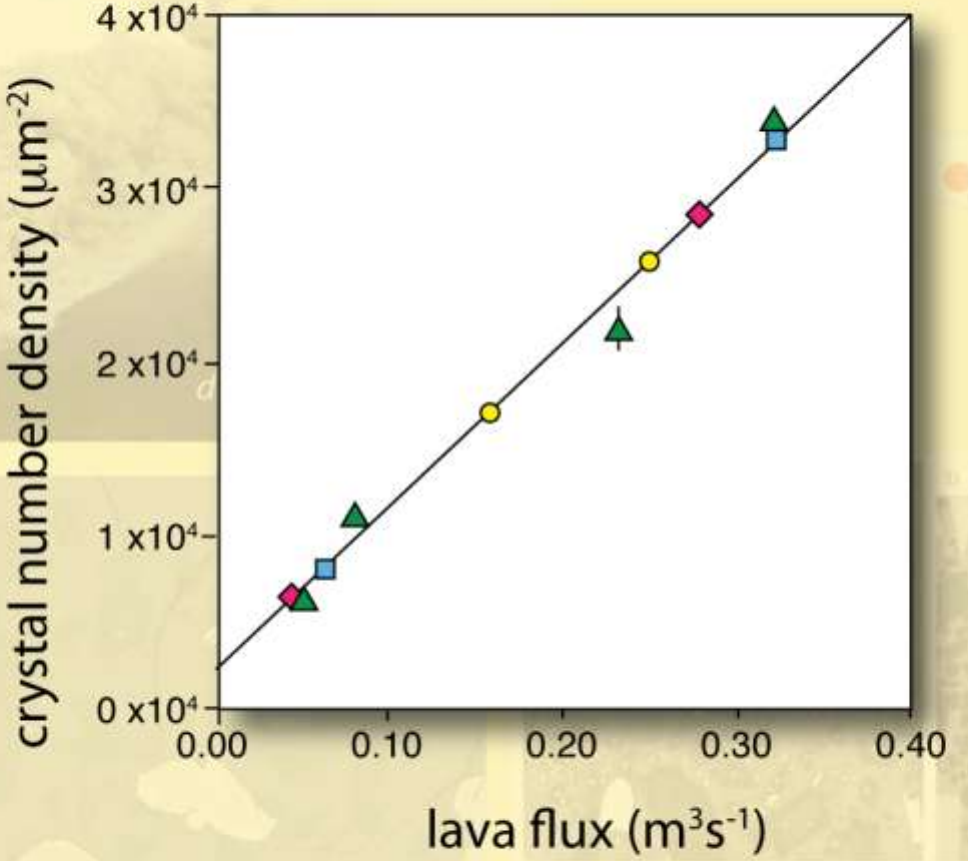

Hammer et al. (2000) J Volcanol Geotherm Res

3D aspect ratio
(Underwood 1968)

interface area per unit
phase volume= 2N/ϕ

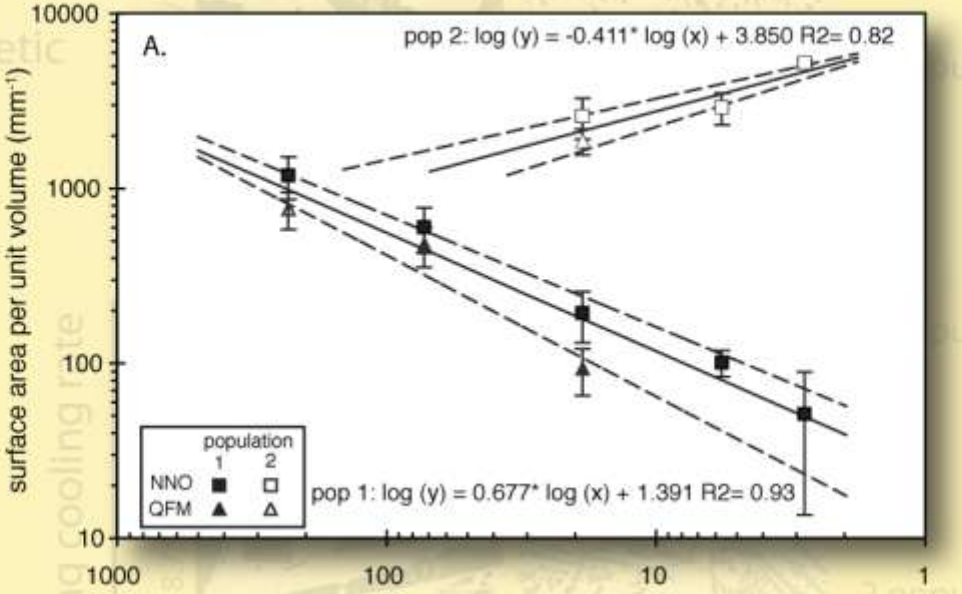

divergence of cpx surface area per unit volume among populations

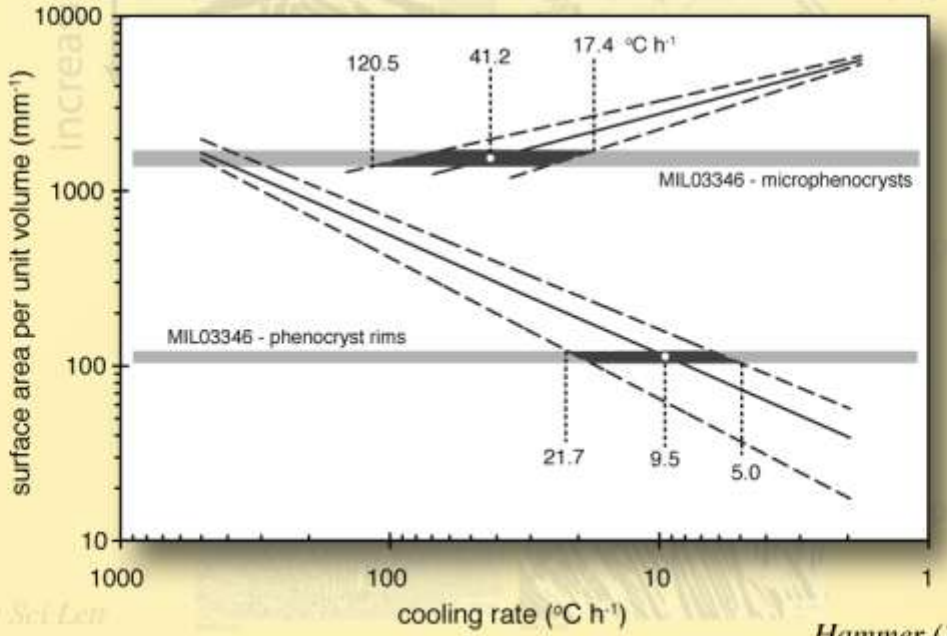

textural geospeedometer applied to Martian meteorite MIL03346

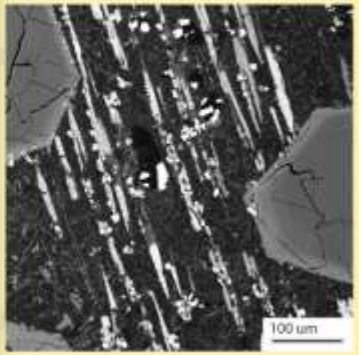

Hammer (2009) Meteoritics Planet Sci

Crystallization mechanisms

nucleation

growth

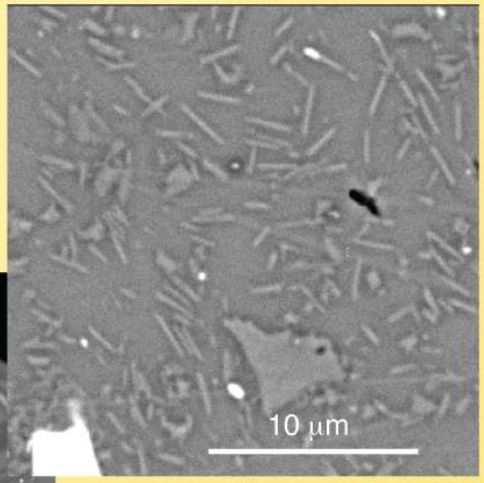

Pinatubo 1991 surge, dacite

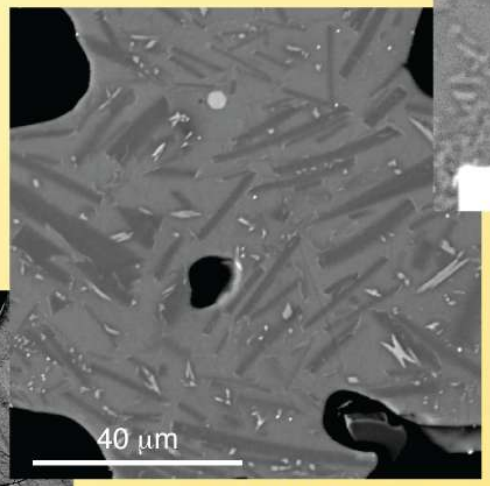

Gareloi 1929 pf, trachyandesite

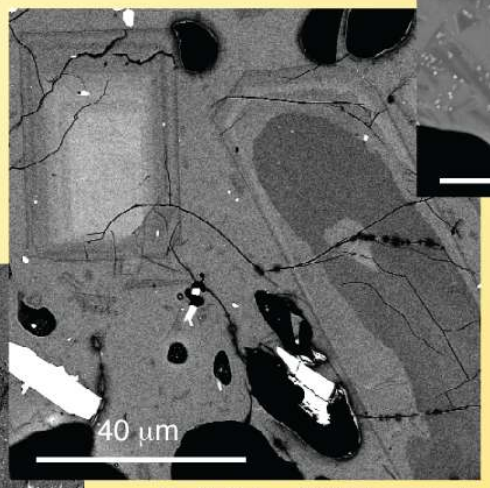

Mt. St Helens 1980 dome, dacite

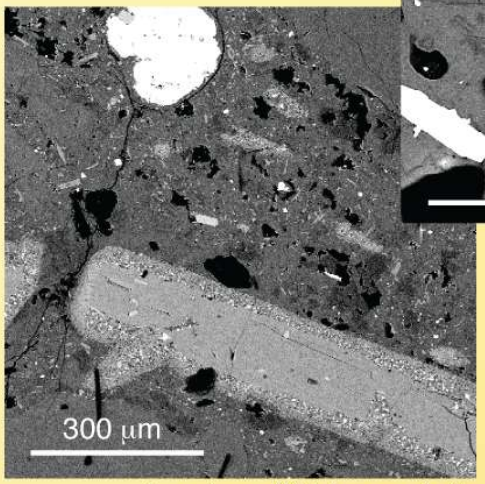

Bezymianny 1956 dome, andesite

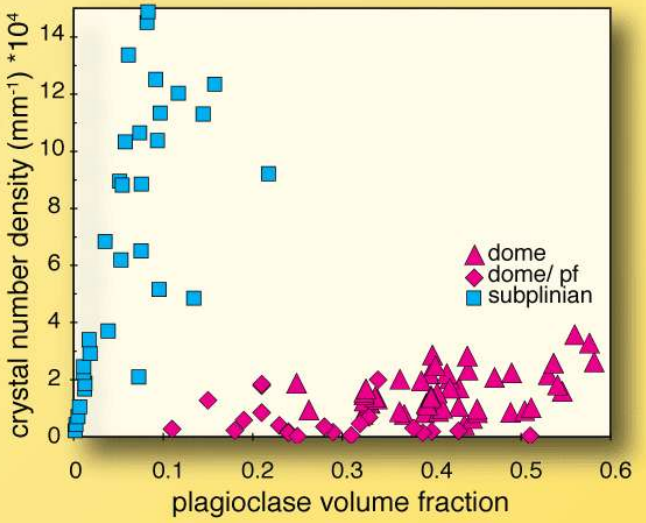

Driving forces for crystallization

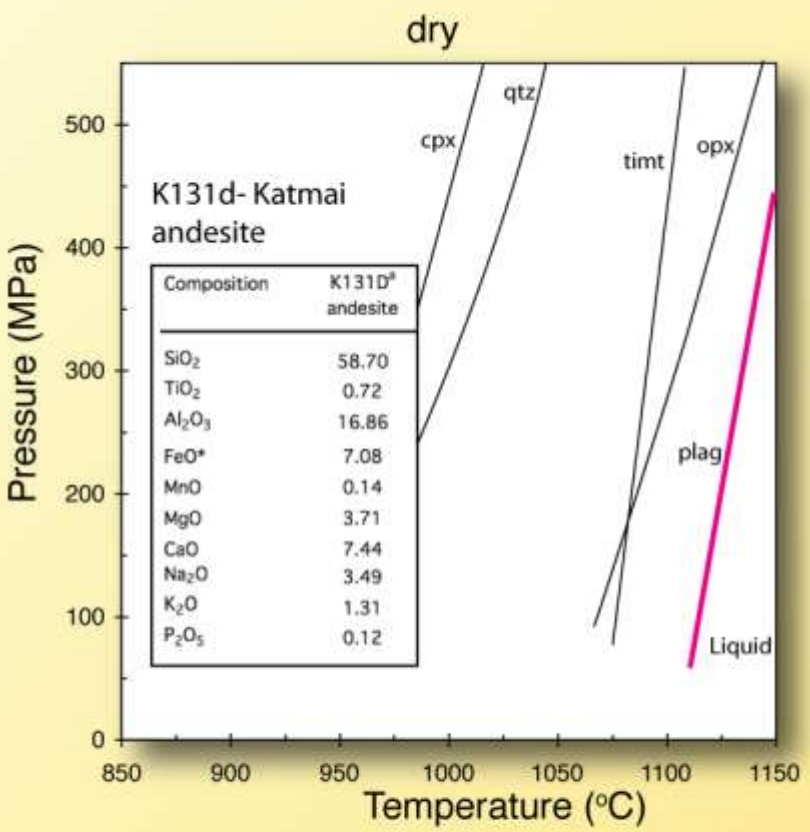

MELTS output, Ghiorso et al. 1995

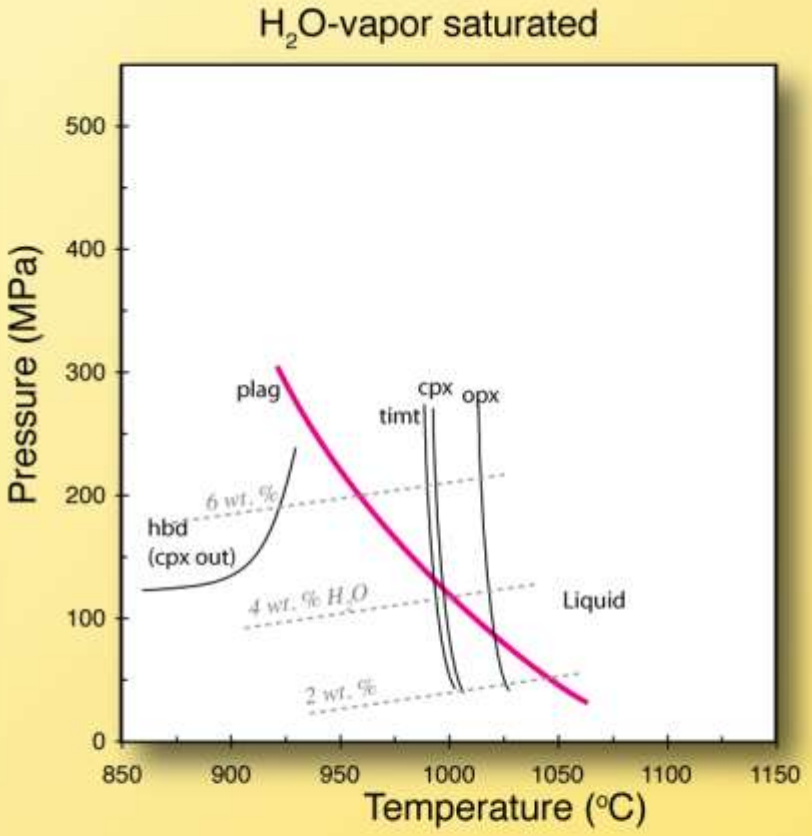

Hammer et al. (2002) Contributions to Mineralogy and Petrology

- plagioclase: tricilinc framework silicate
  clinopyroxene: monoclinic chain silicate
  orthopyroxene: orthorhombic chain silicate
  hornblende: monoclinic chain silicate
  titanomagnetite: cubic Fe-Ti oxide
  quartz: trigonal framework silicate

$CaAl_2Si_2O_8$- $NaAlSi_3O_8$
$(Ca, Na)(Mg,Fe^{2+}, Al, Fe^{3+}, Ti)[(Si,Al)_2O_6]$
$MgSiO_3$-$FeSiO_3$
$[\ ][Ca_2][Fe_4^{2+}Al][(OH)_2[AlSi_7O_{22}]$-$[\ ][Ca_2][Mg_4Al][(OH)_2[AlSi_7O_{22}]$
Fe_3O_4-Fe_2TiO_4
SiO_2

Apparatus

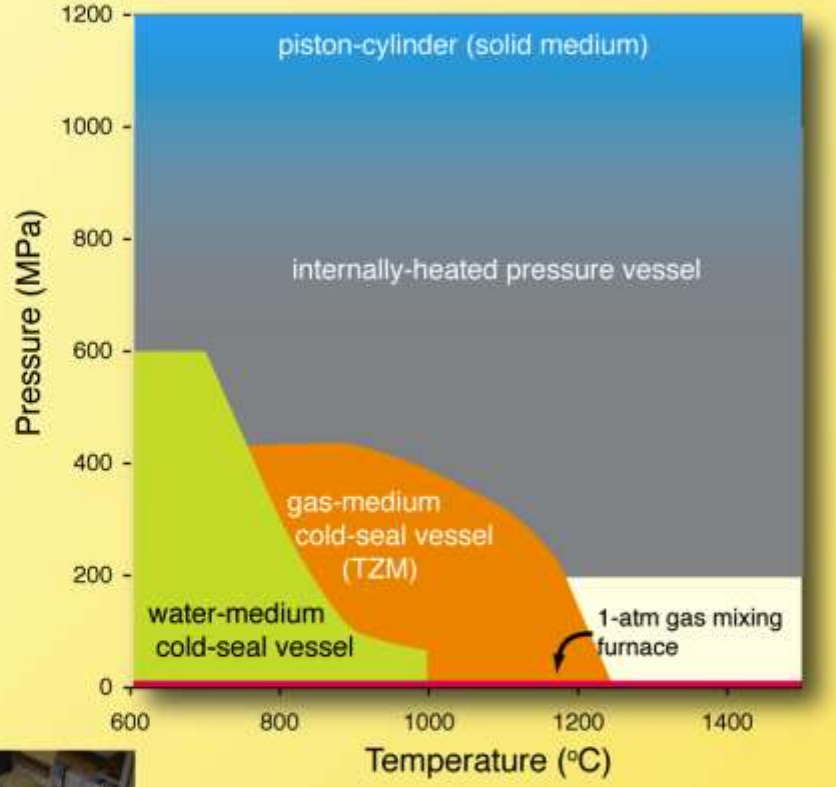
piston-cylinder (solid medium)
internally-heated pressure vessel
gas-medium
cold-seal vessel
(TZM)
water-medium
cold-seal vessel
1-atm gas mixing
furnace
Pressure (MPa)
Temperature (°C)
1200
1000
800
600
400
200
0
600
800
1000
1200
1400

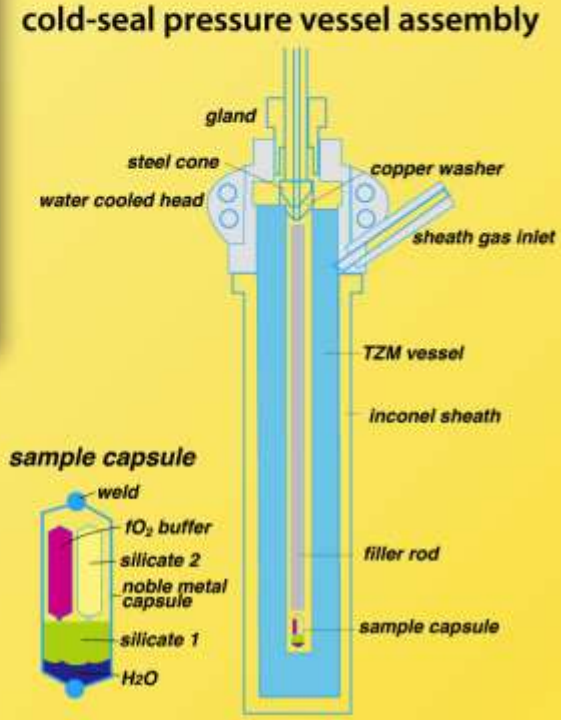
cold-seal pressure vessel assembly
gland
steel cone
water cooled head
copper washer
sheath gas inlet
TZM vessel
inconel sheath
filler rod
sample capsule
sample capsule
weld
fO_2 buffer
silicate 2
noble metal capsule
silicate 1
H_2O

Objectives

Transitions in eruptive style

Lava flow dynamics

Magma ascent rate

Magma degassing

Predictive power of microtexture

- Nucleation rate as a function of undercooling
- Nucleation response to continuous change in temperature or pressure
- Heterogeneous nucleation of major rock-forming minerals

Effects of shear flow

Metastable nucleating phases

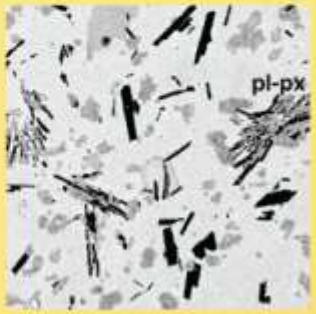

Experiment types

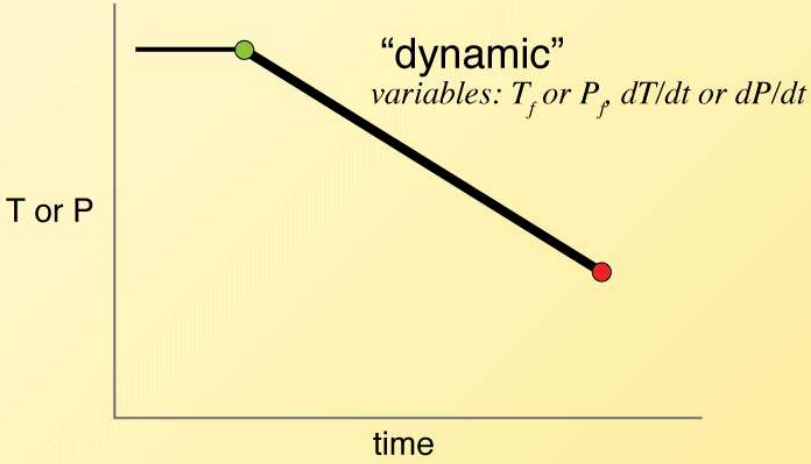

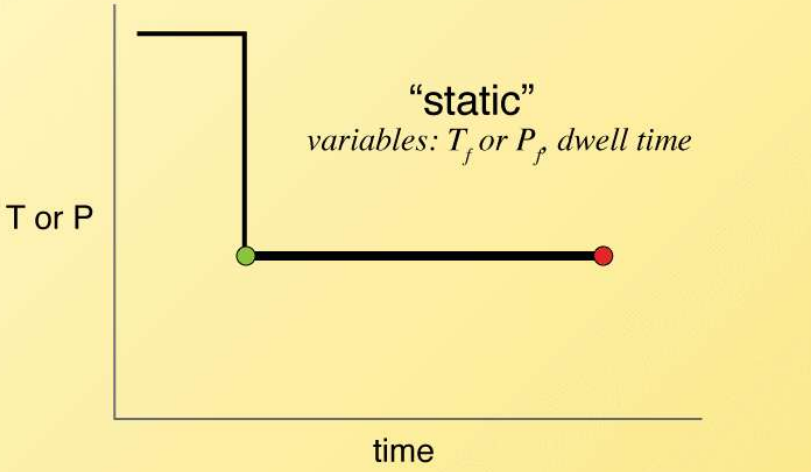

Experiment type determines application

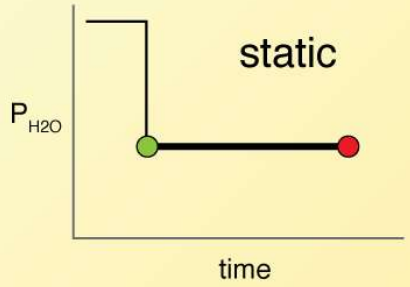

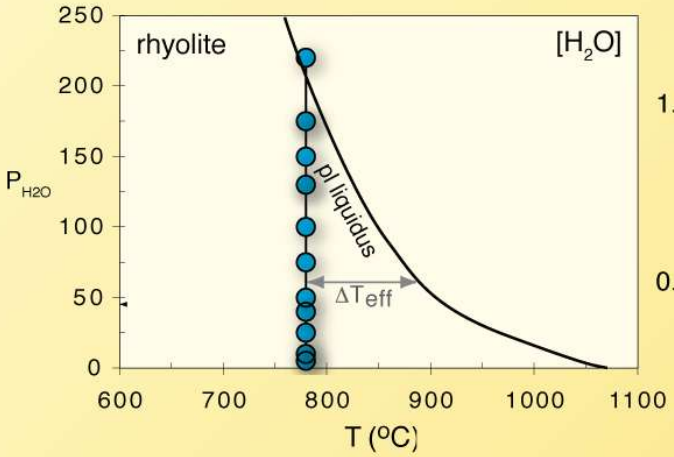

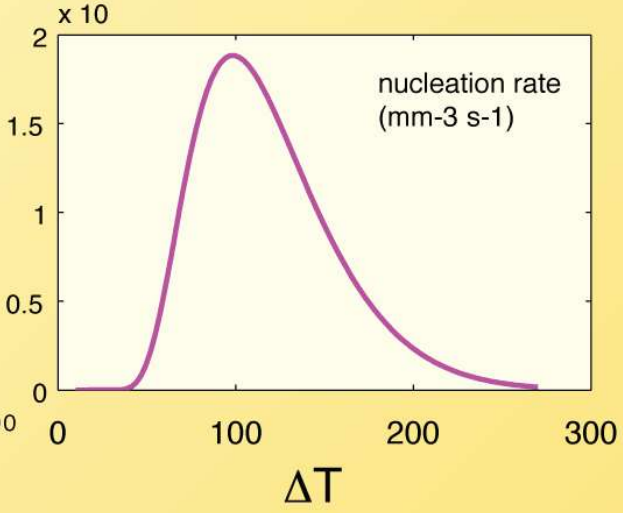

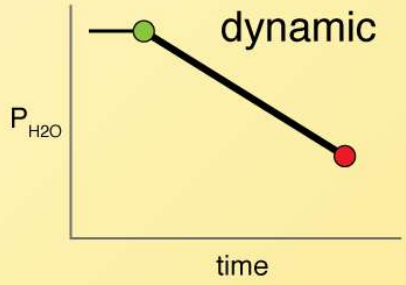

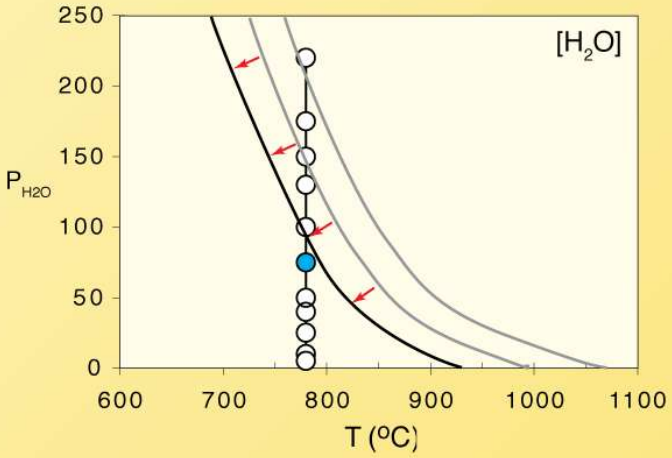

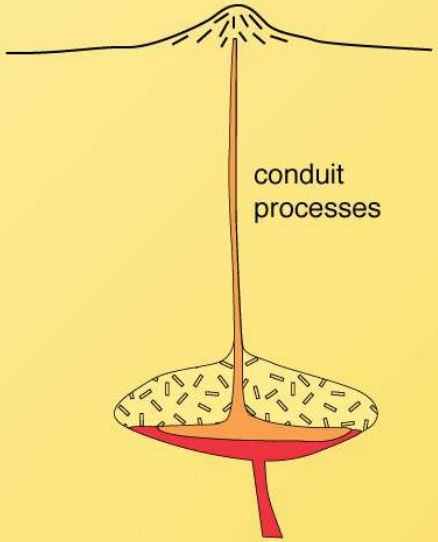

Decompression of H_2O-saturated rhyolite

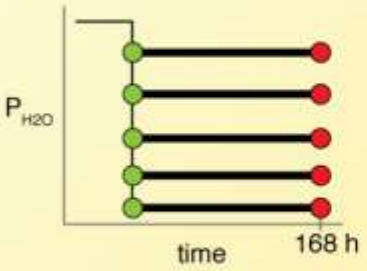

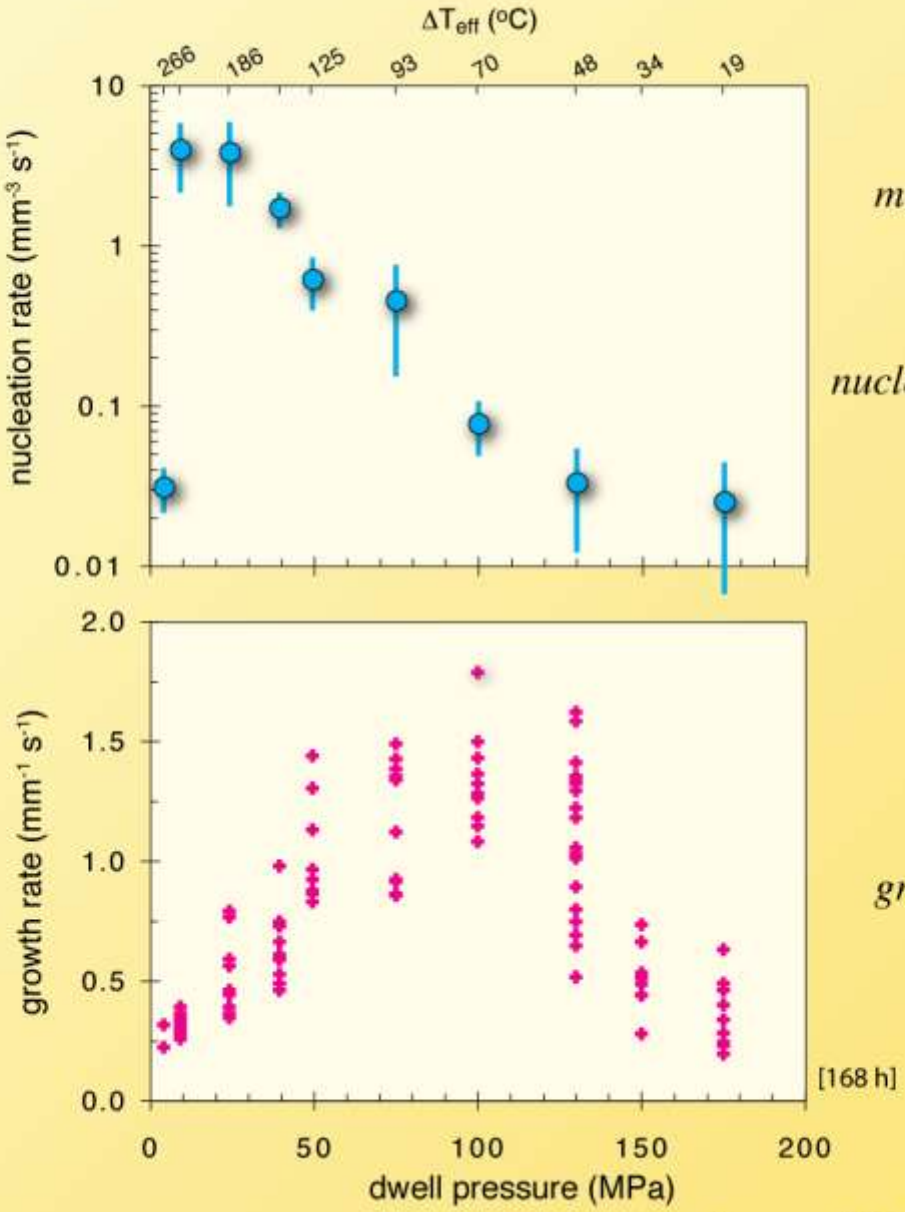

mean size $s_n = \sqrt{\frac{\phi}{N_A}}$

nucleation rate $I = \frac{N_A}{s_n \tau}$

N_A, *number per area*
τ, *dwell time*
ϕ, *area fraction*

growth rate $G = \frac{length}{\tau}$

Hammer and Rutherford (2002) J Geophysical Research

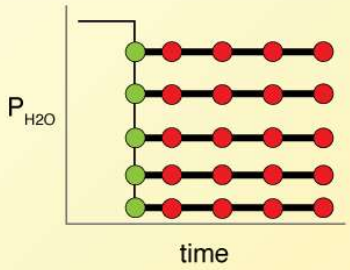

nucleation rate
(mm^{-3} s^{-1})

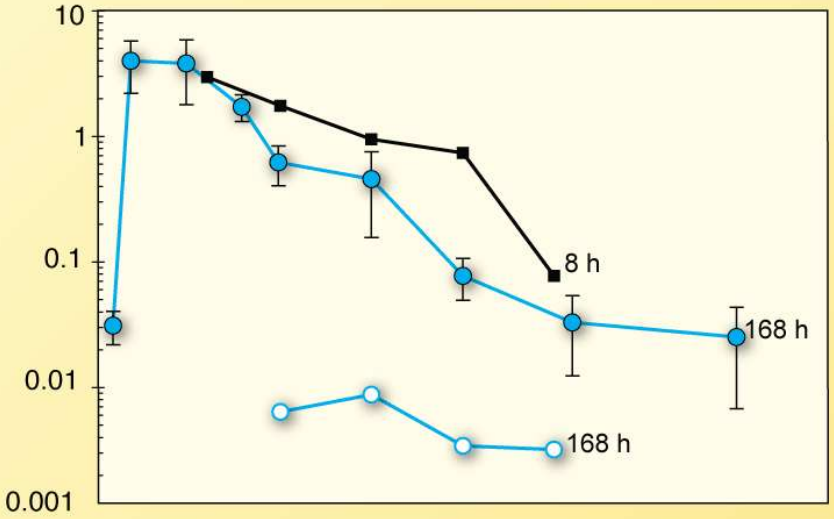

different nucleation rates
in two studies

growth rate
(mm s^{-1})

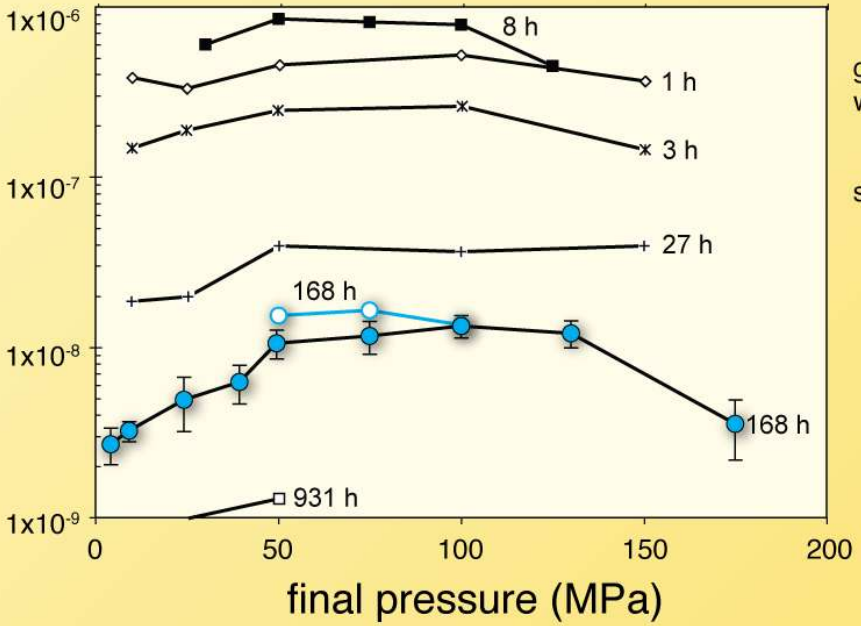

growth rate sharply declines
with increasing dwell time

similar growth rates in two studies

Hammer and Rutherford 2002
Couch 2003

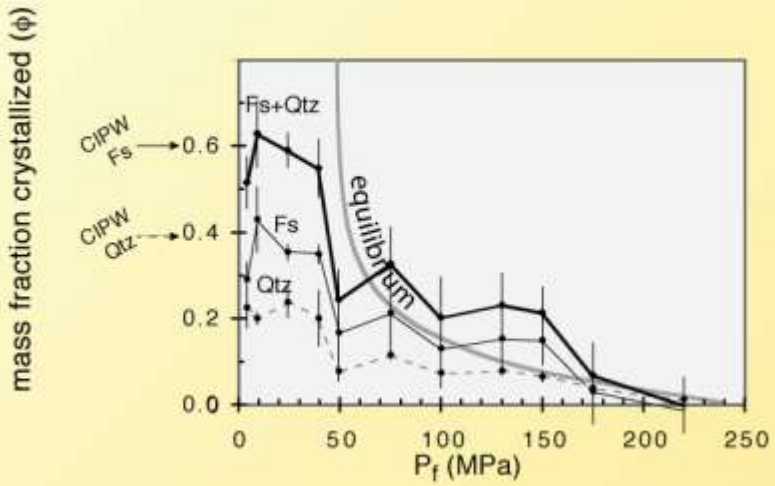

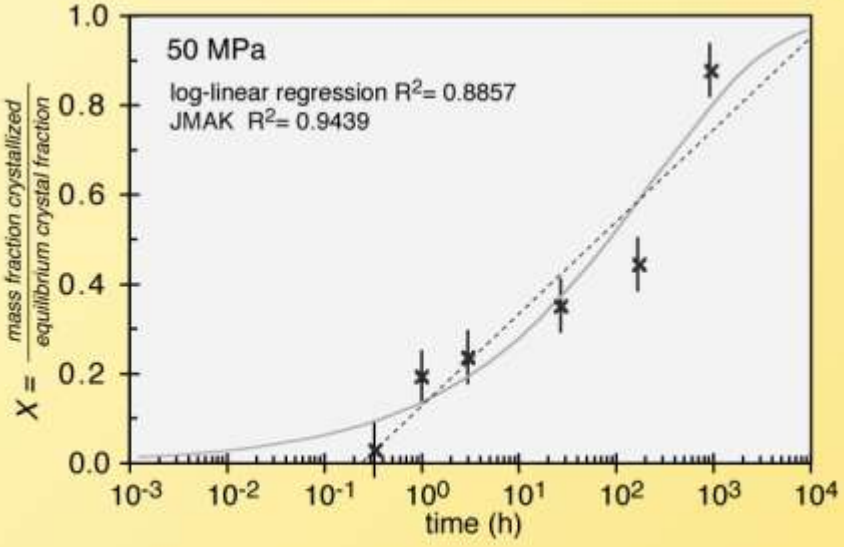

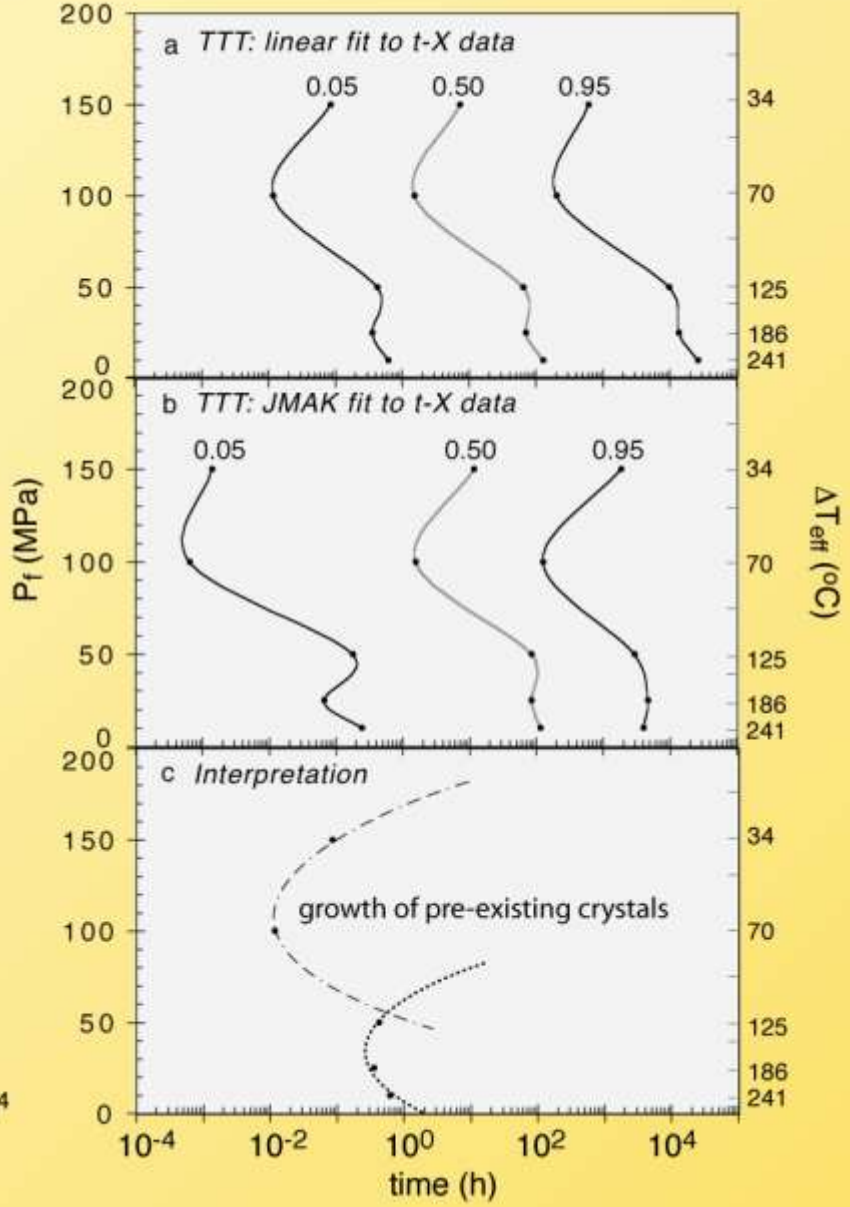

Hammer and Rutherford (2002) J Geophysical Research

Fit data with CNT

$$I = A\exp\left[\frac{-(\Delta G^* + \Delta G_D)}{k_B T}\right]; \Delta G^* = \frac{16\pi\sigma^3}{3\Delta G_V^{\,2}} S(\theta)$$

$$S(\theta) = \frac{(2+\cos\theta)(1-\cos\theta)^2}{4}$$

assumptions:
homogeneous
Stokes-Einstein

$$\Delta G_D = -k_B T \ln\left(\frac{h}{\lambda^3 3\pi\eta}\right)$$

$$I = \frac{A_c}{\eta} T \exp\left(\frac{-\Delta G^*}{k_B T}\right); A_c = \frac{n_V k_B}{3\pi\lambda^3}$$

Turnbull

$$\Delta G = \frac{\Delta H \Delta T}{T_L}$$

ΔT_{eff} for ΔT

$V_M = 1.003 \times 10^{-4}$ m^3 mol
$n_v = N_A / V_M$
$\lambda = 3 \times 10^{-10}$ m
$\Delta H_f = 74300$ J mol^{-1}

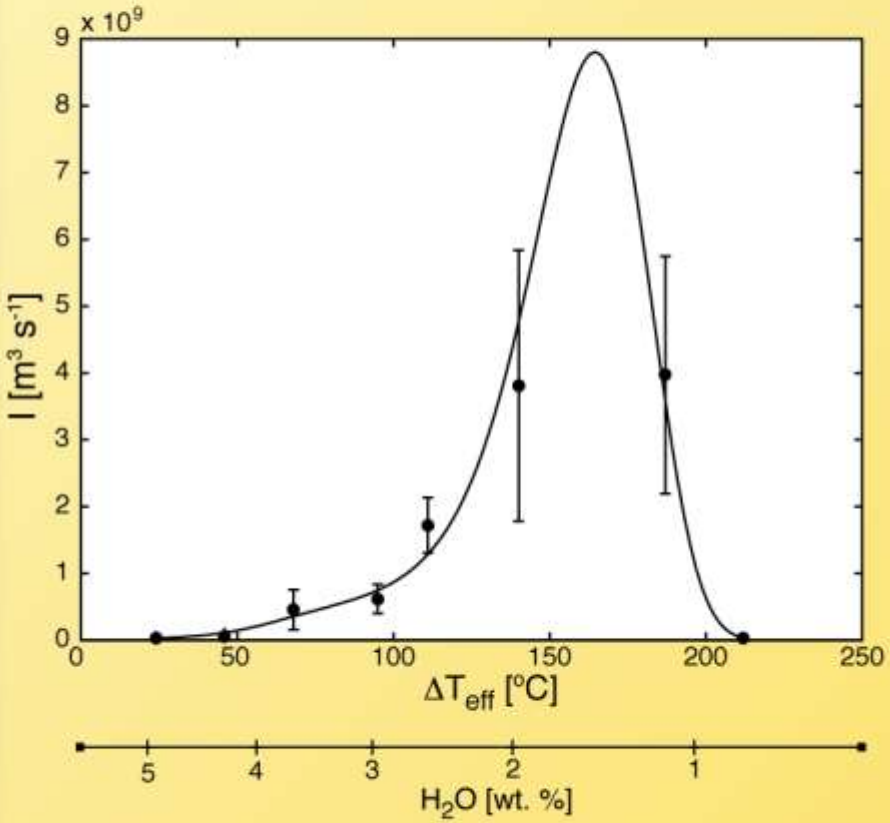

Hammer (2004) American Mineralogist

compositional controls on interfacial energy

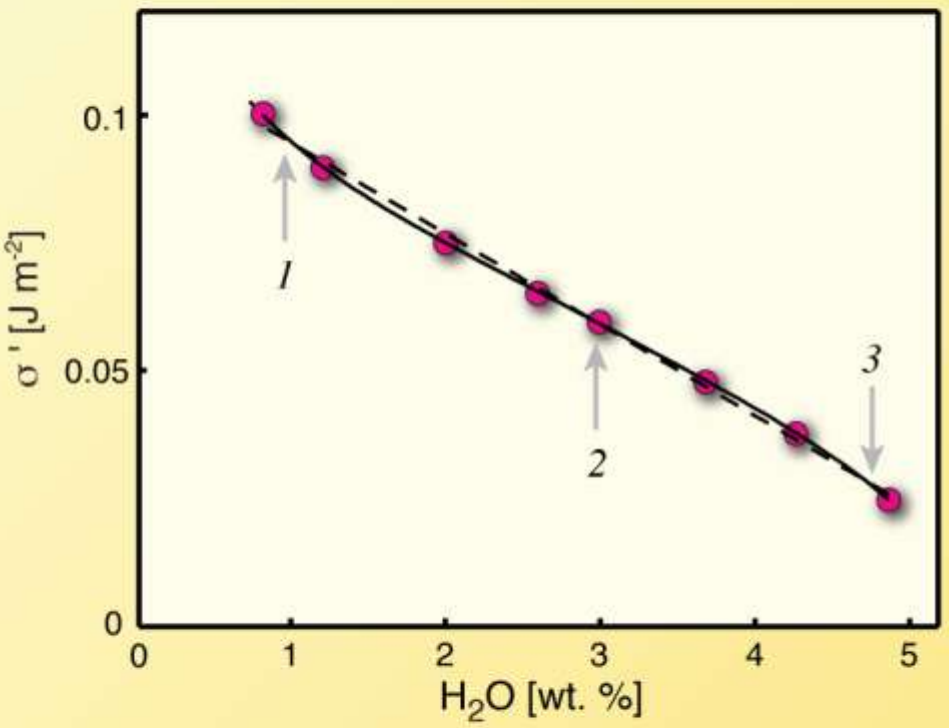

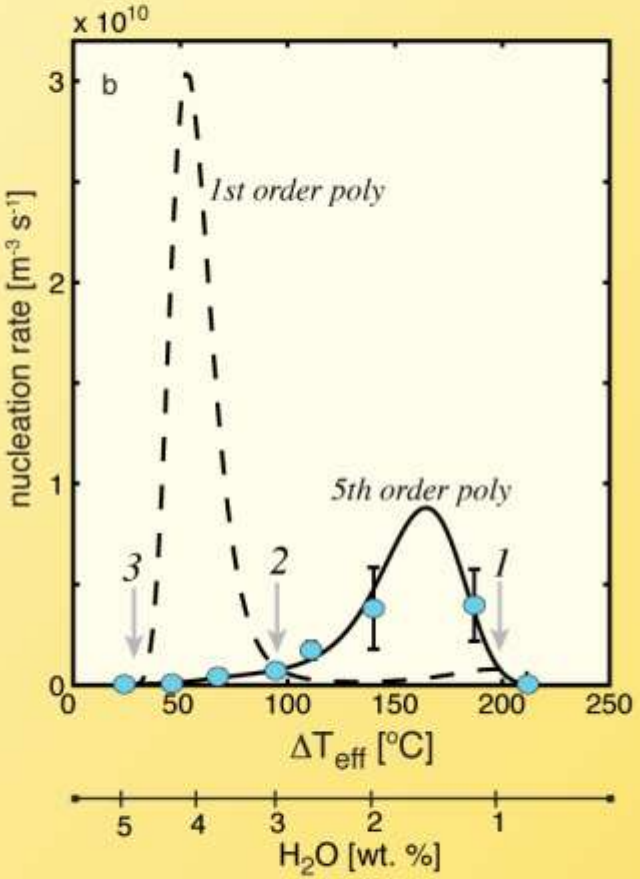

Hammer (2004) American Mineralogist

H_2O solution mechanism in silicate melt:

O^0	+	O^{2-}	=	$2O^-$
(free)		(bridging)		(non-bridging)

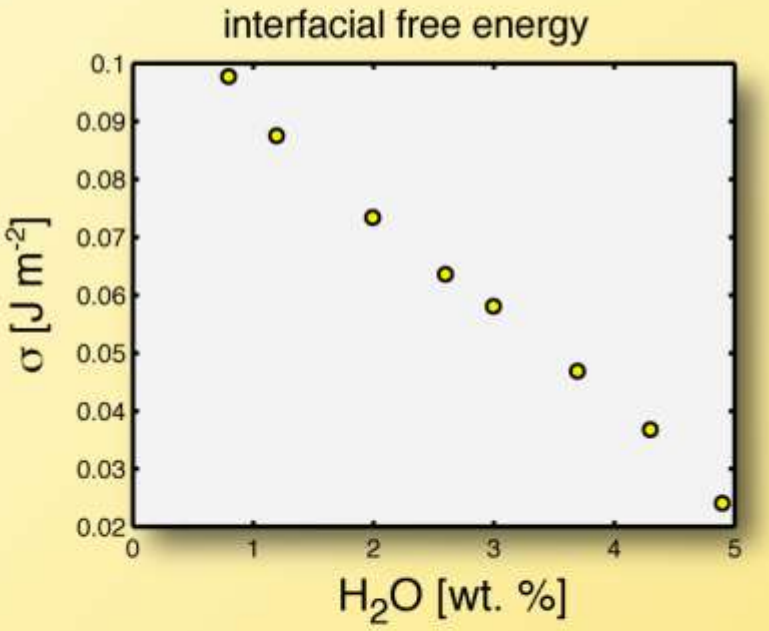

Hammer (2004) American Mineralogist

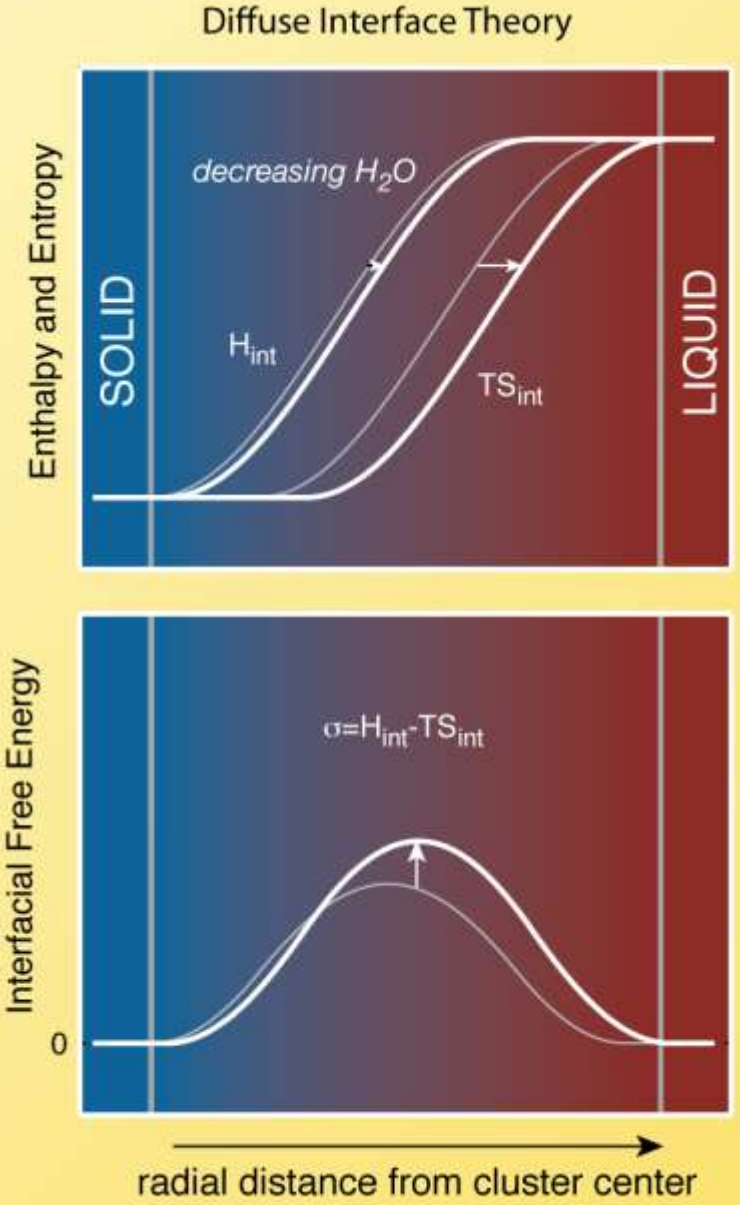

Granasy (1993) J Non-crystalline Solids
Spaepen (1994) Solid State Physics

Continuous decompression experiments

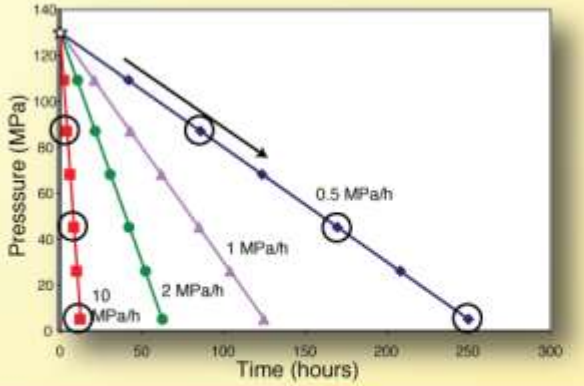

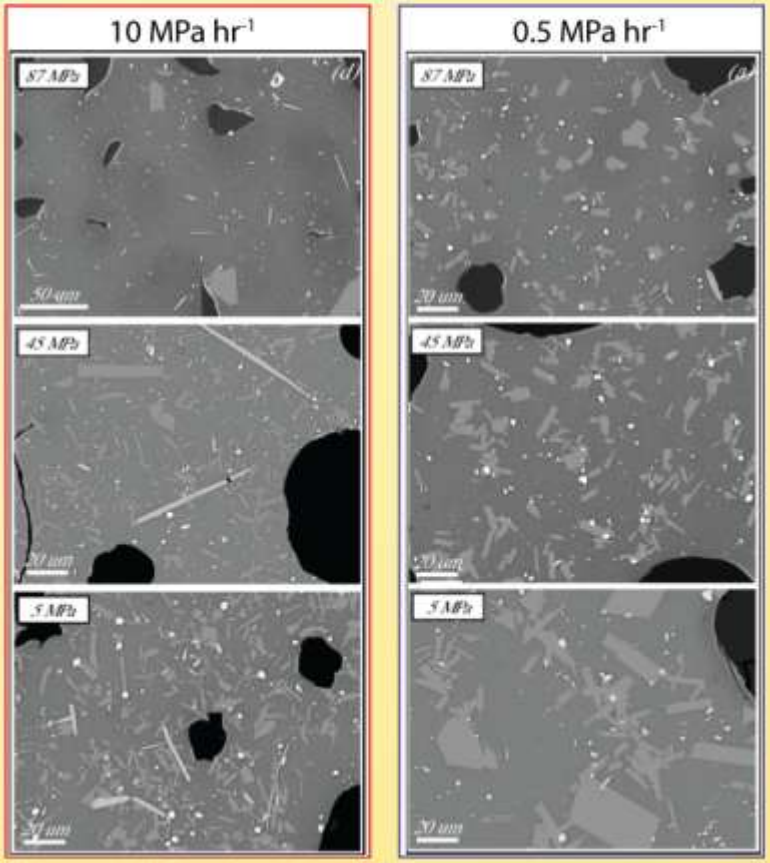

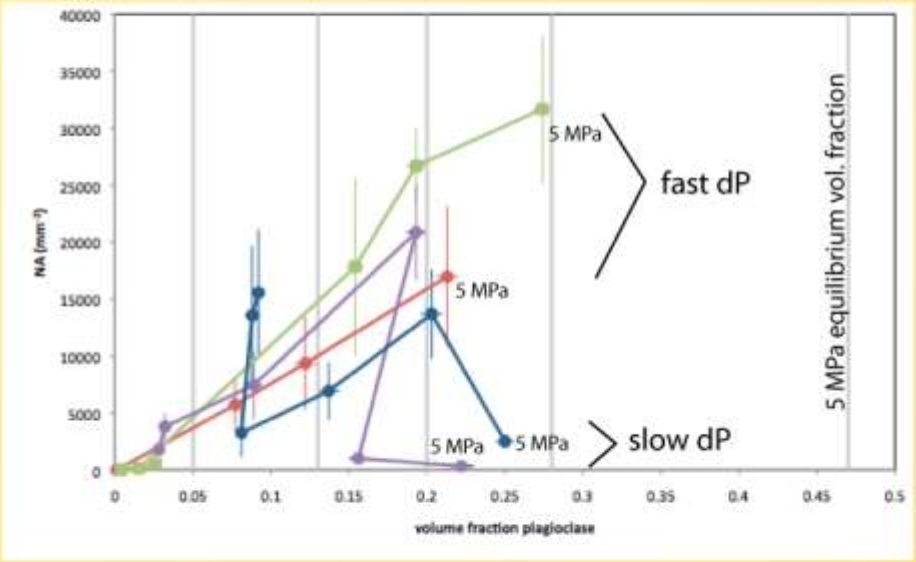

fast decompression: far from equilibrium, NA progressively increases

slow decompression: equally far from equilibrium, coarsening

Brugger and Hammer, submitted, J. Petrology

Conspicuous Contiguity

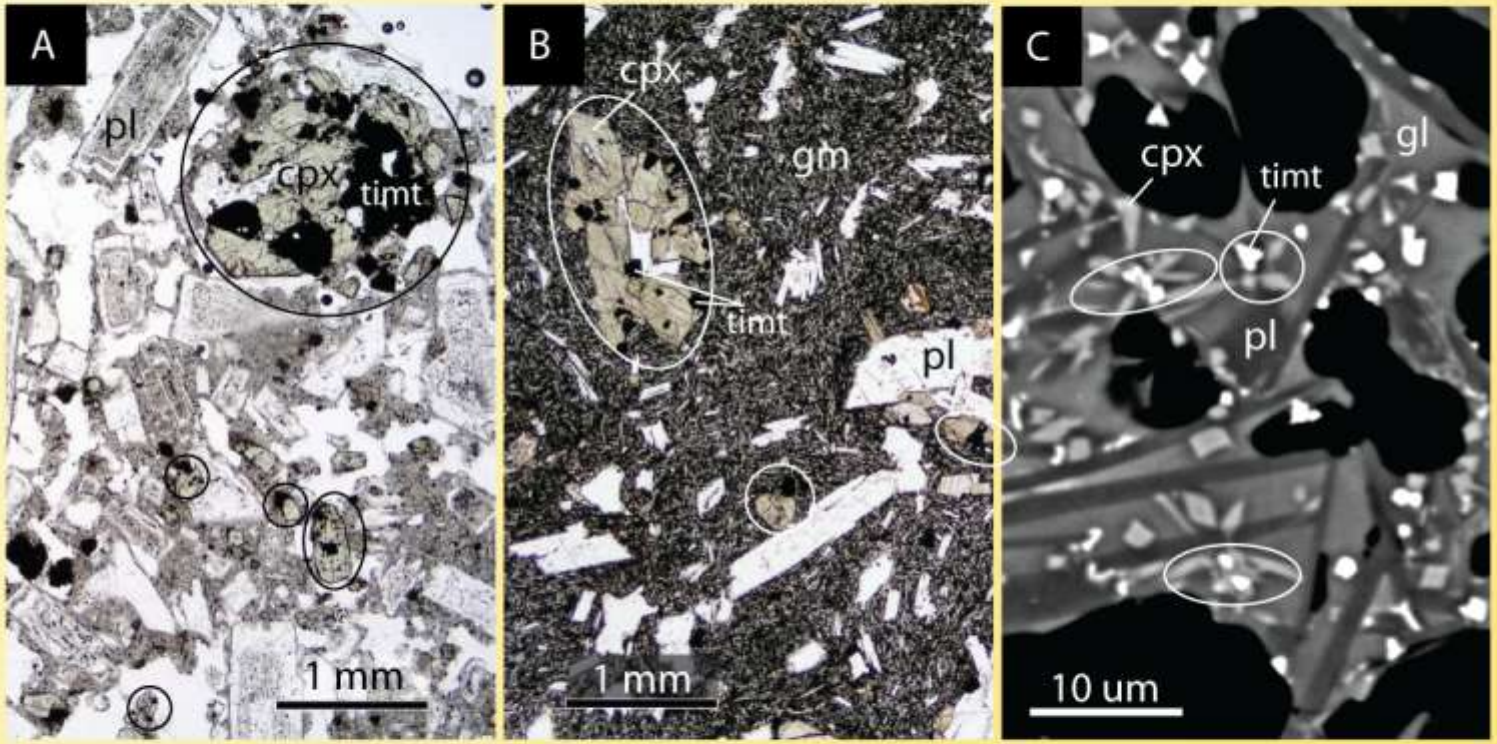

Merapi 1995 andesite dome lava

Etna 122 BC basaltic plinian

Etna 122 BC basaltic plinian

Hammer et al. (2010) Geology

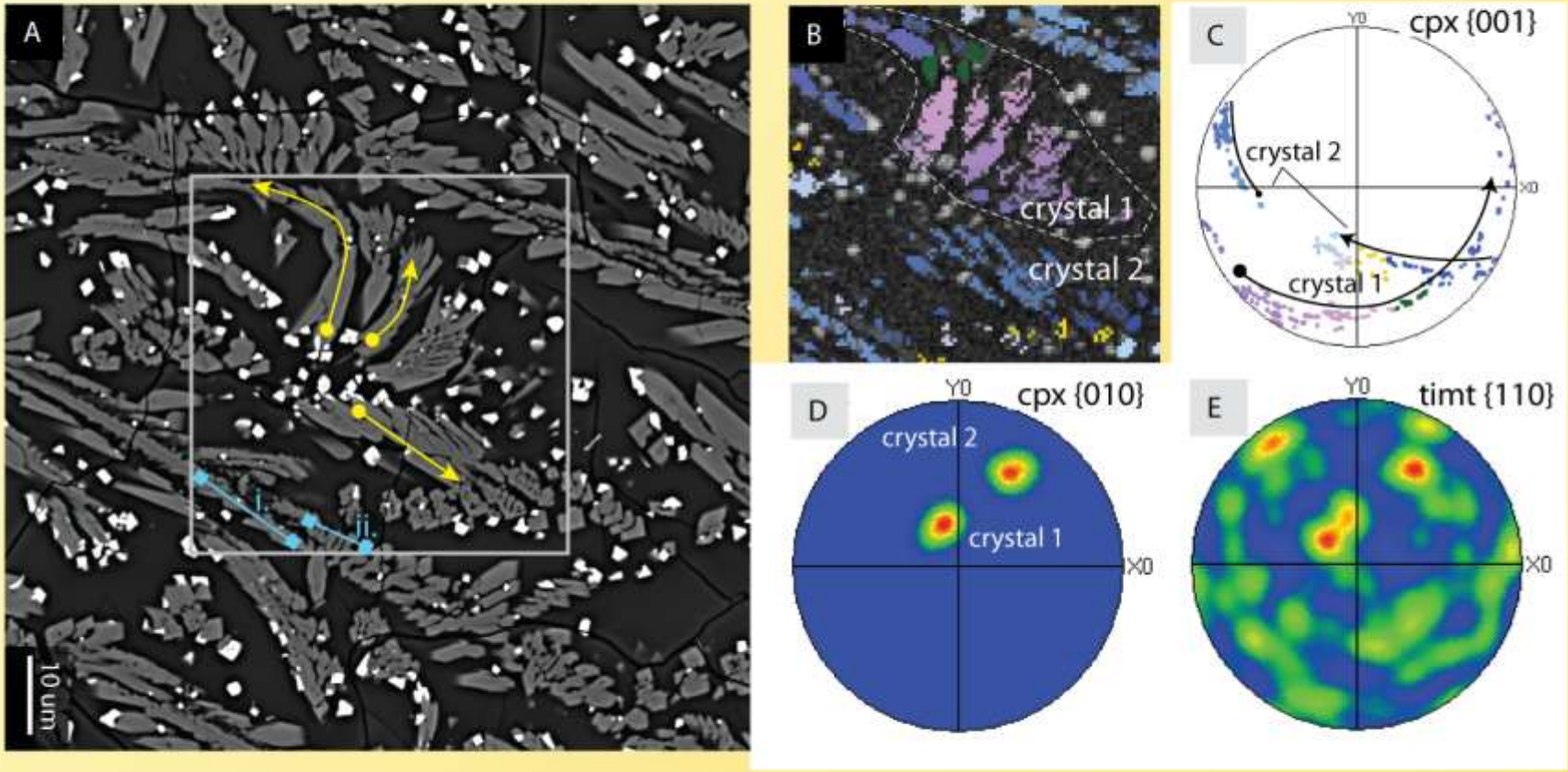

Hammer et al. (2010) Geology

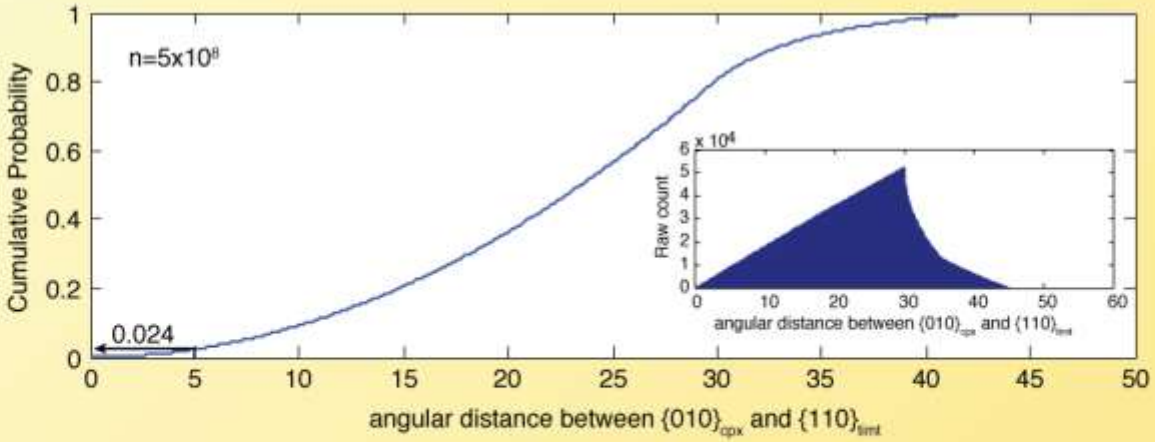

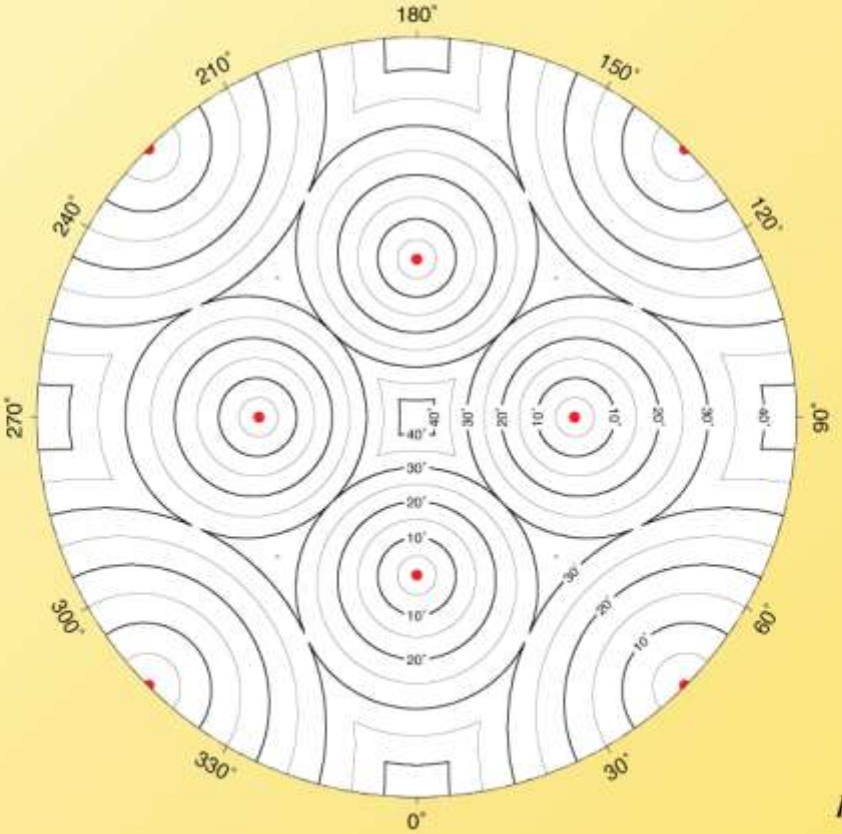

touching cpx-mt pairs exhibiting CPO <5° (%)

random	2.4
natural Etna basalt	22
experimental basalt	80, 84

Hammer et al. (2010) Geology

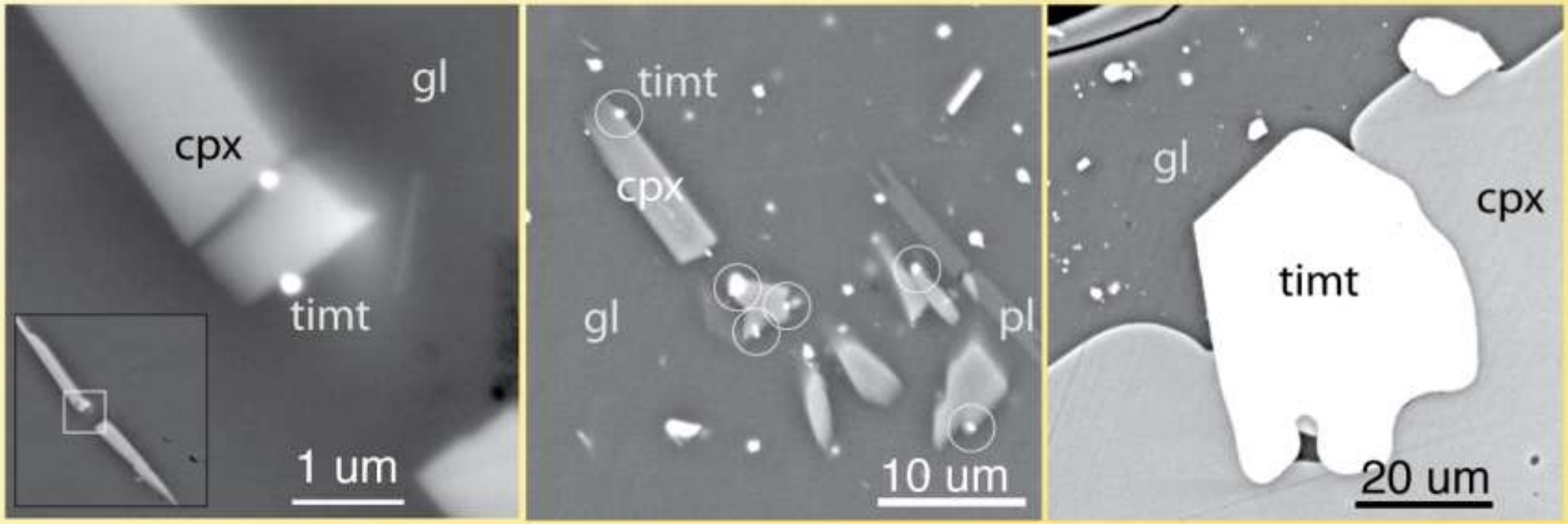

Aniakchak rhyodacite decompression experiment

Hammer et al. (2010) Geology

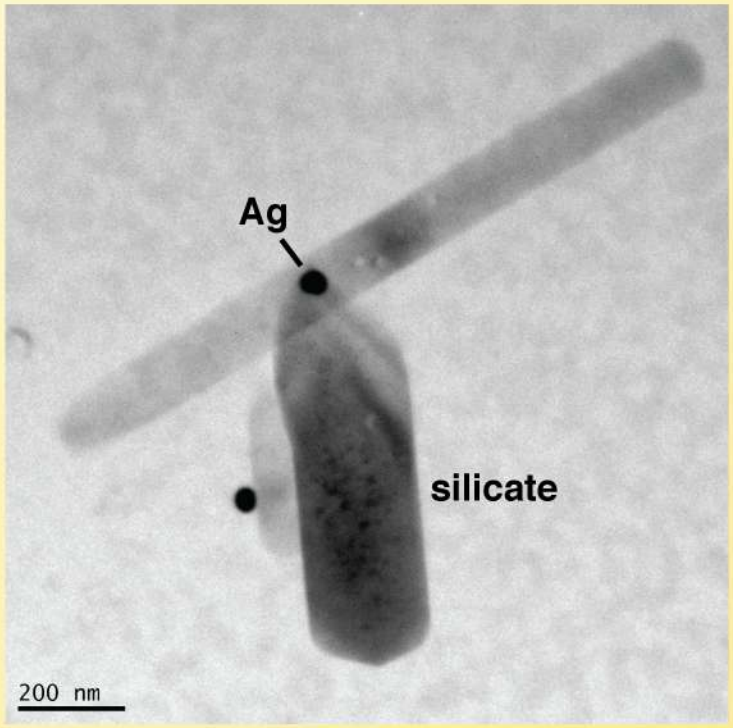

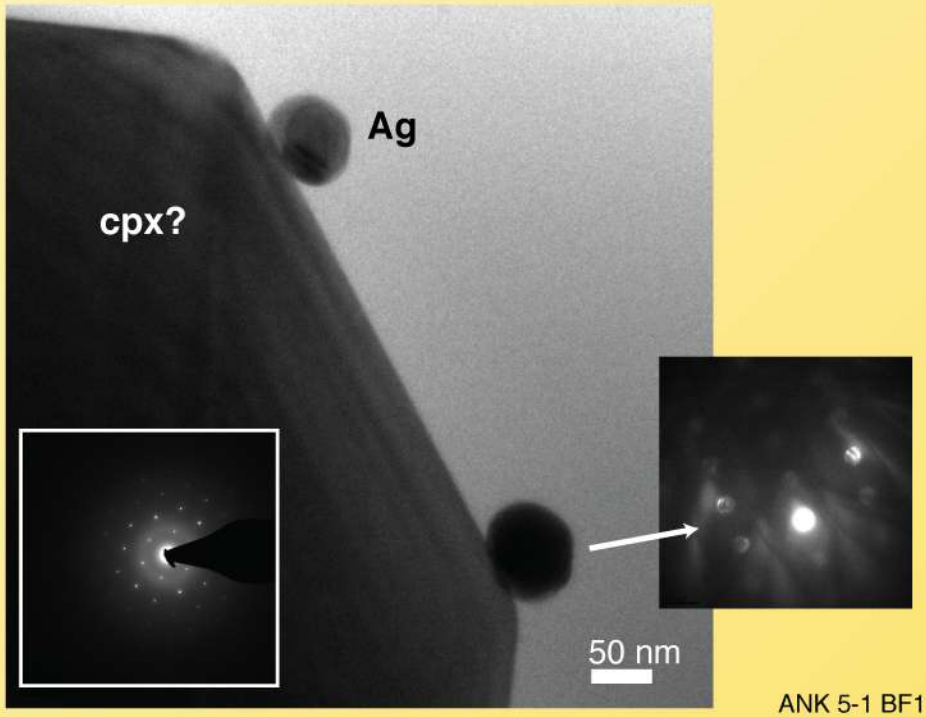

ANK 5-1 BF11

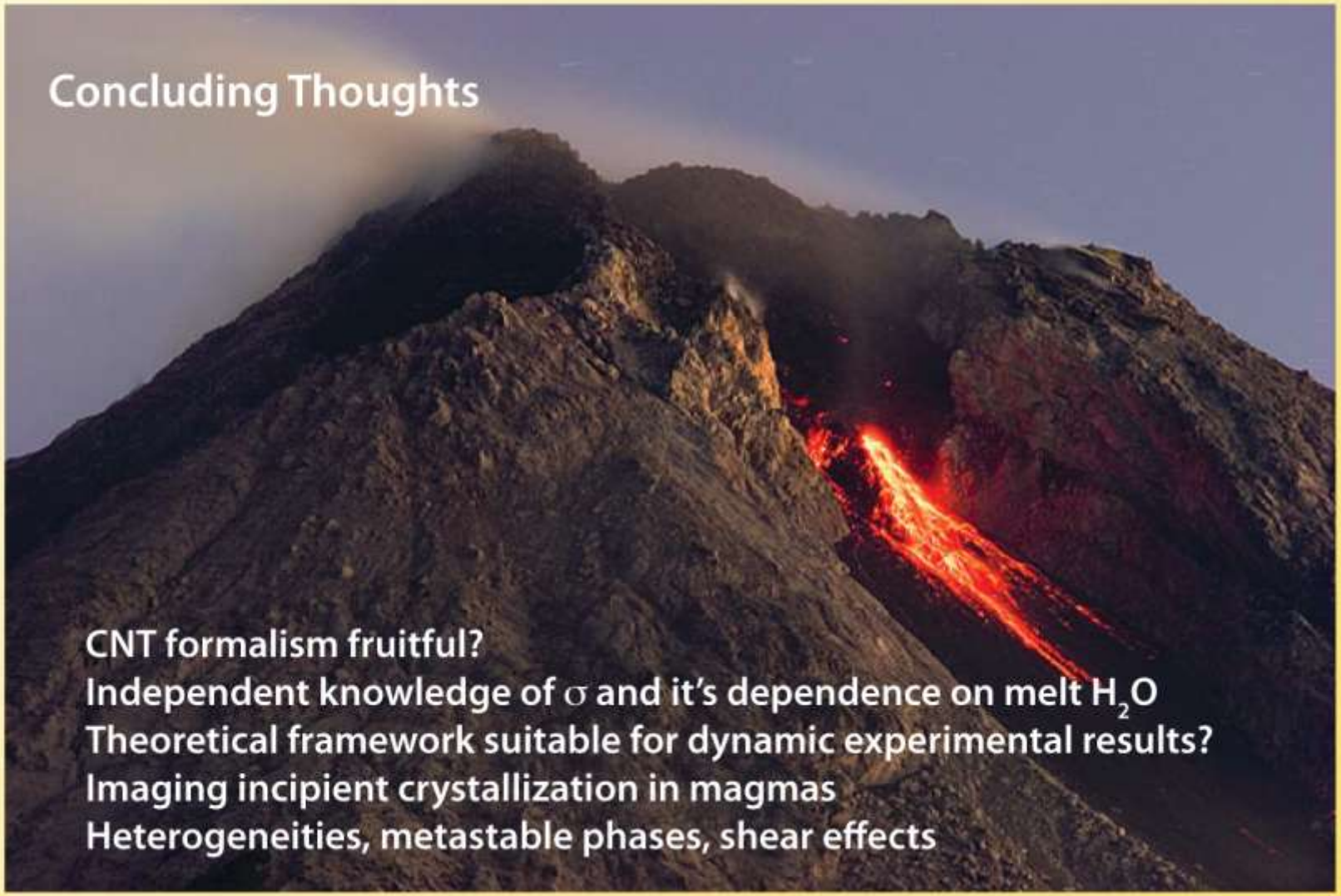
Concluding Thoughts
CNT formalism fruitful?
Independent knowledge of σ and it's dependence on melt H_2O
Theoretical framework suitable for dynamic experimental results?
Imaging incipient crystallization in magmas
Heterogeneities, metastable phases, shear effects

Lawrence Livermore National Laboratory

Quantifying Rapid Solid-state Crystallization Kinetics; Application of the KJMA Equation to High Time Resolution Electron Microscopy Data

Joint AFRL/AFOSR/LLNL Pacific Rim Workshop on Nucleation, May 2nd-7th, 2010

Thomas LaGrange

DTEM TEAM: Geoffrey H. Campbell, Nigel D. Browning, Bryan W. Reed, Melissa Santala, Joseph Mckeown, Katie Jungjohann, Marta Bonds, William J. Dehope, Glenn Huete and Richard Shuttlesworth

Lawrence Livermore National Laboratory, PO Box 808, Livermore, CA 94551

This work performed under the auspices of the U.S. Department of Energy by Lawrence Livermore National Laboratory supported by Office of Science, Office of Basic Energy Sciences, Division of Materials Sciences and Engineering of the U.S. Department of Energy under Contract DE-AC52-07NA27344.

At the nanoscale, structural evolution in materials happens quickly because distances are short.

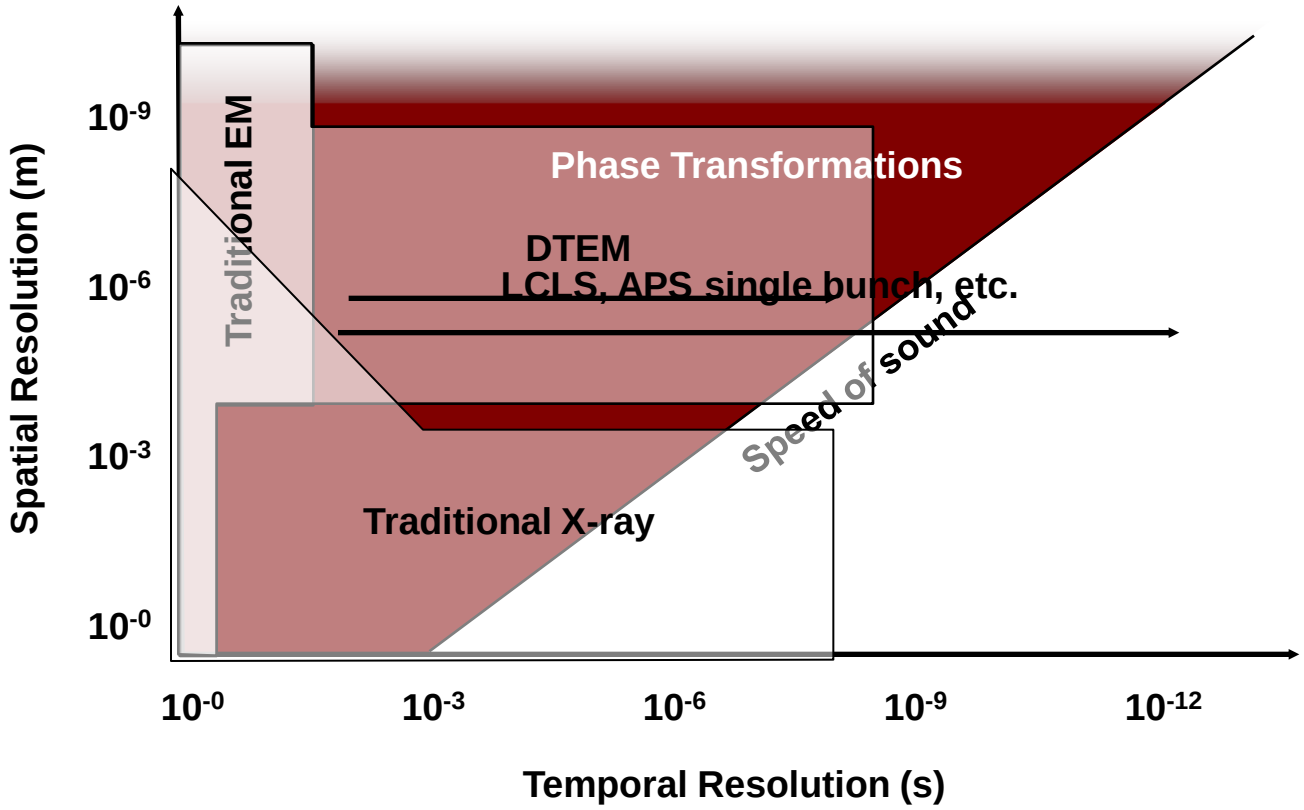

In regimes that have never before been explored, we will observe new and noteworthy features of materials dynamics.

DTEM affords the opportunity to directly study complex transient phenomena in materials

DTEM experiments are on the same length and time scales as large scale atomistic simulation

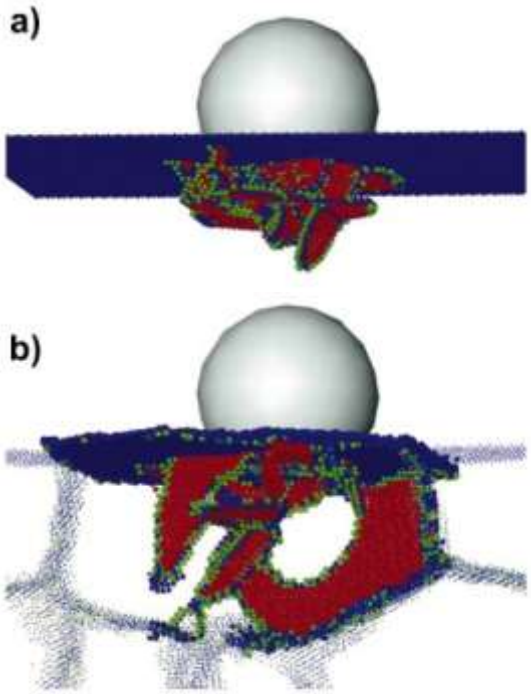

H. Van Swengenhoven, PSI

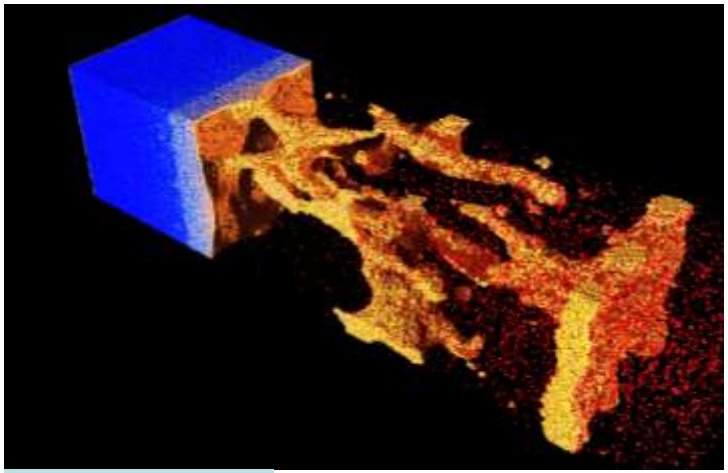

G. Gilmer, LLNL

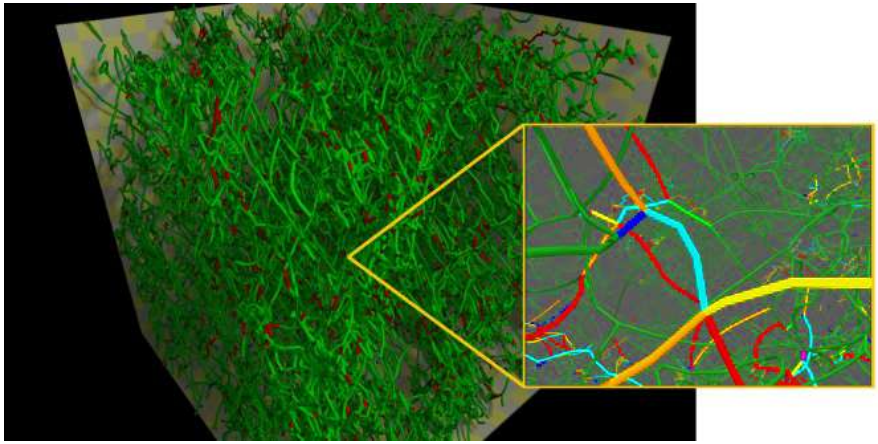

V.Bulatov, LLNL

Overview: The LLNL DTEM is a nanosecond-scale *in situ* TEM with single-shot capability

DTEM adds two lasers to a conventional TEM to enable:

- Driving sample events with extreme spatiotemporal temperature gradients
- Real-space imaging and diffraction with ~15 ns exposures
- Enough signal in one exposure to form an image (up to 2×10^9 electrons)

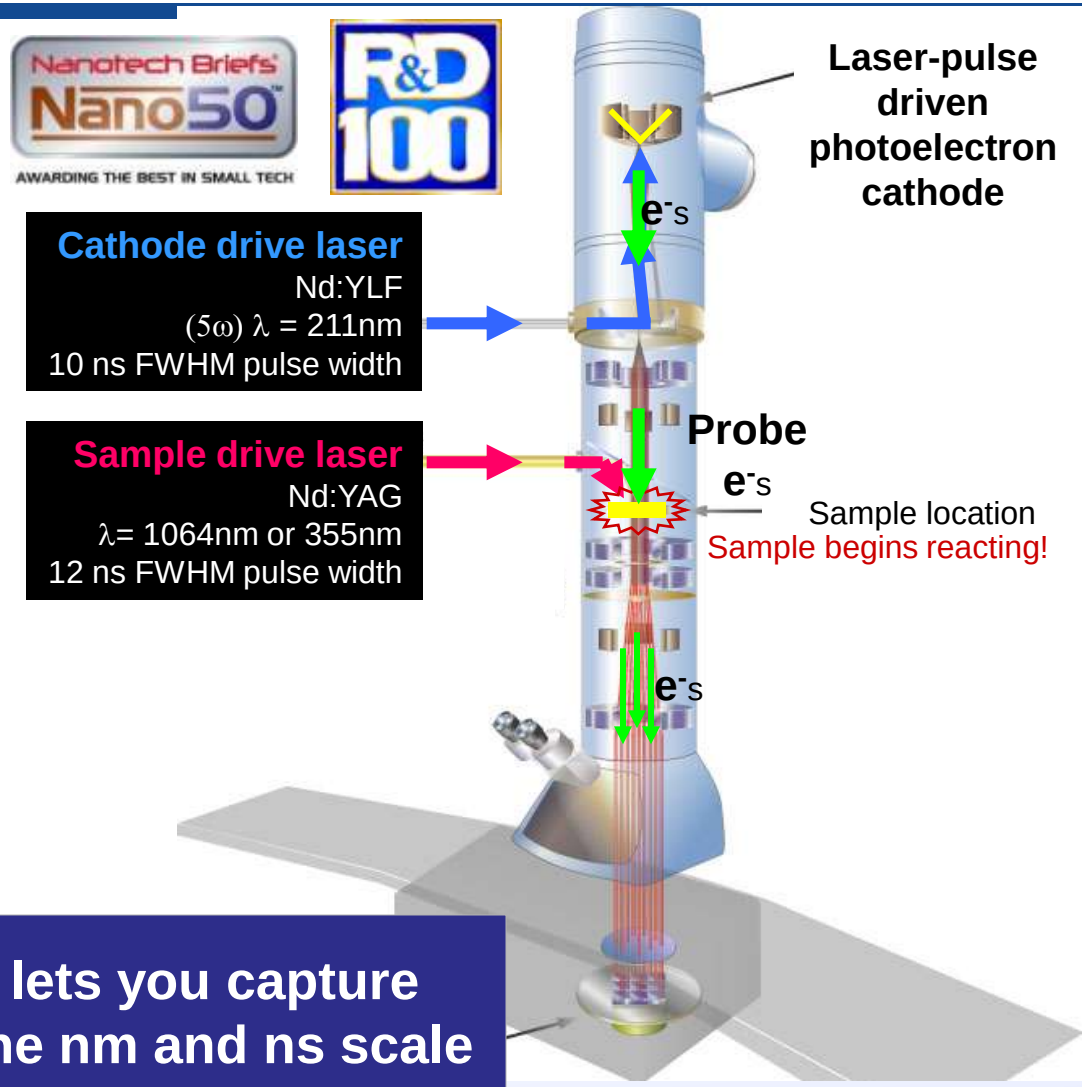

DTEM's single-shot approach lets you capture *unique, irreversible* events on the nm and ns scale

We have achieved performance in DTEM adequate for most materials science investigations we could envision

Conventional TEM Image

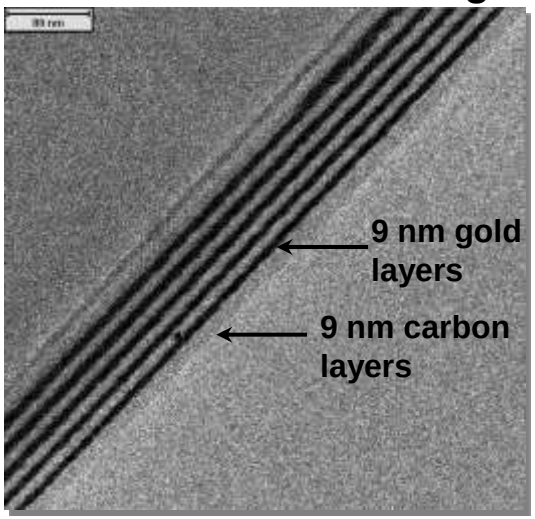

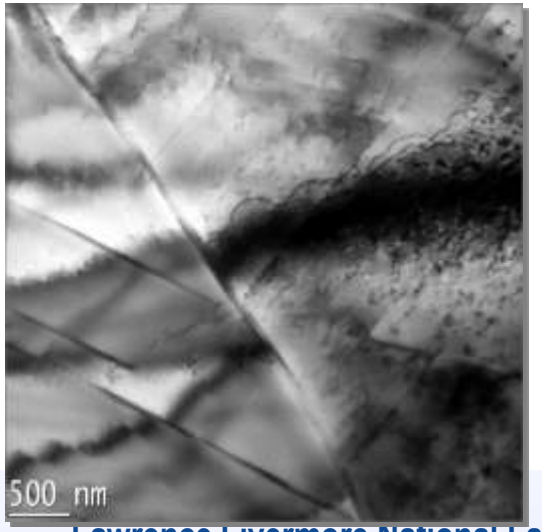

Single-Shot 15 ns DTEM Image

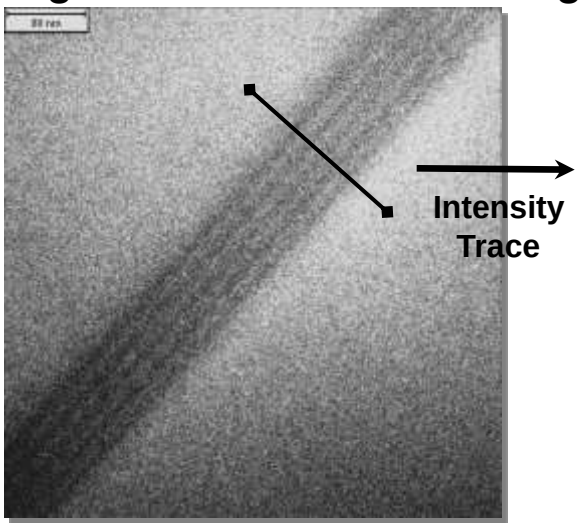

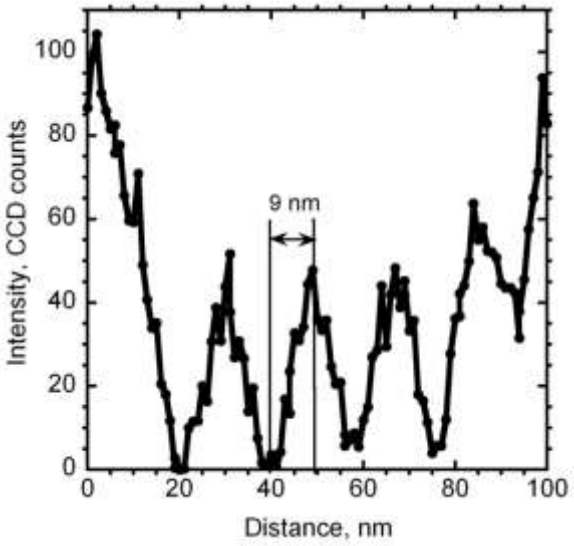

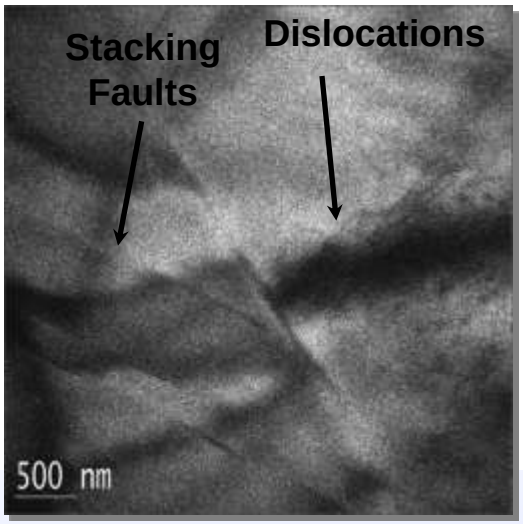

Dynamical contrast formation allows DTEM to image those defect structures that control properties of materials.

Laser heating can be used to tailor microstructure and properties in NiTi thin films for shape memory applications.

- Laser annealing can be used to crystallize amorphous NiTi film and modify grain size
- DTEM laser pulse produces large spatiotemporal temperature gradients
- Kinetics *do not* extrapolate from low temperature studies

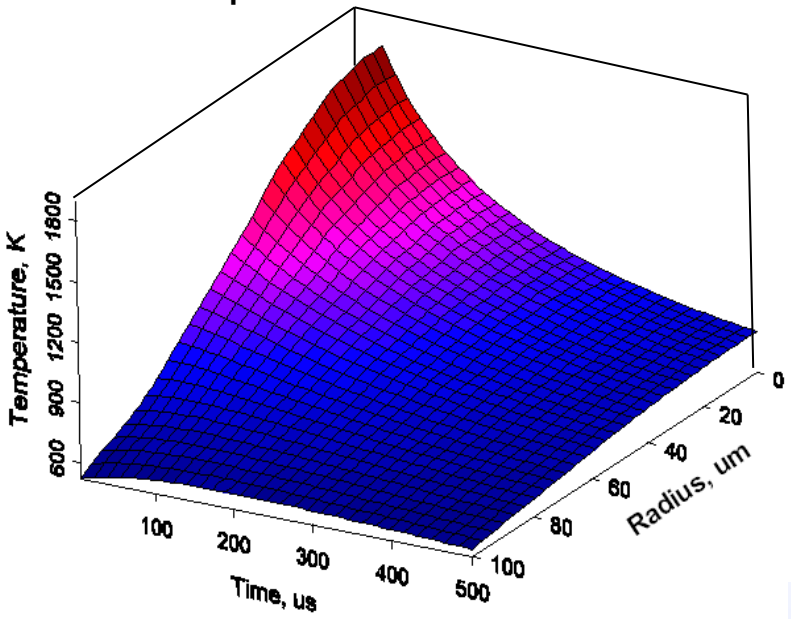

CW laser annealing, Wang et al., *Acta Mater.* 2005

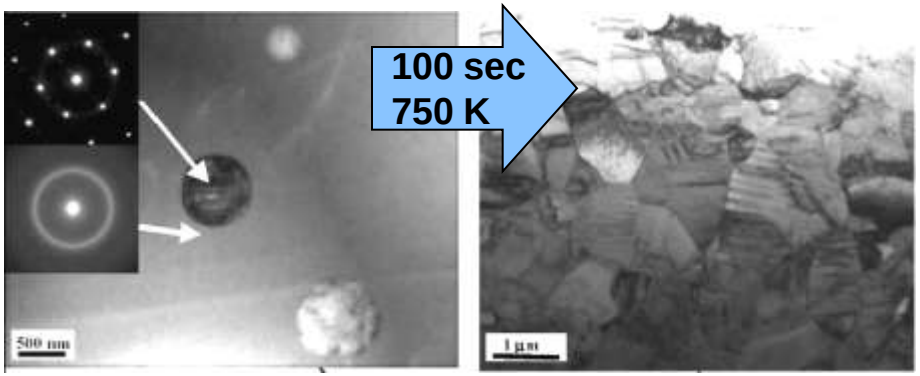

Pulsed laser annealing in DTEM (~1500 K)

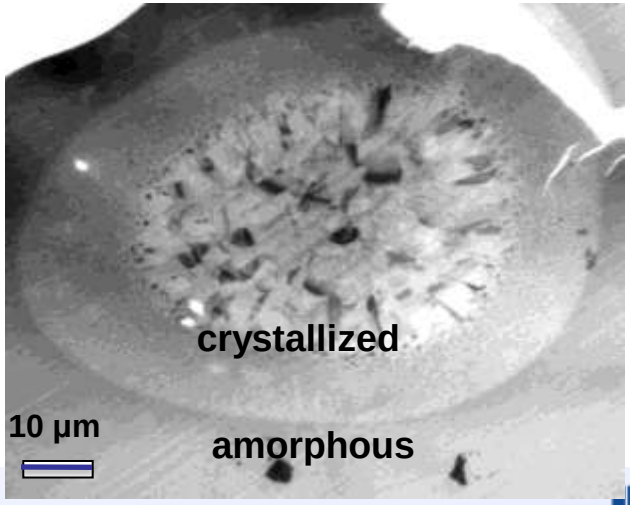

Conventional annealing and *in situ* TEM studies were used to determine the kinetic parameters for crystallization.

- We studied crystallization processes in 250 nm thick amorphous, equiatomic NiTi films.
- Films were annealed at 768K using *in situ* TEM heating holder.
- Crystallization processes were recording using a video camera.
- Comparable crystallization kinetics to CW laser annealing experiments.

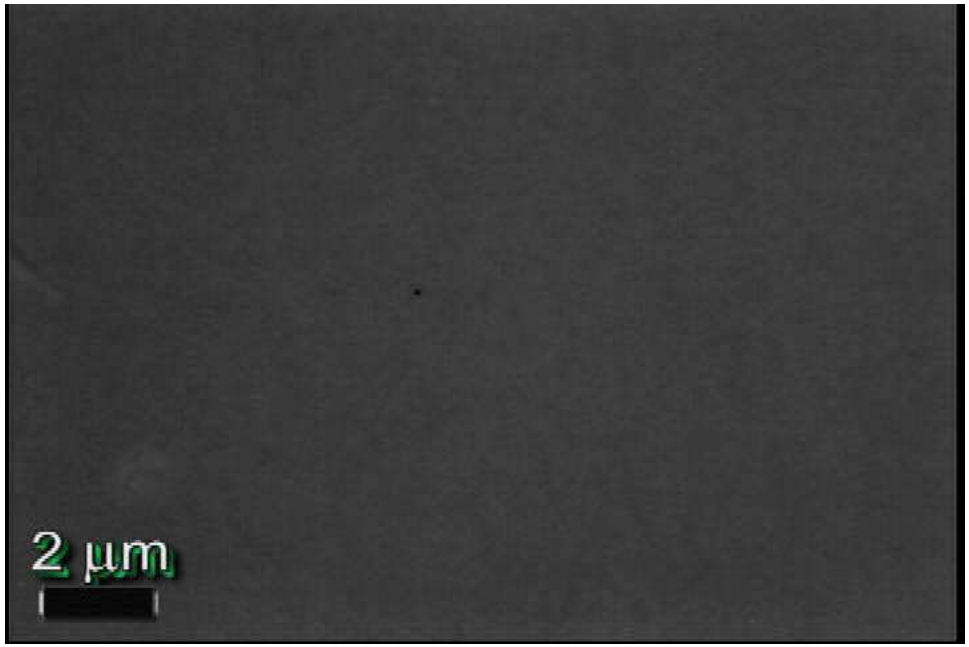

Conventional *in situ* hot stage microscopy used to determine crystallized fraction as a function time for JMAK analysis

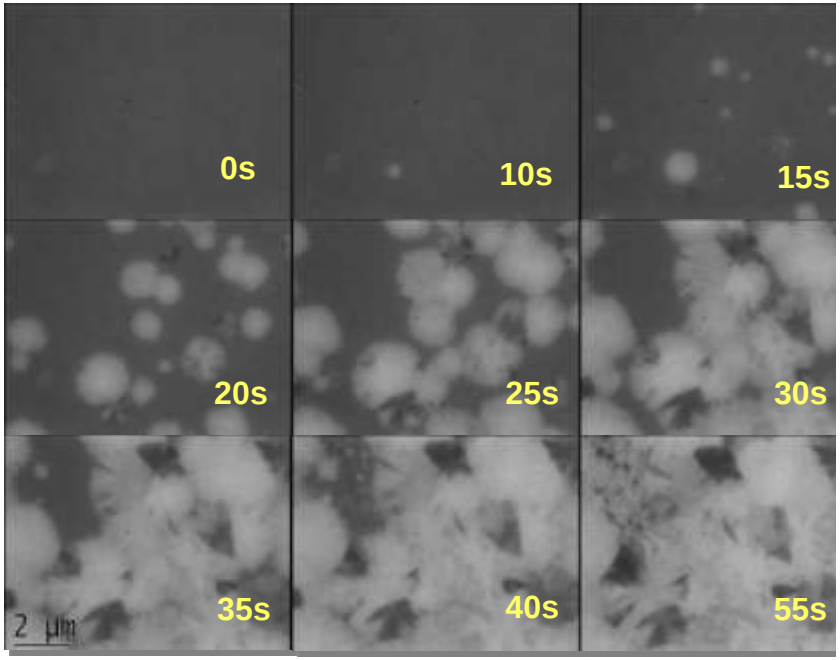

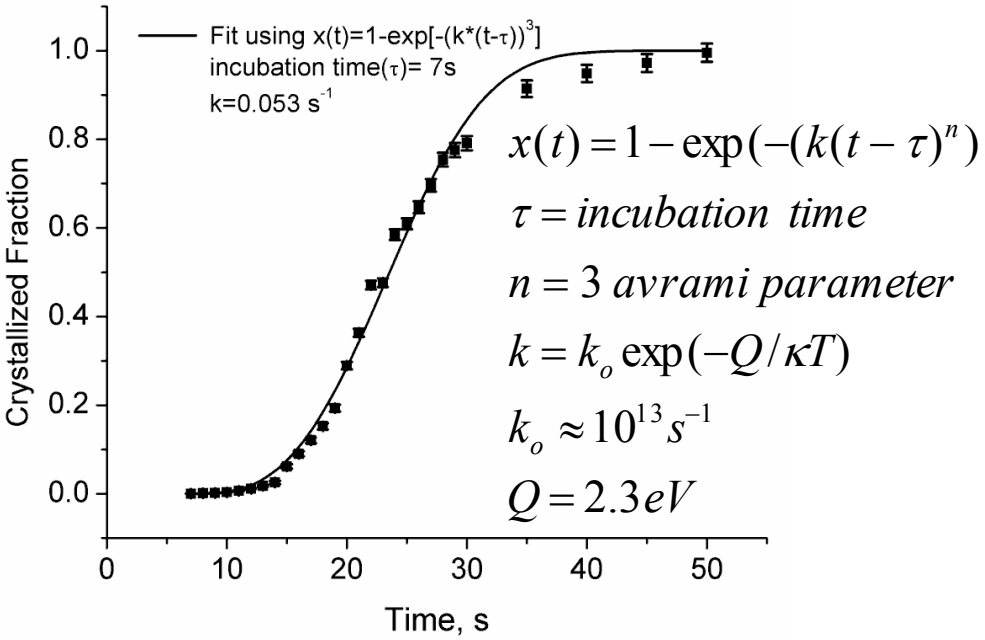

- Crystallization data were fit with the Johnson-Mehl-Avrami-Kolmogorov model to determine the kinetic parameters.
- Consistent with previous reports for NiTi in the literature.
- Kinetic data was extrapolated and compared with DTEM data measured at high temperatures (850-1550K).

Crystallization of amorphous NiTi films occurs on the µs timescale, much faster than expected from known kinetics.

t=0s Before laser heating

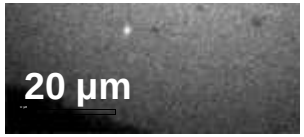

t=1 µs After drive laser pulse

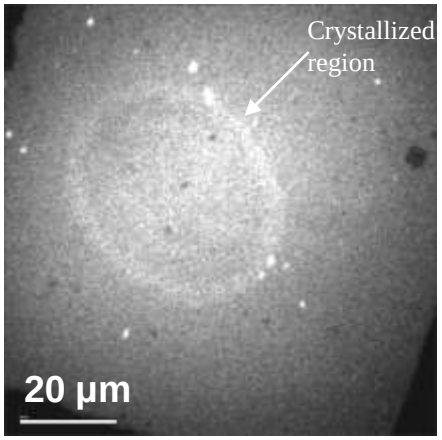

t=∞ After laser heating

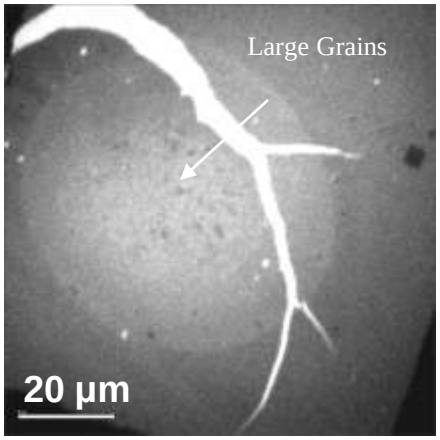

Nucleation is different under pulsed laser heating.

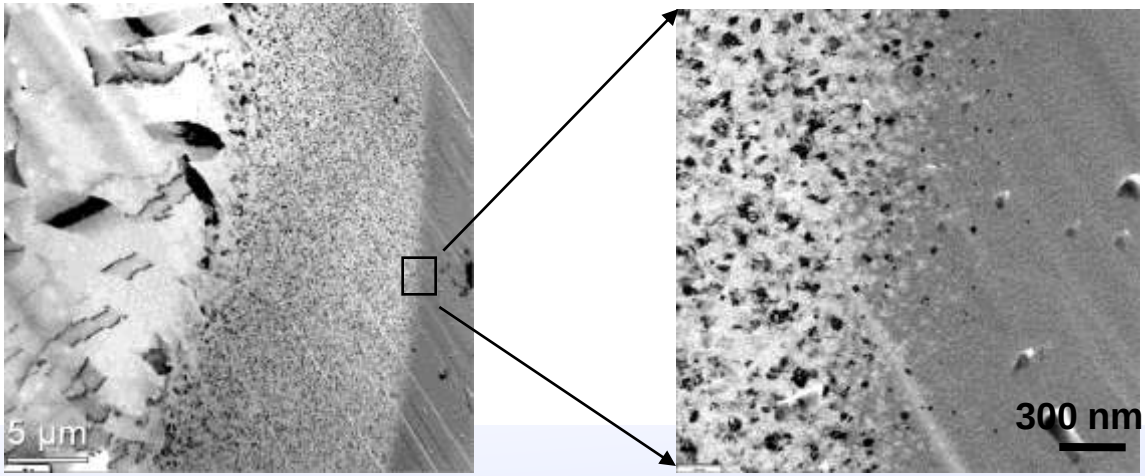

Crystallization kinetics depend strongly on laser fluence, film thickness and heat transport.

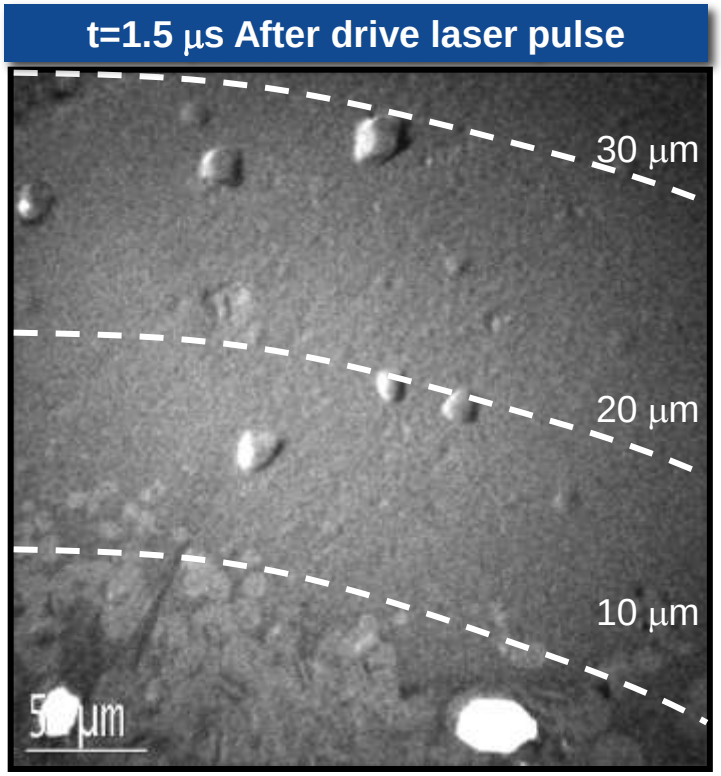

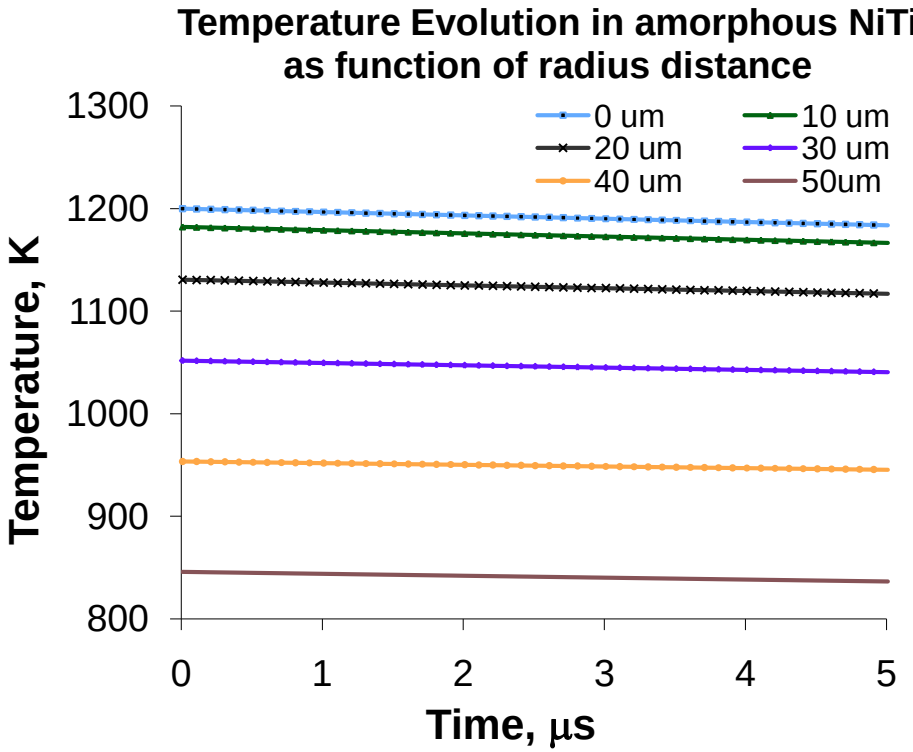

- Temperature rise was calibrated using ex-situ reflectivity measurements and observations of liquefaction.
- Radial temperature and cooling rate calculation assume Gaussian laser energy distribution and heat loss by lateral conduction in an infinite medium.

Time-resolved brightfield imaging used to study rapid nucleation rate under pulsed laser annealing.

- Nucleation rate can be determined by the change in the number of new sites as a function of time normalized to the untransformed volume.
- Requires multiple single-shot experiments.

$$J(t_i) = \frac{1}{1 - X(t_i)} \frac{dN}{dt}$$

$$= \frac{1}{1 - X(t_i)} \frac{(N_i - N_{i-1})}{(t_i - t_{i-1})}$$

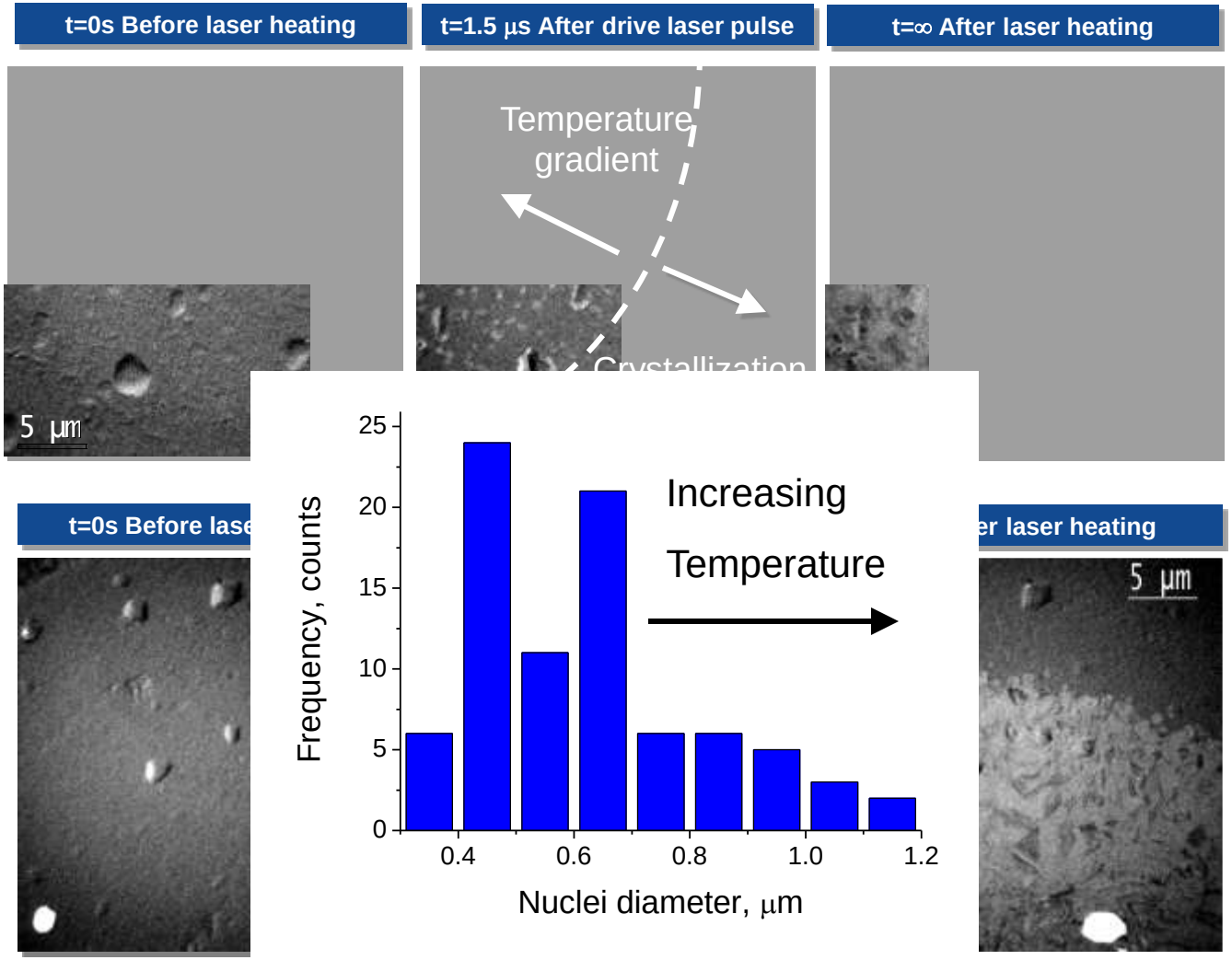

Extraordinarily high nucleation rate occur under pulsed laser heating.

Conventional *In situ* TEM at 768K

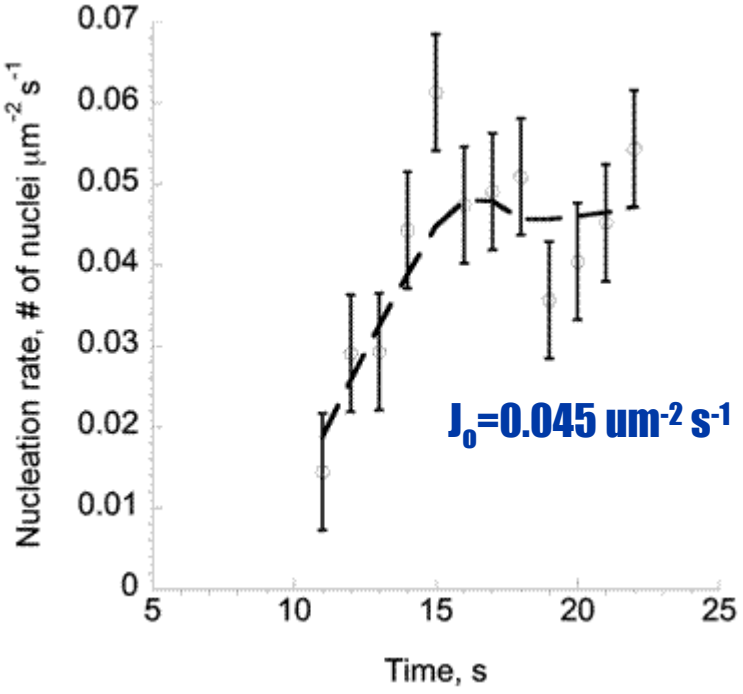

Pulsed laser heating in DTEM to 1200K

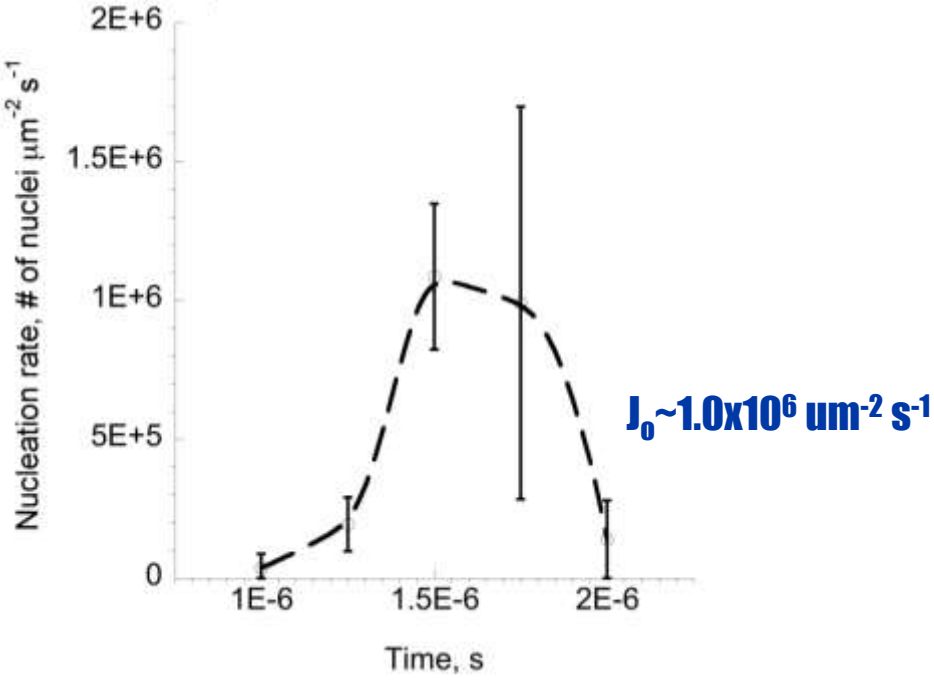

- Nucleation rate is 8 orders of magnitude higher under pulsed irradiation.
- Extrapolation of data acquired at 768K using JMAK kinetics still leads to a predicted nucleation rate that is orders of magnitude different. **$J_o \approx 370\ \mu m^{-2}\ s^{-1}$**

Crystallization data were fit with the Johnson-Mehl-Avrami-Kolmogorov model to determine the kinetic parameters.

- Assuming that k_o is the Debye frequency ~10^{13} s^{-1},

$$k = k_o \exp(-Q/\kappa T)$$

Q_{DTEM}=1.7±0.3 eV

$Q_{slow\ anneal}$=2.3±0.17 eV

- Assuming that n=3 and crystallization occurs under steady state nucleation and growth, the growth rate can be calculated, V_o=6.7x10^5 μm s^{-1}

$$k = \sqrt[3]{(\pi/3) J_o V_o^2}$$

- The associated grain size can also be predicted,

$$\bar{d} = 1.2\sqrt[3]{V_o / J_o} = 1.05\mu m$$

Crystallized volume fraction as a function of time at an estimated temperature of 1200K

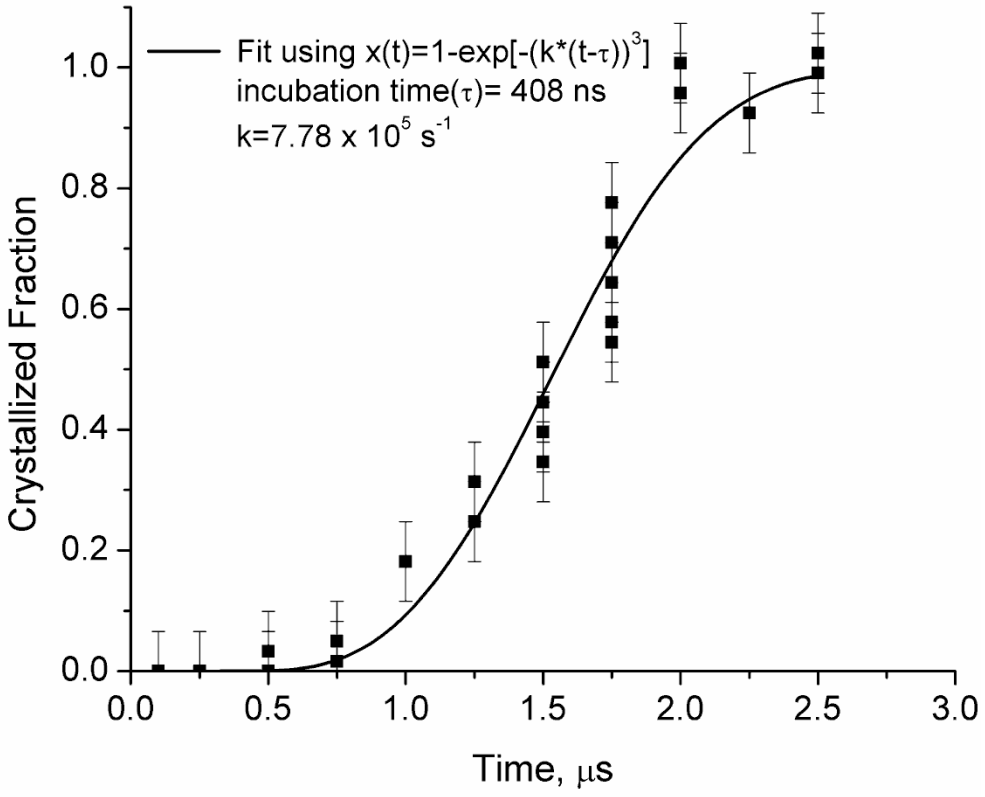

Crystallization rate varies strongly with laser intensity showing a C-curve like behavior which has not been previously observed.

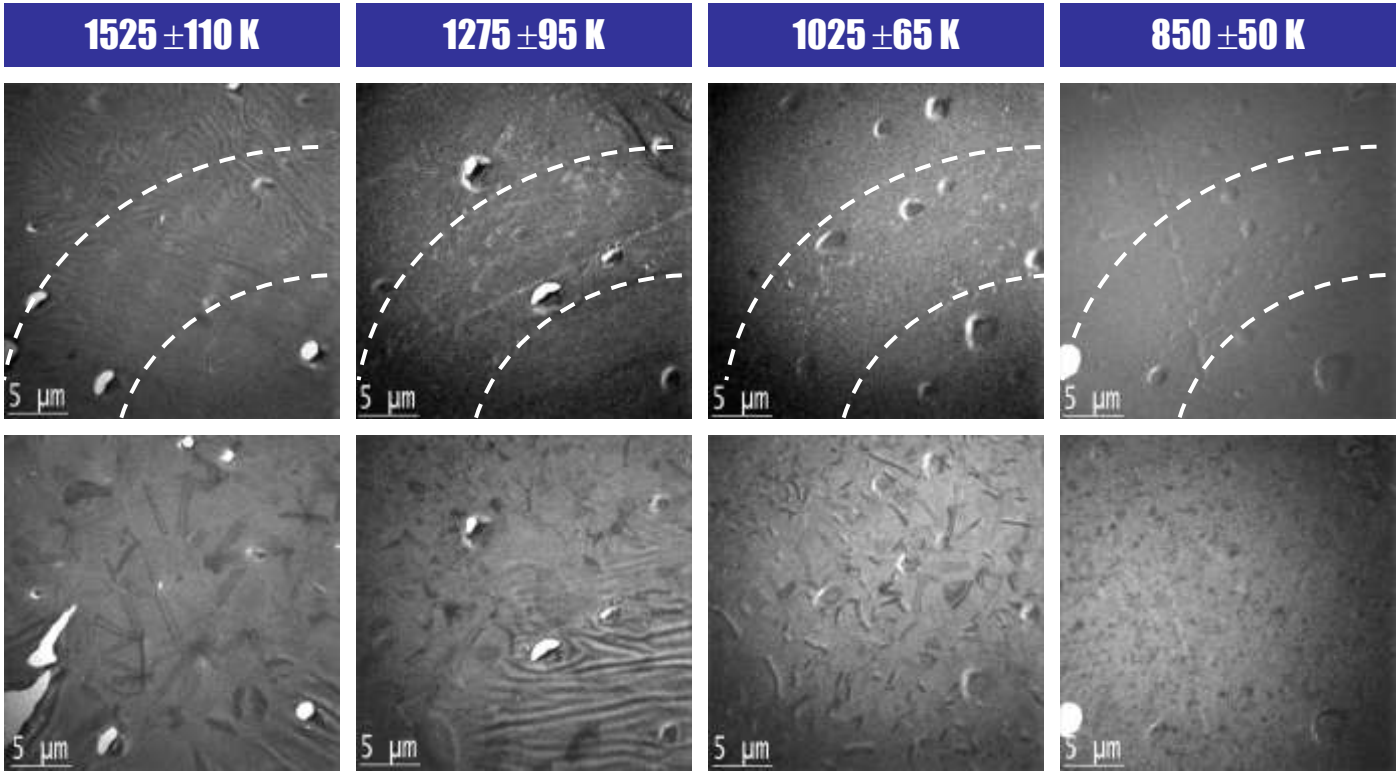

- Final microstructure varies strongly with initial pulsed laser annealing temperature.
- Crystallization rates appear to be highest at temperatures around 1200K.
- The threshold temperature for pulsed laser crystallization is ~850K

C-curve like behavior cannot be predicted from data obtained in the slow-heating experiments.

- Large discrepancy between pulsed laser heating and slow annealing.
- Extrapolation of DSC data using the JMAK equation show that mechanism occurring under pulsed laser annealing are not captured
  nal thermal

  navior m
  results from increased entropy (lower driving force) at high temperatures.

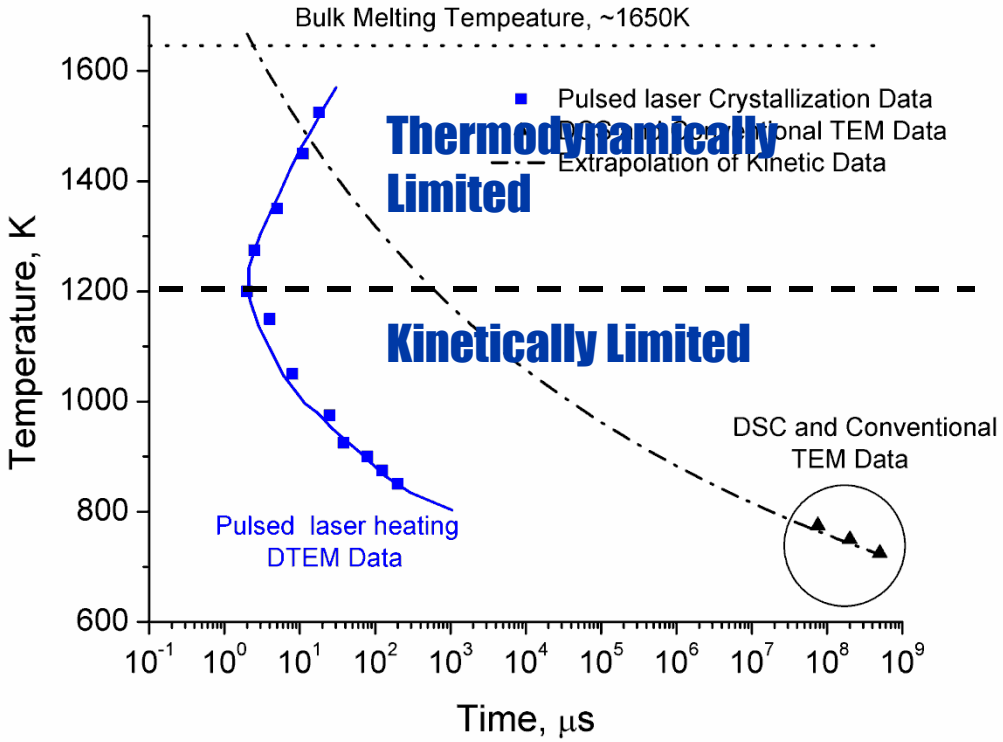

Future experiments will strive to measure precise growth rates and approximate interfacial energies.

Conclusions

- Using the DTEM, one can quantitatively measure the nucleation and growth rates associated with phase transformations with ns time resolution.
- We can gain insight into the subtle details of materials processes in previously unexplored regimes (kinetically driven and high temperature states).
- The discrepancy between pulsed laser and slow annealed induced devitrification kinetics is captured by the JMAK analysis and is not understood!

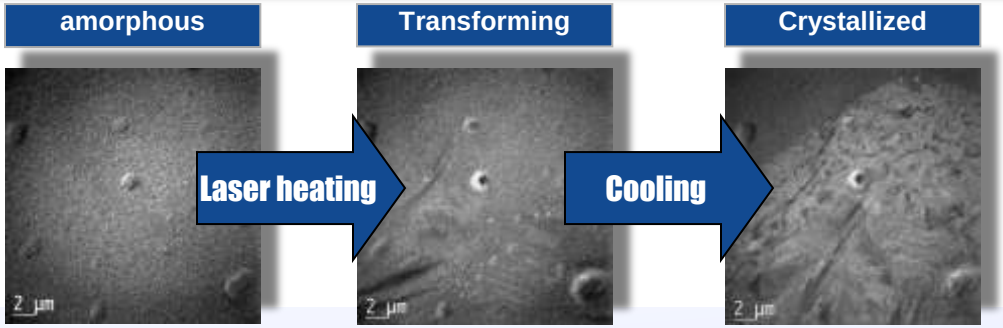

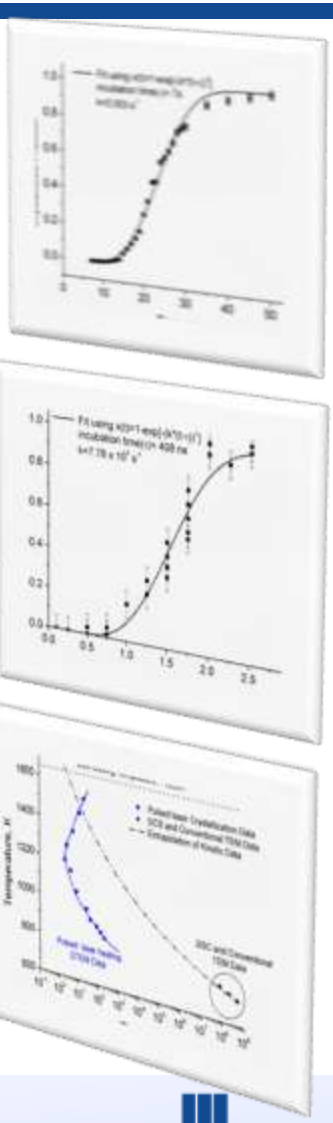

To follow the microstructural and defect evolution, multiple images must be acquired from drive event.

- Measurement of the growth rates requires multiple images of a moving interface to reveal its velocity.
- A time sequence of multiple images (a movie) allows the position of a given moving interface to be measured and its speed determined.

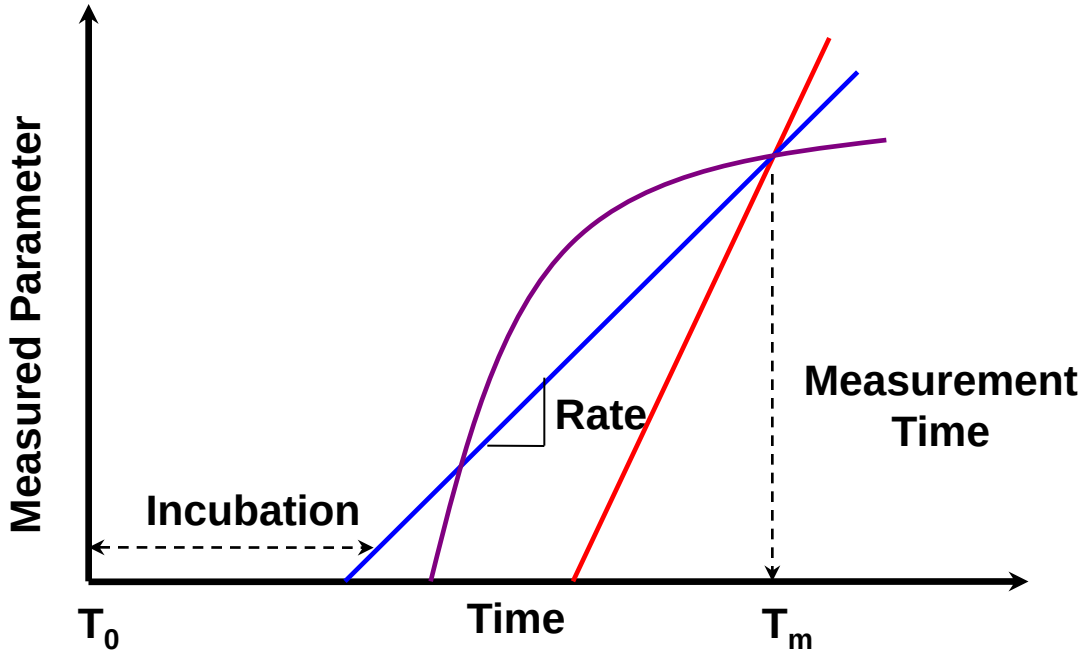

Movie Mode will let us capture a series of images from a single sample drive event.

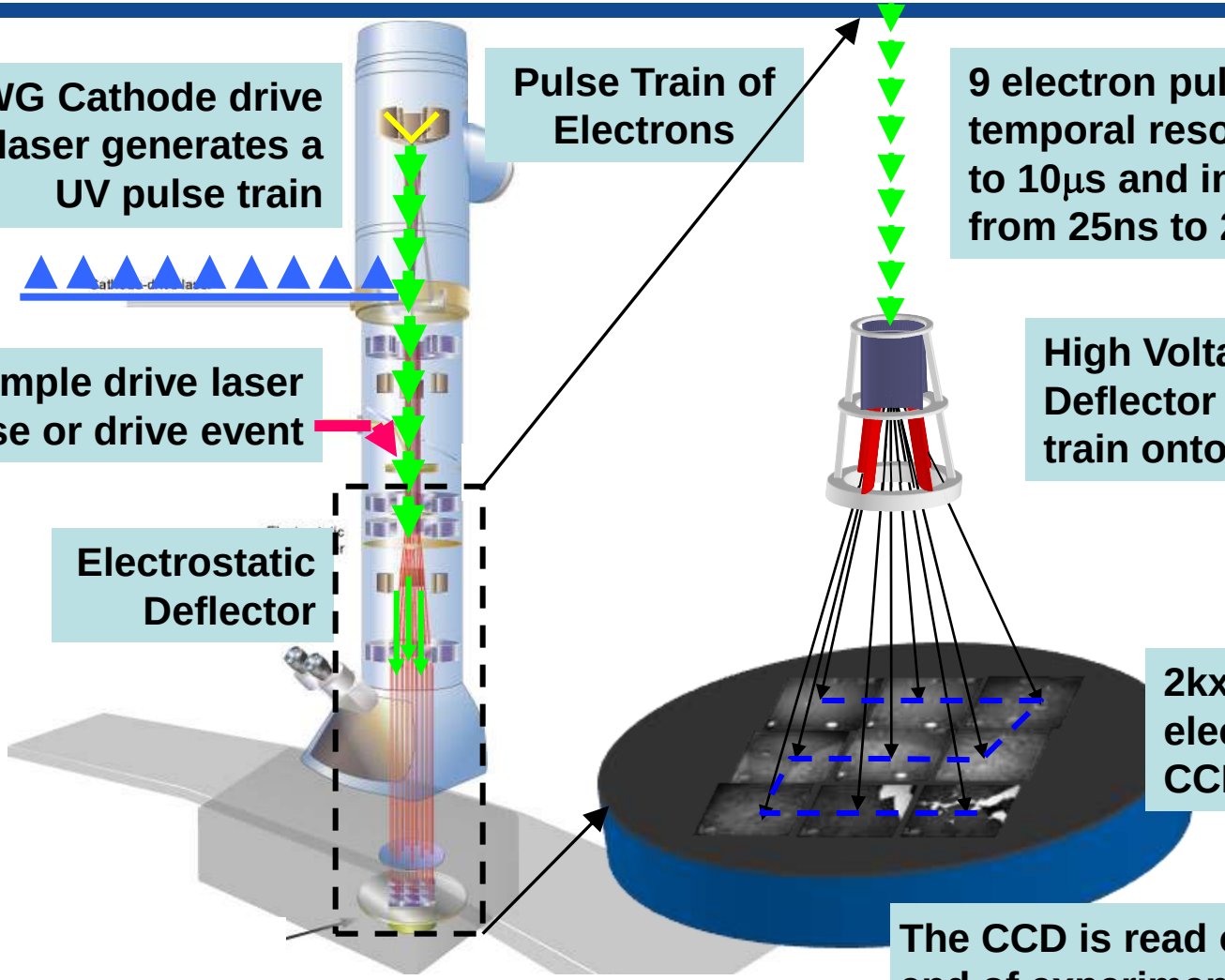

AWG Cathode drive laser generates a UV pulse train

Pulse Train of Electrons

9 electron pulses with temporal resolution from 5ns to 10μs and interframe times from 25ns to 250μs

Sample drive laser 1 pulse or drive event

High Voltage Electrostatic Deflector rasters pulse train onto the CCD

Electrostatic Deflector

2kx2k Single-electron Sensitive CCD camera

The CCD is read out at the end of experiment and segmented into frames.

DTEM needs bright sources, but ultimately higher time resolution limits spatial resolution!

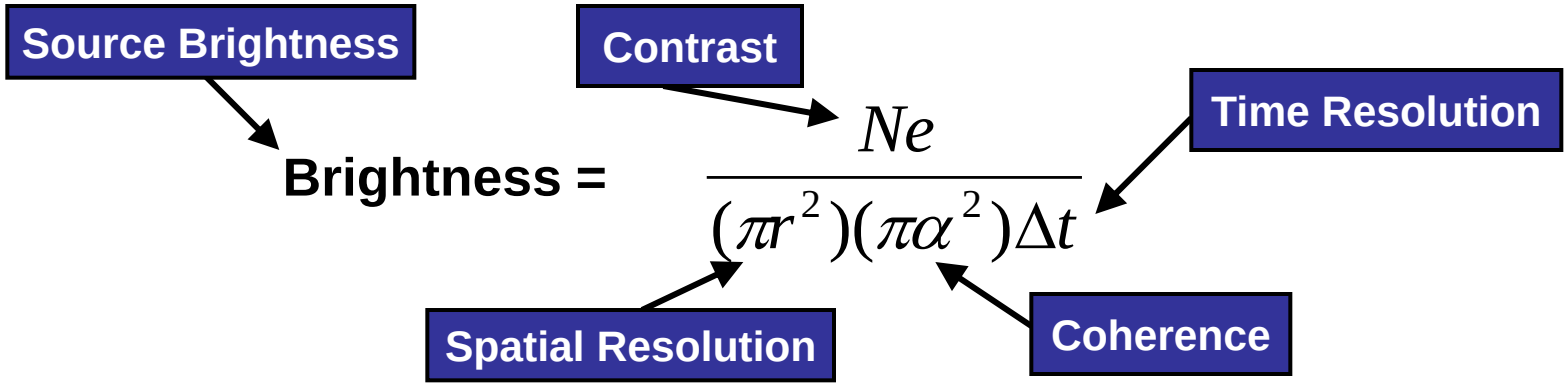

Resolution is governed by the fixed normalized brightness of the gun!

Lens aberrations and electron-electron interactions can reduce your effective average brightness in your system.

A high quality image needs N ~ 10^8 electrons.

Suppose r = 1 μm, α = 10 mrad, Δt = 1 ns.

Brightness = 1.6x10^9 A cm^{-2} $steradian^{-1}$, with 16 mA at the camera.

This is the brightness of a typical field emitter, but with vastly more current.

DTEM currently has brightness of ~1x10^8 A cm^{-2} $steradian^{-1}$

With high electron currents, electron-electron interactions limit brightness and spatial resolution.

Longitudinal Space Charge

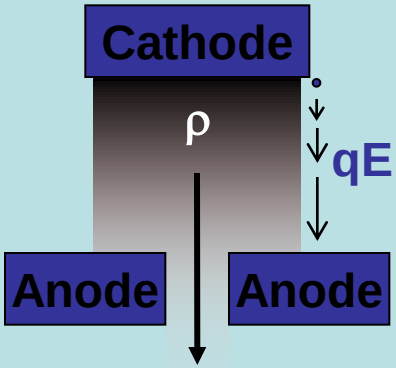

Child's Law:

- Field from recent electrons retards emission
- Fundamentally limits current density:

$$j \propto V^{3/2} / d^2$$

Lateral Space Charge

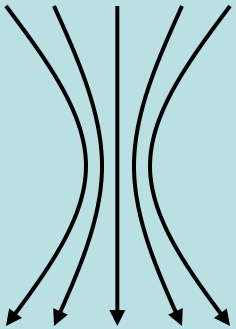

Defocusing:

- To first order, it's just a diverging lens
- Higher orders create spherical aberration

Longitudinal Inhomogeneous

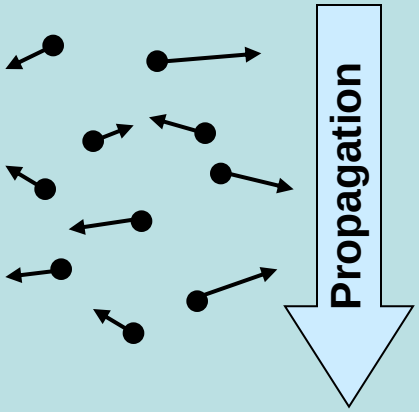

Boersch Effect:

- Pulse viewed in rest frame
- Most velocity is lateral
- Equilibration increases ΔE

Lateral Inhomogeneous

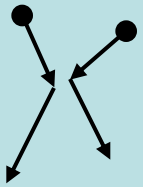

Trajectory Displacement:

- Random electron-electron scatter
- High-resolution information stored in lateral velocities is gradually destroyed

History: DTEM grew out of developments in time-resolved TEM that date back to the 1960's

- "Stroboscopic" TEM uses many synchronized pulses to capture a cyclic process
  - Magnetic domain wall motion (Spivak et al., *Bull Acad. Sci. USSR* **30**, 822 (1966))
- Groups in Europe and Japan developed pulsed TEM and SEM through the 1980's and 1990's
  - Multi-frame movies with 30 μs exposure, ms interframe time (Takaoka & Ura, *J. Elect. Mic.* **32**, 299 (1983))
  - Nanosecond-scale single-shot TEM with 3-frame movies (Domer & Bostanjoglo, *Rev. Sci. Inst.* **74**, 4369 (2003))
- Advances in lasers, TEM's, and ultrafast techniques have re-ignited the field in the last few years

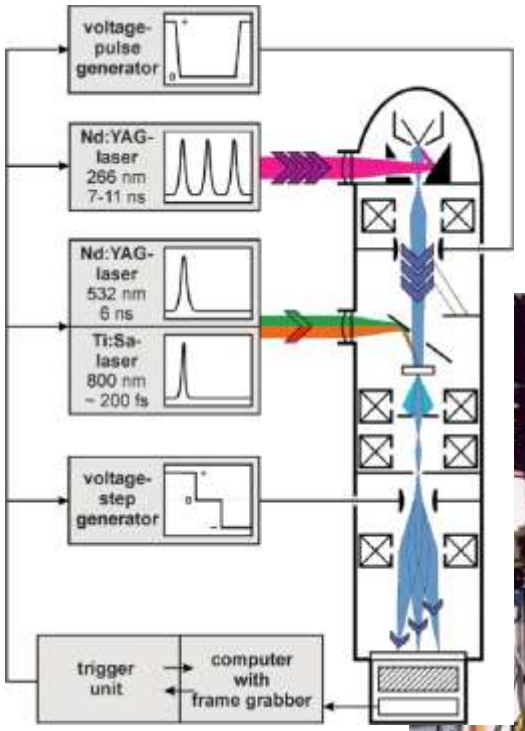

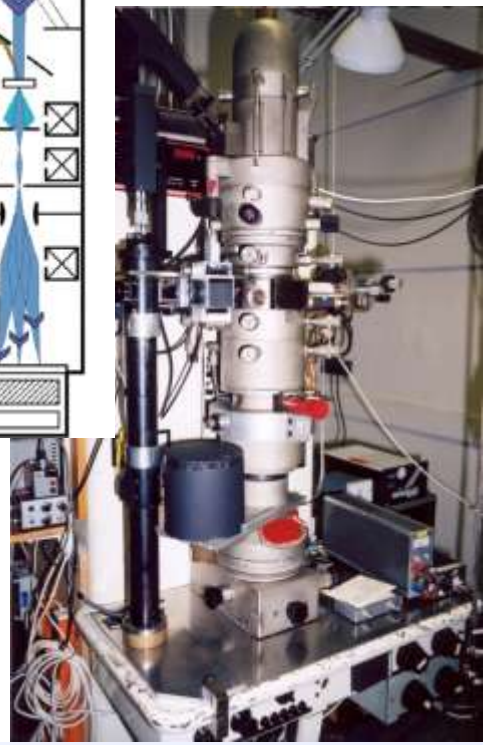

A femtosecond stroboscopic approach was developed by the Zewail group at Caltech

- 120 keV G12 Twin Tecnai
- Gatan Ultrascan 1000 UHS 2048 x 2048
- Results reported were acquired with 1 electron per pulse
- More recently developed a second-generation machine

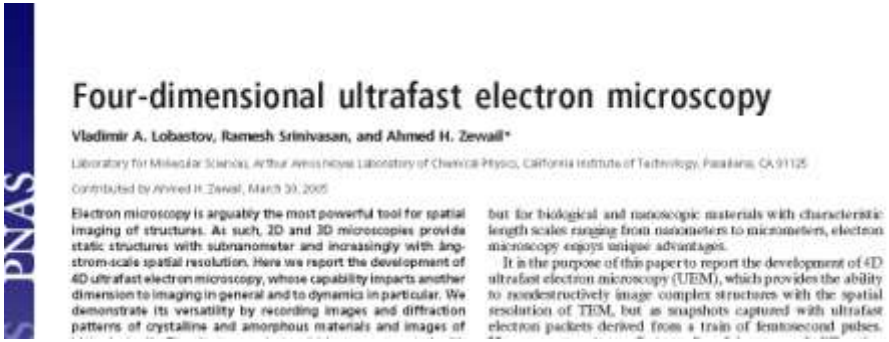

PNAS

Four-dimensional ultrafast electron microscopy

Vladimir A. Lobastov, Ramesh Srinivasan, and Ahmed H. Zewail*

Laboratory for Molecular Sciences, Arthur Amos Noyes Laboratory of Chemical Physics, California Institute of Technology, Pasadena, CA 91125

Contributed by Ahmed H. Zewail, March 30, 2005

Electron microscopy is arguably the most powerful tool for spatial imaging of structures. As such, 2D and 3D microscopies provide static structures with subnanometer and increasingly with ångstrom-scale spatial resolution. Here we report the development of 4D ultrafast electron microscopy, whose capability imparts another dimension to imaging in general and to dynamics in particular. We demonstrate its versatility by recording images and diffraction patterns of crystalline and amorphous materials and images of

but for biological and nanoscopic materials with characteristic length scales ranging from nanometers to micrometers, electron microscopy enjoys unique advantages.

It is the purpose of this paper to report the development of 4D ultrafast electron microscopy (UEM), which provides the ability to nondestructively image complex structures with the spatial resolution of TEM, but as snapshots captured with ultrafast electron packets derived from a train of femtosecond pulses.

PNAS 2005;102[20]:7069-73

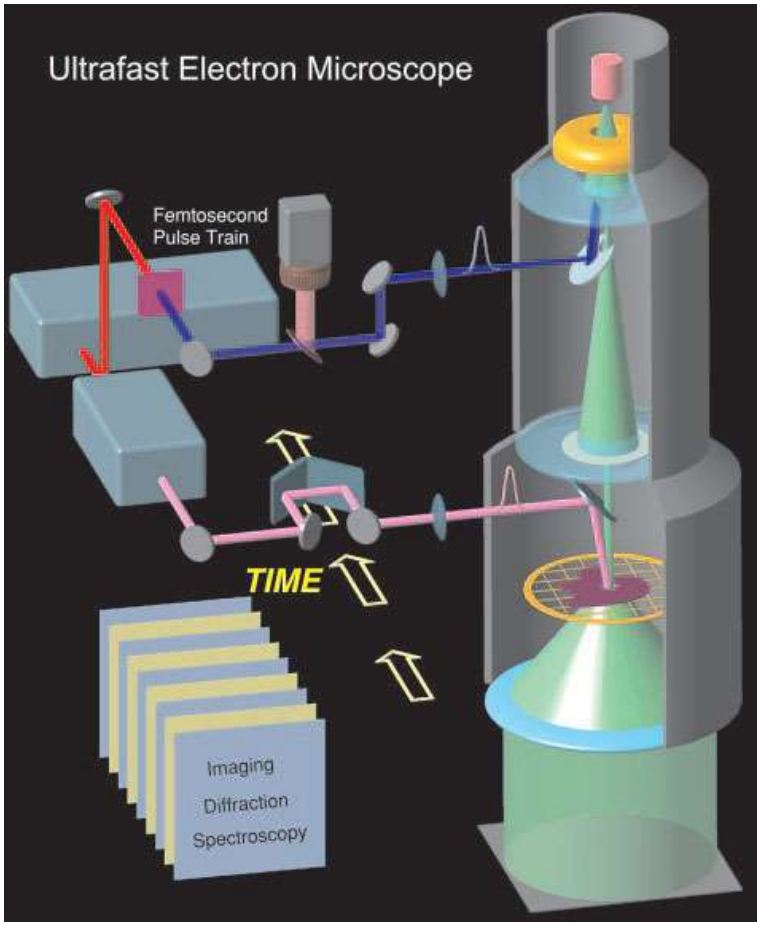

Time-resolved electron probes divide roughly into three categories

	Stroboscopic	Intermediate	Single Shot
Example	UFTEM	UED	DTEM
Electrons/Pulse	~1-10^3	~10^3-10^6	~10^7-10^9
Pulses/Image	10^5+	Few-100	1
Time Resolution	Sub-ps	sub-ps to few ps	15 ns
Spatial Resolution	Å	Many µm	~10 nm
Energy Spread	~1 eV	~100 eV	~10 eV
Spectroscopy	Yes	Not demonstrated	Not demonstrated
Main Strength	Spatiotemporal resolution	Great for diffraction; systems are simple	Capture unique, irreversible events in real space
Main Weakness	Extremely repeatable processes only	Imaging is difficult	Resolution

Trajectory displacement will limit resolution to at best 5 nm at 1 ns, 200 keV

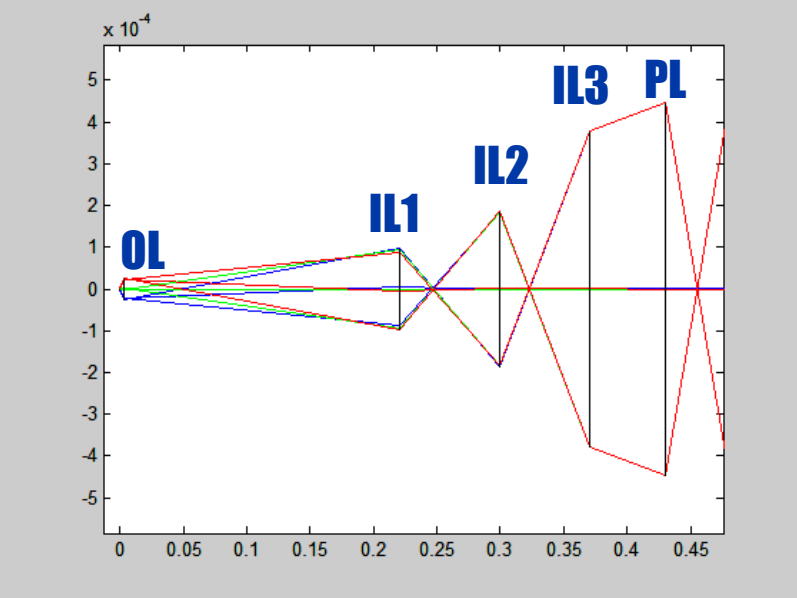

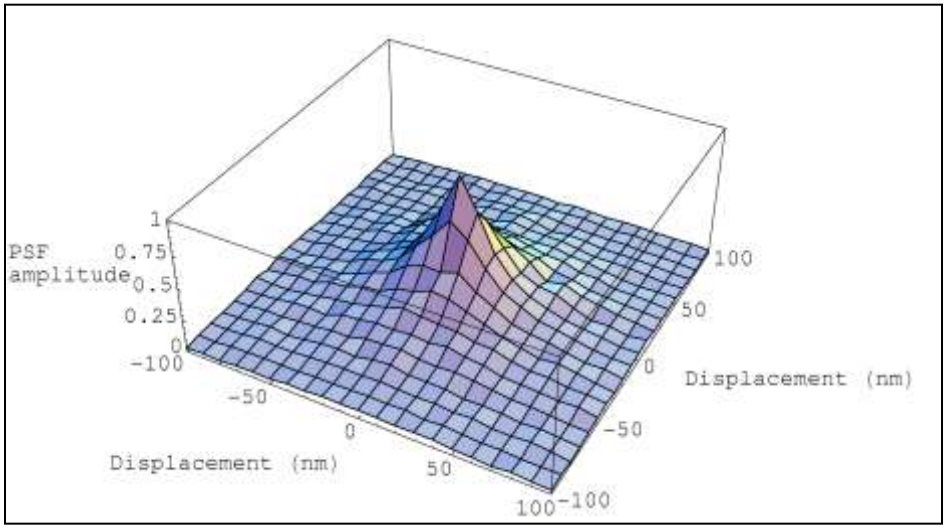

Analytical formulas were applied to optical model of post-sample lens system.

Result: 5-50 nm resolution limit, depending on current and lens settings

Numerical multi-particle simulation of electron point spread function after sample interaction

Result: 5-50 nm resolution limit, depending on current and spot size

Simulation has suggested the feasibility of ultrafast (< 10 ps) electron imaging

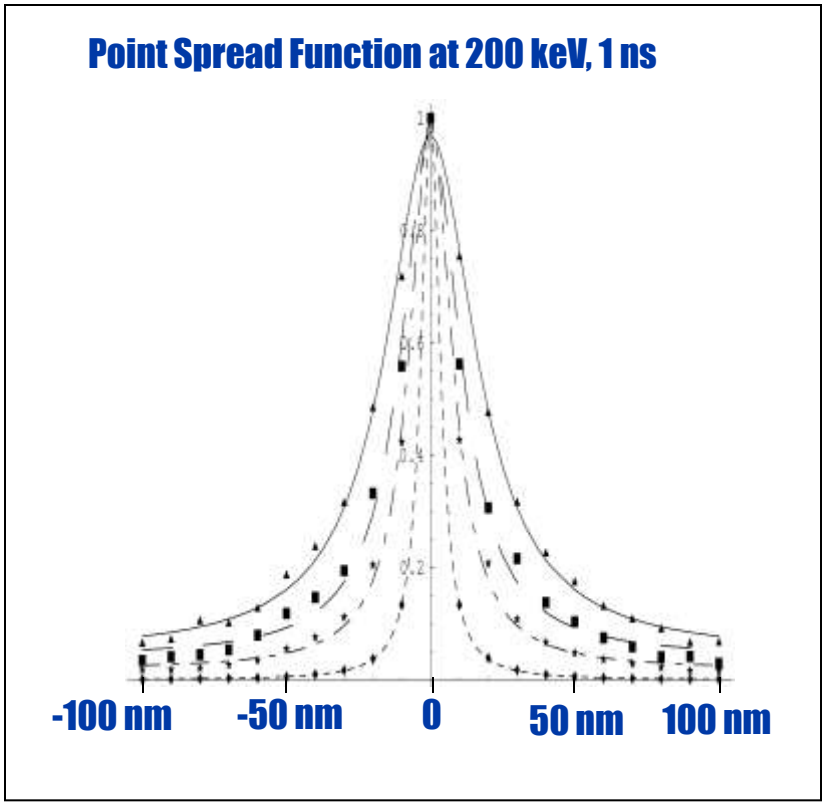

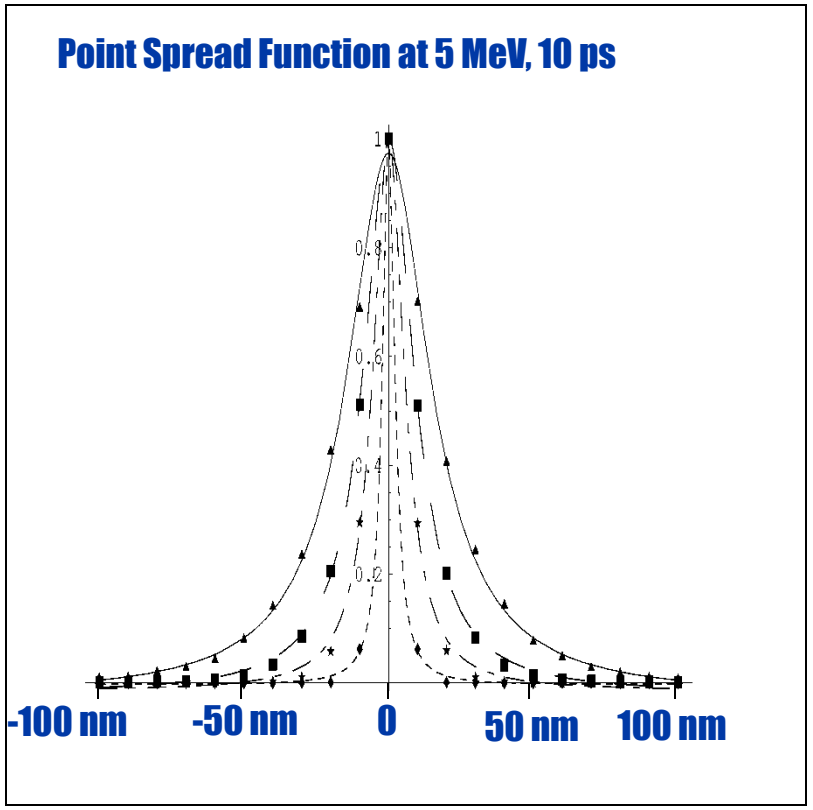

For picosecond resolution imaging, relativistic energies may be the only way to obtain high spatial resolution.

Relativistic pulses significantly mitigate stochastic blur.

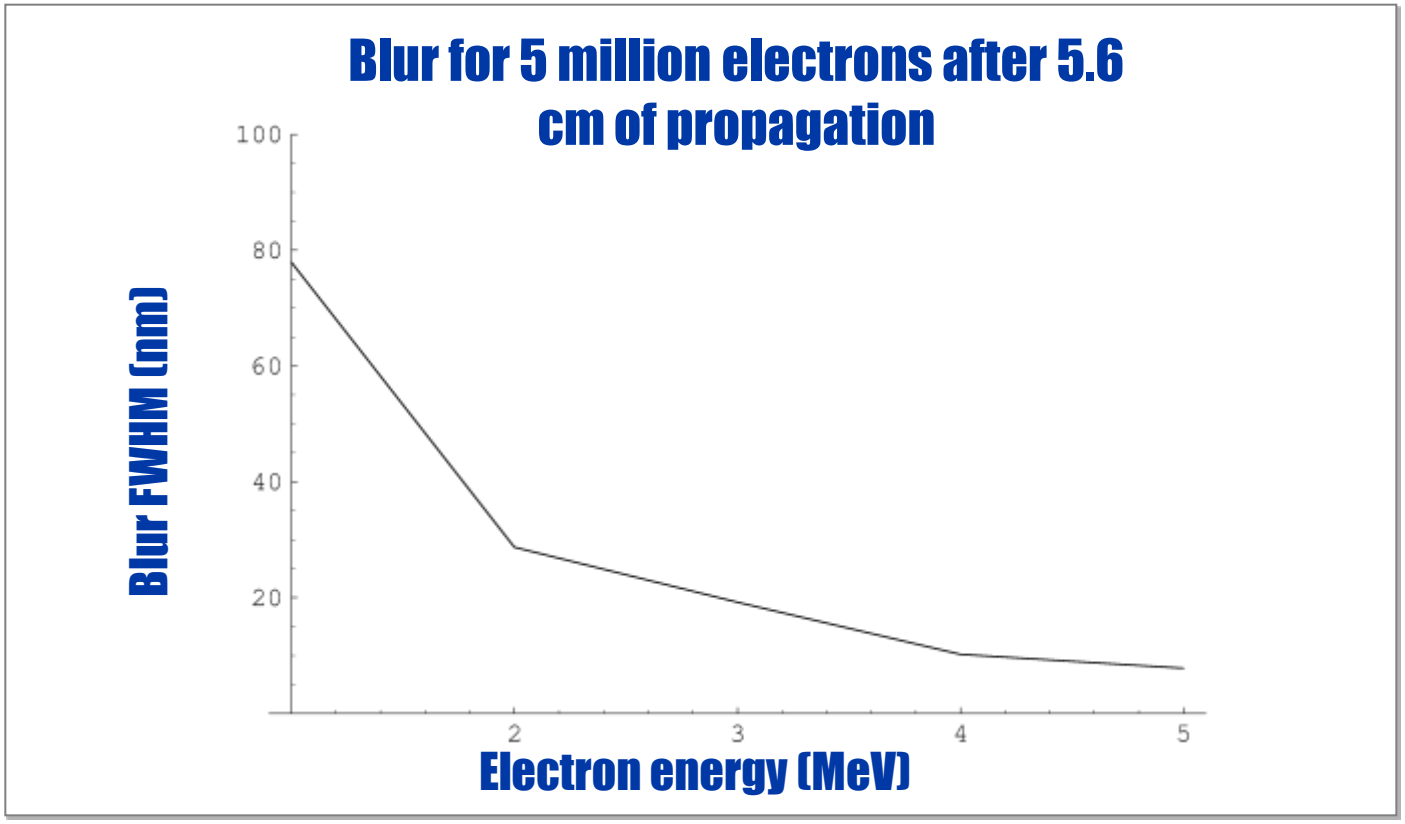

Relativistic electrons have a shorter (proper) propagation time, diverge more strongly, and have smaller current density.

A future DTEM might look more like a particle accelerator

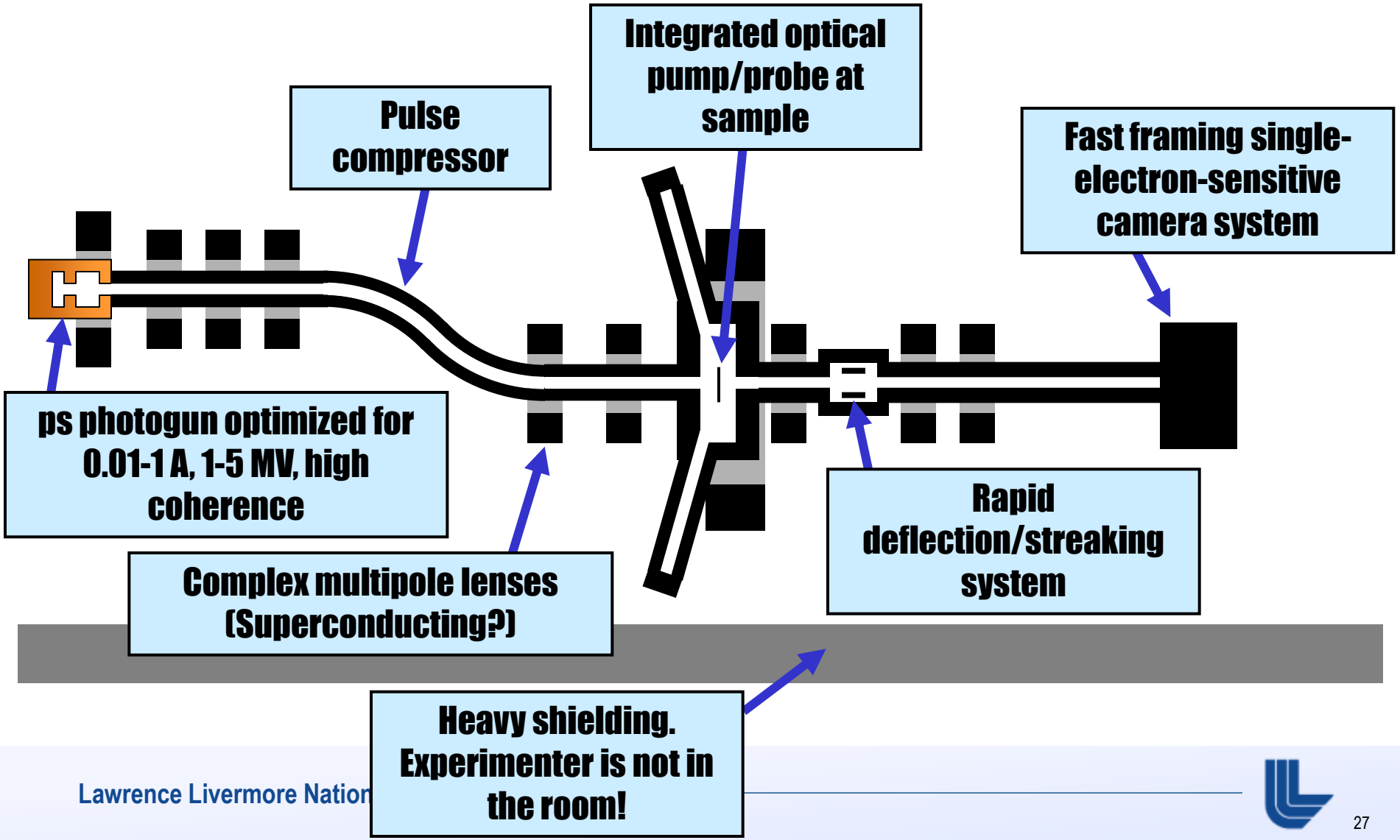

NUCLEATION IN AMORPHOUS Al ALLOYS

Influence of Solute Distribution

Joint AFRL/AOARD/LLNL Workshop on Nucleation During Solid-Solid Phase Transformations in Metallic Systems

5 May 2010

J.E. Spowart[a], D.B. Miracle[a] and H.M. Mullens[b]

a. AF Research Laboratory
Materials and Manufacturing Directorate
Dayton, OH USA

b. Southwestern Ohio Council for Higher Education (SOCHE)
Materials and Manufacturing Directorate
Dayton, OH USA

AFRL
THE AIR FORCE RESEARCH LABORATORY

Cleared for Public Release: ASC 02-0416

"~~metallurgists~~ experimentalists are apt to be practical down-to-earth people who stand no nonsense, but the ~~non-metallurgists~~ theoriticians are probably more lyrical and imaginative"

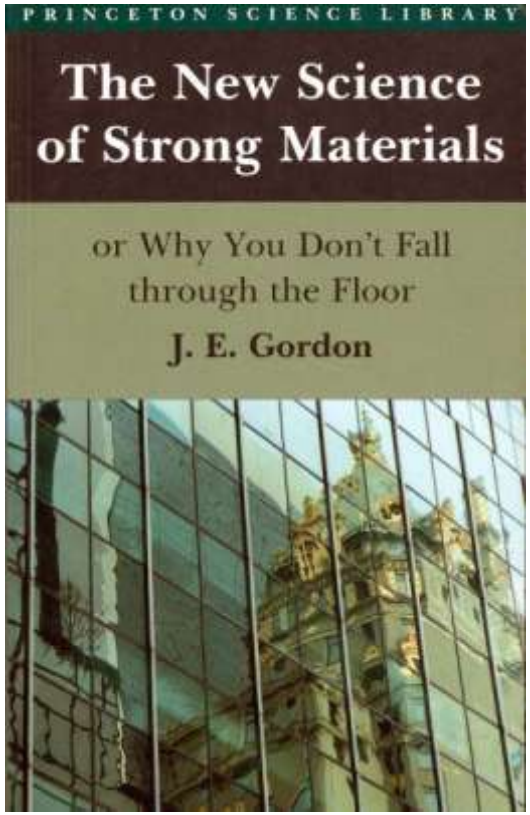

OUTLINE

INTRODUCTION

Properties and Applications of Metallic Glasses

NUCLEATION IN AMORPHOUS Al

MODELING OF NUCLEATION SITES

CONCLUSIONS

MULTIFUNCTIONAL METALS OF DISTINCTION

Unique balance of properties distinguish metallic glasses as a distinct class of metals

- **Mechanical**
  - *Very high hardness*
  - *Strength twice that of conventional metals*
  - *Fracture toughness can be very high*
  - *High resilience and low mechanical damping*
- **Magnetic**
  - *High magnetic permeability &low hysteresis losses*
  - *Highly tailorable magnetic properties*
- **Corrosion**
  - *Lack of crystal defects (grain boundaries) and unique formulations give exceptional corrosion behavior*
- **Processing**
  - *High viscosity and low strain rate sensitivity of the supercooled liquid enables thermo-plastic forming that was previously impossible*
  - *Low solidification shrinkage and lack of grain structure gives high precision and finish in castings*

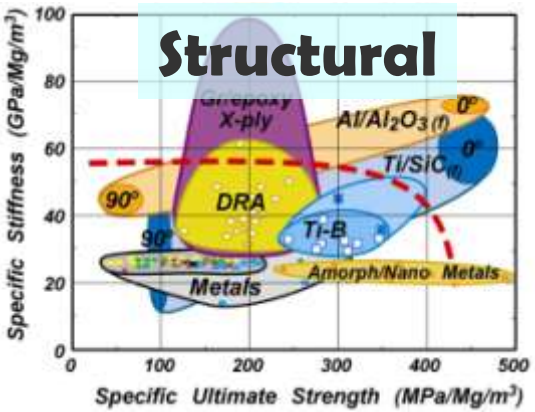

AMORPHOUS METALS
Current Applications

Low loss magnetic material
- ❖power and current transformers
- ❖video recording heads
- ❖electronic surveillance tags

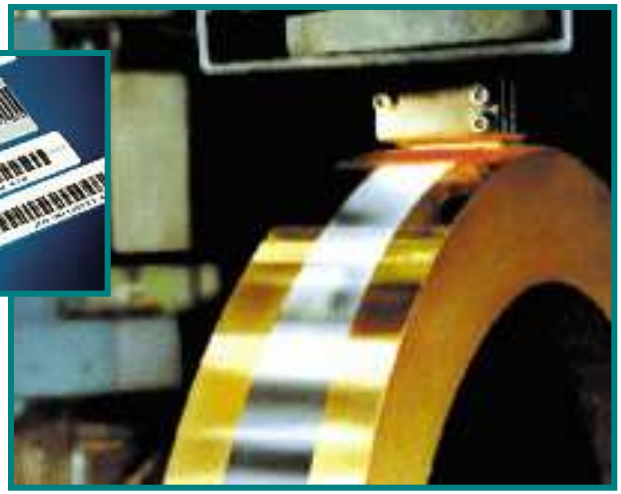

Corrosion resistance
- ❖corrosion resistant coatings for safety razors
- ❖nuclear containment coatings being validated

Structural applications
- ❖micro-mirror hinges for digital projection systems
- ❖golf club heads, tennis racquets, baseball bats
- ❖electronics cases for cell phones, laptops, PDAs
- ❖brazing alloy

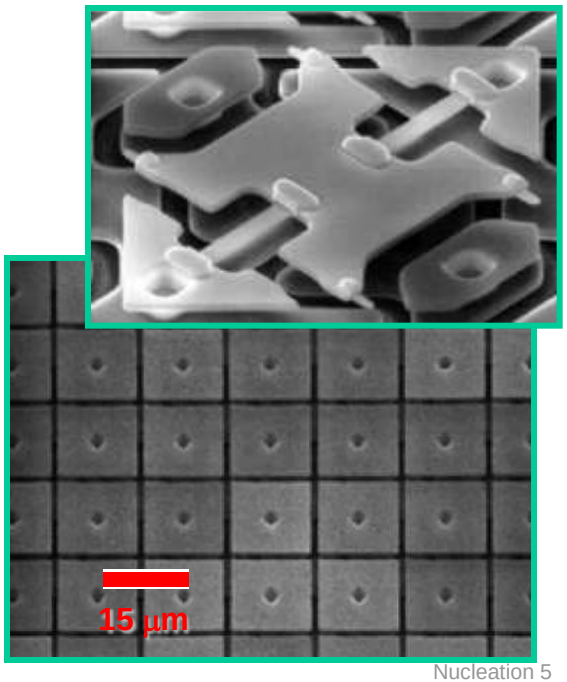

MAGNETIC APPLICATIONS OF METALLIC GLASSES

Power transformer cores for electricity distribution

- Significant reduction in hysteresis losses, especially in systems with higher harmonics introduced by non-linear loads in modern electronics
  - *Non-linear power supplies, variable speed motors, lighting controls, electronic power sources in personal computers and telecommunications…*

Electronic power supplies and power conditioners

Magnetic read/write heads

- Also takes advantage of high hardness and excellent wear resistance

Magnetic shielding

Industries impacted by metallic glass applications

- Electrical power distribution
- Electronics
- Communications
- Computers
- Electronic article surveillance

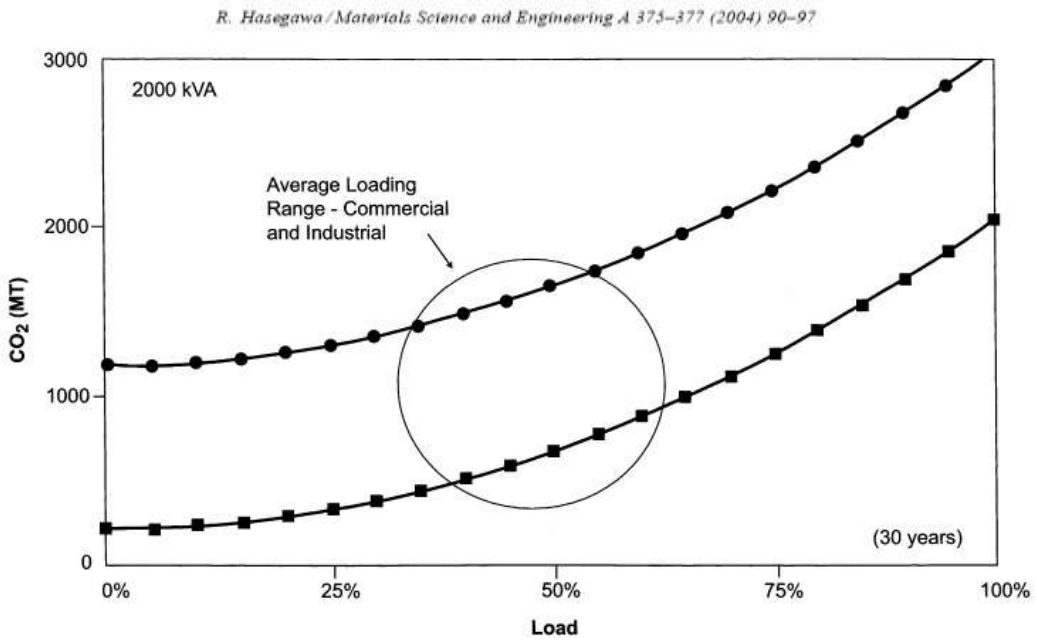

TAILORABLE *B-H* CHARACTERISTICS

'Square' *B-H* Curve for Voltage Control

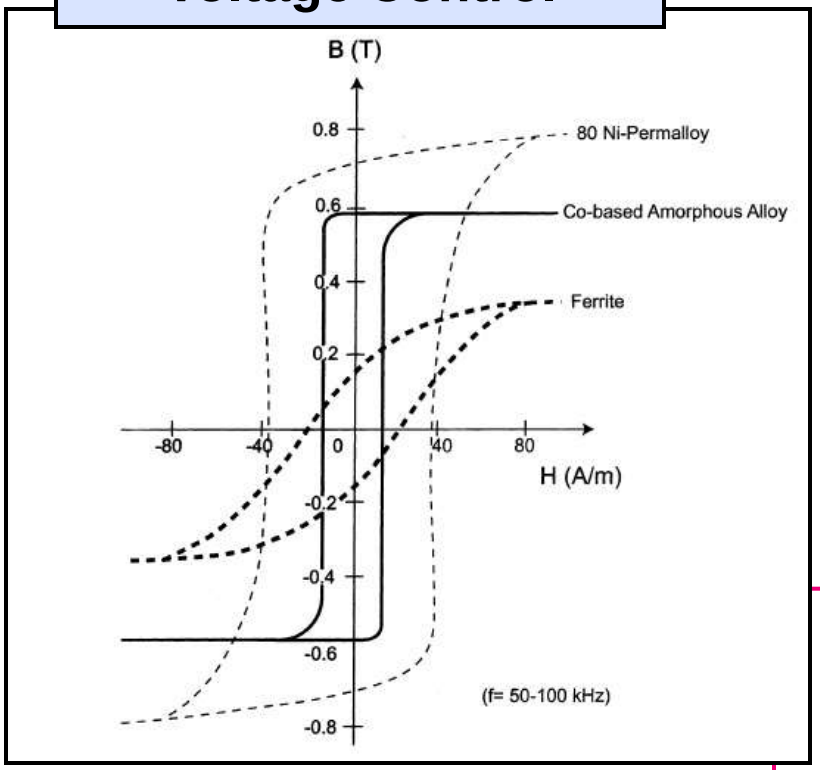

Linear permeability for interface transformers

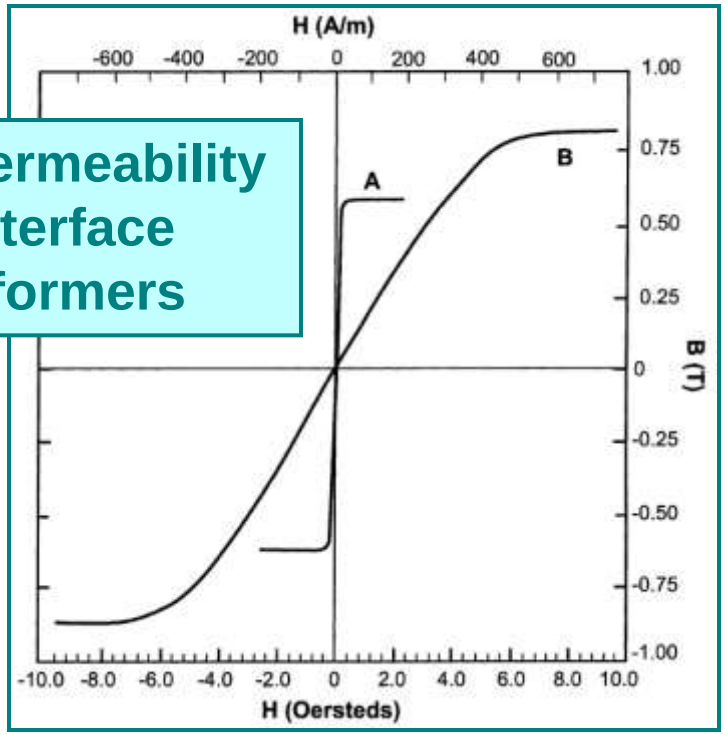

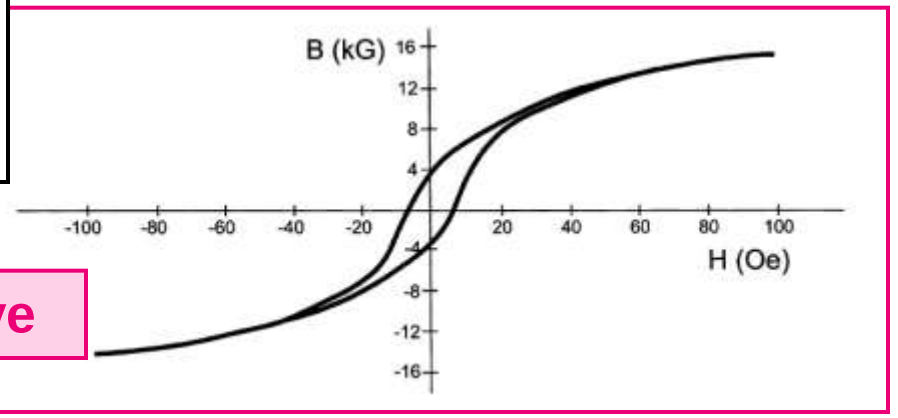

'Choke coil' *B-H* Curve

Hasegawa; *MSE*, **A375-377** (2004) 91-97

ELASTIC LIMIT v. STIFFNESS

Springs

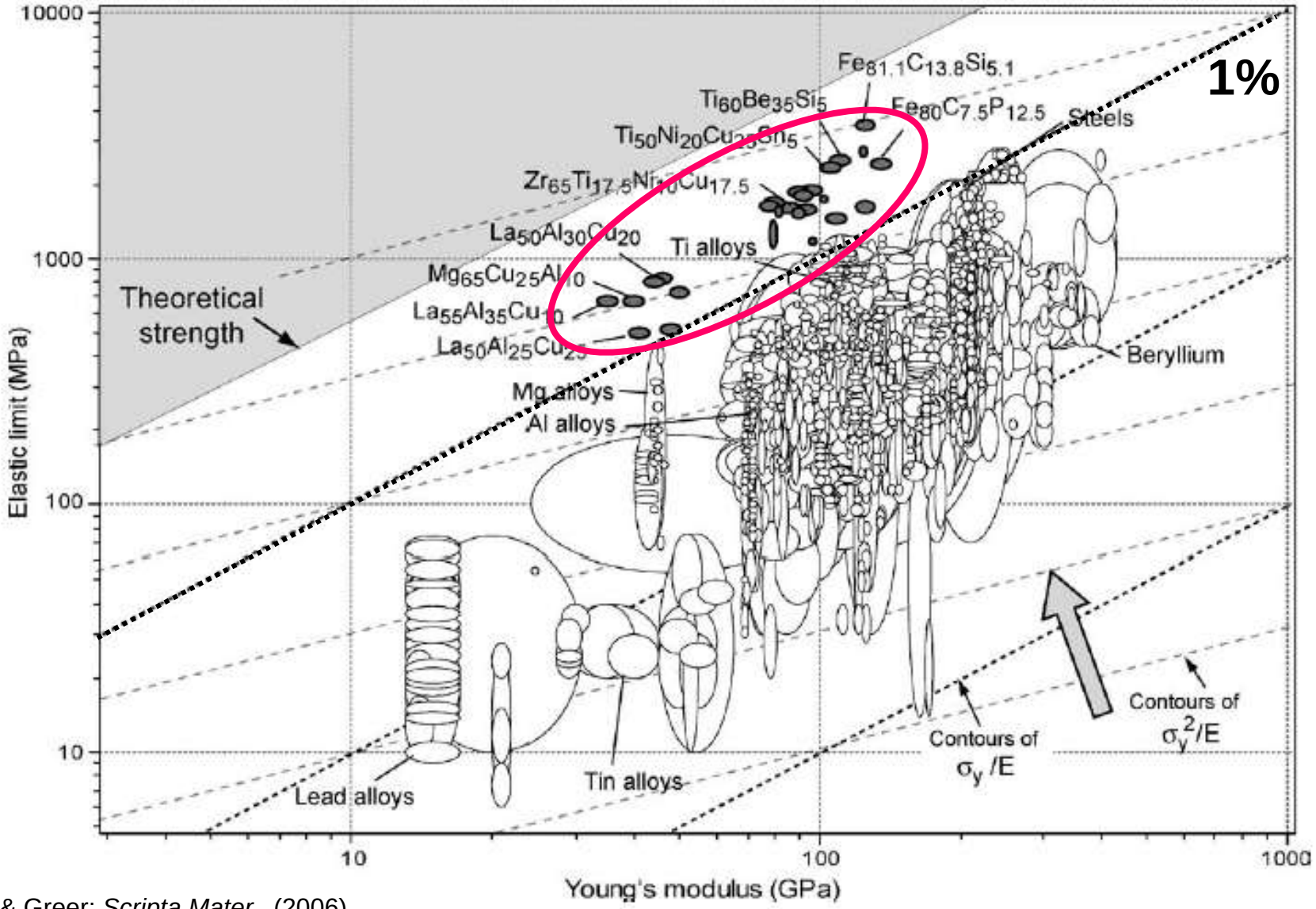

Ashby & Greer; *Scripta Mater.*, (2006)

RESILIENCE *v.* LOSS COEFFICIENT
Vibrating Reeds

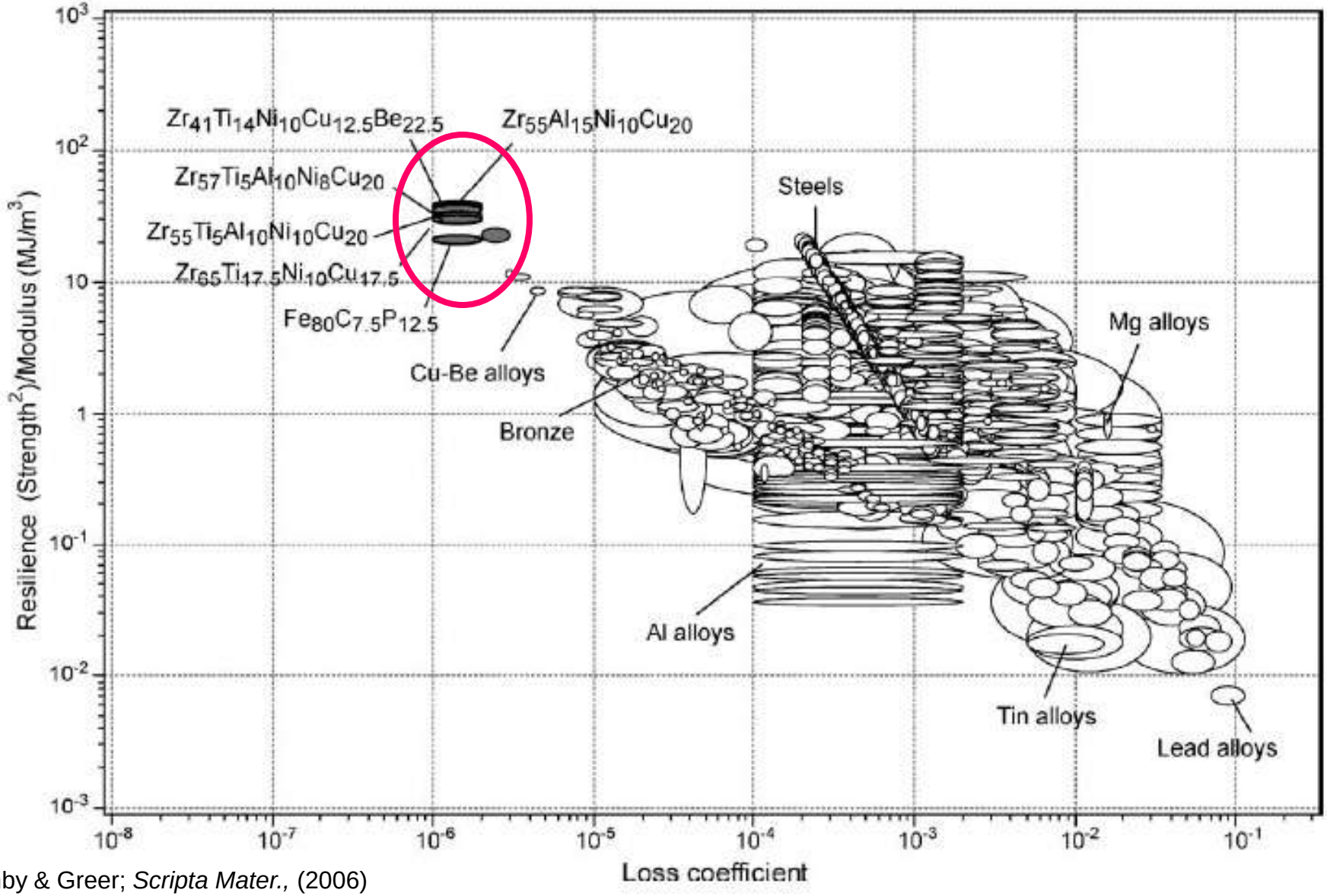

Ashby & Greer; *Scripta Mater.*, (2006)

FRACTURE TOUGHNESS v. STIFFNESS

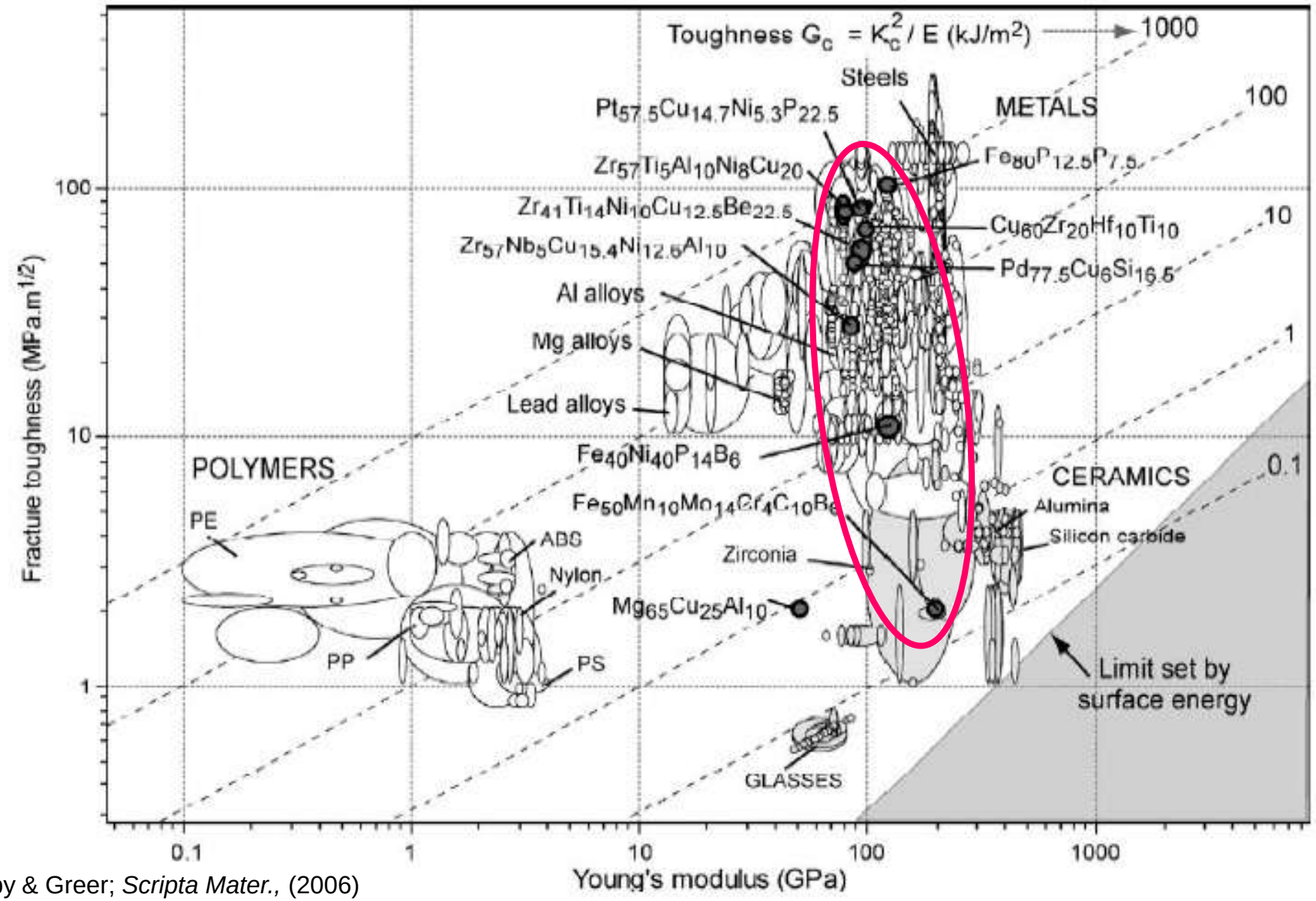

Ashby & Greer; *Scripta Mater.*, (2006)

PLASTIC-LIKE PROCESSING OF AMORPHOUS METALS

Conventional metals cannot be practically supercooled for processing
- ❖ Crystal nucleation occurs quickly at low undercooling, followed by rapid growth

The liquid is stabilized far below T_m in metallic glasses
- ❖ Chemical and topological contributions stabilize the metallic glass structure

Enables injection molding to produce net shape metallic components
- ❖ process time increases dramatically after cooling below the 'nose'
- ❖ thick sections (>1 cm) can be formed in bulk metallic glasses

Metal injection molding provides important processing capability
- ❖ enables unitized construction of complex shapes where part volume is important
- ❖ metals compete successfully with plastics for both cost and performance

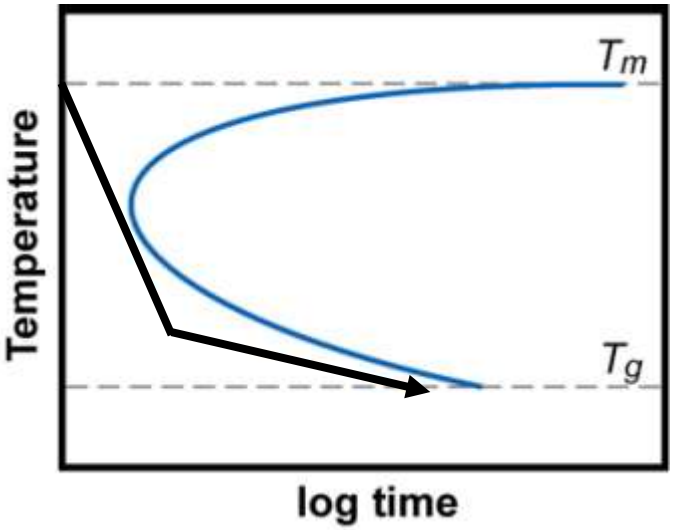

BLOW-MOLDING: No contact area

Courtesy J. Schroers

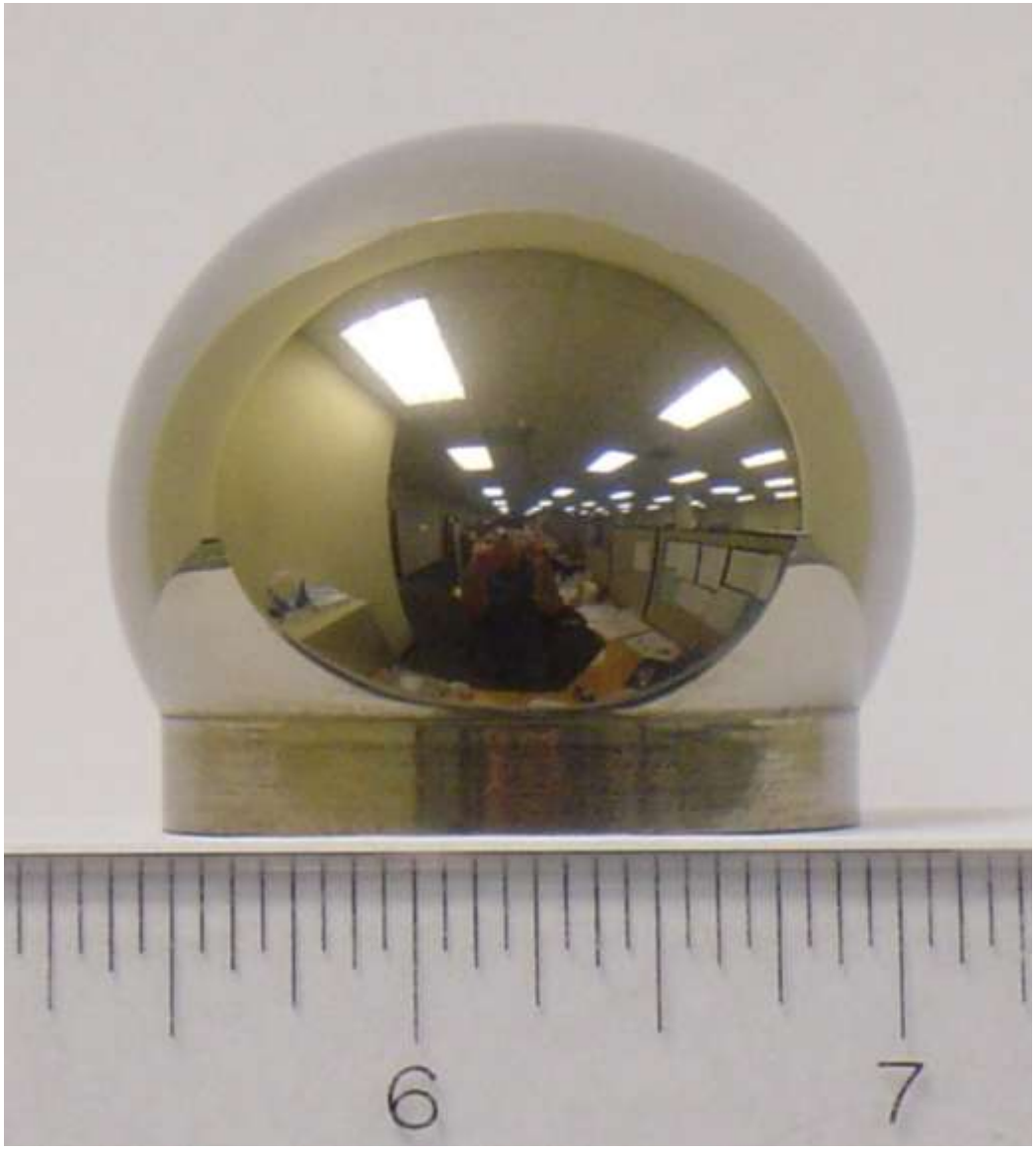

Zr44Ti11Cu10Ni10Be25 (LM1b)

T=460°C, t =40 sec

10^5 Pa, 400% strain

J. Schroers, T. Nguyen, A. Peker, N. Paton, R. V. Curtis, Scripta Materialia, 57, 341 (2007)

Unachievable shapes for metals?

Courtesy J. Schroers

Yale

Hollow, thin, seamless, complex parts

J. Schroers, *Processing of bulk metallic glass. Advanced Materials, 21, 2009*

TPF OF BMG-How small can you go?

Courtesy J. Schroers

ZrTiNiCuBe on C (a) AlN (b)

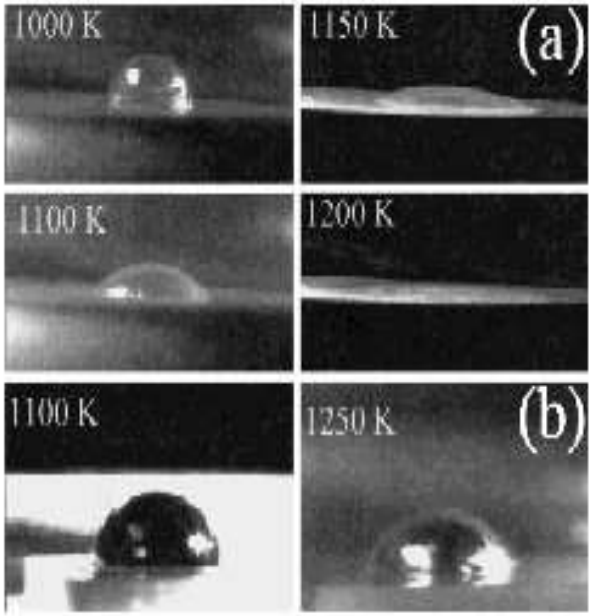

J. Schroers, K. Samwer, F. Szuecs, W.L. Johnson, JMR, 15, 1617 (2000)

PtNiCuP into porous Al2O3

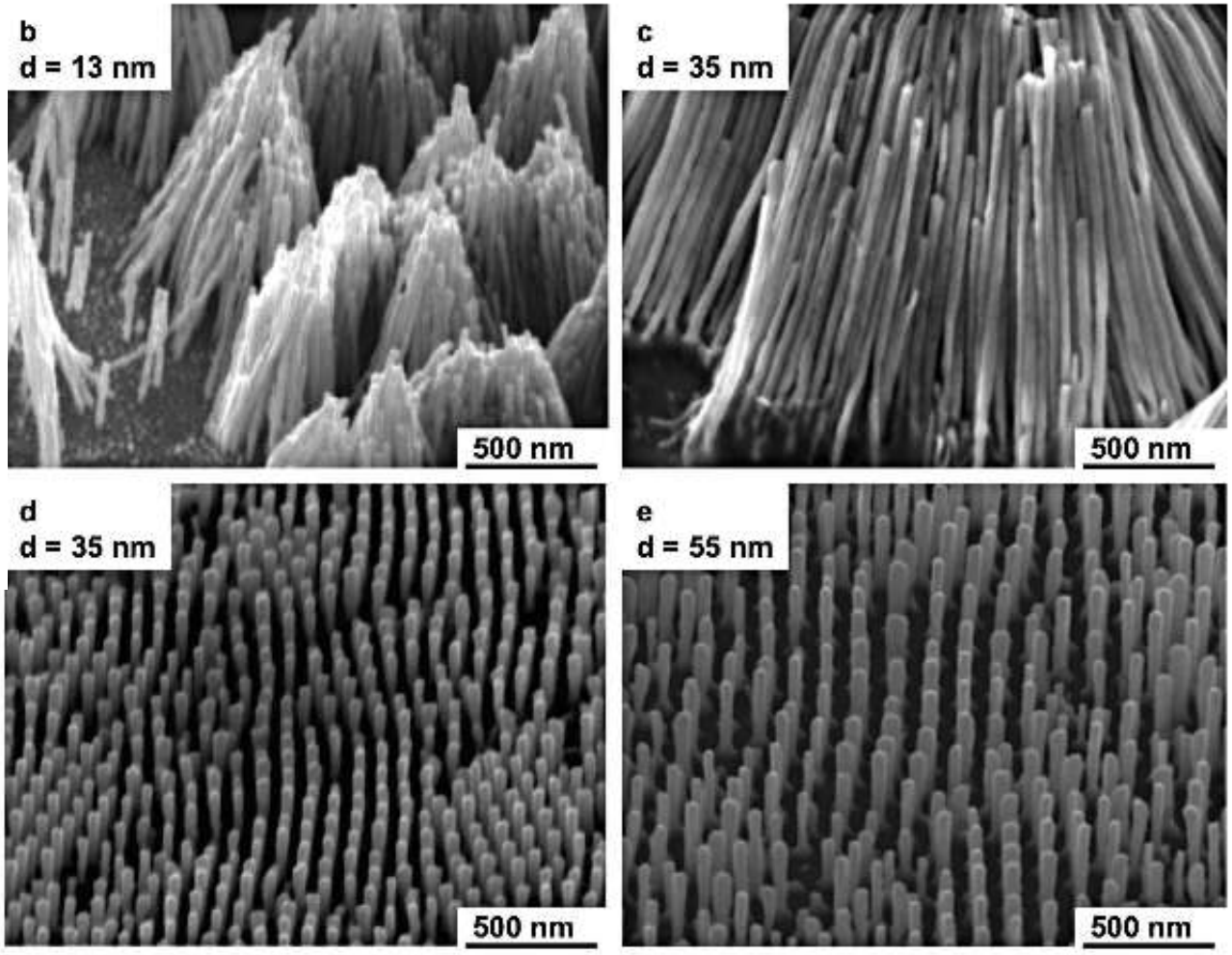

G. Kumar, H. Tang, and J. Schroers, Nature 457, 868 (2009)

AMORPHOUS METALS
Potential Aerospace Applications

Metallic glasses properties motivate important applications

- Sensor/actuator applications
  - *exceptional soft and hard magnetic properties*
  - *magneto-strictive and GMR behavior*
  - *remote sensing of temperature, stress, strain*
- Power transformers
  - *exceptional soft magnetic properties*
- Structural applications
  - *enabling specific strength*
  - *good fracture toughness*
  - *penetrators*
- Environmental applications
  - *exceptional corrosion resistance*
  - *unusual friction, wear resistance*
- Information storage and reproduction
  - *ability to reproduce very fine surface details*

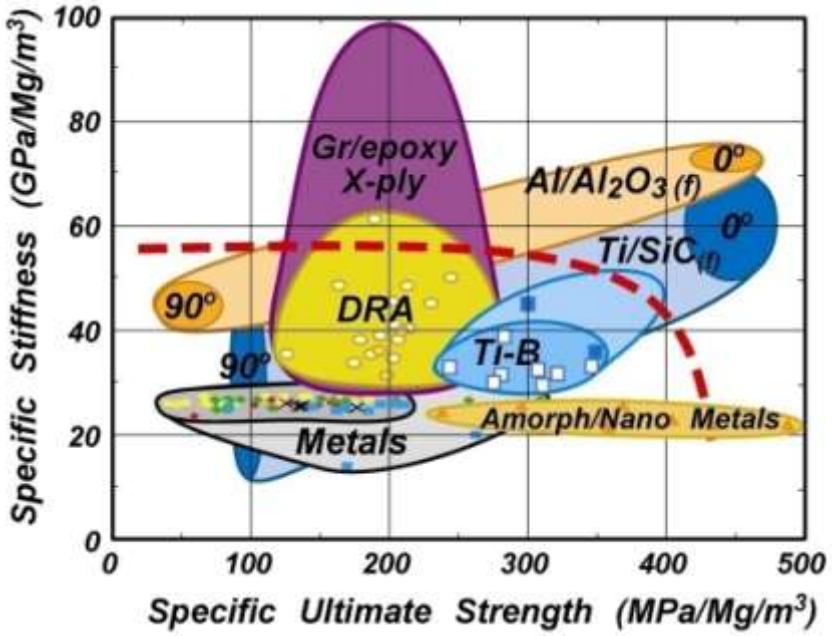

NUCLEATION IN AMORPHOUS METALS

- No fundamental differences from crystal nucleation in undercooled liduids and supersaturated solids
- Systems are characterized as far from equilibrium
- A significant number of systems show nucleation of icosahedral and quasicrystalline phases
- Some alloys show an exceptionally high number density of nuclei (~10^{21} to 10^{23} m^{-3})

OUTLINE

INTRODUCTION

NUCLEATION IN AMORPHOUS Al

- *Characteristics*
- *Influence on Properties*

MODELING OF NUCLEATION SITES

CONCLUSIONS

In Situ NANOCRYSTALS IN AMORPHOUS METALS

Nanocrystal dispersions can be formed *in situ* in amorphous Al

- Al nanocrystals are 5-30 nm in diameter
- Al nanocrystals are at an exceptionally high number density (10^{21} to 10^{23} /m^3)

Improves strength and ductility

- mechanisms unknown

Nucleation mechanism unknown

- conventional homogeneous and heterogeneous nucleation do not fit experimental observations

Control of nanocrystalline precipitation gives an approach to control properties of a-Al

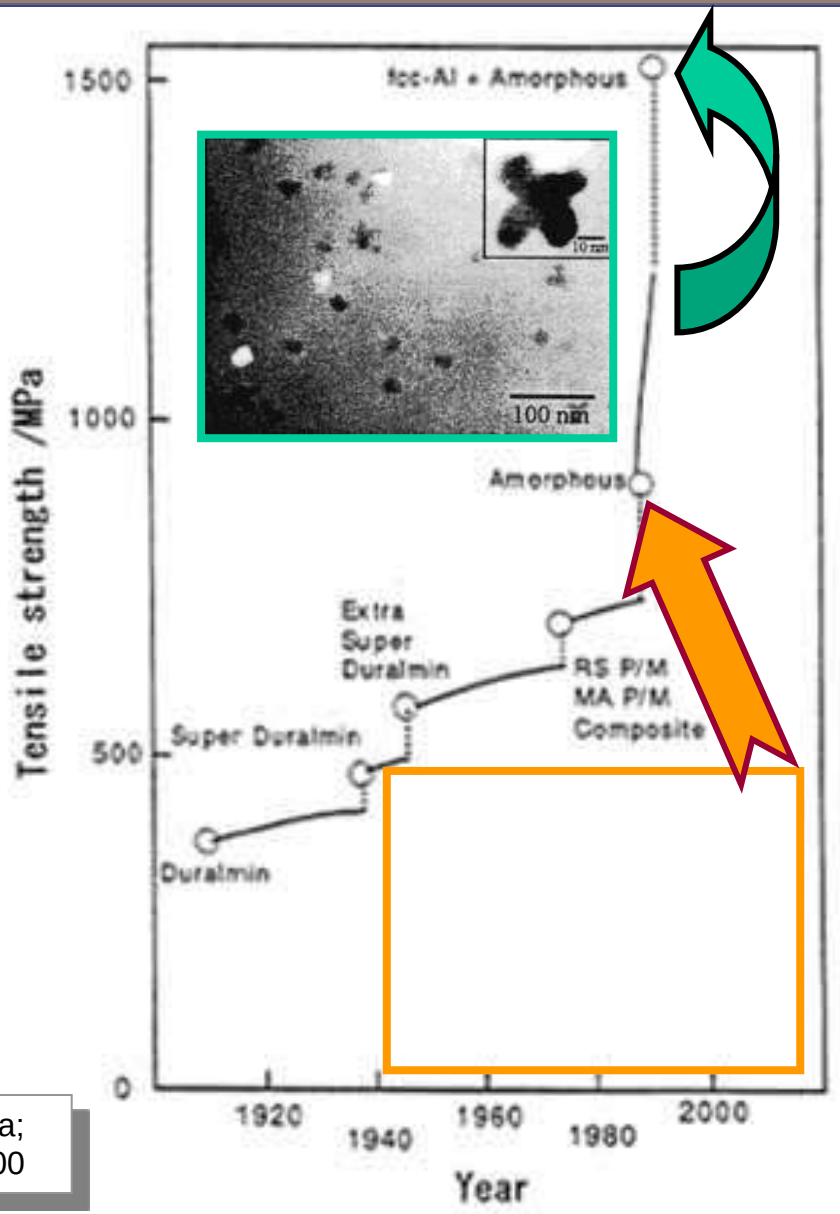

A. Inoue, H. Kimura; *Mat. Sci. Eng.*, 2000

CRYSTALLIZATION OF a-Al

Melt spinning produces amorphous product and crystallization initiates above T_x

Al crystallites are very small (~10-30 nm), and occur at an exceptionally high volume density (~$3x10^{21} m^{-3}$)

- typical volume density for standard metals is ~10^{16} m^{-3}
- Heterogenous nucleation unlikely
- Low apparent activation energy for nucleation
- nucleation at “quenched-in features” may be related to Al-like MRO in a-Al (Perepezko and Imhoff, 2009)
- features responsible for nucleation have not been identified

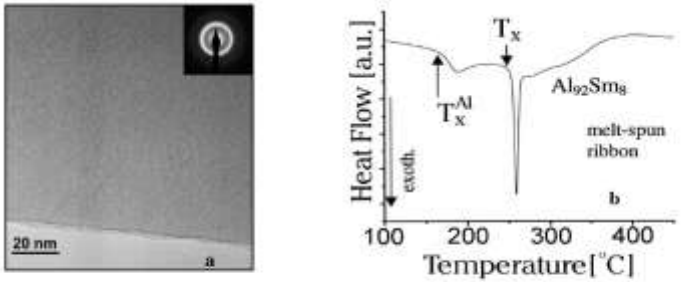

Figure 1: a) Bright-field TEM image and corresponding SAED pattern of as-spun $Al_{92}Sm_8$ ribbon. The analyses do not show any signs of crystallinity. b) Continuous DSC trace of as-spun $Al_{92}Sm_8$ at 20°C.min^{-1} [18]. The crystallization occurs in two steps. The primary crystallization peak with an onset at 172°C corresponds to the development of a high number density of Al-nanocrystals in the amorphous matrix. The second peak is attributed to the crystallization of the remaining amorphous phase.

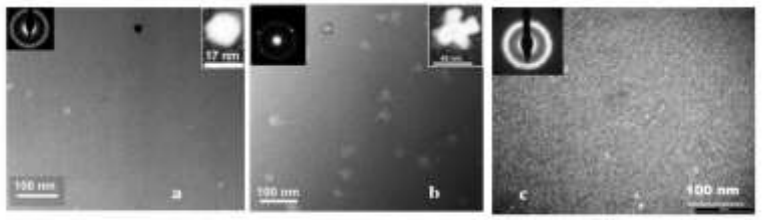

Figure 5 : TEM images of $Al_{88}Y_7Fe_5$ a) and b) Bright-field and corresponding SAED images of as-spun samples that have been annealed at 245°C for 10 and 60 min, respectively. c) Dark-field and corresponding SAED images of an as-spun sample that has been cold-rolled to a true strain of $\varepsilon = -10$. Both, thermal treatments and plastic deformation induce the development of Al-nanocrystals. The Dark-field TEM images in the inset show the shape evolution of nanocrystals from a spherical to a dendritic morphology with increasing annealing time.

Boucharat and Wilde, 2009.

"Gentleman, we have run out of ~~money~~ models. Now we must think."

Winston Churchill

OBJECTIVE

Provide a structural description of the sites responsible for the high nucleation density in partially devitrified amorphous Al

OUTLINE

INTRODUCTION

NUCLEATION IN AMORPHOUS Al

MODELING OF NUCLEATION SITES

CONCLUSIONS

STRUCTURAL MODEL FOR AMORPHOUS METALS

The structure of amorphous Al can be described as an organized arrangement of Y-centered clusters

- Y surrounded by ~14 Al and ~3Ni atoms
- Ni and Y solutes appear to be correlated
- Supported by measurement of partial coordination numbers

Intercluster regions are Al-rich and have a relatively high free volume

- high free volume produces local high internal energy, and also enables more rapid mass transport
- both of these favor nucleation of crystalline phases

Miracle, *Nature Materials*, **3**, 697 (2004).
Miracle, Acta mater., **54**, 4317 (2006).
Miracle, Louzguine, Louzguina, Inoue, *International Materials Review*, In press.

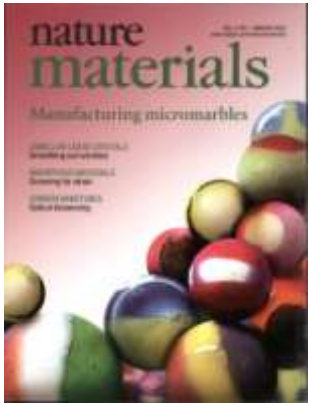

From our readers

SOLVING THE PUZZLE OF EUTECTIC COMPOSITIONS WITH 'MIRACLE GLASSES'

To the editor — The structural model for metallic glasses published in the October issue of *Nature Materials*[1] may account for the observed compositions of binary A_xB_y eutectics, which occur most frequently at integer values of x and y. In 1935, D. Stockdale[2] suggested that, in binary alloy phase diagrams, the compositions of eutectic points should correspond with simple whole-number ratios of the two kinds of atoms A (solvent > 50 at.%) and B (solute < 50 at.%). There was insufficient data to confirm this prediction at the time, but in 1960, W. Hume-Rothery and E. Anderson[3] re-examined the Stockdale suggestion by plotting the frequency of occurrence of binary eutectic compositions versus alloy compositions from the handbook of ... found clear maxima ... corresponded to A/B ... 1, 2/1 and 3/2.

Hume-Rothery and Anderson tried to explain this finding on the basis of the local short-range order (SRO) of the atomic structures in binary liquids by postulating that eutectic compositions are likely to form when interatomic interactions ... such that B–B nearest neighbours ...

A.R. Yavari, *Nature Materials*, **4**, 2 (2005)

INEFFICIENT ATOMIC PACKING AROUND Al ATOMS

Table 1. Coordination numbers and bond lengths for Al–RE–TM amorphous alloys.

	Coordination Number	Bond Distance (nm)	Local Atomic Concentration	Packing Efficiency
$Al_{87}Y_8Ni_5$ (7)				
Y–Al	14.3 ± 1.9	0.320	77%	88%
Y–Ni	2.7 ± 0.7	0.297	15%	14%
Y–Y	0.4 ± 0.4	0.356	8%	3%
Al–Al*	7.2 ± 0.8	0.286	84%	57%
Al–Ni*	0.4 ± 0.1#	0.268	4%	3%
Al–Y*	1.2 ± 0.2	0.320	12%	12%
Ni–Al*	6.5 ± 0.2#	0.268	59%&	60%
Ni–Ni&	0&		9%&	~0%&
Ni–Y*	3.5 ± 2.6	0.303	32%&	40%
$Al_{90}Y_{10}$ (7)				
Y–Y	1.1 ± 0.4	0.362	13%	9%
Y–Al	14.1 ± 1.5	0.320	87%	87%
Al–Y*	1.6 ± 0.2	0.320	12%	16%
Al–Al*	10.7 ± 0.8	0.288	88%	85%
$Al_{90}Ce_5Fe_5$ (8,9)				
Ce–Al	14.0 ± 1.6	0.325		85%
Fe–Al	4.9 ± 2.4	0.249		45%
$Al_{90}Ce_3Fe_7$ (8,9)				
Ce–Al	11.0 ± 2.3	0.325		67%
Fe–Al	6.4 ± 2.1	0.249		59%

* Data from total radial distribution functions.
\# Values corrected from original citation.
& Estimated value.

Local packing efficiency is only 72% around Al atoms

Miracle, *J. Non-Cryst. Sol.*, 2004.

FREE VOLUME

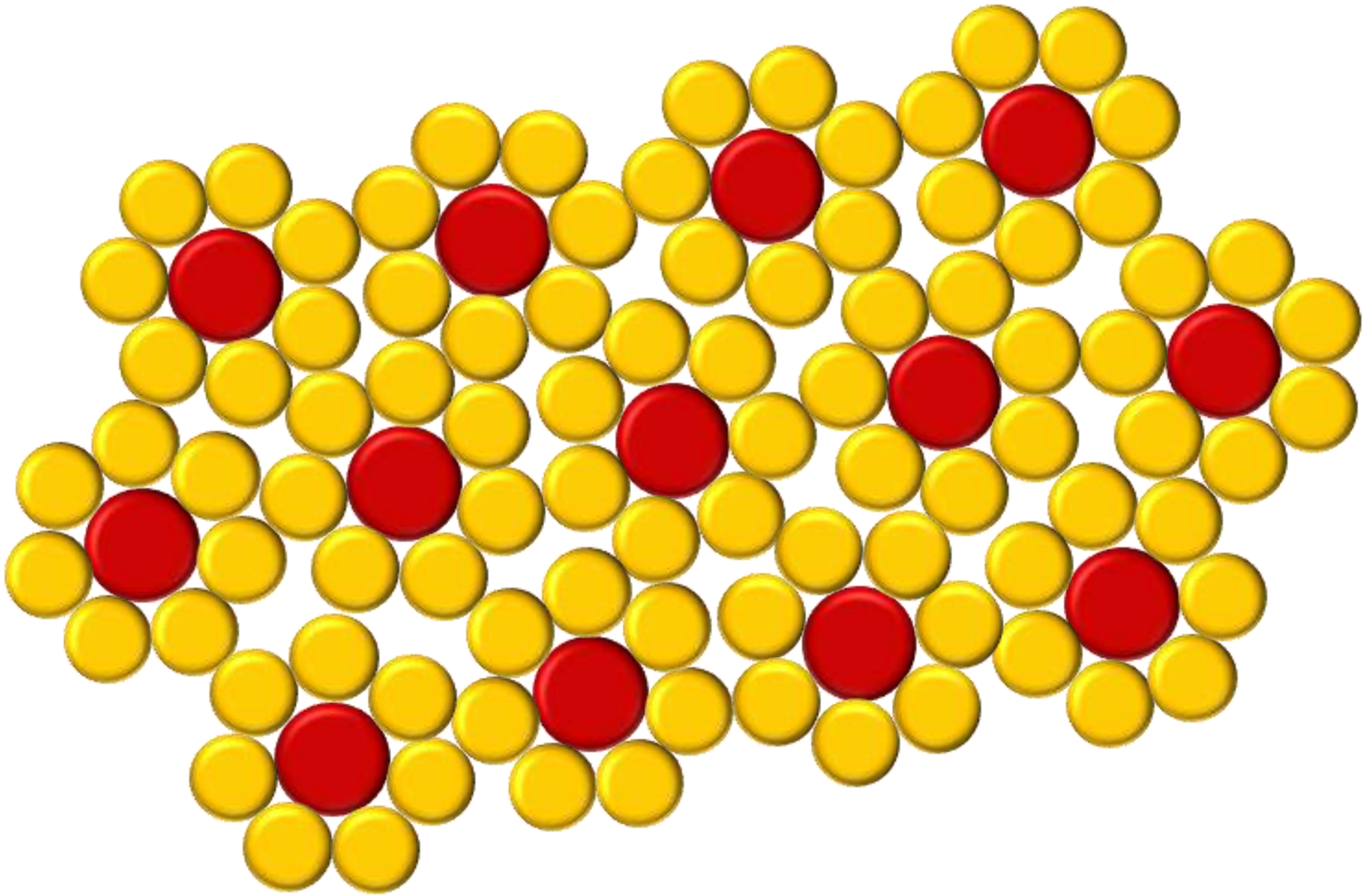

Free volume is locally highest in the regions between Y–centered clusters. These regions are enriched in Al, and depleted in Y and Ni.

SOLUTE ATOMS DESTABILIZE CRYSTALLINE Al

Local lattice strains associated with solutes destabilize crystal (Egami, Waseda, JNCS, 1984.)

- Magnitude of lattice strains decrease with increasing distance from solute

Rare earth metal (RE) solutes are non-interacting, and may be *randomly* distributed in the structure

- *Average* intersolute spacing is ~3 atom spacings
- Spacing between RE atoms will be larger than the average in some cases, producing lower lattice strains and large Al-rich regions
- These regions may be favored for nucleation of crystalline phases

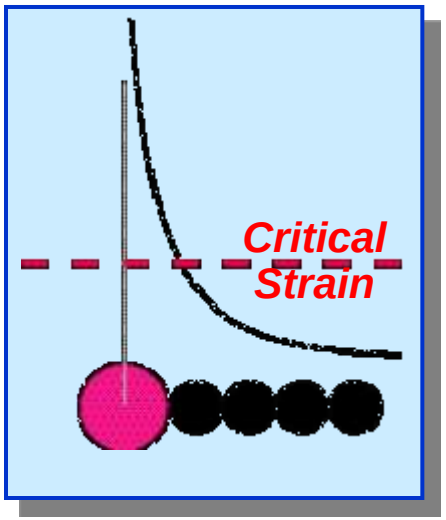

POSTULATE

Critical Al nuclei form in Al-rich areas where Y–Y spacing is sufficiently large to allow formation of a critical cluster

critical nucleus size is generally held to be ~100 atoms

atomic cube ~5 atoms on a side, or atomic sphere ~6 atoms in diameter

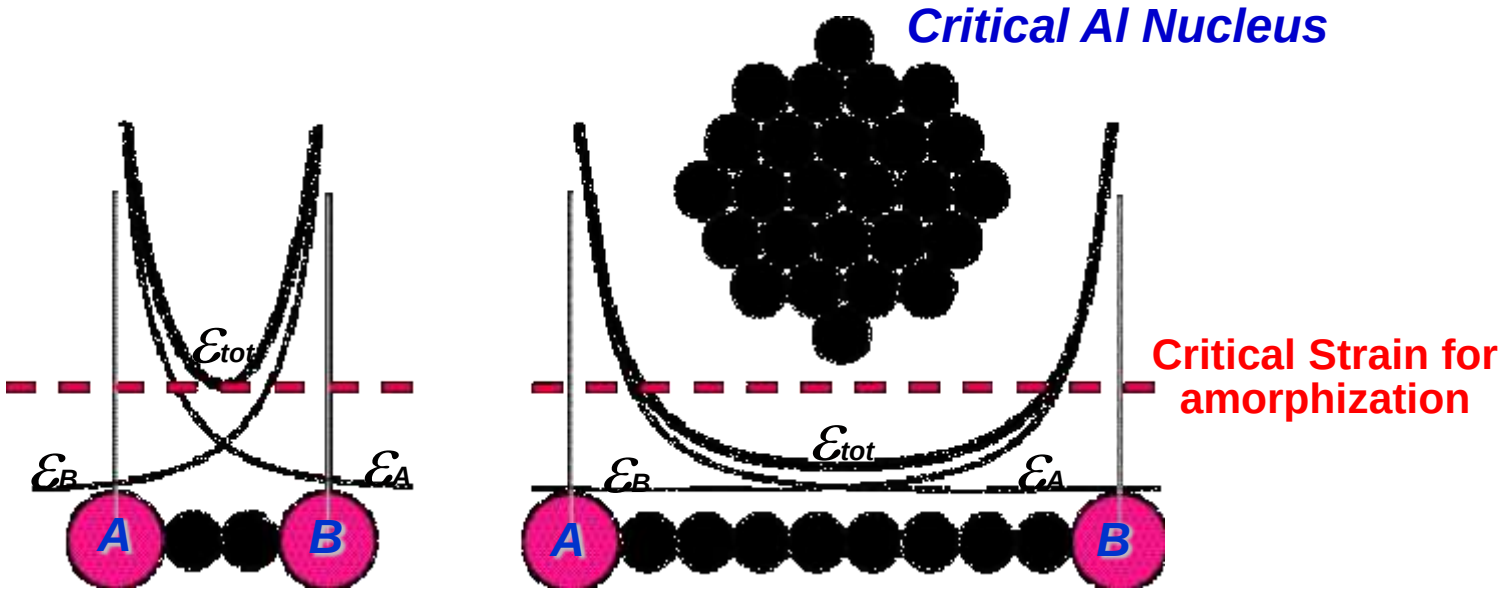

Spowart, Miracle, Mullens, *J. Non-Cryst. Sol.*, **336**, 202 (2004).

Al NUCLEI IN A RANDOM ARRAY OF Y ATOMS

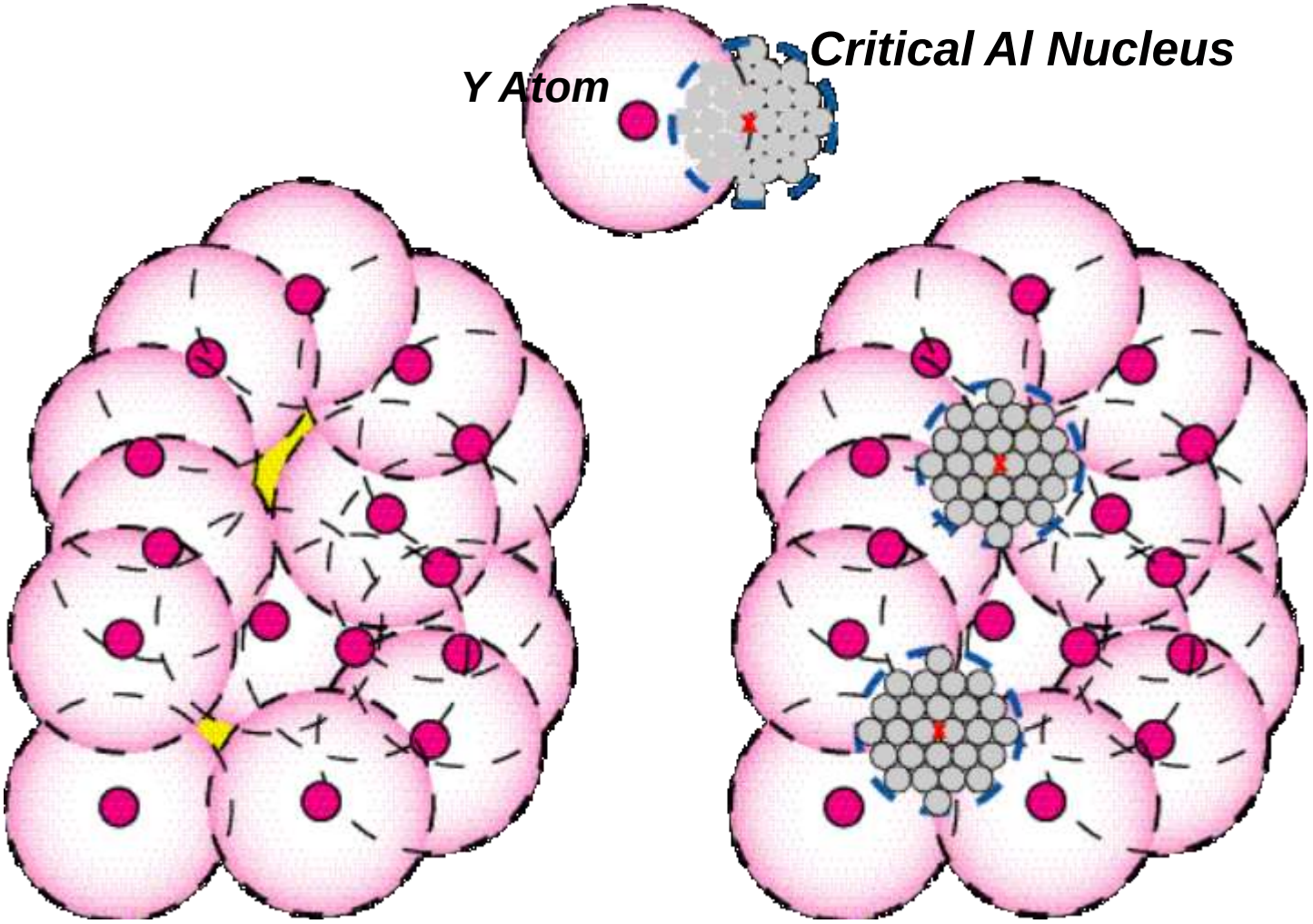

Random Array of Y Atoms

Potential Al Nuclei Sites

APPROACH

Assume a *random* spatial distribution of discrete Y atoms in a continuous matrix of Al atoms

Search for Y-free regions that are large enough to contain a critical Al nucleus

- Suggest that Al atoms in these regions are non-crystalline, but will arrange into a crystal with only a small activation energy needed to rearrange atoms
- Solute diffusion is not required for nucleation, but will be required for growth

Determine the volume density of such sites as a function of the size of these regions and solute concentration

- Model solute concentrations from 0.04 to 0.10

Compare with experimental value of nucleus volume density

MODELING THE ALLOY

Amorphous alloy model:

- hard spheres
- hard edges
- 10^3 to 10^7 atoms

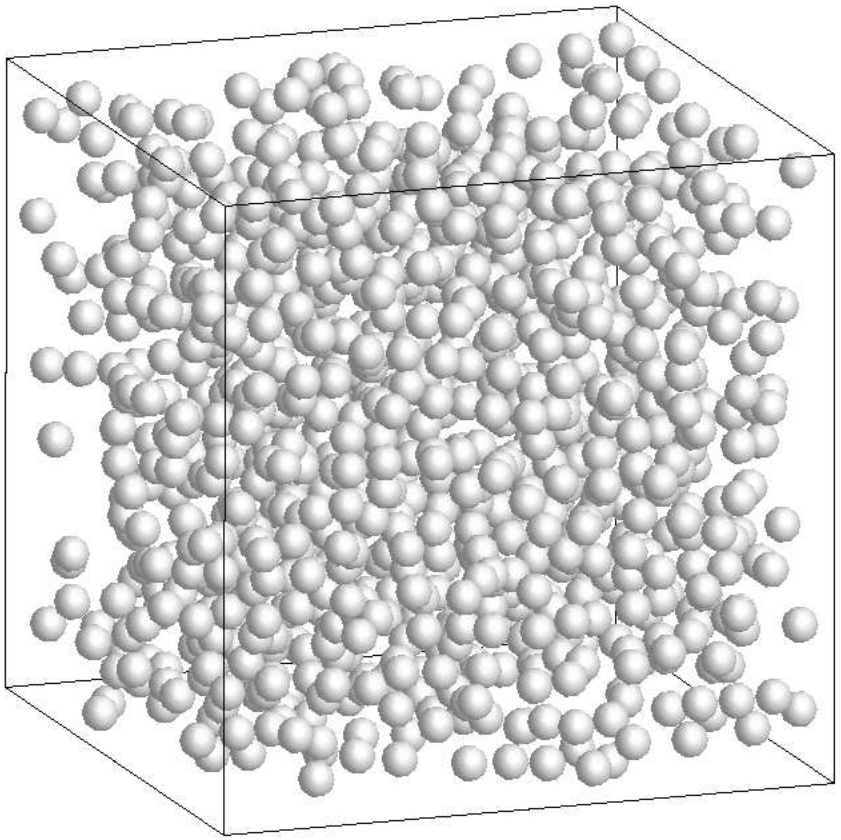

Random (non-overlapping) spatial distribution of 7 At% Y in Al

NUMBER OF NUCLEI vs CRITICAL NUCLEUS SIZE

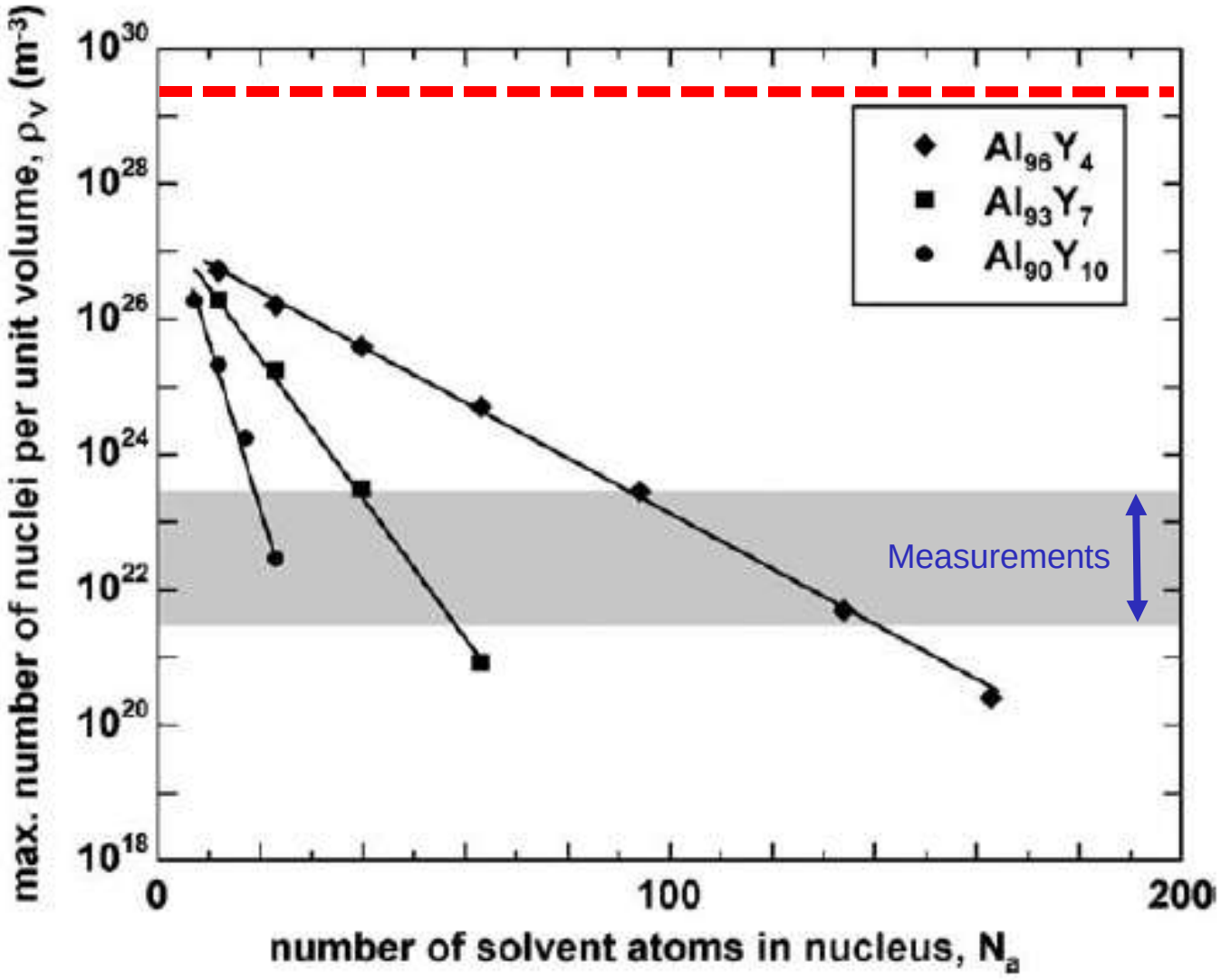

NUMBER OF NUCLEI vs SOLUTE CONCENTRATION

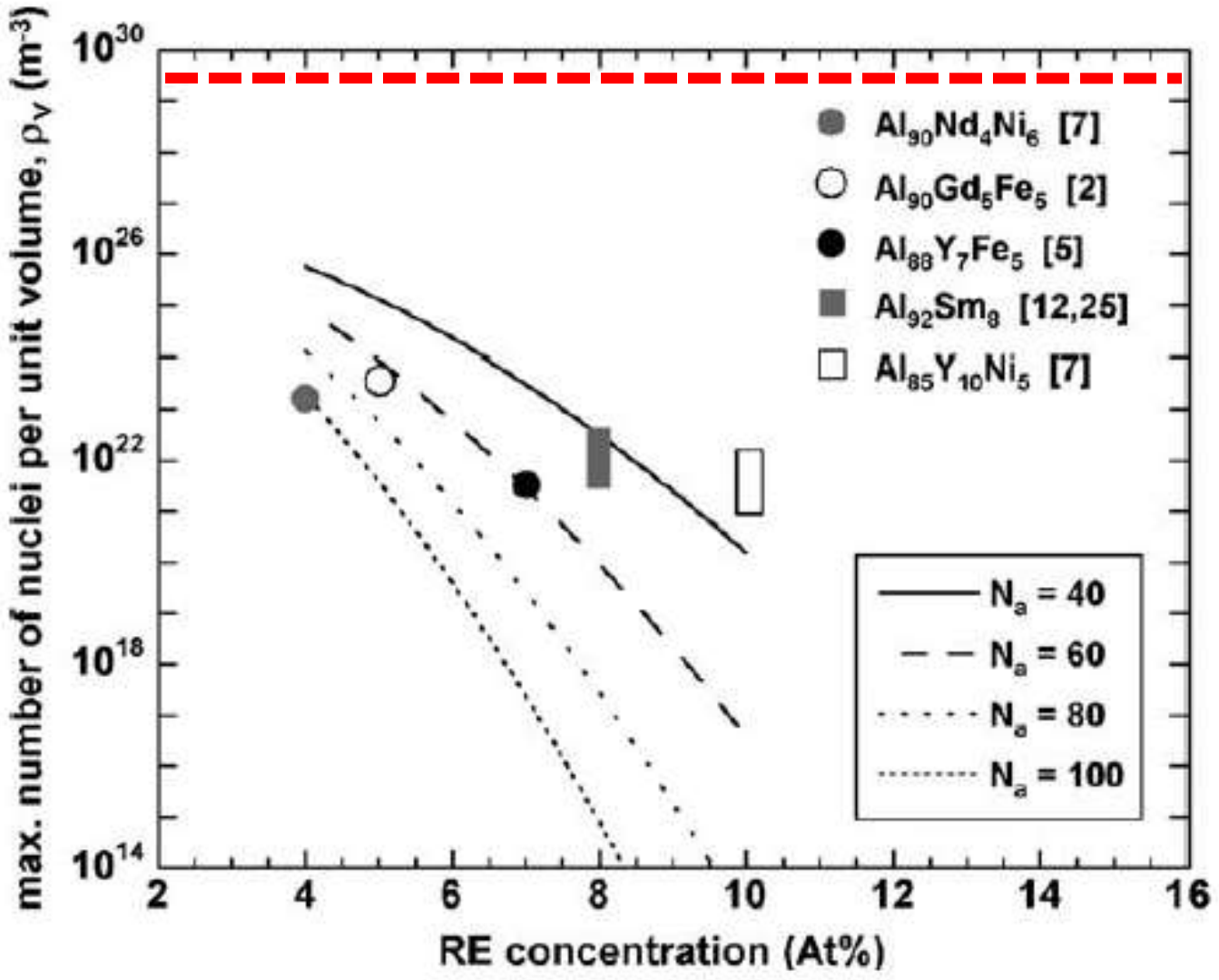

COMPARISON WITH MEASUREMENTS

Table 1
Showing tabulated data from Fig. 4

Alloy system	ρ_V (m^{-3})	n_a (estimated)	Ref.
$Al_{90}Nd_4Ni_6$	$\sim 10^{23}$	100	[7]
$Al_{90}Gd_5Fe_5$	3.6×10^{23}	70	[2]
$Al_{88}Y_7Fe_5$	$3–4 \times 10^{21}$	60	[5]
$Al_{92}Sm_8$	$4 \times 10^{21}–3.5 \times 10^{22}$	40–50	[12,25]
$Al_{85}Y_{10}Ni_5$	$\sim 10^{21}–10^{22}$	30–40	[7]

Values of ρ_V are from experimental measurements, estimates of n_a are obtained by interpolating the modeled relationships between nucleus number density and RE solute concentration.

OUTLINE

INTRODUCTION

NUCLEATION IN AMORPHOUS Al

MODELING OF NUCLEATION SITES

CONCLUSIONS

CLOSING COMMENTS

A simple physical model of the atomic structure responsible for the high volume density of Al nanocrystals in a-Al has been analyzed

- Focuses on random solute distribution
- Thermal defects not addressed but may give similar results
- Does not address nucleation or growth of super-critical nuclei

Observed nucleant volume densities are consistent with critical nuclei containing 40-100 atoms, matching estimated values

Low activation energy conceived thru the local rearrangement of Al atoms

Consistent with subsequent observations of Al-like MRO in a-Al alloys

Need to understand chemical effects that influence solute distribution, especially next-nearest neighbors

THANK YOU!

RULE 1 CONSEQUENCES

Efficient Packing of Primary Clusters

Four topologically distinct atomic species and sites

- Solvent atoms (Ω)
- Primary (α) solutes produce the structure-forming unit clusters
- Cluster-octahedral interstices (β)
- Cluster-tetrahedral interstices (γ)
- $r_\alpha > r_\beta > r_\gamma$

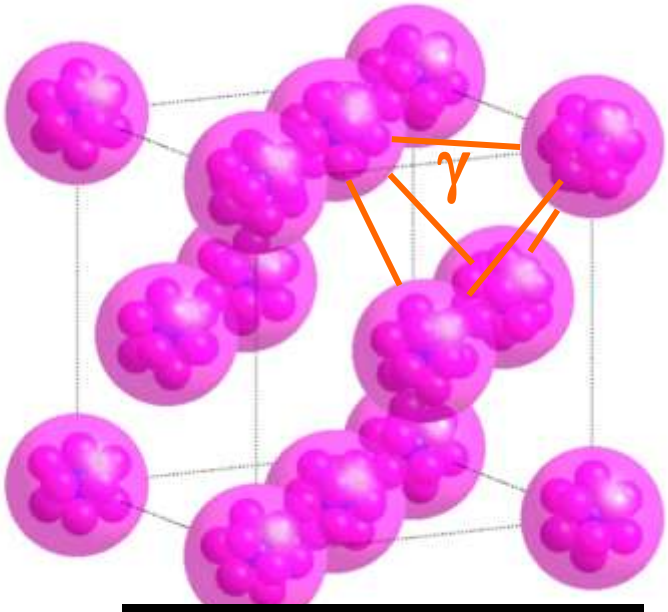

Solute atoms occupy ~ordered sites

- Provides basis for observed medium range atomic ordering (MRO)
- Variable cluster-cluster separation degrade cluster ordering beyond a few cluster diameters

Preferred atom positions introduces the possibility of structural defects

- Vacancy and anti-site point defects
- Constitutional and thermal

“Ninety-nine percent loyalty is 100% disloyalty.”

Napoleon Bonaparte

“He’s not dead. I said he’s *mostly* dead. BIG difference.”

Miracle Max, from “The Princess Bride”

“The Pirate’s Code is more what you’d call ‘guidelines’ than actual rules.”

Captain Barbossa, from “The Pirates of the Caribbean”

THERMAL DEFECT PAIR

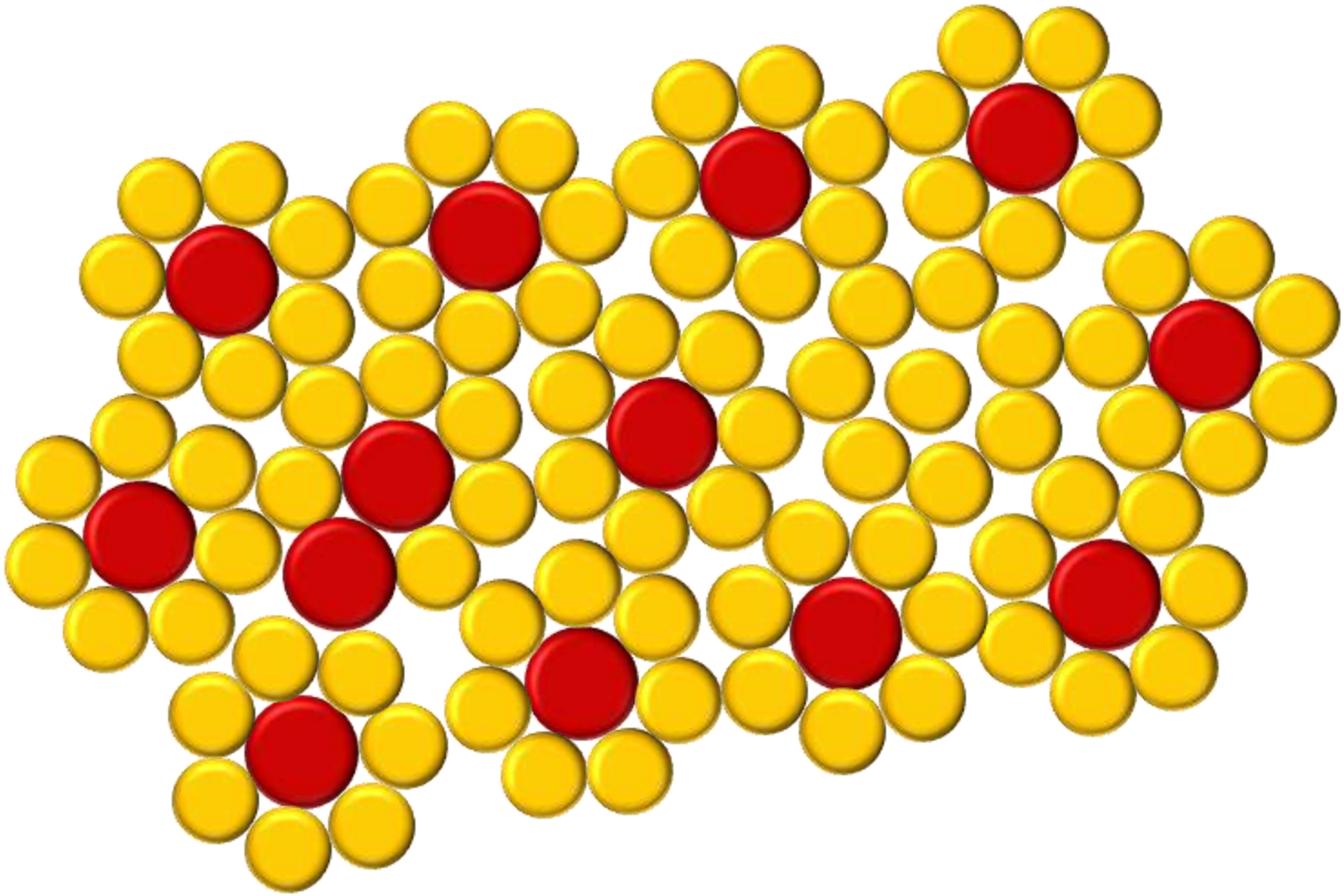

DIRECT COUNTING METHOD

Count the number of cubic volumes of side Q within the model system which contain no Y atoms

Considerations :

- fixed lattice
- cubic volume, (Q^3) not spherical volume ($4/3\pi r_{cluster}^3$)

Bounded Problem:

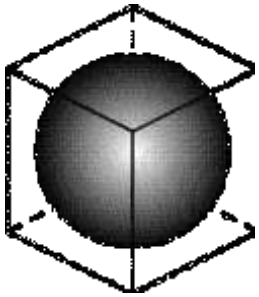

Q = 2.89 d_{Al}

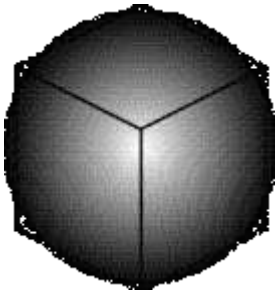

Q = 3.52 d_{Al}

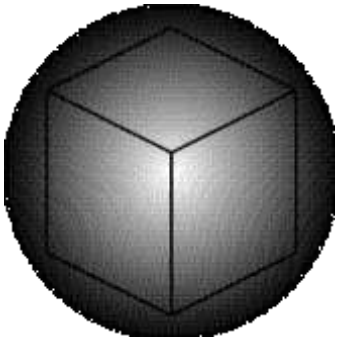

Q = 5 d_{Al}

RESULTS

Direct Counting:

- limited by size of domain
- computationally intensive
- fixed lattice

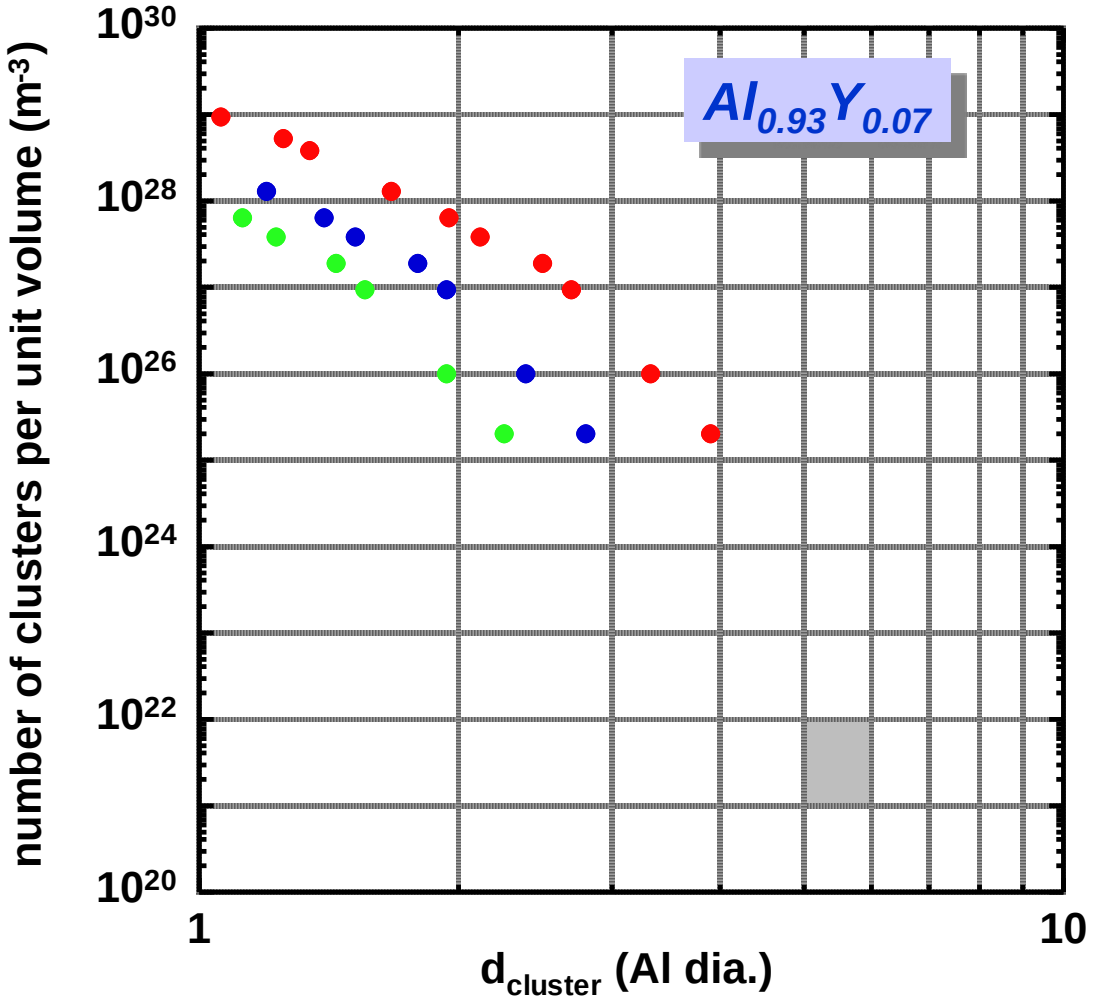

PROBABILISTIC METHOD

Measure the distribution of local V_f at length scale Q:

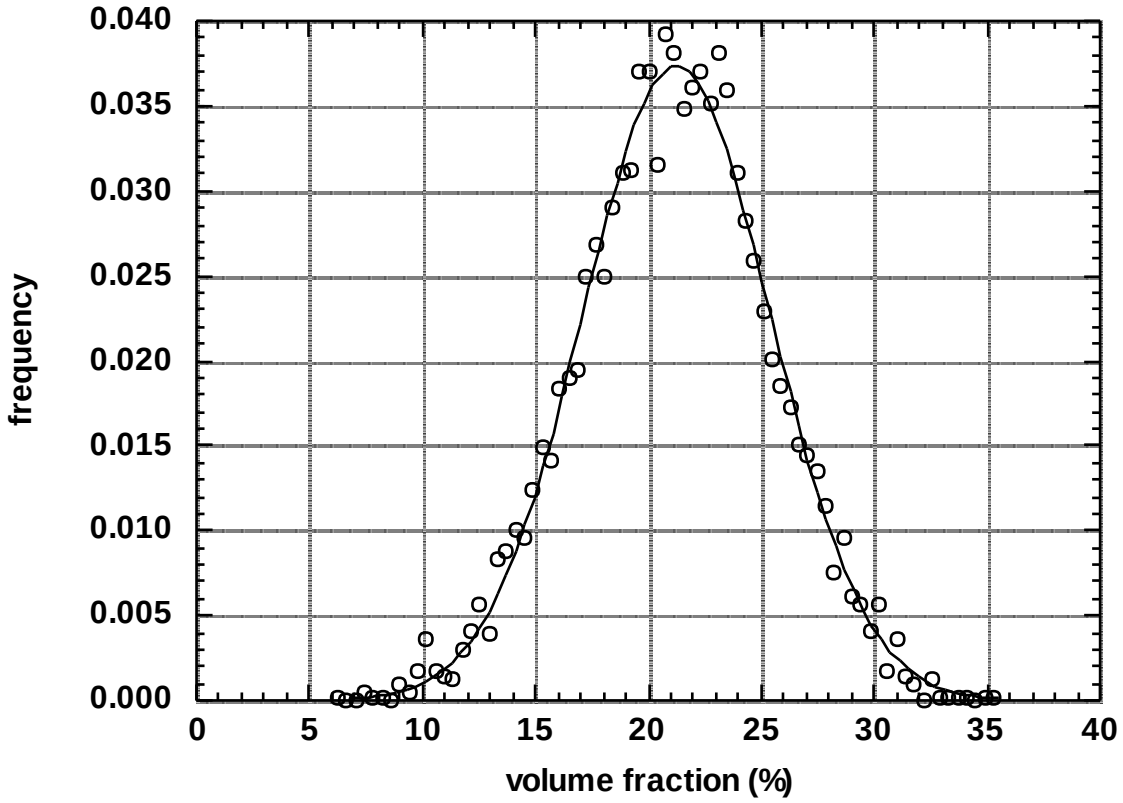

Random (non-overlapping) spatial distribution of 11 At% Y in Al sampled at length scale Q = 2.29 d_p (4096 volume elements)

PROBABILISTIC METHOD

Model the distribution of local V_f :

$$\phi(f) = \frac{1}{\sqrt{2\pi\sigma_f}} \exp\left[-\left(f - f_0\right)^2 \Big/ 2\sigma_f^2\right]$$

(Gaussian)

Calculate statistics :

- mean $V_f = f_0$
- std. dev. of $V_f = \sigma_f$

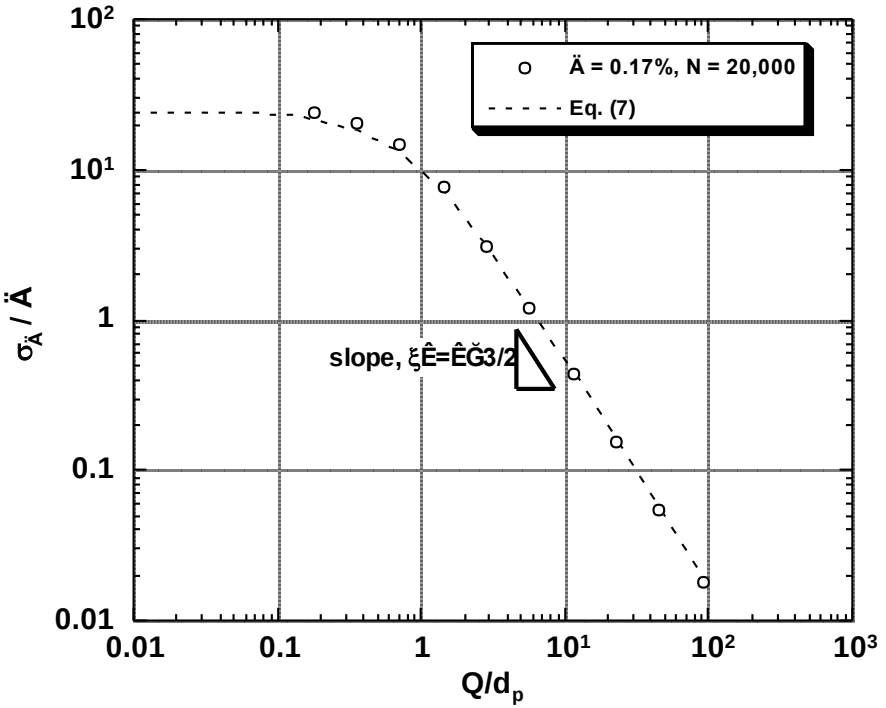

PROBABILISTIC METHOD

Calculate the probability of finding $V_f = 0$, over a length scale Q:

$$\Pr\{f : f + \Delta f\} = \int_{f}^{f+\Delta f} \phi(f)\, \mathrm{d}f$$

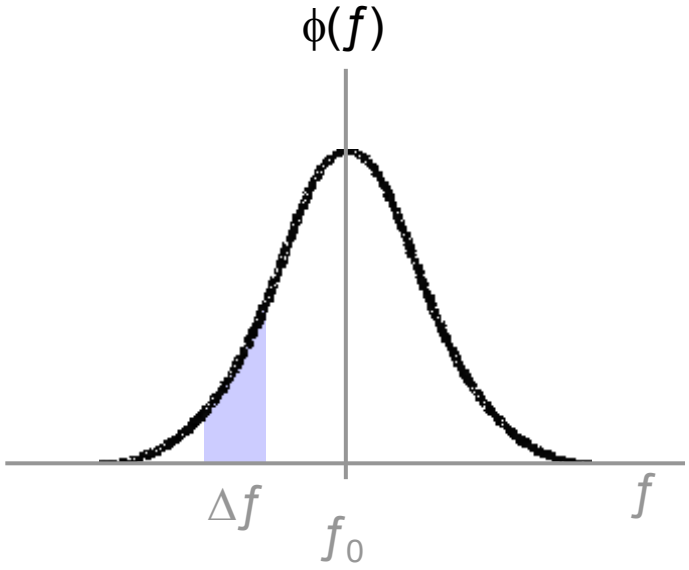

Assumptions :

- $f = 0$
- $\Delta f = 0.005$

RESULTS

Probabilistic Method:

- limited by statistical model
- fixed lattice

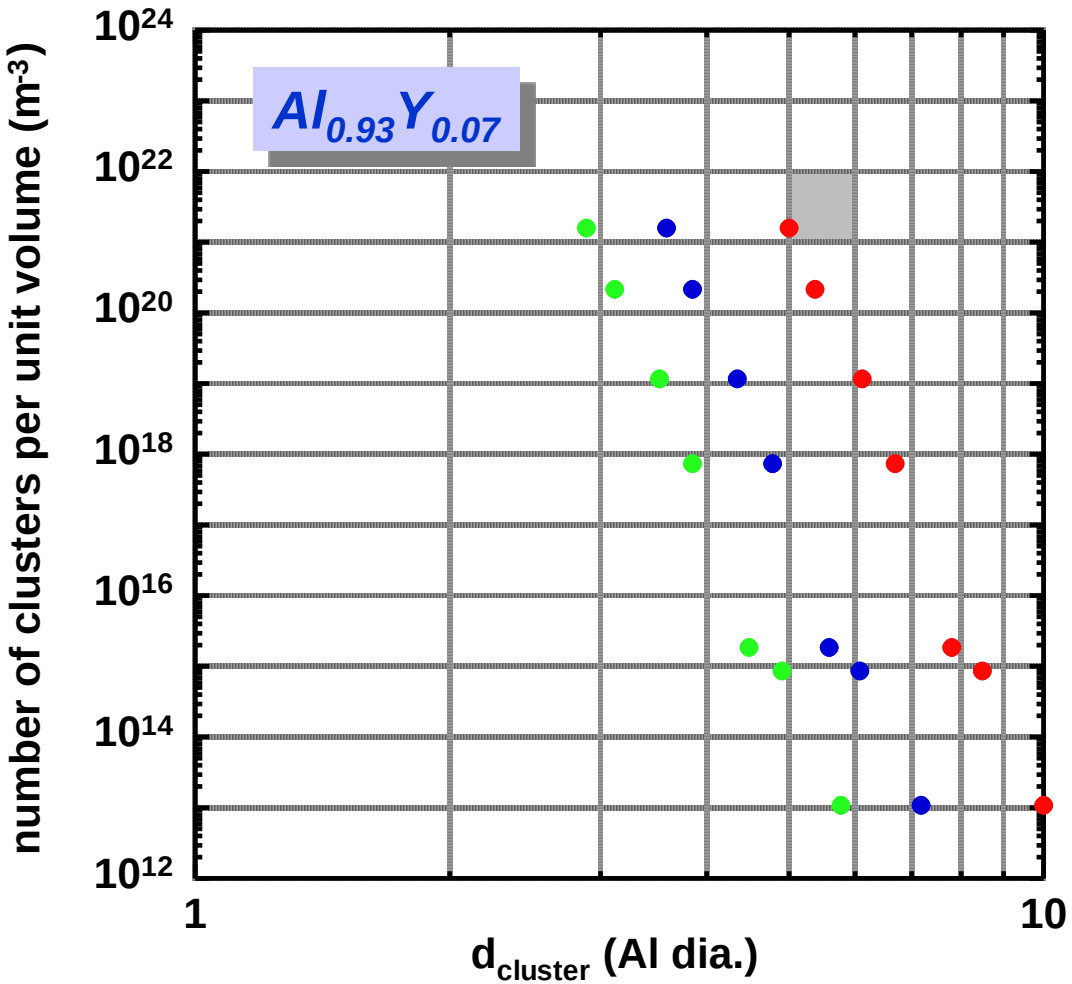

COMBINED RESULTS

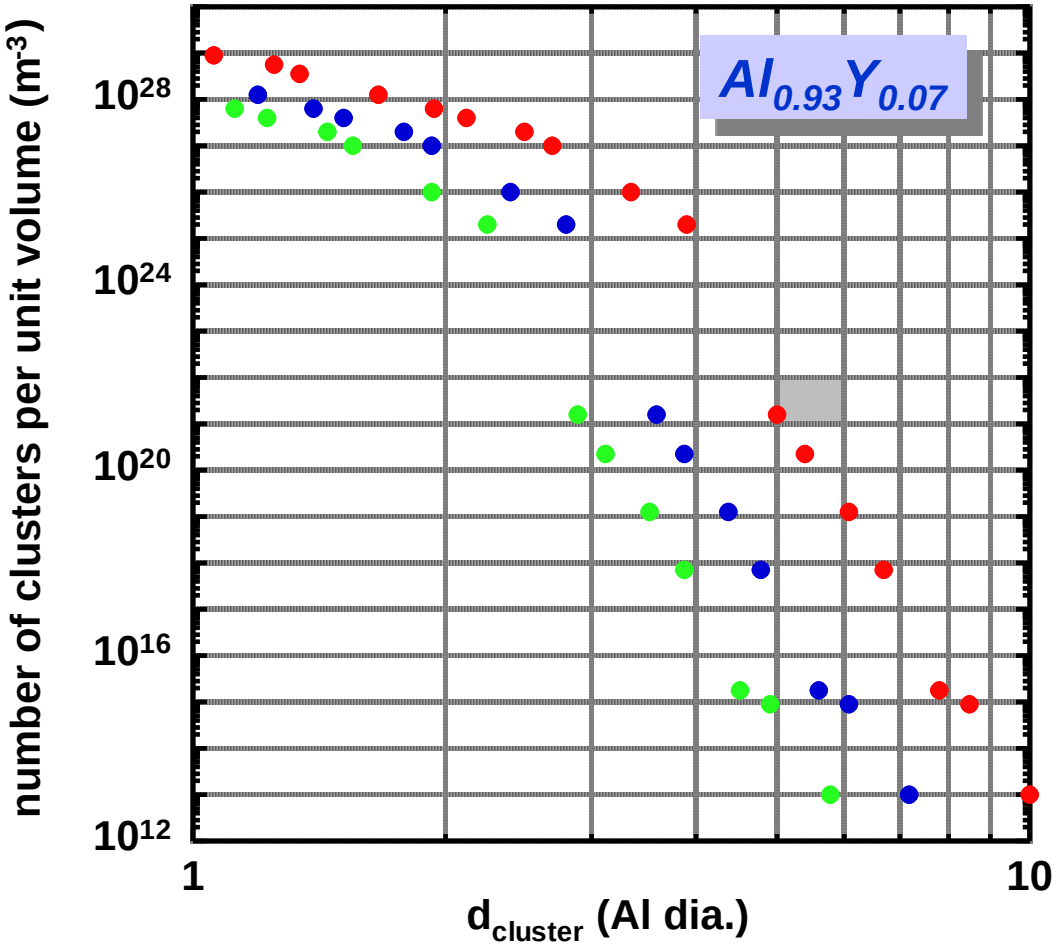

Future Work:

- close the gap!
- new compositions
- multiscale effects: clustered clusters

CLUSTER MODELS
Cluster Linking

Configurations producing a Y–Y separation of 2Al atoms

- *Link adjacent clusters by nestling an Al atom from one cluster in a low-energy position of a 2nd cluster, then rotating to a final low-energy configuration*
  - ➢ *. . . into a trigonal array yields a tetrahedron*
    - trigonal arrays exist in all clusters, so this may be a common linking configuration
  - ➢ *. . . into a four-fold array yields an octahedron*
    - these are intrinsic to the $Al_{15}Y$ cluster, and can occur in terminations of all other clusters discussed
  - ➢ *. . . into a five-fold array forms a portion of a low-energy icosahedron*
- *Another possibility is to link two trigonal arrays to form an Al_6 octahedron*

Configurations producing a Y–Y separation of 1Al atom

- *Adjacent Y atoms share a common trigonal array of Al atoms*

Configurations producing adjacent Y–Y atoms

- *Substitute an Al or Ni atom in a Y–centered cluster with Y*
- *“Linear molecules” obtained by stacking a given cluster upon itself*
  - ➢ *can be accomplished with each of the four clusters discussed*

Significant structural diversity is enabled via linking

Inter-Solute Spacing

- Consider a regular distribution of solute atoms of concentration, c_i, which occupy the corners of a cube of edge length, x_i atoms. Then:

$$c_i = 1/x_i^3$$

- If we know C_i, then we can determine the mean inter-solute spacing, x_i:

$$x_i = 1/c_i^{1/3} = c_i^{-1/3}$$

- for $C_j = 0.09$, $L_j = 2.2$ atoms; for $C_j = 0.13$, $L_j = 2.0$ atoms
  - *on the average, every Y atom is separated by 1 – 1.2 other atom diameters*

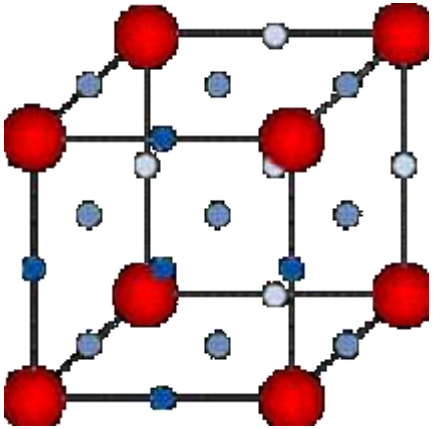

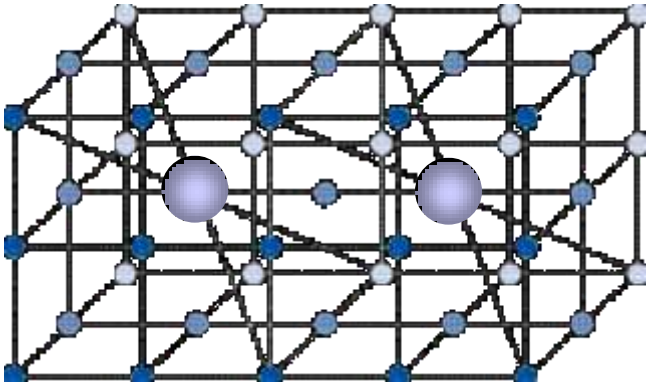

For $L_i = 2$,

$C_i = 1/8 = 0.125$

Each Y and its nearest neighbors may be treated as a RVE

ARC Centre of Excellence
Design in Light Metals

Australian Government
Australian Research Council

Heterogeneous Nucleation of Plate-shaped Transformation Products

Barry C Muddle
ARC Centre of Excellence for Design in Light Metals
Monash University 3800 Victoria AUSTRALIA

Acknowledgements: **Y Kryvasheyeu, J Rosalie, GB Winkelman, L Bourgeois, JF Nie**

Joint AFRL/AOARD/LLNL Workshop

'Nucleation During Solid-Solid Phase Transformations in Metallic Systems'

2-7 May, Maui, Hawaii

MONASH University

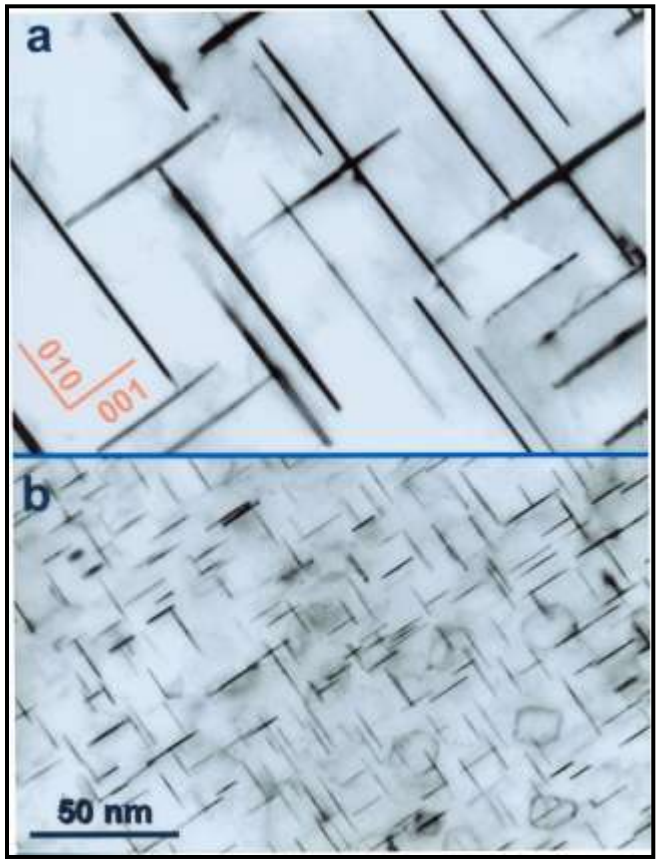

(a) Al-4Cu Alloy, and

(b) Al-4Cu-0.05Sn Alloy

18h at 190ºC

B ~ <100>$_\alpha$

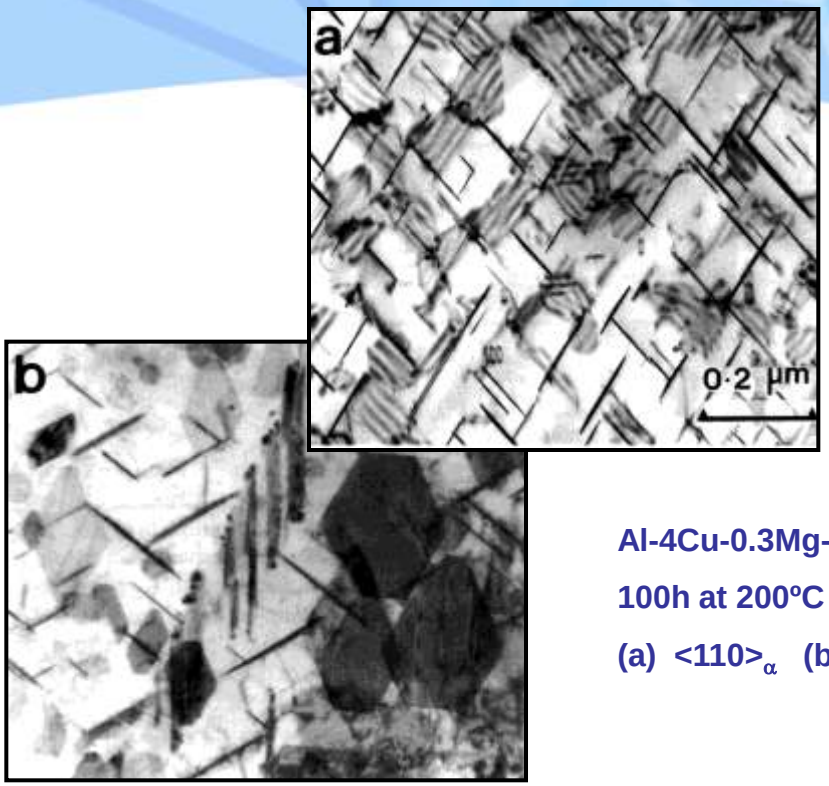

Al-4Cu-0.3Mg-0.4Ag Alloy

100h at 200ºC

(a) <110>$_\alpha$ (b) <111>$_\alpha$

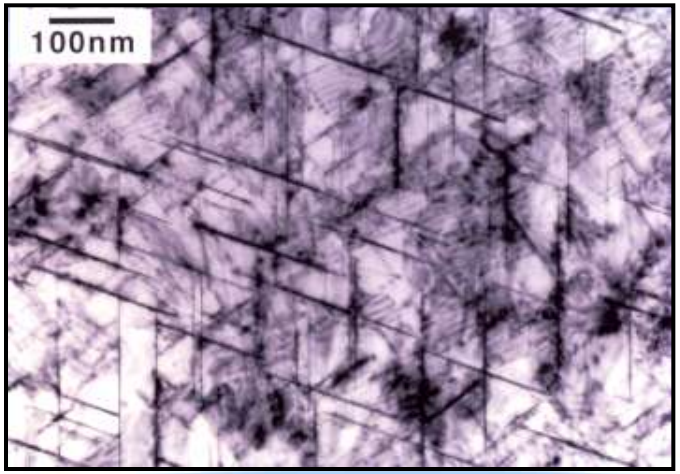

Al-4Cu-1.0Li-0.3Mg-0.4Ag Alloy

5h at 200ºC

B ~ <111>$_\alpha$

Australian Government
Australian Research Council

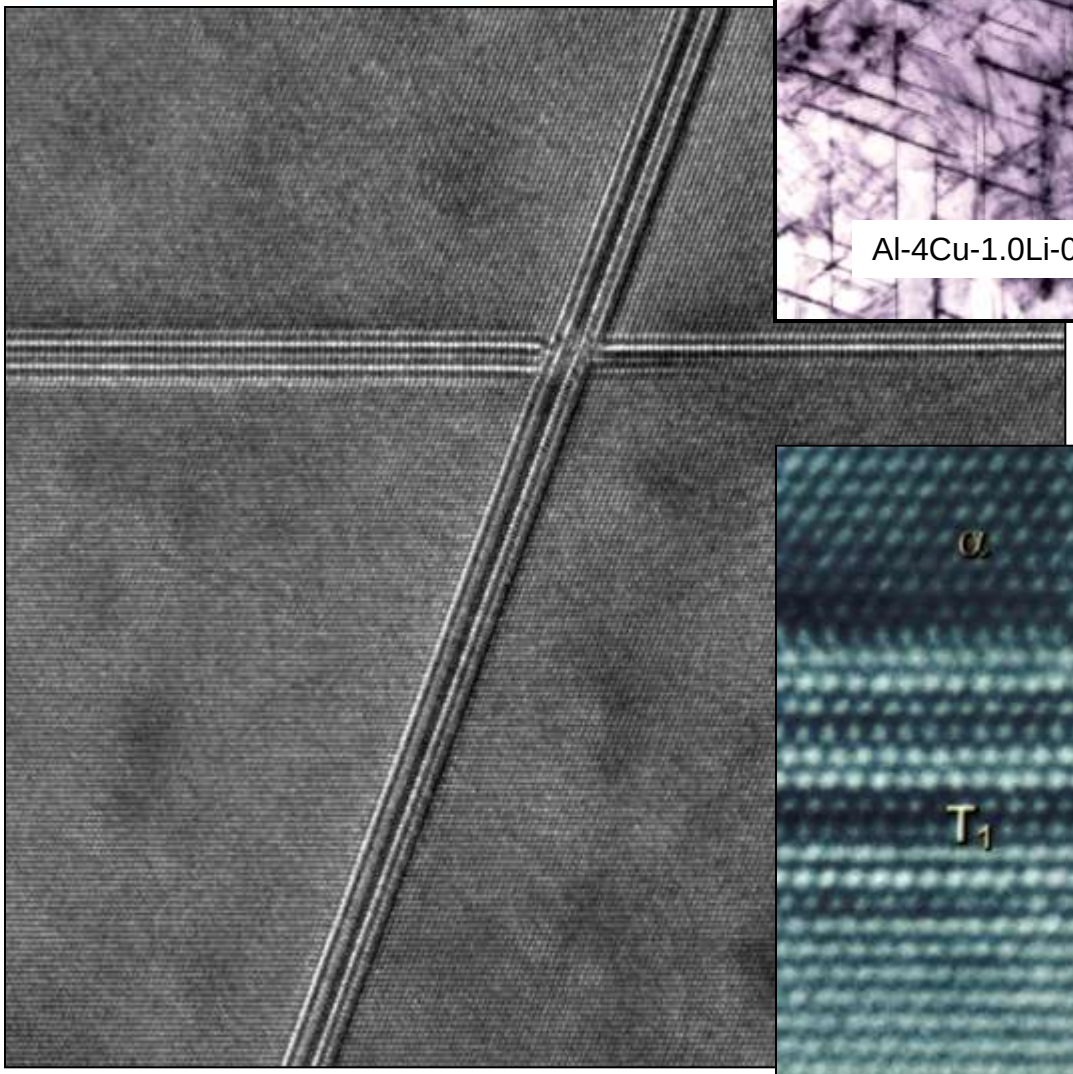

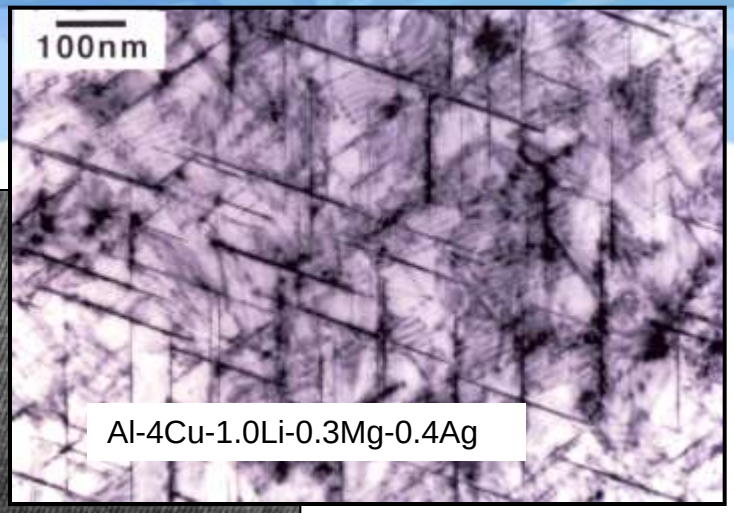

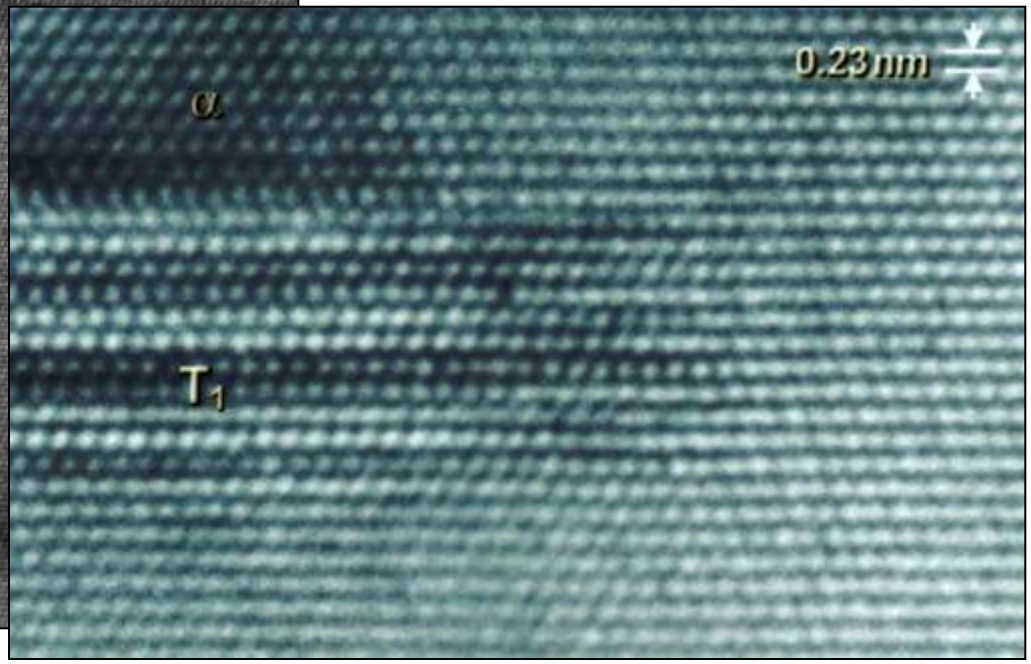

T_1 Phase (Al_2CuLi) in Al-Cu-Li Alloys

Formation of γ' Phase (Ag_2Al) in Al-Ag Alloys

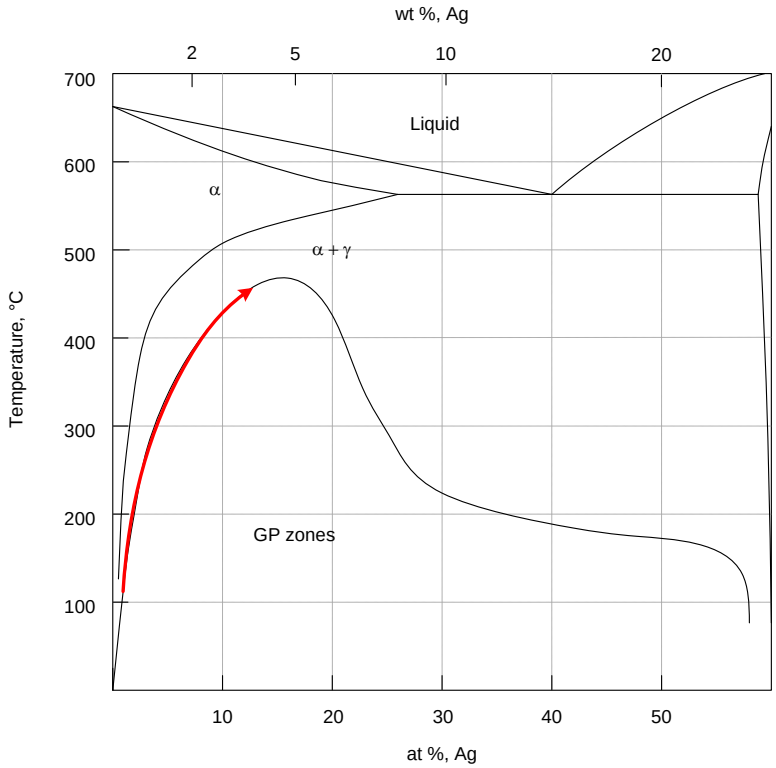

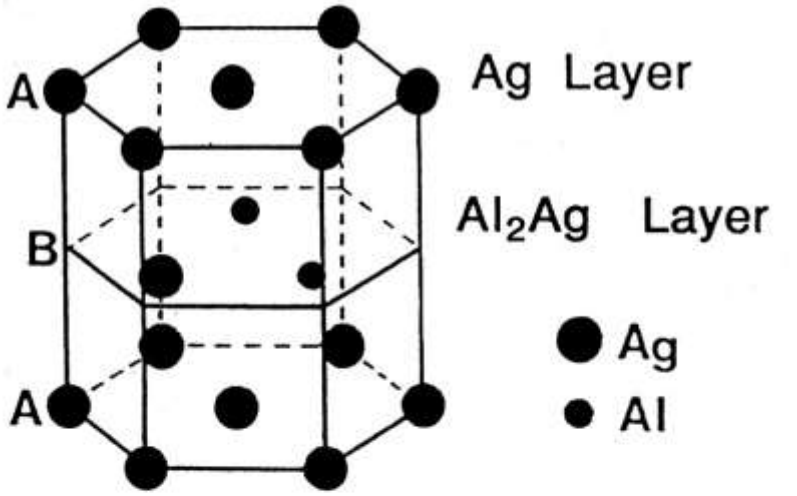

Fig. 2—Schematic representation of the crystal structure proposed for the γ phase (Ag_2Al) in Al-Ag alloys.[23]

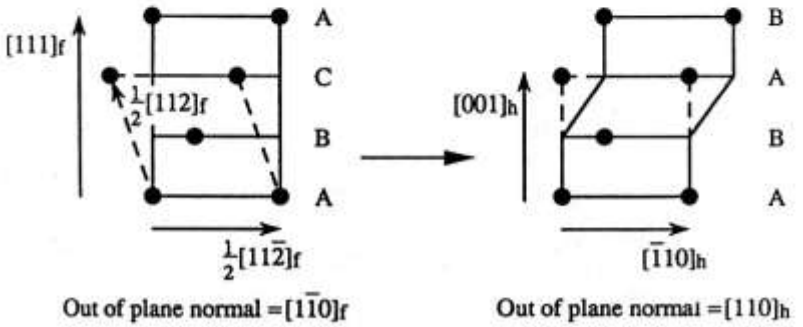

Fig. 3—Schematic representation of the lattice correspondence between parent and product lattices for the fcc to hcp transformation.

Muddle, Nie, Hugo, *Metall.* Mater. Trans. **25A** p. 1841 (1994)

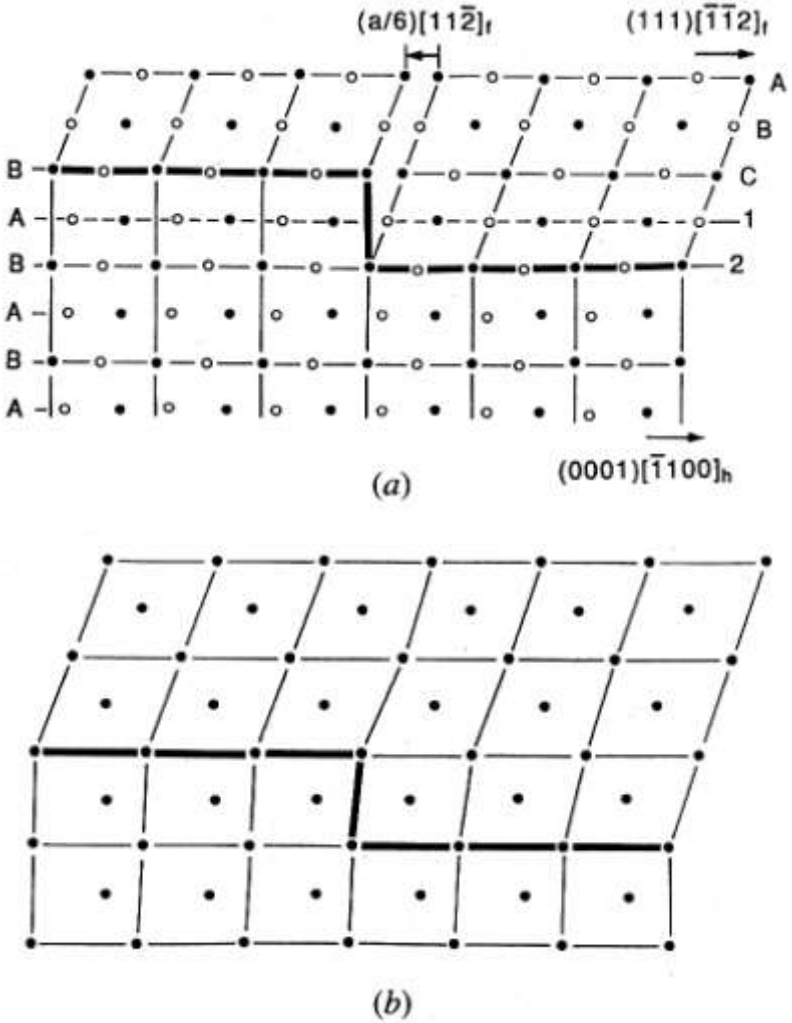

$$\mathbf{b_T} = hm\mathbf{d} = h\tau\mathbf{t} + h\xi\mathbf{n}$$

$$\mathbf{b_T} = \frac{a}{6}\langle 112\rangle + \frac{2\xi a}{3}\langle 111\rangle$$

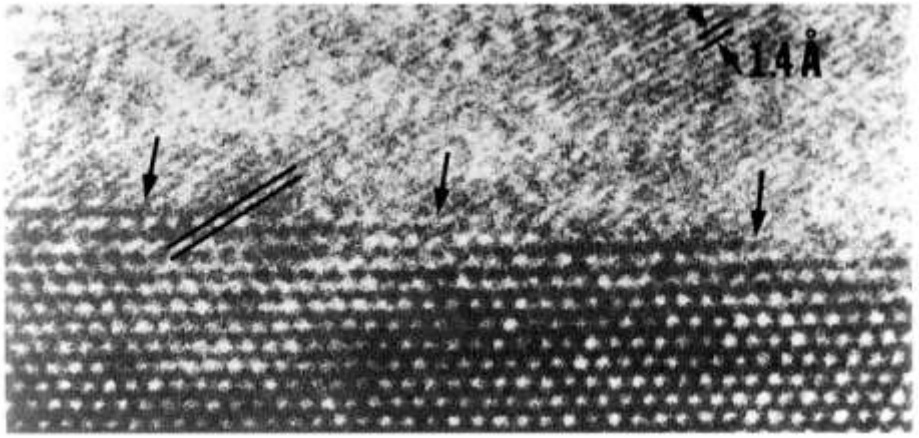

Muddle, Nie, Hugo, *Metall.* Mater. Trans. **25A** p. 1841 (1994)

Howe, Dahmen, Gronsky, *Philos. Mag.* **56A** p. 31 (1987)

Consider a platelet of the product phase to take the form of a thin oblate spheroid, with radius a and semi-thickness c, and an aspect ratio, $A = c/a$, such that $a >> c$.

$$\Delta F^0 = \frac{4}{3}\pi a^3 A(\Delta F_v + E_{el}) + 2\pi a^2 [1 + f(A)]\gamma_s$$

$$f(A) = \frac{A^2}{\sqrt{1-A^2}} \tanh^{-1}\sqrt{1-A^2}$$

Unconstrained transformation strain is an invariant plane strain, comprising a uniaxial expansion ξ normal to the invariant plane and a simple shear τ in the habit plane

J.K. Lee, H.I. Aaronson and D.M. Barnett, *Metall. Trans.* 8A(6), pp. 963-70, 1977

For small A, the **shape-independent energy due to the uniaxial expansion** alone may be expressed in the form:

$$E_\xi = \frac{\pi}{4(1-\nu)} A\mu\xi^2$$

μ – shear modulus

ν – Poisson's ratio

The **strain energy per unit volume for the constrained shear** τ is given by:

$$E_\tau = \frac{\pi(2-\nu)}{8(1-\nu)} A\mu\tau^2 \qquad E_\tau >> E_\xi$$

The **total elastic strain energy** $E_{el} = E_\xi + E_\tau$ tends to a minimum of zero as the aspect ratio A goes to zero. However, surface energy of a thin plate-like form:

$$E_\gamma = 2\pi a^2(1+A)\gamma_s$$

increases with square of plate radius. Equilibrium shape at nucleation will be that which achieves an appropriate balance in the competing needs to minimize both elastic strain energy and surface energy.

J.W. Christian, *Acta Metall.* **6** pp. 377-9 (1958)

$$\Delta F^0 = \frac{4}{3}\pi a^3 A(\Delta F_v + E_{el}) + 2\pi a^2 [1 + f(A)]\gamma_s$$

Under the combined influence of interfacial energy and elastic strain energy, the energy barrier to nucleation ΔF^* may be considered a function of the critical values a^* and A^* which simultaneously satisfy the conditions

$$[\partial(\Delta F^o)/\partial a]_A = 0 \quad \text{and} \quad [\partial(\Delta F^o)/\partial A]_a = 0$$

$$a^* = \frac{-2\gamma_s}{(\Delta F_v + E_{el})} \frac{1 + f(A)}{A}$$

In the limit of $A \rightarrow 1$ $\qquad a^* = -2\gamma_s/(\Delta F_v + E_{el})$

The corresponding ($a = a^*$) value of ΔF_o is:

$$\Delta F^* = \frac{2}{3} \frac{\pi \gamma_s^{\ 3}}{(\Delta F_v + E_{el})^2} \frac{[1 + f(A)]^3}{A^2}$$

J.K. Lee, H.I. Aaronson and D.M. Barnett, *Metall. Trans.* 8A(6), pp. 963-70, 1977

Interface	γ mJ/m^2	Method/Reference
α/θ′, habit plane	30	Nearest neighbour, regular solution model [2]
	156	MEAM (MD, empirical potentials calculations) [5]
	190	Ab initio, DFT [4]
	235	Ab initio, DFT [3]
	510	Experiment, isothermal calorimetry [1]
α/θ′, semicoherent edges	360	Nearest neighbour, regular solution model [7]
	615	Ab initio, DFT [3]
	694	MEAM [5]
	21500	Experiment, isothermal calorimetry [1]
α/γ, habit plane	115	Nearest neighbour, regular solution model [2]
	150	[6]
α/γ′, habit plane	4-7	Discrete-lattice plane, regular solution model [6]
	60	Nearest neighbour, regular solution model [2]
	117	[6]

1. JD Boyd and RB Nicholson, *Acta Metall.*, 1971. **19**(10): p. 1101-9.
2. HI Aaronson, JB Clark, and C Laird, *Metal Sci. J.*, 1968. **2**: p. 155-158.
3. V Vaithyanathan, C Wolverton and LQ Chen, *Phys. Rev. Lett.*, 2002. **88**(12): p. 125503-1.
4. V Vaithyanathan, C Wolverton and LQ Chen, *Mater. Sci. Forum*, 2004. **449-452**: p. 19-24.
5. SY Hu, MI Baskes, M Stan, and LQ Chen, *Acta Mater.*, 2006. **54**(18): p. 4699-707.
6. RV Ramanujan, JK Lee and HI Aaronson, *Acta Metall. et Mater.*, 1992. **40**(12): p. 3421-32.
7. HI Aaronson and C Laird, *Ford Motor Co. Scientific Laboratory Report*, 1967.

ΔF_V J/m^3	$\xi = 0, \tau = 0$			$\xi = 0.025, \tau = 0.0$			$\xi = 0.05, \tau = 0$		
	a^* nm	A^*	ΔF^* k_BT	a^* nm	A^*	ΔF^* k_BT	a^* nm	A^*	ΔF^* k_BT
γ_h=0.03 J/m^2 , γ_e=3γ_h									
1.0 10^8	3.6	0.33	85.1	4.0	0.28	96.3	5.2	0.20	131.2
2.0 10^8	1.8	0.33	21.3	1.9	0.30	22.7	2.2	0.25	26.9
3.0 10^8	1.2	0.33	9.5	1.3	0.31	9.9	1.4	0.27	11.1
4.0 10^8	0.9	0.33	5.3	0.9	0.32	5.5	1.0	0.28	6.0
5.0 10^8	0.7	0.33	3.4	0.7	0.32	3.5	0.8	0.29	3.8
γ_h=0.05 J/m^2 , γ_e=3γ_h									
1.0 10^8	6.0	0.33	394.0	6.7	0.28	445.8	8.7	0.20	607.4
2.0 10^8	3.0	0.33	98.5	3.2	0.30	105.0	3.7	0.25	124.6
3.0 10^8	2.0	0.33	**43.8**	2.1	0.31	45.7	2.3	0.27	**51.5**
4.0 10^8	1.5	0.33	24.6	1.5	0.32	25.4	1.7	0.28	27.9
5.0 10^8	1.2	0.33	15.8	1.2	0.32	16.2	1.3	0.29	17.4
γ_h=0.1 J/m^2 , γ_e=3γ_h									
1.0 10^8	12.0	0.33	3152.1	13.5	0.28	3566.9	17.4	0.20	4859.6
2.0 10^8	6.0	0.33	788.0	6.4	0.30	839.5	7.4	0.25	996.7
3.0 10^8	4.0	0.33	350.2	4.2	0.31	365.5	4.7	0.27	411.7
4.0 10^8	3.0	0.33	197.0	3.1	0.32	203.5	3.4	0.28	222.9
5.0 10^8	2.4	0.33	126.1	2.5	0.32	129.4	2.6	0.29	139.3

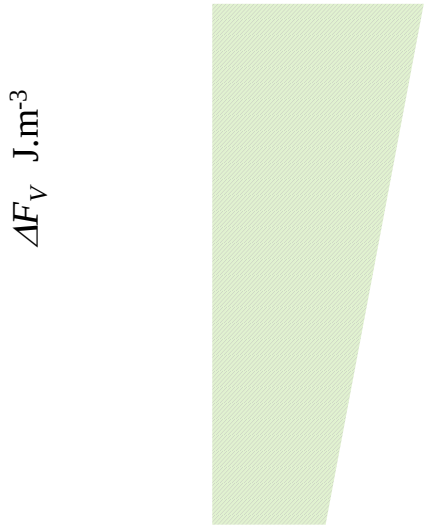

Activation barrier (expressed in $k_B T$) for the nucleation of circular disc

ξ = 0.045, τ = 0

Transformation temperature = 520 K (250°C)

ΔF_V J/m^3	$\xi = 0, \tau = 0$			$\xi = 0.05, \tau = 0.3$		
	a^* nm	A^*	ΔF^* k_BT	a^* nm	A^*	ΔF^* k_BT
1.0 10^8	6.0	0.33	394.0	72.1	0.02	21148.0
2.0 10^8	3.0	0.33	98.5	19.9	0.04	1754.5
3.0 10^8	2.0	0.33	**43.8**	9.7	0.05	**442.3**
4.0 10^8	1.5	0.33	24.6	5.9	0.06	173.6
5.0 10^8	1.2	0.33	15.8	4.1	0.07	86.2

Nucleation Barrier

ΔF^* (J)

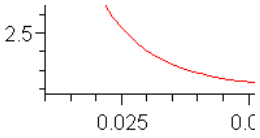

A

Nucleation Barrier

ΔF^* (J)

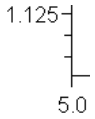

A

Equilibrium shape an implicit function of the effective driving force (ΔF_v reduced by total elastic strain energy E_{el}) and is evaluated numerically as a function of ΔF_v and E_{el}.

ξ = - 0.045, τ = 0.33, γ_s = 0.1 - 0.3 J.m^{-2}, μ = 26 GPa

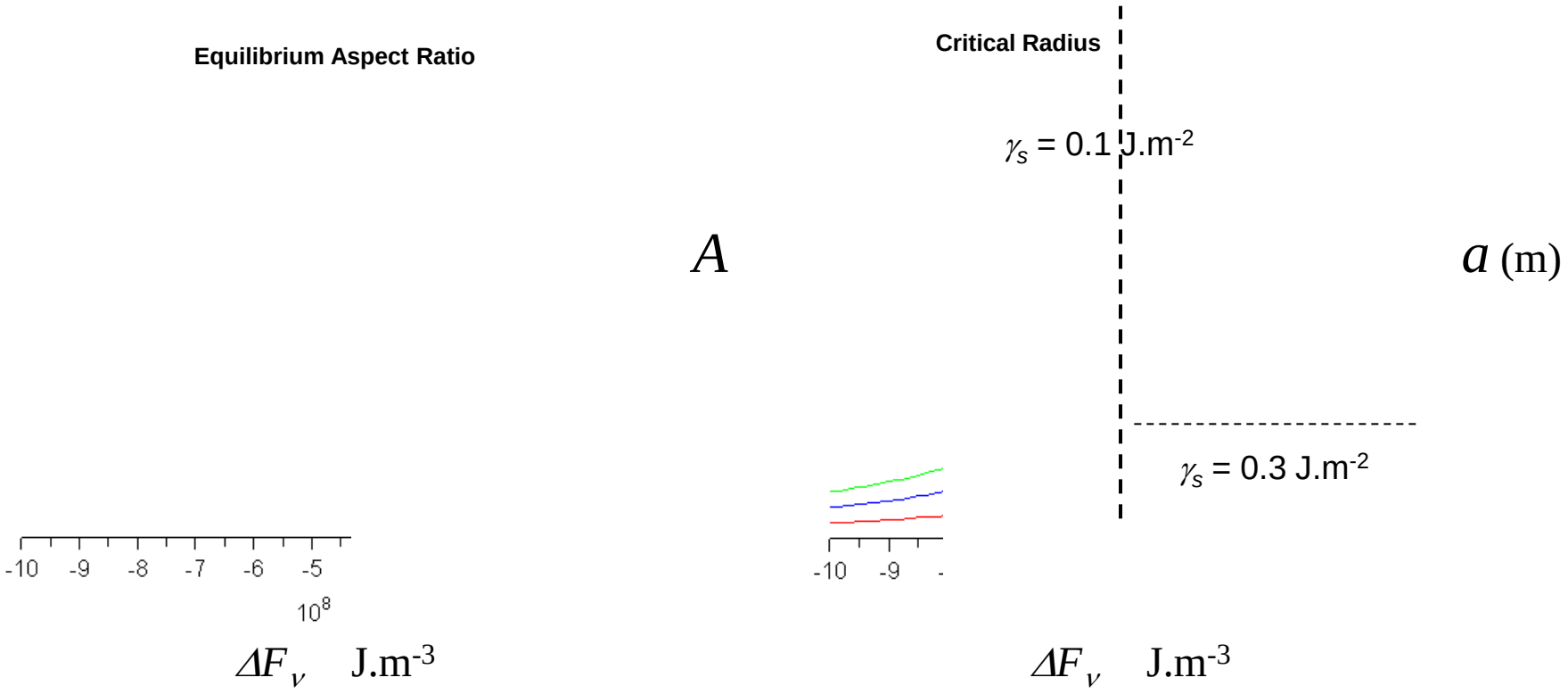

Nucleation Barrier

γ_s = 0.1 J.m^{-2}

γ_s = 0.3 J.m^{-2}

ΔF_v J.m^{-3}

$\Delta F^* / kT$

At 500K and γ_s = 0.2 J.m^{-2}

$\Delta F^* \sim 2.2 \times 10^3 kT$

Accommodation of shear strain energy may occur through:

- self accommodation

or **heterogenous nucleation**:

- coherent nucleation in association with pre-existing defects providing an appropriate strain field
- sympathetic nucleation
- autocatalytic nucleation
- cluster-assisted nucleation

Self Accommodation

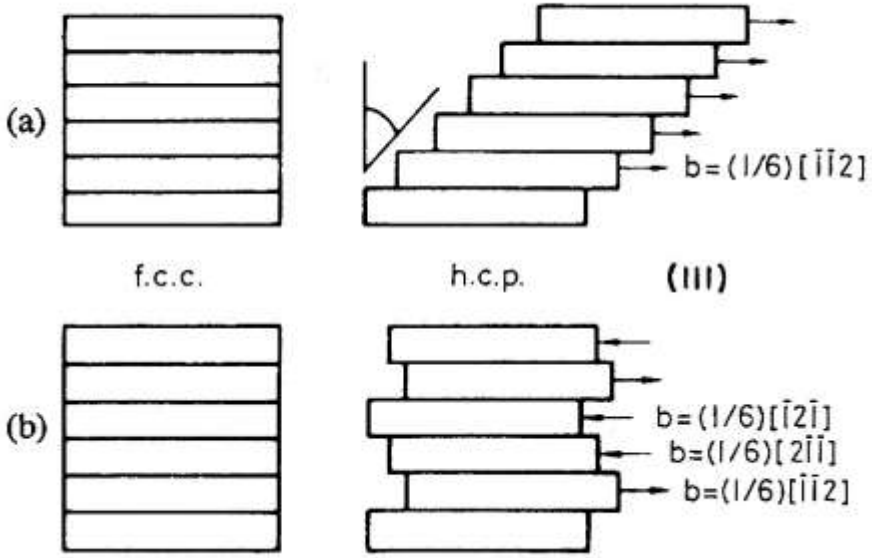

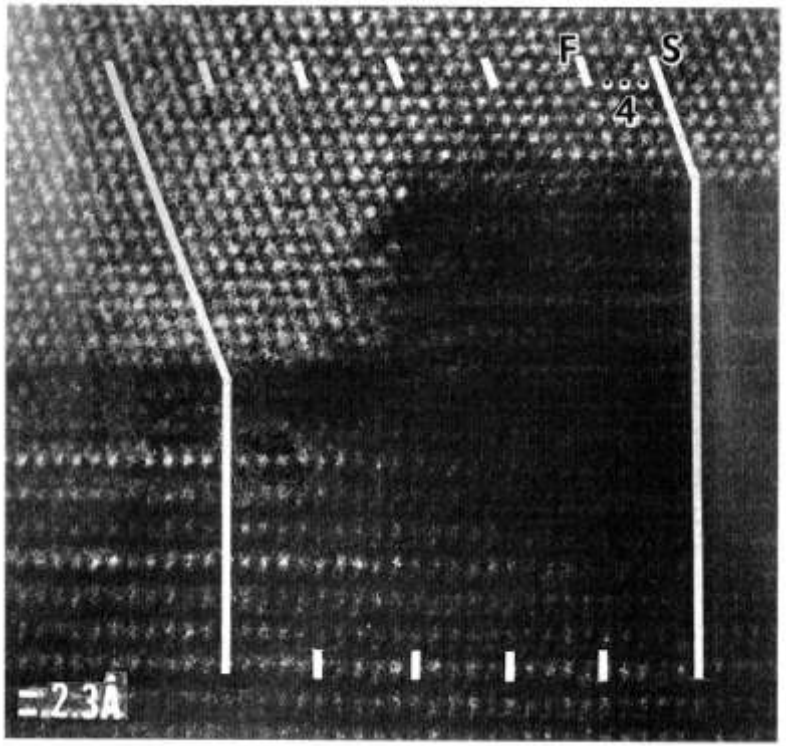

Christian, *The Theory of Transformations in Metals and Alloys* Pergamon (2002)

Howe, Dahmen, Gronsky, *Philos. Mag.* **56A** p. 31 (1987)

Heterogeneous Nucleation

Nucleation at non-random, preferred sites providing assistance in surmounting activation barrier

1. Nucleation at Pre-existing Static Sites

- **1-, 2-, 3-D Structural Defects (in excess of equilibrium concentration)**
  - incoherent nucleation releasing strain energy of the defect
  - coherent or partially coherent nucleation utilizing the strain field of the defect
  - nucleation on stacking faults
- **Sequential Precipitation**
  - e.g. GP zone/θ”/θ’/θ in Al-Cu
  - nucleation on interphase boundaries
  - sympathetic nucleation

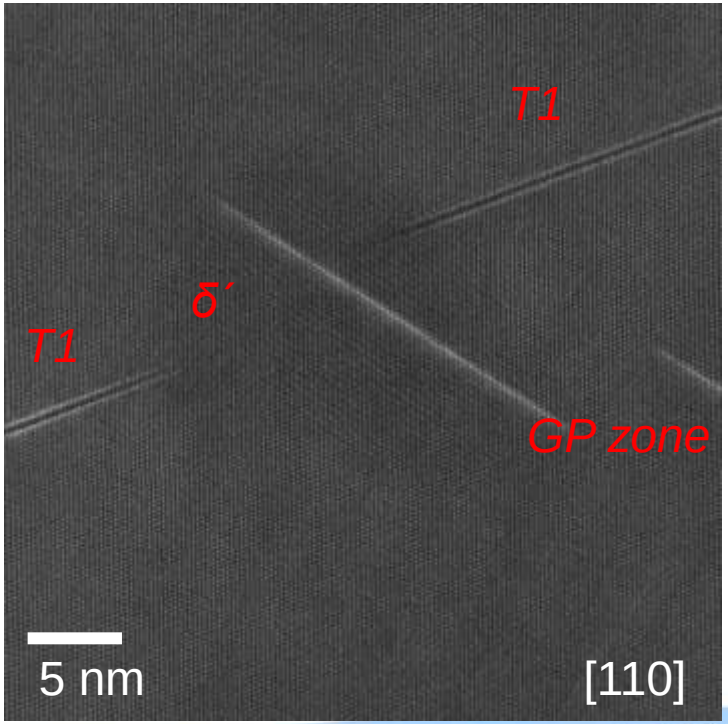

Al-Cu-Li-Mg alloy

Australian Government
Australian Research Council

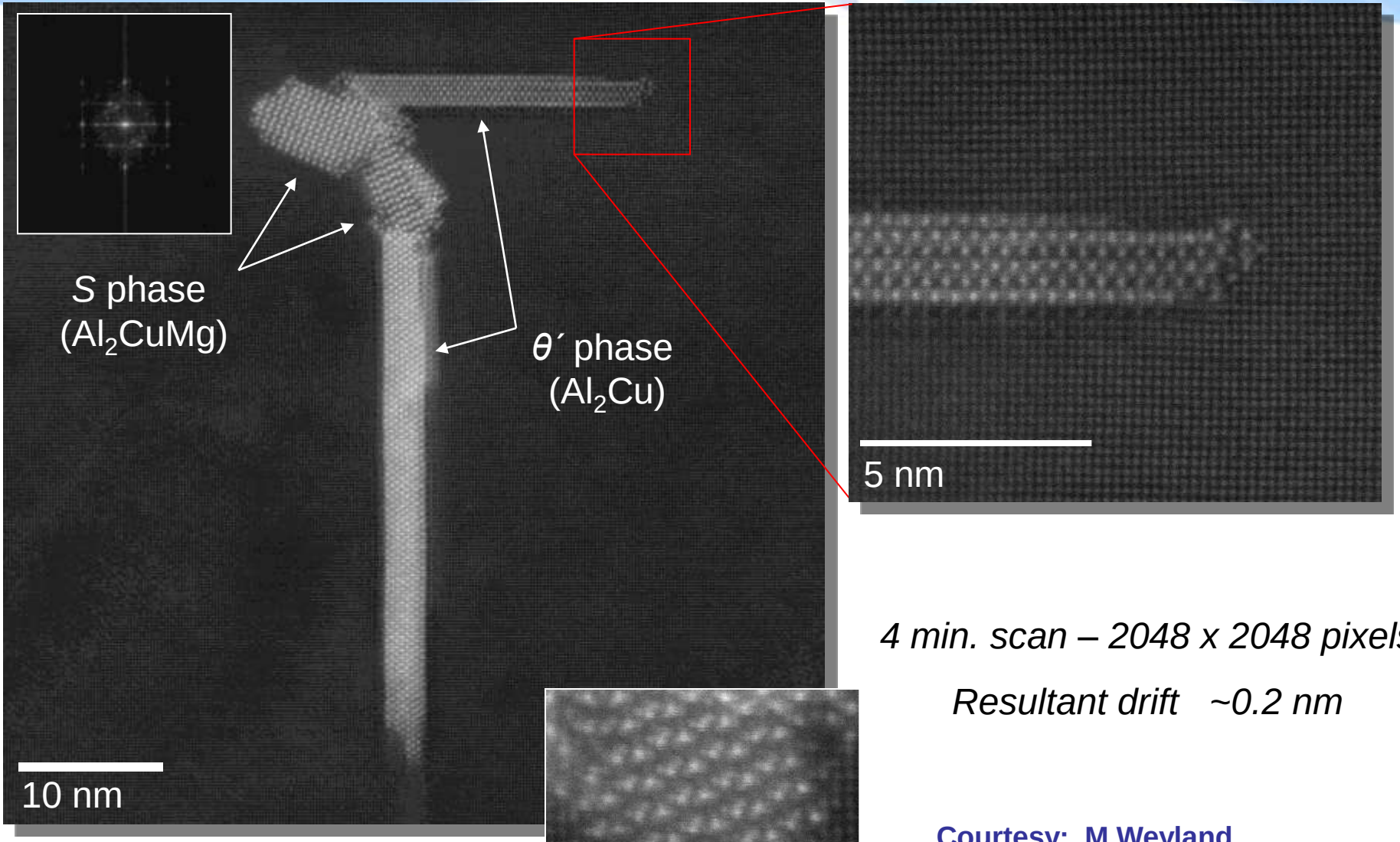

4 min. scan – 2048 x 2048 pixels

Resultant drift ~0.2 nm

Courtesy: M Weyland

Al-Cu-Li-Mg alloy

Heterogeneous Nucleation

2. Nucleation at Preferred Sites defined Dynamically

- **Self-accommodation/Sympathetic Nucleation**
- **Autocatalytic Nucleation**

- formation of preferred heterogeneous arrays as a result of nucleation in the elastic strain fields of existing precipitates

- **Cluster-assisted Nucleation**

- pre-nucleation solute clustering persists through the incubation period required for establishment of a finite nucleation rate

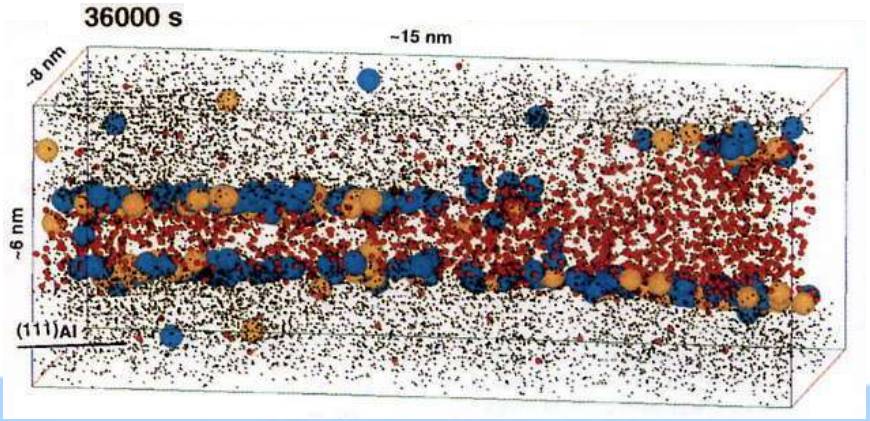

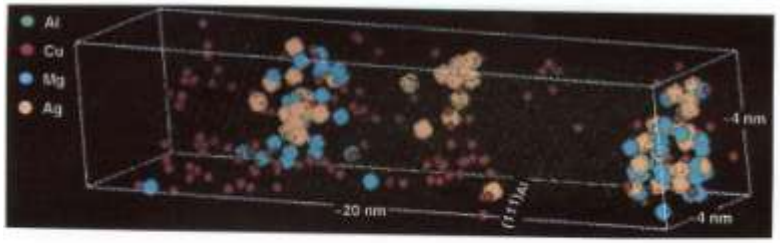

3DAP elemental mapping of an Al-4Cu-0.3Mg-0.4Ag (wt%) alloy aged 5 sec. at 180°C
(*Murayama and Hono, Scripta Mater. 1998*)

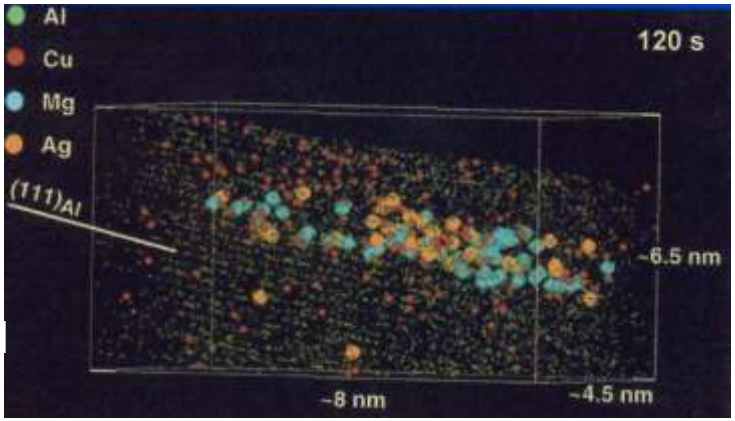

3DAP elemental mapping of a $\{111\}_\alpha$ platelet in an Al-4Cu-0.3Mg-0.4Ag (wt%) alloy aged at 180°C
Reich, Murayama and Hono, Acta Mater., 1998

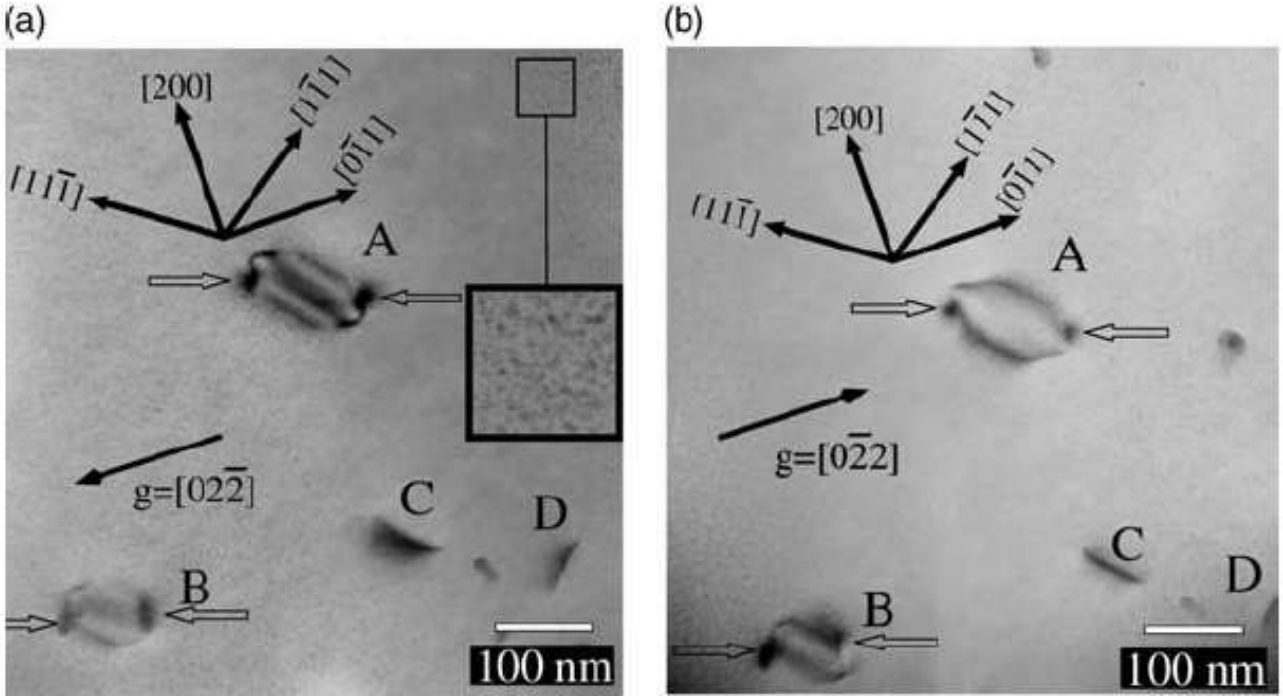

Figure 2. Elec
for 0.083 h at
inside (in (a)) t
line strain cor
a dissociated F
is shown in th

Rosalie, J.M., L.N. Bourgeois and B.C. Muddle, "Precipitate assemblies formed on dislocation loops in aluminium-silver alloys", *Philos. Mag,* Vol. 89, pp. 1267-78, 2009.

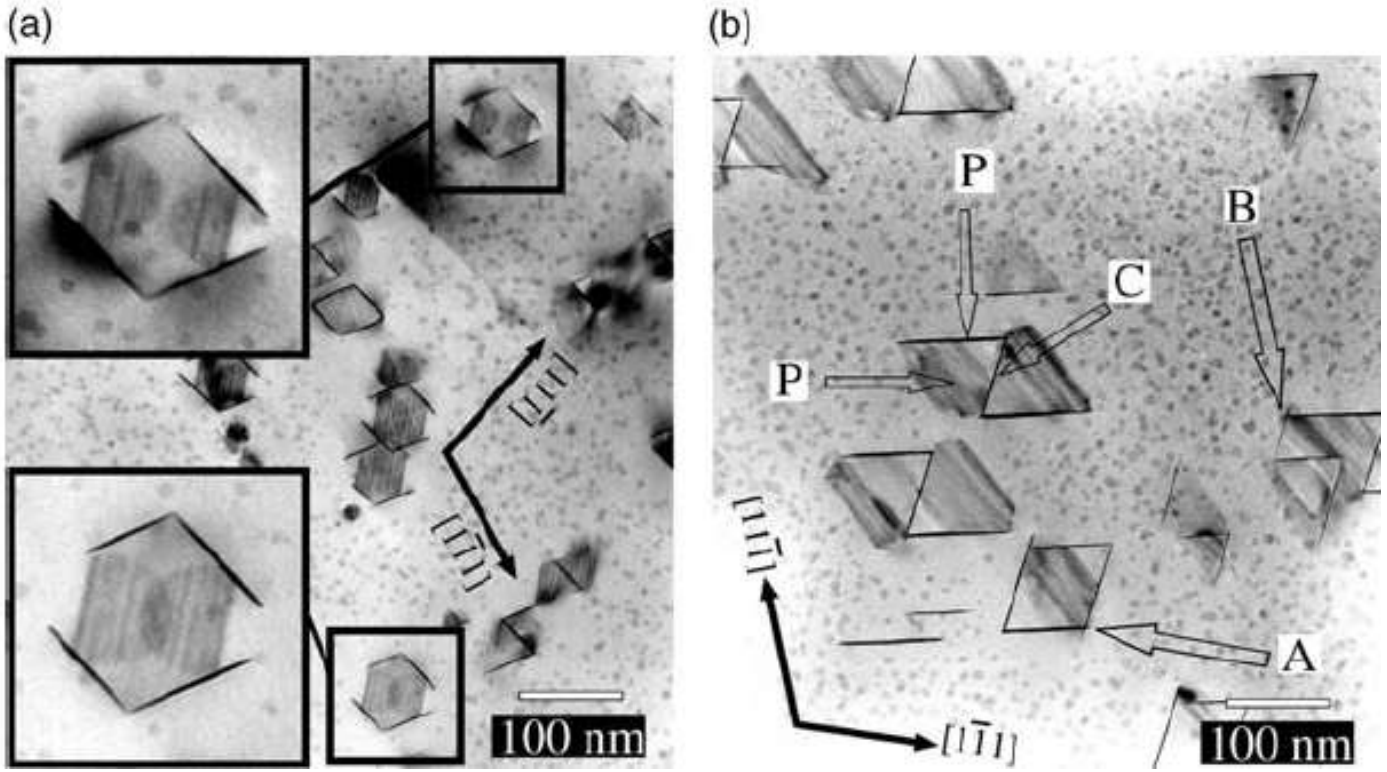

Figure 3. Micr
$Al_{98.3}Ag_{1.7}$ allo
central (*C*) an
showed that the

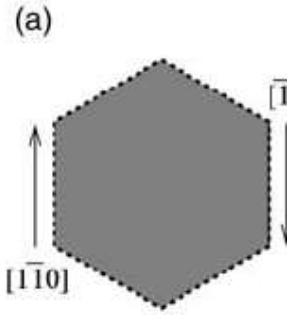

Figure 6. The disso
in (a) where the loop
loop lies. The faulted
of this dislocation in
The (11$\bar{1}$) glide plan
the partial dislocatio
the passage of the Sh
for each {110} facet
which are located alt

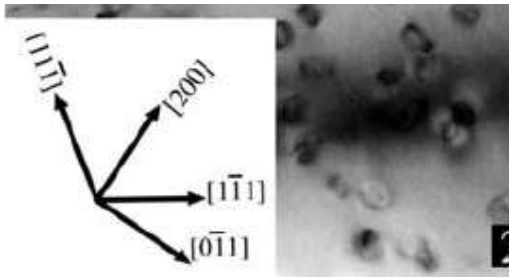

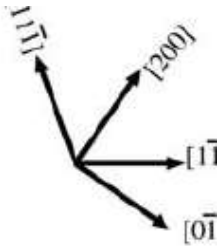

Figure 2. The as-quenched defect structure of the $Al_{98.2}Ag_{0.9}Cu_{0.9}$ alloy, viewed close to the $[011]_\alpha$ zone in a two-beam condition with $g = 11\bar{1}$. The microstructure contains a population of approximately circular dislocation loops and some linear dislocations.

0.2h at 200ºC

Rosalie, J.M., L.N. Bourgeois and B.C. Muddle, "Precipitate assemblies formed on dislocation loops in aluminium-silver-copper alloys", *Philos. Mag.*, Vol. 89, pp. 2195-2211, 2009.

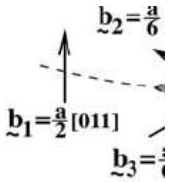
$\underset{\sim}{b}_2=\frac{a}{6}$
$\underset{\sim}{b}_1=\frac{a}{2}[011]$
$\underset{\sim}{b}_3=$

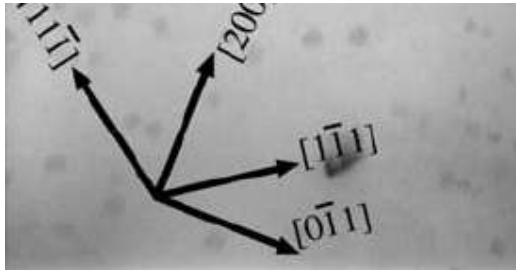
$[1\bar{1}1]$
$[0\bar{1}1]$

2h at 200ºC

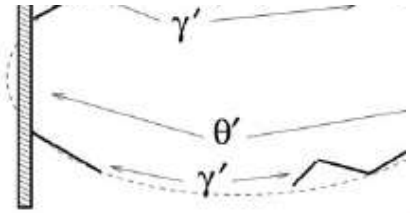
γ′
θ′
γ′

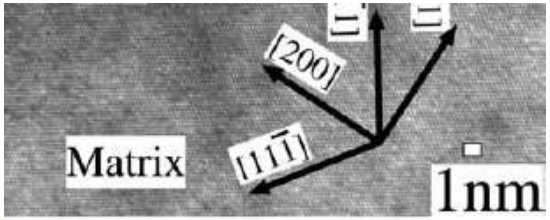
[200]
Matrix
[11$\bar{1}$1]
1nm

0.40 nm

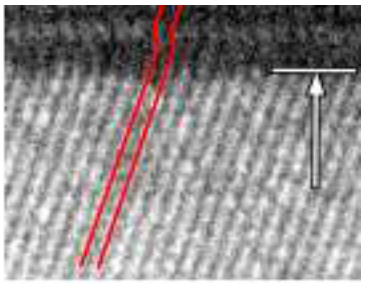

(c)

Australian Government
Australian Research Council

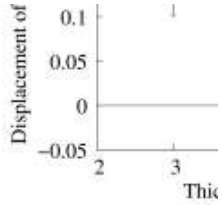

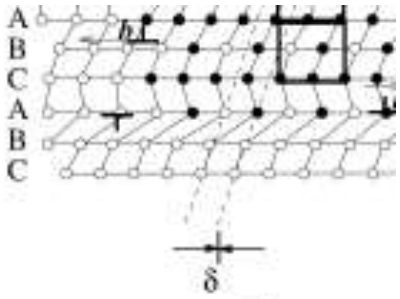

(c)

Al-Cu-Mg Alloys: *Nucleation of S Phase on Dislocation Loops*

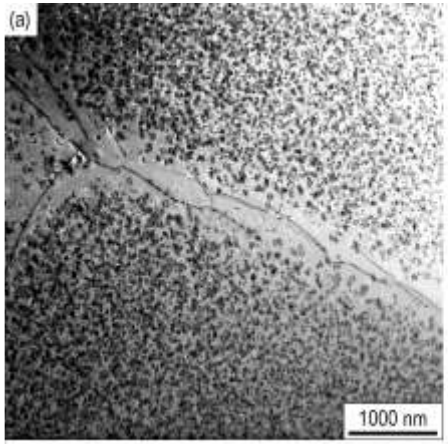

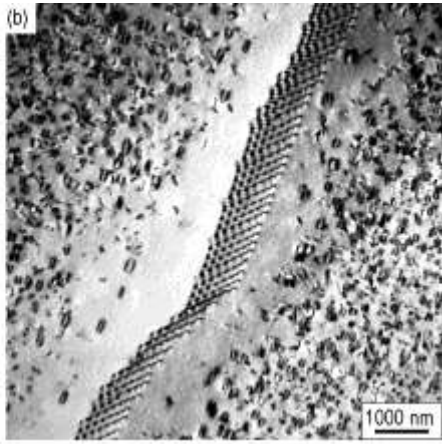

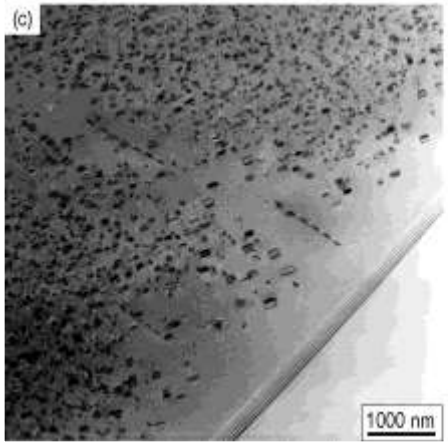

Solution Treat. (525˚C)
+ Quench (20˚C)
+ Age 60s @ 150˚C

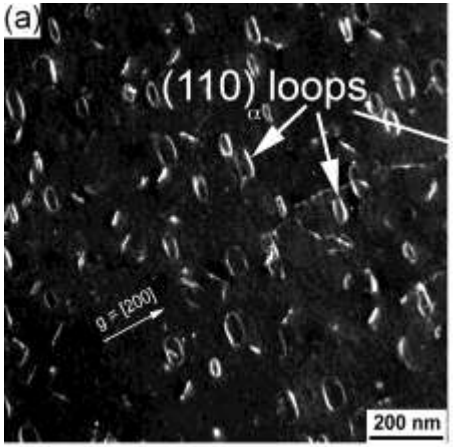

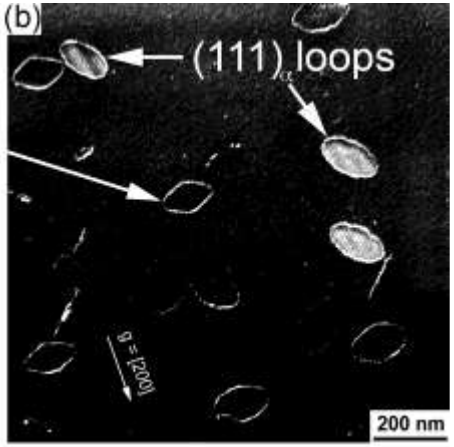

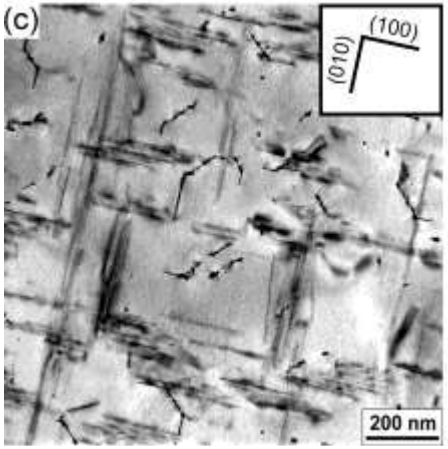

Al-1.1Cu-0.5Mg

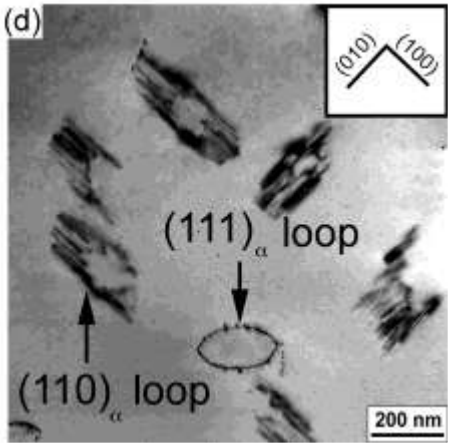

Al-0.2Cu-1.7Mg

Winkelman, G.B., R. Krishnamurthy and B.C. Muddle, "Orientation Relationships and Lattice Matching for the S Phase in Al-Cu-Mg Alloys", *Acta Mater.*, Vol. 55, pp. 3213-28, 2007.

Al-Cu-Mg Alloys: *Nucleation of S Phase on Dislocation Loops*

$\{111\}_\alpha$-type Loop

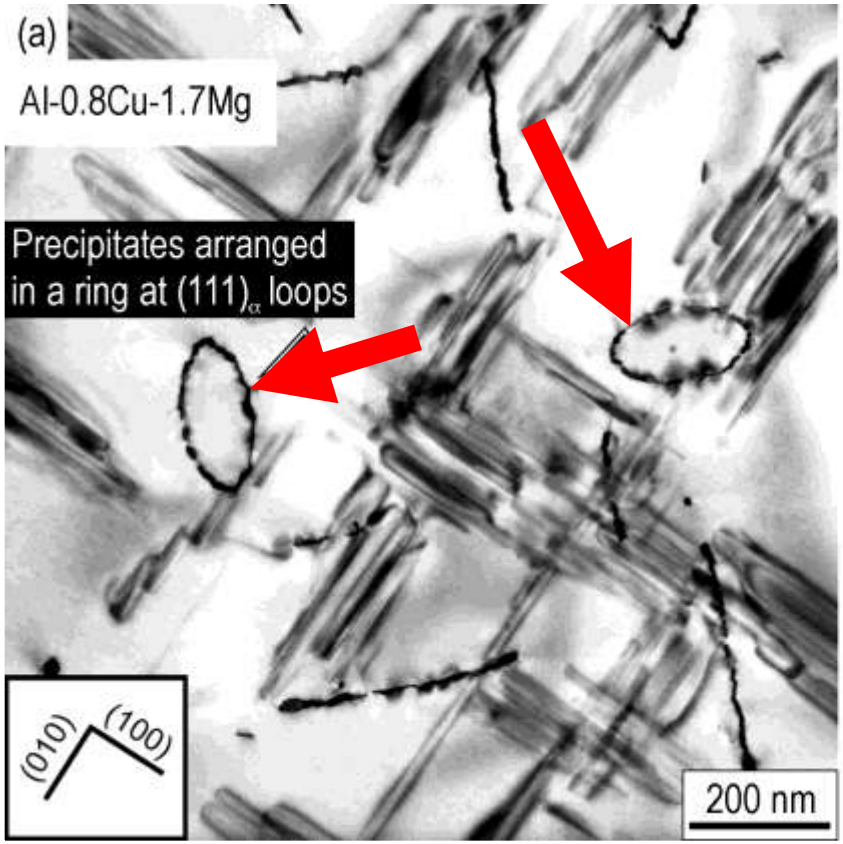

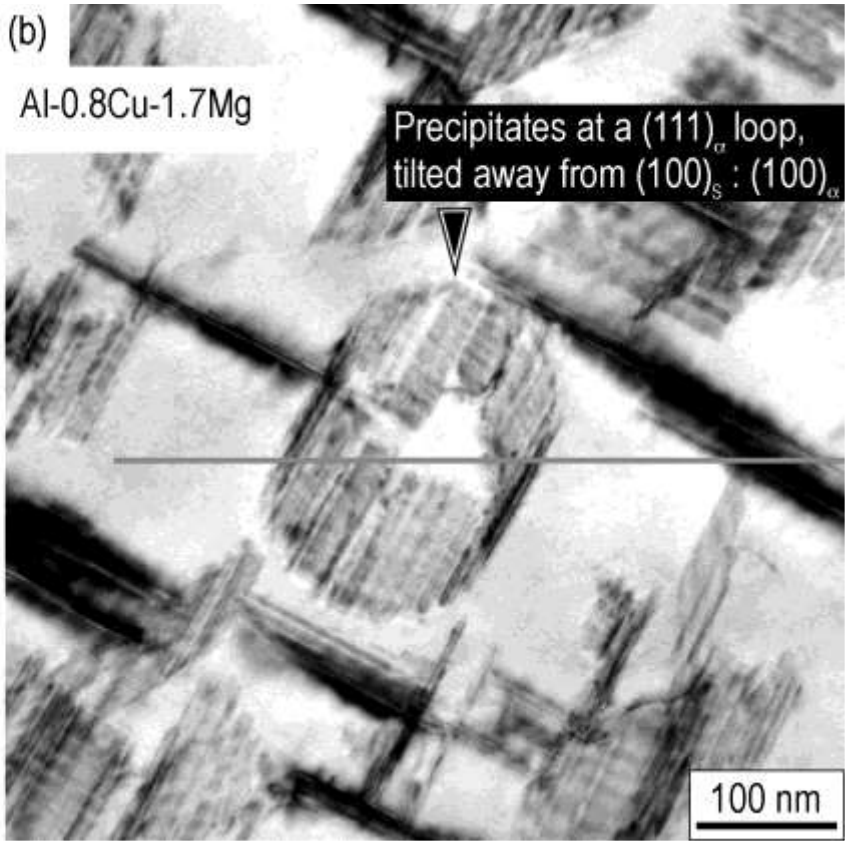

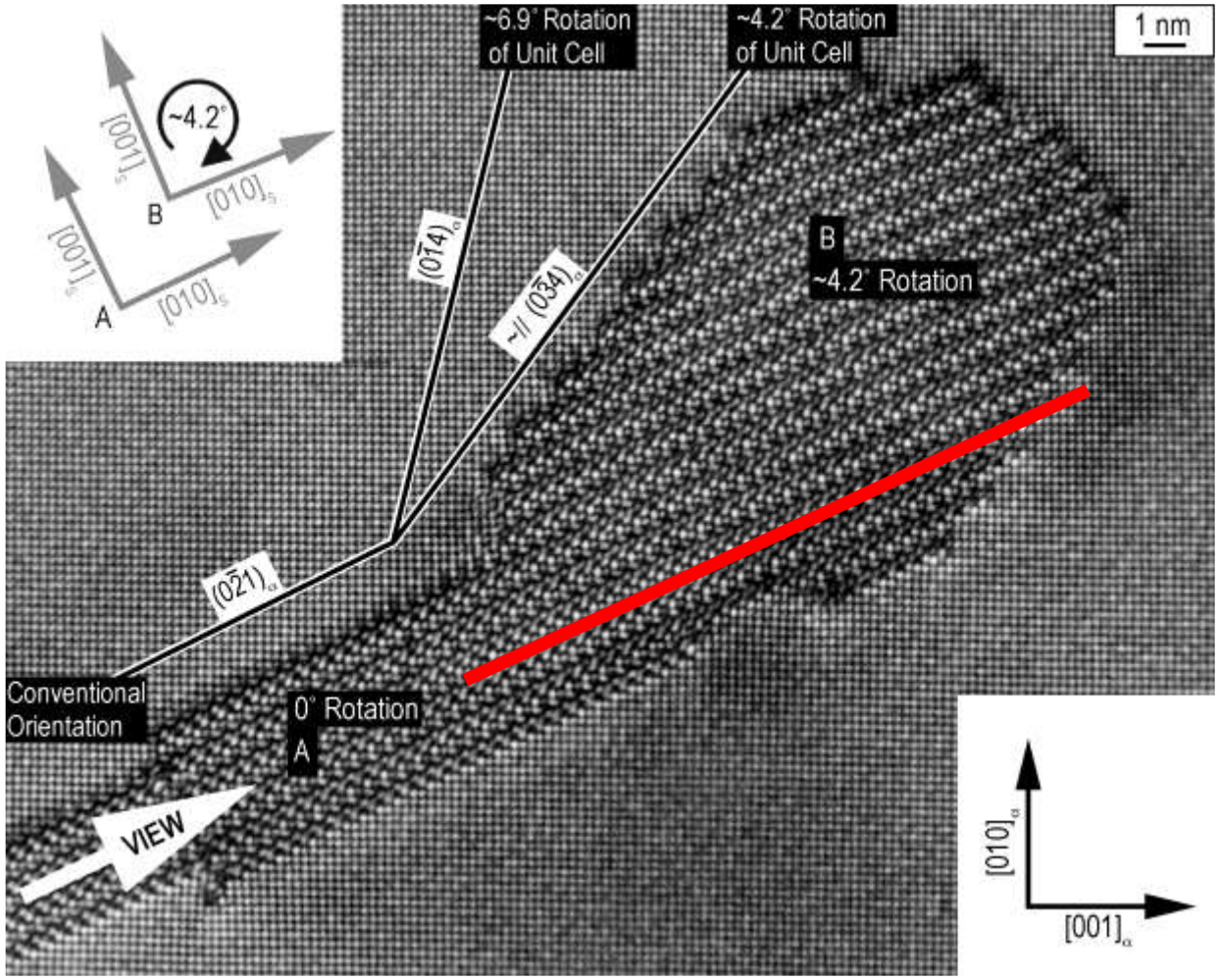
~6.9° Rotation of Unit Cell
~4.2° Rotation of Unit Cell
1 nm
~4.2°
[001]β
[010]β
B
[001]α
[010]α
A
(0$\bar{1}$4)α
~// (03$\bar{4}$)α
B
~4.2° Rotation
(02$\bar{1}$)α
Conventional Orientation
0° Rotation
A
VIEW
[010]α
[001]α

$\{111\}_\alpha$- type Loop

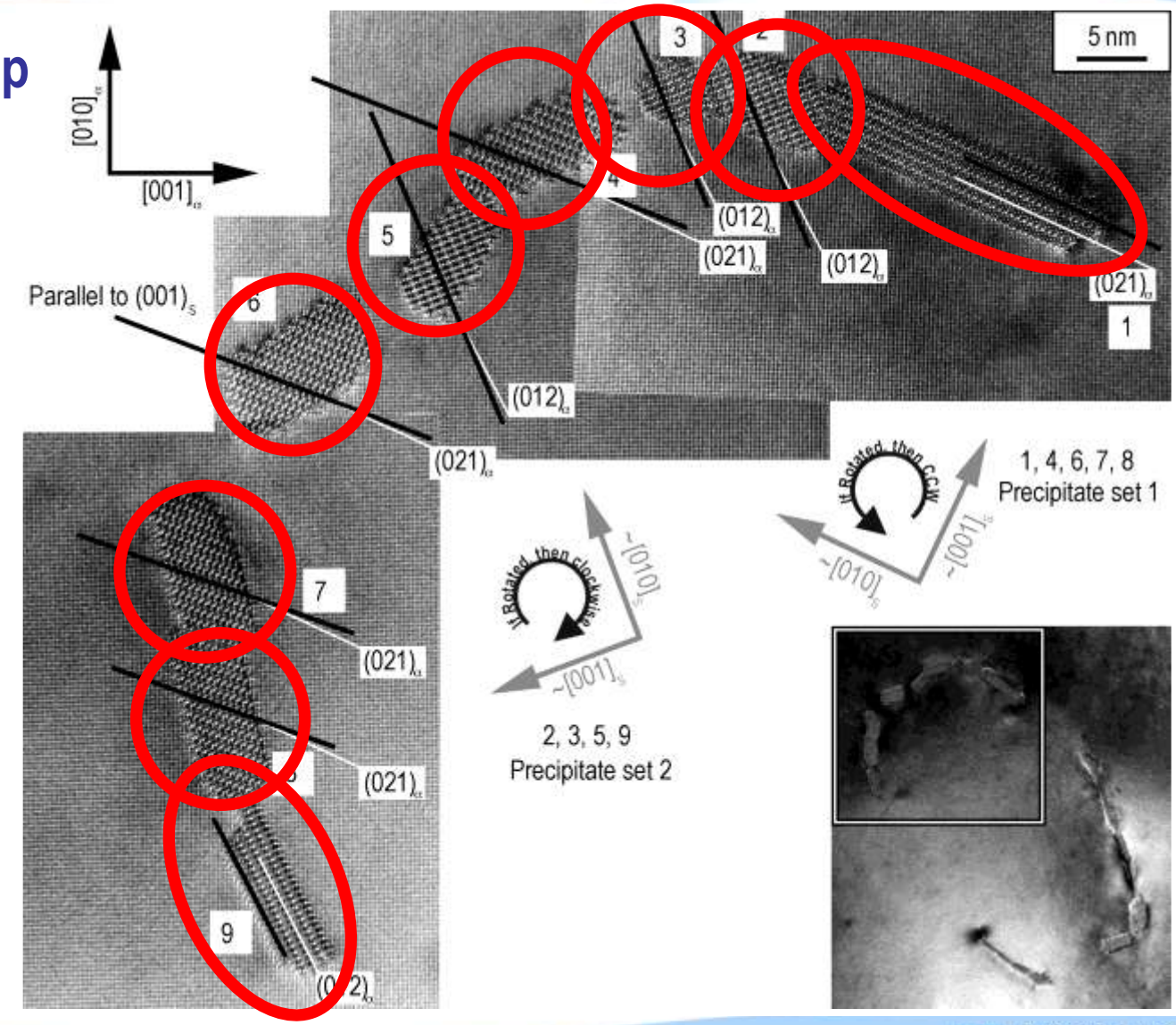

Autocatalytic Nucleation

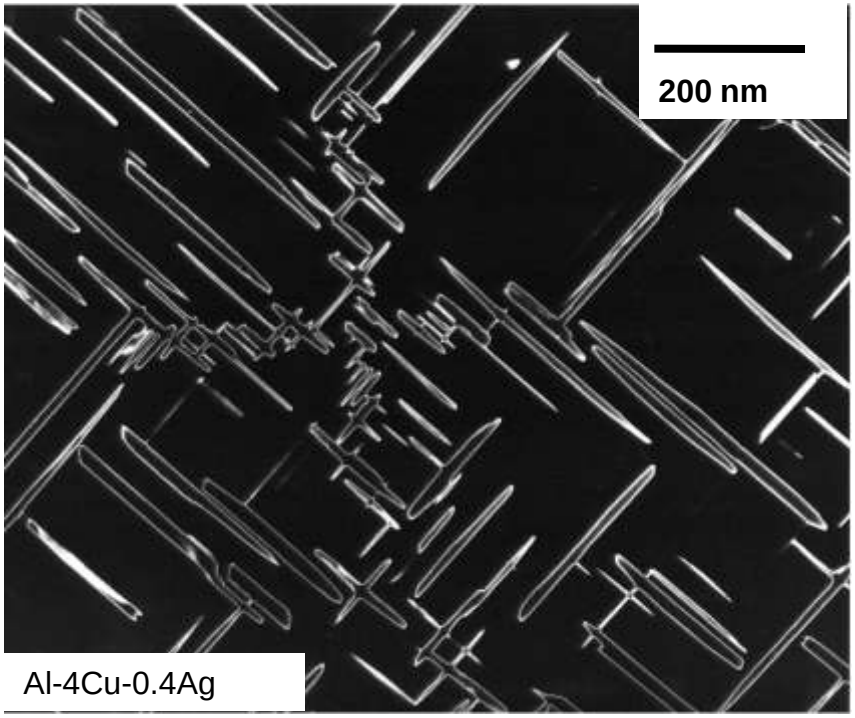

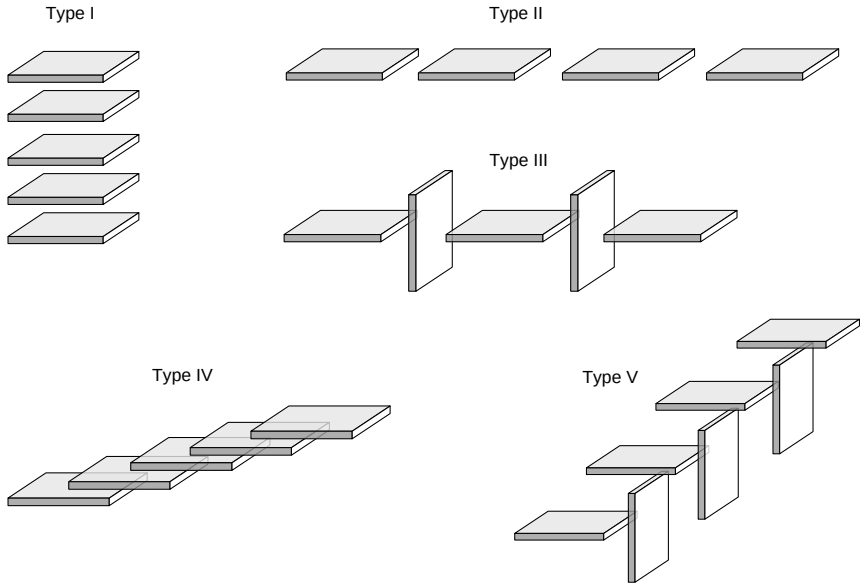

Autocatalytic nucleation of θ'
in Al-Cu alloys

LM Brown, RH Cook, RK Ham and GR Purdy, *Scripta Met*., **7** 815-20, 1973

V Perovic, GR Purdy and LM Brown, *Acta Metall*., **27** 1075-84, 1979

V Perovic and GR Purdy, *Acta Metall*., **29** 889-902, 1981

V Perovic, GR Purdy and LM Brown, *Scripta Metall*., **15** 217-21, 1981

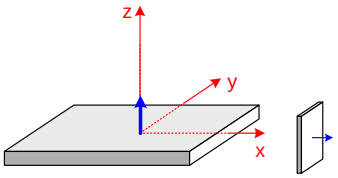

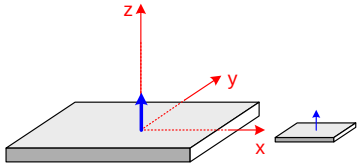

Courtesy: Y Kryvasheyeu

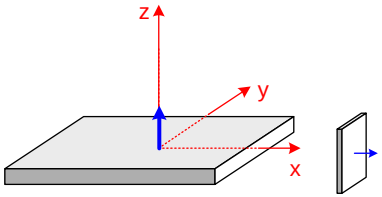
z
y
x

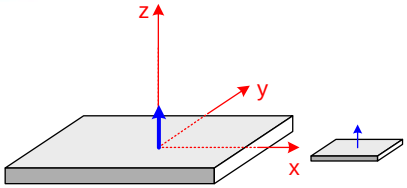
z
y
x

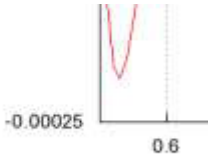
-0.00025
0.6

-0.0002
-0.0003

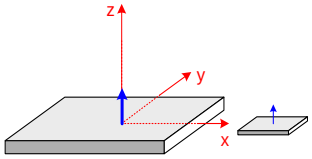
z
y
x

-1.5
-1

-0.0005
-0.1

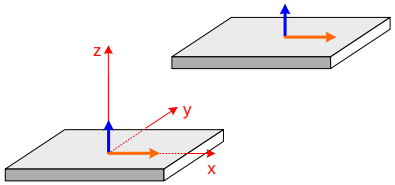
z
y
x

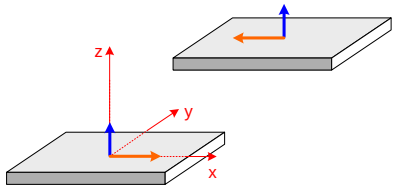
z
y
x

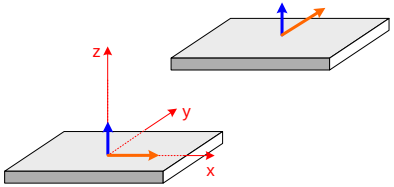
z
y
x

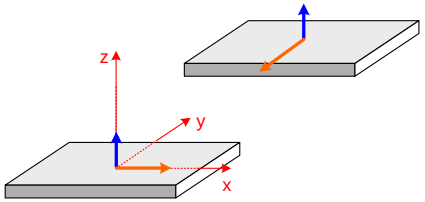
z
y
x

y
x

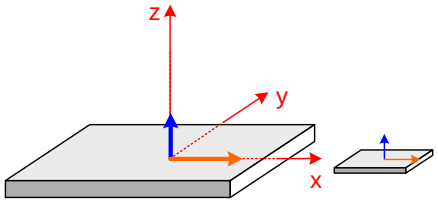
z
y
x

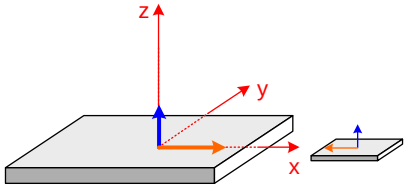
z
y
x

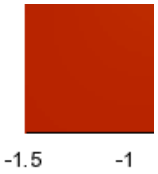
-1.5
-1

Cluster-assisted Nucleation

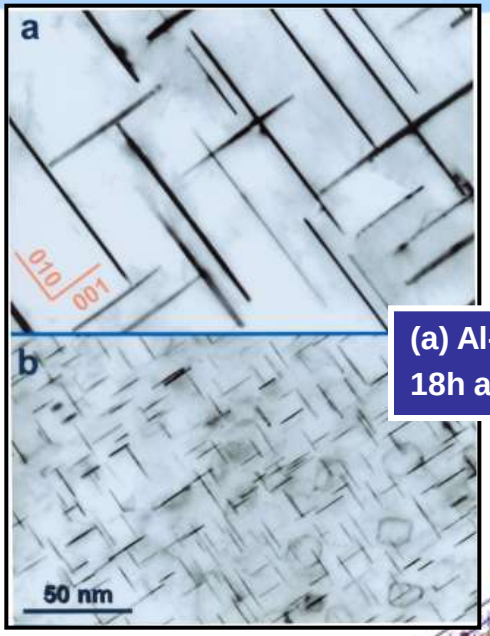

(a) Al-4Cu, and (b) Al-4Cu-0.05Sn
18h at 190ºC

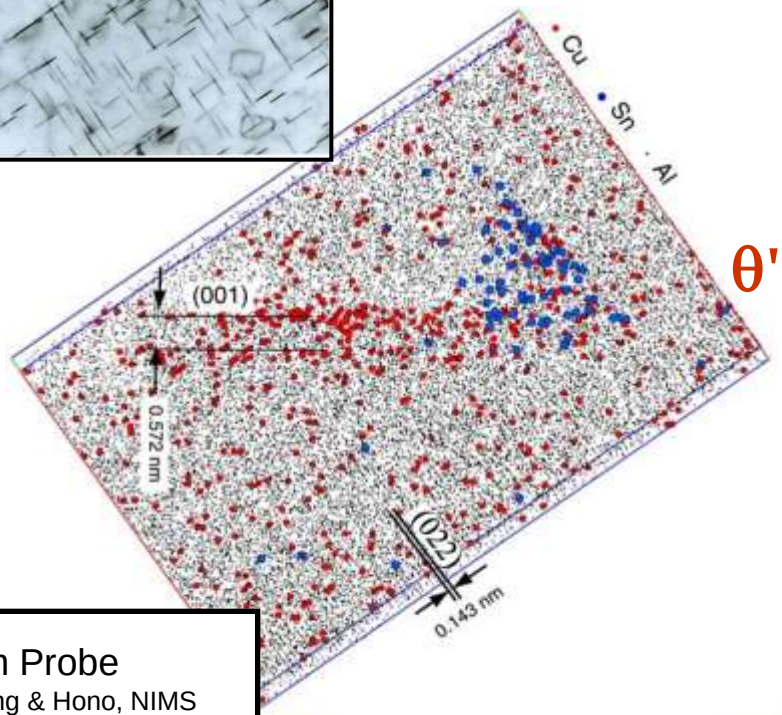

3-D Atom Probe
Courtesy Ping & Hono, NIMS

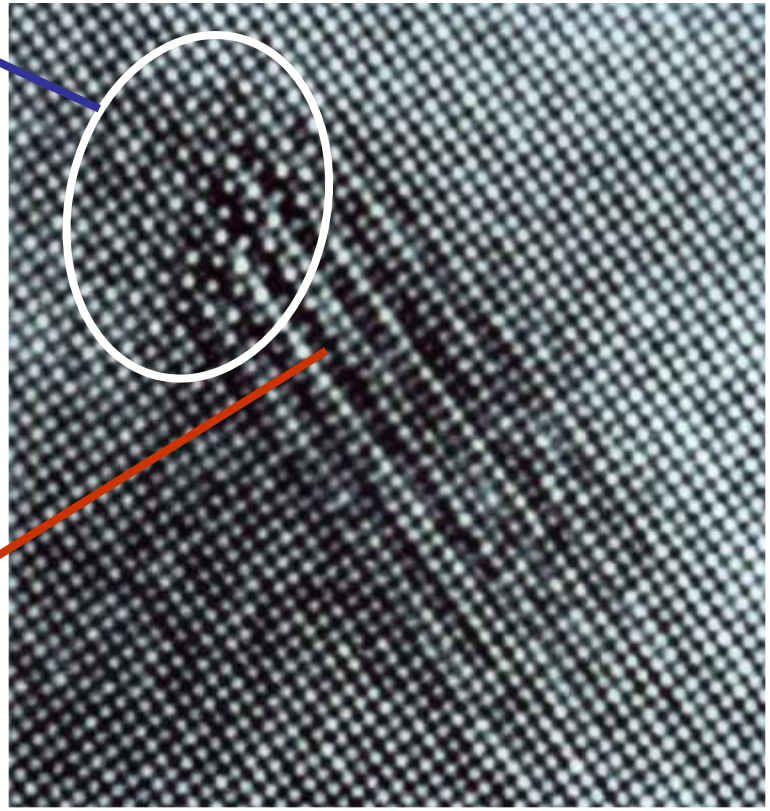

Al-Cu-Sn 300 s ageing at 200°C

Courtesy L Bourgeois

Electron diffraction patterns using focused TEM probe ***1nm*** *diameter.*

Orientation relationship between β-Sn and matrix not found in the binary alloy Al-0.01Sn:

(100)β // (110)α,

[010]β // [001]α

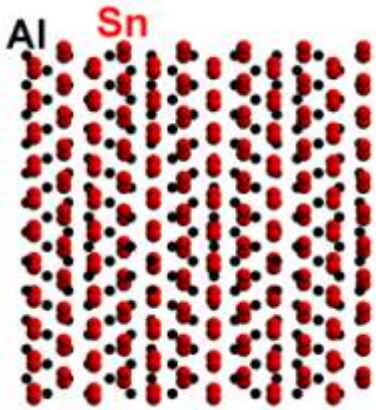

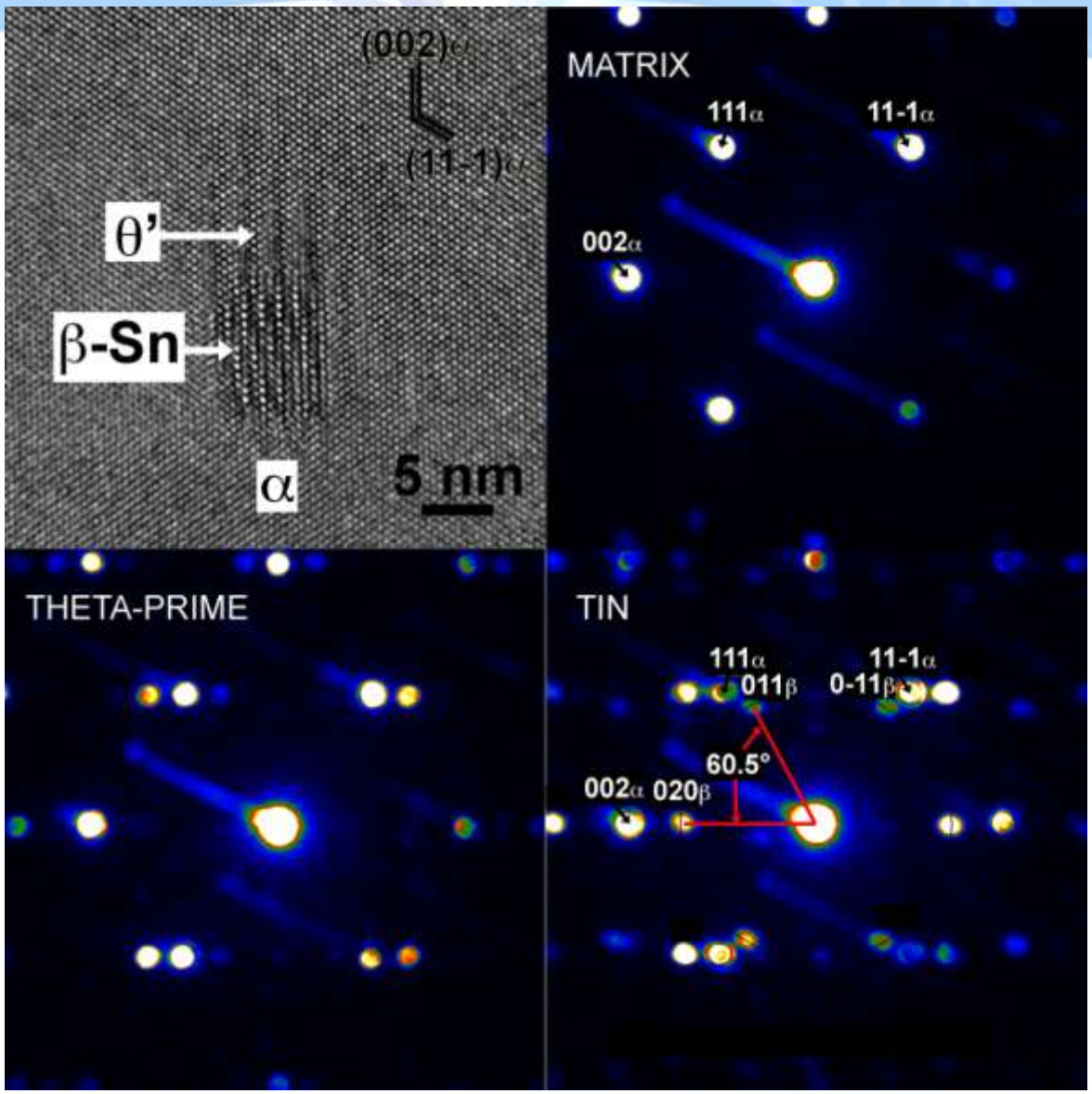

Al-1.7Cu-0.01Sn
2min@200°C, [110]$_\alpha$

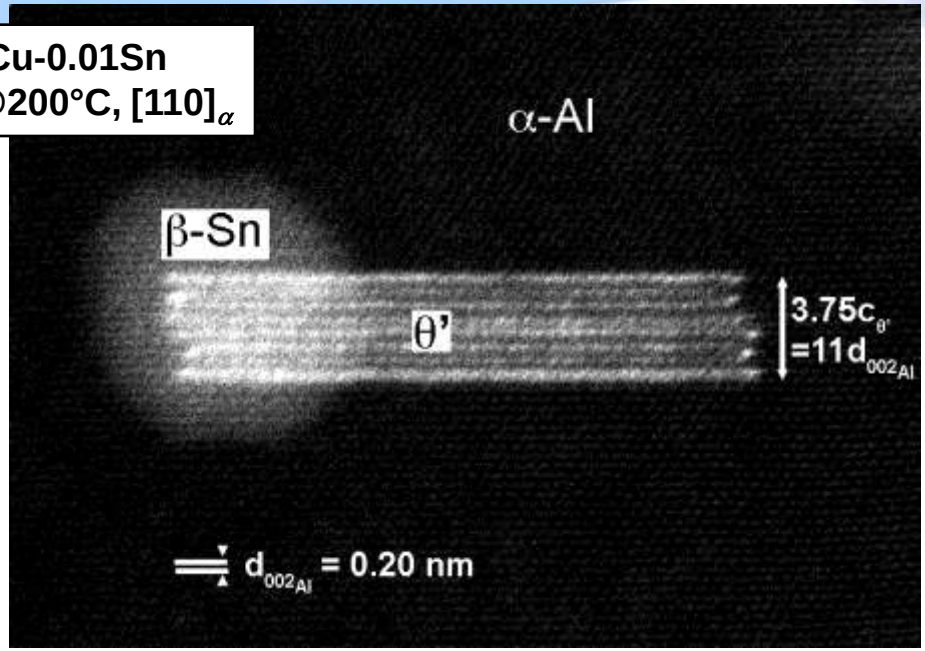

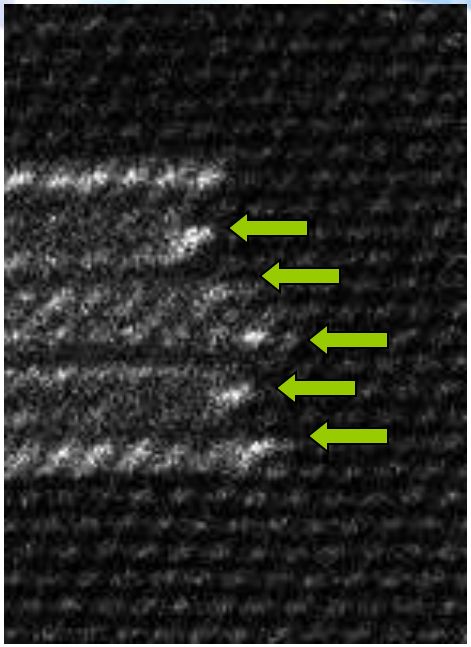

HAADF-STEM
FEI Titan
E. Yucelen

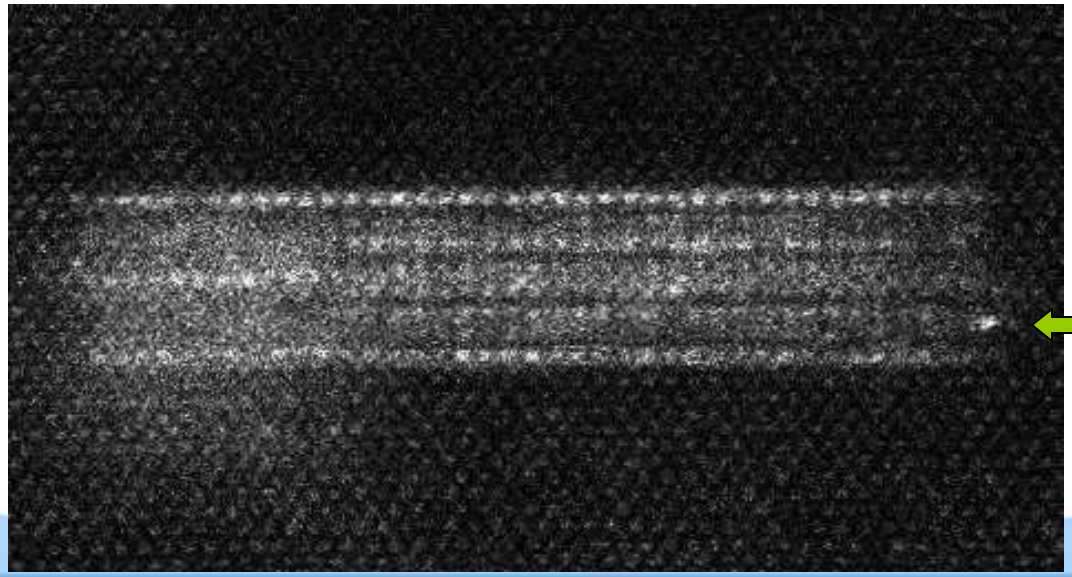

HAADF-STEM,
JEOL 2100F

Sn atoms and/or localised strain at θ'-matrix interface.

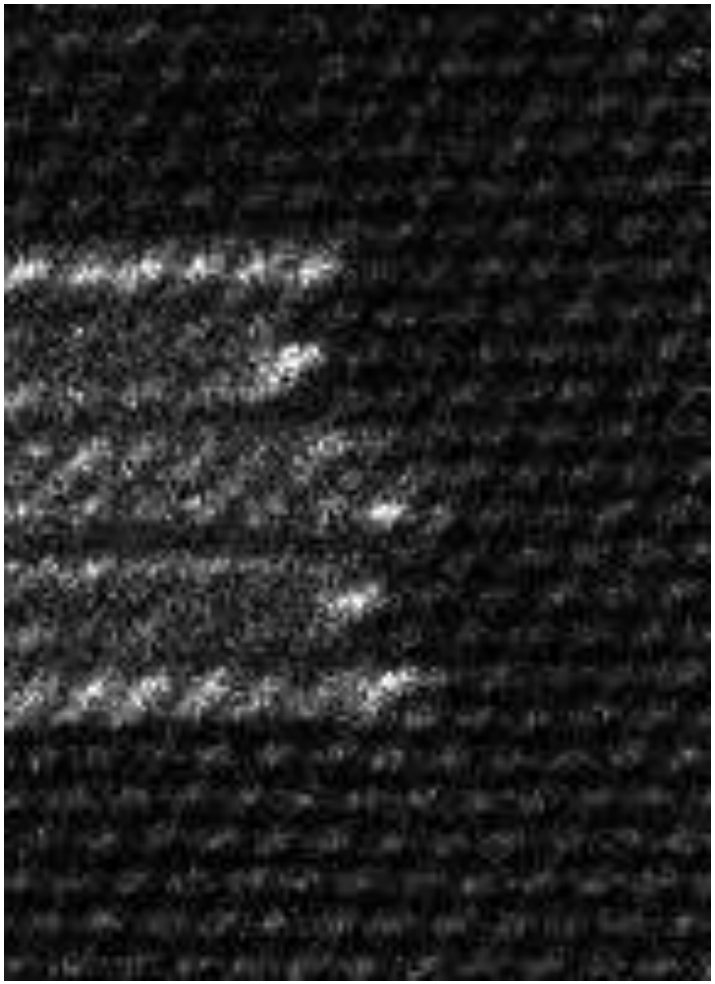

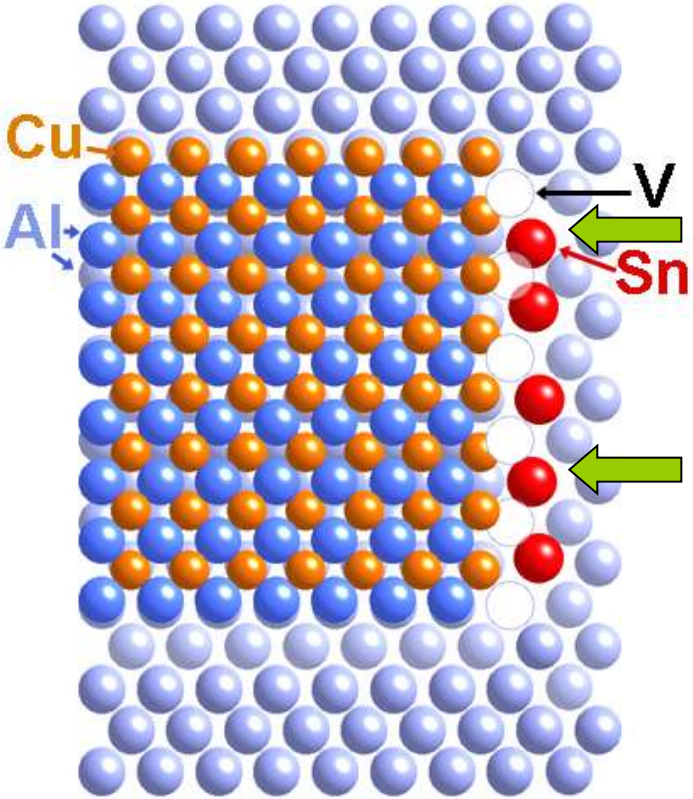
Cu
Al
V
Sn

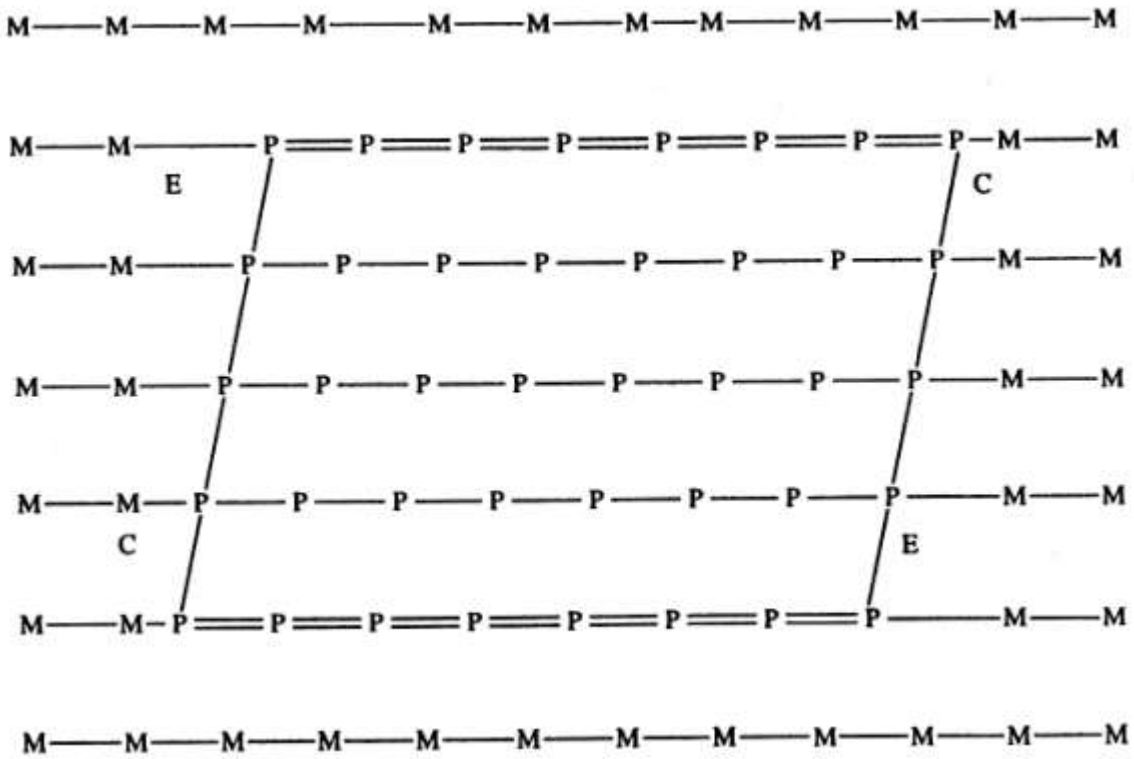

Christian, *Progress in Materials Science* **42** p. 101 (1997)

Summary

- those transformations giving rise to plate- or lath-shaped transformation products, and classically regarded as *diffusional*, are likely ***diffusional-displacive*** with a significant shear component
- at nucleation, the accommodation of shear strain energy may be at least as important as interfacial energy and may play a critical role in determining equilibrium nucleus shape – nucleation likely involves formation of 'loop' of transformation dislocation of critical form
- accommodation of shear strain energy may occur through:

  (i) self-accommodation

  (ii) coherent nucleation in association with pre-existing defects providing an appropriate strain field

  (iii) autocatalytic nucleation

  (iv) cluster-assisted nucleation

MONASH University

Go Boldly.

Shape Strain and Its Accommodation during Precipitation of Precipitate Plates

Jian-Feng Nie

Department of Materials Engineering
Monash University, Australia

Joint AFRL/AOARD/LLNL Nucleation Workshop, Maui Hawaii, 2-7 May, 2010

www.monash.edu

Acknowledgements

Zhou Xu
Matthew Weyland
Hong Liu
Yuman Zhu
Allan Morton
Yunzhi Wang
Barry Muddle
Australian Research Council
ARC Centre of Excellence for Design in Light Metals

Questions

- Is there a **shape strain** in the formation of precipitate plates, and if so, how to quantify it
- What is the role of **shape strain** in nucleation and thickening of precipitate plates & what are the implications for alloy design

Plate-shaped precipitates are often key strengthening or toughening constituents in engineering materials

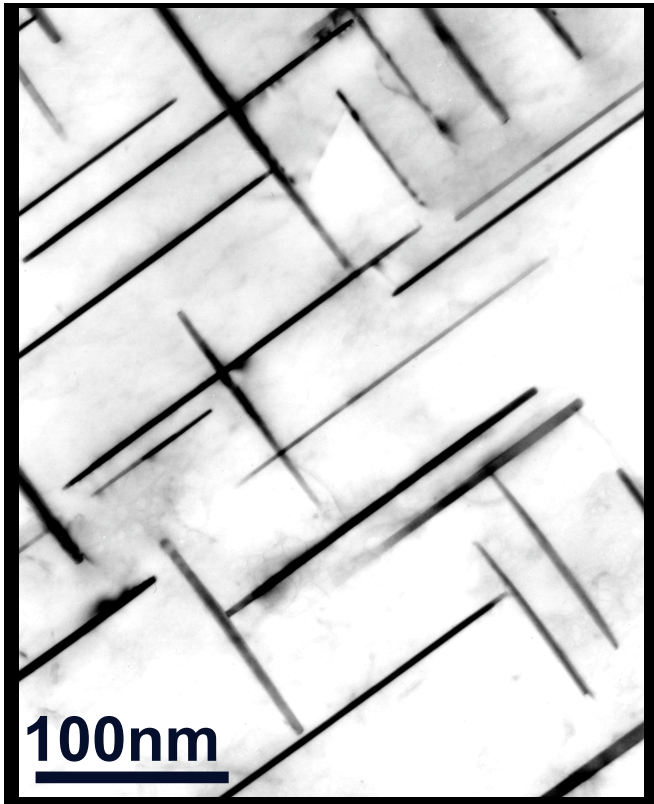

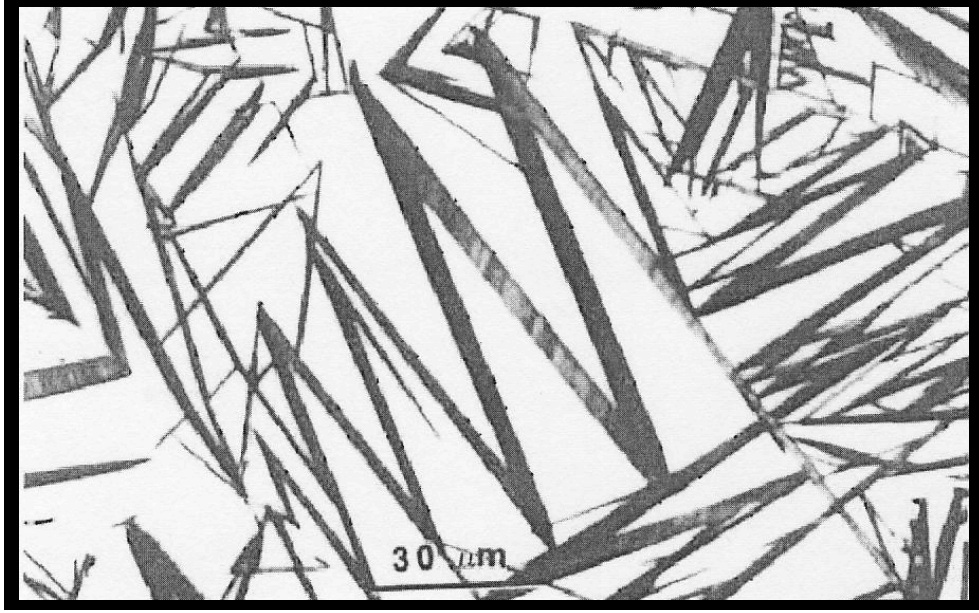

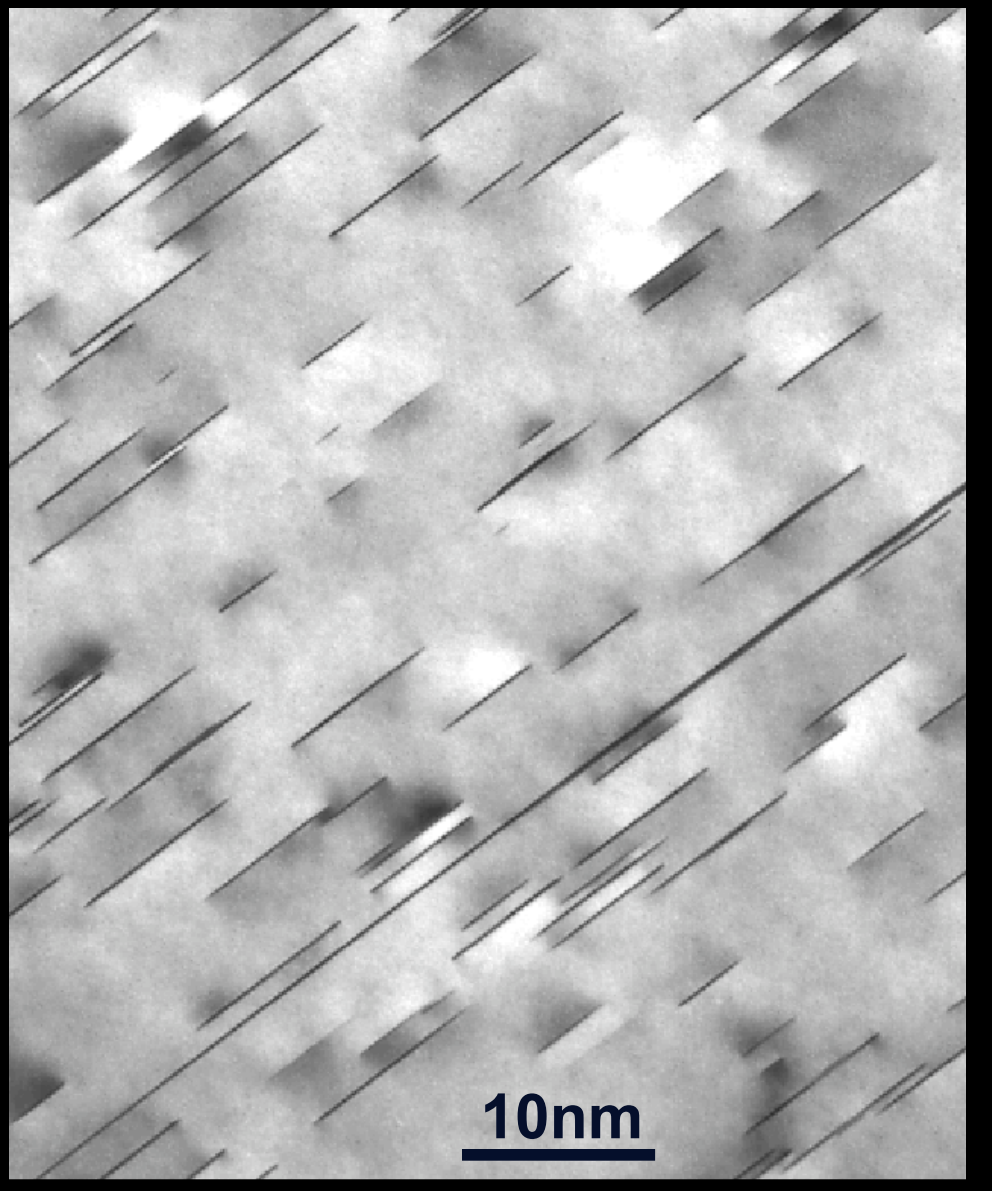

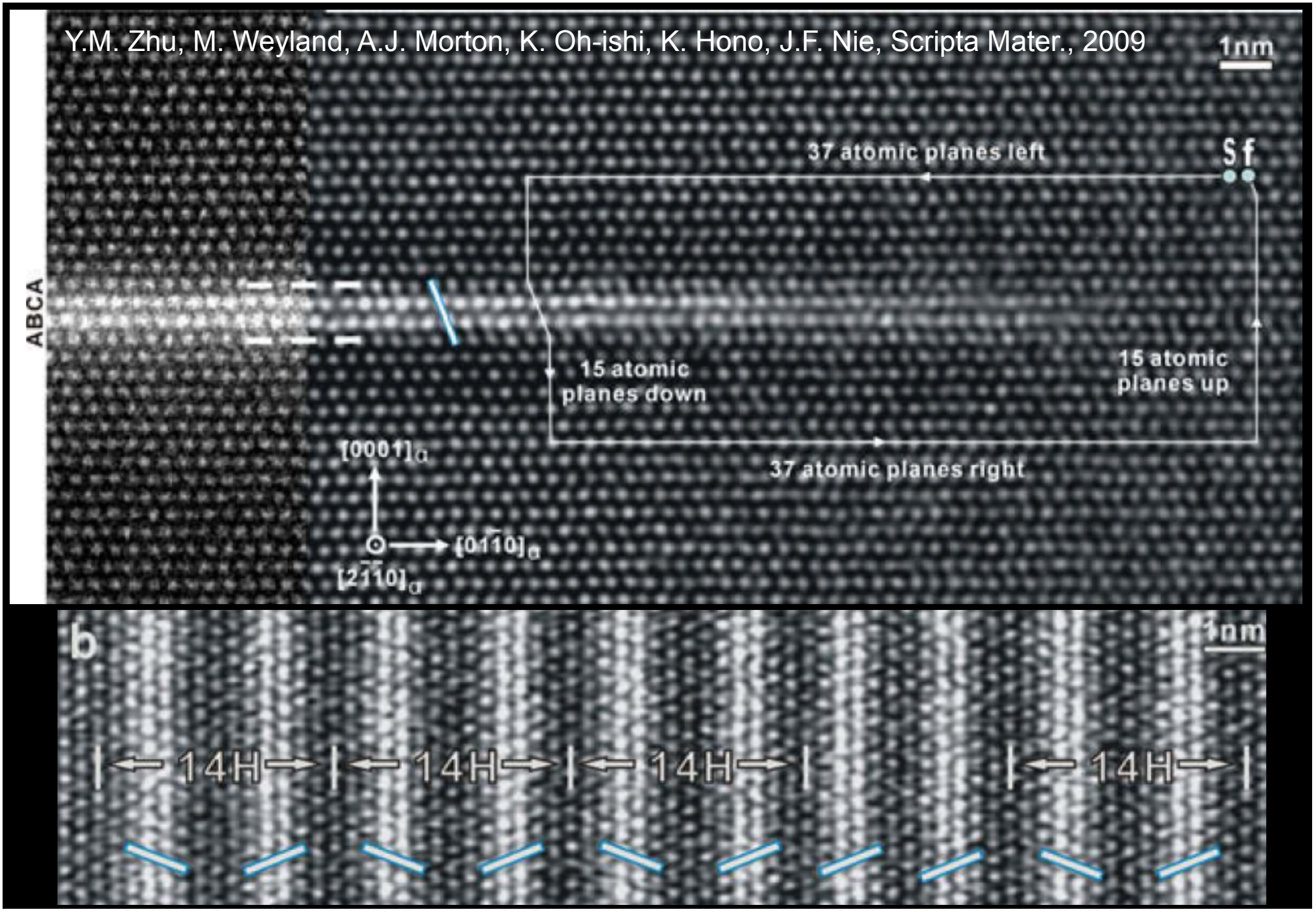
Y.M. Zhu, M. Weyland, A.J. Morton, K. Oh-ishi, K. Hono, J.F. Nie, Scripta Mater., 2009
1nm
37 atomic planes left
Sf
ABCA
15 atomic planes down
15 atomic planes up
37 atomic planes right
[0001]α
[01$\bar{1}$0]α
[2$\bar{1}\bar{1}$0]α
b
1nm
14H
14H
14H
14H

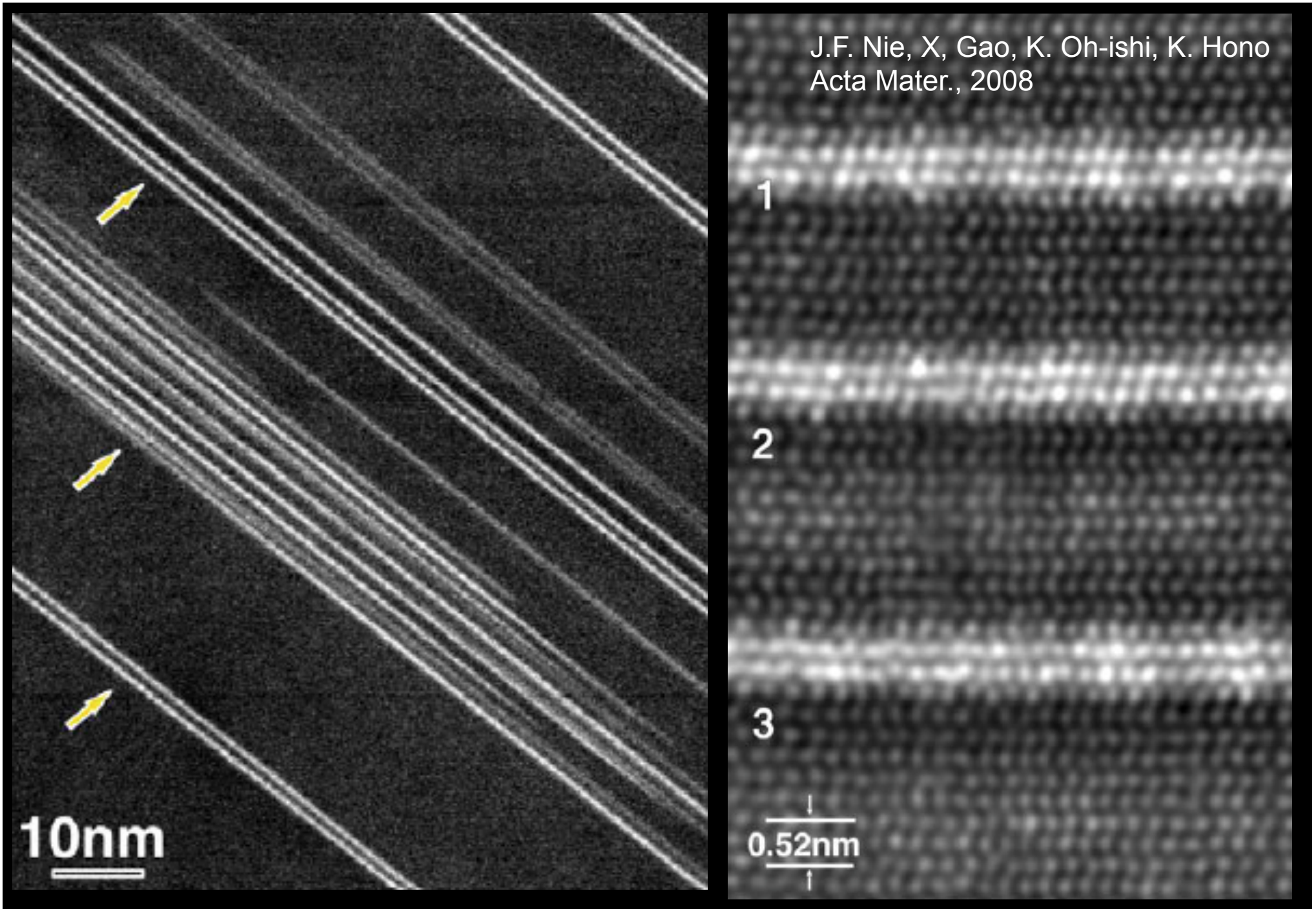
10nm
J.F. Nie, X, Gao, K. Oh-ishi, K. Hono
Acta Mater., 2008
1
2
3
0.52nm

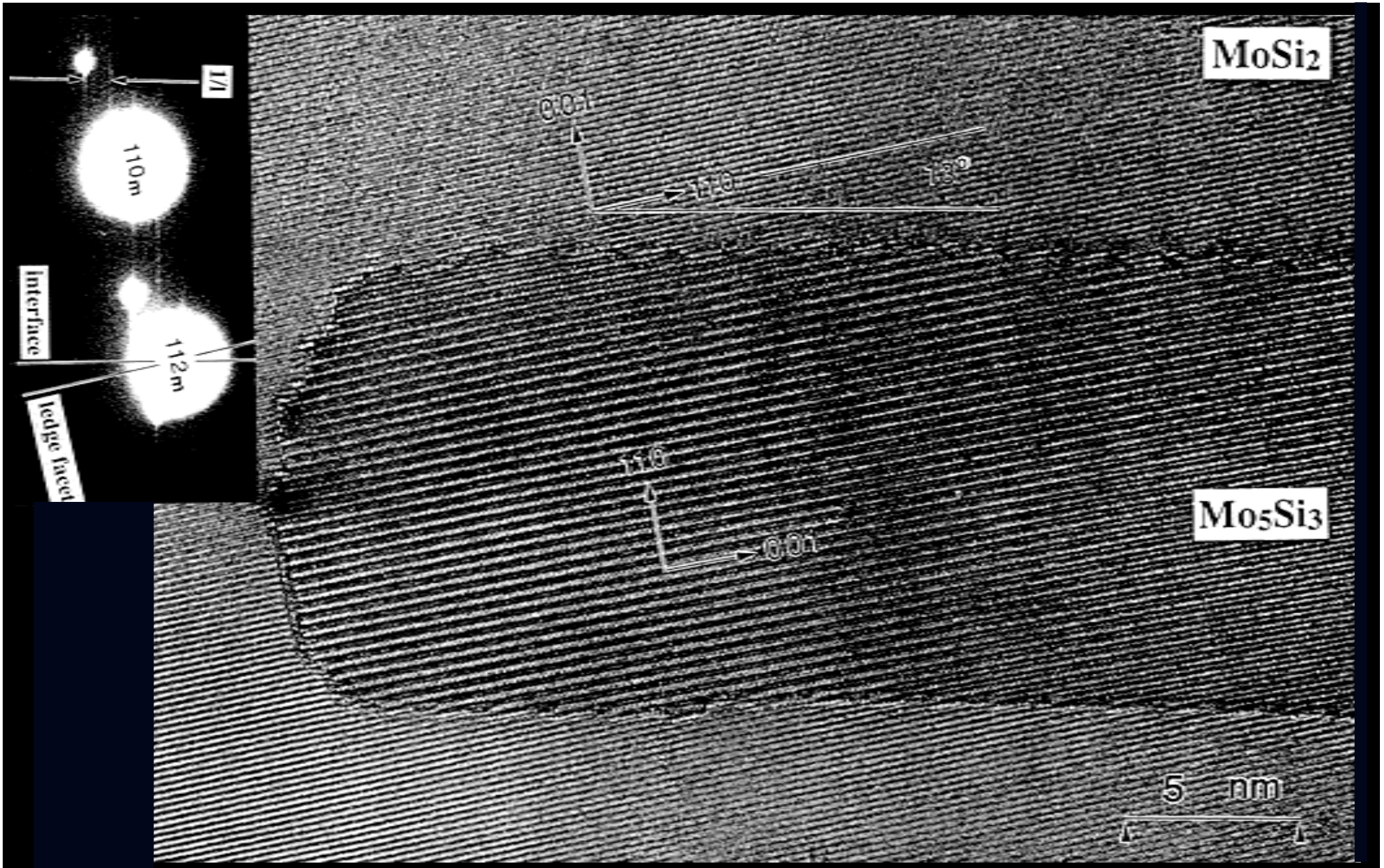

Mo_5Si_3 Precipitates in $MoSi_2$

S.Q. Xiao, S.A. Maloy, A.H. Heuer and U. Dahmen, Phil. Mag. A, 1995

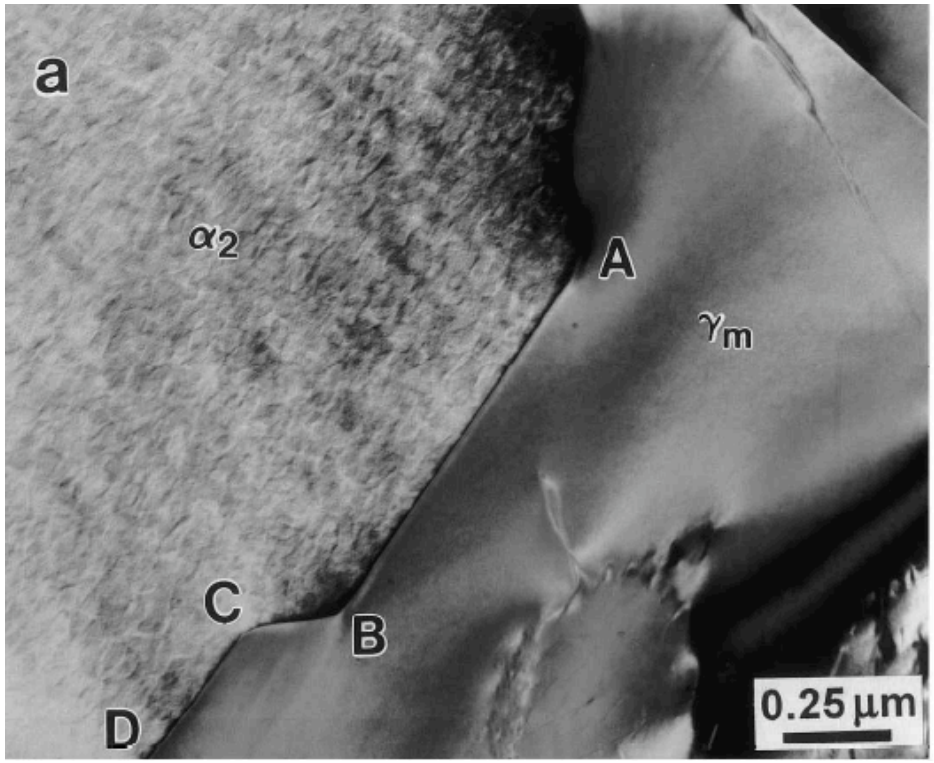

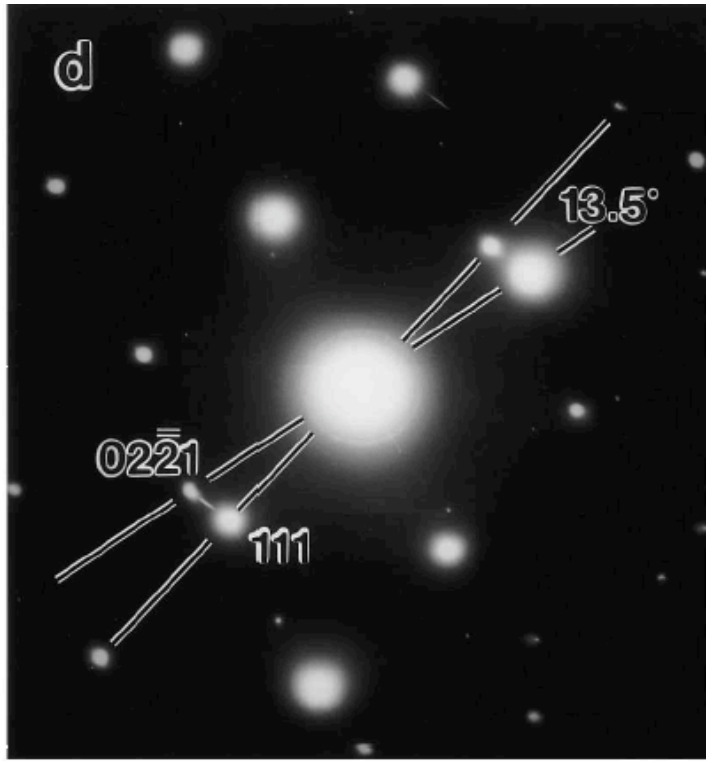

TiAl

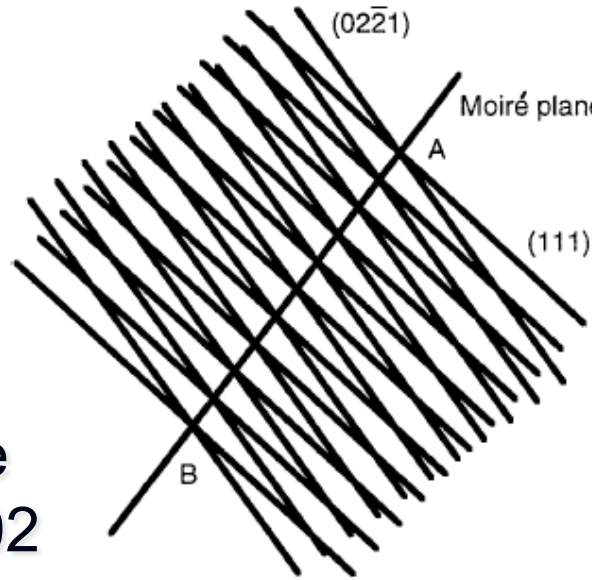

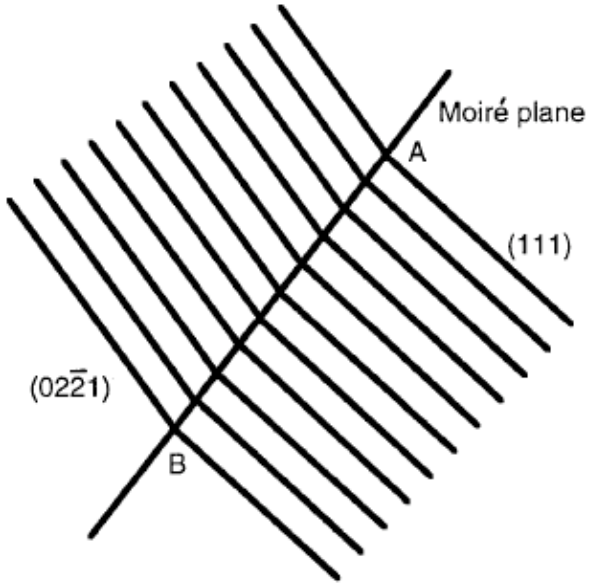

J.F. Nie and B.C. Muddle
Metall. Mater. Trans. 2002

Lattice Plane Deformation and Matching

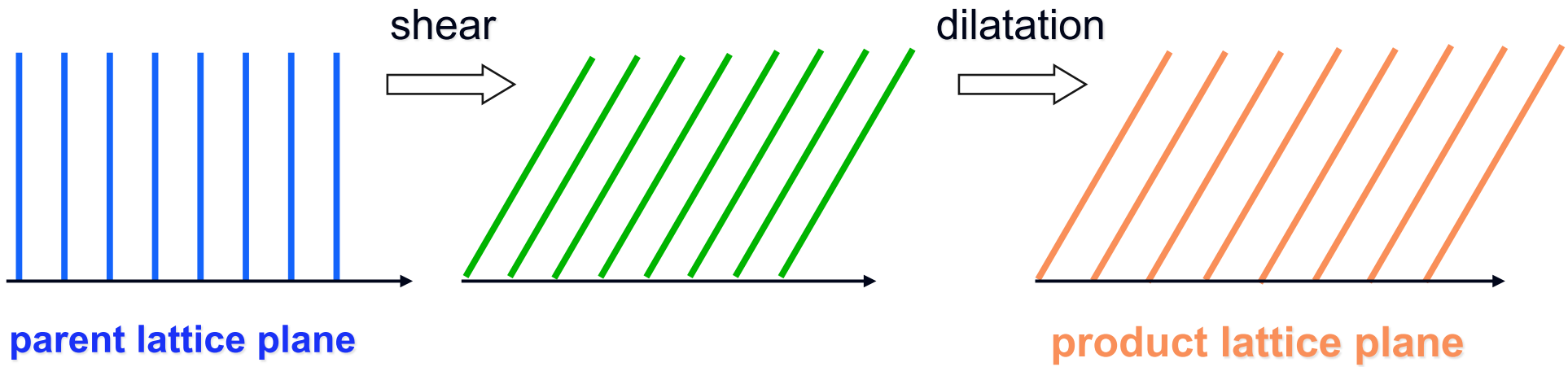

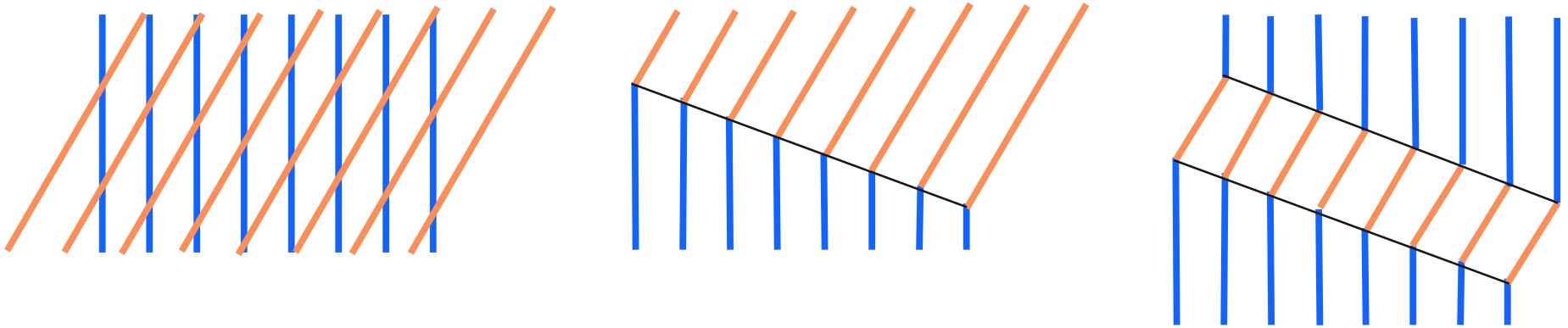

planar interface is parallel to moire plane

J.F. Nie *Acta Mater.* 2004

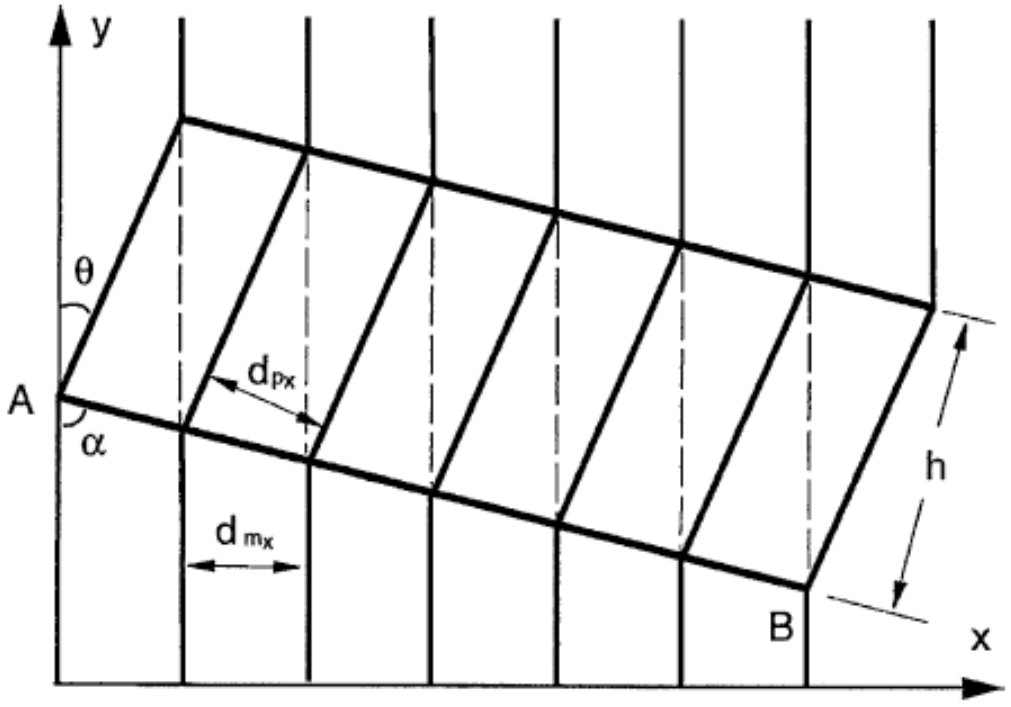

$$\sin\alpha = \frac{d_{m_x}\sin\theta}{\sqrt{d_{m_x}^2 + d_{p_x}^2 - 2d_{m_x}d_{p_x}\cos\theta}} = \frac{s}{\sqrt{s^2 + (\varepsilon_x - 1)^2}}$$

J.F. Nie
Acta Mater. 2004

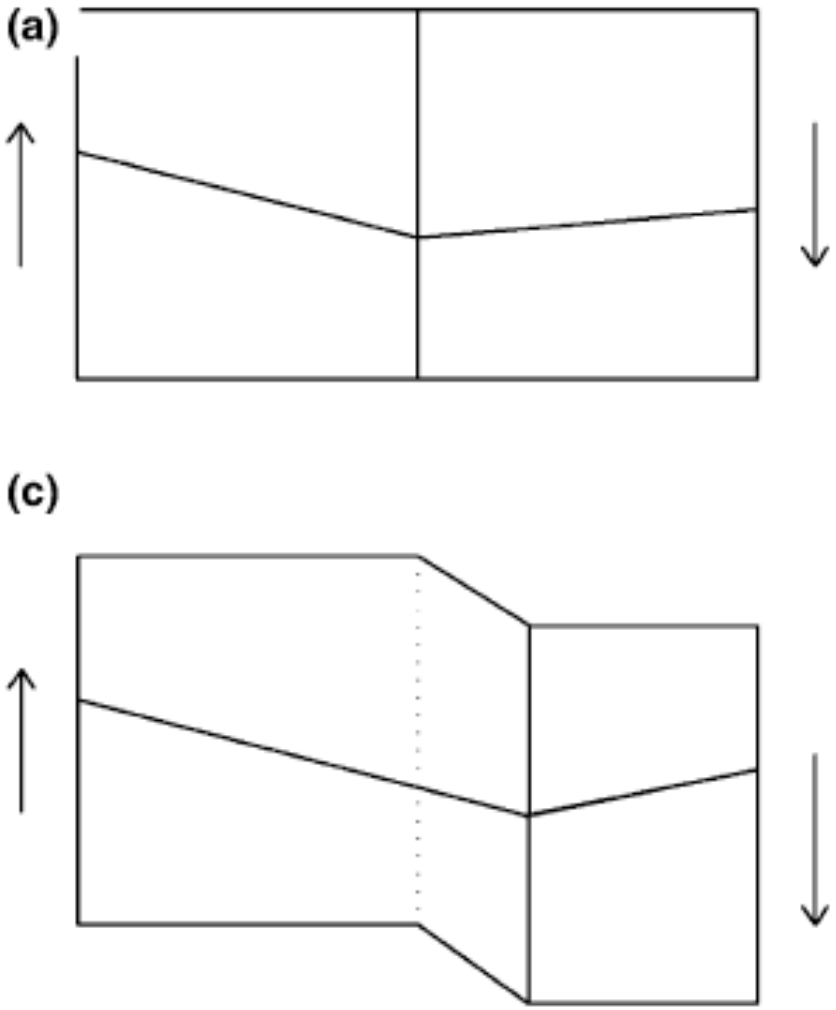

J.W. Cahn, J.E. Taylor
Acta Mater. 2004

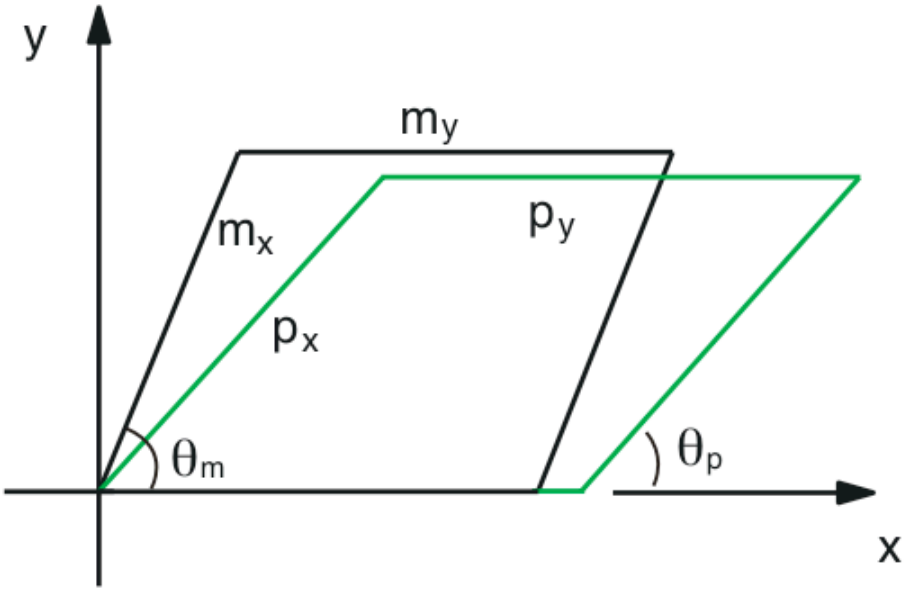

Lattice Deformation Strain

$$s_1 = \frac{\eta_y}{tan\theta_p} - \frac{\eta_x}{tan\theta_m}$$

$$\eta_x = \frac{d_{px}}{d_{mx}} \frac{\sin\theta_m}{\sin\theta_p}$$

$$\eta_y = \frac{d_{py}}{d_{my}}$$

η_y

η_x

OR (φ)
HP (α)

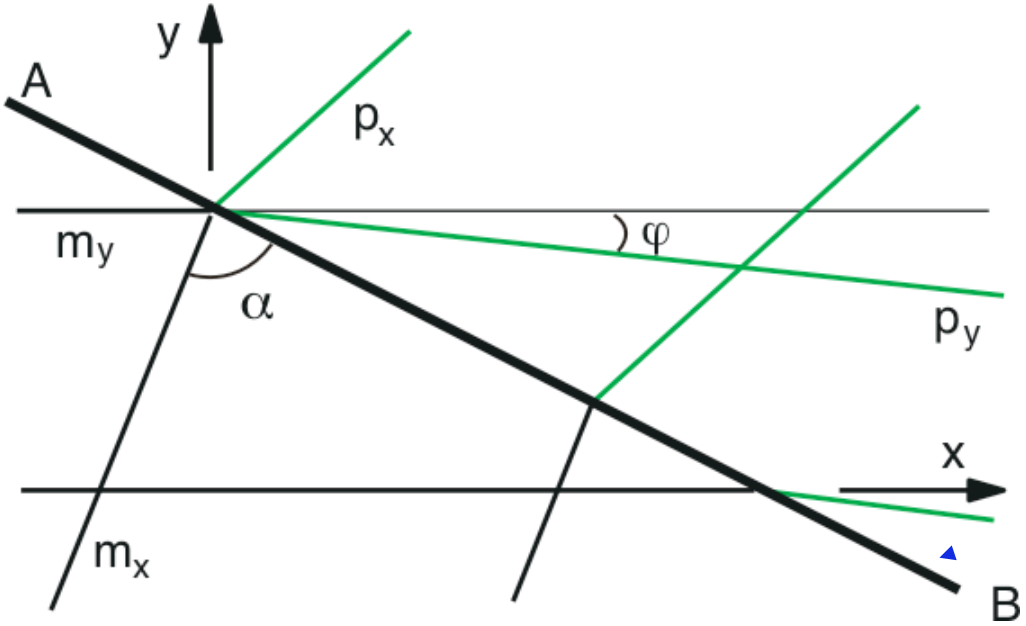

habit plane

J.F. Nie
Acta Mater. 2004

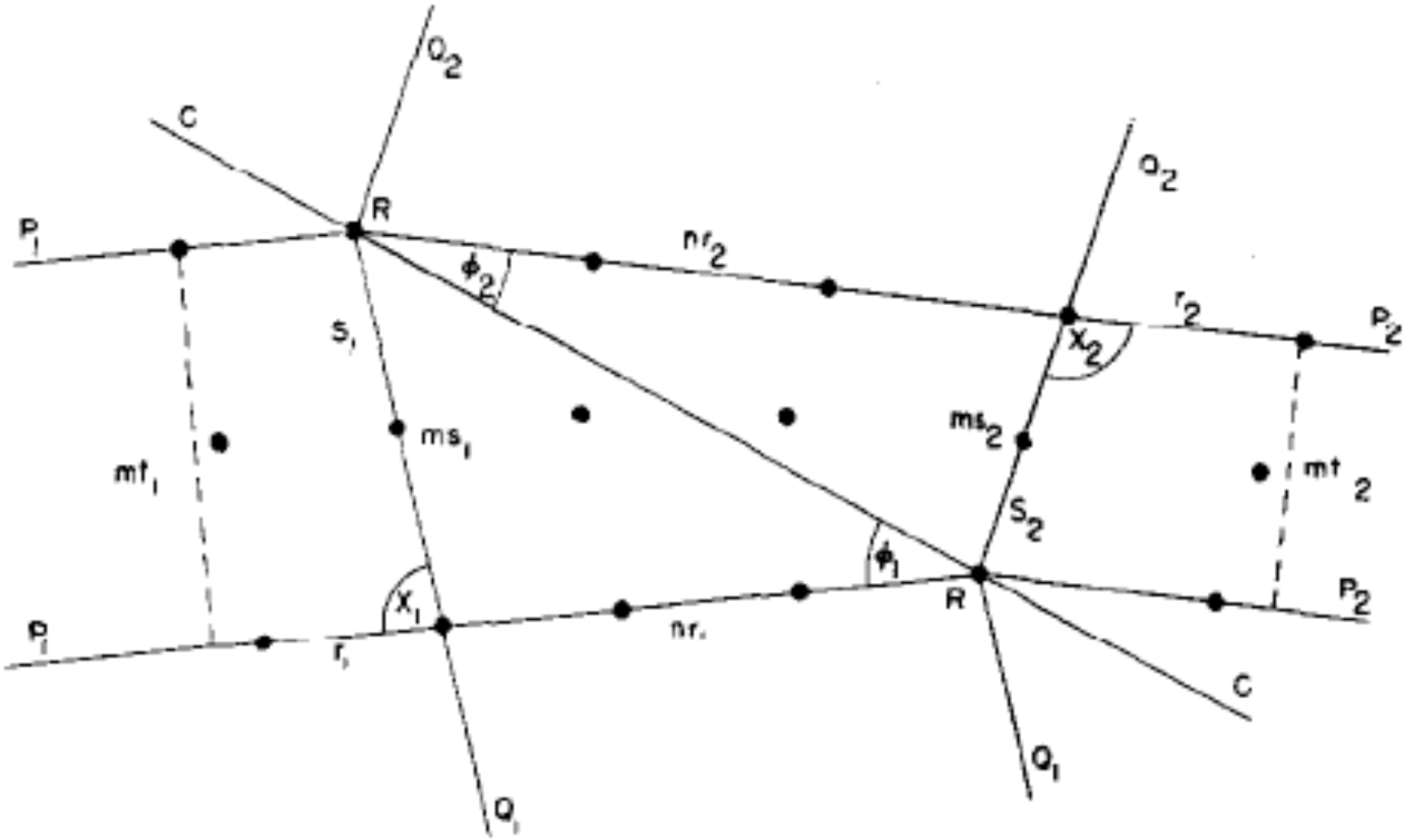

MARTENSITE*

F. C. FRANK†

*Received August 5, 1952.

†The H. H. Wills Physical Laboratory, University of Bristol, England.

ACTA METALLURGICA, VOL. 1, JAN. 1953

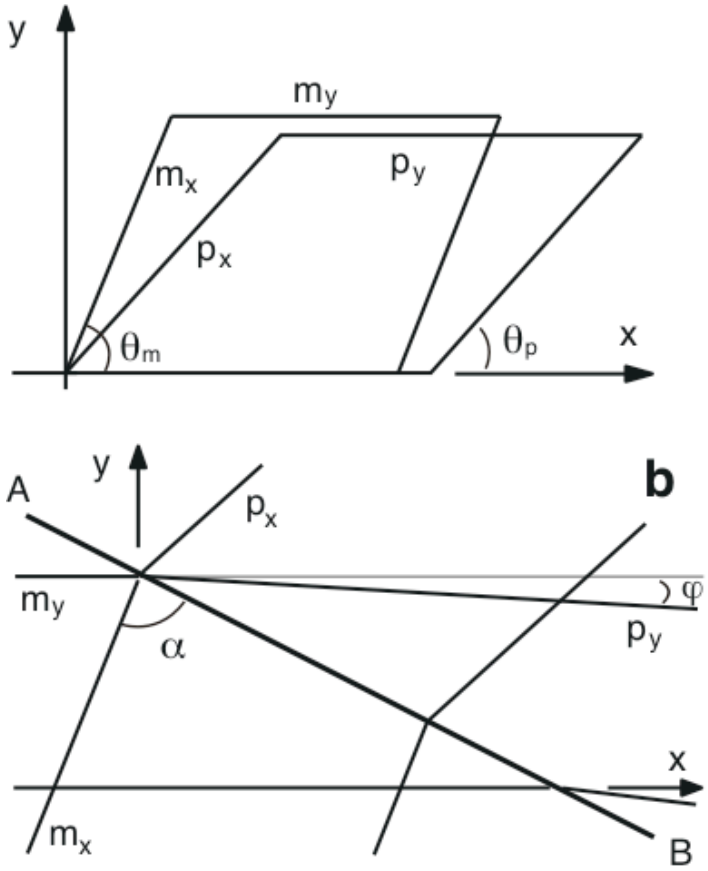

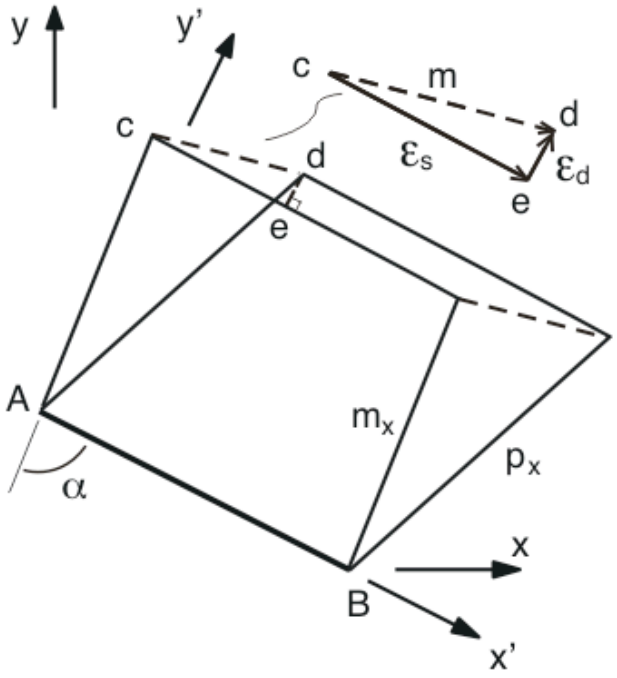

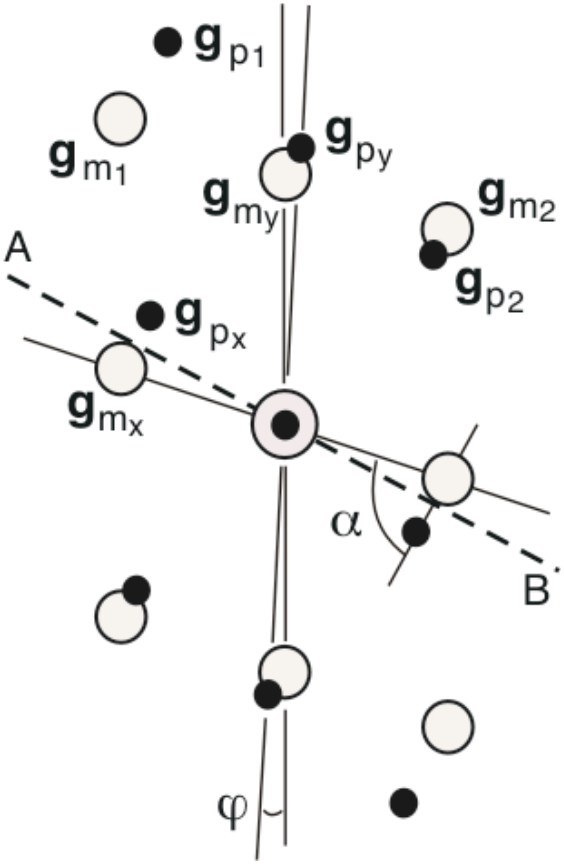

Input Data: $\mathbf{g}_{mx}$, $\mathbf{g}_{my}$, $\mathbf{g}_{px}$, $\mathbf{g}_{py}$, θ_m, θ_p

Output: α (or β), φ, lattice deformation strains, shape strain

J.F. Nie, *Acta Mater*. 2008

$s_i > 0$	$\eta_y < 1$	$\eta_y = 1$	$\eta_y > 1$
$\eta_x < 1$	**a** 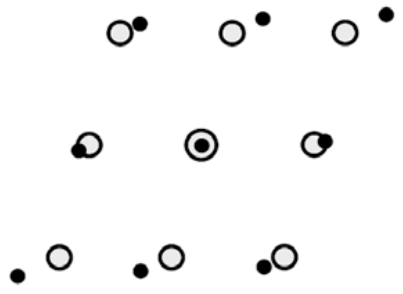	**b** 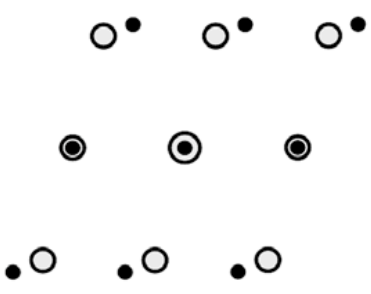	**c** 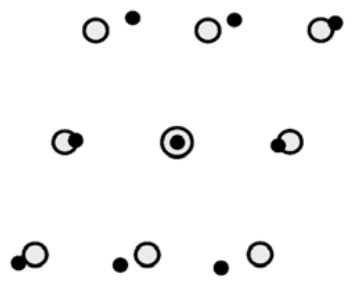
$\eta_x = 1$	**d** 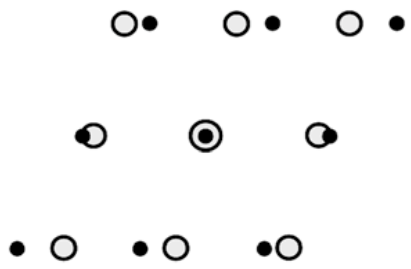	**e** 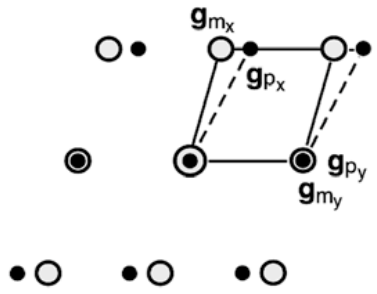	**f** 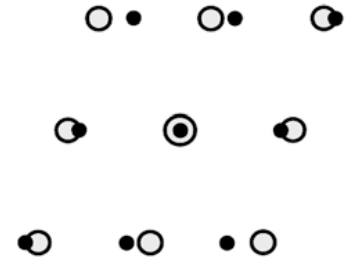
$\eta_x > 1$	**g** 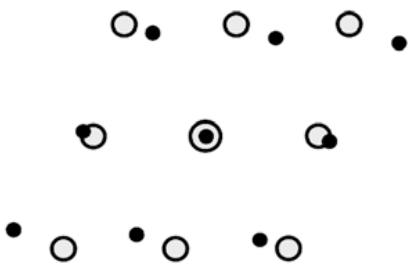	**h** 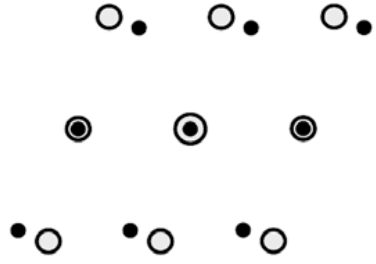	**i** 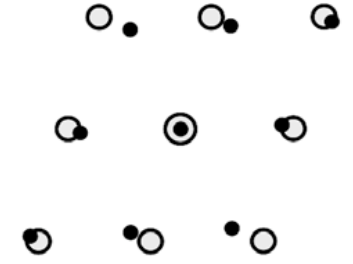

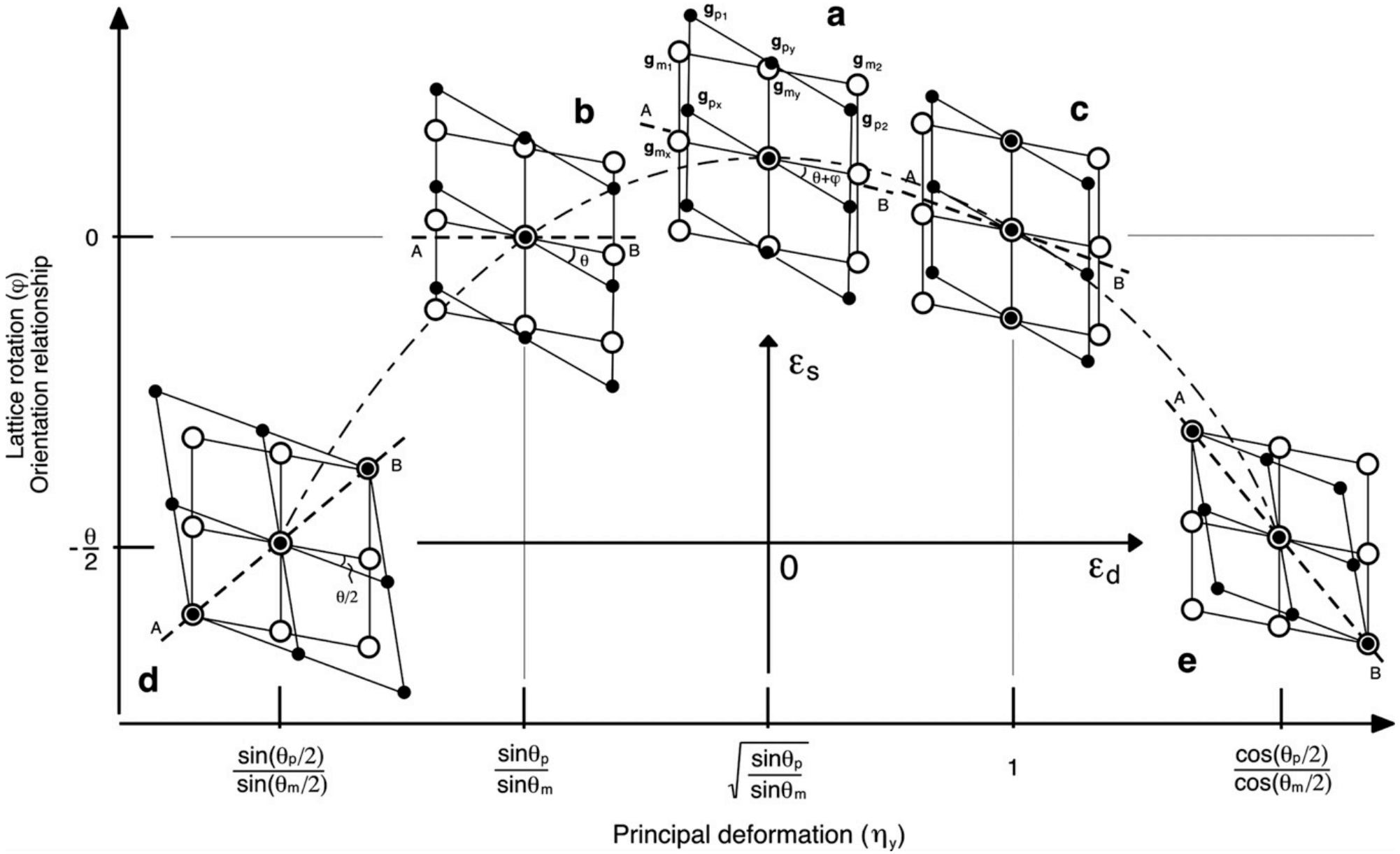

J.F. Nie, *Acta Mater*. 2008

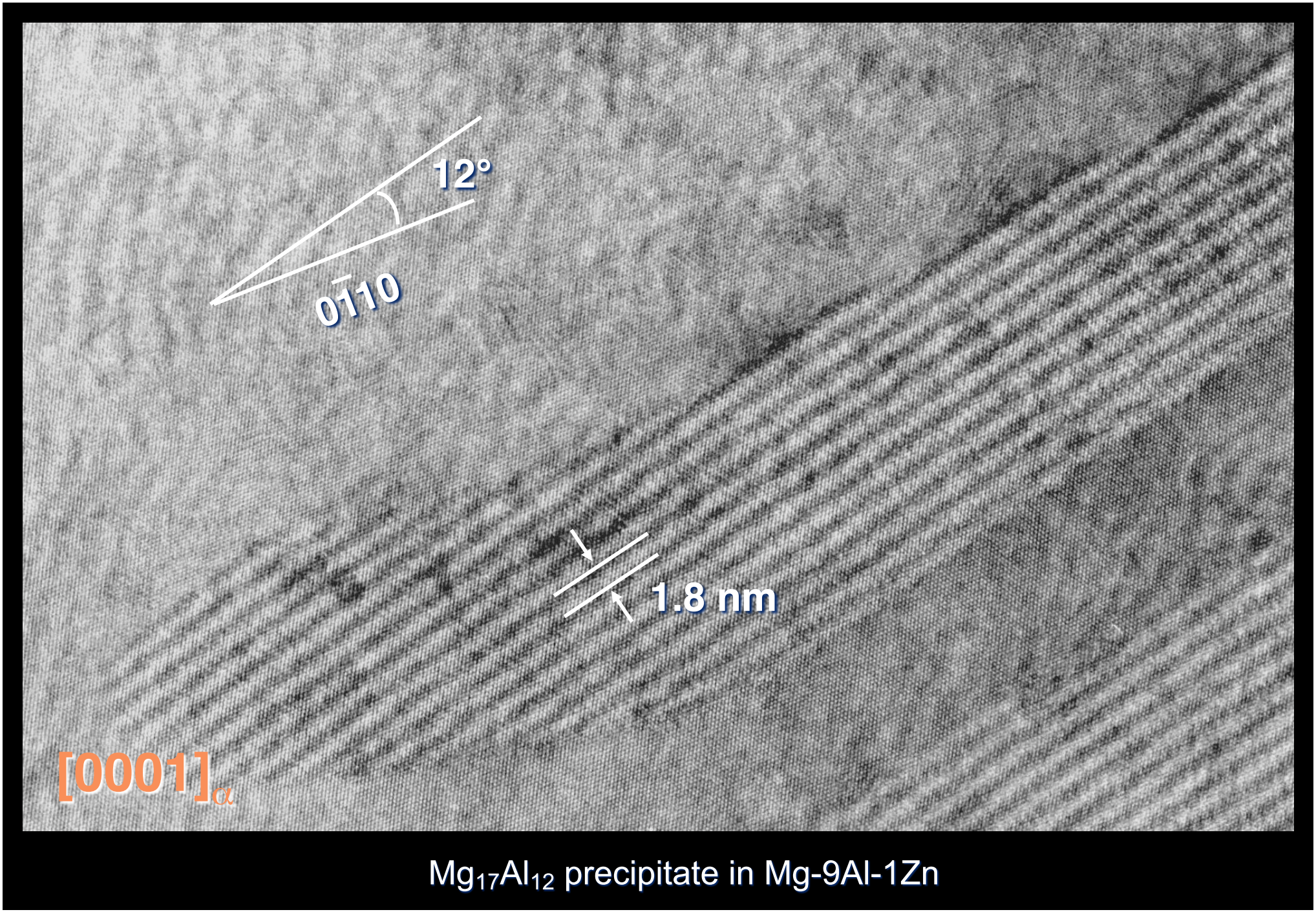

$Mg_{17}Al_{12}$ precipitate in Mg-9Al-1Zn

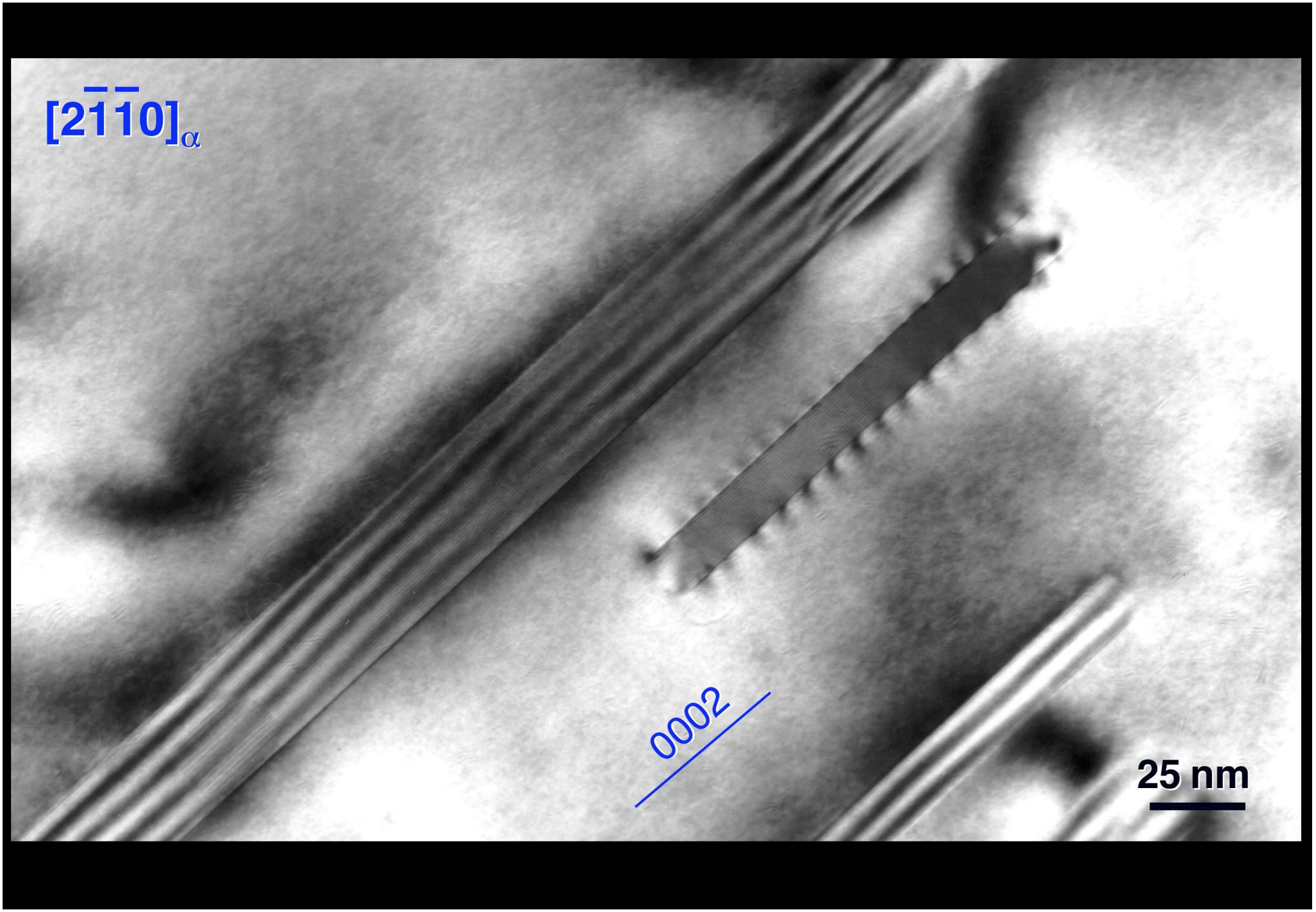
$[2\bar{1}\bar{1}0]_\alpha$
0002
25 nm

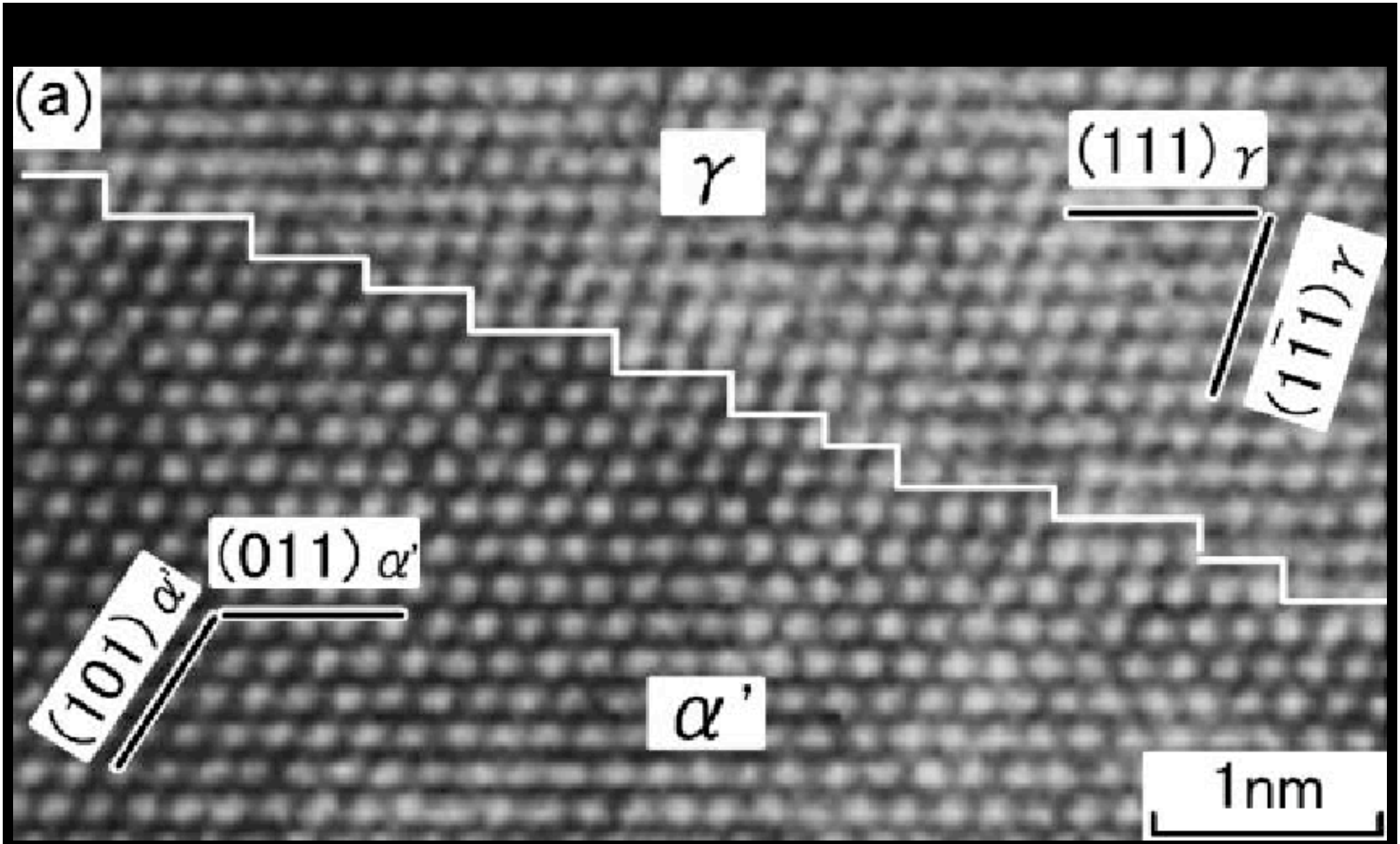

Lath Martensite in Fe-20.2Ni-5.4Mn

T. Moritani, N. Miyajima, T. Furuhara and T. Maki, Scripta Mater. 2002

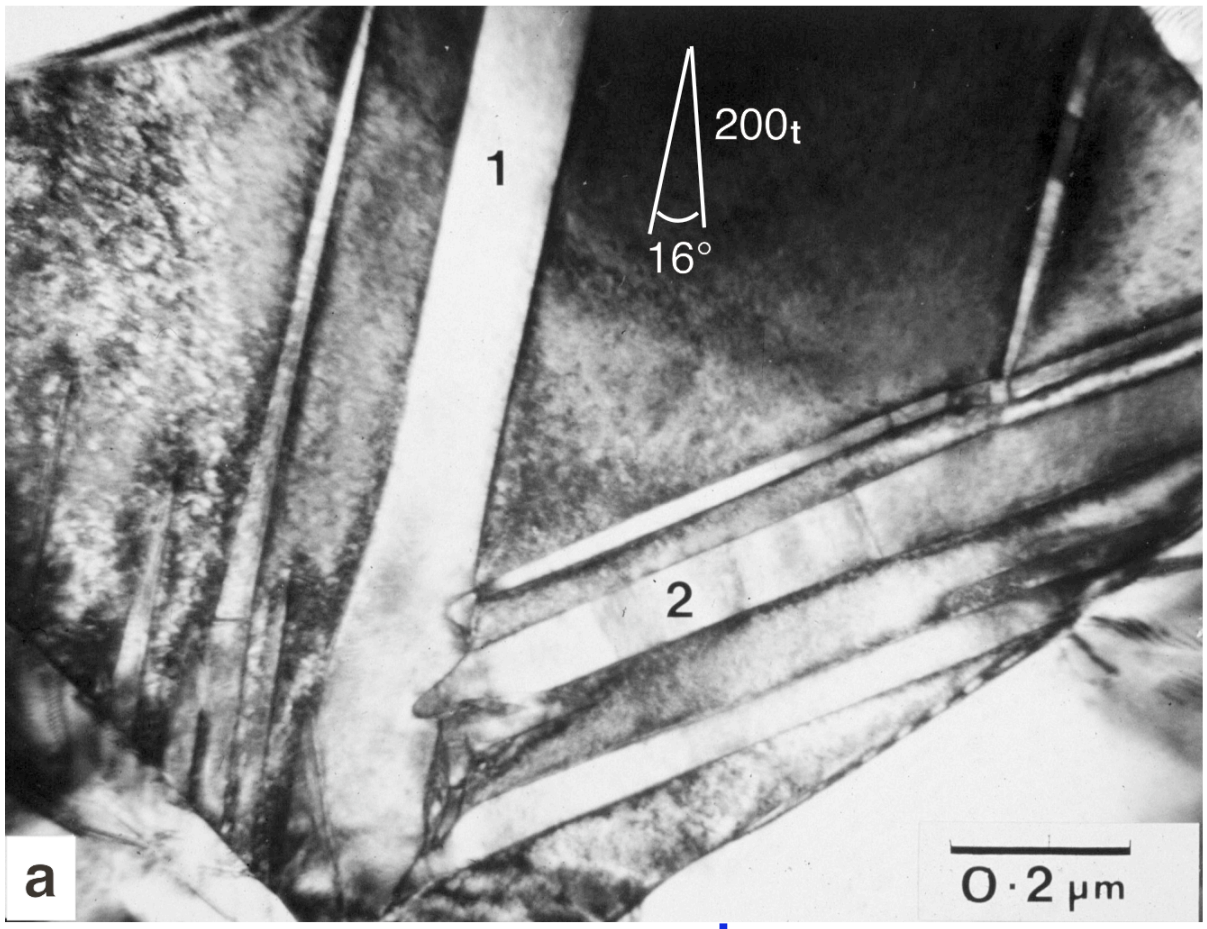

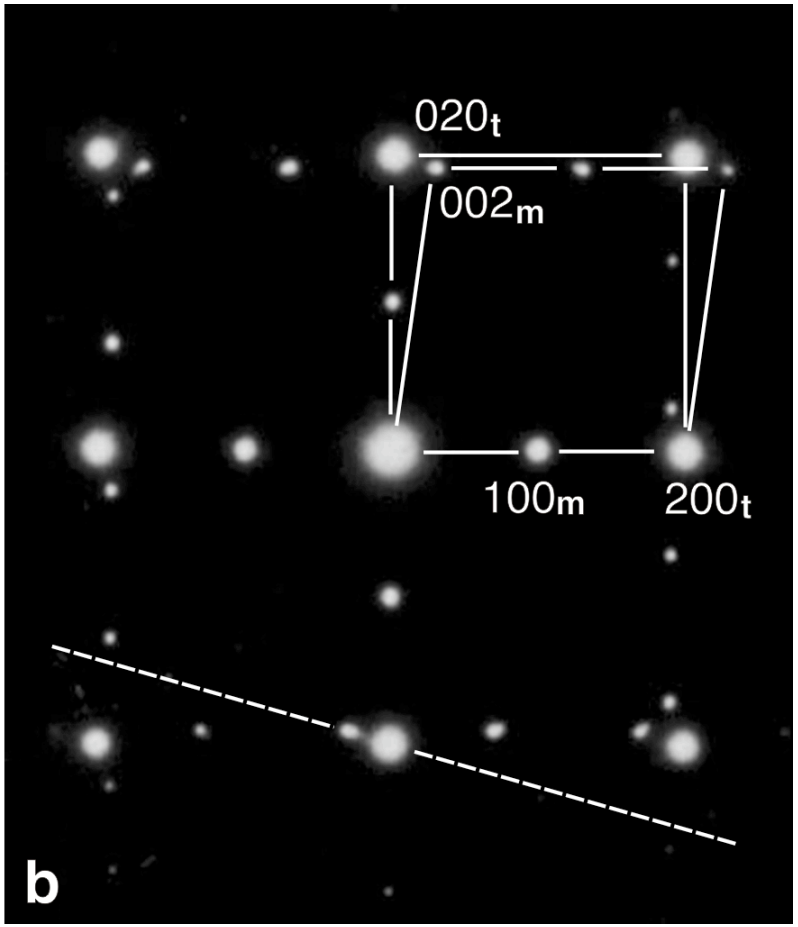

Input

ratio of $g_{(002)m}/g_{(002)t}$

$g_{(200)m}/g_{(200)t}$, θ_m, θ_p

Output

$\varphi = 0°$ $(200)_m$ // $(200)_t$, $[0\bar{1}0]_m$ // $[001]_t$

$\beta = 16.15°$

$\varepsilon_d = 0.0448$; $\varepsilon_s = 0.1548$

J.F. Nie, B.C. Muddle, *Mater. Sci. Eng.*, 2006

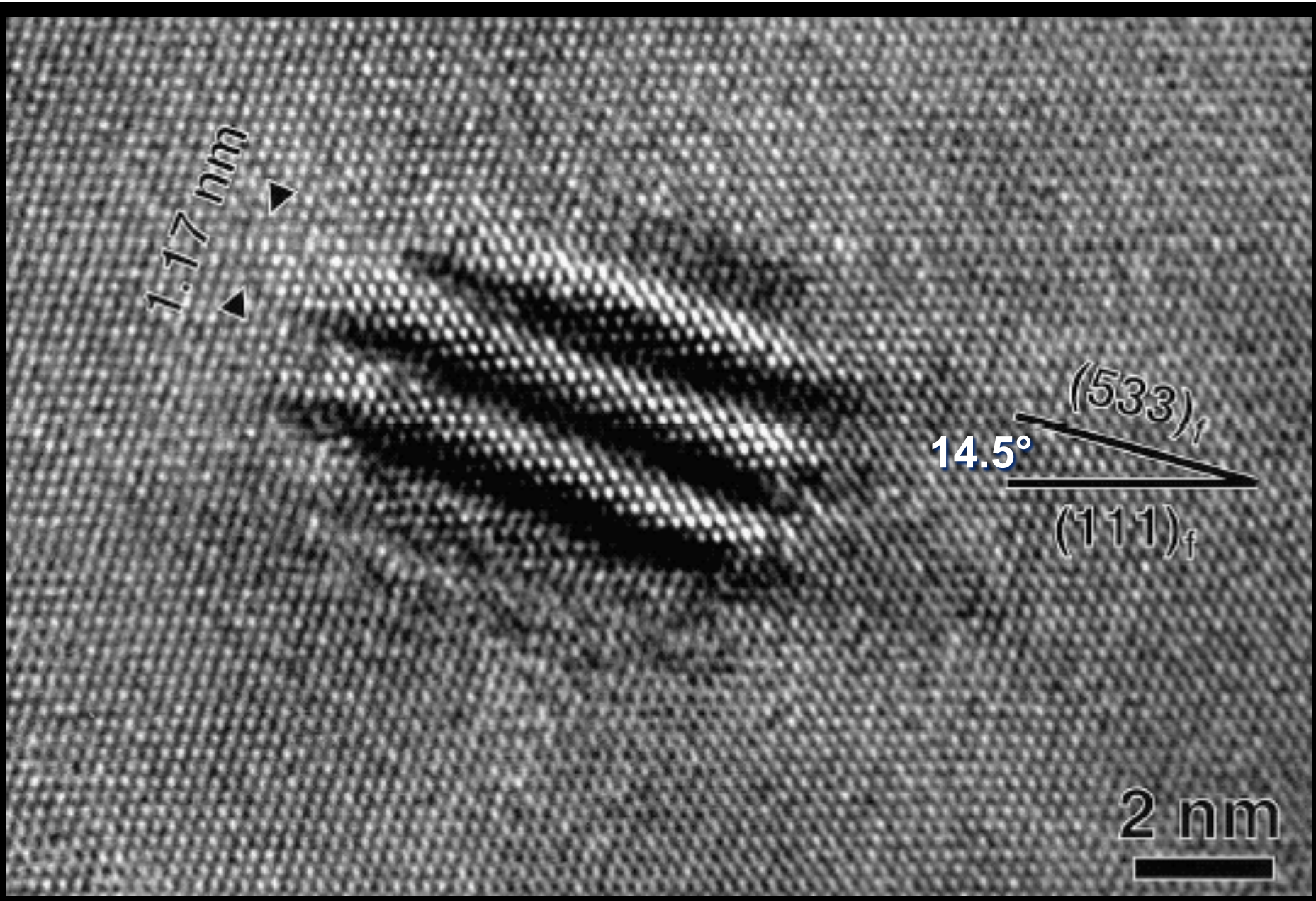

Cr Precipitate in Cu - K.S.

T. Fujii, H. Nakazawa, M. Kato and U. Dahmen, *Acta Mater.*, 2000

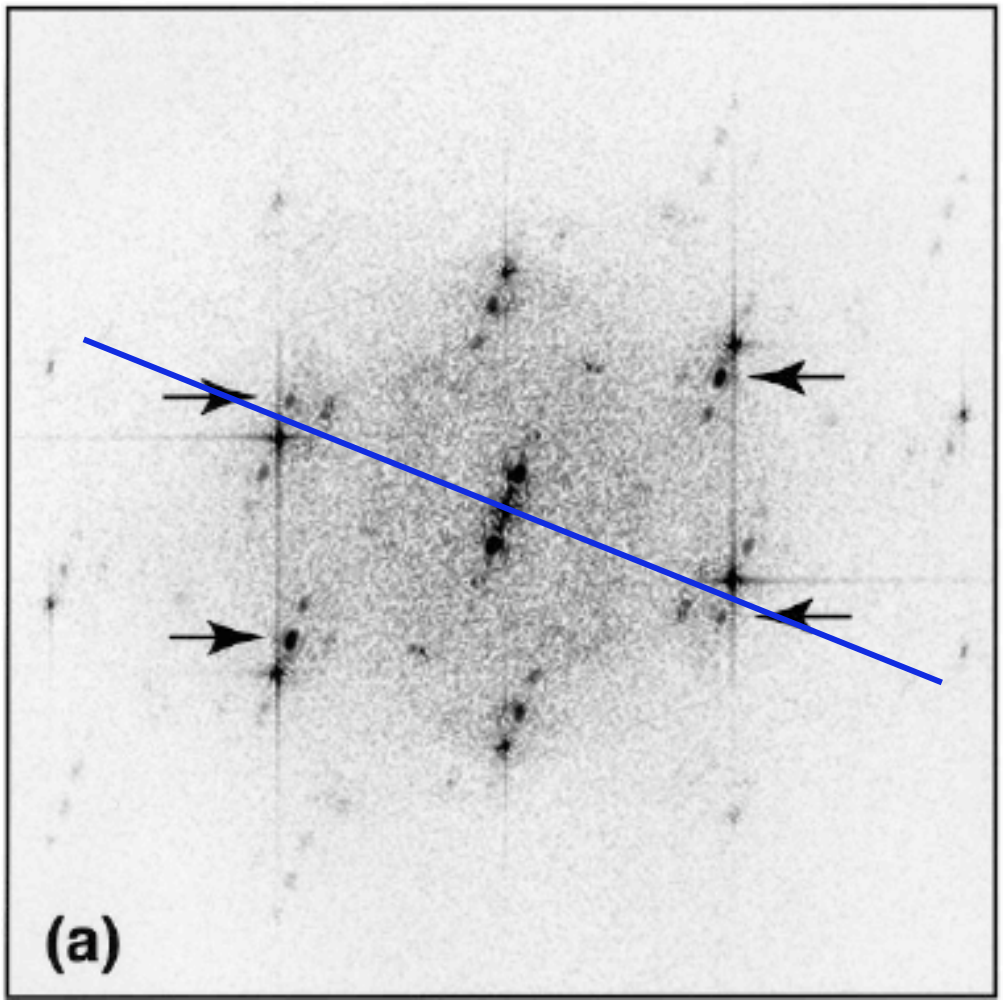

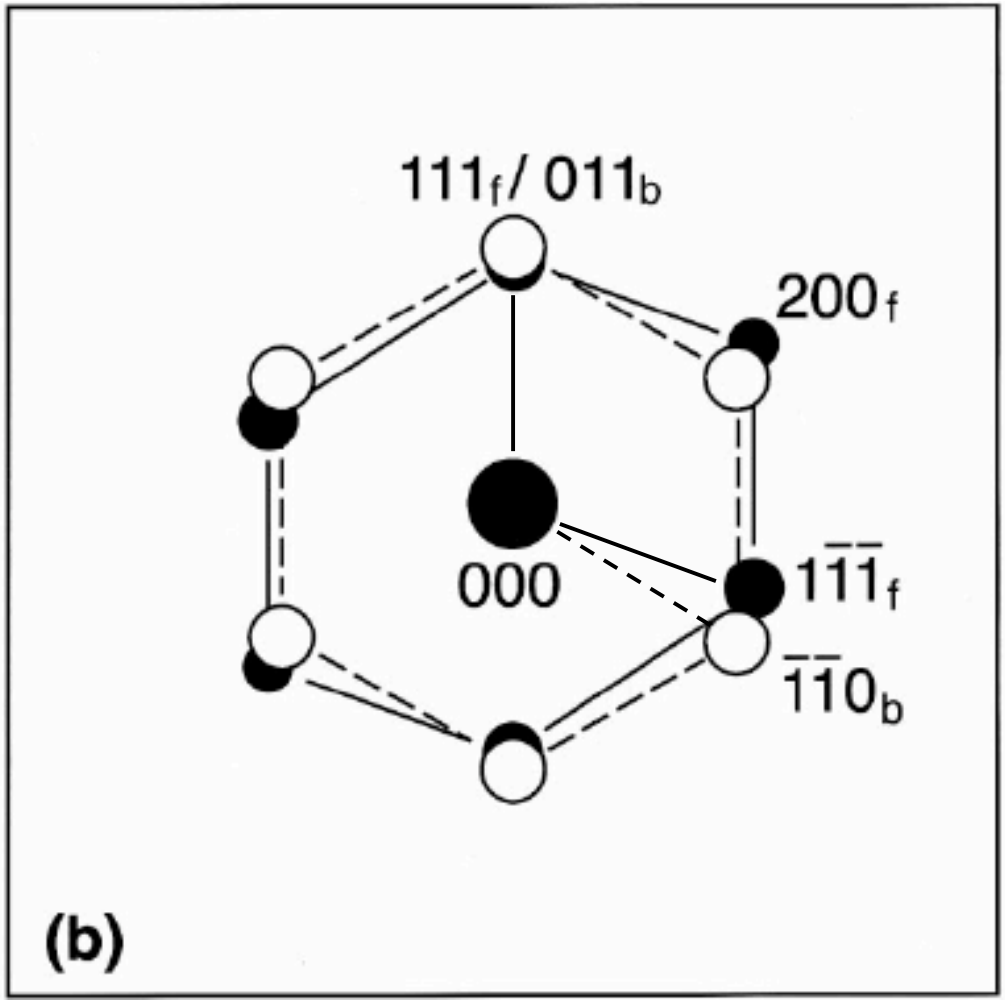

Input

ratio of $g_{(1\text{-}1\text{-}1)f}/g_{(\text{-}1\text{-}10)b}$

$g_{(111)f}/g_{(011)b}$, θ_m, θ_p

OR and HP

$(111)_f$ ~// $(011)_b$

$[\text{-}110]_f$ // $[1\text{-}11]_b$

φ = 0.52°

β= 14.49°

ε_d = 0.0133; ε_s = 0.2040

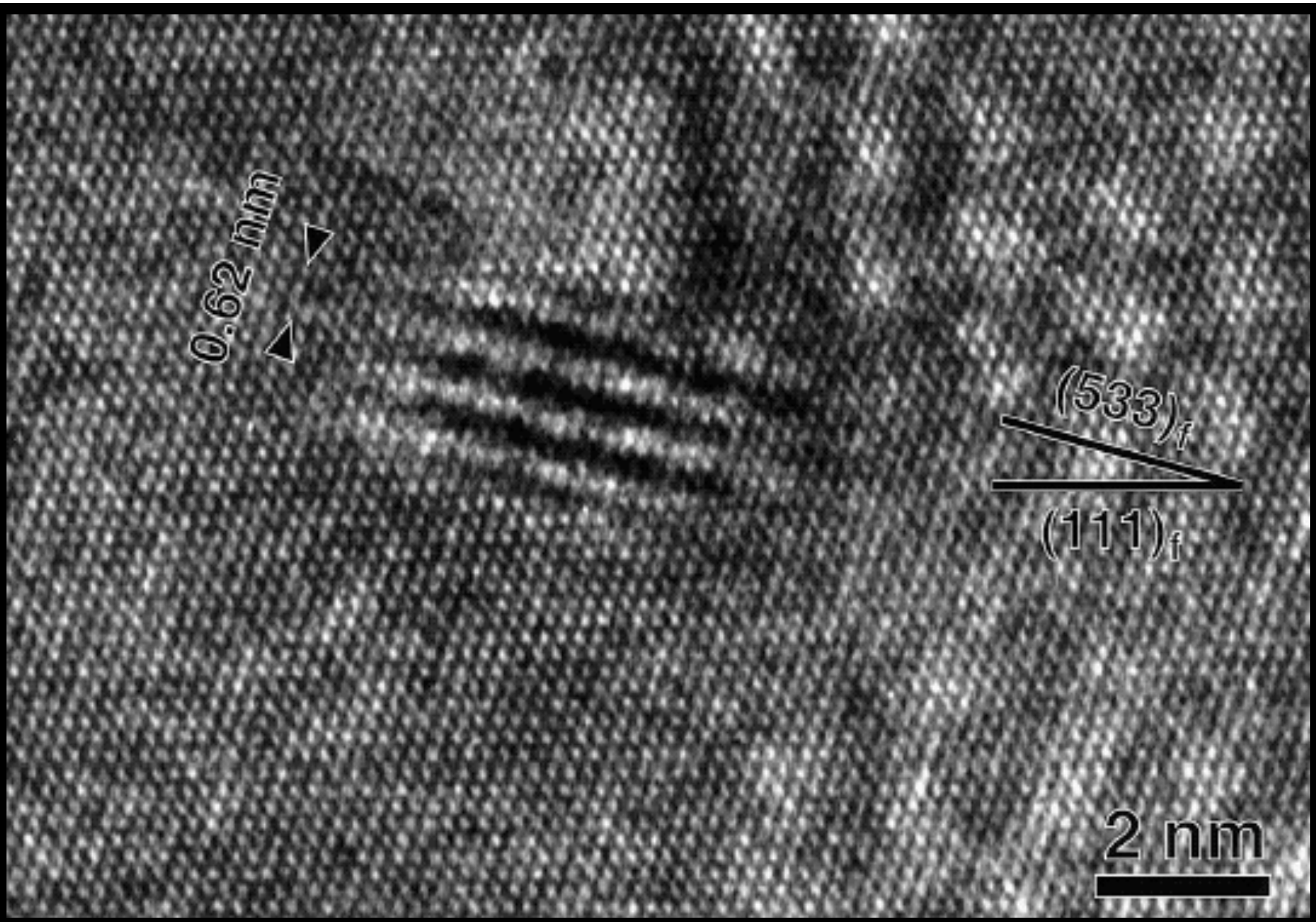

Cr Precipitate in Cu - N.W.

T. Fujii, H. Nakazawa, M. Kato and U. Dahmen, *Acta Mater*., 2000

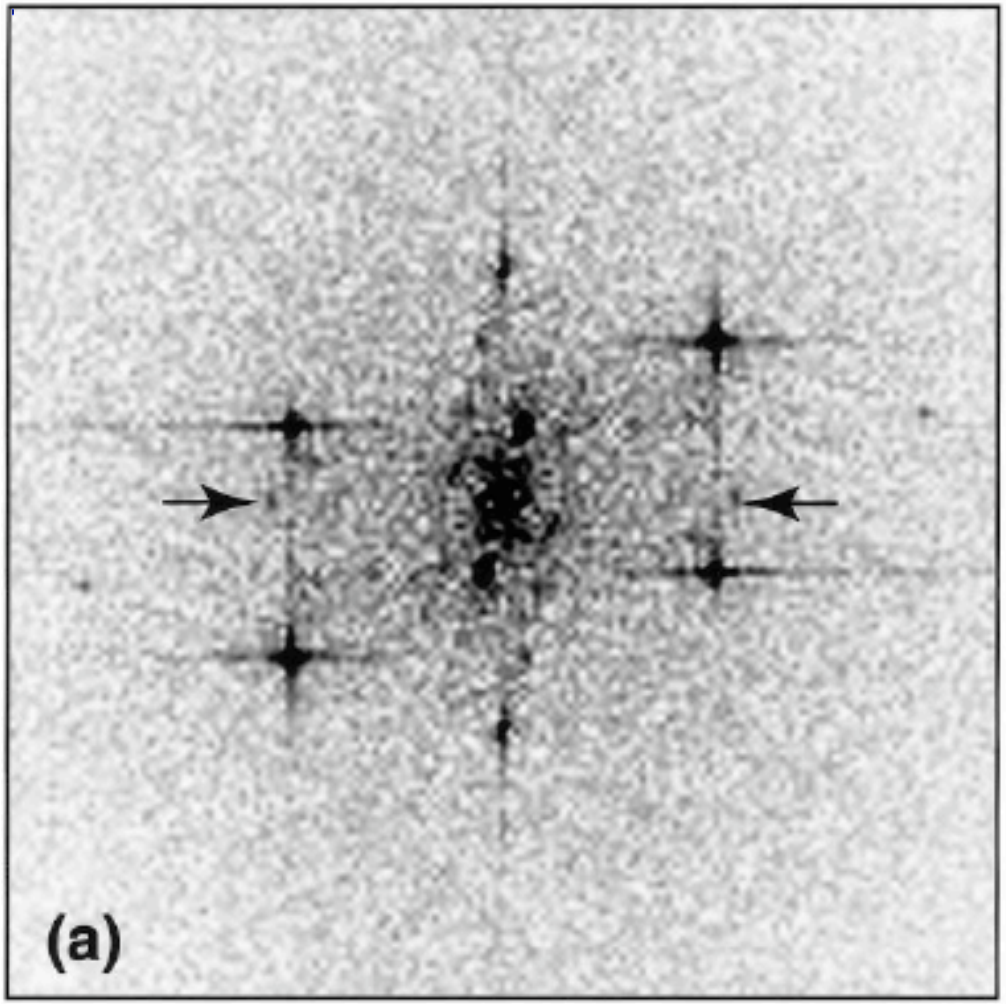

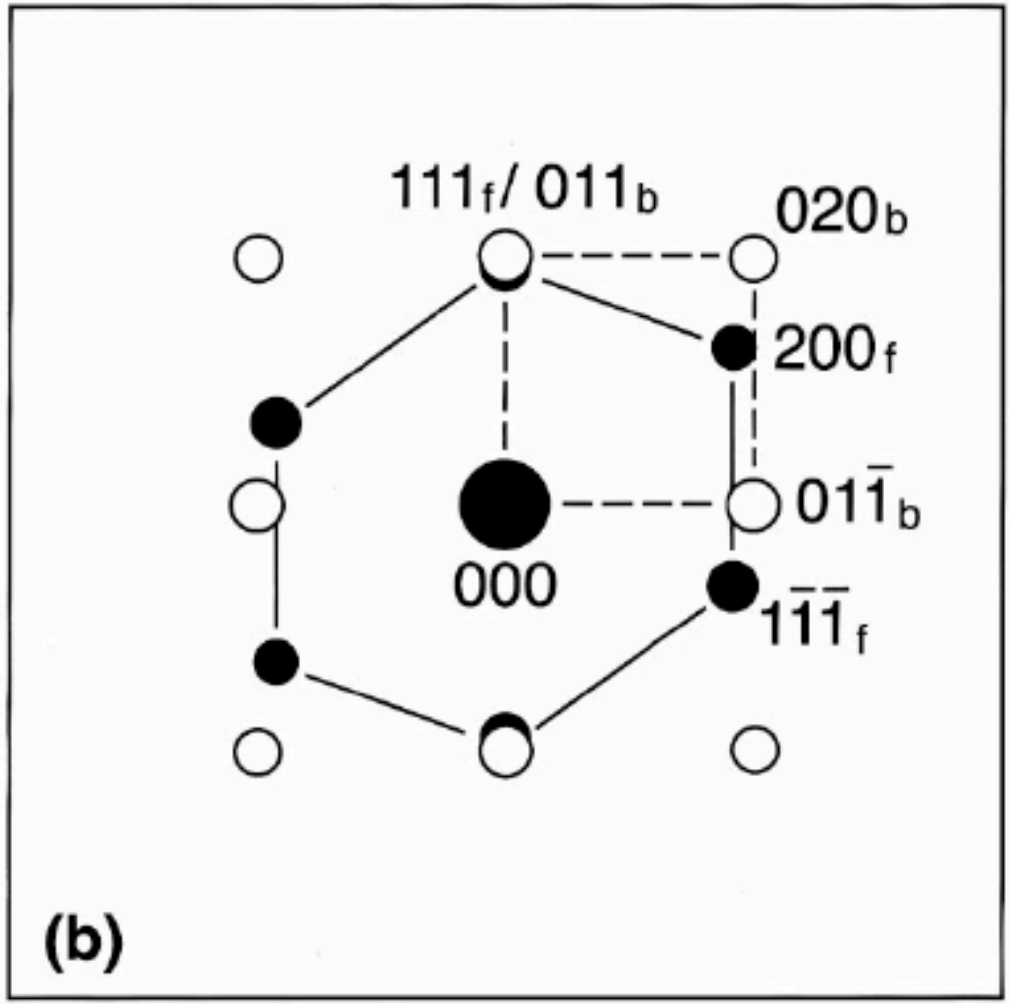

LDS

$$T = \begin{pmatrix} 1.092 & 0.365 \\ 0 & 1.030 \end{pmatrix}$$

OR and HP

φ = -0.44° $(111)_f$ ~// $(011)_b$

β= 14.50° $[011]_f$ // $[100]_b$

ε_d = 0.1246; ε_s = 0.3477

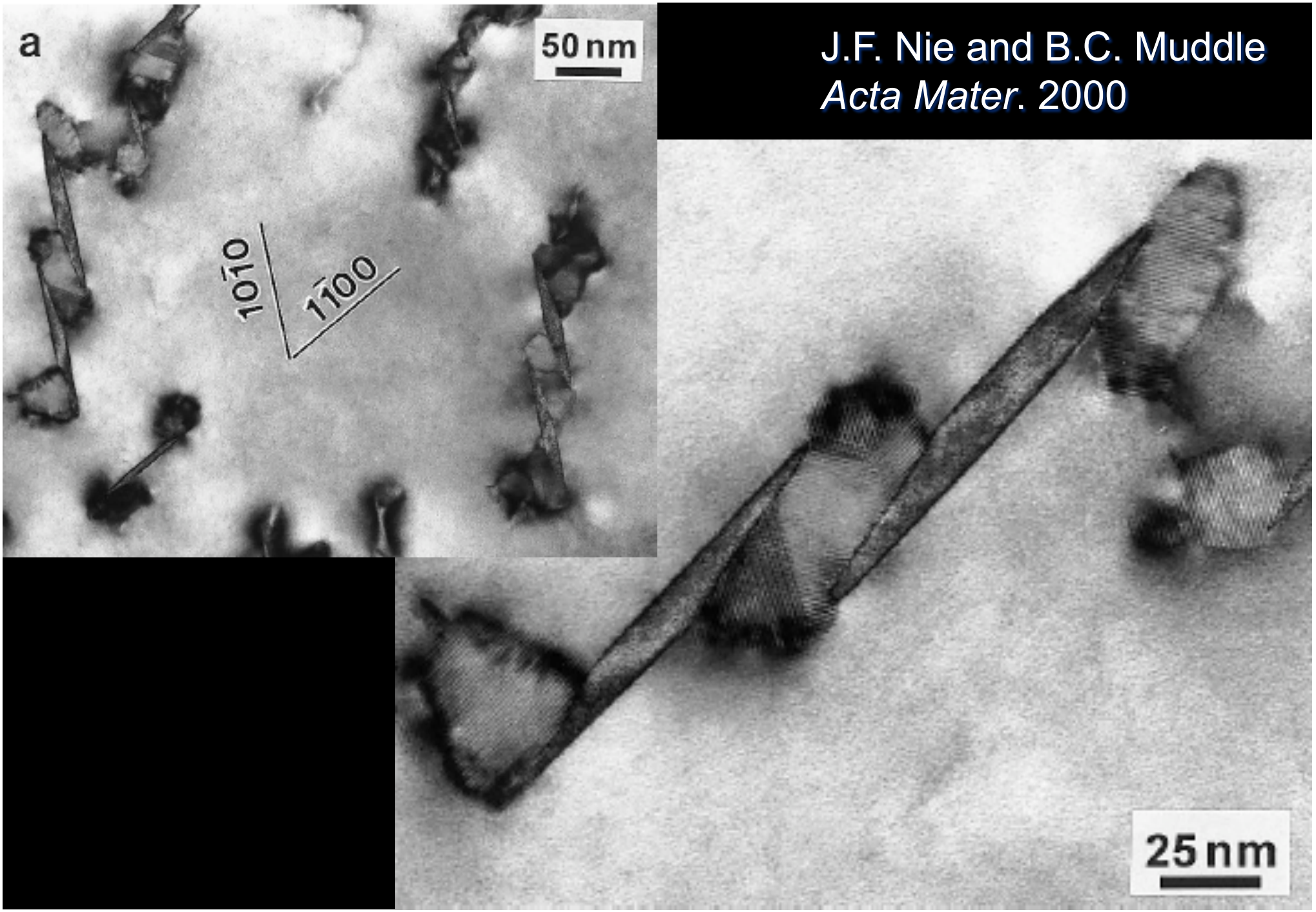
a
50 nm
$10\bar{1}0$
$1\bar{1}00$
J.F. Nie and B.C. Muddle
Acta Mater. 2000
25 nm

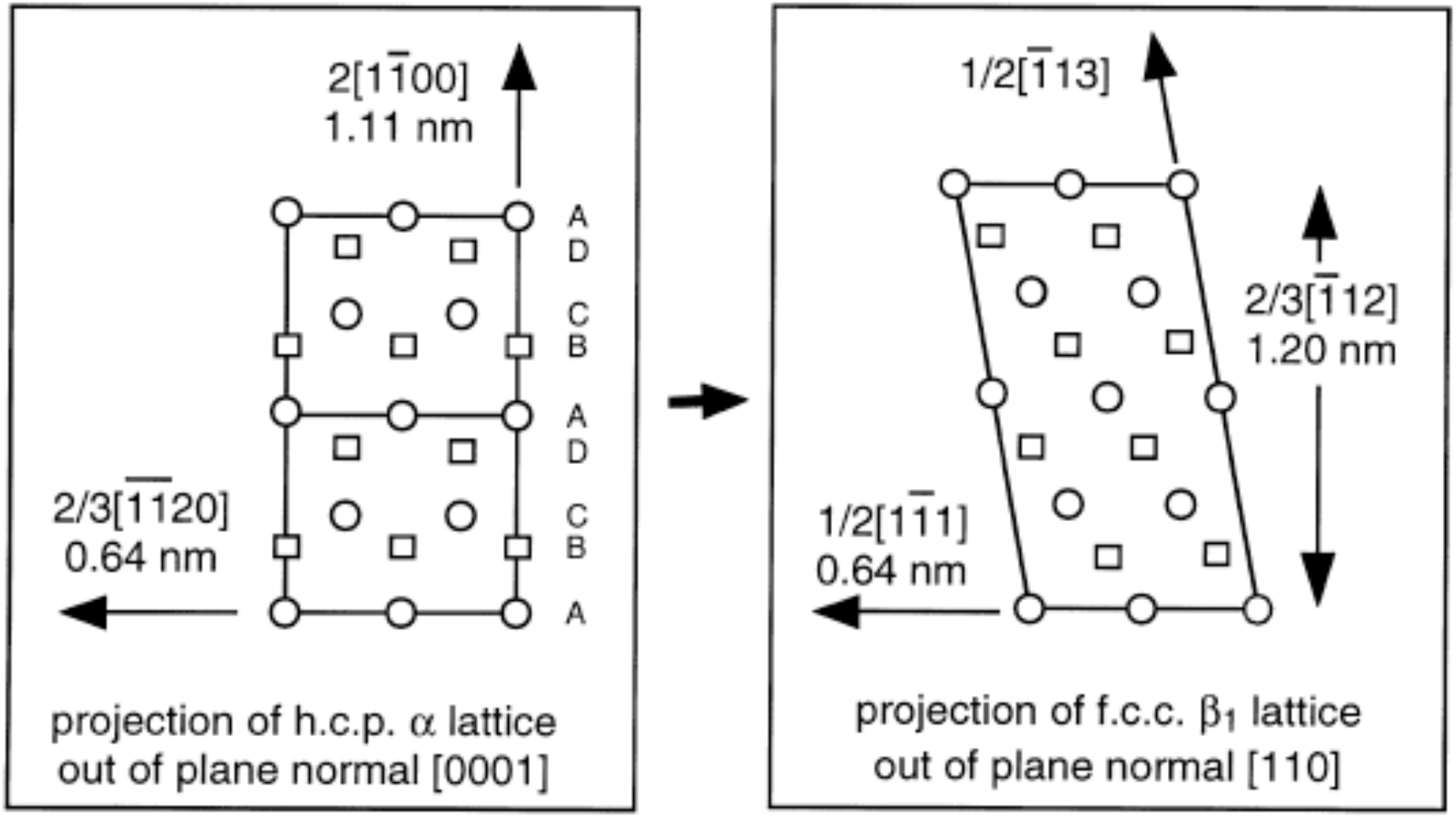

Output: $\varphi = 0°, \beta = 0°$

$\varepsilon_d = 0.086; \varepsilon_s = 0.227$

J.F. Nie and B.C. Muddle
Acta Mater. 2000

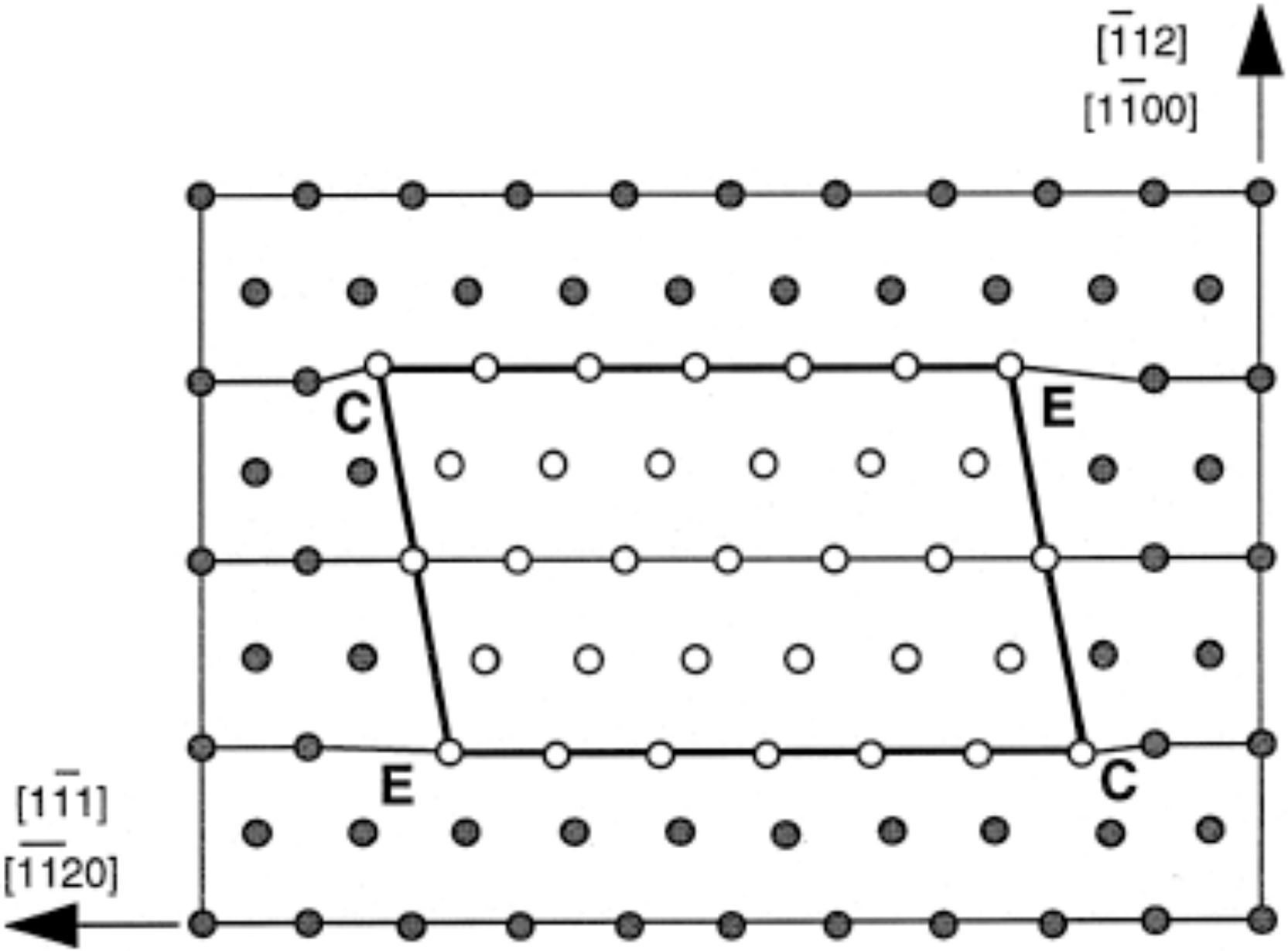
[$\bar{1}$12]
[1$\bar{1}$00]
C
E
E
C
[1$\bar{1}$1]
[$\bar{1}$120]

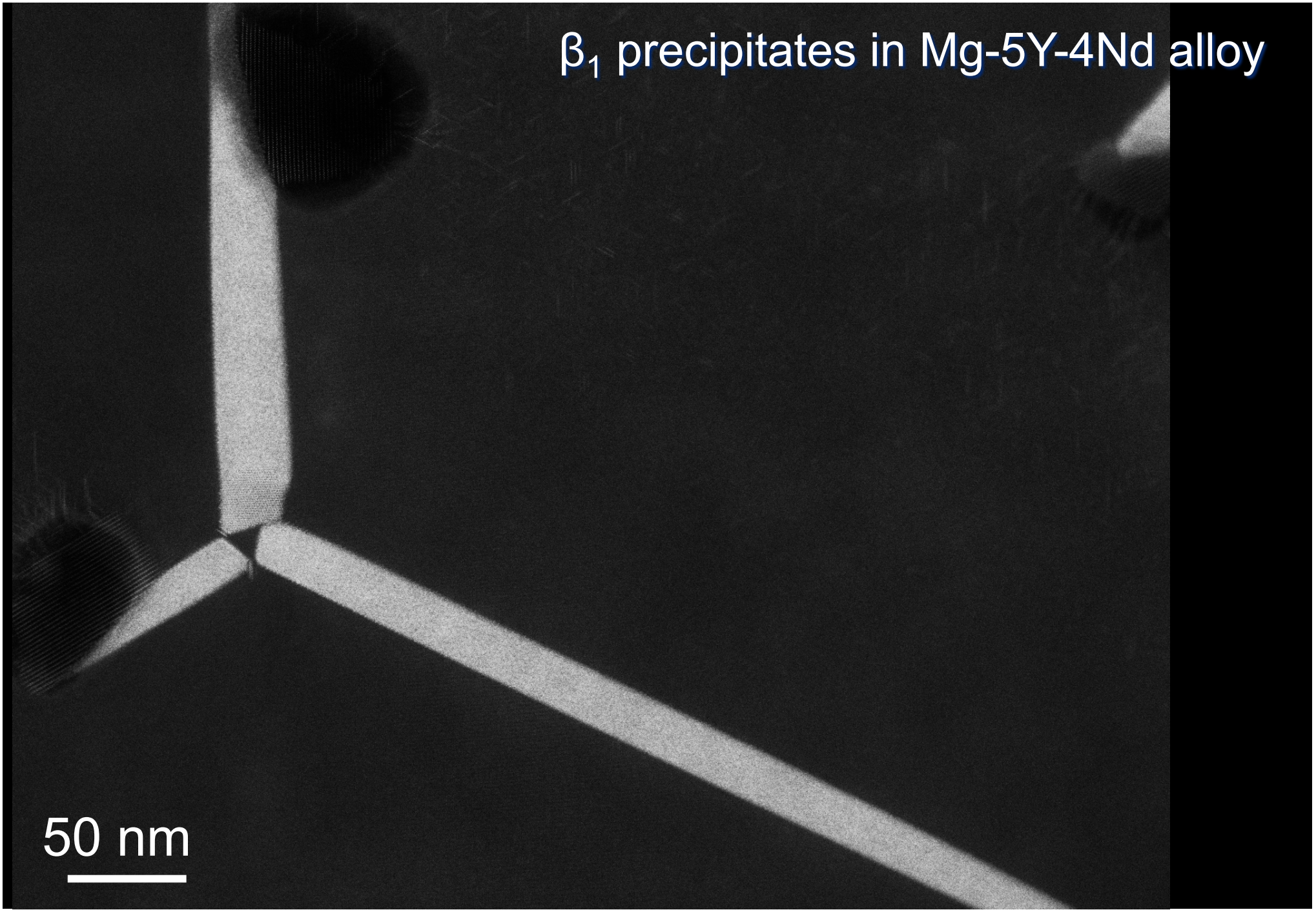
β_1 precipitates in Mg-5Y-4Nd alloy
50 nm

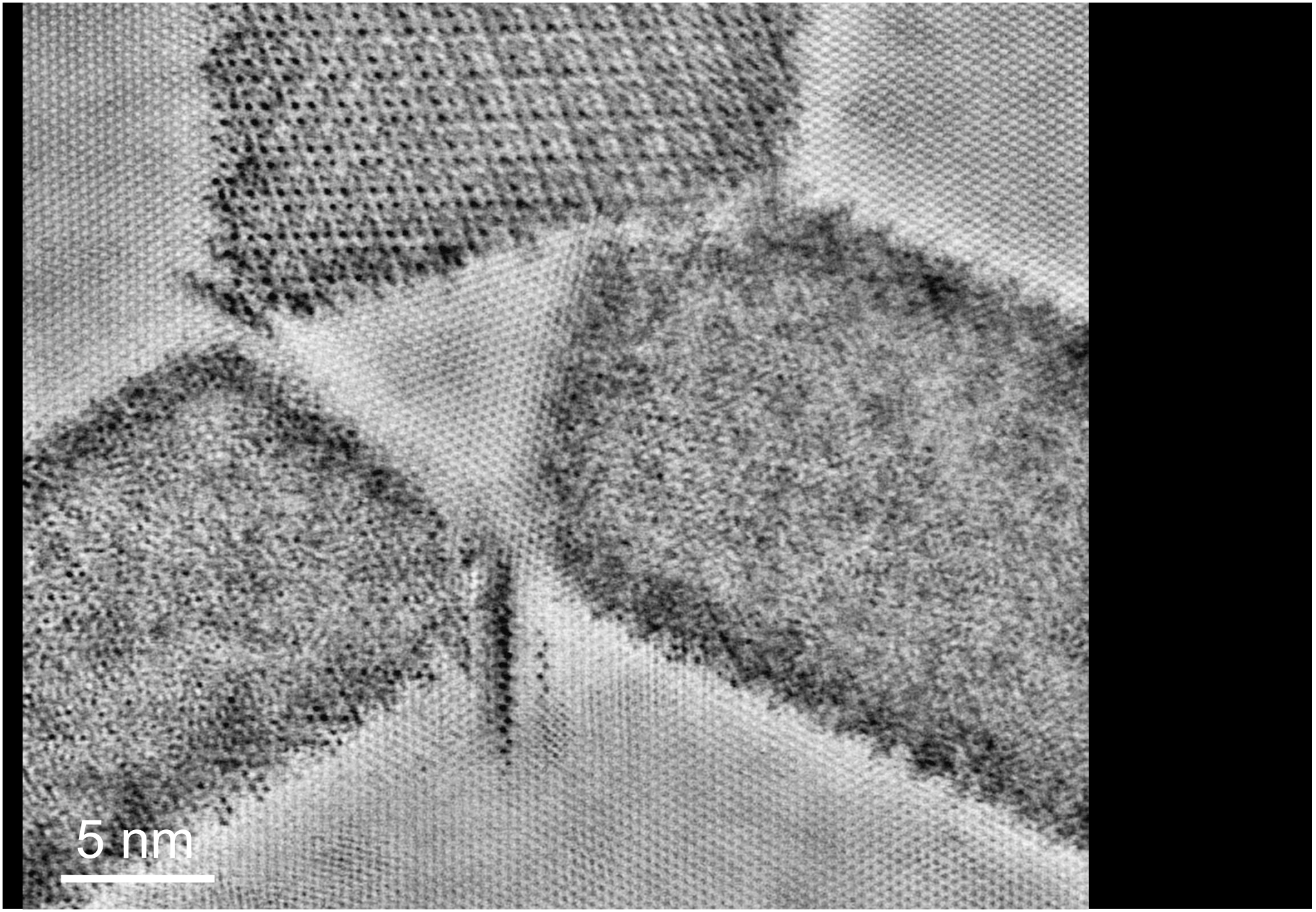
5 nm

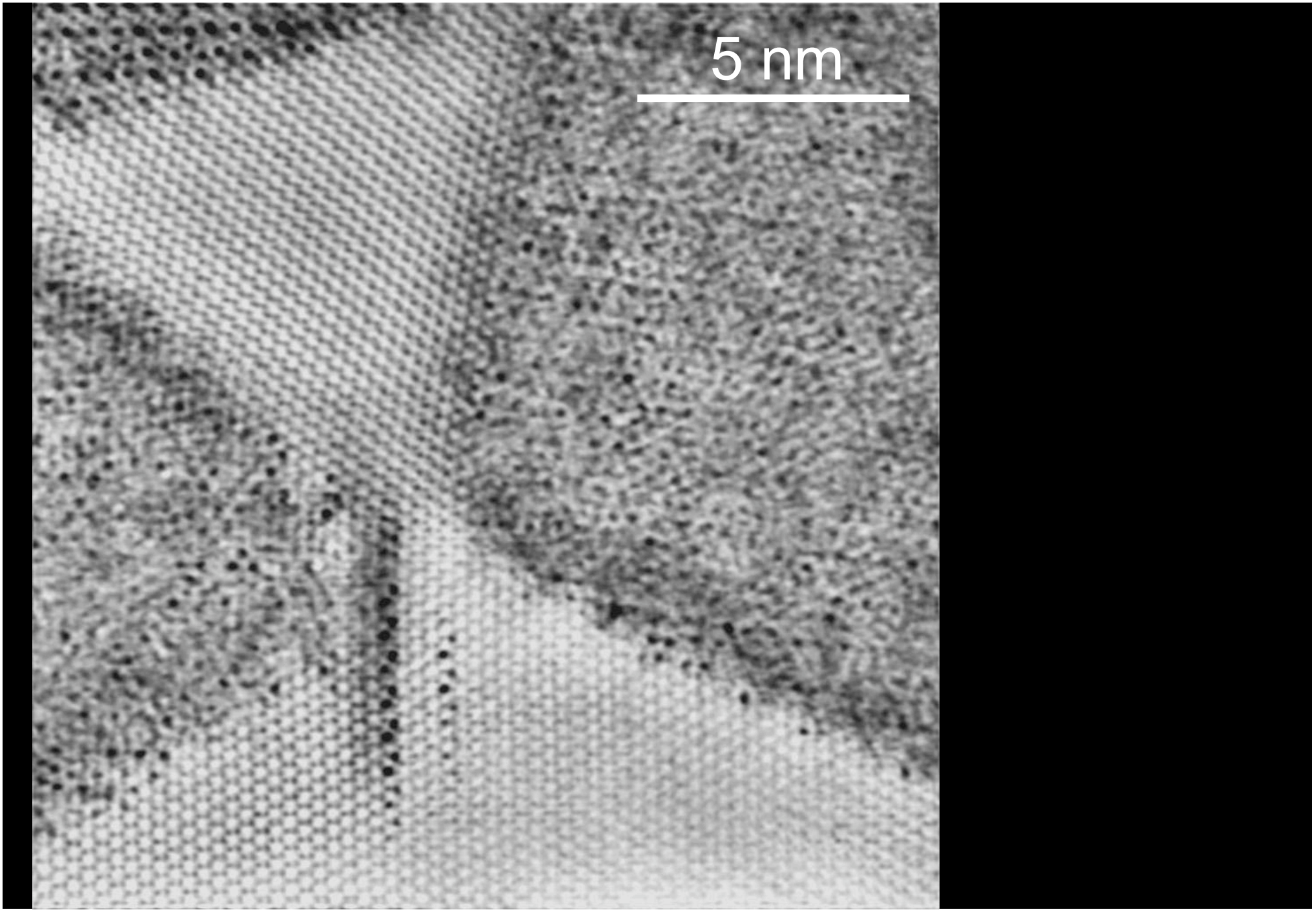
5 nm

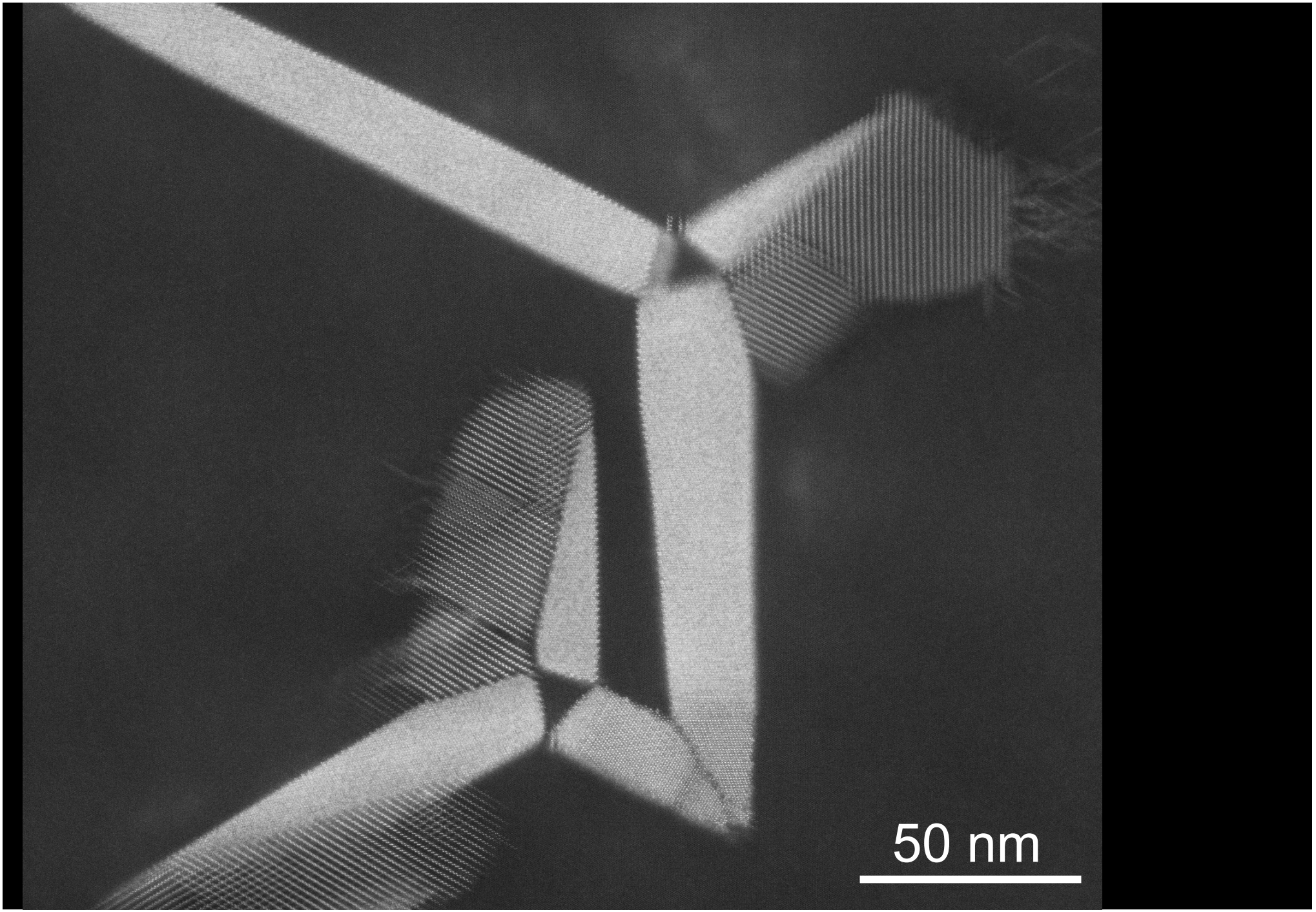
50 nm

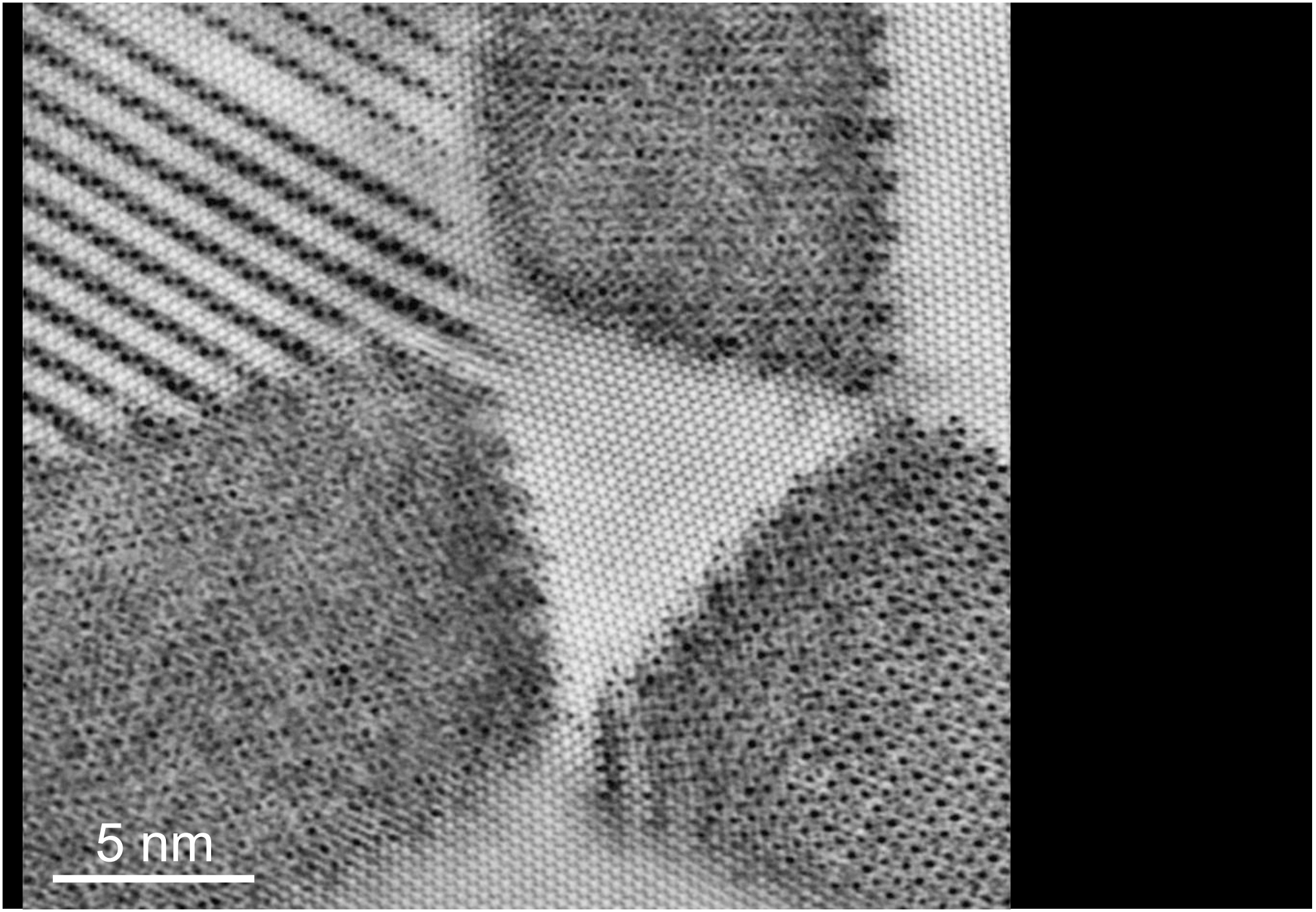
5 nm

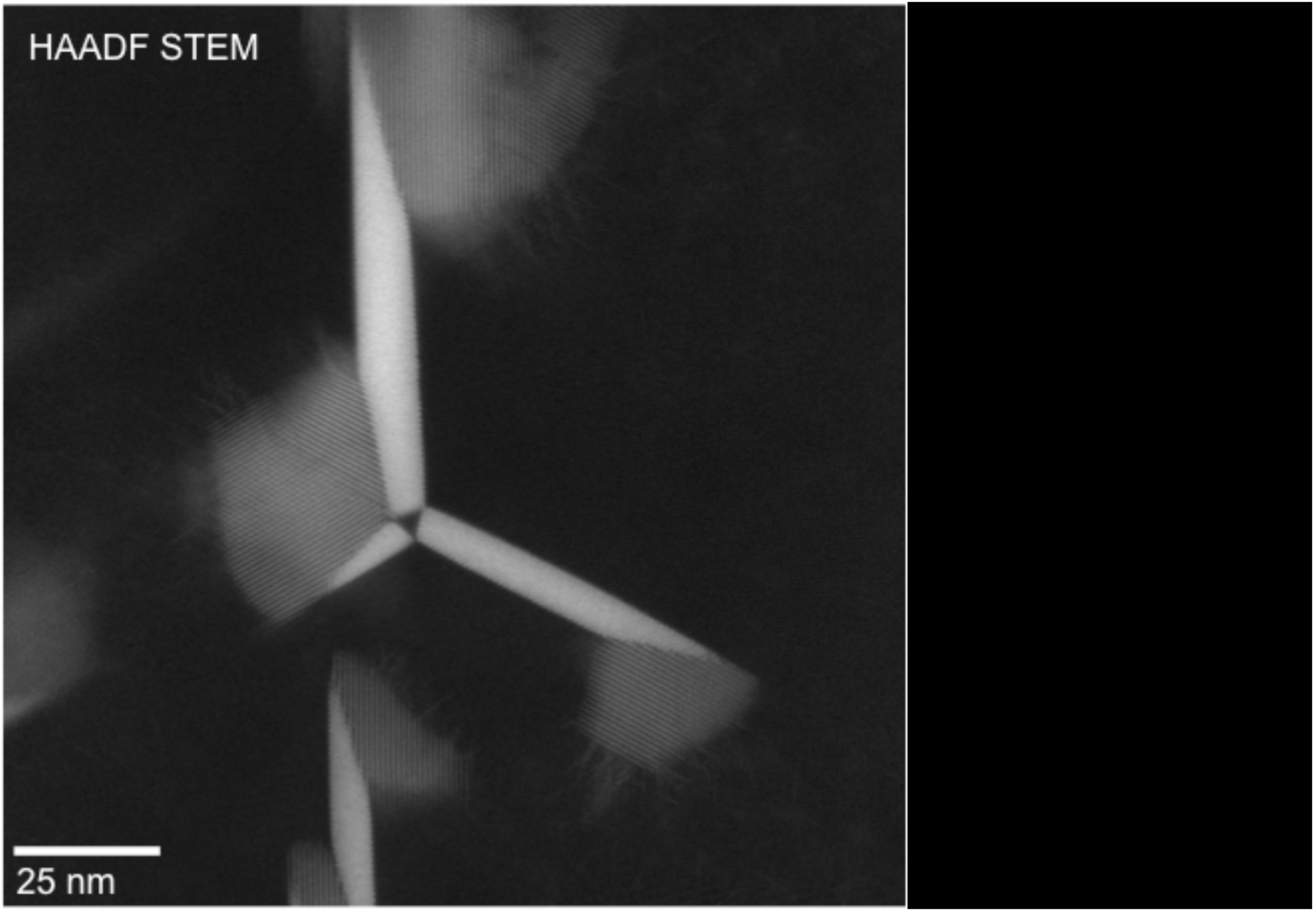
HAADF STEM
25 nm

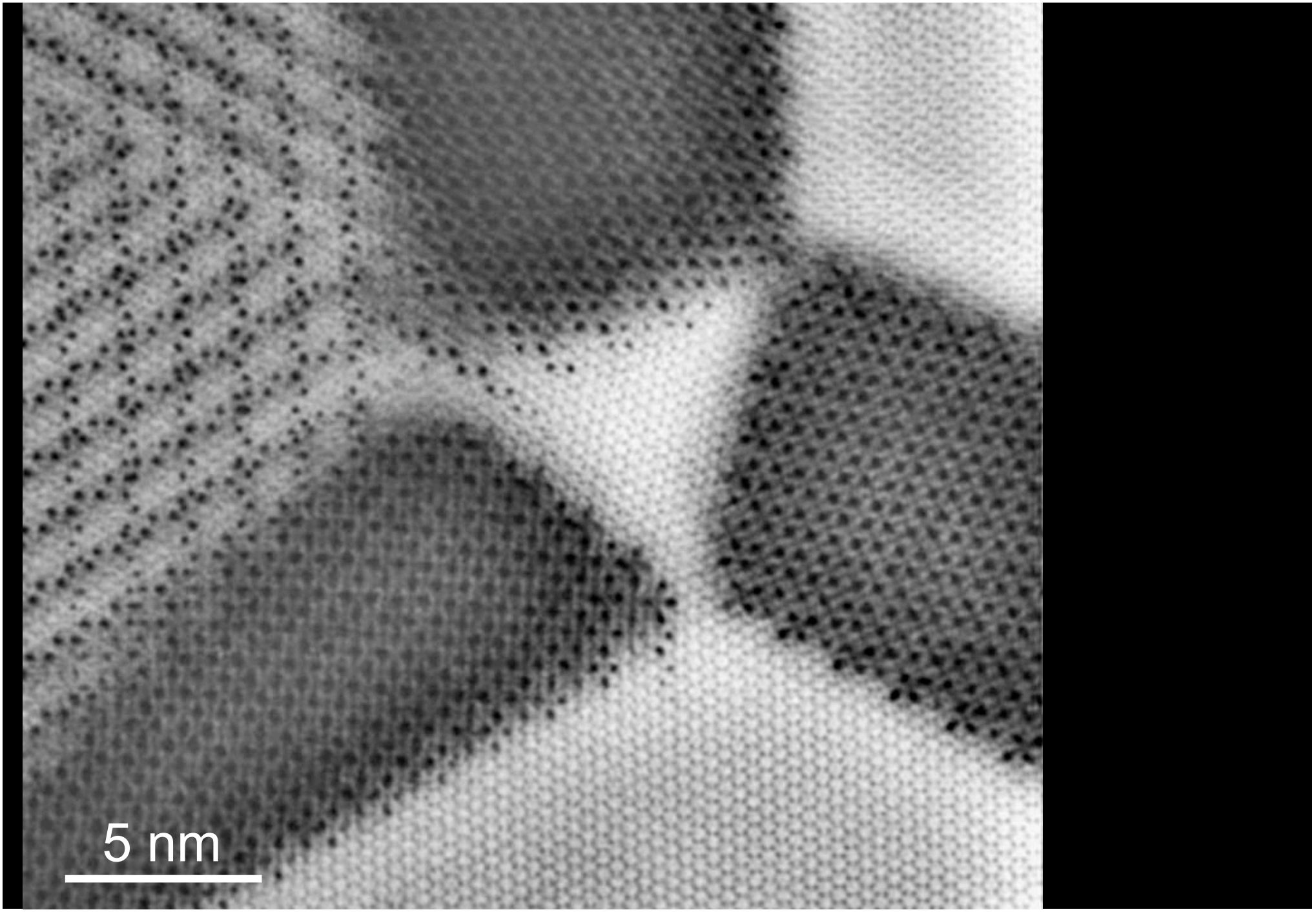
5 nm

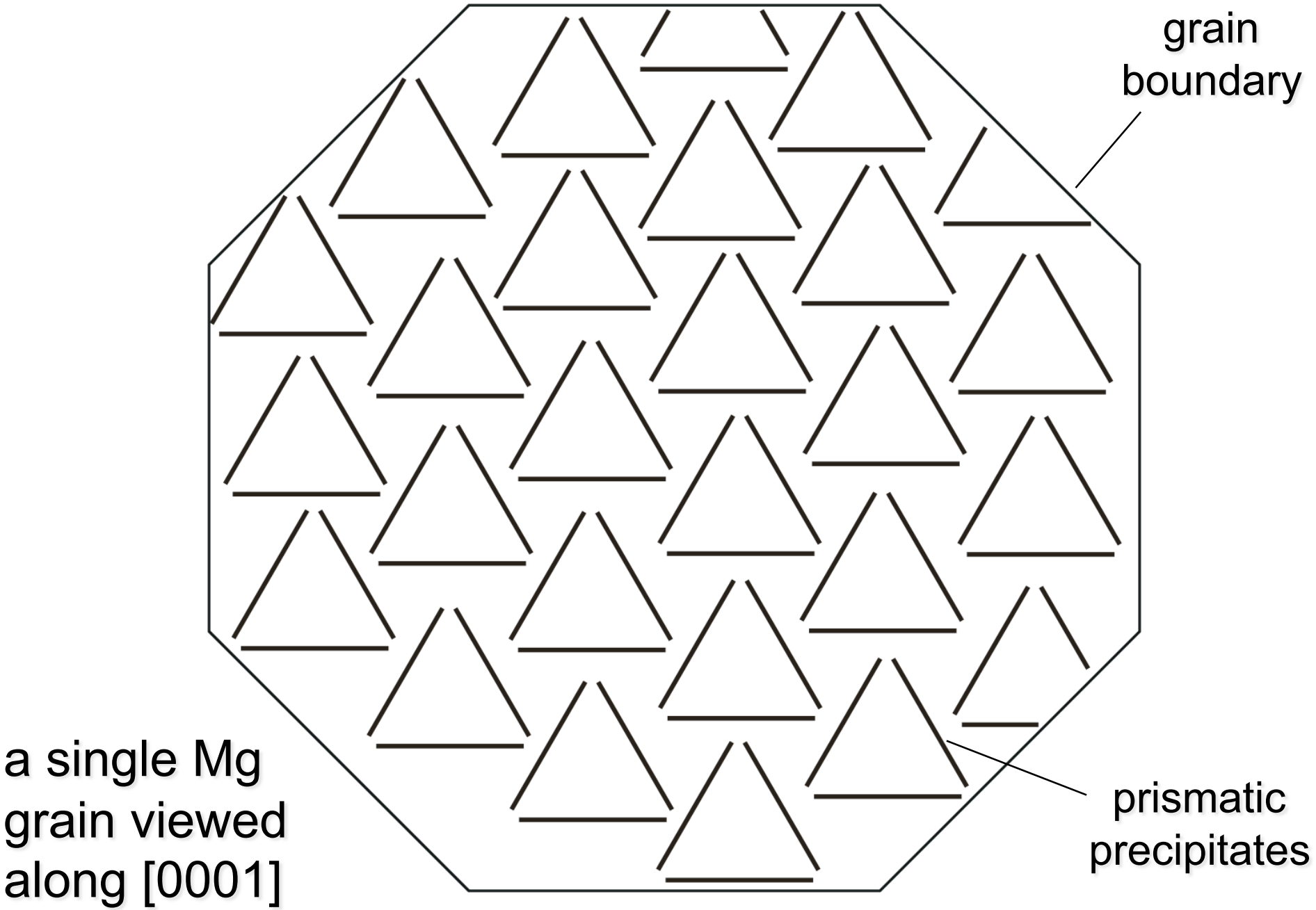

a single Mg
grain viewed
along [0001]

Nucleation Engineering: Multiscale Integration

G.B. Olson

Northwestern University & QuesTek Innovations LLC

Evanston, IL

NORTHWESTERN
UNIVERSITY

QUESTEK
INNOVATIONS LLC

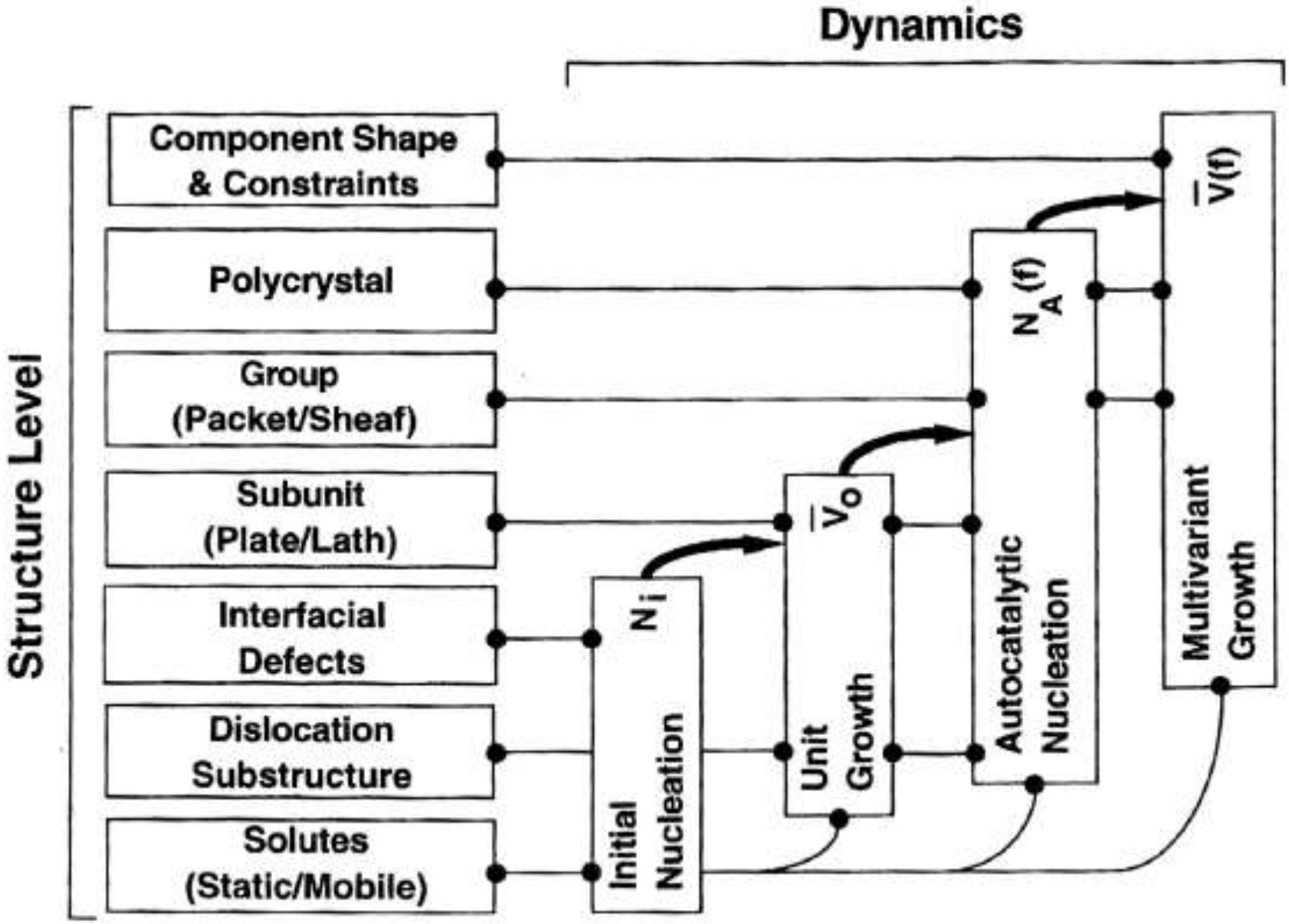

Fig. 1 Dynamic Hierarchy of Martensitic Microstructure [5].

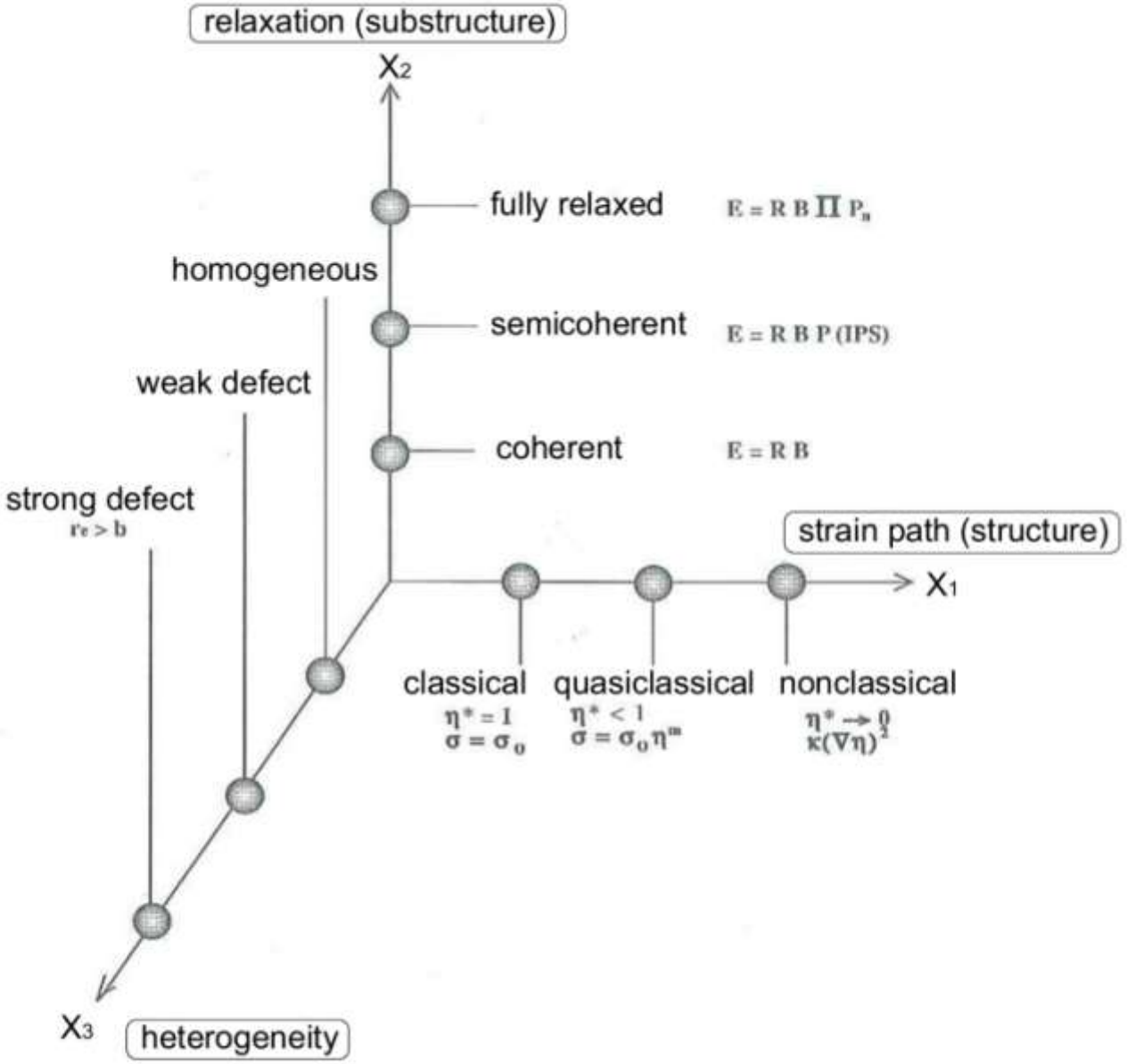

Principal parameters defining a "theory space" for martensitic nucleation

Reference: Olson, G.B., and Roitburd, A.L., 'Martensitic Nucleation', Ch. 9 in *Martensite,* ed. Olson, G.B. and Owen, W.S., ASM International (1992), p. 154

Hierarchy of Design Models

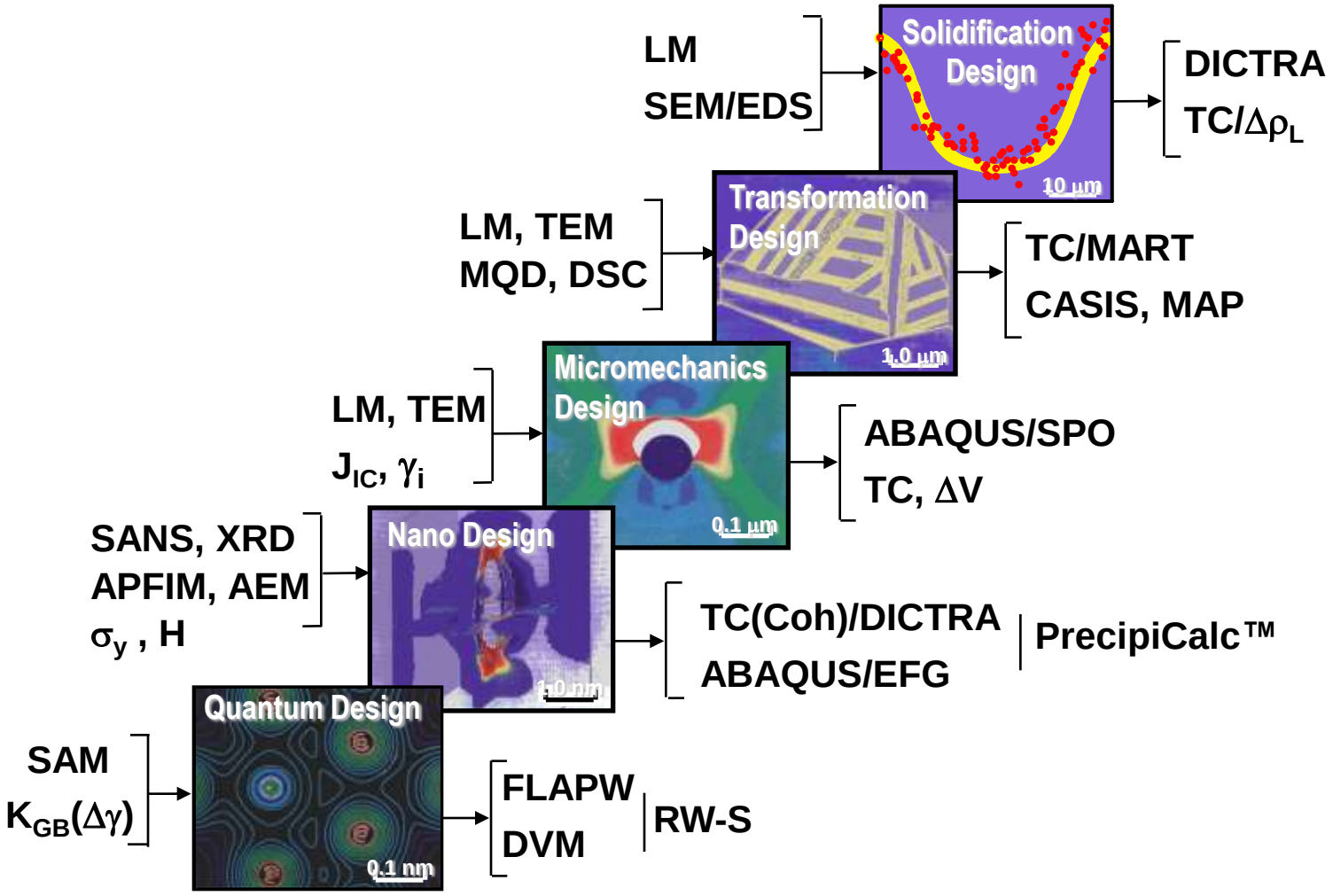

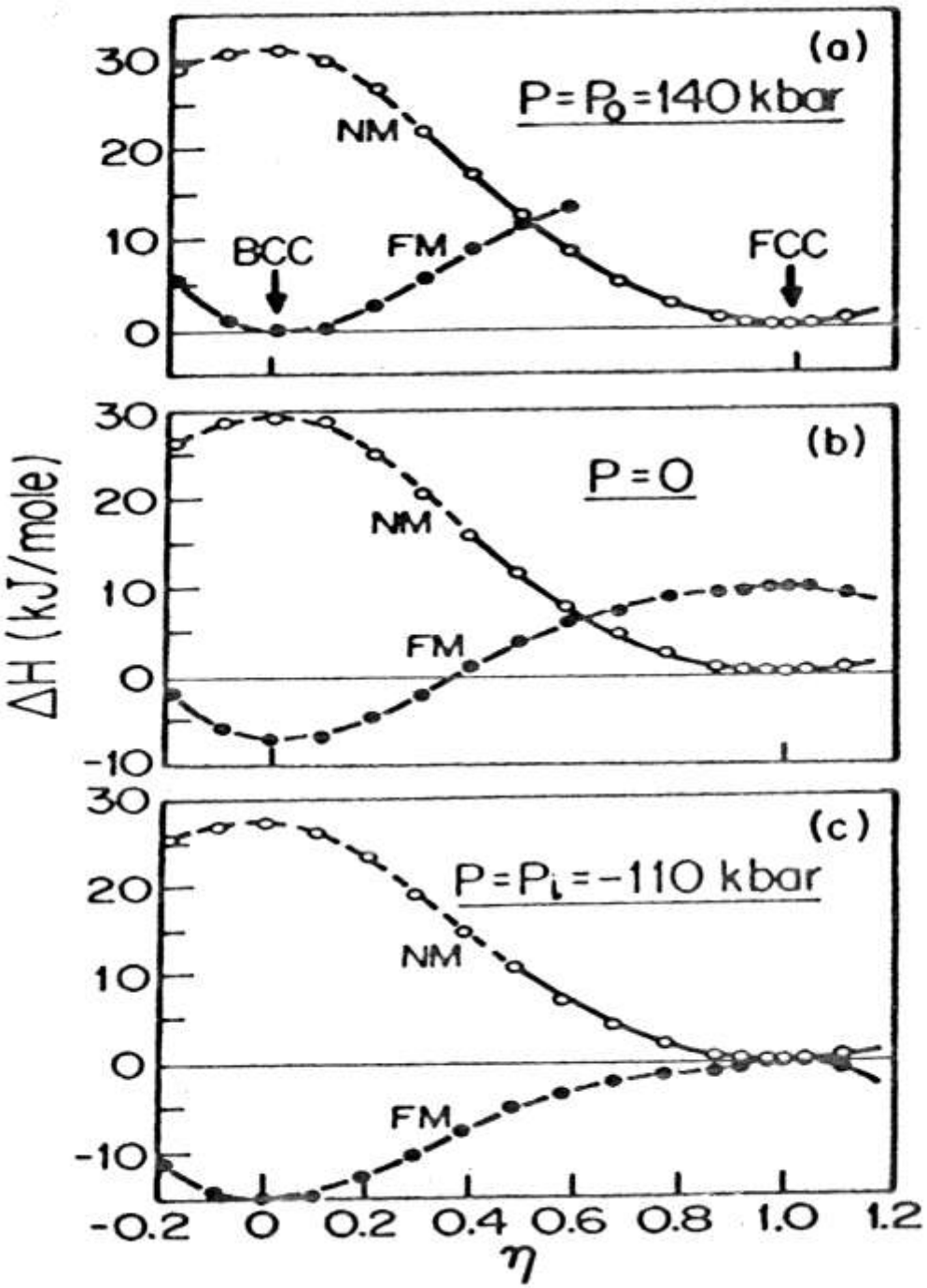
(a)
P=P0=140 kbar
NM
FM
BCC
FCC
(b)
P=0
NM
FM
(c)
P=Pi=-110 kbar
NM
FM
ΔH (kJ/mole)
30
20
10
0
-10
-0.2
0
0.2
0.4
0.6
0.8
1.0
1.2
η

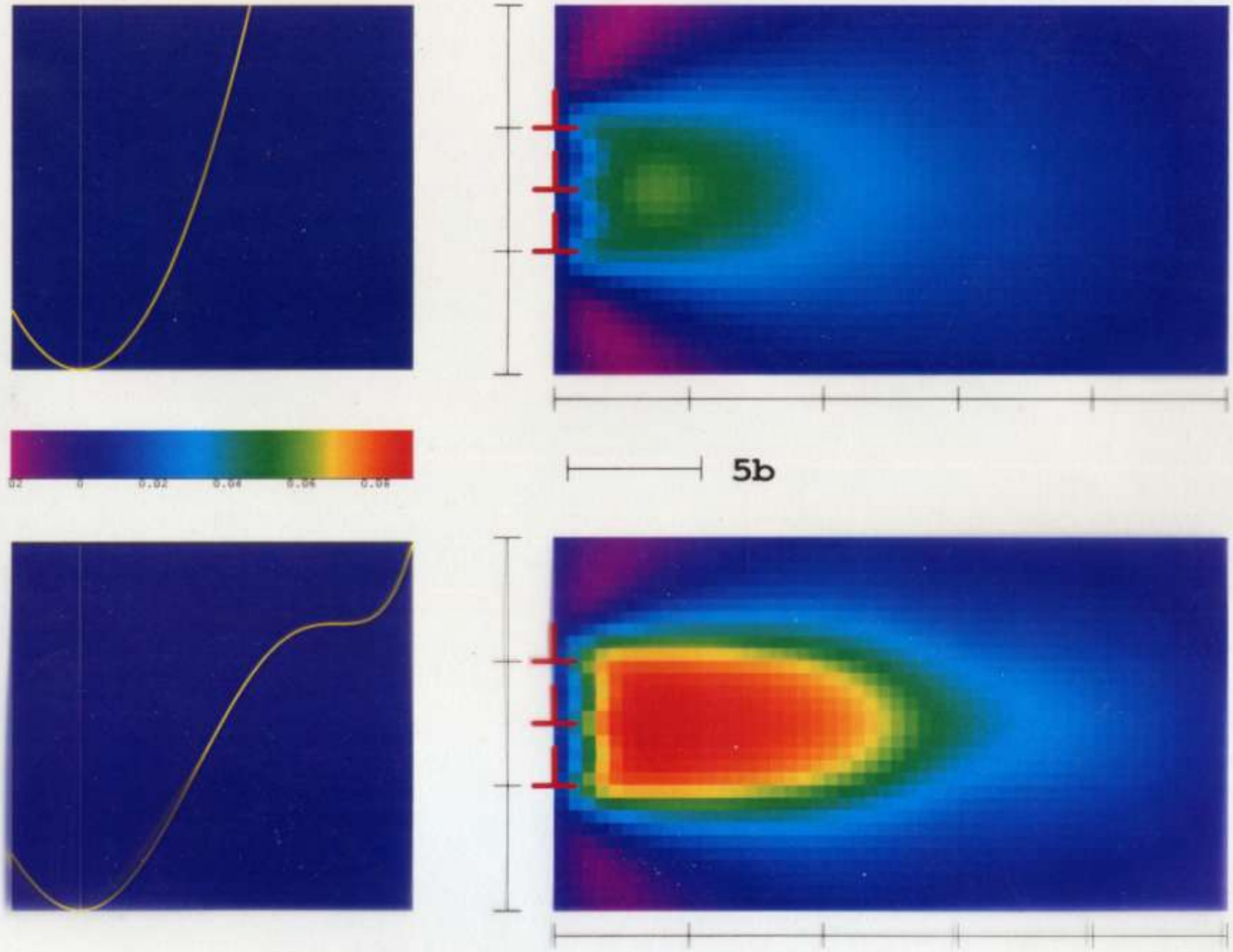
0.02
0
0.02
0.04
0.06
0.08
5b

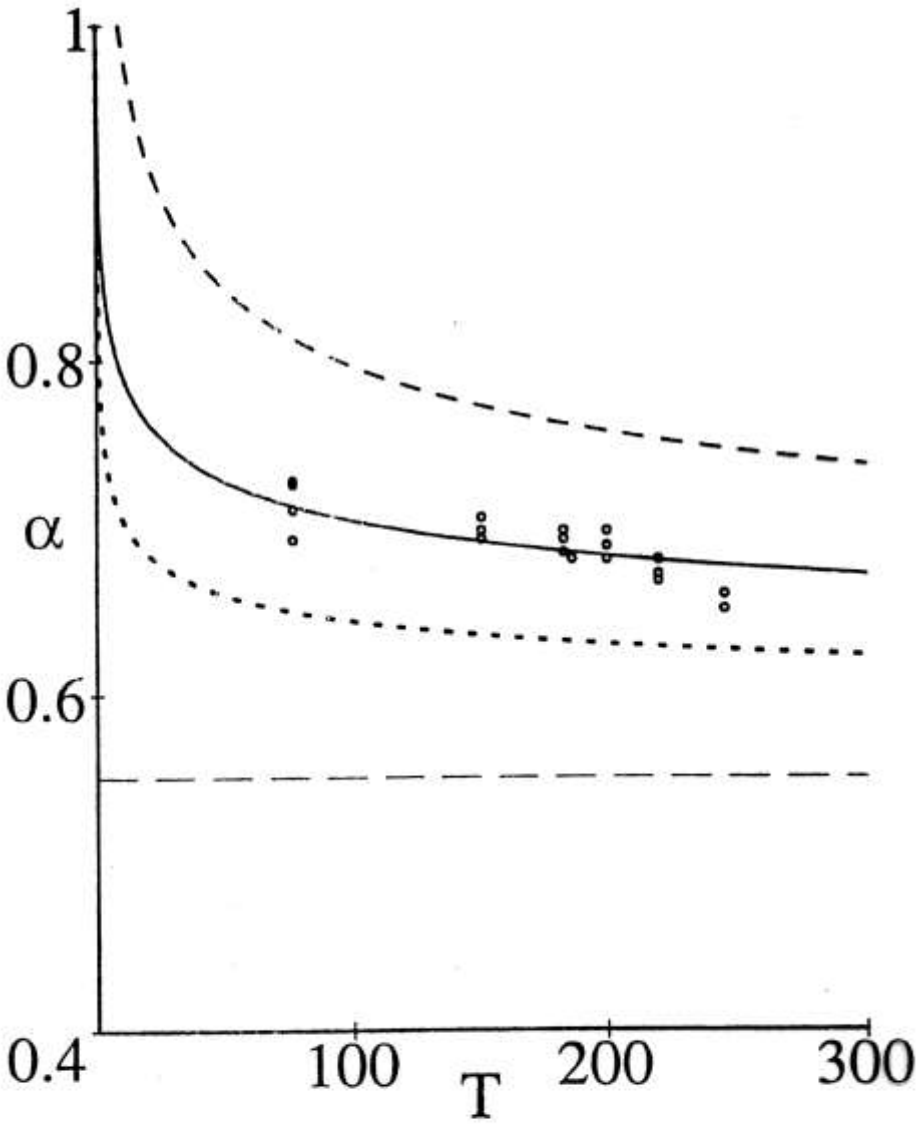

Fig. 11—Critical driving force for homogeneous, coherent nucleation in Fe-Co as a function of temperature. Circles are data from the article of Lin *et al.*[15] The lower dotted line is the prediction of the nonclassical nucleation model with the material parameters taken directly from Lin *et al.* The solid line is a fit of the nonclassical model to the data

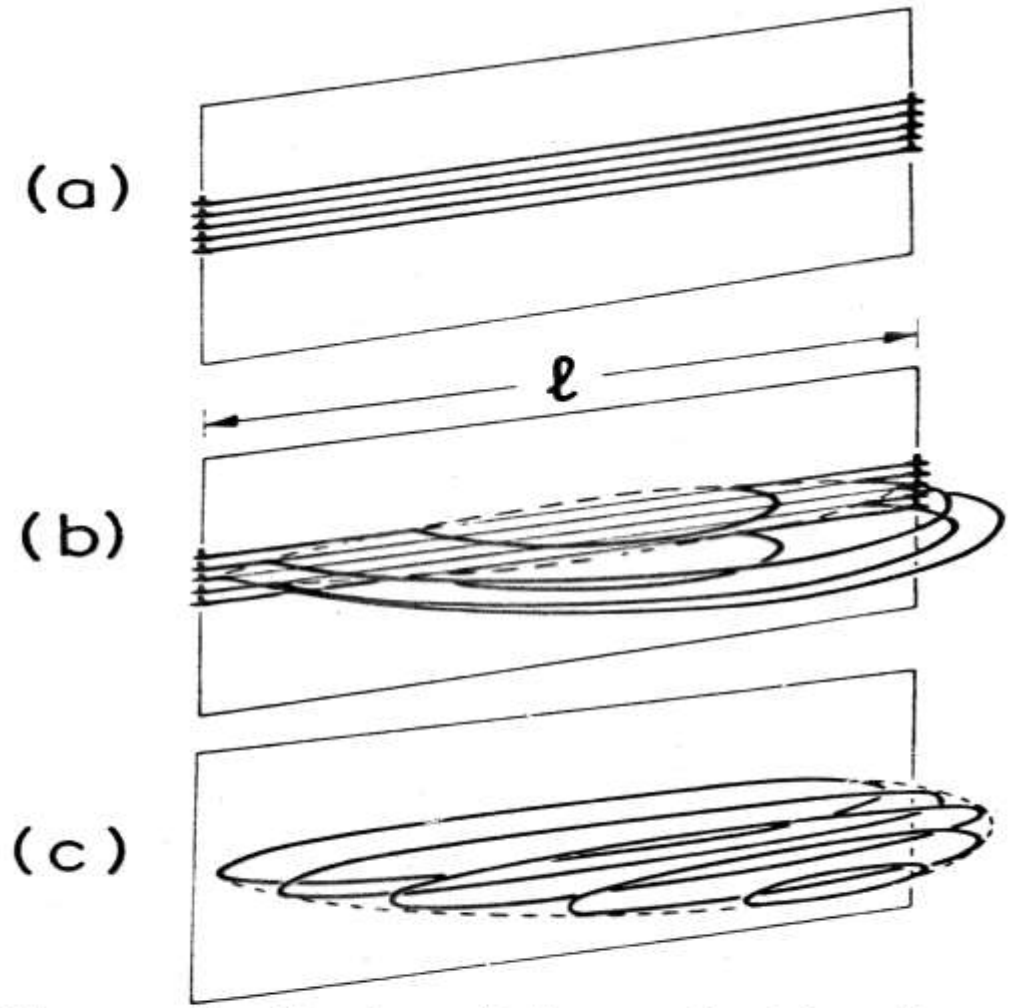

Figure 5. Martensitic nucleation by dislocation dissociation: (a) nucleating defect, (b) dissociation of defect to produce a/18 [1$\bar{2}$1] partial dislocations of Figure 4, (c) simultaneous generation of lattice dislocations of Figure 4.

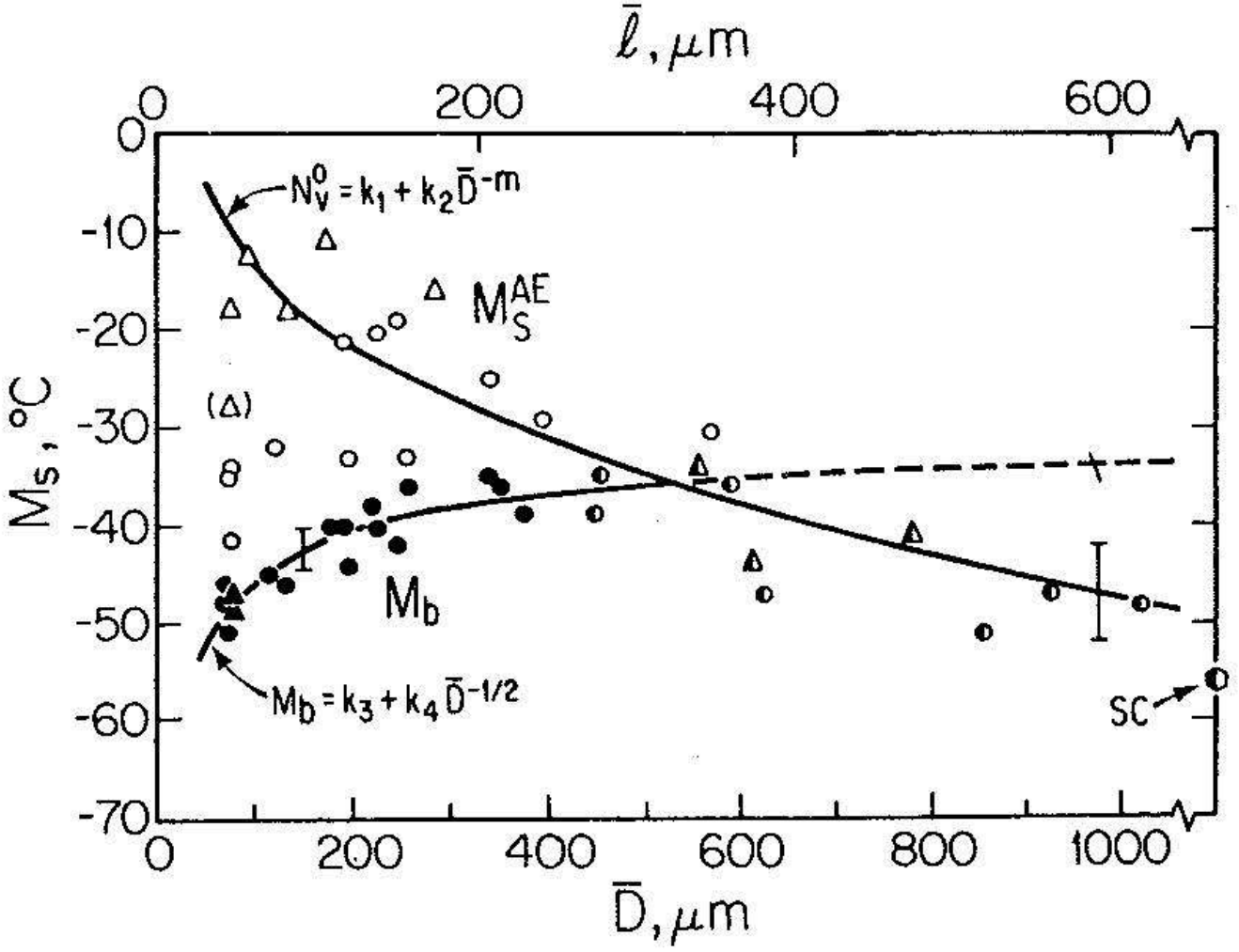

Grain-size dependence of acoustic-emission M_s^{AE} (open symbols) and electrical-resistivity M_b (closed symbols) measured in Fe-32.3Ni. Circles represent acoustic emission experiments conducted at 70 dB gain; triangles denote more sensitive measurements at 90 dB gain.

Reference: Olson, G.B., and Roitburd, A.L., 'Martensitic Nucleation', Ch. 9 in *Martensite,* ed. Olson, G.B. and Owen, W.S., ASM International (1992), p. 169

Distributed Heterogeneous Nucleation: CryoMART Simulator

$$martensite\ \ fraction\ \ f(t)=\overline{V}(f)\int_0^{\infty} N_v(n,t)dn,\quad \overline{V}(f)=V_1 f^{-m}$$

$$\frac{dN_v(n,t)}{dt}=\left[\frac{dN_i(n)}{dn}+f\frac{dP(n)}{dn}-N_v(n,t)\right](1-f(t))\upsilon\, exp\left(-\frac{Q(n,\Delta g_{ch})}{kT}\right)$$

$$Q=Q_0\left[1-\left(\frac{\Delta g}{\Delta \hat{g}}\right)^p\right]^q,\qquad \Delta g=\Delta g_{ch}+g_0+\frac{2\gamma_s}{nd}+w_\mu$$

- n — defect potency size
- $N_v(n)$ — plate number density
- $N_i(n)$ — pre-existing defect
- $P(n)$ — autocatalytic defect
- $Q(n)$ — activation energy
- g_0 — stored energy
- d — interplanar spacing
- γ_s — interfacial energy
- w_μ — athermal frictional work

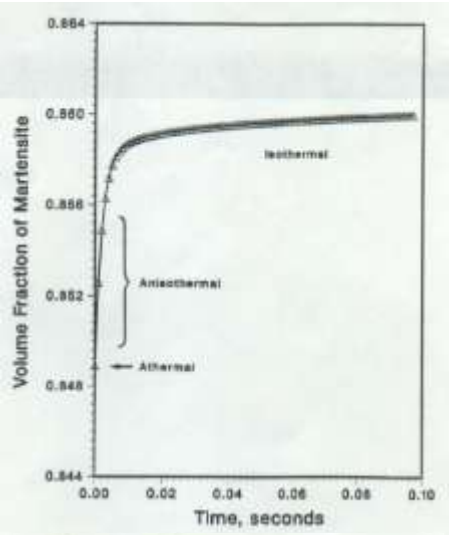

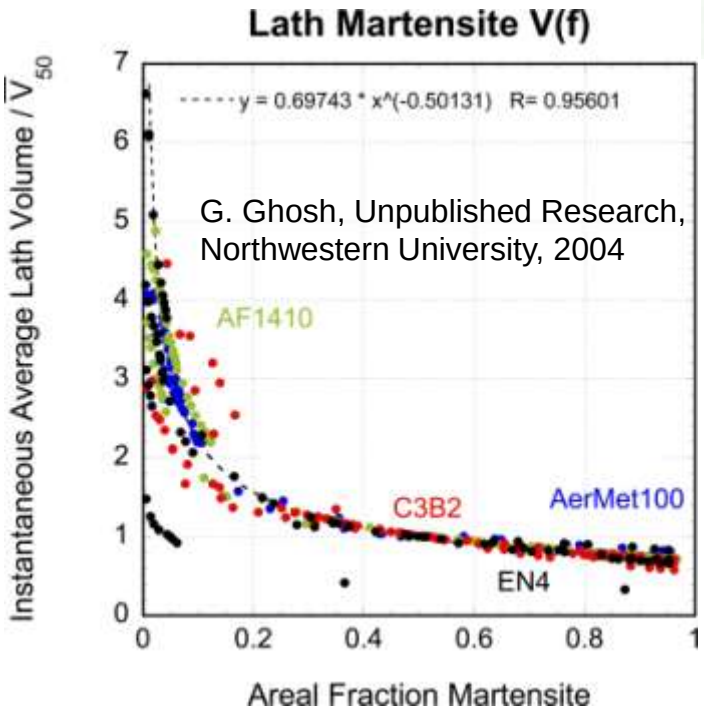

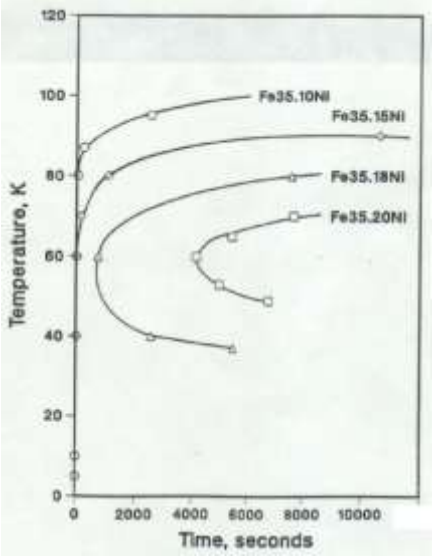

Basic *PrecipiCalc* Equations: Particle Growth

$$\text{Growth: } \frac{dR}{dt} = \frac{\left(1 + R\sqrt{4\pi N_v \langle R \rangle}\right)}{\left(R\Gamma + s(R) \Big/ \left(M_0 \exp \frac{-Q}{RT}\right)\right)} \left\{ \Delta G_m - \frac{2\sigma(R)\bar{V}_m^{\beta}}{R} \right\}$$

$$\text{where } \Delta G_m = \left[\Delta C_i\right]^T \left[\frac{\partial^2 \bar{G}^{\alpha}}{\partial C_i \partial C_j}\right] \left[\Delta C_j^{\infty}\right] + \left[\bar{C}_m^{\beta}\right] \bullet \left(\left[\bar{\mu}_m^{\alpha}\right] - \left[\bar{\mu}_m^{\beta}\right]\right)$$

$$\Gamma = \left[\Delta C_i\right]^T \left[\frac{\partial^2 \bar{G}^{\alpha}}{\partial C_i \partial C_j}\right] \left[\bar{D}_{jk}\right]^{-1} \left[\Delta C_k^{e}\right]$$

Thermodynamics

Diffusivity

Interfacial Property

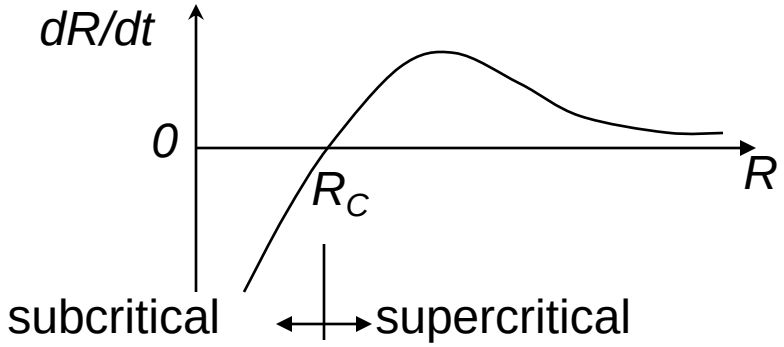

Basic PrecipiCalc Equations: Classical Homogeneous Nucleation

Steady State Nucleation Rate $J_{SS} = Z\beta^* \frac{N_a}{V_m^{\alpha}} e^{\frac{-W_R^*}{k_B T}} = \int_0^{\infty} \bar{J}_{SS}(R) dR$

where Zeldovitch factor $Z = \left[\frac{V_m^{\beta 2} \sigma}{4\pi^2 N_a^{\ 2} k_B T R_C^{\ 4}} \right]^{1/2}$

work to form a critical nucleus $W_R^* = \frac{16\pi\sigma^3}{3\left(\Delta G_m / V_m^{\beta}\right)^2}$

rate of atomic impingement $\beta^* = 4\pi R_C \frac{N_a}{V_m^{\beta}} \frac{\Delta G_m}{\Gamma}$

N_a is Avogadro's number, k_B is Boltzmann's constant

R_C is critical radius where $dR/dt = 0$, T is temperature

Incubation Time τ calculated from

$$\begin{cases} \int_0^{\tau} \beta^*(t')dt' = \frac{1}{\theta Z(t)^2}, & \text{if } \tau < t \\ \int_0^{\tau} \beta^*(t')dt' + \beta^*(t)(\tau - t) = \frac{1}{\theta Z(t)^2}, & \text{if } \tau > t \end{cases}$$

, where $2 < \theta < 4\pi$

which gives $\tau = \frac{1}{\theta \beta^* Z^2}$, at isothermal conditions. Note $t = 0$ at the start of incubation.

nucleation rate distribution is a normal distribution with mean and variance scaled by (R_{kT} - R_C), where *dR/dt=0* at R_C

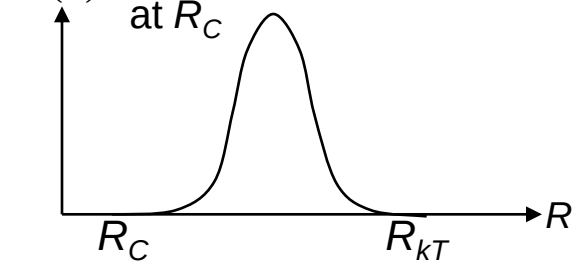

$$R_{kT} = \left[R_C^{\ 3} + \frac{3V_m^{\beta}}{4\pi\sqrt{\pi} N_a Z} \right]^{1/3}$$

NASA Microstructure Modeling: 3rd Generation Disk Alloys

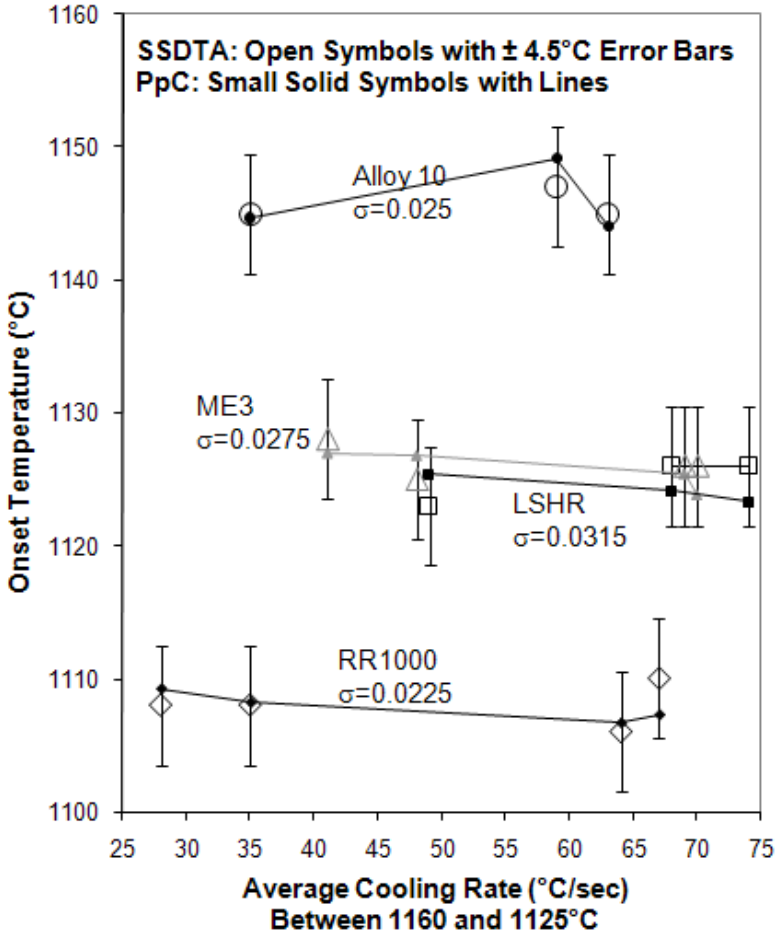

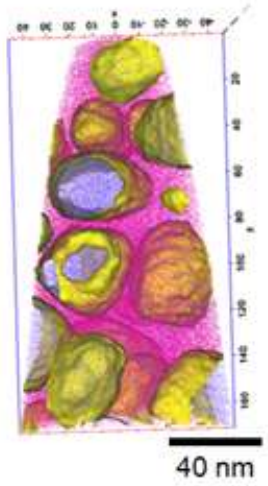

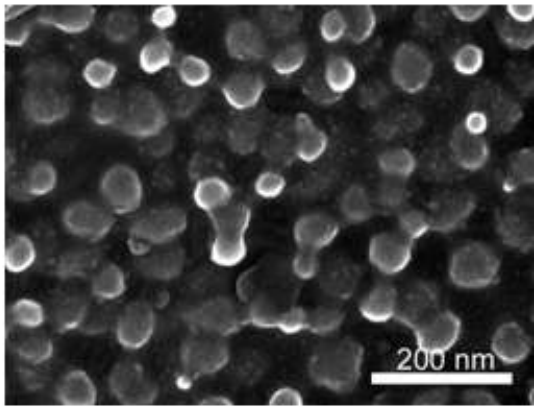

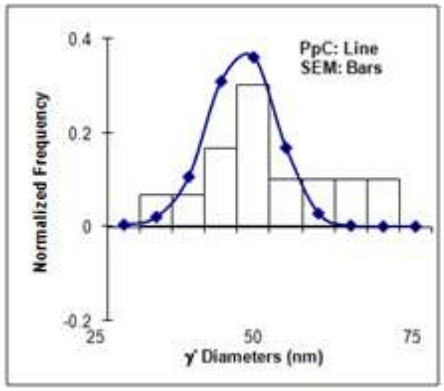

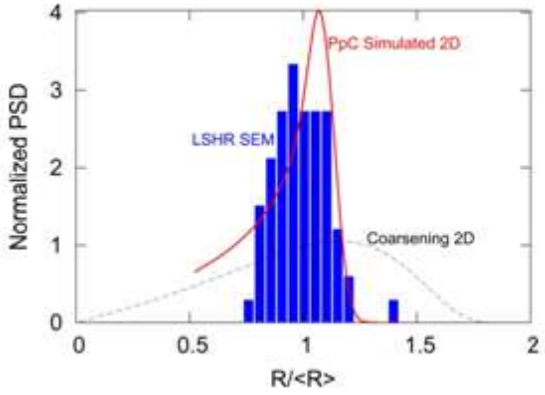

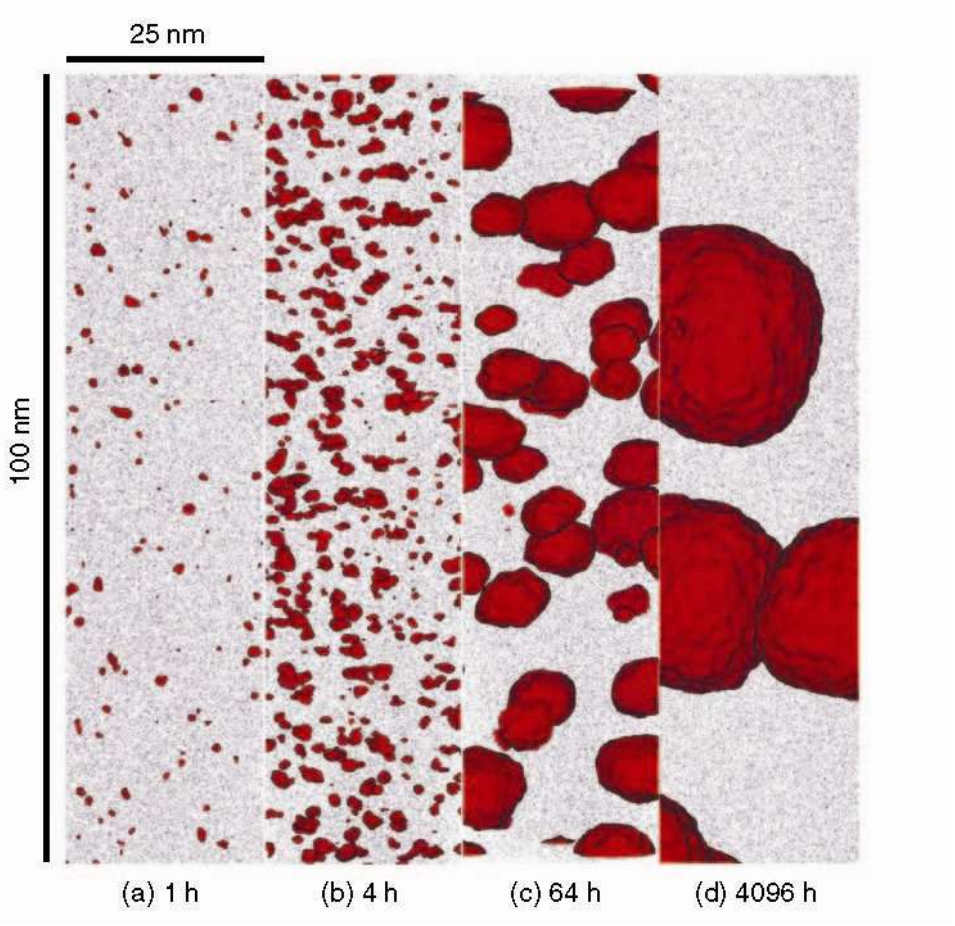

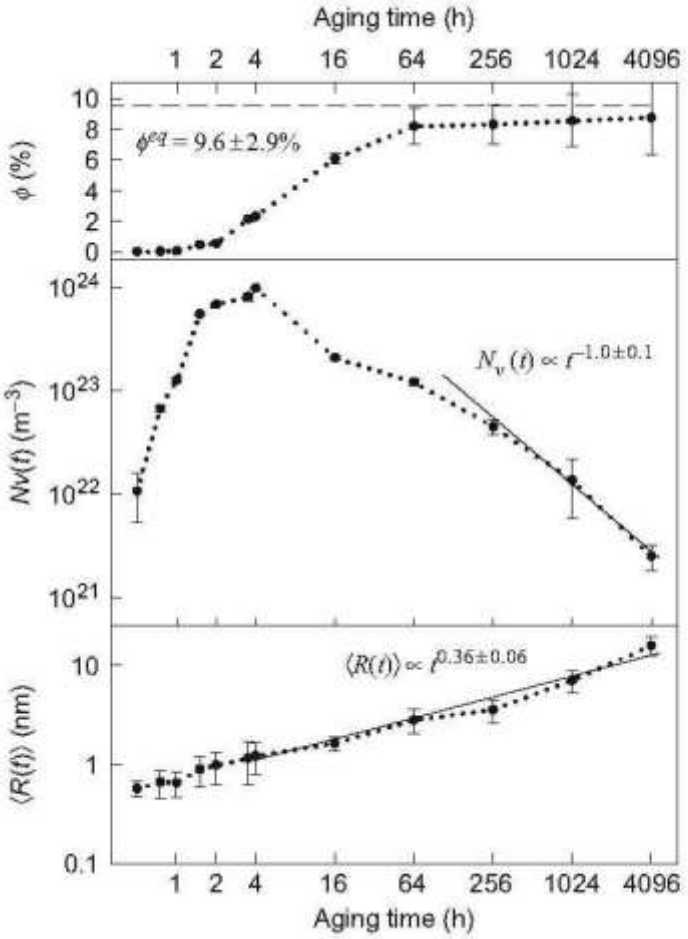

Ni-6.5 Al-9.5Cr at. % alloy aged at 873K

Reference: Booth-Morrison, C., Zhou, Y., Noebe, R.D., and Seidman, D.N., (2009) 'On the nanometer scale phase separation of a low-supersaturation Ni-Al-Cr alloy', *Philosophical Magazine*, 99999:1.

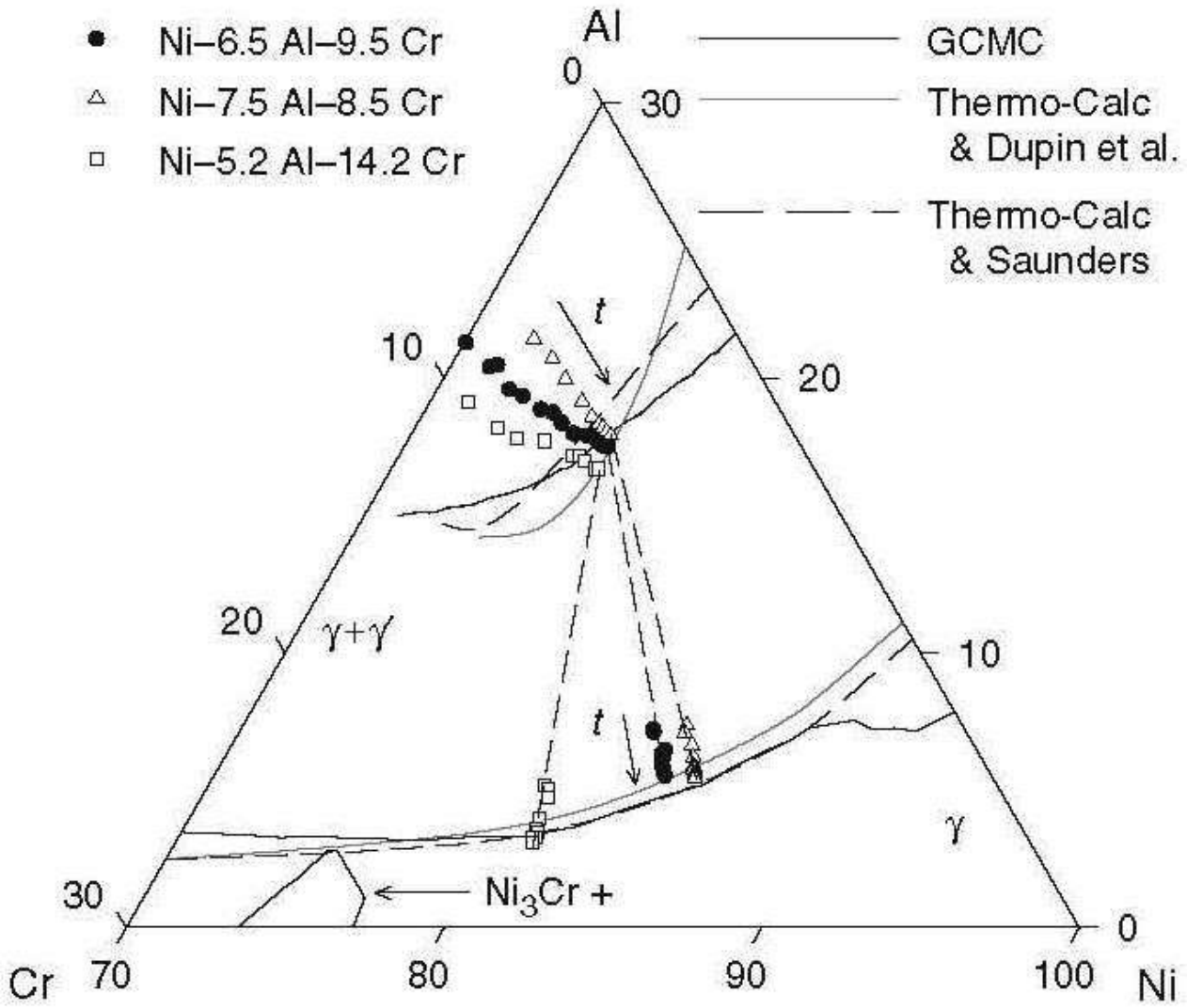

The compositional trajectories of the γ-matrix and γ'-precipitate phases of Ni-6.5 Al-9.5 Cr at. %, displayed on a partial Ni-Al-Cr ternary phase diagram at 873K.

Reference: Booth-Morrison, C., Zhou, Y., Noebe, R.D., and Seidman, D.N., (2009) 'On the nanometer scale phase separation of a low-supersaturation Ni-Al-Cr alloy', Philosophical Magazine, 99999:1.

D 3-D digital structure

NRL Atlas

DARPA

Design Research Tools

matCAT Characterization & Visualization Toolset

FSL/LOM Tomography [Pollock, Olson] Toughness, Fatigue Strength [Olson, Kern]

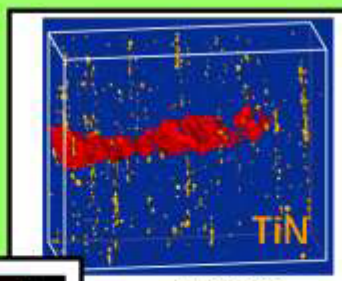

Ductile Fracture [Moran, Liu, Parks] Fatigue Nucleation [McDowell, Olson]

FSL/FIB Tomography [Pollock] Shear Instability [Olson, Kern]

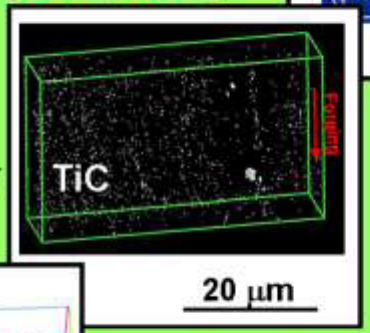

Microvoid Shear [Moran, Liu, Parks] Fatigue Propagation [McDowell]

LEAP Tomography [Seidman] Yield Strength [Olson, Kern]

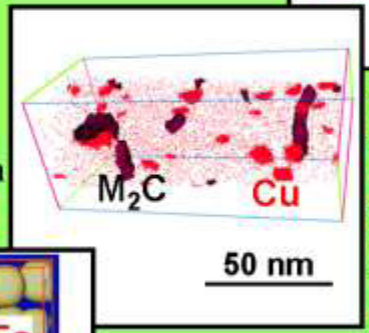

Transformation Toughening [Parks, Olson] Precipitation Strengthening [Voorhees, Wang, Jou]

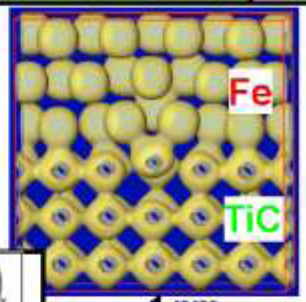

Semicoherent IPB Adhesion [Freeman, Jerome, Wang]

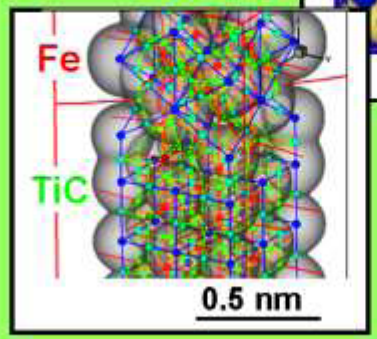

Bond Topological S/P Relations [Eberhart]

DFrac-3D

PrecipiCalc-3D

FLAPW

TECD

iSIGHT/CMD Integration

QuesTek INNOVATIONS LLC

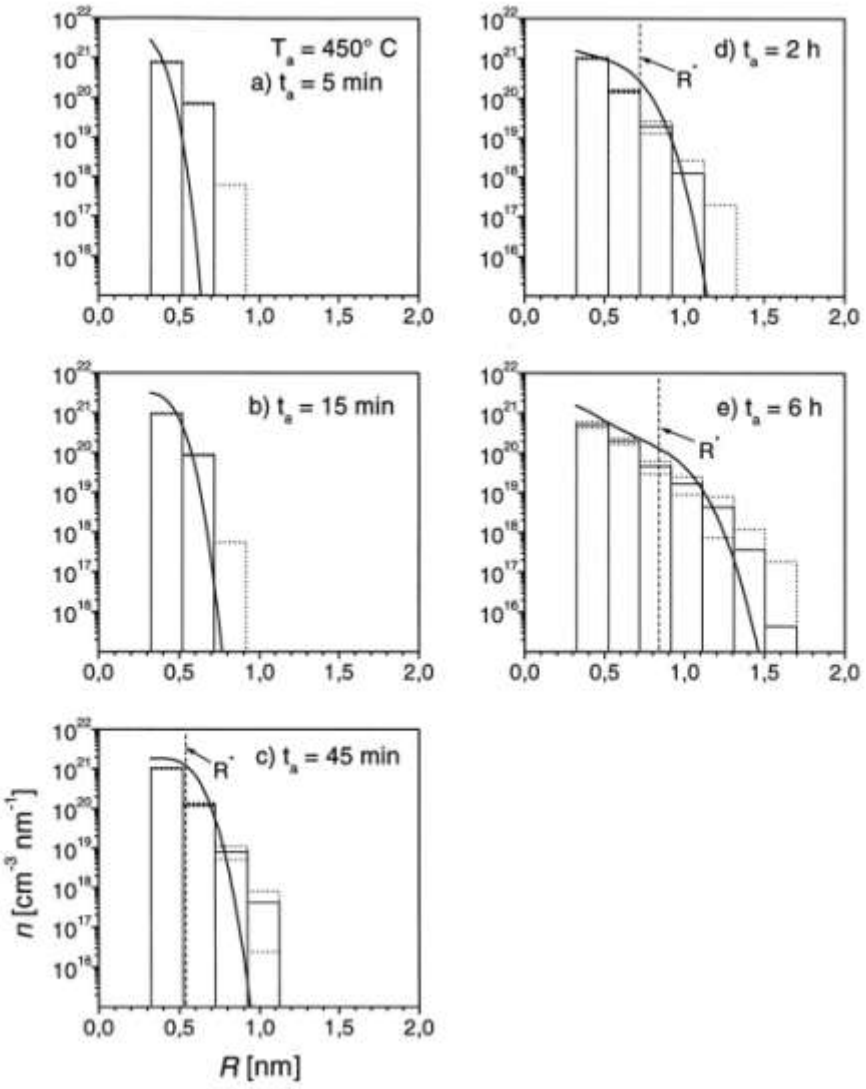

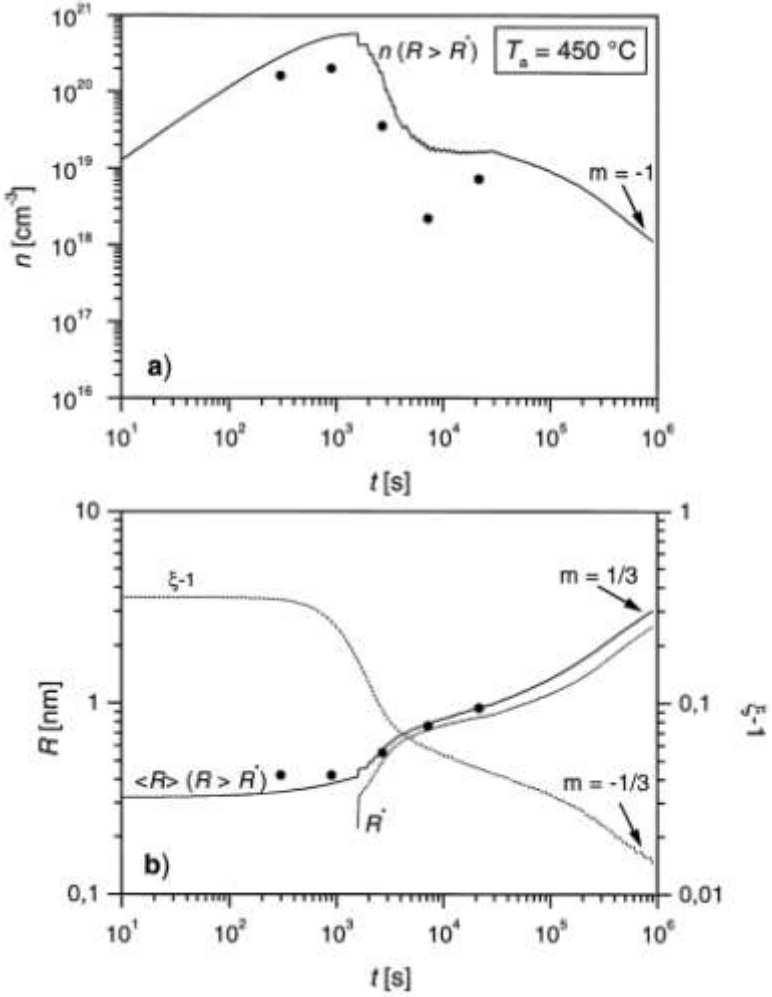

Ni-13 at.% AL aged at T_a=450˚C

Reference: Staron, P. and Kampmann, R., (2000) 'Early-stage decomposition kinetics in Ni-Al alloys—I. Small and wide-angle neutron scattering investigation on Ni-13 at.% Al and clusterdynamic modelling', *Acta Materialia*, 48:701-712.

$$\frac{dC_{n_X}}{dt} = J_{n_X-1\to n_X} - J_{n_X\to n_X+1} \quad \forall\, n_X \geqslant 2,$$

$$J_{n_X\to n_X+1} = \beta_{n_X} C_{n_X} - \alpha_{n_X+1} C_{n_X+1},$$

$$\frac{dC_1}{dt} = -2J_{1\to 2} - \sum_{n_X\geqslant 2} J_{n_X\to n_X+1},$$

Condensation Rate (long range diffusion control)

$$\beta_{n_X} = 4\pi r_{n_X} \frac{D_X}{\Omega} C_1,$$

Dissolution Rate (equilibrium cluster size distribution)

$$\alpha_{n_X+1} = 4\pi r_{n_X} \frac{D_X}{\Omega} \exp\left[(36\pi)^{1/3} a^2 \left((n_X+1)^{2/3}\sigma_{n_X+1} - n_X^{2/3}\sigma_{n_X} - \sigma_1\right)/kT\right].$$

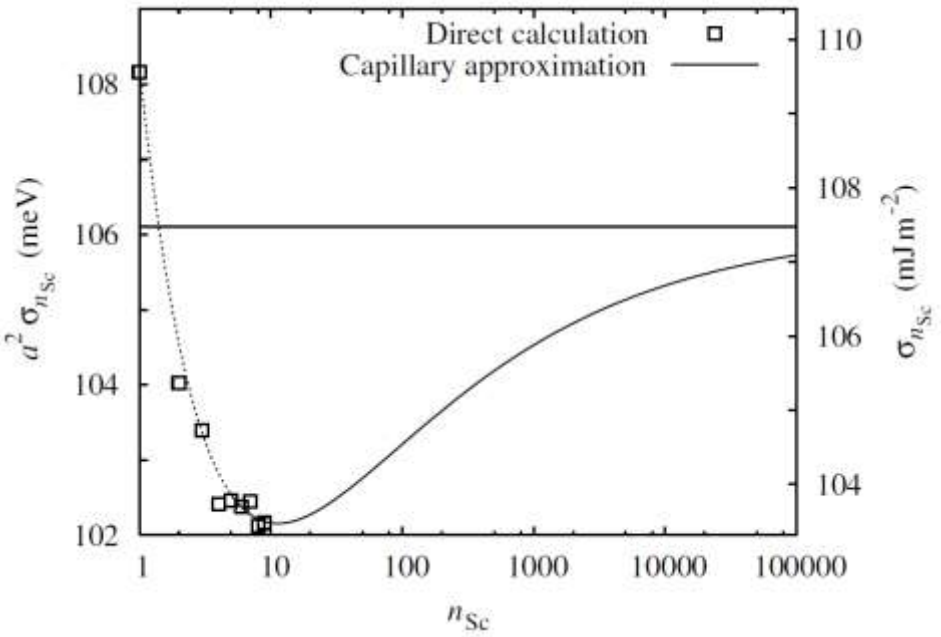

E. Couet, A. Barbu, L. Laé, and G. Martin, *Acta Mater*., **53** (2005) 2313-2325.

Heterogeneous Nucleation at Grain Boundaries

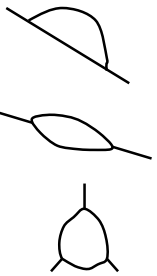

(a) coherent particle on flat impurity

(b) incoherent particle on grain boundary

(c) trijunction edge line

Nucleation Rate $J = \exp\left(-\frac{\tau}{t}\right) Z\beta^* N(1-f_s) e^{\frac{-W^*}{k_B T}}$, k_B is Boltsman constant and T is temperature

Energy Barrier $W^* = W_h^* f$, where f is a volumetric correction factor:

$$f = \begin{cases} (2-3\cos\theta+\cos^3\theta)/4, \text{(a)} \\ (2-3\cos\theta+\cos^3\theta)/2, \text{(b)} \\ \frac{6}{4\pi}\left[\pi - 2\sin^{-1}\left(\frac{1}{2}\csc\theta\right) + \frac{1}{3}\cos^2\theta\sqrt{4\sin^2\theta-1} - \cos^{-1}\left(\cot\theta/\sqrt{3}\right)\cos\theta\left(3-\cos^2\theta\right)\right], \text{(c)} \end{cases}$$

Available Nucleation Sites $N = \begin{cases} 2N_0\left(\delta/\overline{D}\right), \text{(a)}, \ \delta \approx 0.1\text{nm}, \ \overline{D} \text{ is grain diameter} \\ N_0\left(\delta/\overline{D}\right), \text{(b)} \\ N_0\left(\delta/\overline{D}\right)^2, \text{(c)} \end{cases}$

Nucleation Site Consumption Ratio $f_s = \begin{cases} \left(\pi N_v \overline{R}\sin^2\theta\right)/\frac{3}{\overline{D}}, \text{(a)}, \ \overline{D} \text{ is grain diameter}, \ \overline{R} \text{ is mean size} \\ \left(\pi N_v \overline{R}\sin^2\theta\right)/\frac{6}{\overline{D}}, \text{(b)} \\ N_v \overline{R}^2\left(1-4\cos^2\theta/3\right)^{1/2}/\frac{3\alpha_e}{\overline{D}^2}, \text{ where } \alpha_e \approx 30 \text{ (c)} \end{cases}$

Zeldovitch factor $Z = Z_h f^{1/2}$

Incubation Time $\tau = \frac{1}{\Theta\beta^* Z^2} = \frac{1}{\Theta\beta^* Z_h{}^2 f}$, where $\Theta \in (2, 4\pi)$

Impingement Rate $\beta^* = gR_c{}^2 \frac{N_a}{V_m^\beta} \begin{cases} dR/dt, \text{ for mass tranport controlled nucleation}, R_c \text{ critical size} \\ D/6a, \text{ for interfacial controlled nucleation}, V_m^\beta \text{ molar volume} \end{cases}$

Surface correction factor $g = \begin{cases} 2\pi(1-\cos\theta), \text{(a)} \\ 4\pi(1-\cos\theta), \text{(b)} \\ 6\pi - 12\sin^{-1}\left(\frac{1}{2}\csc\theta\right) - 12\cos\theta\cos^{-1}\left(\cot\theta/\sqrt{3}\right), \text{(c)} \end{cases}$

mass balance $V^\beta = \frac{4\pi}{3} fR^3$

Heterogeneous Nucleation on Dislocations

Nucleation Rate $= Z\beta^* N e^{\frac{-fW_R^*}{k_B T}} e^{-\tau/t}$, with a defect interaction factor f

Available Nucleation Site Density, $N = \frac{N_a}{V_m^\alpha}\left(\pi(1.5b)^2\right)\left(\rho - 2N^{\text{tot}}\overline{R}\right)$

Incubation Time, $\tau = \frac{1}{\theta\beta^* Z^2 f}$

Energy Barrier for Nuclation, $W_R^* = \frac{16\pi\sigma^3}{3\left(\Delta G_m / V_m^\beta\right)^2}$

Atomic Impingement Rate, $\beta^* = 4\pi R_c \frac{N_a}{V_m^\beta}\frac{\Delta G_m}{\Gamma}$

Heterogeneous M_2C Nucleation on Dislocations

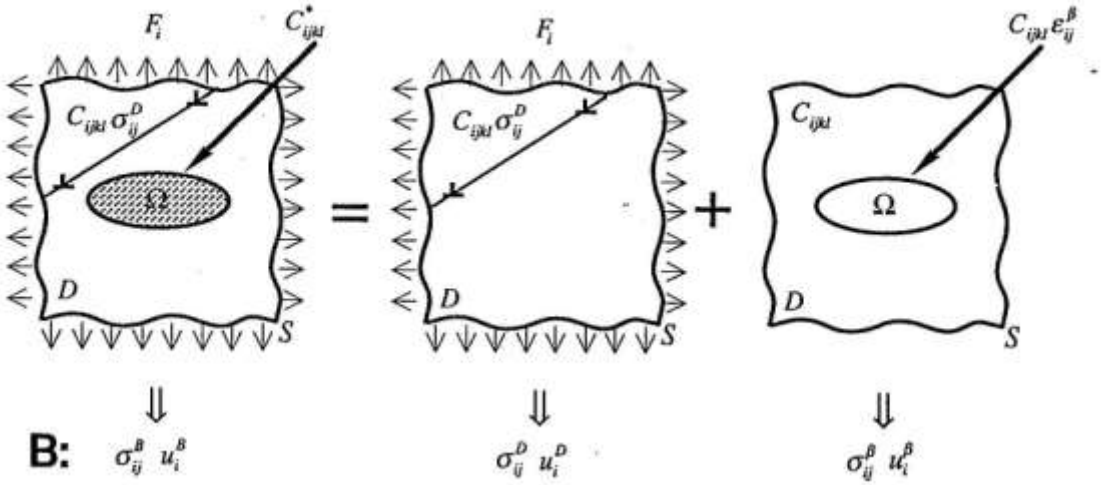

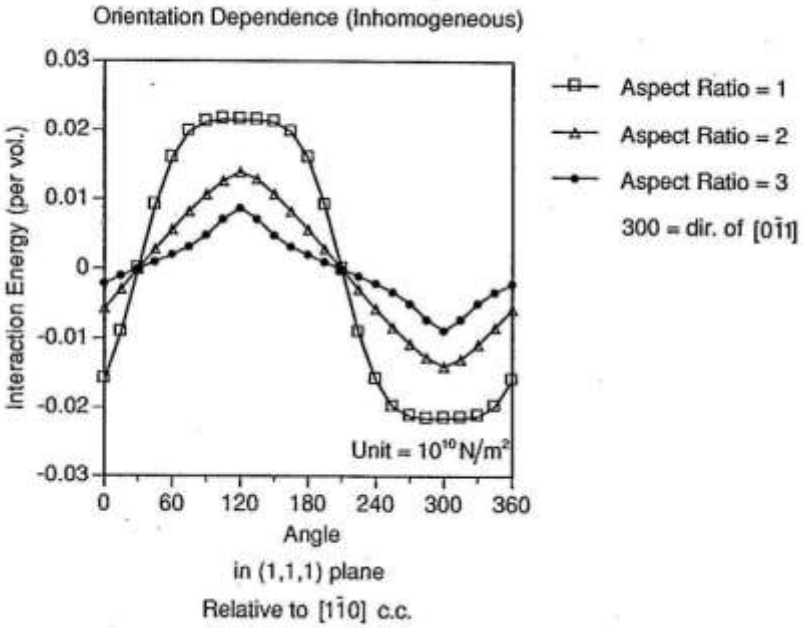

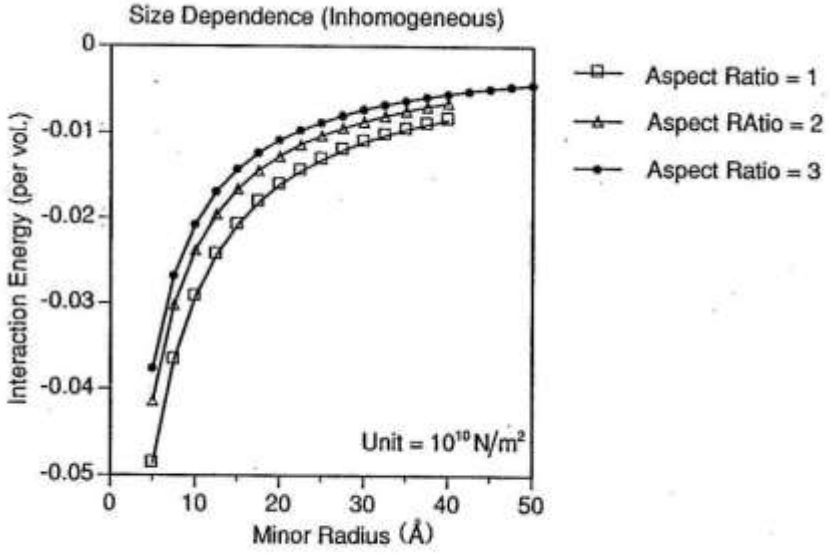

Reference: King, K.C., Olson, G.B., and Mura, T., 'Elastic Energy of Coherent Precipitation at Dislocations in an Anisotropic Matrix', Ch. 7 in *Modern Theory of Anisotropic Elasticity and Applications*, ed. Wu, J.J., Ting, T.C.T., Barnett, D.M., Society for Industrial and Applied Mathematics (1991), pp.103-121.

AF1410 Precipitation Simulation

Isothermal M_2C precipitation simulation of AF1410 steel at 510°C, along with the experimental results from G.B. Olson, T.J. Kinkus and J.M. Montgomery, *Surface Science 246* (1992) 238. Parameters used in the simulation include: surface energy σ_{coh}=0.25J/m^2, σ_{incoh}=1.0J/m^2, ρ=2.5x10^{14} (1/m^2), f=0.55, ΔR_{tran}=5, D_{pipe}/D_{vol}=100.

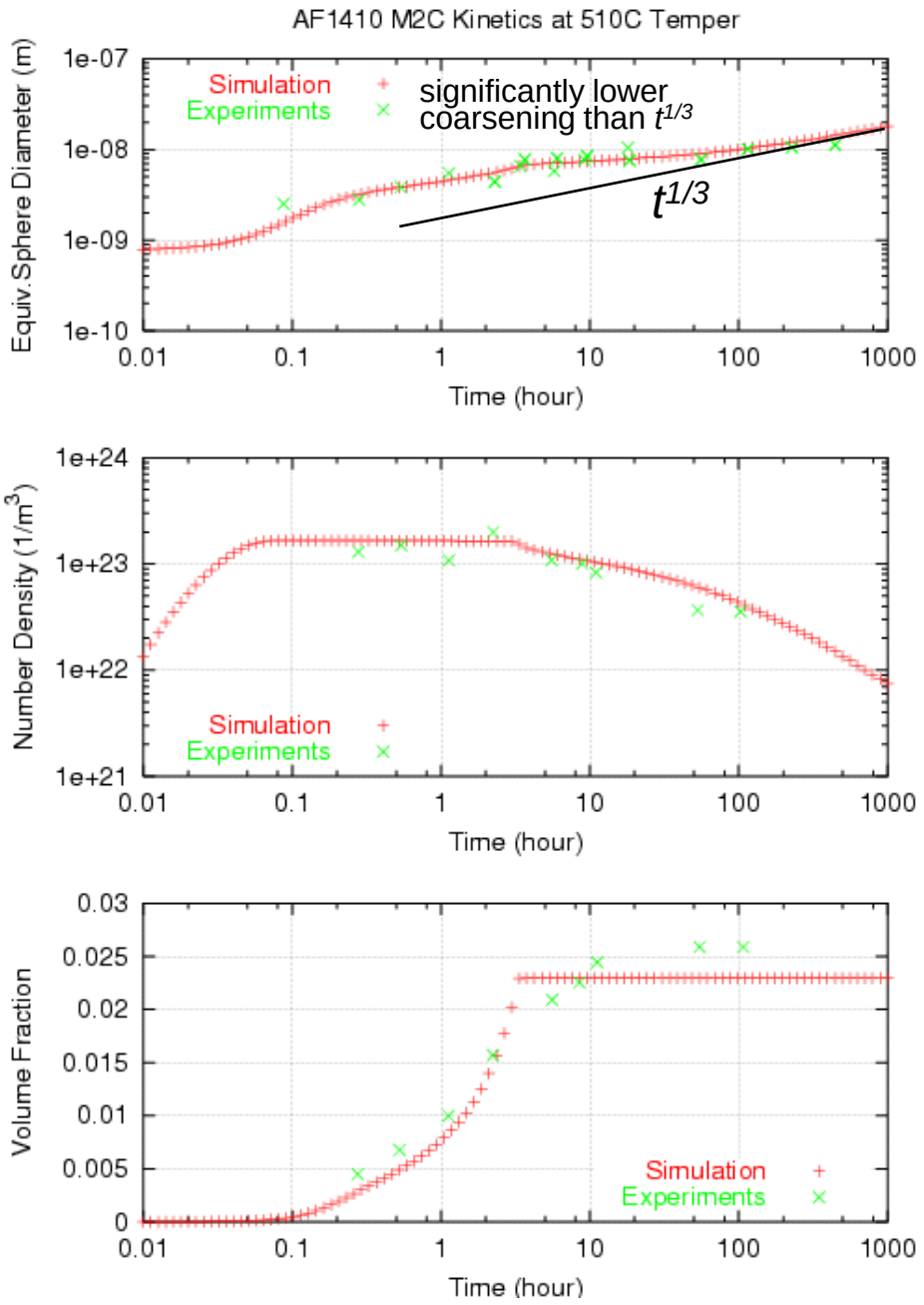

Materials Science and Engineering, A 132 (1991) 107-118

Heterogeneous nucleation of solidification in atomized liquid metal droplets

M. Libera, G.B. Olson and J. B. Vander Sande

Department of Materials Science and Engineering, Massachusetts Institute of Technology, Cambridge, MA 02139 (U.S.A)

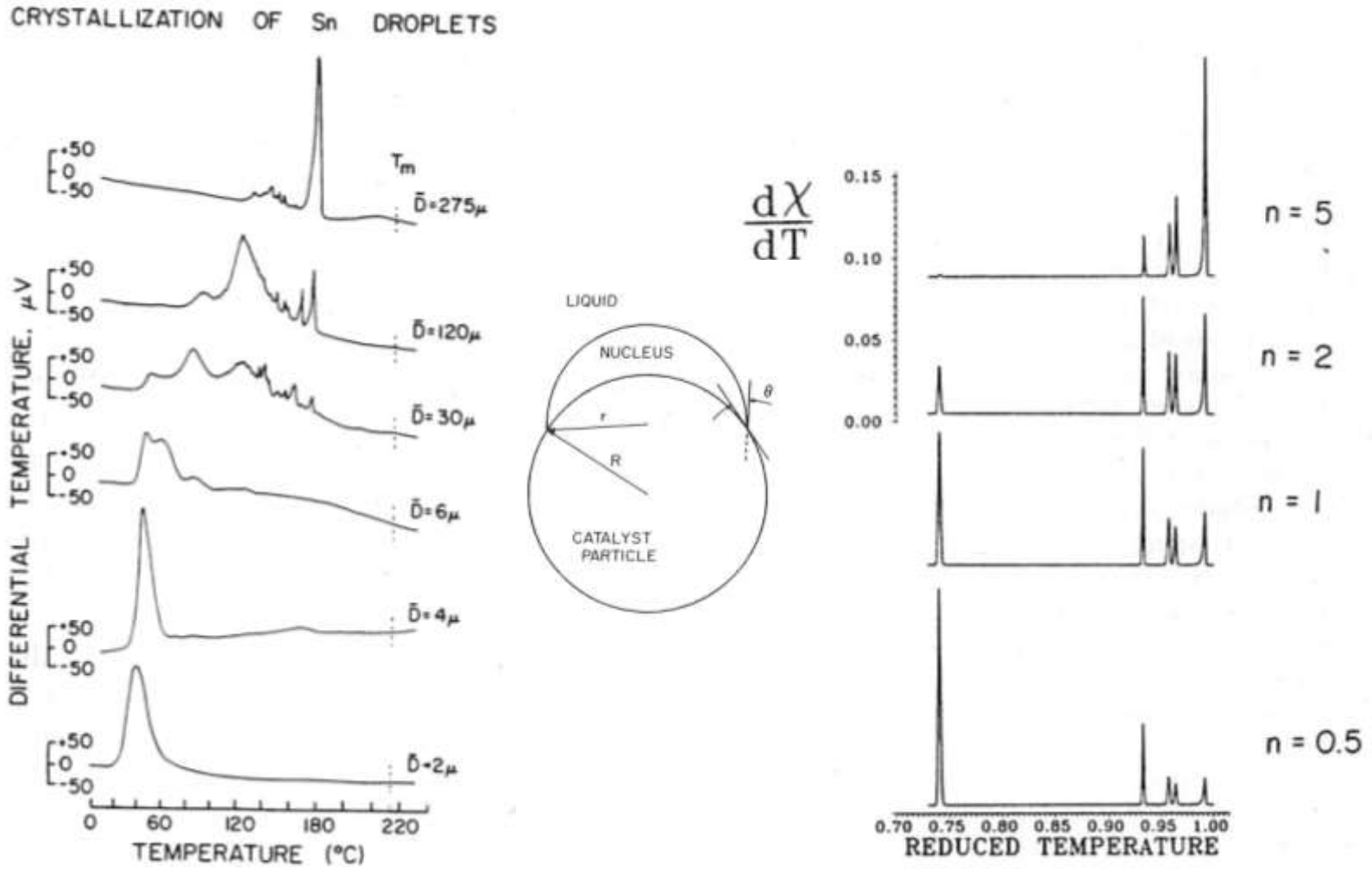

Fatigue Nucleation

- Fatigue in gear steels:
  - Sliding-Rolling Contact
  - Single Tooth Bending
- Minimum bending fatigue strength controlled by subsurface inclusions:
  - Not all inclusions are equally potent
  - Al_2O_3 vs La_2O_2S inclusion clusters in GearMet C61 and C67

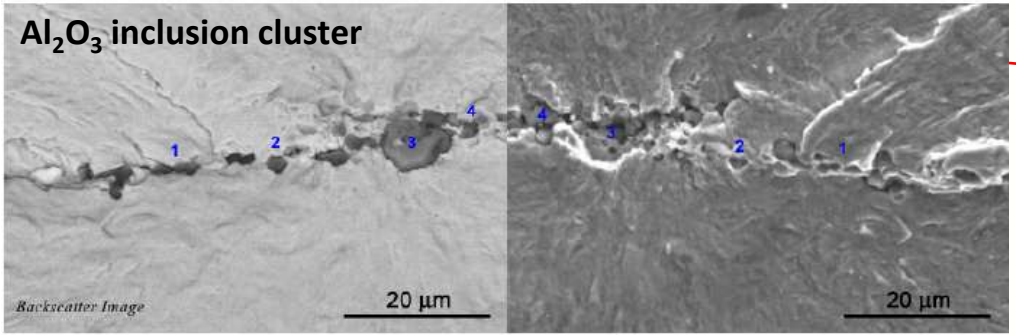

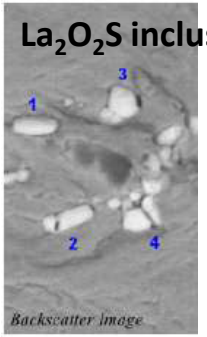

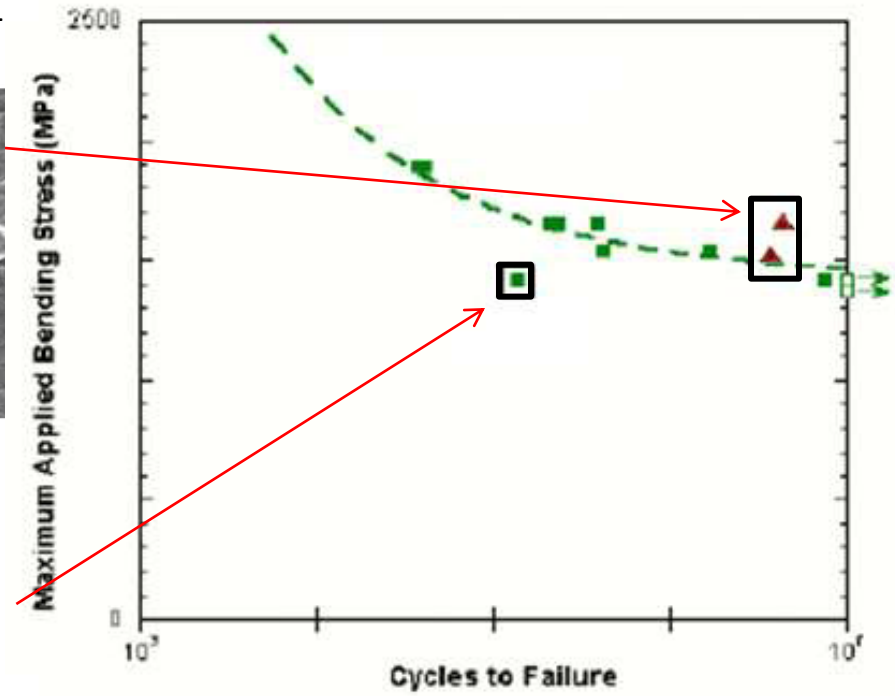

Tiemens, B., Ph.D. Thesis, NU, 2006.

Inclusion Clusters: 3D Tomography

Damaged TiN Pair in Mod4330
(J. Sebastian, H.-J. Jou, QuesTek;
M. Uchic, AFRL)

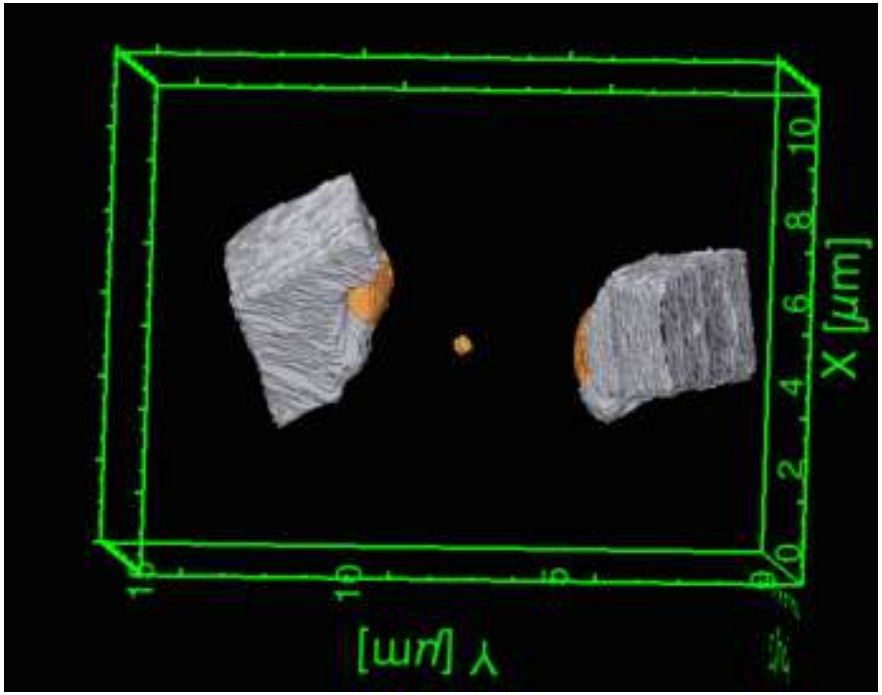

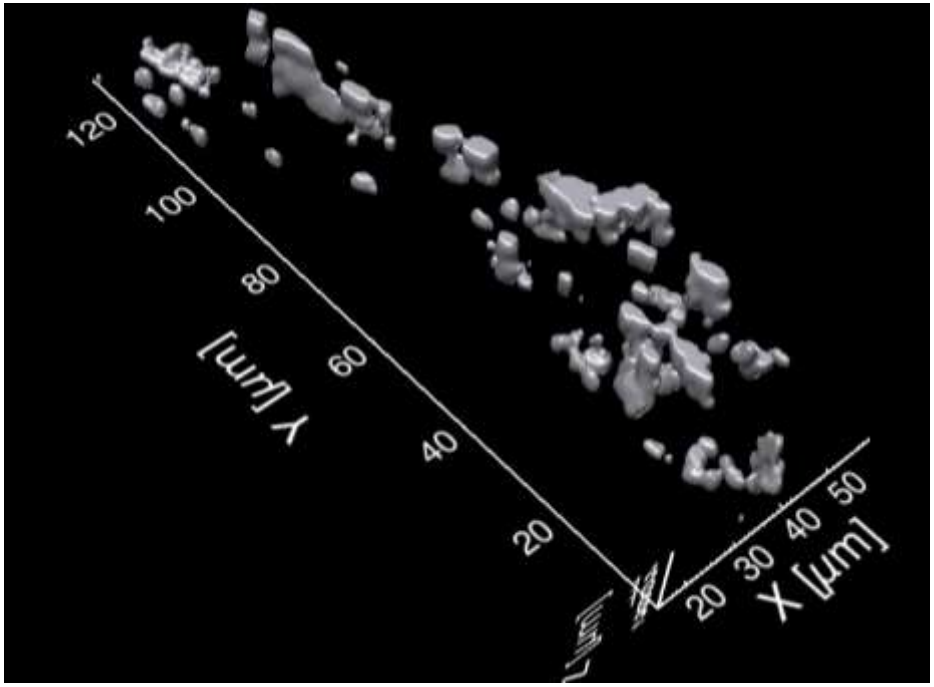

La_2O_2S Cluster in C61-La Gear Steel
(S. Chan, NU; G. Spanos, NRL)

Design Research Tools Consortium
Contract No. N00014-05-C-0241

3D Microstructure-Sensitive Fatigue Simulator

- Process simulation for prediction of critical locations
- 3D representation of observed potent nucleant clusters
- Micromechanical simulation of FIP evolution

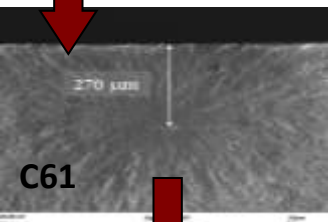

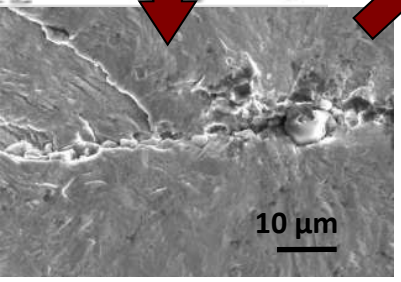

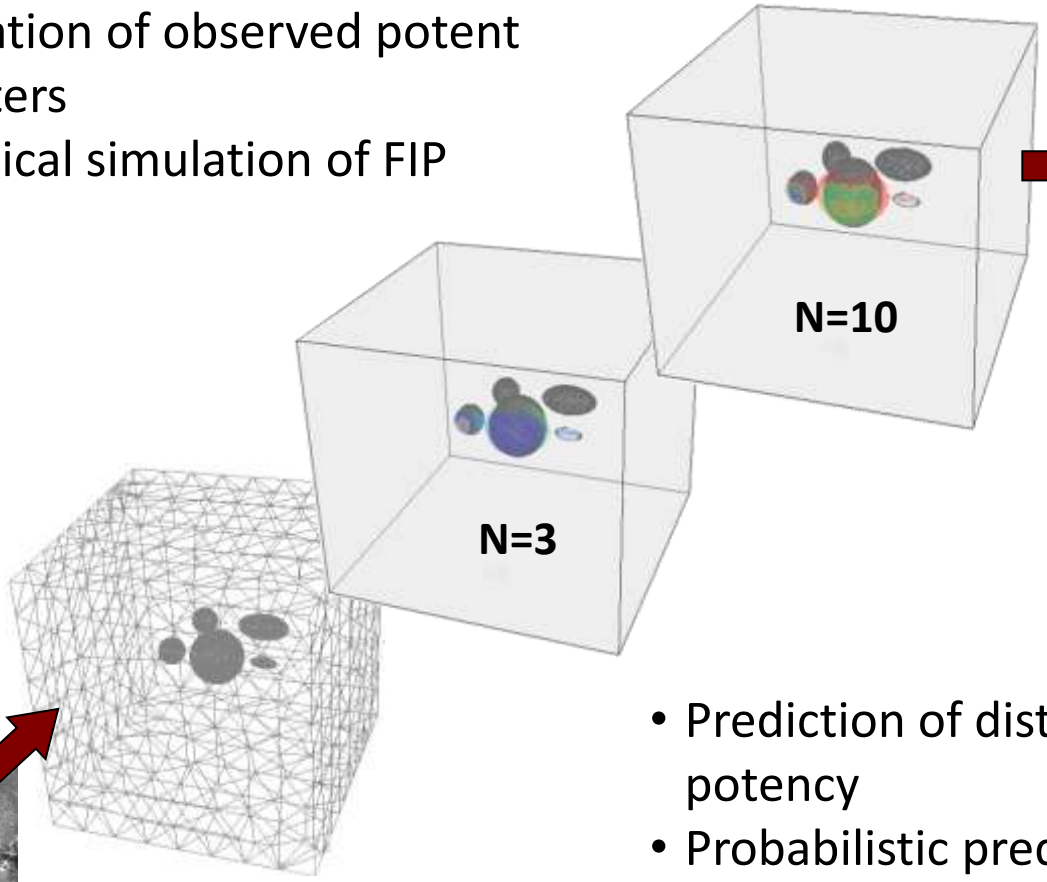

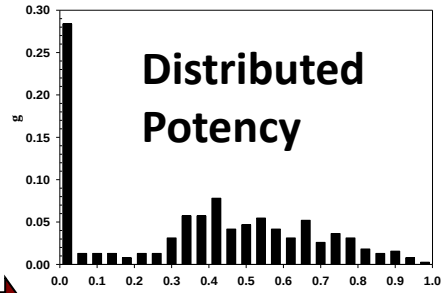

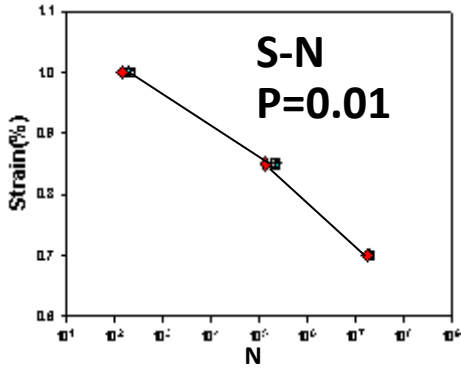

- Prediction of distributed nucleant potency
- Probabilistic prediction of minimum fatigue properties

R. Prasanna, D. McDowell, Georgia Institute of Technology

Modeling fatigue in Ni base superalloys

- **Demonstrated feasibility of microstructure-sensitive fatigue simulation and fatigue life prediction (p.2 & 3)**

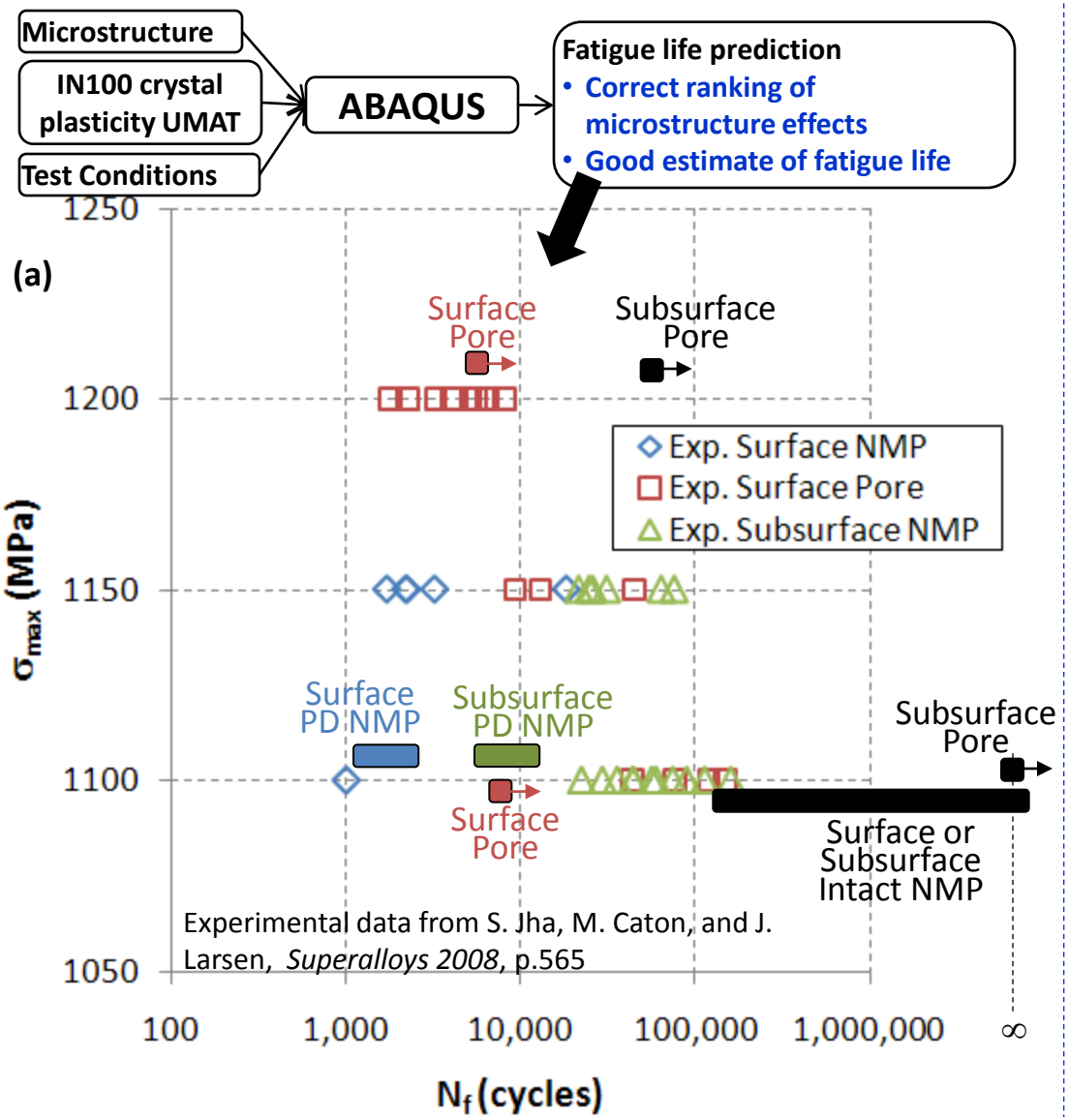

- **3D Tomographic Reconstruction Illustrated Microstructure Features Around Fatigue Initiation Site (p.4&5)**

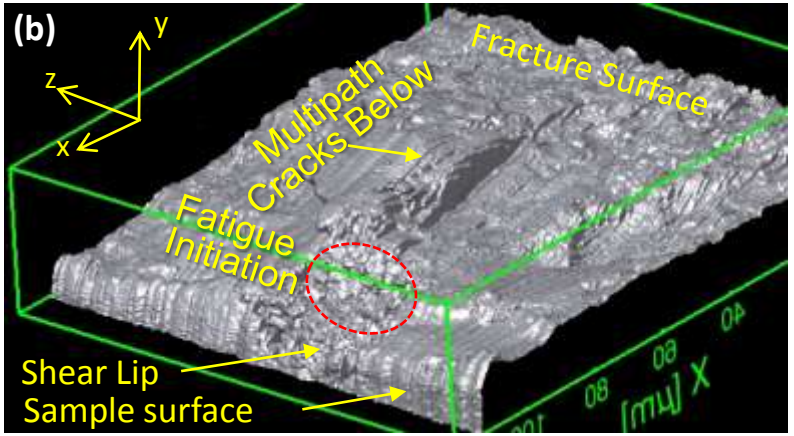

- **Synthesized fractographic and metallograhic data for NMP/pores (p.6)**

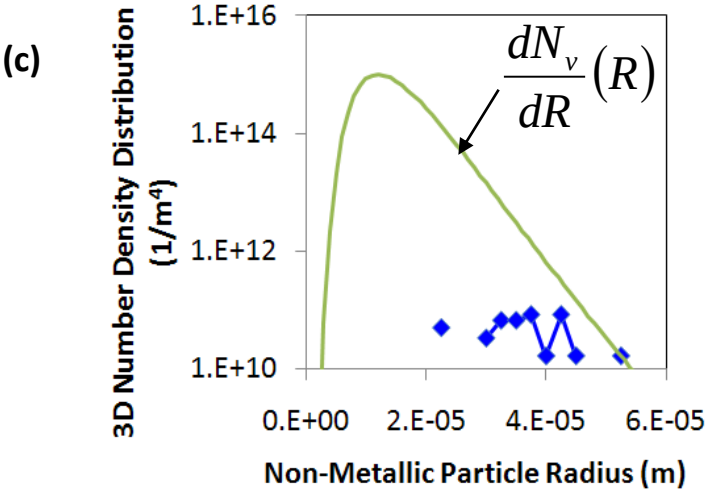

- **Developed approaches to incorporate dwell effects in transition zone (p.7)**

Fig. 4

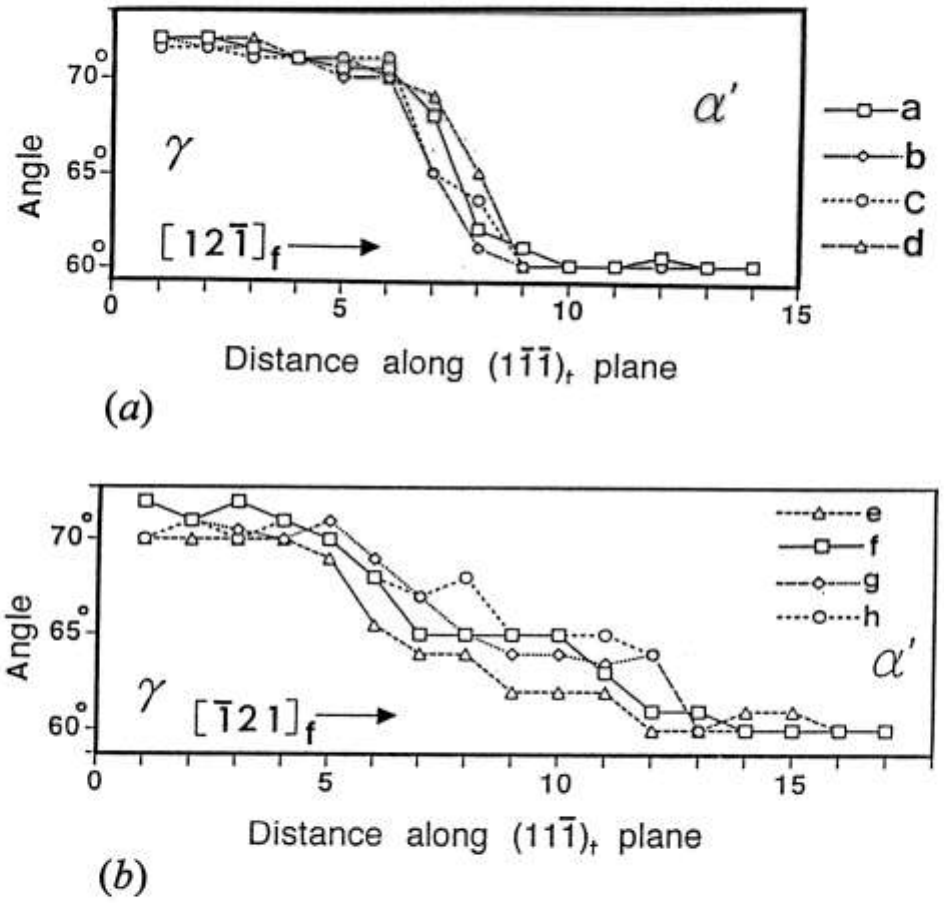

(*a*) Change in angle between $(11\bar{1})_f$ and $(1\bar{1}\bar{1})_f$ when crossing the interface in the $[12\bar{1}]_f$ direction on the $(1\bar{1}\bar{1})_f$ plane from the austenite region to the martensite region. The abscissa represents distance along the $(1\bar{1}\bar{1})_f$ plane in the $[12\bar{1}]_f$ direction in units of $a_f\sqrt{6}/4(= 0{\cdot}2192\,\text{nm})$. (*b*) Change in angle between $(11\bar{1})_f$ and $(1\bar{1}\bar{1})_f$ when crossing the interface in the $[\bar{1}21]_f$ direction on the $(11\bar{1})_f$ plane. The abscissa represents distance along the $(11\bar{1})_f$ plane in the $[\bar{1}21]_f$ direction in the same units as in (*a*).

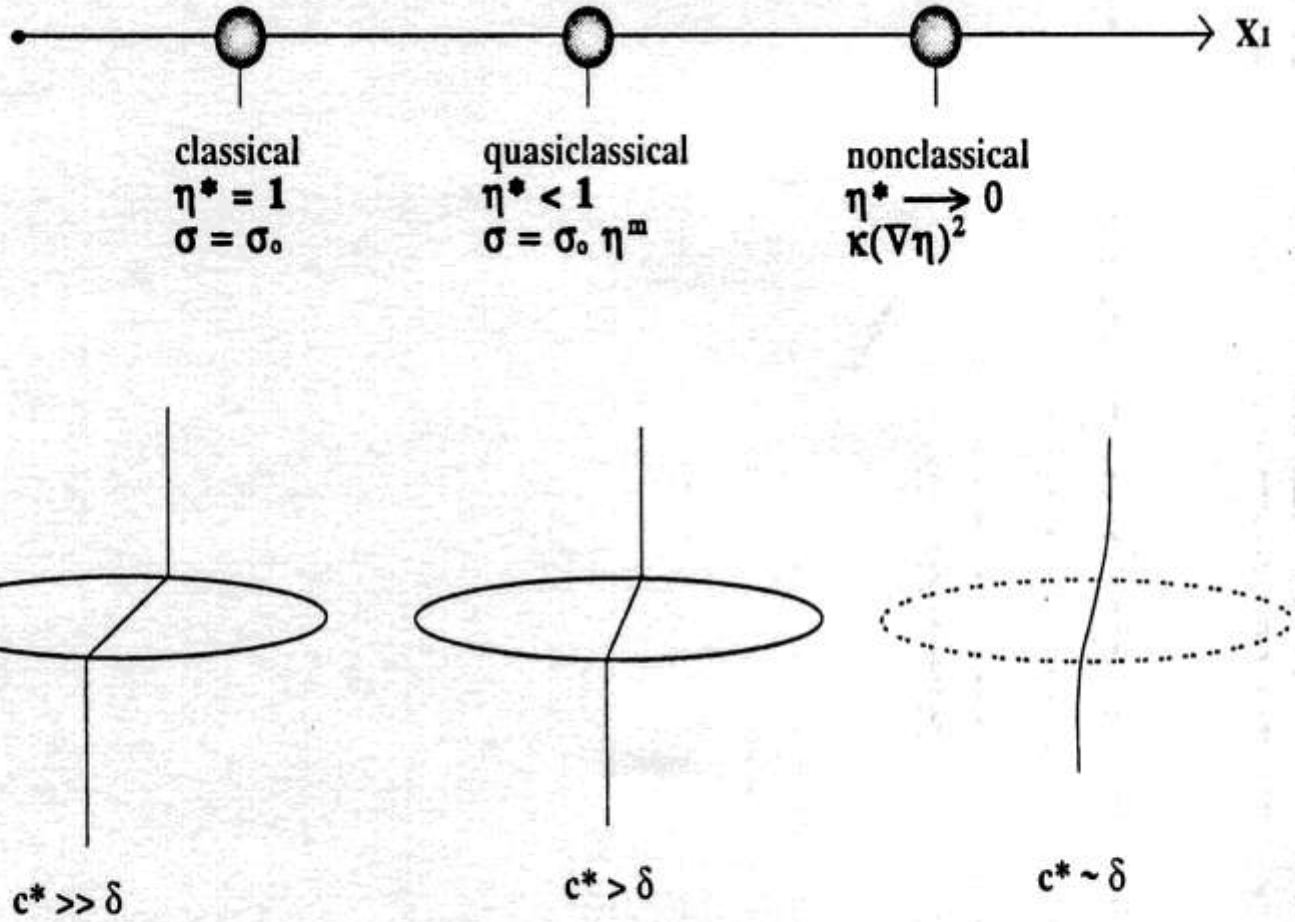

Fig. 8 Nucleation strain path. Schematic illustrations of nucleus structure in three regimes of behavior, with associated theoretical approximations

Fig8

Heterogeneous Martensitic Nucleation

Discrete Dislocation

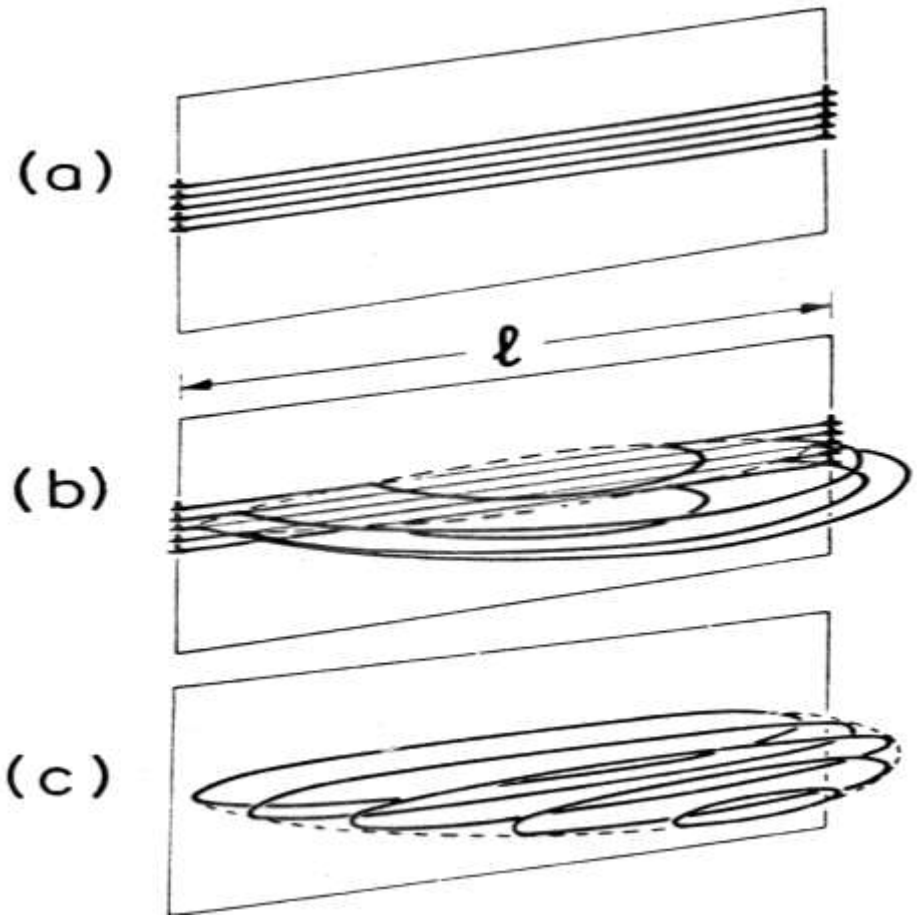

Ginzberg-Landau Continuum

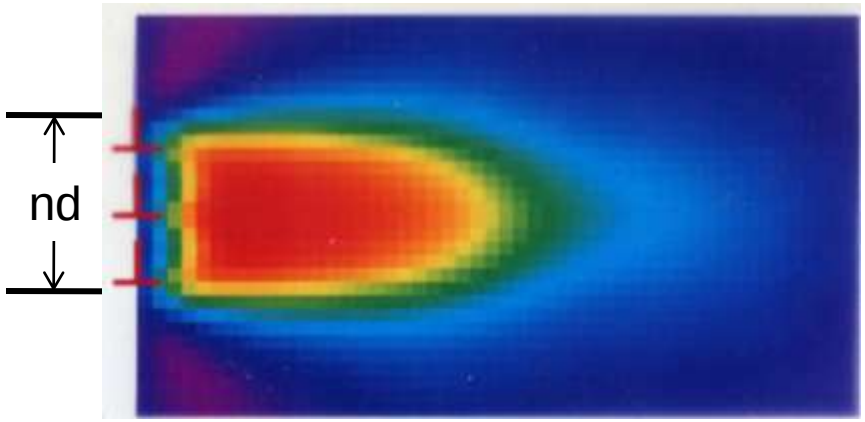

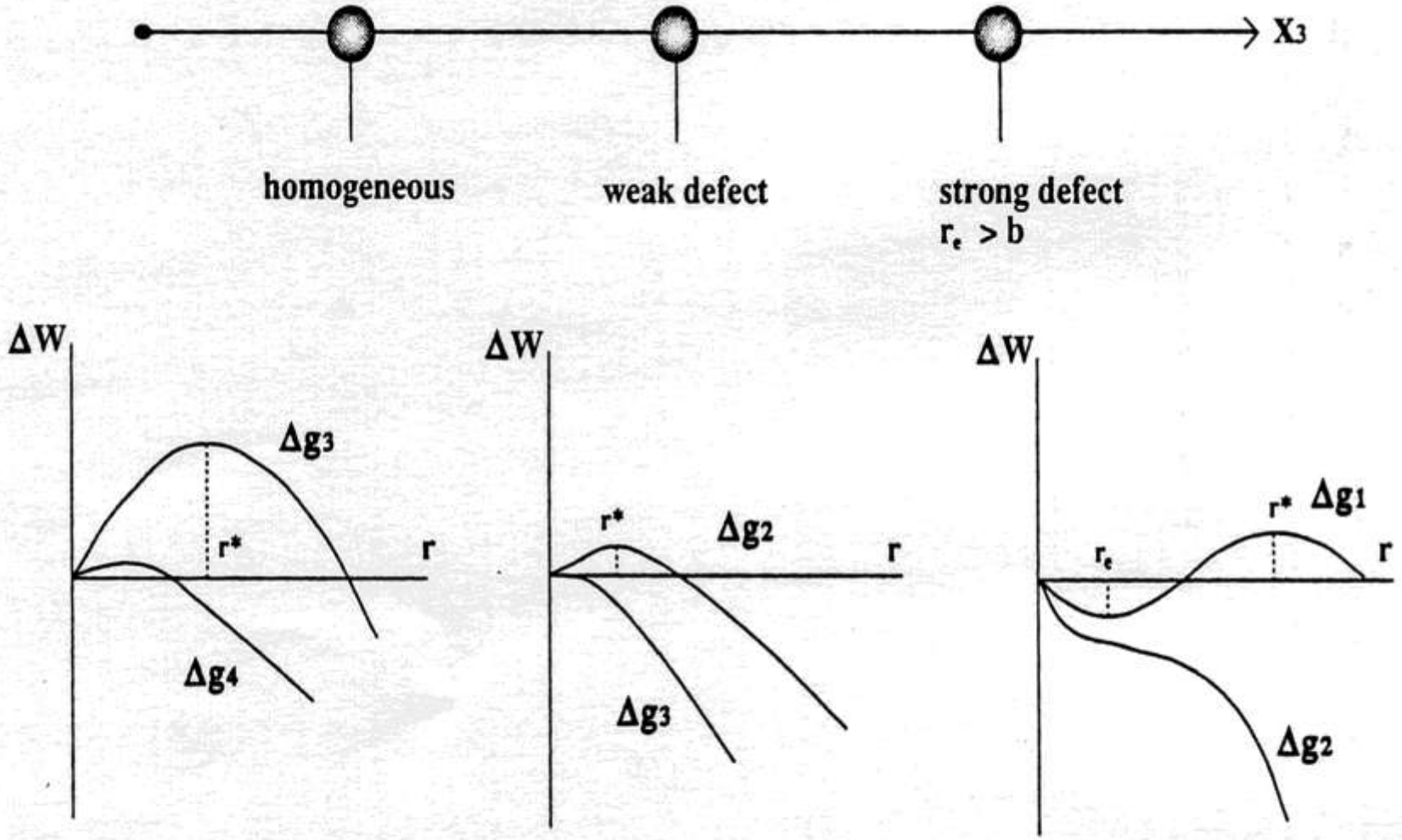

Fig. 15 Role of heterogeneity of nucleation. Schematic curves of energy (ΔW) versus size (r) depict behavior for homogeneous, weak-defect heterogeneous, and strong-defect heterogeneous nucleation at four levels of driving force (Δg).

M_s Temperature Validation

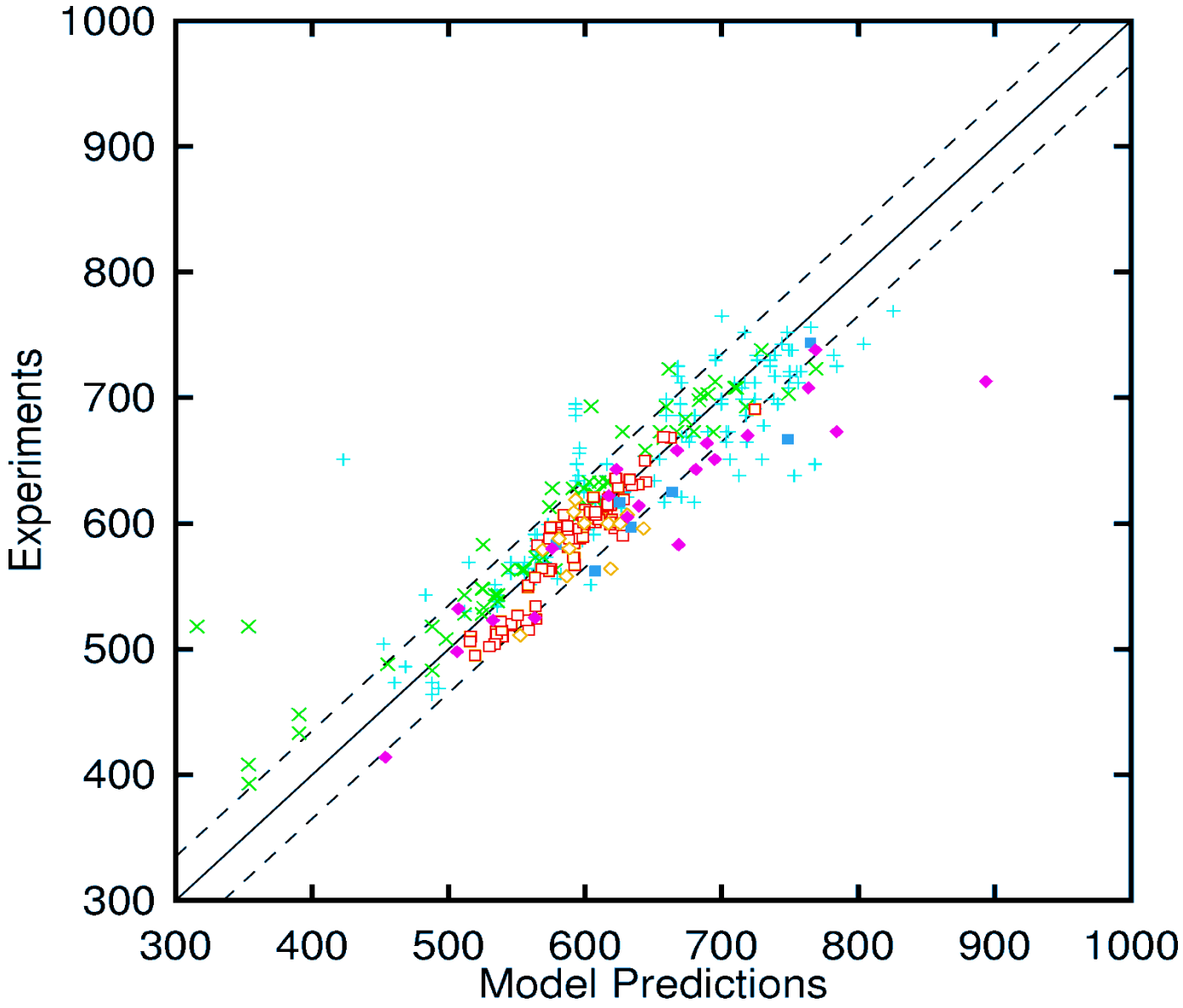

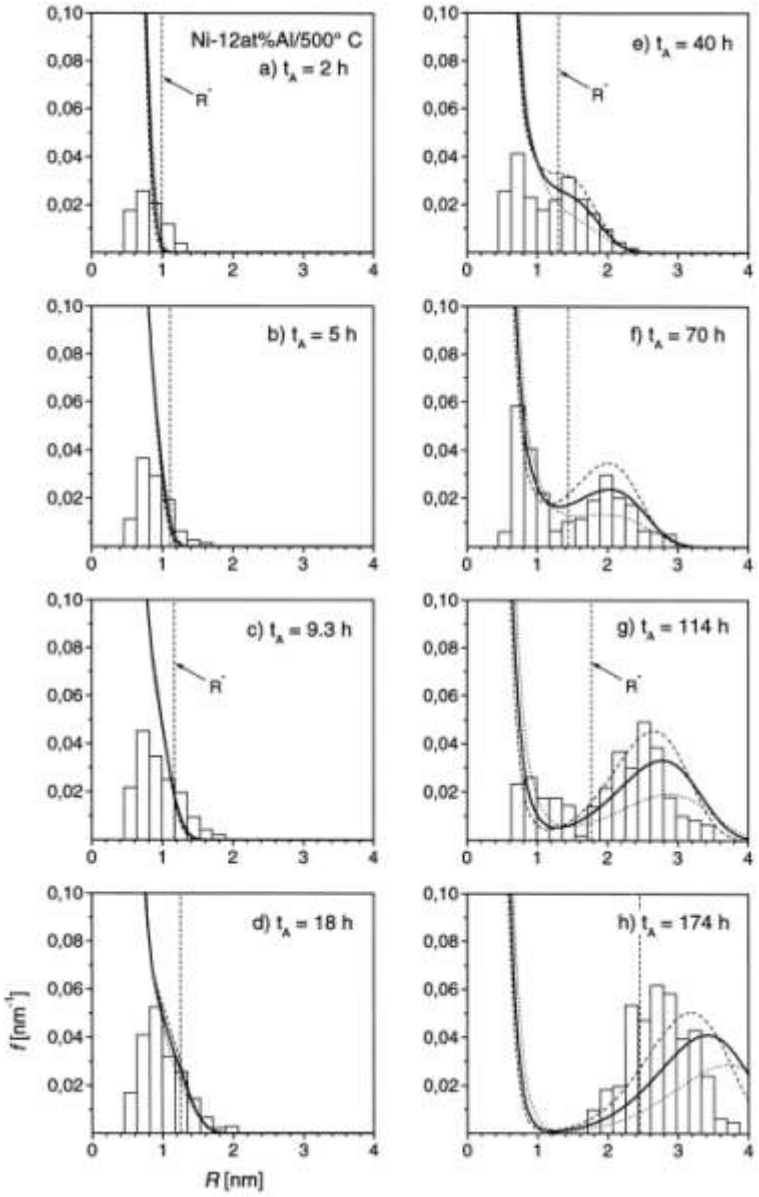

Ni-12 at.% Al aged at 500˚C

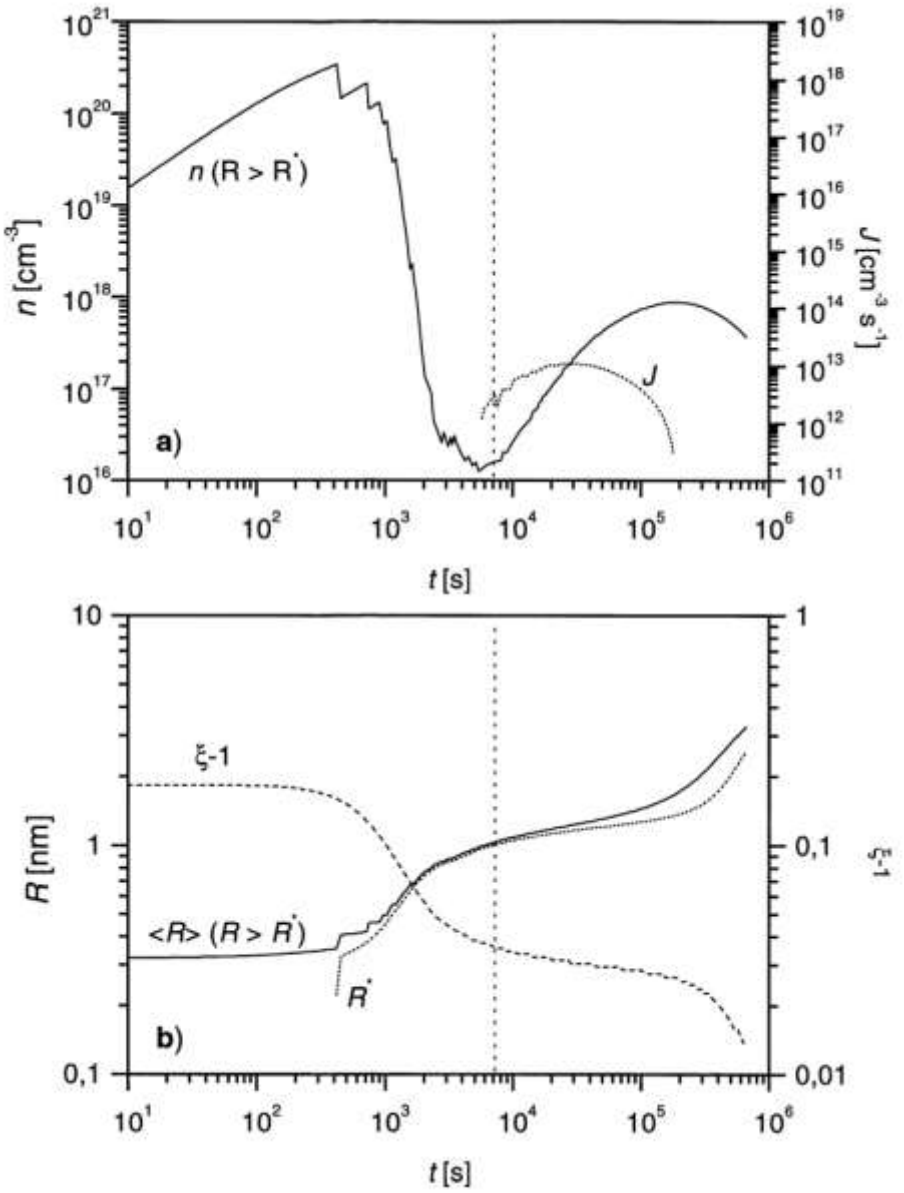

Reference: Staron, P. and Kampmann, R., (2000) 'Early-stage decomposition kinetics in Ni-Al alloys—II. Cluster dynamic modelling of former experimental results', *Acta Materialia*, 48:713-720.

High Pressure: *a new Realm*

Daniel Orlikowski

Condensed Matter and Materials Division

Physical and Life Sciences Directorate

Lawrence Livermore National Laboratory, Livermore, CA

Maui, Hawai`i

UCRL-PRES-xxxx

This work performed under the auspices of the U.S. Department of Energy by Lawrence Livermore National Laboratory under Contract DE-AC52-07NA27344.

Melt-line Kinetics Team: spanning time scales

Nucleation & Growth:

- Molecular Dynamics: D. Richards, J. Glosili
- DTEM: T. Lagrange, B. Reed
- dDAC: W. Evans + Post Doc.
- Any universal scaling of rates, heterogeneity, phase fraction

Coalescence:

- Phase Field Simulations: J. Belak, M. Tang
- DTEM + dDAC
- Compression experiments + X-ray: J. Hawreliak, D. Swift
- Growth and micro-structure: M. Kumar

Continuum strength:

- crystal continuum modeling: N. Barton
- Compression experiments
- “physics” code: thermo-mechanical, poly-crystal

Model: R. Minich, D. Orlikowski

- self-consistent, homogenization, final continuum model

Materials on Demand :: Pressure induce phase transitions

Amorphous Sulfur via Pressure

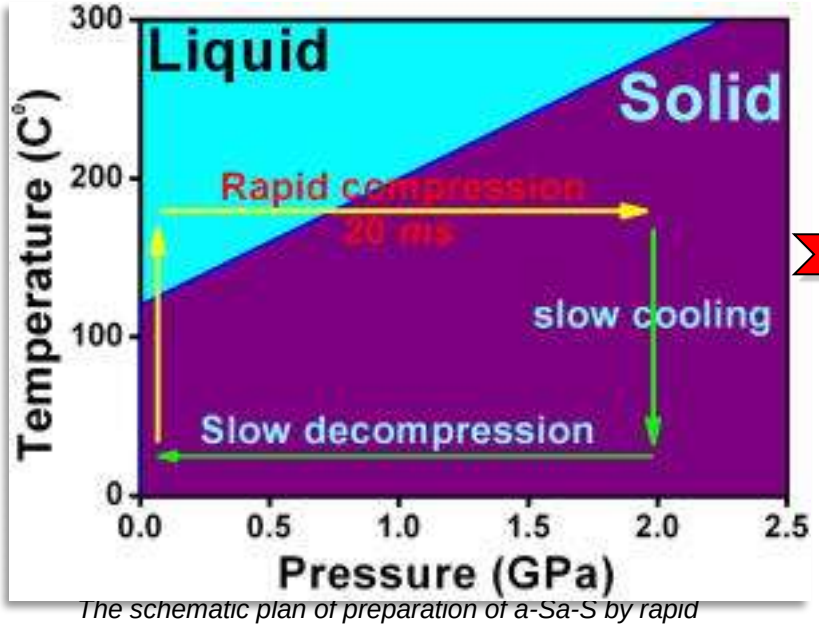

The schematic plan of preparation of a-Sa-S by rapid compression based on the liquid-solid phase diagram of sulfur.

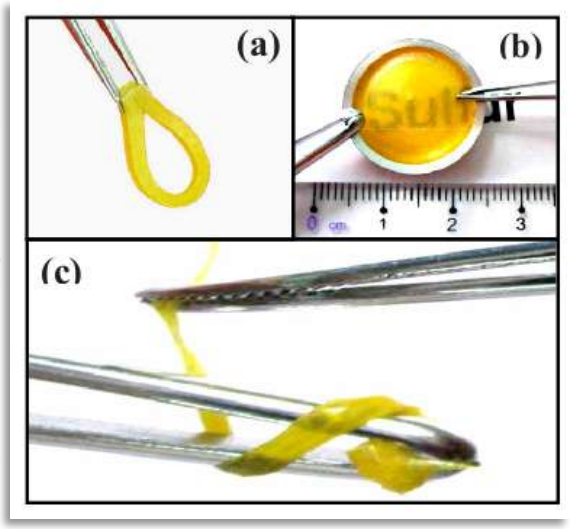

Yu et al. App. Phys. Lett. 2009

Mypolex Nano-diamond abrasive

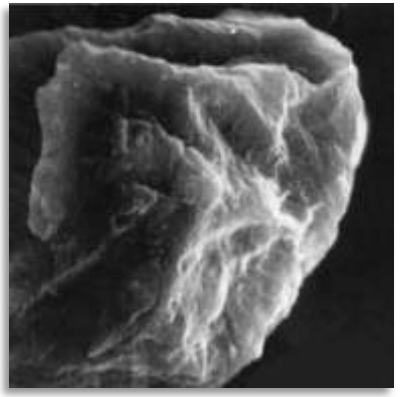

Vereshagin, et al. 1993

➡ Materials for industrial applications

Icy planets: Water phases make the difference

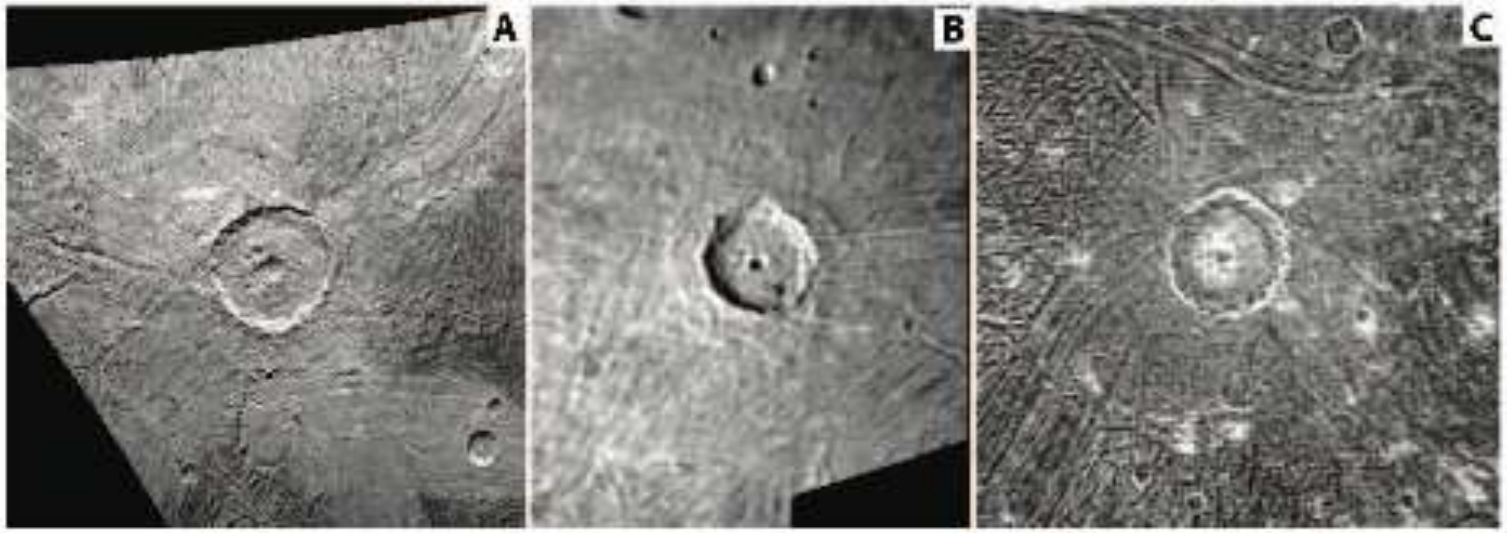

Figure 9: Examples of central pit craters on Ganymede: Isis crater, 73 km in diameter (A); Sebek crater, 64 km in diameter (B); and Bes crater, 62 km in diameter (C). (Voyager images FDS 20640.33, 16405.48, and 20637.41.)

The character of these craters are determined by the ice phases of Water.

(Senft & Stewart 2009)

Kinetics model was not implemented.

Path Contributions to a Final State: sketch

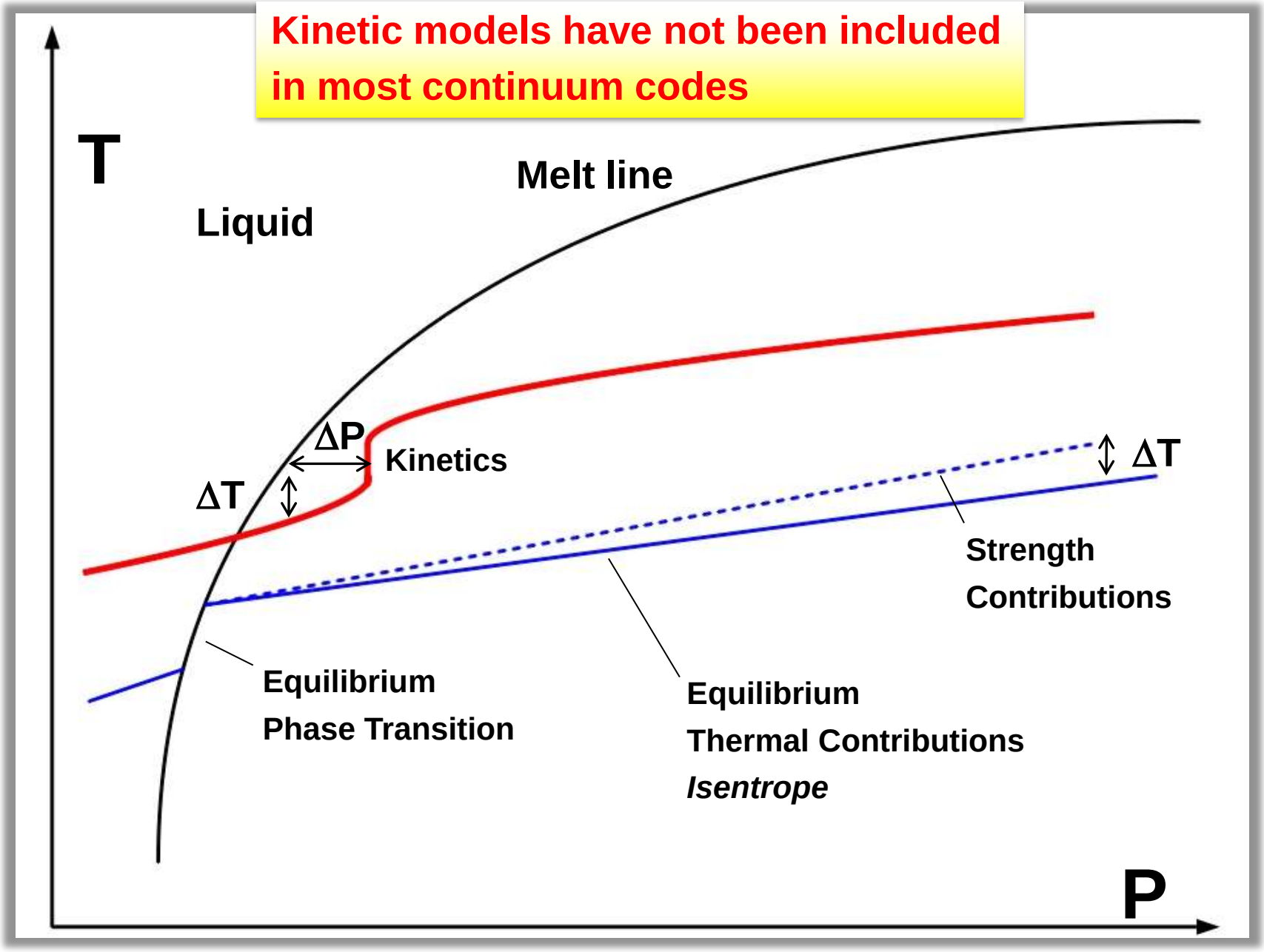

Recent observations: water

Intensity measurement

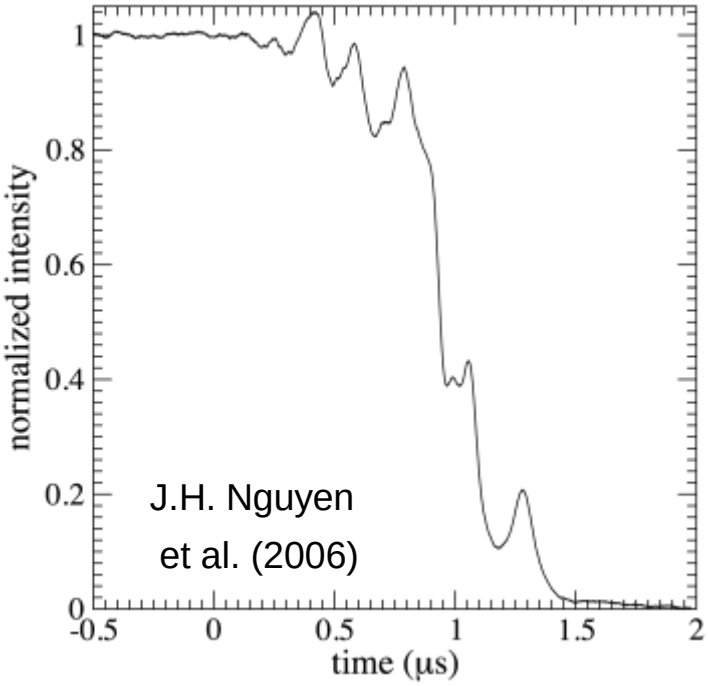

Imaging Ice Formation

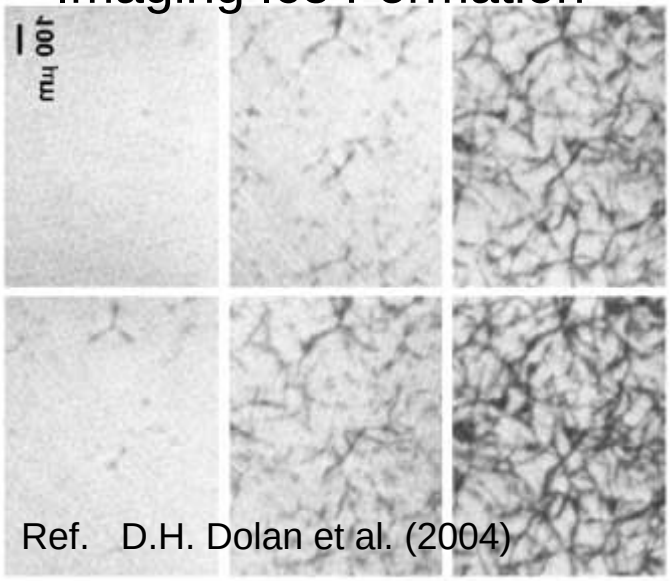

Dyna-DAC: G.W. Lee et al. (2006)

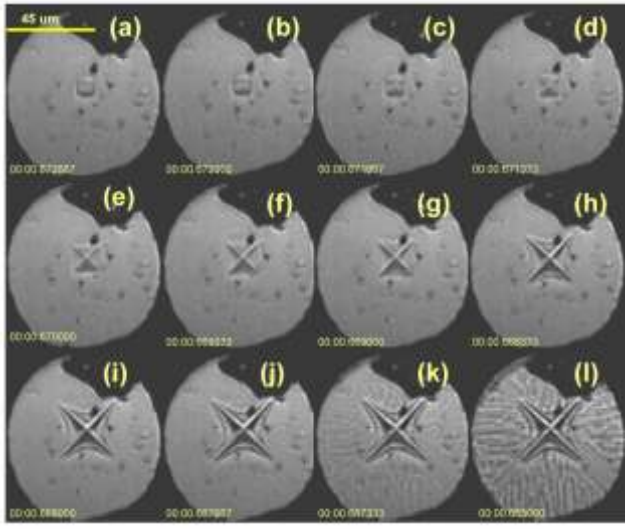

0.1mHz-20kHz => 0.1-10^4 1/s

Intensity measurements of Ice nucleation/growth at an interface

Dendritic or fractal growth

Interface particle velocities that indicate over-driven and relaxation processes occur.

Pressure loading dependence:

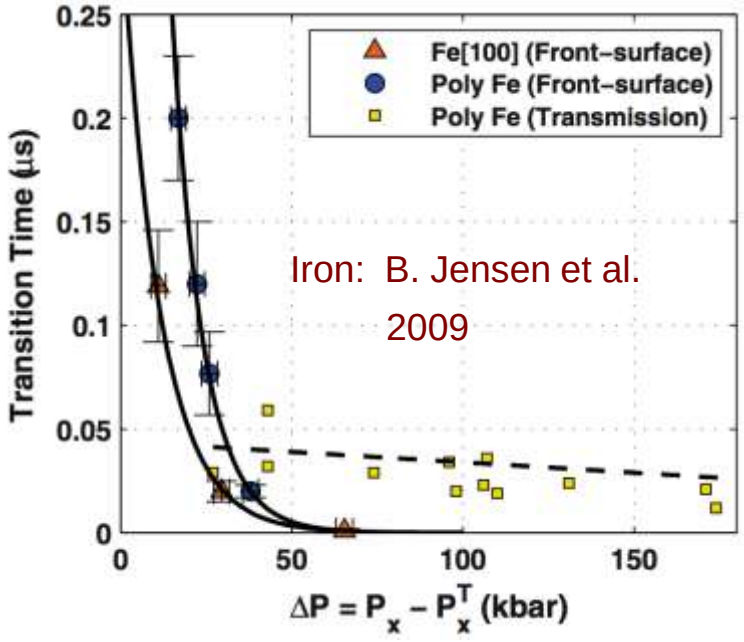

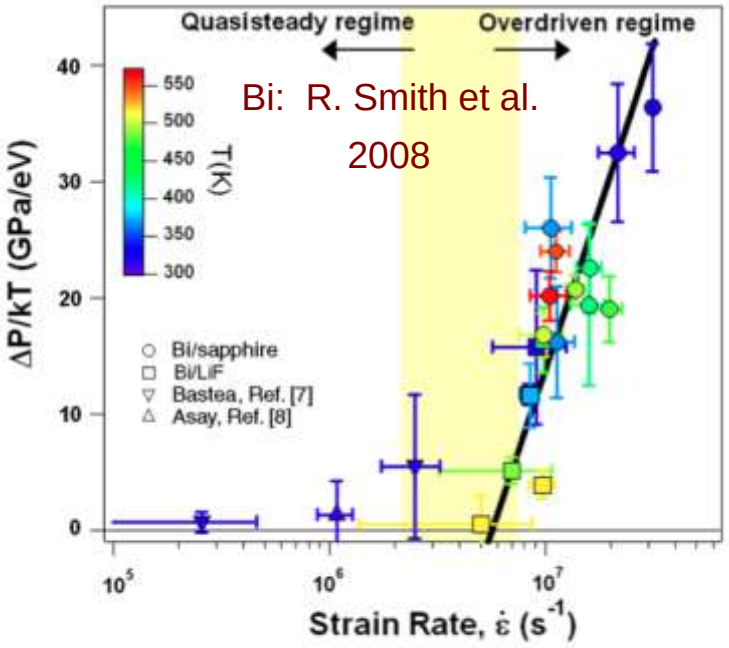

FIG. 5 (color online). $\Delta P/kT$ as a function of strain rate across equilibrium Bi I-II equilibrium phase boundary.

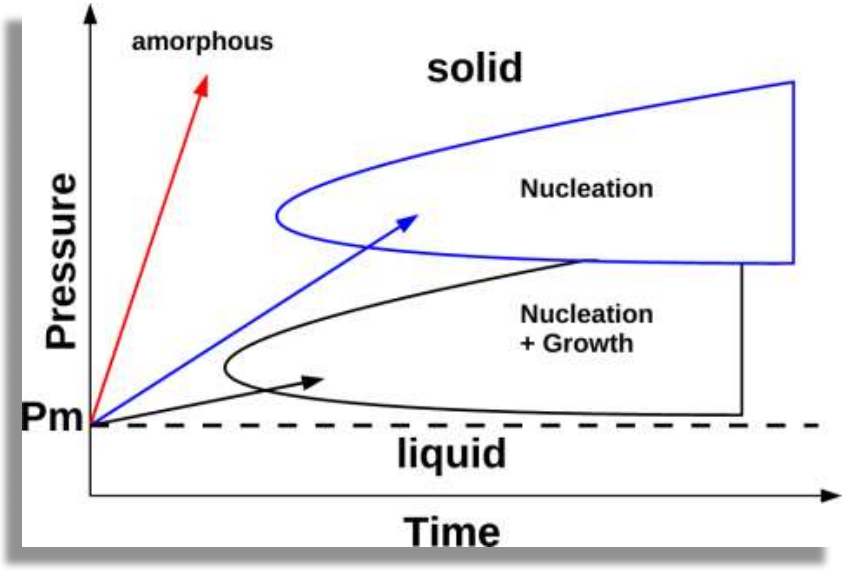

Driver rate may result in varying morphology

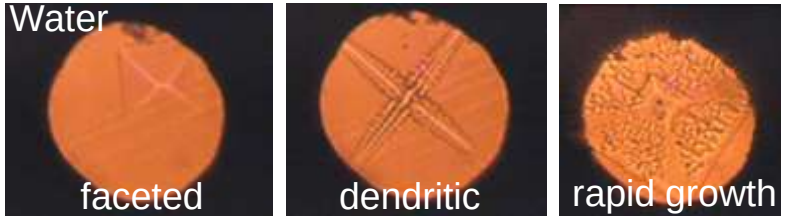

Increasing compression rate

Ref. W.J. Evans

Melt-line kinetics project flow:

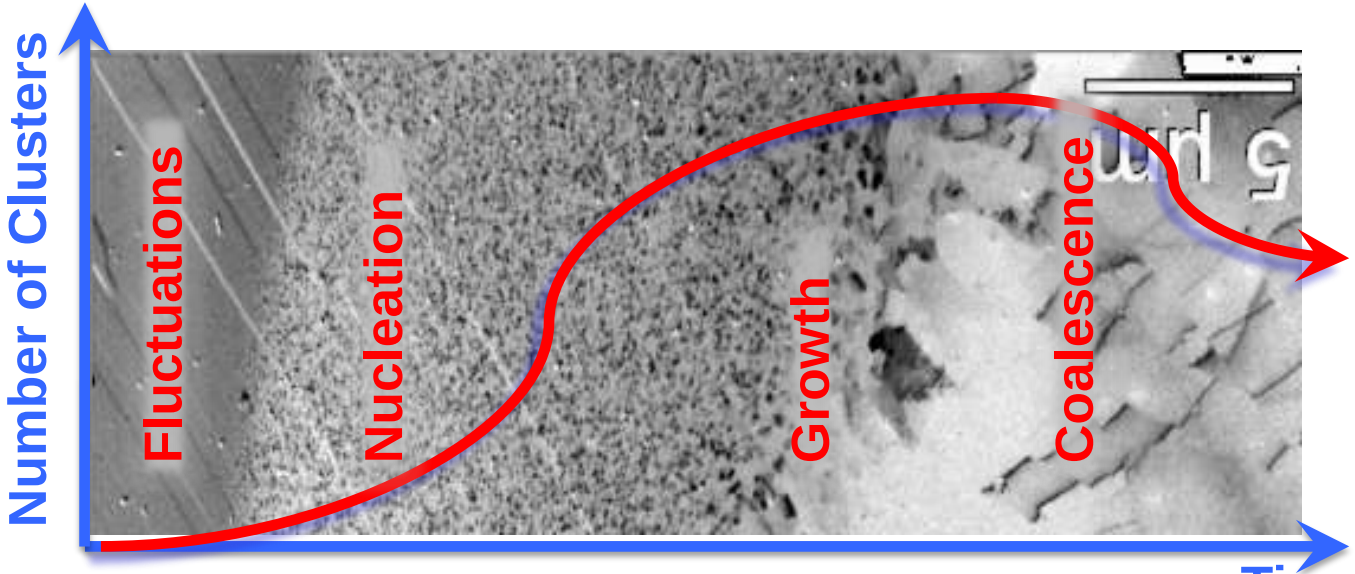

ps - ns

ns - μs

μs +

DTEM, dDAC, LPXP ↔ DTEM, dDAC ↔ Compression experiments

Atomistic Modeling — Phase Field Modeling — Crystal Continuum Modeling

Hydro-code Model ↔ Validation Exp.

Each time scale needs to be benchmarked against experiment.

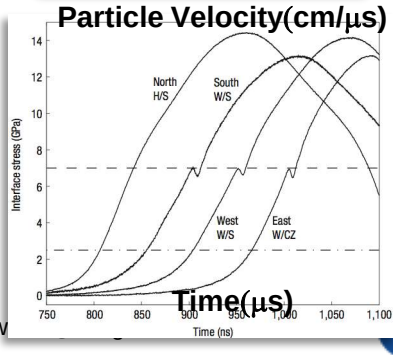

From atomistics to the continuum…

Simulations

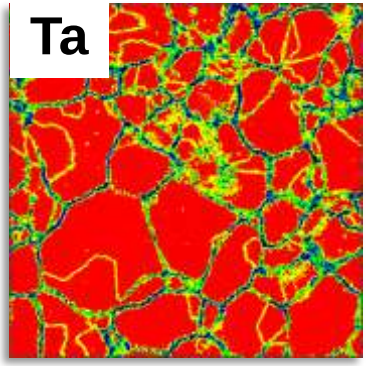

D. Richards, et al.

Nucleation Rates

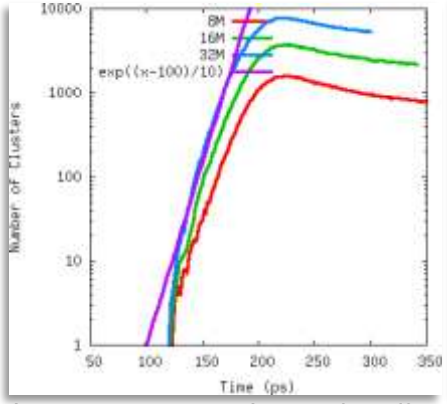

j=1e-12 to 5e-10 clusters/A^3/fs

Growth Rates

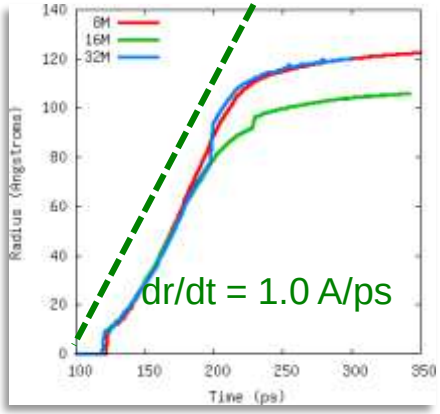

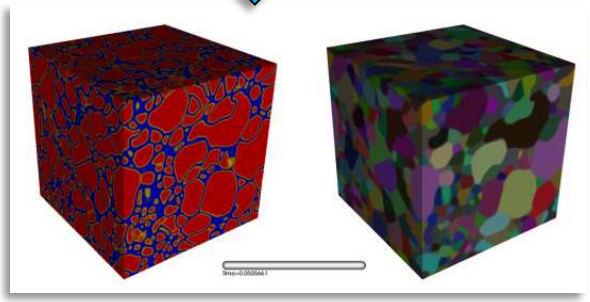

Phase Order Parameter

Crystallographic Quaternion Order Parameter

J. Belak, et al.

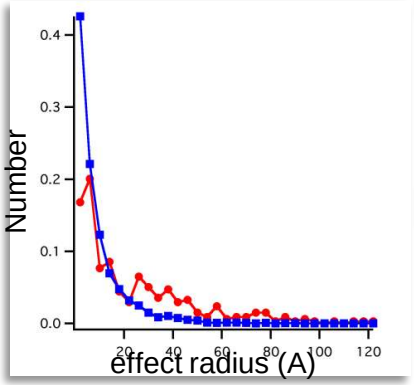

Model

Continuum

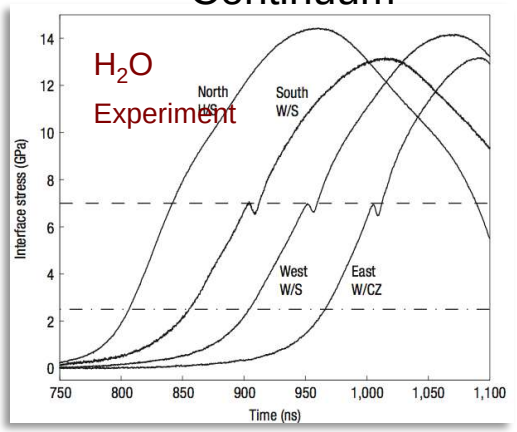

D. Dolan et al.(2007)

Development toward a more physical model (Minich)

CNT:

Free Energy accounting for surface energy

$$\Delta G(N,P,T) = \underbrace{a\,\sigma\,N^{\frac{2}{3}}}_{\text{Surface}} - \underbrace{N\Delta\mu}_{\text{Volume}}$$

Critical Energies and lengths

$$\Delta G_c(N_c,P,T) \approx \frac{\sigma^{\alpha}}{\Delta\mu^{\beta}}$$

Distribution of size and shapes

$$J_n = \int j_n(R,t)dR$$

Phase fraction (iterative)

$$\dot{\phi} \propto \Delta G\, J(N,P,T)\ [1-\phi]\ \Delta\mu(N,P,T)$$

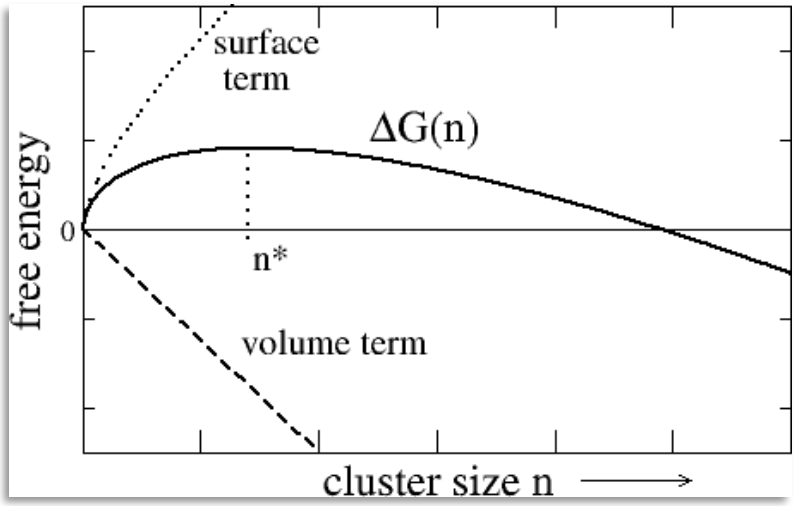

Phase fraction does **NOT** describe distribution: size/shape of nucleants

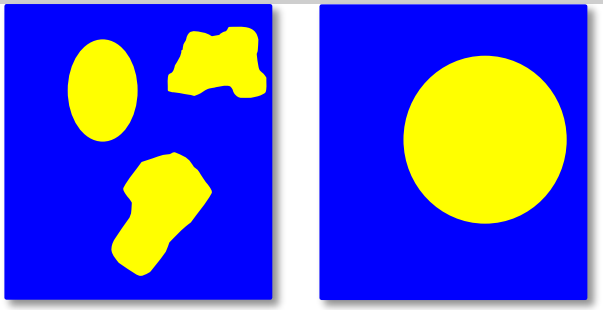

Kolmogorov type phase fraction

$$f_2 = 1 - exp\left[-\frac{A}{4}J_d v_{int}(t-t_0)^4\right]$$

Phase fraction evolution (Minich)

Phase fraction rate:

$$\dot{\Phi} = \Lambda \Delta G^{\Gamma} \, Exp\left[-\frac{B}{\Delta G}\right] \, (1-\Phi) \, \left[a \Delta G^{\gamma} \Phi - b \Phi^{\alpha}\right]$$

Driven Nucleation Percolation Growth

Self-consistent hydro-code time step:

$$\delta t \, \frac{dP_r}{d\Phi} \, \dot{\Phi} + P_{rm} = P_r$$

Melt-line: Pc and Tc

Exponents are left open b/c of possible fractal crystallites, not smooth nor round

Four open parameters:

nucleation rate, over-pressurization, phase fraction dependence, percolation

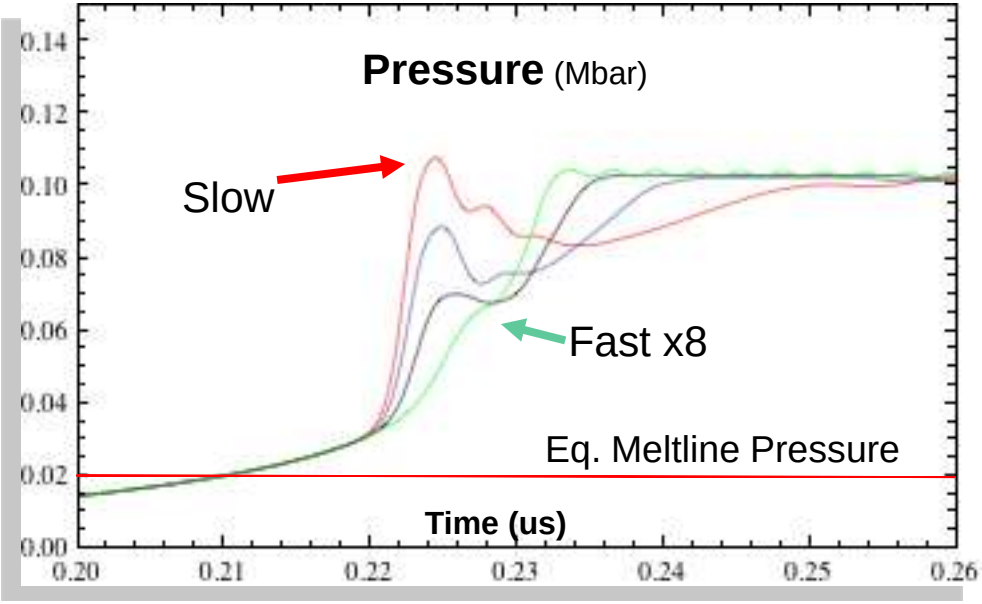

Over-driven transition with relaxation similar to exp.

Parameterization is meant to be bottom-up

Lambda rate ~ 10^5

Critical pressure is

considered the meltline: P~ 2 GPa

Rate of change of Order parameter

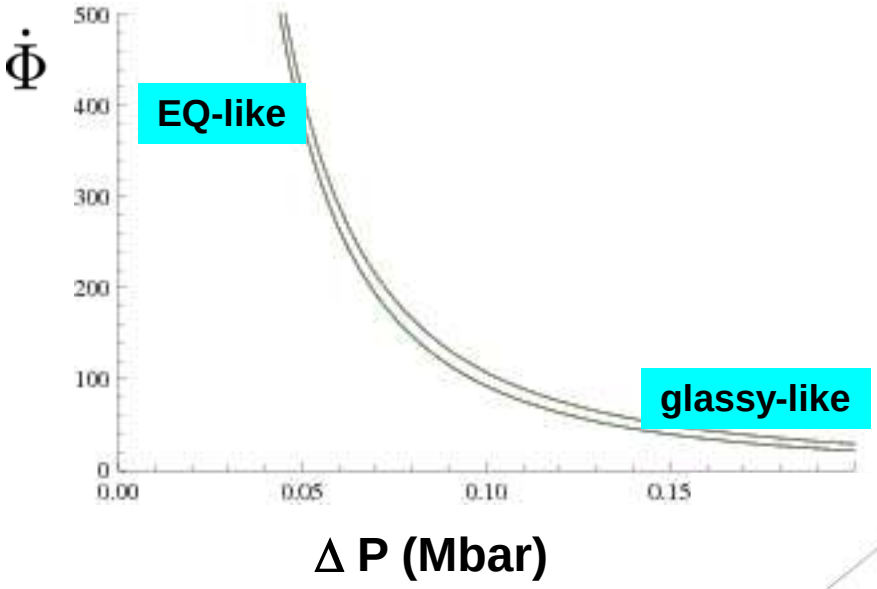

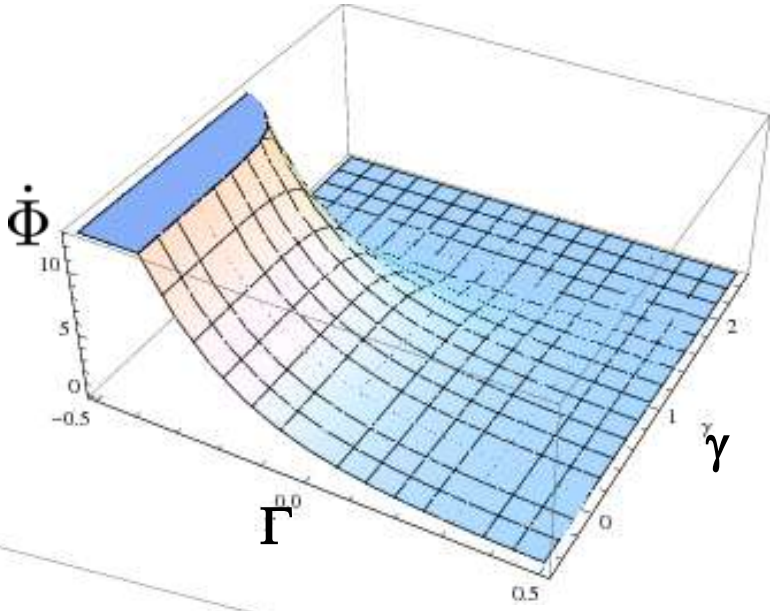

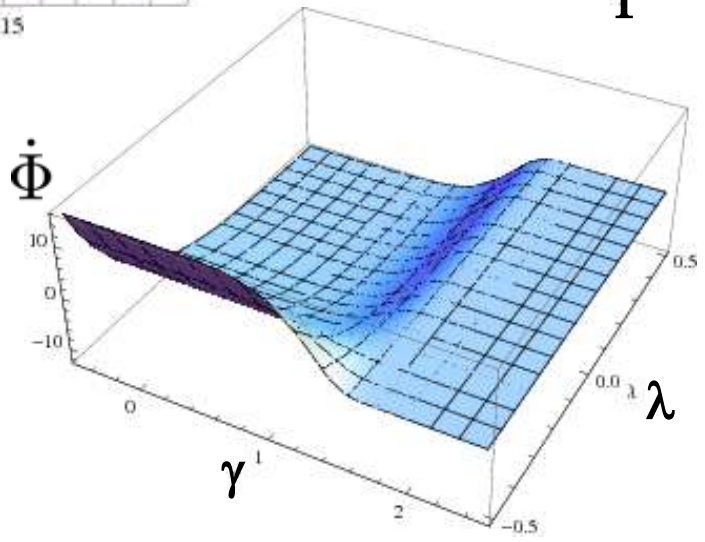

$$\dot{\Phi} = \Lambda(P_r - P_c)^{\Gamma}\ Exp[-\frac{B}{(P_r - P_c)^{y}}]\ (1-\Phi)\ [a(P_r - P_c)^{\lambda}\ \Phi - b\Phi^{\alpha}]$$

Water phase diagram

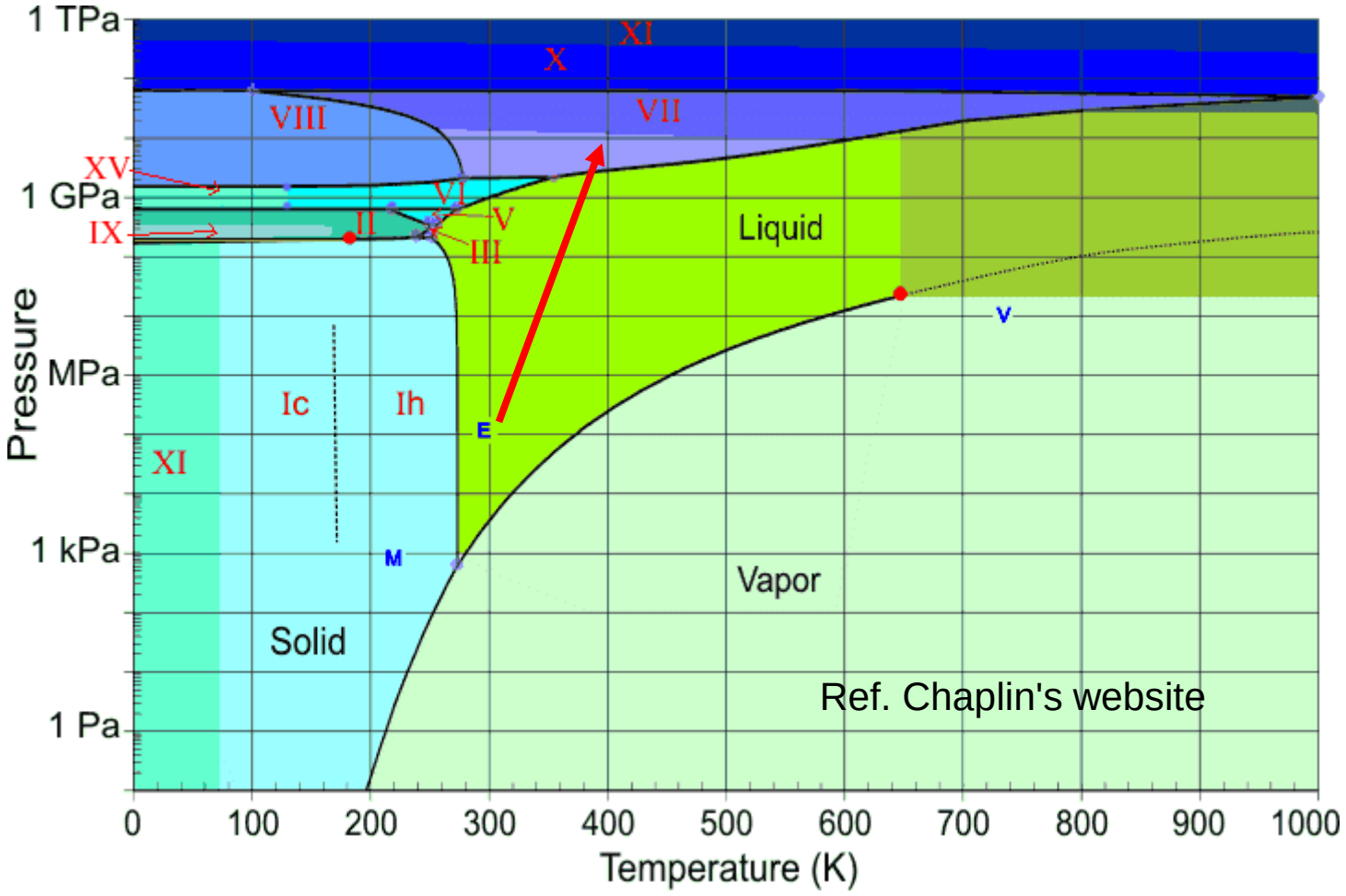

Prototypical observations to be modeled: compressed water

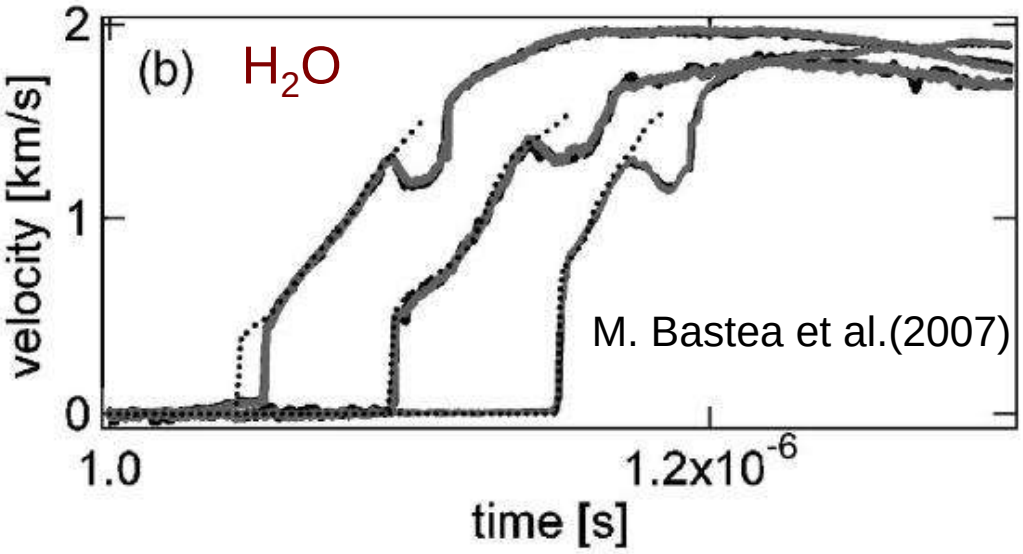

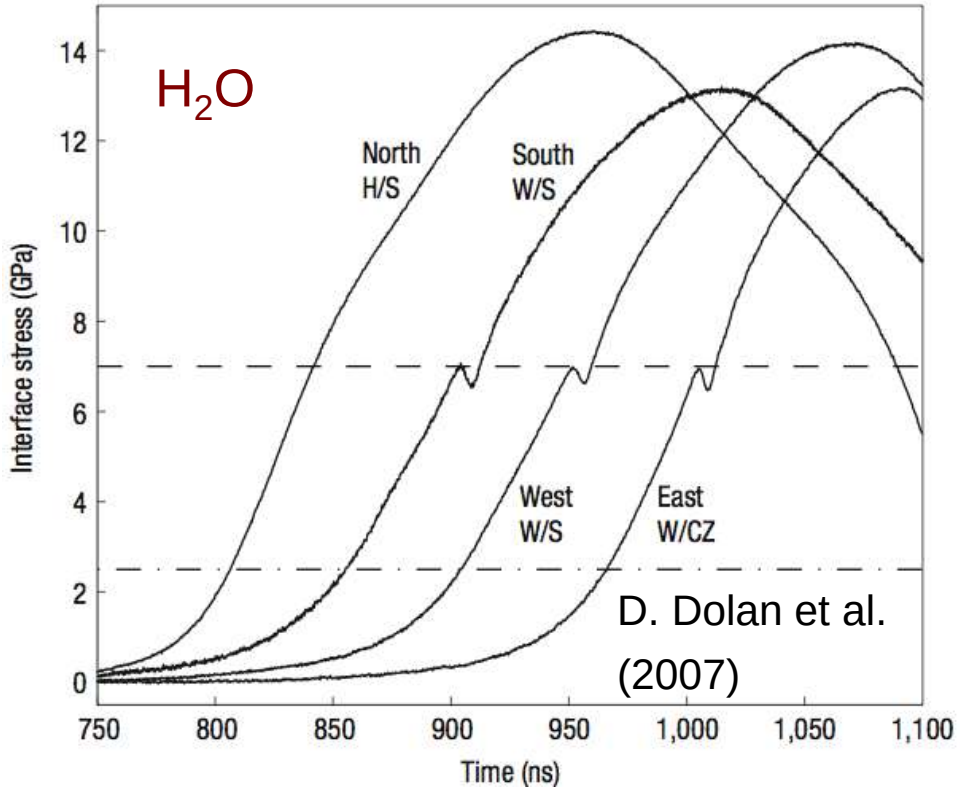

PMMA

Sapphire

Exp. Input wave are not known well
Impurities have been minimized

Hydro phase transformation: compression rate dep.

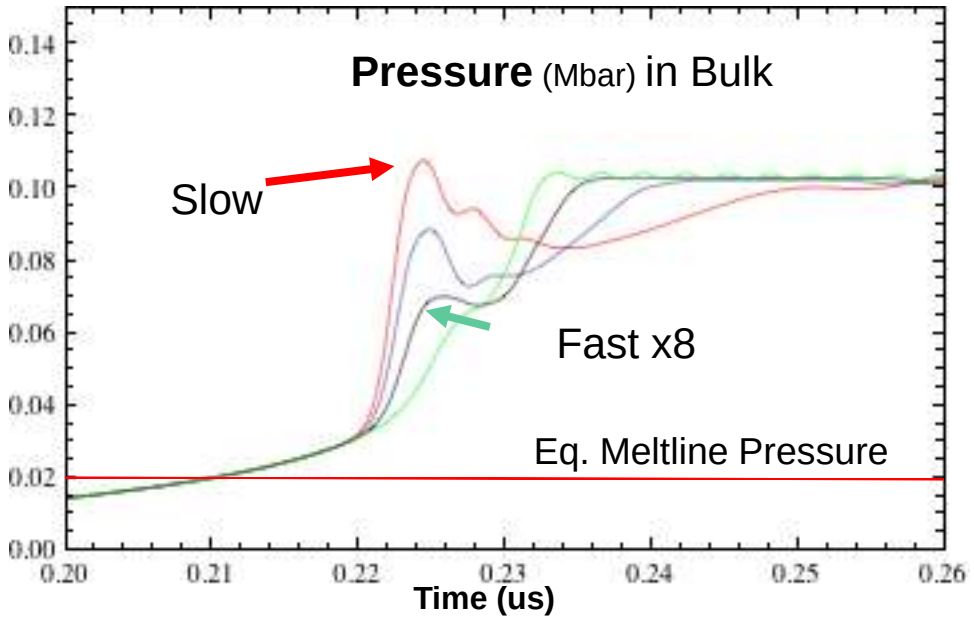

Over-driven transition
with relaxation similar to exp.
Parameterization is
meant to be bottom-up

Nucleation rate
Critical pressure is
considered the meltline: P~ 2 GPa

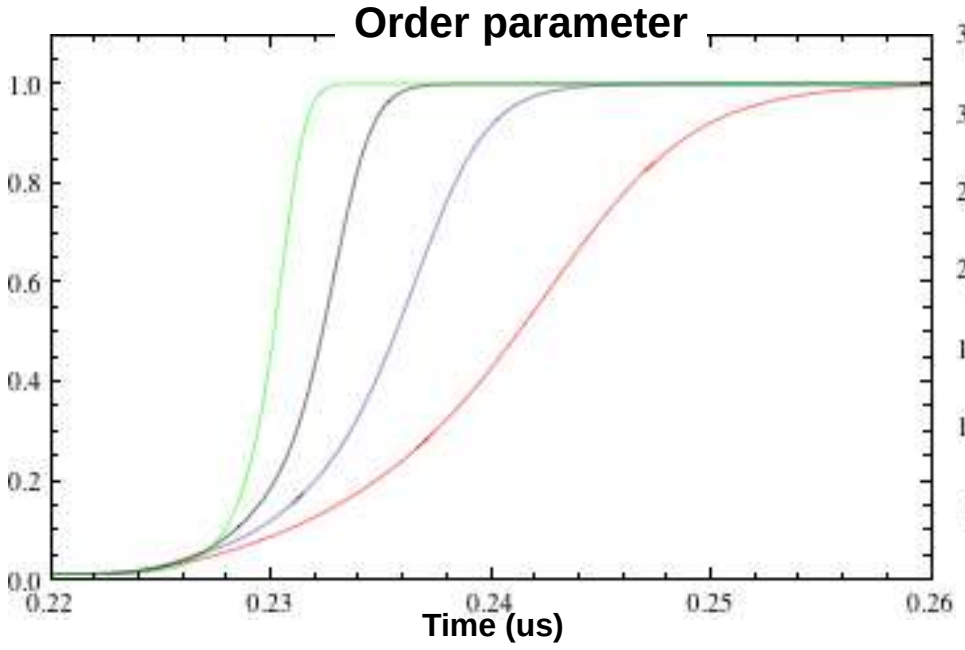

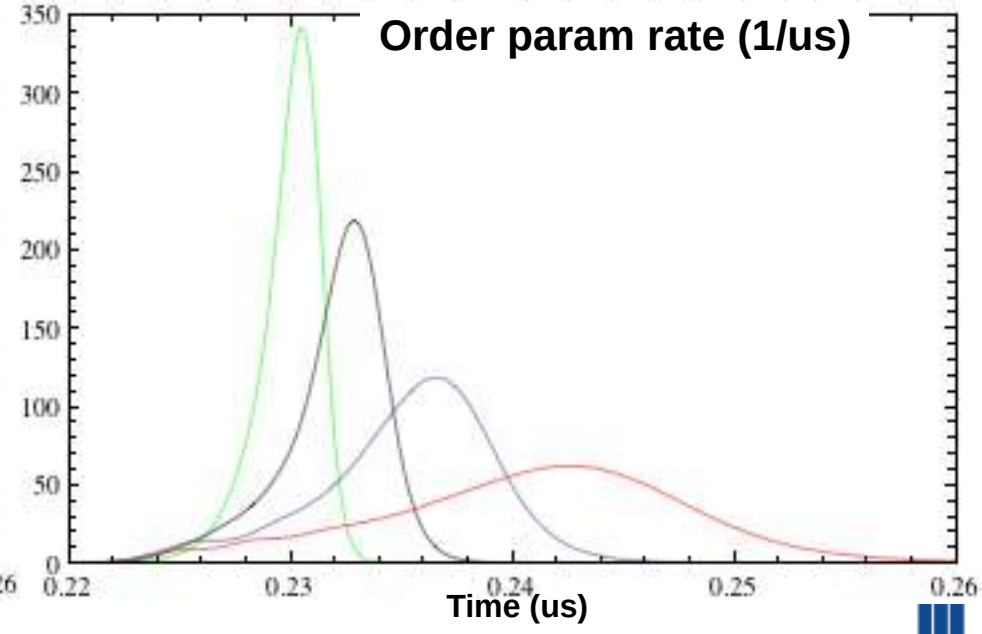

Evolution of compression as function of distance

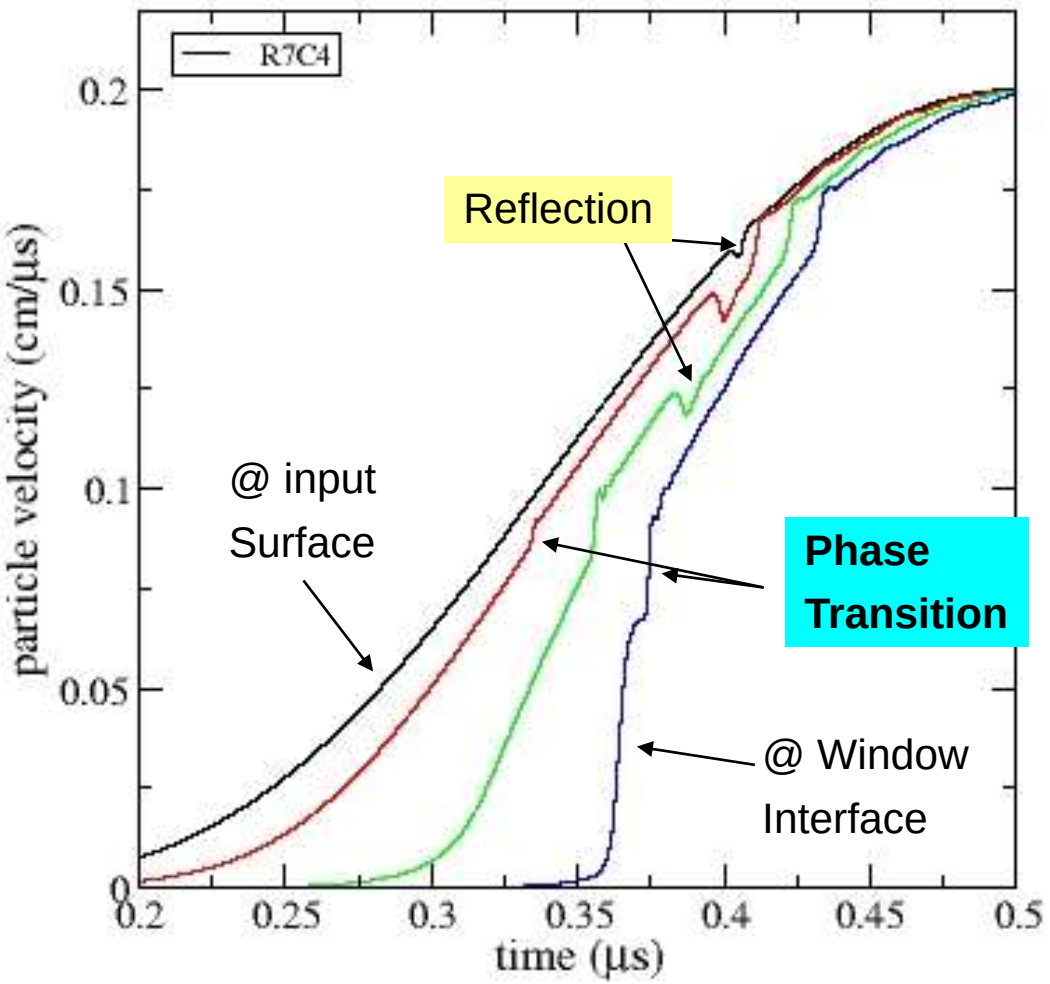

With the model,
Interpretations are difficult

Non-linear effects between
Compression wave
PT model
Reflections

Pressure Wave Snapshots without phase transition

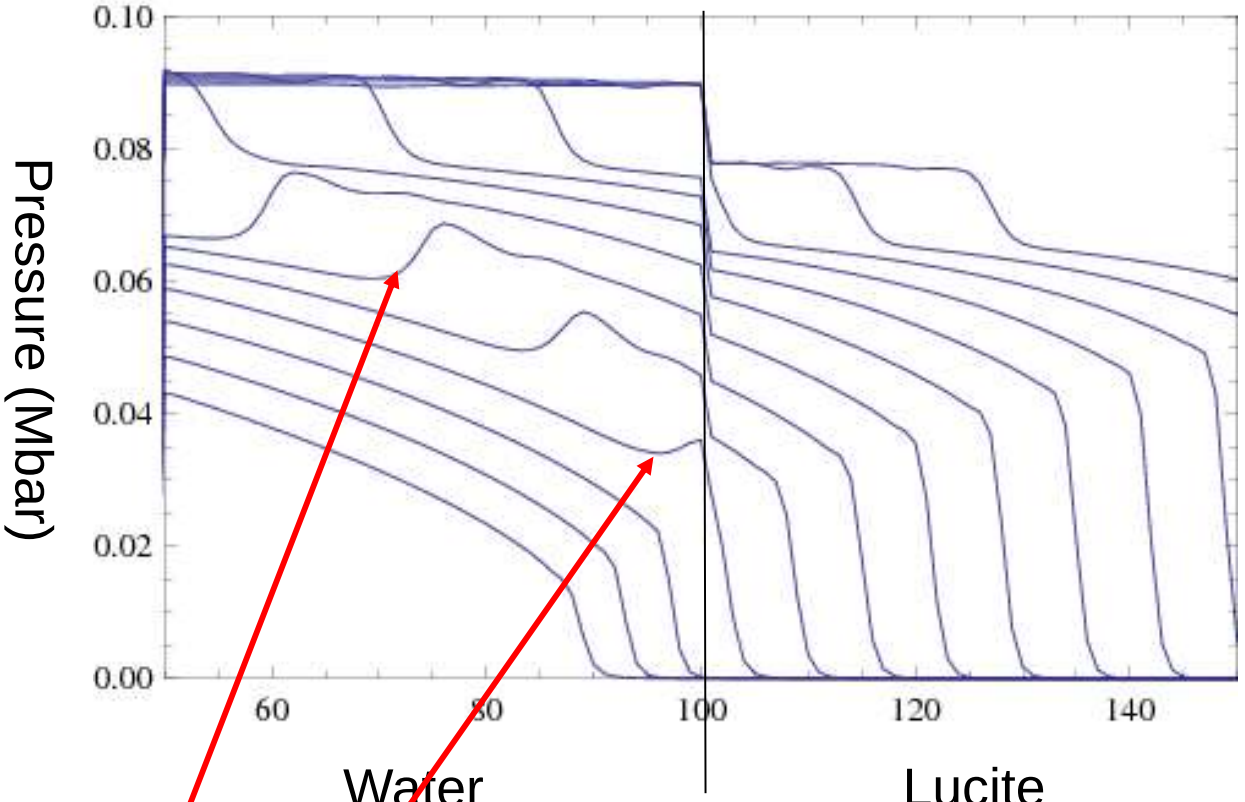

Particle velocity @ window

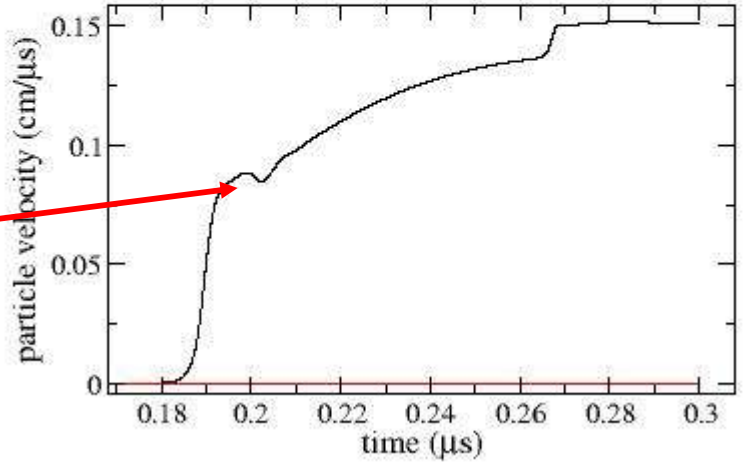

Reflected Compressive Wave

Wave Reflections con't.

Particle velocities @ 2/3 position

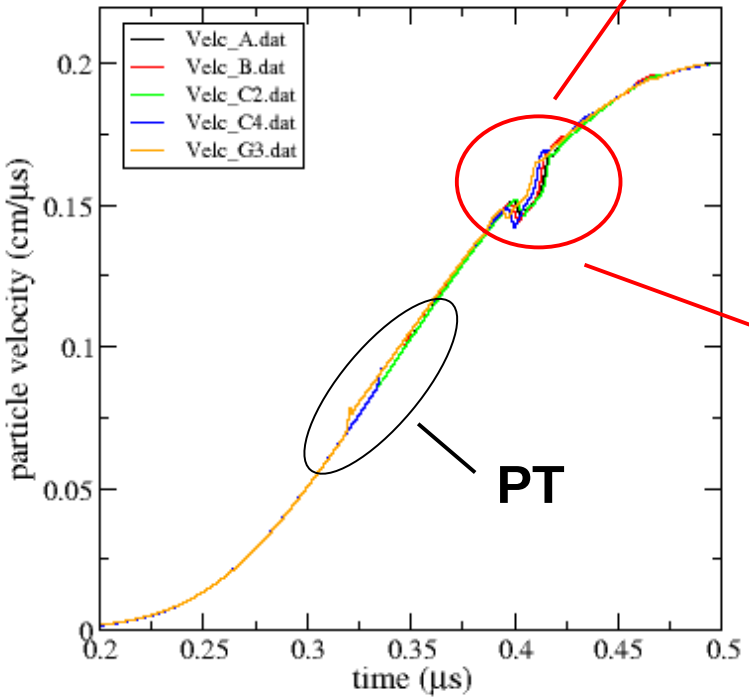

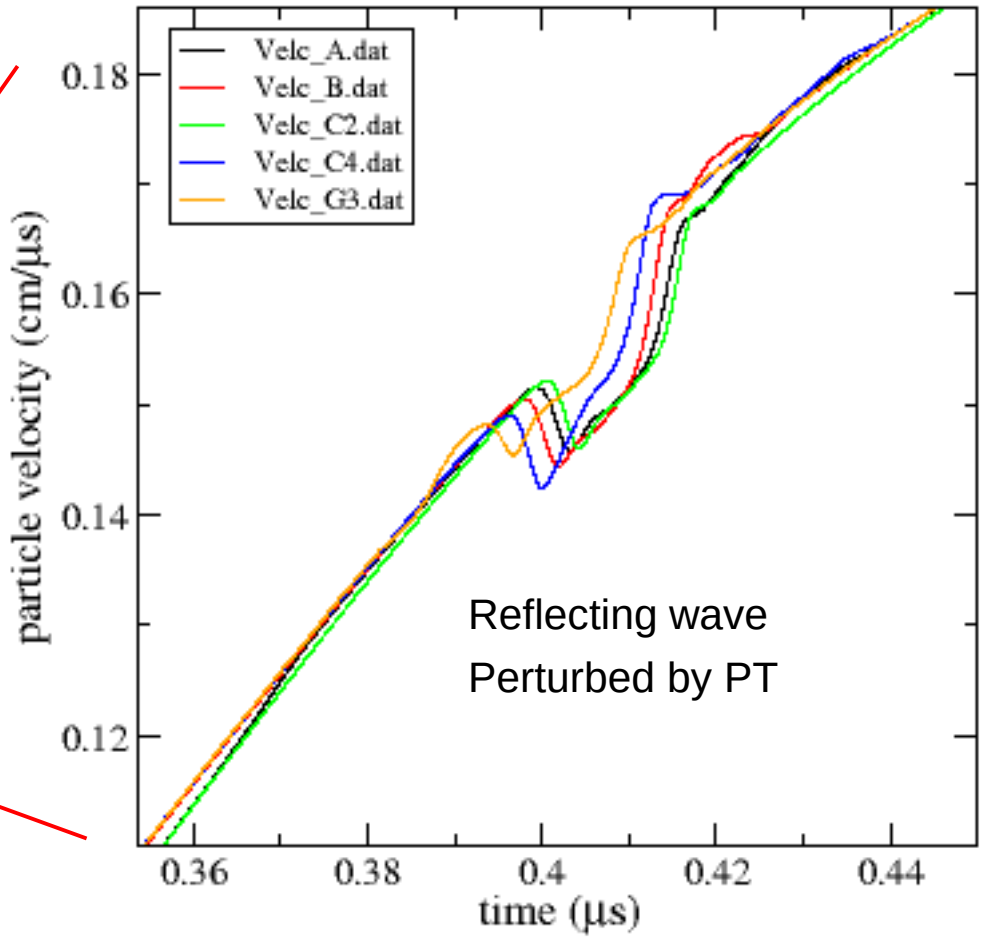

Wave interactions can be misleading

Increasing the duration of the phase transition

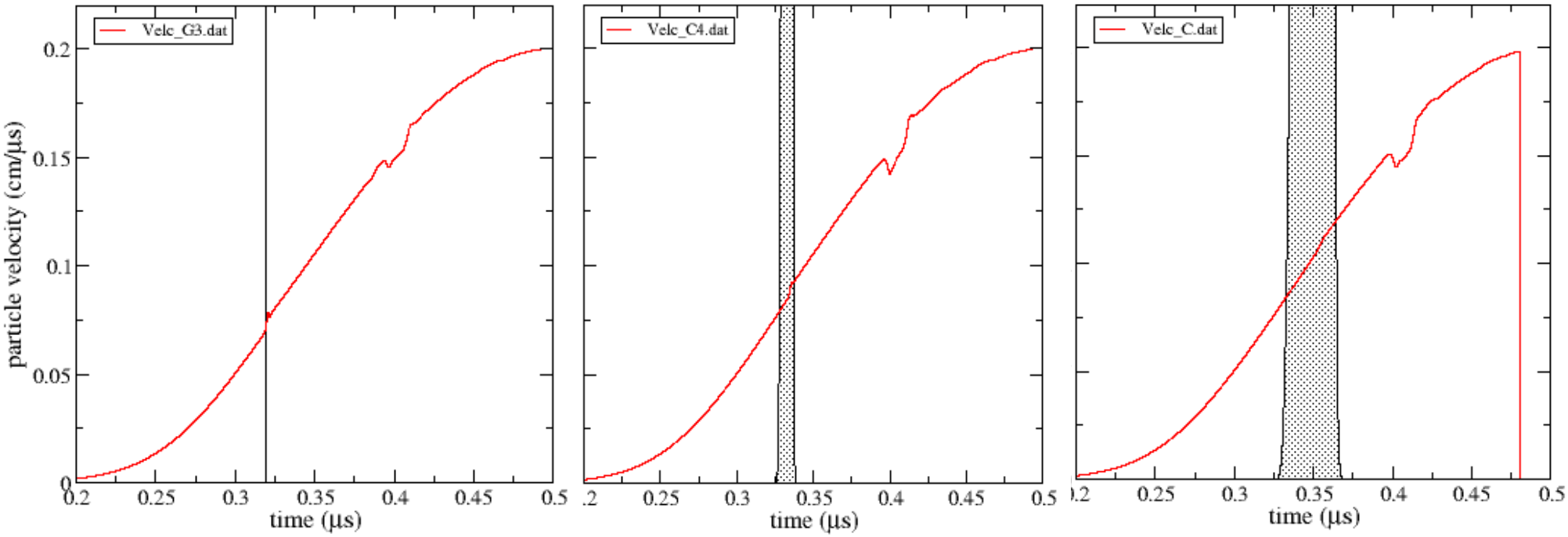

The particle velocity may or may not give clear indications.

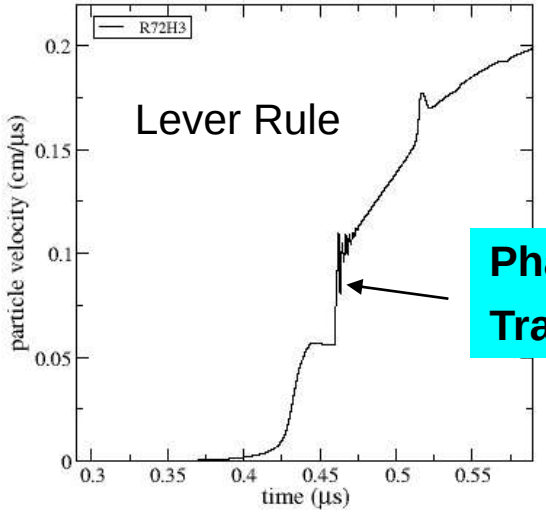

Summary/ Objectives

We plan to bring together the necessary components for a Melt-line phase transition model:

- Spans nanosec to microsec time scales.
- Atomistic, phase-field, crystallographic and continuum modeling will be used.
- Understand missing physics.
- Verify with experiments.
- Understand sensitivities at the continuum level.

A comprehensive, physics-based model would incorporate

I) Probabilistic Nucleation size/shape distribution

II) Kinetics of the surface

III) Percolation

IV) Over-pressurization and relaxation

V) Amorphous formation or freezing

VI) Strength

Some Concerns::

Time: why is the delay time different---Exp. And Simulations
Rare events?

Ion-interaction descriptions: what needs to be included
---viscosity, transition path ways
➡ DFT and metadynamics

Sensitivities: errors, “real” system variations, ….

The overly ambitious path

To develop a robust continuum phase transition model that incorporates modern theory and simulates recent observations of pressure-induced phase transitions....

I) Probabilistic variations
   Nucleation size/shape distribution
II) Kinetics of the surface

III) Percolation

IV) Over-pressurization and relaxation

V) Amorphous formation or freezing

VI) Strength

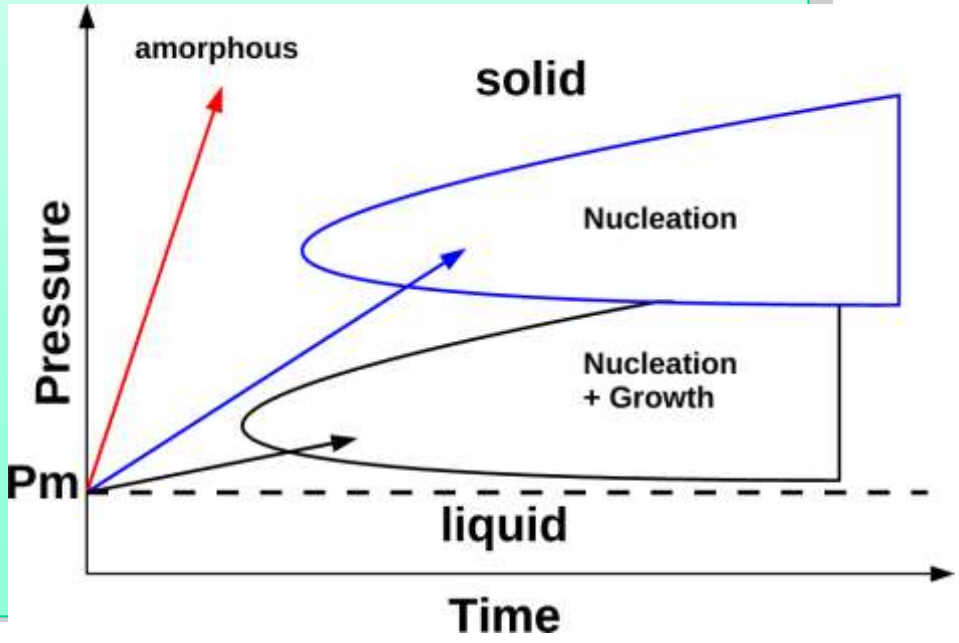

Recent insight into past large-scale MD simulations(Belak)

$$R_c \approx \frac{2\gamma_{sl}}{\Delta S_f (T_m - T)}$$

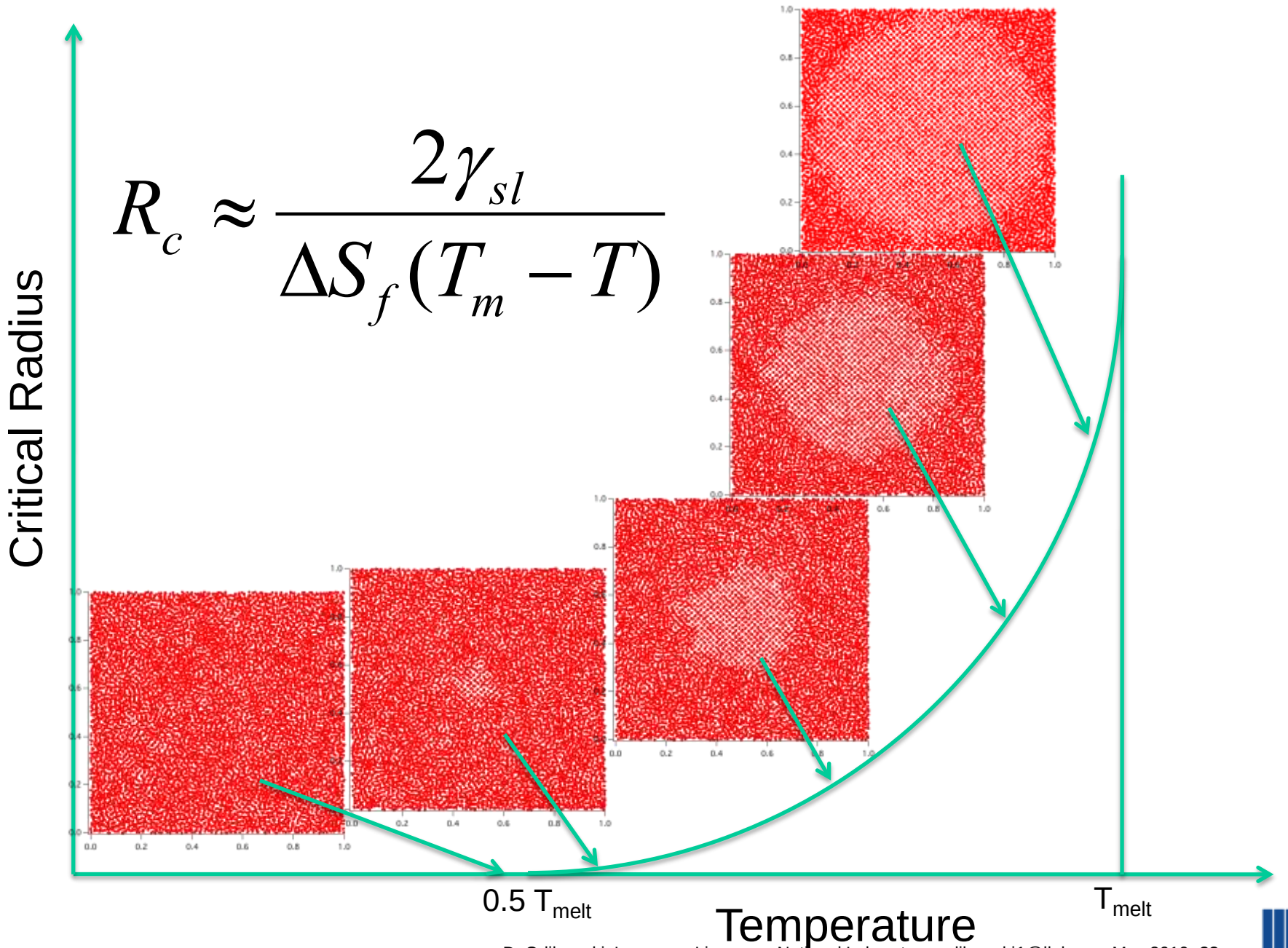

Development toward a more physical hydro model (Minich)

CNT:

Free Energy accounting for surface energy

$$\Delta G(N,P,T) = a\,\sigma\,N^{\frac{2}{3}} - N\Delta\mu$$

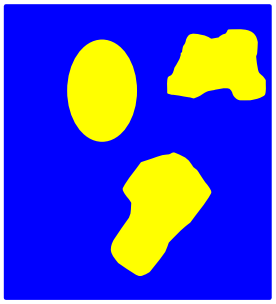

Critical Energies and lengths

$$\Delta G_c(N_c,P,T) \approx \frac{\sigma^{\alpha}}{\Delta\mu^{\beta}}$$

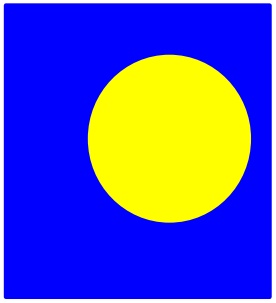

Distribution of size and shapes

$$J_n = \int j_n(R,t)dR$$

Phase fraction (iterative)

$$\dot{\phi} \propto \Delta G\, J(N,P,T)\ [1-\phi]\ \Delta\mu(N,P,T)$$

Kolmogorov type phase fraction

$$f_2 = 1 - exp\left[-\frac{A}{4}J_d v_{int}(t-t_0)^4\right]$$

Phase fraction evolution (Minich)

Phase fraction rate:

$$\dot{\Phi} = \Lambda(P_r - P_c)^{\Gamma}\ Exp[-\frac{B}{(P_r - P_c)^{y}}]\ (1-\Phi)\ [a(P_r - P_c)^{\lambda}\ \Phi - b\Phi^{\alpha}]$$

Self-consistent hydro-code time step:

$$\delta t\ \frac{dP_r}{d\Phi}\ \dot{\Phi} + P_{rm} = P_r$$

Melt-line: Pc and Tc

Four exponents are left open b/c of possible fractal crystallites, not smooth nor round

Four open parameters:

nucleation rate, over-pressurization, phase fraction dependence, percolation

Melt-line kinetics project flow:

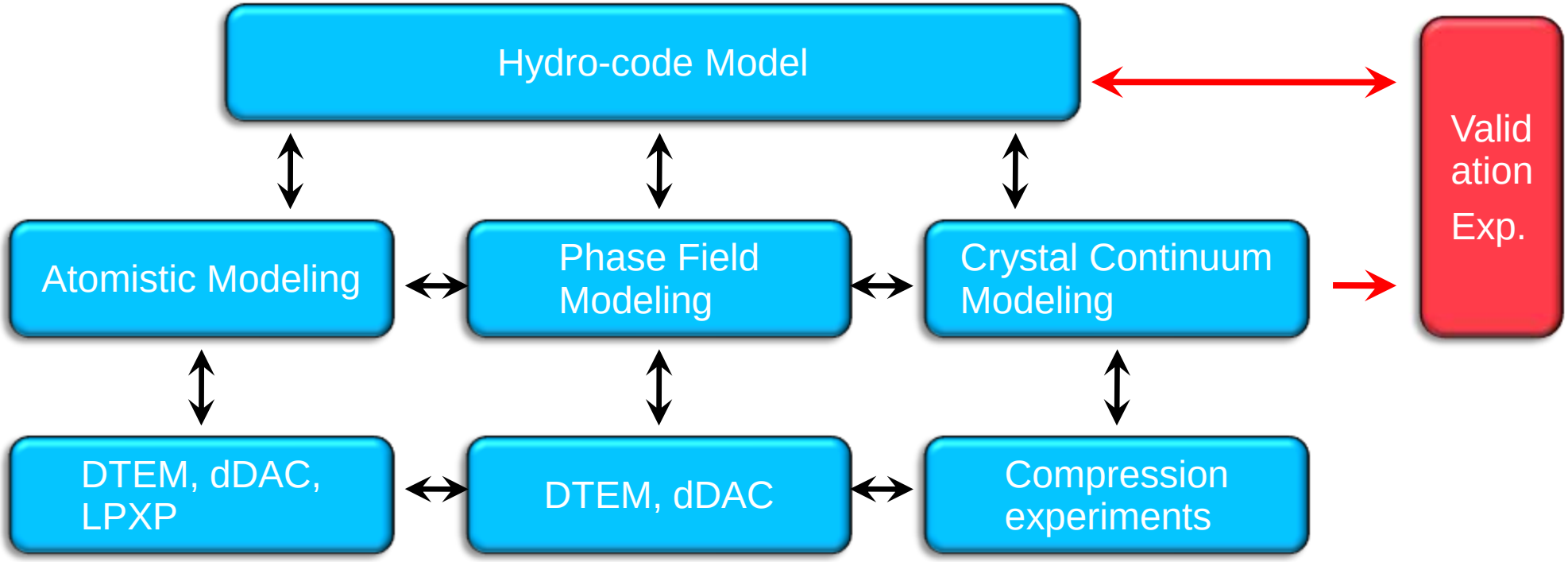

Three contributing time scales:

- ps to ns: atomistics
- ns to μsec: phase field
- μsec + : continuum modeling

Each time scale needs to be benchmarked against experiment.

Materials on Demand :: understanding the pressure dependent kinetic barriers

Ammonia borane stores 8-12 wt% hydrogen at 6 Gpa

$NH_3BH_3 + H_2$

- Hydrogen storage at pressure
- Not stable at ambient pressure

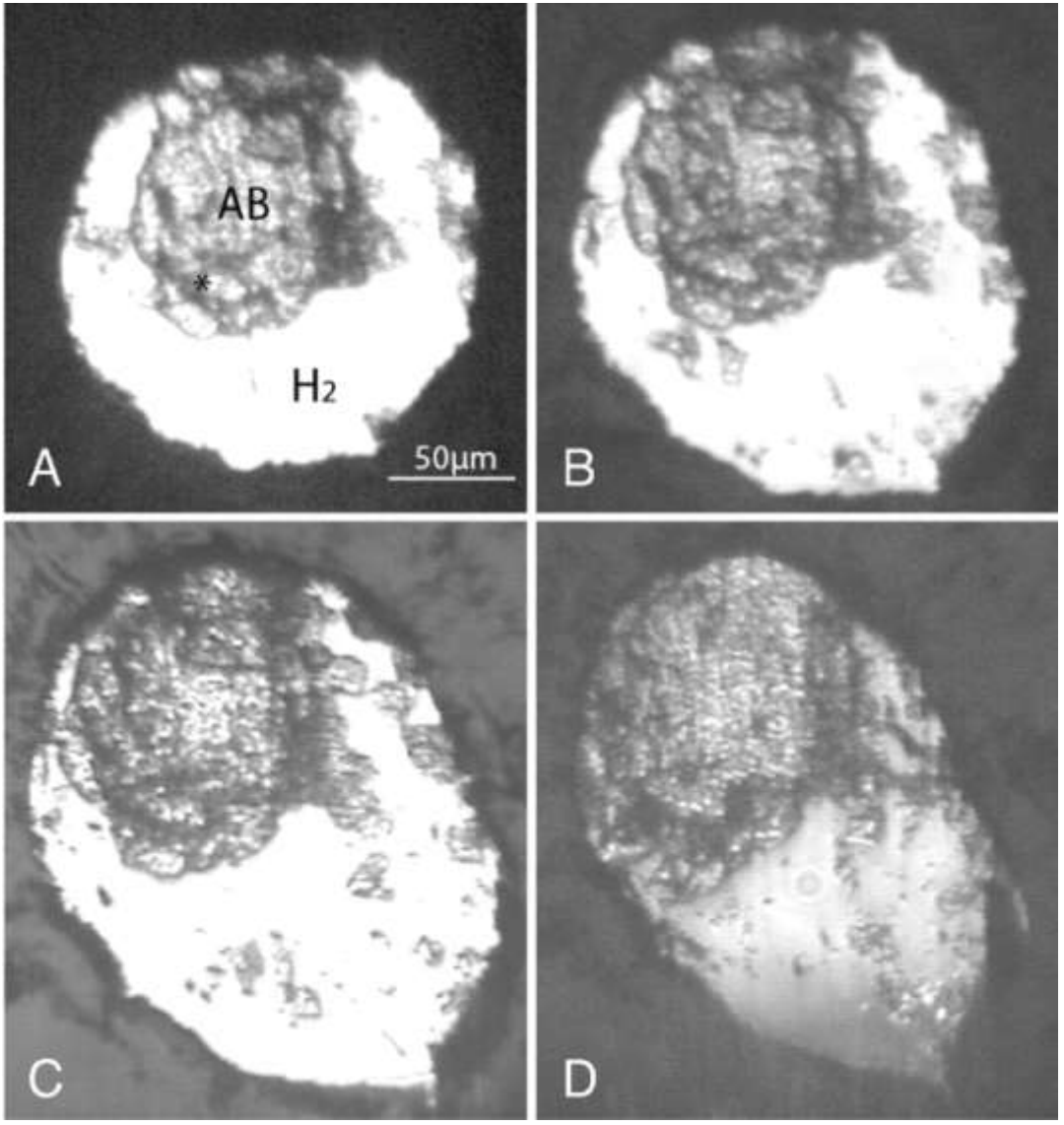

Lin Y et al. PNAS 2009;106:8113-8116

Experiments: capturing the solidification front

Physics Quantity	Diagnostic	Facility	Platform
Nucleation Distribution Function(R,t)	SAXS Imaging	APS, LCLS LLNL	dDAC DTEM
Atomic Solidification Front	Coherent Diffractive X-ray Imaging	LCLS	dDAC LPXP
Nucleation, Growth, Coalescence	Imaging X-ray	APS, LCLS	dDAC LPXP
Solid Phase Fraction(t)	*in situ* X-ray Diffraction + Streak	JLF, LLE, SNL	Janus, OMEGA, Z-pinch
Indirect Material Response(t)	Velocimetry	JLF, LLE, SNL	Janus, OMEGA, Z-pinch

Prototypical observations to be modeled: compressed water

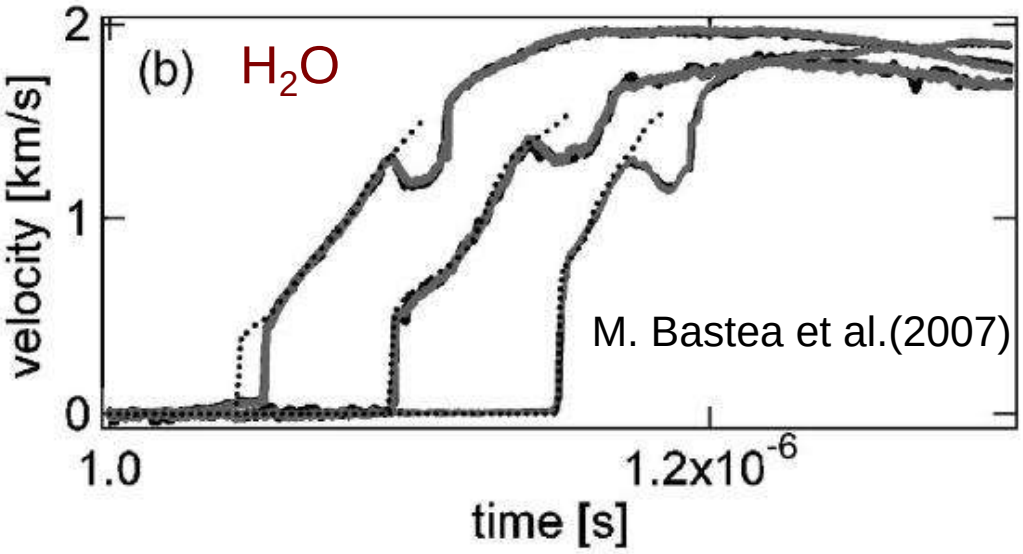

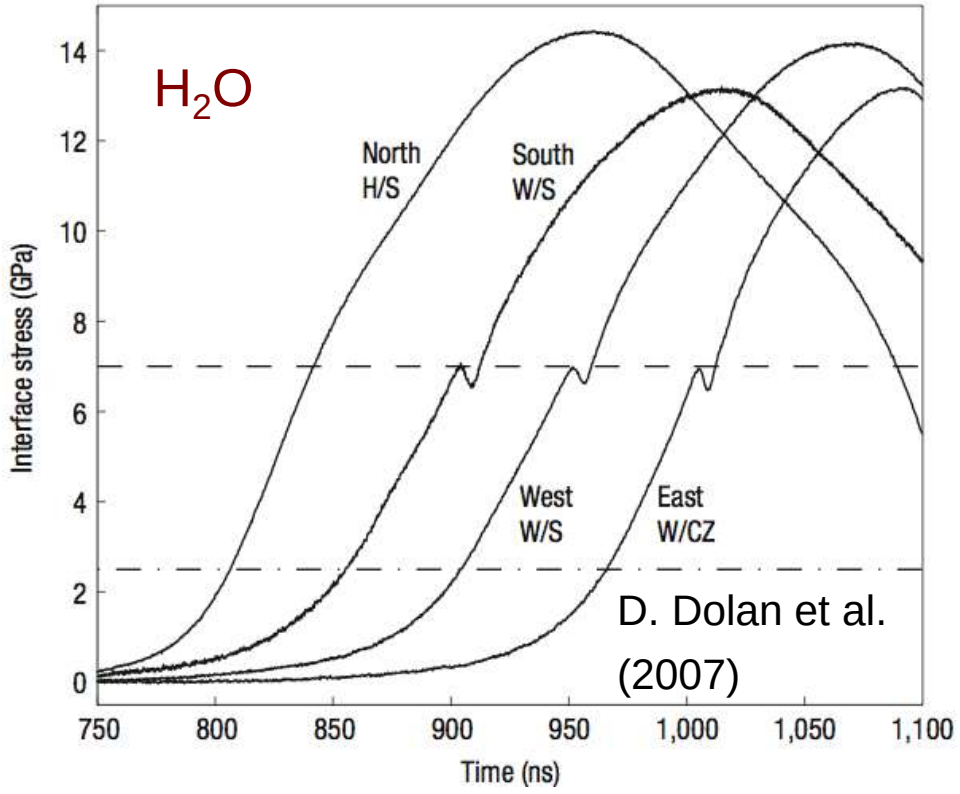

For Liquid-Solid transition,
there is limited experimental evidence, in general.
The over pressurization may be a strain-rate dependent.

Continuum models do not capture this relaxation

Atomistics: nucleation rates (Richards)

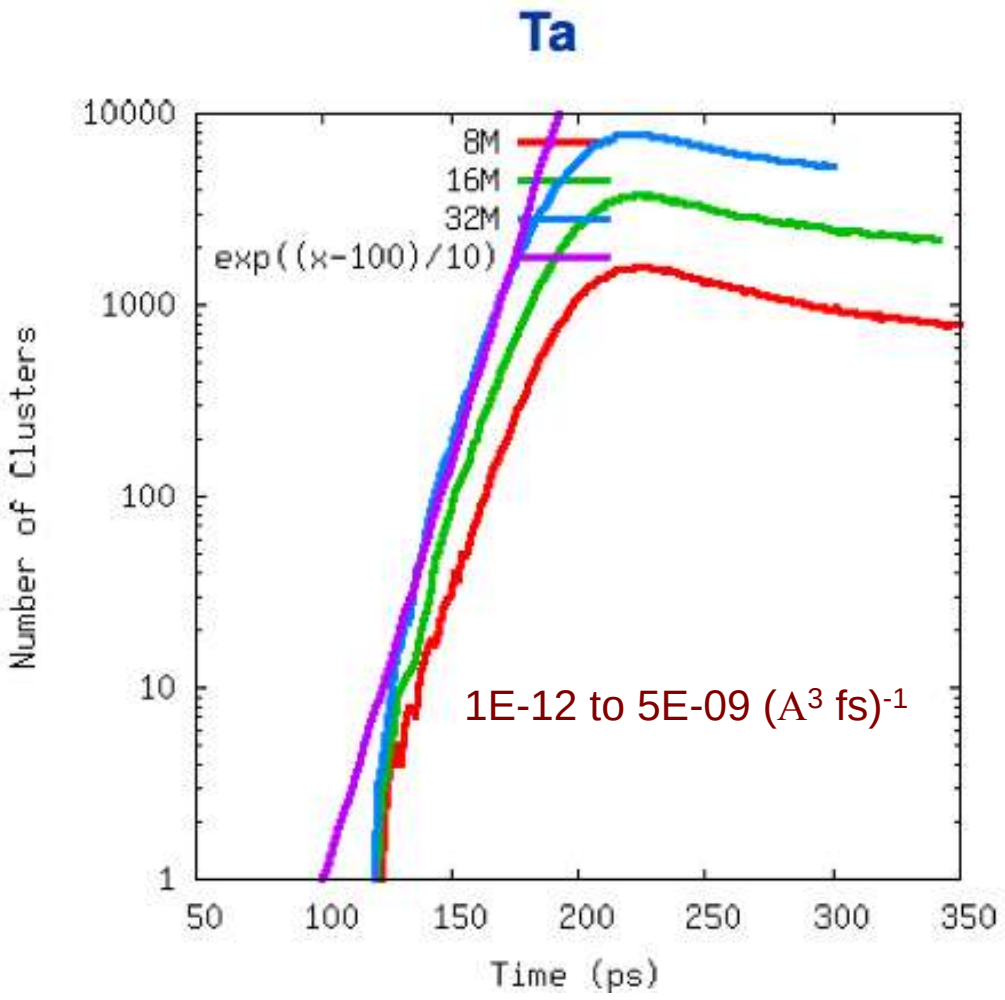

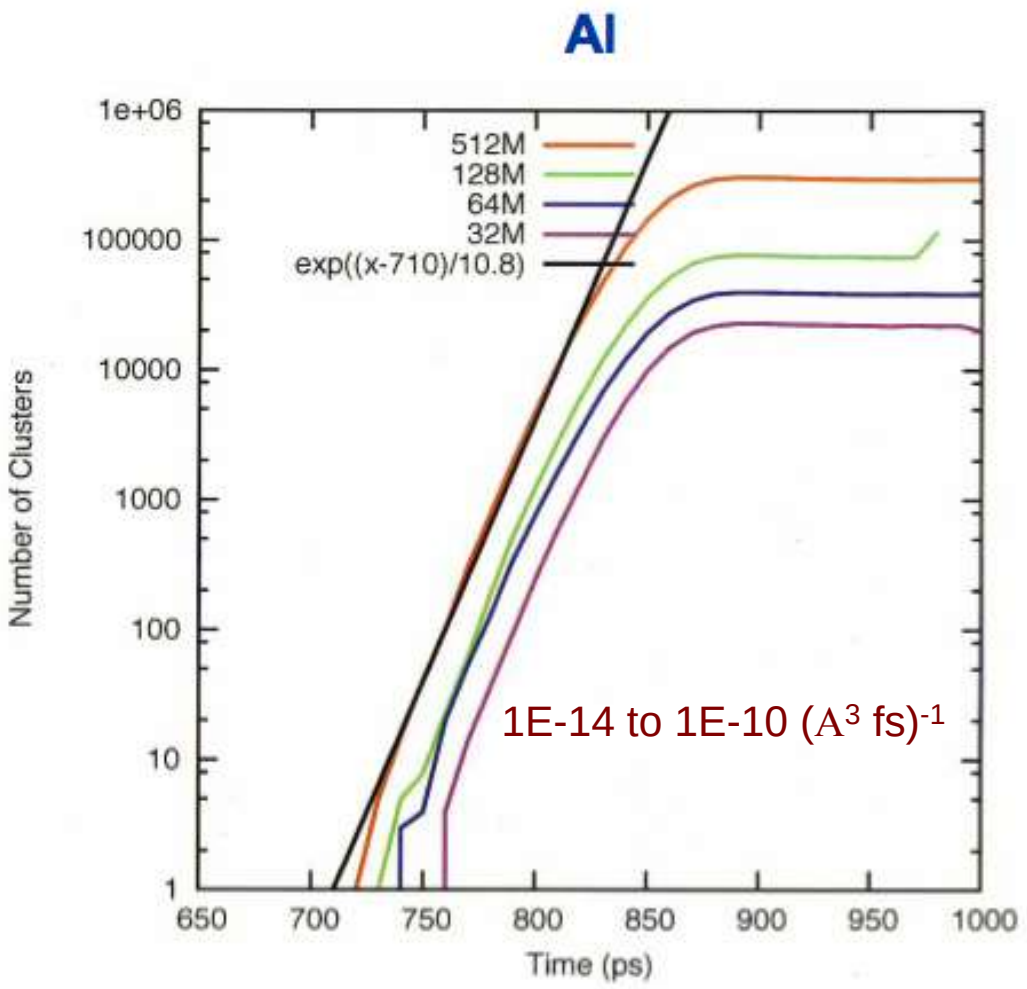

Atomistics: growth rates (Richards)

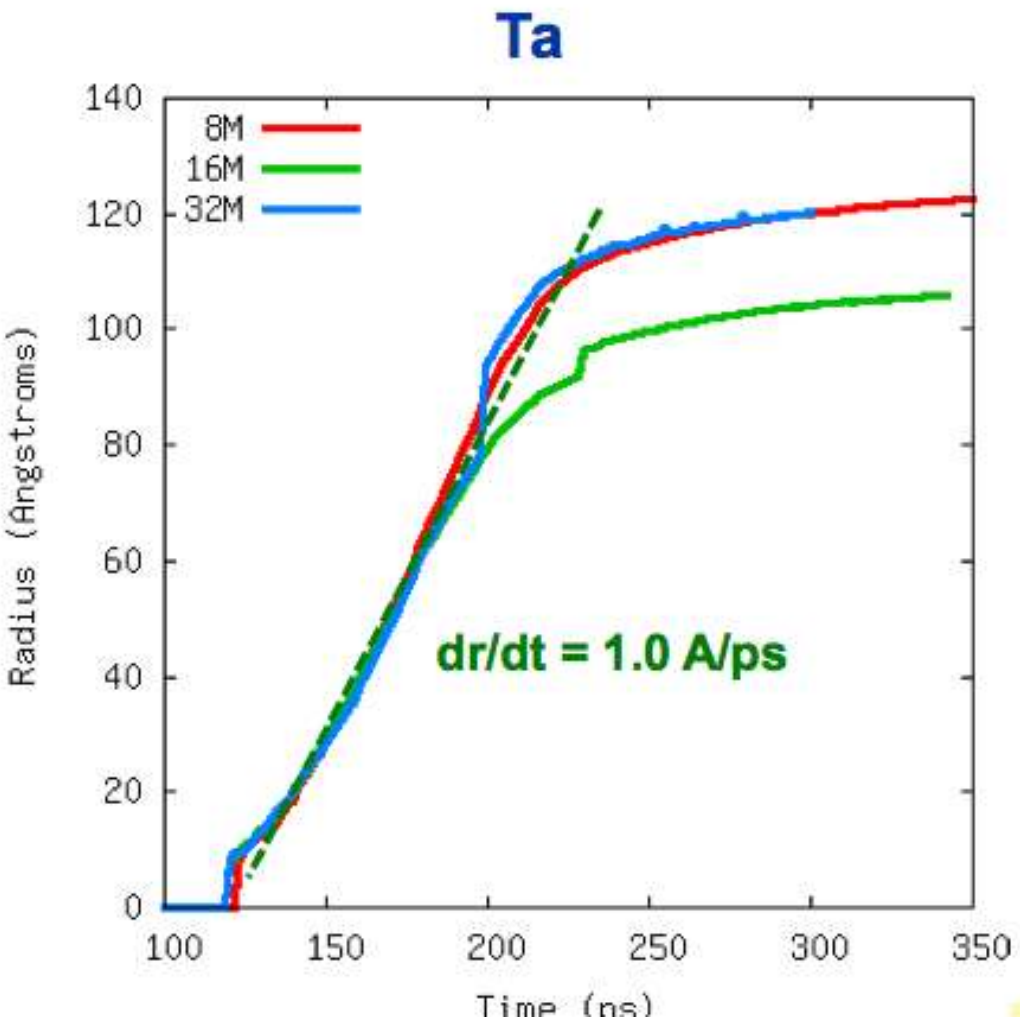

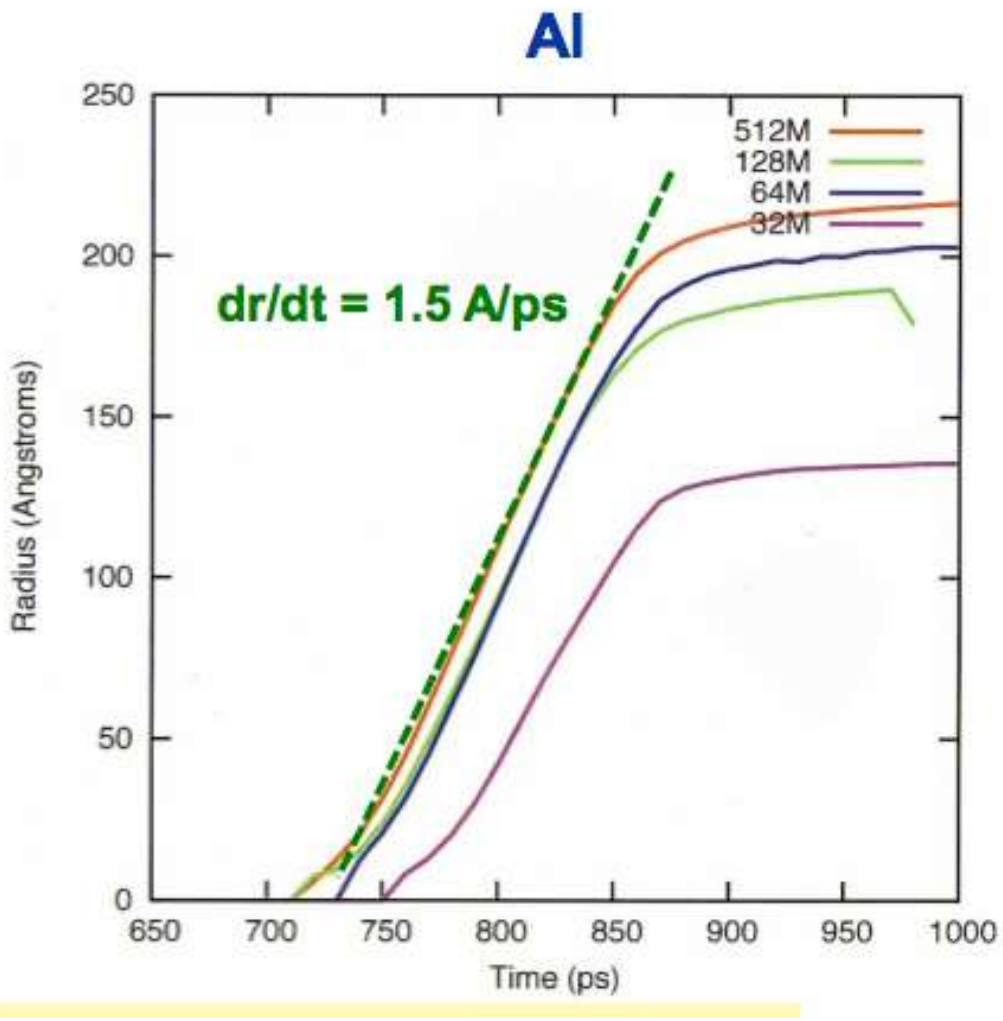

Atomistics: (Richards)

Nucleation Rates

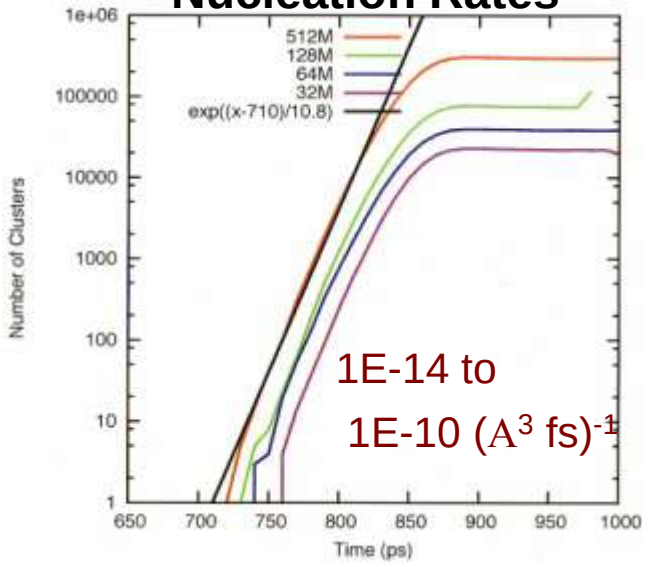

Growth Rates

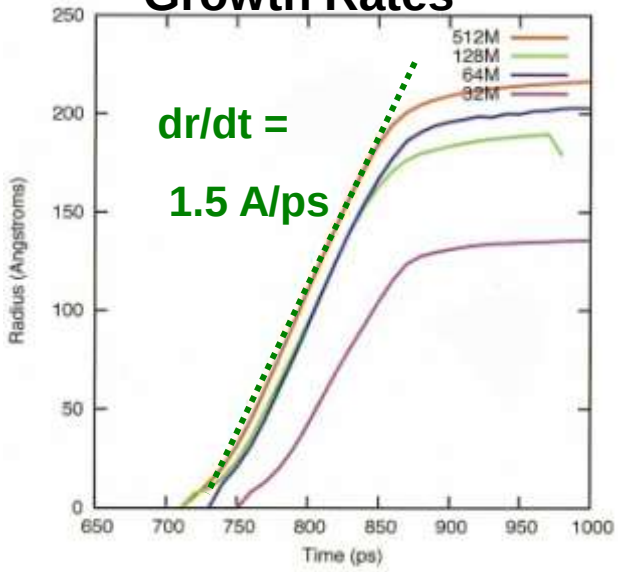

Al: 32m atoms

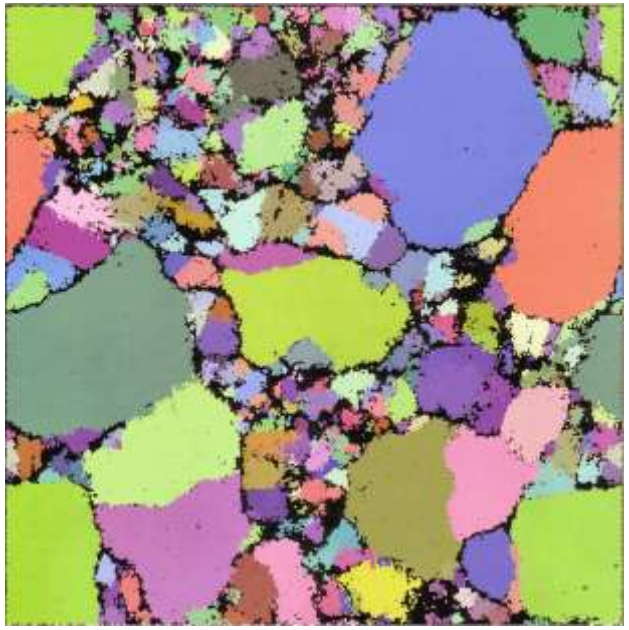

Issues:
Ion potentials
Rates
Scale

MD will not get us to the hydrodynamic time of interest: Belak

100's nm

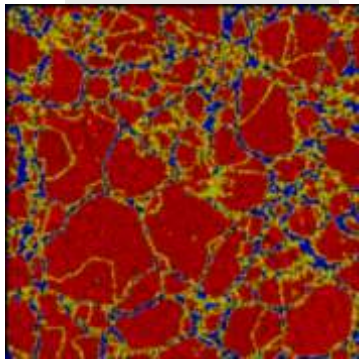

MD Simulation

Nucleation:
Poisson
Distribution

Late Time:
Log-Normal
Distribution

100's μm

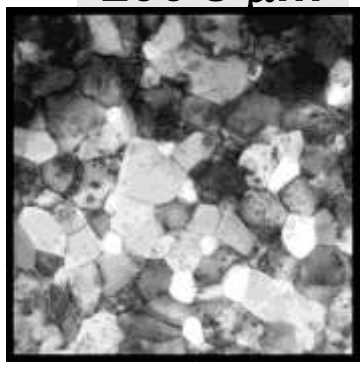

Recovery
Experiment

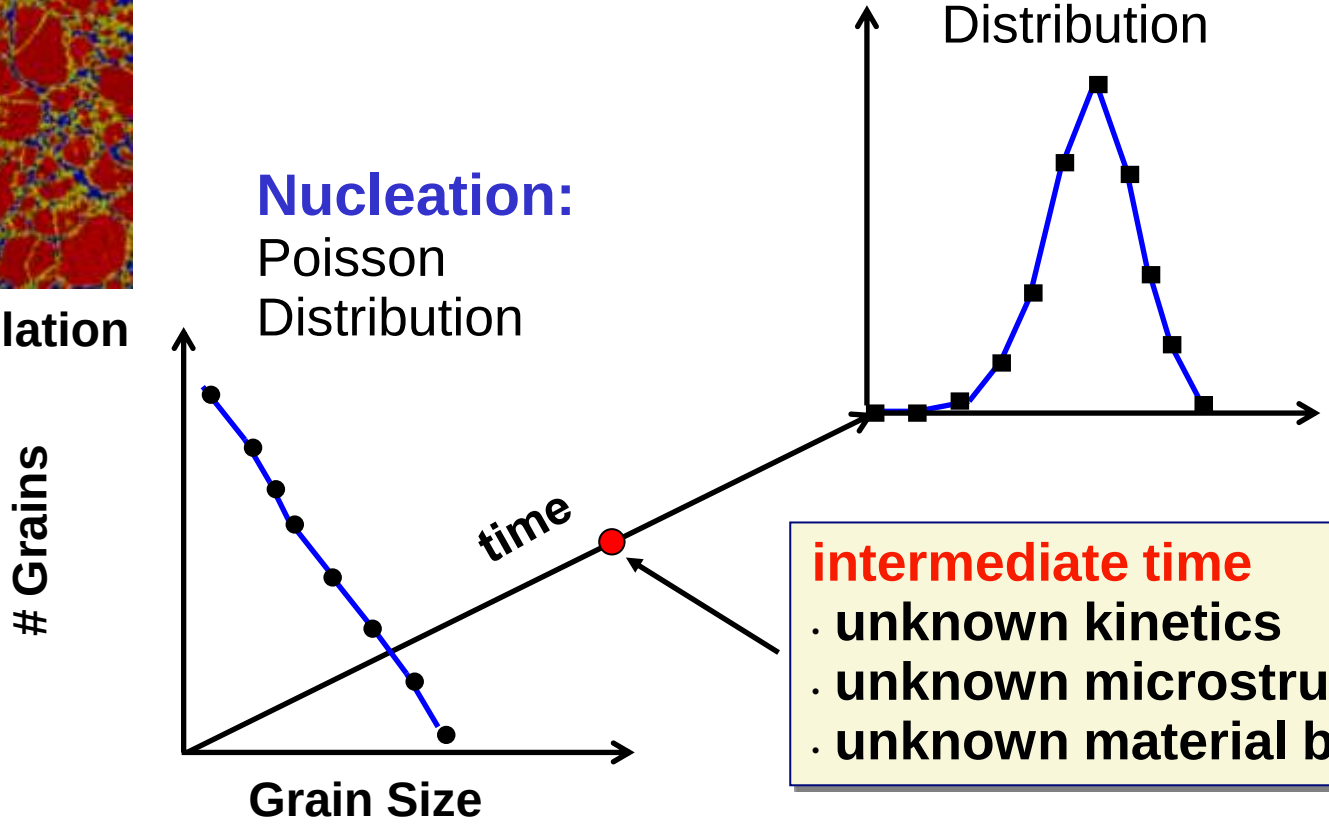

intermediate time
- **unknown kinetics**
- **unknown microstructure**
- **unknown material behavior**

Phase Field Modeling (PFM) will get us to the hydrodynamic time of interest

MD nucleated microstructure onto phase field model: linking time scales (Belak)

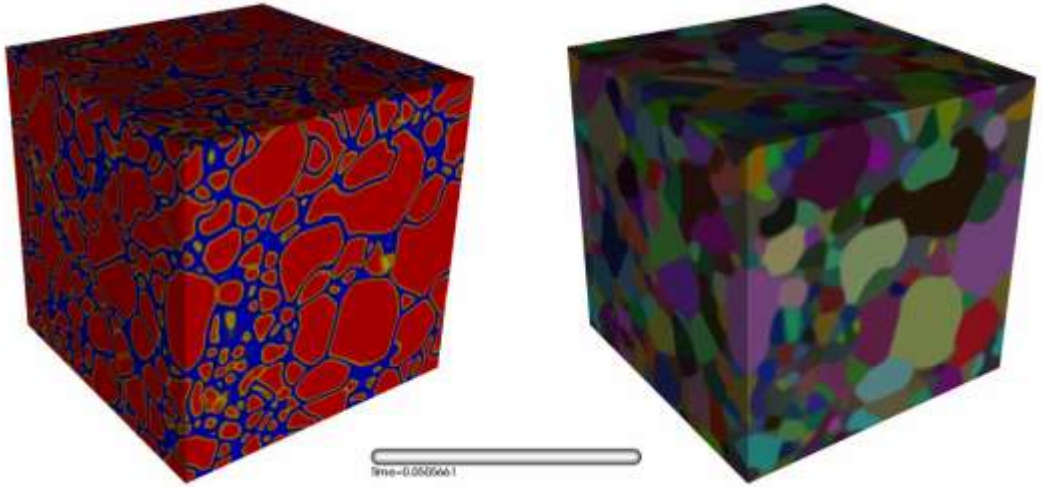

Phase Order Parameter

Crystallographic Quaternion Order Parameter

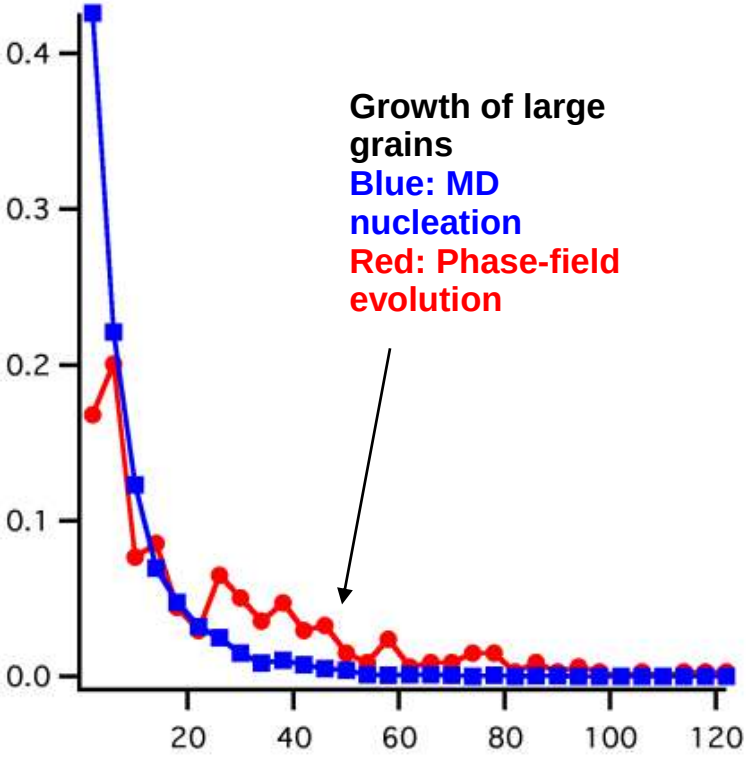

While significant grain coarsening has occurred on the microsecond scale, the microstructure is far from log-normal

Quasi-static polycrystal compression of Fe: transformation progresses from grain boundaries (Barton)

- Phase transformation with concurrent elastic and plastic accommodation
- Uses power-law transformation kinetics
- Burgers transformation mechanism, with habit plane based interaction energy

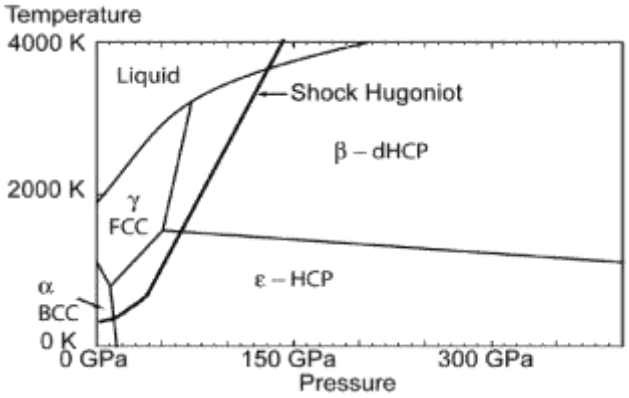

Saxena and Dubrovinsky, *Am. Miner.*, 2000.

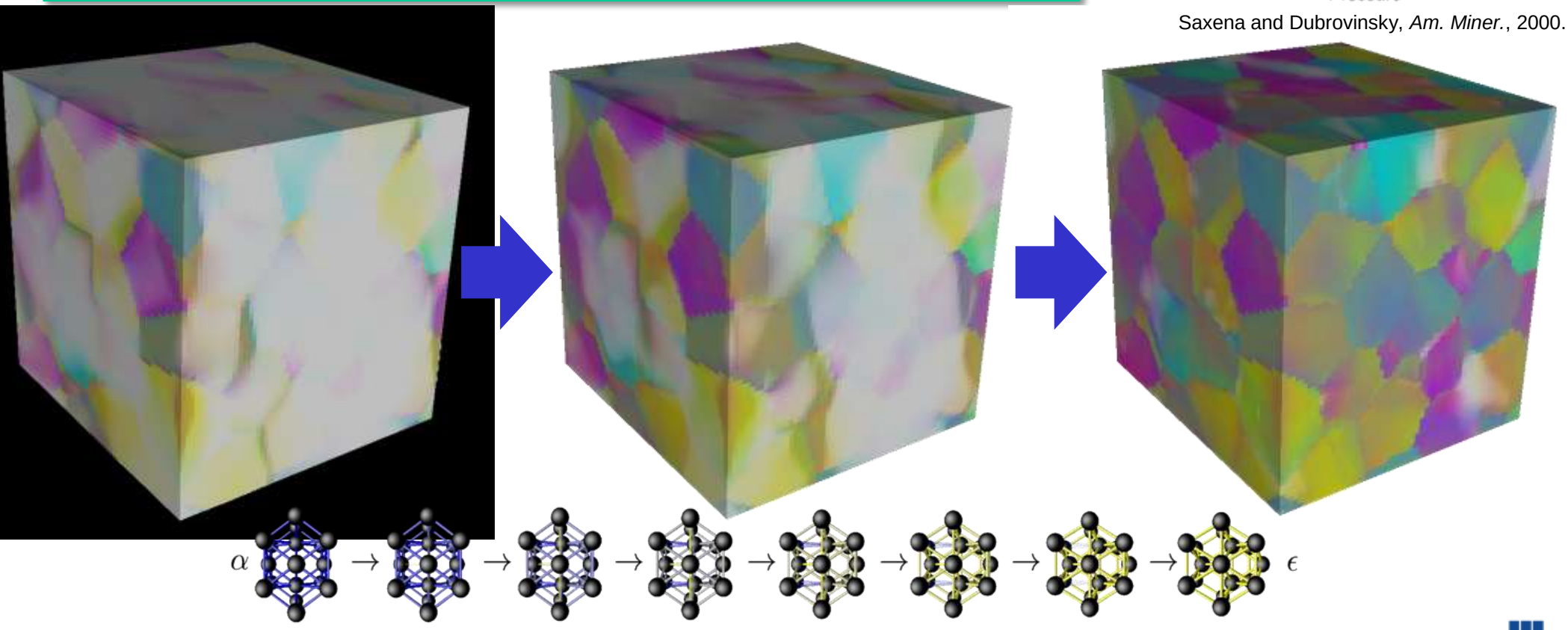

Interaction energy influences response and microstructure (Barton)

See von Bargen & Boehler, *High Pres. Res.*, 1990.

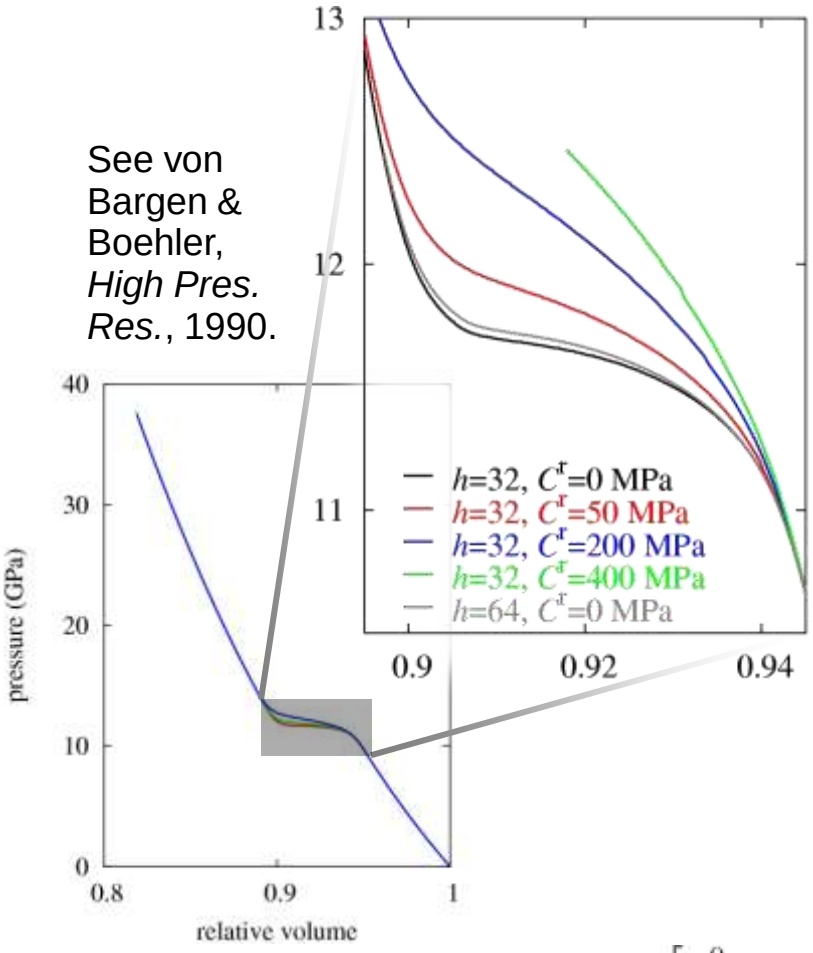

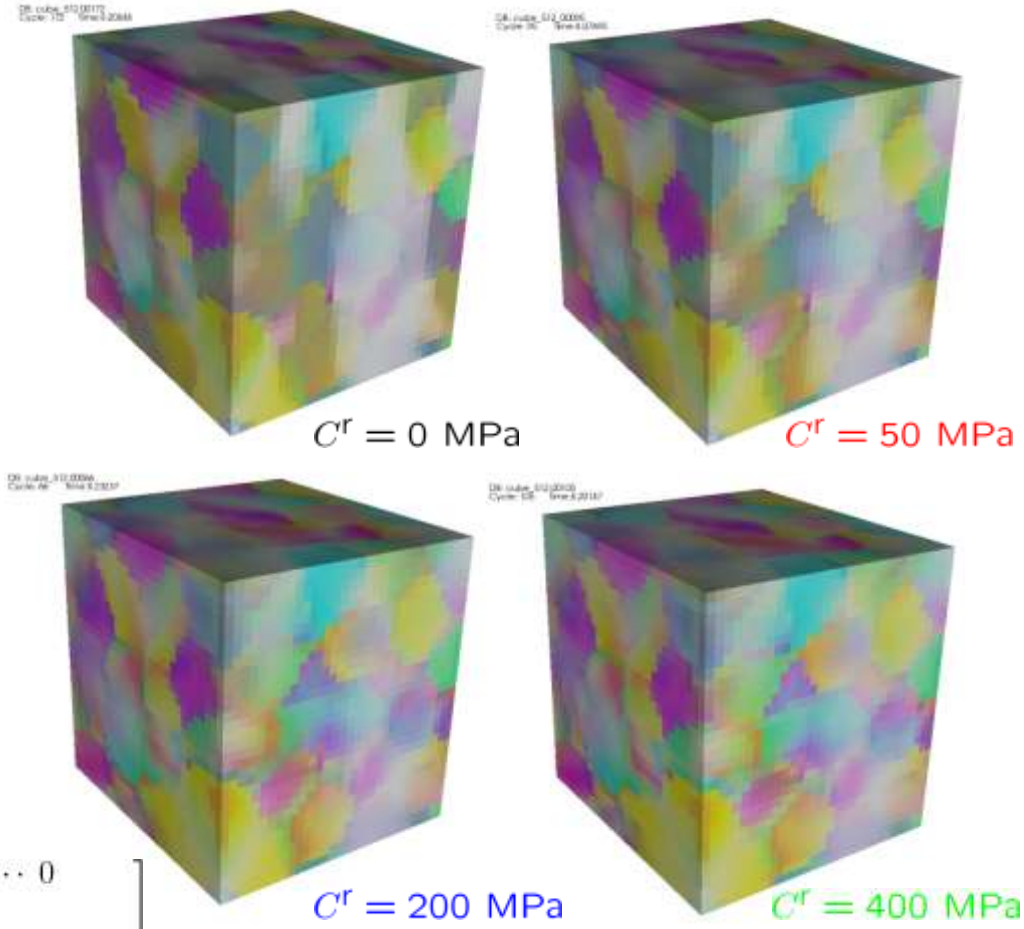

$$E^r = C^{r_b}(1 - m_p)^2 + \sum_{i,j=1}^{n_c} m_i A_{ij}^r m_j \qquad A_{ij}^r = \begin{bmatrix} 0 & 0 \cdots 0 \\ 0 & \\ \vdots & C^{r_a}(1 - |\mathbf{n}_i \cdot \mathbf{n}_j|) \\ 0 & \end{bmatrix}$$

What is Phase Field modeling? Basic Equations

Phase Field modeling is time-dependent Ginzburg-Landau theory

Solid **Liquid**

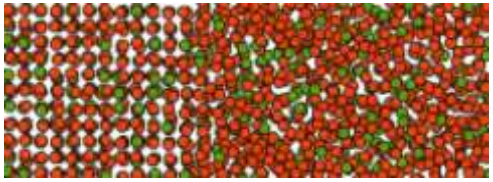

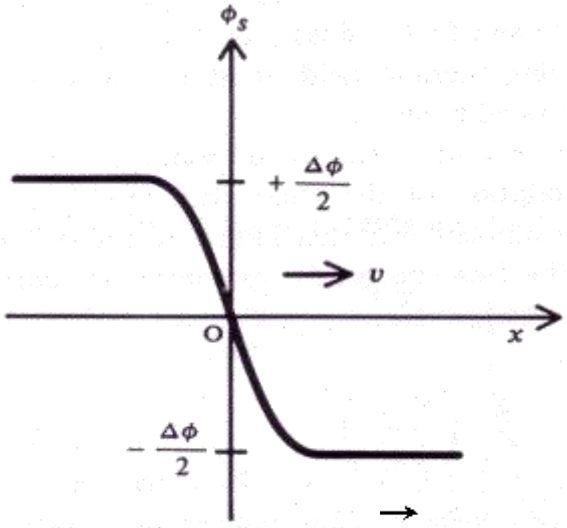

Order Parameter $\vec{\phi}(r,t)$

$$F(\phi) = \int dx[\frac{1}{2}|\nabla\phi|^2 + f(\phi,P,T) + f_{GB}(\nabla\theta) + f_{el}]$$

Total Free Energy of multi-phase material

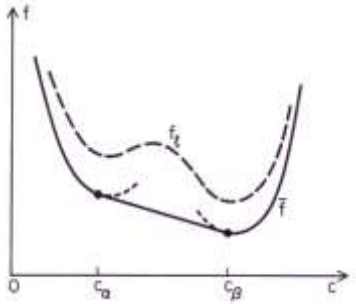

Local Free Energy Density $f(\phi) \approx \phi(1-\phi)(1+\phi)$

$$\frac{\partial\phi}{\partial t} = -\Gamma(-\nabla^2)^a \frac{\delta F}{\delta\phi} + noise$$

Kinetic Equation with Thermal Noise

What does a crystallographic-aware phase-field model of polycrystal solidification look like?

Pusztai et al., have proposed a 3D quaternion-based phase-field model

- Represents crystal orientation with quaternion order parameter
- Quaternions are widely used to analyze crystallography of polycrystal interfaces
- Quaternion algebra is fast, efficient, avoids singularities, …

Free Energy

$$F = \int \left[\frac{\varepsilon_\phi^2}{2} |\nabla \phi|^2 + f(\phi, c, T) + HT[1 - p(\phi)] \left(\sum_i (\nabla q_i)^2 \right)^{1/2} \right] d^3 r$$

Evolution

$$\frac{\partial q_i}{\partial t} = -M_q \frac{\delta F}{\delta q_i} + \zeta_i = M_q \left[\nabla \cdot \left(D \frac{\nabla q_i}{|\nabla q_i|} \right) - 2\lambda q_i \right] + \zeta_i$$

Where q_i is the quaternion order parameter, M_q is the associated mobility and ζ is the fluctuation in q.

We have implemented the Pusztai model in our 3D AMR code

- Enhance energy functional to represent energetics of grain boundaries
- Crystal symmetry aware quaternion mathematics
- Extend energy functional to include elasticity and alloy concentration

Refs: T. Pusztai, G. Bortel, and L. Granasy, “Phase field theory of polycrystalline solidification in three dimensions,” Europhys. Lett, 71 (2005) 131-137; R. Kobayoshi and J.A Warren, “Modeling the formation and dynamics of polycrystals in 3D,” Physica A 356 (2005) 127-132.

A shift in dimension during the phase transition

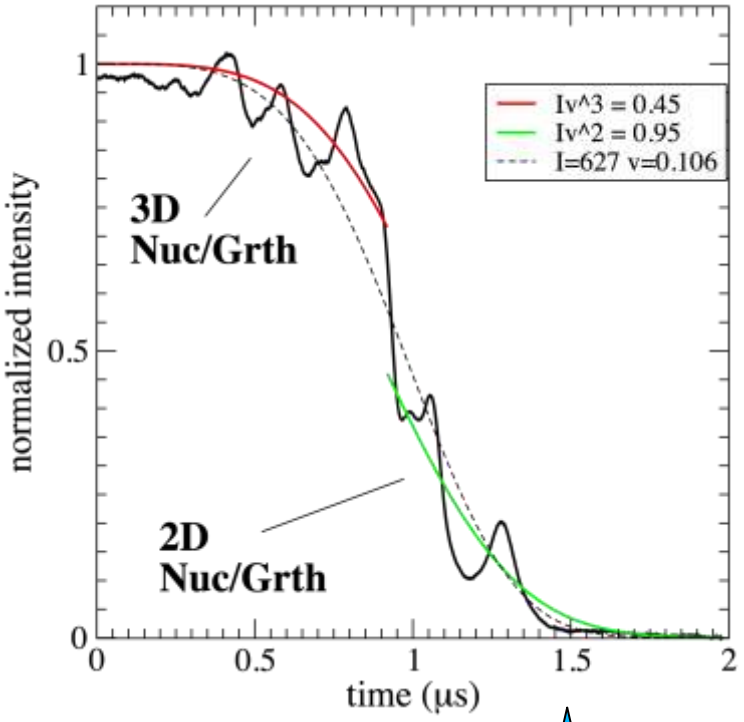

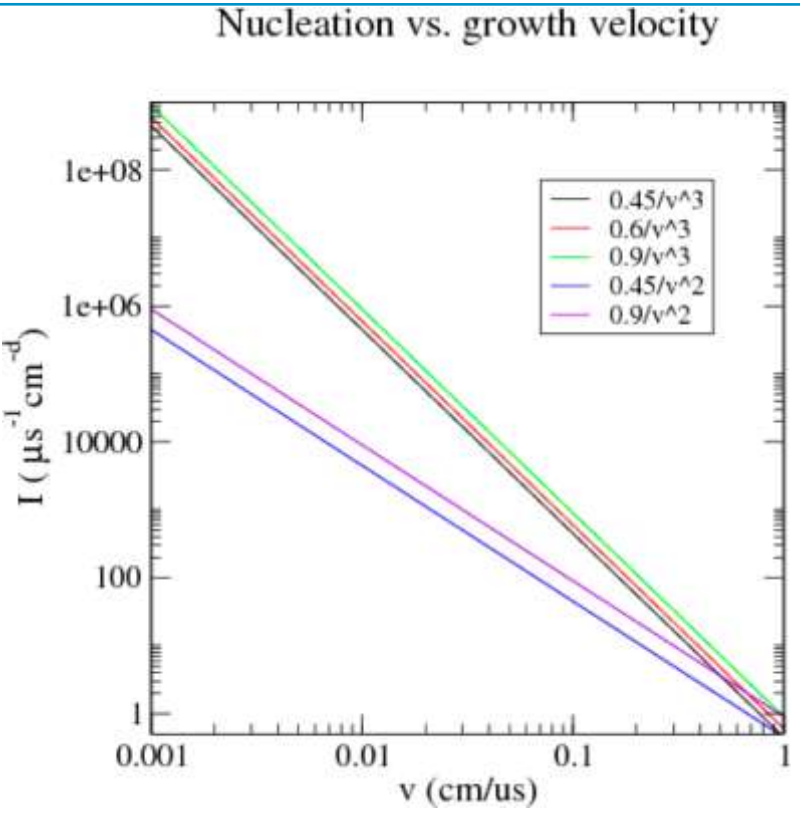

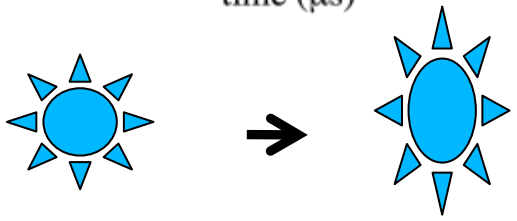

$$f_2 = 1 - exp\left[-\frac{A}{4} J_d v_{int} (t - t_0)^4\right]$$

Oscillations indicate bifringence

1/e decay of intensity gives τ ~ 110 ns

Time scale τ~ 5-15 ns (M. Bastea 2007)

Parameterization of simulations: Water

Linear phase fraction

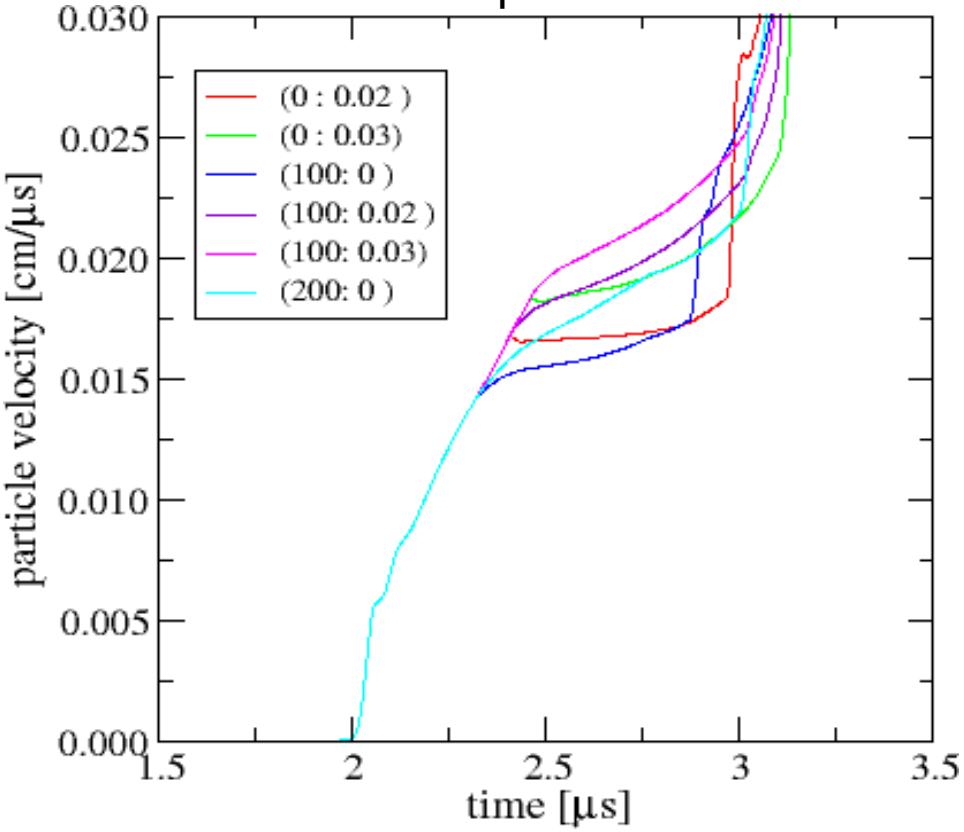

Exponential phase fraction

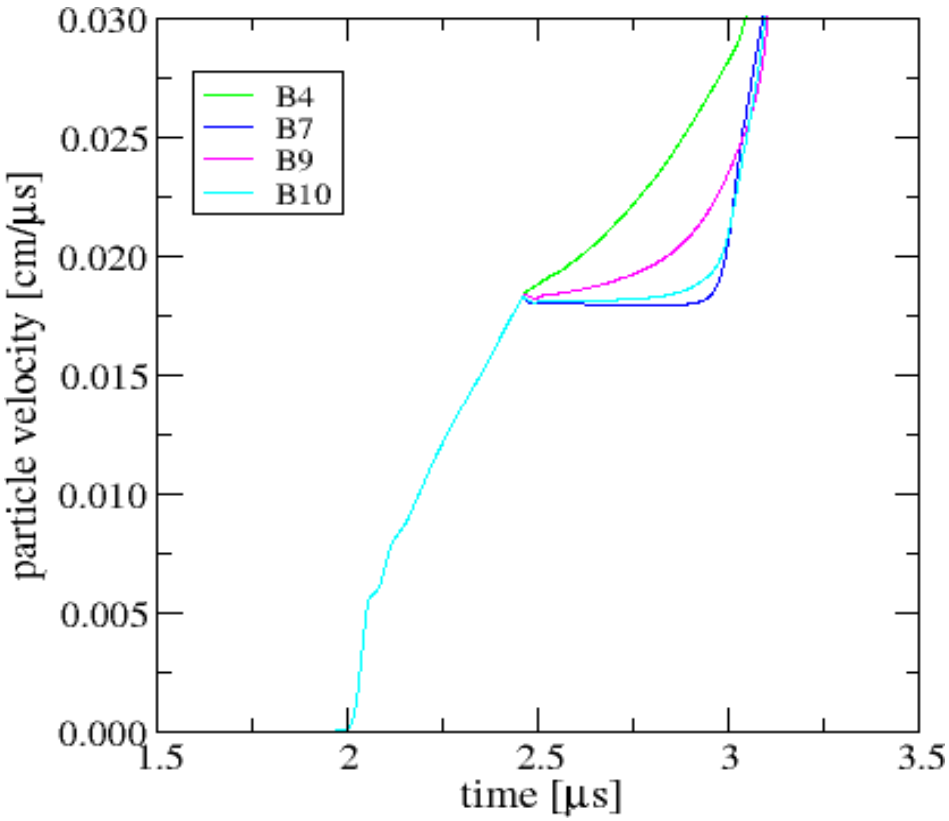

(♦, x): ♦ is a time constant[ns];

x is the % shift of liquidus in volume.

Corresponding pressure of the transition:

(100: 0) P_{PT}= 2.0 GPa

(0: 0.02) P_{PT}= 2.3 GPa

(0: 0.03) P_{PT}= 2.6 GPa

Label	A	B
B4:	-4.8e-3	8.0e-4
B7:	-4.8e-3	8.0e-5
B8:	-4.8e-3	4.4e-4

♦ = 100 ns

Liquidus shifted 3%.

1D dynamic simulations using ALE3D explore interactions between plasticity and phase transformation (Barton)

Bain transformation mechanism, with full reverse transformation modes

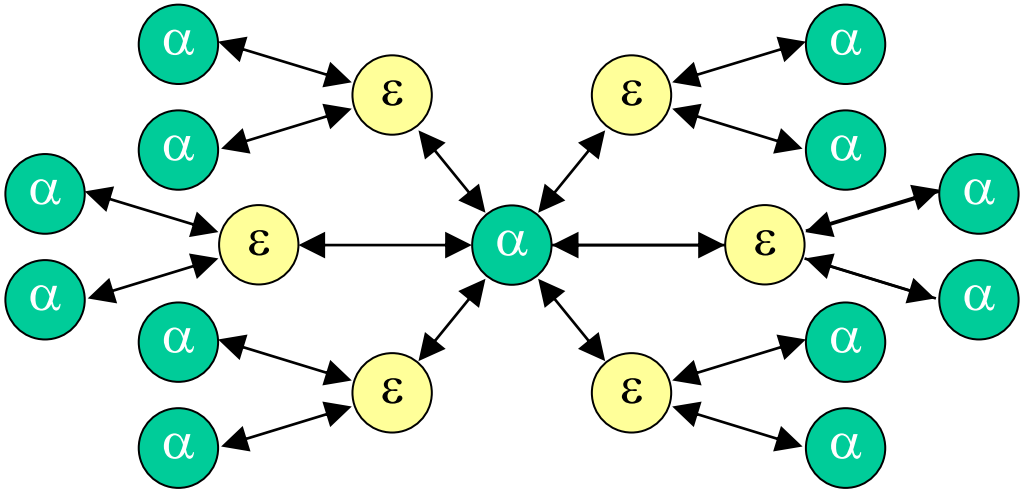

case	$\dot{\gamma}_{ro}\ (\mu s^{-1})$	c_s
a	10^{-3}	1
b	10^{0}	1
c	10^{3}	1
d	10^{6}	1
e	10^{3}	0.5
f	10^{3}	0.25

For example:

Armstrong *et al*., *JAP*, 2009

Barton *et al*., *MSMSE*, 2009

- Initially cube-oriented alpha single crystal
- Pressure BC on loading face: peak pressure of 20 GPa, 4 ns pulse duration
- Periodic lateral BCs
- 100 microns in depth

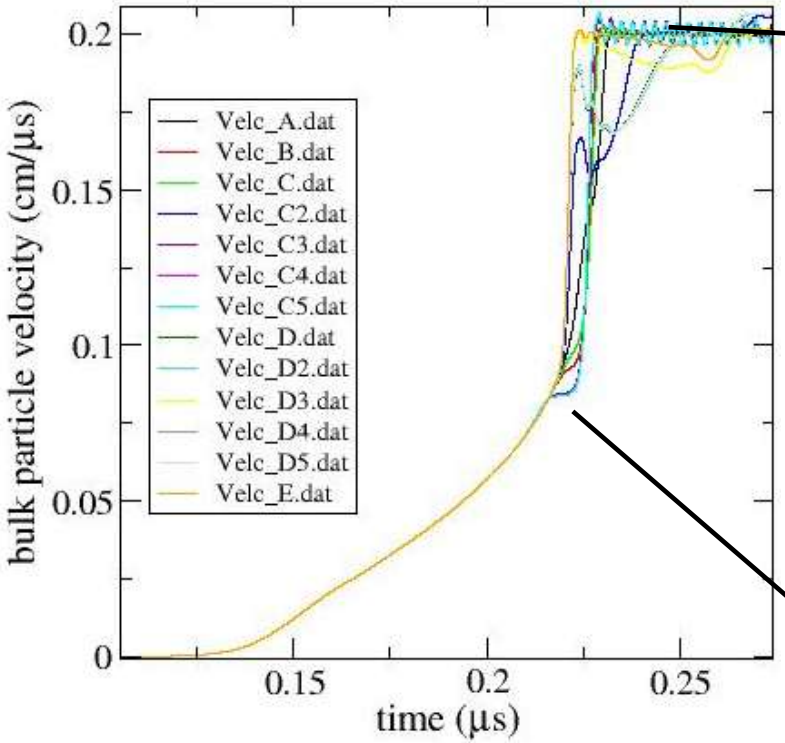
bulk particle velocity (cm/μs)
time (μs)
0
0.05
0.1
0.15
0.2
0.15
0.2
0.25
Velc_A.dat
Velc_B.dat
Velc_C.dat
Velc_C2.dat
Velc_C3.dat
Velc_C4.dat
Velc_C5.dat
Velc_D.dat
Velc_D2.dat
Velc_D3.dat
Velc_D4.dat
Velc_D5.dat
Velc_E.dat

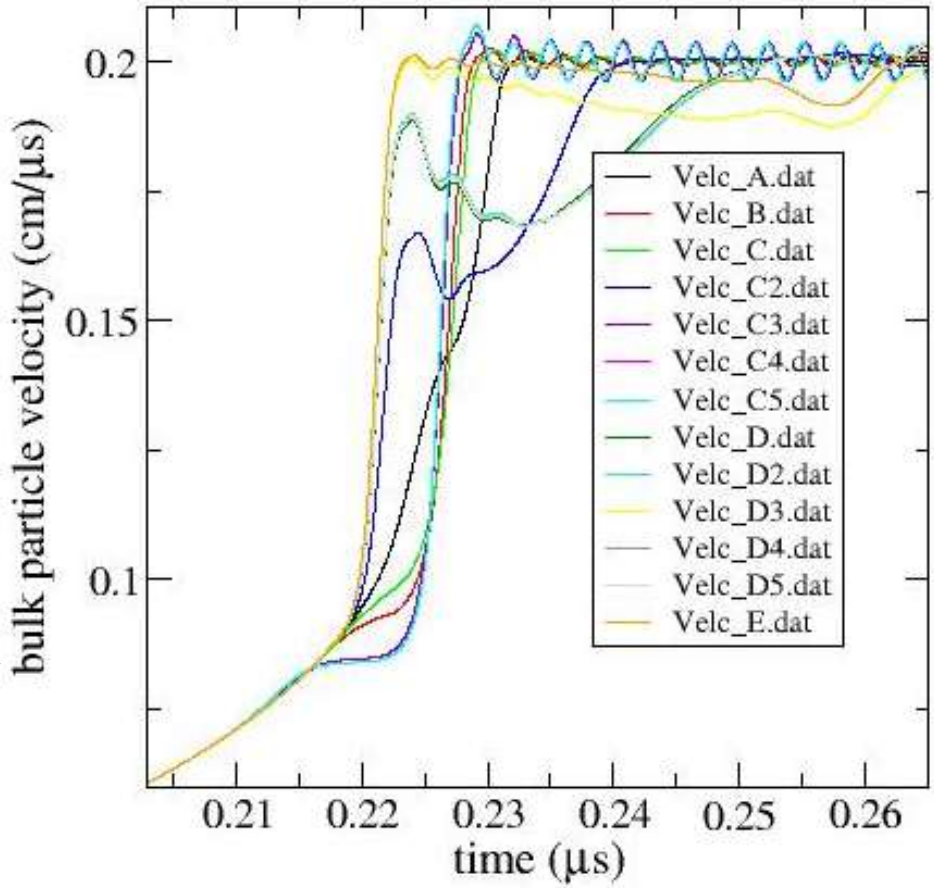
bulk particle velocity (cm/μs)
time (μs)
0.1
0.15
0.2
0.21
0.22
0.23
0.24
0.25
0.26
Velc_A.dat
Velc_B.dat
Velc_C.dat
Velc_C2.dat
Velc_C3.dat
Velc_C4.dat
Velc_C5.dat
Velc_D.dat
Velc_D2.dat
Velc_D3.dat
Velc_D4.dat
Velc_D5.dat
Velc_E.dat

Varying the compression wave

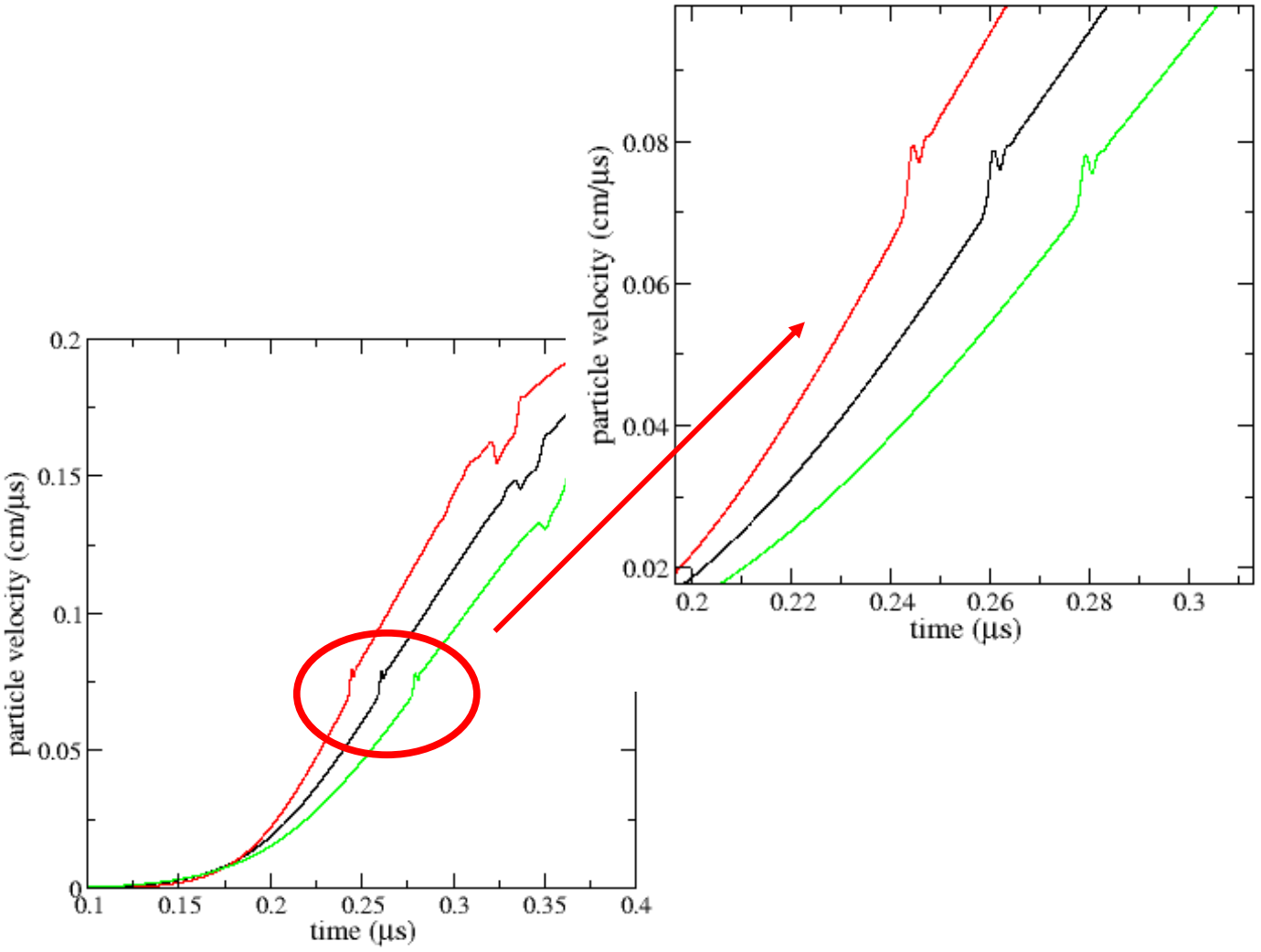

With P(V,T) = P(V,T=0) + Pe(V,T) + Pi(V,T) + Pie(V,T)

There are several contributions that effect the final density rho(P,T) or rho(P,E):

- The cold and the electron (Pe) and/or ion (Pi) thermal contributions (blue solid)
- The material strength also contributes to the entropy or heat (blue dashed)
- The kinetics associated with every traversed phase line (red solid line)
  Delays in transition, developing shocks, not fully transformed material

We think we know (reasonably):

The cold contribution P(V,T=0), comparison to DAC

And to some extent the thermal contributions, comparison to Hugoniots
and to *known* phase lines

Kinetics will contribute a min. of 100 ns in wave propagation arrival time,
Comparison to experiment(J. Nguyen)

Unknown aspects:

The phase diagram in general is not well determined
---liquid-liquid transition, high temperature phases (suggested),
high pressure melt line

The strength is not well defined b/c of the unknown phases and
still is under development theoretically

Kinetics are completely unknown
---general theory is still developing, experiments are minimal to zero

Continuing LLNL's tradition as a forerunner…

Pressure component of phase transitions has not been significantly studied:

- ➡ gives new insights into Classical Nucleation Theory(CNT) via pressure
- ➡ asserts LLNL as an authority in phase transitions at pressure
- ➡ begins to understand pressure-dependent kinetic barriers

Improved understanding and modeling enables:

- ➡ new materials on demand to be obtained/understood from high pressure
- ➡ significant computational resources for *quantitative results and analysis to overlap with experiments, in length and time.*
- ➡ models that are high impact for Stockpile Stewardship Science and Boost

UNIVAC

Dawn

Omega

Analysis and Modeling of Nucleation Controlled Reactions

Professor John H. Perepezko
University of Wisconsin--Madison
Dept of Materials Science and Engineering
1509 University Avenue Madison, WI 53706
AFOSR Nucleation Workshop
Maui, Hawaii, May 2-6, 2010

- INTRODUCTION
- Classical Theory – Highlights
- Applications and Limitations
    - Nucleation Theorem
    - Grain Refinement
    - Dynamics
    - Phenomenological
- Experimental Approaches
    - Indirect
    - Direct
        - Nucleation Density
        - Size Distribution
        - Transient time
        - Nucleation Statistics
- Experience
    - Primary Nanocrystallization
    - Nucleant Refining
- Open Issues-Future Directions

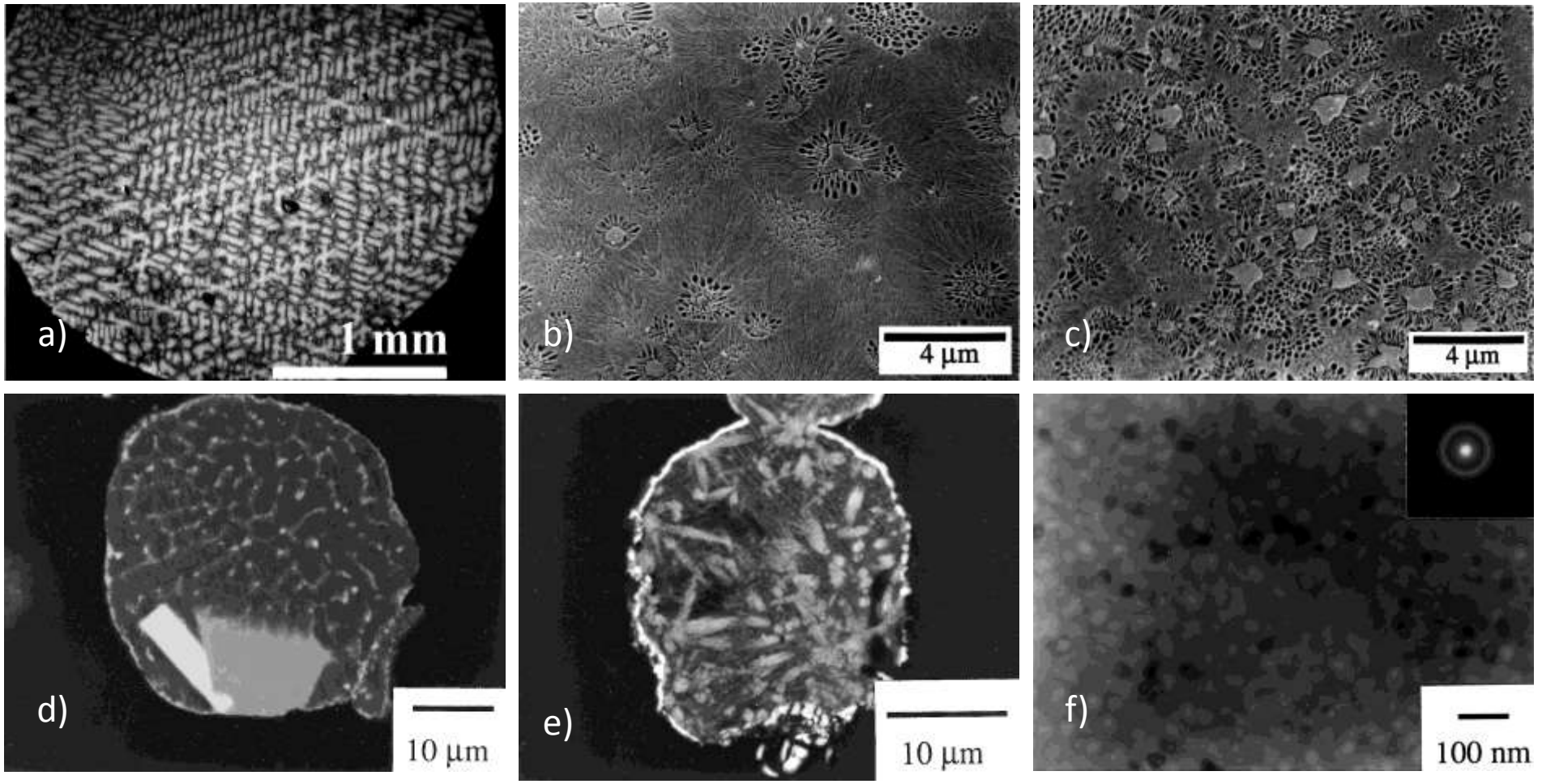

(a) large Ni- base single-crystal droplet after 20ºC/min cooling from a very pure melt; (b)/(c) laser processed Al-26%Si, laser velocity 100 mm/s (b) and 500 mm/s (c), showing fine equiaxed silicon crystals surrounded by a-Al cells and distributed in a fibrous eutectic matrix (plane view); (d)/(e) AlY_7Fe_5 droplets, cooled in the DTA with two intermetallic particles surrounded by a eutectic matrix (d) or water quenched with numerous intermetallic particles (e); (f) AlY_7Fe_5 melt spun ribbon after an isothermal annealing treatment for 10 min at 275ºC, density of nanocrystals is greater than 10^{22} m^{-3}.

Classical Nucleation Theory

- **Kinetic Model**
- Clusters of particles originate when two atoms come together.
- These clusters are in equilibrium with the surroundings and can grow or shrink by the addition or removal of single particles.
- Most clusters will break up into single particles, but there will be some (small) probability that a cluster will grow large enough (i.e. to the critical size) that the number of particles that leave the cluster will just equal those that come to it.
- If the cluster grows larger that this critical size, it will not shrink, but will grow to a macroscopic size particle.

Nucleation Kinetics

In nucleation cluster size is a configurational coordinate. A flux is the net number of clusters/cm^3-sec. growing from size n to (n+1).Let C(n,t) represent the number of clusters of size n that exist in the system at time t. Then,

$$\frac{\partial C}{\partial t} = \beta A'(n-1)C(n-1,t) + \alpha A'(n)C(n+1,t) - \beta A'(n)C(n,t) - \alpha A'(n-1)C(n,t)$$

Where β is the impingement frequency of a monomer (for nucleation in vapors) α is the evaporation frequency and A'(n) is the area of space around the cluster which will hold an impingement monomer. This procedure is called Detailed Balancing. By definition, at equilibrium ∂c/∂t=0 and C=Co. Thus, at equilibrium:

$$\beta A'(n-1)Co(n-1,t) + \alpha A'(n)Co(n+1,t) = \beta A'(n)Co(n,t) + \alpha A'(n-1)Co(n,t)$$

If there is no steady state growth of clusters through the size classes (i.e. for steady state conditions), the preceding equation can be made more restrictive,

$$\beta A'(n-1)Co(n-1,t) = \alpha A'(n-1)Co(n,t)$$

or

$$\alpha = \beta \frac{Co(n-1,t)}{Co(n,t)}$$

It should be noted that by using an equilibrium condition, α has been determined by invoking the principle of time reversibility. This principle requires that at equilibrium every microscopic process takes place at the same rate as its reverse. Substituting for a in the rate equation

$$\frac{\partial C}{\partial t} = \beta A'(n) Co(n,t)\left[\frac{C(n+1,t)}{Co(n+1,t)} - \frac{C(n,t)}{Co(n,t)}\right]$$

$$= \beta A'(n-1) Co(n-1,t)\left[\frac{C(n,t)}{Co(n,t)} - \frac{C(n-1,t)}{Co(n-1,t)}\right]$$

The preceding is the difference-differential equation for nucleation. This equation can be greatly simplified if we assume that C/Co and Dco vary slowly with n and if we disregard terms of higher than second order. To proceed, we define

$$D(n) = \beta A/(n) = \beta A(n)$$

where A(n) is the surface area for size n, A'(n) is the area around a cluster of size n that can accept a monomer, and D(n) is the diffusion coefficient of cluster in cluster size space. Now, we expand in a Taylor series about n the following functions

$$\frac{C(n+1)}{Co(n+1)} \qquad \frac{C(n-1)}{Co(n-1)} \qquad D(n-1)Co(n-1)$$

Substituting these into the difference differential equation yields:

$$\frac{\partial C}{\partial t} = \frac{\partial}{\partial n}\left[D(n)Co(n)\frac{\partial\left(\frac{C(n)}{Co(n)}\right)}{\partial n} \right]$$

The above is the isothermal nucleation equation and has the form of Fick's 2nd law of diffusion in a force field. This observation is consistent with the view that nucleation is a random-walk process through cluster size space.
We can rewrite the nucleation equation as an equation of continuity as follows:

$$\frac{\partial C}{\partial t} + \frac{\partial J(n)}{\partial n} = 0 \qquad \textit{and} \qquad J(n) = -DCo\frac{\partial}{\partial n}\left(\frac{C}{Co}\right)$$

where J(n) is the net number of clusters growing from size n to (n+1).
Equation (4) can also be written as:

$$J(n) = -D\frac{\partial C}{\partial n} + UC \qquad \textit{and} \qquad U = D\frac{1}{Co}\frac{\partial Co}{\partial n} = D\frac{\partial}{\partial n}(\ln Co)$$

random walk term drift velocity, U, term

The Steady State

We now consider the possibility that a steady state current of clusters exists without any change in C (i.e. In order to produce such a situation, we must continuously supply monomers to keep C(1) constant and remove all the clusters equal to or larger than a certain size, n, so that size will not go to infinity). This scheme was first proposed by Becker and Döring, Ann. Physik, 24, 719 (1935). Using the equation for the nucleation rate we have.

$$J_S = -DCo\frac{\partial}{\partial n}(Cs/Co)$$

where the subscript s indicates steady state. Also, from the steady state model we can write

$$(C_S/Co)_{n=1} = 1 \qquad and \qquad (C_S/Co)_{n=\hat{n}} = 0$$

Integrating the equation for J_s yields

$$\int_{n=1}^{n=\hat{n}} -\frac{J_S}{DC_O}dn = \int_1^{\hat{n}} d(Cs/Co) = -1 \qquad or \qquad J_S = \frac{1}{\int_1^{\hat{n}} dn/DCo}$$

In general

$$Co(n) = C(1)\exp\left[\frac{-\Delta G(n)}{kT}\right]$$

Where C(1) is the number of monomers and ΔG(n) is the free energy to form a cluster of size n. C_o has a sharp minimum when ΔG is maximized, or when $n=n_c$. Thus, we can set $D=D_c$ and approximate C_o by expanding ΔG(n) about n_c to the second order to get

$$J_S = D_C C_O(n_C)\left[\frac{\partial^2 \Delta G(n_C)}{\frac{\partial n^2}{2\pi kT}}\right]^{1/2} = DC_O Z$$

where

$$Z = \left[\frac{\partial^2 \Delta G(n_C)}{\frac{\partial n^2}{2\pi kT}}\right]^{1/2} = \left[\frac{-1}{2\pi}\left(\frac{\partial^2 \ln C_o(n_C)}{\partial n^2}\right)\right]^{1/2}$$

Z is generally called the Zeldovich Factor.

Nucleation Product Phase Size Distribution

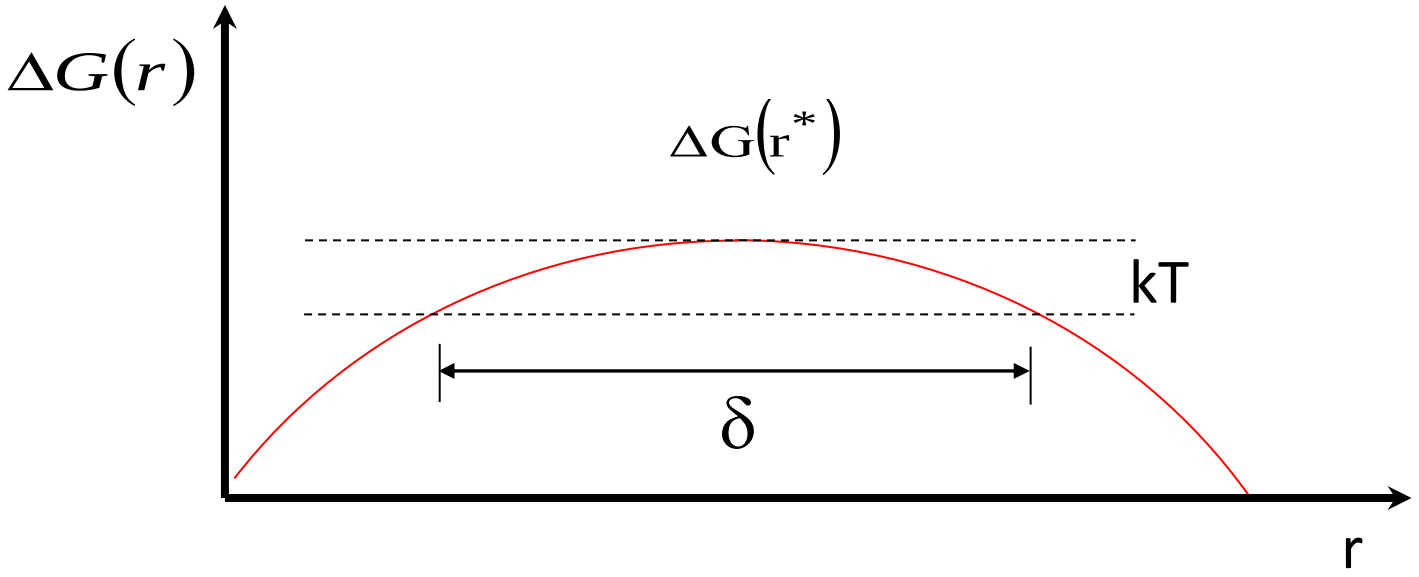

Of ten, observations on nucleation processes yield a product phase size distribution. However, the usual analysis of nucleation does not seem to treat this result in a clear manner. We expect that the size distribution is Gaussian in nature. To develop an analytical expression we can examine a spherical nucleus geometry as an illustration.

The work to form a cluster of radius, r is given by
at the critical size, $d\Delta G(r)/dr = 0$ and

$$\Delta G(r) = 4\pi r^2 \sigma + \frac{4}{3}\pi r^3 \Delta G_v$$

which yields

$$r^* = -2\sigma / \Delta G_v$$

$$\Delta G^* = \frac{16\pi\sigma^3}{3\Delta G_v^2}$$

Now, ΔG^* can be expressed in terms of r^* by substituting $\Delta G_v = -2\sigma/r^*$ so that

$$\Delta G^* = \frac{4\pi\sigma r^{*2}}{3}$$

Thus, the nucleation barrier is 1/3 of the surface energy of the cluster. Also , the concentration of clusters is given by

$$c\left(r^*\right) = c\left(1\right)\exp\left(\frac{-\Delta G^*}{kT}\right)$$

where c(1) is the concentration of monomers. If we examine cluster sizes near r^* (i.e. (r^*-r)) and expand $\Delta G(r)$ we obtain

$$G\left(r\right) = \Delta G\left(r^* - \Delta r\right) = \Delta G\left(r\right)_{r^*} + \left[\frac{d\Delta G\left(r\right)}{dr}\right]_{r^*} \Delta r + \left[\frac{d^2\Delta G\left(r\right)}{dr^2}\right]_{r^*} \frac{\Delta r^2}{2}$$

Since $\left[\frac{d\Delta G\left(r\right)}{dr}\right]_{r^*} = 0$

$$\Delta G\left(r\right) = \frac{4\pi\sigma r^2}{3} + \left[\frac{d^2\Delta G\left(r\right)}{dr^2}\right]_{r^*} \frac{\Delta r^2}{2}$$

We can also note that

$$\left[\frac{d^2\Delta G\left(r\right)}{dr^2}\right]_{r^*} = 8\pi\sigma + 8\pi r^*\Delta G_v = 8\pi\sigma + 8\pi r^* \left(-2\sigma/\Delta G_v\right) \Delta G_v = -8\pi\sigma$$

then, $$\Delta G(r) = \frac{4\pi\sigma r^2}{3} - 8\pi\sigma\frac{\Delta r^2}{2}$$

so that $$c(r) = c(r^*)\exp\left(\frac{4\pi\sigma\Delta r^2}{kT}\right)$$

The normal distribution is

$$P(x) = \frac{1}{s(2\pi)^{1/2}}\exp\left(-\frac{\left(x-\bar{x}\right)^2}{2s^2}\right)$$

which indicates that

$$s = \left(\frac{kT}{4\pi\sigma}\right)^{1/2} \quad \text{and that} \quad \bar{x} = r^*$$

Thus, the measured distribution parameters can be used to determine r^* and σ which in turn will give ΔG^* and J.

Nucleation Theorems

Most of the existing methods of analyzing nucleation behavior are linked to specific models. Nucleation theorems developed by Kashchiev offer a general model independent analysis to determine properties of the critical nucleus. Since the initial introduction, several variants have been developed

1st Nucleation Theorem

$$\left.\frac{\partial W^*}{\partial \mu_{oi}}\right|_T = -\Delta n_i^*$$

Δn^* is the excess number of atoms of type i in the nucleus over that present in the same volume of the original phase

1st Nucleation Theorem (cont'd)

$$\left.\frac{\partial W^*}{\partial \mathrm{T}}\right|_{\mu} = -\Delta S^*$$

$$\left.\frac{\partial W^*}{\partial \mathrm{P}}\right|_{\mathrm{T}} = -\nu_0 \Delta n^*$$

Application

$$J = A\exp(-W^* / k\mathrm{T})$$

$$W^* = -k\mathrm{T}\ln J + k\mathrm{T}\ln A$$

$$-\Delta n^* = \left.\frac{\partial W^*}{\partial \mu_{oi}}\right|_{\mathrm{T}} = -\frac{\partial(k\mathrm{T}\ln J)}{\partial \mu_{oi}} + \frac{\partial(k\mathrm{T}\ln A)}{\partial \mu_{oi}}$$

Binary Systems

- Measure “critical supersaturation” (or constant J)

$$kTd\ln J = 0 = kTd\ln A - dW^* \cong -dW^*$$

$$W^* = f(a_1, a_2)$$

$$0 = -dW^* = -\left(\frac{\partial W^*}{\partial \ln a_1}\right)_T d\ln a_1 - \left(\frac{\partial W^*}{\partial \ln a_2}\right)_T d\ln a_2$$

Binary Systems (cont'd)

$$kTd\ln a_1 = d\mu_{o,1} \quad \text{and} \quad kTd\ln a_2 = d\mu_{o,2}$$

$$O = \Delta n_1^* d\ln a_1 + \Delta n_2^* d\ln a_2$$

or

$$\left(\frac{\partial \ln a_2}{\partial \ln a_1}\right)_{T,\,J} = -\frac{\Delta n_1^*}{\Delta n_2^*}$$

2nd Nucleation Theorem

$$\left(\frac{\partial(W^* / \mathrm{T})}{\partial \mathrm{T}}\right)_p = -\frac{1}{\mathrm{T}^2}\ (\Delta E^* - h_0 \Delta n^*)$$

ΔE* is the energy change through creation of the critical cluster and h_0 is the enthalpy per atom in the parent phase.

$$\left(\frac{\partial \ln J}{\partial \mathrm{T}}\right)_{P_0} = \left(\frac{\partial \ln A}{\partial \mathrm{T}}\right)_{P_0} + \frac{1}{k\mathrm{T}^2}(\Delta E^* - n^* L_f)$$

Delay Time and Steady State Nucleation

$$J = Z\beta C(n^*) \qquad \tau = (\theta\beta Z^2)^{-1}$$

$$J\tau = C(n^*)/\theta Z$$

$$Z = [\Delta G(n^*)/(3\pi k\mathrm{T})n^{*2}]^{1/2}$$

$$Z = (1/8\pi v_b)(\sigma/kT)^{-3/2}(\ln S)^2$$

$$\ln(J\tau) = \ln(N_0/\theta Z) - (16\pi\sigma^3 v_b^3/3k^3)/[\mathrm{T}^3(\ln S^2)]$$

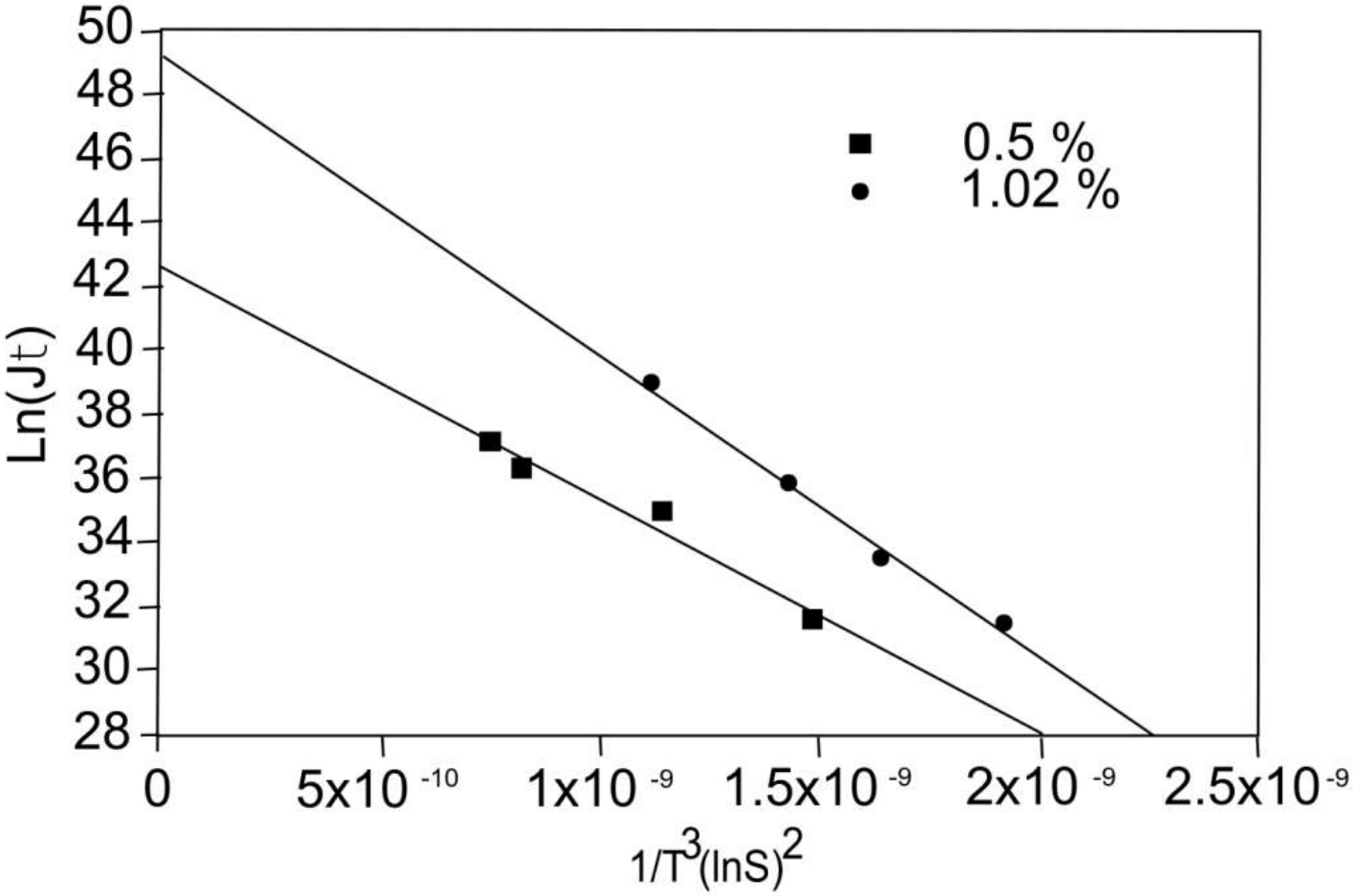
50
48
46
44
42
40
38
36
34
32
30
28
Ln(Jt)
0
5x10 -10
1x10 -9
1.5x10 -9
2x10 -9
2.5x10 -9
1/T3(lnS)2
0.5 %
1.02 %

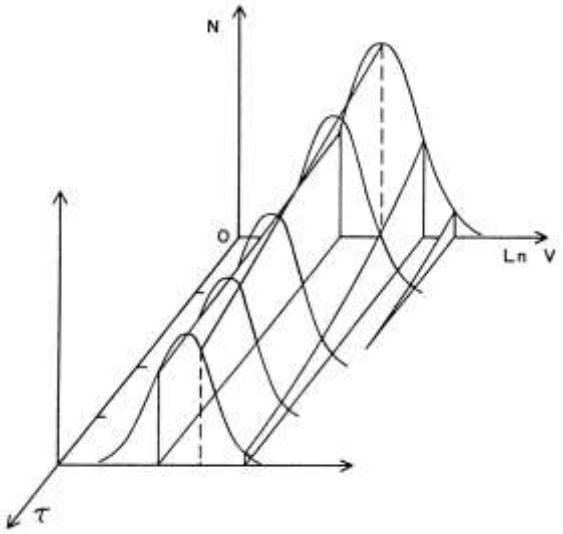

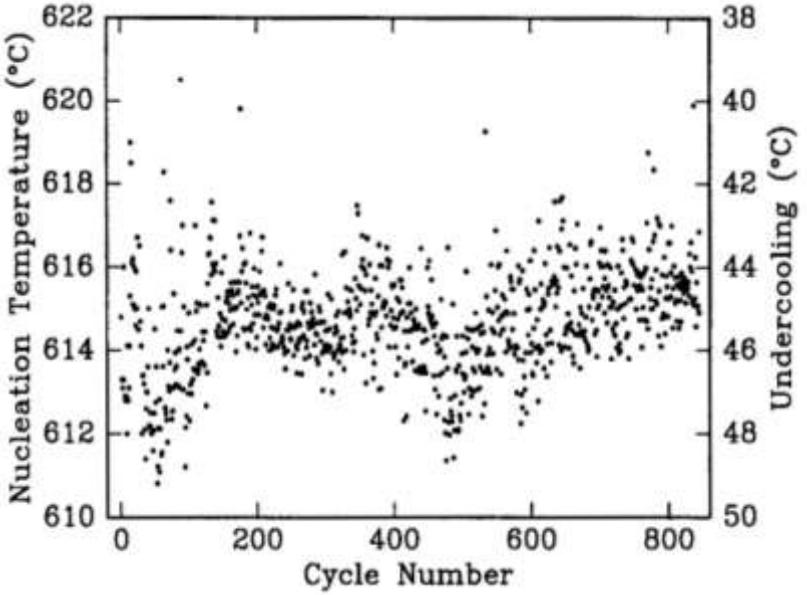

Single Run, Multiple Droplets	Single Droplet, Multiple Runs
average behavior of large number of independent nucleation events	direct observation of individual nucleation event
convolute nucleation statistics / multiple sites	convolute nucleation statistics / site development
identical thermal history for all droplets	identical droplet for all nucleation events
traces average behavior	traces the most potent site in a particular droplet

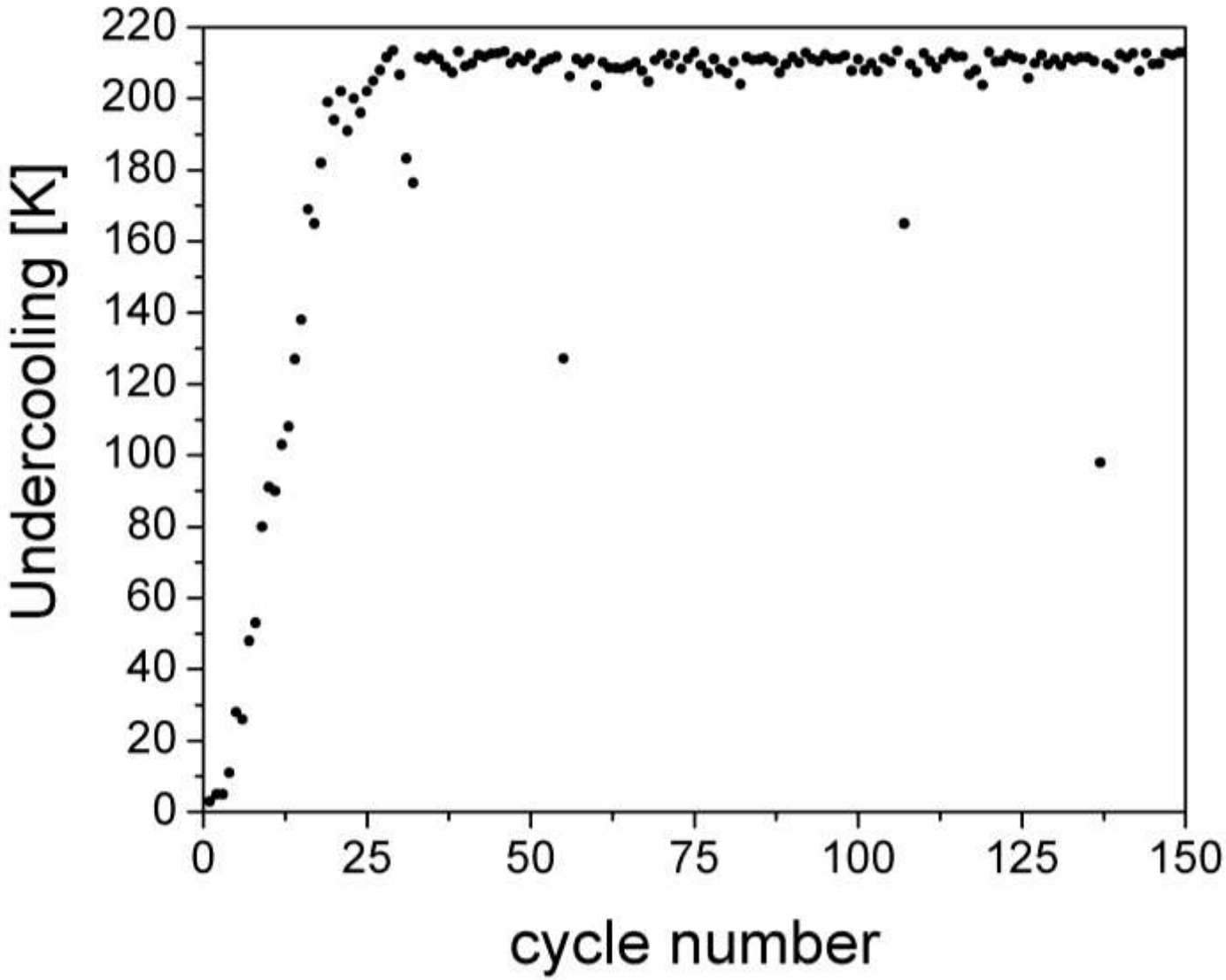
Undercooling [K]
220
200
180
160
140
120
100
80
60
40
20
0
0
25
50
75
100
125
150
cycle number

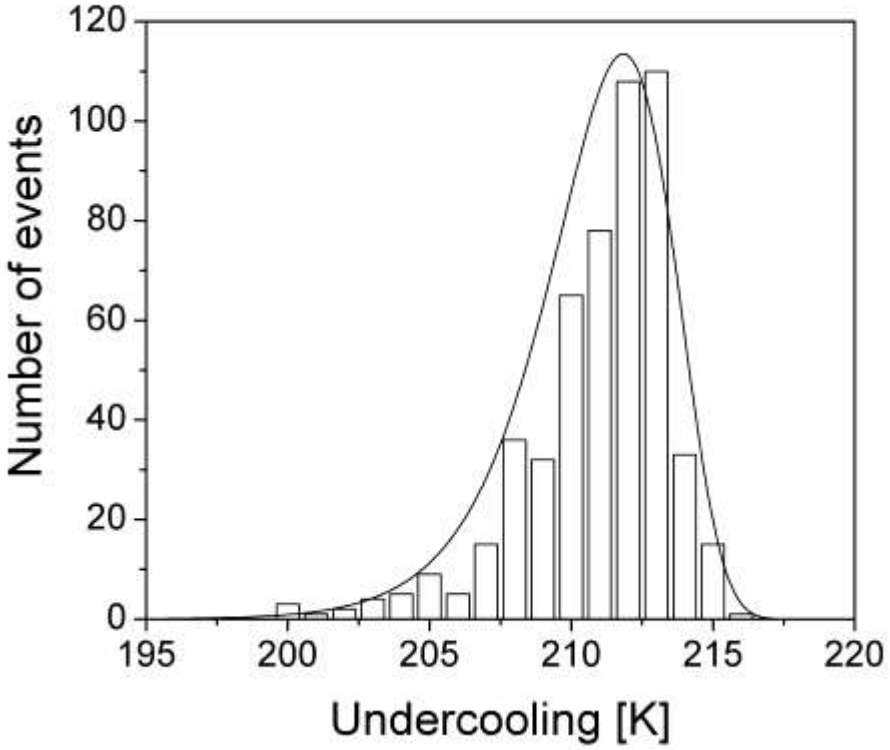

$$\lambda_i = \frac{1}{h_i} \frac{d_i}{(s_i + 0.5 d_i)}$$

λ_i = nucleation probability/unit time
h_i = interval width
d_i = # events/ h_i
s_i = # unfrozen
$J = \lambda / v$ (nucleation rate)

$$J = \rho \frac{D_l}{a_0^2} \frac{2\pi r^2 (1 - \cos[\theta])}{a_0^2} \exp\left[- \frac{\Delta G^* f(\theta)}{kT} \right]$$

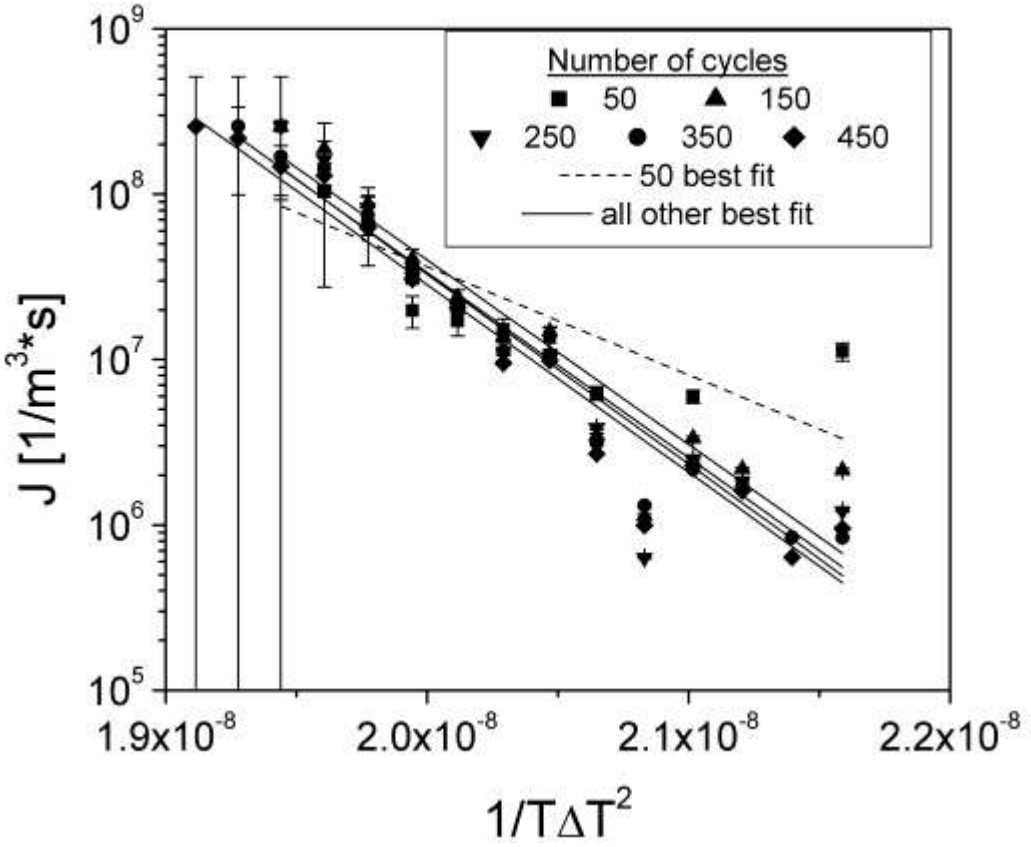

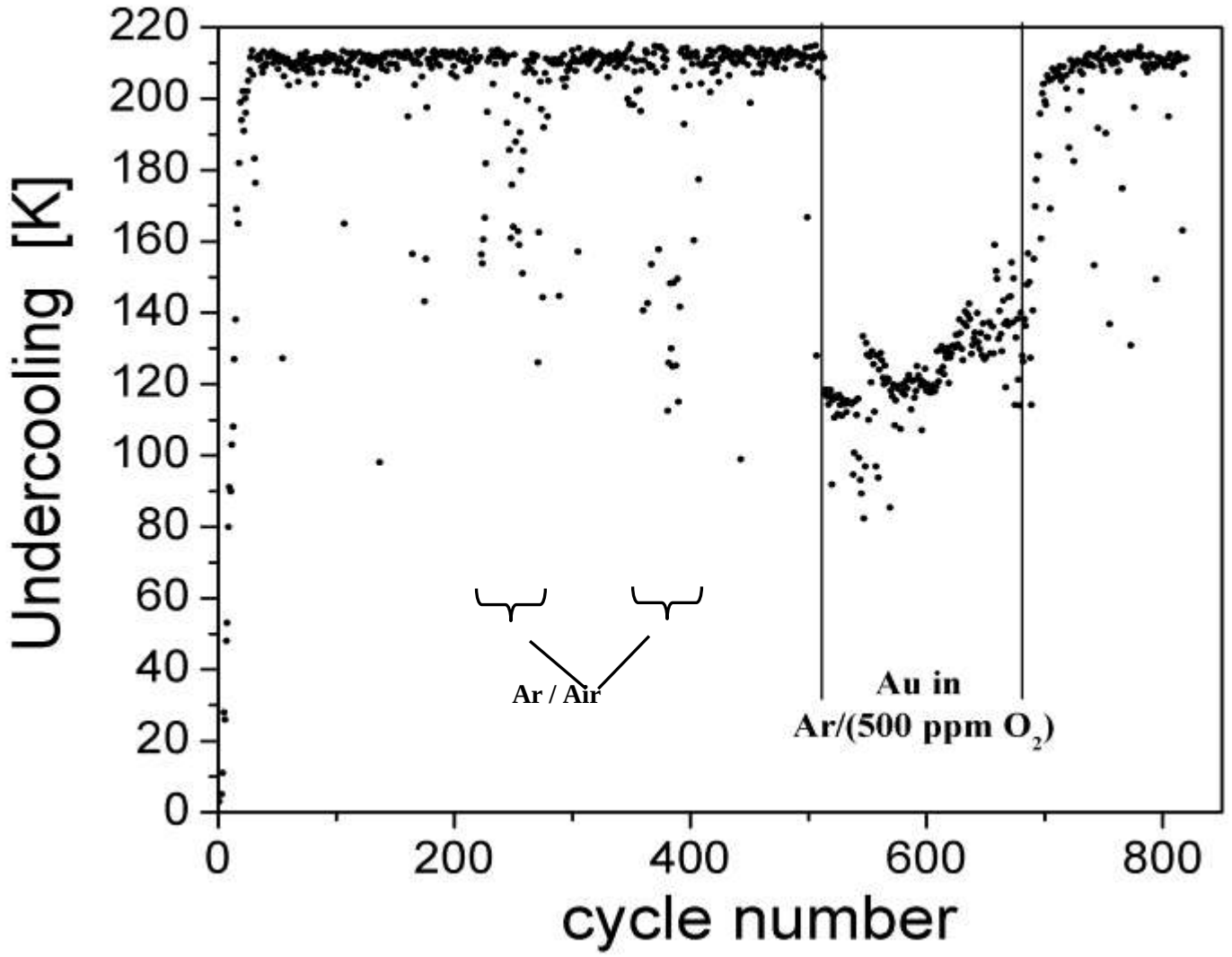
Undercooling [K]
220
200
180
160
140
120
100
80
60
40
20
0
0
200
400
600
800
cycle number
Ar / Air
Au in
Ar/(500 ppm O2)

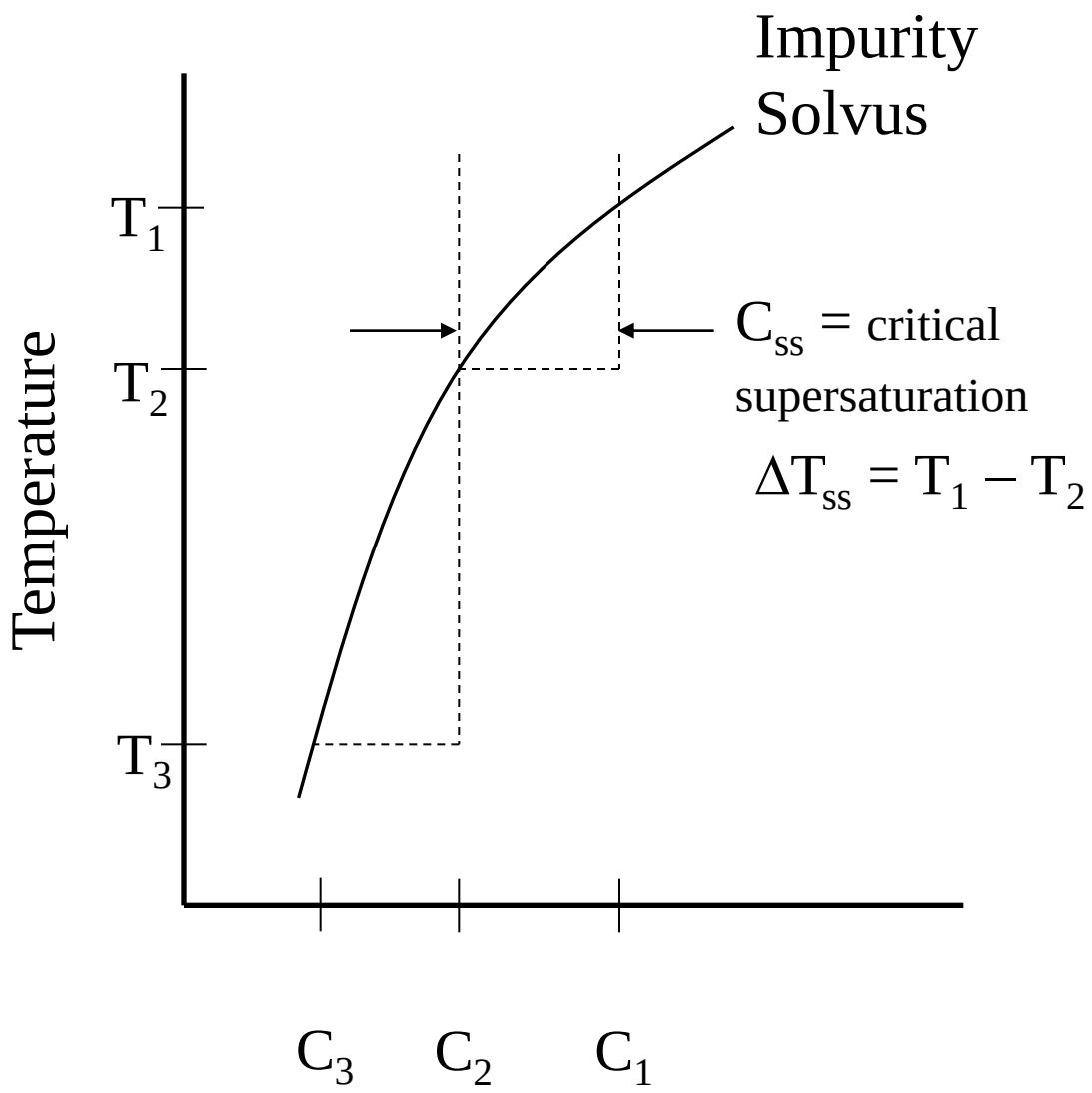

$$\Delta G_v = RT_2 \ln(C_{ss}) = \frac{-\Delta H_s \, \Delta T_{ss}}{T_1}$$

- Homogeneous Nucleation
  - Nucleation rate

$$J_v = n_v \nu \exp\left[\frac{-\Delta G_A}{kT}\right]\exp\left[\frac{-a\sigma_{sl}^3}{\Delta G_v^2 kT}\right]$$

- Heterogeneous Nucleation

$$n_v \Rightarrow n_s$$

$$a \Rightarrow a\,f(\theta)$$

$N_v = n_{v0}\exp(\beta\Delta T)$

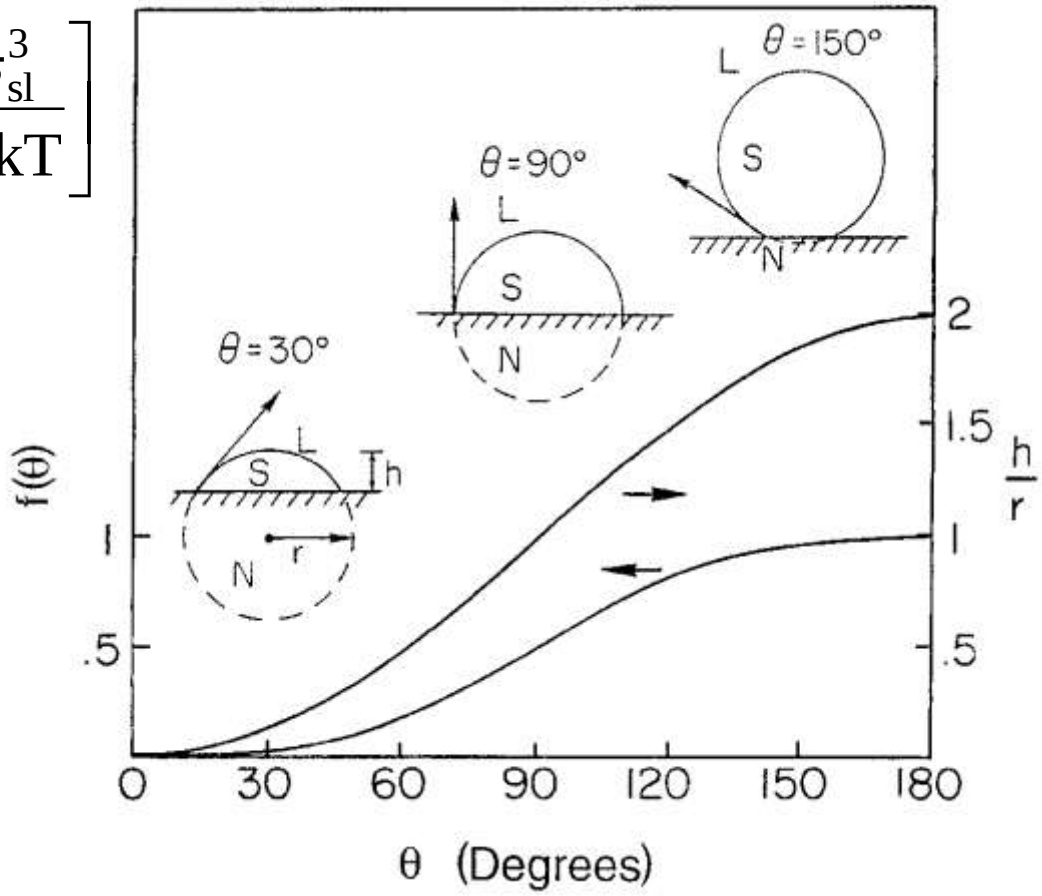

50 nm

und
0.2
0

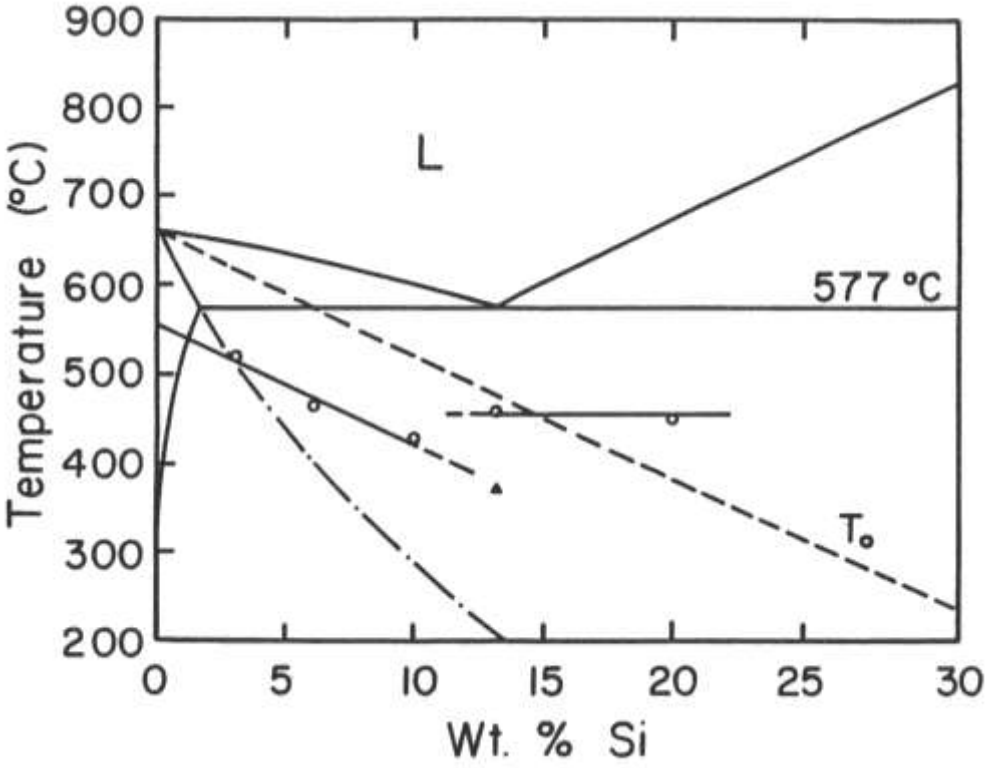

Undercooled behavior of Al-Si alloys.The triangle point represents the quenched eutectic signal.

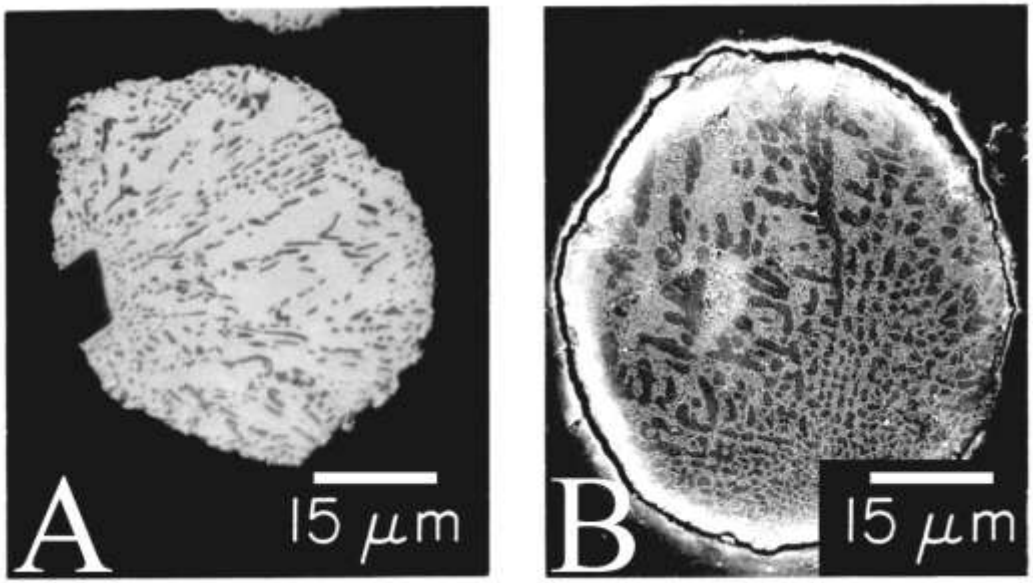

Microstructure developed in eutectic Al-Si powders (A) cooled in the DTA, 20K/min [primary Si-dark faceted particle] and (B) quenched, 500 K/sec [primary Al dendrites].

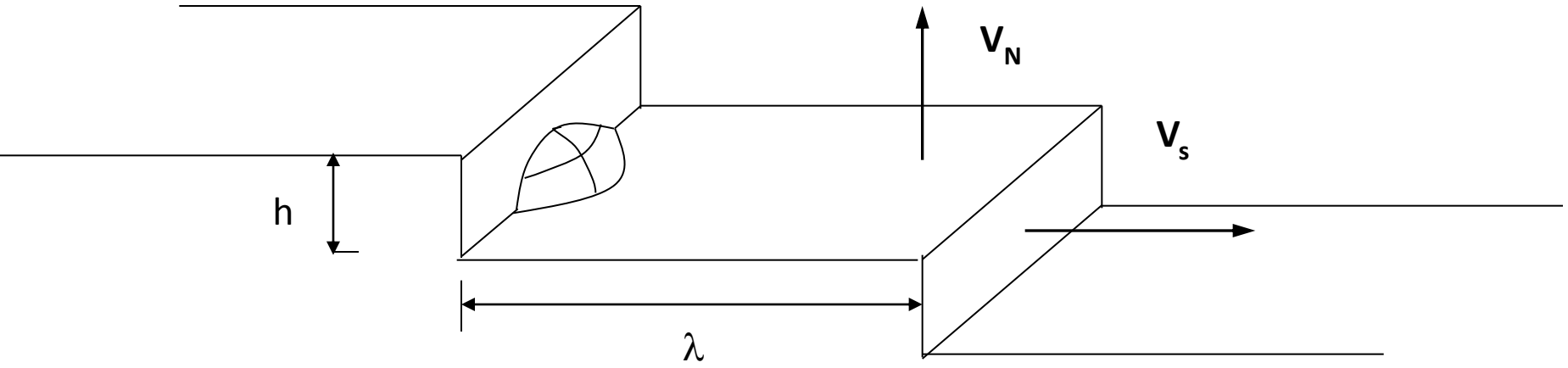

Variety of Possible Scenarios

V_s = 0.01 m/s;

$\tau \cong n^{*2} / \beta$

$\tau \cong 10^{-8} – 10^{-6}$ s (liquid)

$\tau \cong 0.1 – 10$ s (glass)

$V_N = f(h, \lambda, , , \ldots)$

$\beta \cong 10^{10}$ /s (liquid); $\beta \cong 10^{4}$ /s (glass)

n*: 10 – 100

$$f(\theta) = \frac{\Delta G^*_{het}}{\Delta G^*_{hom}} = \frac{V^*_{het}}{V^*_{hom}} = \frac{(l_i - \tau v_s) l_0^2}{l_0^3}$$

Mechanical Properties

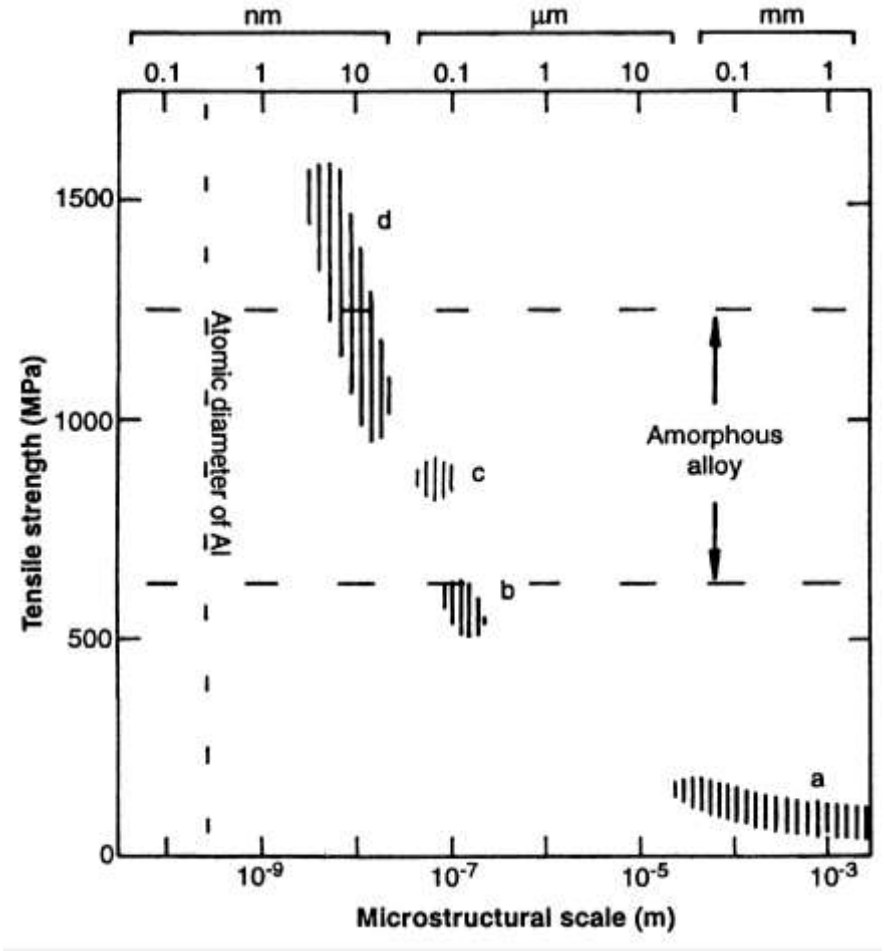

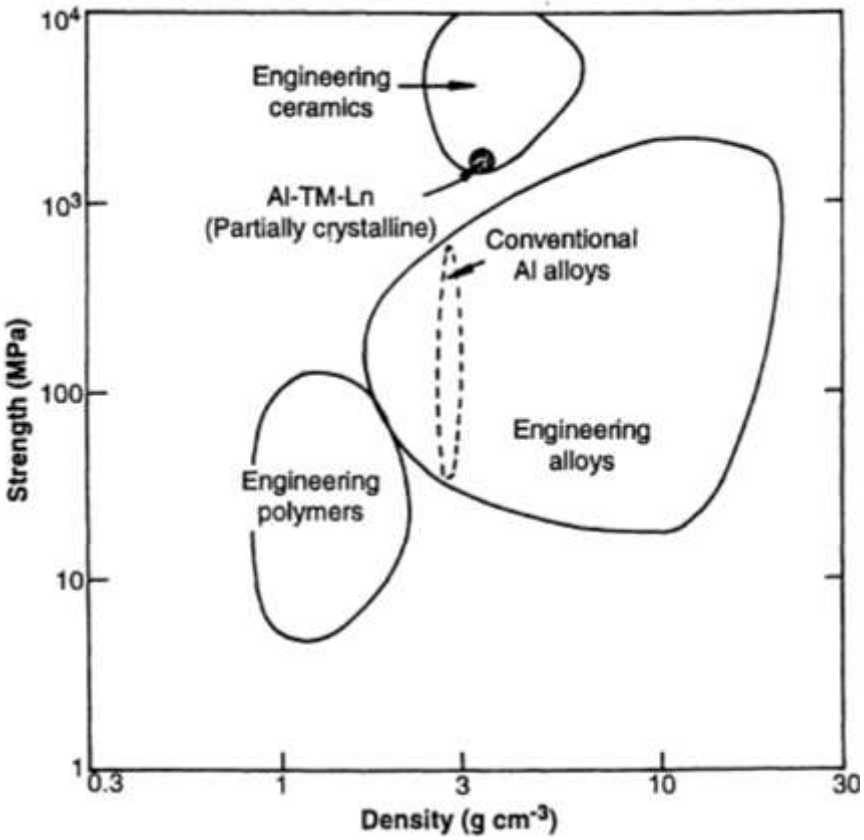

*A. L. Greer, "Metallic Glasses", Science, **267** (1995) pp. 1947*

Annealing of Melt-Spun $Al_{88}Y_7Fe_5$

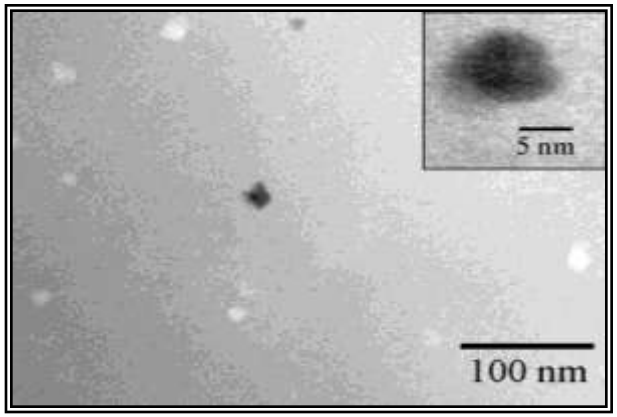

Isotherm at 245ºC 10 min

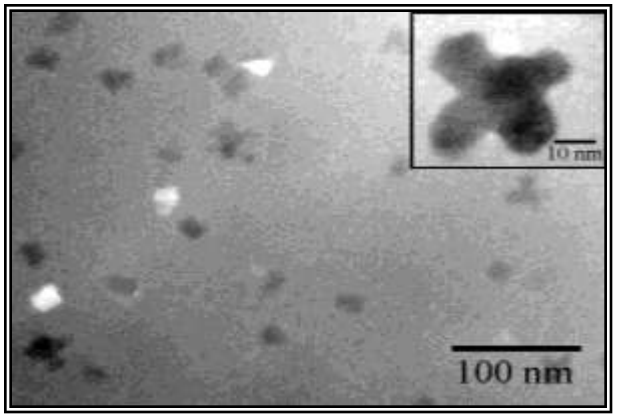

30 min

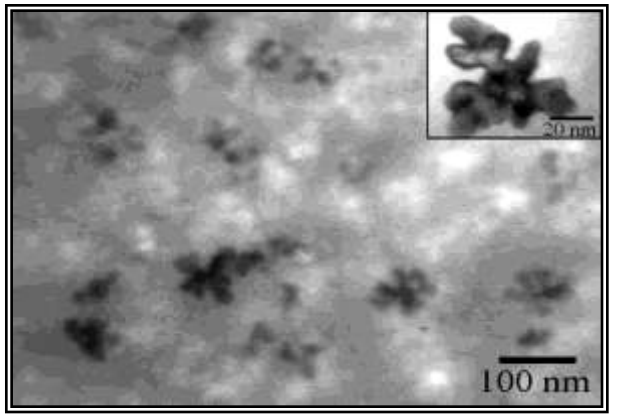

100 min

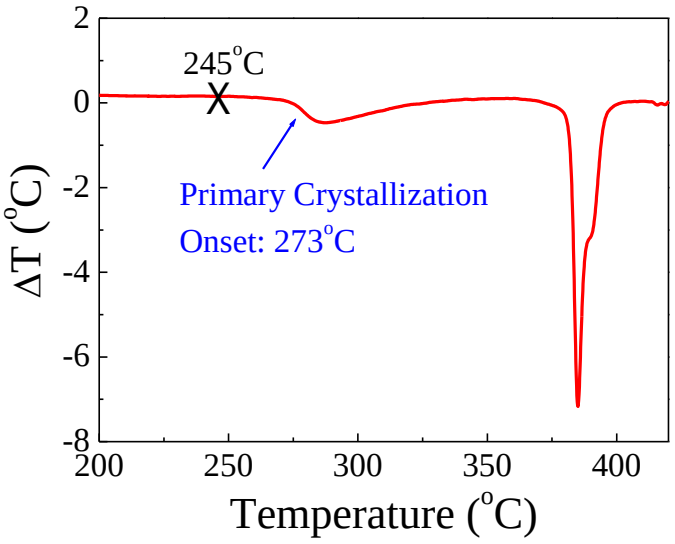

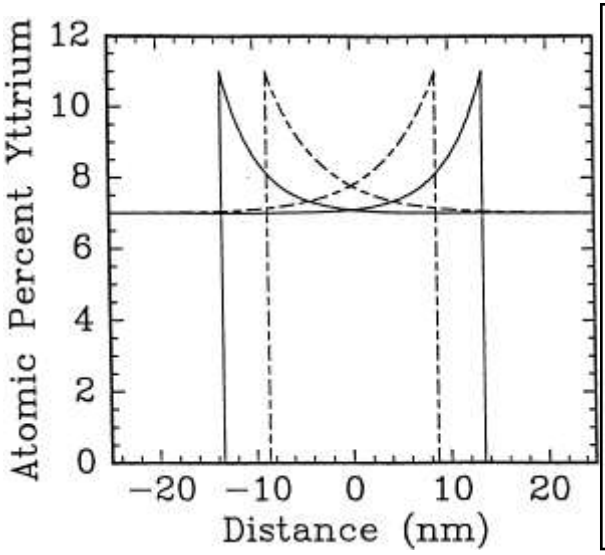

Crystallization of α-Al nanocrystals occurs at temperatures below 273ºC and the growth of the nanocrystals is impeded when the diffusion field impingement occurs

General Features of Nanocrystals

- NC's are pure Al
  - Al_{fcc} is NOT favored thermodynamically
  - Competing against the intermetallic phase
- Growth velocity limited by RE diffusion

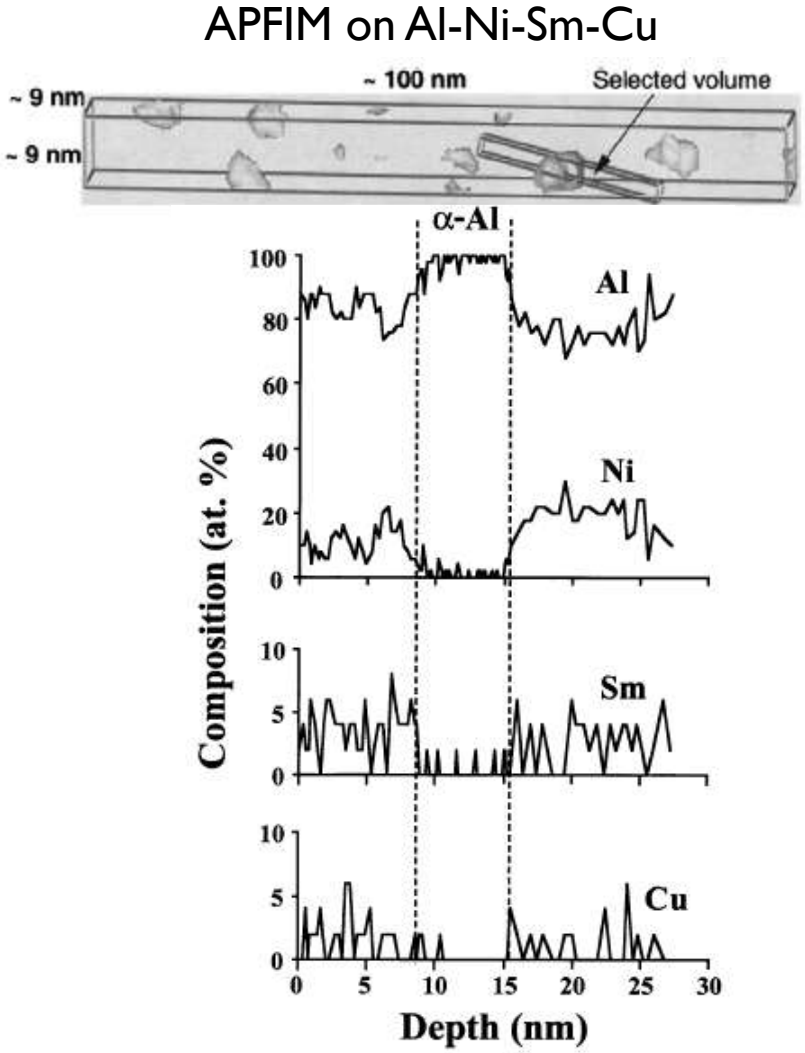

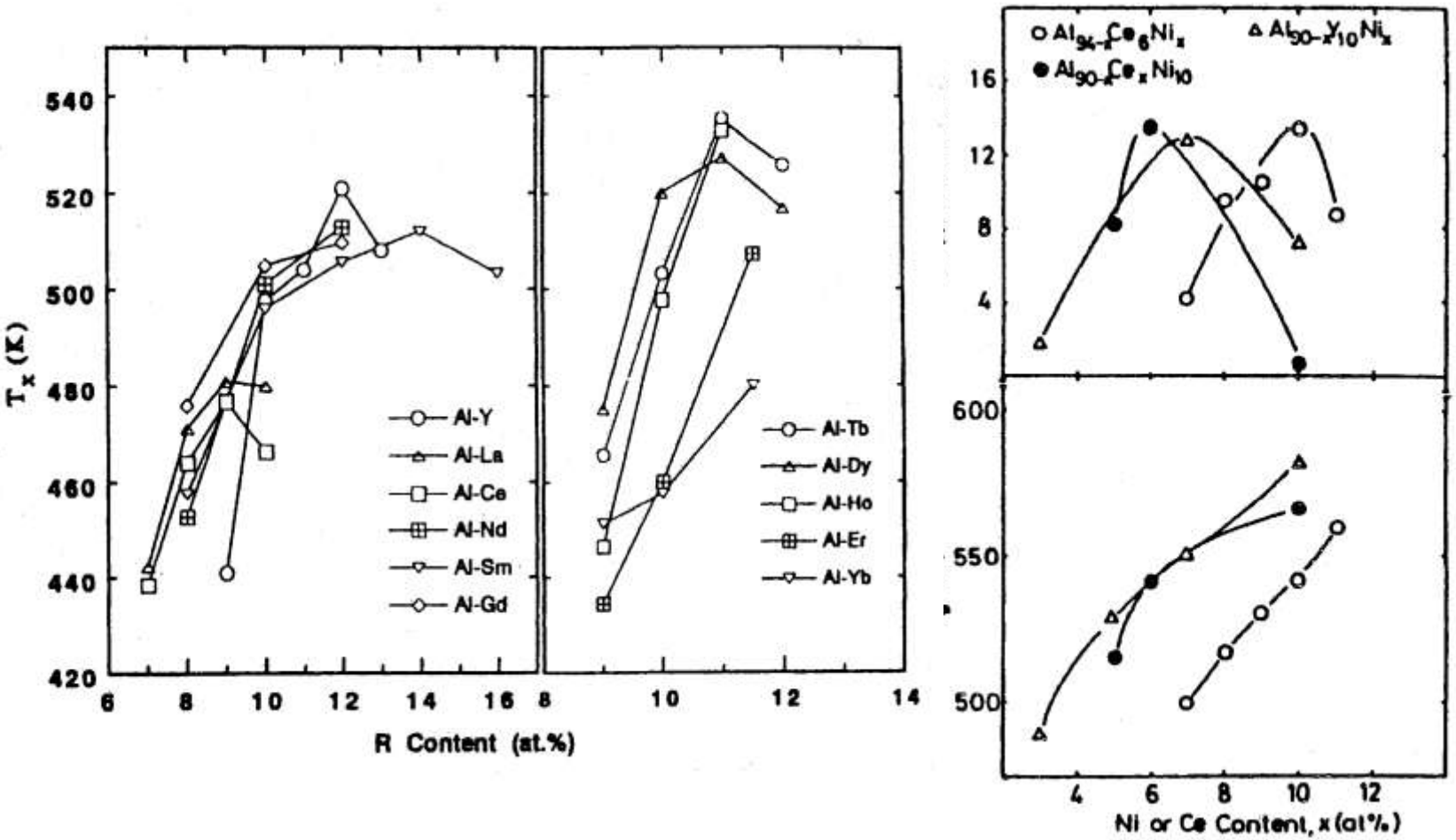

A. Inoue, Progress in Mat. Sci., ***43****, (1998)*

Nucleation Control

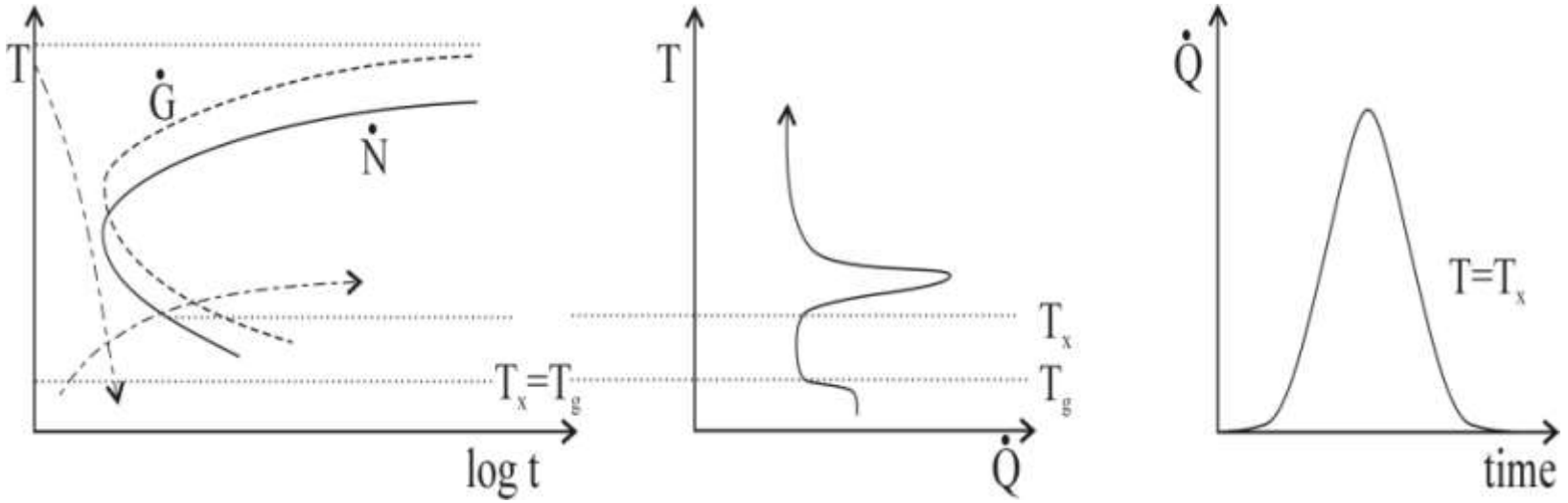

Growth Control

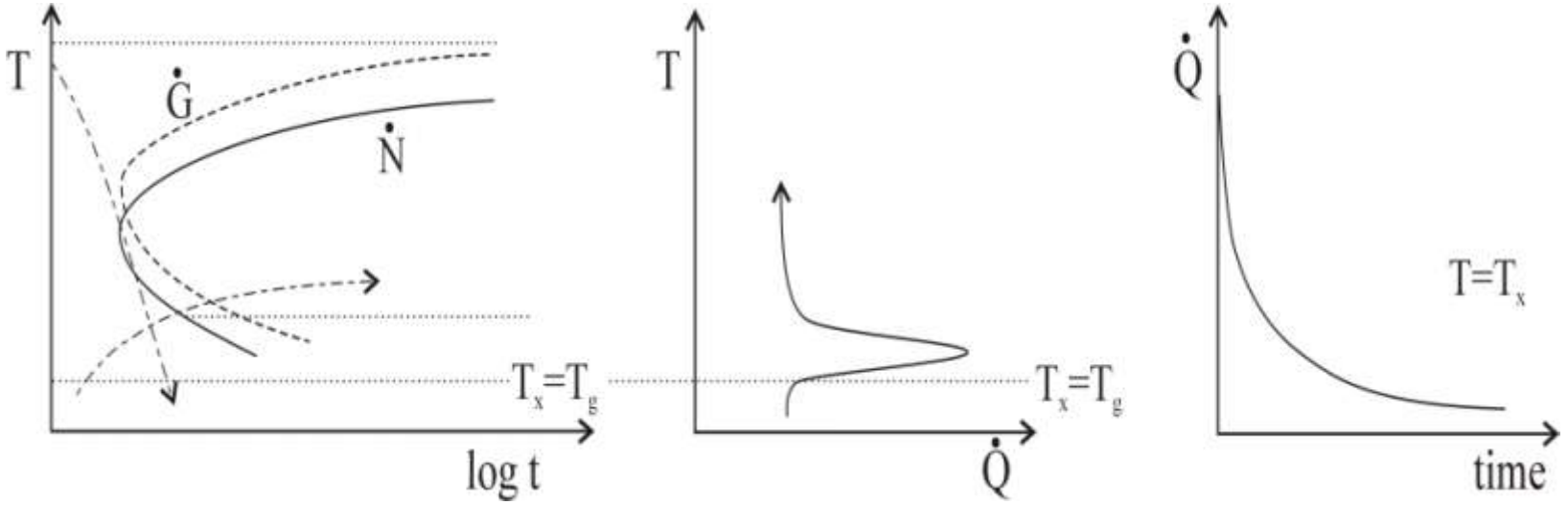

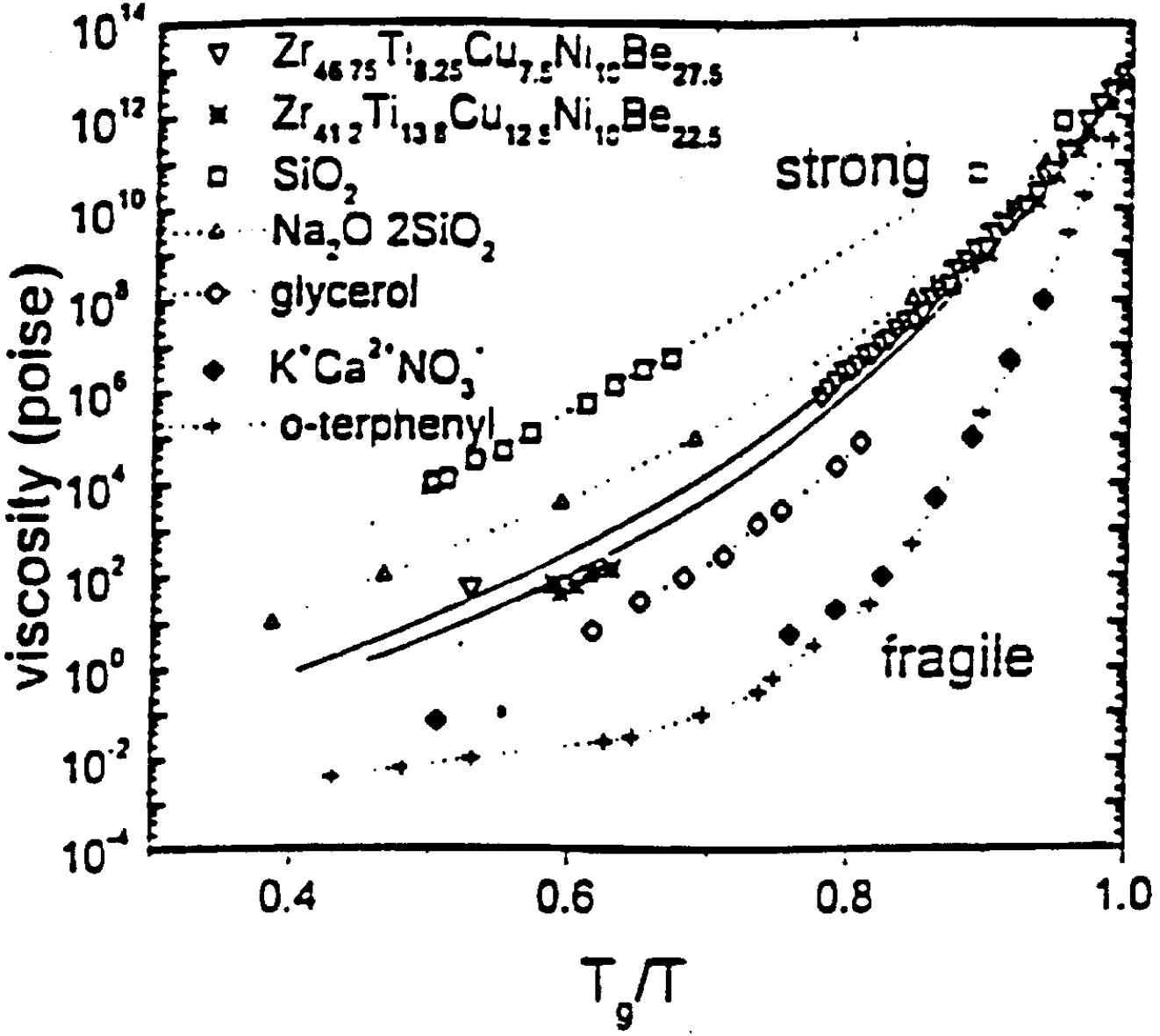

*C. A. Angell, Science, **267**, (1995) pp. 1924*

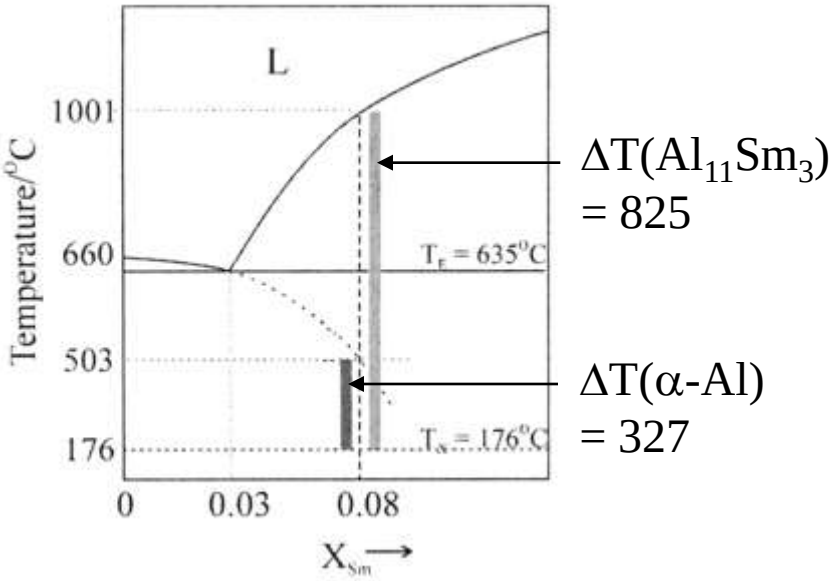

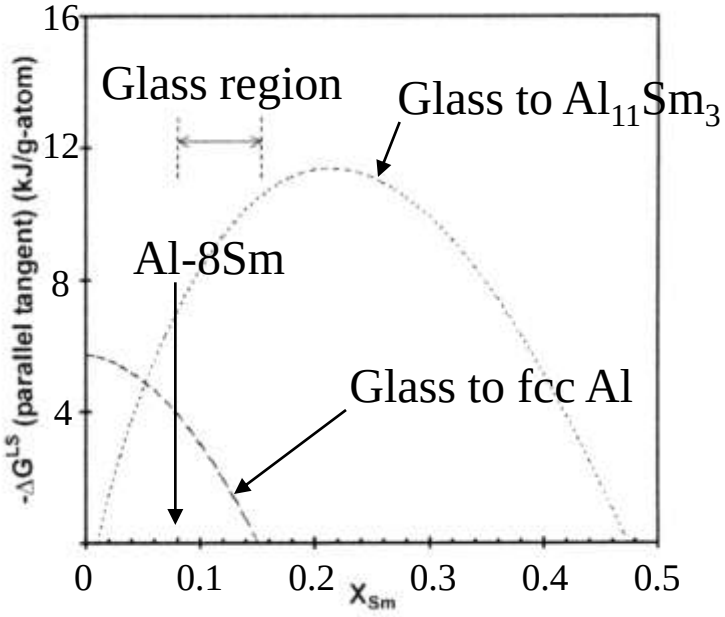

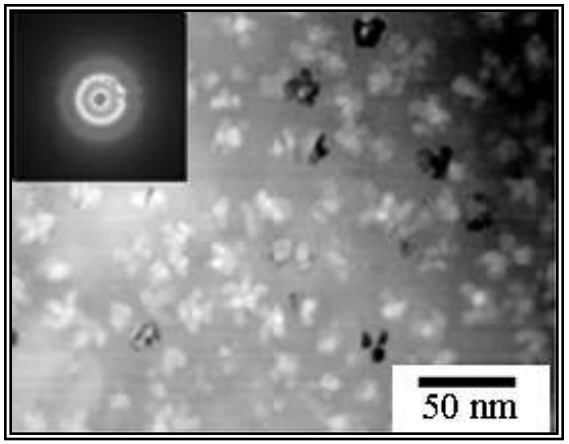

Annealed:150 °C, 10 min

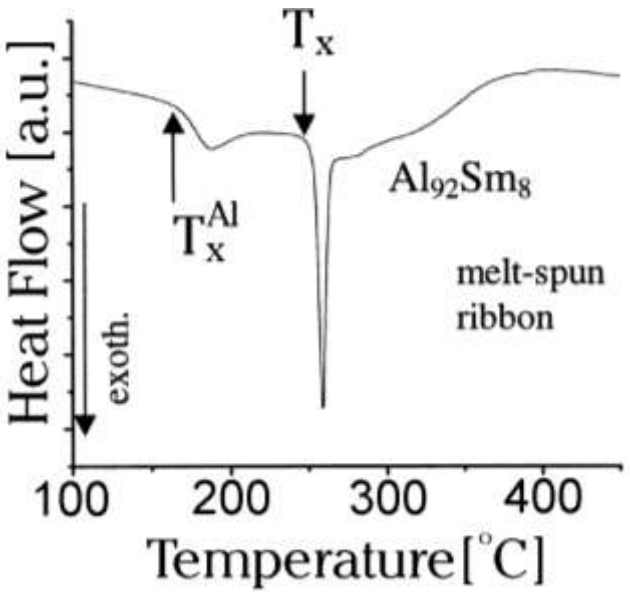

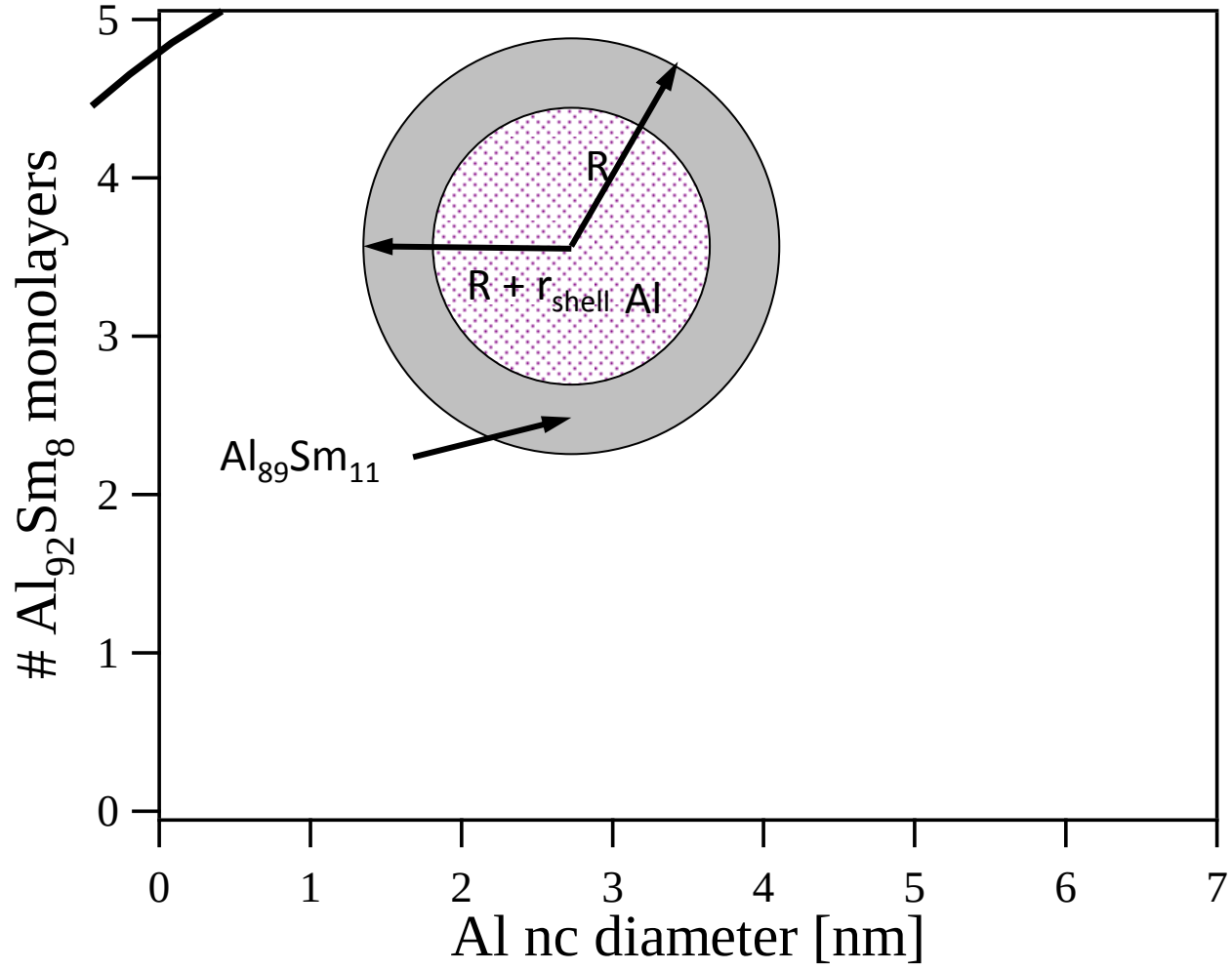
5
4
3
2
1
0
$Al_{92}Sm_8$ monolayers
0
1
2
3
4
5
6
7
Al nc diameter [nm]
R
R + r_{shell} Al
$Al_{89}Sm_{11}$

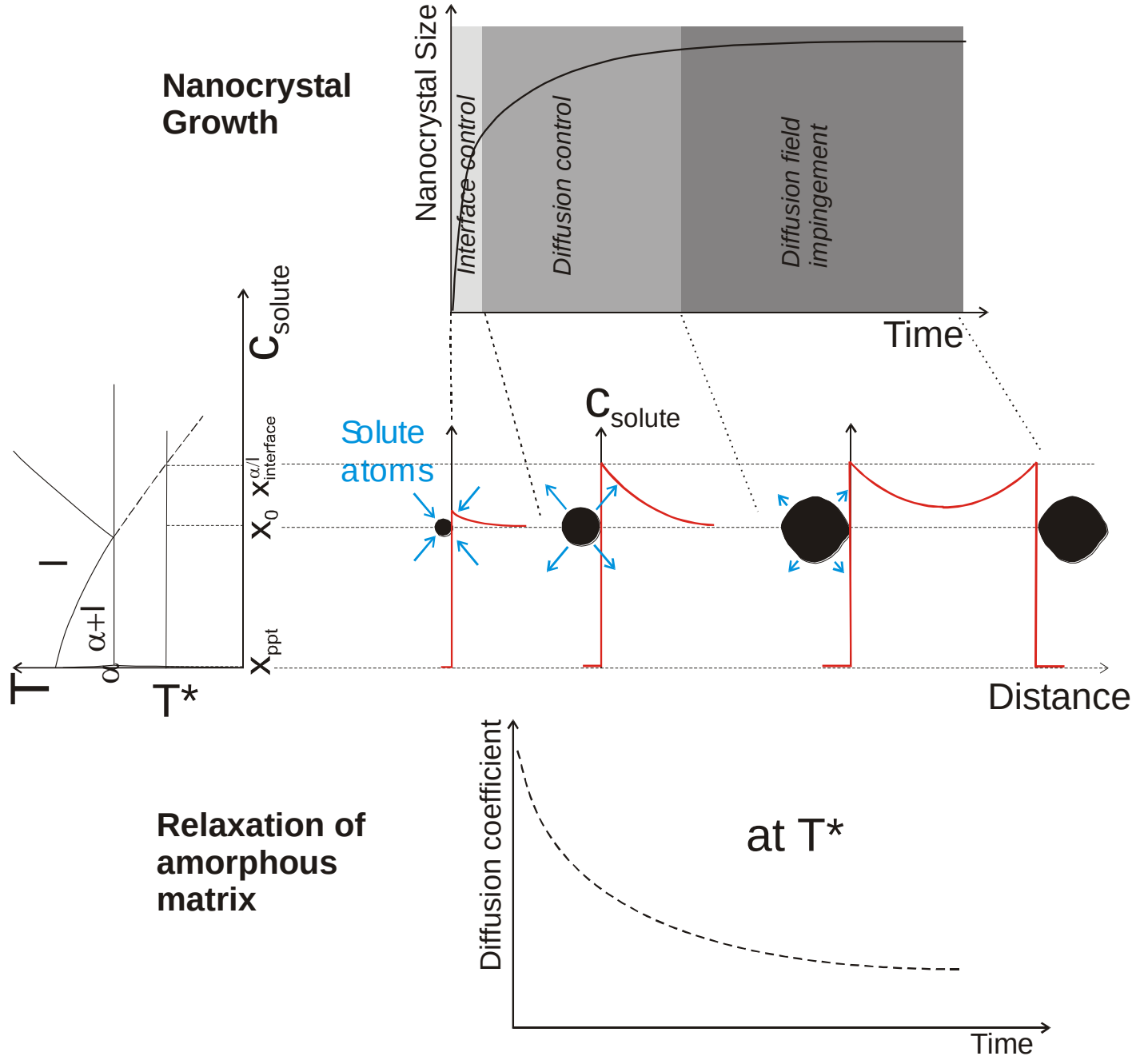

Nanocrystal Growth
Nanocrystal Size
Interface control
Diffusion control
Diffusion field impingement
Time
C_{solute}
x_0
$x_{interface}^{\alpha/l}$
x_{ppt}
α
$\alpha+l$
l
T
T*
Solute atoms
C_{solute}
Distance
Relaxation of amorphous matrix
Diffusion coefficient
at T*
Time

Heterogeneous Catalysis

- Precursor Liquid Phase Separation
  - Site Density
  - Thermodynamics
- Clustering By Linked Fluxes
  - Site Density
- Homophase/Heterophase Catalysis
  - Local Structure
    - Solute Centered
    - Solvent MRO
  - Impurity Cores

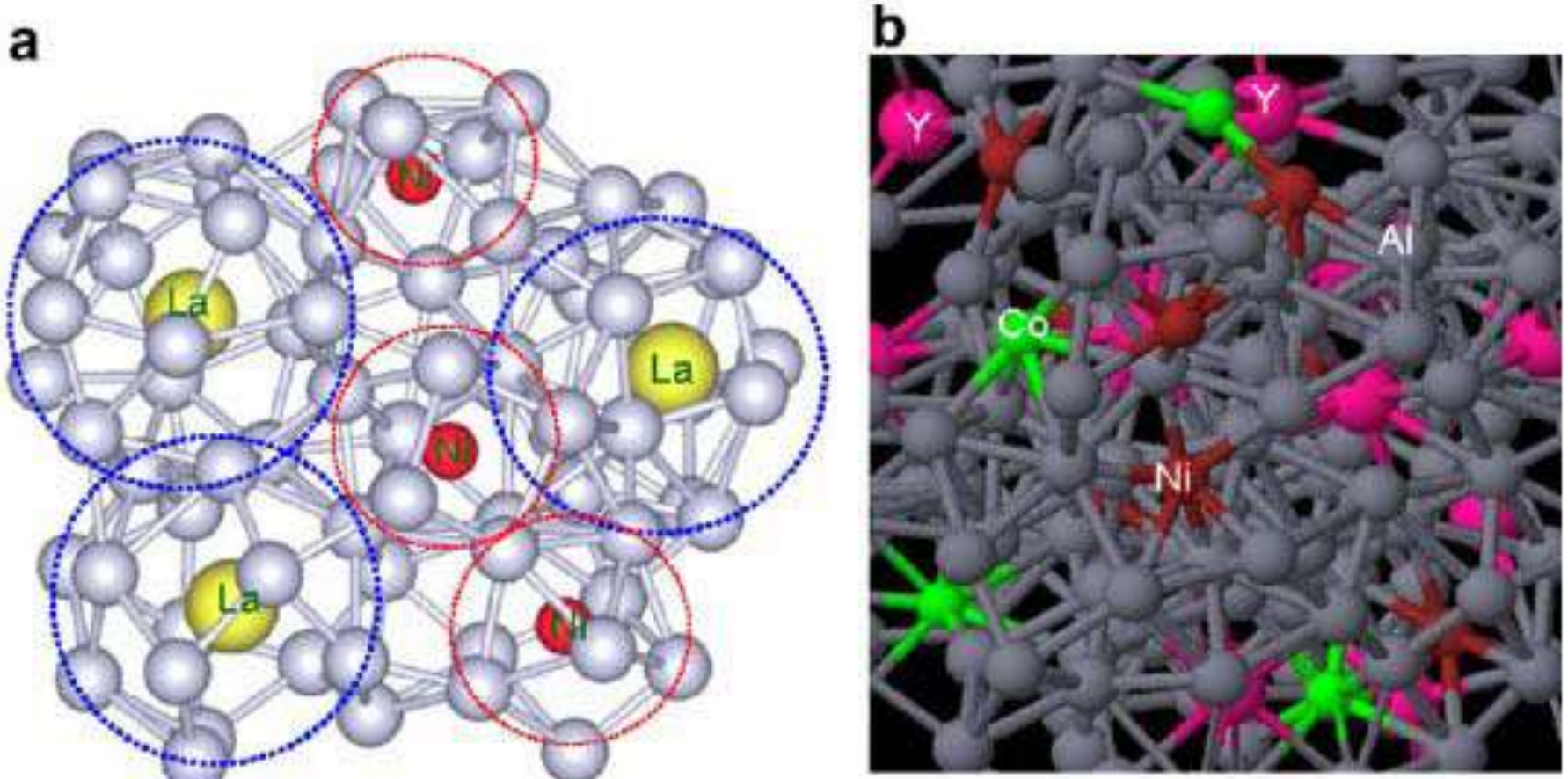

Sheng,et al, Acta Mat. 56, 6264 (2008)

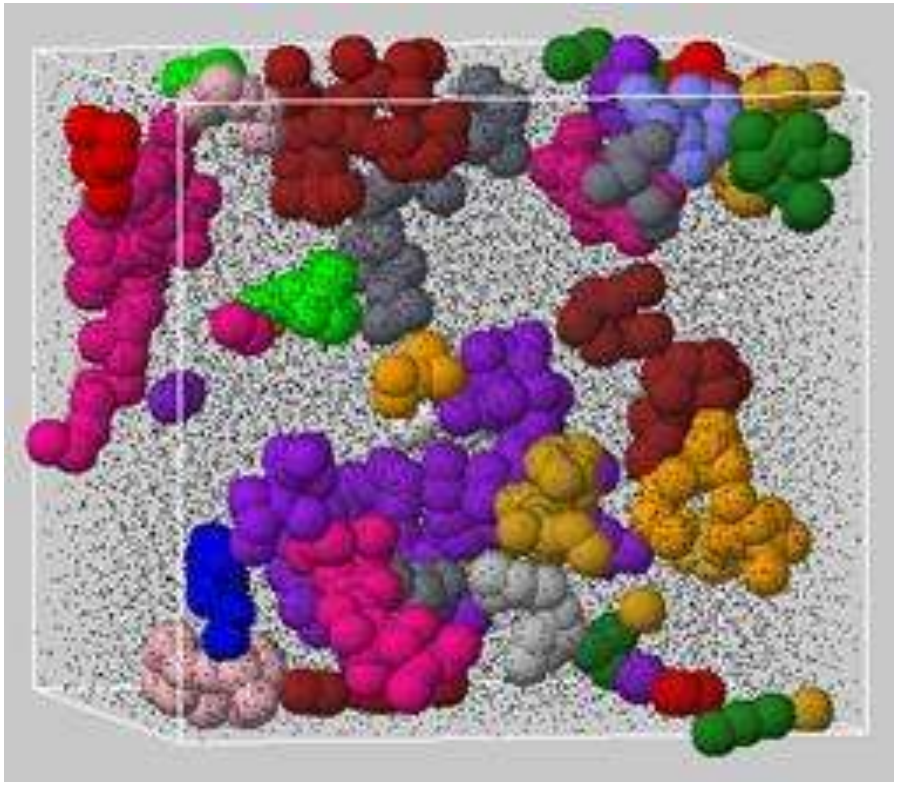

Spatially heterogeneous dynamics
Simulation by Glotzer group (U. of Michigan)

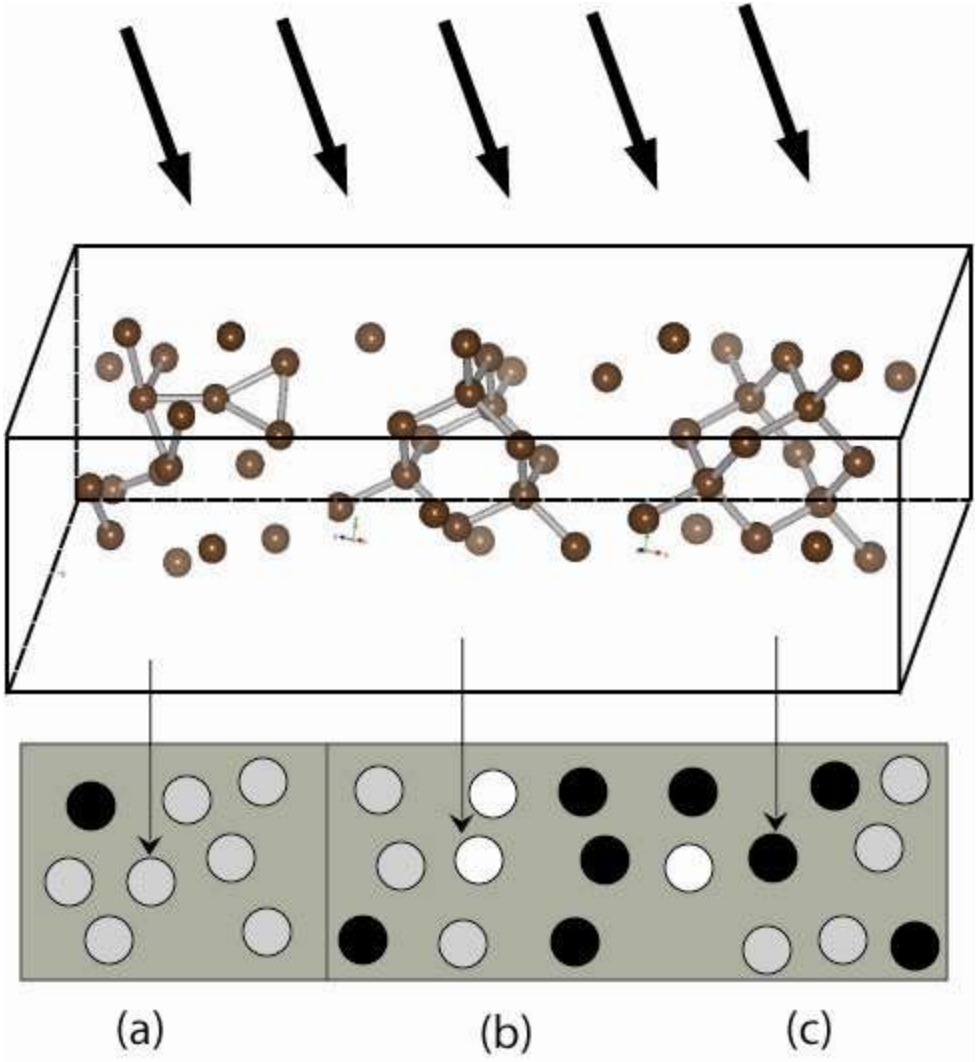
(a)
(b)
(c)

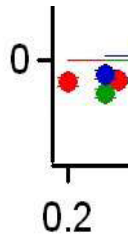
0
0.2

MRO Character

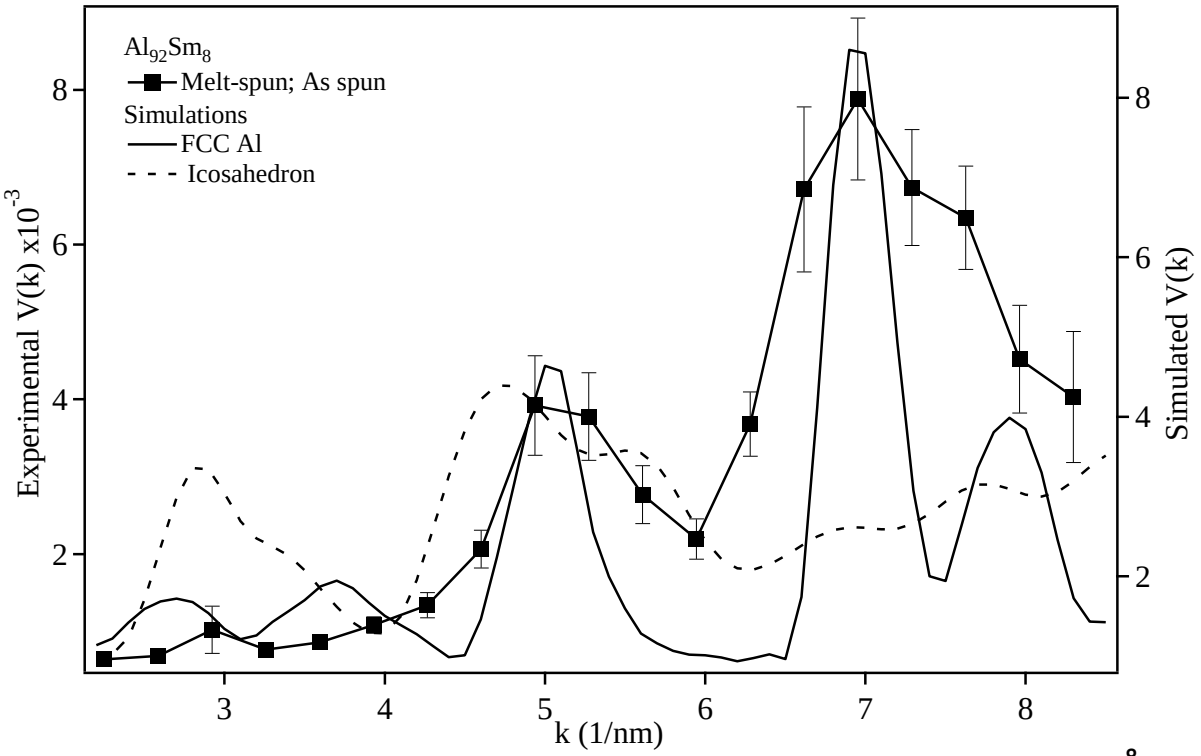

Measured *V*(*k*) for melt-spun as spun and simulated *V*(*k*) for a 30 Å Al sphere and a Sm-centered icosahedra. The Al sphere reproduces the peak positions and relative heights. The simulations have been multiplicatively scaled to match the data.

Crystallization behavior of Al-Y-Fe-Cu

- Primary (Al_{fcc}) crystallization onset shift due to substitution of Cu for:
  - Fe: ΔT_X = -50 (1 at%)
  - Y: ΔT_X = -45 (1 at%)
  - Al: ΔT_X = +10 (1 at%)

- Changes also occur in the intermetallic crystallization
  - While not as significant, show the strong composition dependence.

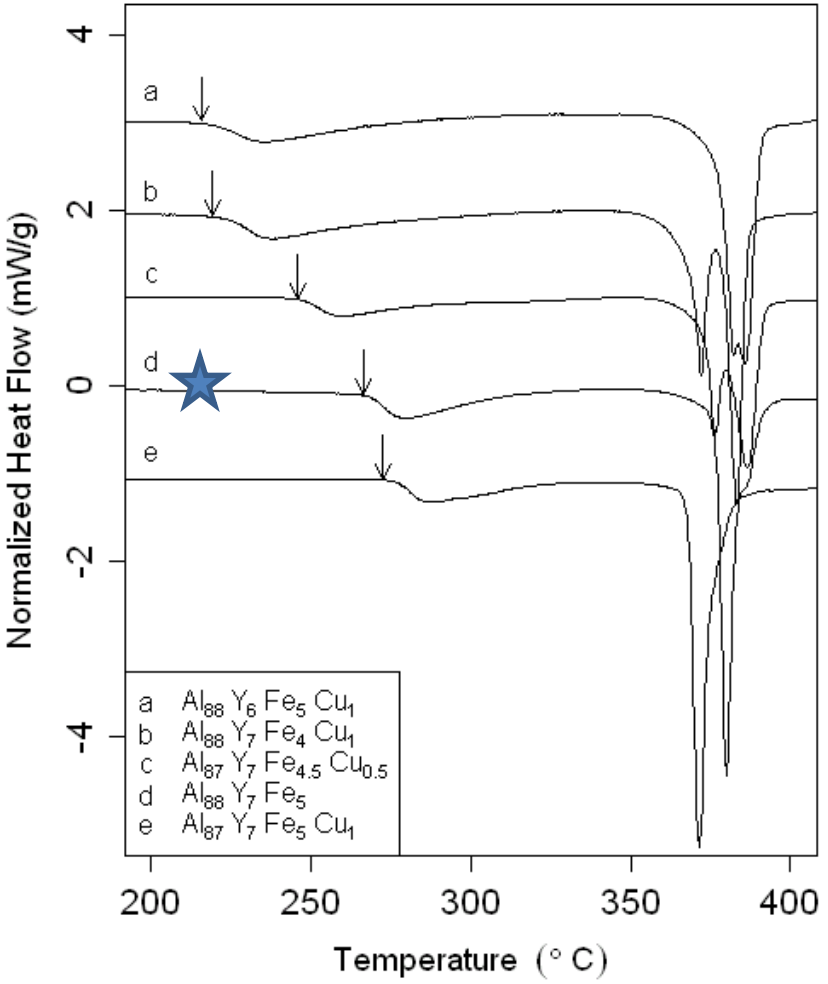

Nucleation product density

$N_v=6.9\times10^{20}$ m^{-3} $N_v=3\times10^{21}$ m^{-3} $N_v=1.1\times10^{22}$ m^{-3}

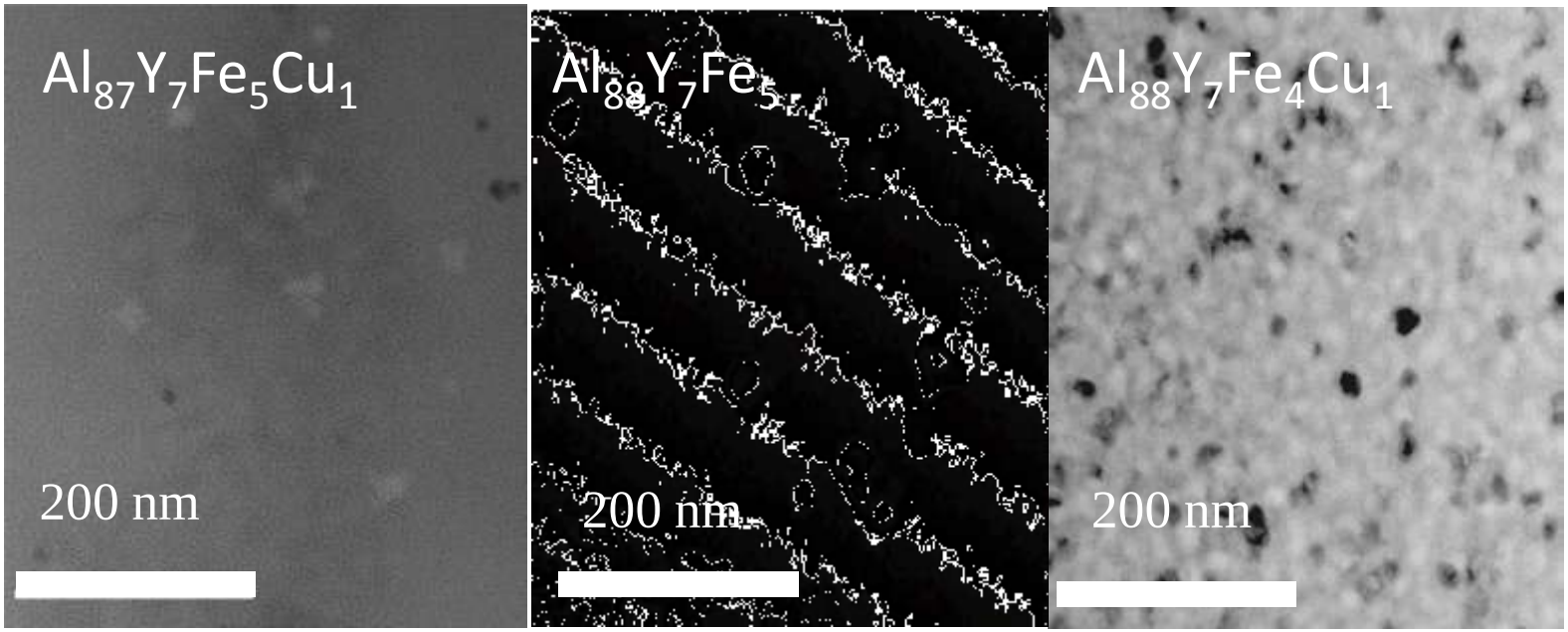

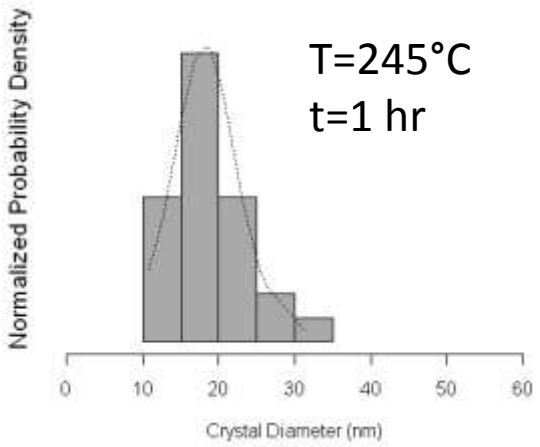

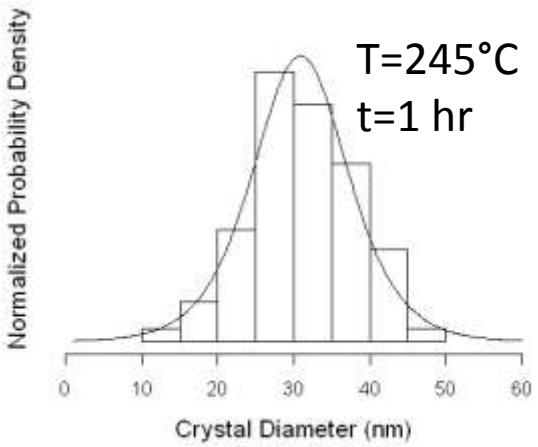

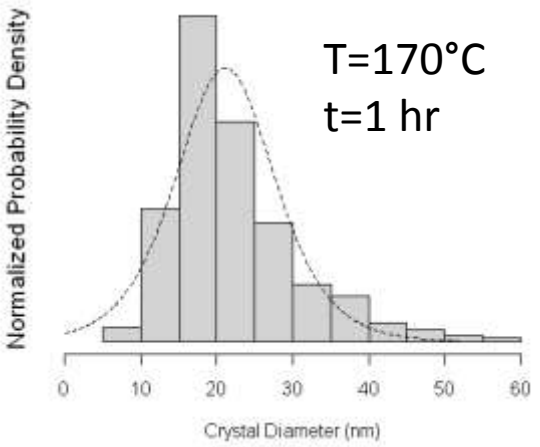

MRO Changes with composition

- Number Density
  - $N_{m,no} = 1.2\times10^{27}\ m^{-3}$
  - $N_{m,Cu} = 1.7\times10^{27}\ m^{-3}$
- Average Size = .755 nm
- Volume Fraction
  - $\Phi_{m,no} = 25\%$
  - $\Phi_{m,Cu} = 41\%$

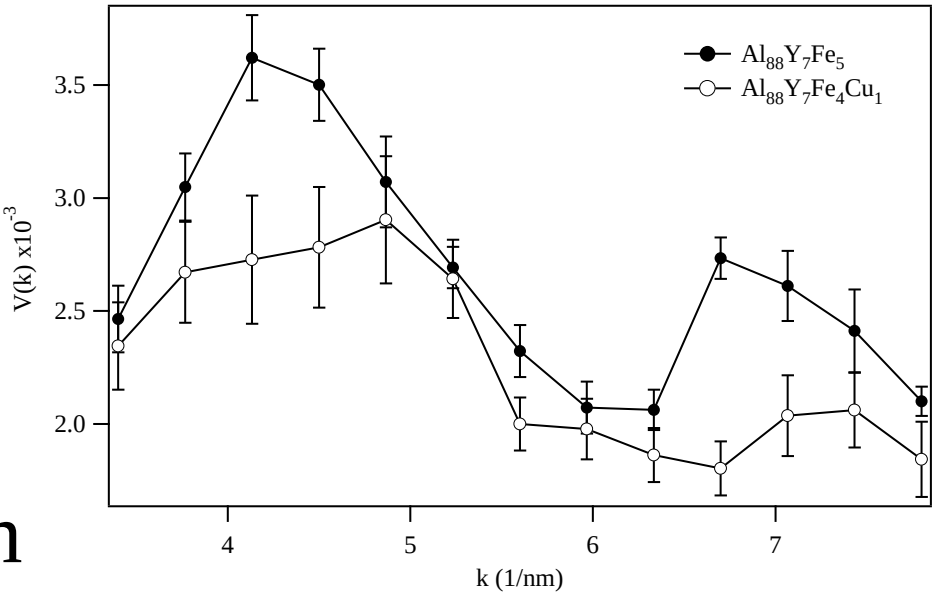

FEM data for $Al_{88}Y_7Fe_5$ and $Al_{88}Y_7Fe_4Cu_1$ at 1.6 nm spatial resolution. The peak positions occur at the Aluminum 200 and 220 reflections. The lower peaks in $Al_{88}Y_7Fe_4Cu_1$ indicate a more spatially homogeneous structure at a length scale of 1.6 nm.

Post-anneal Microstructure

- High density of nanocrystals
  - N_{no} = $2.94*10^{21}$ #/m^3 (9min)
  - N_{Cu} = $1.09*10^{22}$ #/m^3 (2min)
  - d_{no} = 31nm
  - d_{Cu} = 21nm
  - Roughly equal final $Al_{nc,fcc}$ volume fraction
    - $\Phi_{m,no}$ = 4.6 %
    - $\Phi_{m,Cu}$ = 5.2 %
  - To put these numbers in perspective, for each crystal that grows, 2 to $4*10^5$ MRO are annihilated.

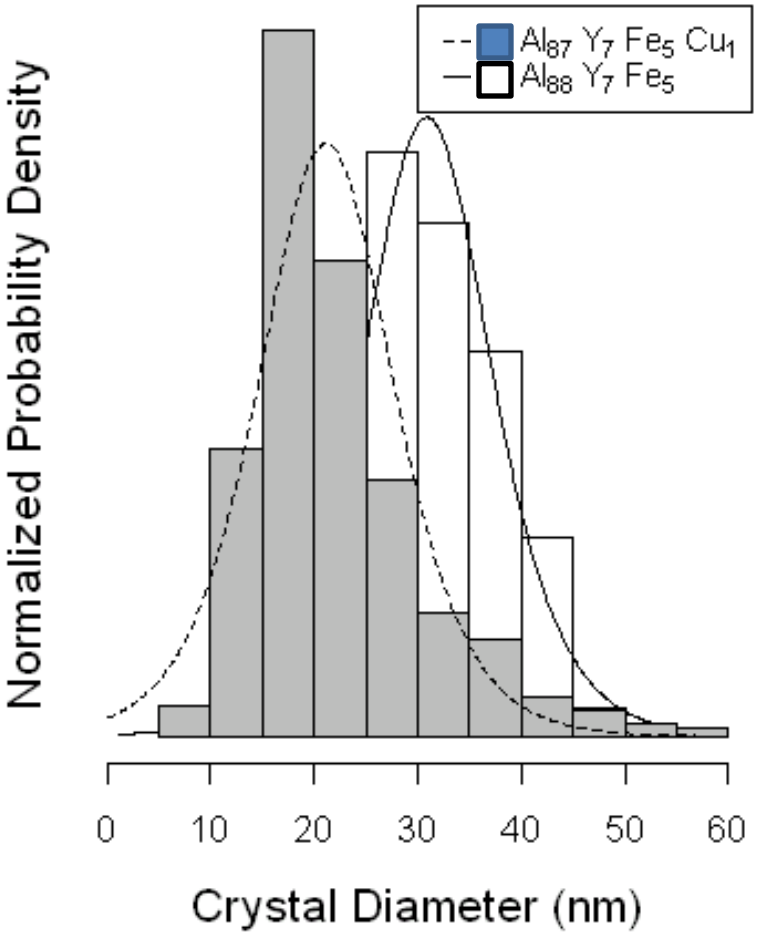

Cluster Concentration

- In an undercooled liquid the equilibrium cluster size concentration is

$$C(n)=C_1\exp(-\Delta G_n/kT)$$

- It is highly improbable that the MRO concentrations would be retained C(n) from the quench.

Monomer concentration

MRO concentration

MRO Interpretation

- Within an undercooled liquid there are energetically preferred configurations of Al MRO regions.
- The MRO regions persist and evolve by a classical thermal fluctuation mechanism.
- The MRO is disordered/defective Al that acts as a seed for NC

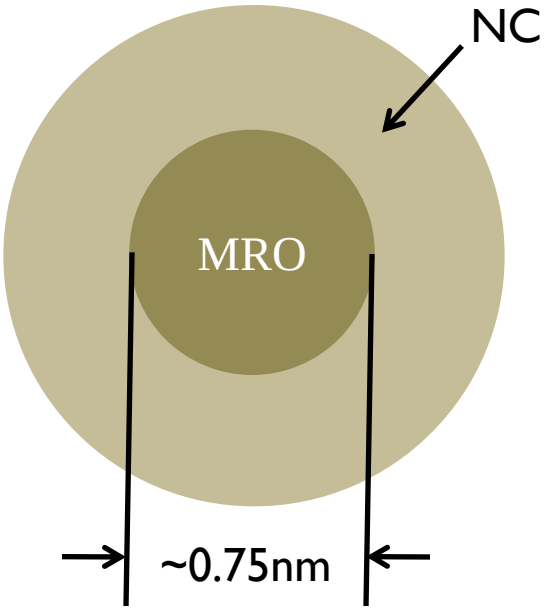

Energetic Treatment of MRO

$$\Delta G_s = 4\pi r_0^2(\sigma_{c/x} - \sigma_{c/g}) + 4\pi r^2 \sigma_{x/g} = 4\pi\sigma_{x/g}(r^2 - r_0^2)$$

$$\Delta G(r, r_0) = 4\pi r_0^2 \sigma_{nc/g}(r_2 - r_0^2) + \frac{4\pi}{3}(r^3 - r_0^3)\Delta G_V$$

$$\Delta G^* = \frac{16\pi\sigma_{nc/g}^3}{3\Delta G_V^2} - 4\pi\, r_0^2 \left(\sigma_{nc/g} - \frac{r_0 \Delta G_V}{3}\right)$$

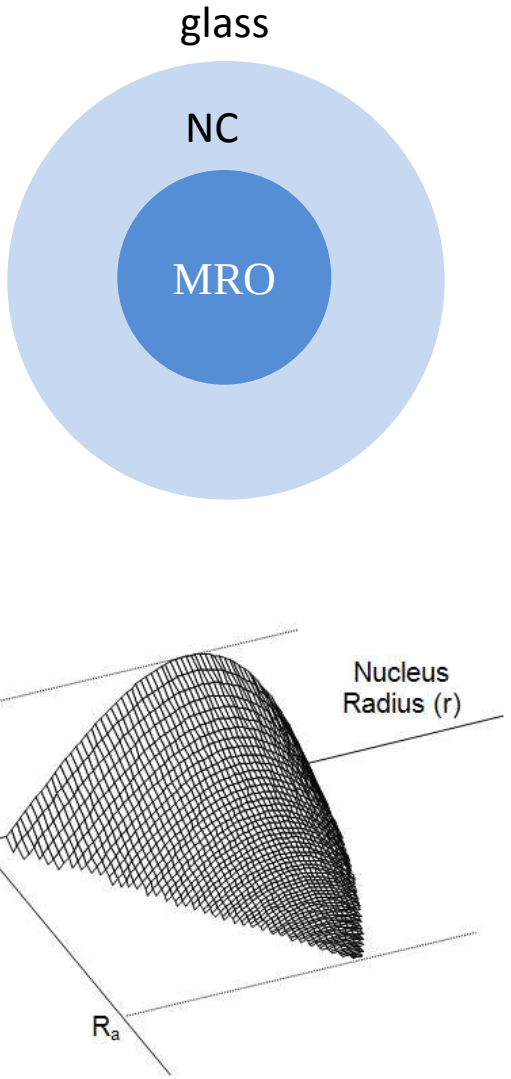

Seeded Nucleation Cont.

$$\Delta G(r) = 4\pi\sigma_{x/g}(r^2 - r_0^2) + \frac{4\pi}{3}(r^3 - r_0^3)\Delta G_V$$

$$r^* = \frac{-2\sigma_{x/g}}{\Delta G_V} = \frac{-2(0.0104 + 8*10^{-5}T)}{-1.087*10^9 + 1.29*10^6 T}$$

$$r^* = \frac{0.296}{3.736*10^8} = 0.79 \text{ nm at } 553 \text{ K}$$

For $d_0 = 0.74$ nm and $r_0 = 0.37$ nm

$$\Delta G^* = 4\pi\sigma_{x/g}(0.487) + \frac{4\pi}{3}(0.49 - 0.05)$$

$$\Delta G^* = 0.217*10^{-18} \text{ J}$$

$$k_B T = 1.38*10^{-23}*553 = 7.63*10^{-21}$$

$$\frac{\Delta G^*}{(k_B T)} = 28.4 \text{ (reasonable)}$$

Steady State Model

Volume Dependent Heterogeneous Nucleation

$$J_{SS} = \rho\beta Z \exp\left(-\frac{\Delta G^*}{k_B T}\right)$$

$\rho =$ MRO number densty

$\beta = 4\pi r^{*2} D C_0 a^{-4}$ = Attachment Frequency

$$Z = \frac{\Delta G_V^2 v_a}{8\pi\sqrt{k_B T \sigma^3}} = \text{Zeldovich factor}$$

$$Jss = \frac{\rho 4\pi r^{*2} D C_0 \Delta G_v^2 v_a}{8a^4\pi\sqrt{k_B T \sigma^3}} \exp\left(\frac{-\Delta G^*}{k_B T}\right)$$

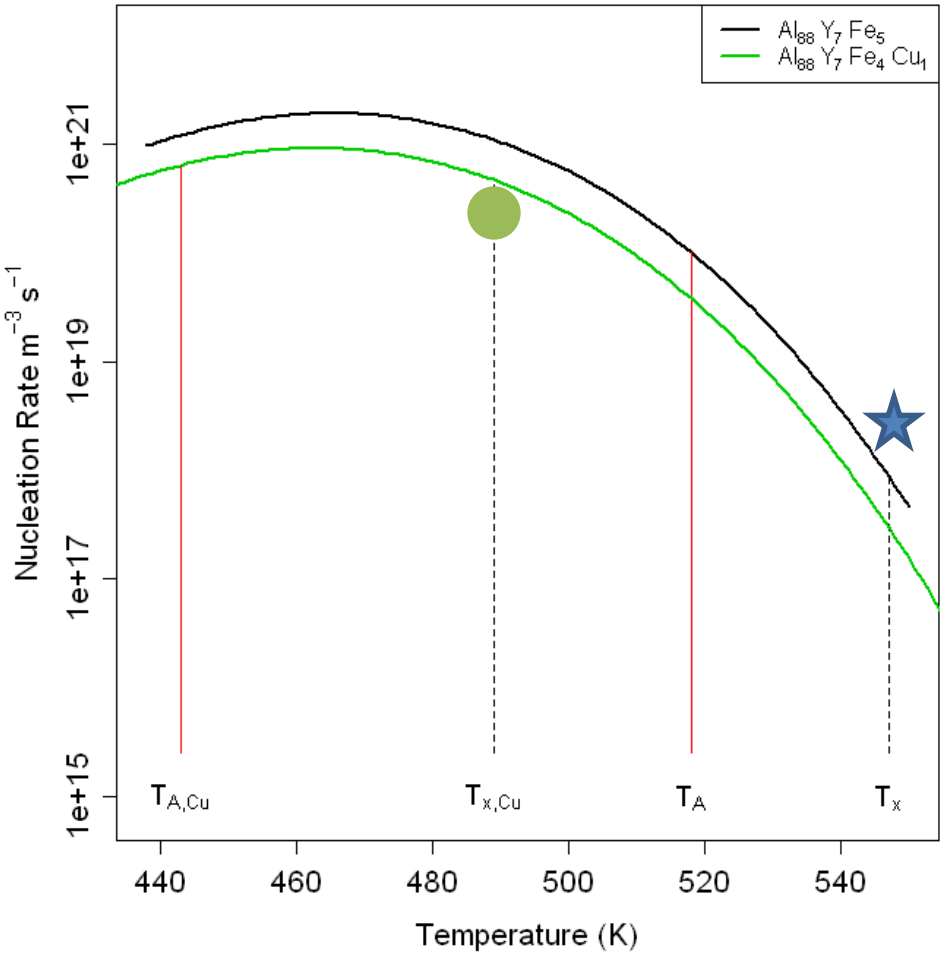

Transient Nucleation

- Changes in MRO number density do not account for nucleation enhancement
- The base model can now be used to analyze number densities observed at different temperatures

$$J_t = J_{SS} \exp\left(-\frac{\tau}{t}\right)$$

Solving for τ,

$$\tau = \frac{1}{\beta Z^2} = \frac{8 k_B T \sigma a^4}{D \Delta G_v^2 C_0 v_a^2}$$

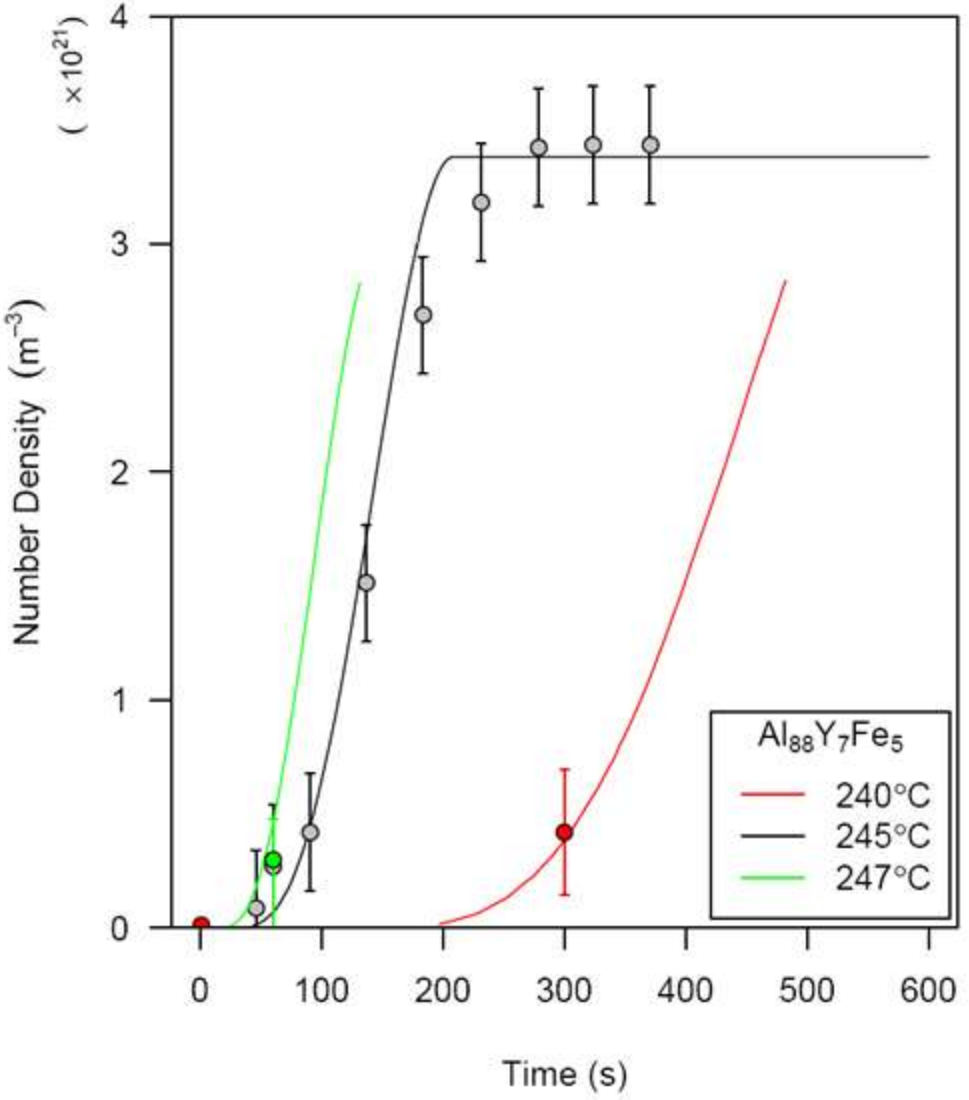

Transient Nucleation

- Transient time constant evaluated for AlYFe.

$$J_T = J_{SS} \exp(-\frac{\tau}{t})$$

$$\tau = \frac{1}{\beta Z^2} = \frac{8 k_B T \sigma a^4}{D \Delta G_v^2 C_0 v_a^2}$$

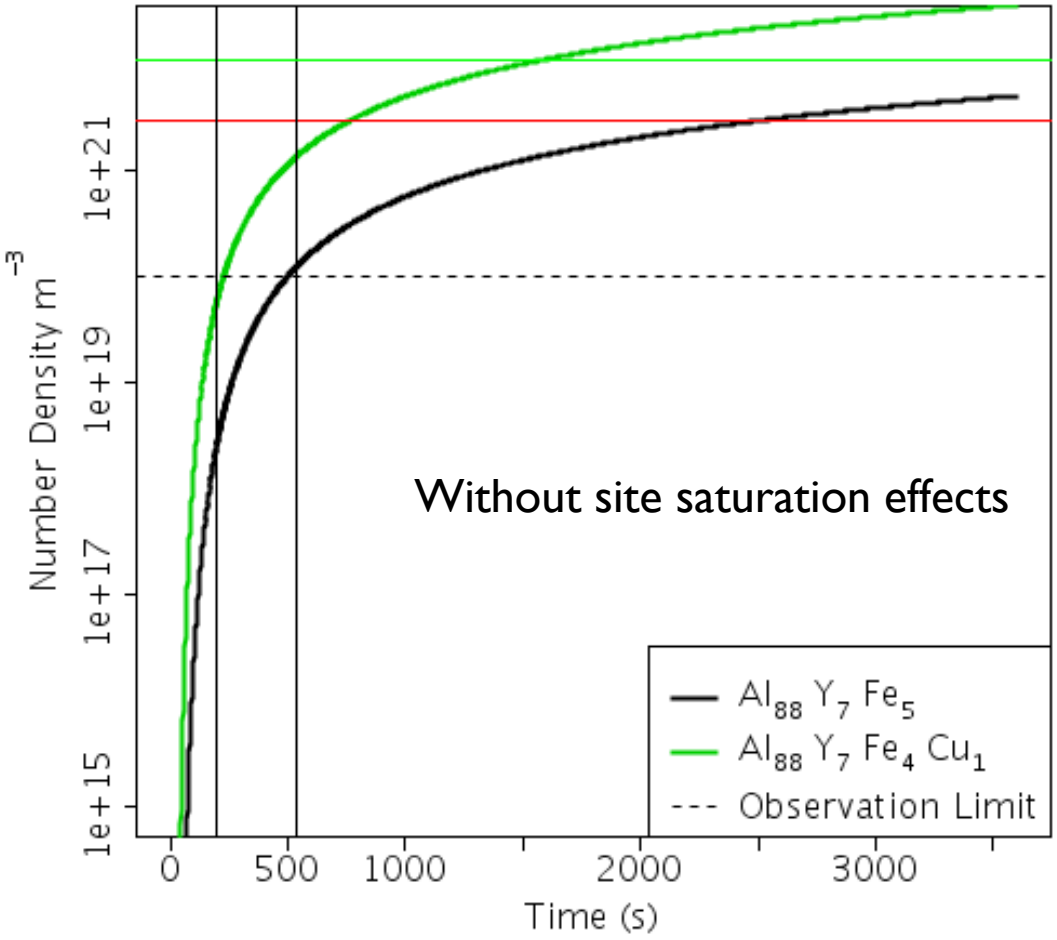

Growth Modeling

- Rapid size increase due to interfacial growth mechanism
- Diffusion controlled growth of larger particles
- Growth inhibited by diffusion field impingement.
- Interfacial instability leads to dendritic type growth

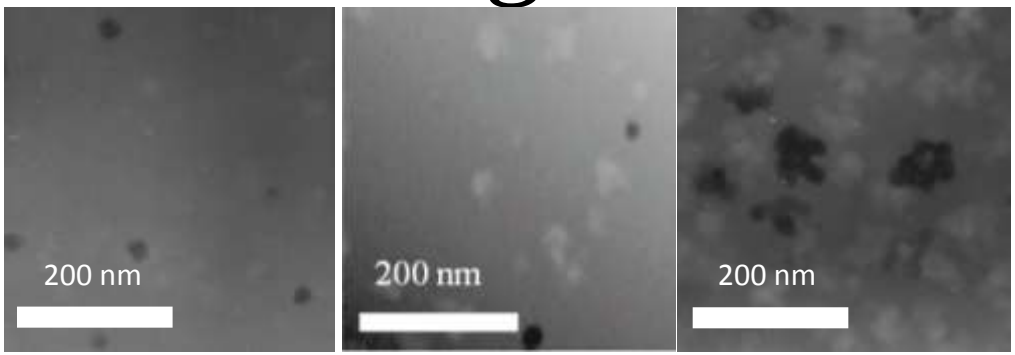

Spherical growth

Dendritic growth

Current status of combined model

- Crystallization start temperatures can be reproduced over a range of compositions and heating rates.
- Poor fitting during the later stages of the reaction is attributed to the complicated growth.
- Improved growth/transport analysis will also aid the interpretation of nucleation

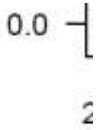

Nucleation Product Density Calculation

Extended Volume Fraction: $X_e = \int_0^t J_s \frac{4\pi}{3}[v(t-\tau)]^3 dt = \frac{4\pi J v^3}{3}\int_0^t t^3 dt$

$$X_e = \frac{\pi}{3} J v^3 t^4$$

Now, X, the real volume fraction transformed is:

$$X = 1 - \exp(-X_e)$$

For $X = 0.99\,;\ X_e \sim 5$

The number density, ρ, of nanocrystals is given by

$$\rho = \int_0^t J(1 - X(t))\,dt = J\int_0^t \exp(-X_e)\,dt$$

to find the maimum in ρ we let $t \to \infty$

$$\rho_m = J\int_0^\infty \exp\left(\frac{-\pi}{3} J v^3 t^4\right) dt = J\int_0^\infty \exp(-k t^4)\,dt$$

$$k = \frac{\pi}{3} J v^3$$

Product Density Continued

Where: $\int_0^\infty \exp(-y)\, y^{-3/4}\, dy$ is the Γ function

$$\Gamma(n) = \int_0^\infty e^{-y}\, y^{n-1}\, dy \qquad \text{So,}$$

$$n-1 = -3/4 \quad ; \quad n = 1/4$$

$$\Gamma(1/4) = \Gamma\frac{(1.25)}{0.25} = \frac{0.9064}{0.25} = 3.63$$

$$\rho = \frac{3.63\, J}{4\, k^{1/4}} = 0.897 \left(\frac{J}{v}\right)^{3/4}$$

For $\rho = 2.9 * 10^{21}$

$$\frac{J}{v} = 4.7 * 10^{28} \quad \text{For } J = 10^{18} \text{ and } v_a = 10^{-10}\,(\text{m/s})$$

Now, for 1 hr, $d = 21\, nm$

$$\frac{r}{t} = \frac{10 \text{ nm}}{3600 \text{ s}} = 2.7 * 10^{-3}\,\text{nm/s} = 2.7 * 10^{-12}\,\text{m/s}$$

For $v = 2.7 * 10^{-12}$ m/s

$$J \rightarrow 1.2 * 10^{17} \text{ m}^{-3}$$

Transport Question

- The magnitude of change in the transient behavior is very large (>$10^{2)}$ for a single atomic percent substitution. This is puzzling if it is dependent upon the simple change in diffusion.

- How do we consider cluster development by atomic addition in this partially ordered environment with different time constants?

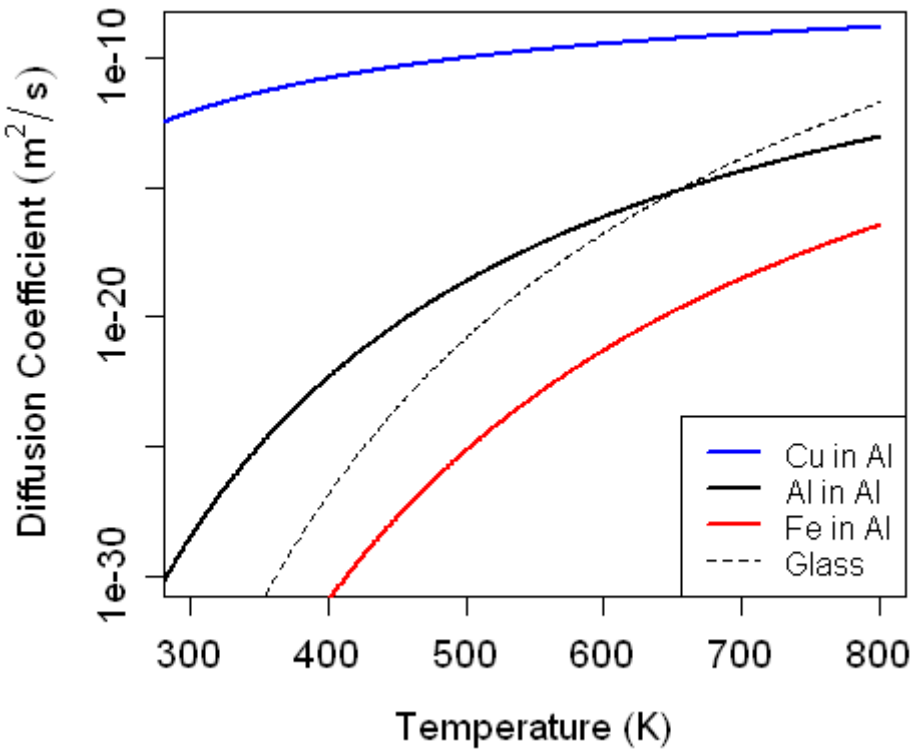

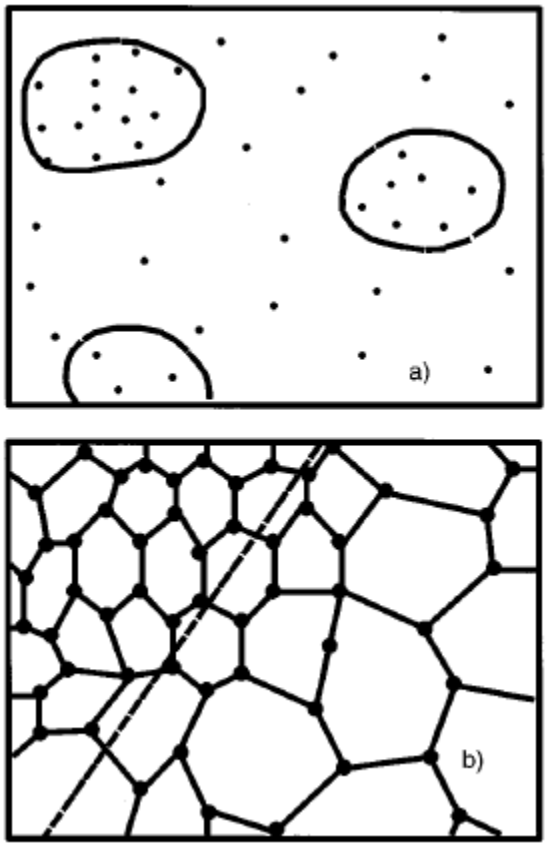
a)
b)

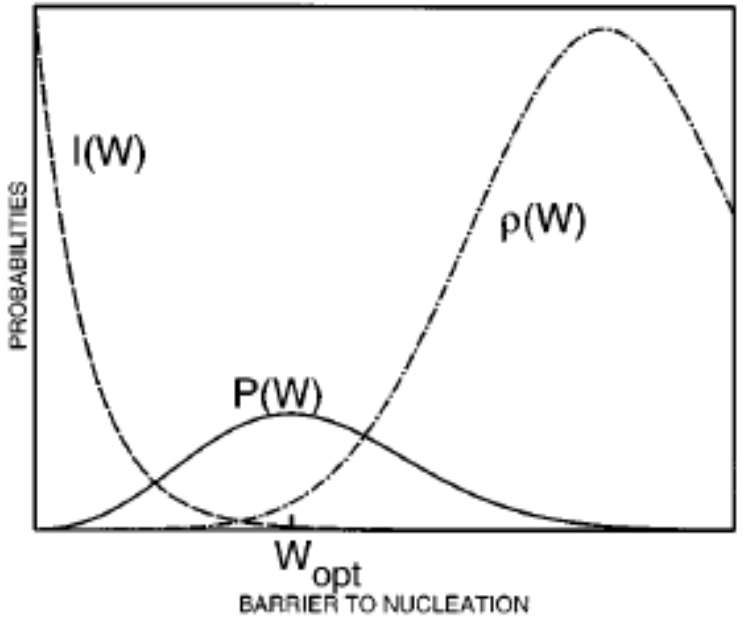
I(W)
ρ(W)
P(W)
PROBABILITIES
W opt
BARRIER TO NUCLEATION

Intermediate Phase Nucleation During Interdiffusion

- Initial Phase Establishes Phase Sequence
- Role of 👍C – Precursor Stage
  i.e. $r^* \propto \Delta C/$👍C
- Influence of ΔD
- $\Delta J \propto \Delta D$👍C
- Growth Kinetic Competition
- Multicomponent Pathways

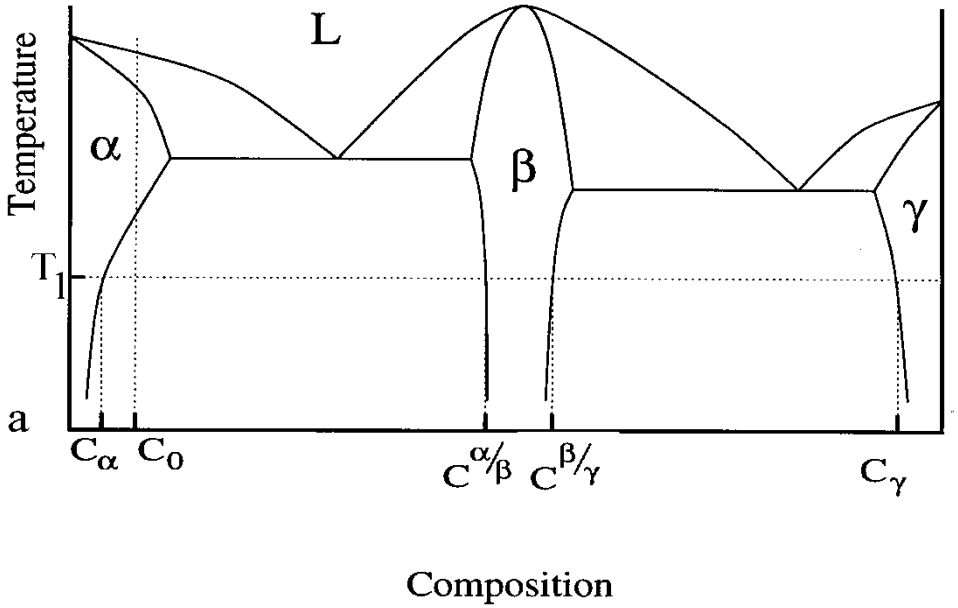
Temperature
L
α
β
γ
T_1
C_α
C_0
$C^{\alpha/\beta}$
$C^{\beta/\gamma}$
C_γ
Composition

a

b

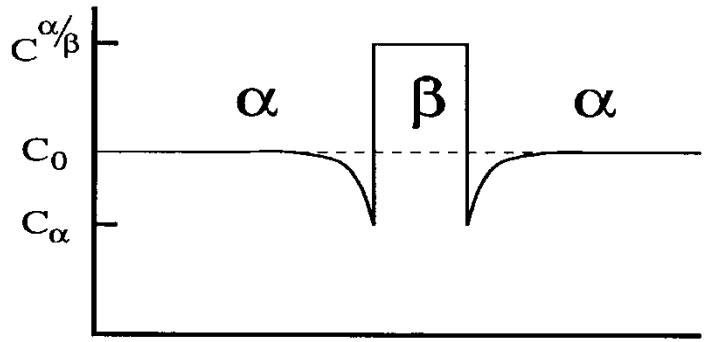
$C^{\alpha/\beta}$
α
β
α
C_0
C_α

c

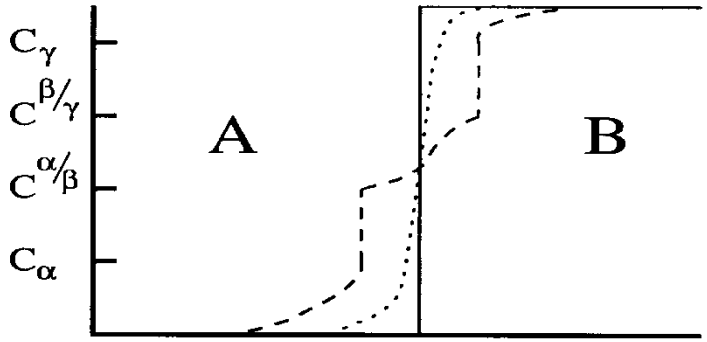
C_γ
$C^{\beta/\gamma}$
$C^{\alpha/\beta}$
C_α
A
B

d

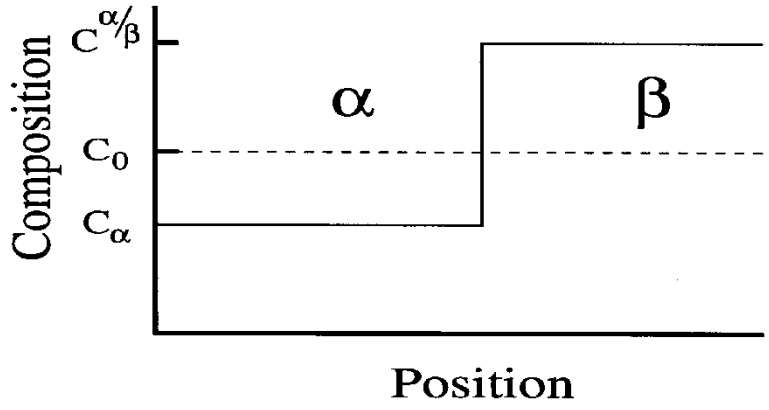
Composition
$C^{\alpha/\beta}$
α
β
C_0
C_α
Position

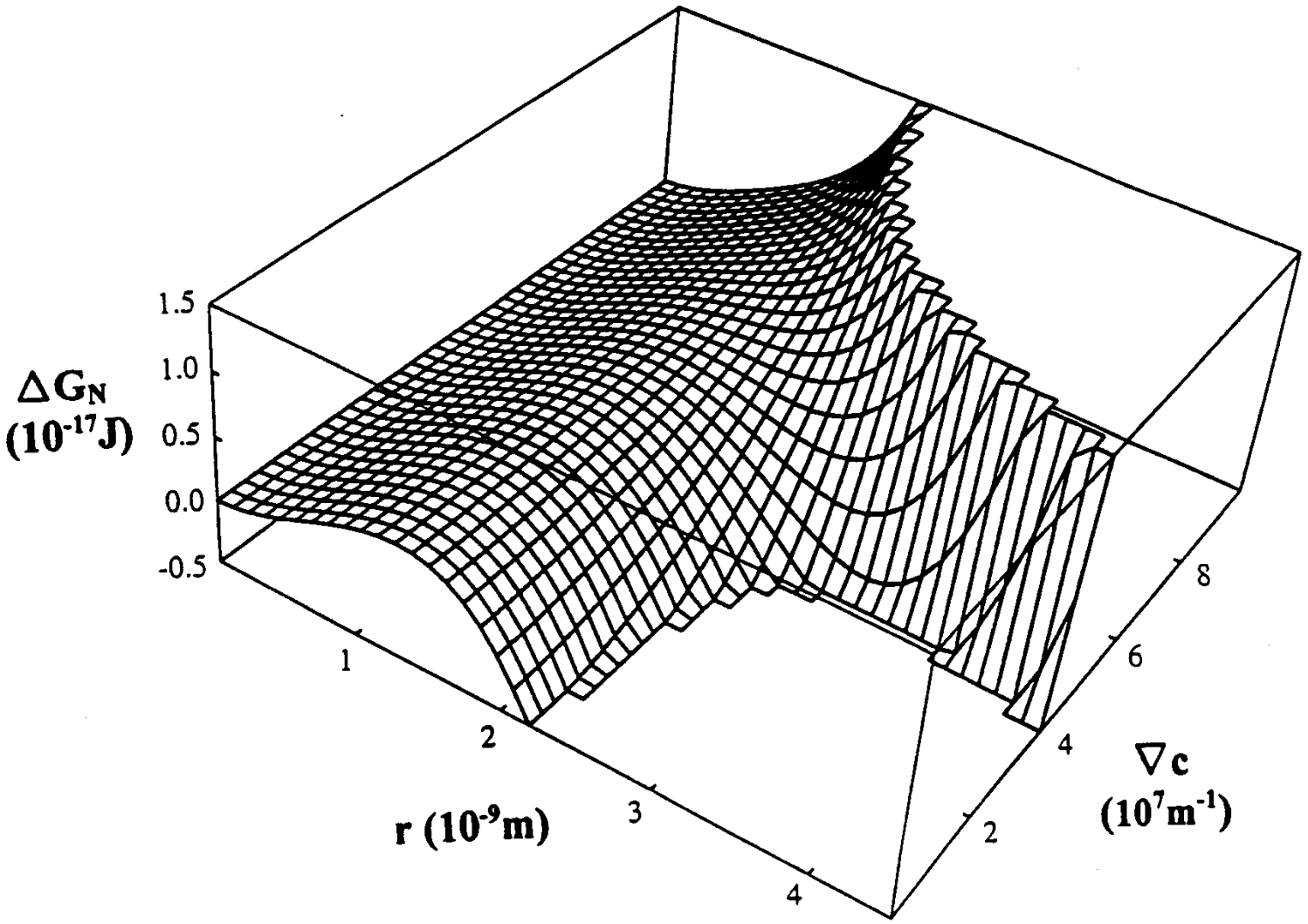

$$\Delta G_N = A\sigma r^2 + B\Delta G_v r^3 + G_{xx}\nabla C^2 r^5$$

(a)

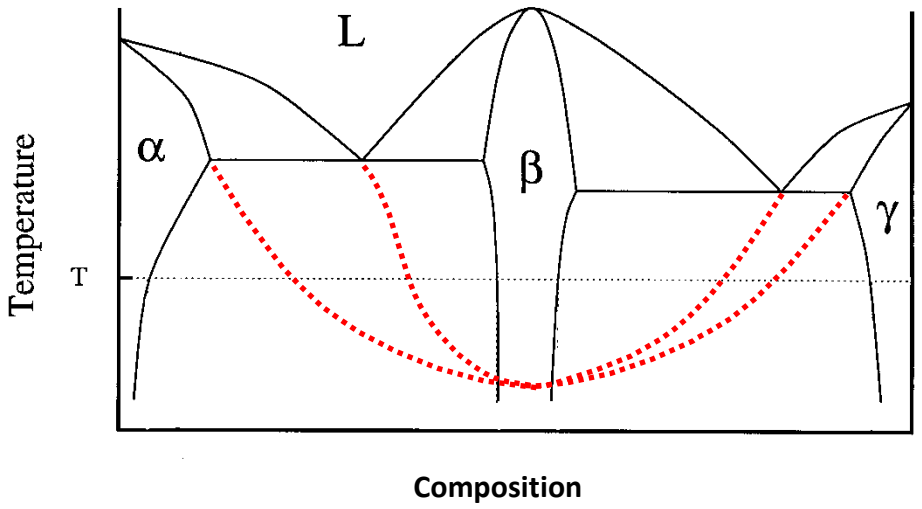
L
α
β
γ
Temperature
T
Composition

(b)

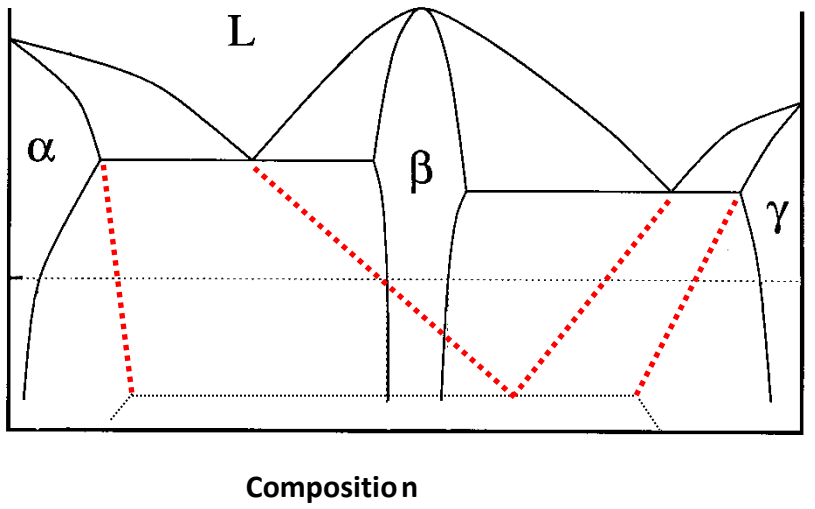
L
α
β
γ
Composition

(c)

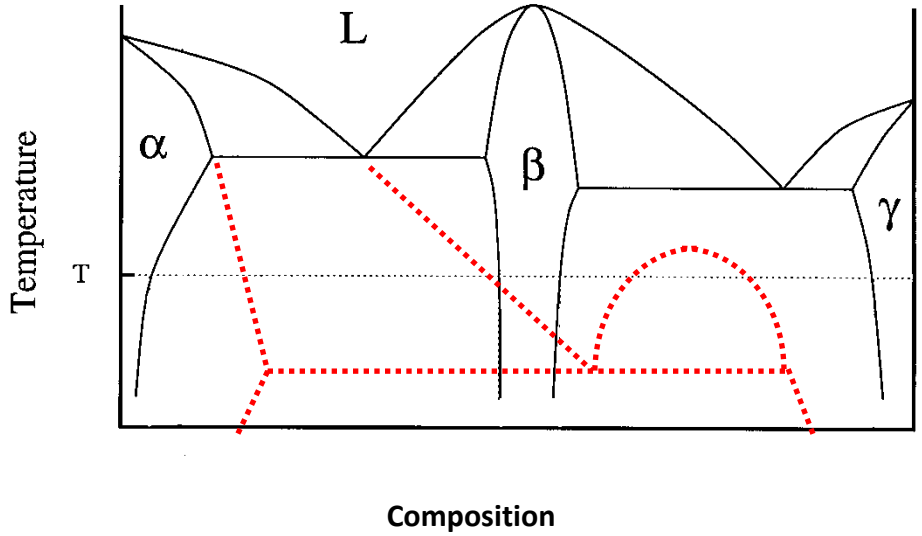
L
α
β
γ
Temperature
T
Composition

Interdiffusion Preceeds Intermetallic Phase Formation During Interfacial eactions

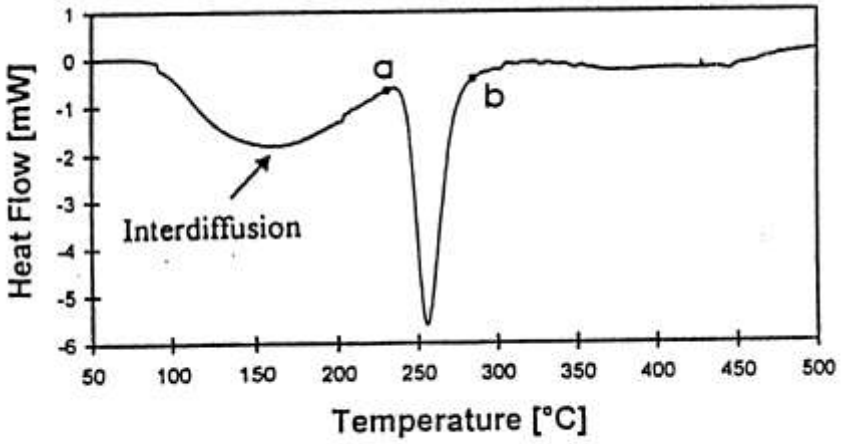

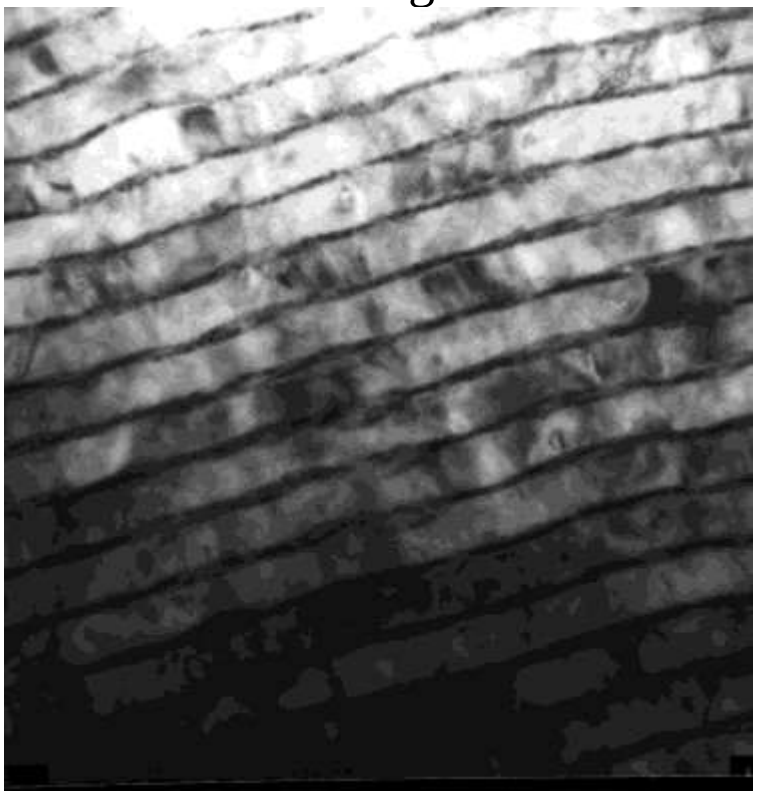

XTEM of Al/Ni multilayer at point (a) of DSC trace without phase formation.

Table-I: Summary of the nature of the first phase formed

Λ \ <C>	$Al_{82}Ni_{18}$	$Al_{75}Ni_{25}$	$Al_{50}Ni_{50}$
Short (10-14.4 nm)	Al_3Ni	Al_3Ni	AlNi
Intermediate (22.2-100 nm)	Al_9Ni_2	Al_9Ni_2	Al_9Ni_2
Large (400 nm)	----------	----------	Al_9Ni_2

- Initial phase formation requires minimum volume with phase compositional range
- Interdiffusion is required to develop dc/dx for the critical volume
- Gradient can be modified by layer thickness which in turn can control phase selection and sequencing

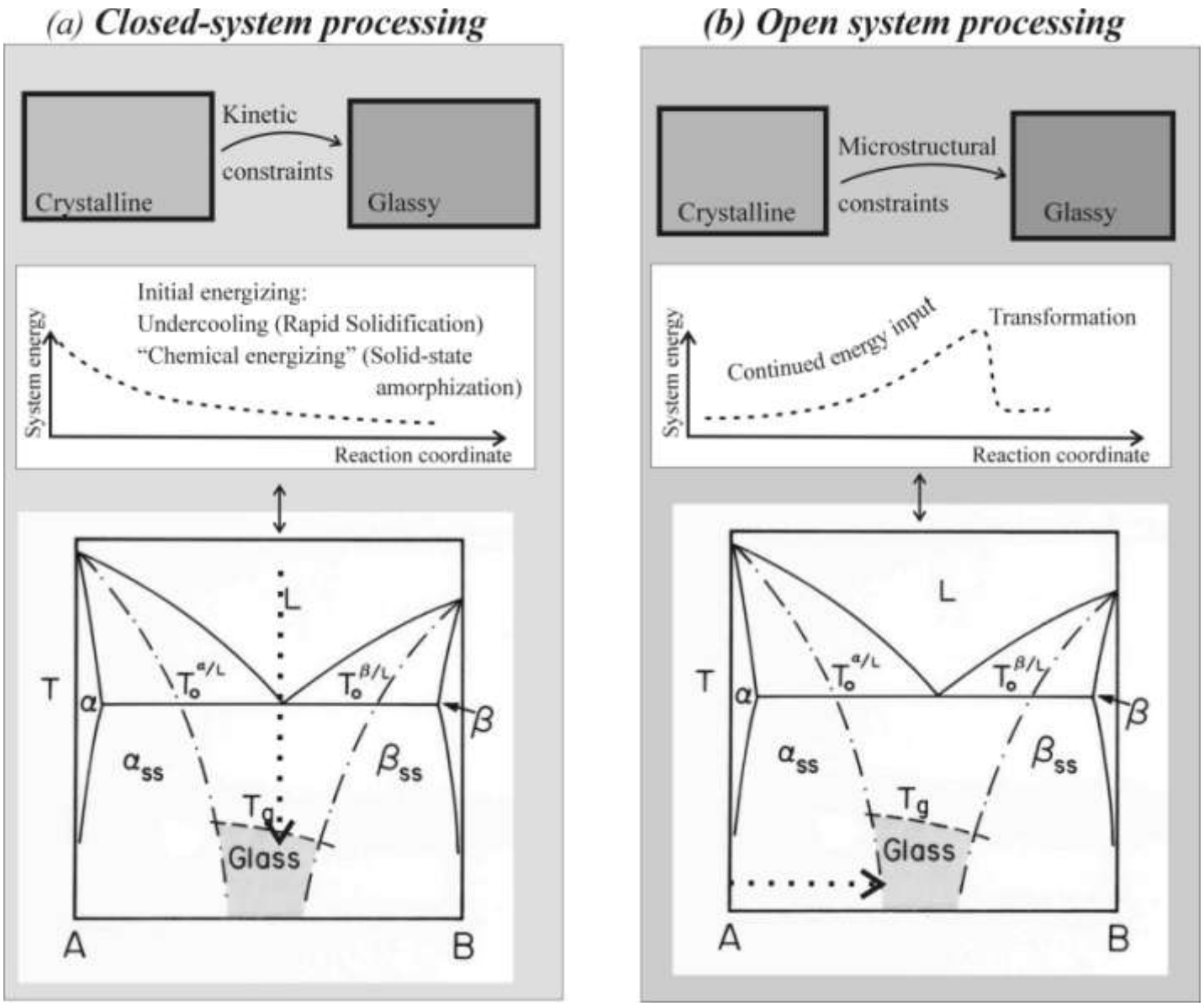
(a) Closed-system processing
Crystalline
Kinetic
constraints
Glassy
Initial energizing:
Undercooling (Rapid Solidification)
"Chemical energizing" (Solid-state
amorphization)
System energy
Reaction coordinate
L
T
α
$T_o^{\alpha/L}$
$T_o^{\beta/L}$
β
α_{ss}
β_{ss}
T_g
Glass
A
B
(b) Open system processing
Crystalline
Microstructural
constraints
Glassy
System energy
Continued energy input
Transformation
Reaction coordinate
L
T
α
$T_o^{\alpha/L}$
$T_o^{\beta/L}$
β
α_{ss}
β_{ss}
T_g
Glass
A
B

Effective Temperature

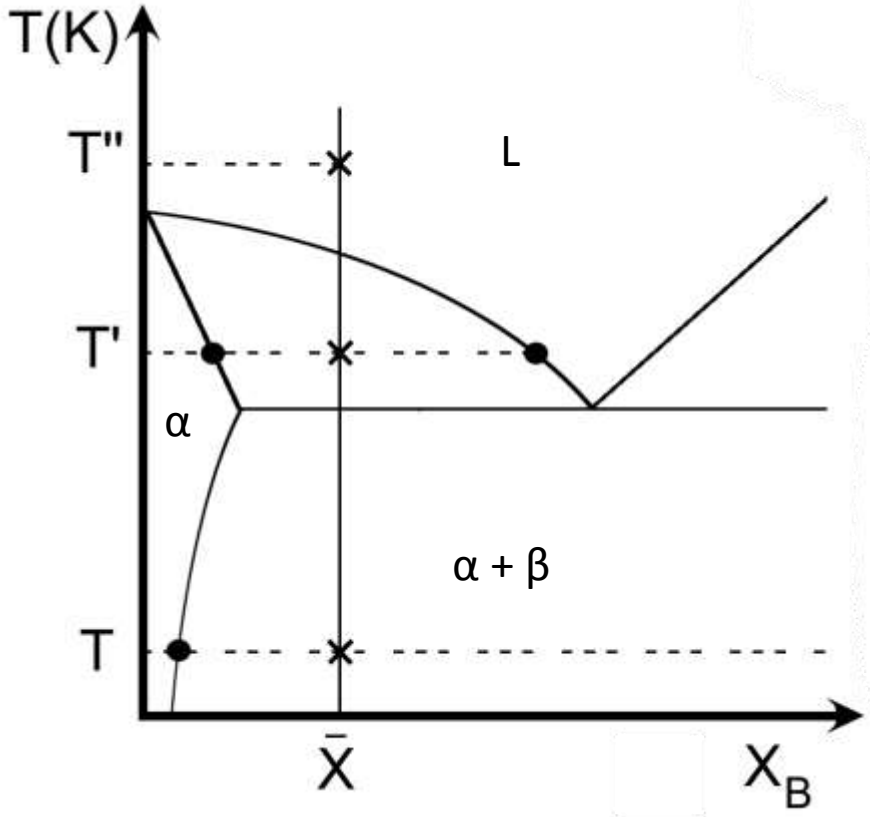

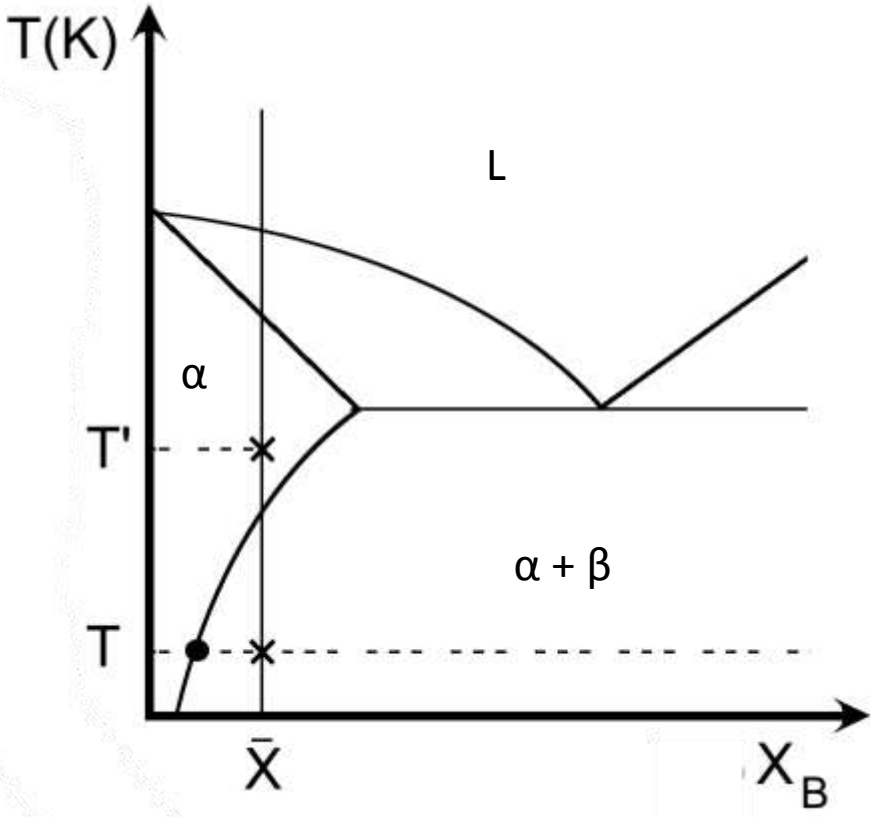

$T' = T(1+\Delta)$

$\Delta = D_{bal} / D_t$

Amorphization Mechanism ($Al_{60}Dy_{20}Ni_{20}$)

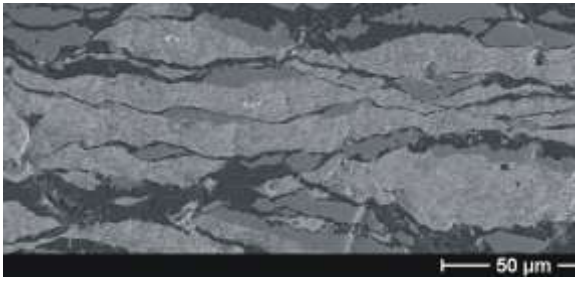

ε_{true}= -7.5
Cr6

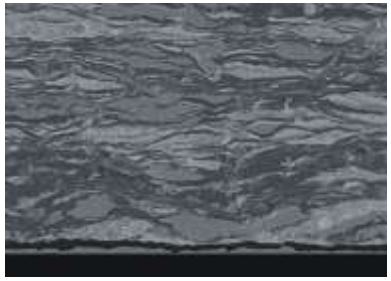

ε_{true}= -15.2
Cr15

ε_{true}= -28.9
Cr30

Mechanism

- Overall layer refinement (T_m + crystal structure significant)
- Shear-mixing at individual interfaces
  (Negligible solubility, negative heat of mixing, importance of dislocations?)

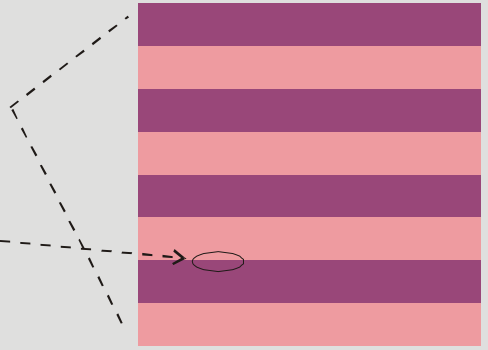

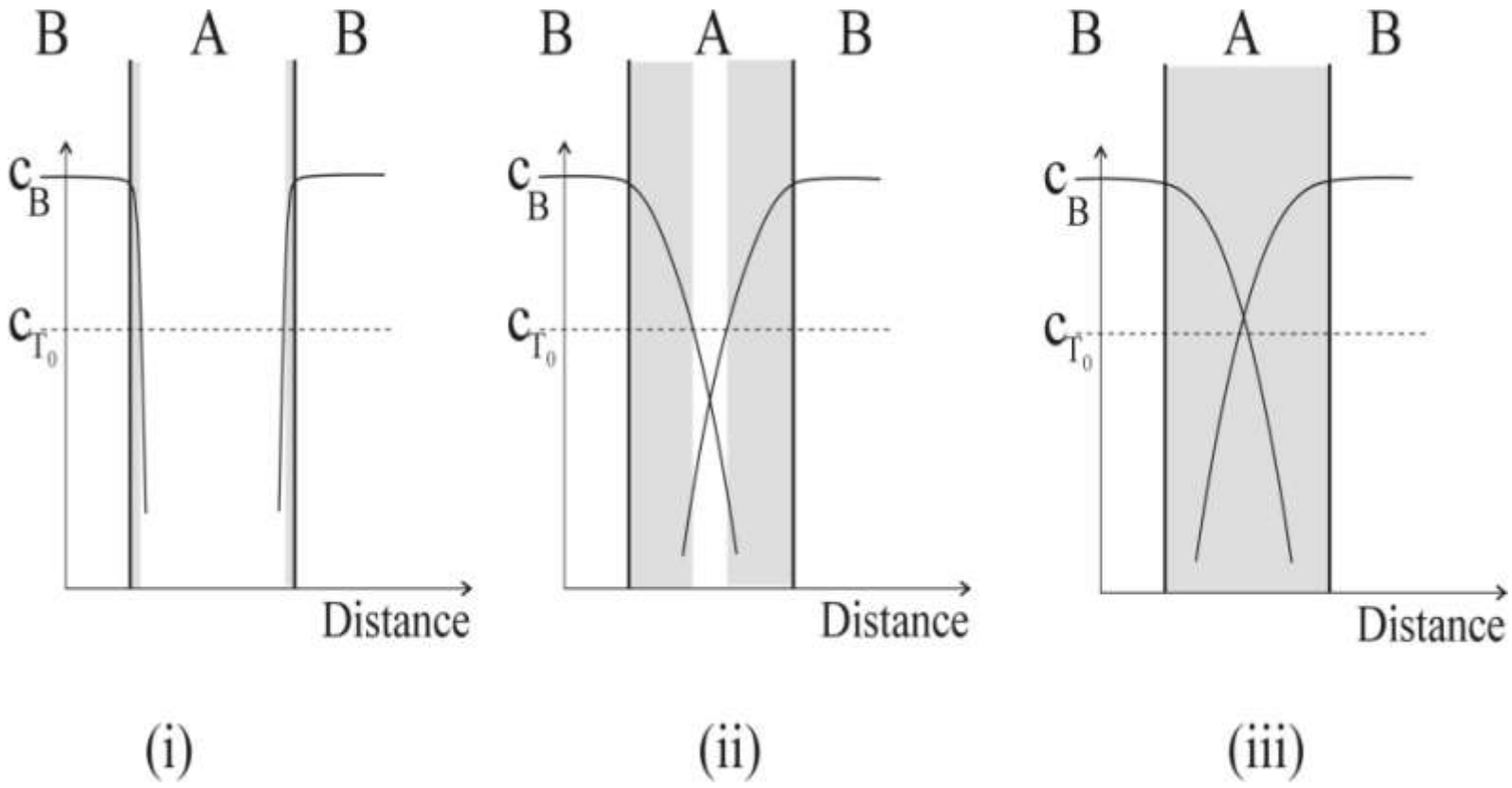
B
A
B
c_B
c_{T_0}
Distance
(i)
(ii)
(iii)

Al-Sm Metallic Glass formed by Different Processes

Cold-rolled sample:

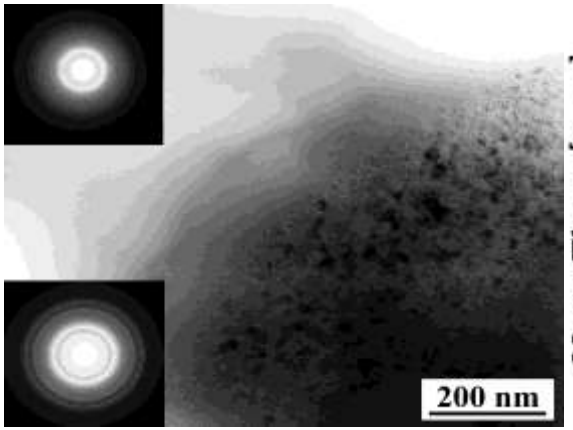

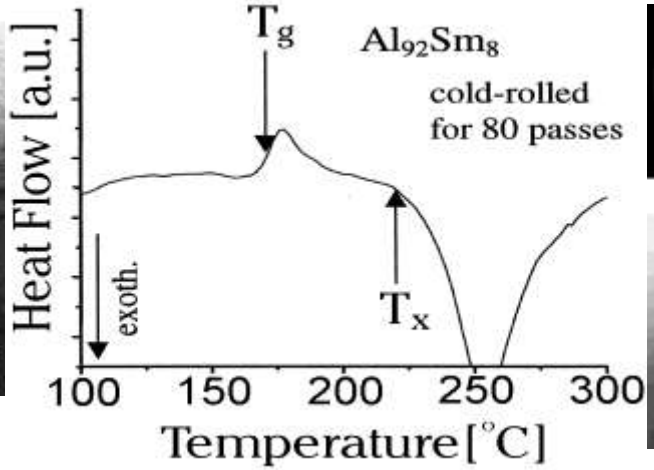

After annealed at 150°C, 60min:

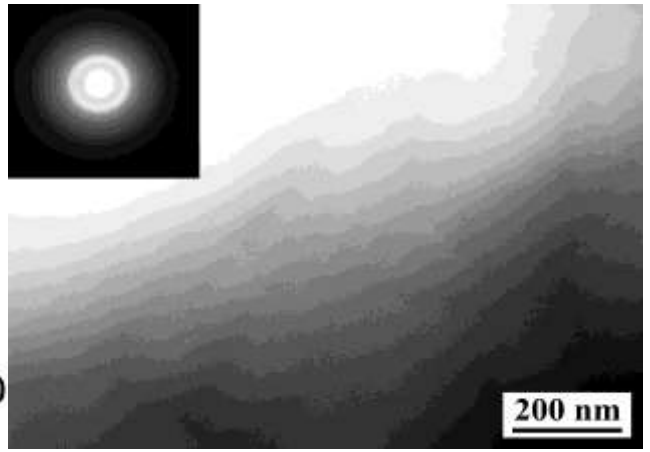

Melt-spun sample:

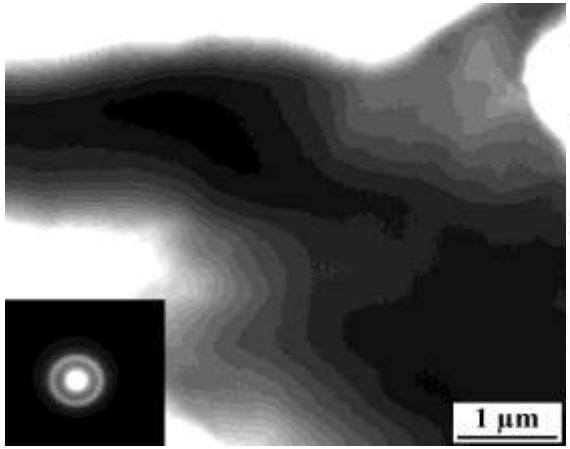

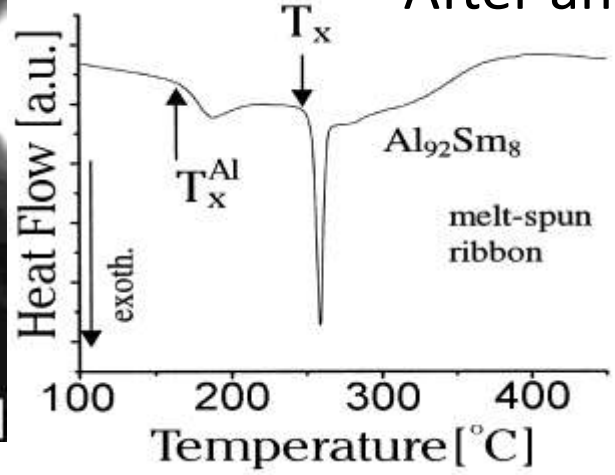

After annealed at 150°C, 10min:

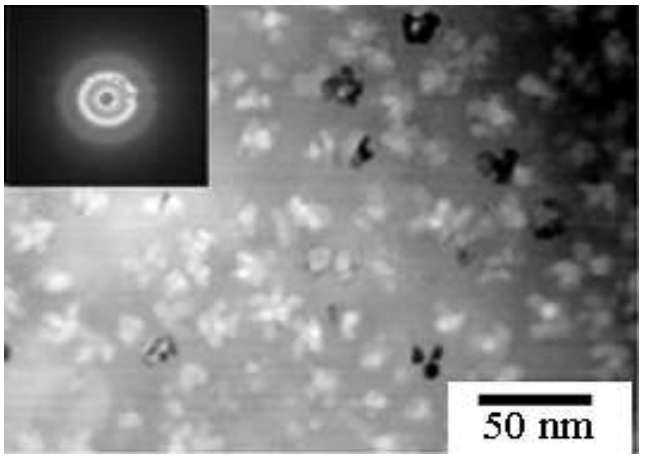

Summary

Nanostructure Synthesis During Devitrification and Deformation of Al Glass

Strong Composition Dependence

-T_x , T_g Relatively Stable: Tx> 250°C [Al-RE-TM]

- Phase Selection

- Solute Substitution Effects

Structural Heterogeneity---

-MRO (Processing and Solute Sensitivity)

Kinetics -Heterogeneous; Transient Nucleation

In AlYFe low level substitution of Cu for Fe results in:

- Increase in the MRO number density
- Transient nucleation time constant decrease
- Low level substitution of Cu for Al may promote BMG

Open Issues: Nucleation and Atomic Transport in Spatially Heterogeneous Glass

Deformation Induced reactions

Deformation driven mixing provides a distinct kinetic pathway unavailable through thermal treatment. Alloying develops in stages through layer refinement and interface roughening with enhanced atomic exchange.

New Pathways for Nanostructure /BMG Synthesis

We Have Met the Enemy and He Is PowerPoint

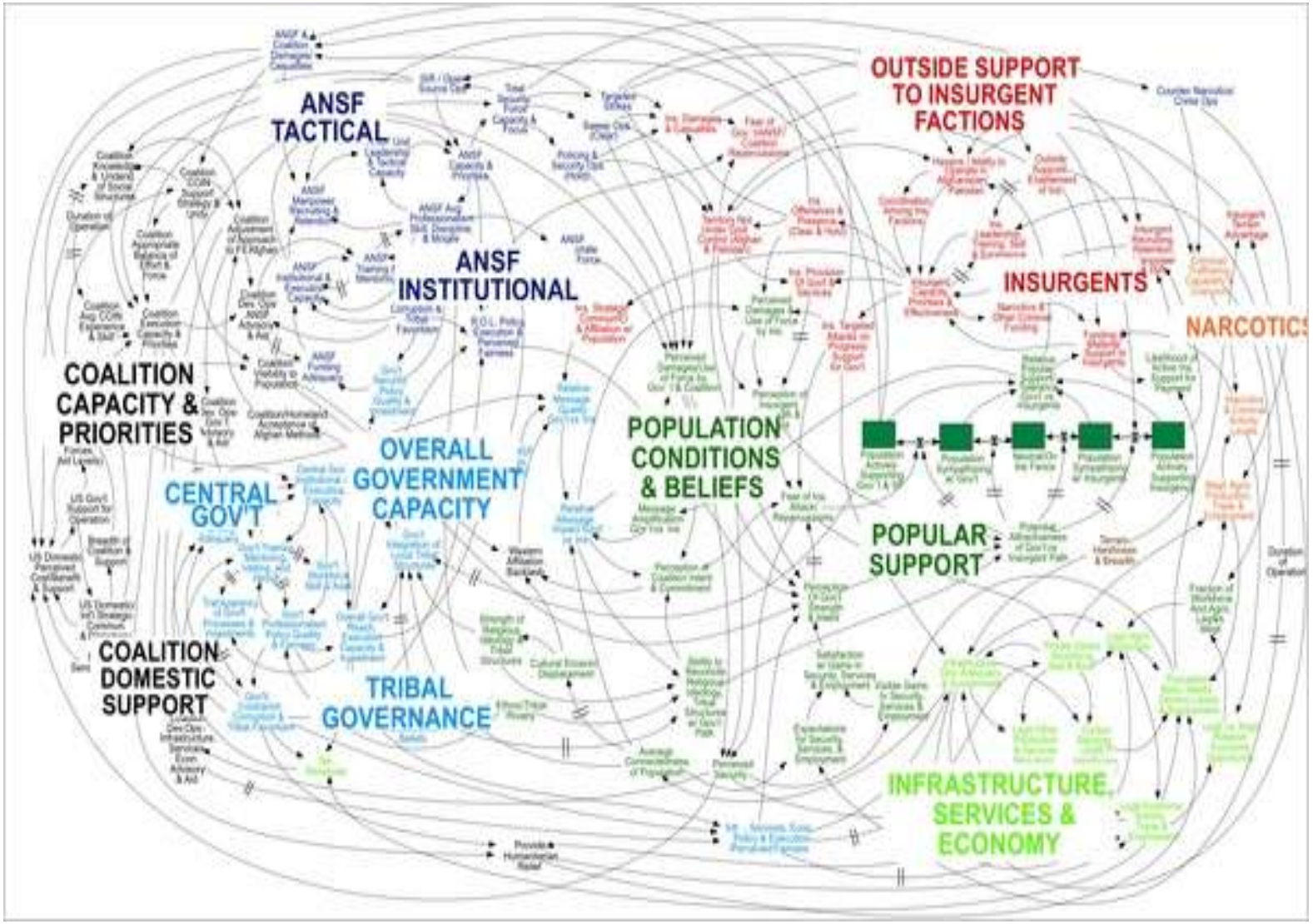

A PowerPoint diagram meant to portray the complexity of American strategy in Afghanistan certainly succeeded in that aim. (NY Times, April 26, 2010)

Al88Y7Fe5 Annealed at 235C/508K

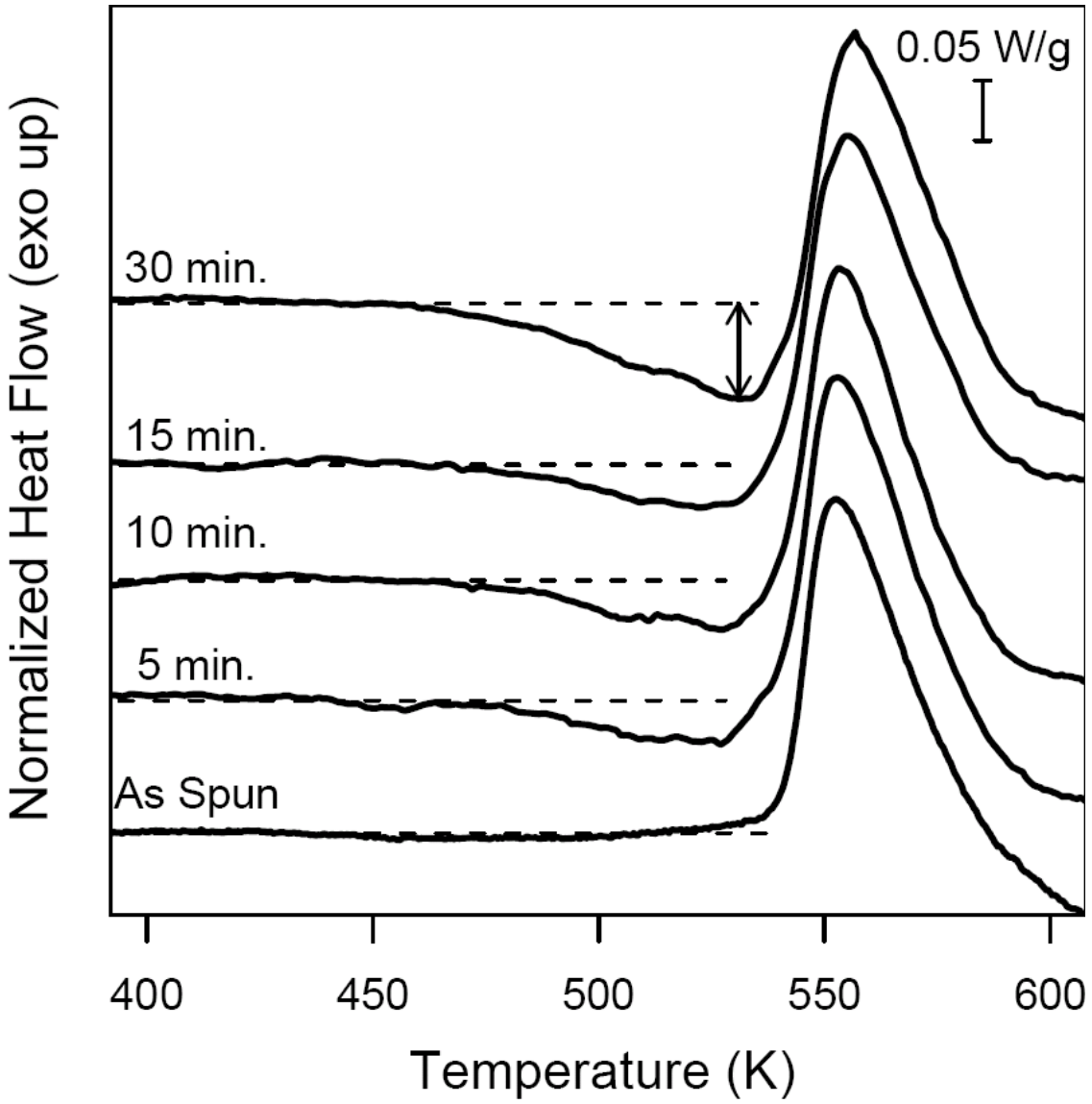

Al88Y7Fe4.5Cu0.5 Annealed at 205C/478K

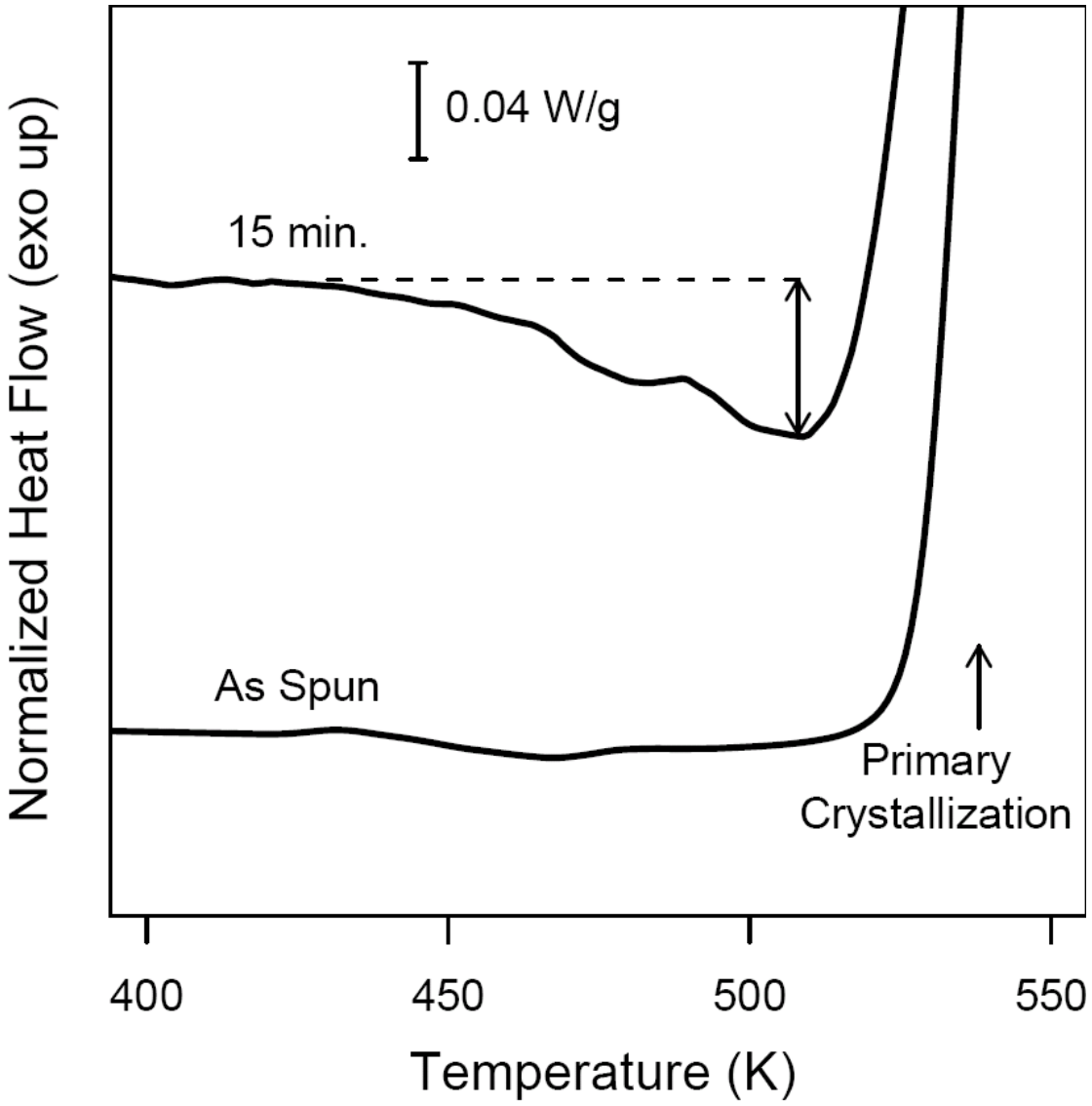

Nucleation and Growth Model

- Measured nanocrystal and MRO densities and sizes act as the direct input to develop the model
- Analysis results are tested to reproduce the measured data

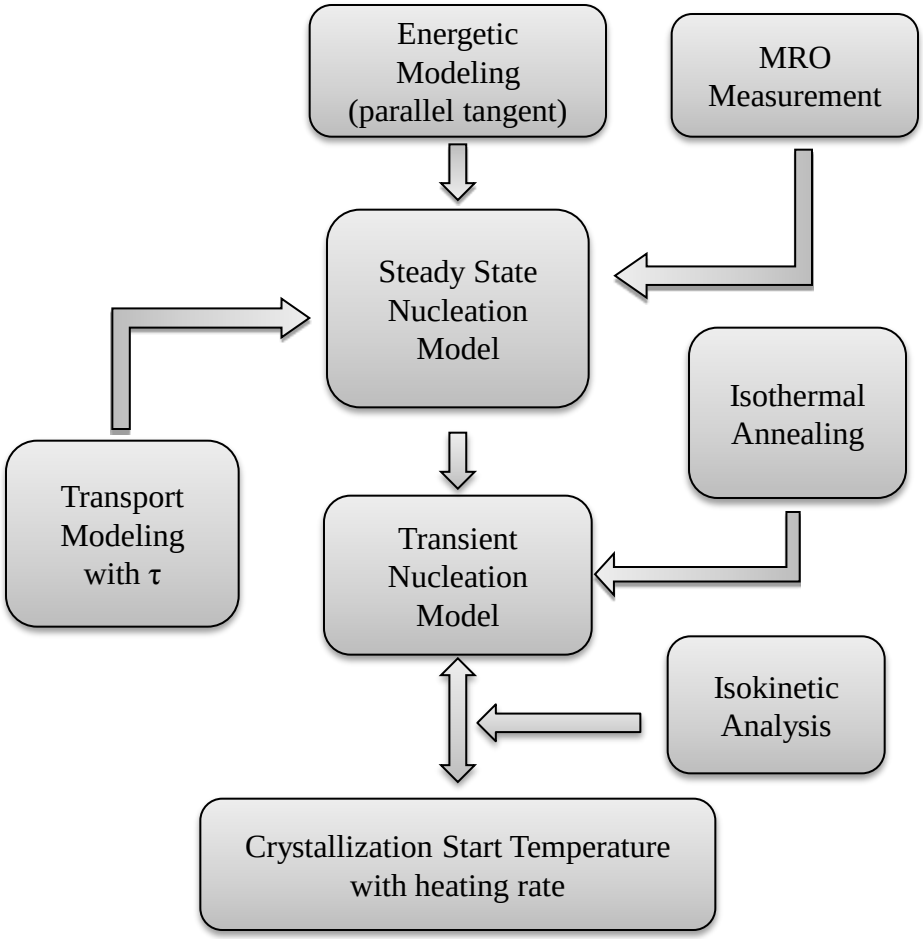

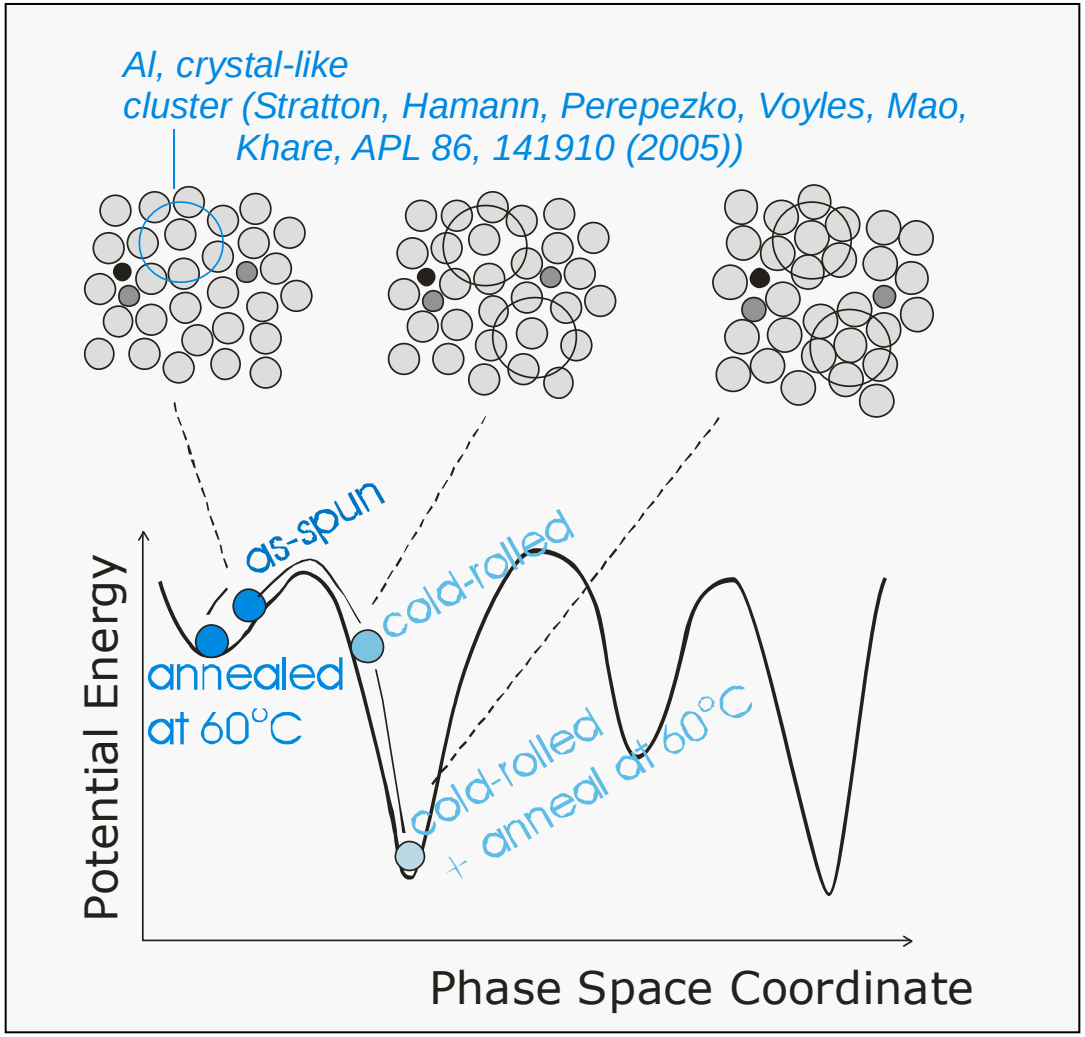

Volume per transformation zone: $10^{-28}m^3$ Heat per t. zone: $10^{-20}J$

With 10^{26} transformation zones per m^3 Heat released: $10^6J/m^3$

MRO and FEM mode

- Medium range order in $Al_{88}Y_7Fe_5$ and with Cu substitution refers to Al crystal-like structure (0.6 to 2 nm in *d*)
- In nanodiffraction FEM mode, we can control the resolution by controlling the probe size
- Advantages in nanodiffraction mode:

1. Enhanced coherence
2. Resolution can vary continuously
3. High *k* range

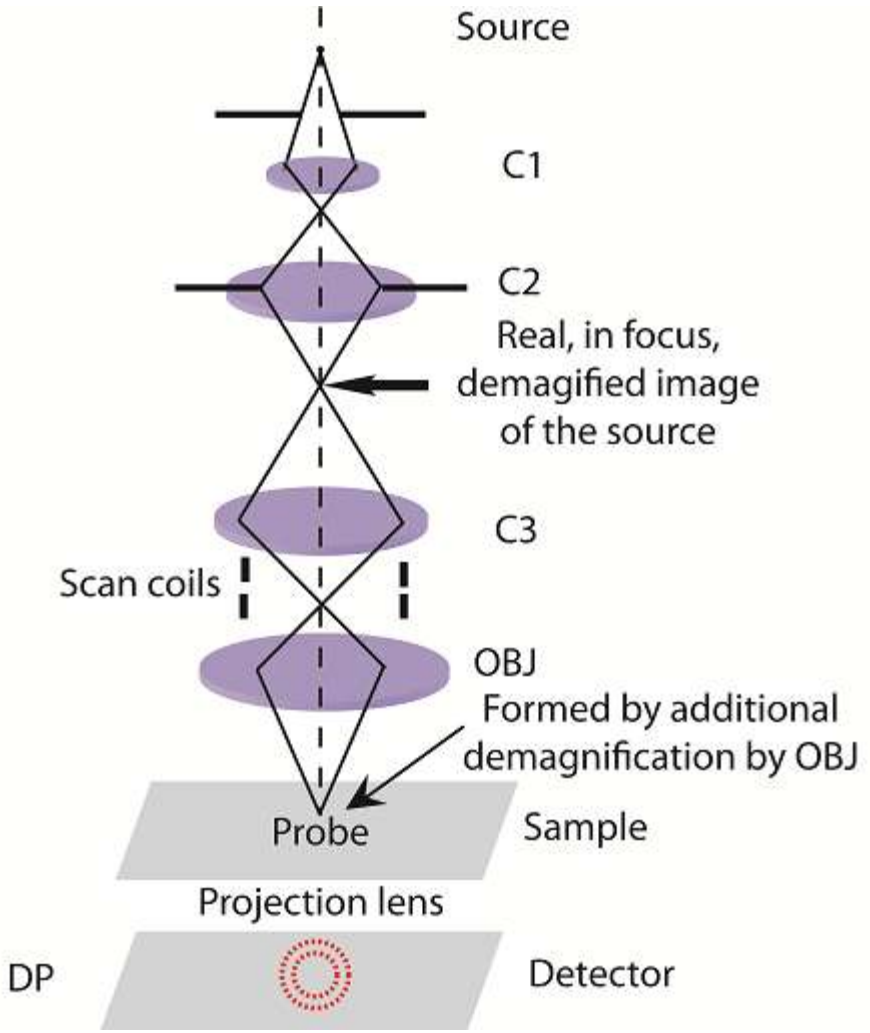

Nano-diffraction

Resolution controlled by probe

Nucleation in Magnetic Nanomaterials

R.V. Ramanujan

School of Materials Science and Engineering

Nanyang Technological University

Singapore

Team: H.F. Li, S.W. Du, Y. Zhang

Soft Magnetic Nanomaterials

- Applications
  - Energy devices
    - Generators
    - Transformers
    - Motors
  - Electromagnetic shielding
  - Data Storage
  - Biomedical devices
  - Surveillance tags

- ↑ energy efficiency by making softer magnetic materials
- Solution: Go Nano!

What do we want?

- Many amorphous magnetic materials are very soft
- High density of soft magnetic nanocrystals in a soft magnetic amorphous matrix ➔ magnetically softer!
- High nucleation rate of crystals + low growth rate
- Herzer Model: Nano ppts: $H_C \sim (\text{crystal size})^6$
- Crystallize amorphous magnetic material by heat treatment

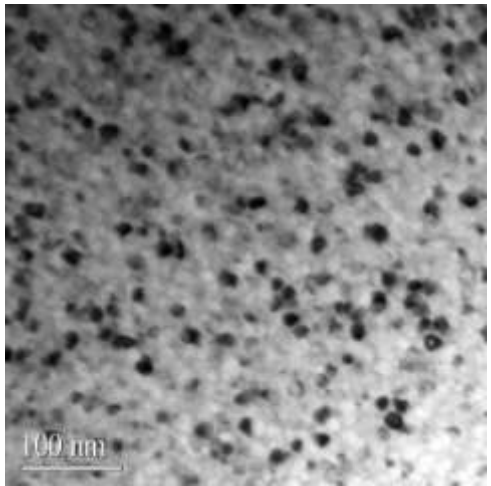

Challenge

- Can a microstructure of high density of soft magnetic precipitates in a soft magnetic amorphous matrix be magnetically softer than the famous
  - Permalloy (Fe-Ni)
  - Fe-Co for high temp. aircraft applications
  - Fe-Si-B (transformer steel)

  YES!
- Which elements will increase nucleation rate and reduce growth rate of precipitates?
- Commercial nanocrystalline magnetic alloys
  - $Fe_{73.5}Si_{13.5}Nb_3B_9Cu_1$ (FINEMET)
  - $Fe_{88}Zr_7B_4Cu_1$ (NANOPERM)
  - $Fe_{44}Co_{44}Zr_7B_4Cu_1$ (HITPERM)

Application of nucleation and growth concepts to produce soft magnetic nanostructures

- Fe-Ni-B-Mo
- Fe-Co-B-Zr
- Fe-Si-B-Nb-Cu

Nucleation in Permaloy based Fe-Ni-B-Mo magnetic nanomaterials

Objective

- Fe-Ni-B-Mo
  - To understand role of Mo and B in producing high nucleation rate and low growth rate

J. Alloys Compounds, 425, 251-260 (2006)

J. Non-Crystalline Solids, 351, 3105-3113 (2005)

Initially amorphous $Fe_{40}Ni_{38}B_{18}Mo_4$ crystallized by heat treatment

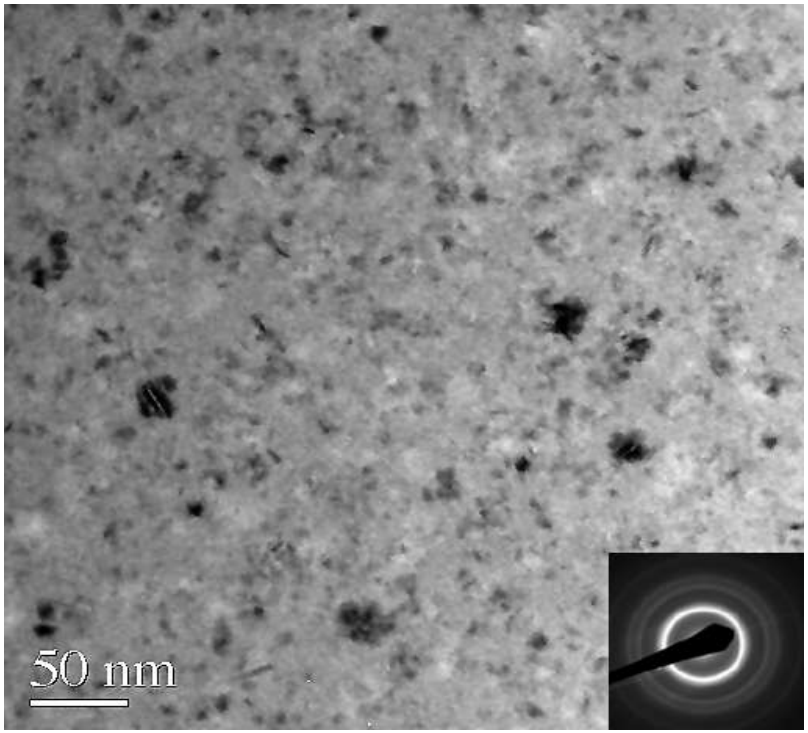

HEAT TREATED AT 400°C FOR 1 H.

Formation of Fe-Ni nano precipitates

Size distribution of crystals

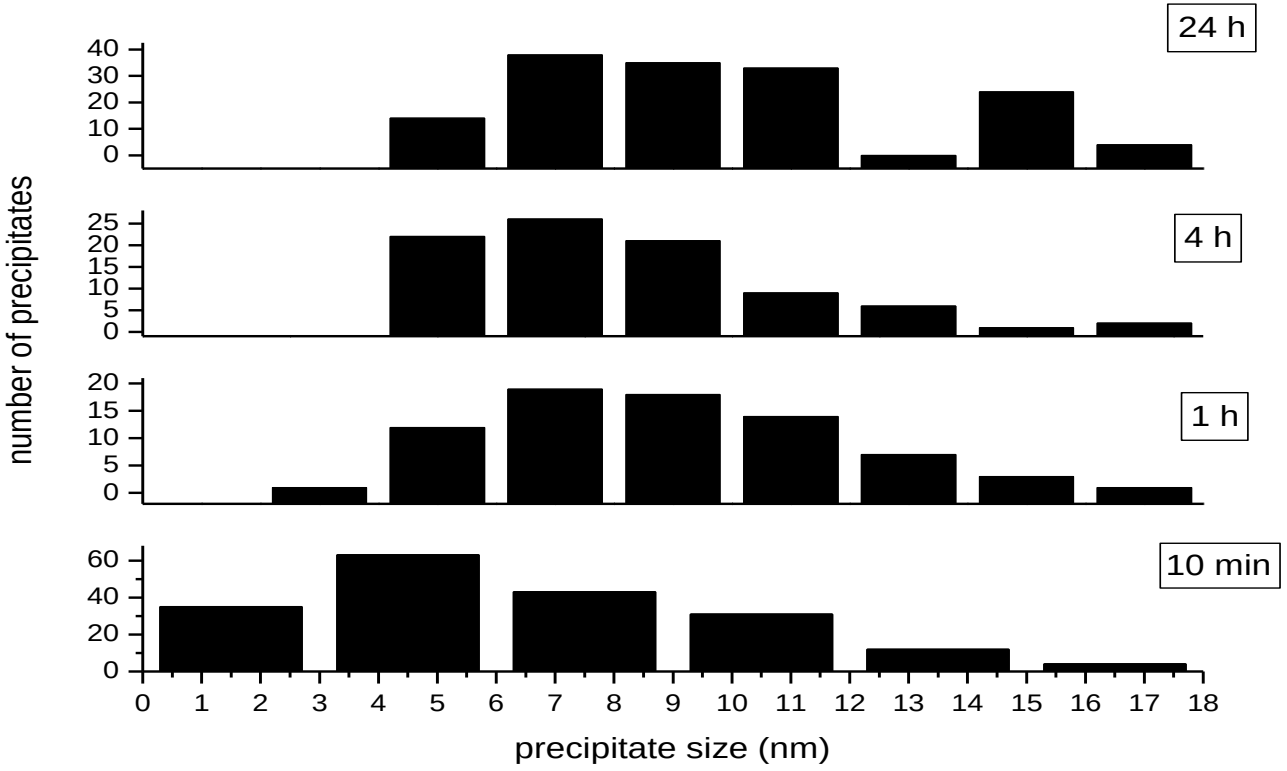

Size distribution of alloy heat treated 350 ^{o}C

Precipitate size almost constant with heat treatment time

Johnson-Mehl-Avrami Plot

- Johnson-Mehl-Avrami
  - $y=1-exp(-Kt^n)$
- Avrami exponent
  - $n=0.39$
  - Usual value 1-4
- Counterpart alloys
  - $Fe_{40}Ni_{40}B_{20}$: 3
  - $Fe_{40}Ni_{40}P_{14}B_6$: 4

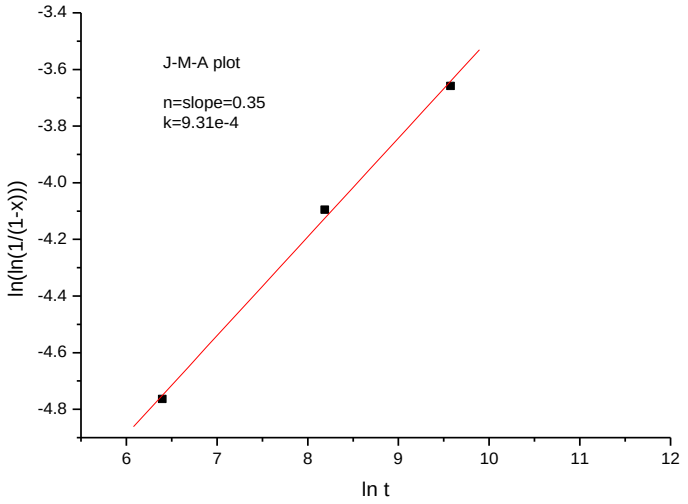

Low value of Avrami exponent n

Effect of boron on nucleation

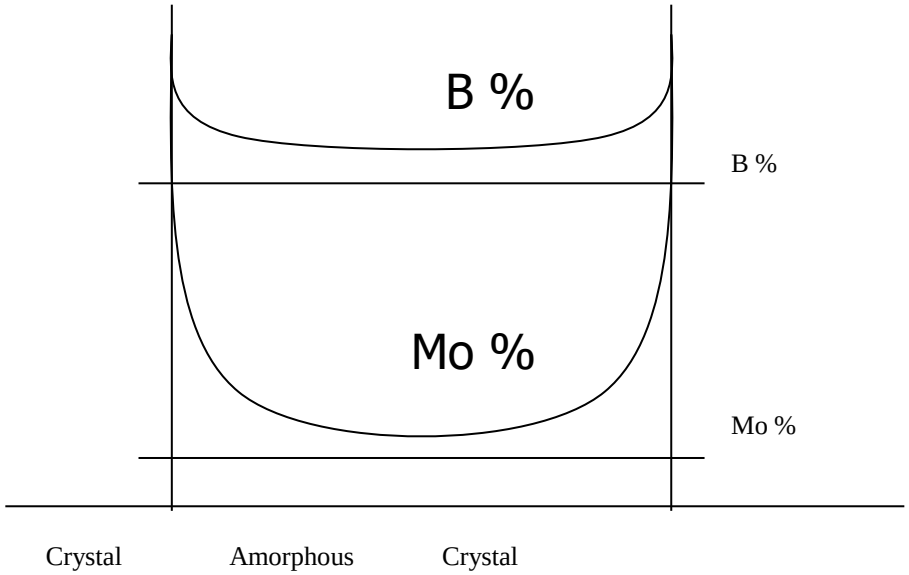

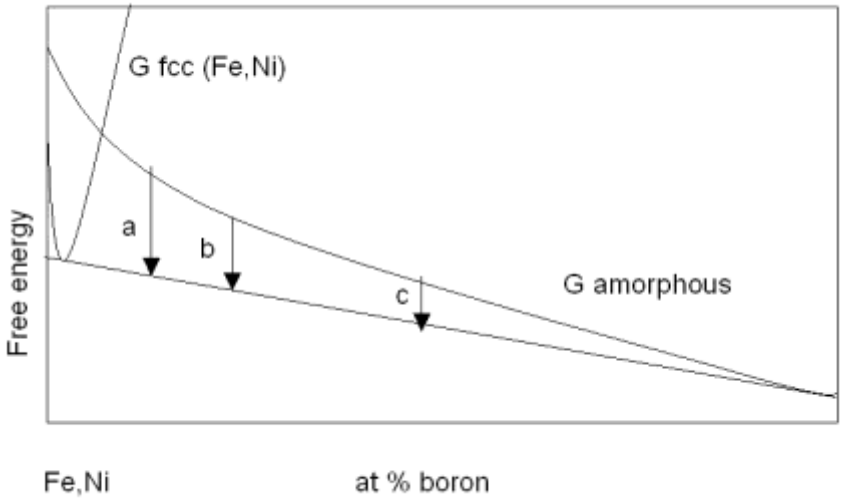

Schematic profile of B and Mo concentration in the amorphous matrix

Free energy for the amorphous phase and the crystalline phase

Boron decreases the nucleation rate

Model of effect of Mo on growth

- Hillert's theory on normal grain growth

$$\frac{dR}{dt} = \frac{A}{R} \Rightarrow R^2(t) - R^2(0) = 2At$$

- Michels' Model

$$\frac{dR}{dt} = \frac{A}{R} - f(R)$$

- Boundary condition

$$\frac{dR}{dt} = 0, R \to R_{\max}$$

Concentration of Molybdenum

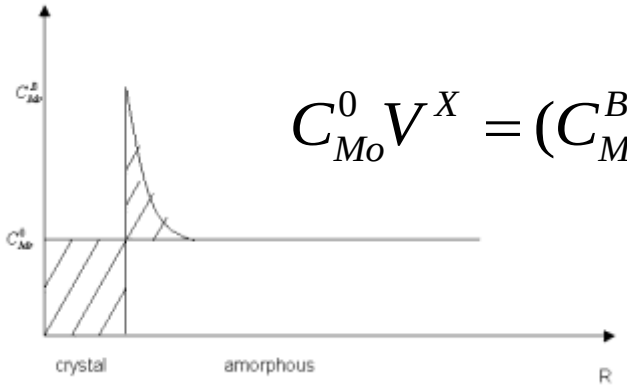

$$C_{Mo}^{0} V^{X} = (C_{Mo}^{B} - C_{Mo}^{0}) A^{B} L$$

$$\frac{dR}{dt} = \frac{A}{R} - \frac{AR}{R_{\max}^{2}}$$

Molybdenum pile up at the crystal:amorphous interface

$$R(t) = \{R_{\max}^{2} - (R_{\max}^{2} - R^{2}(0)) \exp[-2At / R_{\max}^{2}]\}^{1/2}$$

Crystal size and effect of Mo

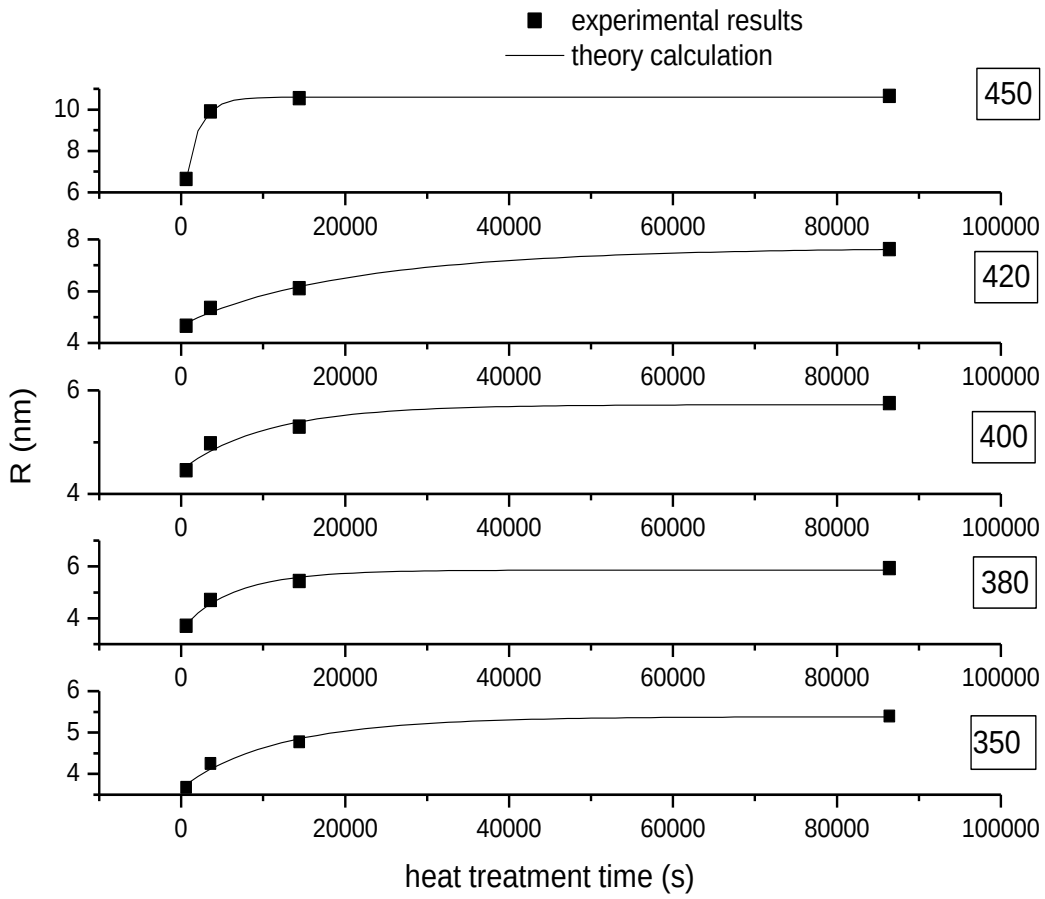

Crystal growth is retarded by the pile up of Mo atoms at interface

Good agreement of the experimental result and

Magnetic Properties

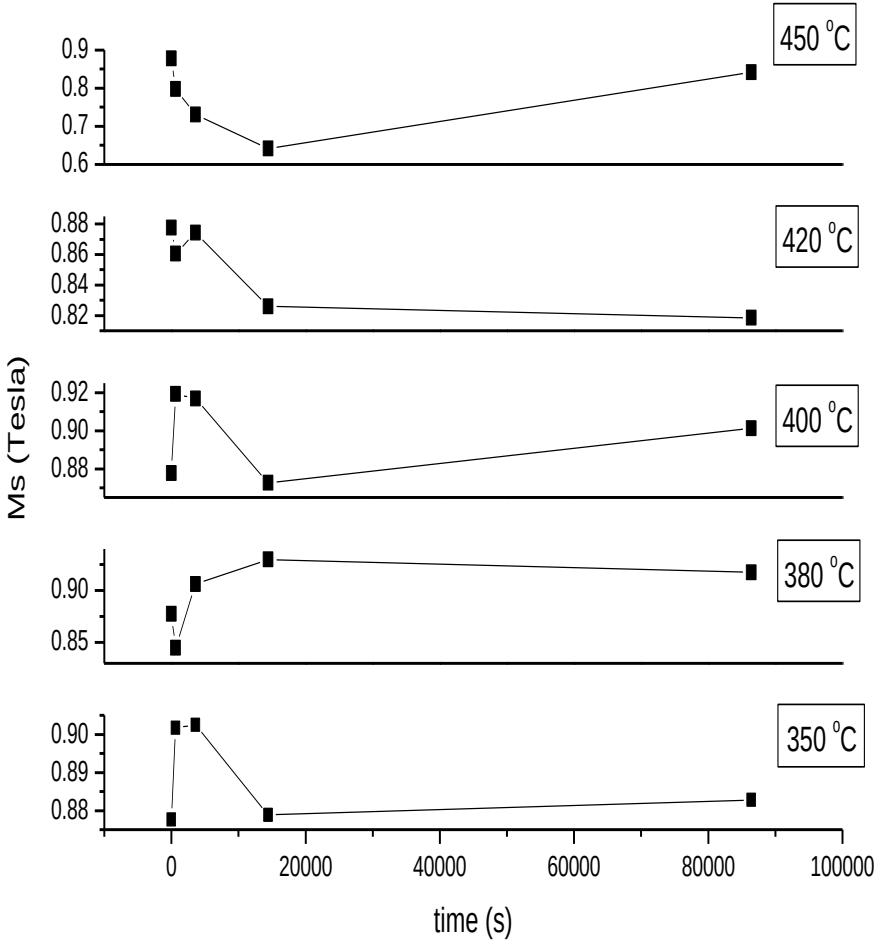

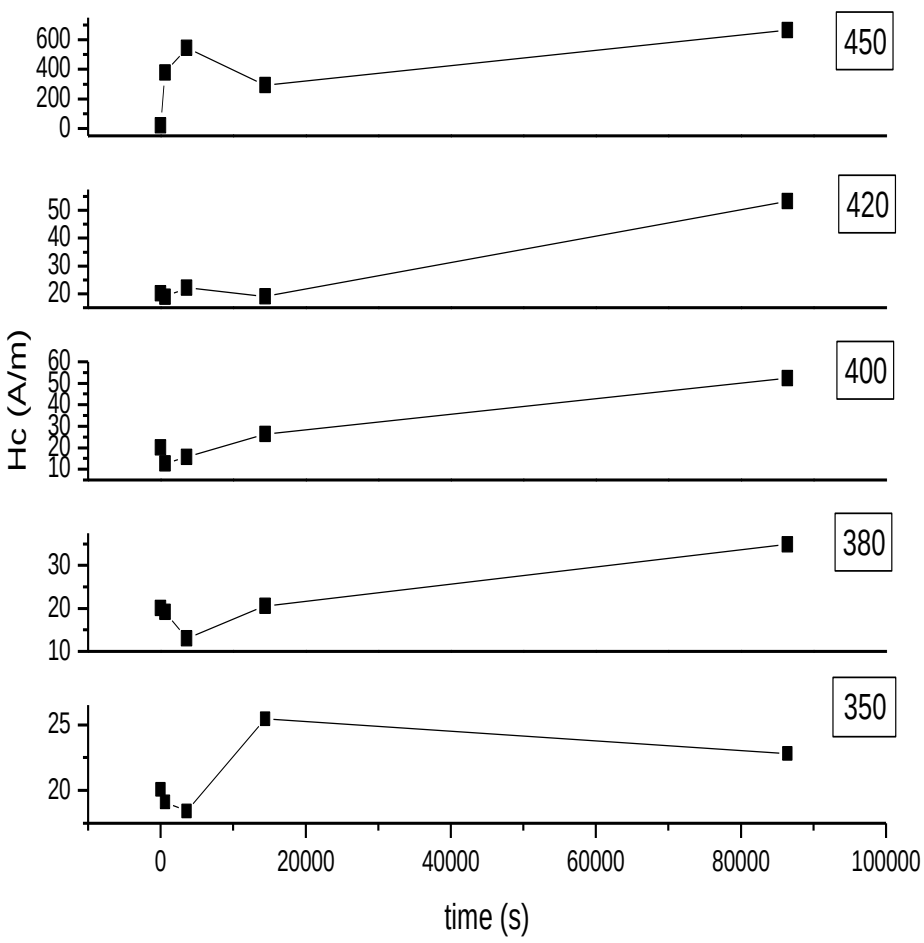

Improved magnetic properties was achieved at

Application of nucleation and growth concepts to produce soft magnetic nanostructures

- Fe-Ni-B-Mo
- Fe-Co-B-Zr
- Fe-Si-B-Nb-Cu

Nanocrystallization of HiTperm $Co_{44.5}Fe_{44.5}Zr_7B_4$

IEEE Trans. Nanotechnology, 6, 177-185 (2007)

IEEE Trans. Nanotechnology, 5, 295-300 (2006)

Nanocrystallization of initially amorphous HiTperm $Co_{44.5}Fe_{44.5}Zr_7B_4$

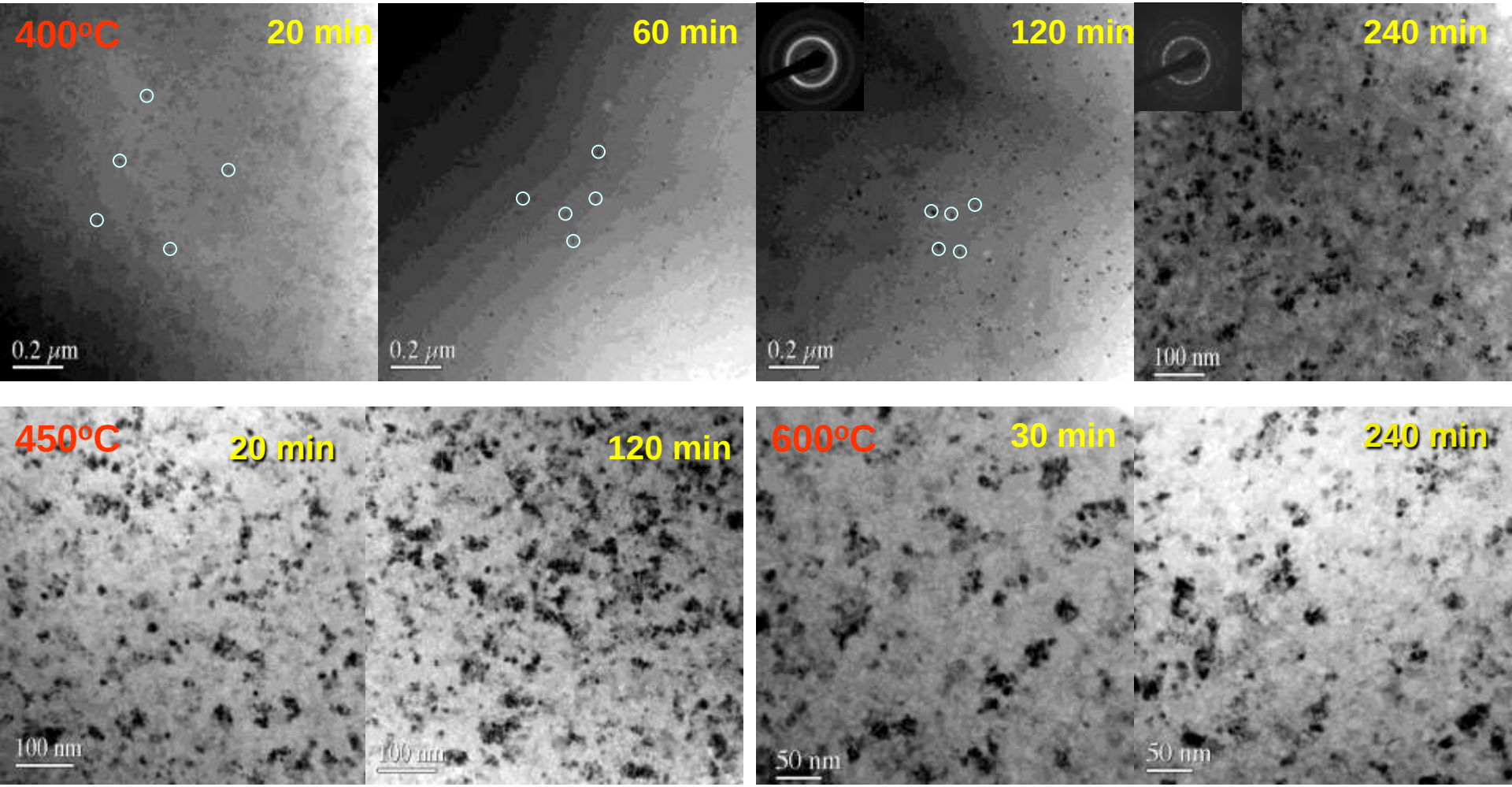

- High nucleation rate, low growth rate

Application of nucleation and growth concepts to produce soft magnetic nanostructures

- Fe-Ni-B-Mo
- Fe-Co-B-Zr
- Fe-Si-B-Nb-Cu

Finemet type alloys

- Fe-Si-B-Cu-Nb alloys (transformer steel based)

- Excellent magnetic properties with **combined** Cu & Nb alloying additions in Fe-Si-B alloy due to nanostructure formation

- Conventional (incorrect) view:
  - Role of Cu is to↑ nucleation
  - role of Nb is to ↓ growth.

Objective

- What is the role of Cu and Nb alloying additions in nanostructure formation in Fe-Si-B-Cu-Nb alloys?

Methodology

- Effects of alloying additions: 1 at% Cu and 3 at% Nb in amorphous Fe-Si-B-Cu-Nb alloy.

Morphology after primary crystallization

Fe-Si-B

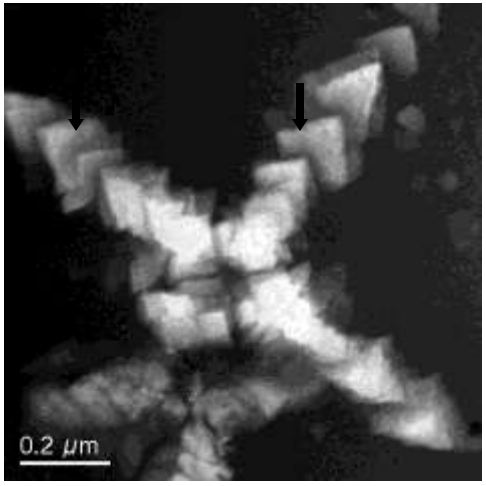

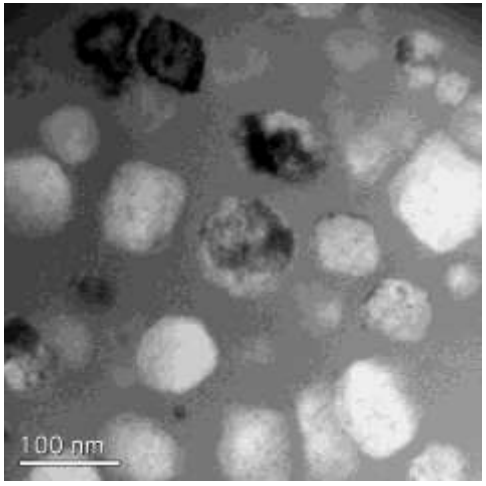

Fe-Si-B-Cu

Fe-Si-B-Nb

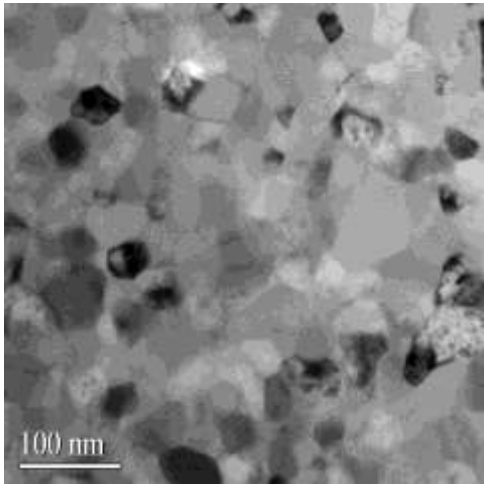

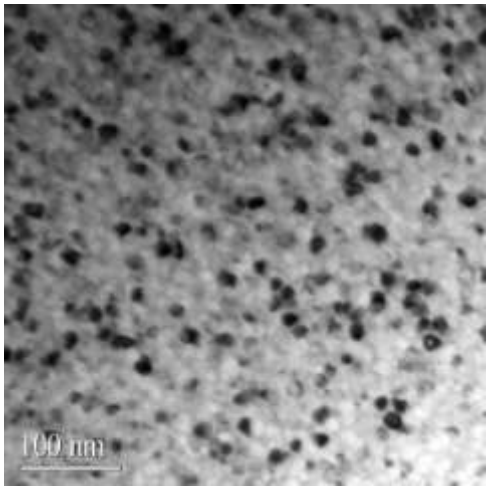

Fe-Si-B-Cu-Nb

(1)$Fe_{77.5}Si_{13.5}B_9$

Large microstructure difference due to alloying addition

Fe-Si-B alloy

Equiaxed to dendrite morphological transition in Fe-Si-B

Appl. Phys. Lett., 88, 182506, 2006

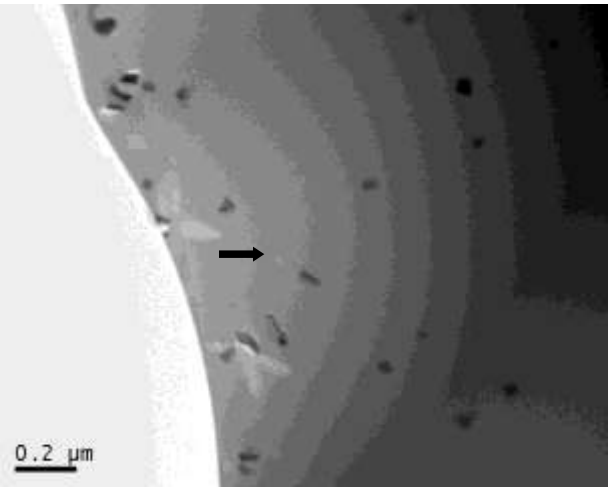

0s

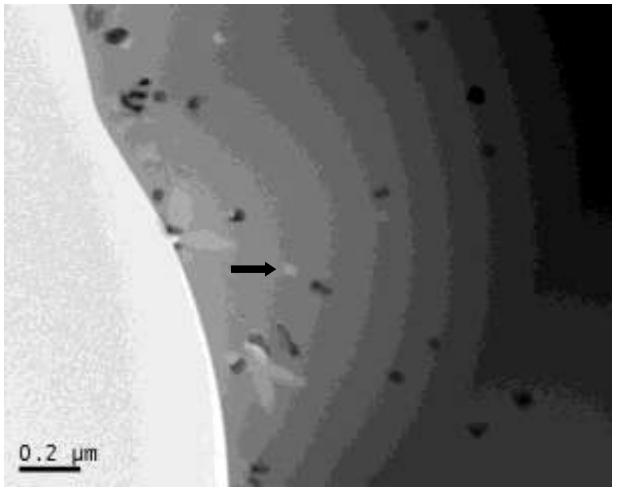

6s

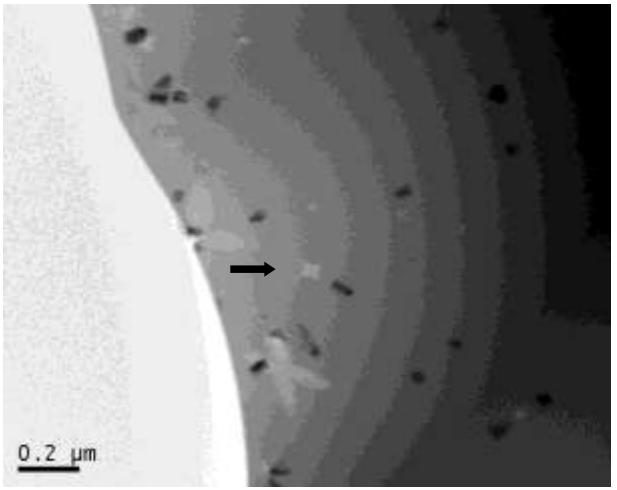

12s

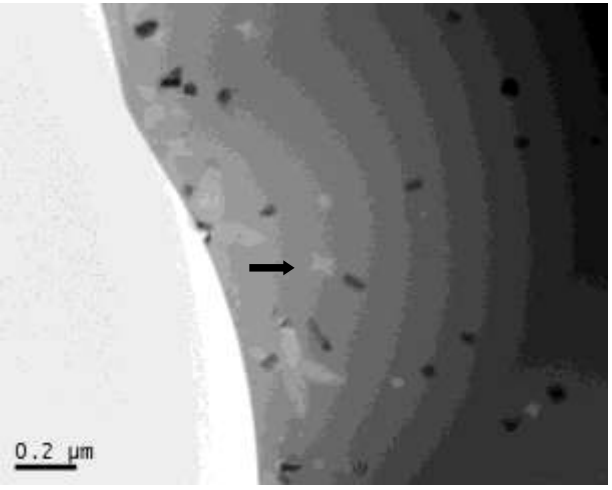

18s

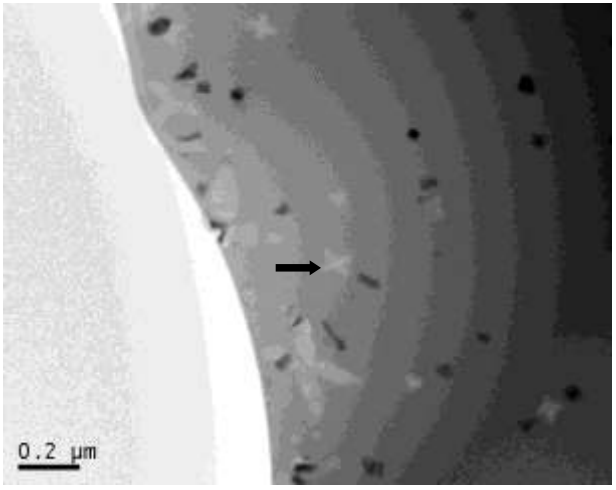

24s

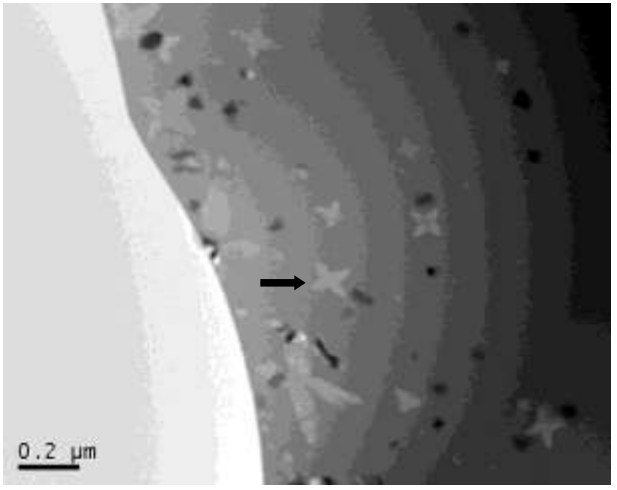

30s

Fe-Si-B alloy

- Dendrites of closely spaced Fe-Si crystals, spacing ~ nanometers.

- In-situ hot stage TEM: equiaxed → dendritic morphological transition at critical size of ~ 45 nm . Explained by morphological stability theories.

Effect of Cu addition

In-situ hot stage TEM of Fe-Si-B-Cu

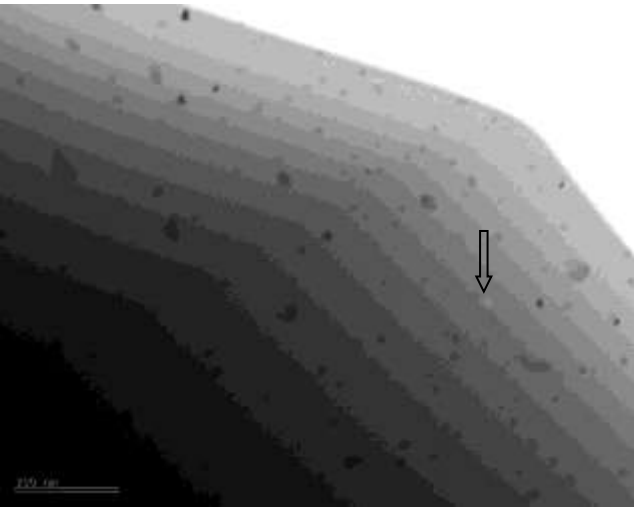

- 400°C for 306s

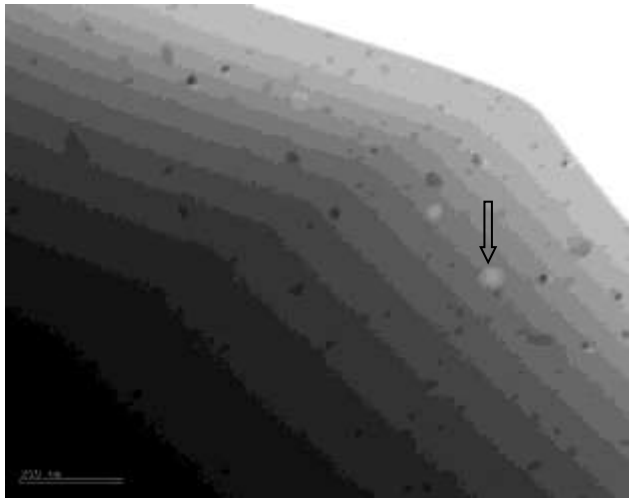

- 400°C for 318s

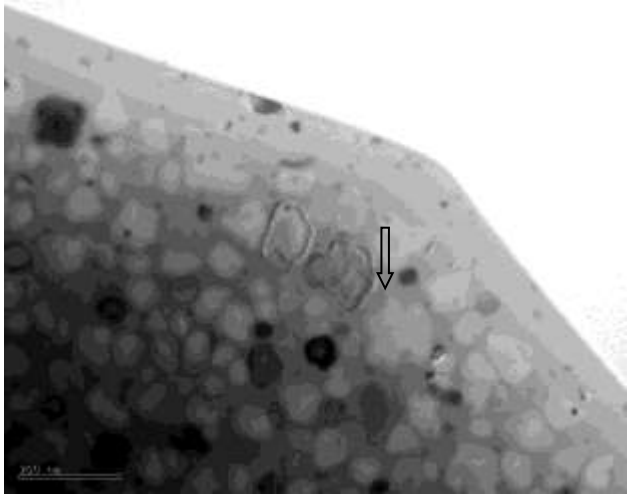

- 450°C for 600s

Unstable interface of spheroidal crystal when crystal size > than 100nm.

Effect of Cu alloying addition

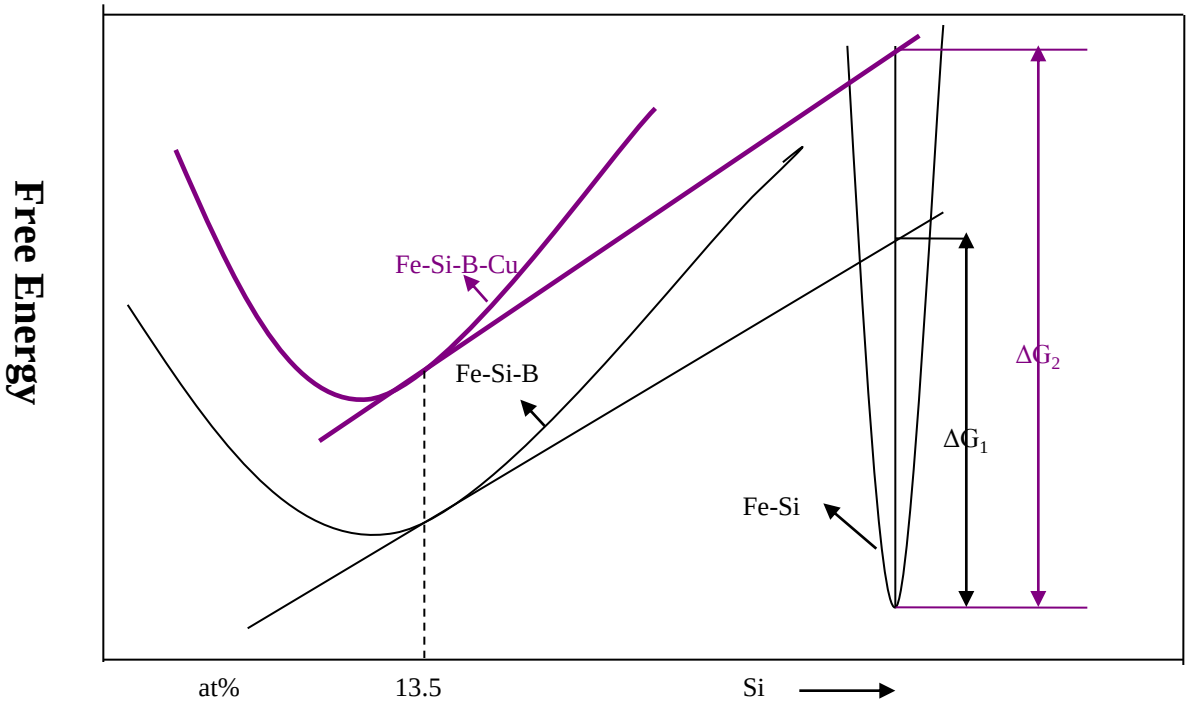

Free energy G-curve for amorphous matrix and crystallization product

Fe-Si-B-**Cu**

- Cu addition influenced **both** nucleation and growth
  - spheroidal crystals ~ 100 nm, rough interfaces .

- Crystal density ↑, crystal size ↓. However, crystal density << than in Fe-Si-B-Nb-Cu.

- Driving force for nucleation ↑.

Effect of Nb addition

Eutectic crystallization of Fe-Si-B-Nb alloy

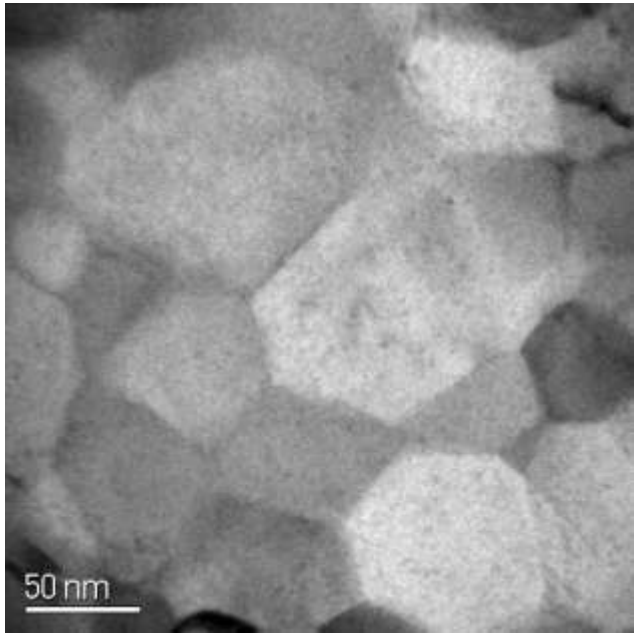

(1)

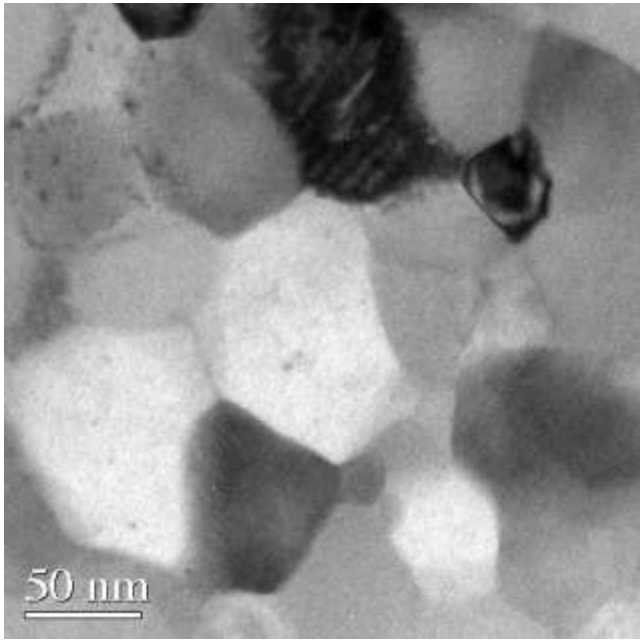

(2)

TEM micrographs of the alloy with **Nb**, after heat treatment at 550 ^{o}C for (1)0.5 h and (2)24 h

Equiaxed

Effect of Nb addition

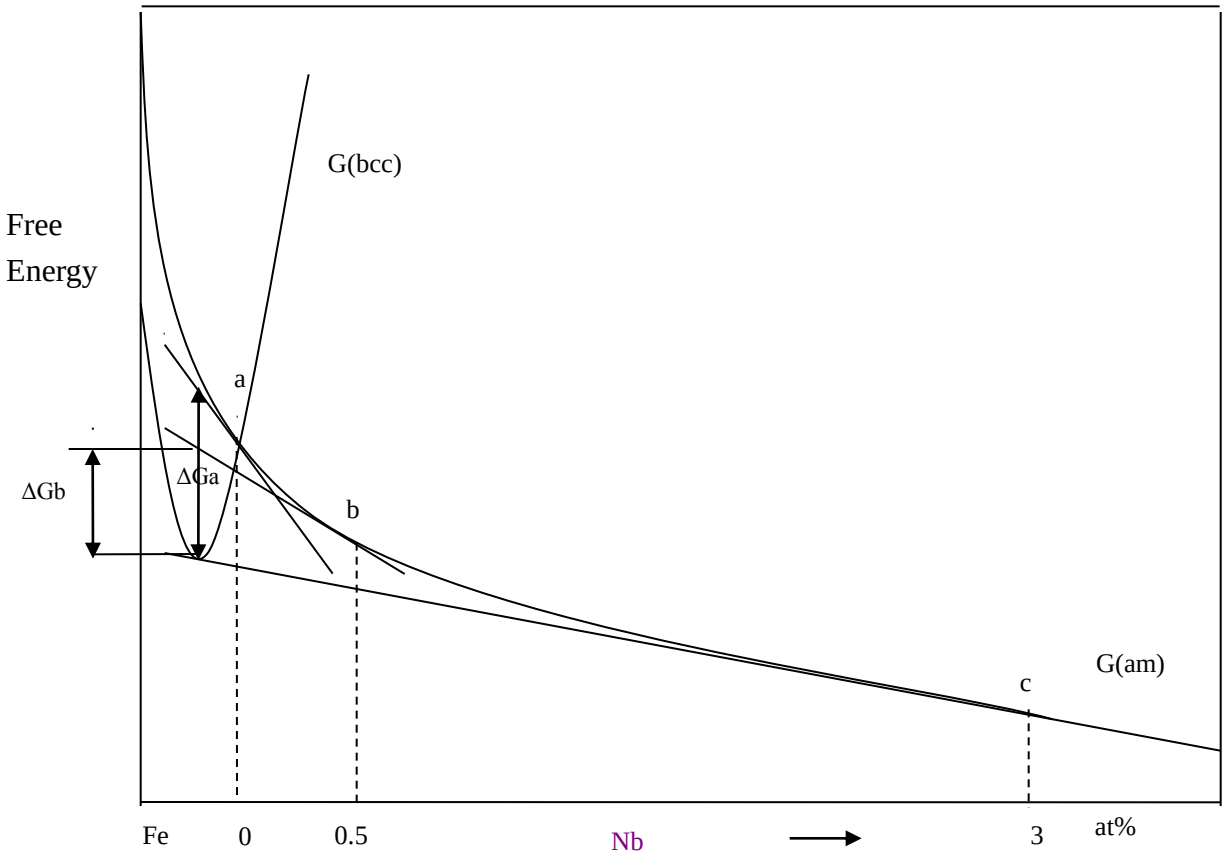

Free energy G-curve for amorphous matrix and crystallization product

Fe-Si-B-**Nb**

- Eutectic crystallization:Fe-Si, Fe_3B and $Fe_{23}B_6$
- Greater ↑ in crystal density, ↓ of crystal size compared to Cu addition.
- But, cannot obtain high crystal density and small crystal size of Fe-Si-B-Nb-Cu.
- Hence, synergetic effects of combined Cu and Nb additions key to nanostructure formation

Effect of both Cu and Nb additions

Cu and Nb EELS map at initial stage of crystallization

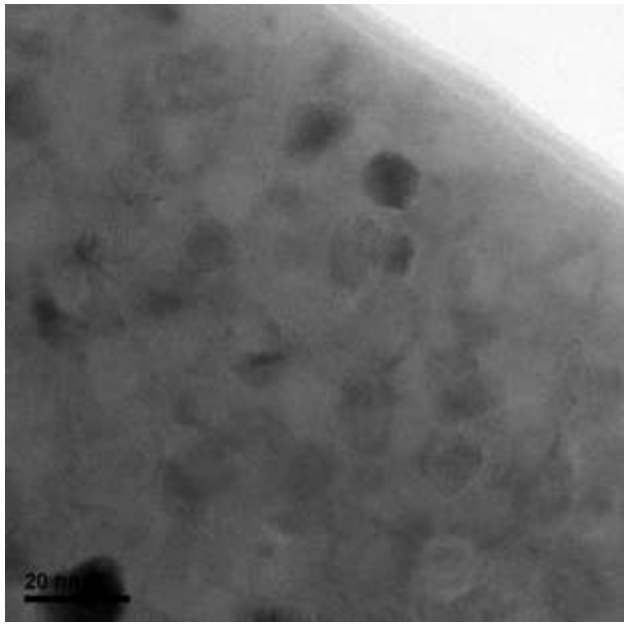

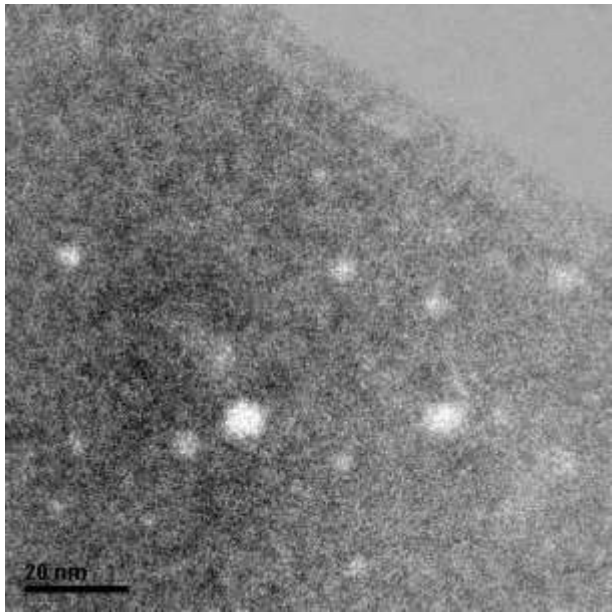

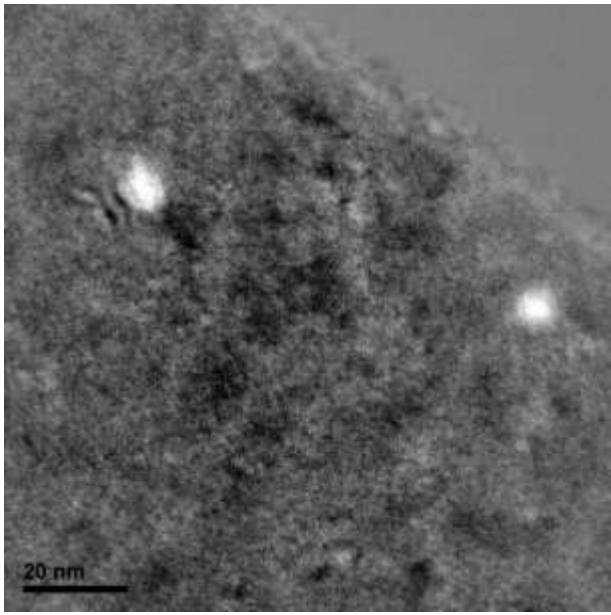

(a) **(b)** **(c)**

(a) BF TEM micrograph of Fe-Si-B-Nb-Cu alloy after heat treatment at 500 ^{o}C for 10 min (b) EELS map of Cu (c) EELS map of Nb

Cu AND Nb rich regions

Quantitative analysis of crystallization

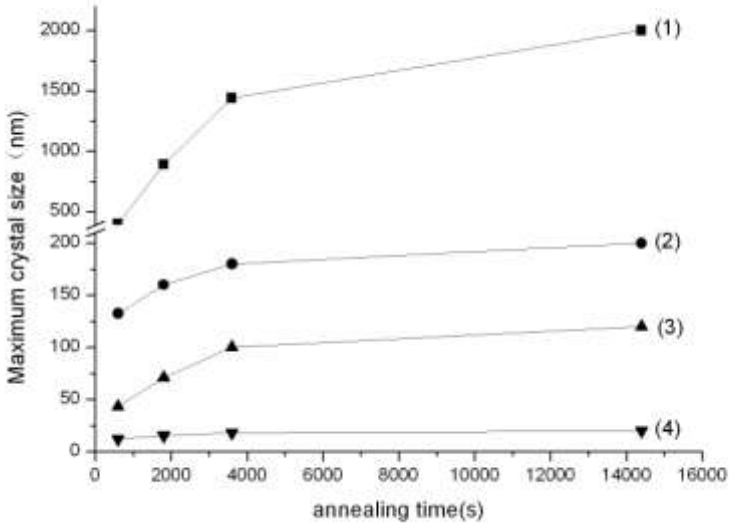

Maximum crystal size as function of annealing time: (1)Fe-Si-B (2)Fe-Si-B-Cu (3)Fe-Si-B-Nb (4)Fe-Si-B-Nb-Cu alloy at 500 °C

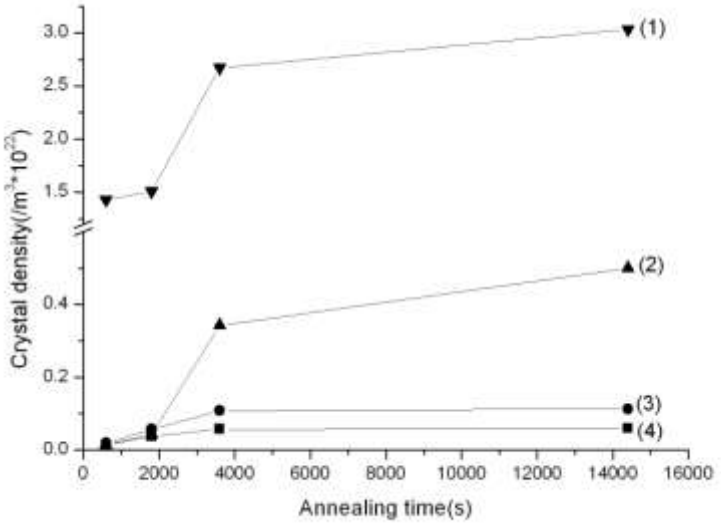

The number of crystal per unit volume as function of annealing time: (1) Fe-Si-B -Nb-Cu (2) Fe-Si-B-Nb (3) Fe-Si-B-Cu (4) Fe-Si-B alloy at 500 °C

Johnson-Mehl-Avrami-Kolmogorov Plot

- JMAK equation

  $X=1-exp[(Kt)^n]$

- Avrami exponent

  $n=0.25$

  Usual value 1-4

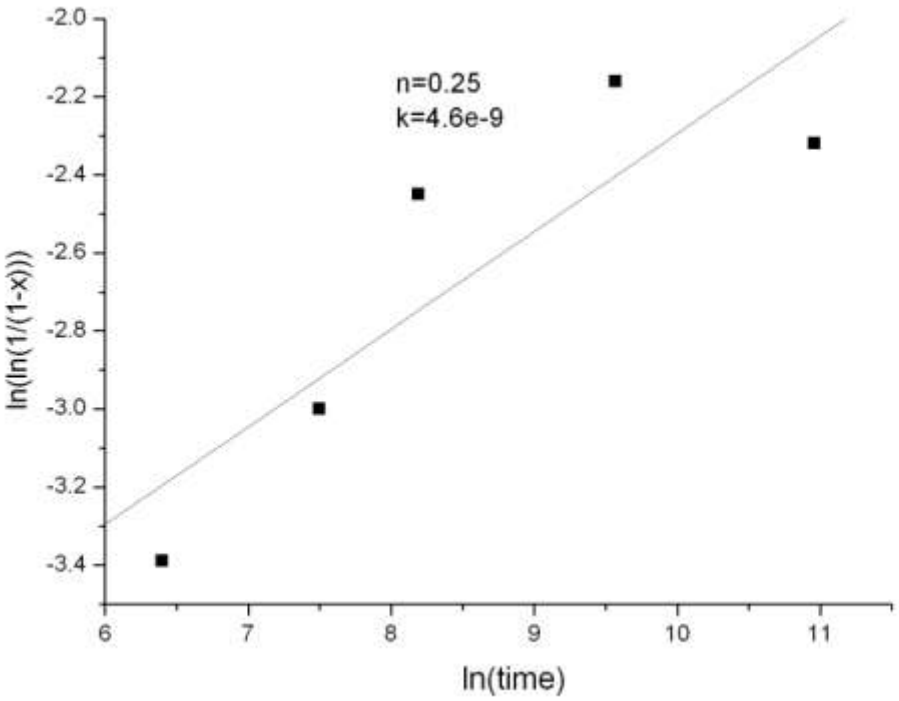

Conclusions

- Alloying with Cu, Nb had dramatic effects on nanostructure formation in iron-based soft magnetic materials

- Studied by DSC, XRD, EDX , EELS, conventional & in-situ hot stage TEM.

Fe-Si-B-Nb-Cu

Novel mechanism of nanostructure formation (synergetic effects of combined Cu and Nb)

- Contrary to most models, we find that **both** Nb and Cu influence nucleation and growth processes.
- Combined additions ➔ small crystal size and high crystal density.
- High nucleation rate ➔ **both** Cu and Nb rich regions ➔ high number of heterogeneous nucleation sites.
- Low growth rate due to strong interaction of Cu, Si, Nb and B atoms, consistent with Hunziker model.

Summary

- A high density of soft magnetic nanoprecipitates in an amorphous matrix yield superior soft magnetic properties
- Nucleation and growth concepts have been used to produce novel soft magnetic nanostructures in iron and Co based soft magnetic materials

Related Publications-1

- H.F. Li and R.V. Ramanujan, Coarsening of the nanolamellar structure in a soft magnetic alloy, *IEEE Trans. Nanotechnology*, 6, 177-185 (2007).
- R.V. Ramanujan and Y. Zhang, Quantitative transmission electron microscopy analysis of the nanocrystallization kinetics of soft magnetic alloys, *Phys. Rev. B*., 74, 224408-1 to 224408-7 (2006). *This paper was selected by American Inst. of Physics and American Phys. Soc. for J. of Nanoscale Sci. Tech., Dec. 26, 2006.*
- R.V. Ramanujan and S.W. Du, Nanocrystalline structures obtained by the crystallization of an amorphous Fe40Ni38B18Mo4 soft magnetic alloy, *J. Alloys Compounds,* 425, 251-260 (2006).
- H.F. Li and R.V. Ramanujan, Nanolamellar structure obtained by simple crystallization of an amorphous cobalt based magnetic alloy, *IEEE Trans. Nanotechnology*, 5, 295-300 (2006). *XRD data from this paper has been incorporated in the Powder Diffraction file of the International Centre for Diffraction Data (USA).*
- Y. Zhang and R.V. Ramanujan, The effect of copper alloying additions on the crystallization of an amorphous Fe-Si-B alloy, *J. Mater. Sci.*, 41, 5292-5301 (2006).
- H.F. Li and R.V. Ramanujan, In situ hot stage transmission electron microscopy observations of nanocrystal formation in a Co65Si15B14Fe4Ni2 amorphous magnetic alloy, *Thin Solid Films*, 514, 316-322 (2006).
- R.V. Ramanujan and Y. Zhang, Solid state dendrite formation in an amorphous magnetic Fe77.5Si13.5B9 alloy observed by in-situ hot stage transmission electron microscopy, *Appl. Phys. Lett.*, 88, 182506 (2006).
- H.F. Li, D.E. Laughlin and R.V. Ramanujan, Nanocrystallization of an Fe44.5Co44.5Zr7B4 amorphous magnetic alloy, *Phil. Mag.*, 86, 1355- 1372 (2006).
- H.F. Li and R.V. Ramanujan, Crystallization behavior of the cobalt based metallic glass Co65Si15B14Fe4Ni2, *Mater. Sci. Engg. A*, 375-377, 1087-1091 (2004).

Related Publications-2

- Y. Zhang and R.V. Ramanujan, Microstructural observation of the crystallization of amorphous Fe-Si-B based magnetic alloys, *Thin Solid Films*, 505, 97-102 (2006).
- Y. R. Zhang and R.V. Ramanujan, Characterization of the effect of alloying additions on the crystallization of an amorphous magnetic Fe73.5Si13.5 B9Nb3Cu1 alloy, *Intermetallics*, 14, 710-714 (2006).
- Y. Zhang and R.V. Ramanujan, A study of the crystallization behavior of an amorphous Fe77.5Si13.5B9 alloy, *Mater. Sci. Engg.*, A416, 161-168 (2006).
- S.W. Du and R.V. Ramanujan, Crystallization and Magnetic Properties of Fe40Ni38B18Mo4 Amorphous Alloy, *J. Non-Crystalline Solids,* 351, 3105-3113 (2005).
- Y. Zhang and R.V. Ramanujan, The effect of niobium alloying additions on the crystallization of a Fe-Si-B-Nb alloy, *J. Alloys Compounds*, 403, 197- 205 (2005).
- H.F. Li and R.V. Ramanujan, In-situ TEM observations of the coarsening of a nanolamellar structure in a cobalt based magnetic alloy, *J. Mater. Sci.*, 40, 1901-1907 (2005).
- S.W. Du and R.V. Ramanujan, Mechanical alloying of Fe-Ni based nanostructured magnetic materials, *J. Magn. Magn. Mater*., 292, 286-298 (2005).
- H.F. Li and R.V. Ramanujan, Mechanical alloying of FeCo nanocrystalline magnetic powders, *J. Electronic Mater.*, 33, 1289-1297 (2004). *Special Issue*.
- H. F. Li and R.V. Ramanujan, Microstructural evolution during crystallization of a Co65Si15B14Fe4Ni2 magnetic material, *Intermetallics*, 12, 803-807 (2004).
- S.W. Du and R.V. Ramanujan, Characterization of Fe40Ni38B18Mo4 nanomagnetic alloy, *Mater. Sci. Engg. A*., 375-377, 1040-1043 (2004).

Thank You !

Thermodynamic Modeling of the Early Stages of Solid State Precipitation in Alloy Sysems

S.Rangnathan
National Metallurgical Laboratory
Jamshedpur 831 007, INIA

AFRL-AOARD-LLNL WORKSHOP ON NUCLEATION, May 2010

Nucleation

Not always an equilibrium process

Nucleus – different from equbm. Phase

can transform to non-equbm. phase

true of composition

interface composition – crucial

Modelling the non-equilibrium process

Non-Equilibrium Process

Many phase transformations

do not reach equilibrium

checked by kinetics

mass transfer

heat transfer

chemical reaction

Non-equilibrium state

compositional (eg. Super-saturated solutions)

structural (eg. Amorphous solids)

morphological

Modelling - Equilibrium Phenomenon

Equilibrium State

- Unique
- Well-defined
- Easy to target and predict

Equilibrium State

Free energy of s system

minimum at equilibrium

$dF = 0$

$F = \Sigma k_i \mu_i$

k_i = co-efficient terms

μ_I = potential terms

μ - temperature, pressure, chemical potential

At constant temperature, pressure

$F = \Sigma m_i \mu_I$

m – mass

μ - chemical potential

i - phase - i

Non-Equilibrium Transformation

Consider a system A-B

Phases α,β

Equilibrium Processes
Free Energy-Composition Diagram

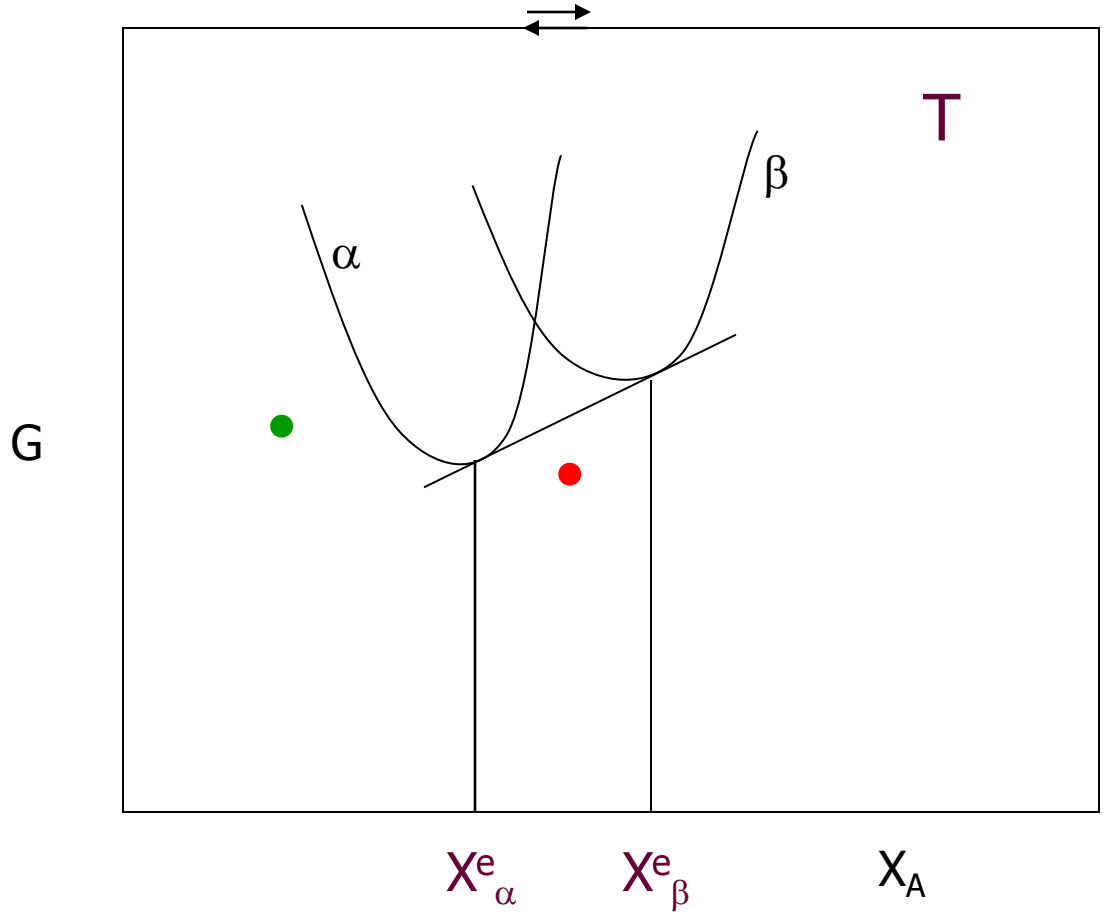

Free Energy–Composition Diagram Invariant Composition Phases

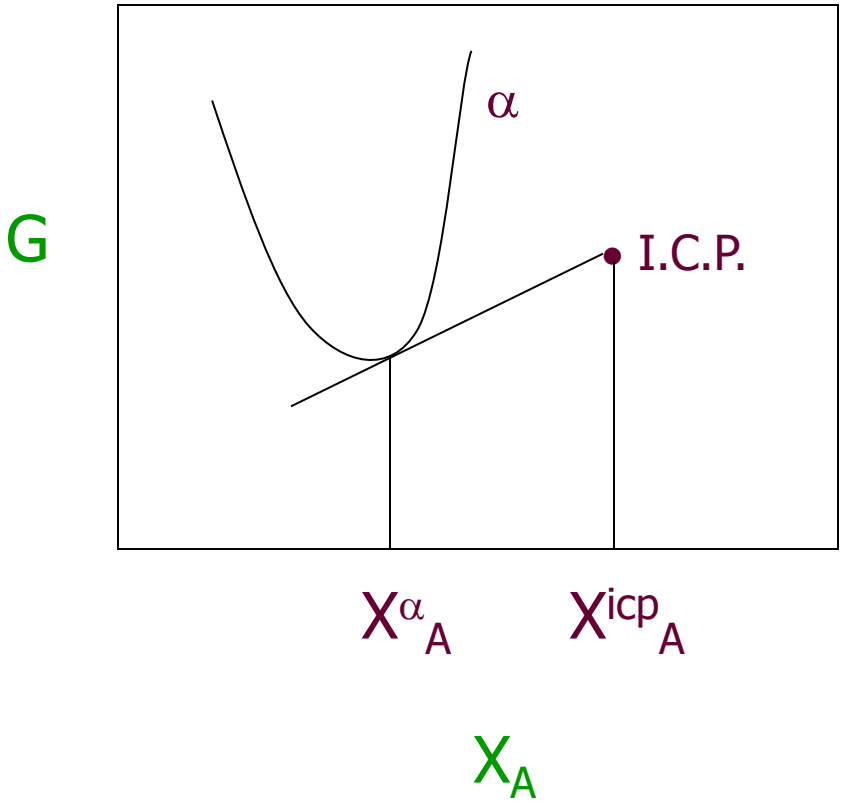

Criterion for Non-Equilibrium Process

Consider system A-B (constituents)

Possible phases α,β

Chemical potentials μ_A^{α} , μ_A^{β}, μ_A^{α}, μ_A^{β}

For transformation

$$\alpha \rightarrow \beta$$

$$\Delta G^{\alpha\beta} = X_A^{\alpha}\, \Delta\mu_A + X_B^{\alpha}\, \Delta\mu_B$$

$$\Delta\mu_i = \mu_i^{\alpha} - \mu_i^{\beta}$$

$\Delta G^{\alpha\beta} < 0$ for process to occur

Non-equilibrium process

α,β can be solution phases or compounds

Relevant for material synthesis

Transformation Diagrams

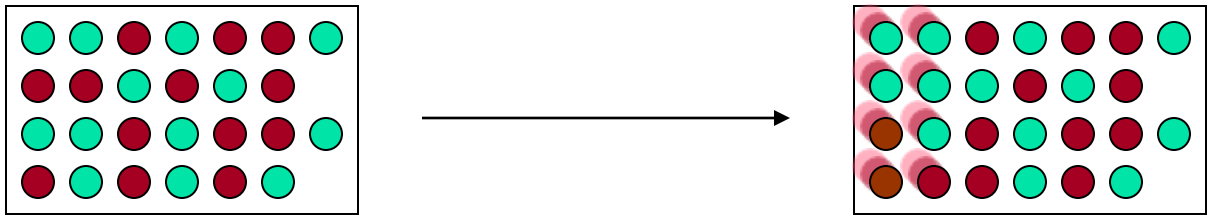

State A State B

Free Energy Change = (G_B-G_A)

Non - equilibrium process - nucleation

$\Delta G<0$

States A and B can be aqueous solution and compound

Calphad, 2002

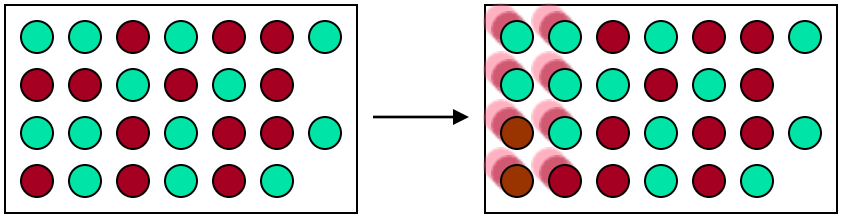

State A State B

Transformation Diagram

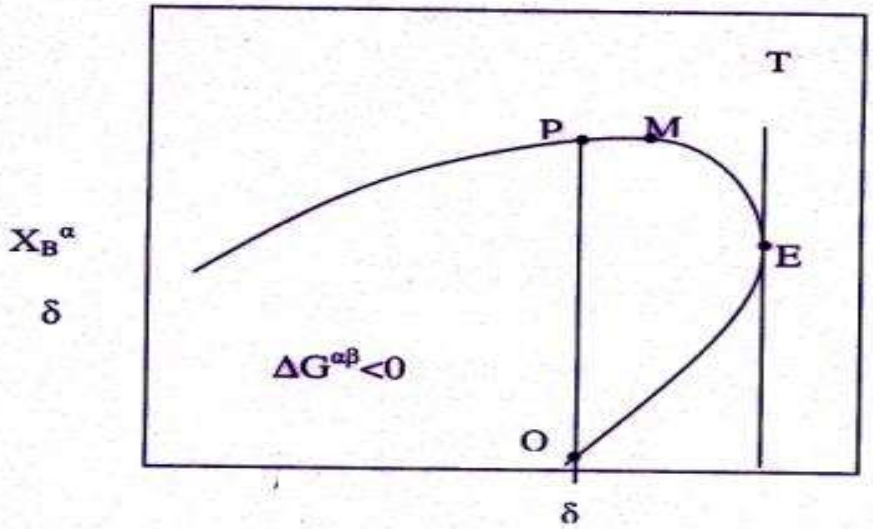

$$\Delta G^{\alpha\beta} = X_A^\alpha \Delta\mu_A + X_B^\alpha \Delta\mu_B$$

$$\Delta\mu_i = \mu_i^\alpha - \mu_i^\beta$$

Transformation Diagram

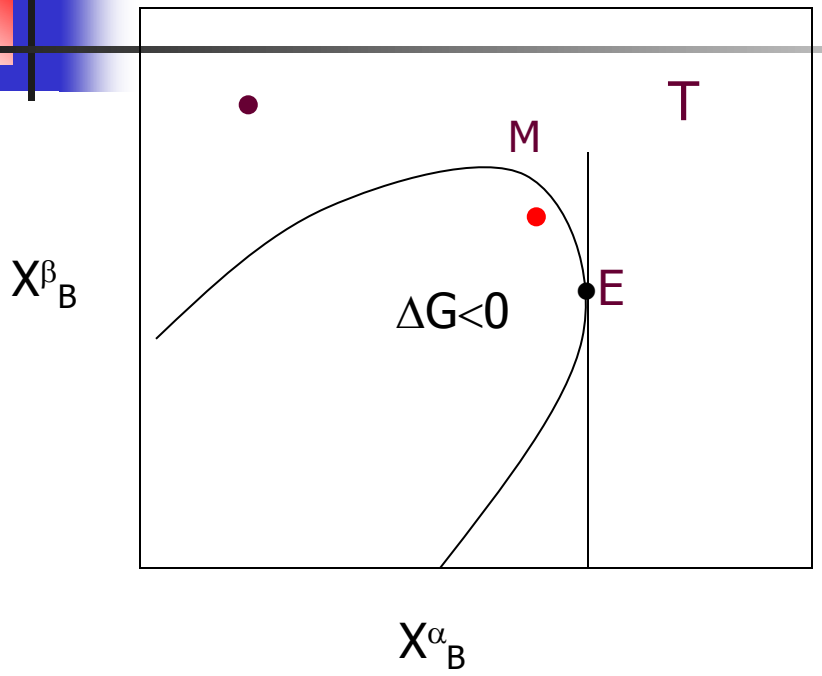

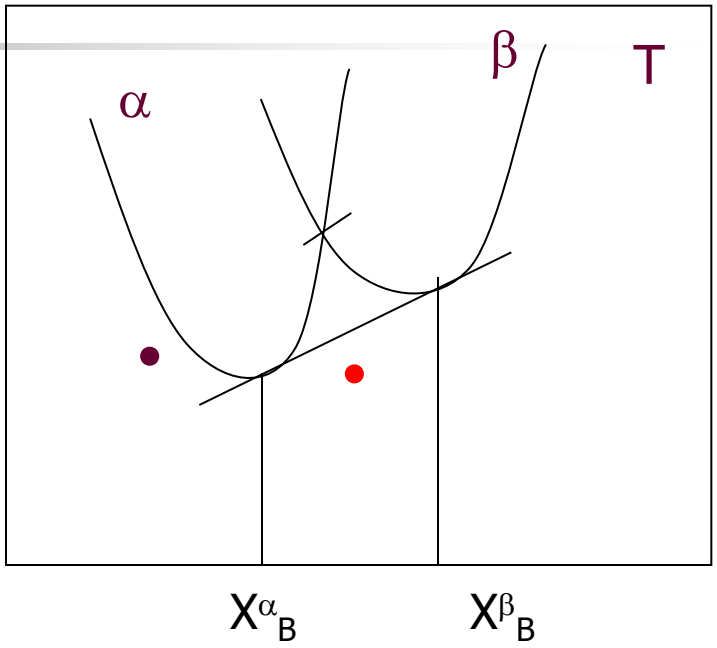

The Bi-directional Transformation Diagram

$\alpha \rightarrow \beta$ possible at X^{β}_{X}

$X^{\alpha}_{X} \rightarrow X^{\beta}_{X}$

Will β at X^{β}_{B} transform to α ?

In other words, will β go back into solution?

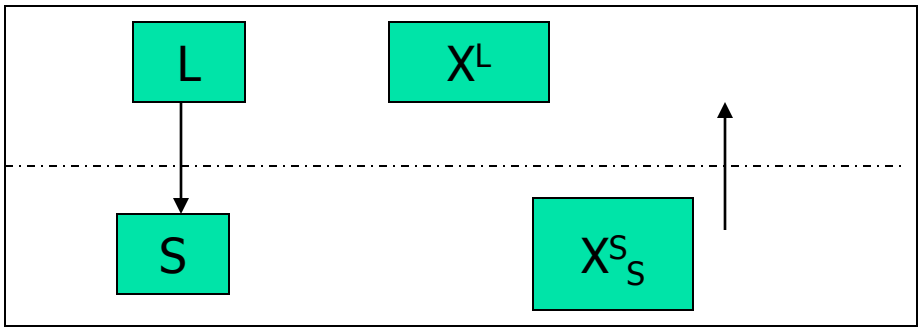

Will the nucleus Redissolve?

Bi – Directional Transformation Diagram

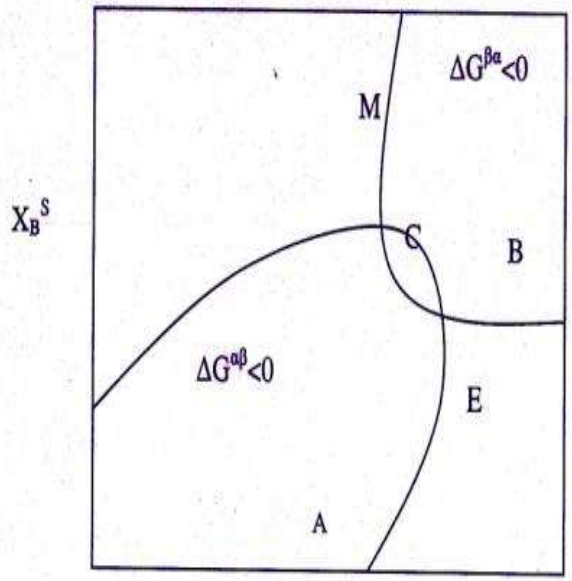

$$\Delta G^{\alpha\beta} = X_A^{\alpha}\,\Delta\mu_A + X_B^{\alpha}\,\Delta\mu_B$$

$$\Delta G^{\beta\alpha} = -\left[\left(X_A^{\beta}\,\Delta\mu_A\right) + \left(X_B^{\beta}\,\Delta\mu_B\right)\right]$$

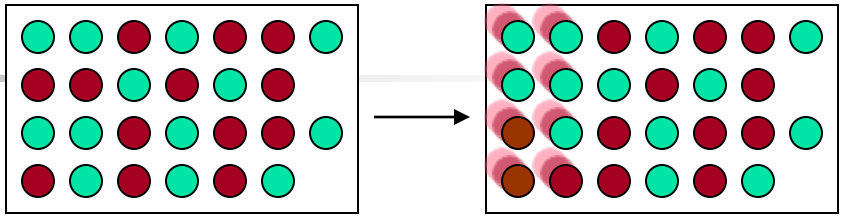

State A State B

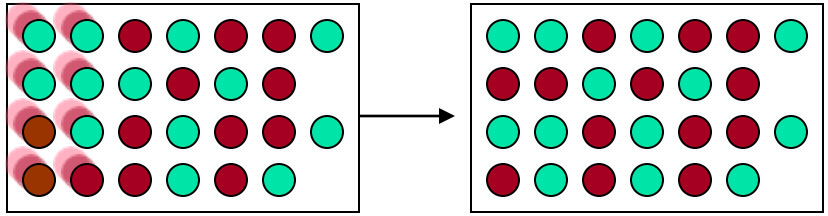

State B State A

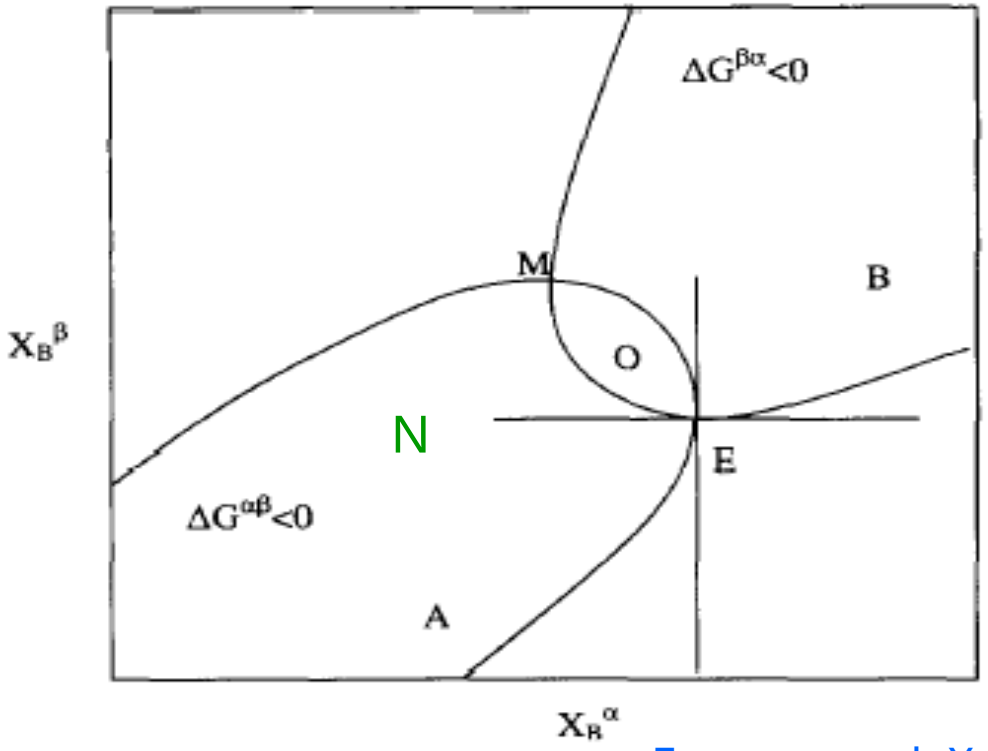

For compound, X is replaced with μ

Loci for $\alpha \rightarrow \beta$ and $\beta \rightarrow \alpha$ transformation

Example : Transformation - closer in composition

Possible at short time intervals

May not be the equilibrium state

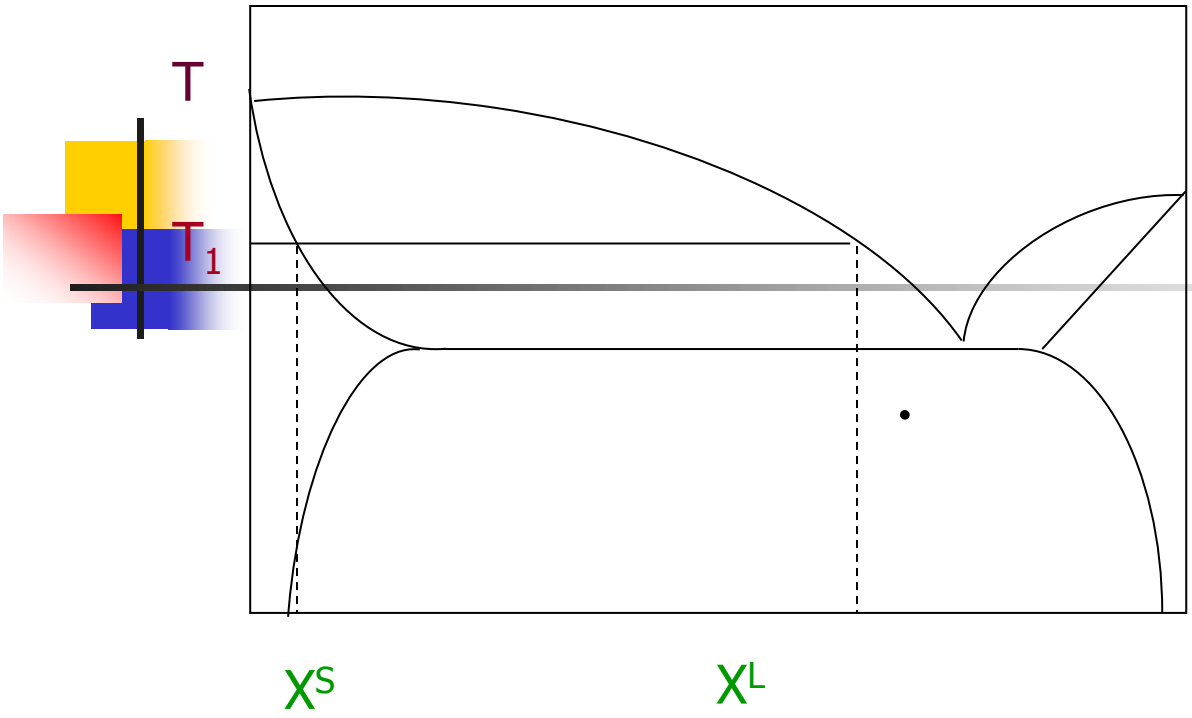
T
T1
XS
XL
X

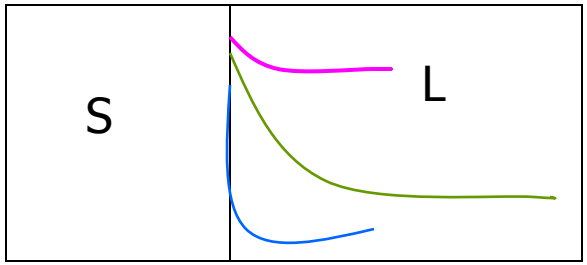
S
L

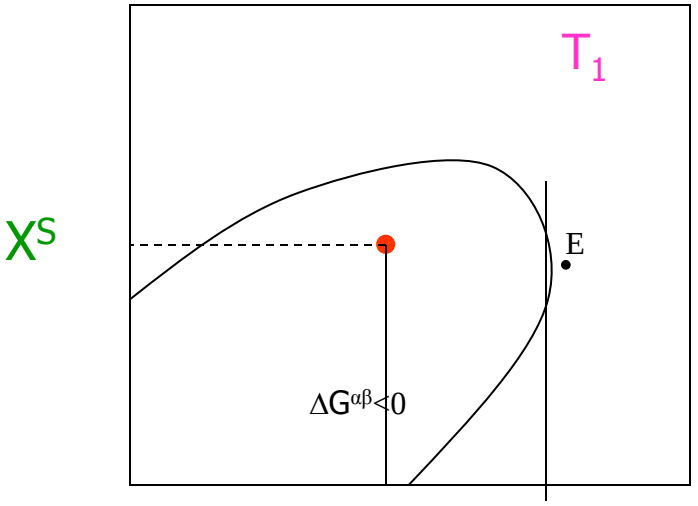
T1
XS
E
ΔGαβ<0
XL

Interfacial Composition

- Solid solution-nucleus interface
  - composition different from bulk
  - plays a crucial role
  - growth rate
  - controlled by
    - thermodynamics
    - surface area
    - mass transfer kinetics

Predict – use transformation diagrams

Non-equilibrium solidification of Steel

L->Austenite (non-equilibrium) observed

L->Ferrite (equilibrium)phase diagram

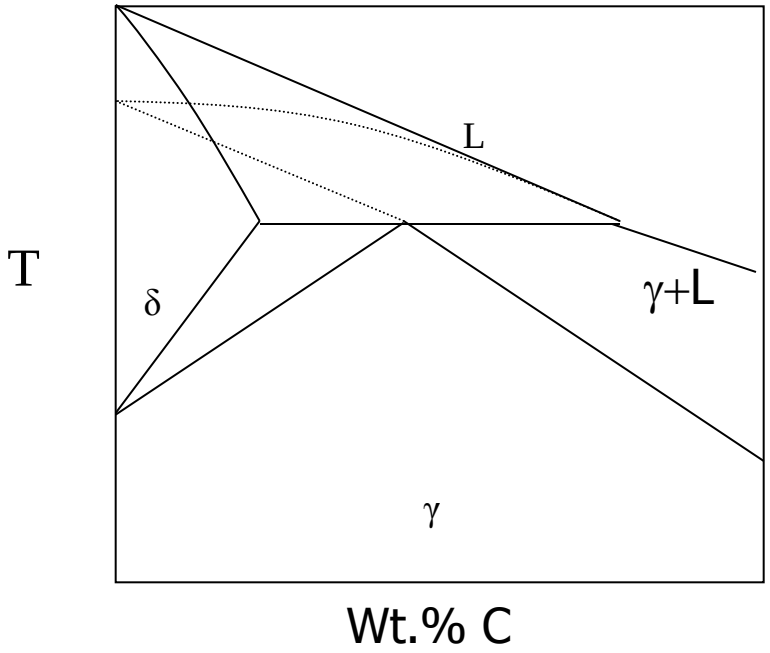

Usually explained

On the basis of phase diagram

Meta-stable extension of (γ+L) field

Again, an equilibrium assumed (meta-stable)

However, this approach does not explain why this route is preferred

Transformation Diagram Solidification of Steel

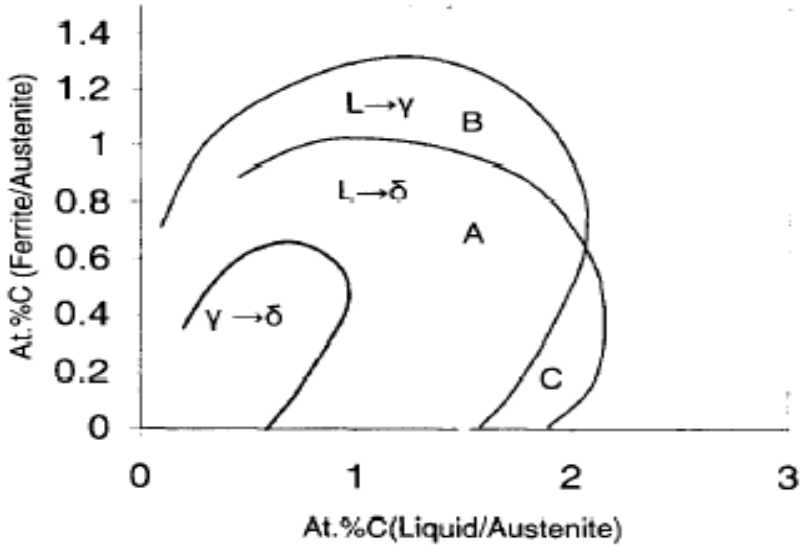

Region B: smaller fluctuations in composition required for L→γ; L->δ not feasible in this region

Larger fluctuations required for L->δ equilibrim

Hence L→γ transformations occurs

Transformation Diagram
Invariant-Composition Phase

Invariant composition phase

- any chemical compound
- fixed composition
- no solution phase

Fe_3C ,Cr_7C_3

Composition axes cannot be used

Axis transformed chemical potential

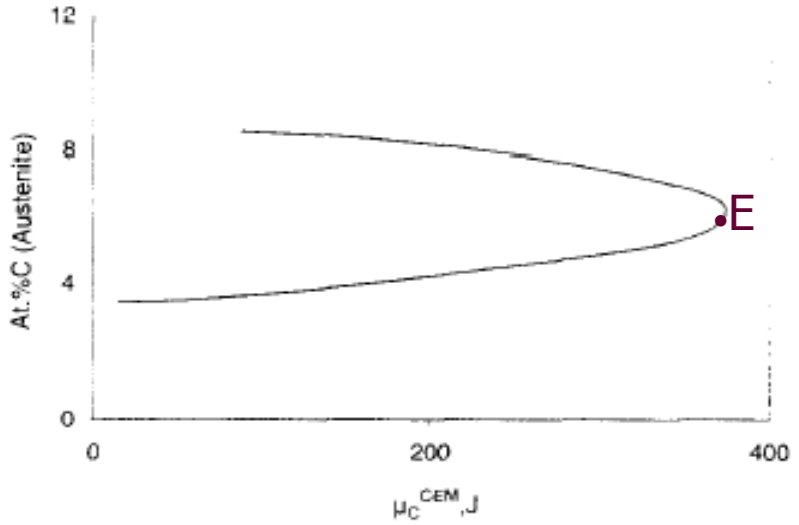

bcc-
$Cr_{23}C_6$

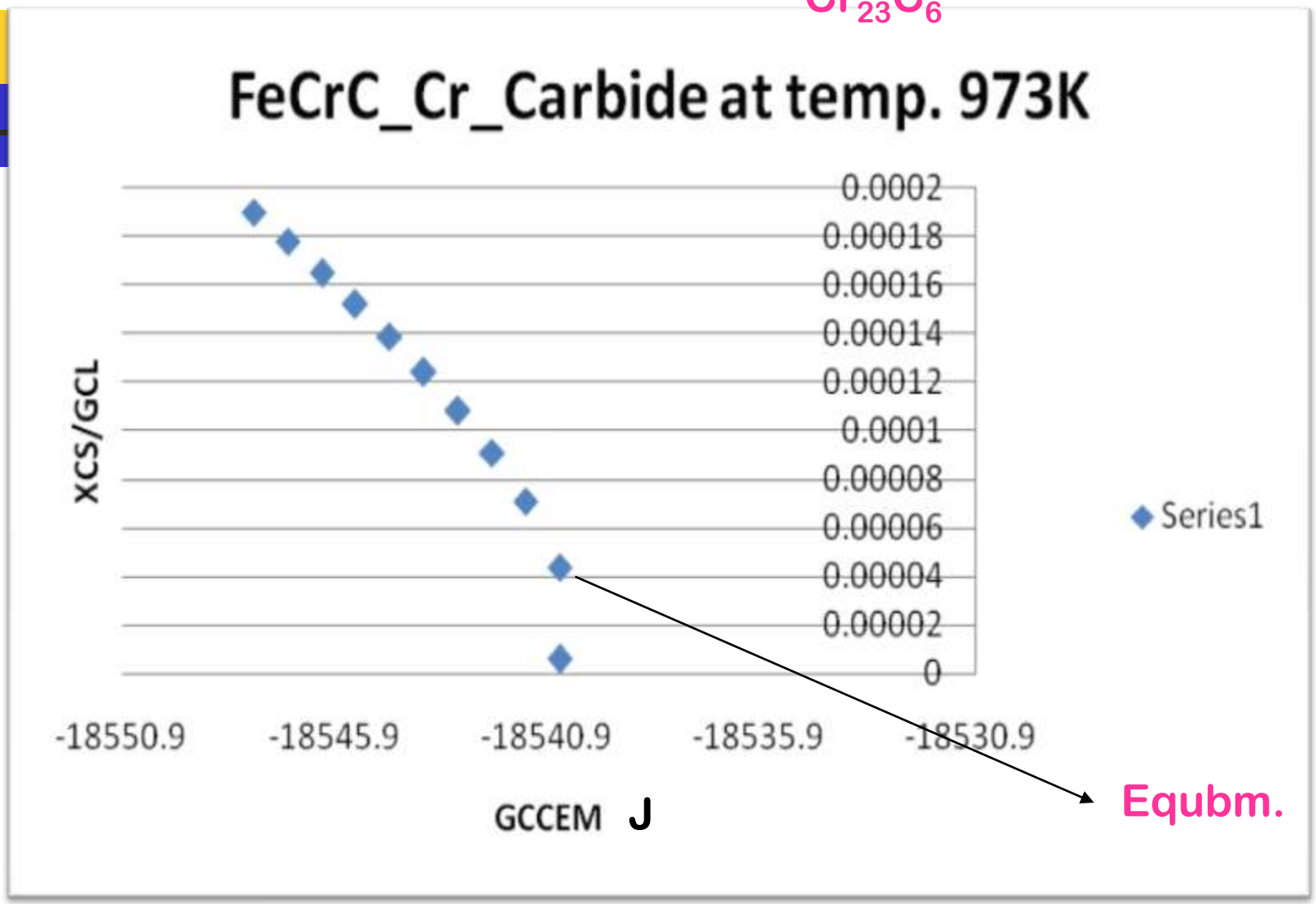
FeCrC_Cr_Carbide at temp. 973K
XCS/GCL
0.0002
0.00018
0.00016
0.00014
0.00012
0.0001
0.00008
0.00006
0.00004
0.00002
0
-18550.9
-18545.9
-18540.9
-18535.9
-18530.9
GCCEM J
Series1
Equbm.

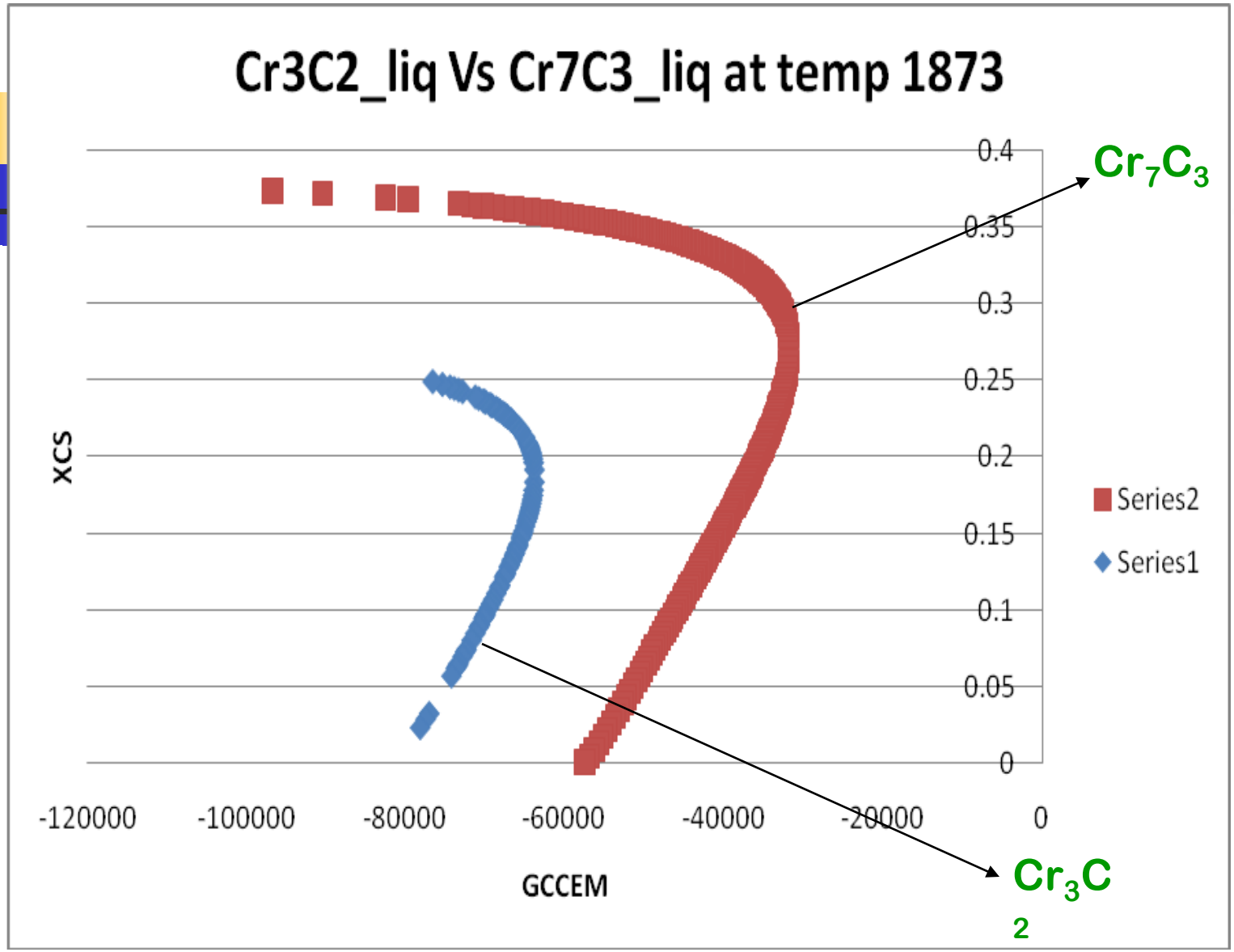
Cr3C2_liq Vs Cr7C3_liq at temp 1873
XCS
GCCEM
0.4
0.35
0.3
0.25
0.2
0.15
0.1
0.05
0
-120000
-100000
-80000
-60000
-40000
-20000
0
Series2
Series1
Cr7C3
Cr3C2

Ti-Cr

Transformation at 873 K (α/β)

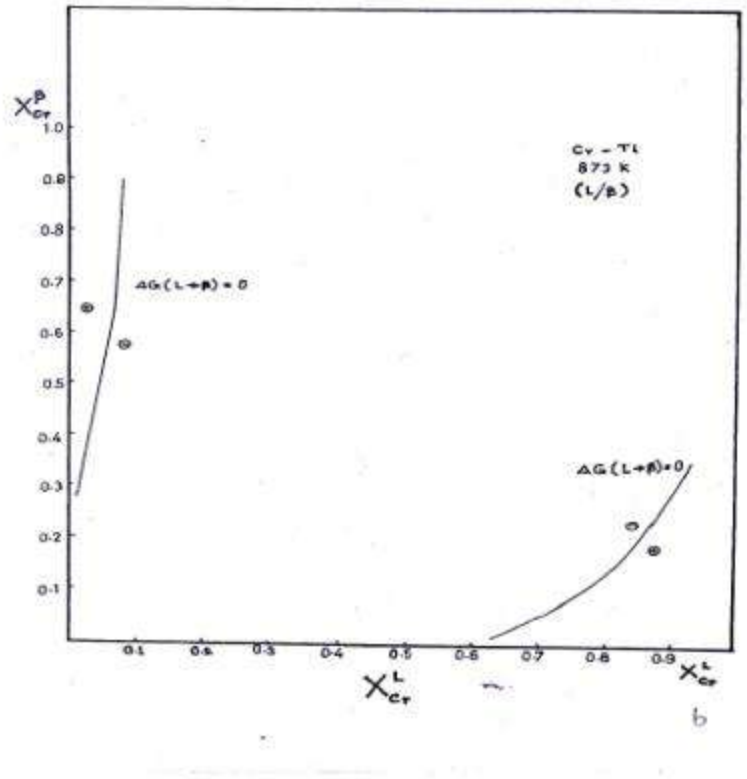

Ti-Cr

Transformation at 873 K (α/β)

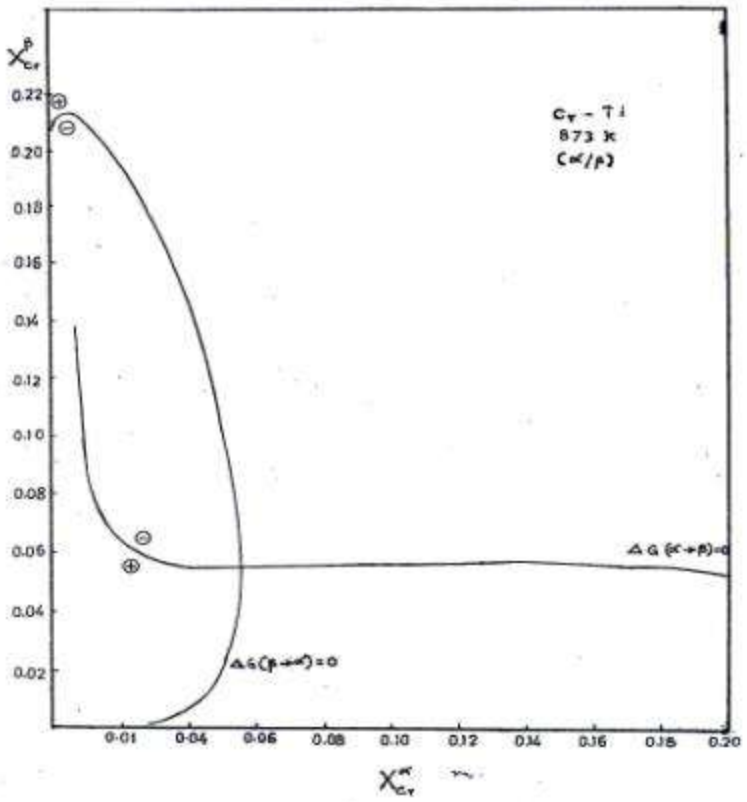

Ti-Cr

Transformation at 873 K (α/β)

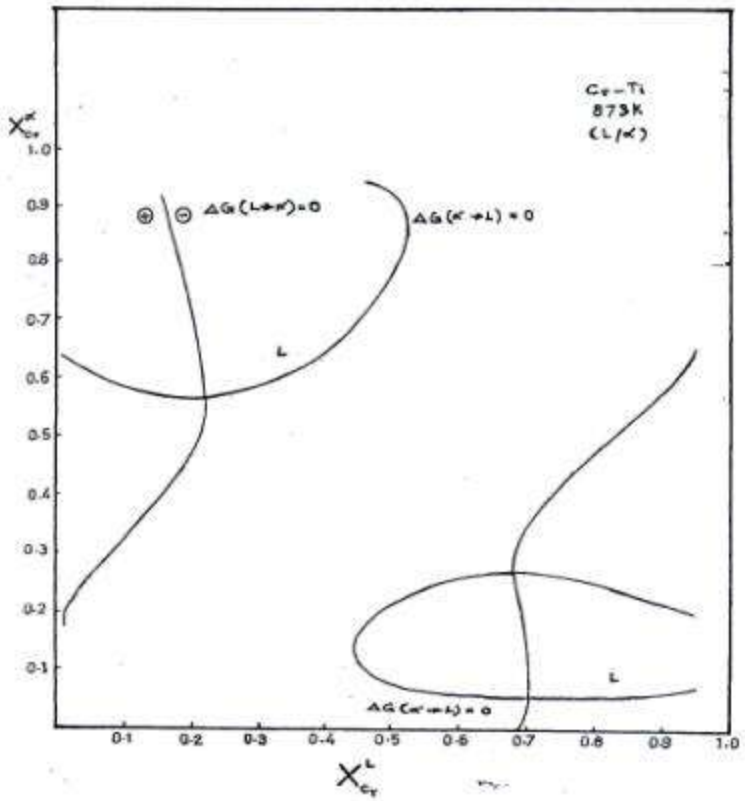

α/L

Amorphous Phase

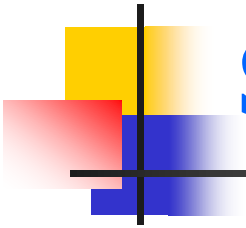

Summary

Nucleant – free energy criterion

Can transform to alternative phases

Trace the non-equilibrium – Transformation Diagrams

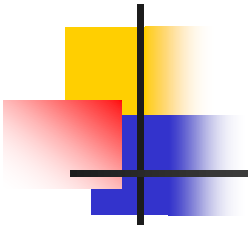

Acknowledgement

P. Ramachandra Rao

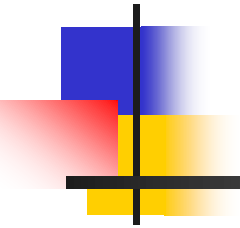

Thank You

LLNL-PRES-430016

Lawrence Livermore National Laboratory

Grain Boundary Engineered Materials as Correlated Networks: Large-Scale Implications of Twin Nucleation

May 3, 2010

B. W. Reed, M. Tang, J. F. Belak, J. V. Bernier, V. V. Bulatov, T. LaGrange, and M. Kumar

Lawrence Livermore National Laboratory, P. O. Box 808, Livermore, CA 94551

This work performed under the auspices of the U.S. Department of Energy by Lawrence Livermore National Laboratory under Contract DE-AC52-07NA27344 and supported by the Office of Science, Office of Basic Energy Sciences, Division of Materials Sciences and Engineering, of the U.S. Department of Energy by SISGR Grant

This is a multi-institutional collaboration
(Institutions listed at the time of most active collaboration)

MSU: Phil Duxbury, Erin McGarrity

University of Michigan: Gary Was

GE Global Research Center: Peter Andresen, Martin Morra

University of California–Berkeley: Robert Ritchie

University of California–Davis: N. Sukumar, A. Tabarraei

Washington State University: David Field

Lehigh University: David Williams

University of Minnesota: Barry Carter

LANL: Mark Cola, Vivek Davé

MIT: Chris Schuh, Megan Frary

RWTH (Germany): Myrjam Winning

CMU: Tony Rollett

LLNL: Kerri Blobaum, Wayne King, Roger Minich, Robert Rudd, Adam Schwartz, Eira Seppälä, James Stölken, Ken King, Bob Etien

What is grain boundary engineering?

- Simple processing can enhance resistance to intergranular failure/degradation by 3X-5X or more
- Based on using "special" grain boundaries (e.g. coherent twin) to break up the network of weaker "random" grain boundaries
- Works on many different failure modes
  - Stress corrosion cracking
  - Impurity embrittlement
  - Microstructural coarsening
  - Magnetic flux penetration in superconductors

Key concept: Context matters!
The grain boundary *network* is essential.

Consider two grain boundary networks.

Suppose red boundaries are strong, blue boundaries are weak.

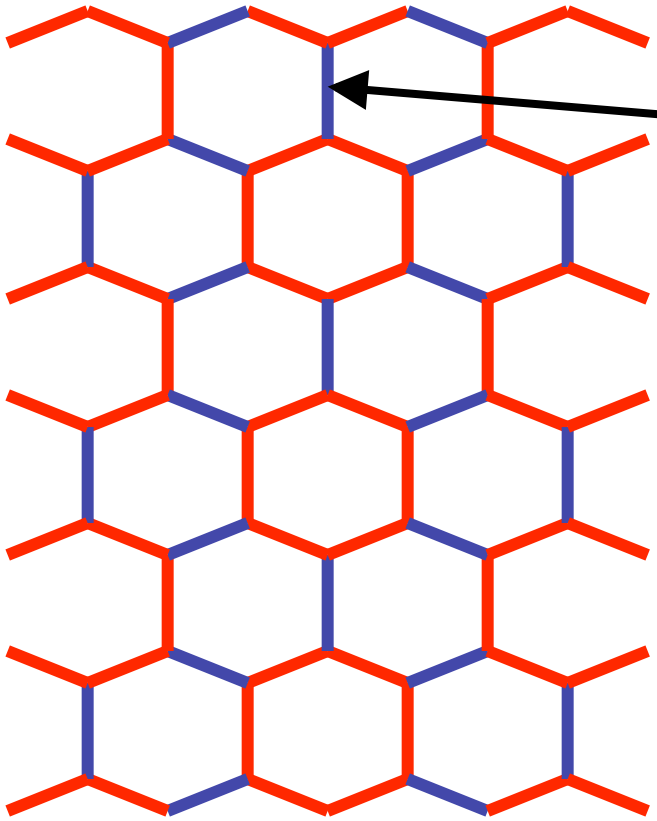

If this boundary fails, not much happens.

If this boundary fails, the whole material can come apart.

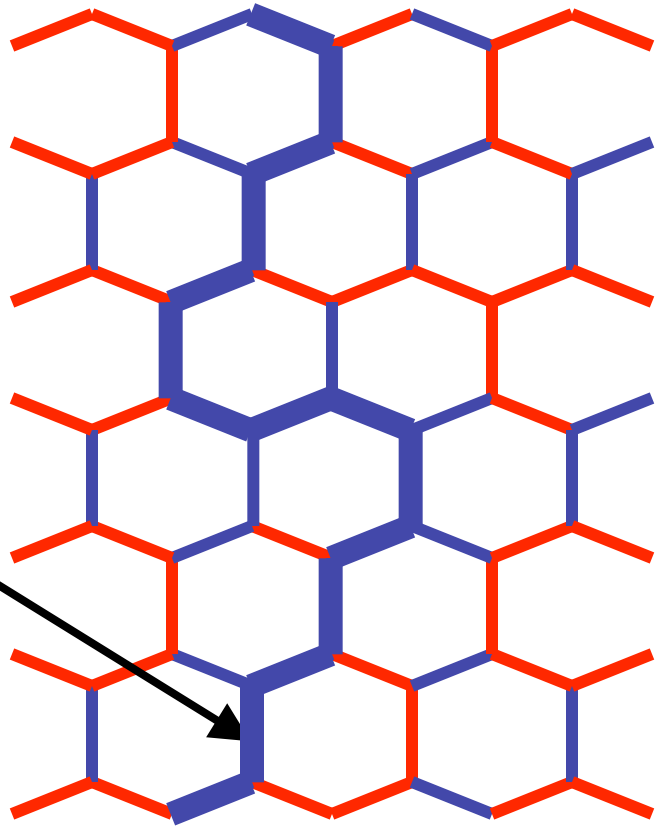

Focus of this talk: What does nucleation and growth of twins do on the scale of the grain boundary network?

Given the characteristics of the nucleation and growth, . . .

- Crystallography
- Anisotropy and texturing
- Combinatorics governed by crystallographic constraints
- Dominant morphologies

. . . what does this do to the network properties?

- Special/random percolation thresholds
- Correlation lengths and supra-grain structure
- Large-scale resistance to intergranular degradation

For many metals, the dominant special boundary is the Σ3 {111} twin

- Low stacking fault energy fcc materials (e.g. Cu, Ni)
- Two mirror-image grains sharing a {111} plane
- Twins form as deformed material anneals
- Twin boundaries tend to be large, flat, smooth, and stable
- When Σ3's meet, they can generate Σ9's, Σ27's, etc.
- $\Sigma 3^n$ "twin-related" grain boundaries dominate the statistics

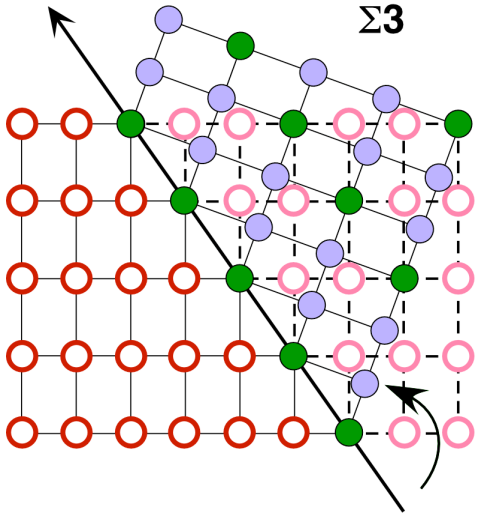

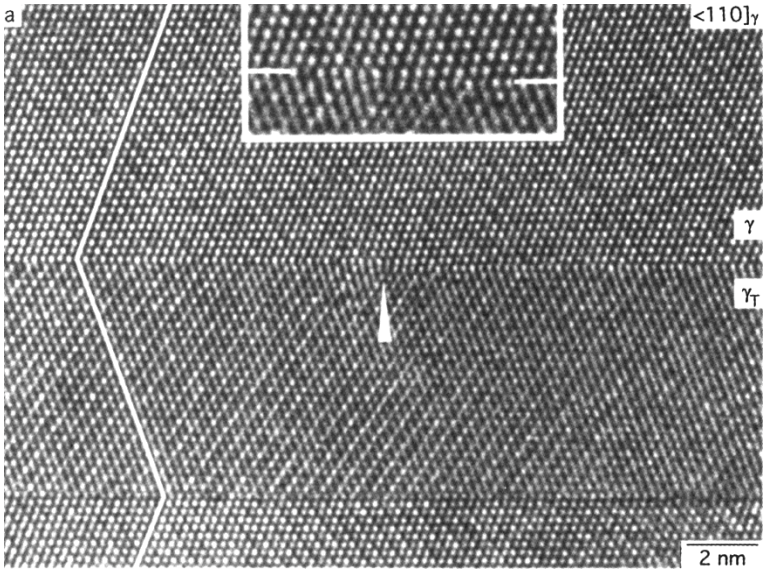

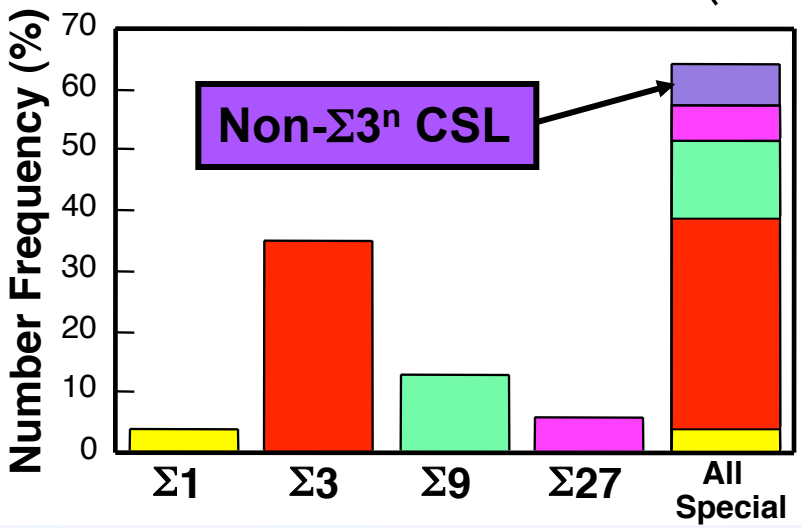

Definition: CSL = Coincident Site Lattice

Cyclic thermomechanical processing enhances the populations of twin-related boundaries

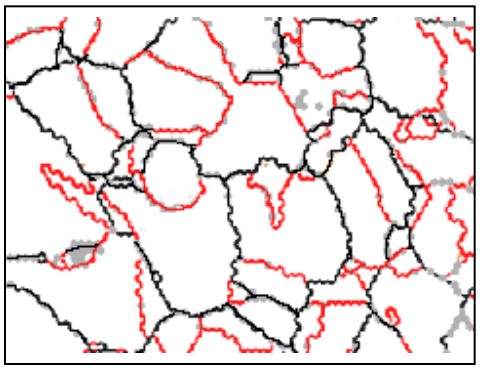

Initial microstructure

~45% special

Multi-step thermomechanical processing sequence*

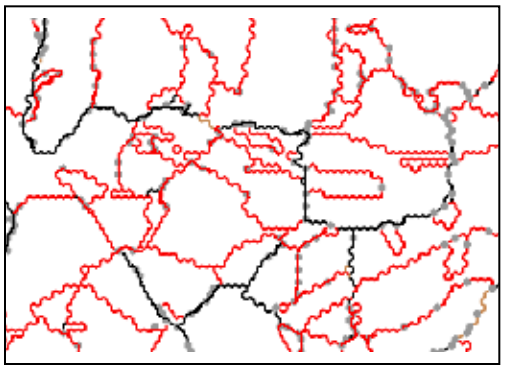

Final microstructure

~80% special

Repeat
3 - 7 times

Rolling
5 - 20% reduction

Annealing
$T \approx \frac{T_m}{2}$

Red = Σ3 boundaries
Black = Random boundaries

G. Palumbo, US Patent 5,702,543 (1997); and Kumar, King, Schwartz Acta Materialia (2000)

There are two often-cited mechanisms for nucleating annealing twins in fcc materials

- **Growth accidents**
  - One layer of hcp within fcc (ABCBA stacking)
  - Possible mechanism: Shockley partials forming on moving, faceted boundaries
  - Often makes simple morphologies ("back-and-forth" twinning)

- **Recrystallization**
  - Driven by plastically stored energy
  - Nucleation frequently at existing boundaries or triple junctions
  - More isotropic; which variant you gets depends on unknown local factors

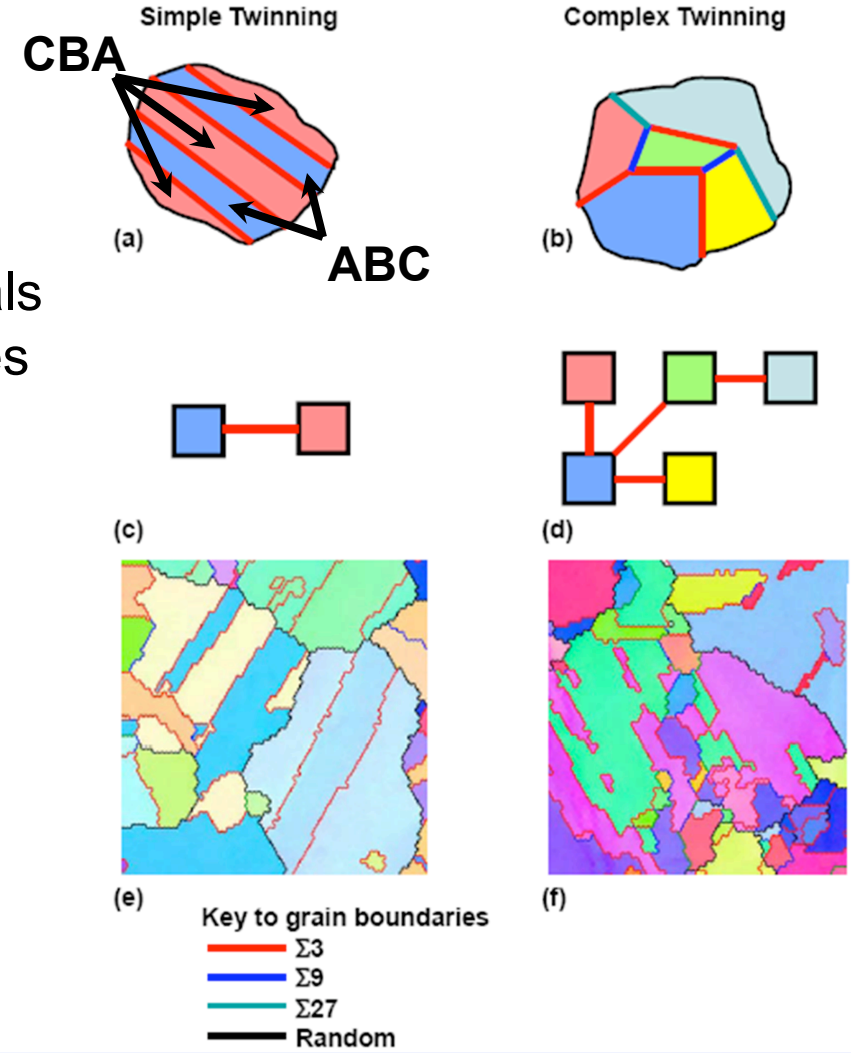

Recrystallization produces twins that have far more interesting effects on the boundary network

- Nucleate at boundaries (or junctions)
- Nucleation can be far more isotropic than for growth accidents
  - This facilitates cross-twinning, including creation of Σ9, Σ27, etc.
- Fueled by dislocation energy, leaving behind well-annealed crystal
- Σ3 boundaries include both coherent and incoherent segments
  - Complex morphology facilitates more complex network
  - Mobile incoherent segments can move into neighboring grains

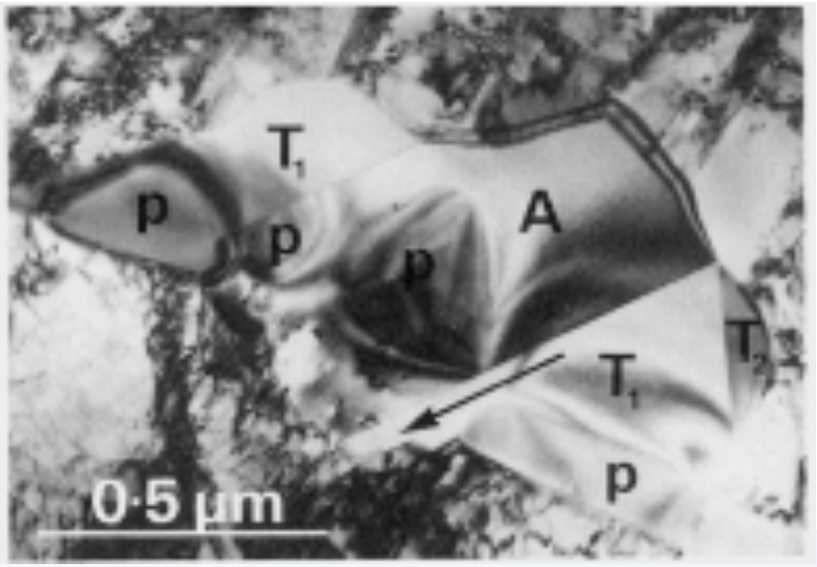

TEM image of annealing twins in steel, from A. R. Jones, J. Mat Sci 16, 1374 (1981)

The grains develop into clusters that we call Twin-Related Domains (TRD)

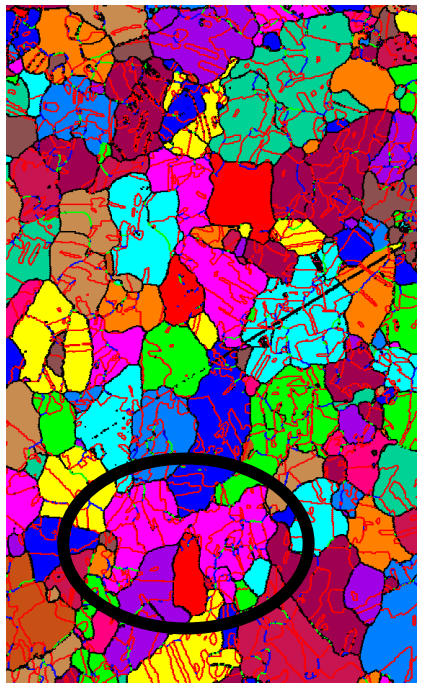

200.0 μm = 80 steps

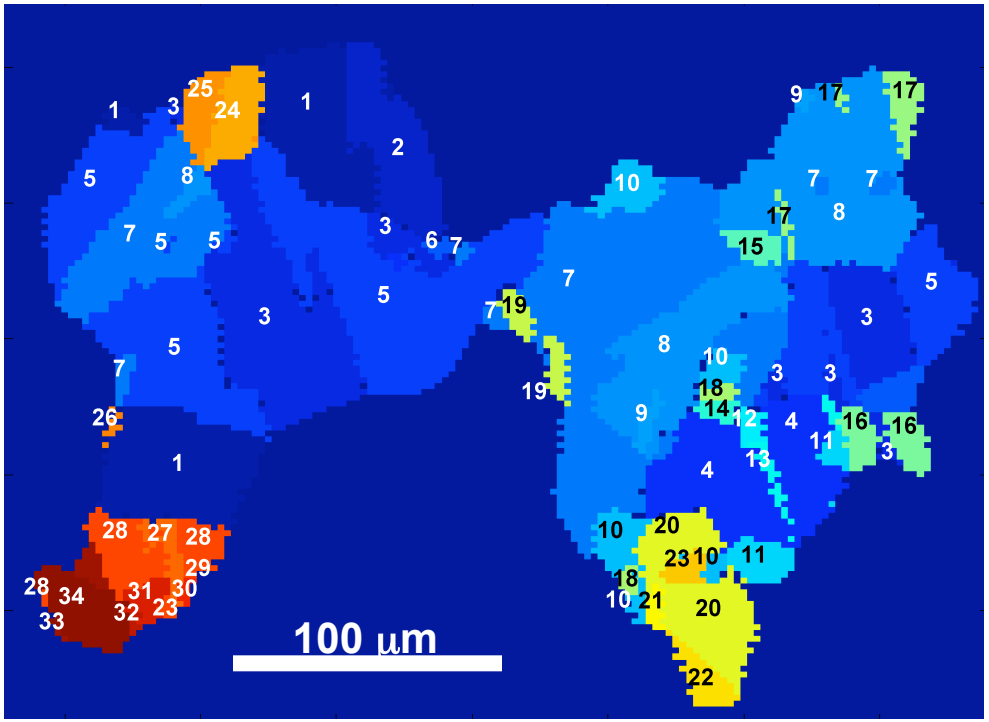

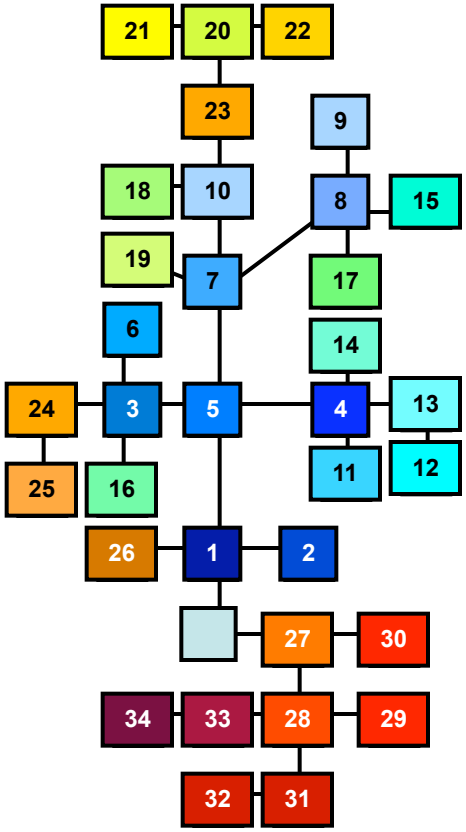

An initial grain grows and forms multiple twins, making an extended complex structure with hundreds of grains

When the domains are well developed, we pass through a percolation threshold.

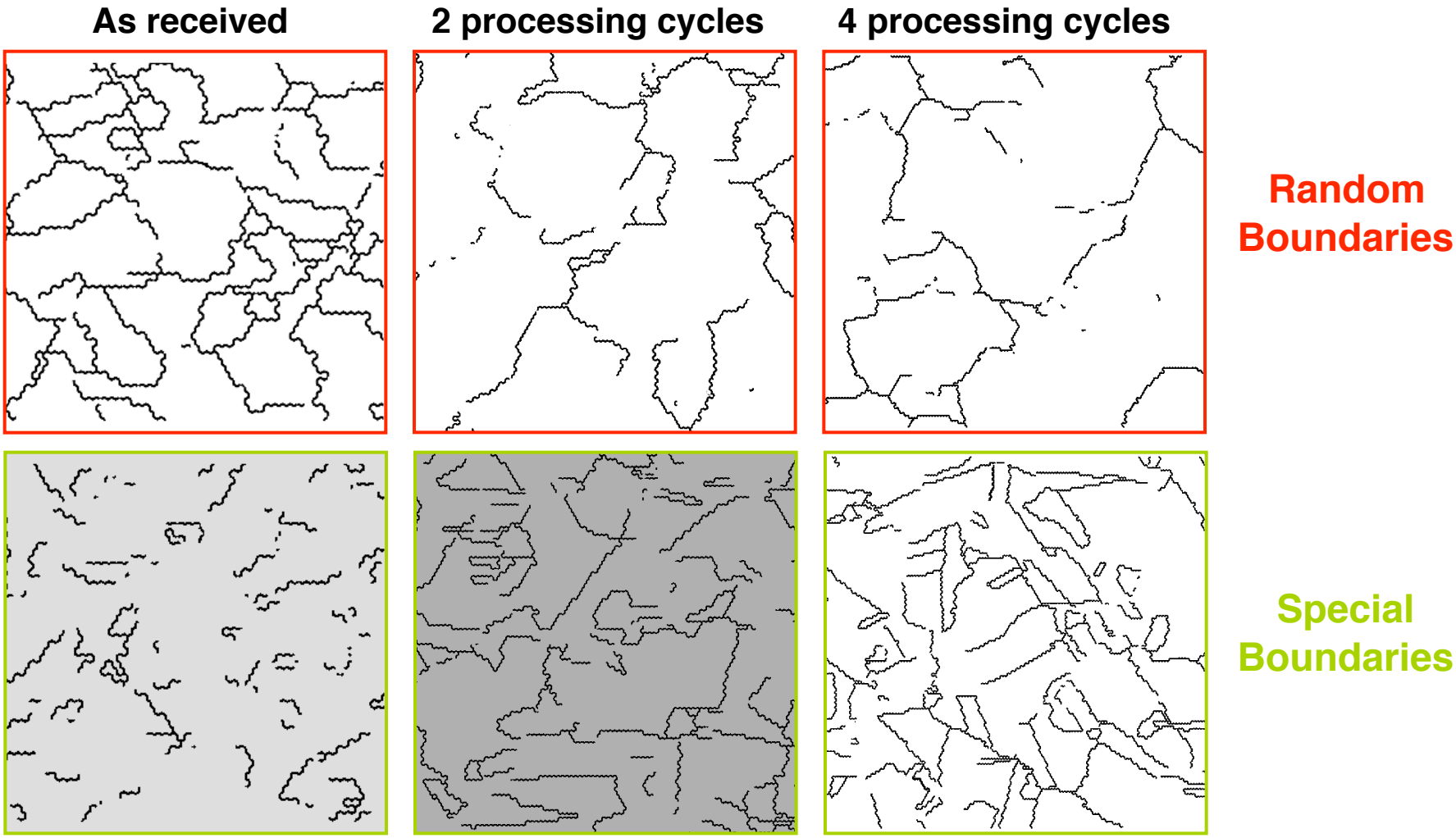

The surfaces created by intergranular cracking look completely different in normal and engineered materials

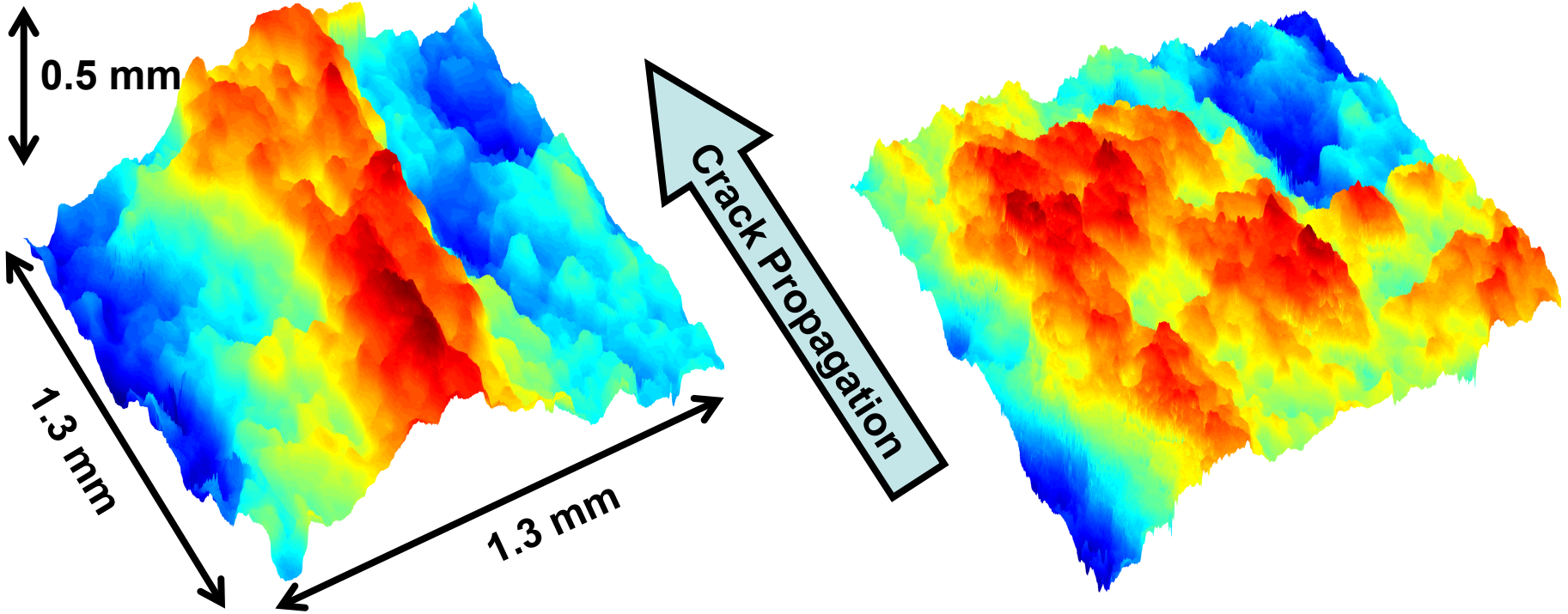

Normal Material

- Anisotropic ridges parallel to crack propagation over wide range of length scales

Engineered Material

- Isotropic, uniform, more randomly rough (like a random walk)

Conventional representations of grain orientations don't handle multiple twinning well.

- There are specific mechanisms that produce, for a given grain, one of four variant twin orientations
- These are high-angle grain boundaries (60° <111>) that aren't going to be found in a local fluctuation
- The new misorientation is very nearly perfect, usually within 1°

You want to have a representation that explicitly includes these exact, discrete possibilities; nucleating "by chance" in quaternion space will waste a lot of CPU cycles.

Real microstructures can have twin chains 10 or 11 units long! This needs *a lot* of orientations to be in the ensemble.

Importance of misorientation relationships: To stop a random boundary path in two dimensions, you need a "J_2" triple junction

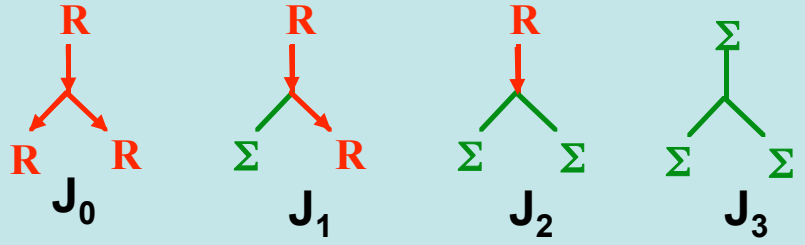

Preferred crack paths (red arrows) only stop at J_2's

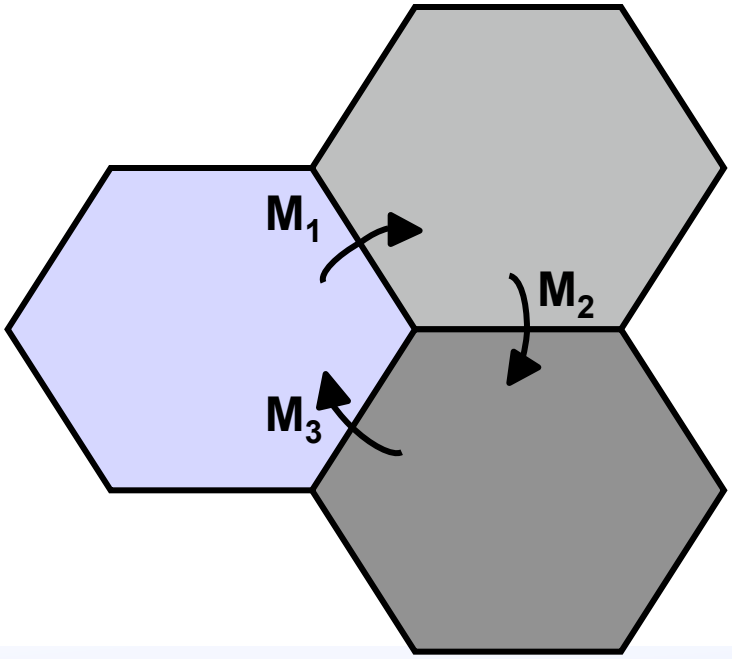

But there's a constraint:

$$M_1M_2M_3 = I$$

And special misorientations tend to be related to each other.

$$\Rightarrow J_2 \text{ is suppressed!}$$

$J_2/(1-J_3)$ correlates with clustering behavior.
(Kumar, King, Schwartz Acta Mater. 48, 2081 (2000))

The Σ combination rule governs Coincident Site Lattice combinations allowed at a triple junction

If two boundaries at a triple junction are CSL boundaries, then so is the third.

The three Σ values are related:

$$XY = k^2 Z,$$

$$\frac{X}{k}, \frac{Y}{k} \text{ are integers}$$

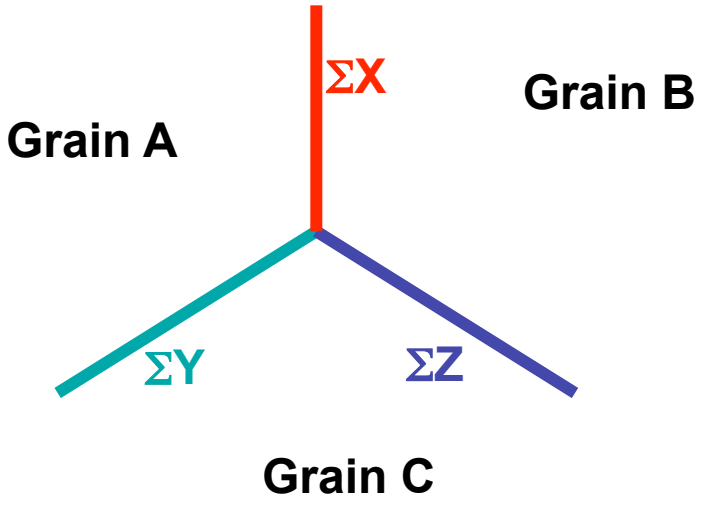

Allowed:

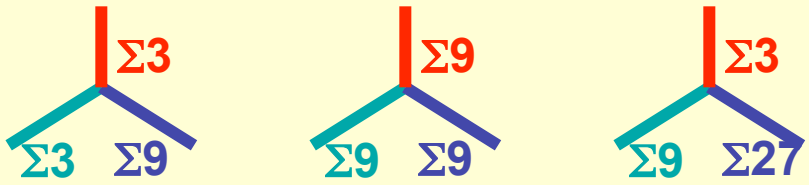

Disallowed:

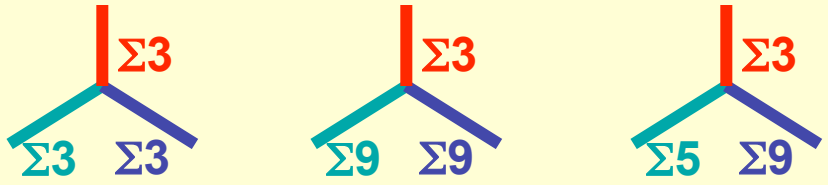

Miyazawa et al (1996). *Acta Cryst.* **A52,** 787.

Gertsman, V. Y. (2001). *Acta Cryst.* **A57,** 369.

The Σ combination rule alone significantly alters the statistical properties of the network.

(From Minich, Schuh, and Kumar, Phys. Rev. B **66,** 052101 (2002) and Schuh, Minich, and Kumar, Phil. Mag. **83,** 711 (2003).)

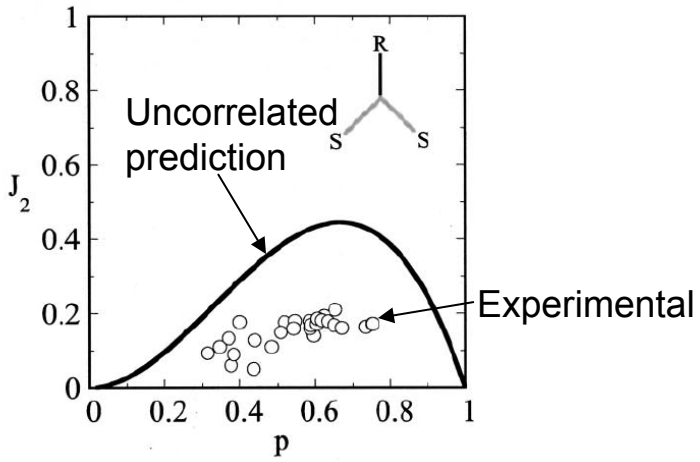

Triple Junction Distributions

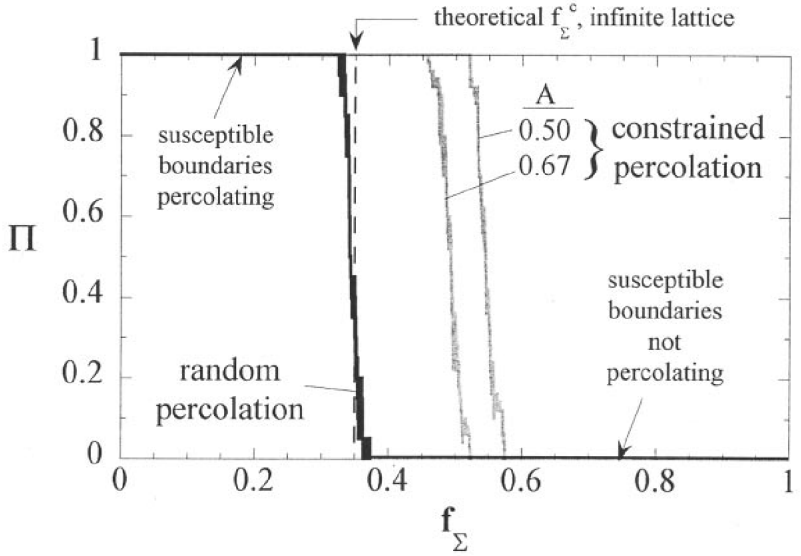

Weak Boundary Percolation Probability vs. Special Fraction

Simple model:

Σ combination rule at triple junctions

Σ3, Σ9, Σ27, Random

Explains most of the observed correlations.

But how many more correlations are hiding?

The Σ combination rule can be generalized by working out the structure of the entire group.

Vertex = grain orientation

Link = one of the four Σ3 twinning operations (a,b,c,d)

Each vertex has exactly 4 neighbors

There are no loops

Tree is infinite and highly symmetric

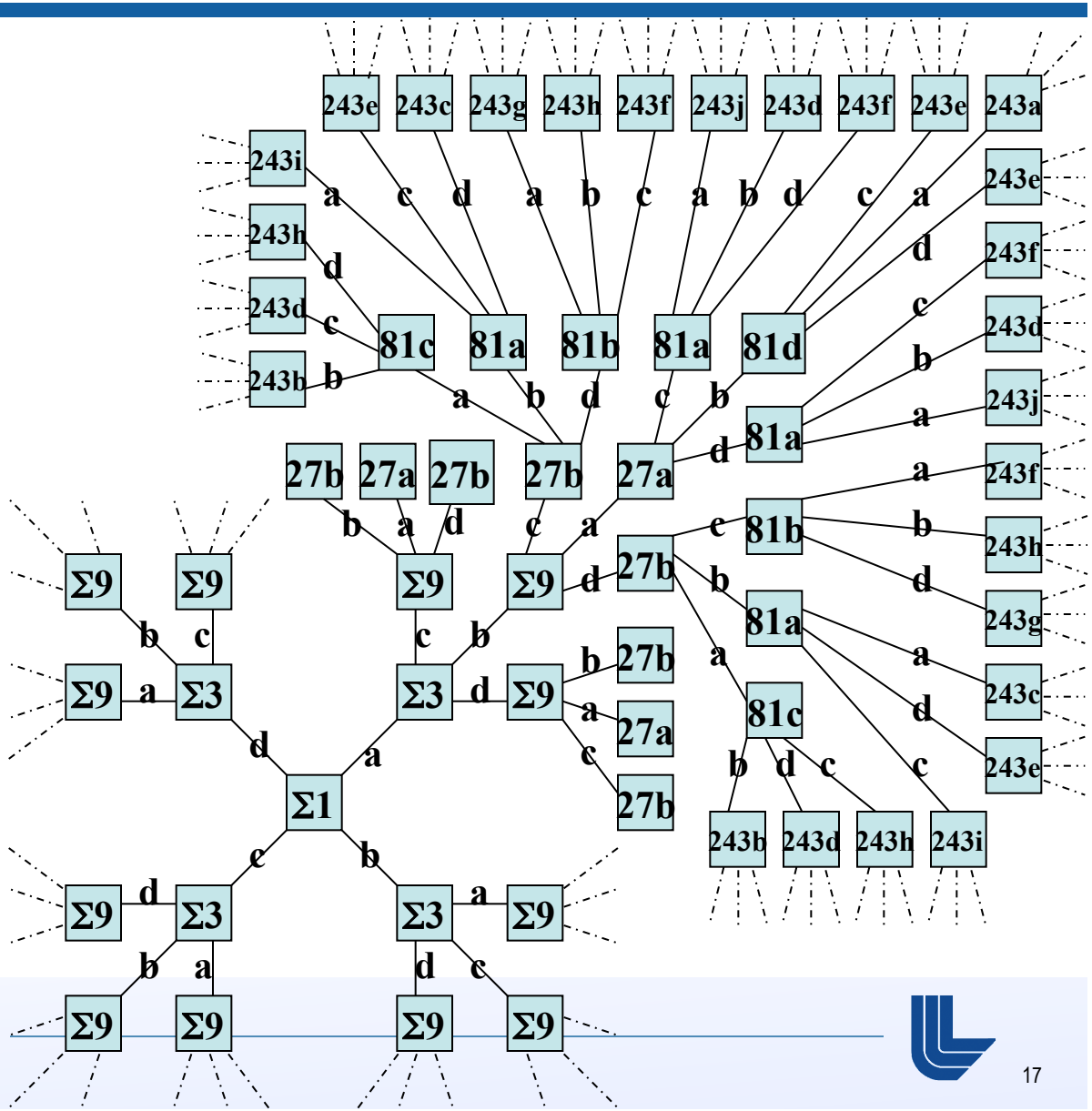

Reed, Minich, Rudd, Kumar, Acta Crystallographica A (2004)

There is potentially an infinite number of constraints on the network.

Σ combination rule satisfied, yet triple junction invalid

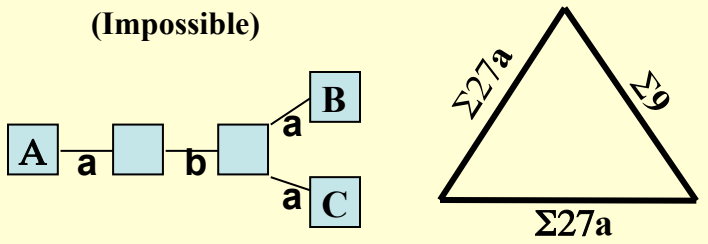

All triple junctions valid, yet quadruple node invalid

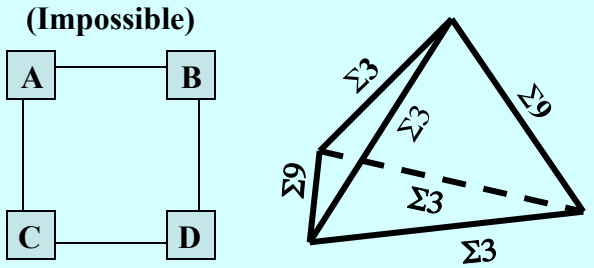

All quadruple nodes valid, yet larger cluster invalid

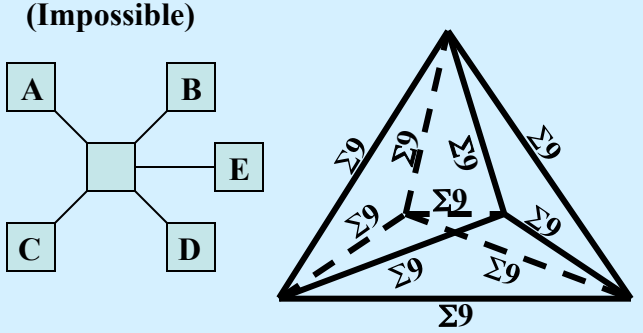

It's possible to efficiently account for the constraints in a model developed for highly-twinned materials.

- Treat everything as a perfect $\Sigma 3^n$ orientation
- Use string representation with 4-letter alphabet
- Define energy metric:

Σ	Comment	Typical Energy
1	No boundary at all	-1 (grain growth) or ∞ (static topology)
3	Perfect twin	-0.9 (Cu) to -0.3 (Al)
9	Twin variant	-0.5 to -0.2
27	2nd twin variant	-0.3 to -0.1
81+	Random	0

- Pick a topology (2-D or 3-D, random or ordered)
- Assign initial orientation strings to each grain
- Pick a temperature $1/\beta$ and run a Metropolis Monte Carlo calculation

The Potts-like Monte Carlo simulations yield statistically realistic microstructures with very few free parameters

Potts-like model including grain growth and twinning, efficiently calculated using $\Sigma 3^n$ strings, and guaranteed to satisfy all constraints

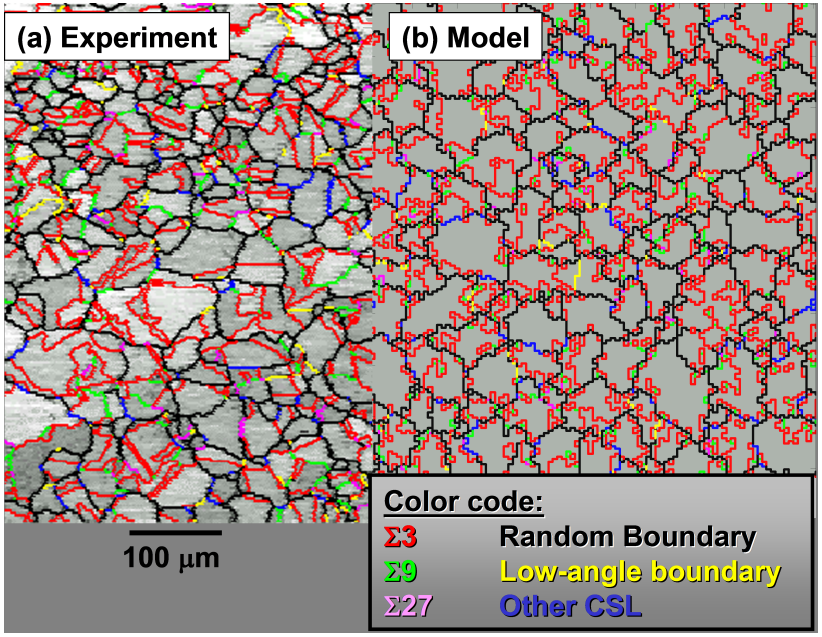

	Experimental (EBSD)		Model (Average of 10 runs)	
	Number Fraction	Length Fraction	Number Fraction	Length Fraction
Σ3	27.3	44.1	27.1	43.7
Σ9	10.7	6.9	10.0	7.3
Σ27	3.9	2.9	3.5	2.6
Other Σ	6.2	4.9	6.5	5.0
Random	51.8	41.2	52.9	41.3
J_0	14.4		13.6	
J_1	51.1		51.6	
J_2	14.3		14.4	
J_3	20.2		20.4	

- Designed to mimic topology of a specific engineered Cu sample
- 5 free parameters
- <10 CPU-seconds to generate

- Designed to match detailed statistics of a specific engineered Cu sample
- ~10 CPU-hours to optimize over 5-parameter space
- All metrics match within uncertainty

Work in progress: Combine the twin nucleation algebra with phase field modeling

- Monte Carlo run rapidly produces statistically realistic initial structure and a useable ensemble of grain orientations
- Phase field evolves this using a grain boundary energy and mobility metric
  - Multi-variable phase-field model for grain growth distinguishes among random boundaries, special boundaries and vicinal boundaries.
  - Assign GB energies and mobilities that depend on misorientation and will include grain boundary plane dependence in near future
  - Track evolution of grain size, GB character distribution, and network connectivity in phase-field simulations
- Progress towards efficient simulation of crystallographically realistic multiple-twinning model including nucleation of new twin grains

Adjusting the energy is not enough—low special boundary mobility is important for realistic stabilization of the network

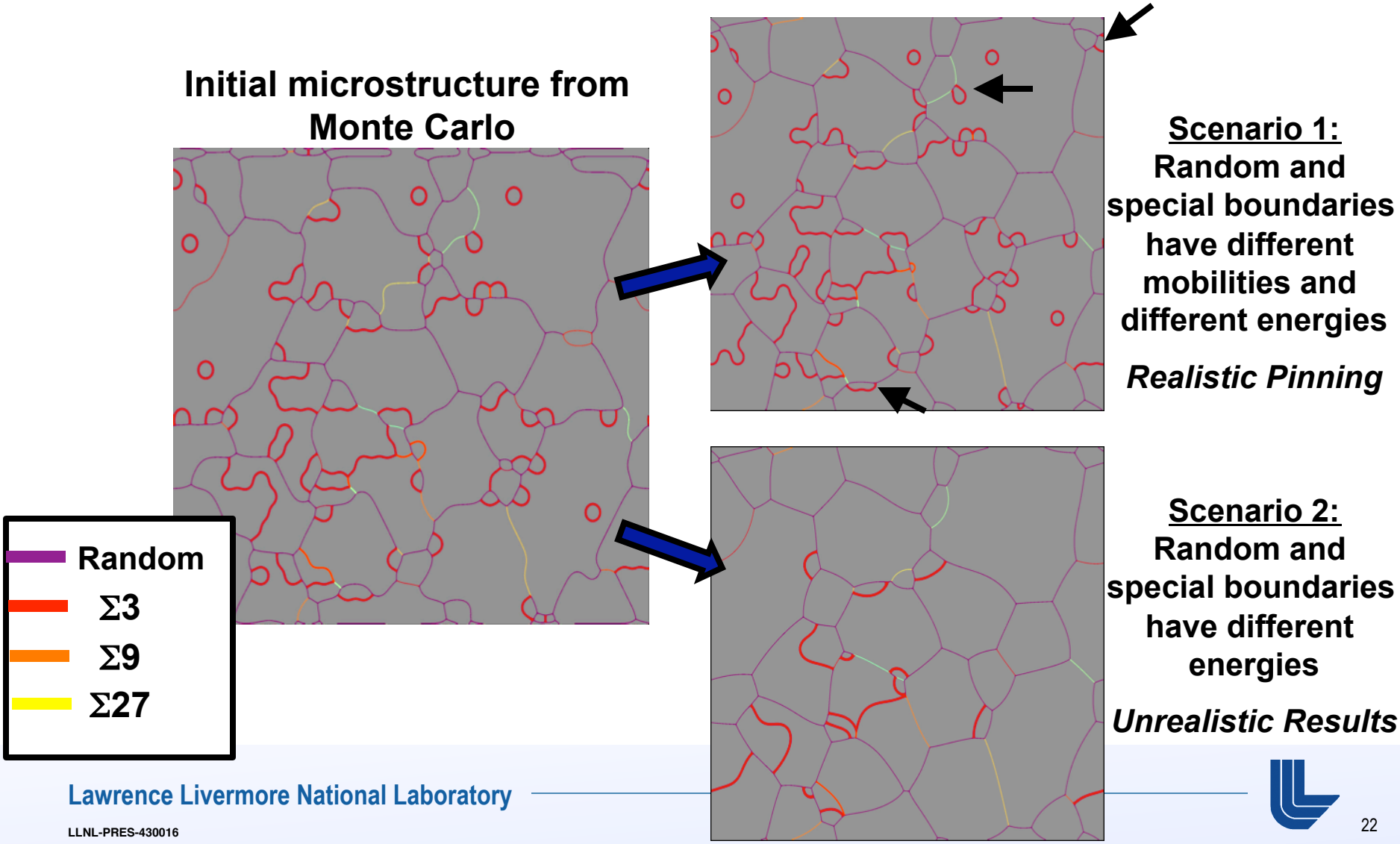

Grain boundary plane anisotropy is necessary to get the model to nucleate while remaining stable

No GB Plane Anisotropy

To nucleate twins, a transition like this should be energetically favorable:

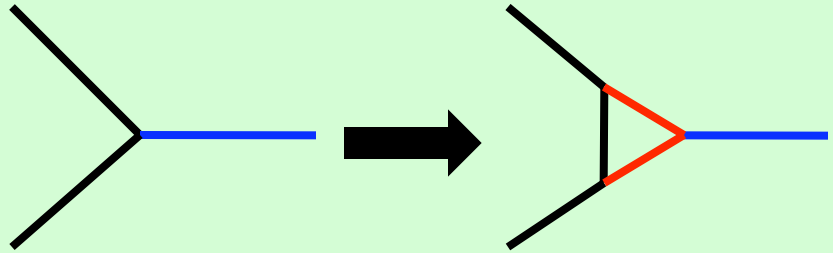

But then nothing stops the triple junctions from "unzipping" out of existence!

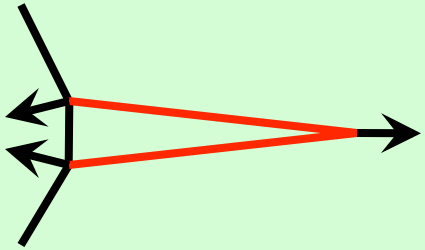

Σ3

Σ9

Random

GB Plane Anisotropy

In reality, a Σ3 is only really low energy close to a particular {111} plane

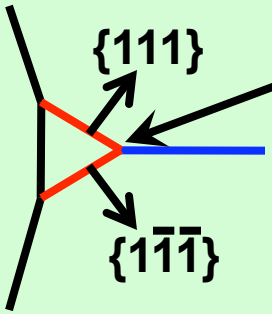

Very stable triple junction

The most interesting morphologies depend on some parts of the boundary being far more mobile than others

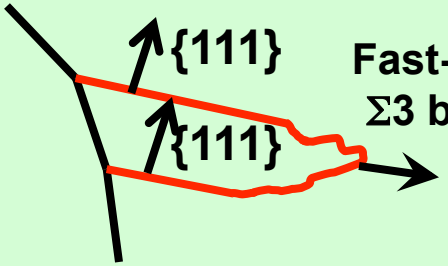

Fast-moving incoherent Σ3 boundary segment

Multiply-twinned nanoparticles offer clues for making a finite orientation ensemble for the phase field model

- Many fcc nanoparticles (< 10 nm) form icosahedral multi-twinned structures
- 20 grains, 10 grain orientations, 30 twin boundaries, 12 twin pentajunctions
- Each grain exposes low-energy {111} faces to the outside world and to its neighbors
- Each link in the graph is a 72° <110> rotation, a good approximation to the 70.5° <110> Σ3
- Downsides:
  - Each grain is rhombohedrally distorted
  - Each orientation only has 3 neighbors in the network instead of 4
  - Pentajunctions are far too easy to form

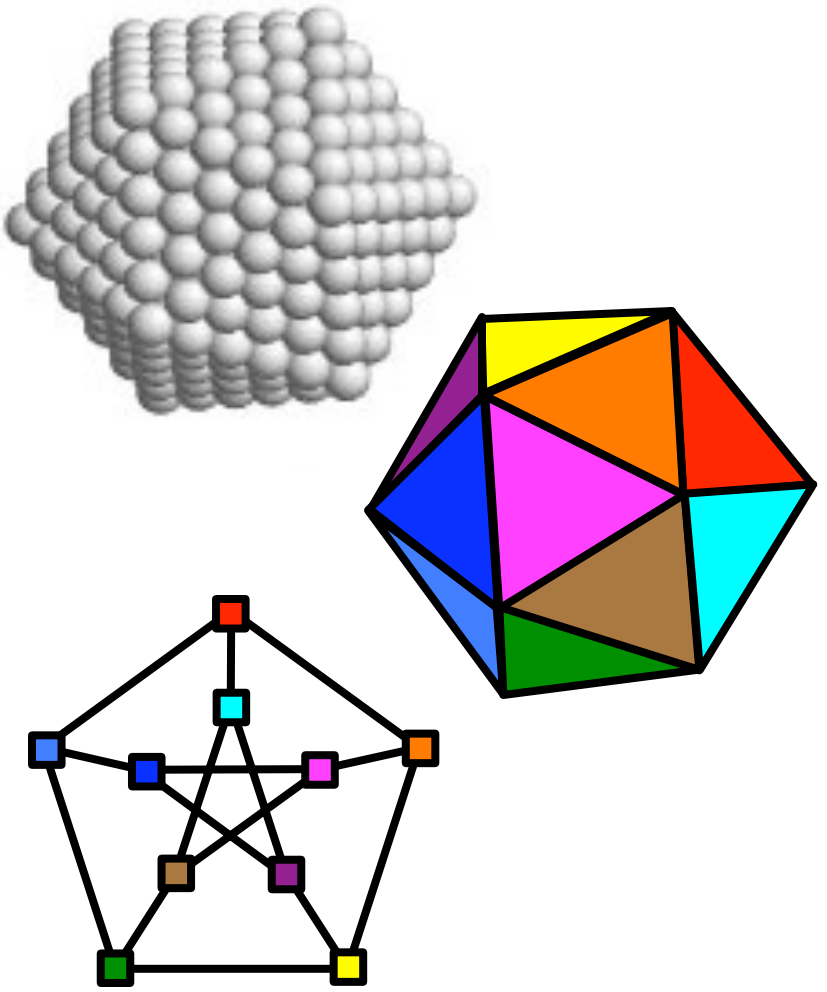

X. Yang et. al, J. Phys. Chem. A. 111 (2007) 5048
C. Y. Yang, J. Crystal Growth 47, 274 (1979)
D. Reinhard et al., Phys. Rev. B 55, 7868 (1997)
K. J. Koski et al., Phys. Rev. B 78, 165410 (2008)

Summary and Future Directions

- Grain boundary engineered materials have complex network properties that depend heavily on mathematical constraints on twin nucleation, growth, and interaction
- These properties produce supra-grain correlations that are important for large-scale material properties
- We are developing simulation approaches that efficiently handle the mathematics of multiple twinning
  - Capturing the essence of the network constraints is demonstrated
  - Group theoretical formalism handles twin nucleation efficiently in Monte Carlo simulations
  - More predictive phase field simulations are under development
- Realistic network properties are easy to get. Realistic evolution needs a great deal more physics to be in the model.

Neighboring TRD's are usually separated by random boundaries

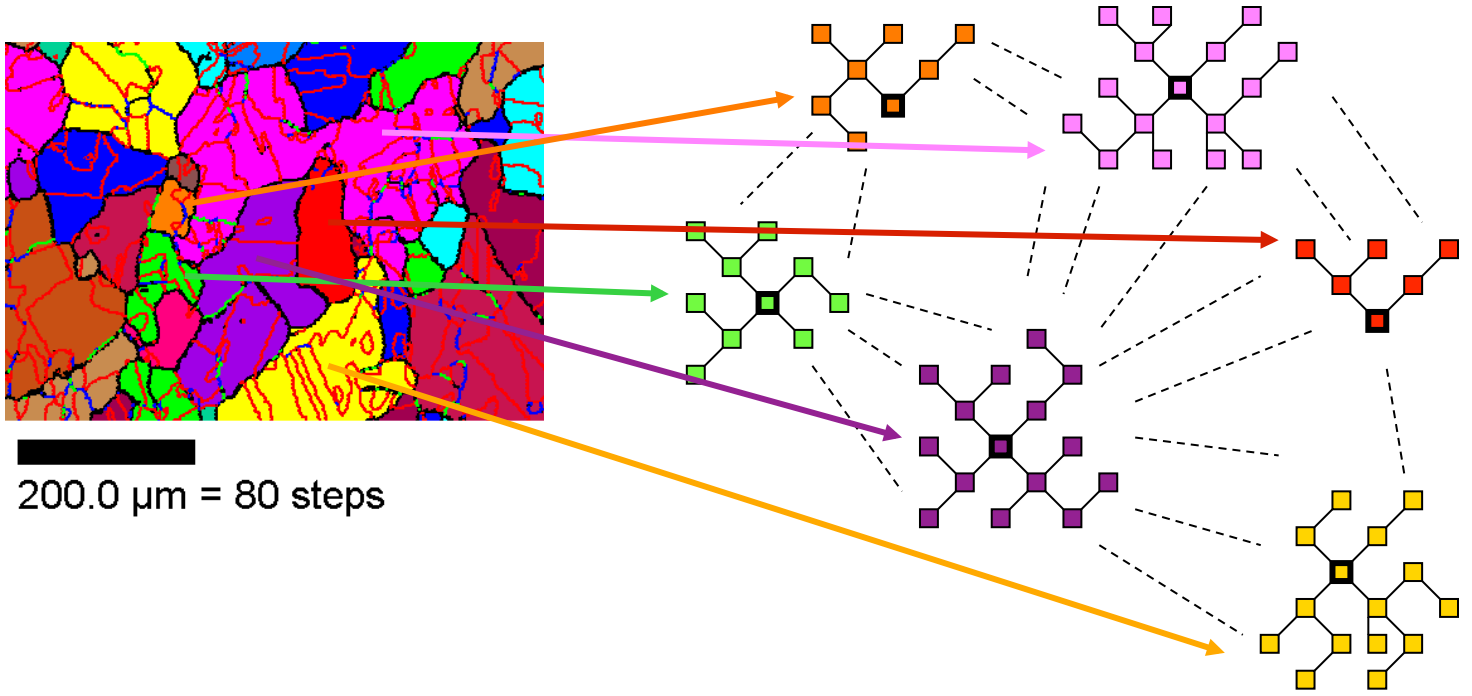

- The grain orientations in neighboring TRD's are unrelated.
- They still form special boundaries occasionally, breaking up the random boundary clusters.

Grain boundary networks in conventional and engineered materials are qualitatively different

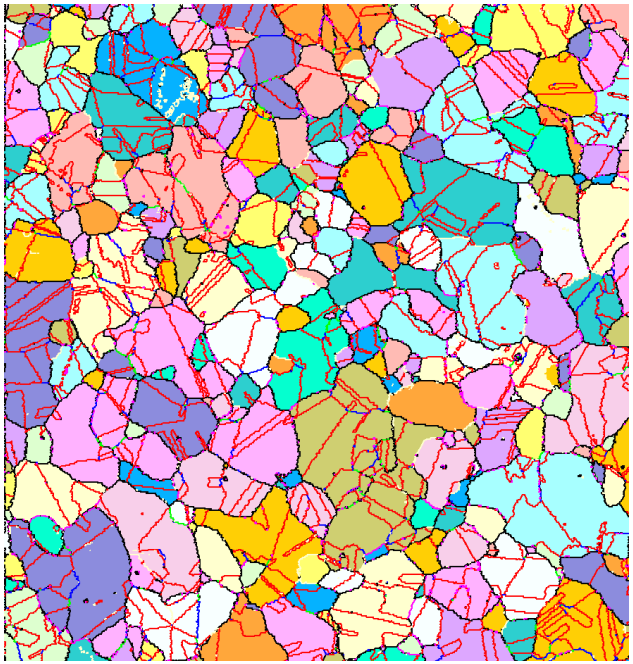

300 μm Normal Material, *f* = 0.49

- Mostly flat Σ3's, twinning back-and-forth on the same {111} planes
- Simple intra-TRD networks
- Few distinct orientations in each TRD

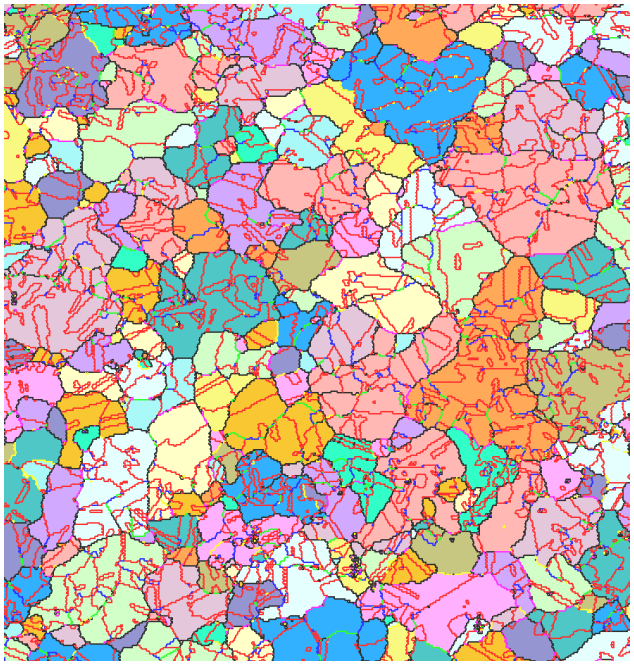

300 μm Engineered Material, *f* = 0.60

- Highly complex intra-TRD networks
- More frequent inter-TRD special boundaries
- Many distinct orientations in each TRD

Definition: *f* = fraction of CSL boundaries

Weak boundary paths exist on length scales that match measurements of fracture surface roughness

- Red boundaries are strong (special)
- Black boundaries are weak (random)
- Background colors are twin-related domains

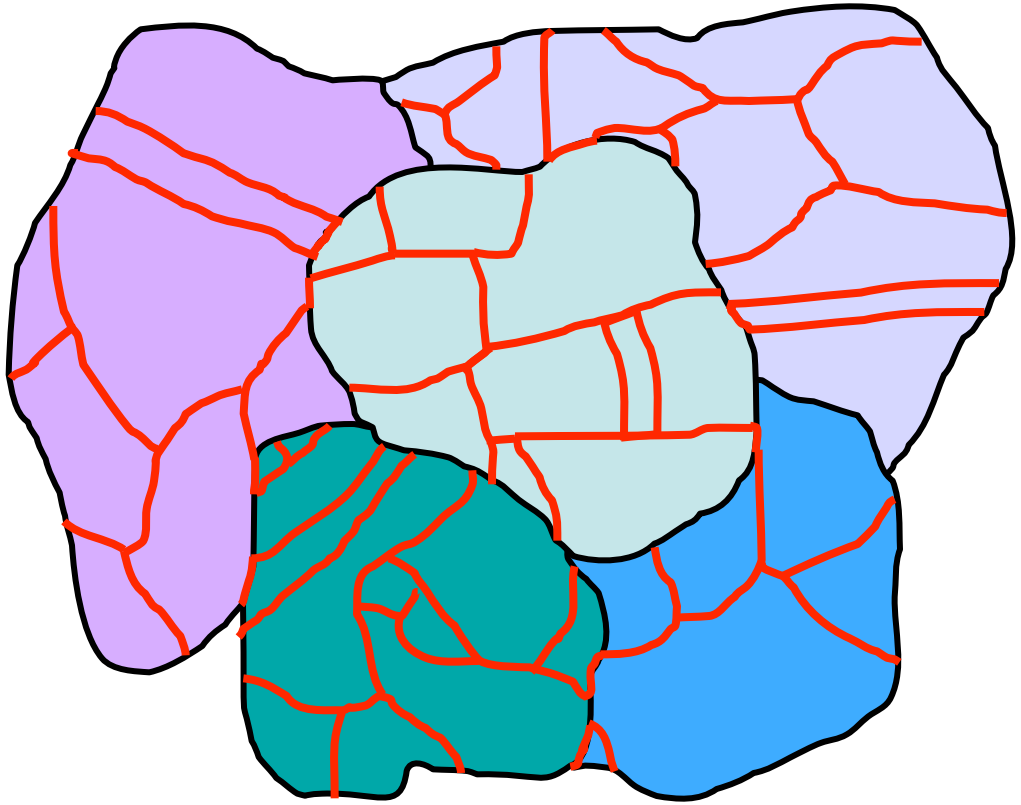

Size Scales

Grain diameter 35-70 μm

TRD diameter 70-160 μm

Isolated Random Boundary 10-20 μm

Shows up in the roughness scaling of both materials

Large Random Boundary Cluster 140-160 μm

Shows up in the roughness scaling of the normal material

Example results from Reed et al., Acta Mat. 56, 3278 (2008)

The group structure can be efficiently represented by strings on a four-letter alphabet

- There are four "generators." Call them a, b, c, and d.
- Each represents a twin on a specific {111} plane.
- Each is its own inverse. aa = bb = cc = dd = ϕ
- Any orientation in the group can be reached by a finite string of these 4 letters.
- Any orientation at all can be approximated by a string of length <16.
- After doing maximal pair cancellation, the string is unique, and the "type" of the rotation is $\Sigma 3^{\text{string length}}$
  - Example: abccbd = abbd = ad is a $\Sigma 3^2 = \Sigma 9$
- The inverse of a string is the same string in reverse order
- The misorientation between two strings is $\text{String}_1^{-1}\text{String}_2$
  - Example: Misorientation between abd and abcd is $(\text{abd})^{-1}\text{abcd}$ = dbaabcd = dbbcd = dcd, which is a $\Sigma 27$.

These are <u>all</u> of the rules. Following these lets you efficiently handle all twin-related orientations while guaranteeing crystallographic consistency.

Computer Simulations of Evolving Microstructures: Nucleation, Growth, & Coarsening

J. M. Rickman
Dept. of Mat. Sci. & Eng. and Dept. of Physics
Lehigh University

Collaborations

K. Barmak
W. S. Tong
S.-B. Lee
A. D. Rollett
J. D. Gunton

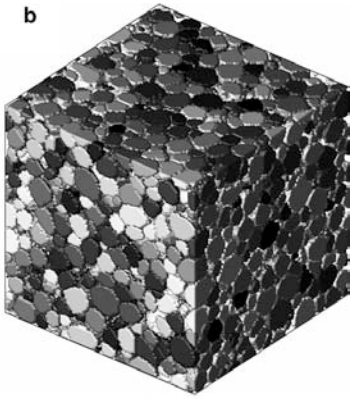

Petroleum Research Fund

Outline

- Nucleation and Growth: Simulation and Analysis

Simulation Methodology

Correlation Functions

Microstructural Descriptors

Homogeneous vs. Heterogeneous Nucleation

Non-Isothermal Transformation

Non-Euclidean Geometry

- Applications

Deducing Nucleation Conditions From a Microstructure

Tailoring Microstructures in Transforming Films

Input to Coarsening Models

Stochastic Geometry

- kinetics of nucleation & growth to coalescence
- microstructural features

Distribution of nuclei $\longrightarrow$ **Generator of point process**

Tools

- computer simulation (Monte Carlo)
- nonequilibrium correlation functions
- neighbor distributions

- Can one deduce nucleation conditions from kinetic data?

- Can one deduce nucleation conditions from a coalesced microstructure?

Simulating Nucleation and Growth

Partitioning of Space - burst of nuclei

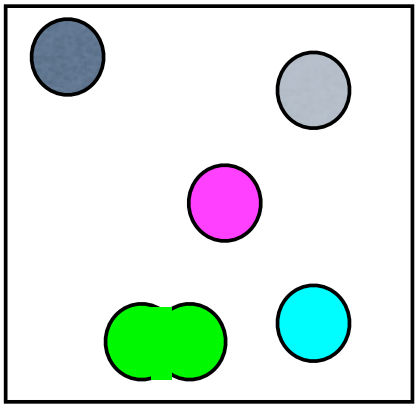

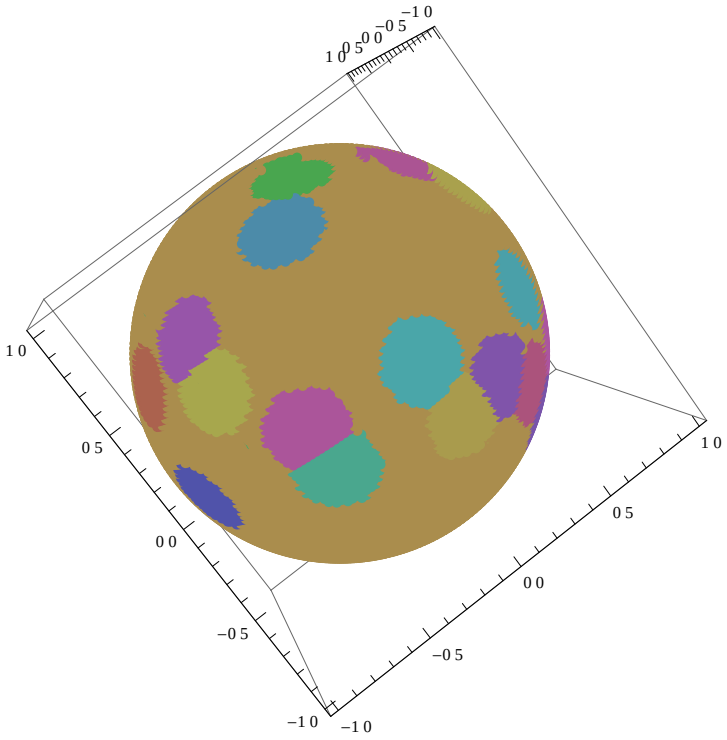

- burst of nuclei (Poisson process)
- constant growth rate
- growth stops at impingement

Partitioning of Space - time-dependent nucleation rate

- Constant nucleation rate → Poisson process in space and time

- kinetic Monte Carlo (N-fold way) used to model time-variable rate of non-isothermal case

Simulating Nucleation and Growth

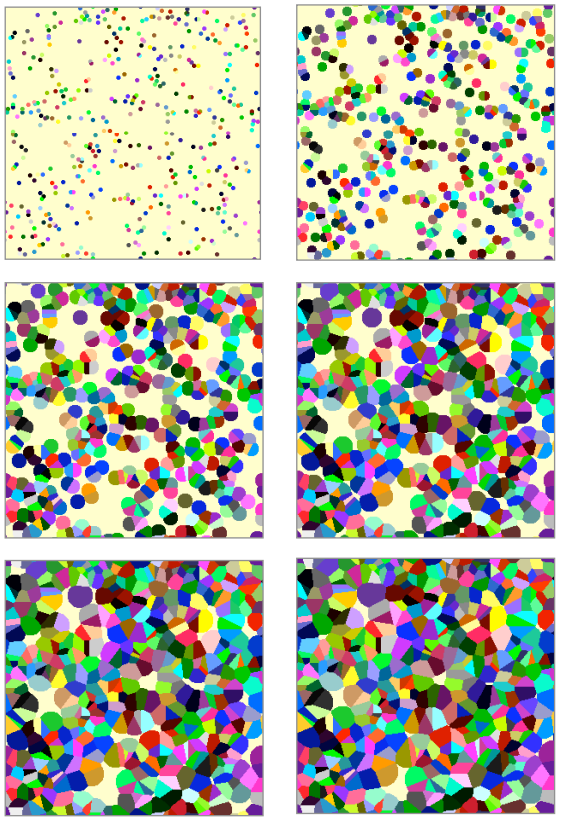

Burst of nuclei in plane
Constant growth rate

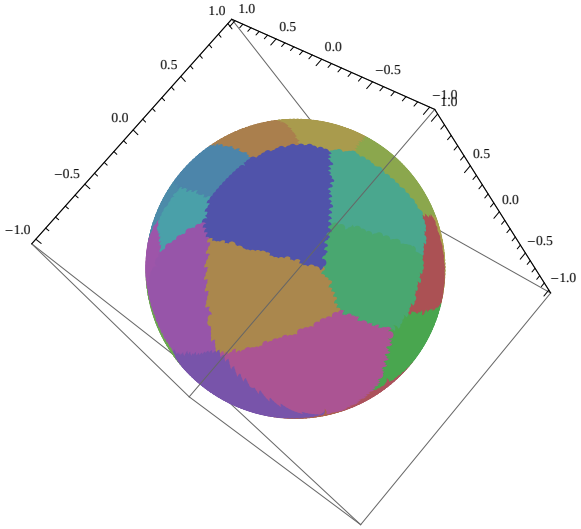

Burst of nuclei on sphere
Constant angular growth rate

Non-isothermal conditions
Temperature ramp

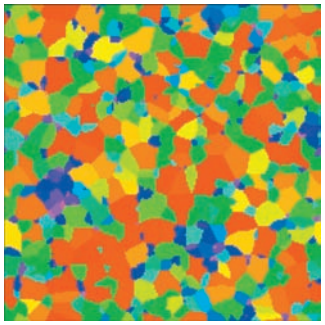

Transformation Fraction (JMAK)

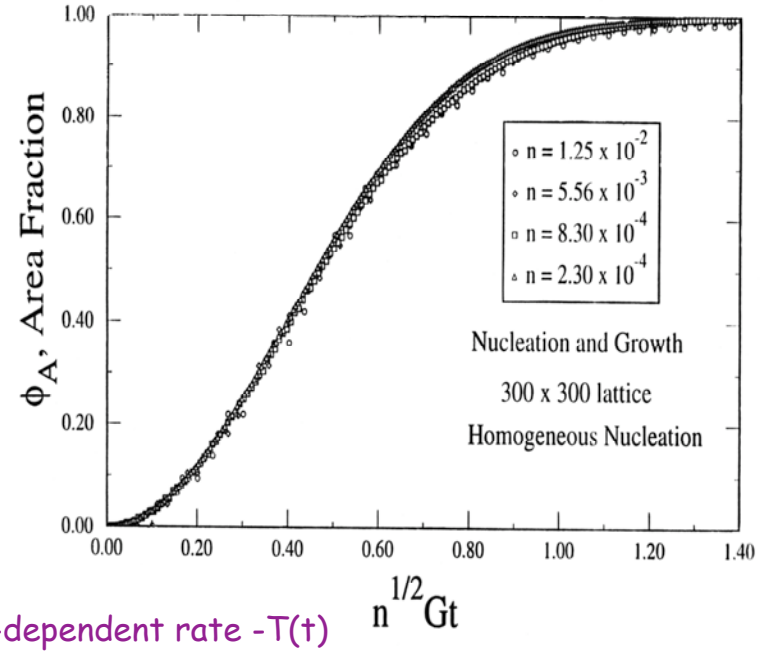

time-dependent rate -T(t)

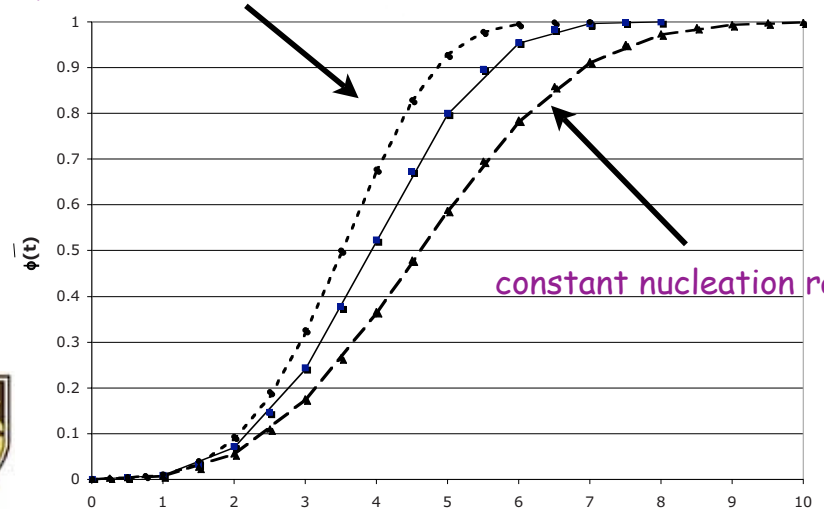

Sekimoto n-point correlation function

$$C_n\left(\vec{r}_1,\vec{r}_2,\ldots,\vec{r}_n,t\right)=\exp\left[-\int d^2r'\int d\tau\, I(\vec{r}',\tau)\left(1-\prod_{i=1}^{n}D\left(\vec{r}_i,t;\vec{r}',\tau\right)\right)\right]$$

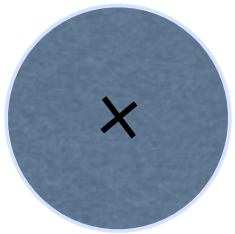

Poisson Statistics

$$\text{Prob. } untransformed \propto \exp\left[-n\pi r^2\right]$$

- Fraction transformed determined from stochastic geometry (Poisson process).

- Correlated nuclei - other point processes.

- Non-Euclidean spaces - other metrics.

Two-Point Function - Planar Geometry

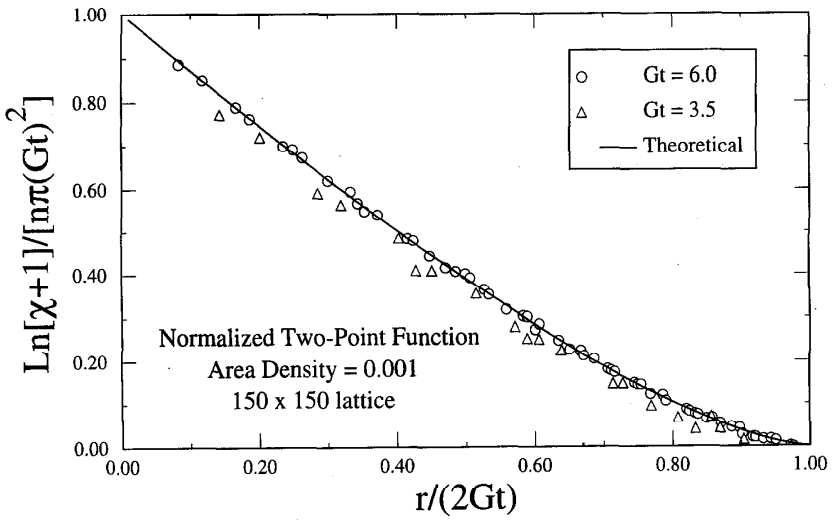

Planar Surface

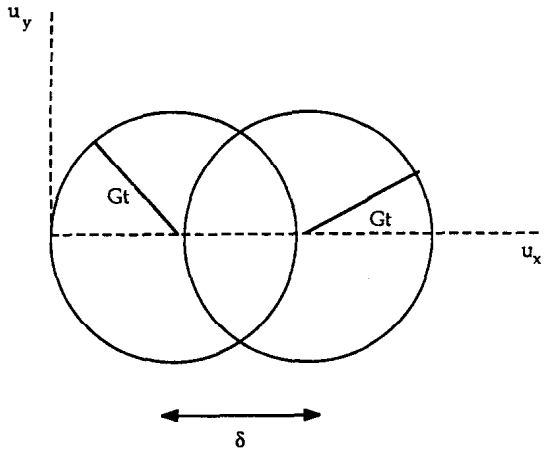

Geometry - overlap integral

$$C_2(\vec{r}_1, \vec{r}_2, t) = \exp[- n \int d^2r'(1 - D(\vec{r}_1;t:\vec{r}';0)D(\vec{r}_2;t:\vec{r}';0))]$$

$$C_2(\delta, t) = [C_1]^2 \exp\,(n\pi G^2 t^2 \gamma(s)),$$

$$\gamma(s) = \frac{2}{\pi}\,[\,\sin^{-1}\sqrt{1 - s^2} - s\sqrt{1 - s^2}]\,\Theta(1 - s).$$

Two-Point Function - Special Cases

Non-Isothermal System

$$\chi(\vec{r}_1,\vec{r}_2,t) = \frac{C_2(\vec{r}_1,\vec{r}_2,t) - C_1(\vec{r}_1,t)C_1(\vec{r}_2,t)}{C_1(\vec{r}_1,t)C_1(\vec{r}_2,t)}$$

$$\chi(|\vec{r}_1 - \vec{r}_2|,t) = \exp\left[\frac{2G_0^2 I_0 t^3}{3}\left(\arccos(y) - 2y\sqrt{1-y^2}\right.\right.$$
$$\left.\left. + y^3 \ln\left(\frac{1+\sqrt{1-y^2}}{y}\right)\right)\Theta(1-y)\right] - 1,$$

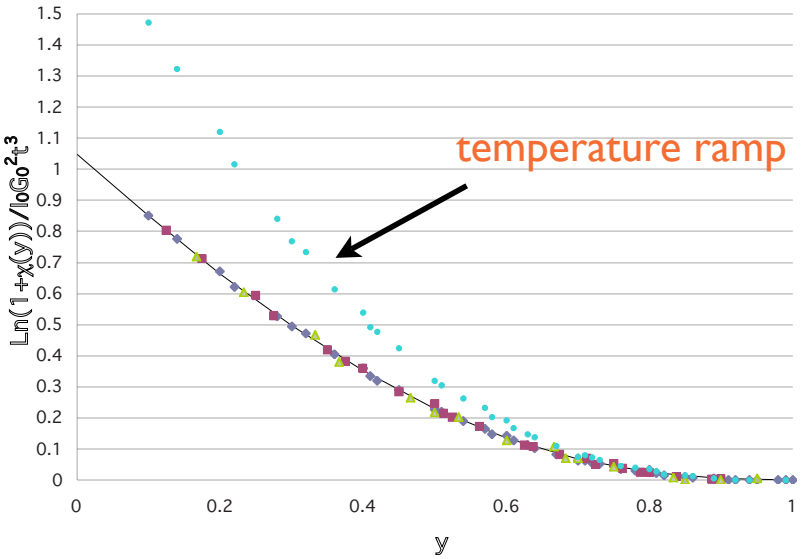

Spherical Surface

$$\chi(\Phi,t) = \frac{\left[1 - A_{\cup}(\Phi,t)/4\pi\right]^N}{\left[1 - f(t)\right]^{2N}},$$

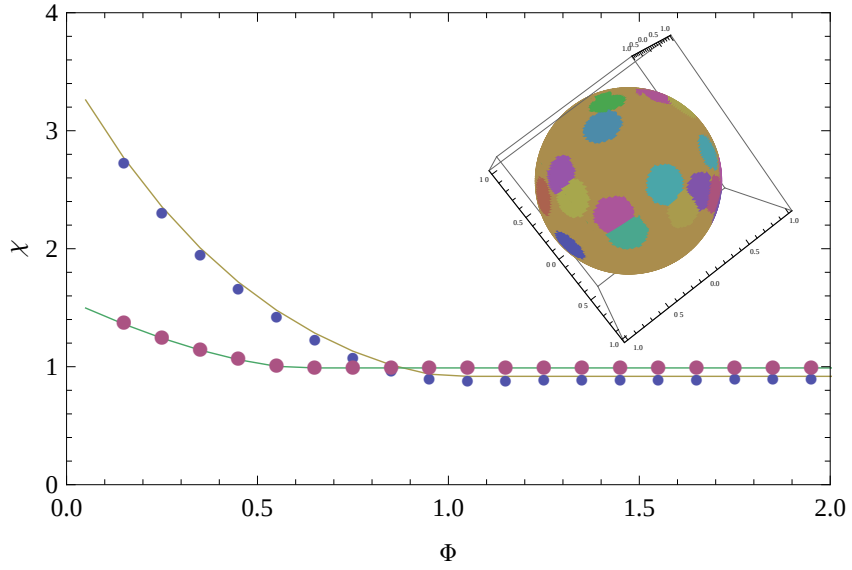

Heterogeneous Nucleation - Kinetics

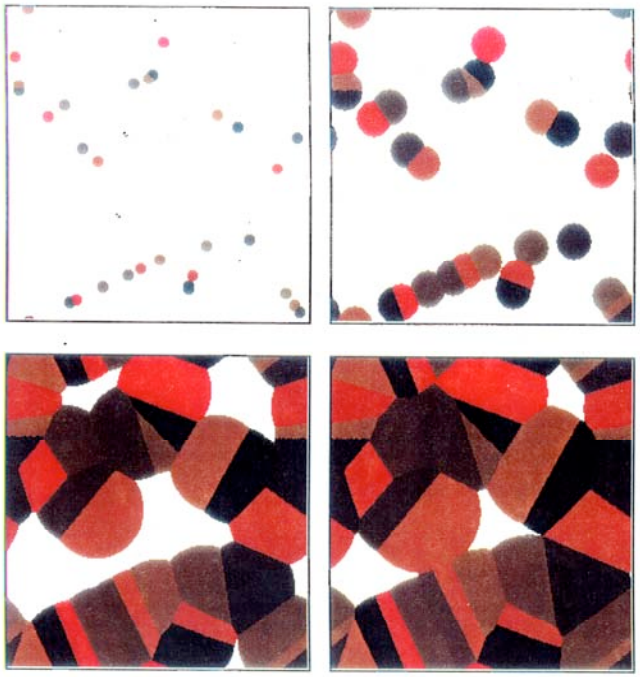

Transformation Fraction

Nucleation on Grain Boundaries

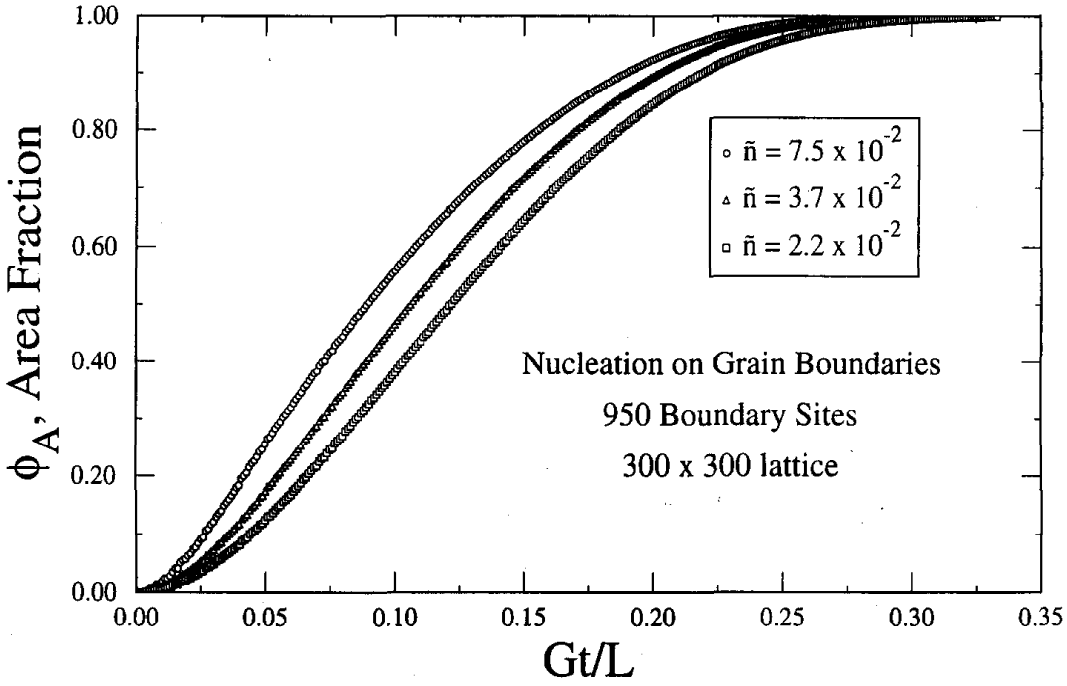

Correlated Nuclei

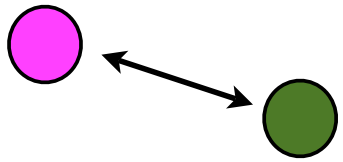

- long-range interactions (e.g., stress)

- correlated point process

↓

- build g(r), etc., into multipoint correlation function

↓

- g(r) can be approximated by Percus-Yevick

Transformation Kinetics: Nb/Al Thin Films

Working Backwards From Calorimetry Traces

Calorimetry traces

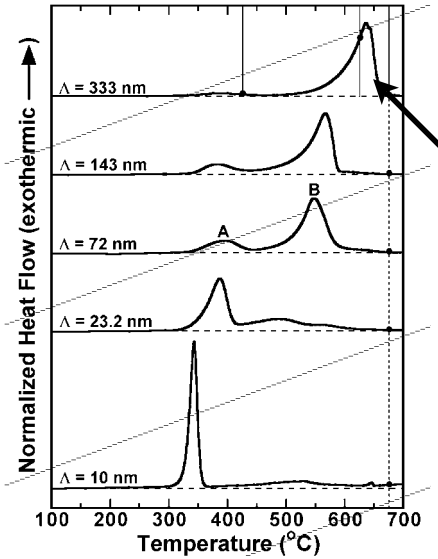

related to fraction transformed

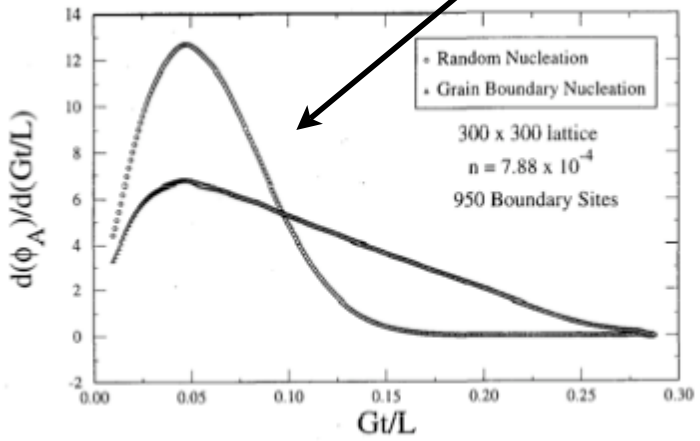

simulation, calculation

Microstructural Analysis

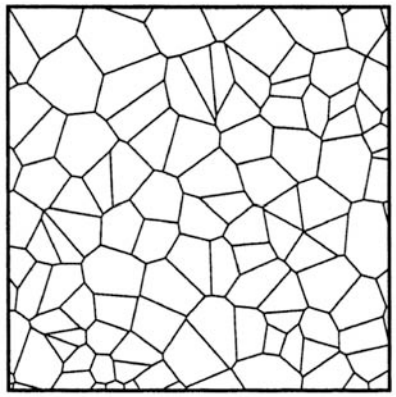

Final microstructure (burst of nuclei in plane)

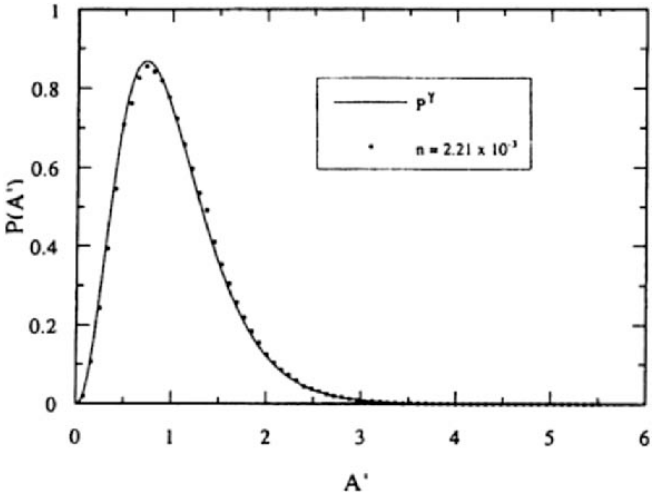

Grain area distribution - comparison with gamma dist. (Kiang)

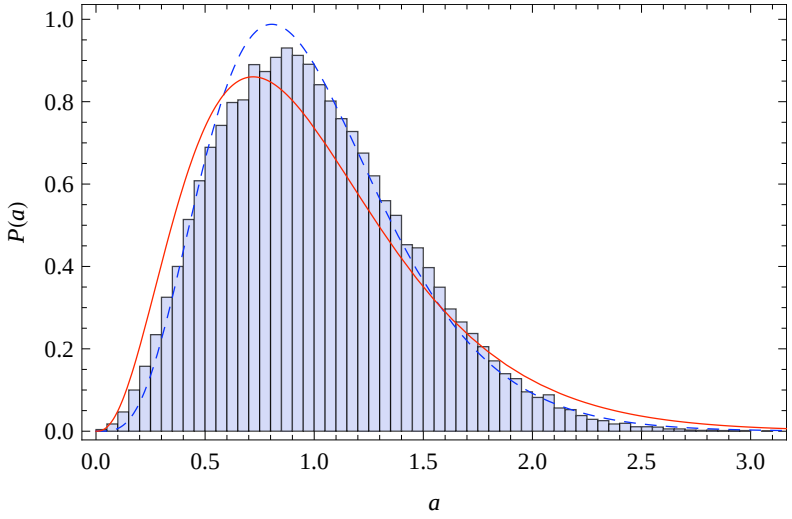

$$P^{\gamma}(A') = \frac{1}{\beta^{\alpha}\Gamma(\alpha)}(A')^{\alpha-1}\exp(A')$$

Correction due to spherical geometry

Heterogeneous Nucleation - Microstructures

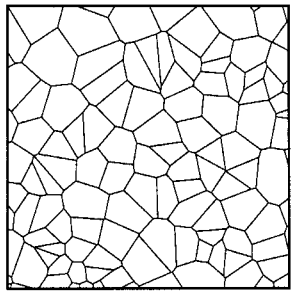

random distribution of nuclei

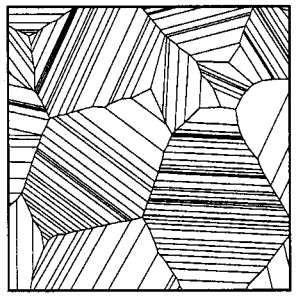

GB catalyzed

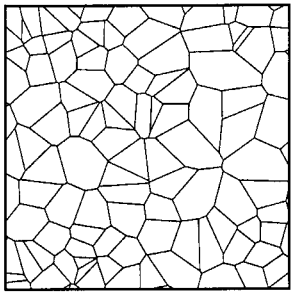

grain corner catalyzed

Pair Correlation Function - Corner Sites

Shows nonrandomness of sites.

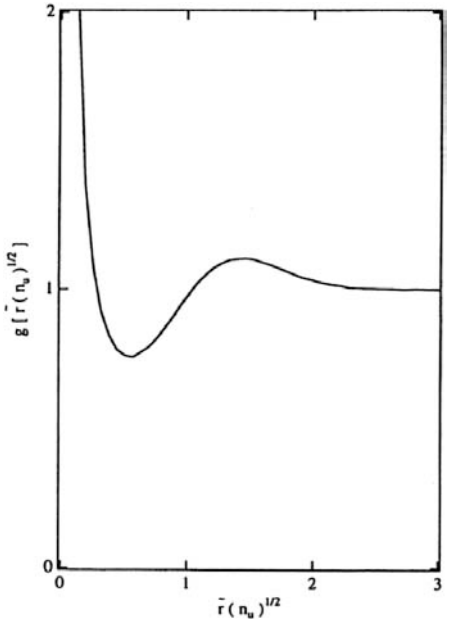

Distinguishing Among Nucleation Scenarios

r = internucl. sep. (boundary)/grain size

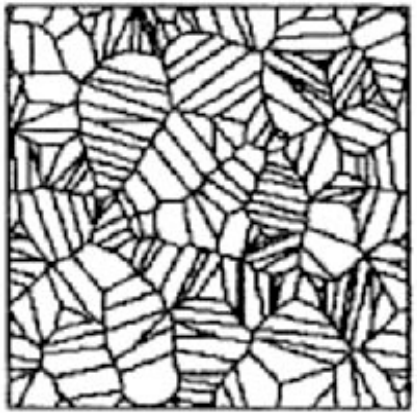

r<1

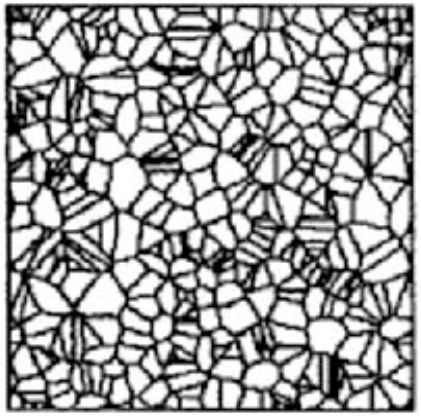

r~1

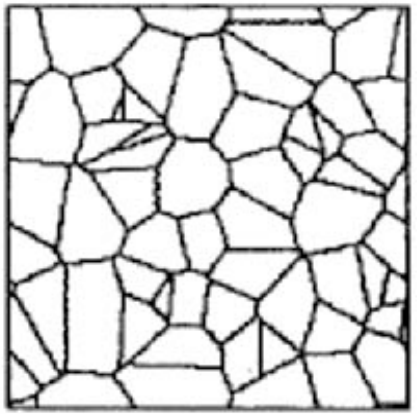

r>1

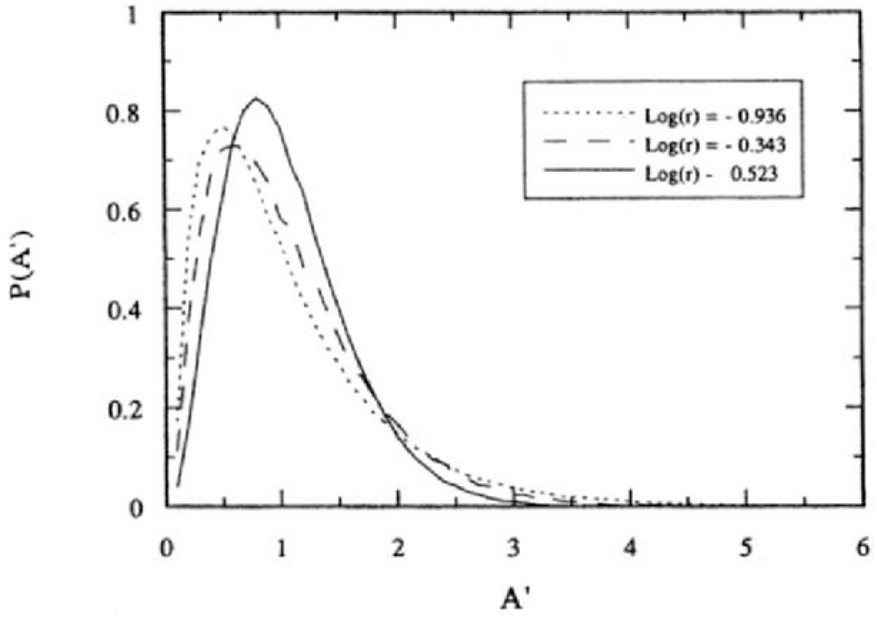

Grain-area distribution

Shifts with r

Other Microstructural Descriptors - Stochastic Geometry

Neighbor distributions - useful if locations of nuclei are known

$$\langle r_k \rangle = \frac{1}{\sqrt{\pi}(\lambda_d)^{1/d}} \left[\Gamma\left(1+\frac{d}{2}\right)\right]^{1/d} \frac{\Gamma(k+1/d)}{\Gamma(k)}$$

first moment of k-th neighbor distribution

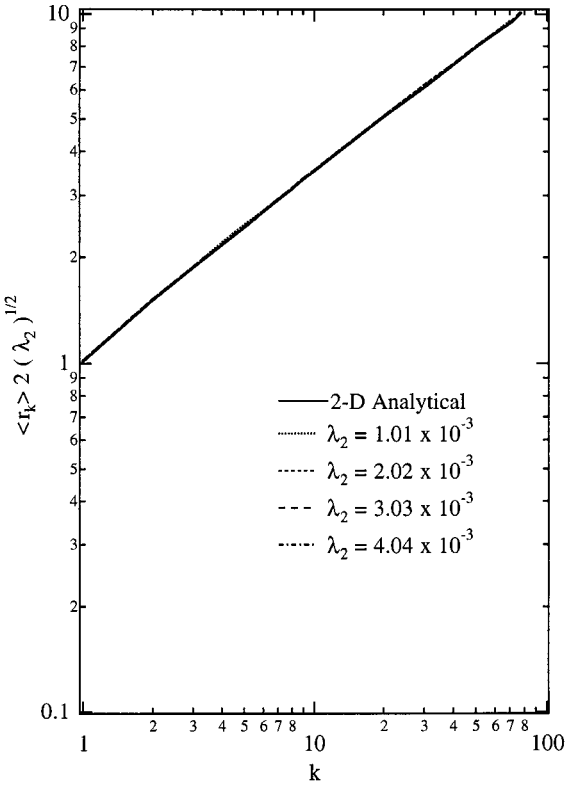

random distribution of points

nucleation on GB

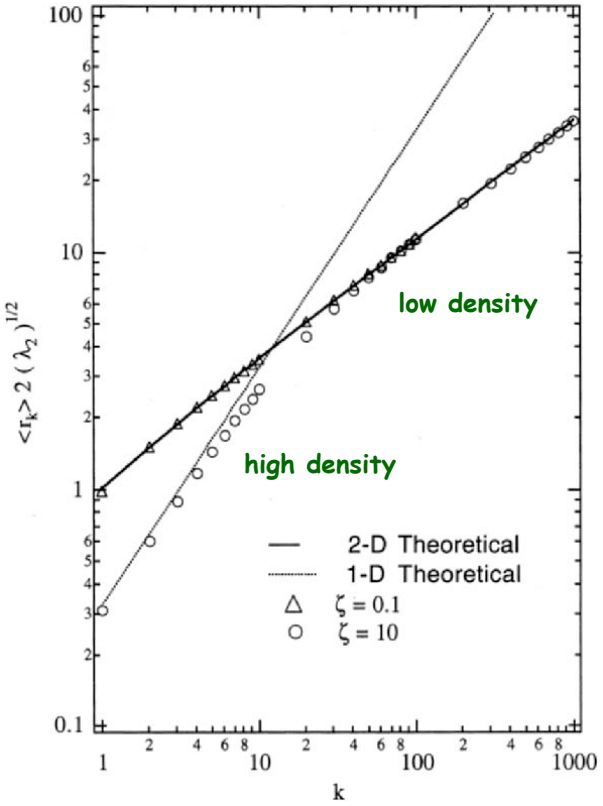

Locating Nuclei from Coalesced Microstructure

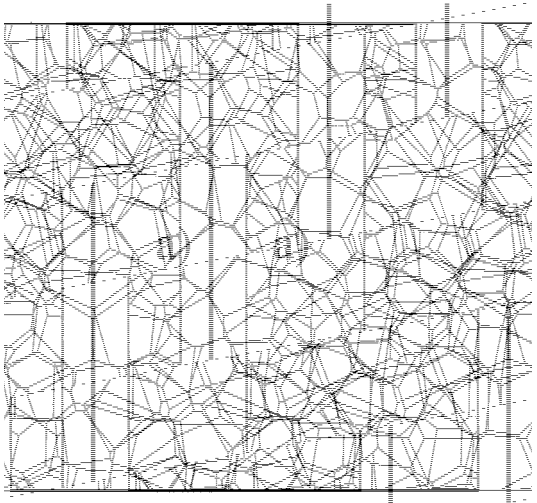

trial microstructure based on grain centroids

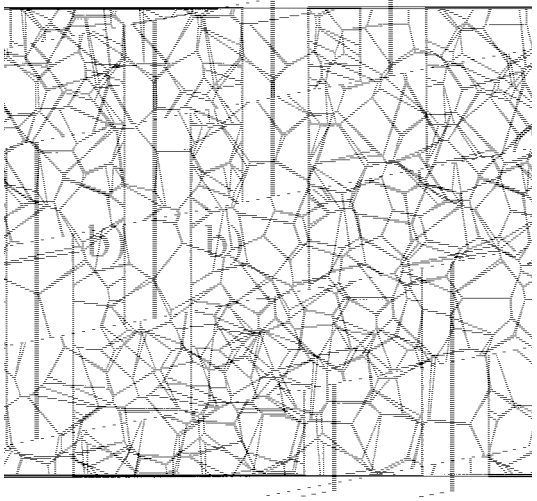

microstructure after successive iterations

Reverse Monte Carlo Procedure

- choose trial positions for nuclei

- generate associated microstructure

- calculate objective function for markers

- reject/accept criterion

Microstructure - Non-Isothermal Conditions

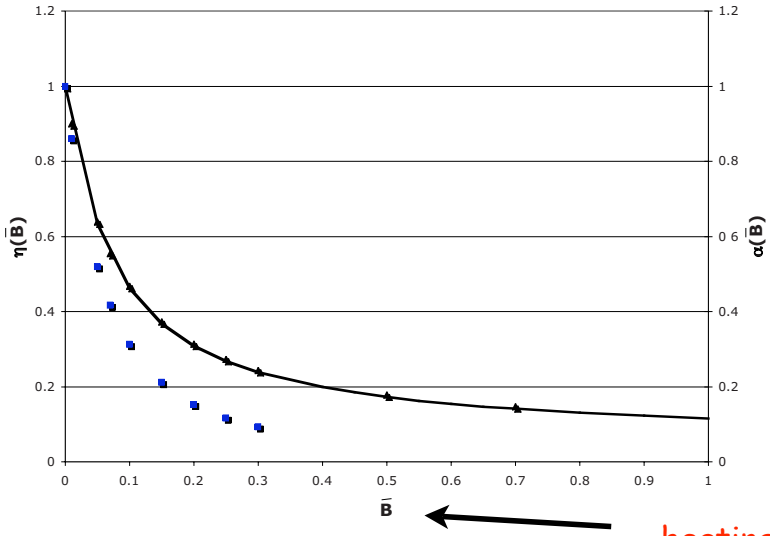

heating rate

constant nucleation rate (isothermal)

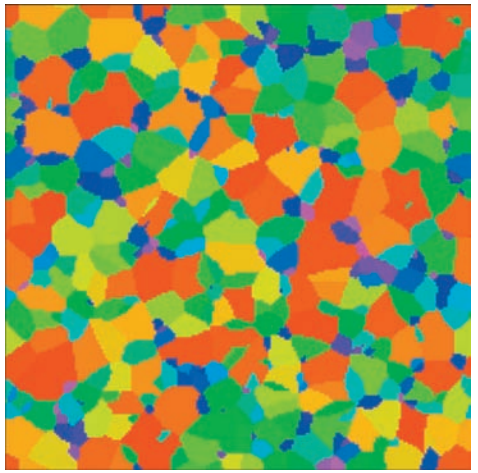

$$\langle N(B=0)\rangle = I_0 \int_0^\infty dt \exp\left[-\frac{\pi I_0 G_0^2 t^3}{3}\right]$$

$$= \left(\frac{3}{\pi}\right)^{1/3} \Gamma\left(\frac{4}{3}\right)\left(\frac{I_0}{G_0}\right)^{2/3}.$$

constant heating rate

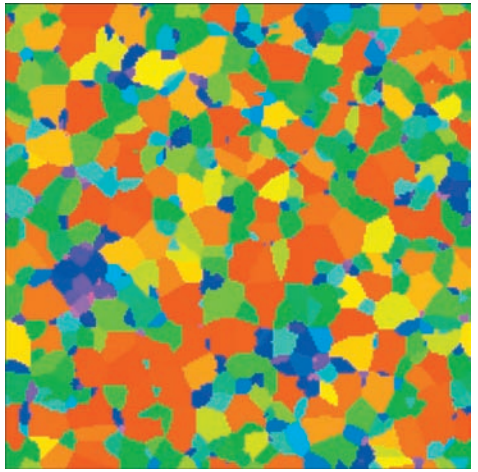

$$\langle N(B)\rangle = I_0 \int_0^\infty dt \exp\left(\frac{-\epsilon_I}{k_B T(t)}\right)(1-\phi(t))$$

$$\approx \langle N(B=0)\rangle \left[1 + \frac{5B}{6T_0}\left(\frac{3}{\pi I_0 G_0^2}\right)^{1/3} \frac{\Gamma\left(\frac{2}{3}\right)}{\Gamma\left(\frac{1}{3}\right)} \overline{\epsilon}\right],$$

Applications

- tailoring microstructure in a transforming thin film

- starting microstructure for models of coarsening

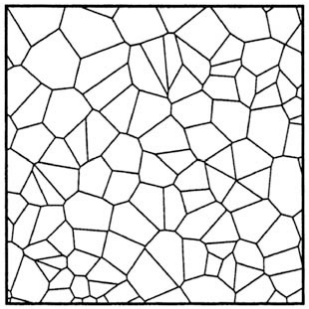

reverse MC

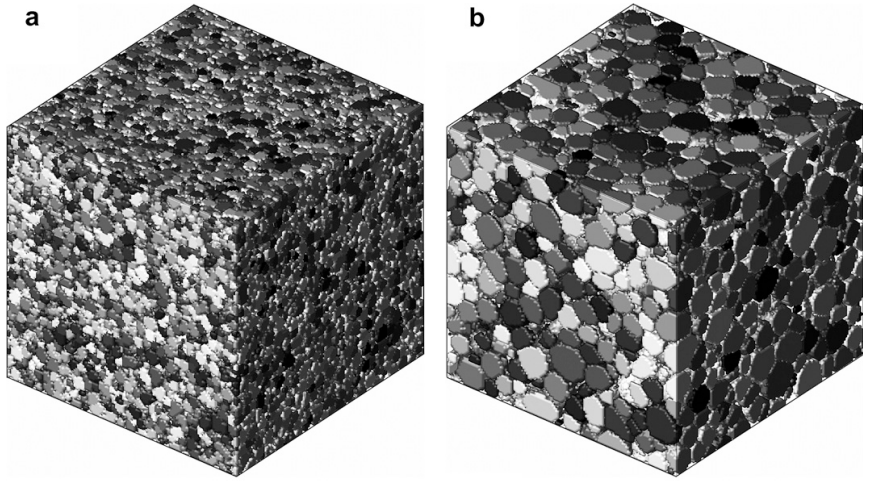

microstructural evolution by coarsening

Biased Nucleation - Thin Film

transforming
film

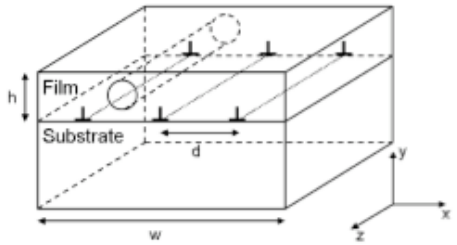

misfit dislocation ->
biasing stress

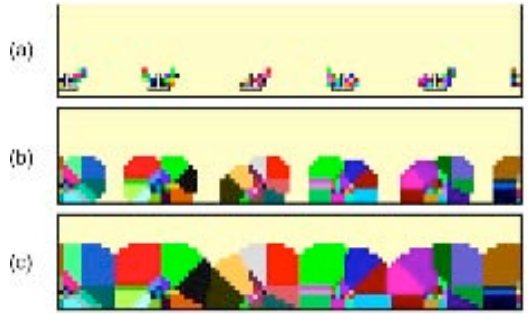

biased nucleation and growth

Microstructural Evolution

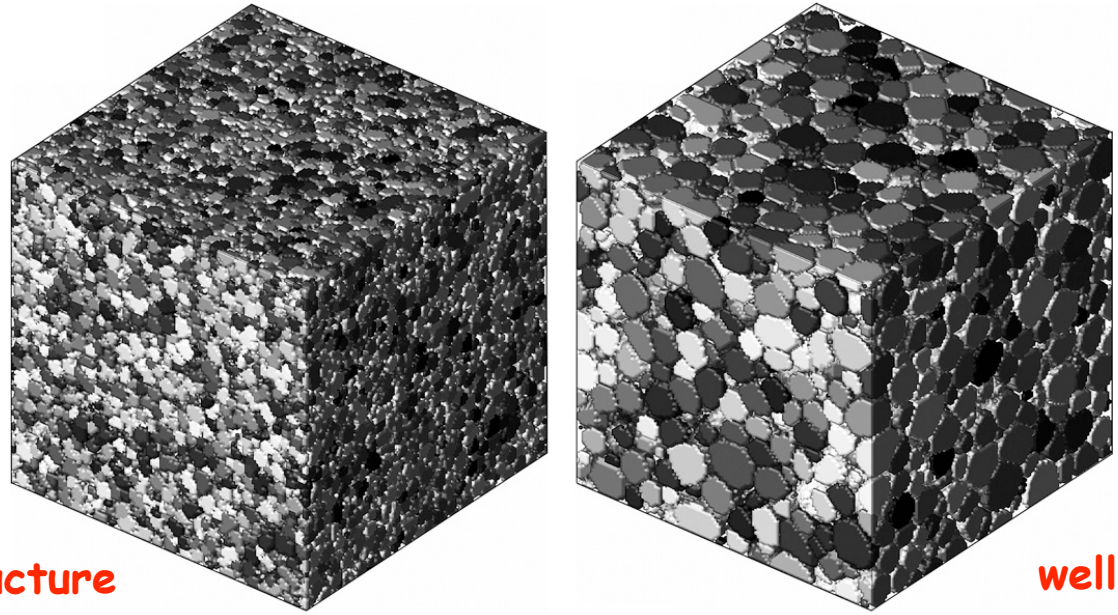

seed microstructure

well-coarsened microstructure

Connection with Nucleation & Growth Models

Initial (Precoarsened) States

- site-saturation kinetics ⟶ narrow distribution

- constant nucleation rate ⟶ wide distribution

Input For Coarsening Models

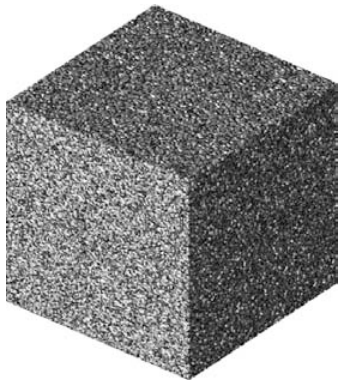

1.) Start with a coalesced microstructure from a nucleation and growth simulation

2.) Map onto a spin model

$$E = \frac{1}{2} \sum_{i}^{N} \sum_{j}^{26} e(s_i, s_j).$$

Q-state Potts Hamiltonian

Voxels: s = 1,2,...,Q

Srolovitz et al. (1983)
Anderson et al. (1984)
Rollett et al. (1989)

3.) Evolve in time to minimize energy.

Example: Liquid-Phase Sintering

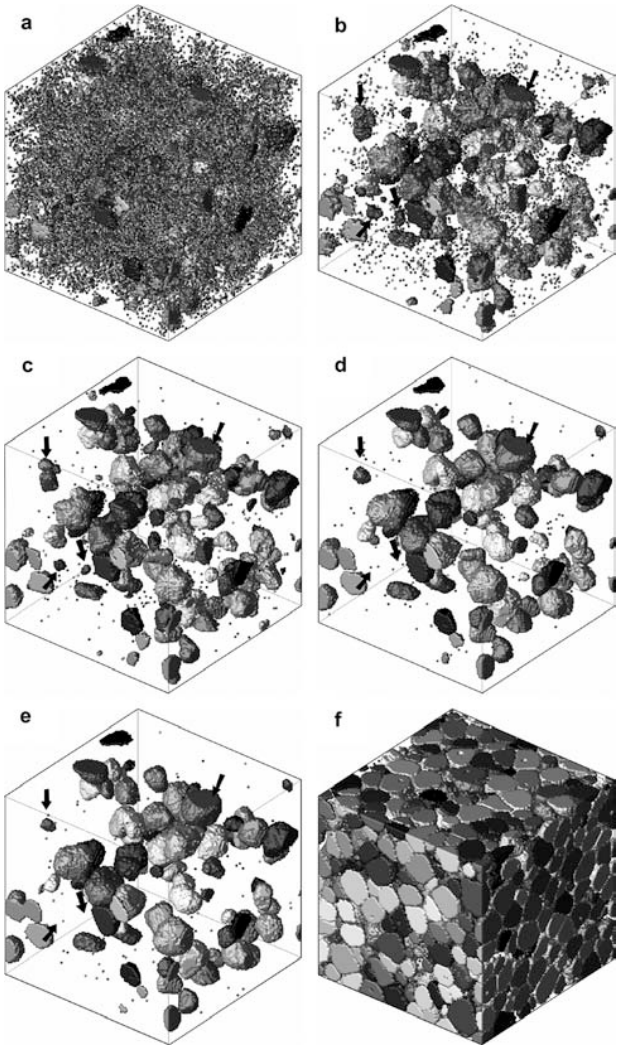

Temporal Evolution

- 128x128x128

-Initial solid fraction: 0.7

-Liquid matrix omitted for visualization.

-Only a portion of the particles present in (a)-(e).

- kT = 1.6

Conclusions

- Concepts from stochastic geometry are useful for describing phase transformation kinetics and associated microstructure.

- In some cases it is possible to deduce nucleation and growth conditions from kinetic data and coalesced microstructures.

-Computer simulation can be used to generate configurations needed for averaging and visualizing microstructures.

- Insights from stochastic geometry can help to tailor transformation microstructures in thin films.

Coarsening

Q-state Potts Model

Used to study grain growth phenomena:

Srolovitz et al. (1983)
Anderson et al. (1984)
Rollett et al. (1989)

- spin orientation ⟶ local phase information
  liquid, solid (grain orientations)

- Hamiltonian: $E = \frac{1}{2} \sum_{i}^{N} \sum_{j}^{26} e(s_i, s_j).$ sum of interfacial energies

Wetting conditions are modeled by fixing interfacial energies

Early Work

- Ostwald Ripening MC Potts Model: Tikare and Cawley (1998)

- two-dimensional model
- fully-wetting condition (interface energy relations)

- MC Potts Model of Solid-State Sintering of Ceramics: Xiangge et al. (2005)

- coarsening in eutectic microstructures

- Geometrical MC Method: Aldazabal et al. (2004)

- simulation of liquid-phase sintering
- no distinction among orientations

Potts Model

Digitized Initial Microstructure

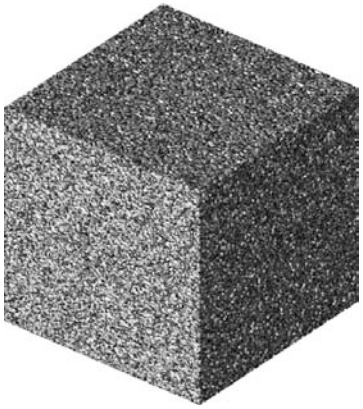

a possible initial state

- Voxel spin value reflects phase and, for solids, orientation

Liquid voxels: $s = -1$

Solid voxels: $s = 1,2,\ldots,Q$

- Interface Energies

$e_{ij}=0,\ s_i=s_j$

$e_{ij}=0.8,\ s_i s_j<0$ (solid/liquid interface)

$e_{ij}=2.0,\ s_i s_j>0,\ s_i=s_j$ (solid/solid interface)

- Significance of Transitions

dissolution
diffusion
precipitation

Size of Critical Nucleus

kT=1.8

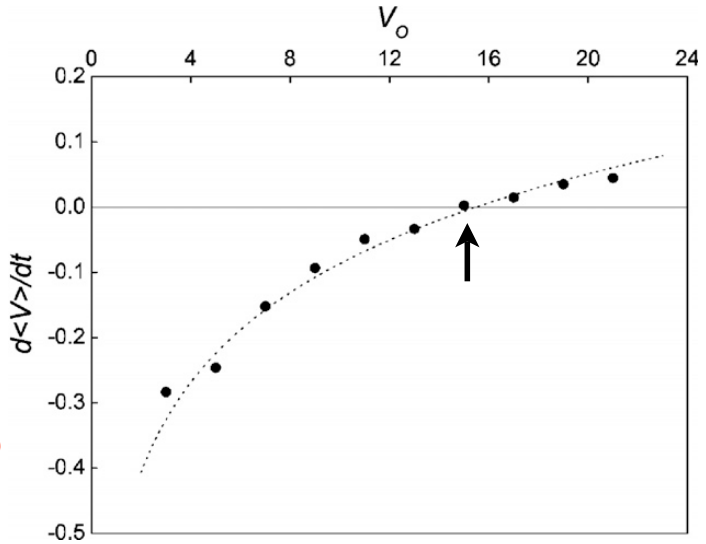

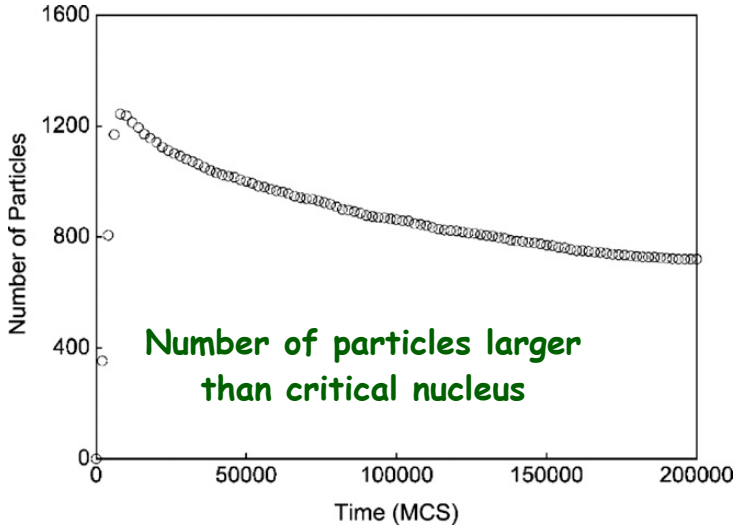

- Determine <V> as a function of time for identical particles.
- V_c is the volume where d<V>/dt = 0.

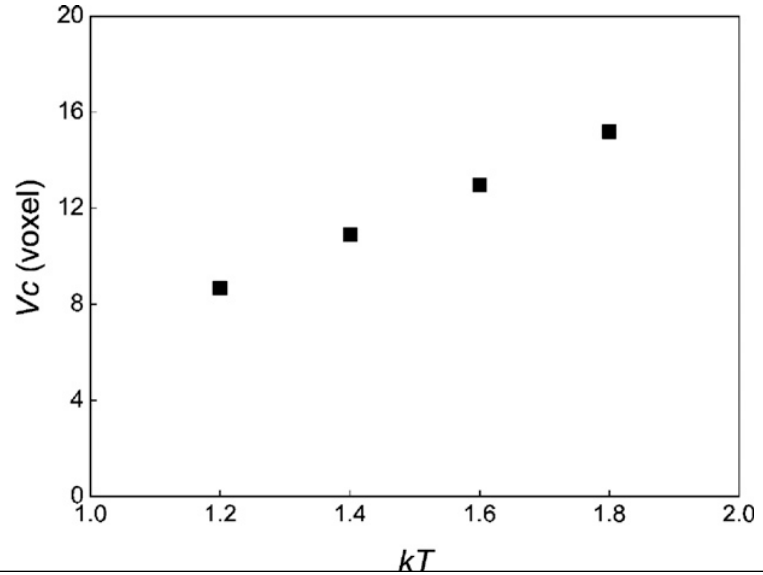

- V_c as a function of temperature

Particle Size Distribution

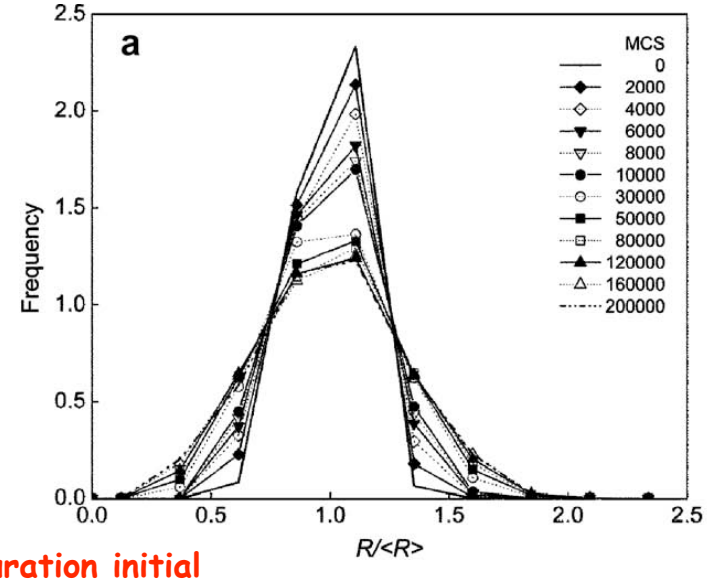

site saturation initial state

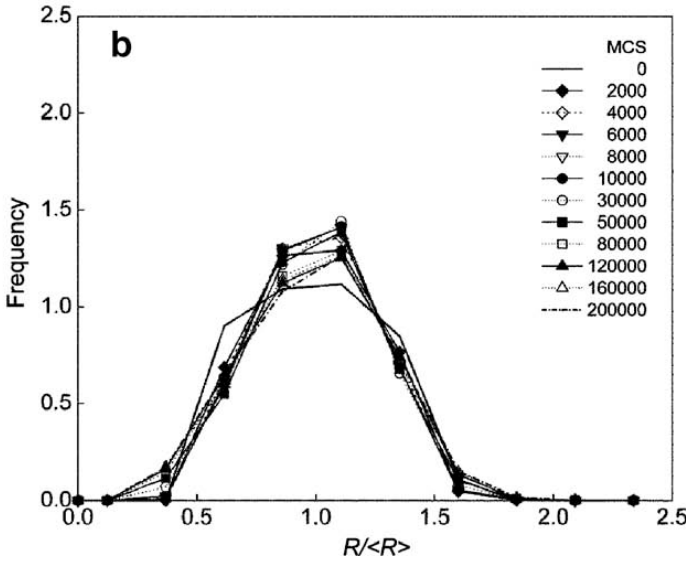

constant nucl. rate initially

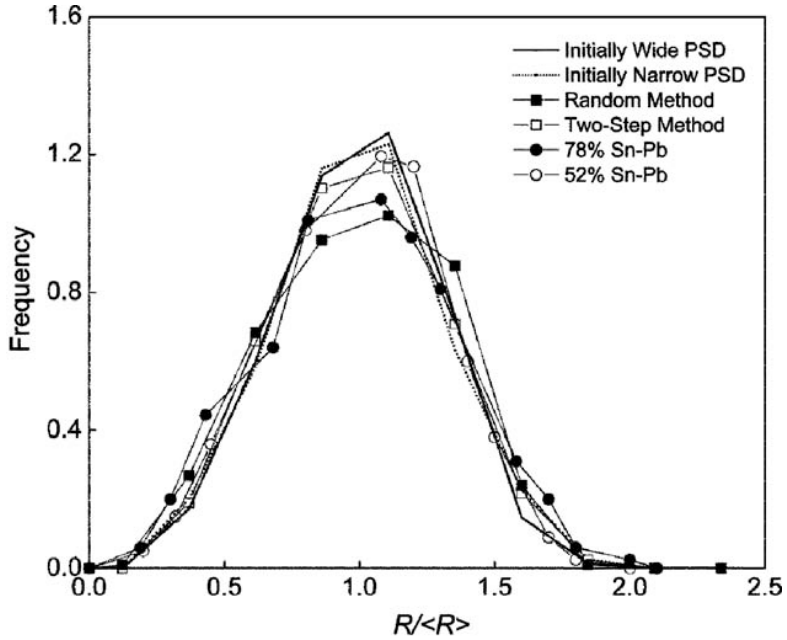

steady-state distribution

self-similar behavior

Coarsening Curves

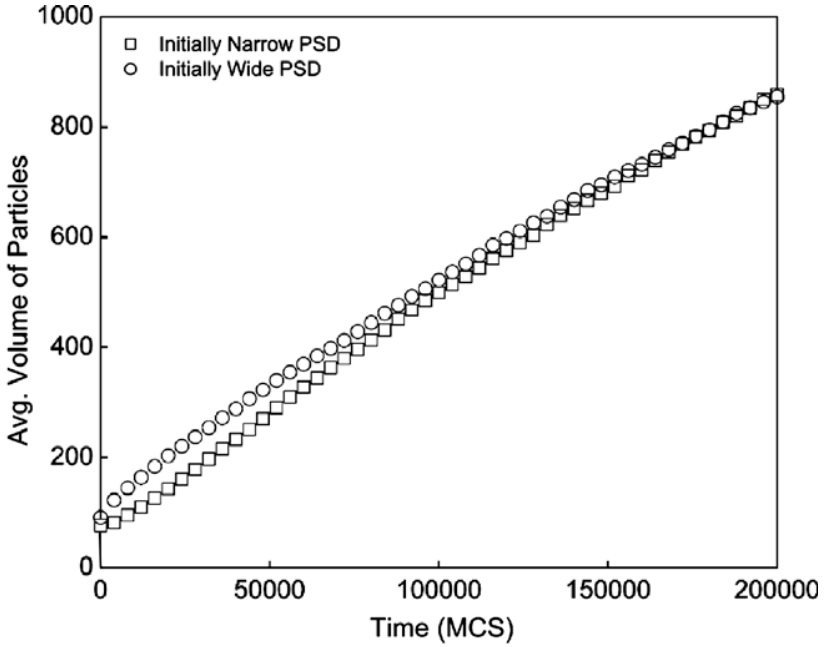

$$\langle V(t) \rangle - \langle V_0 \rangle = Kt$$

$$K = 0.0034\text{-}0.0037\ MCS^{-1}$$

$$\chi\left(\Phi,t\right)=\frac{\left[1-A_{\cup}\left(\Phi,t\right)/4\pi\right]^{N}}{\left[1-f\left(t\right)\right]^{2N}},$$

Another Example: Liquid-Phase Sintering

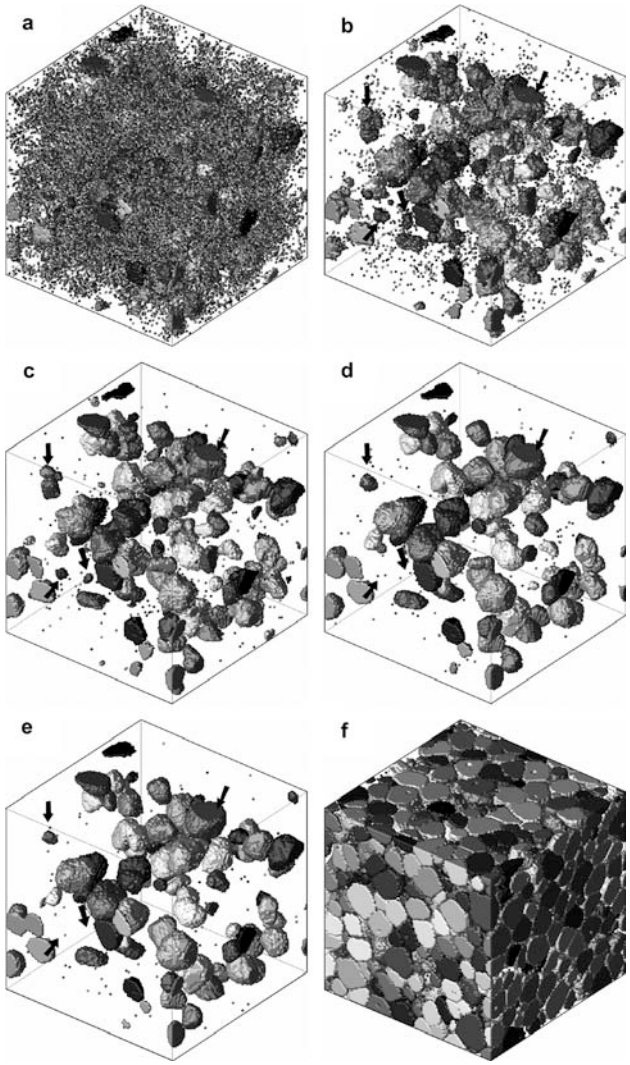

Tailoring Transforming Microstructures in Thin Films

Finding critical configurations
in phase transformations and plastic deformation

Chen Shen[a], Ju Li[b], Yunzhi Wang[c]

[a] GE Global Research
[b] University of Pennsylvania
[c] Ohio State University

Joint AFRL/AOARD/LLNL workshop on nucleation during solid-solid phase transformations in metallic systems, Maui, 2-7 May 2010

imagination at work

Outline

- Energy of nucleus
- Free-end NEB
- Critical nucleus and nucleus along “minimum energy path”
- Dislocation shearing gamma prime
- Summary

Nucleation energetics

Nucleation rate

$$J = J_0 e^{-\Delta F^* / k_B T}$$

Classical nucleation theory
(Volmer & Weber, Becker & Döring)

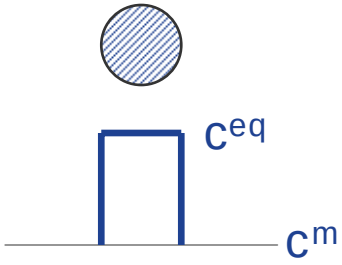

$$\Delta F = \Delta F(R)$$

$$\frac{\mathrm{d}\Delta F}{\mathrm{d}R} = 0 \rightarrow \Delta F^*$$

Non-classical nucleation theory
(Cahn & Hillard)

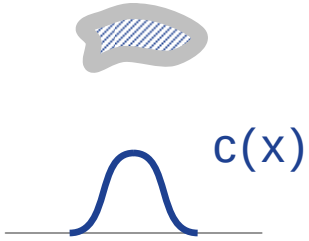

$$\Delta F = \Delta F[c(\mathbf{x})]$$

$$\frac{\delta \Delta F}{\delta c} = 0 \rightarrow \Delta F^*$$

Critical configuration (nucleus)

THE JOURNAL OF CHEMICAL PHYSICS VOLUME 31, NUMBER 3 SEPTEMBER, 1959

Free Energy of a Nonuniform System. III. Nucleation in a Two-Component Incompressible Fluid

JOHN W. CAHN AND JOHN E. HILLIARD

General Electric Research Laboratory, Schenectady, New York

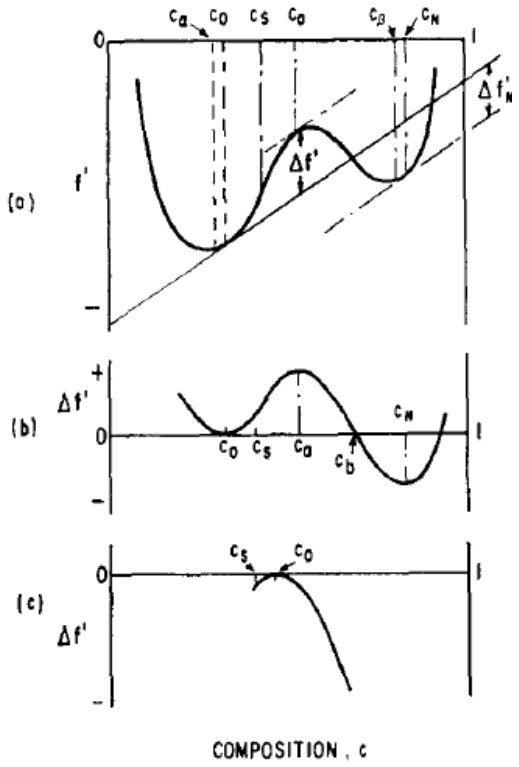

$$W = \int_V [\Delta f' + \kappa(\nabla c)^2] dV,$$

$$c = c(\mathbf{r})$$

$$\Delta f' = f'(c) - f'(c_0) - (c - c_0)(\partial f'/\partial c)_{c=c_0}.$$

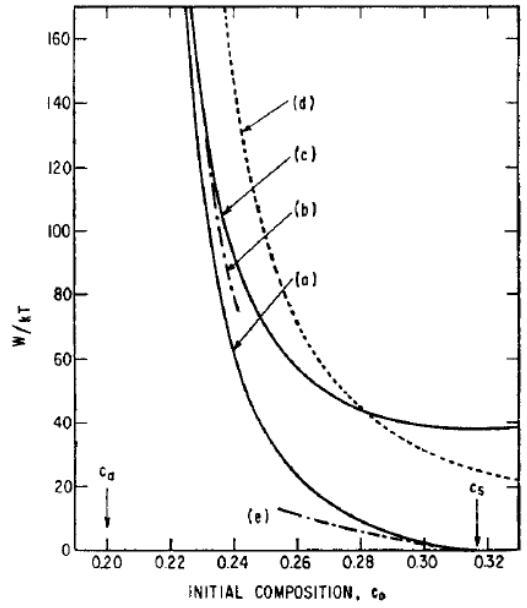

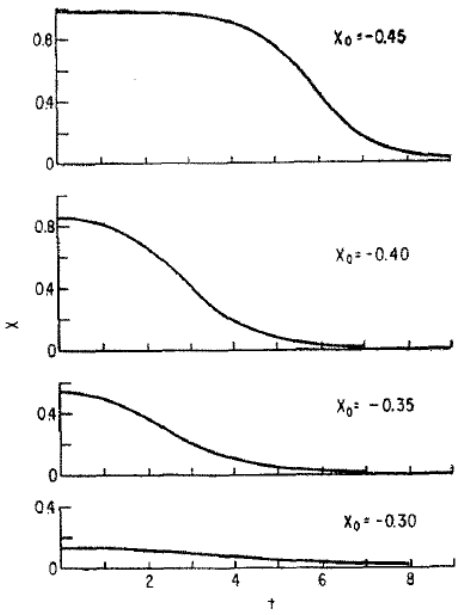

Nudged elastic band (NEB) method

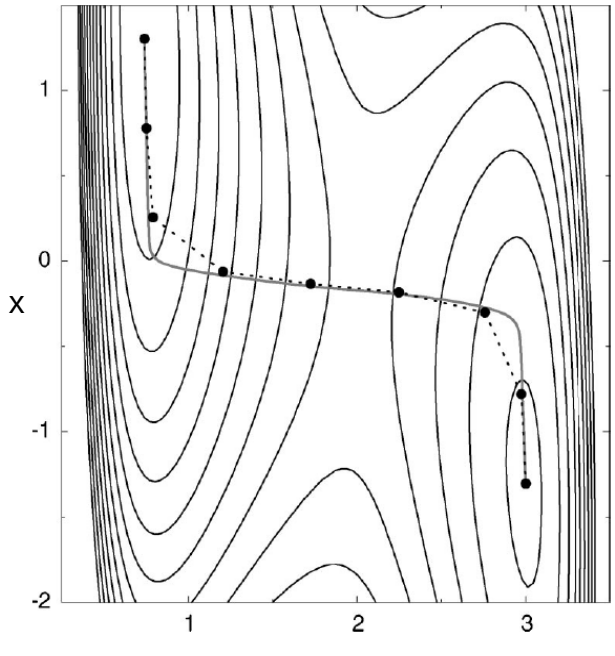

(Mills & Jónsson, 1994; Jónsson et al, 1998; Henkelman & Jónsson, 2000)

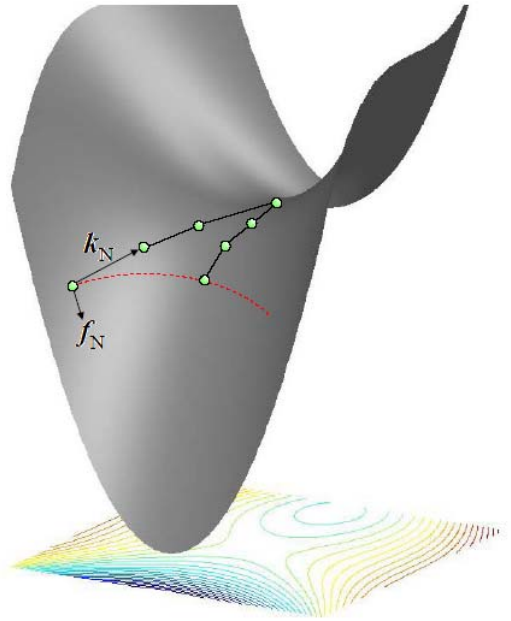

"free-end" NEB

(Zhu, Li, Samanta, Kim, and Suresh: Proc. Nat. Acad. Sci. USA, 2007, vol. 104, pp. 3031–36)

Example: diffusional transformation (precipitation)

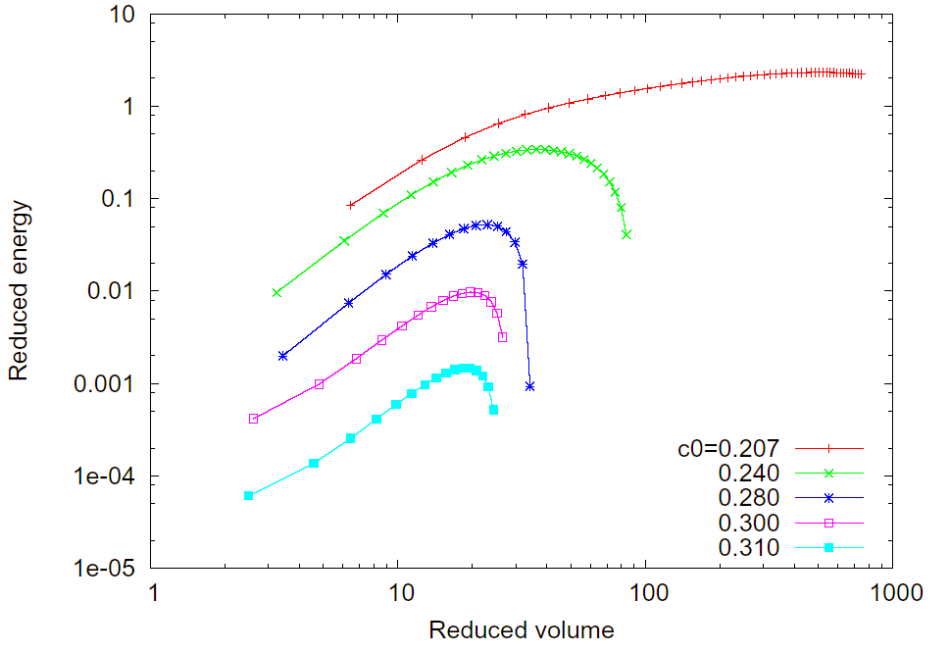

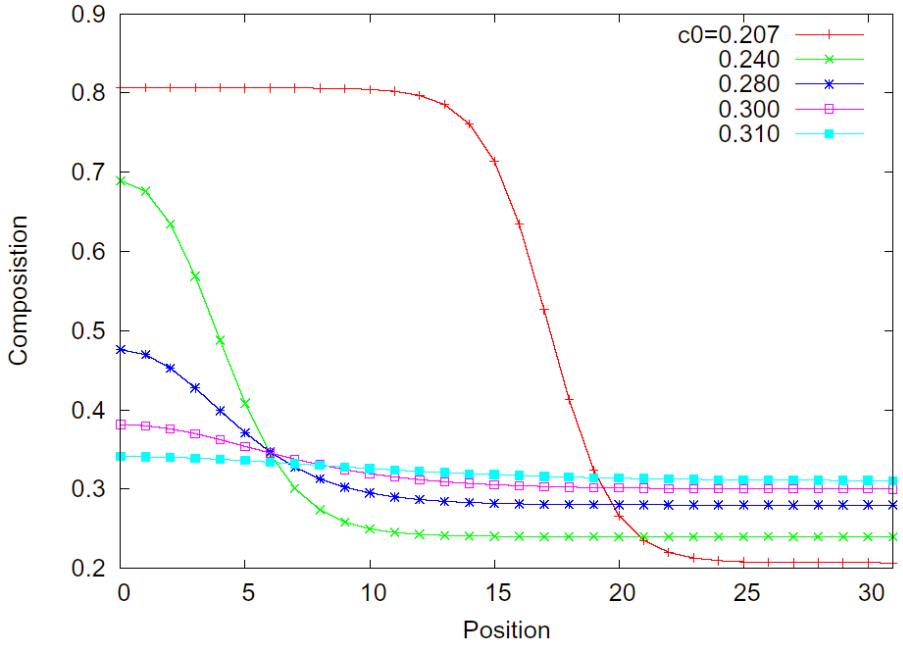

$$\frac{\delta}{\delta c}\left(F-\int \mathrm{d}\mathbf{x}(c(\mathbf{x})-c_0)\mu_0\right)=\frac{\partial f}{\partial c}-\kappa\nabla^2 c-\mu_0=0$$

$$T=\alpha T_0$$

$$f(c)=\frac{\alpha}{2}\Omega[c\ln c+(1-c)\ln(1-c)]+\Omega c(1-c)$$

Example: displacive (cubic → tetragonal) transformation

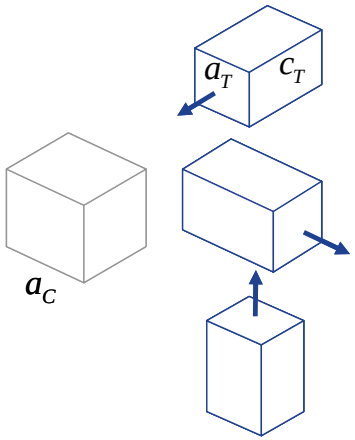

$$\varepsilon_{ij}^{(1)} = \begin{pmatrix} 2 & & \\ & -1 & \\ & & -1 \end{pmatrix}$$

$$\varepsilon_{ij}^{(2)} = \begin{pmatrix} -1 & & \\ & 2 & \\ & & -1 \end{pmatrix}$$

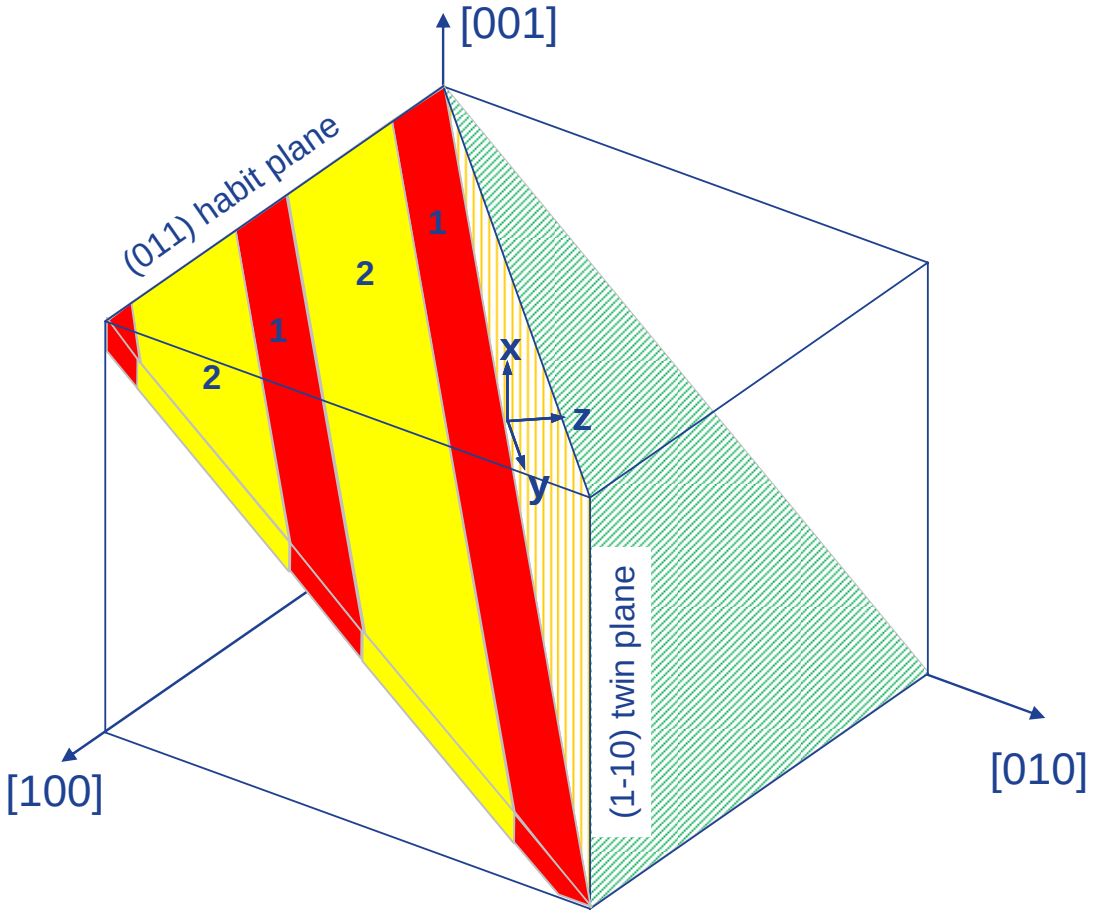

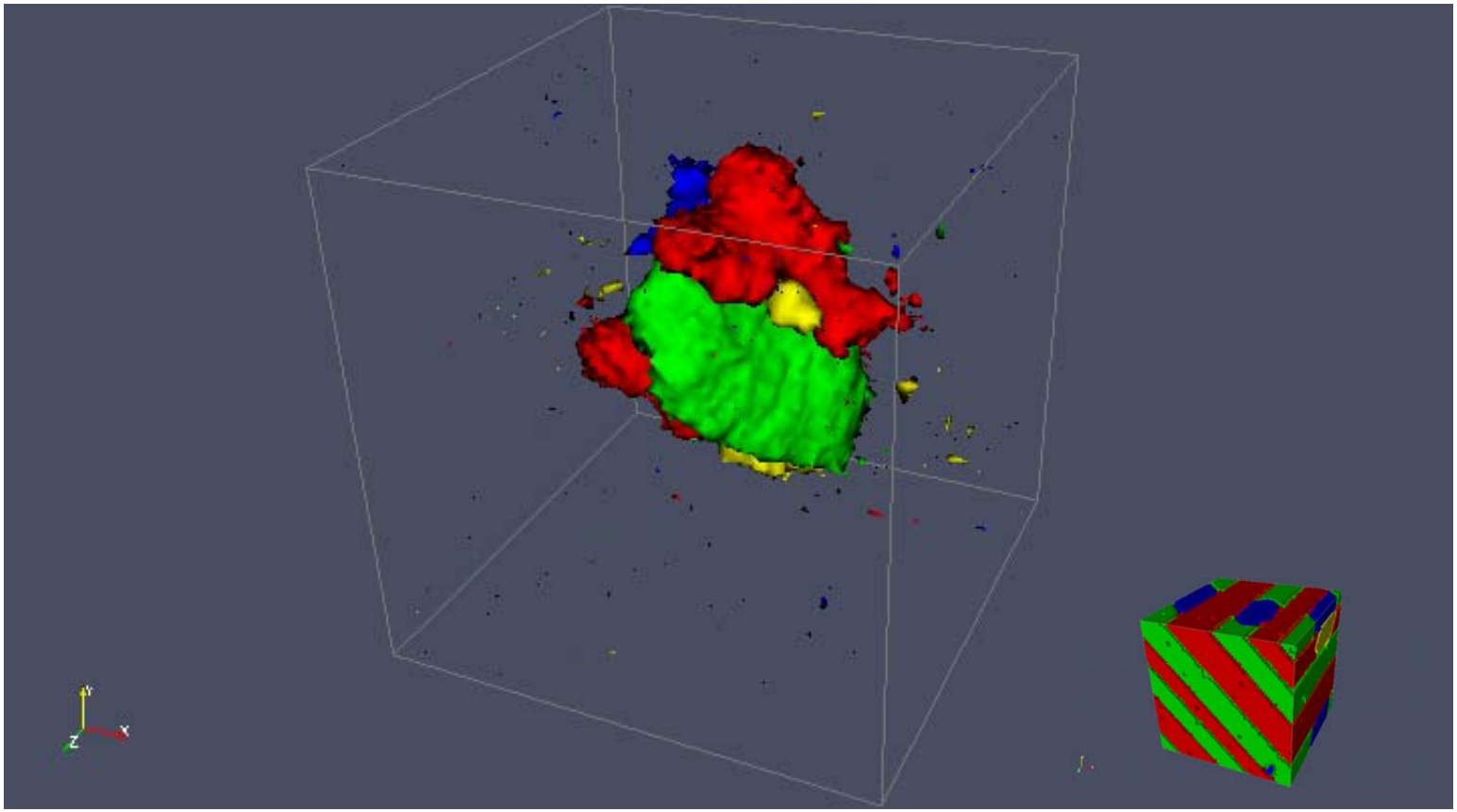

Nucleus along the minimum energy path

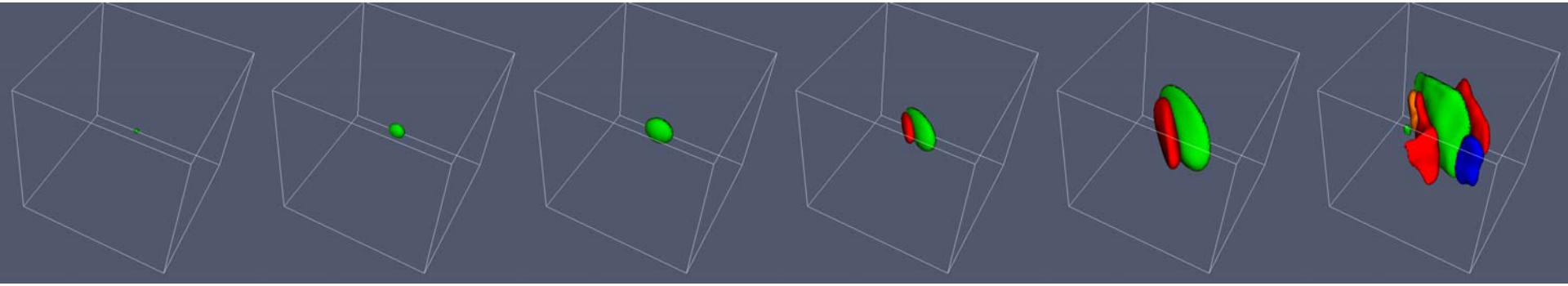

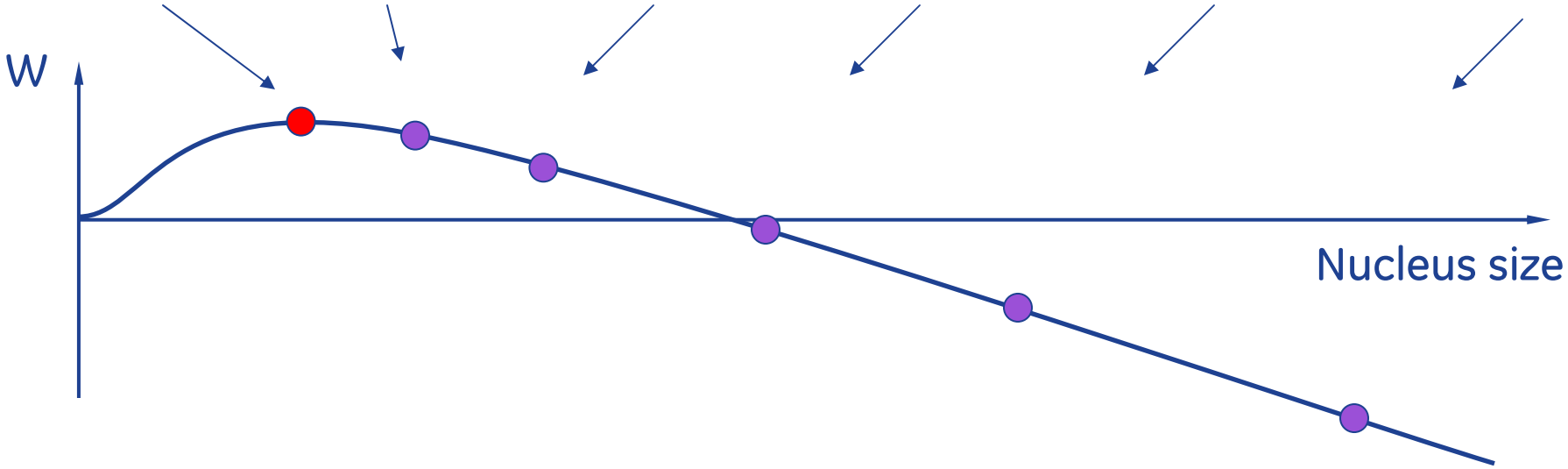

Critical configurations

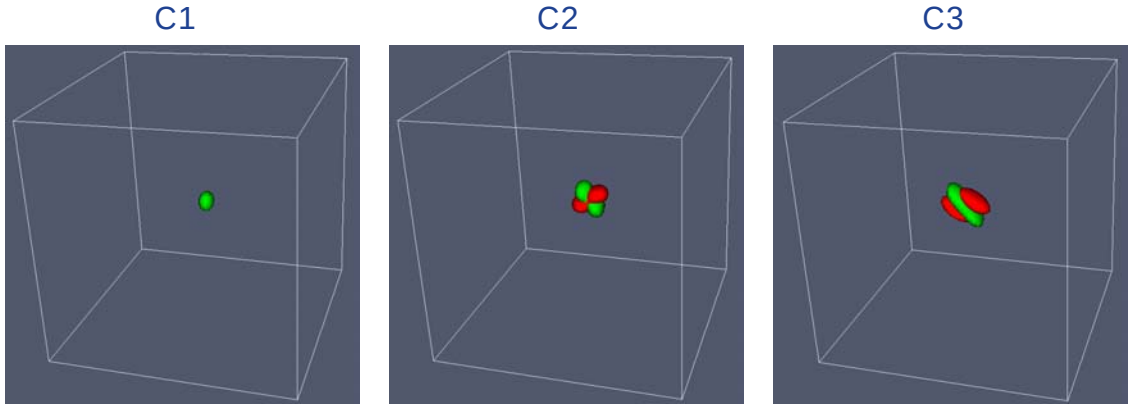

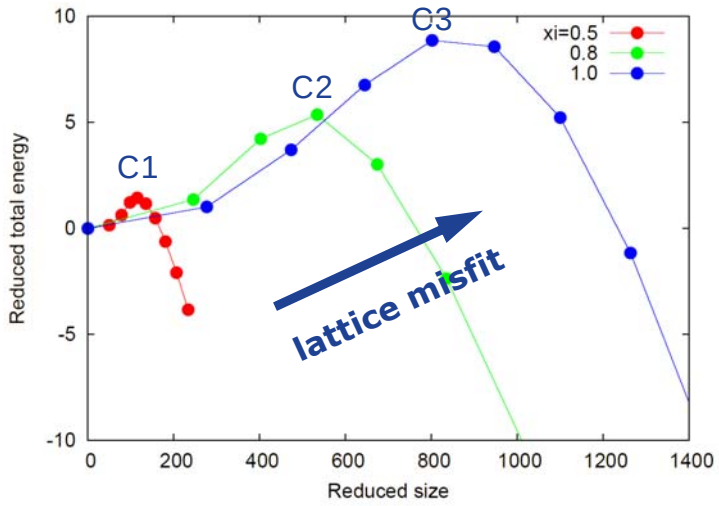

(Shen, Li, Wang, Met Trans, 2008)

What else can we do?

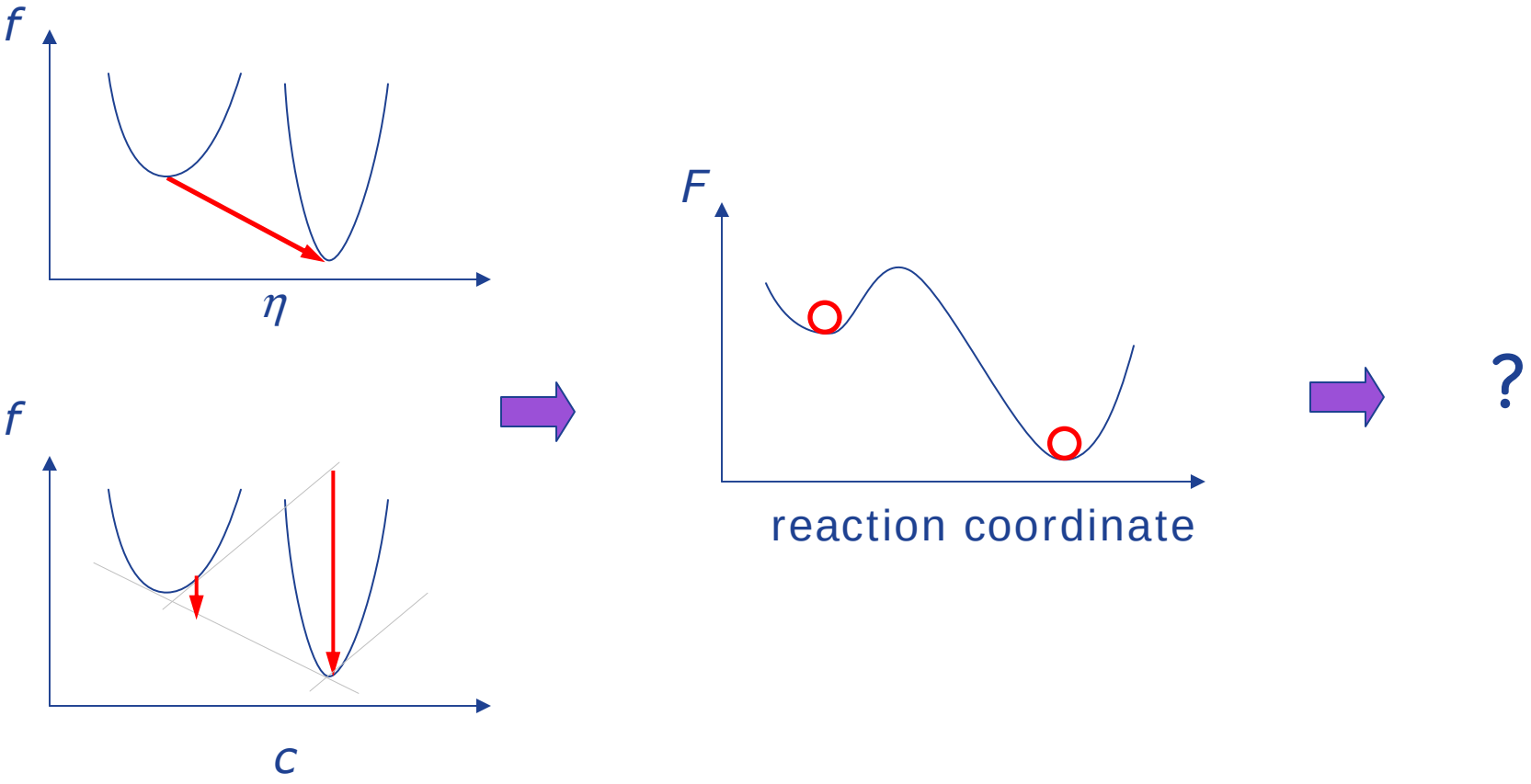

Shearing of gamma prime

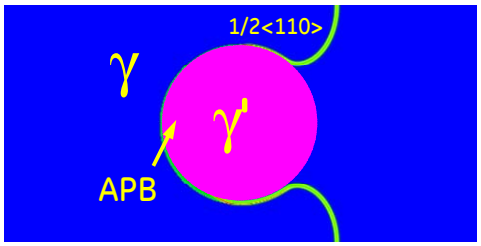

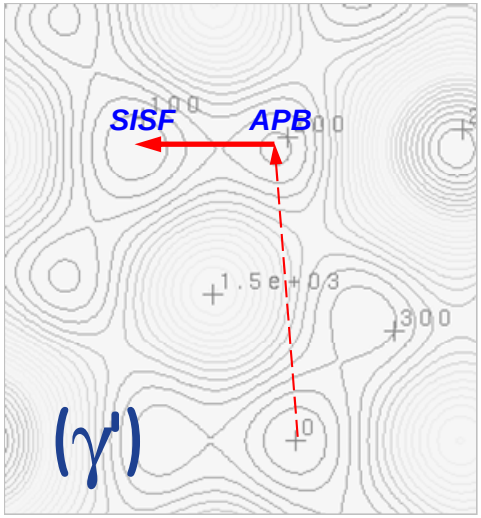

APB → SISF

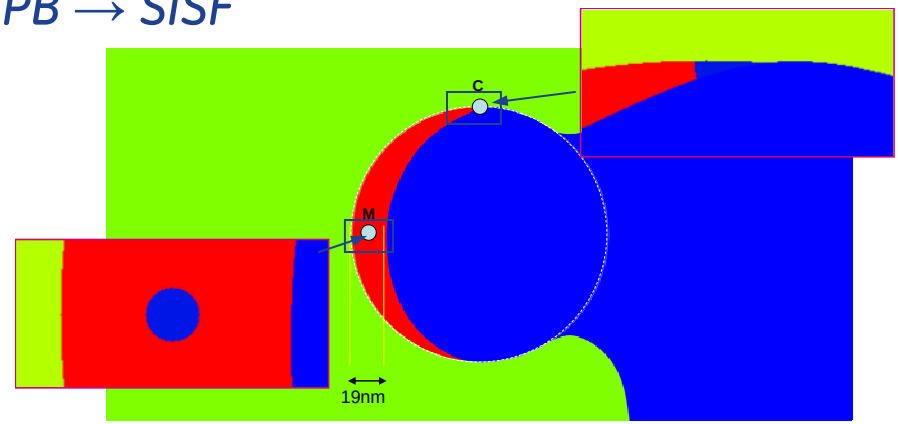

1eV ~ 39kT at R.T.

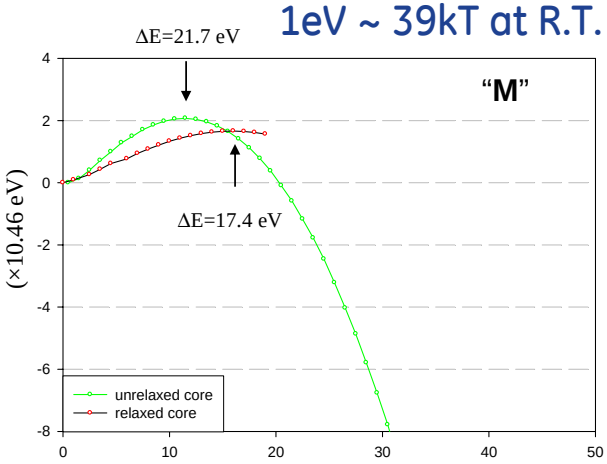

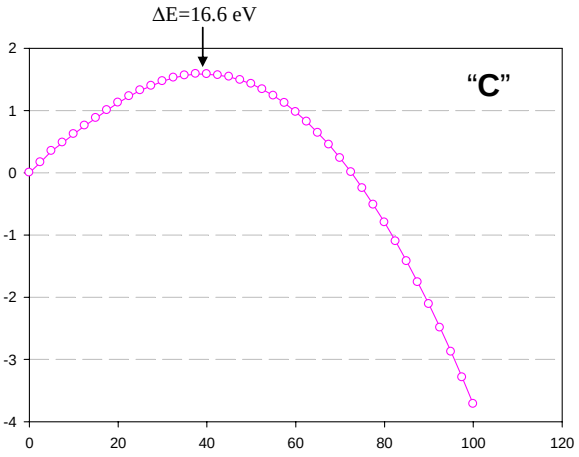

(Shen, Li, Mills, Wang, 2007)

Dislocation core structures

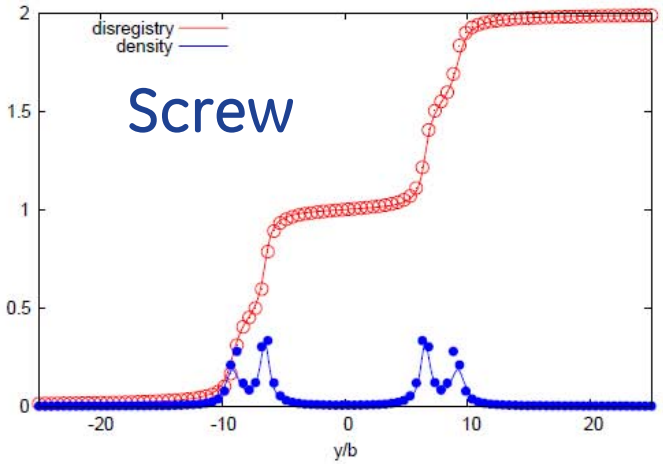

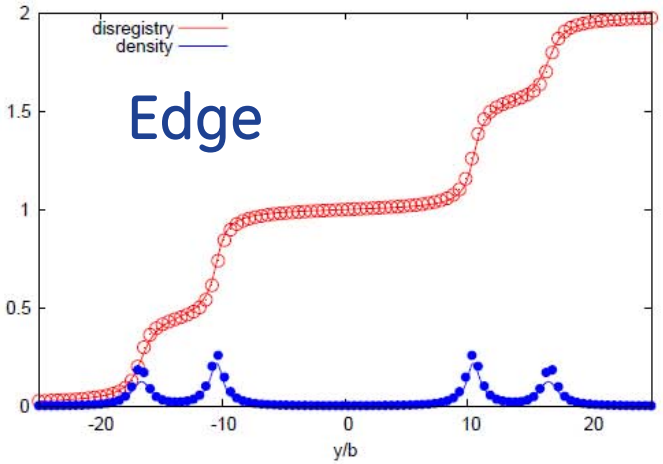

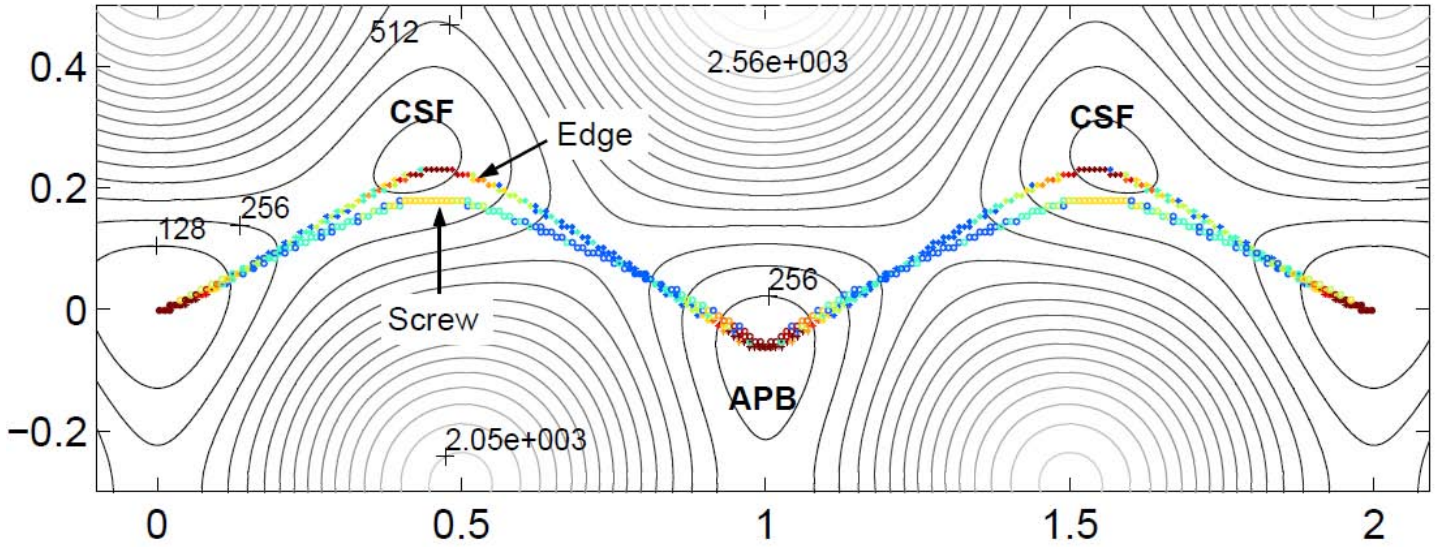

imagination at work

SISF formation at low temperature & high stress

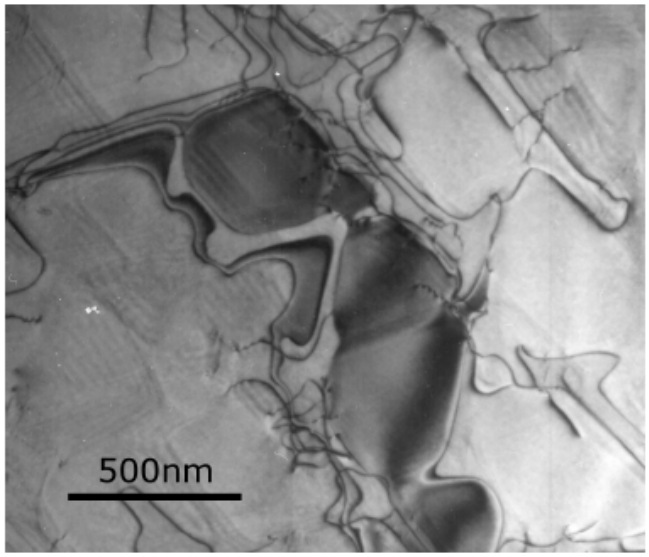

Fig. 1. TEM micrograph showing a {111} section through TMS-82+ superalloy deformed in tension to 1.4% strain at 750°C and 750MPa. Evidence of primary creep is visible: γ channels are populated with $\frac{a}{2}\langle 110\rangle$ dislocations, an $a\langle 112\rangle$ ribbon has nucleated in the matrix and sheared several γ' precipitates leaving intrinsic and extrinsic faults.

(Rae & Reed, 2006)

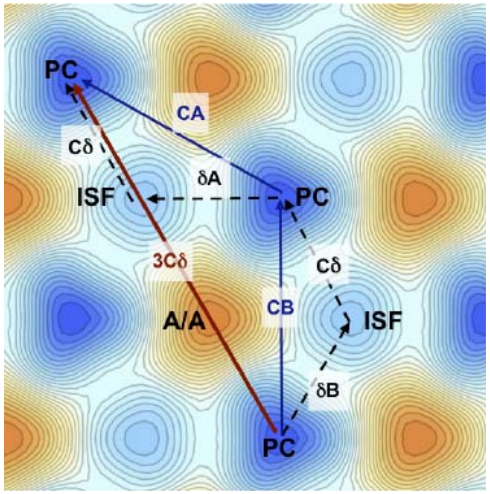

γ

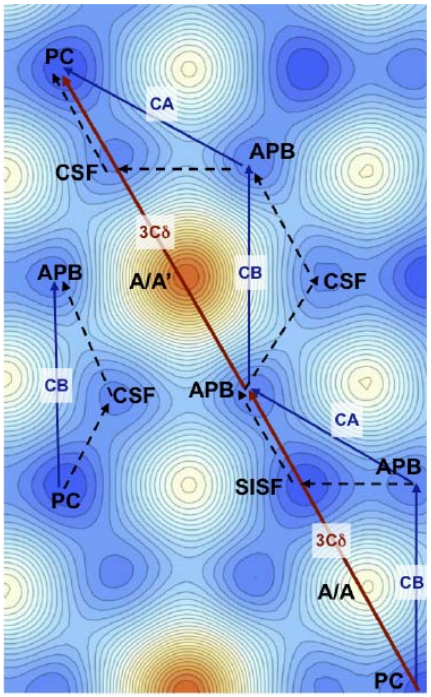

γ'

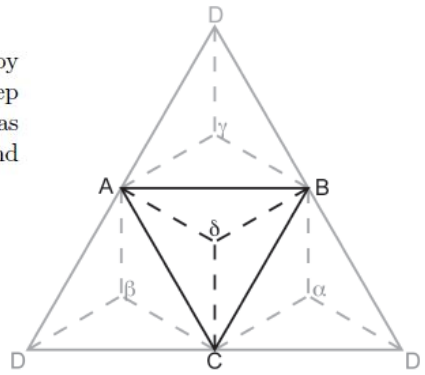

(Vorontsov, Shen, Wang, Dye, Rae, Acta mater 2010)

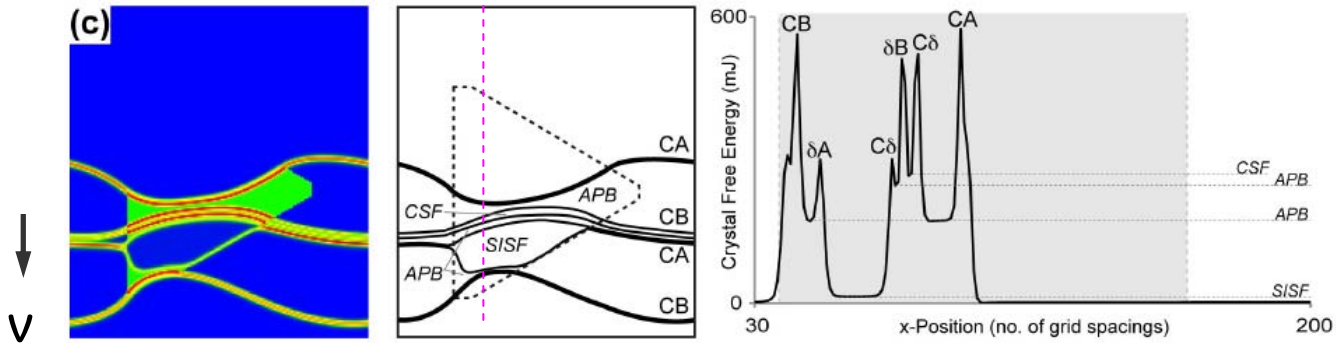

750MPa

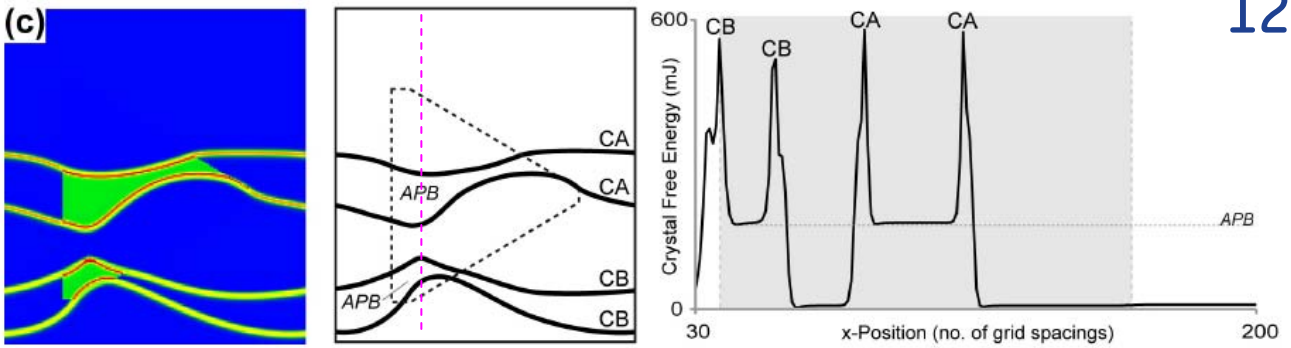

1250MPa

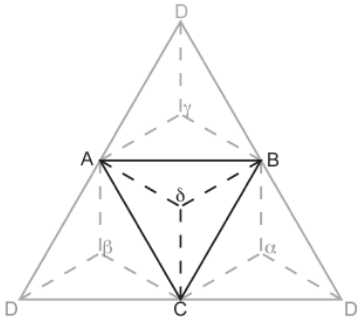

(Vorontsov, Shen, Wang, Dye, Rae, Acta mater 2010)

6Cδ core structures under applied stress

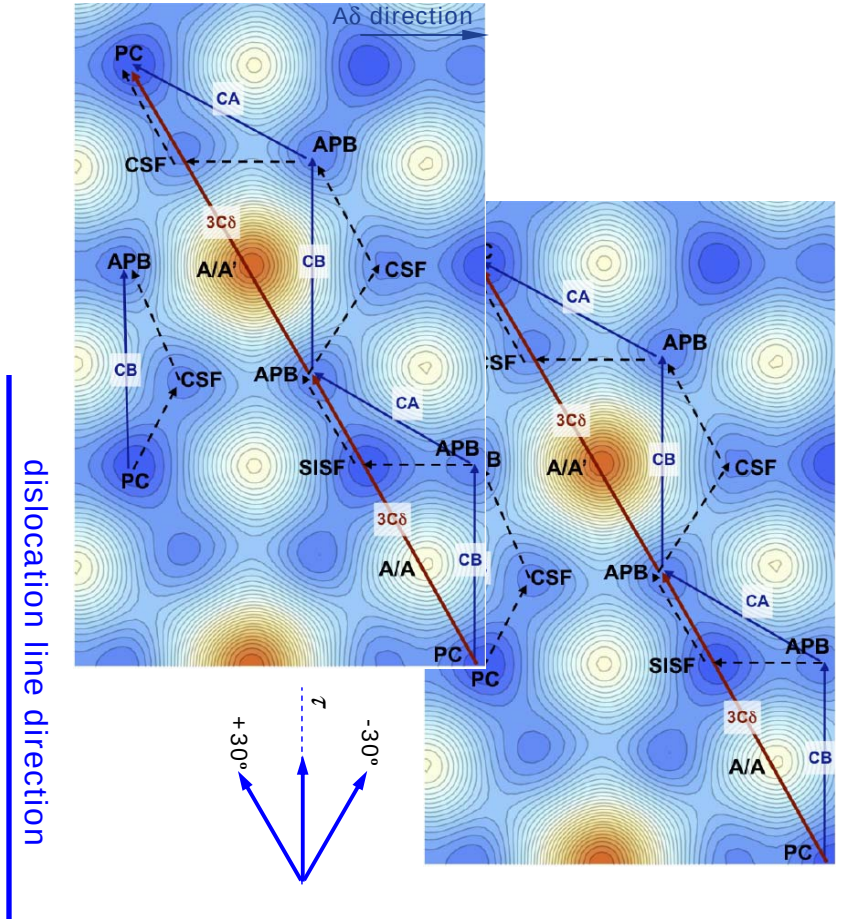

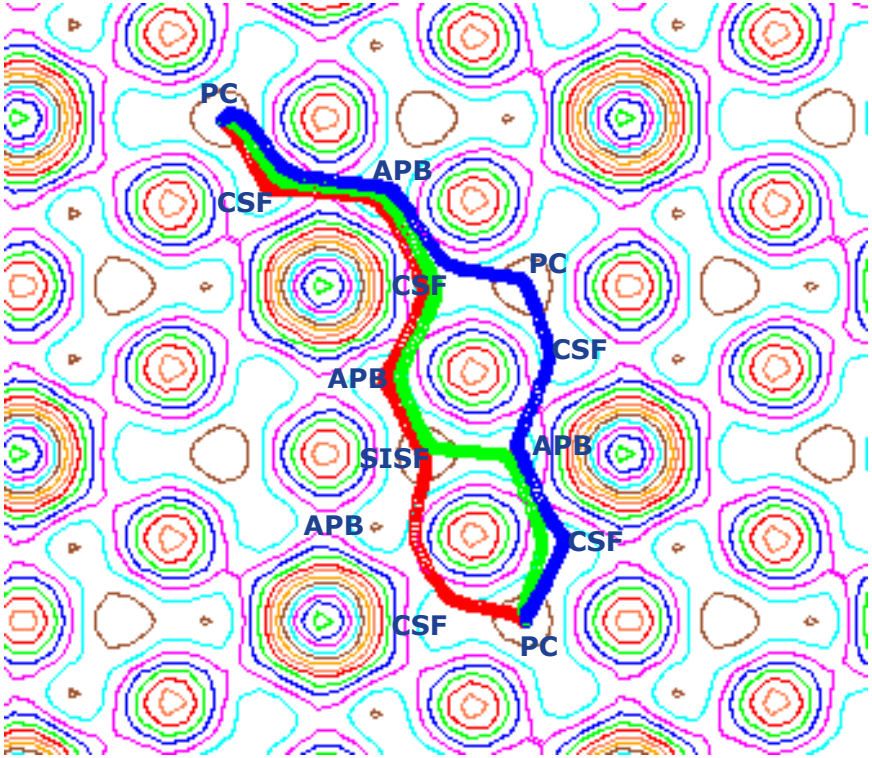

-30°; **τ1=0 < τ2 < τ3**

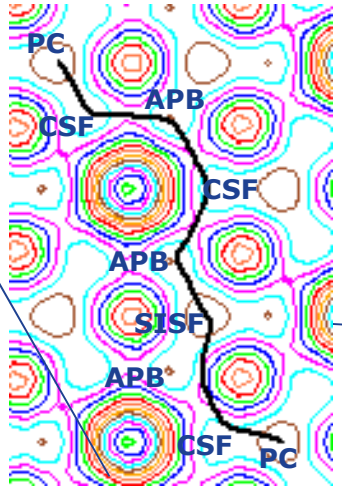

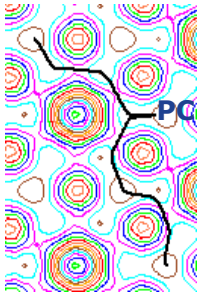

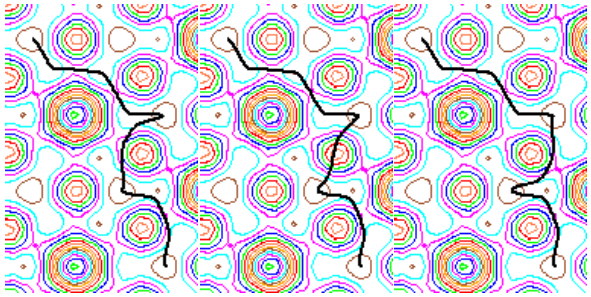

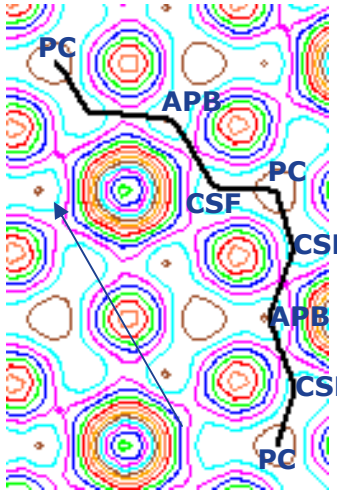

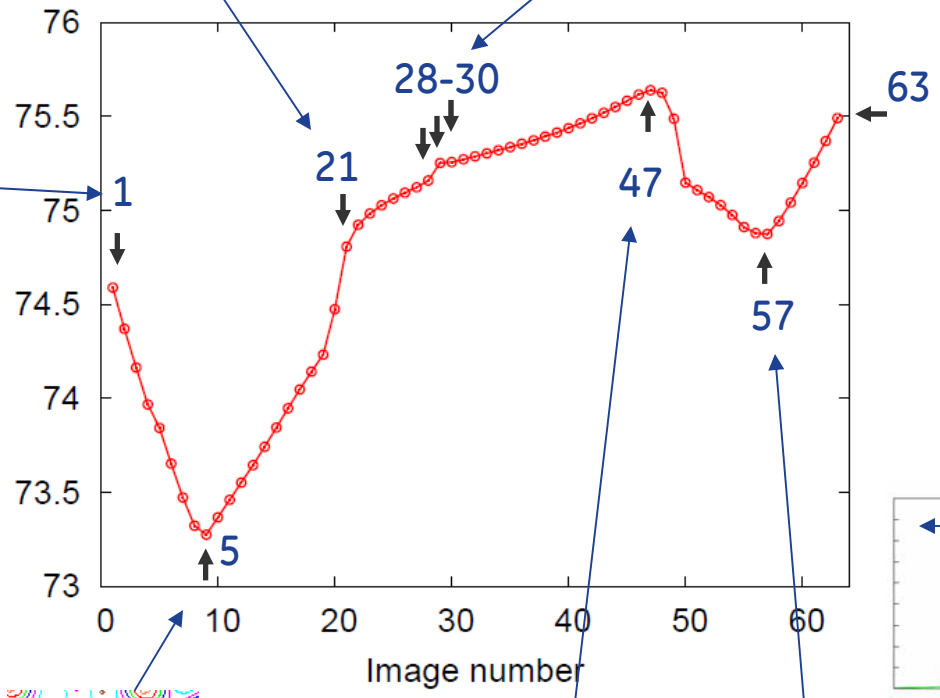

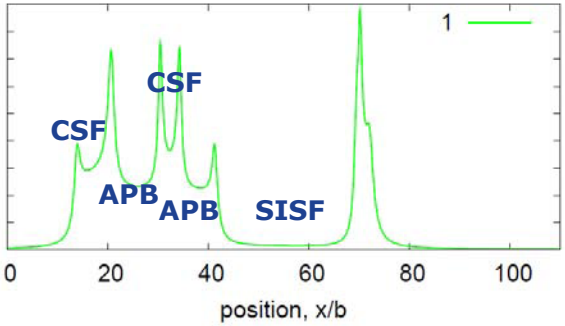

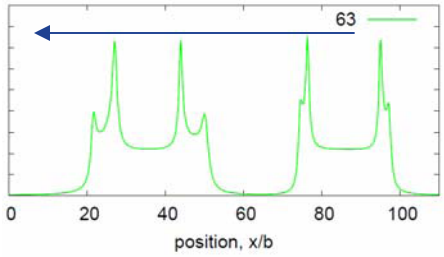

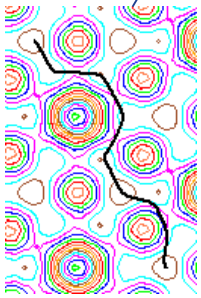

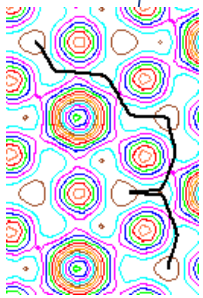

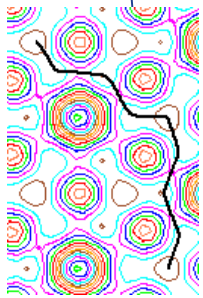

imagination at work

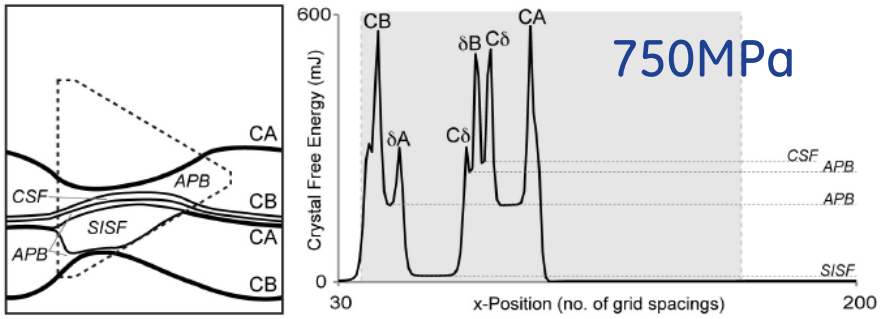

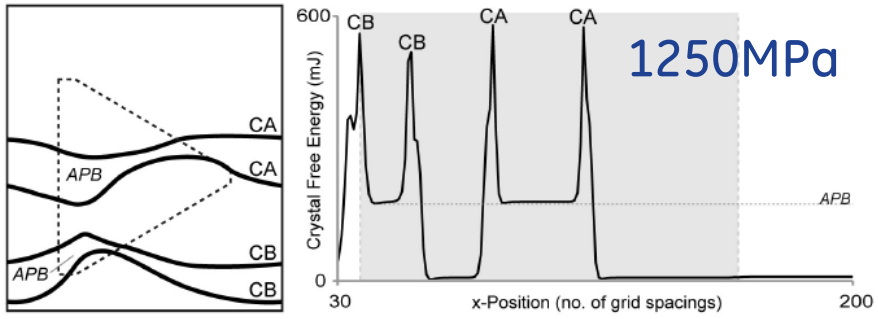

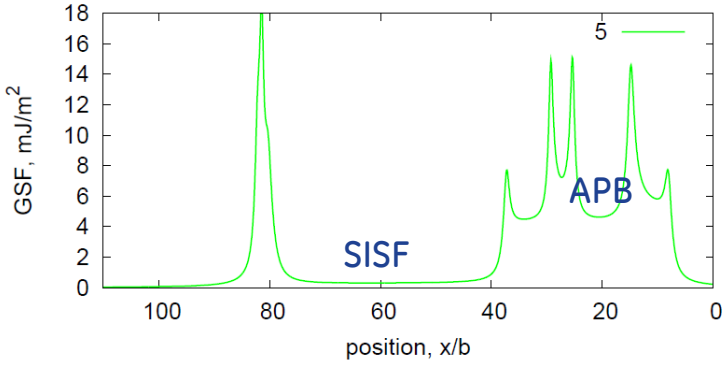

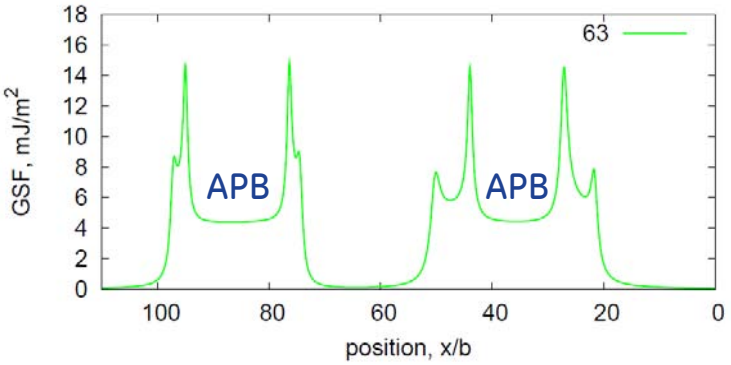

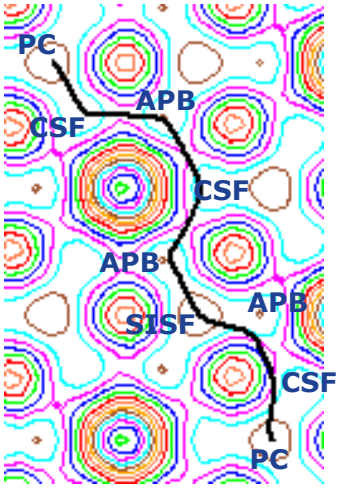

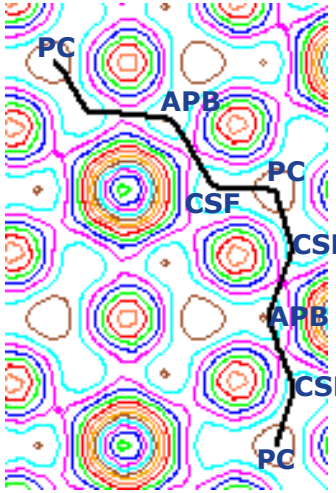

imagination at work

Summary

Non-classical nucleation theory + NEB is a quite open platform to study nucleation in some details

- greater flexibilities to handle nucleus structure details
- leverage new techniques from phase-field community
- combine new data from other computational methods (ab initio, CALPHAD) or from experiment (e.g., 3DAP)
- at thermodynamic level. Perhaps the only way in the near future to handle chemically complex (multi-component) alloys

Commonality with other 'non-nucleation' problems

Can we control embryo properties?

GJ Shiflet

SJ Poon, EA Starke, A. Zhu, M. Widom (CMU)

M.Gao, A. Csontos, B. Gable, A Cheung

UVa; Charlottesville, VA

….it is assumed that solids are so complex that it is better to make approximations first, and then try to show they are consistent with the basic rules of quantum mechanics, and that they yield properties consistent with measured values.

John Gilman “Electronic Basis of the Strength of Materials”

Effect of Trace Additions Cd, In and Sn on the Interfacial Structure and Kinetics of Growth of q' Plates in Al-Cu Alloy; R Sankaran and C Laird, Materials Science and Eng. 1974.

1- Nucleation of θ' takes place by the coalescence of mobile impurity –Cu– vacancy clusters and growth of the precipitates by the movement of these clusters [Hardy 1950; Nobel 1968]

2- Trace elements modfy the α:θ' interface giving an easier match with the matrix lattice, so that the critical size and energy barrier height for nucleation are reduced [Silcock et al; 1955 and Hardy 1956]

3- In the presence of impurity elements, vacancies in the quenched Al-Cu alloy condense to form finer distribution of dislocation loops. An increased density of of θ' precipitate can result from their nucleation on the loops.[Nuyten 1967]

Effect of lattice disregistry variation on the late stage phase transformation behavior of precipitates in nickel-aluminum-molybdenum alloys. Conley, J. G.; Fine, M. E.; Weertman, J. R. Acta Metallurgica (1989), 37(4), 1251-63.

Use controlled lattice disregistry (tune Al+Mo) to affect precipitate morphology (cubes vs spheres) and coarsening kinetics

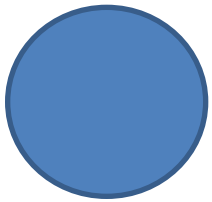

$$\delta = (a_p - a_m)/a_m$$

mostly affected Ni matrix

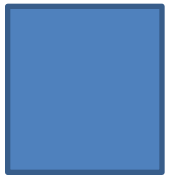

A variety of exptl. techniques were applied to examine how compositional variations in lattice disregistry (**d) affect the coarsening kinetics and particle morphol. evolution of g'-particles in several Ni-Al-Mo alloys. Mo segregates to and increases the lattice parameter of the g-matrix in 2 phase Ni-base Al alloys. Controlled ternary addns. of Mo to dil. binary Ni-Al alloys permit variation of the lattice parameter disregistry between the Ni-base solid soln. and the Ni3Al ordered ppts. Compns. were selected to maintain an approx. .apprx.10 vol.% of the 2nd phase. The coarsening rate of the g'-phase decreases with decreasing lattice disregistry and decreasing Al/Mo ratio. The implications of this observation are discussed with ref. to differences in solid soly., diffusivity, and interfacial energy. The g'-particle shape in low coherency strain alloys is spherical and independent of particle size. In an alloy exhibiting appreciable d and coherency strain, the g'-particles evolve from randomly distributed spheres to sharply aligned cubes and rods as particle size increases. d Increases with aging time. Compression creep of [100] single crystals at 750° did not affect the shape of particles in the low coherency strain alloys while in a higher disregistry alloy, a highly oriented array of plates grew with long edges perpendicular to the applied stress direction. These findings are discussed with regard to stress and thermodn. considerations.**

The precipitate Ω-phase in aluminum-copper-magnesium-silver alloys.
***Muddle, B. C.; Polmear*, I. J.** Acta Metallurgica (1989), 37(3), 777-89.

The combined addn. of small concns. of Ag and Mg to Al-Cu alloys promotes pptn. of a phase, **Ω–πηασε, that forms as thin, hexagonal-shaped plates on matrix {111ña planes. The structure, morphol., and compn. of this phase were examd. in 2 quaternary alloys using TEM, electron microdiffraction and energy dispersive x-ray spectroscopy. Electron microdiffraction patterns from the ppt. phase are indexed in accordance with an orthorhombic structure (a = 0.496 nm, b = 0.859 nm, c = 0.848 nm) and the orientation relationship between ppt. and matrix lattices is such that (001)W||(111)a and [010]Ω||[10.hivin.1]a. The morphol. of the ppt. phase is consistent with the intersection point group (2/m) defined by symmetry elements common to the 2 lattices in the obsd. orientation relationship. The plate shape parallel to (111)a is detd. by a pinacoid parallel to the common 2-fold axis, [010]W. The hexagonal form in this plane is defined by 4 equiv prism facets with a common direction perpendicular to [010]W and the truncation of this prism section by a second pinacoid normal to this 2-fold axis. The 6 facets thus defined are equiv. geometrically and are assocd. with the hexagonal lattice on which the orthorhombic structure of the ppt. phase is based. Energy dispersive x-ray microanal. indicates that the Ag in quaternary alloys partitions to the W phase during aging and there is evidence that segregates at the interface with the matrix. On the other hand, Ag does not partition to the phase q' when it coexists with W in these alloys or is present alone in the ternary alloy Al-Cu-Ag. There is also evidence to suggest that Mg assocs. itself with the Ω phase.**

On the origin of the high coarsening resistance of Ω plates in Al-Cu-Mg-Ag Alloys.

Hutchinson, C. R.; Fan, X.; Pennycook, S. J.; Shiflet, G. J.. Department of Materials Science and Engineering, University of Virginia, Charlottesville, VA, USA. Acta Materialia (2001), 49(14), 2827-2841.

The thickening kinetics of **W plates in an Al-4Cu-0.3Mg-0.2Ag (wt.%) alloy were measured at 200, 250 and 300°C using conventional transmission electron microscopy techniques. At all temps. examd. the thickening showed a linear dependence on time. At 200°C the plates remained less than 6 nm in thickness after 1000 h exposure. At temps. above 200°C the thickening kinetics are greatly increased. At. resoln. Z-contrast microscopy has been used to examine the structure and chem. of the (001)W.dblvert.(111)a interphase boundary in samples treated at each temp. In all cases, two at. layers of Ag and Mg segregation were found at the broad face of the plate. The risers of the thickening ledges and the ends of the plates were free of Ag segregation. The necessary redistribution of Ag and Mg accompanying a migrating thickening ledge occurs at all temps. and is not considered to play a decisive role in the excellent coarsening resistance exhibited by the W plates at temps. up to 200°C. Plates transformed at 200°C rarely contained ledges and usually exhibited a strong vacancy misfit normal to the plate. A large increase in ledge d. was obsd. on plates transformed at 300°C, concomitant with accelerated plate thickening kinetics. The high resistance to plate coarsening exhibited by W plates at temps. up to 200°C, is due to a prohibitively high barrier to ledge nucleation in the strong vacancy field normal to the broad face of the plate. Results also suggest that accommodation of the large misfit that exists normal to the broad face of the plate is unlikely to provide the driving force for Ag and Mg segregation.**

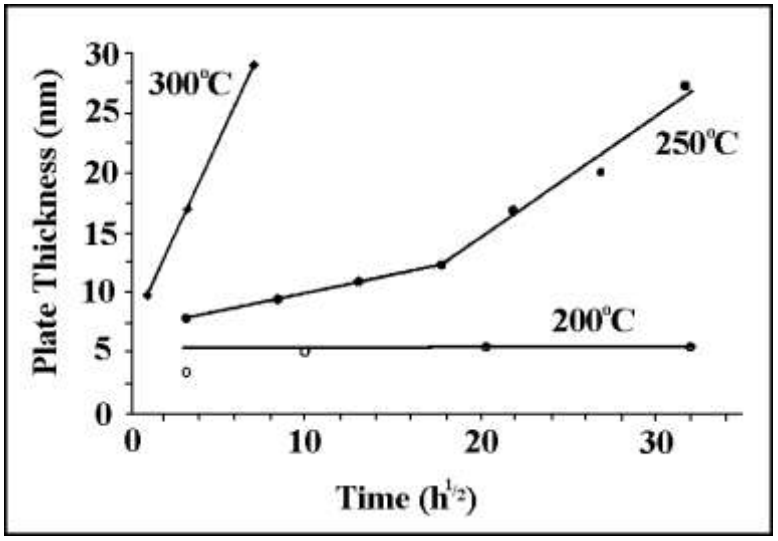

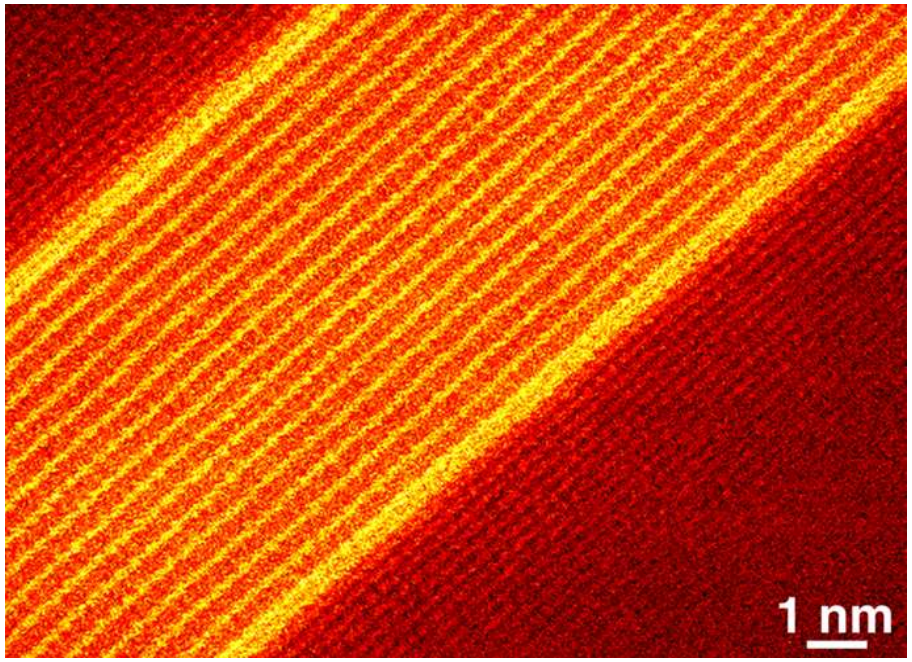

3D-AP: Al-Cu-Mg-Ag

Hono et al: Al-1.9Cu-0.3Mg-0.2Ag (at%), aged at 180 degC

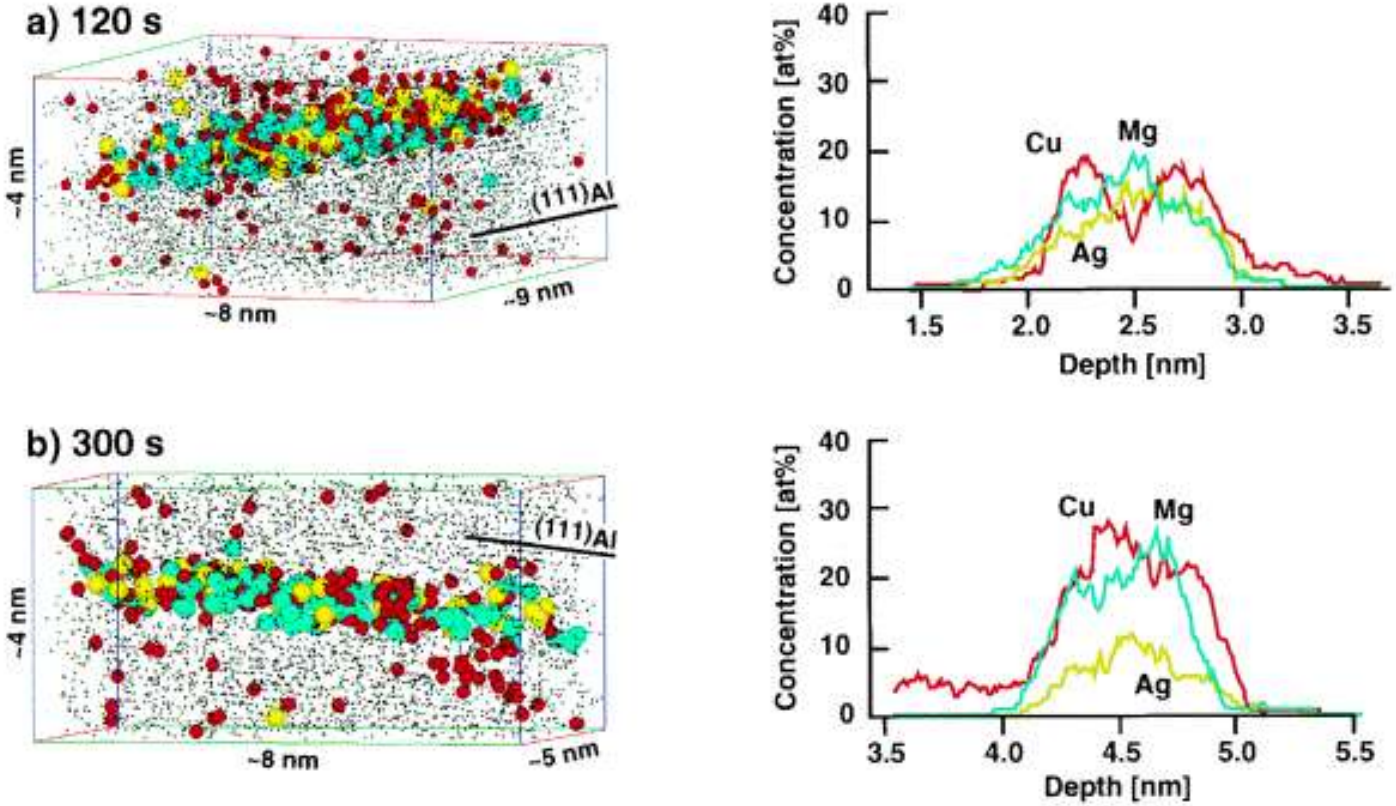

Heterogeneous nucleation of δ ‘ on dislocations in a dilute aluminum-lithium alloy.

Wang, Z. M. & Shiflet, G. J.. Metall and Materials Trans A: (1996), 27A(6), 1599-1609.

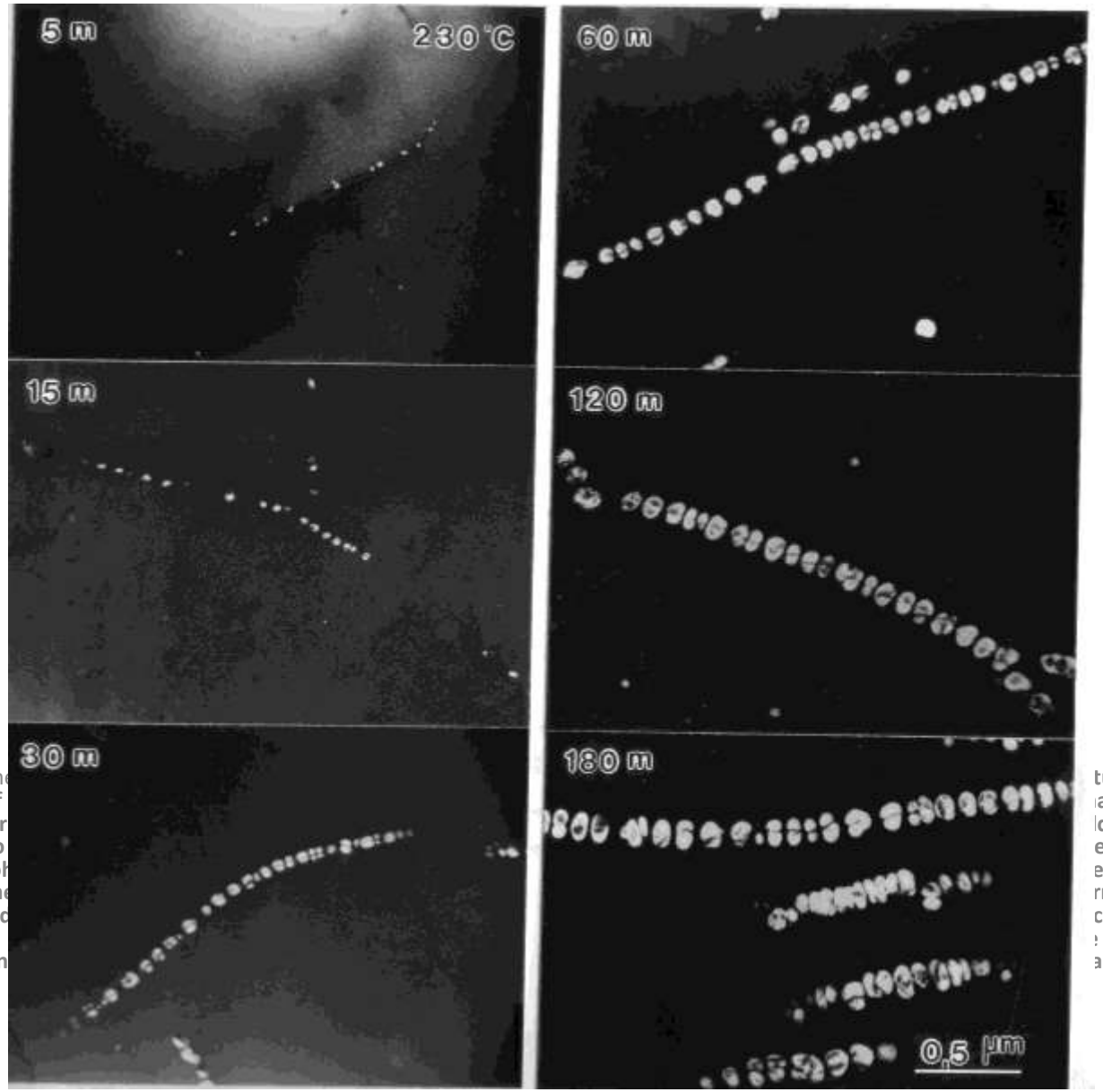

The
of
pr
co
coh
the
and

in

tudy
at d
ld is
e on
e for
rrier
cally,

ain,

δ ' nucleation and growth on low-angle dislocation boundaries in Al-Li.

Wang, Z. M.; Shiflet, G. J.. Physica Status Solidi A: (1995), 149(1), 105-22.

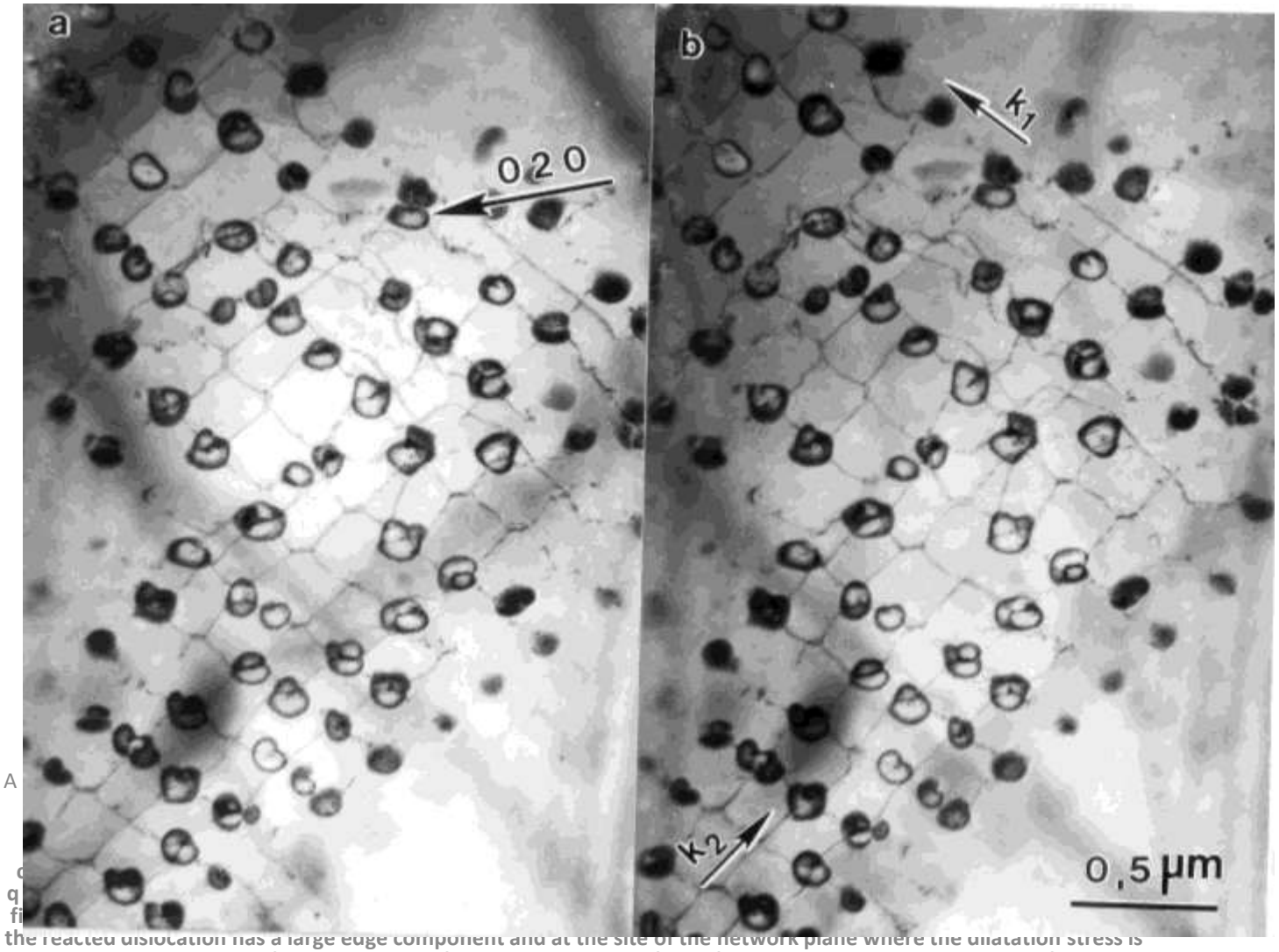

A

q

fi

the reacted dislocation has a large edge component and at the site of the network plane where the dilatation stress is compressive. This is confirmed by calcn. of the dilatation stress field of the dislocation nodes which also further clarifies and is consistent with the exptl. observations.

The effect of plastic deformation on aluminum-copper-lithium Al_2CuLi (T1) precipitation. Cassada, W. A.; Shiflet, G. J.; Starke, E. A., Jr.; Metallurgical Transactions A: Physical Metallurgy and Materials Science (1991), 22A(2), 299-306.

The enhancement of T1 pptn. in Al-Li-Cu alloys by plastic deformation prior to aging (i.e., cold work) and the subsequent increase in alloy strength is investigated. The increased understanding of the role of matrix dislocations in the nucleation and growth of T1 plates, discussed in a previous paper, permits a detailed study of the phenomenon. The effect of different levels of plastic strain on the T1 particle distributions as a function of aging time at 190° **is quantified, and the subsequent influence on tensile properties is thereby described. Plastic deformation decreased the T1 plate length and thickness, increased the no. d. by .apprx.2 orders of magnitude, increased the yield strength by 100 MPa, while simultaneously reaching peak strength in 20% of the time required without plastic deformation.**

Structural Evolution in $Al_{85}Ni_7Gd_8$

- Non-isothermal DSC Heating

before the 1st stage

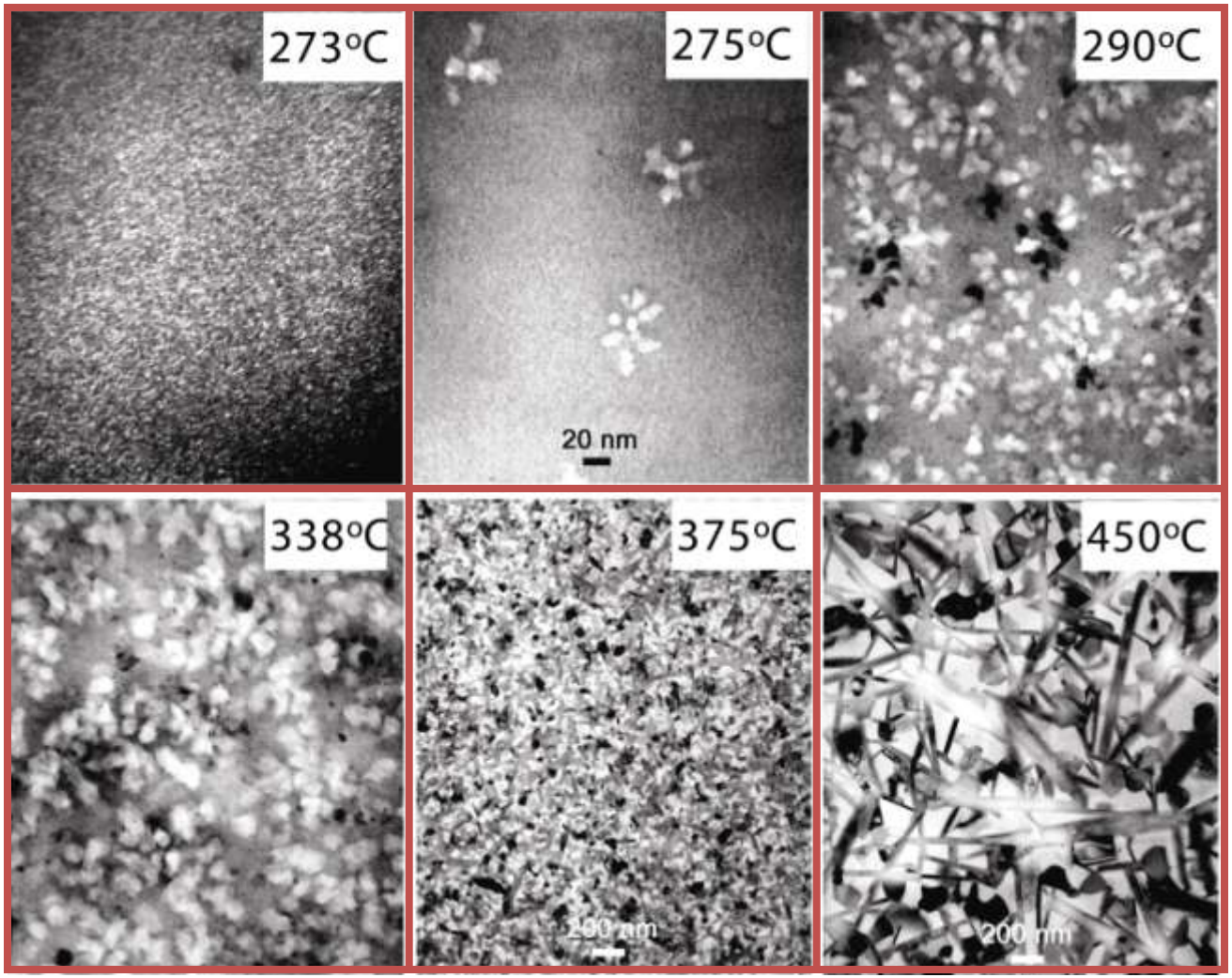

1st stage finished

2nd stage

3rd stage

4th stage

Crystalline Phase Formation Sequences at ≤ 250°C

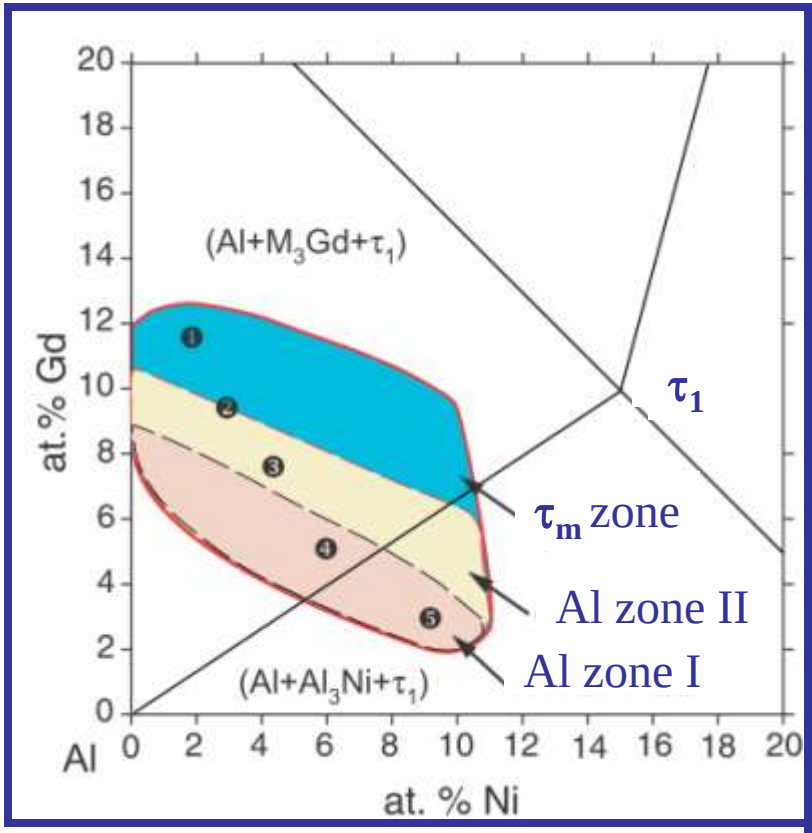

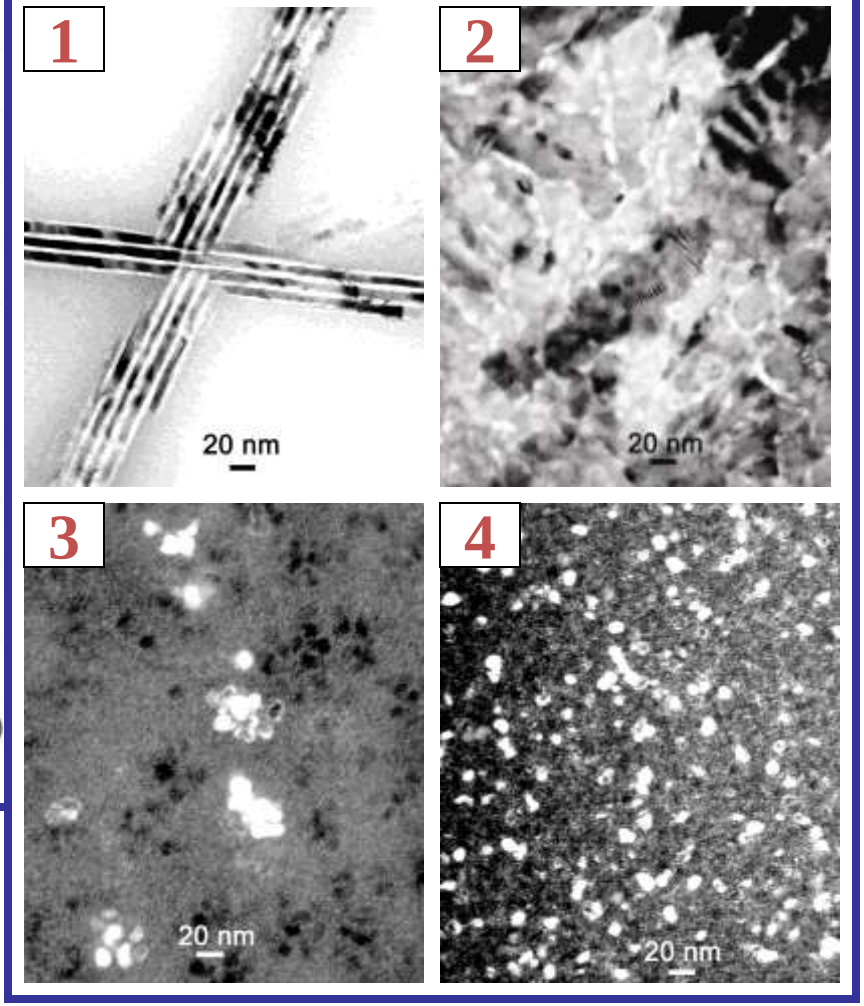

$\tau_m = Al_{34}NiGd_8$

$Al_{90}Fe_5Gd_5$ tensile fracture

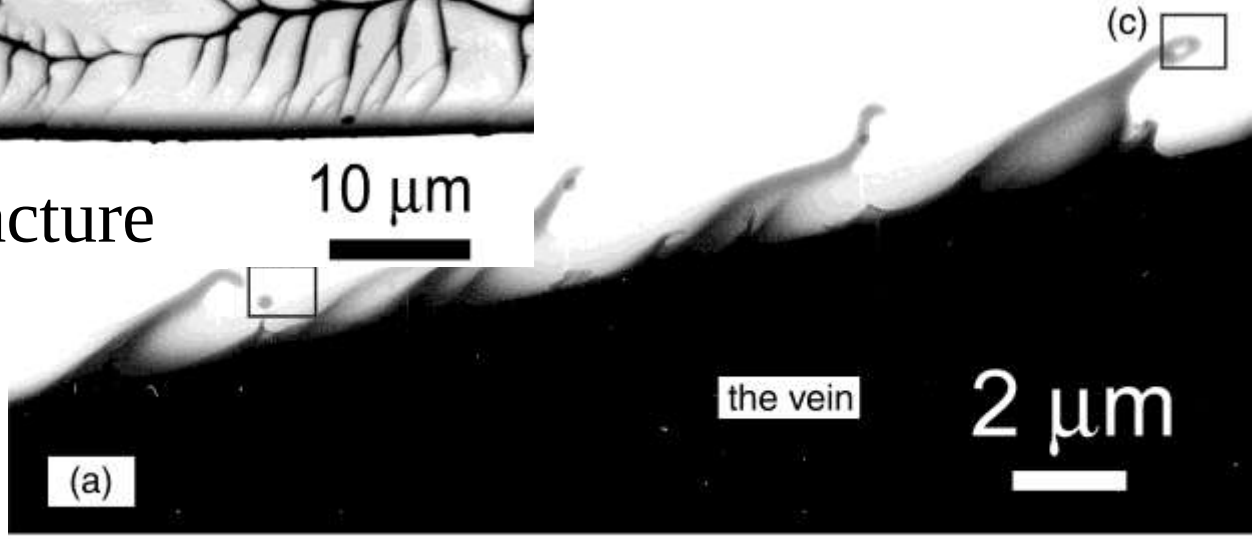

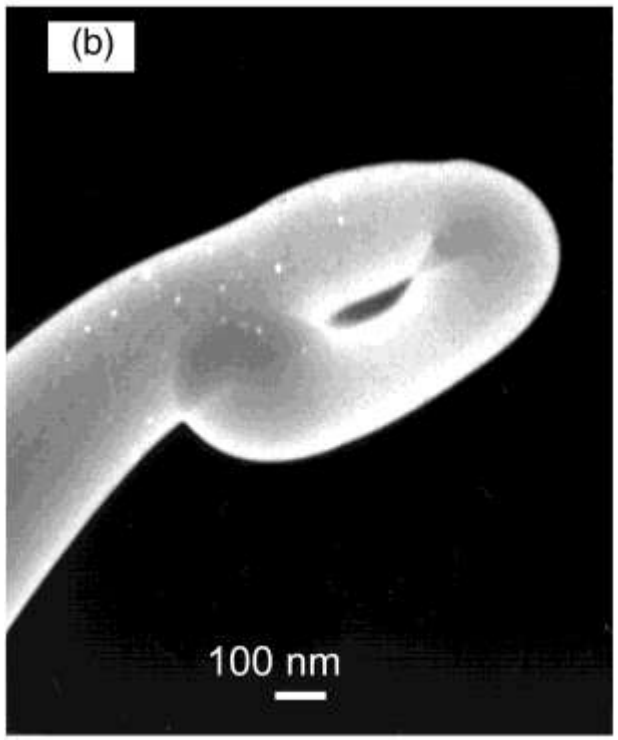

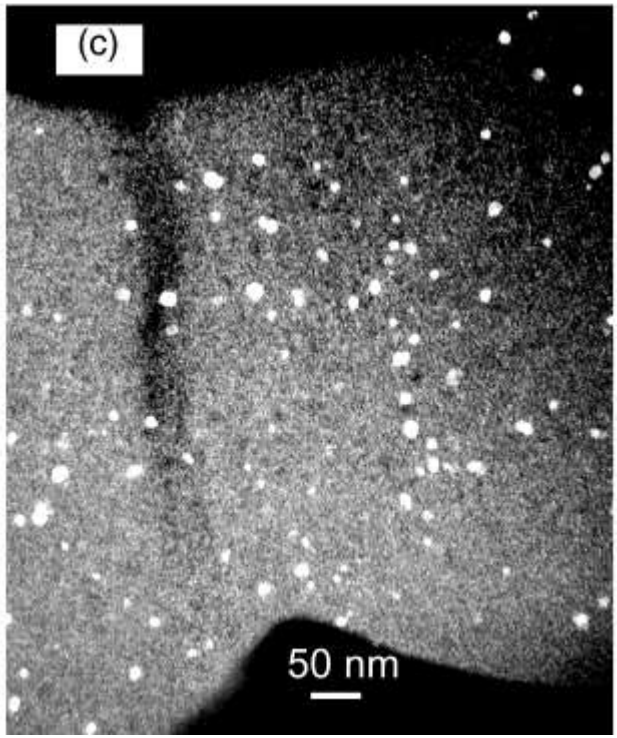

On the Roles of Clusters during Intragranular Nucleation in the Absence of Static Defects

Nie, Muddle, Aaronson, Ringer and Hirth Metall. Mater. Trans, 2002.

- Clusters form and disappear on timescale shorter than embryos
- clusters another form of nucleation site and so are involved in 'cluster-aided intragranular nucleation' heterogeneous nucleation
- reduction of shear strain energy attending precipitate nucleation through segregation of trace solutes and vacancies bound to them to regions of the precipitate interfaces under compressive or tensile strains

Based on all we learned about bonding from amorphous metals – can we transfer ideas to nucleation in conventional alloys?

Balance between calculations and experiments*

- **Focused** calculations are necessary
  - Phase diagrams (partial phase diagrams)
  - Element associations (electronic)
  - Cluster formation f(T)
  - Elastic properties of clusters
  - If working with a modeler –they must work on the problem!
- Experiments are essential
  - Validation of calculations by small adjustments
  - Proof of concept predictive NOT postdictive

*for Shiflet

Information we are interested in from EELS

Near edge

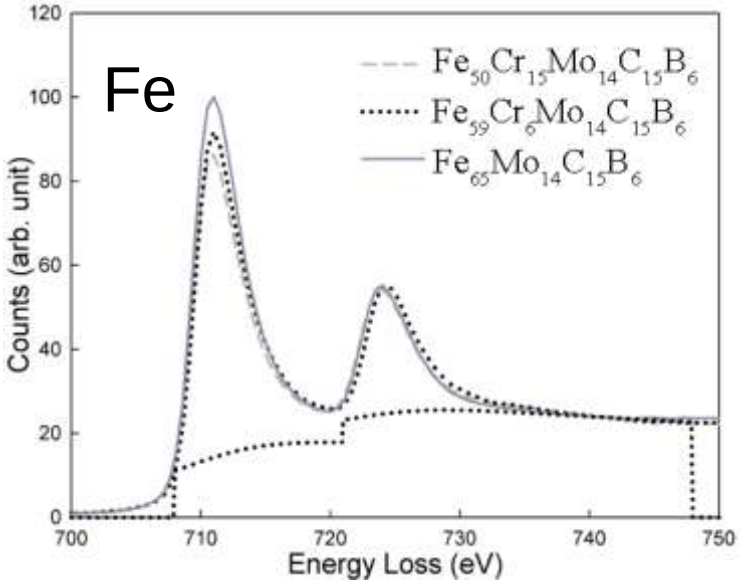

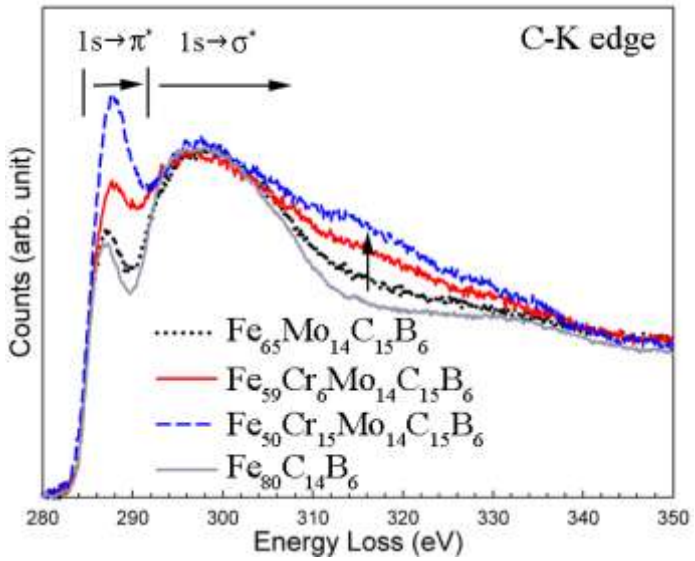

local electronic structure

Extended edge

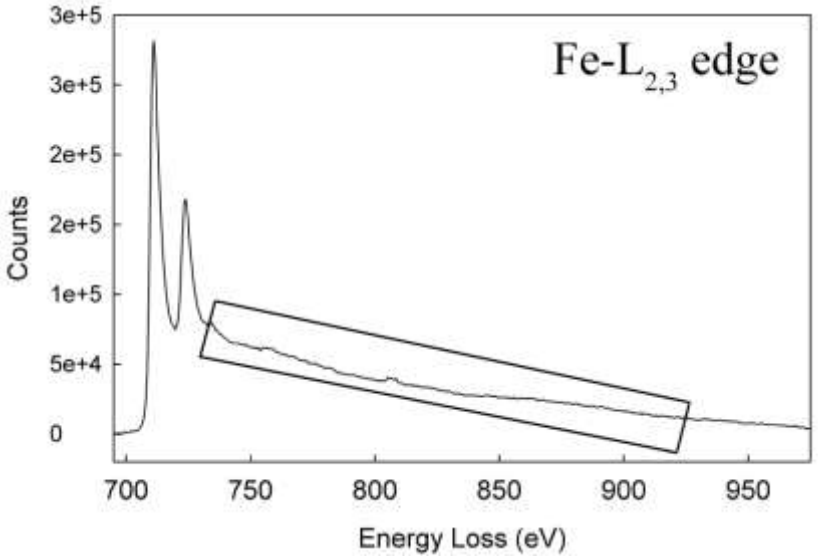

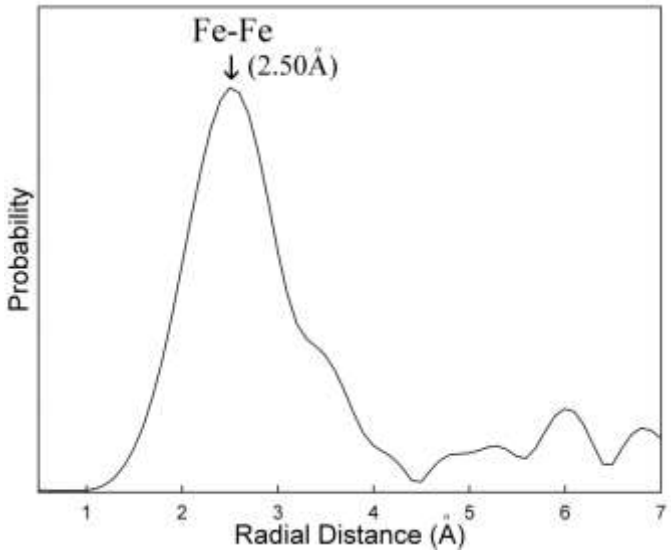

local atomic structure

→ **nearest neighbor atomic distance**

Aluminum nanocrystals form at high densities – 10^{18} cm^{-3}

Fe and Gd rejected into the matrix forming shells

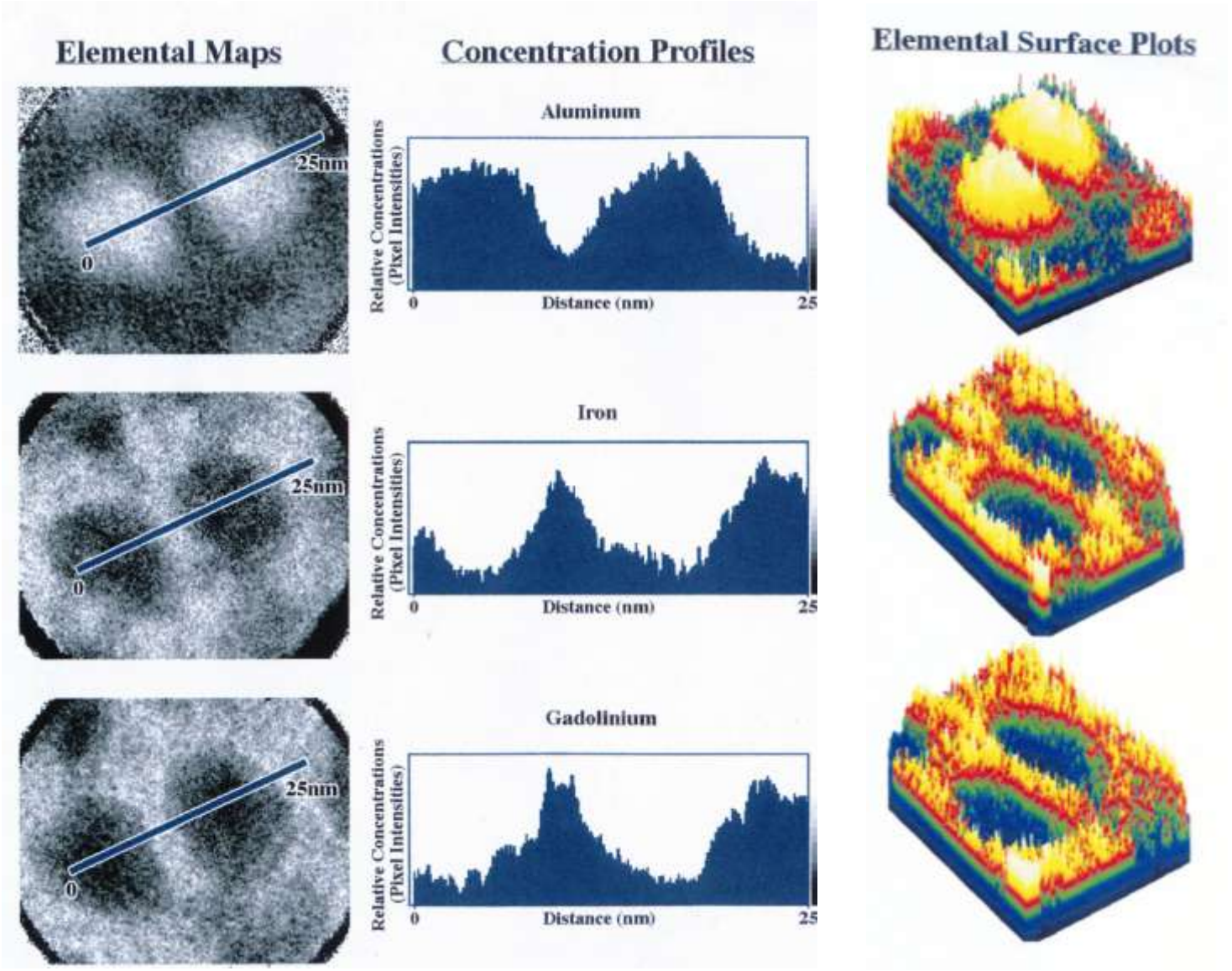

Zero Loss and Plasmon

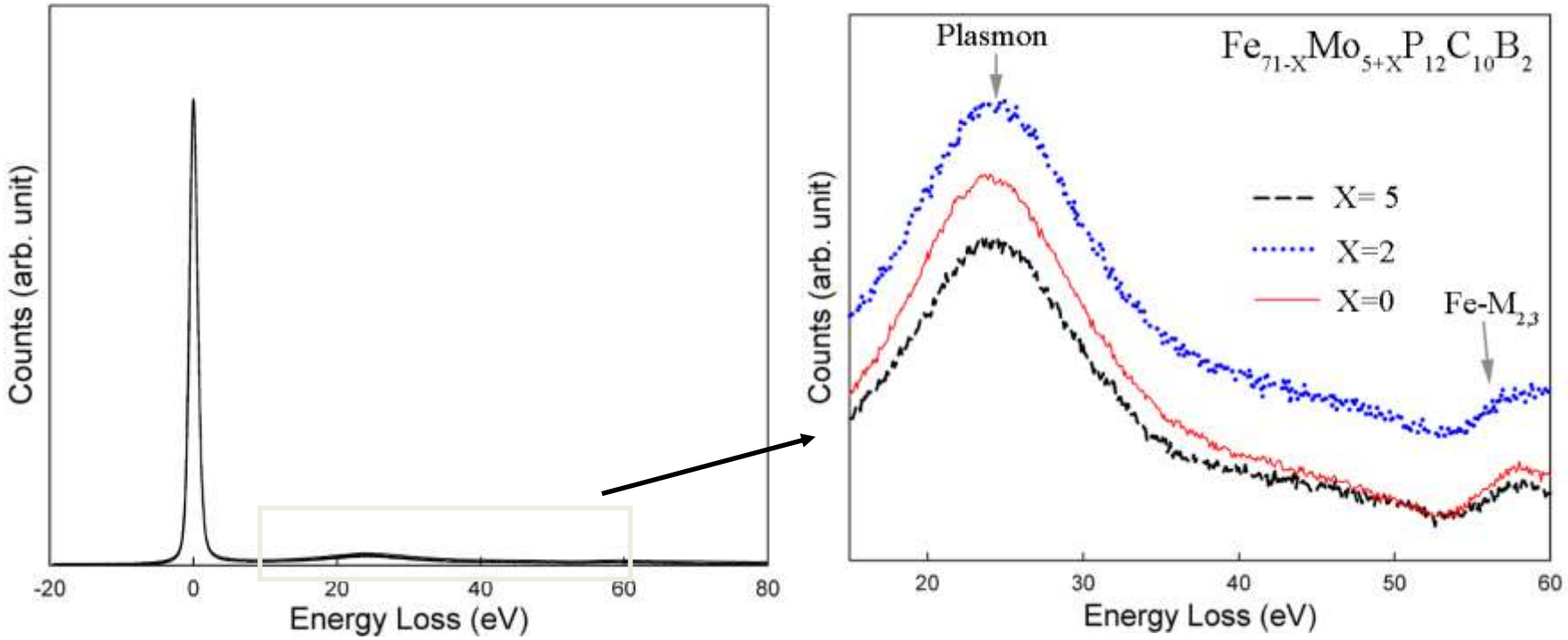

No difference is observed for plasmon peak among as-spun $Fe_{71-X}Mo_{5+X}P_{12}C_{10}B_2$ ribbons

Plasmons and Material Properties

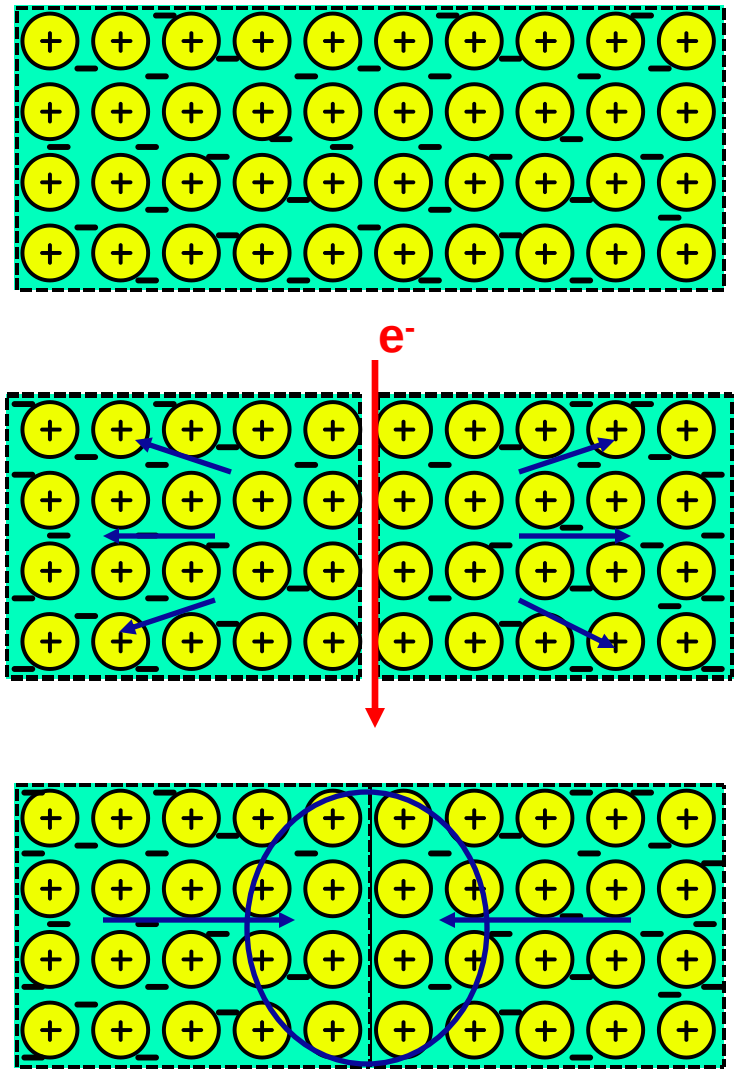

• **Collective oscillation of the valence electron density that occurs at a resonance angular frequency ω_p with a plasmon energy E_p given by:**

$$E_p \cong \hbar\omega_p ,$$

where $\omega_p = [ne^2/(\varepsilon_0 m)]^{1/2}$, n is the valence electron density, e is the electron charge, ε_0 is the permittivity of vacuum, h is Planck's constant, and m is the electron mass.

• **The relation between E_p and n allows one to determine material properties that are governed by the valence electron density.**

Scaling of experimental and calculated single-crystal B_m with E_p

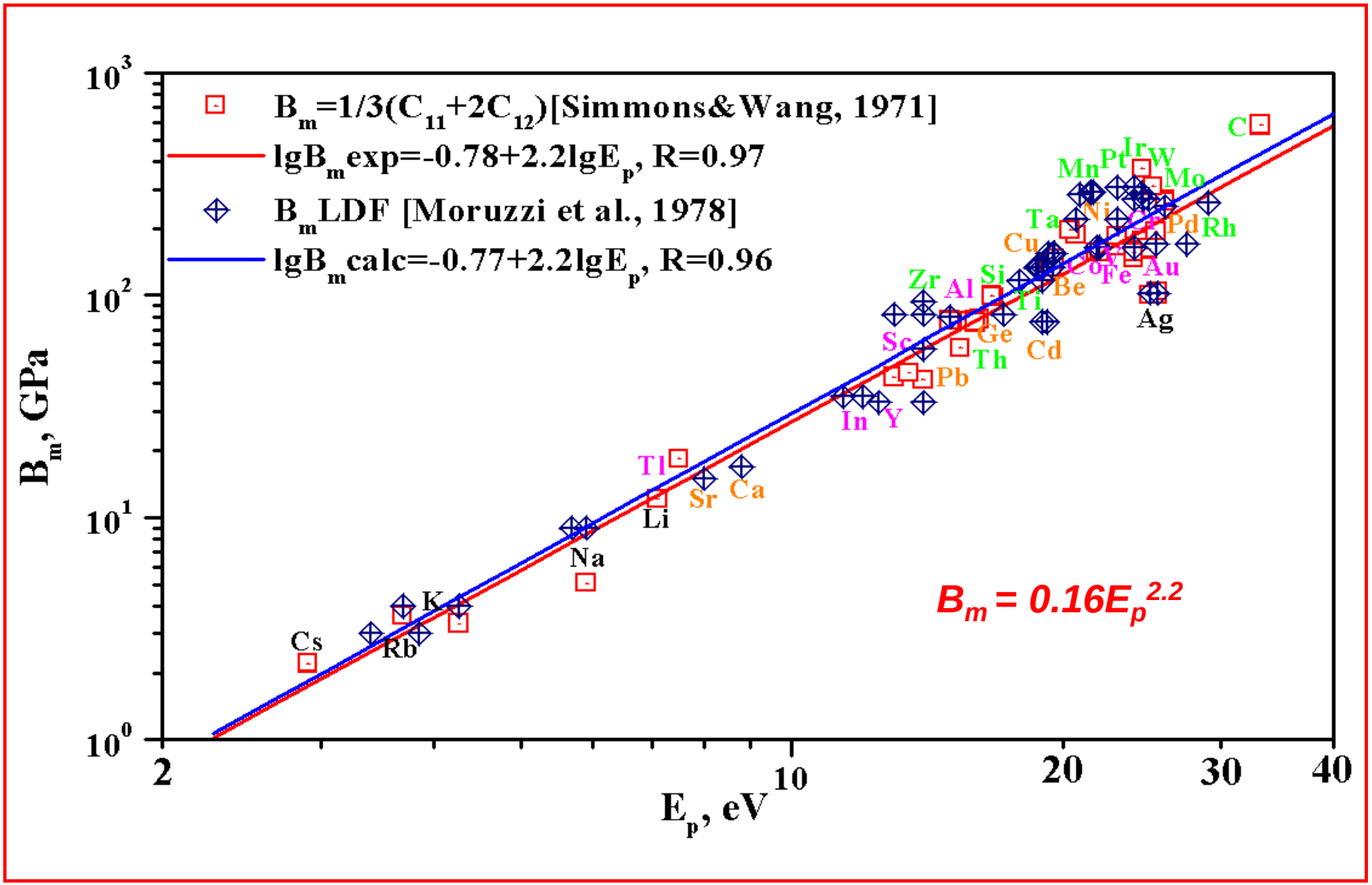

Least-squares-fitted linear regressions for scaling relationships of the power law type $B_m = AE_p^B$ derived using experimental data for single-crystal bulk moduli and LDF quantum mechanical calculations

Properties of Metastable TiH_x precipitates in Ti-H alloy

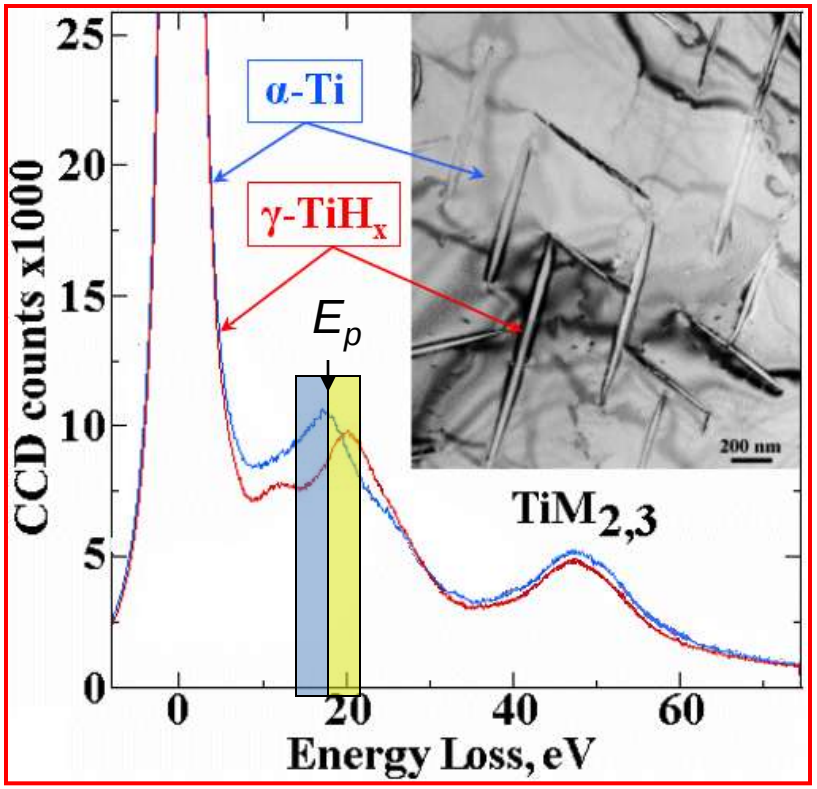

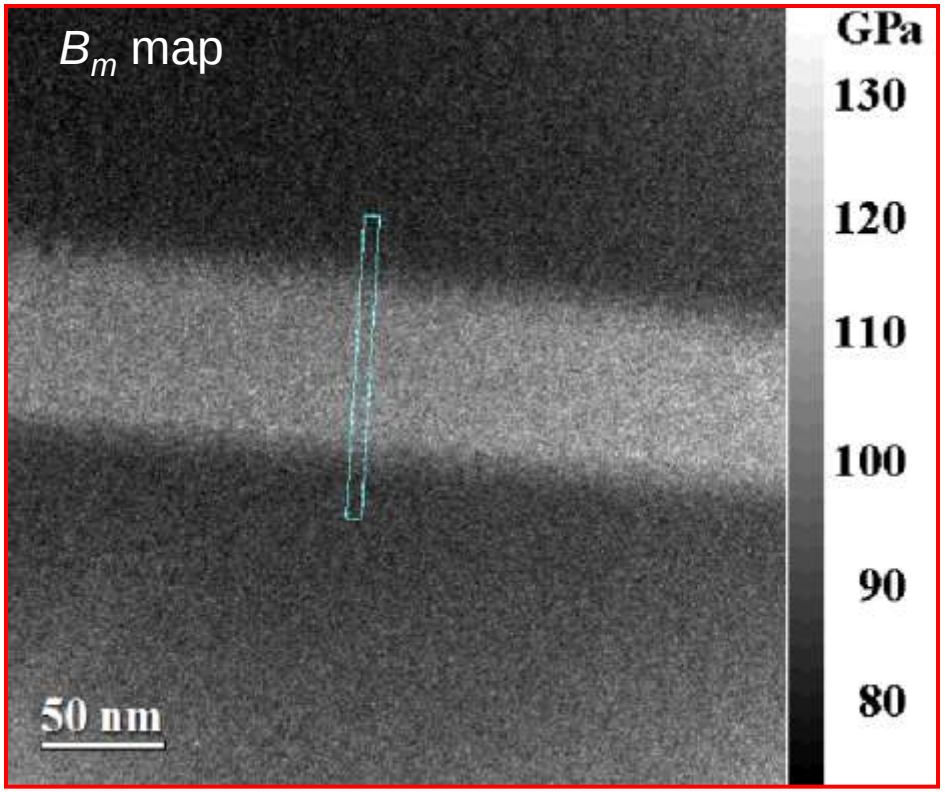

B_m^{Ti} = 85.2 GPa; B_m^{TiHx} = 112.5 GPa

Y_m^{Ti} = 104.7 GPa; Y_m^{TiHx} = 143.9 GPa

G_m^{Ti} = 31.3 GPa; G_m^{TiHx} = 42.4 GPa

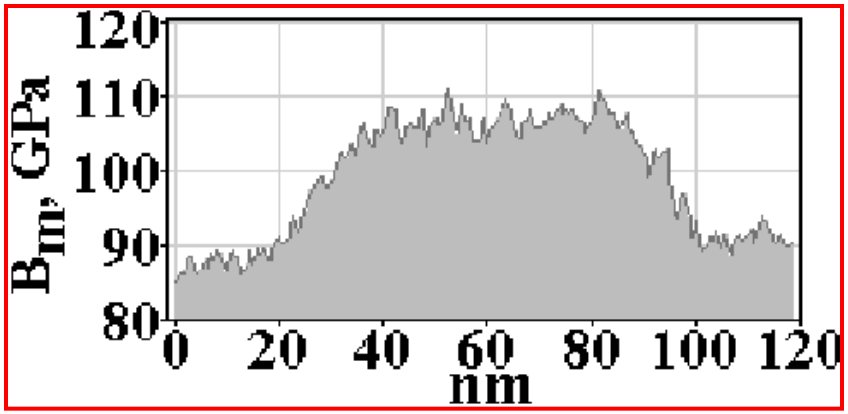

Intensity profile shows B_m versus position with a spatial resolution ~1 nm and modulus resolution of a few GPA; the B_m map is also a H map because B_m scales linearly with H in solid solution in α-Ti alloys

Outline

→ Obtain fundamental scientific understanding concerning

Glass Formability (size)

glass formability ↑

quenching rate ↓

amorphous alloys size ↑

Competing crystalline phase

↓

GFA improvement (Ln effect)

↓

Contributions to Good GFA of amorphous steel

Fracture Behavior (ductility)

Plastic deformation process

→ bond breaking and reforming

Electronic structure

↓ Er, Cr, C, P effects

Local atomic structure

Bonding configuration

↓

Correlation between plasticity (shear modulus) and bonding configuration

Fracture Behavior in *adjusted* Amorphous Steel

Alloy	$D_{max.}$(mm)
$Fe_{65}Mo_{14}C_{15}B_6$	1.5
$Fe_{64.5}Mo_{14}C_{15}B_6\mathbf{Er_{0.5}}$	2.5
$Fe_{64}Mo_{14}C_{15}B_6\mathbf{Er_{1}}$	3.5
$Fe_{63.5}Mo_{14}C_{15}B_6\mathbf{Er_{1.5}}$	3
$Fe_{63}Mo_{14}C_{15}B_6\mathbf{Er_{2}}$	3

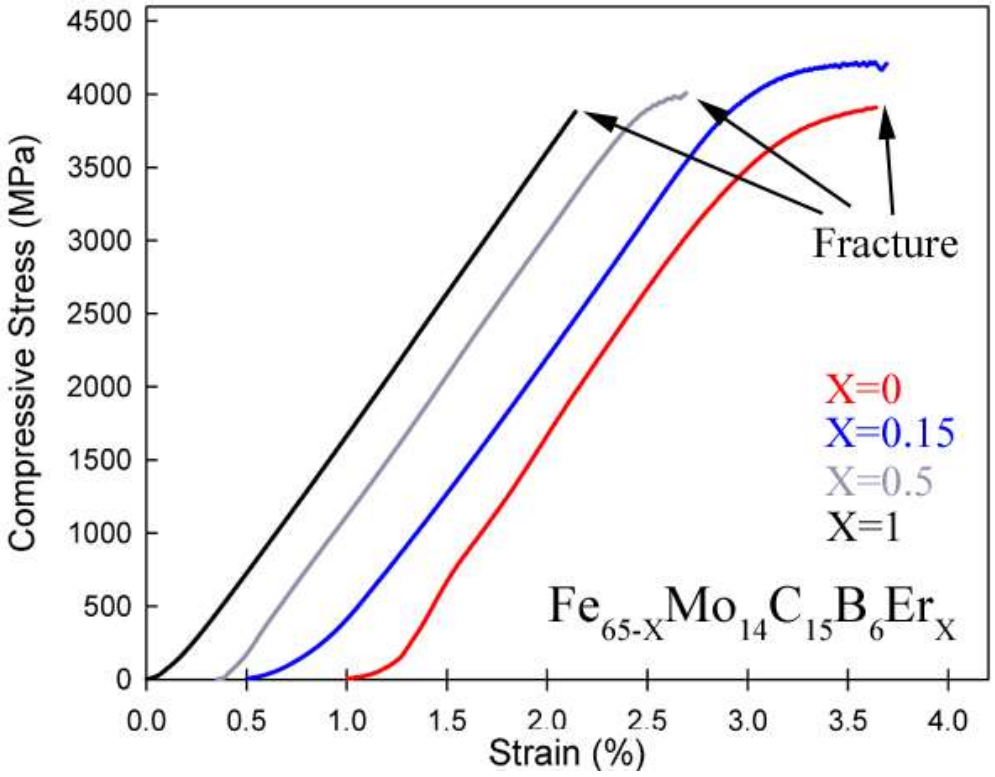

Adding Er to enhance GFA

⟶ occurrence of ductile to brittle transition

Strain rate ~10^{-4} s^{-1}

Tensile fracture ≈ Compressive fracture

(Gu, Poon, Shiflet, J. Mater. Res. (2007))

Reason to be able to make alloys in-house

$Fe_{65-X}Mo_{14}C_{15}B_6Er_X$

0.(

Er

Goal is to develop a strategy for selecting compositions based on microscopic models involving *atomic bonding* & *local structure*

Gu, McDermott, Poon, Shiflet, Appl. Phys. Lett. (2006)

Electronic Structure-Carbon

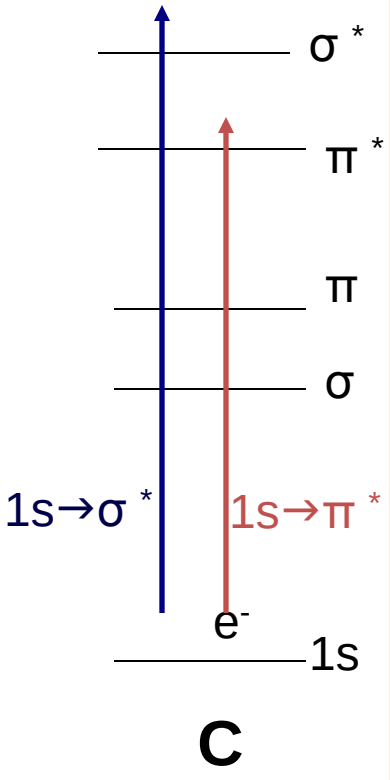

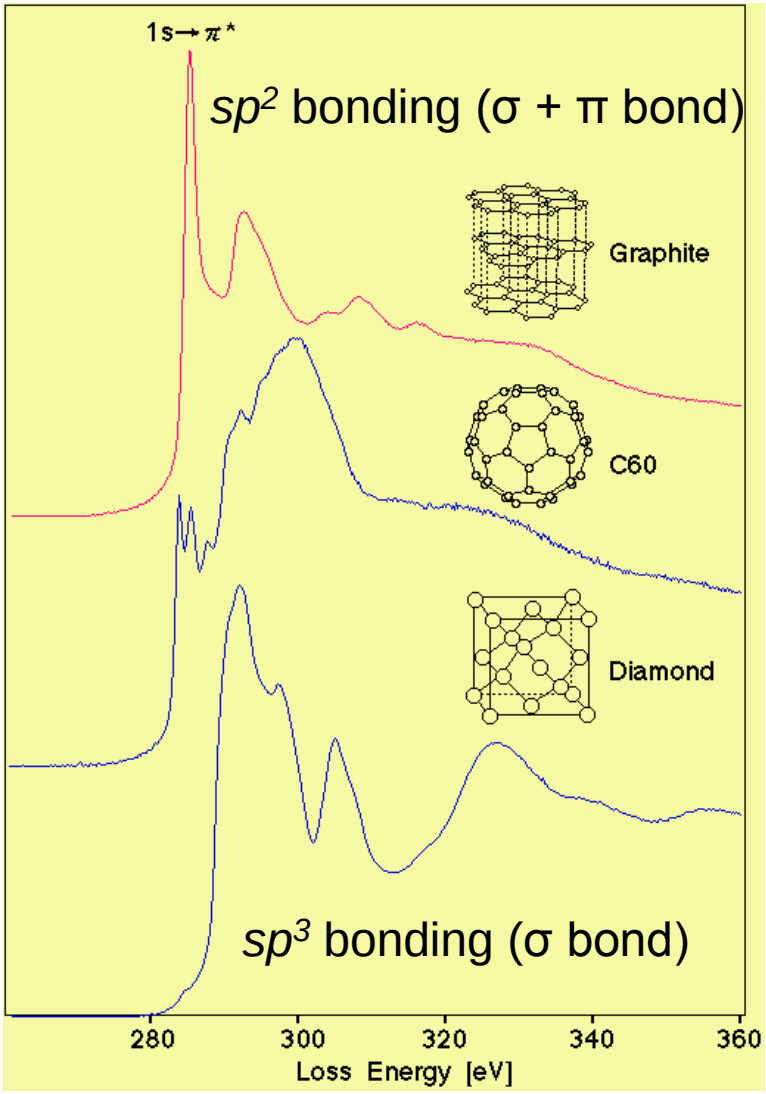

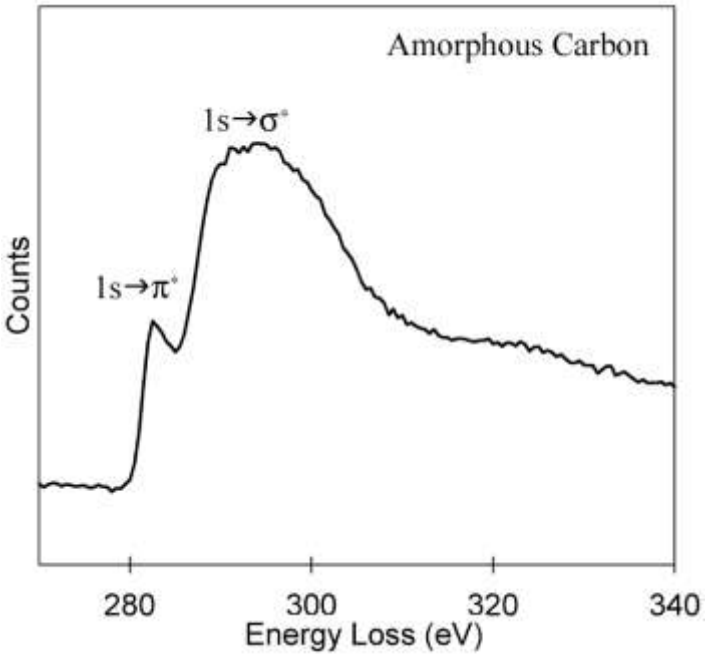

Amorphous C contains both sp^2 and sp^3 hybridization (σ + π bond)- featureless 1s→σ*peak indicates amorphous structure

EELS Result-C-K edge

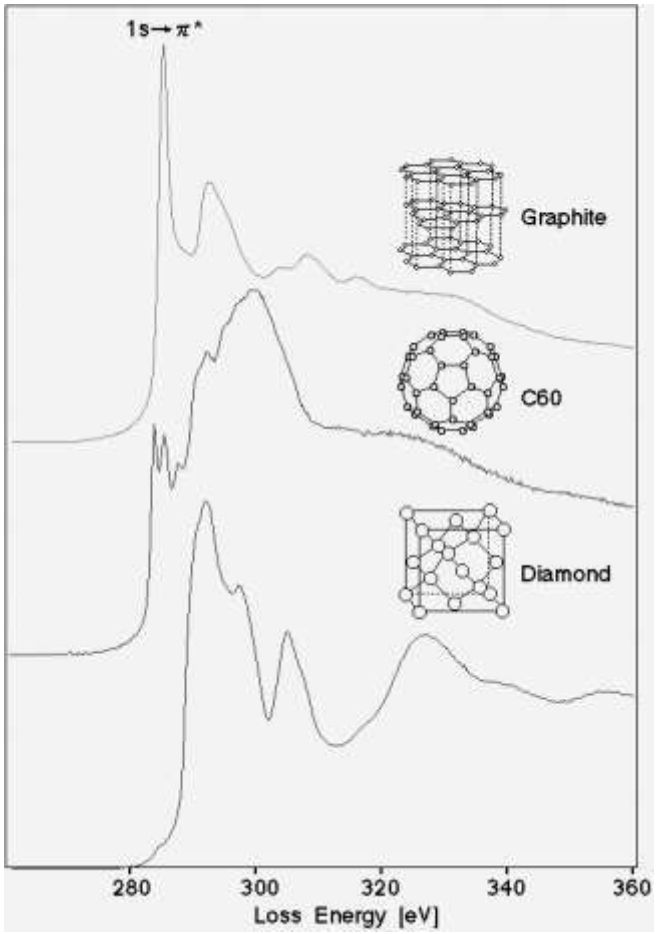

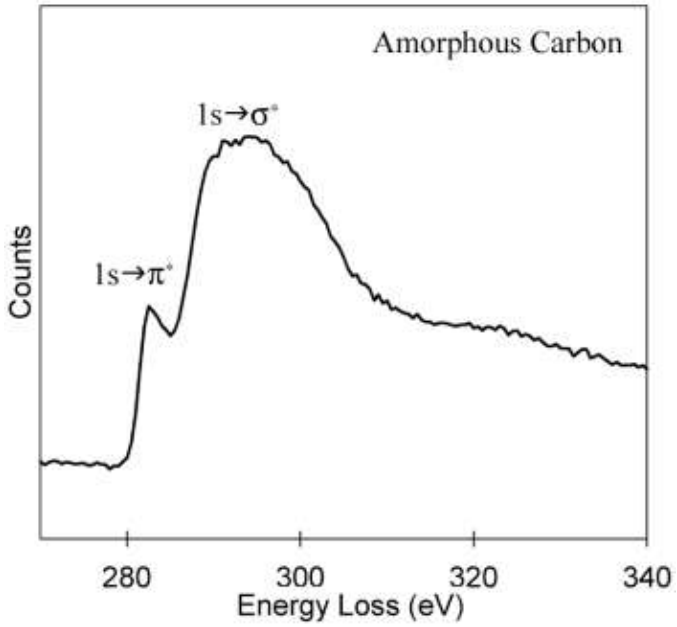

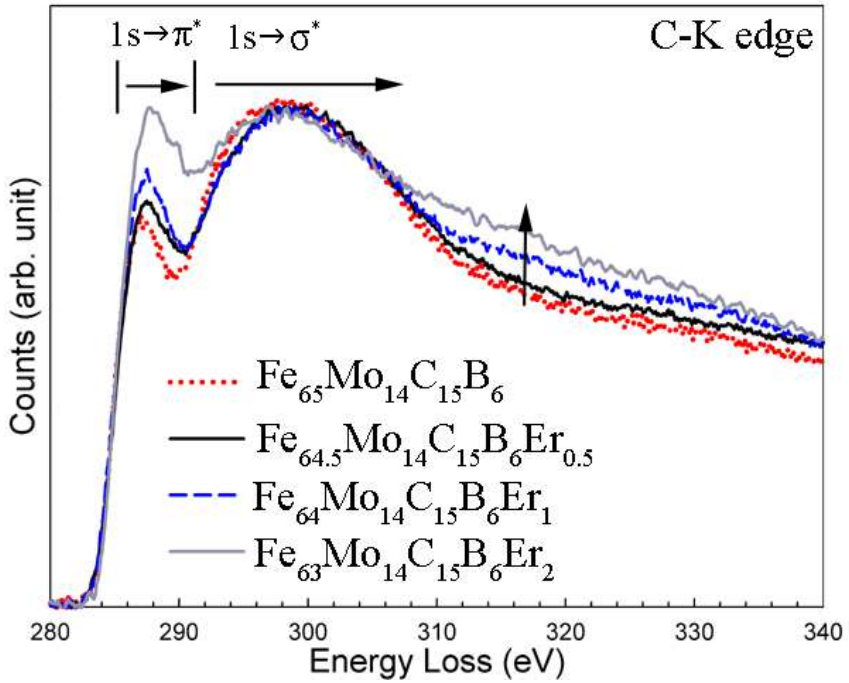

J Wang, Poon, Shiflet, Phys Rev B.

EELS Result-C-K edge

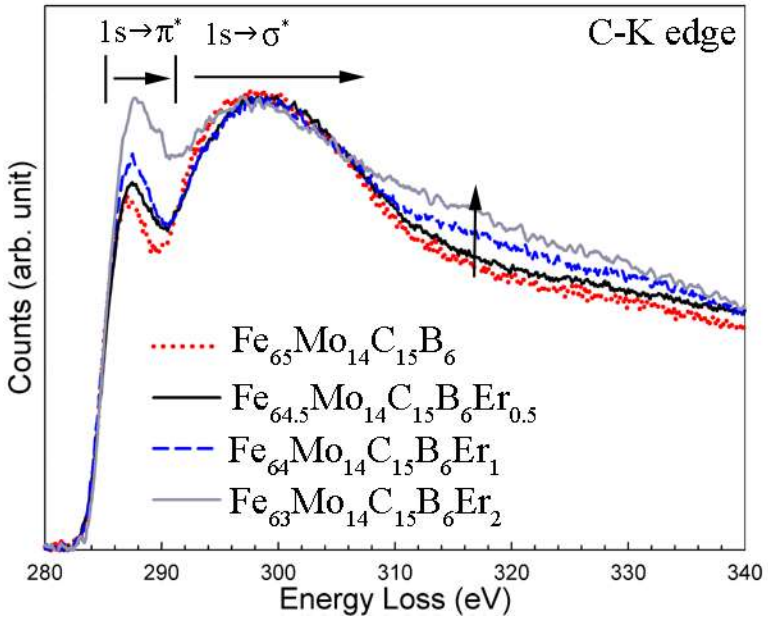

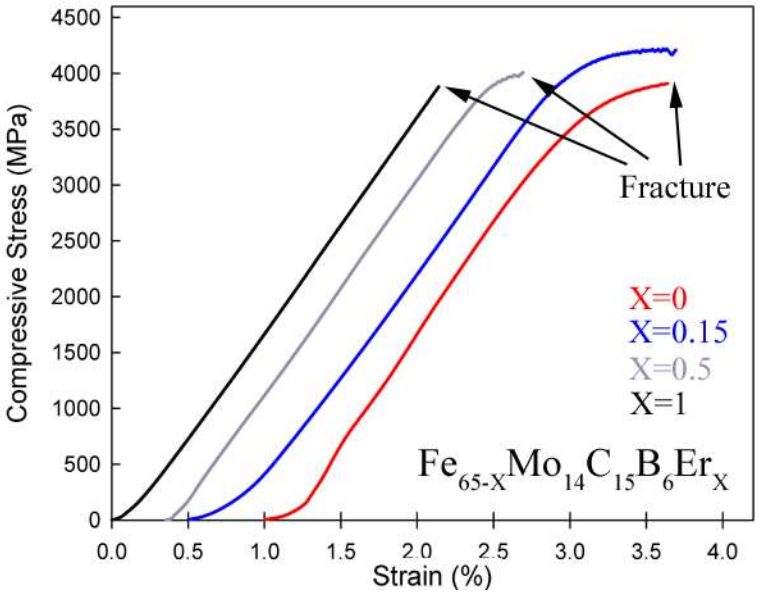

EELS Result-Fe-$L_{2,3}$ edge

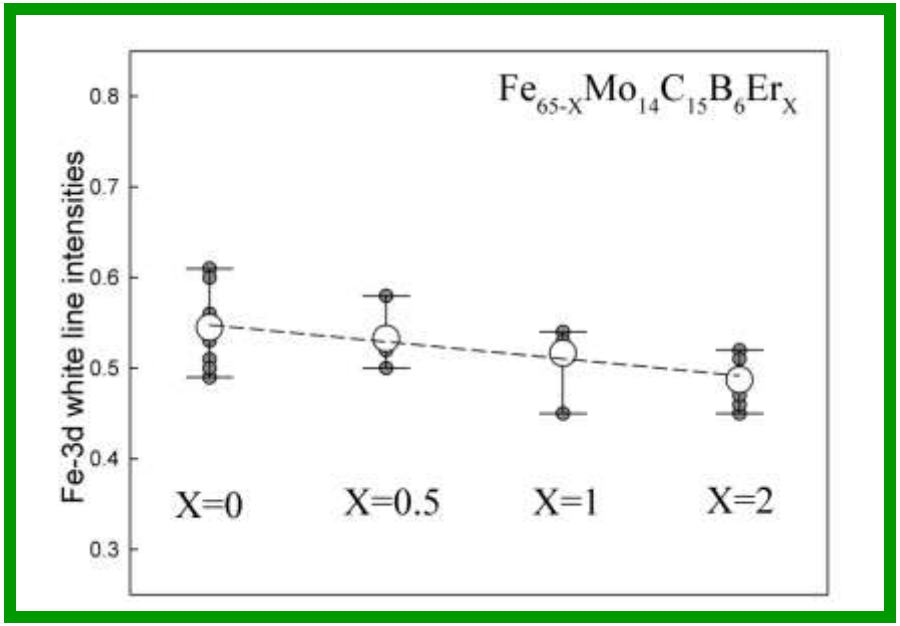

Er effect

Slight increase of 3*d* electrons with Er additions

⟶ Fe regains electrons due to **Er-C formation**

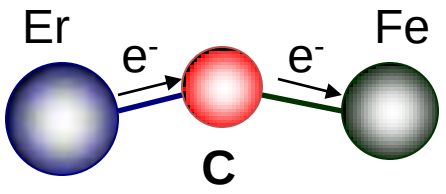

ab initio band calculation shows increase of Fe 3*d*-white intensity for both Er and Cr additions. (M. Widom)
Er is a strong electron donor
Confirmed by XPS

Er-C Effects

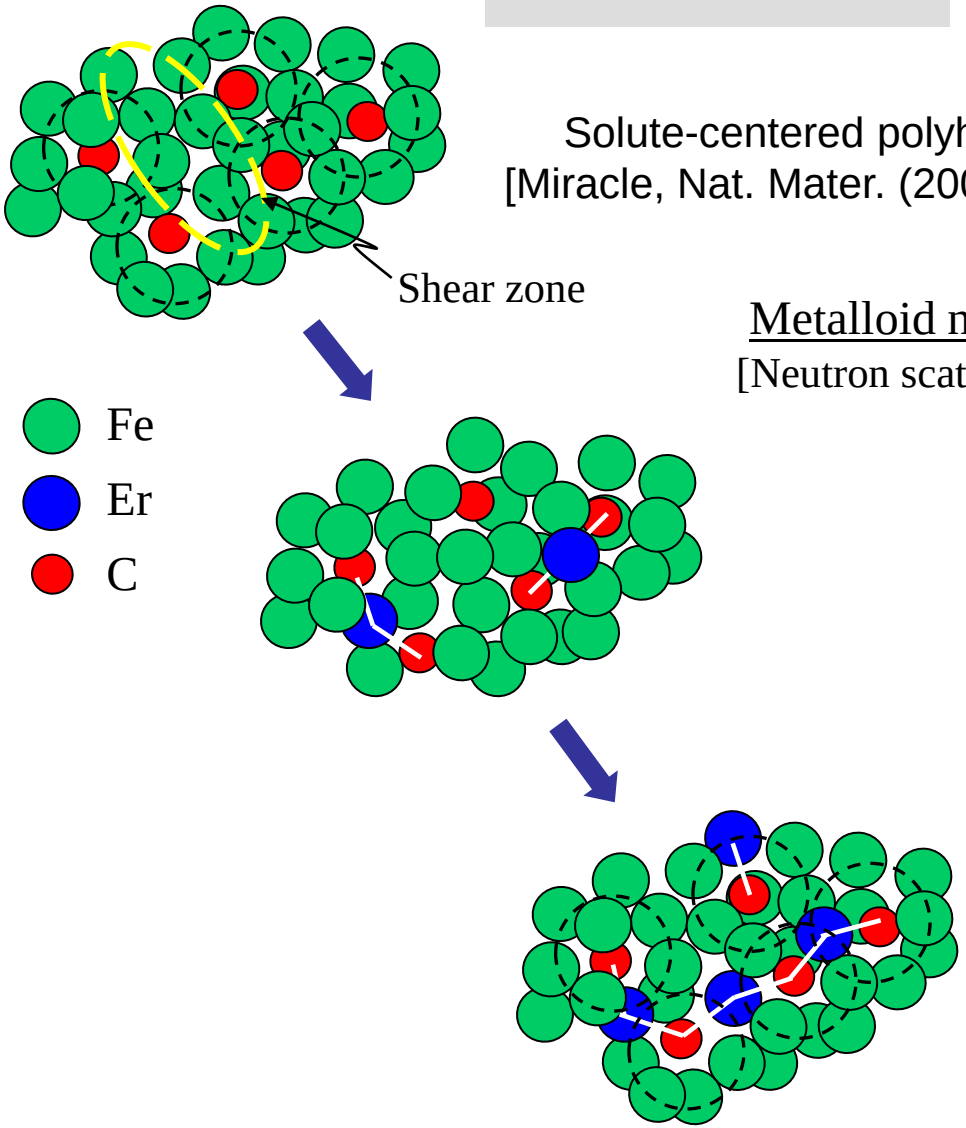

Solute-centered polyhedra as building blocks
[Miracle, Nat. Mater. (2005); Sheng *et al*, Nature (2006)]

Metalloid neighbors around metal atoms in Fe-SAM
[Neutron scattering & ab initio calc. Louca, Widom *et al*]

Fe-(C,B)	**2.2**
Mo-(C,B)	**2.7**
Er-(C,B)	**3.5**
Cr-(C,B)	**?**

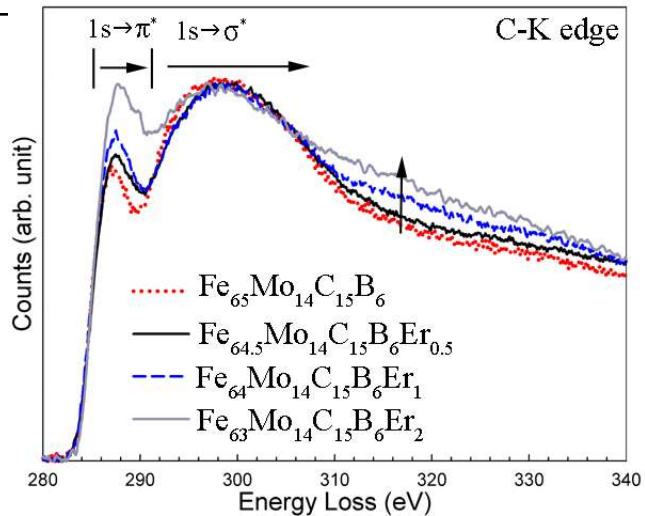

As-spun $Fe_{71-X}Mo_{5+X}P_{12}C_{10}B_2$ amorphous ribbons

X=0

X=2

X=5

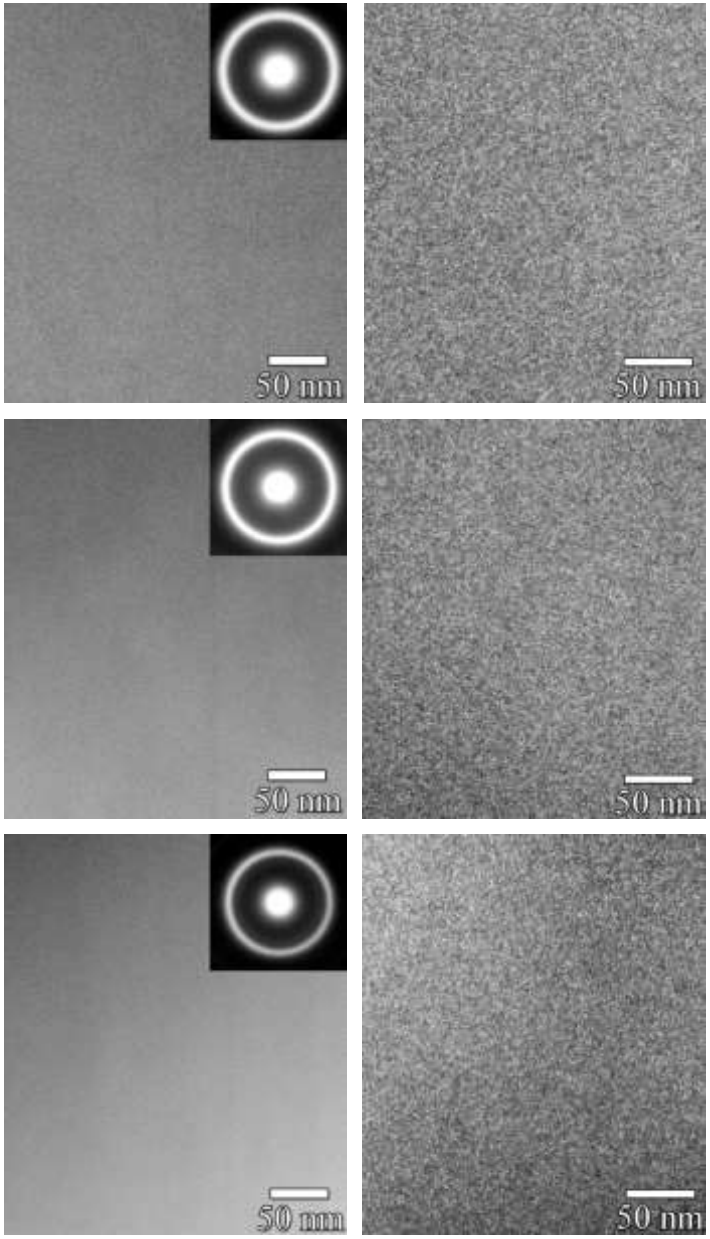

Bright-field Dark-field

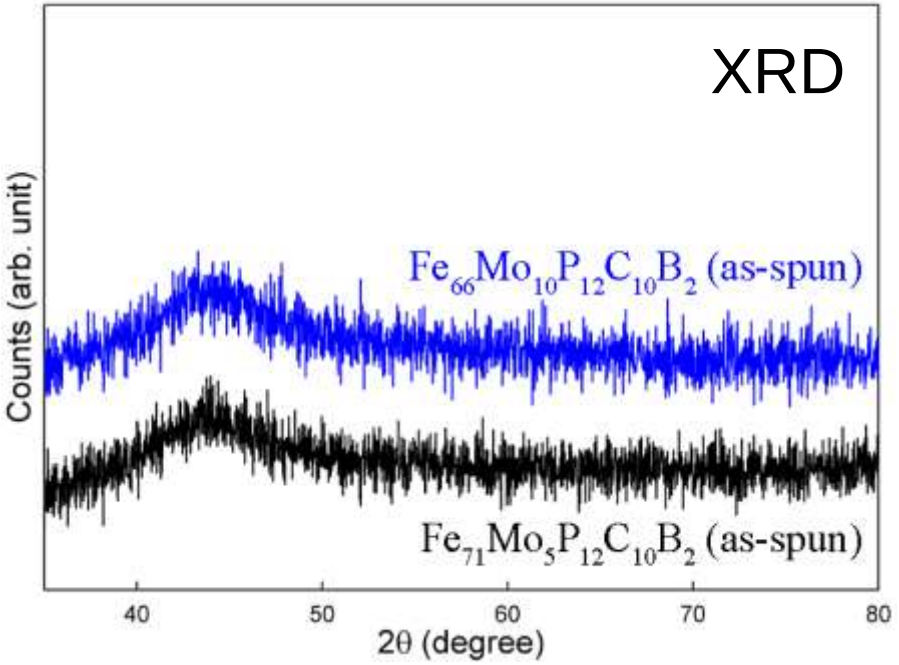

Both TEM and XRD results confirms the amorphicity of all three as-spun ribbons

P- $L_{2,3}$ edge

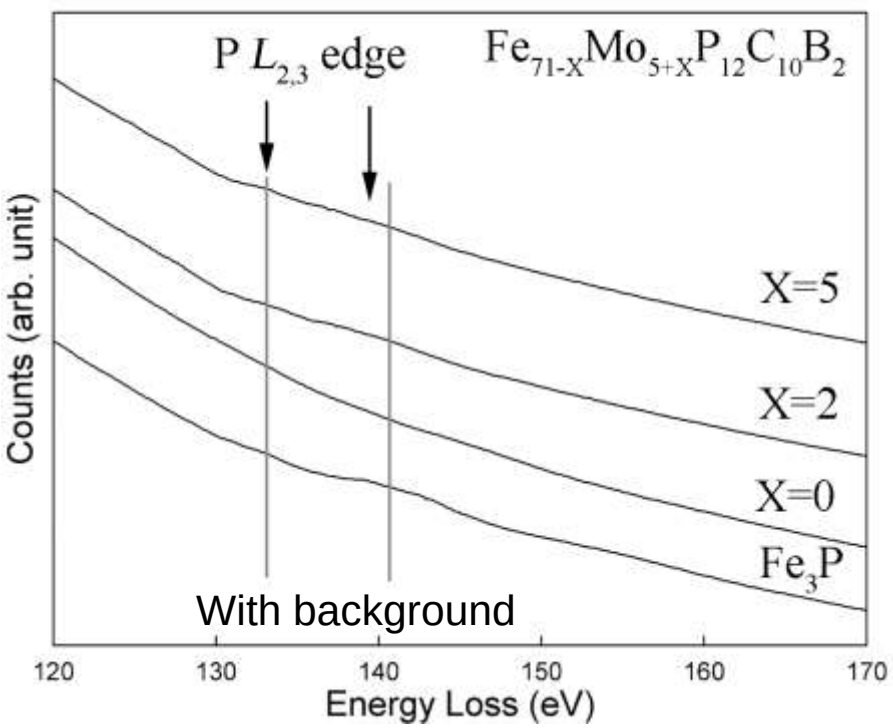

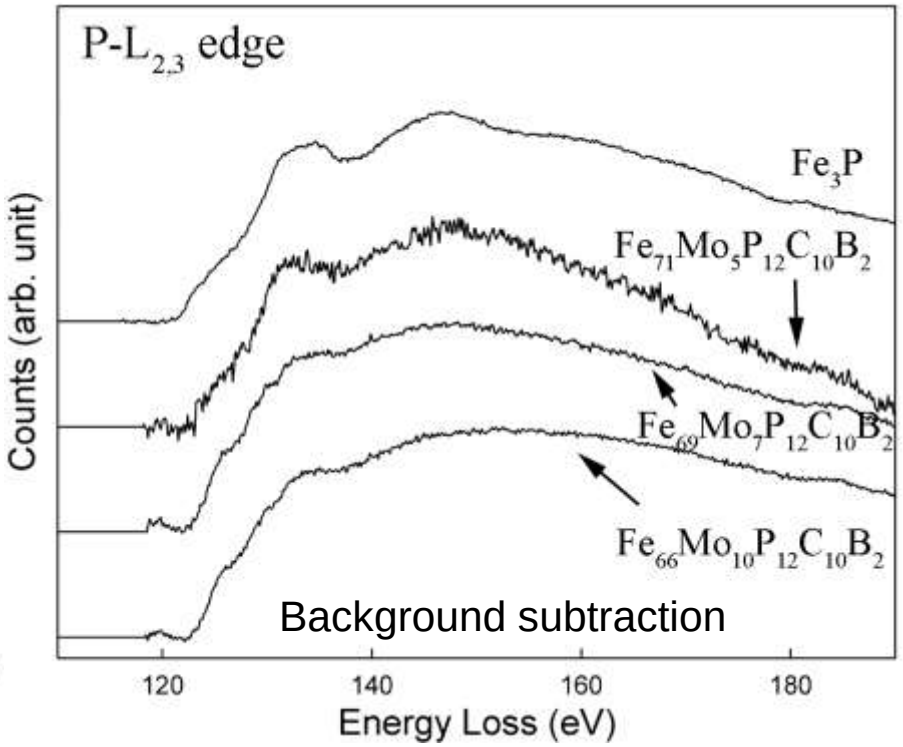

Two humps corresponding to P-$L_{2,3}$ edge are observed for Fe_3P crystalline alloy. $Fe_{71}Mo_5P_{12}C_{10}B_2$ ribbon shows similar but less clear humps of $L_{2,3}$ edge as Fe_3P, indicating the Fe-P bond is the major bond of the bonding surrounding P atom.
As Mo content increases, these two humps are smeared off. This might be due to the formation of stronger Mo-P bonds and thus reduce Fe-P interactions in amorphous structure. (Verified by the increasing 3*d* white line intensities of Fe with increasing Mo content).

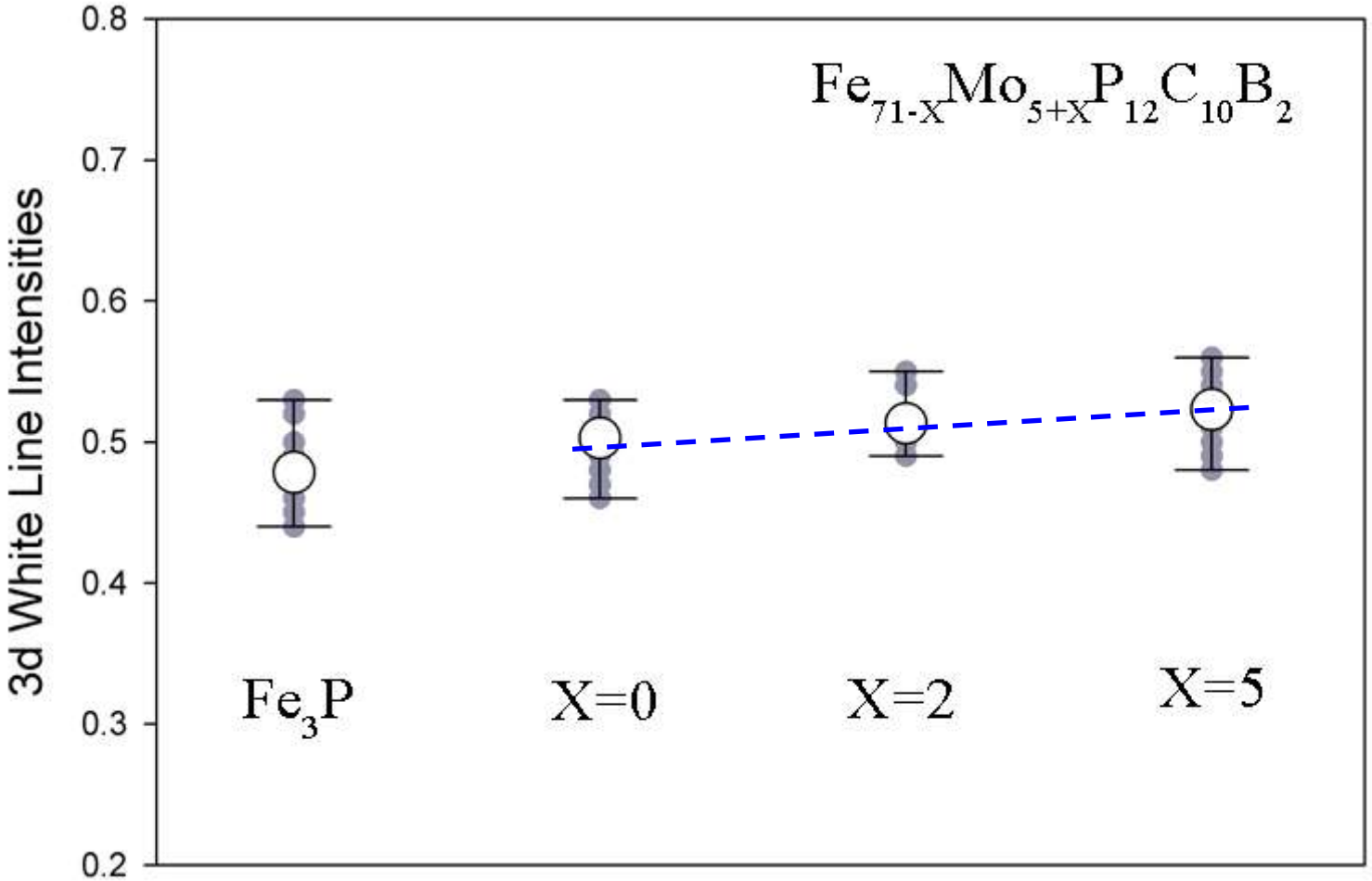

Fe 3*d* white line intensities calculations show a slight increase of Fe 3*d* white line intensities and a decrease of L_3/L_2 ratio with increasing Mo content for as-spun $Fe_{71-X}Mo_{5+X}P_{12}C_{10}B_2$ ribbons.

3*d* electrons number decreases with increasing Mo content, indicating less Fe-P interactions, supporting the P-$L_{2,3}$ edge results.

can be tuned for G

Uniaxial compressive true stress-strain curves for four Fe-Cr-Mo-P-C-B BMGs
(a) Fe63Cr3Mo12**P10**C7B5, (b) Fe64Cr3Mo10**P10**C10B3,
(c) Fe63Cr3Mo10**P12**C10B2, and
(d) Fe71Mo5**P12**C10B2.

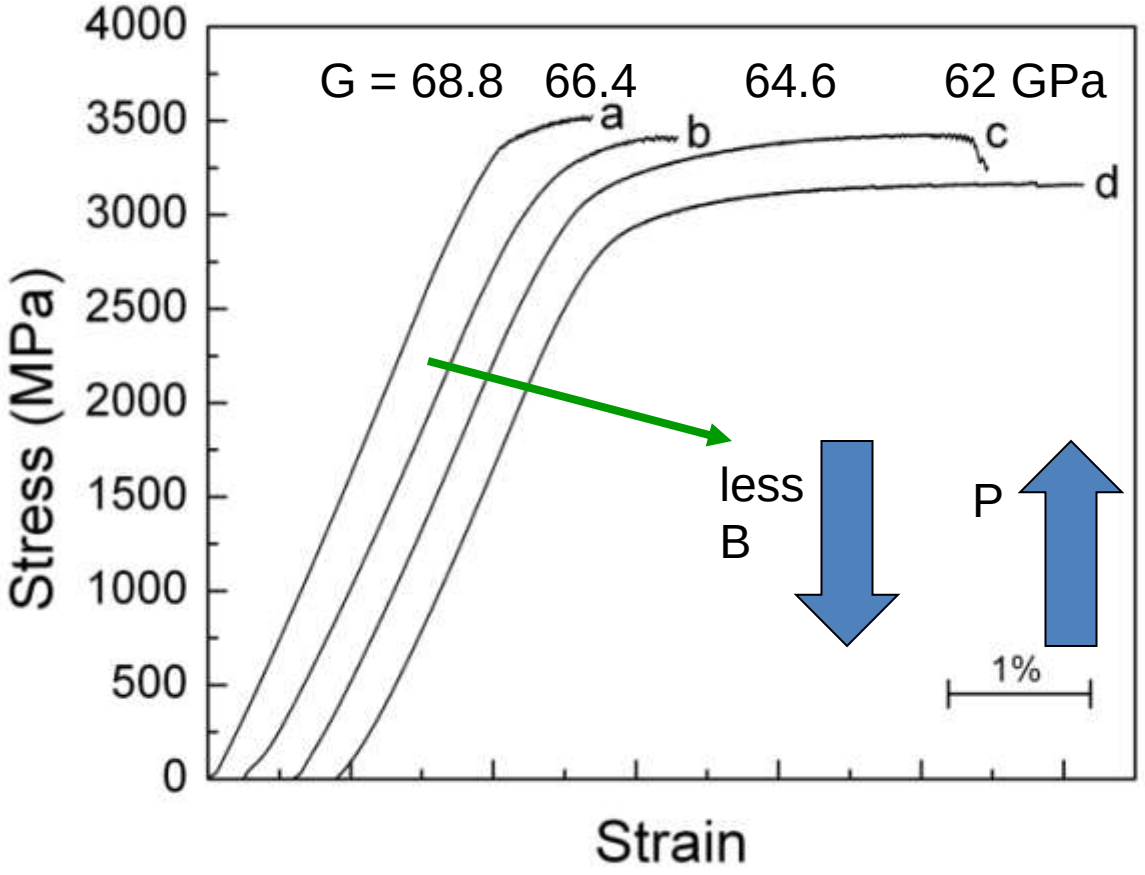

adding electrons to a more than half filled shell weakens the bond
(Pettifor tight-binding model)

Ab-Initial Calculation and Neutron Scattering Measurement

(Michael Widom and Despina Louca)

Partial contributions to total PDF
Charge densities
Bonding enthalpies
Elastic moduli

. Ab-initio MD was performed using the density functional theory. Supercooled liquid of FeMoBC was first simulated; the resulting structures were then quenched using conjugate gradient relaxation to obtain the amorphous structure.

. Density of states and charge transfer were obtained from VASP using projector augmented wave potentials

. Crystal Orbital Hamilton Population COHP (Dronwkowski & Blöchl 1993) was computed to obtain the bonding enthapy. Orbital-projected data was obtained from TB-LMTO calculations.

$$\psi(r) = \sum_{\substack{atom\,i \\ orbital\,\alpha}} c_i^{\alpha} \chi_{\alpha}(r - R_i)$$

$$E = \sum_{\substack{i \\ \alpha}} E_i^{\alpha} + \sum_{\substack{i \neq j \\ \alpha,\beta}} c_i^{\alpha *} c_j^{\beta} H_{\alpha\beta}^{ij}$$

COHP

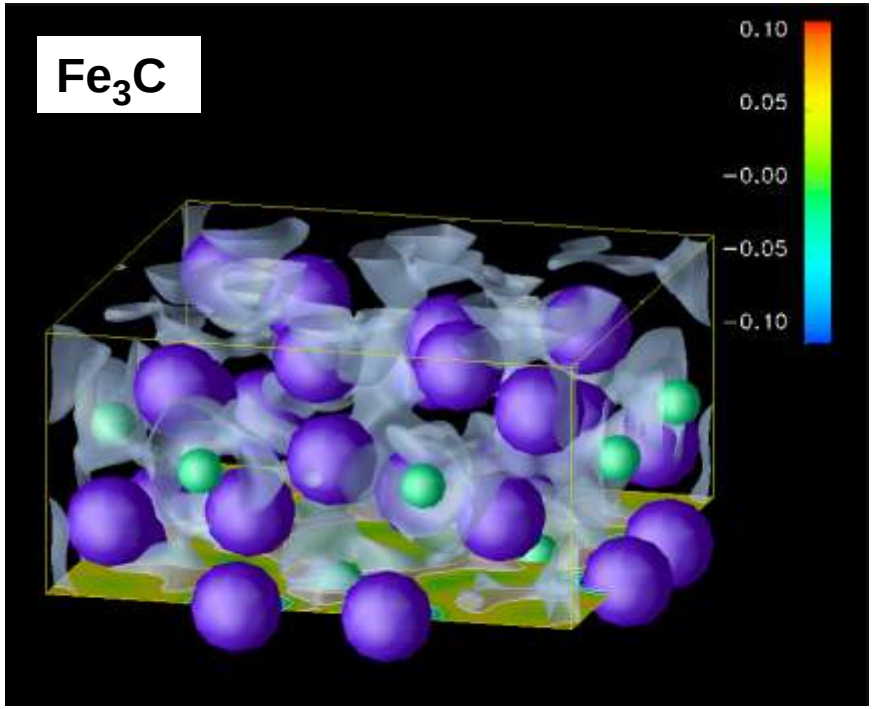

Composing ductile Fe-SAM:

Bonding charge densities of Fe_3C (oP16) and Fe_3P (tI32). Color bar indicates the bonding charge density of electrons in units of $Å^{-3}$ (note that negative (blue) means a *decrease* in electron density). *Isosurfaces enclose regions of bonding charge density greater than 0.06 $Å^{-3}$.*

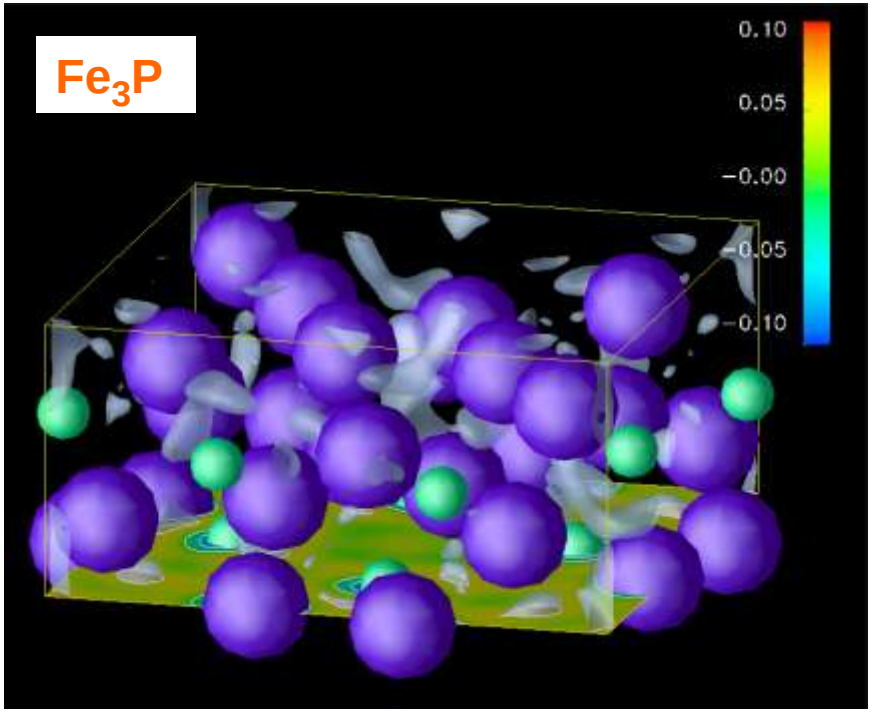

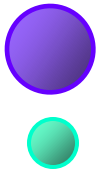

Fe

C or P

Gu, Poon, Shiflet, Widom, Acta Materialia

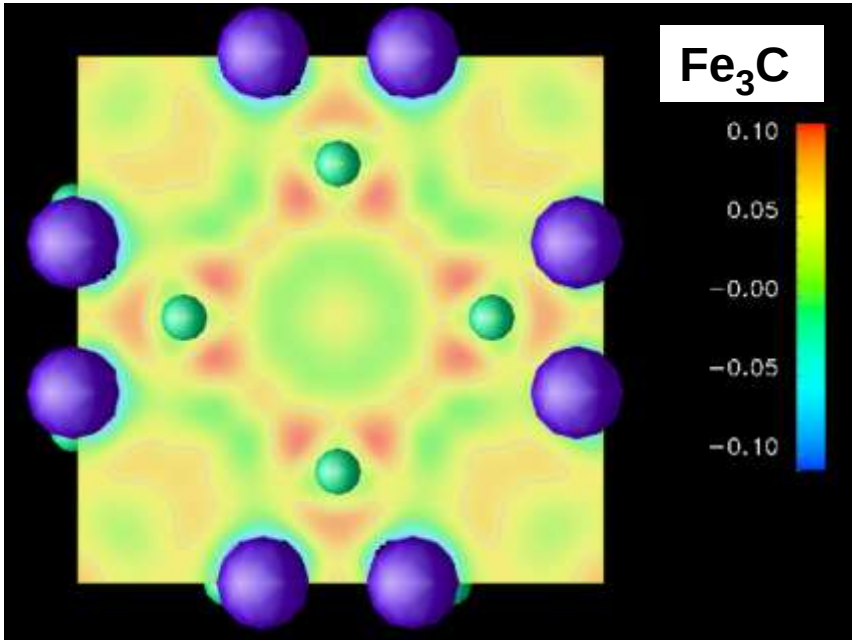

Cut plane view of bonding charge densities. Color bar indicates the bonding charge density of electrons in units of $Å^{-3}$ (negative (e.g blue) means a *decrease* in electron density).

Covalent-like Fe-C bond in Fe_3C
More metallic Fe-P bond in Fe_3P

Charge transfer from (Fe, Mo) to C
Charge transfer from P to (Fe, Mo)

Coexistence of metallic & covalent bonds

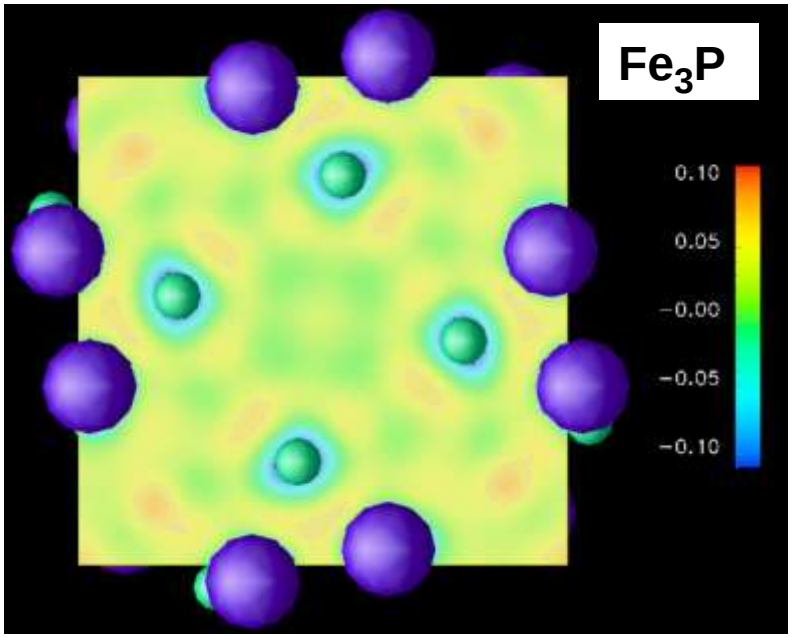

Trace Elements & Nucleation

Clustering of Solute Atoms => Heterogeneous Nucleation Sites

Two questions as to which elements to add or remove:

1) Can they form clusters or co-clusters in the solid solutions?
2) Are the clusters “precursors” or “non-precursors” for desired phases?

Cluster Formation Analysis

Objective: to predict clustering tendency of solute atoms

One Possible Approach:

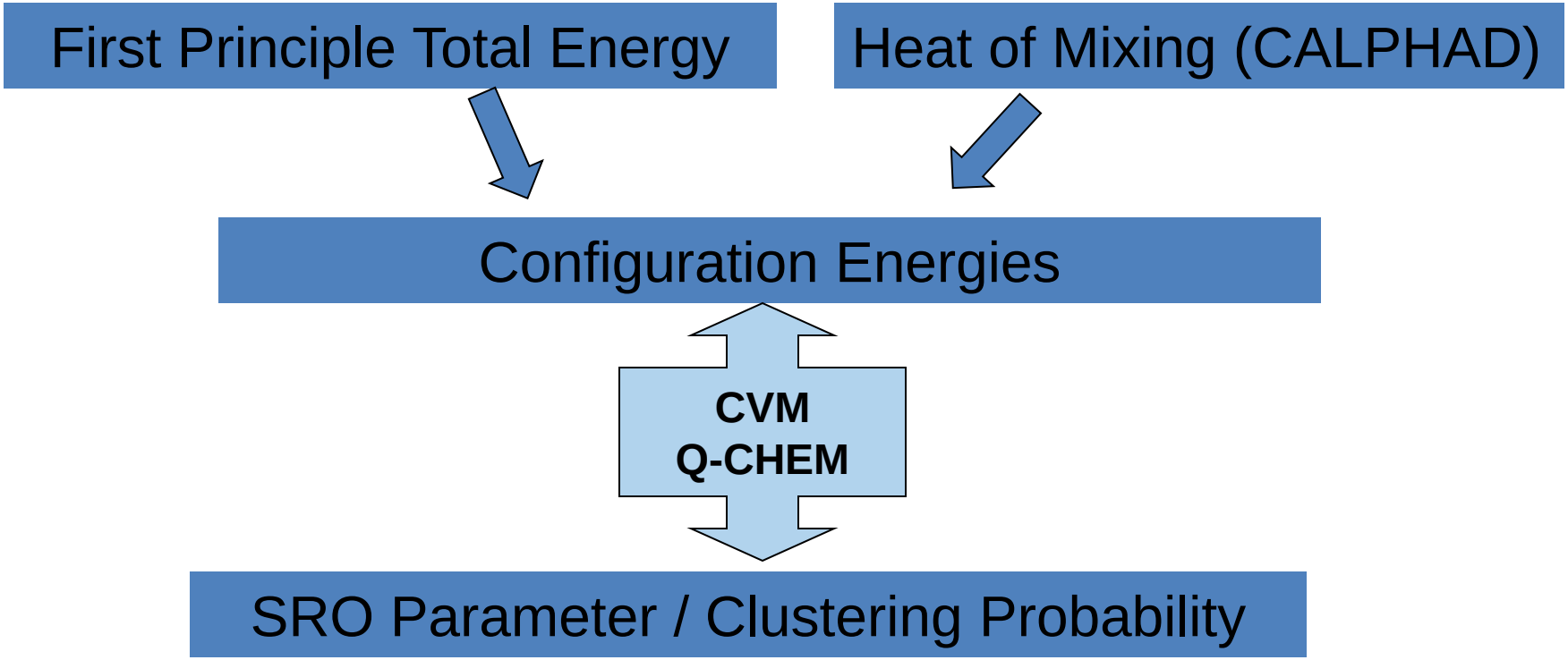

Quasi-Chemical Model of Higher Order Systems

$$G = \sum_i N_{ii} E_{ii} + \sum_{i \neq j} N_{ij} E_{ij} - kT \cdot \ln\left\{ \frac{(zN/2)!}{\prod_i N_{ii}! \cdot (\prod_{i \neq j} (N_{ij}/2)!)^2} \cdot \frac{\prod_i [(z-1)NX_i)!}{[(z-1)N]!} \right\}$$

$$\frac{Y_{ij}^{\ 2}}{(x_i - \sum_{p=i,q} Y_{pq}) \cdot (x_j - \sum_{p,q=j} Y_{pq})} = \exp\left(-\frac{2\Omega_{ij}}{kT} \right)$$

Warren-Cowley SRO parameter

Pairs: $y_{ij} = 1 - Y_{i,j} / x_i x_j$

Triples / Tetrohedrans: $u_{ijk\ldots} = 1 - U_{ijkl} / x_i x_j x_k \ldots$

- positive: clustering
- zero: random
- negative: SRO or co-clustering

SRO Parameters: Al-0.0175Cu-xMg

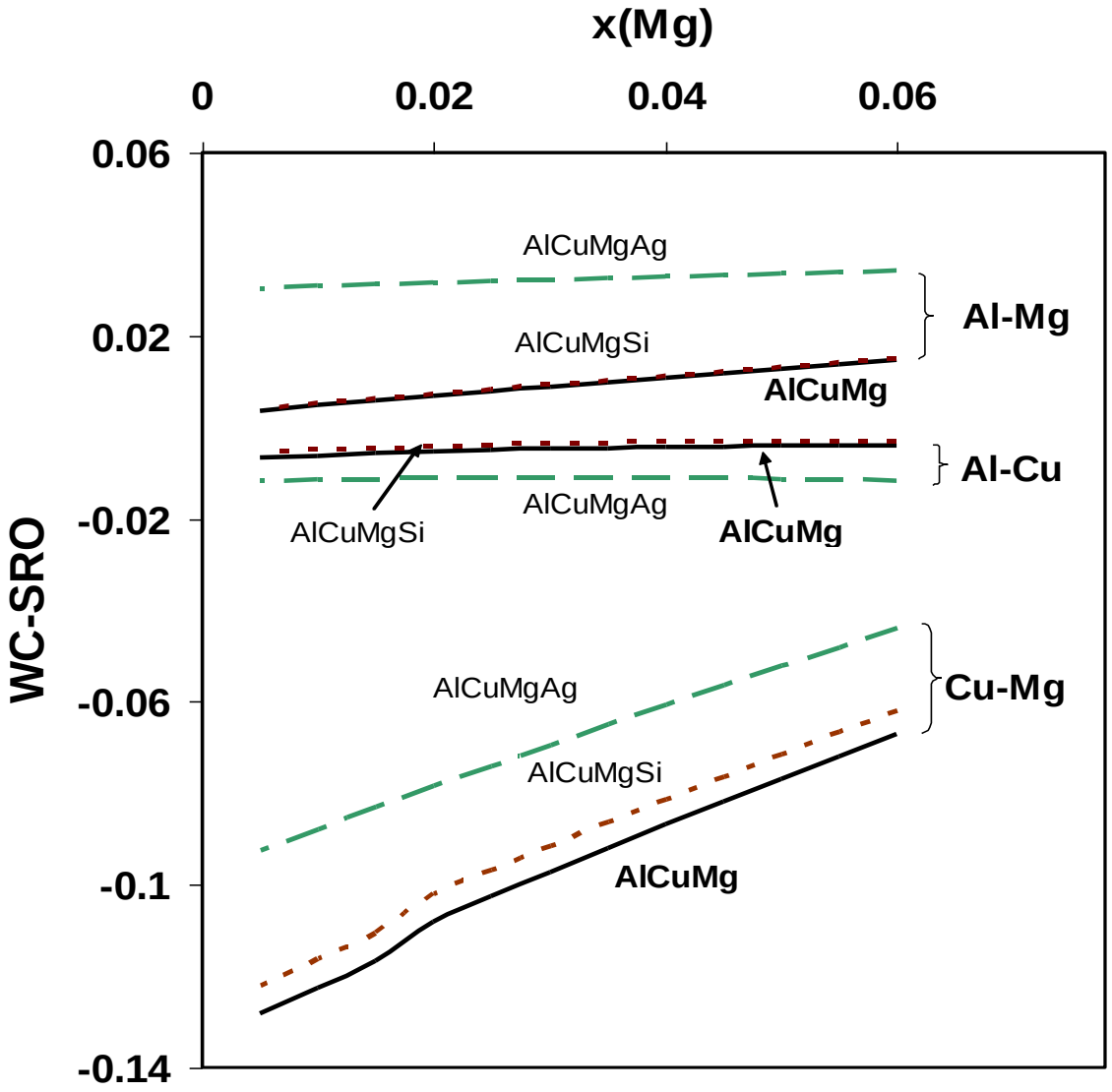

SRO Parameters: Si, Ag Effects

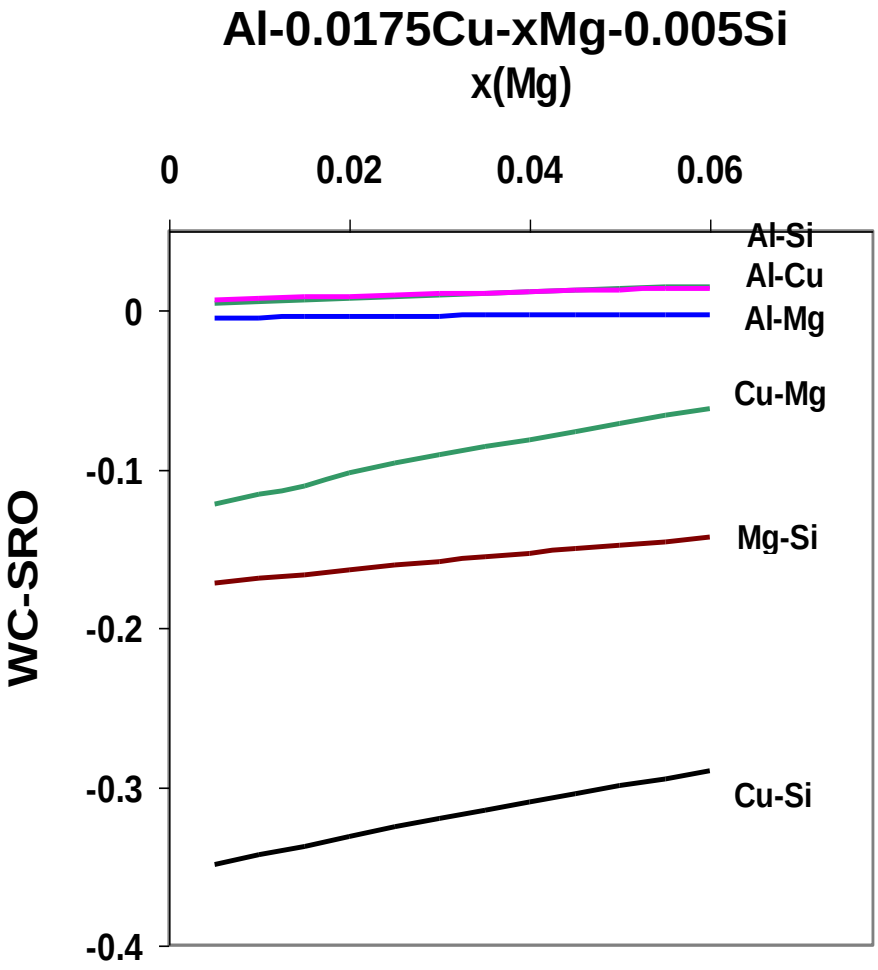

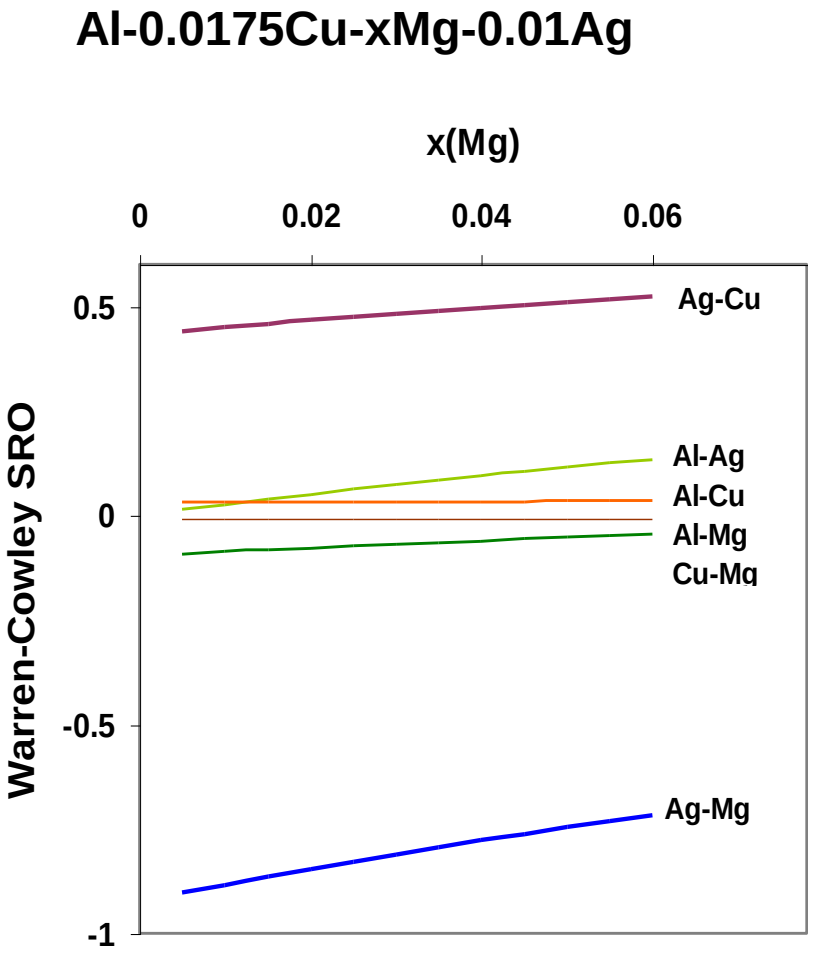

3D-AP: Al-Cu-Mg-Ag

Hono et al: Al-1.9Cu-0.3Mg-0.2Ag (at%), aged at 180□C

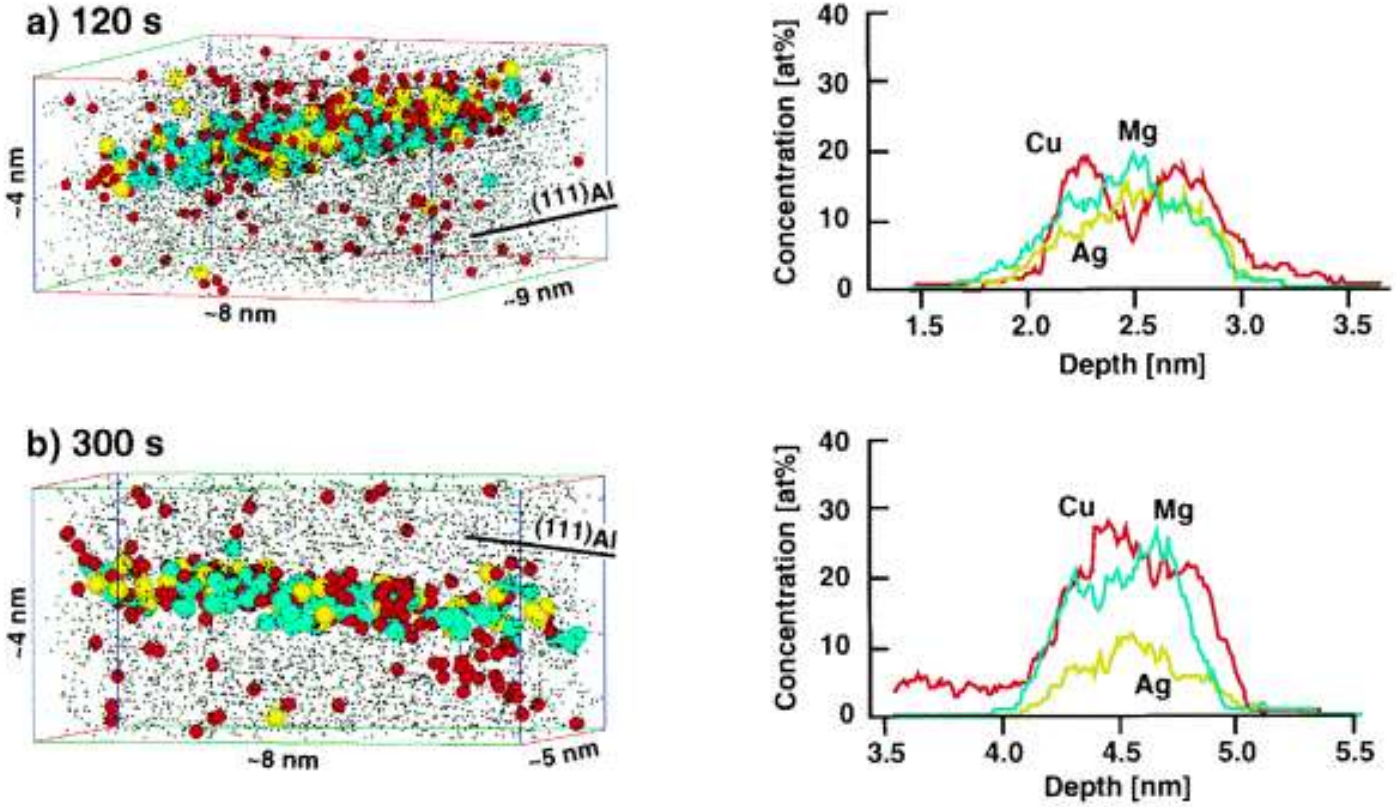

Precursors or Non-Precursors?

- Precursor: enhance nucleation of desired phases, like Cu for θ & Ag for Ω
- Non-precursors: enhance nucleation of undesired phases and/or consume the solute content needed for desired phases, like Si for Omega

Hornstra-Bartels Model

$$E(\xi) = \frac{1}{2} C_{ijkl} (\varepsilon_{mis} \delta_{ij} + b_i \xi_j)(\varepsilon_{mis} \delta_{mn} + b_m \xi_n)$$

Cu-FCC in Al

Mg-FCC in Al

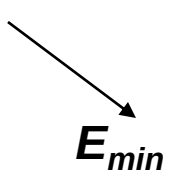

a)

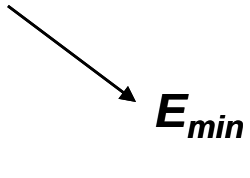

b)

CuMg3-"FCC"

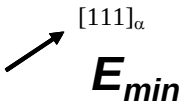

c)

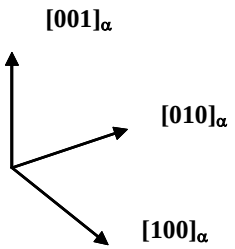

d)

TEM: Si Effect

- Specimens were aged at 250°C for 30min and 2h
- Both aging conditions revealed similar microstructures, with the only difference being the size of precipitates.

Al-4.0Cu-xMg-(0.3Ag)-xSi [$^{wt}/_{o}$]	Mg [$^{wt}/_{o}$]	Mg / Si ratio [$^{wt}/_{o}$] ~ [$^{at}/_{o}$]	Ω Precipitation		
			no	very few	yes
Constant Si content ~0.1 [$^{wt}/_{o}$]	0.1	1	x		
	0.2	2	x		
	0.3	3		x	
	0.4	4			x
Constant Si content ~0.2 [$^{wt}/_{o}$]	0.4	2	x		
	0.6	3		x	
	0.8	4		x	

- These results indicate that a Mg/Si ratio of ~2.0 must be overcome in order to nucleate Ω precipitation.

SRO Parameters: Si, Ag Effects

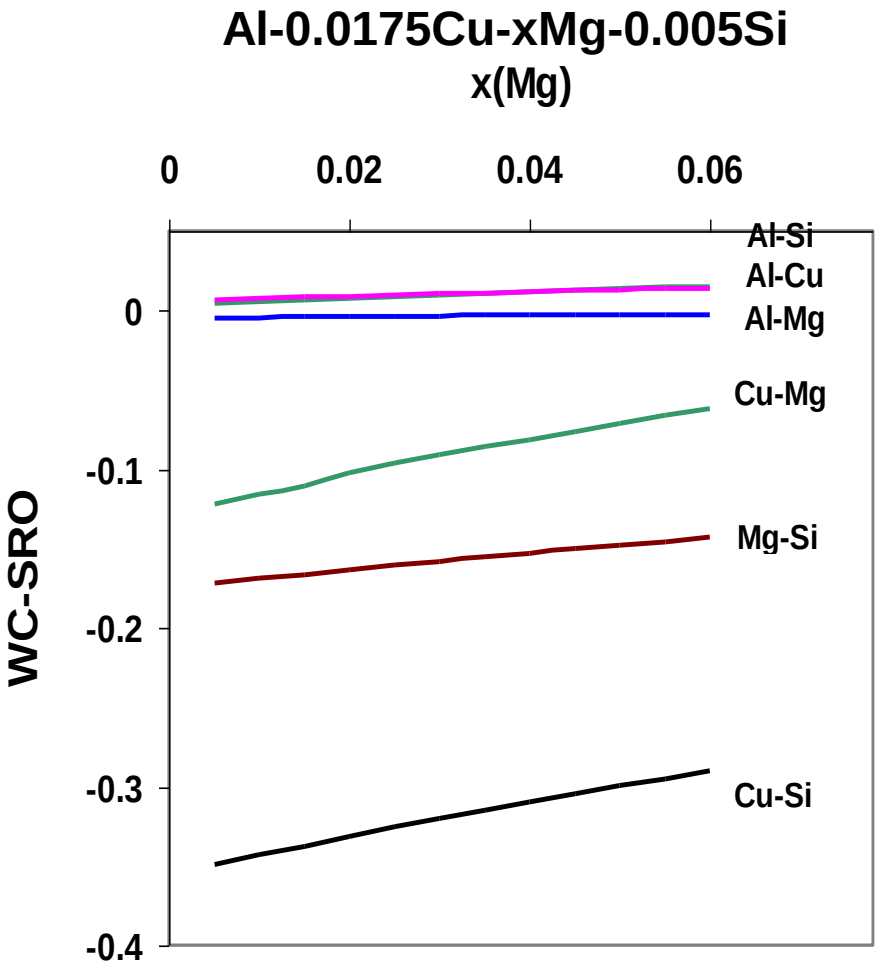

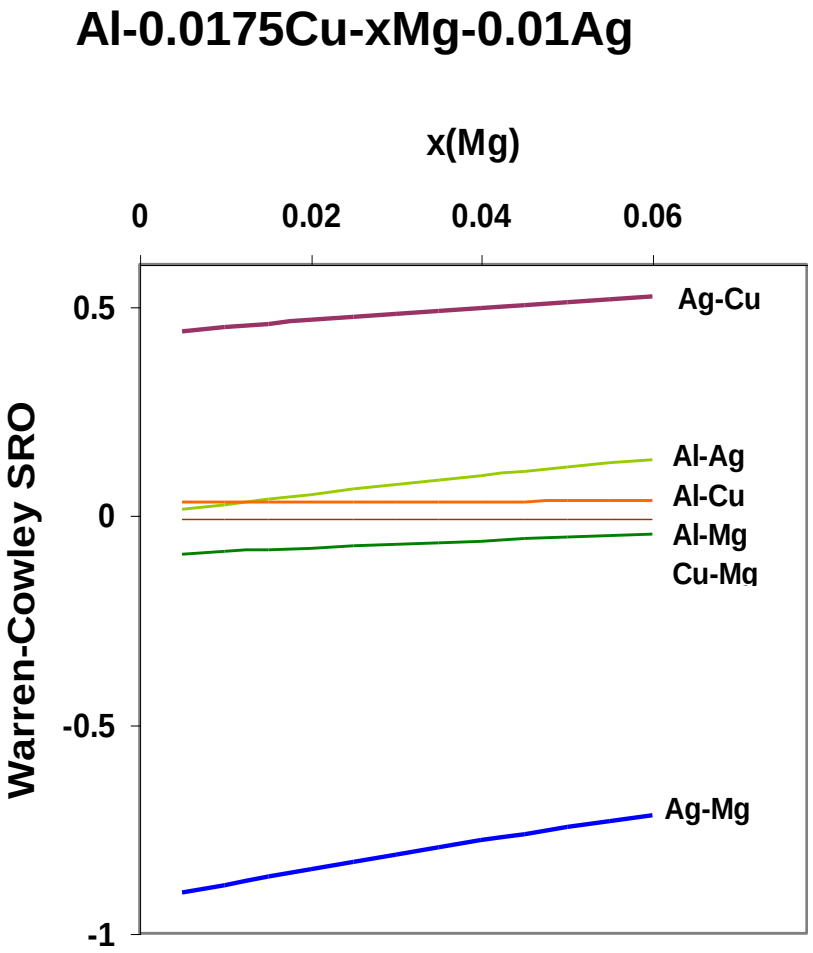

conclusions

- Why not build new precipitates by taking control of:

  clusters→embryos→nuclei→precipitates?

High risk and possible high returns–

Keep close ties on elastic coefficients (electrons)

Use chemical and statistical thermodynamics

Good experimentalist controls the modelers –if possible! Model what is needed.

First Principles Simulations Of Beta To Omega Transformation In Titanium Alloys

Srinivasan G. Srivilliputhur
Department of Materials Science and Engineering
University of North Texas
Denton, Texas, U.S.A.

Acknowledgements

A. Devaraj, N. Gupta, S. Nag, Rajarshi Banerjee
University of North Texas
Denton, Texas, U.S.A.

S. Rajagopalan, H. L. Fraser*
Ohio State University
Columbus, Ohio, U.S.A.
**Now at Exxon Mobil*

Financial support for this work has been provided by the National Science Foundation and the Air Force Research Laboratory

Summary of Experimental Work

- Mechanism of β→ω transformation not completely understood
- β solutionized and quenched Ti-9at%Mo exhibits fine scale ω embryos
  - Different stages of {111} β plane collapse – *aberration corrected HAADF-STEM*
  - Clear evidence of Ti-Ti clustering – *3D atom probe*
  - *Phase separation in β matrix prior to ω formation?*
- Subsequent annealing at 475°C/30mins
  - well-developed ω precipitates – complete collapse of {111} β planes
  - Substantial partitioning of Mo between β and ω

What do we learn from experiments? – Schematic G – X plot for quenched Ti-Mo

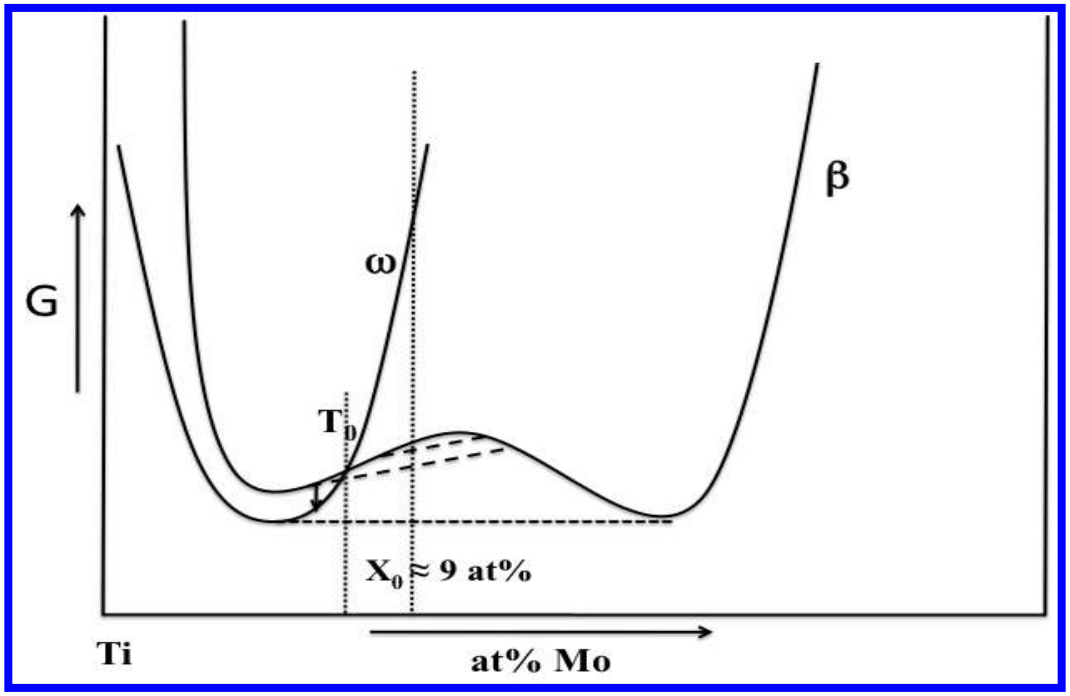

- Phase separation in β matrix required for ω formation in Ti – 9 at% Mo
- Mo-depleted pockets with compositions < T_0 form ω nuclei by displacive collapse
- Is the displacive collapse complete within ω nuclei?

Summary of Experimental Work: Schematic G – η plots for Ti-Mo

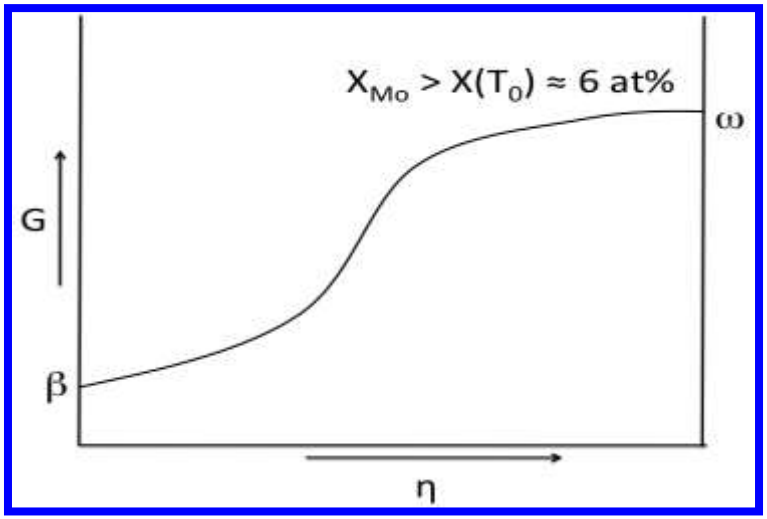

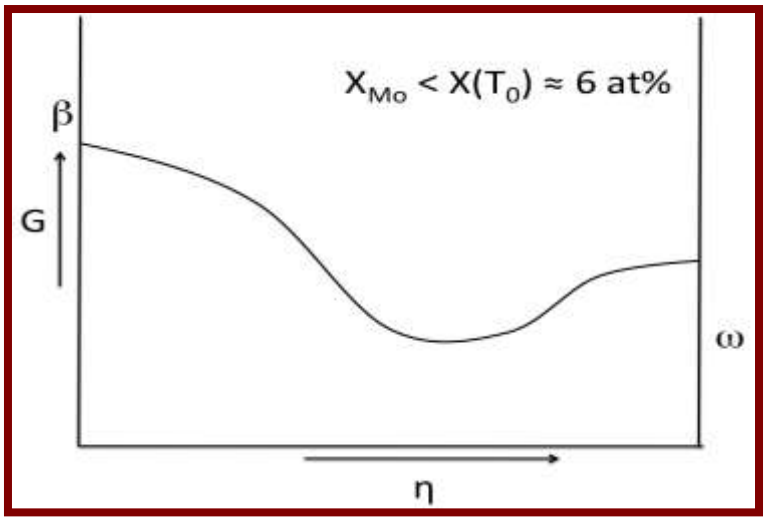

- Mo-depleted pockets with compositions < T_0 form ω nuclei by displacive collapse
- Extent of displacive collapse can be incomplete within ω nuclei – composition dependent amplitude of phonon wave?

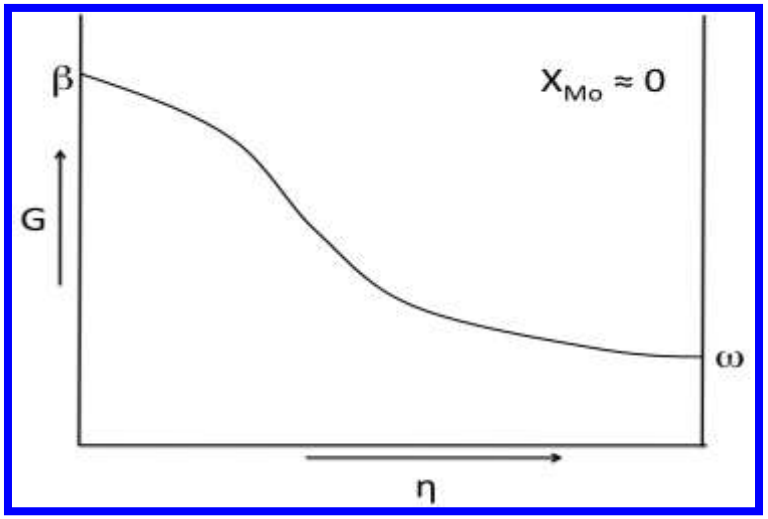

Questions

- Is phase separation in β matrix mandatory for ω formation in Ti-9at%Mo?

- Though ω forms via a displacive collapse of {111} β planes, why is the collapse arrested (partial collapse) in quenched ω embryos

  - Does the extent of collapse depend on ω pocket composition? Why?

- Is there a mixed-mode displacive-diffusional transformation involved in the formation of isothermal ω precipitates?

Simulations Approach Used

- We use first-principles calculations using the Vienna Ab Initio Simulation Package (VASP) (Kresse and Hafnet, PRB 1993)
- β to ω transition path transformation in Ti-Mo system was determined using the Nudged Elastic Band (NEB) (Jónsson , Mills , Jacobsen, 1996)
- We use Projector Augmented Wave (PAW) potentials (Kresse and Joubert, PRB 1999)
- Generalized Gradient Approximation PBE (GGA-PBE) was used (Perdew, Burke, Ernzerhof, PRL 1996)
- Performed convergence tests to determine optimal parameters such as energy of plane wave cutoffs (400eV used) and K-mesh for integration
- Our energy converged to 1 meV /atom

Hexagonal (ω) Phase Precipitation in BCC (β) Titanium

NOTE: Figures Not Drawn to Scale

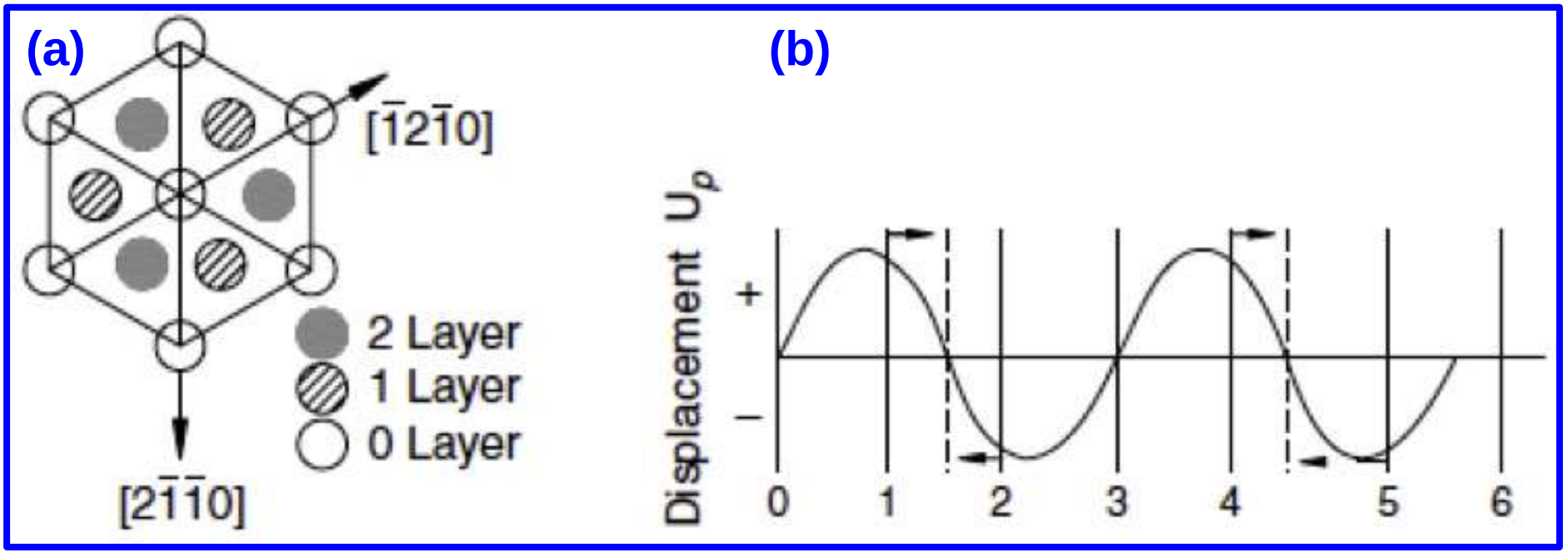

(a) Completed collapsed {222} planes exhibit a 6-fold symmetry and an partial collapse leads to a 3-fold symmetry along <111> axis

(b) The displacement of {222} planes are visualized as a sinusoidal wave with upward and downward motions shown as positive and negative displacements respectively

Banerjee and Mukhopadhyay, Phase Transformations (2007)
de Fontaine, Paton, Williams, Acta Metall. ***19****, 1153(1971)*

Nudged Elastic Band (NEB) Method

- The nudged elastic band (NEB) is a method for finding saddle points and minimum energy paths (MEP) between known reactants and products
- NEB works by first constructing a “chain of images” of the system
- Each image connects to the previous and next image by '*springs*' along the path
- Springs prevent images from sliding down to the nearest minima and forces them to find the lowest energy possible while maintaining equal spacing to their neighbors
- Minimization of the entire system, but with the end structures fixed, provides a MEP

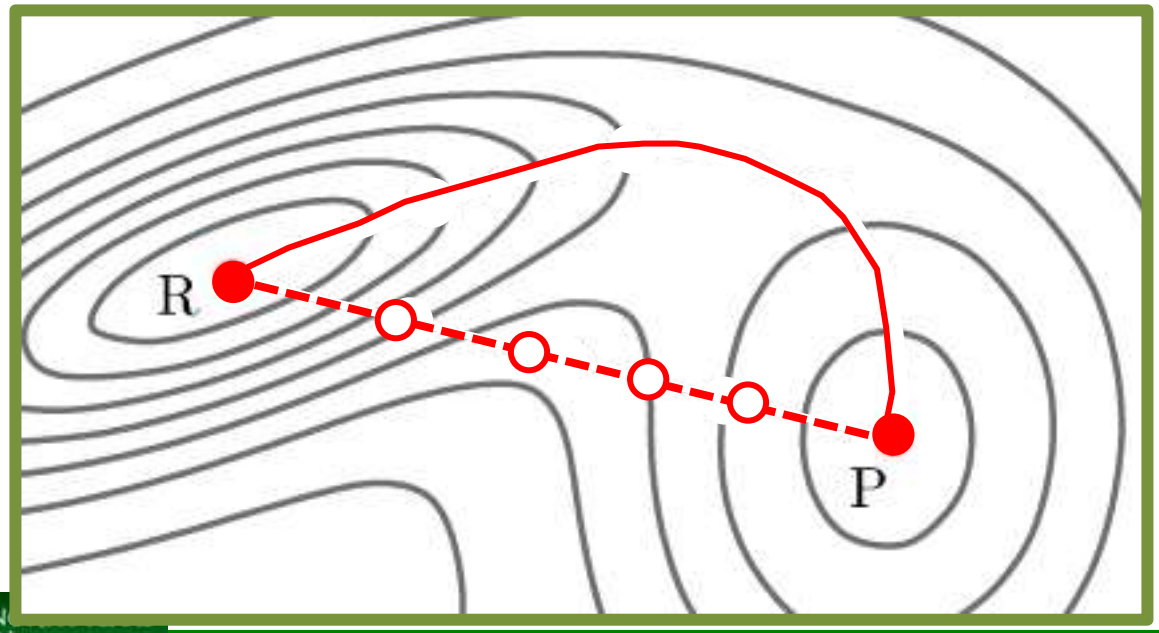

Our Past Success with NEB: Minimum energy path for cross slip of a screw dislocation in Cu

Primary Glide Plane (1-11)

Cross-Slip Plane (-111)

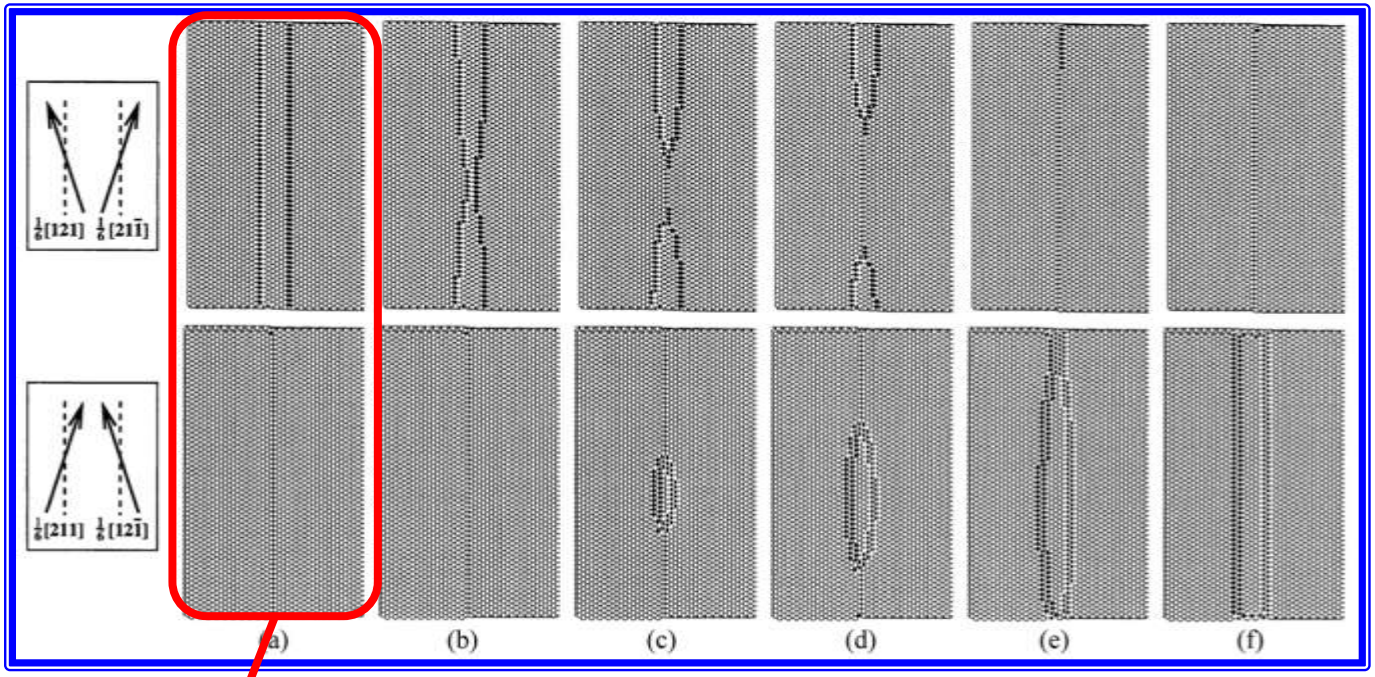

(a) Initial configuration with parallel Shockley partials in the primary glide plane

Rasmussen, Jacobsen, Leffers, Pedersen, Srinivasan, Jónsson (PRL 1997)

Our Past Success with NEB: Understanding α to ω transformation in Pure Titanium

Popular Silcock Mechanism (Acta Metall., 1958)

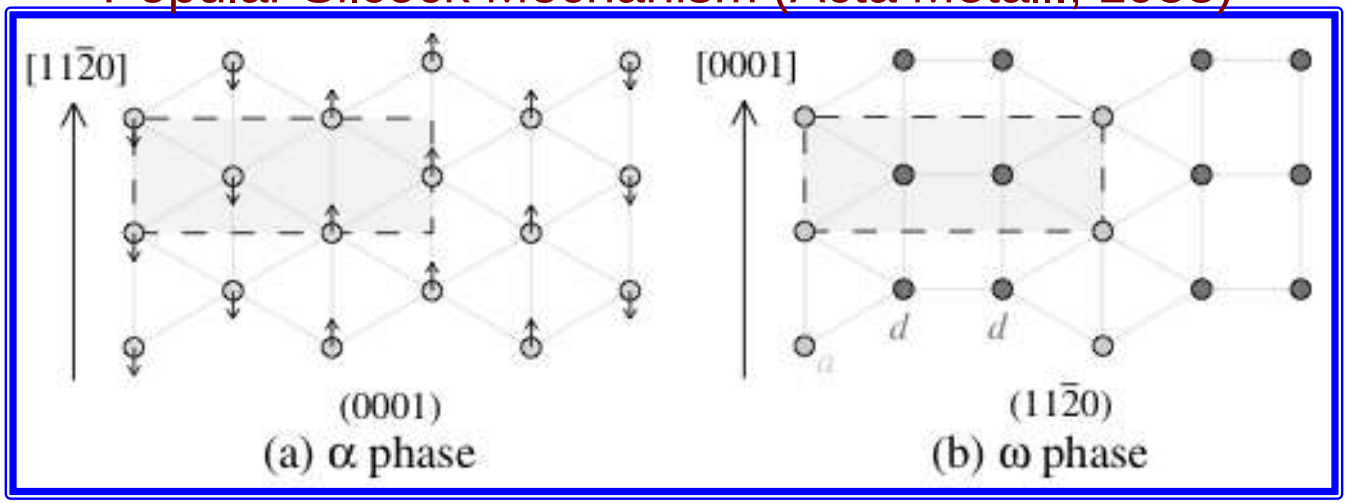

- In each stacking plane, 3 out of every 6 atoms shuffle by 0.74 Å along $[11\text{-}20]_\alpha$ while the other 3 shuffle along $[\text{-}1\text{-}120]_\alpha$
- This shuffle is accompanied by a strain $\varepsilon_{xx} = 0.05$ along $[1\text{-}100]_\alpha$ and $\varepsilon_{yy} = -0.05$ along [11-20] to produce a hexagonal ω cell with the correct c/a ratio.

Our Past Success with NEB: Understanding α to ω transformation in Pure Titanium

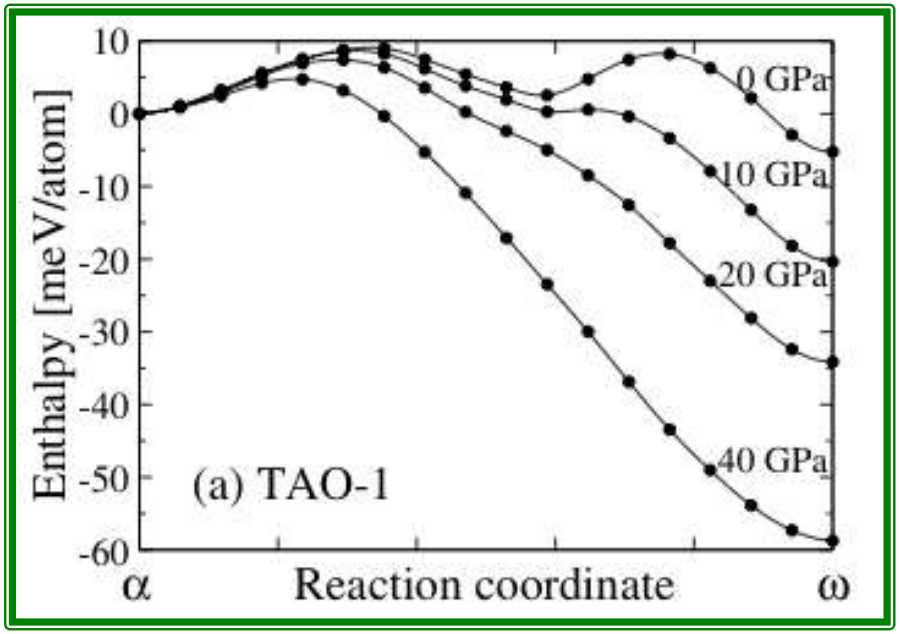

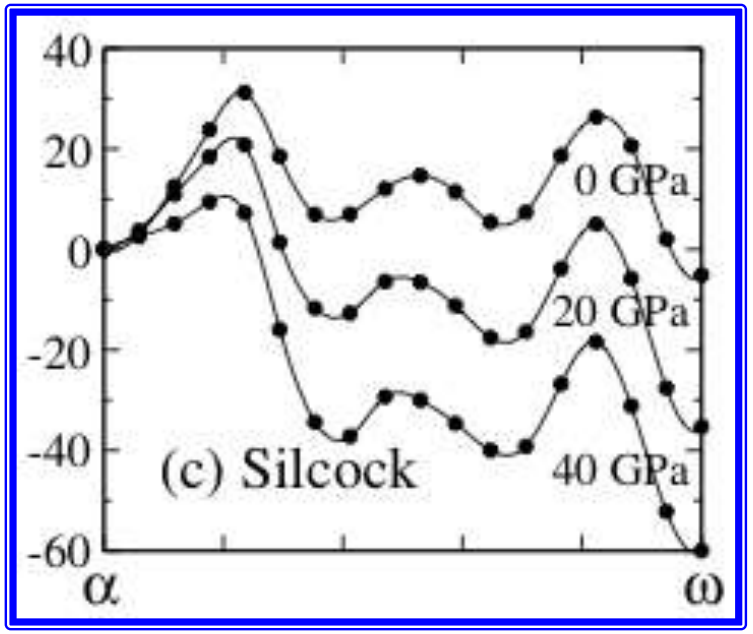

- The TAO-1 path gives the smallest barrier by a factor of 4 at 0 GPa.
- Silcock pathway have larger barriers at from 0 GPa to 40 GPa

Our Past Success with NEB: Understanding α to ω transformation in Pure Titanium

Usikov and Zilbershtein α –> ω transition path
(Usikov & Zilbershtein, Phys. Status Solidi A 1973)

- Mechanism: α –> β –> ω transition via an unstable intermediary β-phase
- α –> β transition occurs via an *inverse Burgers mechanism*, and is followed by β –> ω transition via collapse of 2 out of 3 $(111)_\beta$ planes
- This produces 2 unique pathways called variant-I and variant-2, depending on the direction of $\{111\}_\beta$ planes collapse.
- Allowing variants-1 and 2 to *relax away* from the β-phase yields our TAO-1 and TAO-2 direct transformation pathways

Our Past Success with NEB: Understanding how impurities block α to ω transformation in Titanium

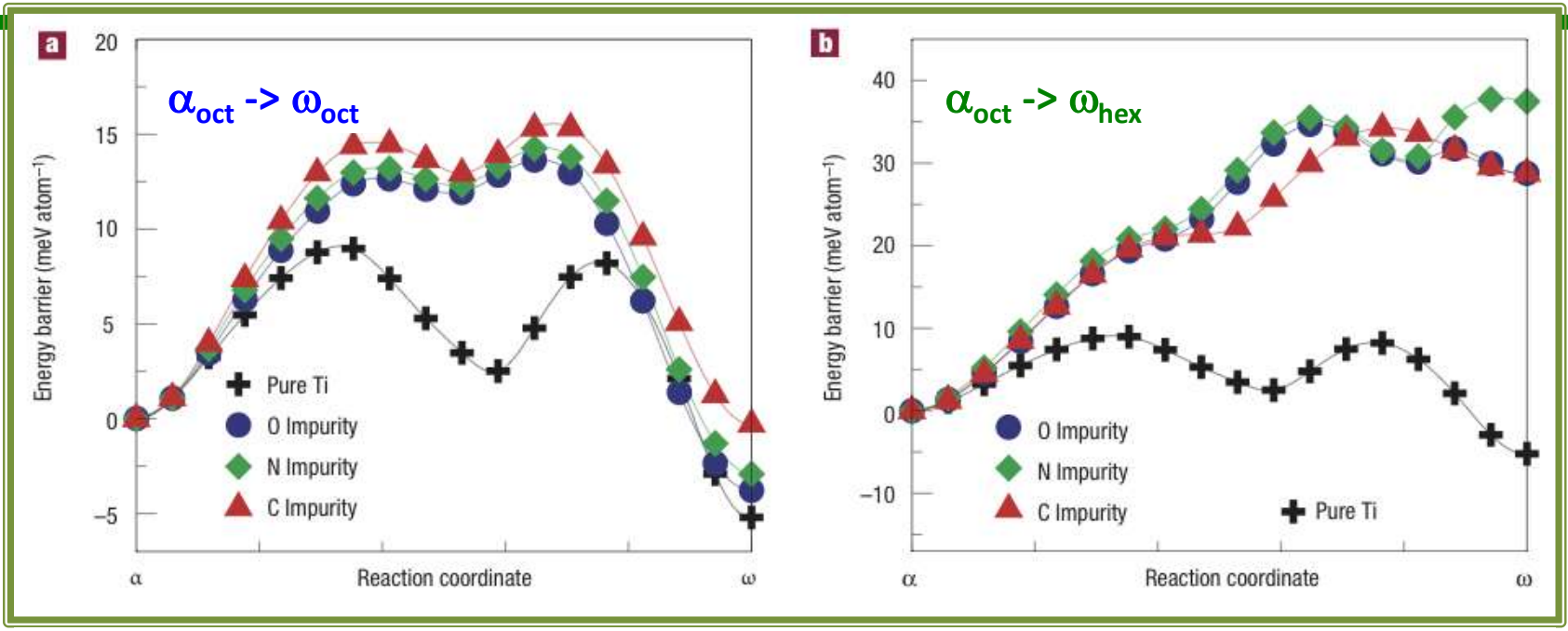

- C, N, O impurities suppresses the ⟨ □ ⌉ transformation by:
  - increasing both the ⌉ energy relative to ⟨ and the energy barrier
- Despite different chemistry, C, N, O increase the energy barrier and the relative energy by nearly the same amount
- This indicates that their primary effect is *steric*

Hennig et al, Nature Materials (2005)

Our Past Success with NEB: Understanding how impurities block α to ω transformation in Titanium

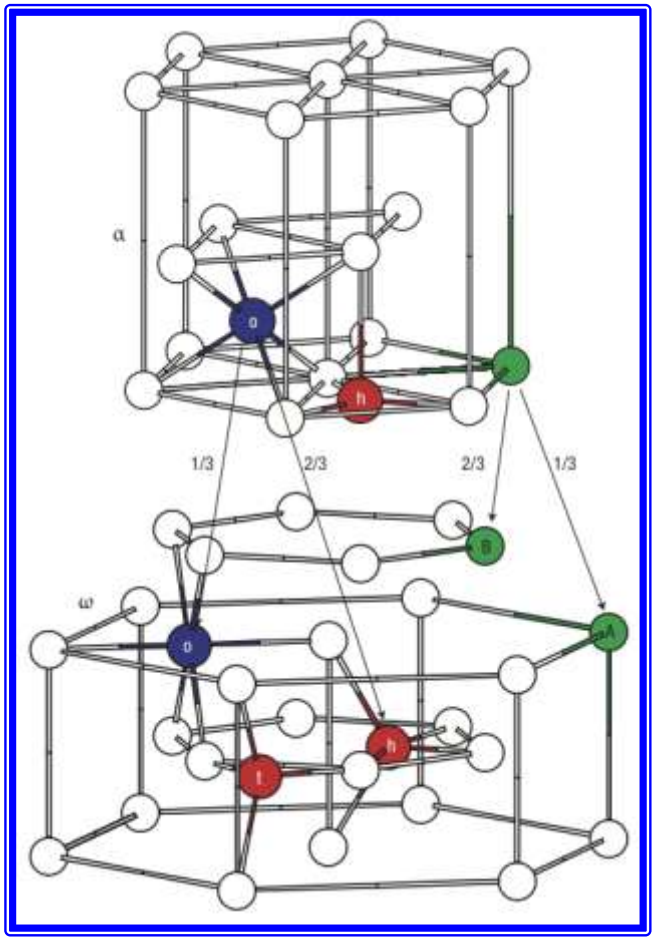

Interstitials in α and ω Ti

- Octahedral (o), tetrahedral (t), and hexahedral (h) sites for interstitial impurities
- A and B are substitutional impurity sites

Hennig et al, Nature Materials (2005)

Pure Ti Lattice Parameter and Energy

parameter	Ti beta super cell	Ti omega supercell	% change
a	4.5995	4.5773	0.5349 %
b	4.5995	4.5773	0.5349 %
c	5.6335	5.6595	-0.369 %
Supercell Energy (ev)	-46.693196	-47.380604	688 meV

- Beta to omega transformation involves:
  - Contraction of 0.53% along a and b axis
  - Expansion of 0.37% along c axis of supercell.
- For pure Ti beta is 688 meV higher than omega

Mo substitution in Ti super cells

- Beta to omega transformation in pure Ti involves:
  - Contraction of 0.53% along a and b axis
  - Expansion of 0.37% along c axis of supercell.
- For pure Ti beta is 688 meV higher than omega

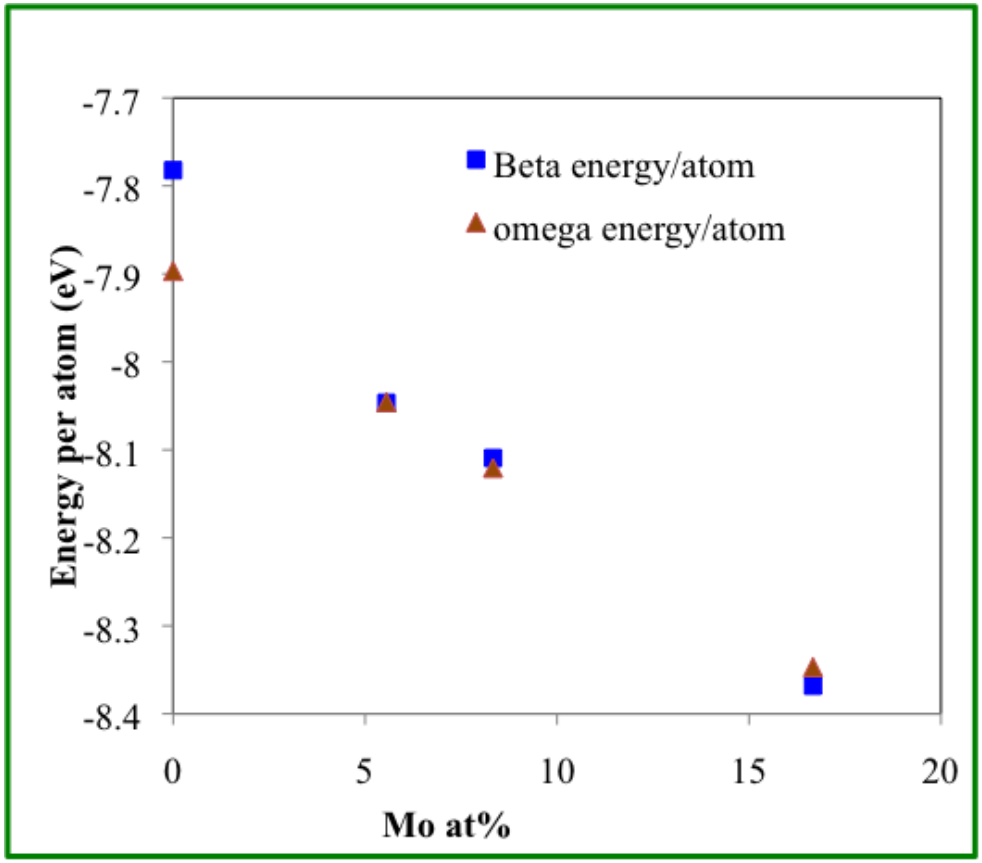

Beta to omega transformation in Pure Ti

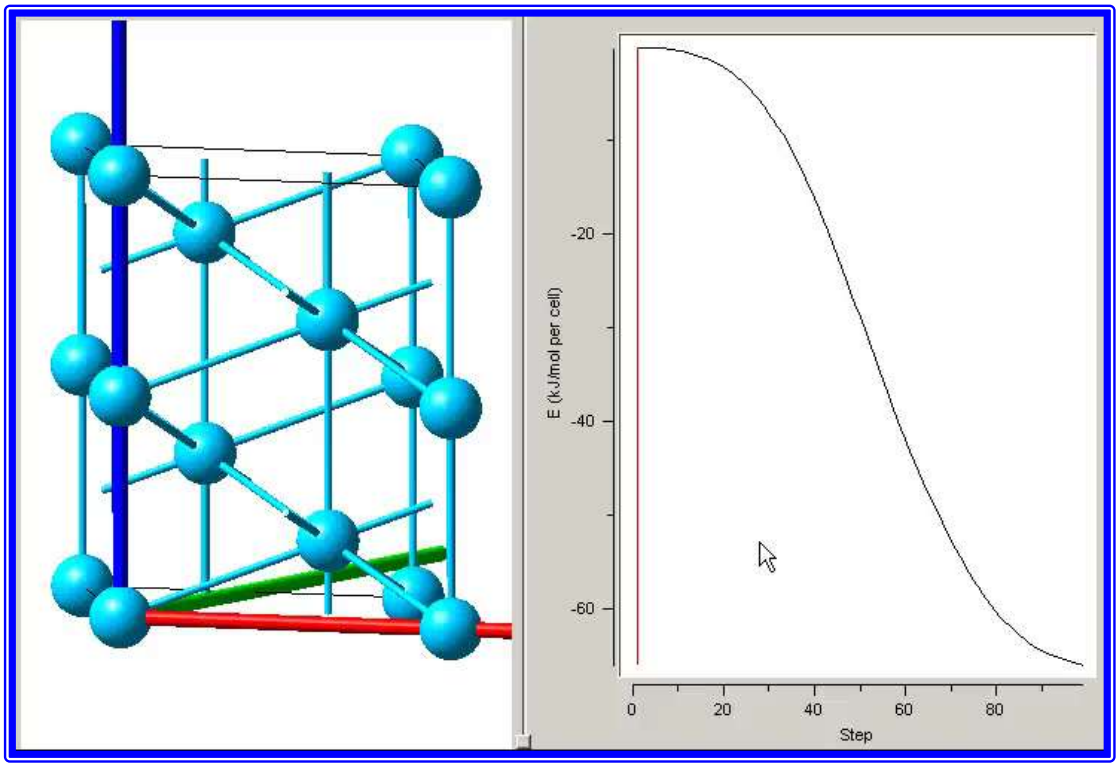

No activation barrier observed in the nudge elastic band method for pure Ti beta to omega transformation

Ti – 16 at% Mo System (1 Mo + 5 Ti atoms in supercell)

- Energy of beta is lower than omega
- Systems with Mo substituted in the collapsing plane positions show same energy
- The omega structure with Mo in noncollapsing planes has a higher energy than omega with Mo in collapsing planes

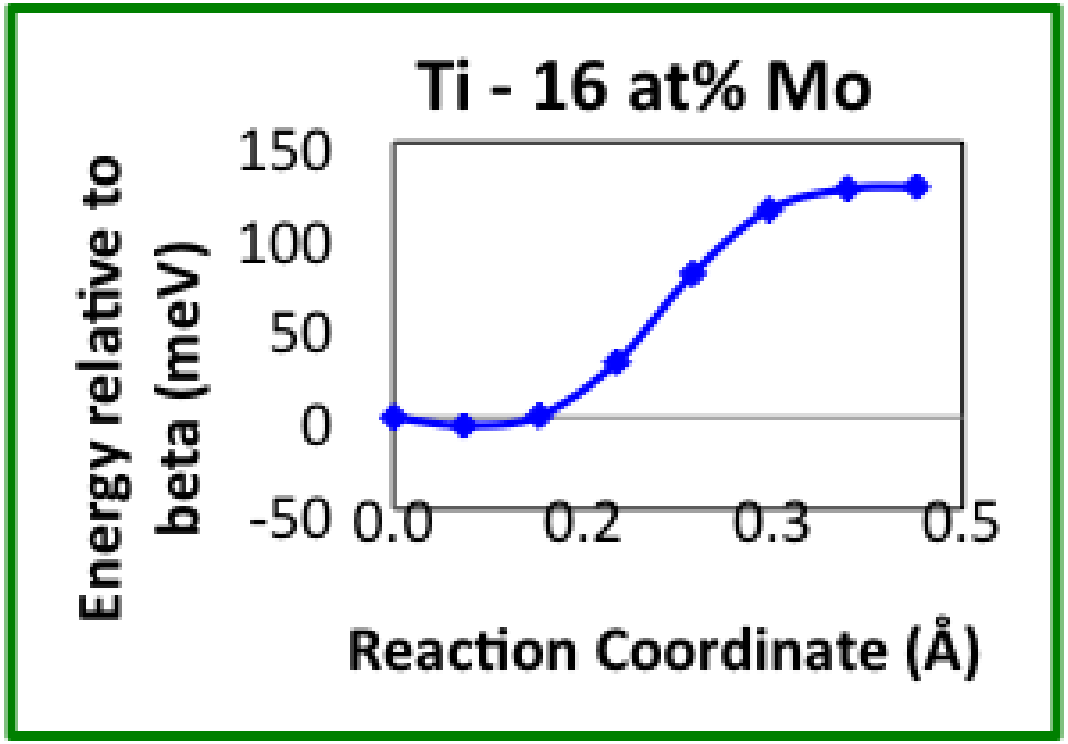

A local minima at 21% partially collapsed structure observed near beta

Ti – 8.33 at% Mo System (1 Mo + 11 Ti atoms in supercell)

- Beta has a higher energy than omega
- A 30 meV activation barrier must be overcome by beta to transform to omega
- There is a local minima close to omega (41 meV) that must be overcome by system to transform fully to omega

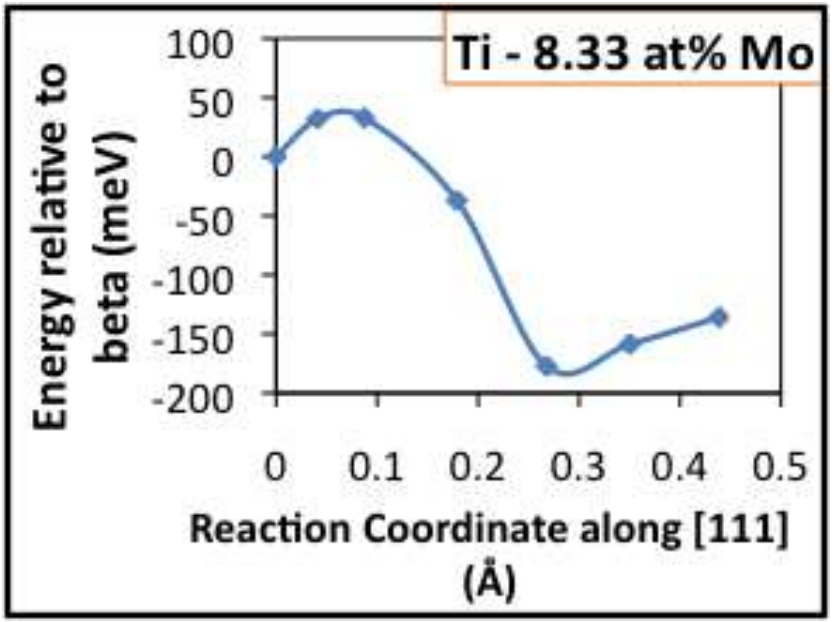

Ti – 5.6 at% Mo System (1 Mo + 17 Ti atoms in supercell)

CALCULATIONS NOT CONVERGED

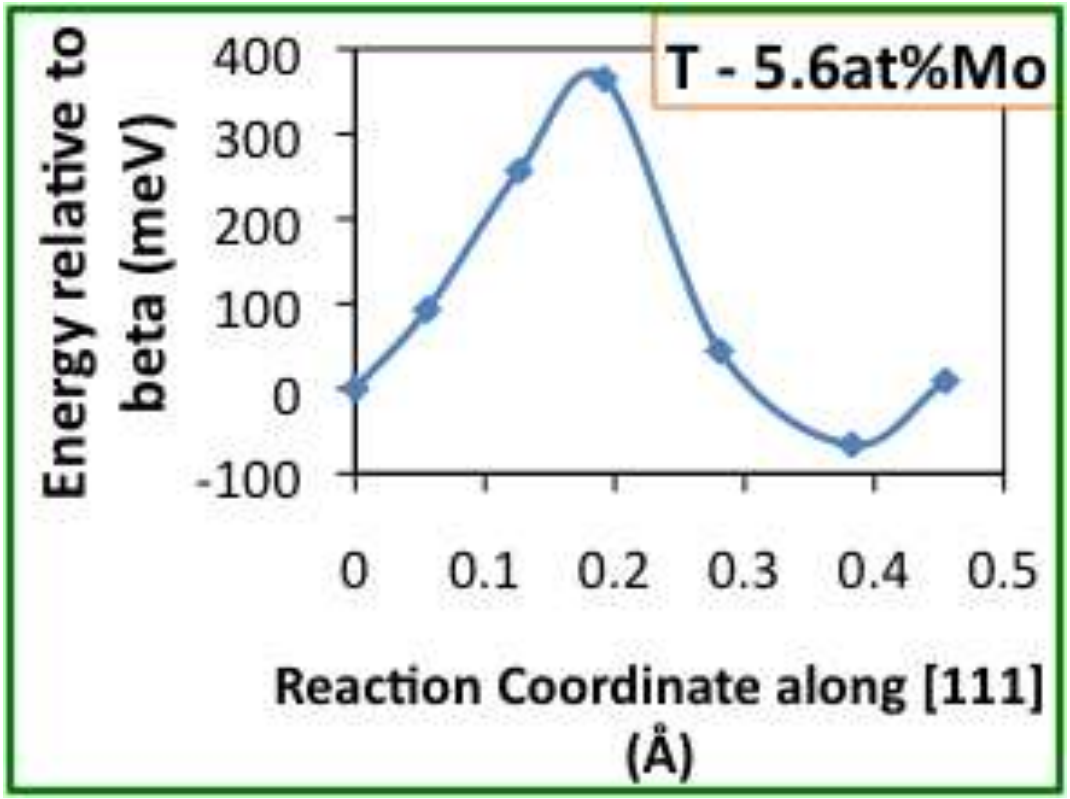

NEB work summary

- In pure Ti beta omega transformation is thermodynamically favorable
- Trends observed in Ti-Mo alloys are
  - 4.16% Mo: Similar to pure Ti, Roll down with some minima close to omega
  - 5.55%Mo: in progress
  - 8.33%Mo: Similar to pure Ti, Roll down with some minima close to omega
  - 16.66%Mo: Opposite to pure Ti, minima close to beta

Points to Ponder …..

- Our preliminary calculations point to the ability of VASP + NEB calculations to determine activation barriers and order parameters for the beta to omega transformations rigorously
- As seen, our current systems are too small to allow variation of composition through out the supercell
- We are currently increasing our systems sizes to a couple of hundred atoms
- Such large systems may not be sufficient
- We may have to use semi-empirical atomisitic models such as MEAM, tight binding, MGPT or bond-order potentials to handle larger systems
- Need to couple these atomistic methods with combinatorial approaches to investigate effect of local compositional environment on saddle points in model binary systems

Thank you for your Attention
Questions?

Accelerated Molecular Dynamics: Methods and Examples

Blas Pedro Uberuaga

Los Alamos National Laboratory

Atomistic Dynamical Simulations 101

- **Goal: simulate time evolution of a system of atoms**
- **Foundations:**
  - Interatomic potential
    - Parameters fit to experiment, high quality calculations
  - Newton's Second Law
    - Tells how system evolves under forces
    - Can directly integrate to get time evolution
- **But!**
  - Can only perform ~2000 force evaluations/second (on Opteron)
  - Typical vibrational period of an atom is 10-100 fs
  - Need ~10 force evaluations per vibrational period for accurate integration
    - Each force evaluation advances system time by 1-5 fs
  - 10^{11} years to simulate 1 second!

MD may *never* get to relevant time scales

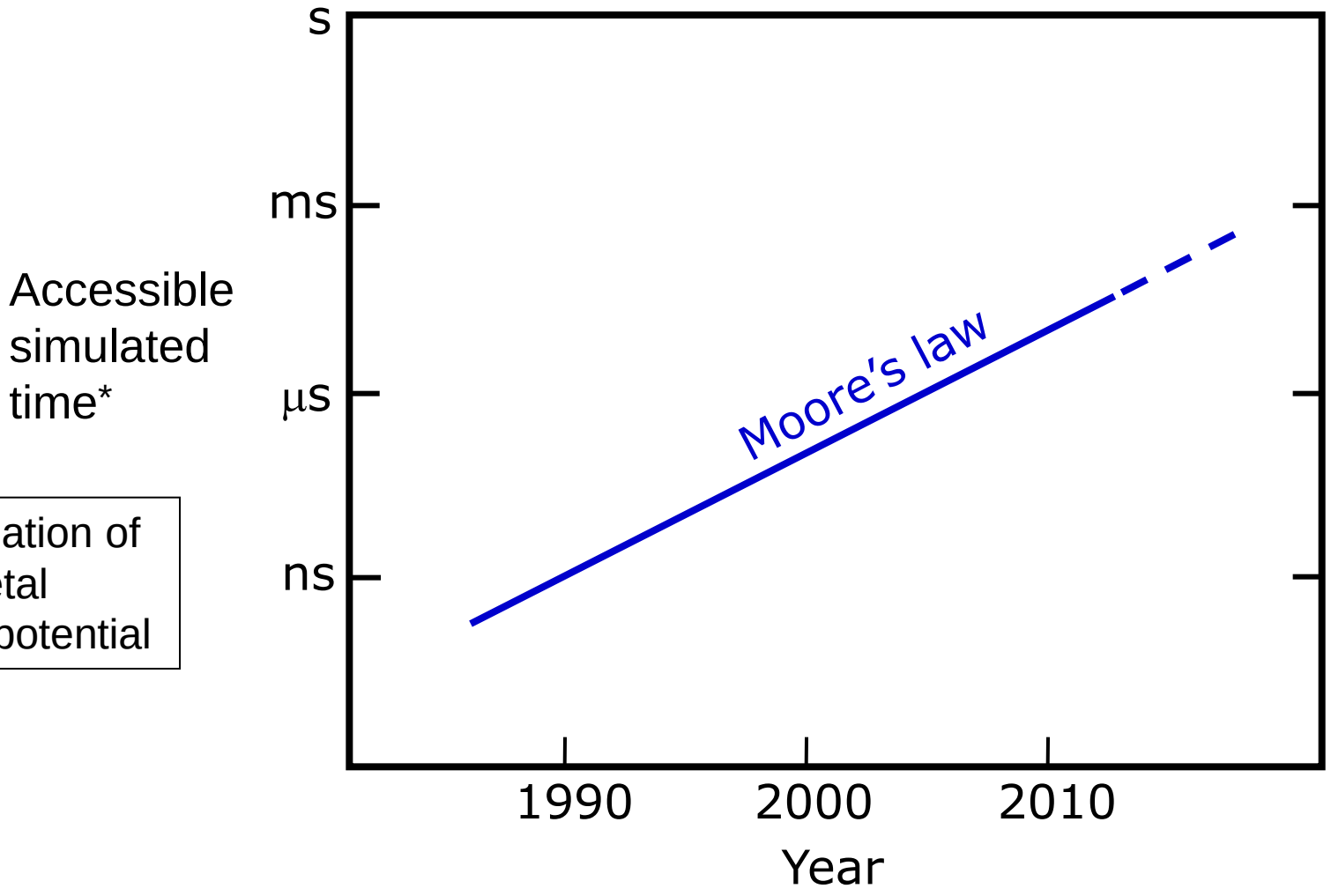

* 1-week simulation of 1000-atom metal system, EAM potential

Brief Introduction to Accelerated Dynamics

- **Many processes occur on much longer timescales than accessible via MD (ps-ns-μs)**
  - e.g. surface growth
  - radiation damage annealing
  - nucleation
  - Etc.
- **Need method to reach experimentally relevant timescales**
- **Three accelerated dynamics methods developed at LANL (Art Voter's team)**
  - Parallel-Replica Dynamics
  - Hyperdynamics
  - Temperature Accelerated Dynamics (TAD)

Infrequent Event System

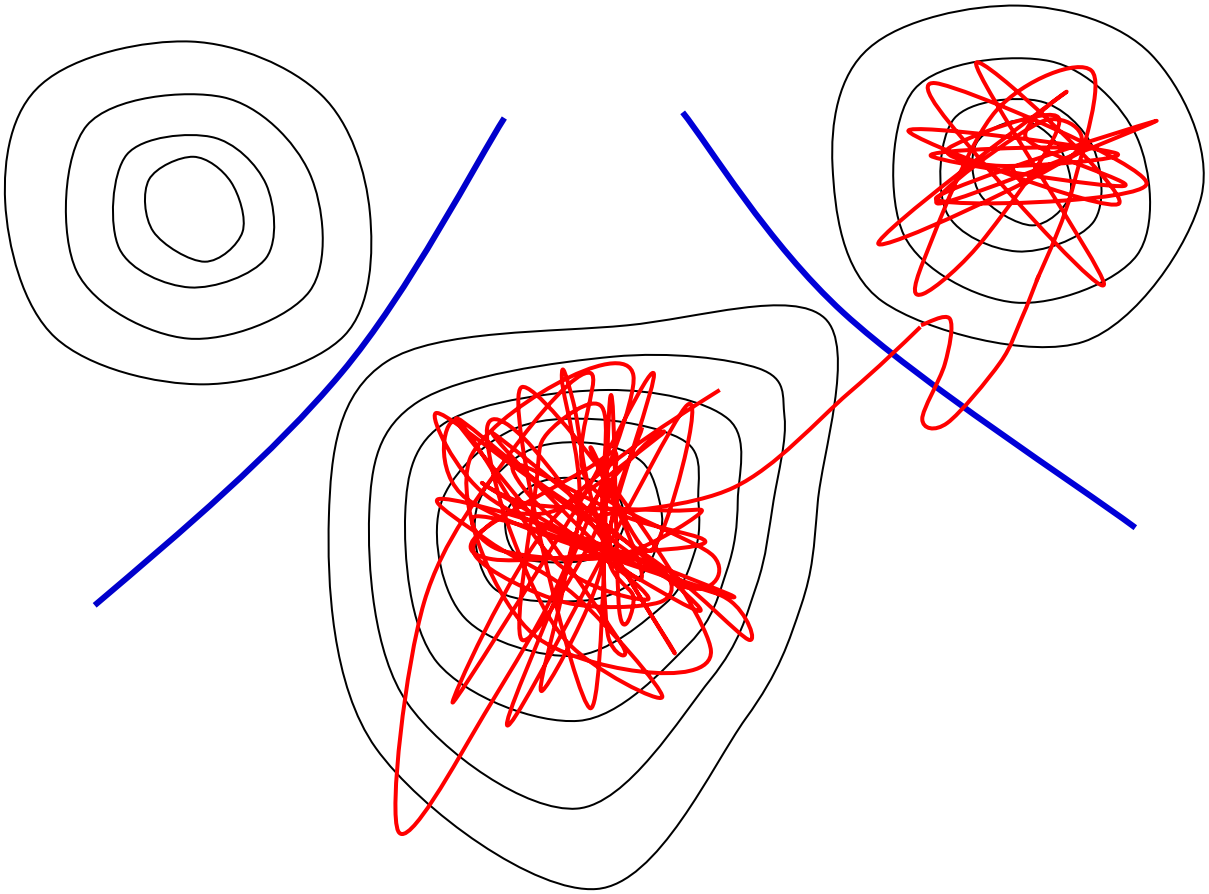

- The system vibrates in 3N-dimensional basin
- Occasionally it escapes, crossing through a dividing surface to a new basin
- This behavior characterizes solid-state diffusion, as well as many other processes

Accelerated Molecular Dynamics Methods

Hyperdynamics	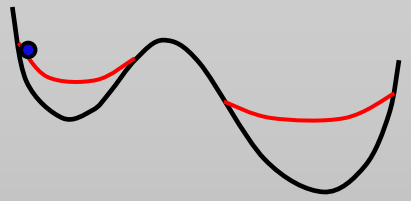	Increase rate by reducing effective barriers	*AFV, J. Chem. Phys., 1997*

Accelerated Molecular Dynamics Methods

Hyperdynamics	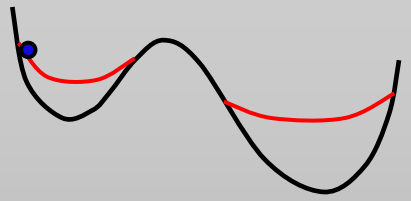	Increase rate by reducing effective barriers	*AFV, J. Chem. Phys., 1997*
Parallel Replica Dynamics	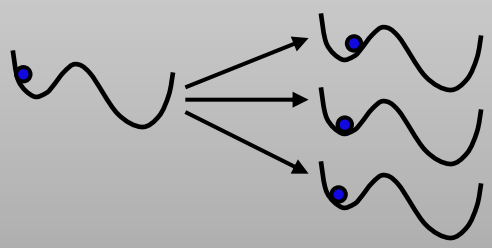	Explore basin with many processors M	*AFV, Phys. Rev. B, 1998*

Accelerated Molecular Dynamics Methods

Hyperdynamics	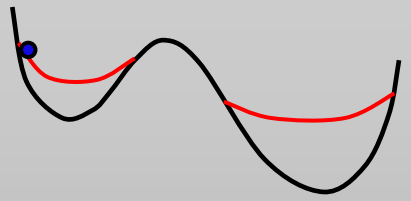	Increase rate by reducing effective barriers	*AFV, J. Chem. Phys., 1997*
Parallel Replica Dynamics	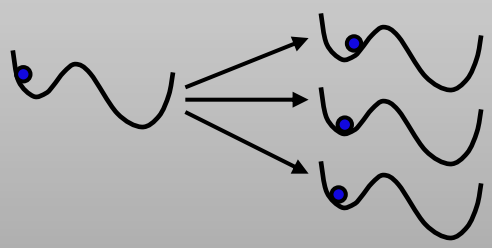	Explore basin with many processors M	*AFV, Phys. Rev. B, 1998*
Temperature Accelerated Dynamics	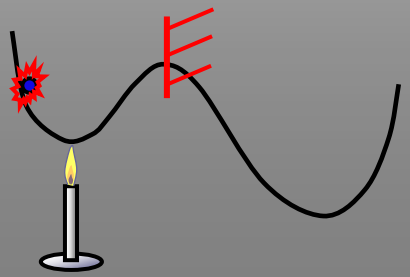	Increase rate by raising temperature	*M.R. Sorensen and AFV, J. Chem. Phys., 2000*

Accelerated Molecular Dynamics Methods

Hyperdynamics	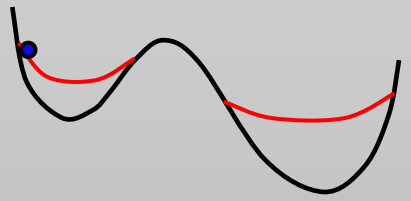	Increase rate by reducing effective barriers	*AFV, J. Chem. Phys., 1997*
Parallel Replica Dynamics	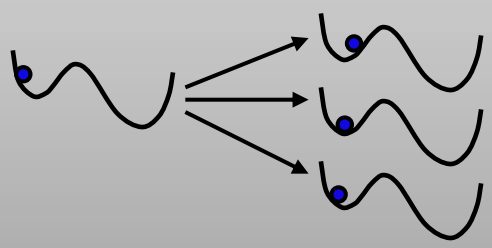	Explore basin with many processors M	*AFV, Phys. Rev. B, 1998*
Temperature Accelerated Dynamics	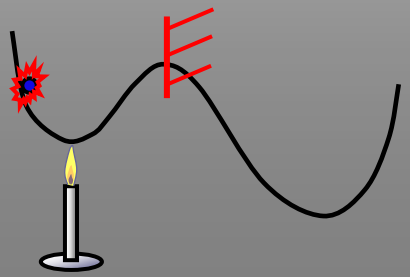	Increase rate by raising temperature	*M.R. Sorensen and AFV, J. Chem. Phys., 2000*

Common Themes: - reduce waiting time for a transition to order of picoseconds;
- let trajectory find transitions "naturally"

Introduction to Hyperdynamics

Voter, *JCP* **106**, 4665 (1997)

- **Builds on umbrella-sampling techniques (e.g., Valleau 1970's); takes it into the time domain**
- **Assumptions:**
  - infrequent events
  - transition state theory (no recrossings)
- **Procedure:**
  - design bias potential ΔV
    - zero at dividing surfaces
    - causes no recrossings
  - run thermostatted trajectory on the biased surface ($V+\Delta V$)
  - accumulate hypertime as

$$t_{hyper} = \Sigma \Delta t_{MD} \exp[\Delta V(R(t))/k_B T]$$

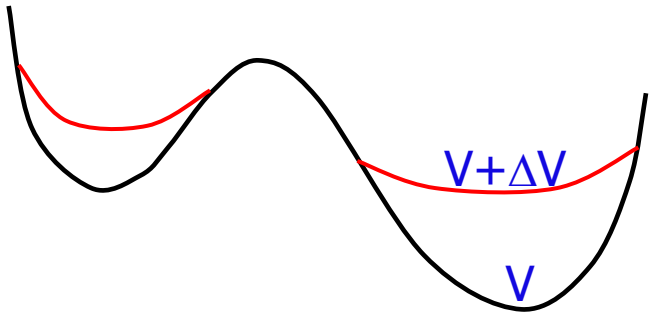

- **Result:**
  - state-to-state sequence correct (because relative rates are preserved)
  - time converges on correct value in long-time limit (vanishing relative error)

Hyperdynamics - characteristics

- **Key challenge is designing a bias potential that:**
  - meets the requirements of the derivation
  - is computationally efficient.
- **Bias potential can be a function of**
  - the shape of the energy surface (AFV, 1997)
  - the energy (Steiner, Genilloud and Wilkins, 1998)
  - the geometry (e.g., bond lengths, Miron and Fichthorn, 2003, 2005)
- **Must be careful that bias is zero on all dividing surfaces or dynamics will be wrong.**
- **When barriers are high relative to T, boost can be many orders of magnitude.**

Introduction to Parallel-Replica Dynamics

Voter, *PRB* **57**, R13985 (1998)

- **Offers parallel speed-up in simulation time**
  - Not as “glamorous” as other methods which offer exponential speed-up on a single processor
- **However, parallel-replica can be applied to systems not suited to the other methods**
  - Rough potentials
  - Floppy systems with fast transitions
  - Driven systems
- **Assumptions:**
  - infrequent events
  - transitions can be detected
  - correlation time known
  - distribution of first-escape times is exponential

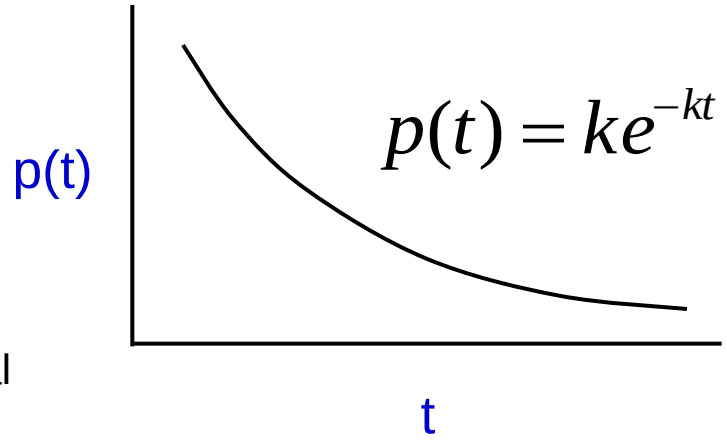

Parallel-Replica Algorithm

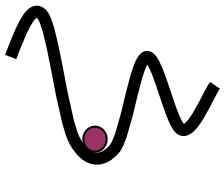

Parallel-Replica Algorithm

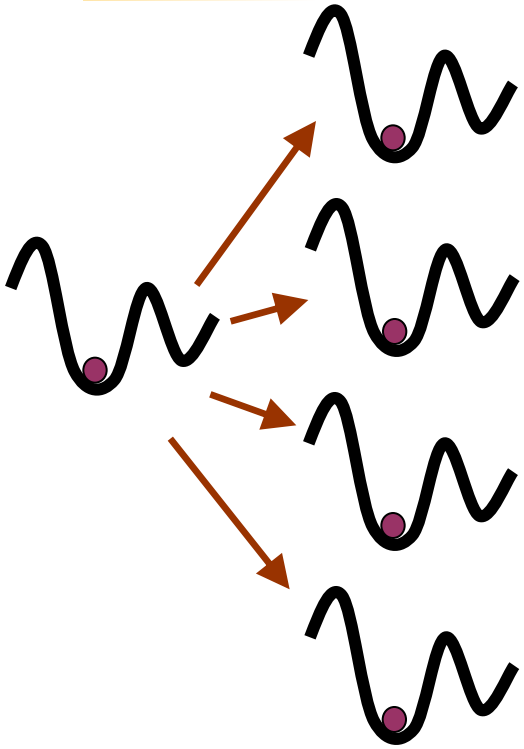

Replicate

Parallel-Replica Algorithm

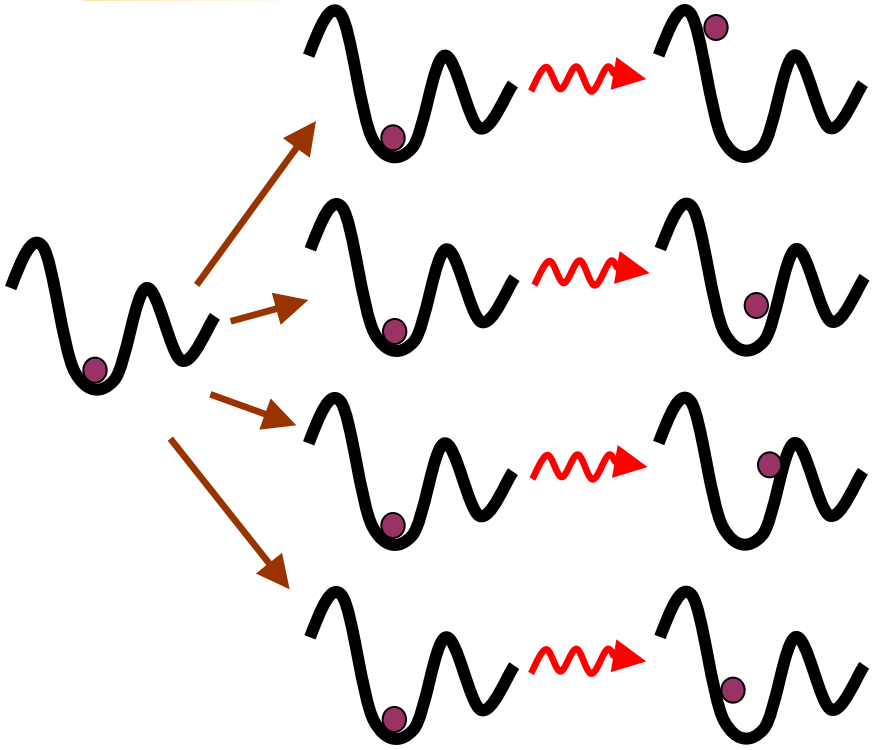

Dephase

Parallel-Replica Algorithm

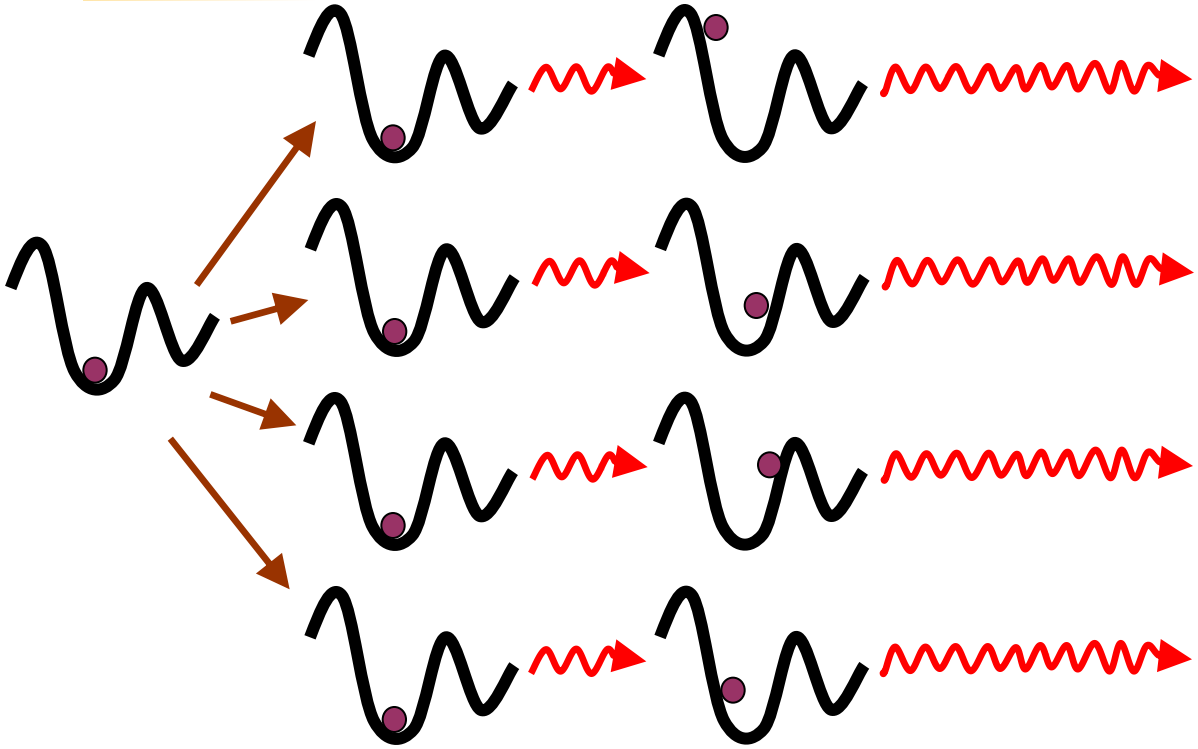

Parallel MD

Parallel-Replica Algorithm

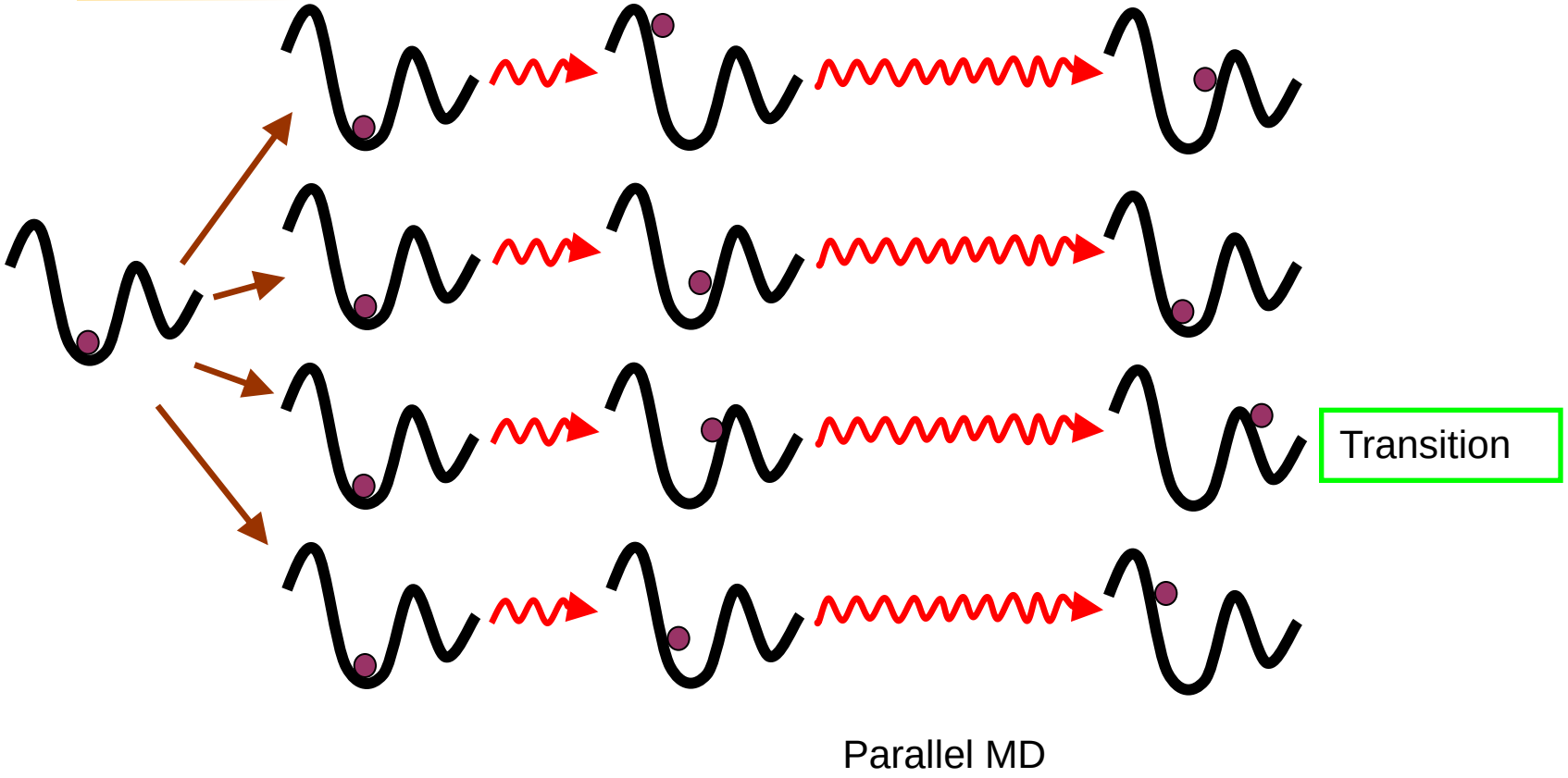

Parallel-Replica Algorithm

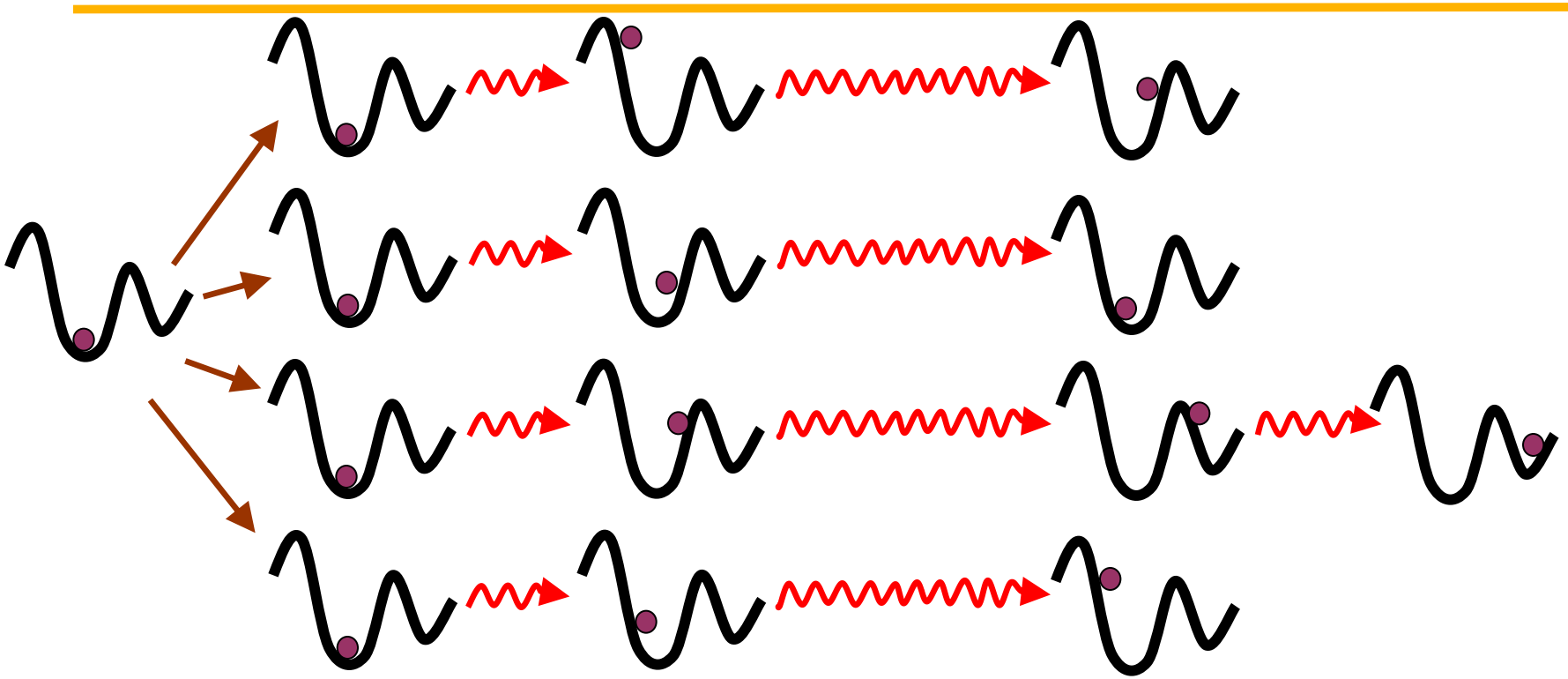

Parallel-Replica Algorithm

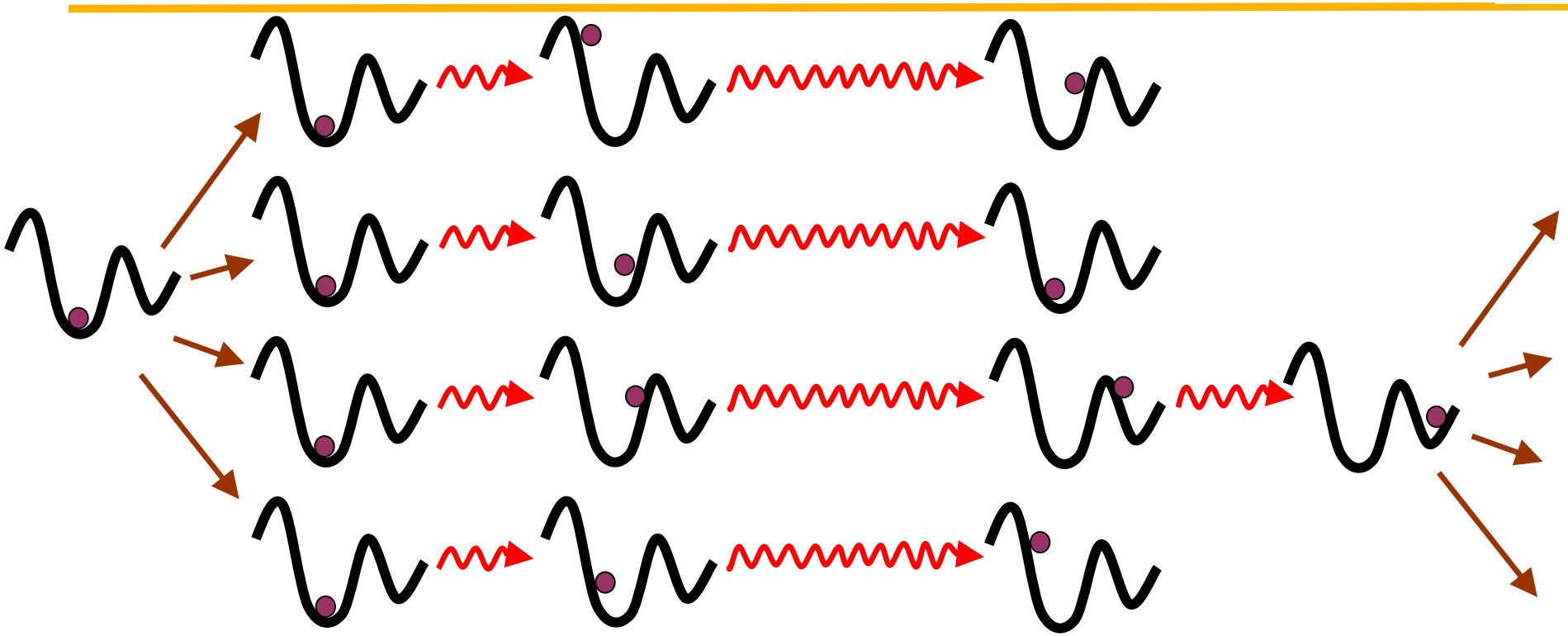

Parallel-Replica Algorithm

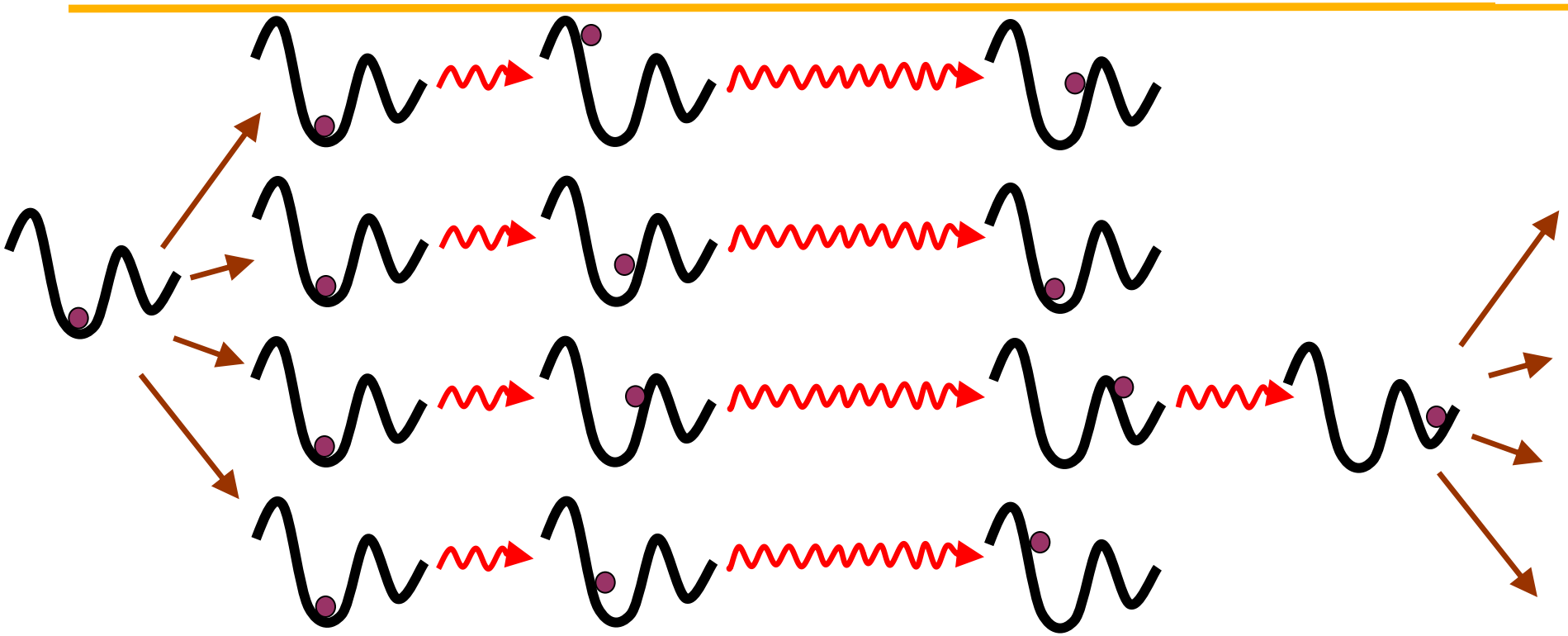

➔ Exact Longtime Dynamics

Parallel-Replica Algorithm

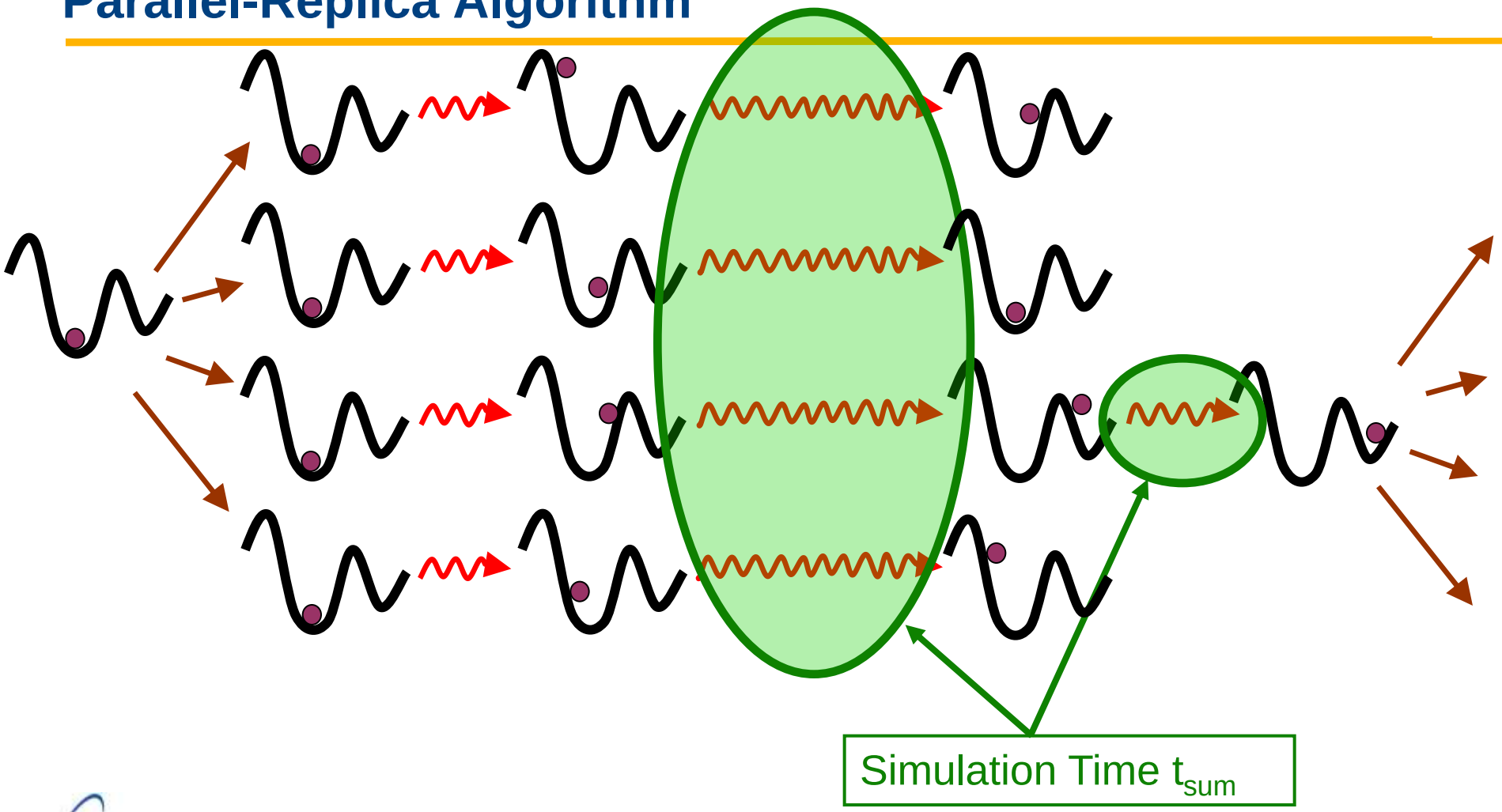

Parallel-Replica Algorithm

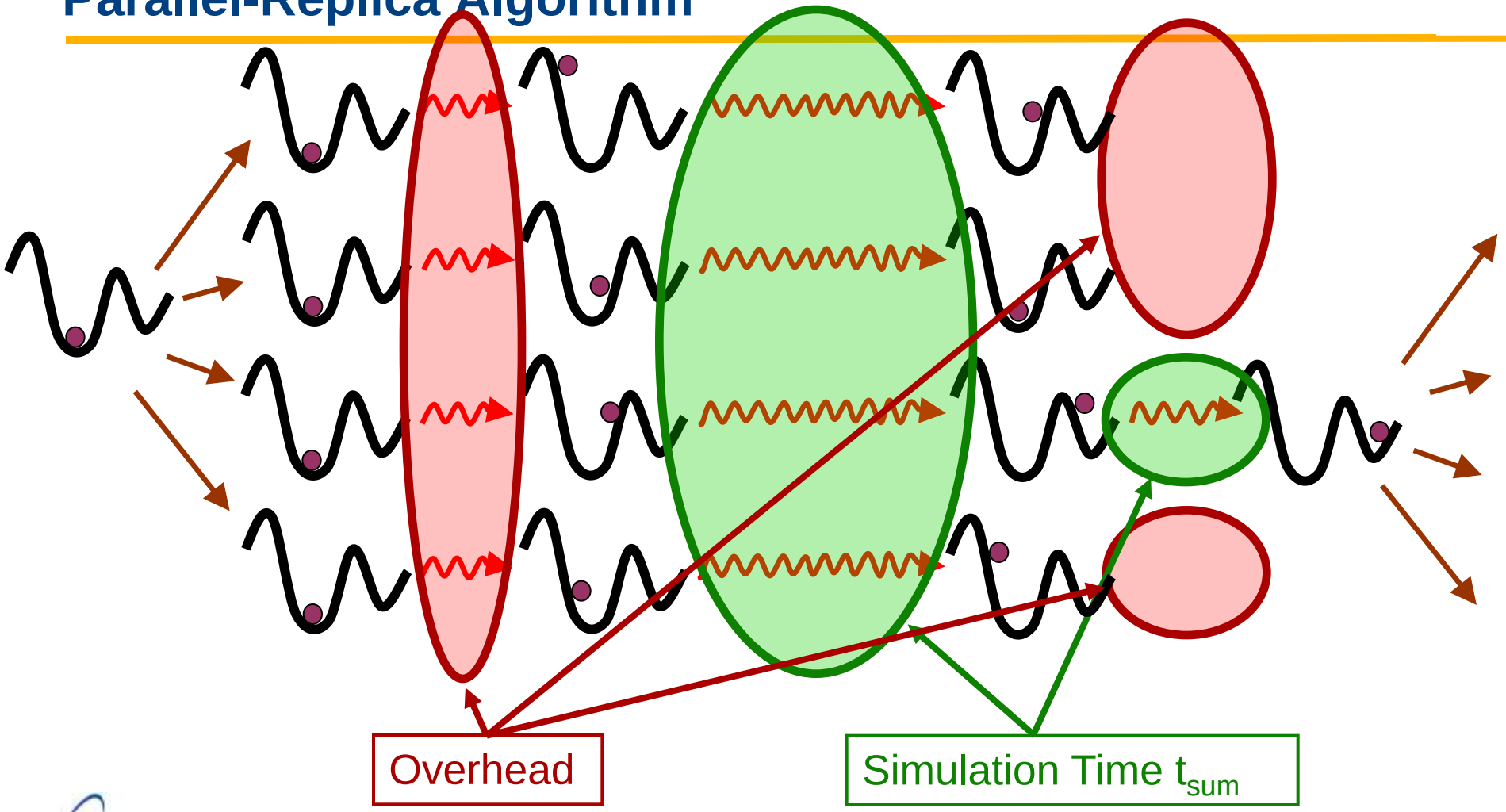

Parallel-Replica Algorithm

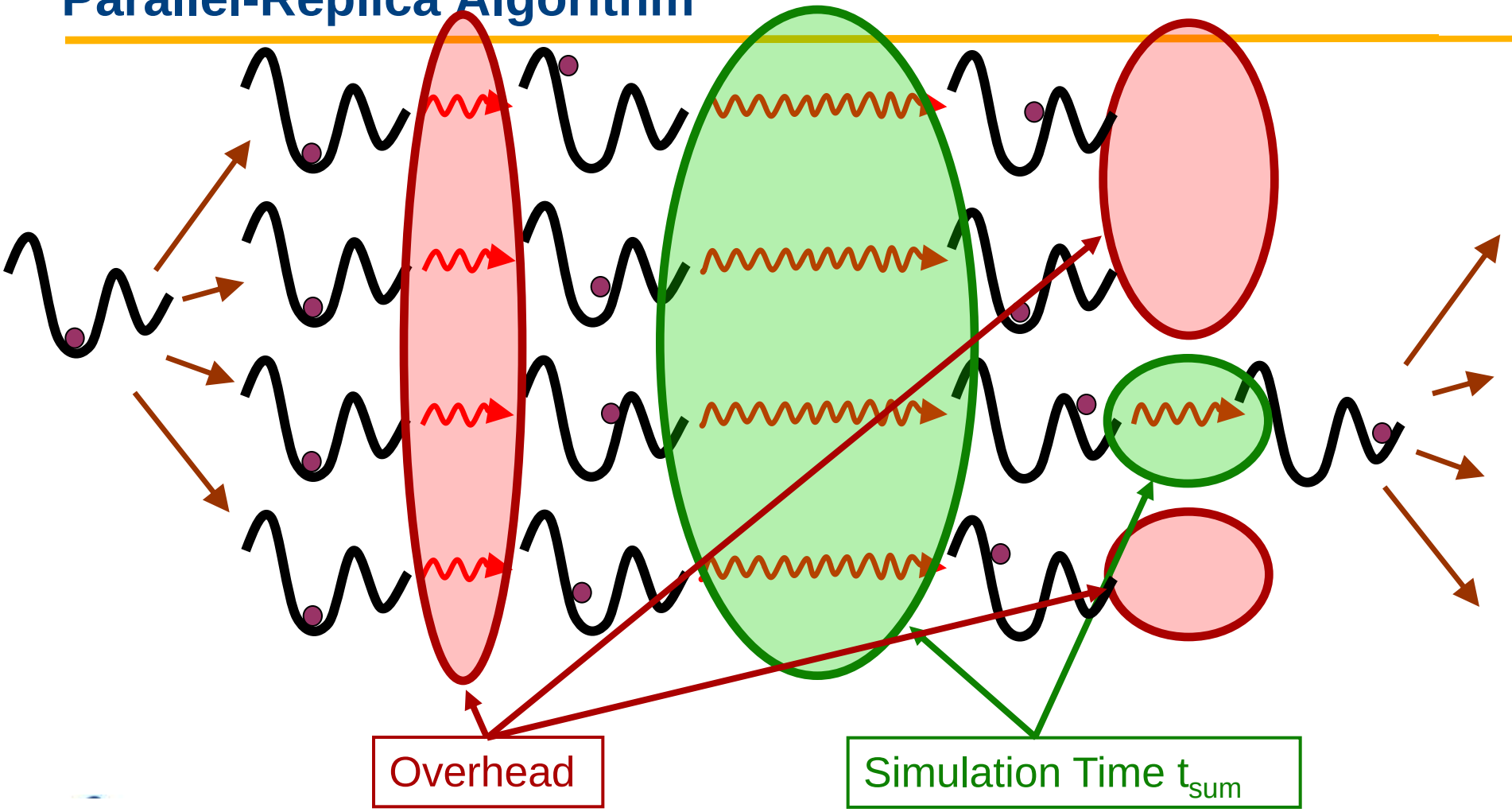

Good parallel efficiency if $t_{rxn} / M >> \tau_{dephase} + \tau_{corr}$

Comparison of Parallel Algorithms

Standard MD

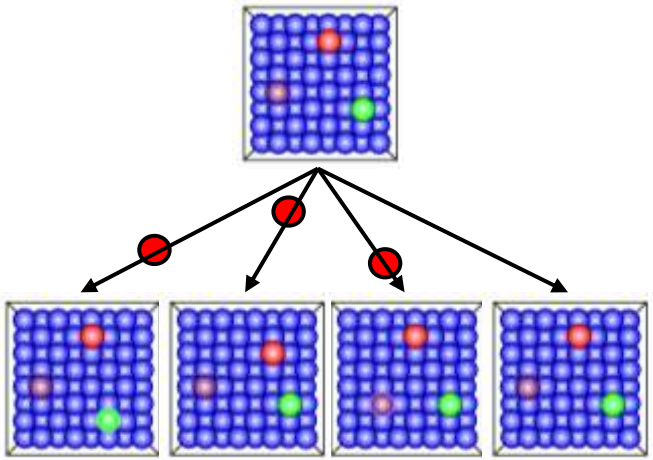

M simulations of
size N for time t

● = event

UNCLASSIFIED

Comparison of Parallel Algorithms

Standard MD

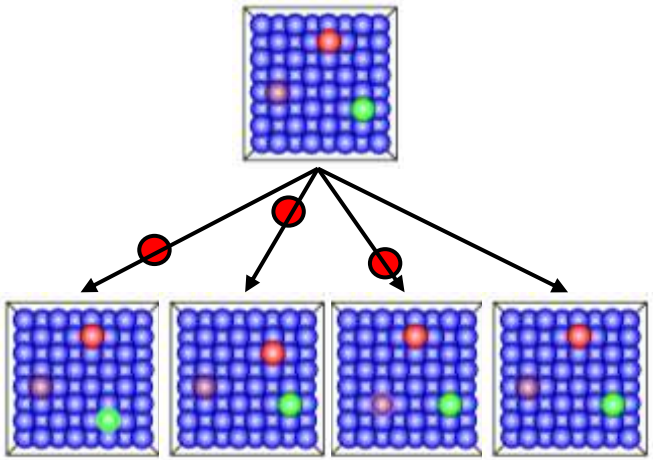

M simulations of
size N for time t

Spatial Parallelization

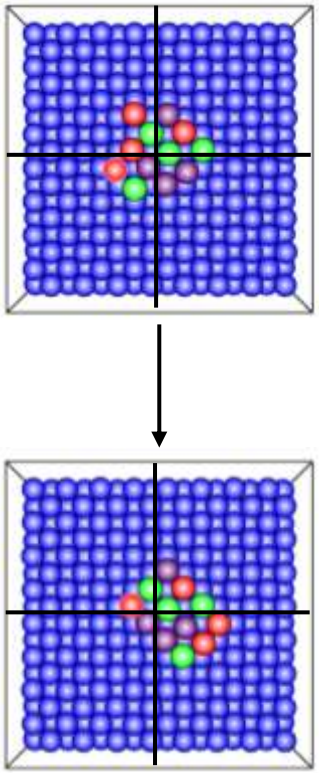

1 simulation of size
MN for time t

● = event

UNCLASSIFIED

Comparison of Parallel Algorithms

Standard MD

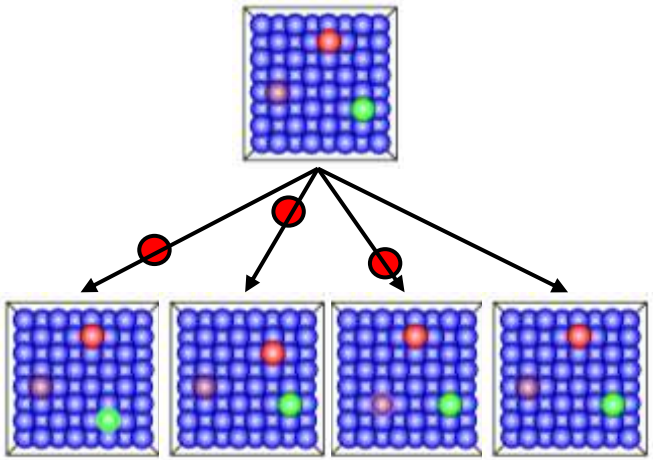

M simulations of
size N for time t

Spatial Parallelization

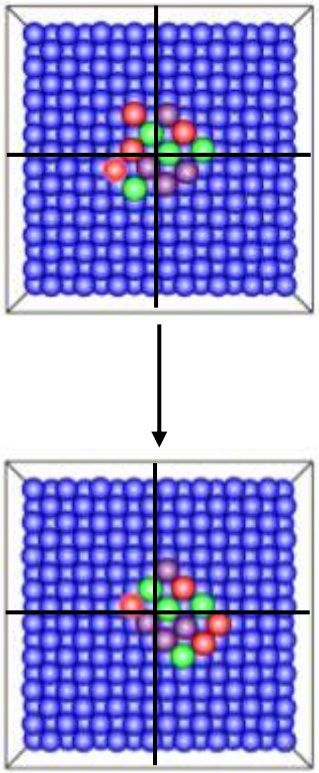

1 simulation of size
MN for time t

Parallel-Replica

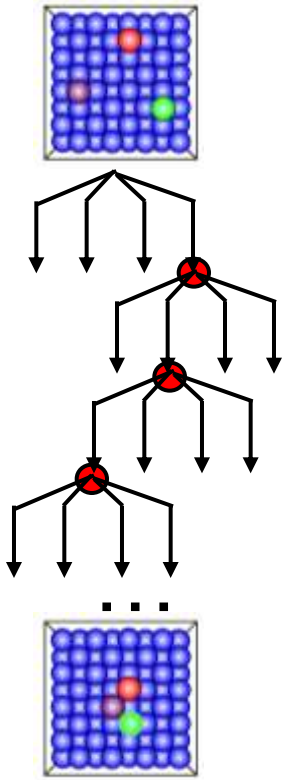

1 simulation of size
N for time Mt

● = event

UNCLASSIFIED

Detecting a Transition

- **Best method depends on the system**
- **Simple method for EAM metal systems:**
  - periodically perform minimization
  - see if geometry at basin minimum has changed

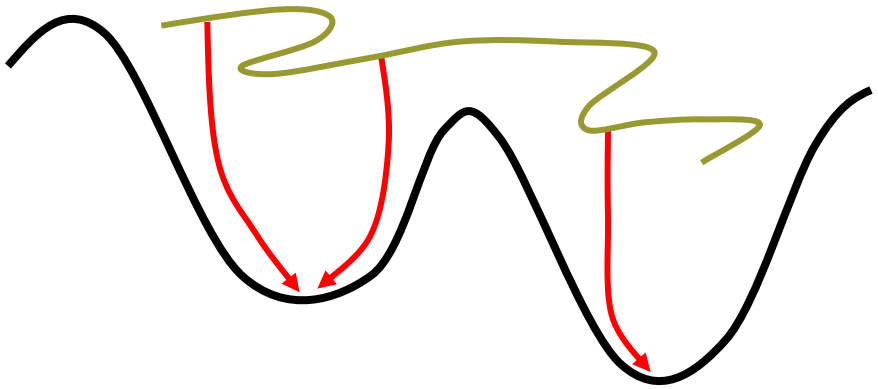

- **Other Methods:**
  - change in bond connectivity/length (covalent systems) (Kum, Uberuaga)
  - change in energy fluctuations (Pande)

Examples of Parallel Replica Simulations

- **Vacancy void annealing in Cu**
  - Motivation
    - Examine void kinetics to understand void swelling under irradiation

- **Stretching of Ag nanowire**
  - Motivation
    - Understand tensile behavior of nano-sized wires

Voids in Cu:
Long time annealing of 20 vacancy

- **EAM Cu**
- **Parallel-replica simulation of 20-vacancy void annealing at 400 K**
  - 20 vacancies is one too many for "perfect" void
- **Total simulation is 7.82 μs**
- **At 1.69 μs, void transforms to SFT**
- **Run on 39 processors for 15 days**
- **Efficiency = 79%**
- **Equivalent single processor time: 1.3 years**

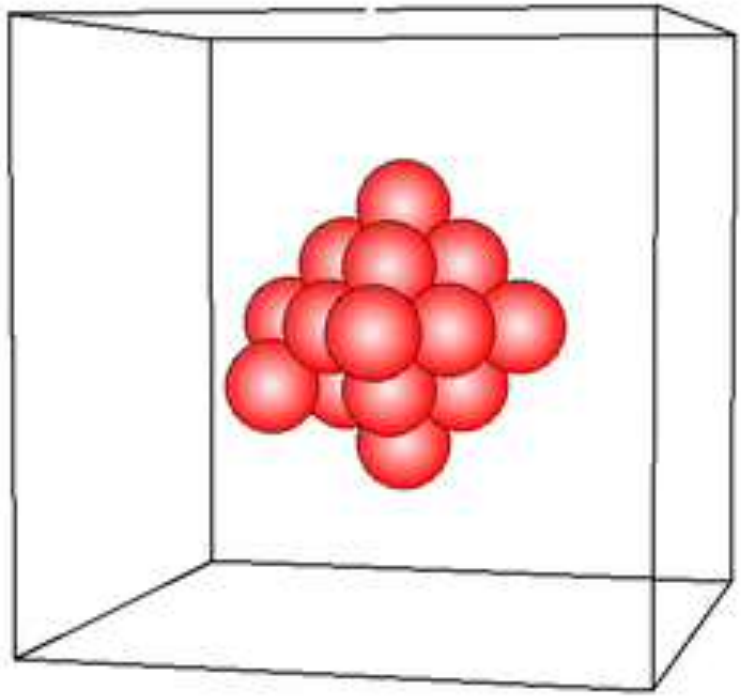

Uberuaga, et. al., *PRL* **99**, 135501 (2007)

Voids in Cu:
Transformation pathway for 20 vacancy void

- **Full path for transformation to SFT calculated with NEB**
- **Initial barrier is > 2 eV**
  - Should have taken >105 years at 400K to occur (assuming standard prefactor)
- **Vineyard prefactor for first step is $2x10^{36}$ s^{-1}**
  - Vineyard rate is faster than one time step at 500K!

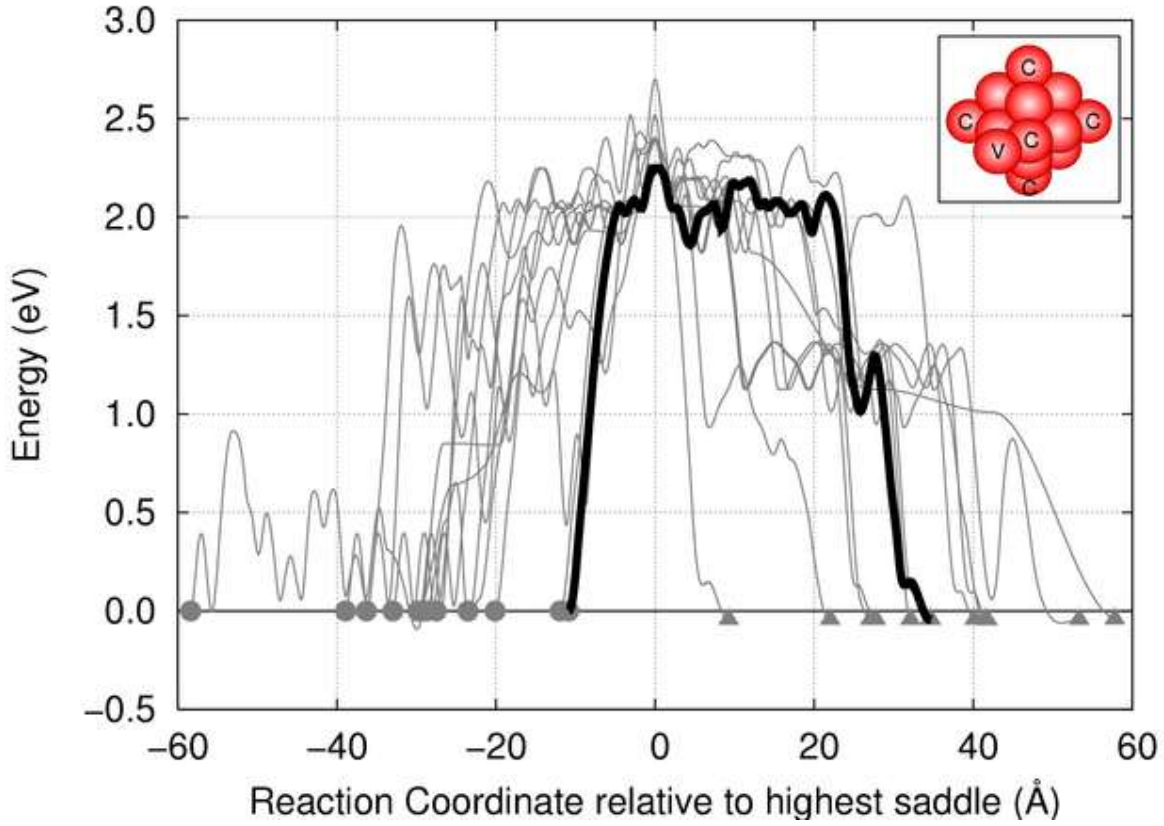

Uberuaga, et. al., *PRL* **99**, 135501 (2007)

Voids in Cu: Origin of Prefactor for Transformation

- **View material containing void as partitioned into two regions**
  - Region I: Cu
  - Region II: void
- **Before transition, volume of Cu is Region I volume**
- **After, volume of Cu is Region I + Region II**
- **Entropy change ΔS due to volume change ΔV: $\Delta S=\alpha B \Delta V$**
  - α=coefficient of thermal expansion, B=bulk modulus
- **Assuming ΔV=10 atomic volumes ⇨ ΔS=67.5/kB ⇨ prefactor enhanced by factor of 10^{29}**
- **Consistent with observed/calculated prefactor of ~10^{40}**

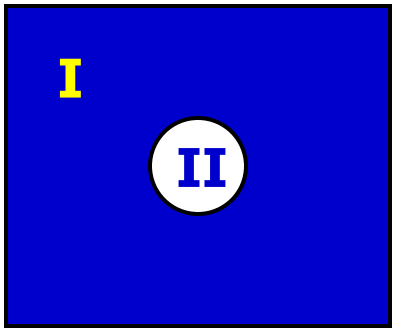

Uberuaga, et. al., *PRL* **99**, 135501 (2007)

Ag nanowire:
ParRep of stretching nanowire

Danny Perez, Chun-Wei Pao, Sriram Swaminarayan, AFV

- **Run on LANL Roadrunner (1 PFLOPS if using all 12,240 cell processors)**
- **Boost good at first; drops as events become more frequent.**
- **Outer edge atoms clamped, advanced 0.01A at regular intervals**
- **Preliminary results…**

Ag[110] nanowire, 1.d5 A/s, 1 us per frame

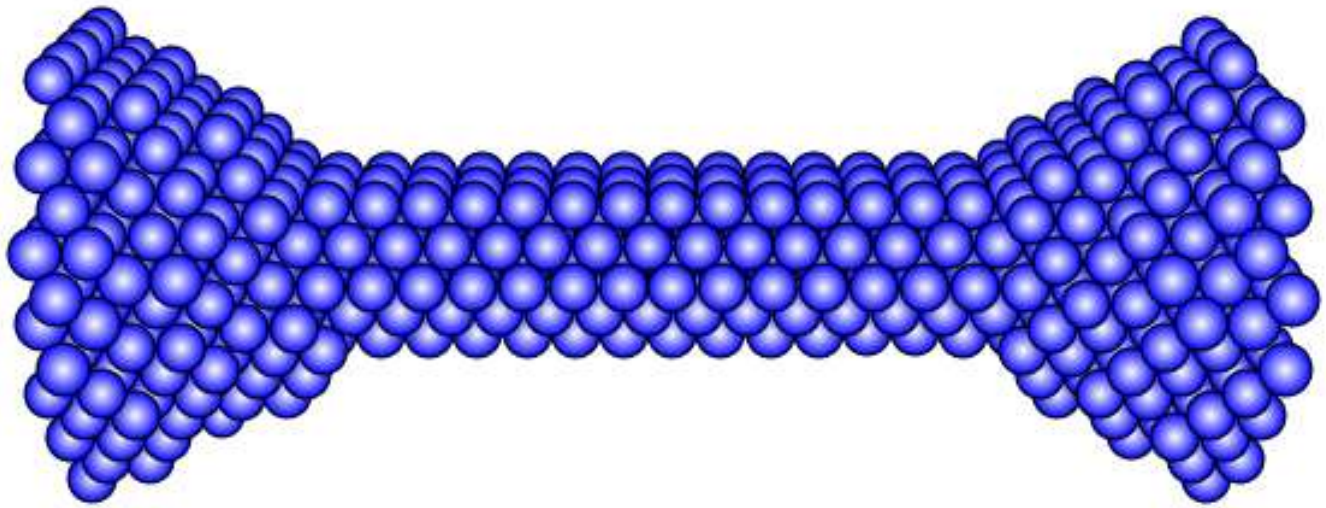

Ag nanowire:
Pulling slower changes behavior

At stretching speeds below ~10^6 Å/s, the system can thin down to four layers, coming back to perfect fcc. At higher speeds, it disorders or necks, never recovering perfect fcc again.

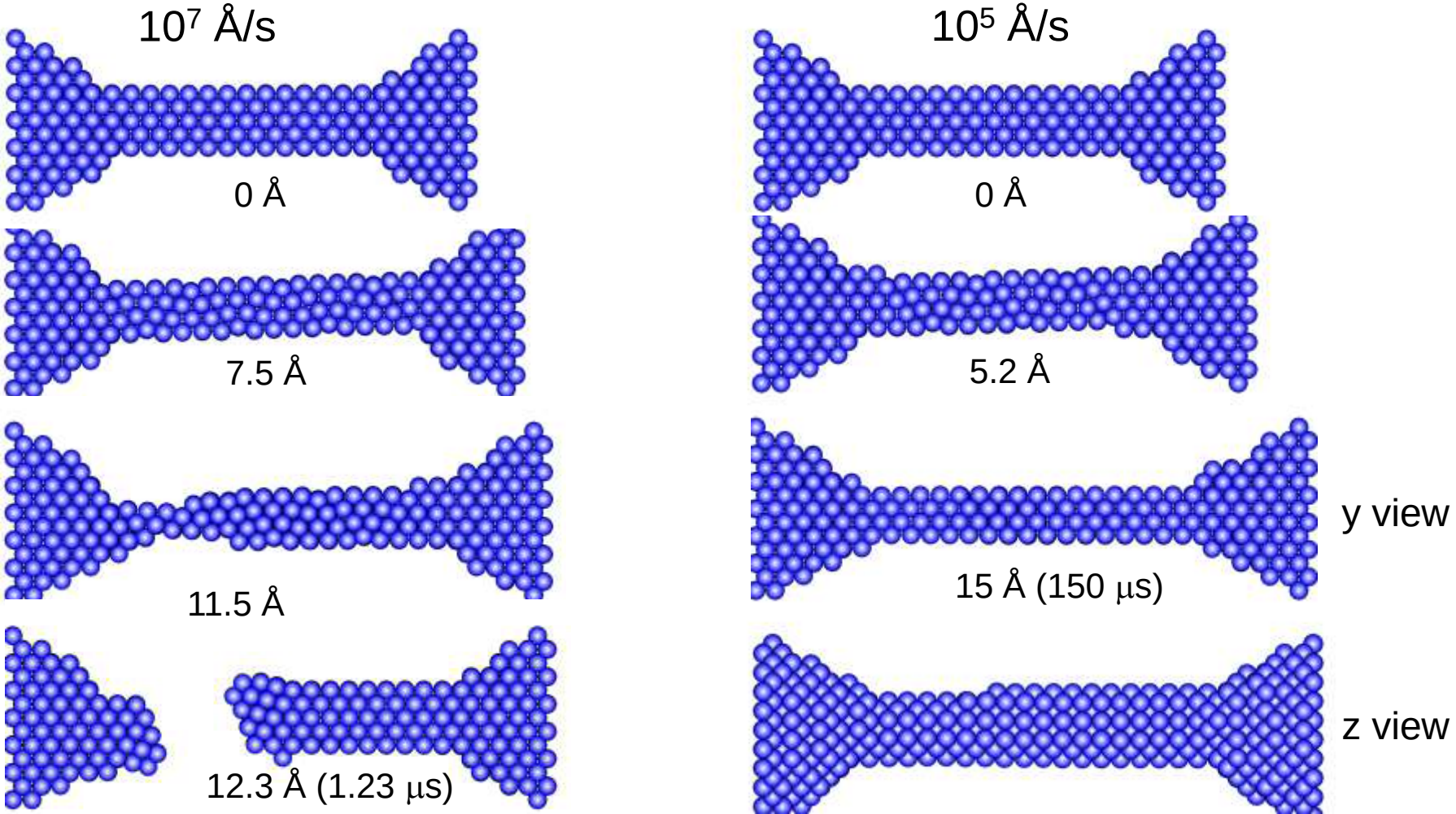

Summary - Parallel-Replica Dynamics

- **Most exact of the accelerated dynamics methods**
  - no harmonic approximation
  - goes beyond TST to include correlated dynamical events
  - no assumption that barrier is energetic - can be entropic
- **Easy to implement – requirements:**
  - transition detection
  - good estimate of correlation time
- **Very general applicability**
  - any system with exponentially distributed events
- **Good match to increasing availability of parallel processing power, distributed computing, etc.**

Limitations - Parallel-Replica Dynamics

- **Only get parallel boost**
  - If statistics are necessary such that number of samples is equal to or greater than number of processors, better to do MD
- **Boost drops off when events are frequent (or become frequent because so many processors)**
  - Requires “tuning” number of processors to temperature of interest
- **Boost especially limited if correlation time is long**
- **For complex systems (e.g., proteins) even transition detection can be tricky**

Introduction to Temperature Accelerated Dynamics (TAD)

Sørensen and Voter, *JCP* **112**, 9599 (2000)

- **Concept:**
  - System characterized by deep energy wells
  - Run basin constrained MD at high temperature
  - Extrapolate behavior to low temperature
- **Approximations:**
  - Harmonic Transition State Theory $\left(k = \nu e^{-\Delta E / k_B T}\right)$
  - Assumed minimum prefactor in system ν_{min}
  - Uncertainty level δ of missing the correct event
- **Very powerful when barriers are high relative to temperature**

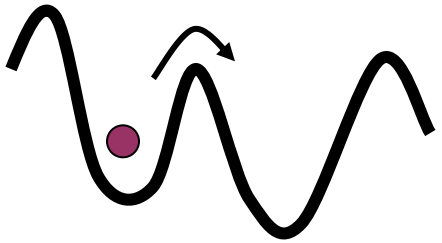

Basin Constrained MD (BCMD)

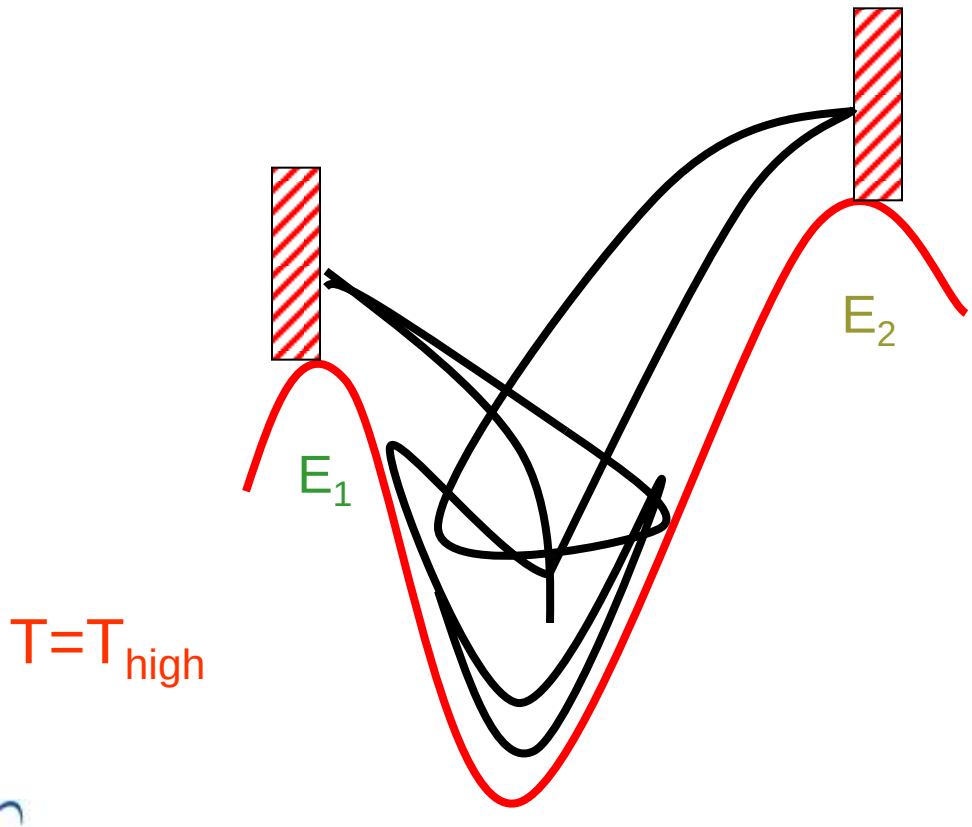

- Run dynamics at T_{high}
- When event occurs, reflect trajectory back into basin
- Continue high-T dynamics
- Reflect trajectory after any other events
- Requires:
  - Detecting transition
  - Finding energy barrier

TAD algorithm

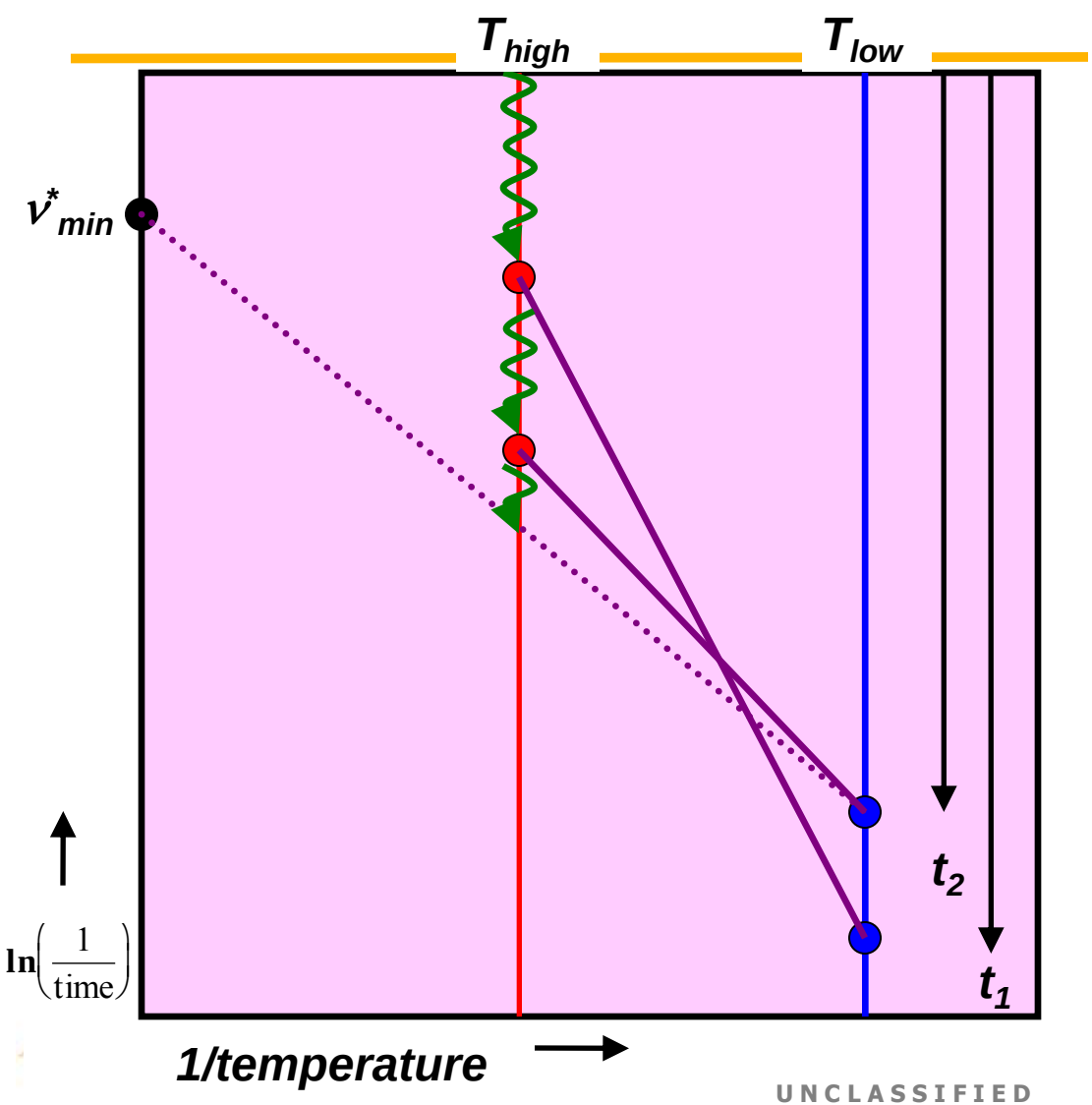

- Do MD at T_{high} until see an event
- Find barrier, extrapolate to T_{low}, find time t_1
- Continue at T_{high} to next event
- Find barrier, extrapolate to T_{low}, find time t_2
- Continue at T_{high} until earlier event not possible (within δ)
- Accept event with earliest time (t_2)

UNCLASSIFIED

Examples of TAD Simulations

- **Interstitial clustering in MgO**
  - Motivation
    - Use MgO as model ceramic to understand radiation damage evolution

- **Interstitial emission at grain boundaries in Cu**
  - Motivation
    - Determine role of GBs in radiation tolerance of nanocrystalline materials

MgO:
Defect aggregation

- **Using standard Buckingham potential with long range Coulomb interaction**
- **Begin with I_2 and I_4**
  - Defects found at end of collision cascade
- **I_2 attracted to I_4, binds forming I_6**
- **Metastable I_6 diffuses very quickly**
  - ns timescale at 300 K
  - diffusion is 1D along <110>
  - decay to ground state takes years
- **Boosts on the order of 10^9**
- **Red=oxygen, Blue=magnesium**
- **Dark=interstitial, Light=vacancy**

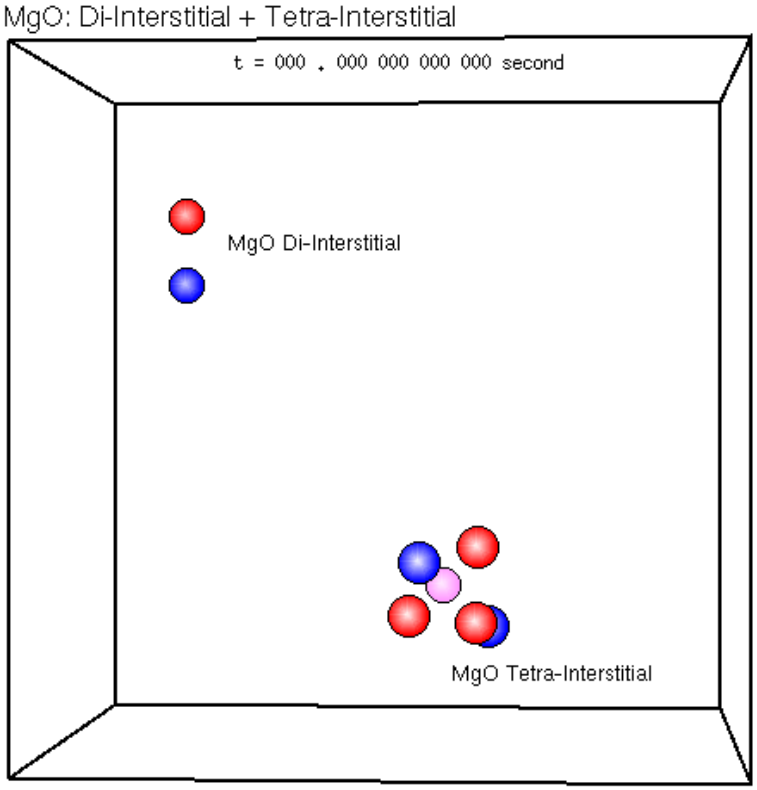

TAD simulation, Uberuaga et al, 2003

Uberuaga, et. al., *PRL* **92**, 115505 (2004); *PRB* **72**, (2005); *NIMB* **28**, 260 (2005)

MgO:
Interstitial cluster kinetics

- TAD simulations of interstitial clusters in MgO
- Diffusion barrier of ground state structures follow no clear pattern
- For clusters of size 5 and greater, there are metastable structures that diffuse faster than the ground state

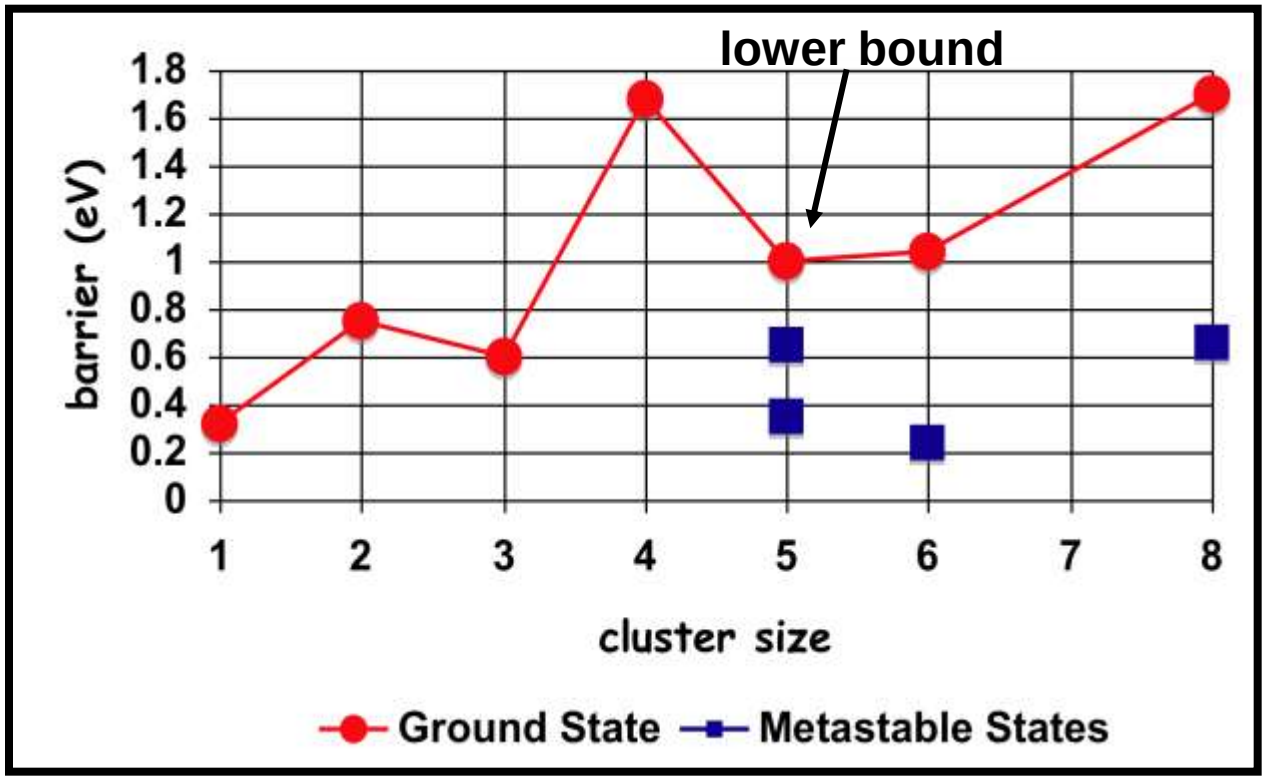

Uberuaga, et. al., *PRL* **92**, 115505 (2004); *PRB* **72**, (2005); *NIMB* **28**, 260 (2005)

MgO:
Effects of cluster mobility on observables

- **1-D reaction rate theory**
  - Mobilities from TAD
  - Steady-state conditions
- **Size of loops increases by more than 3 times when large clusters are mobile**
  - "large" clusters contain more than 1 interstitial
- **Enhanced defect mobility results in fewer, larger loops**

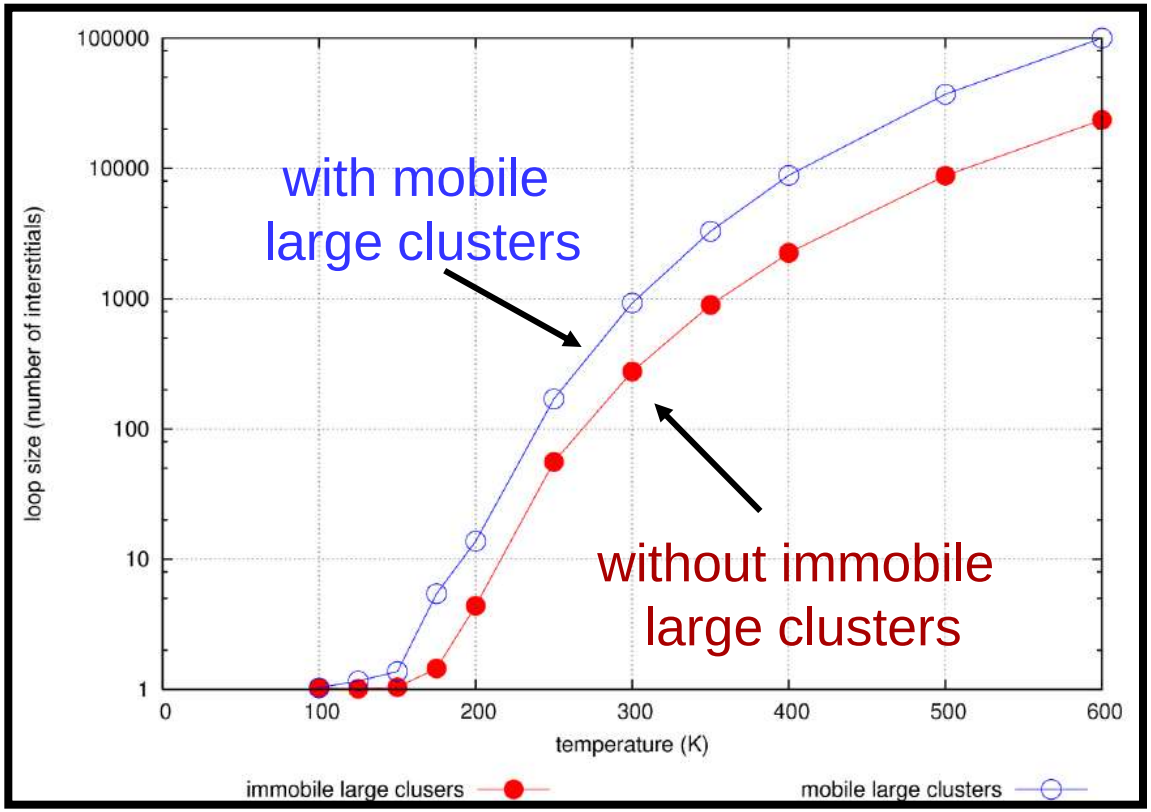

Uberuaga, et. al., *PRL* **92**, 115505 (2004); *PRB* **72**, (2005); *NIMB* **28**, 260 (2005)

Grain boundaries in Cu: Damage production

- Snapshots of a 4 keV cascade initiated 25 Å below Σ11 symmetric tilt GB in Cu at 300 K
- Atoms colored by energy
- After cascade, a number of vacancies remain below the GB, all interstitials absorbed by GB

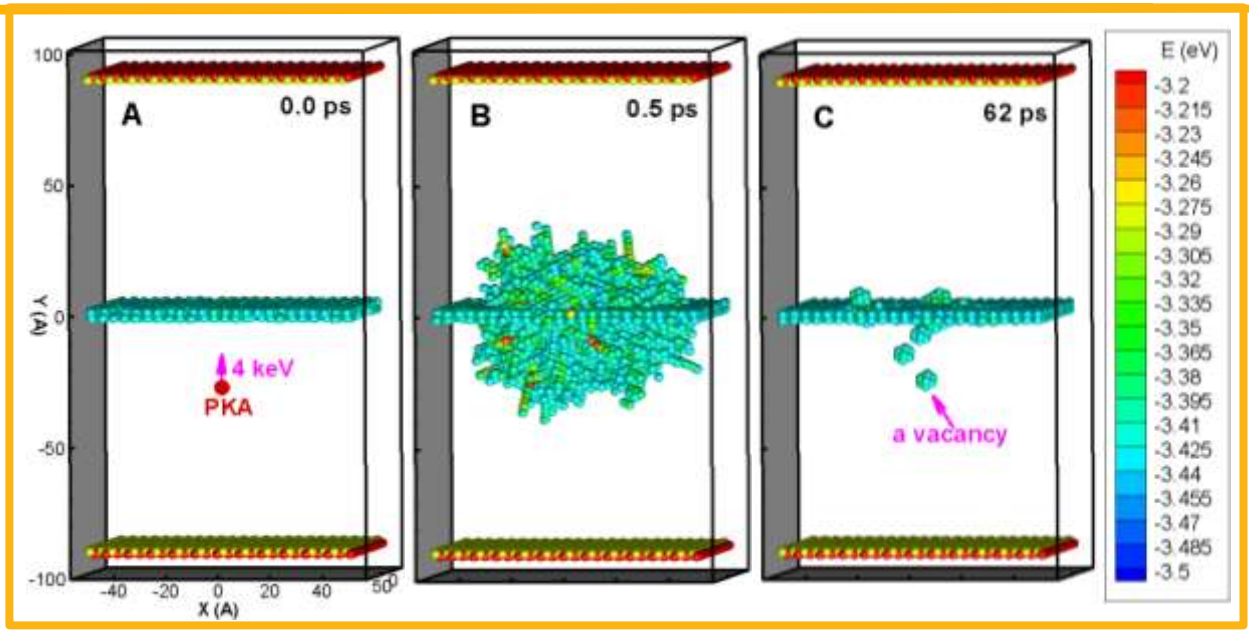

Bai, et. al., *Science* **327**, 1631 (2010)

Grain boundaries in Cu: Damage production

- Snapshots of a 4 keV cascade initiated 25 Å below Σ11 symmetric tilt GB in Cu at 300 K
- Atoms colored by energy
- After cascade, a number of vacancies remain below the GB, all interstitials absorbed by GB
- More vacancies than if GB not there!

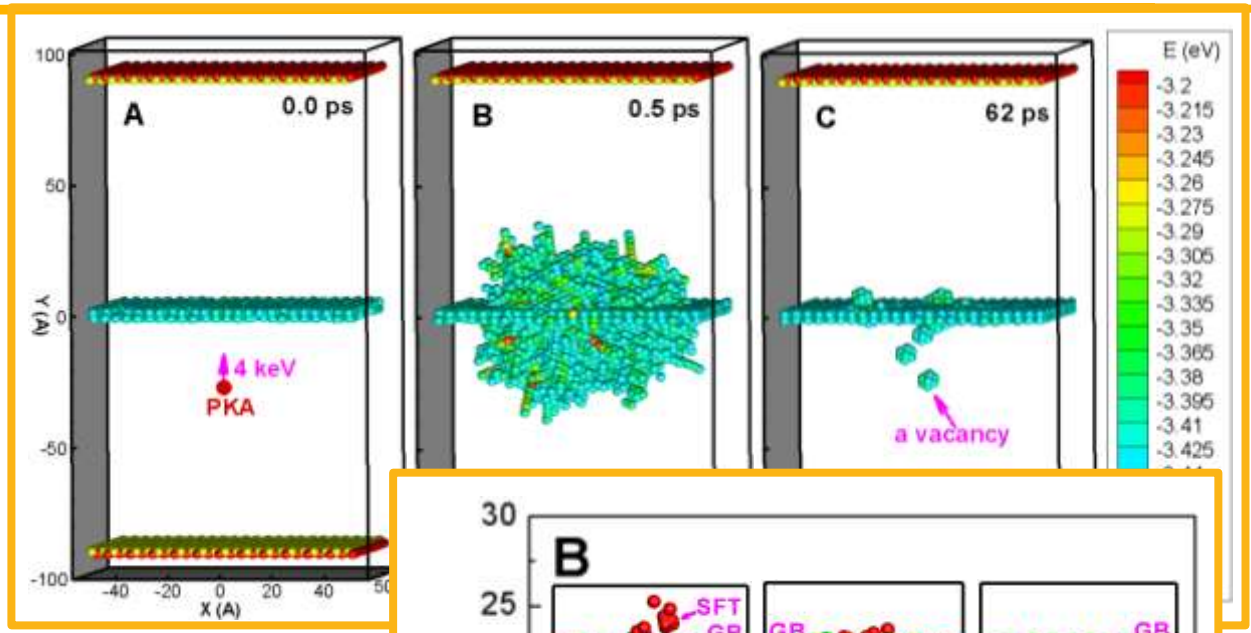

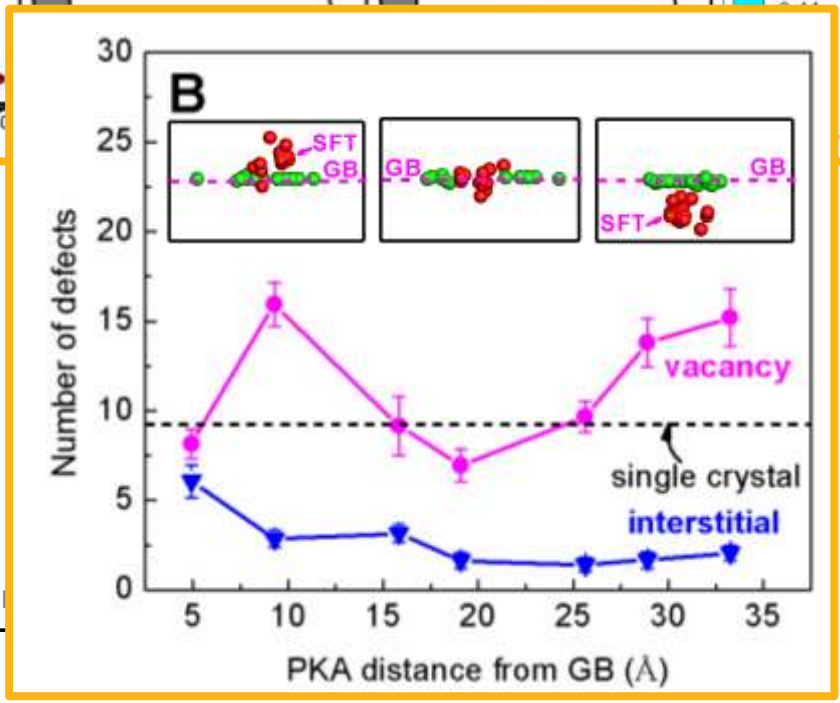

Los Alamos NATIONAL LABORATORY EST.1943
UNCLASSIFIED
Operated by Los Alamos National Security, LLC for the U.S. Department of Energy's NNSA

Grain boundaries in Cu: Snapshots of TAD simulation

- Interstitial emission leads to annihilation of 5 bulk vacancies
- Interstitial emission barriers (0.1-0.2 eV) relatively small compared to bulk vacancy barrier (0.67 eV)
- Interstitial emission extends ~5 atomic spacings into bulk
- Vacancies can diffuse to boundary on longer time scale

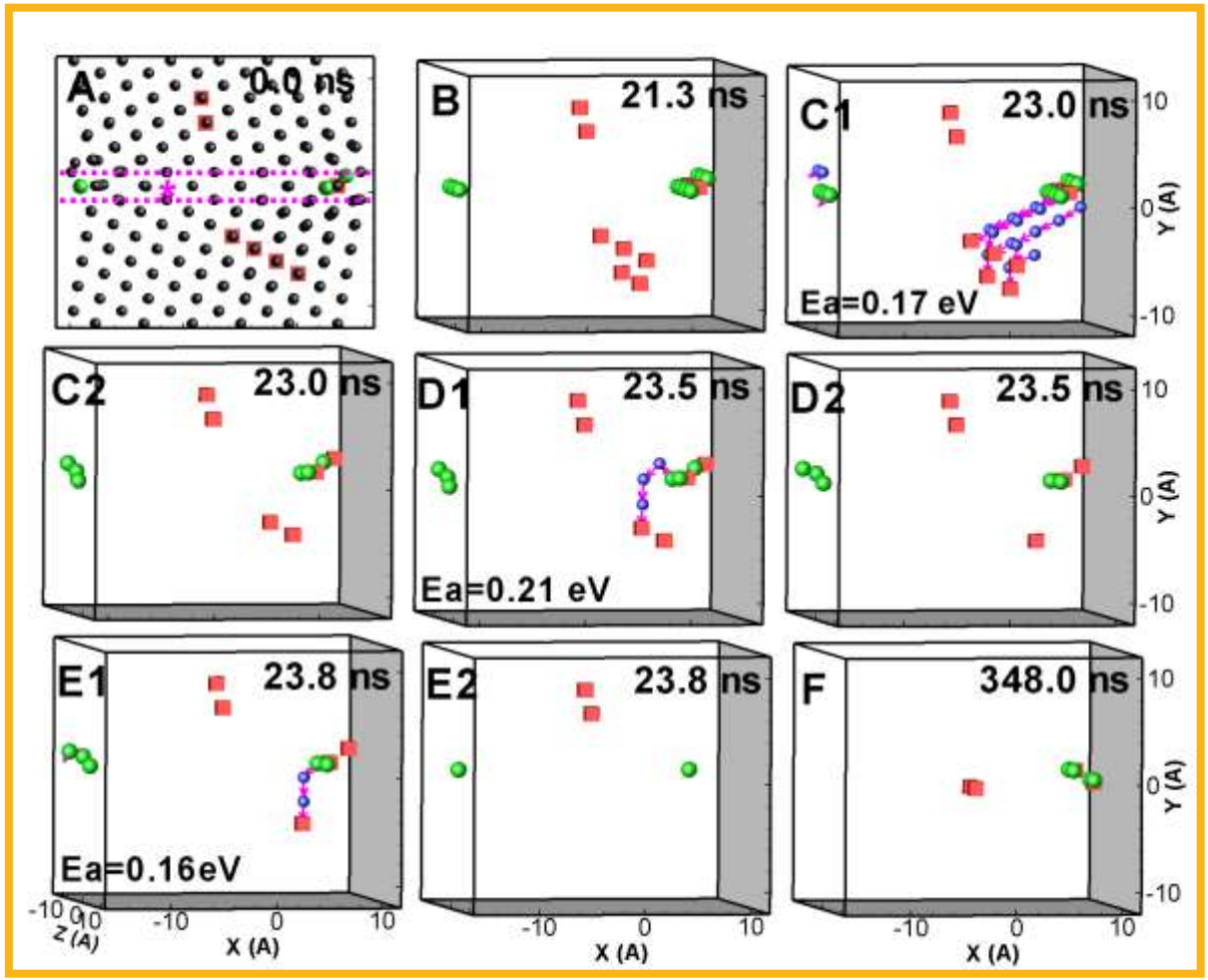

Bai, et. al., *Science* **327**, 1631 (2010)

Summary - Temperature Accelerated Dynamics

- **Potentially most powerful AMD method**
  - Extremely large boosts when temperature is small compared to barriers

- **Basic algorithm is easy to implement – requirements:**
  - transition detection
  - Basin constrained MD
  - Saddle finding method

Limitations - Temperature Accelerated Dynamics

- **Least exact of the accelerated MD methods**
  - Assumes *harmonic* transition state theory
- **For full optimization, requires many bells and whistles**
  - Detect revisited states
  - Ensure events do not involve double jumps, etc
- **Requires the potential to be relatively smooth for efficient saddle point calculations**

AMD characteristics/challenges

- **All three methods can give very large boost factors when events are very infrequent.**
- **Basically, the MD time to next event (+overhead) is collapsed to ~ps time scale.**

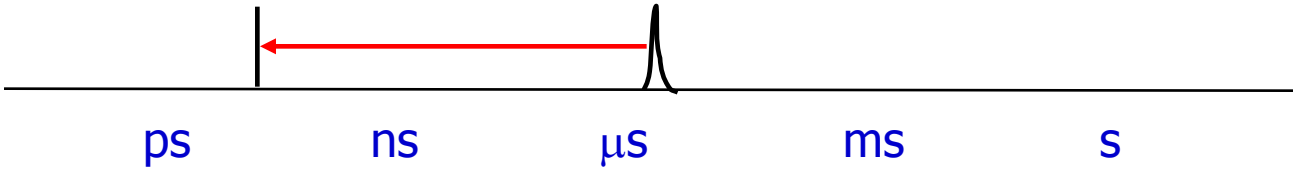

- **Low barriers mean low boost.**
- **Systems with persistent low barriers are our biggest ongoing challenge**
  - e.g., soft-matter systems
- **In principle, electronic structure forces can be used, but they are still pretty expensive**
  - If we cannot reach ~10 ps, we cannot see any events
- **Larger systems are also harder, although we are making progress**
  - ParTAD (Shim, et. al. 2007)
  - TAD-KMC (Chatterjee and Voter, 2010),
  - Local hyperdynamics (Kim, Perez, AFV, 2010).

AMD characteristics/challenges

- **All three methods can give very large boost factors when events are very infrequent.**
- **Basically, the MD time to next event (+overhead) is collapsed to ~ps time scale.**

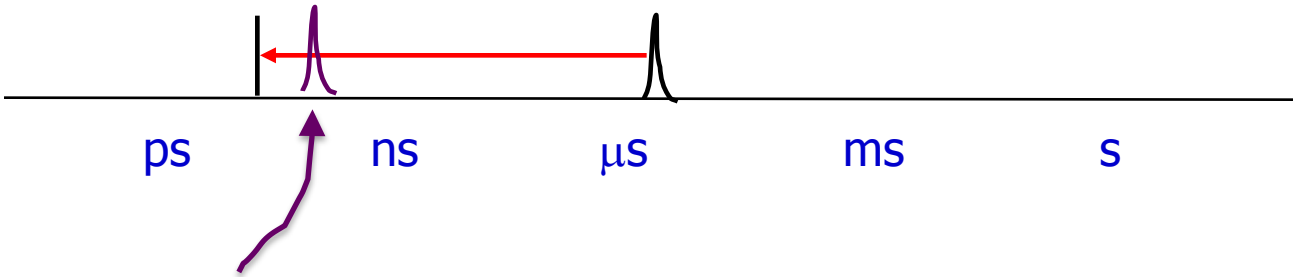

- **Low barriers mean low boost.**
- **Systems with persistent low barriers are our biggest ongoing challenge**
  - e.g., soft-matter systems
- **In principle, electronic structure forces can be used, but they are still pretty expensive**
  - If we cannot reach ~10 ps, we cannot see any events
- **Larger systems are also harder, although we are making progress**
  - ParTAD (Shim, et. al. 2007)
  - TAD-KMC (Chatterjee and Voter, 2010),
  - Local hyperdynamics (Kim, Perez, AFV, 2010).

Comparing AMD Methods: Accuracy

- **Parallel-Replica is most accurate**
  - Only assumes first order kinetics
    - Doesn't even assume TST
  - Accounts for correlated events

- **Temperature Accelerated Dynamics least accurate**
  - Assumes harmonic approximation to TST
  - Has known upper bound to error quantified by δ and ν_{min}

- **Hyperdynamics is intermediate**
  - Assumes TST
    - no harmonic approximation…
    - …but no correlated events
  - Error may creep in via definition of bias potential

Comparing AMD Methods: Efficiency

- **Temperature Accelerated Dynamics possibly most efficient**
  - Large boost when barriers are high relative to T_{low}
- **Efficiency of hyperdynamics really depends on bias potential**
  - With Art's bias potential, computational cost is very high
  - Bond-boost bias overcomes costs
- **Currently, parallel-replica least efficient**
  - Only linear boost with number of processors
  - Right now, typically don't have enough processors to compete with TAD or hyperdynamics
  - In future, this limitation should be reduced
  - Harder to tune accelerating parameter
    - TAD: high temperature
    - Hyperdynamics: bias potential strength
    - Parallel-replica: number of processors
- **All limited by smallest barrier/fastest event in system**

Summary

- **Accelerated molecular dynamics concept:**
  - Let the trajectory find an appropriate way out of state, but coax it into doing so more quickly
- **Significant speedup over standard MD when barriers are high relative to temperature**
- **Often encounter unexpected behavior**
  - Many mechanisms that would be left out of e.g. KMC if intuition alone is used
    - High mobility of interstitial clusters in MgO
    - Transformation of void to stacking fault tetrahedron in Cu
    - Interstitial emission near GBs in Cu
    - Thinning of Ag nanowires
- **Ongoing challenges**
  - low barriers and pesky local minima
  - cuspy potentials
  - scaling with system size

Review: Voter, Montalenti, and Germann, *Ann. Rev. Mater. Res*. **32**, 321 (2002)

Acknowledgements

- **Art Voter (LANL)**
- **Radiation damage evolution in ceramics:**
  - Kurt Sickafus (LANL)
  - Robin Grimes, Antony Cleave, and Jon Ball (Imperial)
  - Roger Smith and Pravesh Bacorisen (Loughborough)
  - Francesco Montalenti (now at University of Milano)
  - Graeme Henkelman (now at University of Texas, Austin)
- **Void evolution in metals:**
  - Steve Valone, Richard Hoagland (LANL)
- **Interstitial Emission at GBs:**
  - Xian-Ming Bai, Richard Hoagland, Mike Nastasi (LANL)
- **Stretching Ag nanowire:**
  - Danny Perez, Chun-Wei Pao, Sriram Swaminarayan (LANL)
- **Funding: BES, Enhanced Surveillance, Motorola, LANL LDRD**

Fine Scale Characterization and Some New Insights into the Precipitation of the Ordered γ' Phase in Nickel base Superalloys

Gopal Babu Viswanathan

Air Force Research Laboratory
Dayton, Ohio, U.S.A.

Partners in the Crime
also called '*Collaborators*'

A. Singh, J.Y. Hwang, S. Nag, R. Banerjee
Center for Advanced Research and Technology
Department of Materials Science and Engineering
University of North Texas
Denton, Texas, U.S.A.

S. Rajagopalan and H. L. Fraser
Center for the Accelerated Maturation of Materials
Department of Materials Science and Engineering
Ohio State University
Columbus, Ohio, U.S.A.

J. Tiley and D. Dimiduk
Air Force Research Laboratory
Dayton, Ohio, U.S.A.

Financial support for this work has been provided by the Air Force Office of Scientific Research and the Air Force Research Laboratory

UNT UNIVERSITY OF NORTH TEXAS Discover the power of ideas

THE OHIO STATE UNIVERSITY

CAMM

AIR FORCE RESEARCH LABORATORY

Microstructural Representations of NASA Developed LSHR Disk Alloy

Motivation

Sam Kuhr &
Hamish Fraser (OSU)

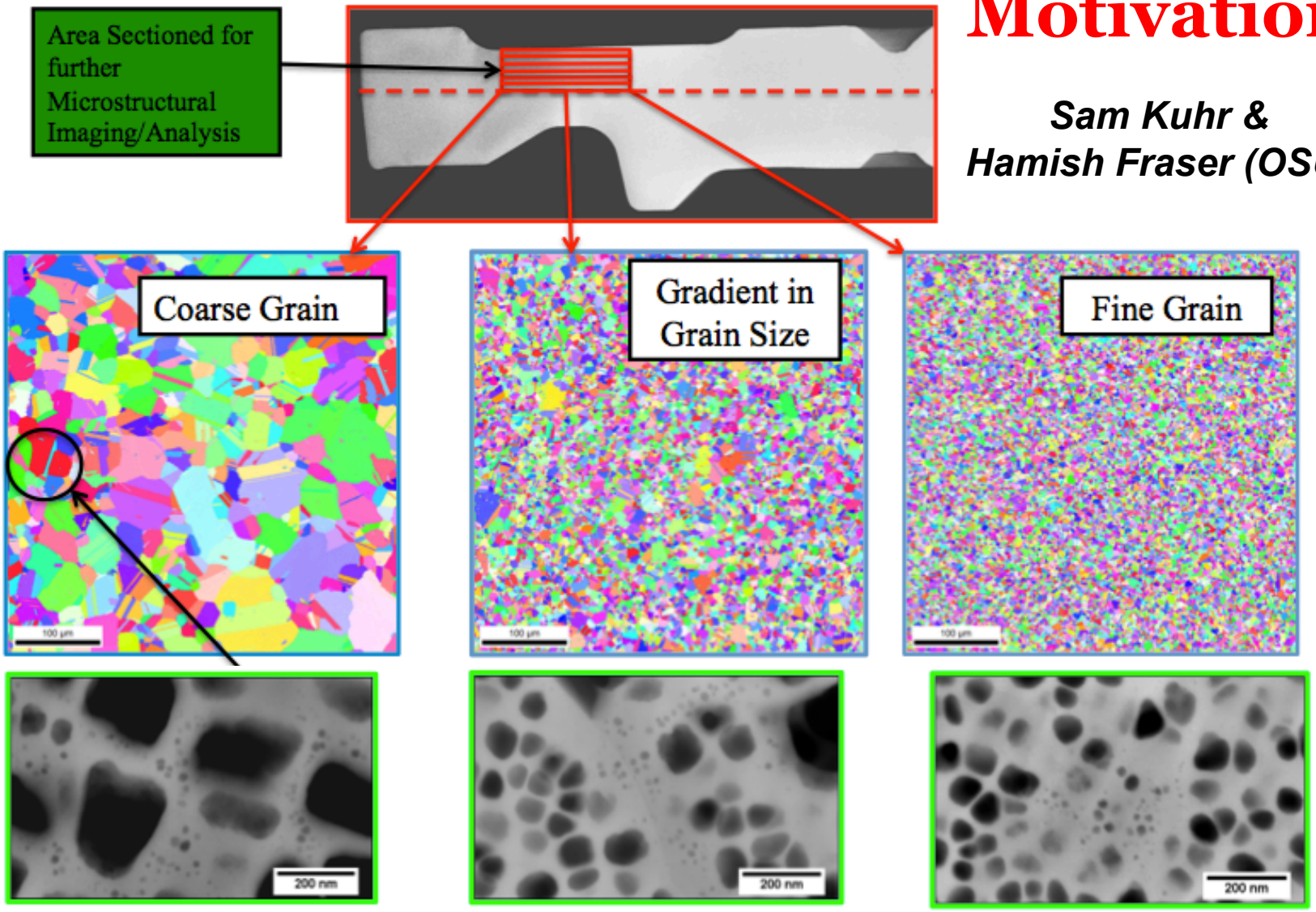

Variations in grain size, γ' size, distribution and volume fraction

Organization

- **γ' precipitation during continuous cooling from single γ phase field**
  - **Rapid cooling (Water Quenched)**
  - **Slow cooling**

- **Evolution of the γ/γ' interface**
  - ***Compositional gradient (or width) across the interface***
  - ***Order-disorder transition width***

- **Application to real multi-component engineering alloys => *study on Rene88 alloy (turbine disk alloy)***
  - **56.53Ni-16.24Cr-13.27Co-3.92Ti-2.09Al-4.08Mo-3.92W-0.76Nb (wt%)**
  - ***Primary alloying elements are Cr, Co, Ti, Al, Mo***

Organization

- **γ' precipitation during continuous cooling from single γ phase field**
  - **Water-quenched (rapid cooling)**
  - **Slow cooling**

- **Evolution of the γ/γ' interface**
  - ***Compositional gradient (or width) across the interface***
  - ***Order-disorder transition width***

- **Application to real multi-component engineering alloys => *study on Rene88 alloy (turbine disk alloy)***
  - **56.53Ni-16.24Cr-13.27Co-3.92Ti-2.09Al-4.08Mo-3.92W-0.76Nb (wt%)**
  - ***Primary alloying elements are Cr, Co, Ti, Al, Mo***

Continuous Cooling Experiments + Aging

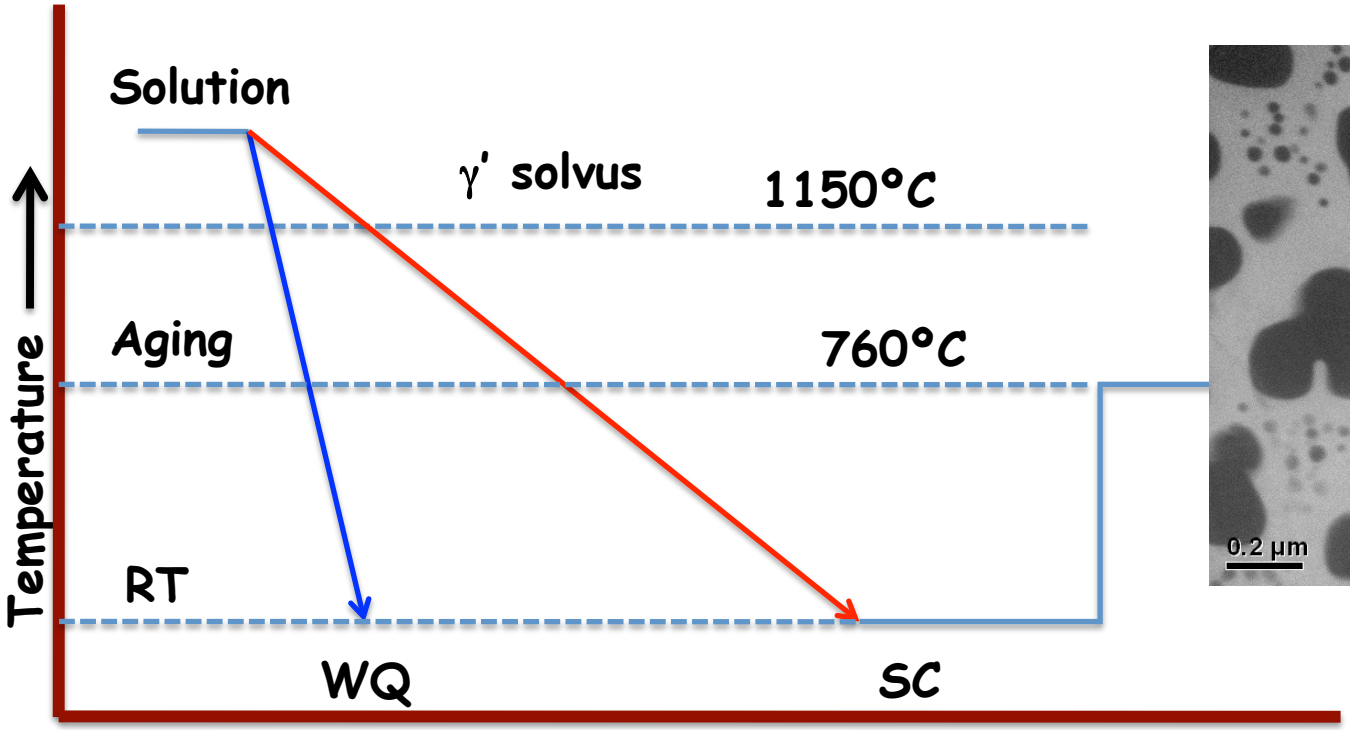

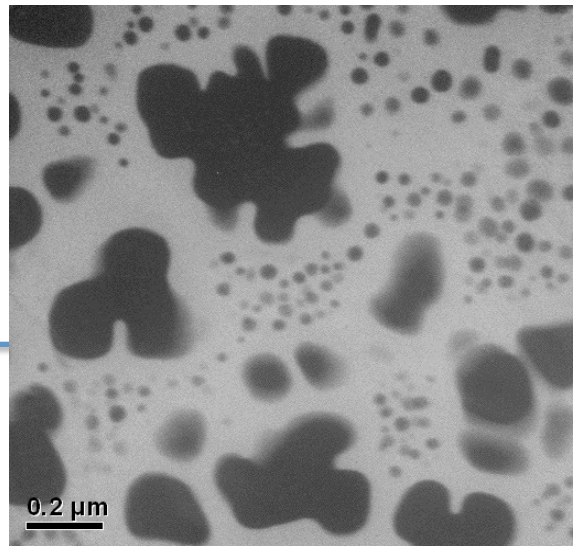

Typical Microstructure: γ' precipitates in a γ matrix

Cooling rates from solution temperature
Water-quenched (WQ) > 300°C / min.
Slow-cooled (SC) = 24°C / min.

Post continuous cooling, samples aged at 760°C for various time periods from 0 – 200 hrs

Typical γ+γ' Microstructures in Rene 88

	Water-Quenched	Slow-Cooled
As-cooled	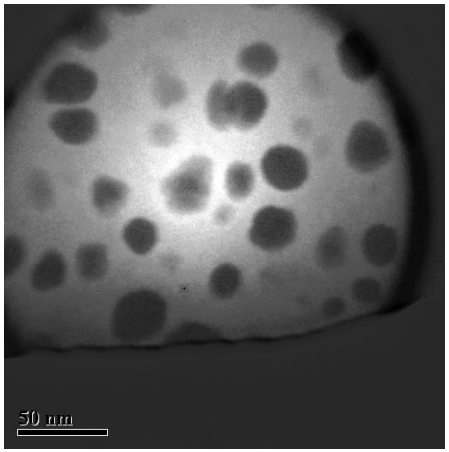	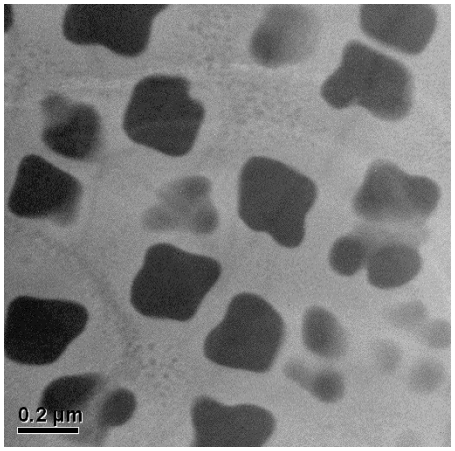
760°C Aged / 200 hours	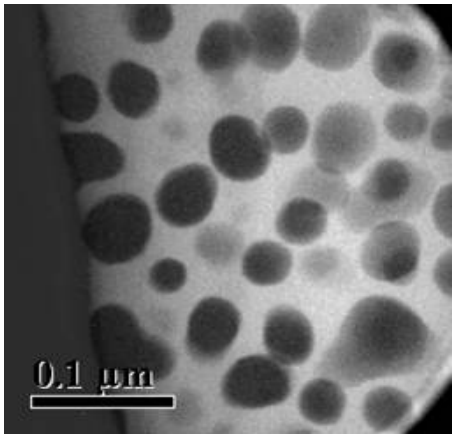	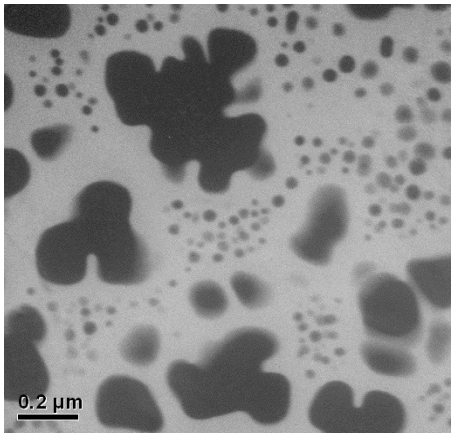
	Monomodal size distribution of γ' precipitates	Bimodal size distribution of γ' precipitates

Cr-M edge Energy-filtered TEM (EFTEM) images

Cr-depleted darker contrast regions – γ' precipitates

Tiley, Viswanathan, Srinivasan, Banerjee, Dimiduk and, Fraser, *Acta Mater.* (2009)

γ' precipitates in Rene 88DT (As Water-Quenched)

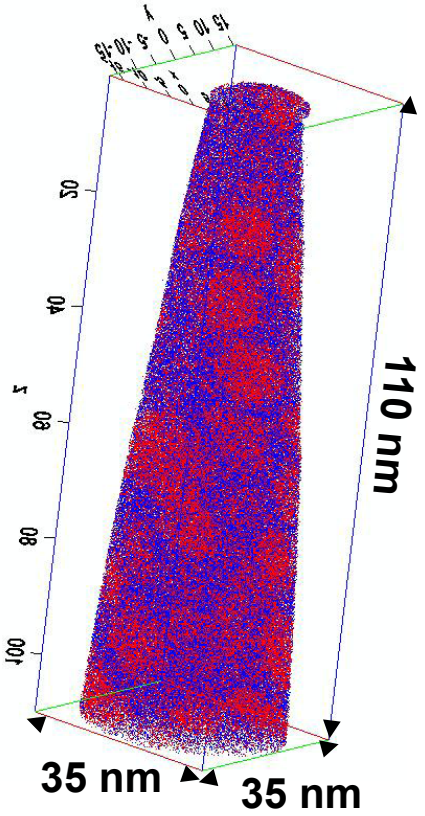

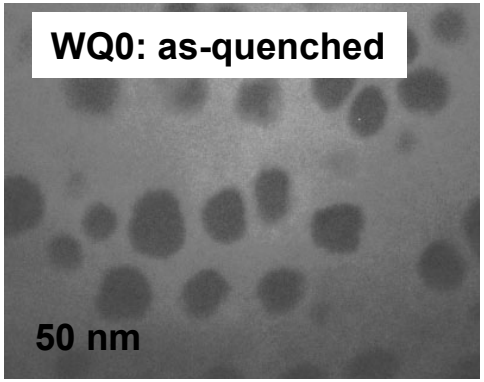

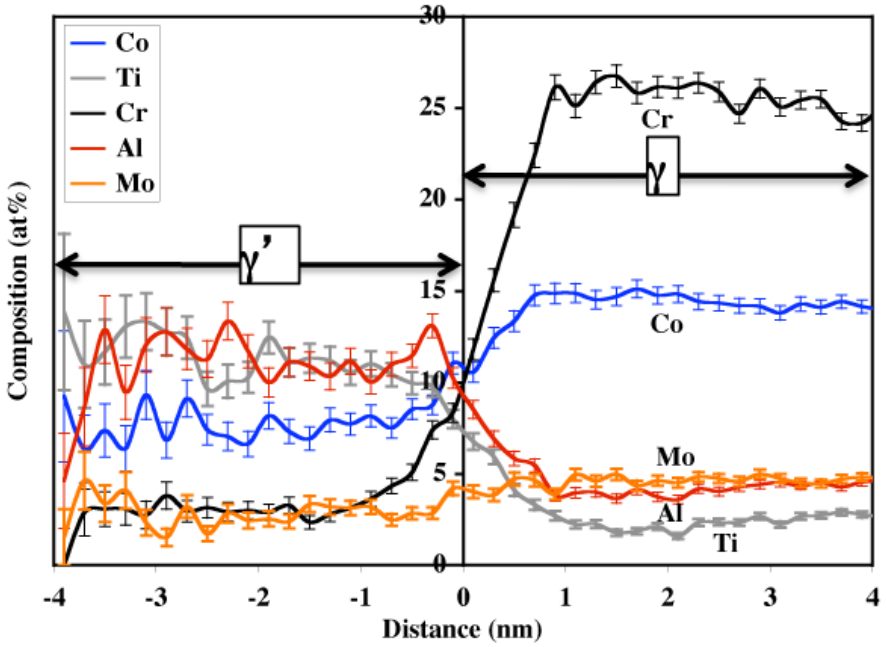

- **Near-spherical primary γ' precipitates are formed on quenching (verified in 3D)**
  - ***Monomodal microstructure***
- **Al, Ti partition to γ'**
- **Cr, Co, Mo partition to γ**

Hwang, Banerjee, Tiley, Srinivasan, Viswanathan, and, Fraser, *Metall. Mater. Trans. A* (2009)

γ and γ' composition in Water-quenched Rene 88

WQ0

	Bulk		γ	γ' (avg)
	Atomic%	Error%	Atomic%	Atomic%
Ni	48.96	0.05	46.10	58.07
Co	12.89	0.02	14.30	8.83
Ti	4.69	0.01	2.50	10.67
Cr	18.92	0.03	23.50	4.68
Al	6.13	0.02	4.20	10.49
Nb	2.32	0.01	2.30	2.97
Mo	4.24	0.01	4.80	3.29
C	0.09	0.00	0.10	0.07
W	1.61	0.01	2.00	1.26
B	0.15	0.00	0.20	0.14

← >5 nm size → ← ~3 nm size →

	γ'1		γ'2		γ'3		γ'4	
	Atomic%	Error%	Atomic%	Error%	Atomic%	Error%	Atomic%	Error%
Ni	59.62	0.65	59.34	0.72	57.10	1.67	51.00	1.92
Co	7.69	0.19	7.45	0.21	10.90	1.05	13.80	1.33
Ti	10.85	0.23	10.90	0.26	10.14	1.02	13.10	1.30
Cr	4.21	0.14	4.06	0.15	5.50	0.77	6.20	0.93
Al	10.55	0.23	11.06	0.26	8.30	0.93	9.70	1.14
Nb	2.72	0.11	2.86	0.13	2.10	0.48	7.00	0.98
Mo	2.86	0.11	2.88	0.13	3.60	0.63	4.10	0.76
C	0.04	0.01	0.07	0.02	0.20	0.15	0.00	0.00
W	1.32	0.08	1.25	0.08	1.90	0.46	1.40	0.45
B	0.13	0.02	0.12	0.03	0.00	0.00	0.00	0.00

- **Compositional partitioning between γ matrix and γ' precipitates**
  - **γ matrix richer in Co, Cr, Mo**
  - **γ' precipitates richer in Al, Ti**

- **Size dependent compositional variation in γ' precipitates**
  - **smaller precipitates are further from equilibrium**
    contain excess of Co but depleted in Al content

Different generations of γ′ precipitation:

Fast Cooling Rates

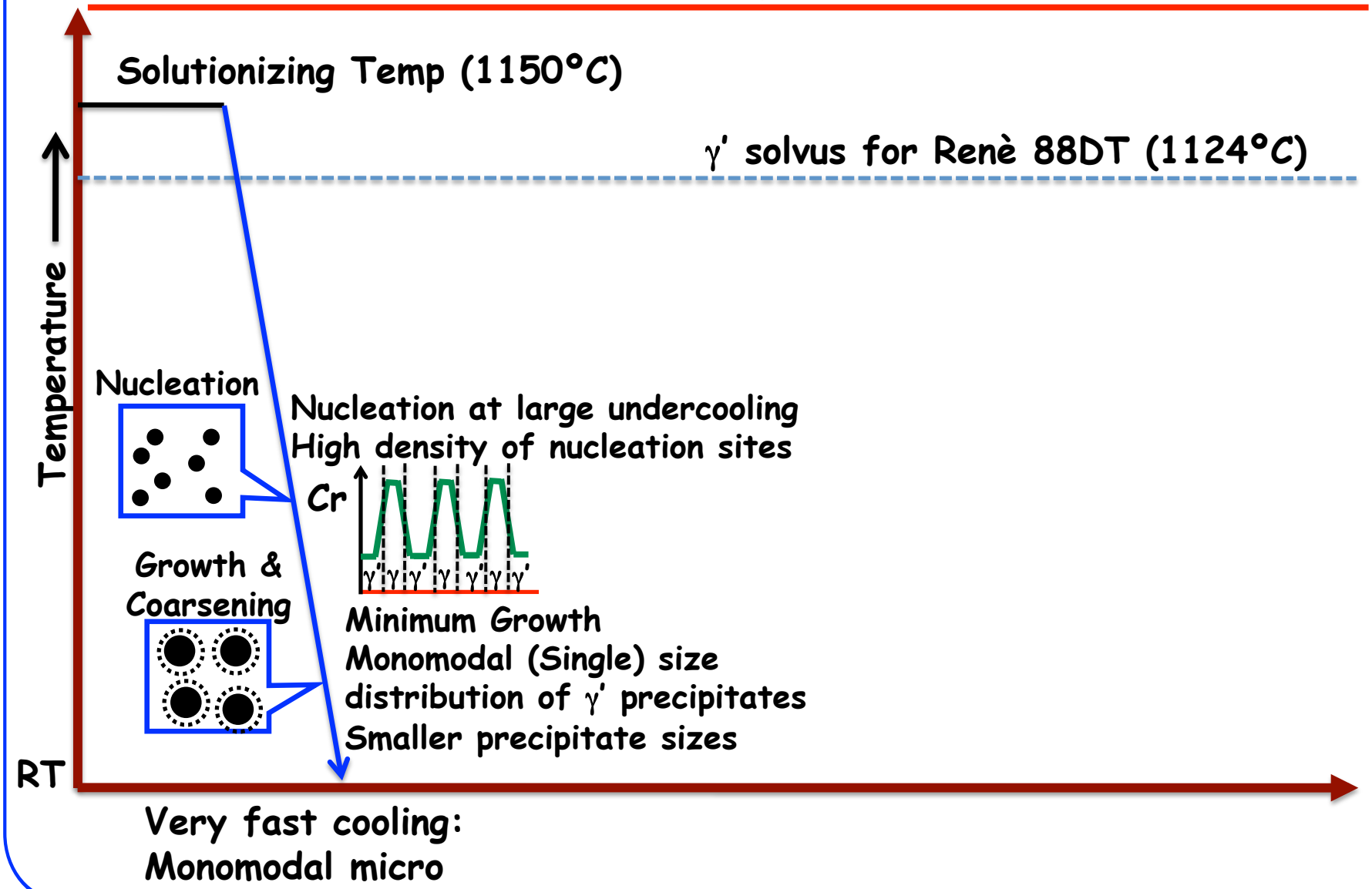

Different Generations of γ' (Primary)

SEM secondary electron images (etched sample)

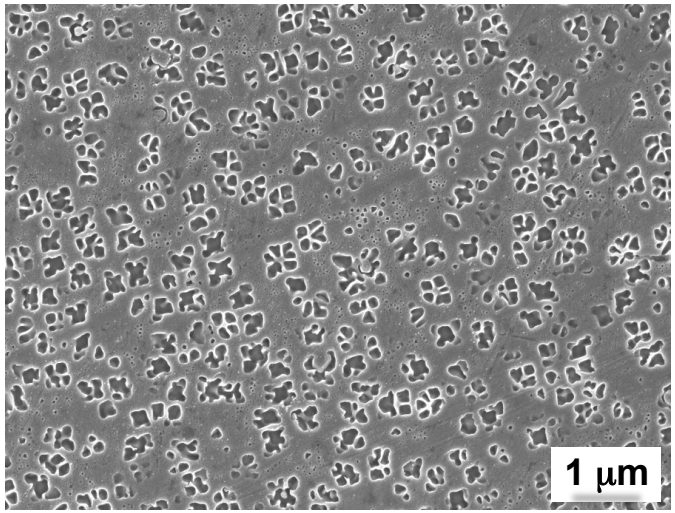

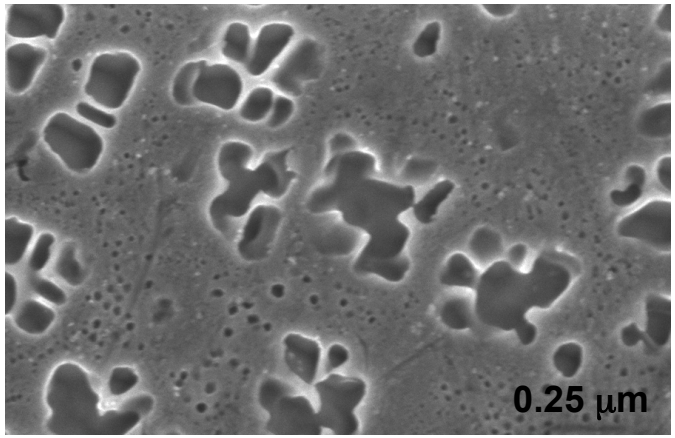

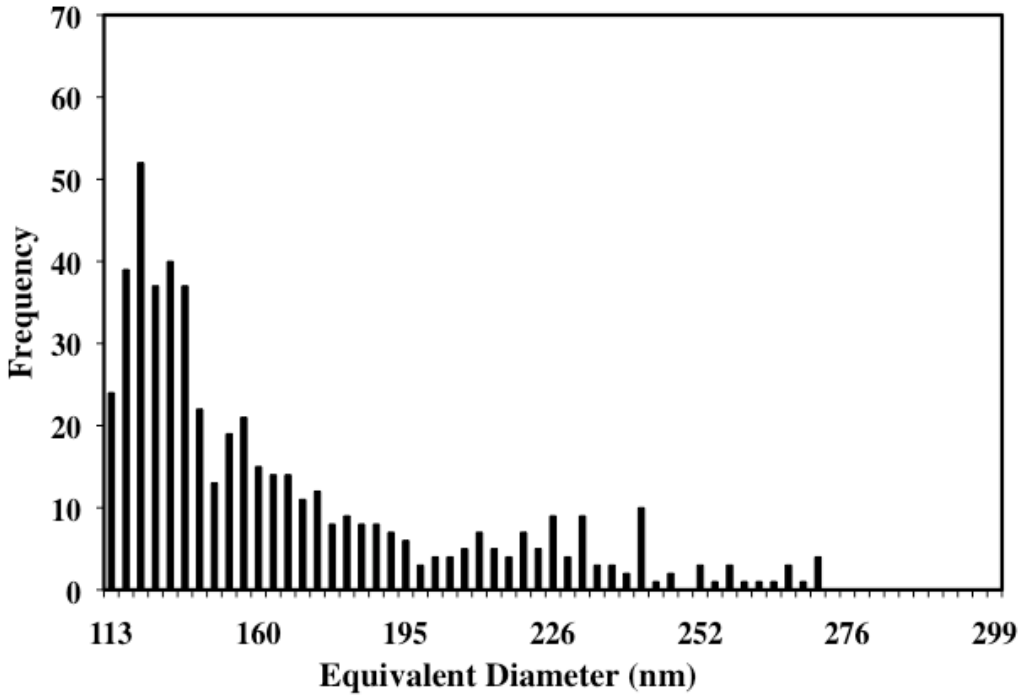

- ***Coarse non-spherical primary γ' precipitates***
- **2D measurement of areas from SEM images – converted to equivalent diameter**
- **Size distribution plot of primary γ' precipitates**

Different Generations of γ' (Secondary)

Energy-filtered TEM images (Cr M-edge)

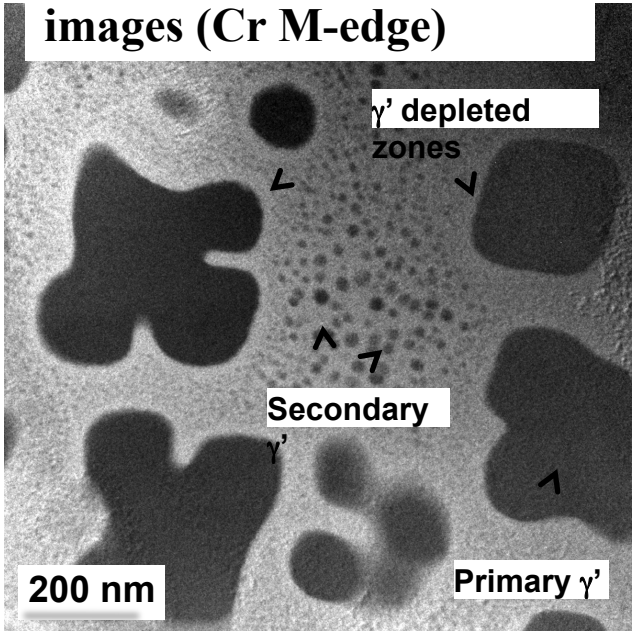

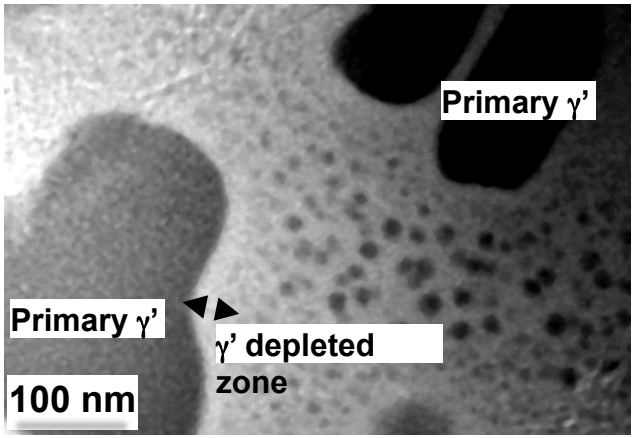

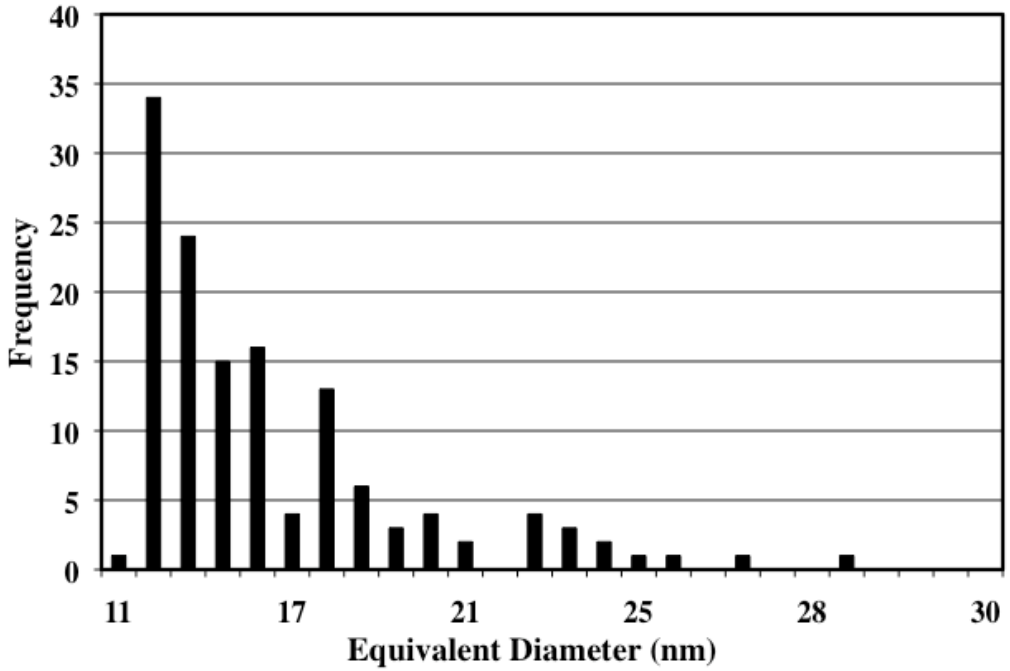

- *Near-spherical secondary γ' precipitates*
- 2D measurement of areas from EFTEM images – converted to equivalent diameter
- Size distribution plot of secondary γ' precipitates

Different Generations of γ' (Tertiary)

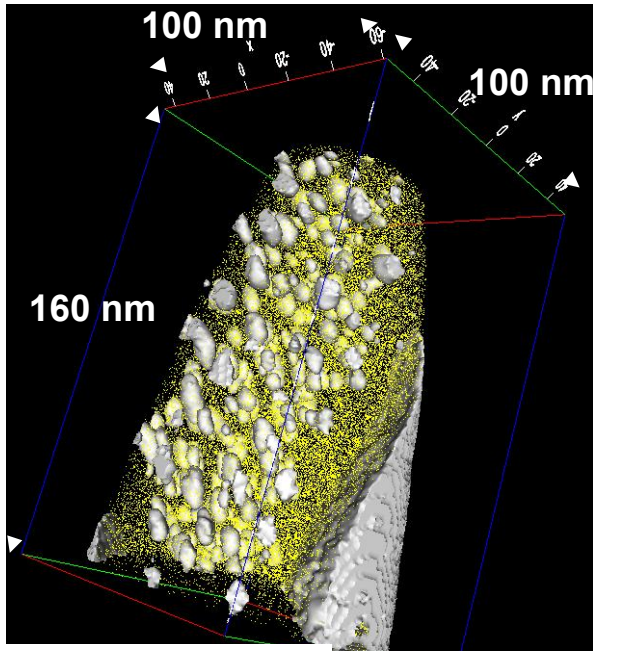

3D atom probe

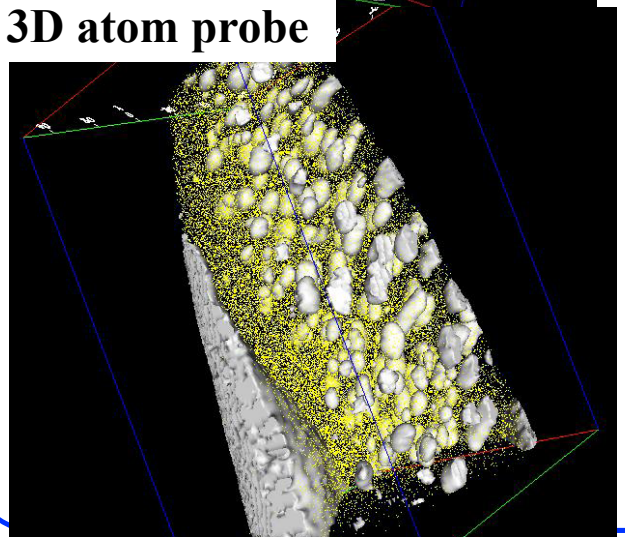

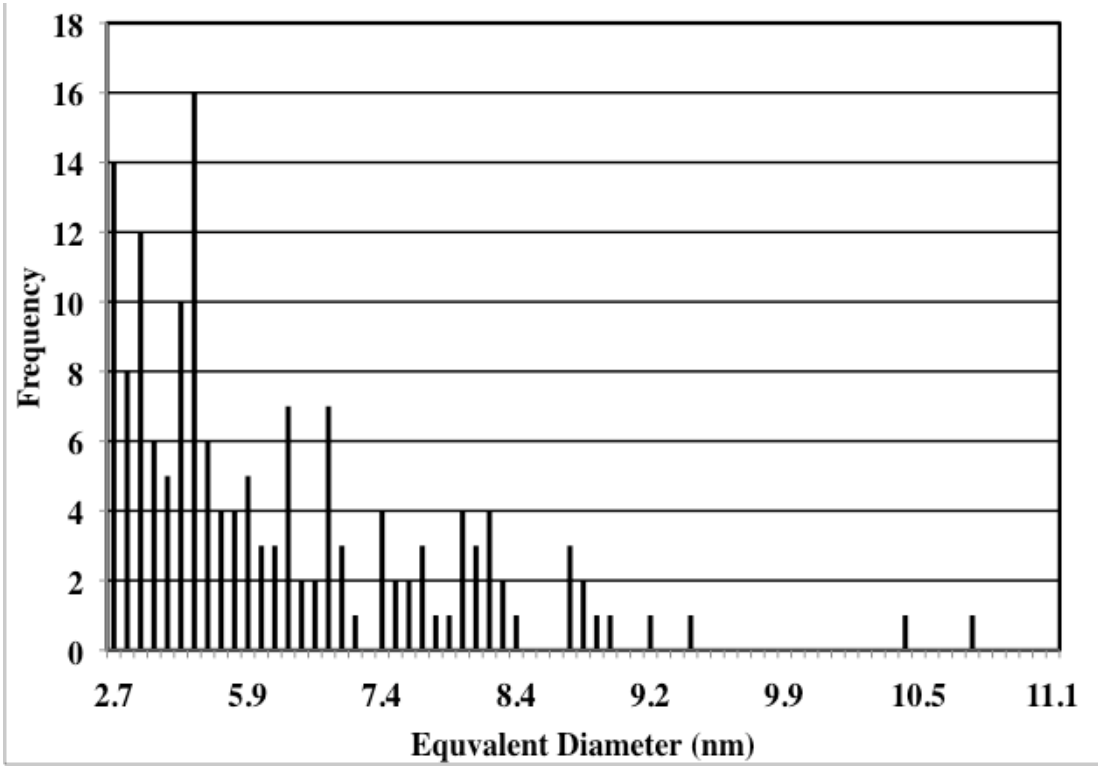

- *Nanometer scale tertiary γ' precipitates*
- 3D measurement of volumes from atom probe tomography – equivalent diameter
- Size distribution plot of secondary γ' precipitates

Three Different Generations of γ'

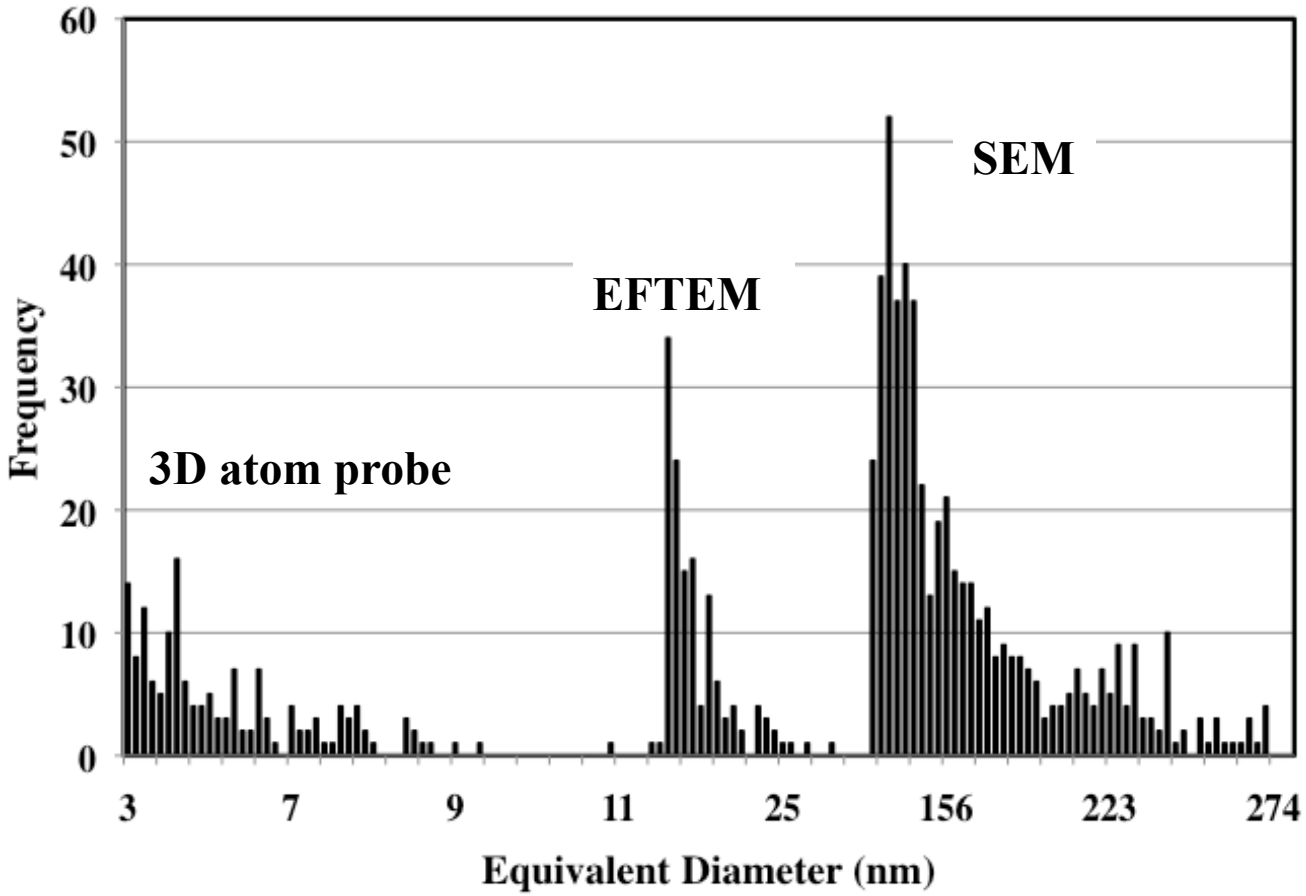

- ***Unique coupling of characterization techniques to identify three different generations of gamma prime precipitates and their relative size distributions***
- **Forming from 3 distinct nucleation bursts**

As Slow-Cooled sample

Cr-M edge EFTEM images

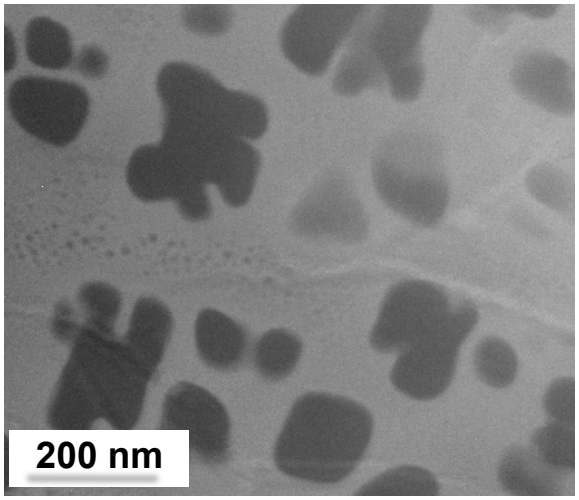

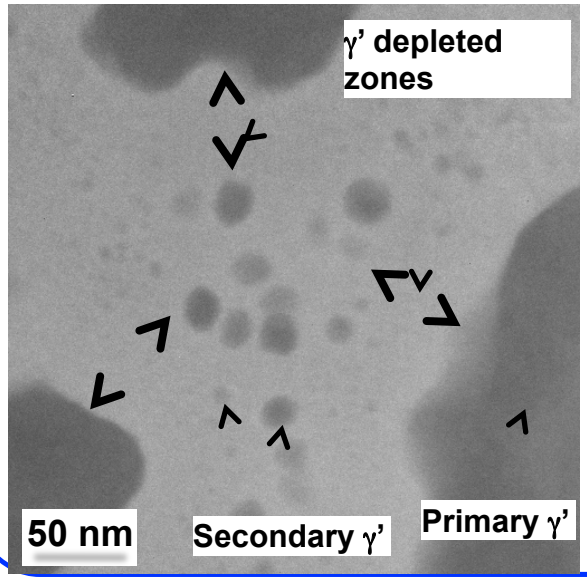

3D atom probe tomography: Cr=14at% isosurface

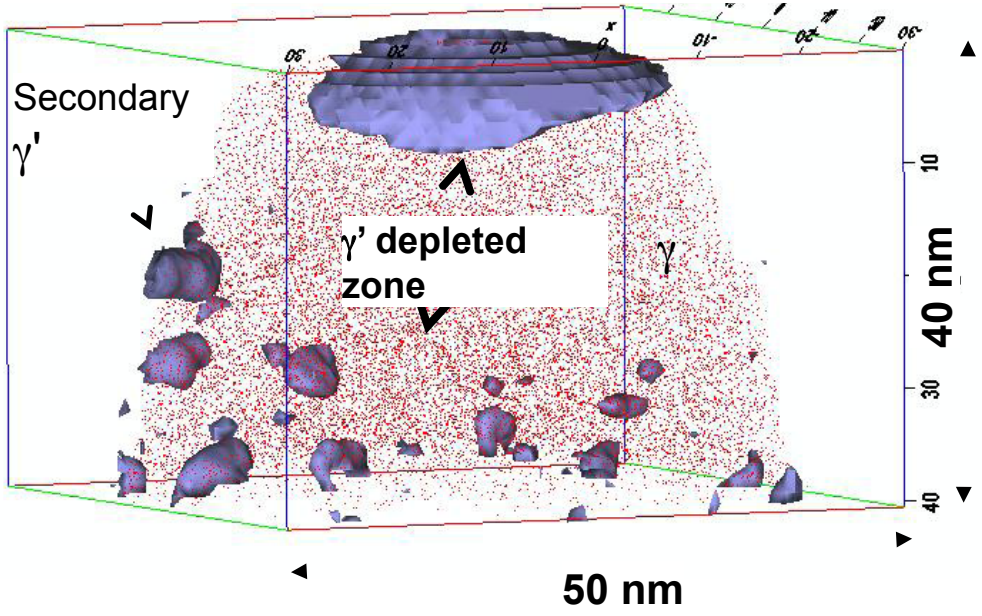

- **Presence of depletion zones between the primary and secondary γ' precipitates**

- Primary γ' : Coarser, non-spherical
- Secondary γ': much finer, near-spherical

As Slow-Cooled sample

	Primary γ'(avg) Atomic %	Secondary (1)γ' Atomic %	Secondary (2)γ' Atomic %
Co	6.70	8.70	10.99
Ti	9.17	7.14	6.43
Cr	1.77	8.23	11.53
Mo	2.84	5.12	4.02

- **Compositional differences between primary and secondary γ' precipitates**
  - **secondary γ' precipitates**
    - **richer in Co, Cr, Mo**
    - **depleted in Ti**
    - ***further from equilibrium***
  - **primary γ' precipitates**
    - ***closer to equilibrium composition***

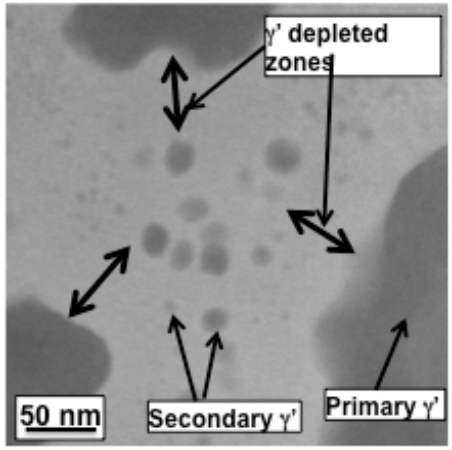

As Slow-Cooled sample

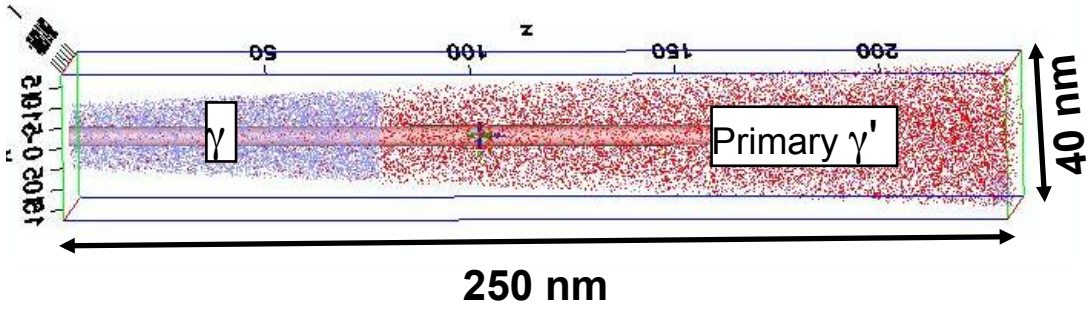

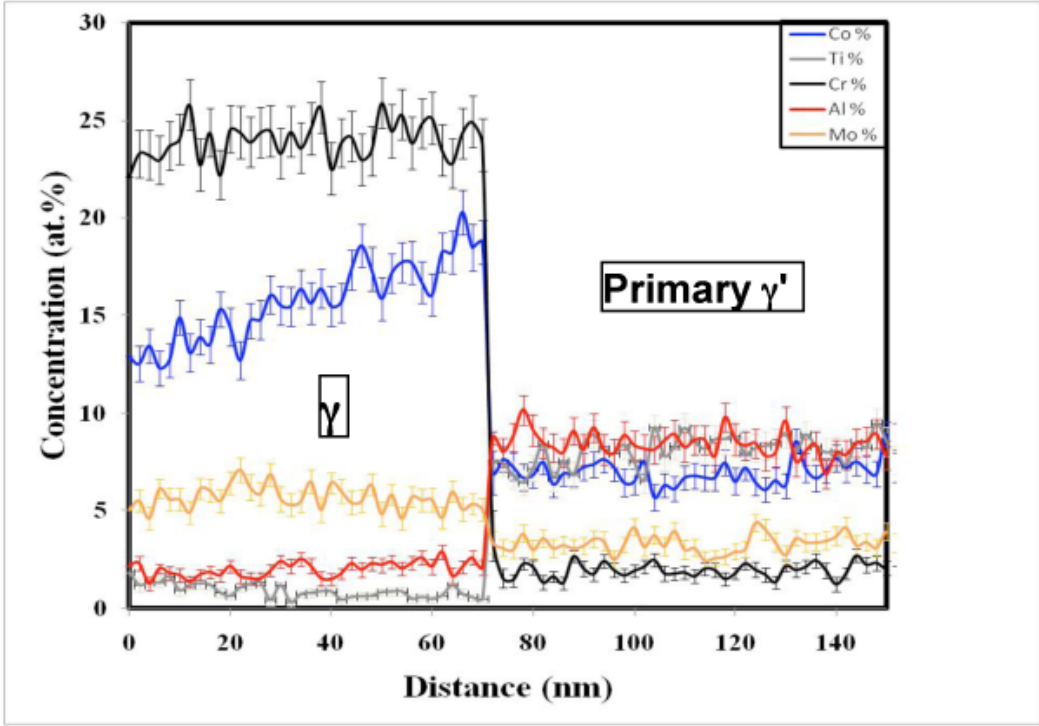

Primary γ' precipitates seem to show a pile-up of Co in the γ matrix near them

- Depletion zone where secondary γ' precipitates cannot nucleate

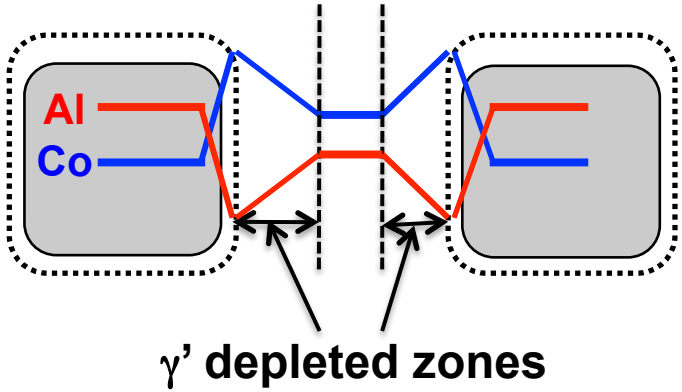

Long-range equilibration of γ composition has not taken place – *limited diffusivity of slow diffusers (e.g. Co)*

As Slow-Cooled sample

SC0	γ near primary γ‘	γ far from primary γ‘	γ near secondary γ‘
	Atomic %	Atomic %	Atomic %
Co	18.63	13.71	15.38
Ti	0.68	1.21	2.68
Al	1.97	1.67	3.76

- **Compositional differences between γ matrix near primary γ' precipitates vs. near secondary γ' preciptates**
  - *γ away from the primary γ' precipitates, near secondary γ' precipitates:*
    - **depleted in Co**
    - **enriched in in Al,Ti**
    - ***further from equilibrium – driving force for secondary γ' nucleation***

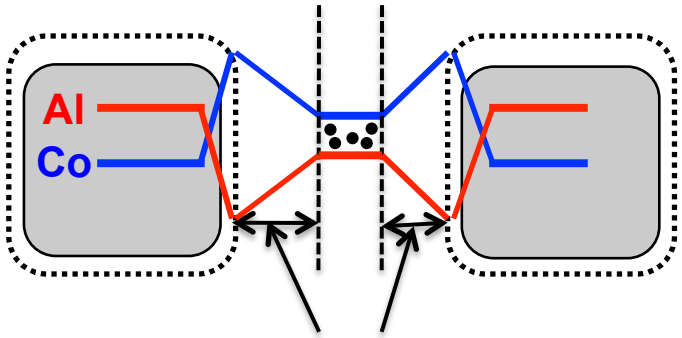

Different generations of γ′ precipitation:

Intermediate Cooling Rates

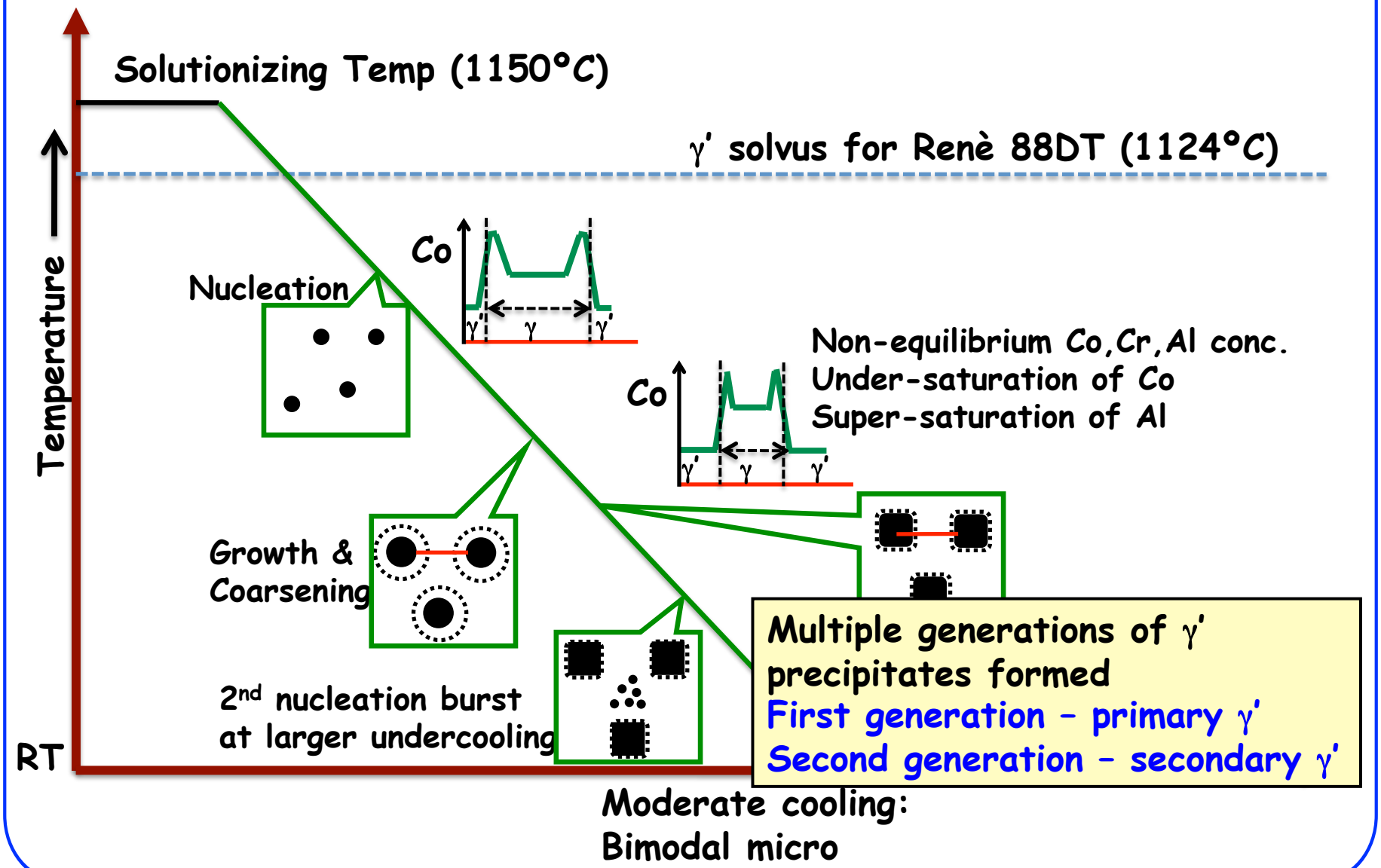

Slow-Cooled + 760°C/50hrs aged sample

Cr-M edge EFTEM images

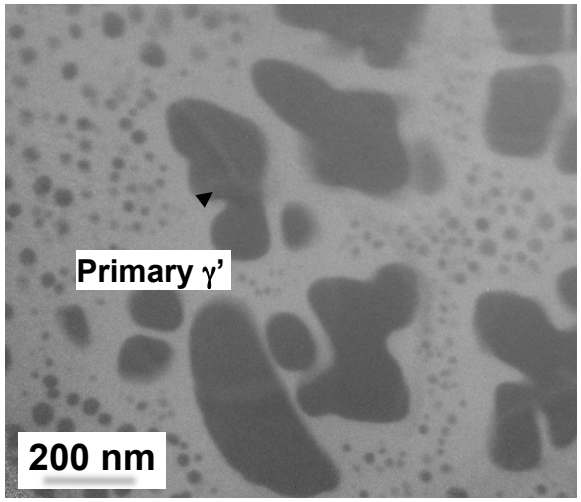

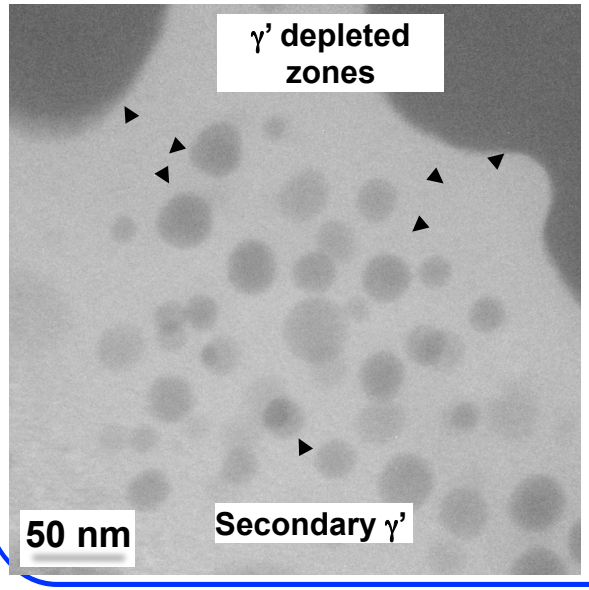

	Primary γ'(avg) Atomic %	Secondary (1)γ' Atomic %	Secondary (2)γ' Atomic %
Co	6.52	7.20	6.13
Ti	9.22	8.31	9.73
Cr	1.71	3.32	1.95
Mo	2.96	1.94	2.10

Lesser compositional variation between the primary and secondary γ' precipitates – *composition of both types of precipitates approaching equilibrium*

Slow-Cooled + 760°C/50hrs aged sample

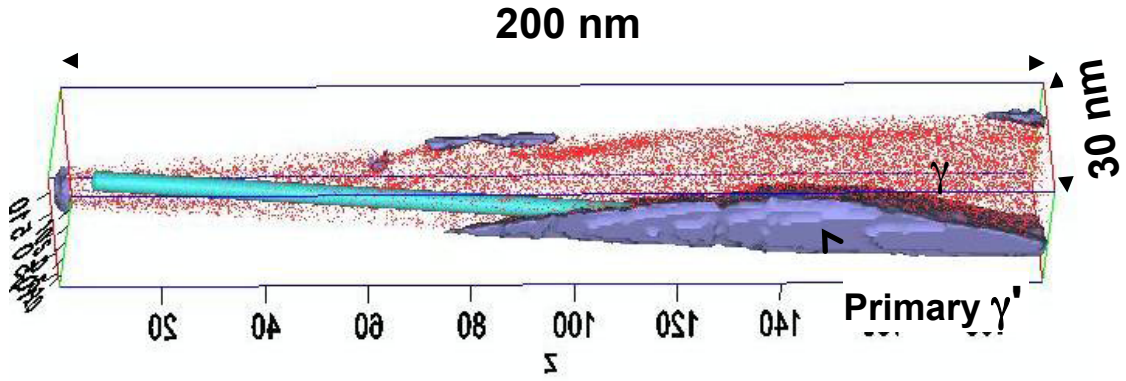

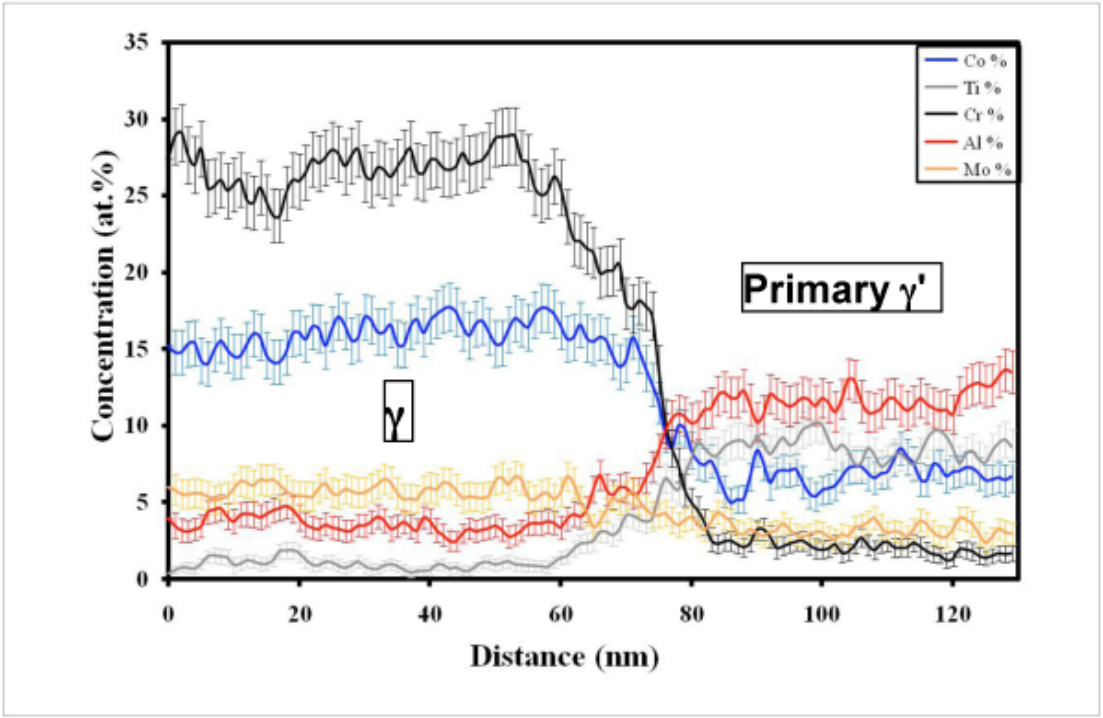

Reduced pile-up of Co and Cr in the γ matrix near the primary γ' precipitates

- Long range composition equilibration in γ matrix due to aging

Organization

- γ' precipitation during continuous cooling from single γ phase field
  - Water-quenched (rapid cooling)
  - Slow cooling

- **Evolution of the γ/γ' interface**
  - ***Compositional gradient (or width) across the interface***
  - ***Order-disorder transition width***

- Application to real multi-component engineering alloys => *study on Rene88 alloy (turbine disk alloy)*
  - 56.53Ni-16.24Cr-13.27Co-3.92Ti-2.09Al-4.08Mo-3.92W-0.76Nb (wt%)
  - *Primary alloying elements are Cr, Co, Ti, Al, Mo*

Demonstration of Z-contrast through HAADF-HRSTEM

γ’ phase

γ phase

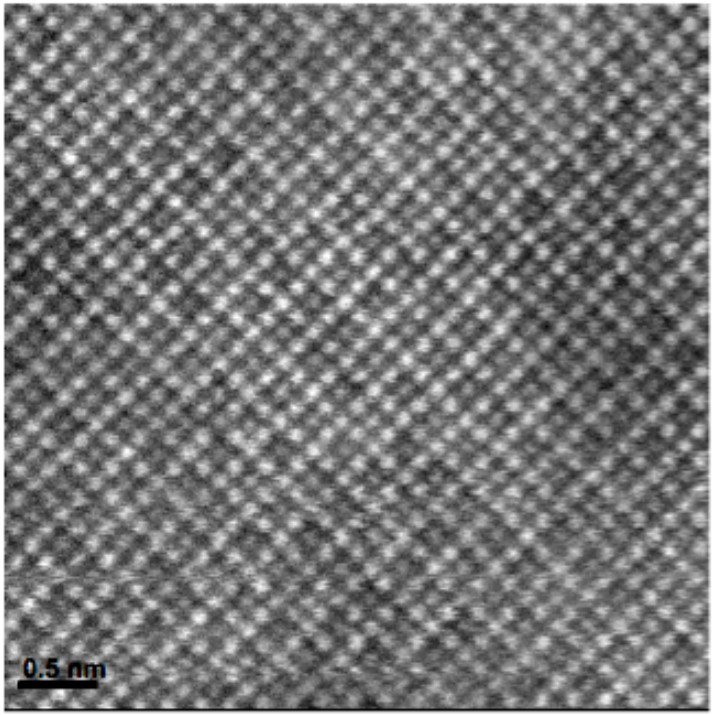

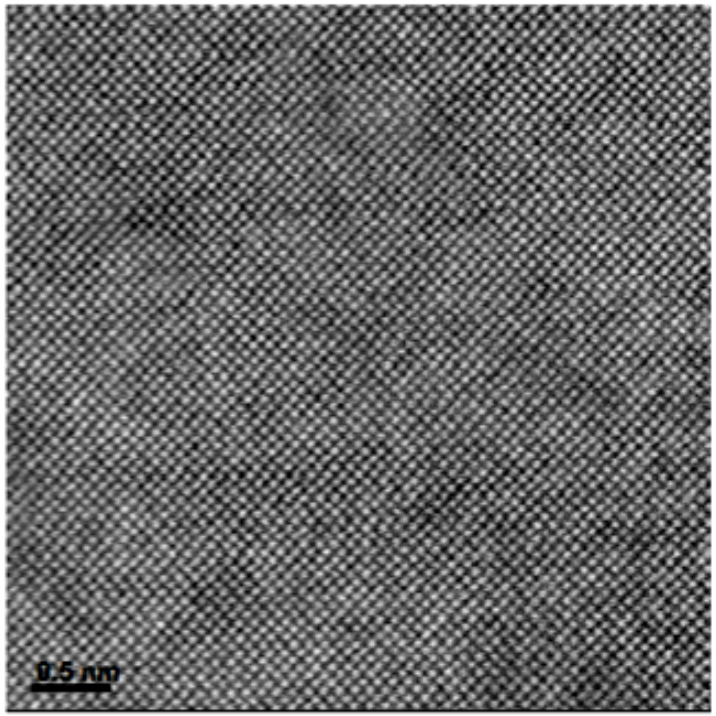

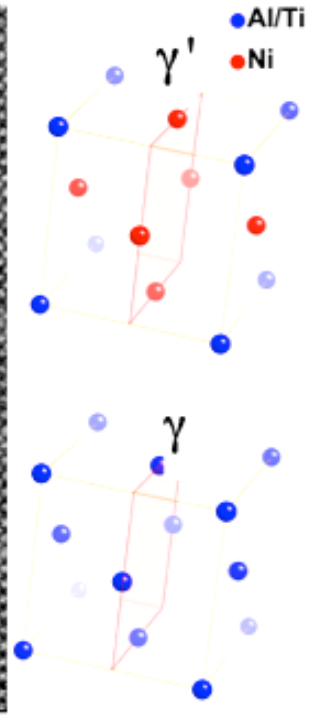

$L1_2$ ordering in γ’ phase – alternate atomic layers of pure Ni and 50%Ni + 50% Al layers

Reflected in experimental HAADF-HRSTEM image

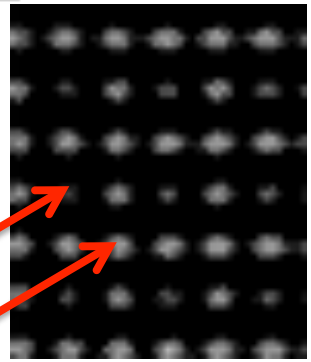

Structural Transition Across γ/γ' Interface

HAADF-HRSTEM image of interface recorded in a C_s corrected TITAN

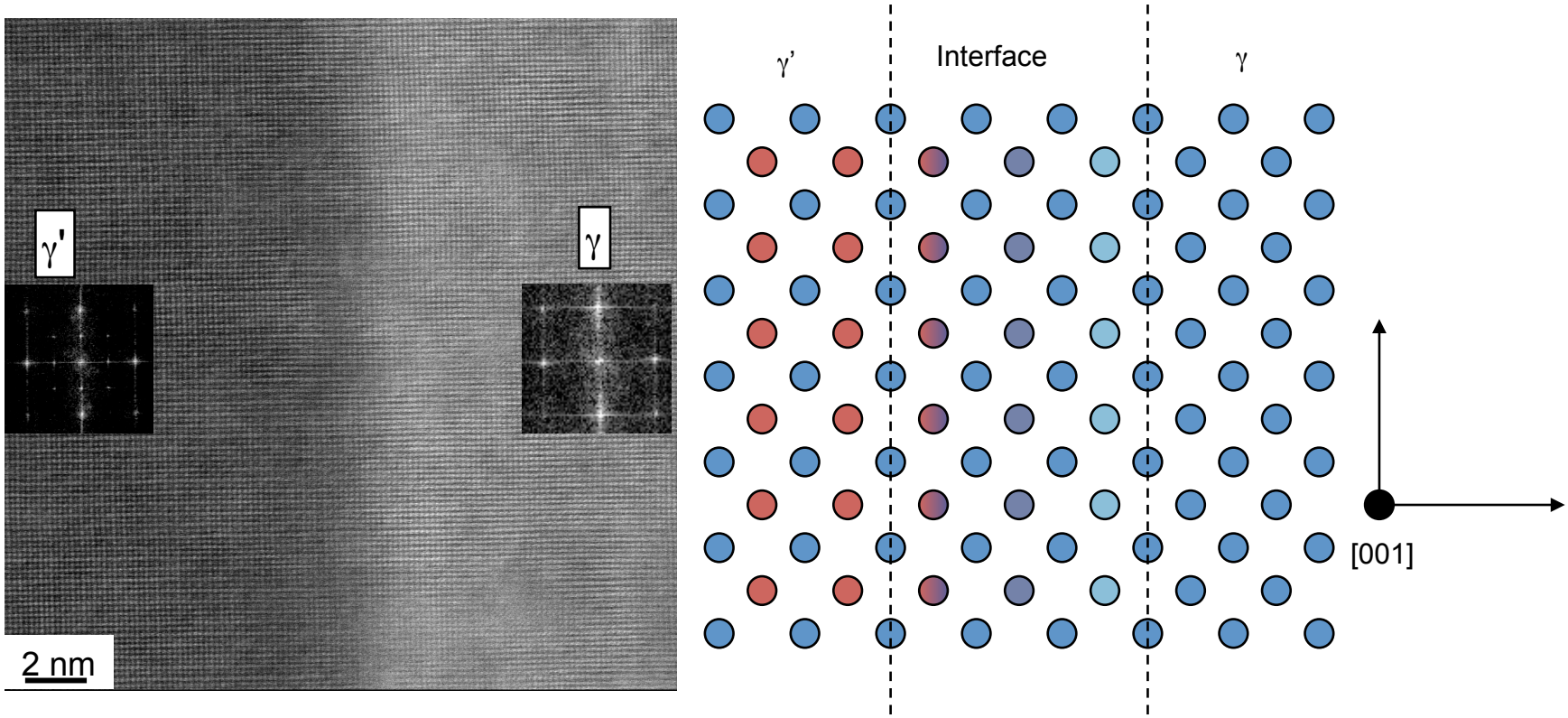

- Interface does not appear to be abrupt, shows transition width
- γ' region exhibits darker contrast as compared with the γ region – γ contains heavier alloying elements (e.g. Cr, Co) – *higher intensity Z contrast in HAADF-STEM*

Structural Transition Across γ/γ' Interface

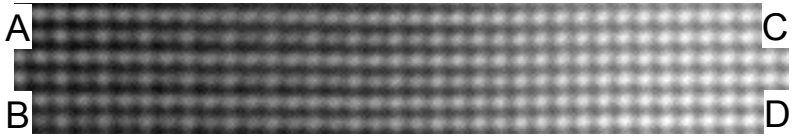

Intensity Profile across interface
(column averaged)

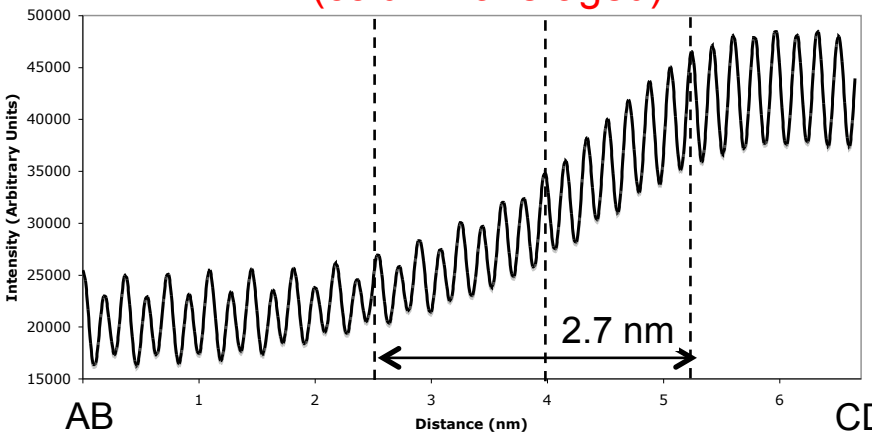

Ratio of Alternate Column Intensities
(measure of long-range order parameter)

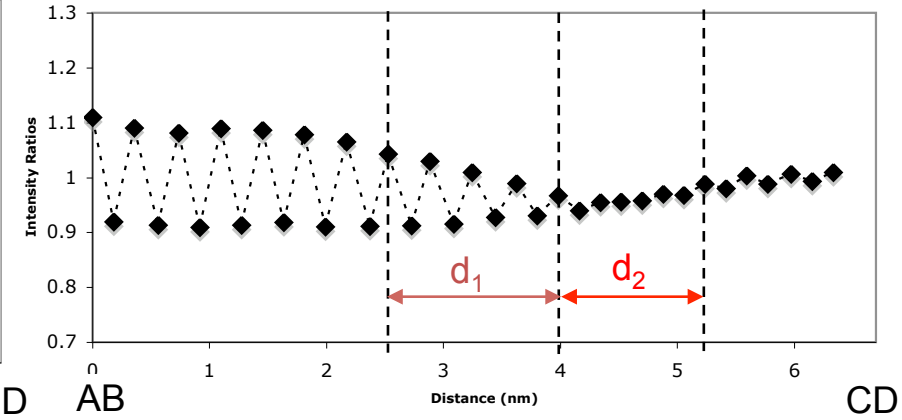

Two distinct interface widths

Avg. width of order-disorder transition (d1): 6-8 (002) planes (~ 1.2 nm)

Avg. width of compositional gradient (d1+d2): 12-14 (002) planes (~ 2.2 nm)

Need to validate with independent measurements (3D atom probe)

Srinivasan, Viswanathan, Banerjee, et. al., *Phys Rev. Lett.* (2009)

3DAP Investigations of Compositional Transition Across Interface

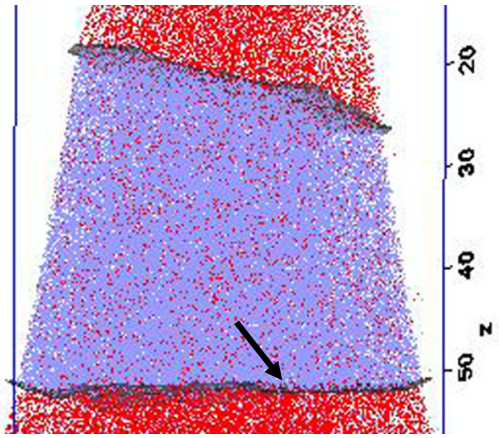

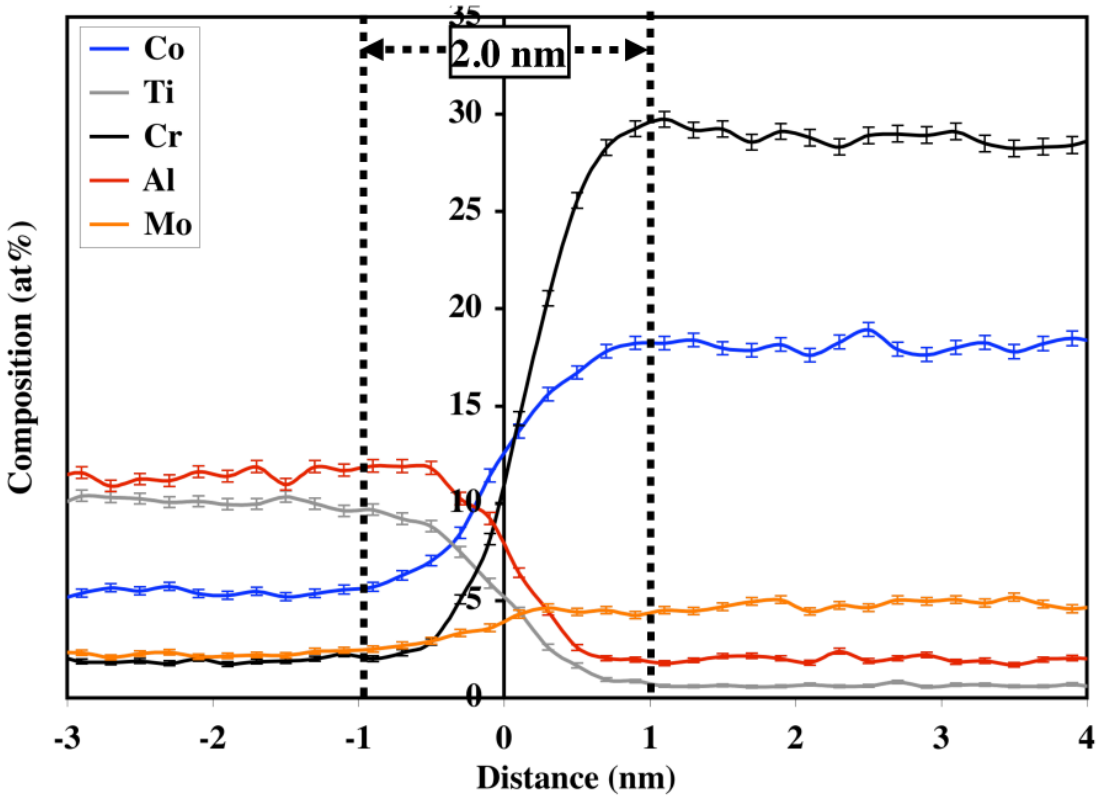

- **Compositional profiles across γ/γ' interface - Proximity Histogram (proxigram) analysis used**
- **Compositional transition across interface occurs over ~ 2 nm**
  - **Non-abrupt compositional interface**
- ***3DAP results in good agreement with HRSTEM results***

Srinivasan, Banerjee, Viswanathan, Tiley and Fraser ., *Phys Rev. Lett.* (2009)

Atomistic Simulations of γ/γ' Interface Structure

EAM simulations of Ni/Ni_3Al interface

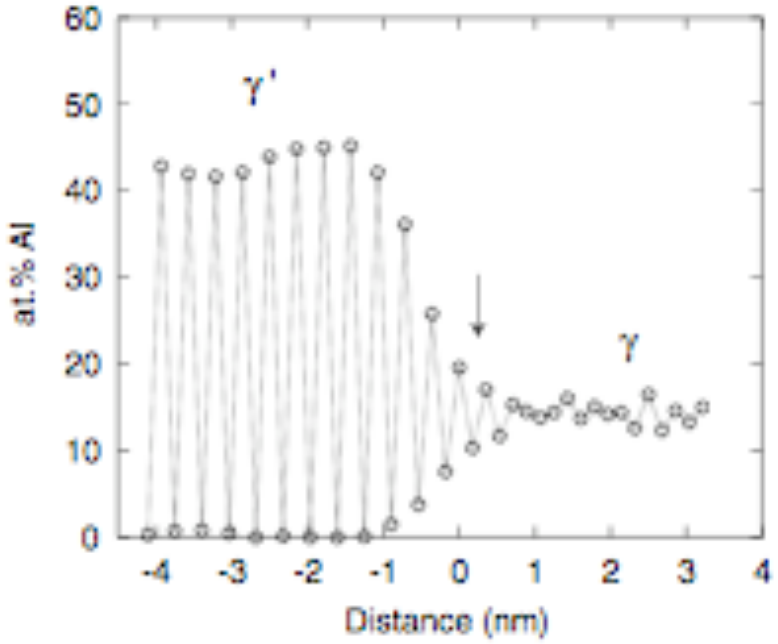

Y.Mishin, *Acta Materialia*, 52 (2004), 1451
Order-disorder transition ~ 6-8 planes

Monte Carlo simulations of γ/γ' interface structure in binary Ni-Al system

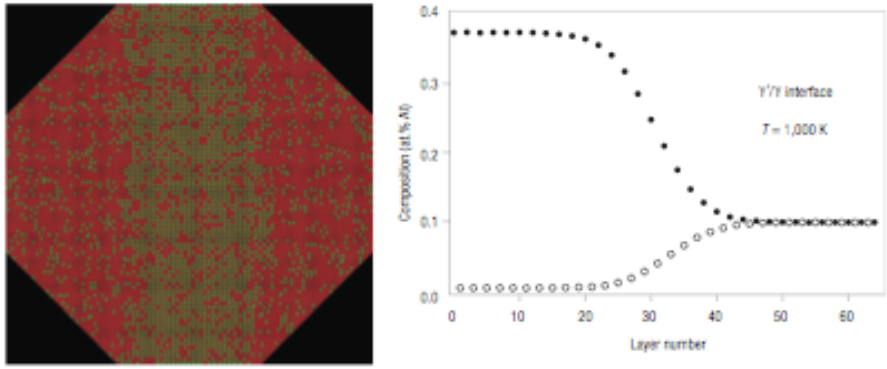

A.J. Ardell, V. Ozolins, *Nature Materials*, 4 (2005) 309
Order-disorder transition ~ 10 planes

- Atomistic simulations predict "ragged", non-abrupt interface structure
- Observed experimental results in very good agreement with atomistic simulations - *partially ordered γ/γ' interface of finite width - slows down diffusivity?*

Organization

- γ' precipitation during continuous cooling from single γ phase field
  - Water-quenched (rapid cooling)
  - Slow cooling

- Evolution of the γ/γ' interface
  - *Compositional gradient (or width) across the interface*
  - *Order-disorder transition width*

- **Application to real multi-component engineering alloys => *study on Rene88 alloy (turbine disk alloy)***
  - **56.53Ni-16.24Cr-13.27Co-3.92Ti-2.09Al-4.08Mo-3.92W-0.76Nb (wt%)**
  - ***Primary alloying elements are Cr, Co, Ti, Al, Mo***

Coarsening Microstructures

Cooling rate → WQ FC SC

Before aging

760°C 200 hr

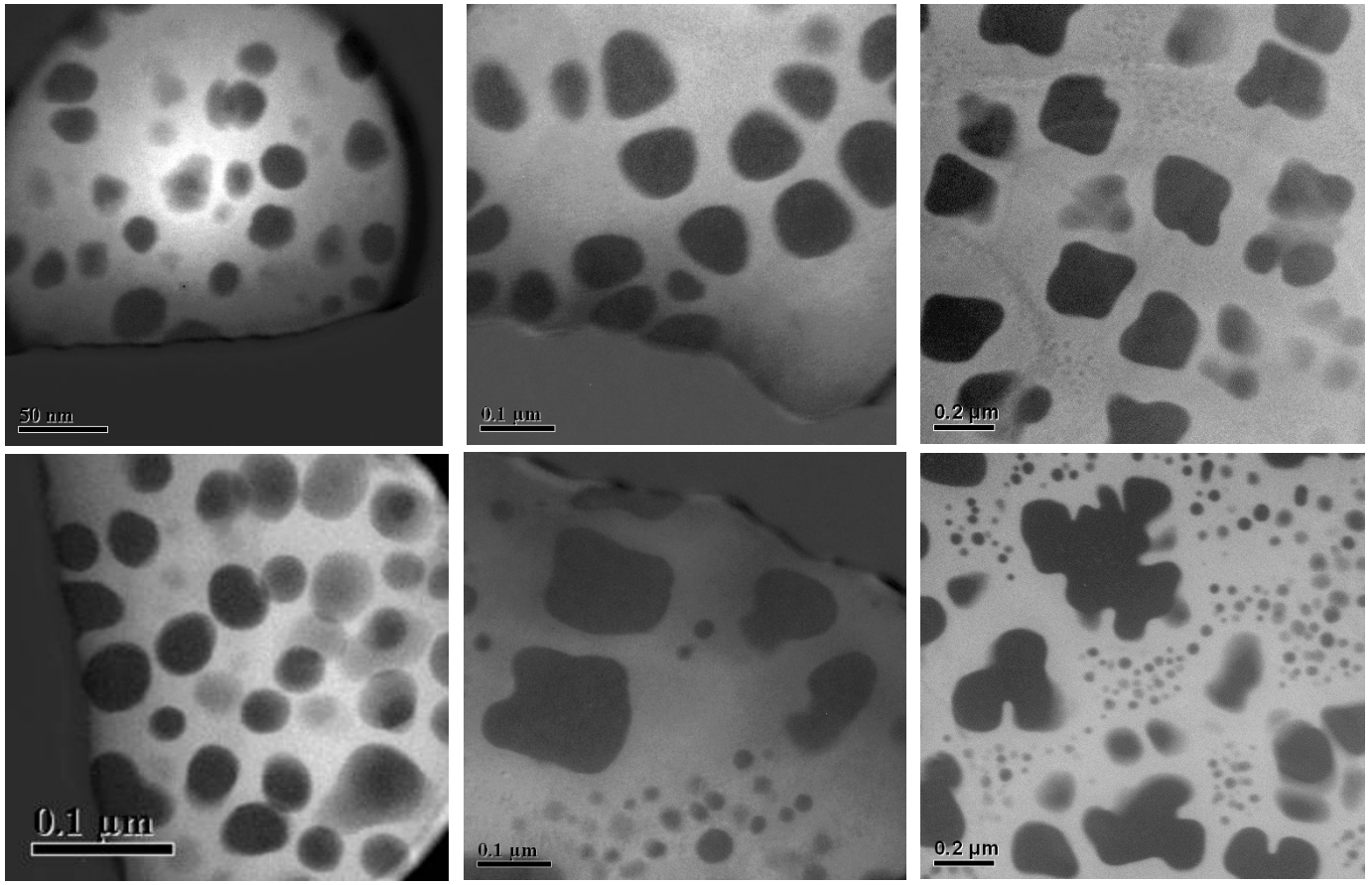

Significant changes in γ' size, morphology as f (cooling rate, aging time)

Experimental coarsening behavior

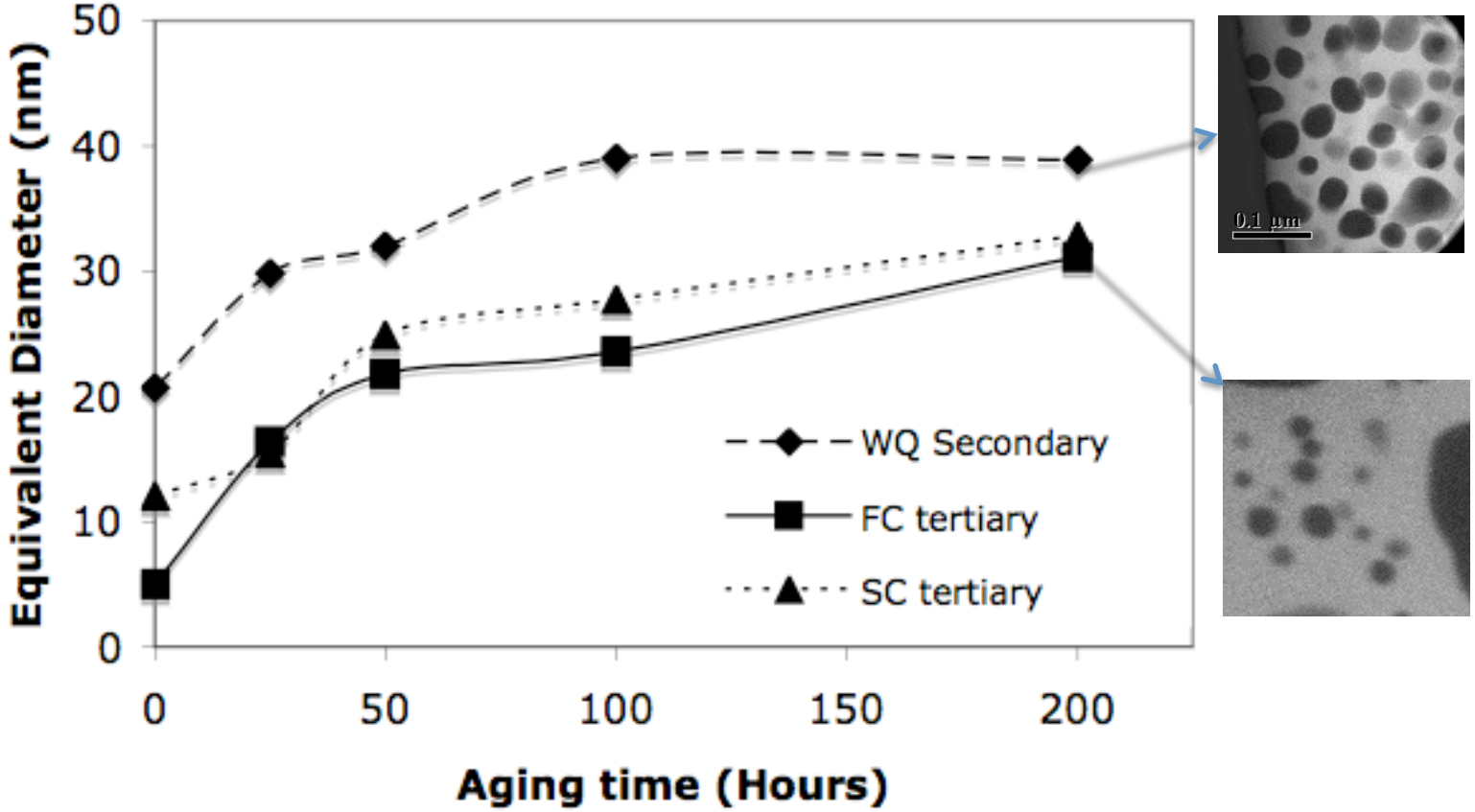

- Coarsening kinetics investigated as f (cooling rate)
- Aging treatment: 760^{0}C for 25,50,100 and 200 hours
- Distinction made between growth and pure coarsening (>25 h aging)

Coarsening kinetics - LSW Model

Classical LSW Model ($r^3-r_o^3=kt$)

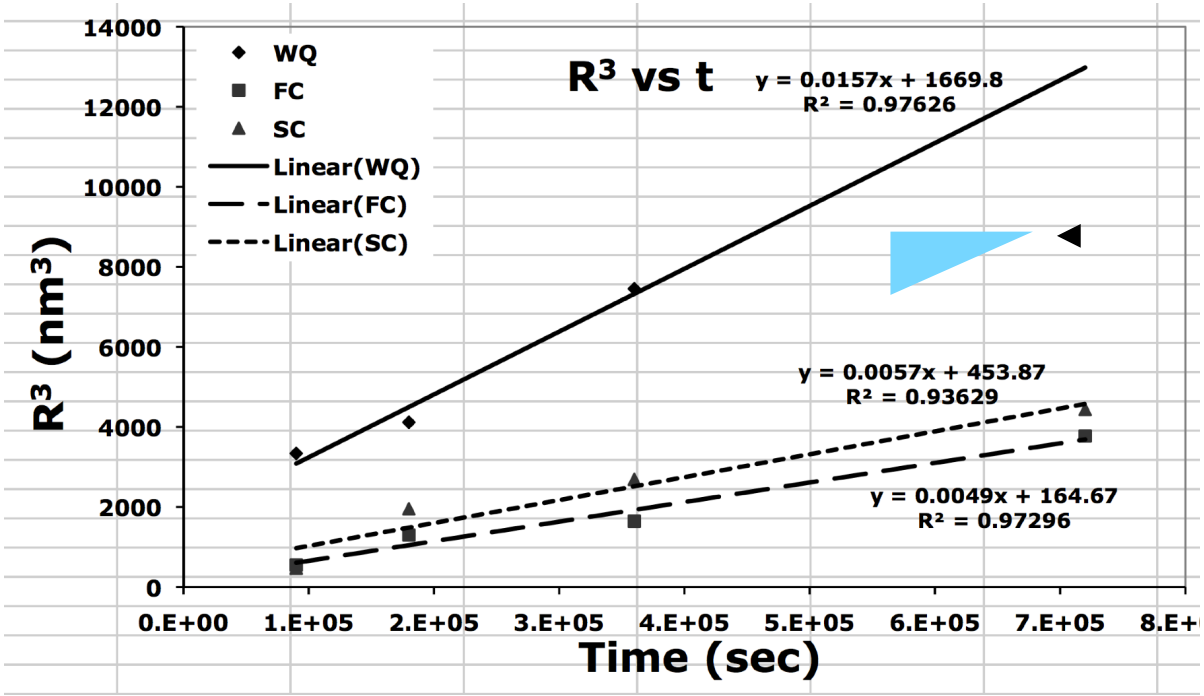

Slopes yield coarsening rate constant, *k*

Experimental rate constants

$k_{WQ} = 0.0157\ nm^3s^{-1}$

$k_{FC} = 0.0049\ nm^3s^{-1}$

$k_{SC} = 0.0057\ nm^3s^{-1}$

Key Assumptions

- Pure coarsening regime
- Constant volume fraction of γ'
- Equilibrium matrix composition

Modeling of Coarsening Kinetics - LSW Model

Coarsening rate constant, k $= \dfrac{A.D.C_e.\gamma_i.V_m}{RT}.10^{27}$

D is the diffusion coefficient of solute in the matrix (m^2s^{-1})

C_e is the atomic fraction of solute in equilibrium with the precipitate

Obtained via 3DAP studies

γ_i is the precipitate/matrix interface energy,

V_m is the molar volume of the precipitate (m^3 mol^{-1}),

R is the universal gas constant (J $mole^{-1}$-K^{-1})

T is the absolute temperature (K).

Substituting experimental values for D, C_e and γ_i the analytically derived coarsening rate constants for primary γ' in WQ sample

k = 0.002 nm^3s^{-1} (using D_{Al})

k = 0.005 nm^3s^{-1} (using D_{Cr}) → **Good Agreement** → Experiment k = 0.0157 nm^3s^{-1}

Coarsening Kinetics - TIDC Model

Trans-Interface Diffusion Controlled ($r^2-r_0^2=kt$) - *(Ardell and Ozolins, 2005)*

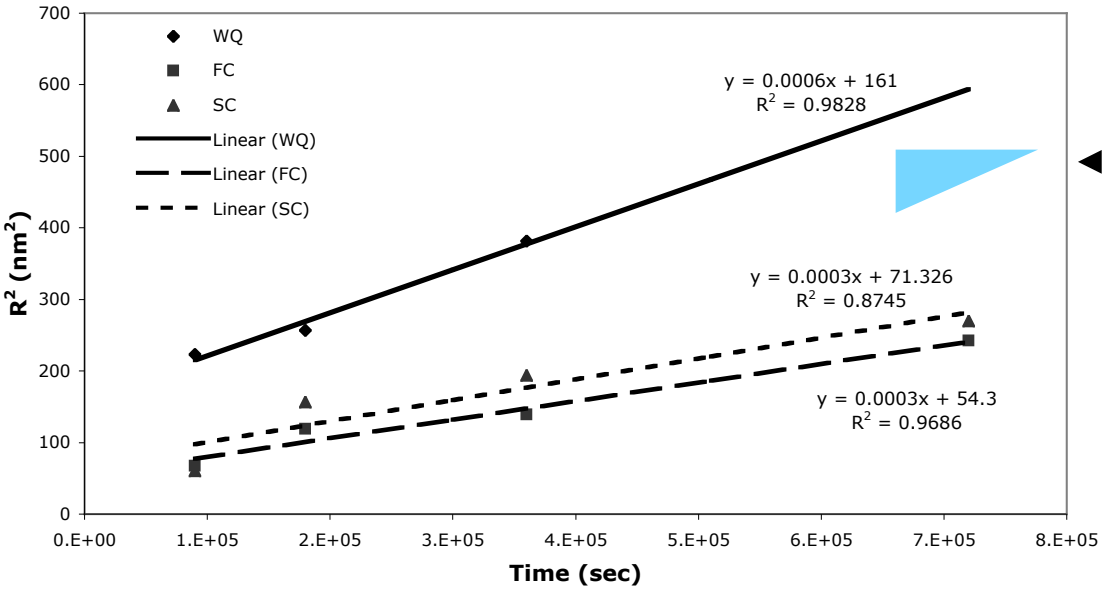

Slopes yield experimental coarsening rate constant, *k*

Experimental rate constants

$k_{WQ} = 0.0006\ nm^2s^{-1}$
$k_{FC} = 0.0003\ nm^2s^{-1}$
$k_{SC} = 0.0003\ nm^2s^{-1}$

Key Assumptions

- Independent of volume fraction
- Diffusion across interface is rate limiting
- Existence of a non-abrupt, ragged interface

Modeling of Coarsening Kinetics - TIDC Model

Coarsening rate constant $$k^i = \frac{32\tilde{D}_i\, l_\gamma}{81\Delta X_e \delta} 10^{18}$$

$\tilde{D}_i$ is the trans interface diffusion coefficient (m^2s^{-1})
l_γ is capillary length
ΔX_e is the difference in the equilibrium solute concentration between γ and γ'
δ is width of the interface

Obtained via 3DAP studies

Substituting experimental values for k^i, ΔX_e and δ the analytically calculated "effective" interface diffusivity in WQ sample is

$D_i \sim 4.33 \times 10^{-19}\ m^2s^{-1}$

(between the diffusivity values for Al in Ni and Ni_3Al)

Summary

- **Nucleation during continuous cooling from above the solutionizing temperature:**
  - **Long range equilibration of γ composition fields away from growing γ' precipitates plays a significant role**
  - **Fast cooling rate results in monomodal distribution of γ' precipitates**
  - **Slower cooling rates result in bimodal or multi-modal γ' precipitates**

- ***Multiple nucleation bursts are different undercoolings clearly identified by coupling SEM, EFTEM, and 3DAP***

- **HRSTEM and 3DAP investigations clearly reveal two distinct transition widths associated with the γ/γ' interface**
  - **order-disorder transition width**
  - **compositional gradient width**

Effect of Coherency and Local Stress on Nucleation

R. Shi, N. Zhou, C. Shen* and Yunzhi Wang

Department of Materials Science and Engineering
The Ohio State University
***GE Global Research Center**

Acknowledgement

ONR and NSF

Joint AFRL/AOARD/LLNL Workshop on Nucleation during Solid-Solid Phase Transformations
Maui, Hawaii, May 2-7, 2010

500nm

10nm

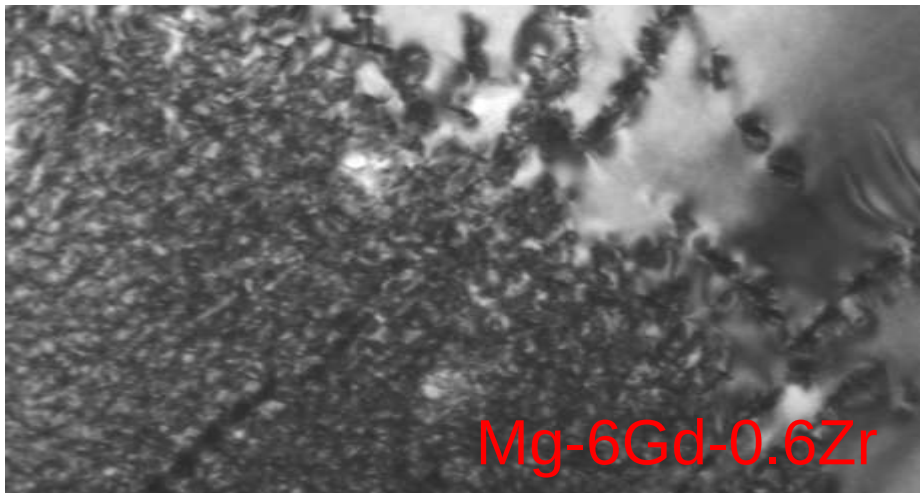

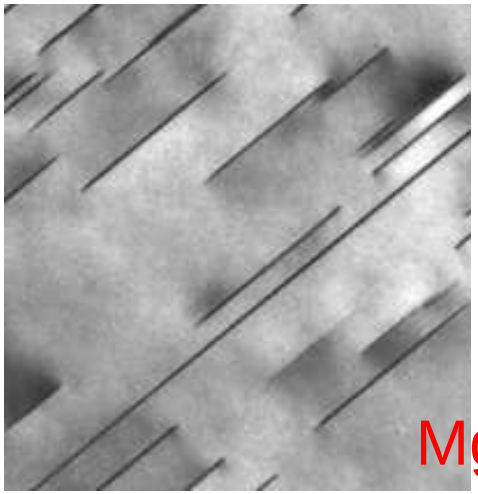

Courtesy of J.F. Nie)

Nucleation in solids is the toughest nut to crack!

K.C. Russell

Challenges:

- Coherency state and defect structure at interfaces/Interfacial energy anisotropy
- Orientation relationship and lattice correspondence
- Concentration non-uniformity in an embryo
- …

Usefulness and limitations of the phase field approaches:

- Langevin dynamics is qualitative in nature
- Interaction energy calculation is at most semi-quantitative
- Phase field total energy functional + Nudged Elastic Band (NEB) – quantitative but energetic only, feeding to explicit algorithm based on classical nucleation theory for kinetics

What we could do using phase field method to study nucleation

I. Quantitative calculation of activation energy and critical nucleus configuration

II. Qualitative understanding of autocatalytic effect and collective nucleation

III. Semi-quantitative study of effects of local stress and pre-existing microstructure on nucleation

Phase Field Modeling of Nucleation

Reprinted from THE JOURNAL OF CHEMICAL PHYSICS, Vol. 28, No. 2, 258–267, February, 1958
Printed in U. S. A.

Free Energy of a Nonuniform System. I. Interfacial Free Energy

JOHN W. CAHN AND JOHN E. HILLIARD
General Electric Research Laboratory, Schenectady, New York
(Received July 29, 1957)

Reprinted from the JOURNAL OF CHEMICAL PHYSICS, Vol. 31, No. 3, 688–699, September, 1959
Printed in U. S. A.

Free Energy of a Nonuniform System. III. Nucleation in a Two-Component Incompressible Fluid

JOHN W. CAHN AND JOHN E. HILLIARD
General Electric Research Laboratory, Schenectady, New York
(Received February 16, 1959)

Comment by Mullins: The fundamental properties associated with an interface and a critical nucleus are expressed in terms of the parameters in the free energy model and there is no need to introduce the artificial dividing surface of Gibbs, nor to define a separate interfacial energy, nor to model the nucleus as homogeneous

Phase field description of defects

Order parameter $\phi(\mathbf{r})$

Chemical non-uniformity: $c(\mathbf{r}), \rho(\mathbf{r}), V_m(\mathbf{r}), \ldots$

Structural non-uniformity: $\eta(\mathbf{r}), \mathbf{u}(\mathbf{r}), \boldsymbol{\varepsilon}(\mathbf{r}), \mathbf{M}(\mathbf{r}),$

Examples:
Martensitic transformation or dislocation, order parameter = inelastic displacement (or strain) $\mathbf{u}(\mathbf{r})$ or $\boldsymbol{\varepsilon}(\mathbf{r})$

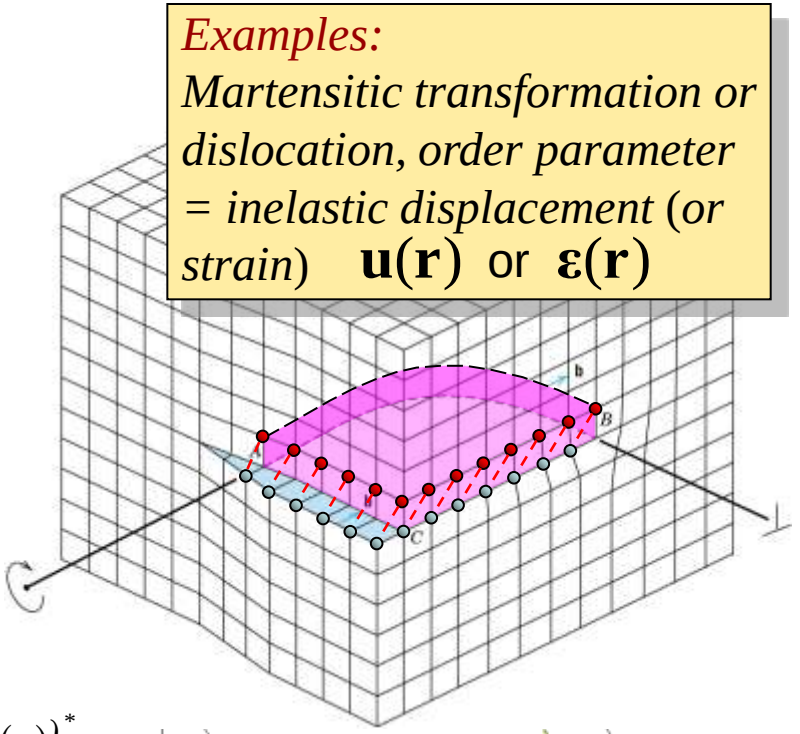

Total energy

Chemical or inelastic energy:

$$F^{ch} = \int [\, f(\phi(\mathbf{r})) + \kappa \,|\nabla \phi(\mathbf{r})|^2]\, \mathrm{d}\mathbf{r}$$

Elastic energy: $\varepsilon_{ij}^T(\mathbf{r}) = \sum_p \varepsilon_{ij}^T(\phi_p(\mathbf{r}))$

$$E^{el} = \frac{1}{2}\sum_{pq}\int \frac{d^3k}{(2\pi)^3} \begin{bmatrix} C_{ijkl}\varepsilon_{ij}^{00}(p)\varepsilon_{kl}^{00}(q) \\ -n_i\sigma_{ij}^{00}(p)\Omega_{jk}(\mathbf{n})\sigma_{kl}^{00}(q)n_l \end{bmatrix} \left\{\phi_p^m(\mathbf{r})\right\}_k \left\{\phi_q^m(\mathbf{r})\right\}_k^*$$

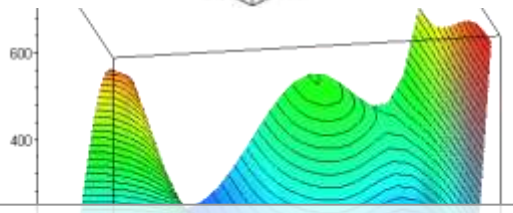

Kinetics

Phase field approach is a superset of the Cahn-Hilliard description of chemical inhomogeneities and the Peierls description of displacive inhomogeneities.

Wang an Li, Acta Mater, Overview 150, 2010

Defect cores are diffuse at their natural length scales

HRSTEM

3D atom probe

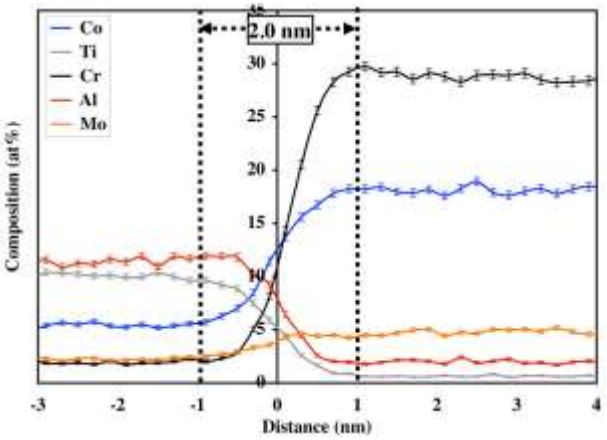

Srinivasan et. al. Phys. Rev. Lett. (2009)

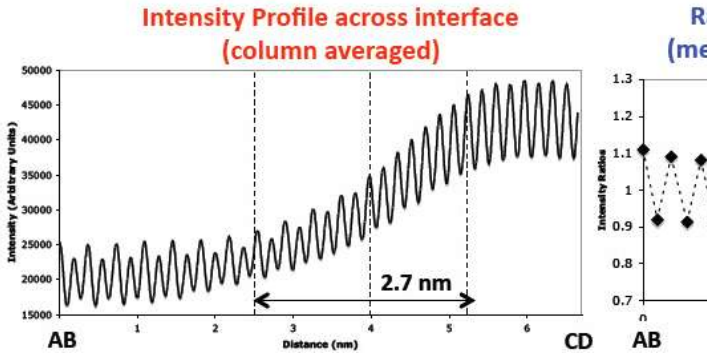

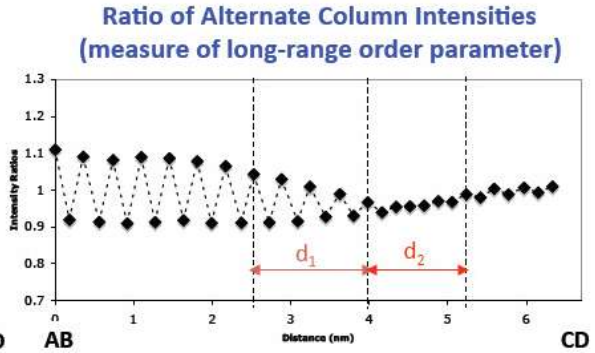

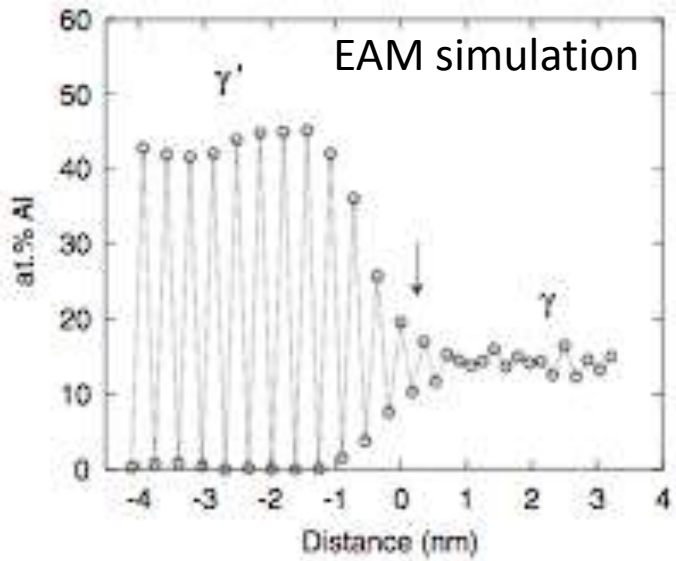

Y. Mishin, *Acta Materialia*, 52 (2004), 1451

Order-disorder transition ~ 6-8 planes

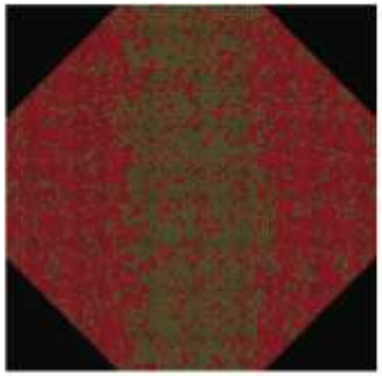

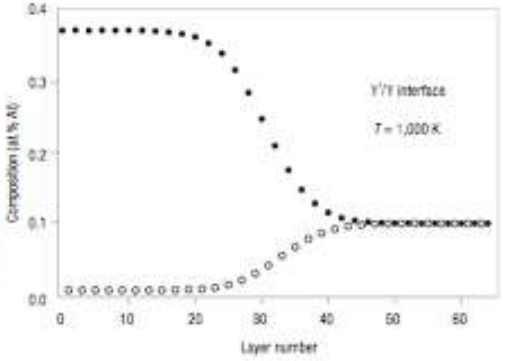

Monte Carlo simulation

A.J. Ardell, V. Ozolins, *Nature Materials*, 4 (2005) 309

Order-disorder transition ~ 10 planes

Interface width – atom probe data

Results indicate a wider γ/γ' interface for the tertiary γ' than for the larger secondary γ'

P. Sarosi (OSU)

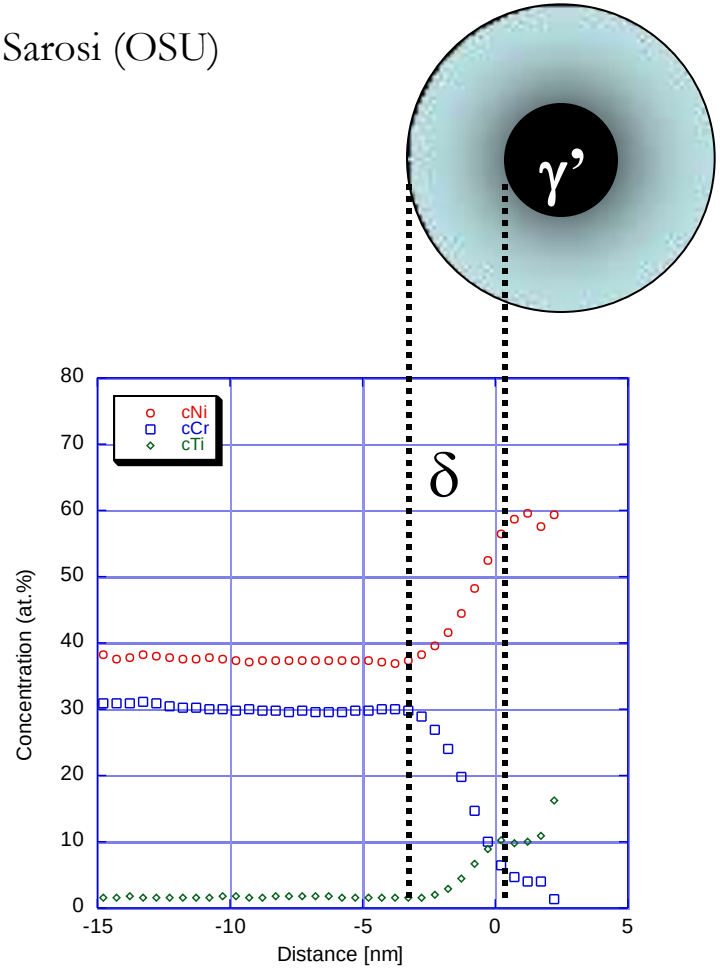

Compositional profile of tertiary γ' (from 30 precipitates)

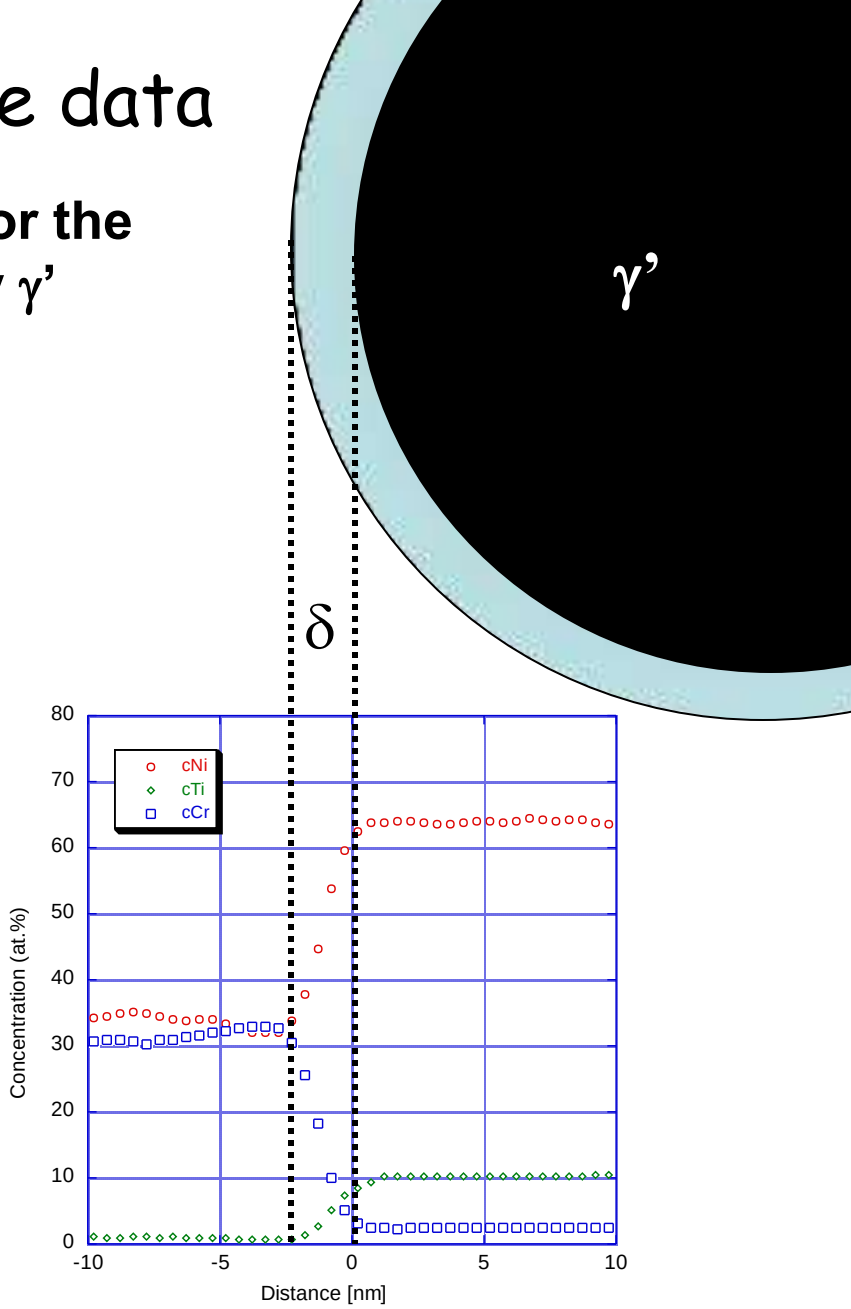

Compositional profile across a secondary γ' and matrix interface

Example I. Quantitative Calculations

- Works at natural length scales of extended defects (~nm)
- Using DFT calculations of GSF/MGSF and Landau free energy as direct inputs and **predict defect structure, chemistry and energy**
- Probe the total energy landscape using NEB for **saddle point configuration and activation energy of defect nucleation**
- When combined with experimental characterization, it could serve as a powerful tool to explore **deformation/transformation mechanisms** and provide critical inputs to coarse-grained phase field simulations

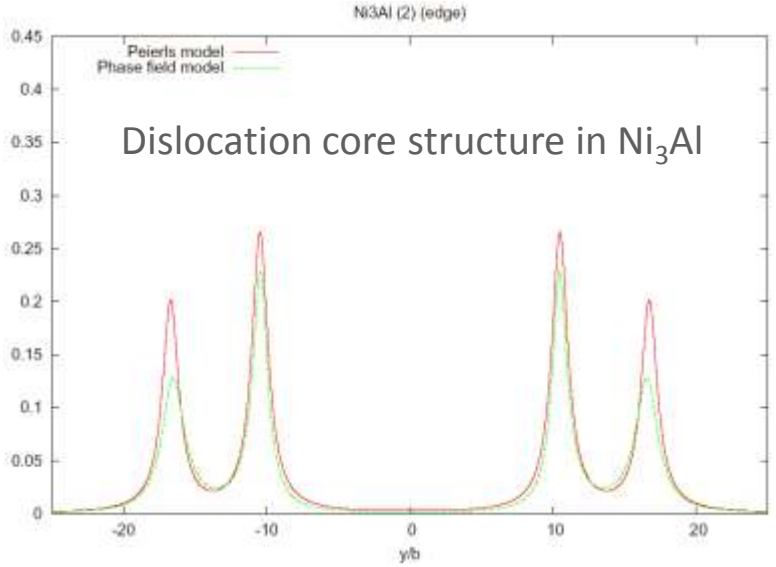

Wang and Li, Acta Mater, Overview 150, 2010

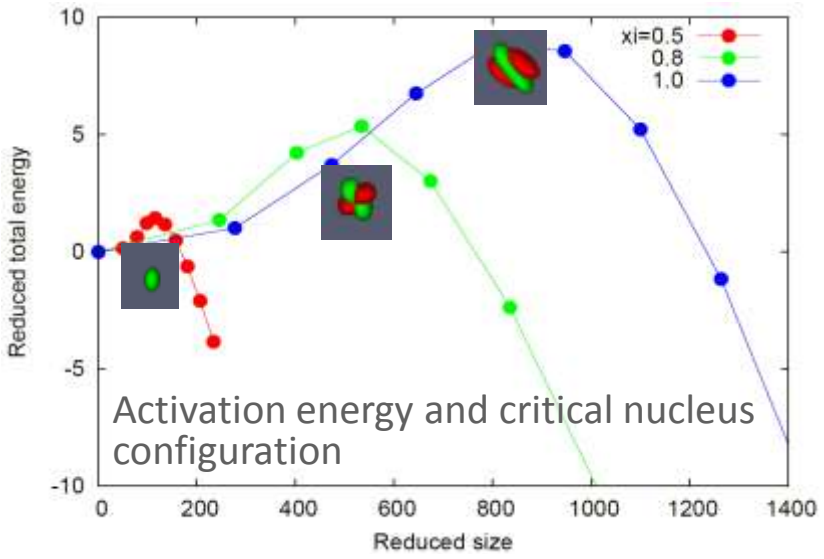

Shen. et. al. Met. Trans. 39A:976 (2008)

Energy landscape calculation by *ab initio*

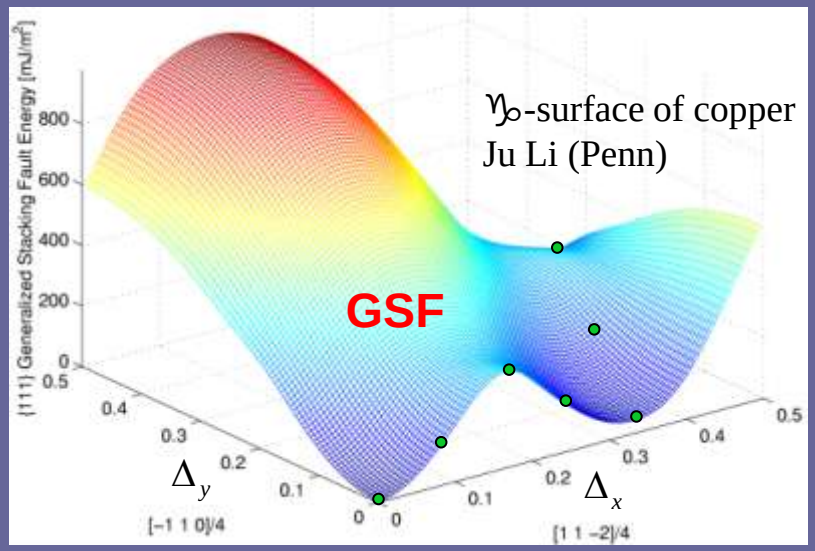

ϒb-surface of copper
Ju Li (Penn)

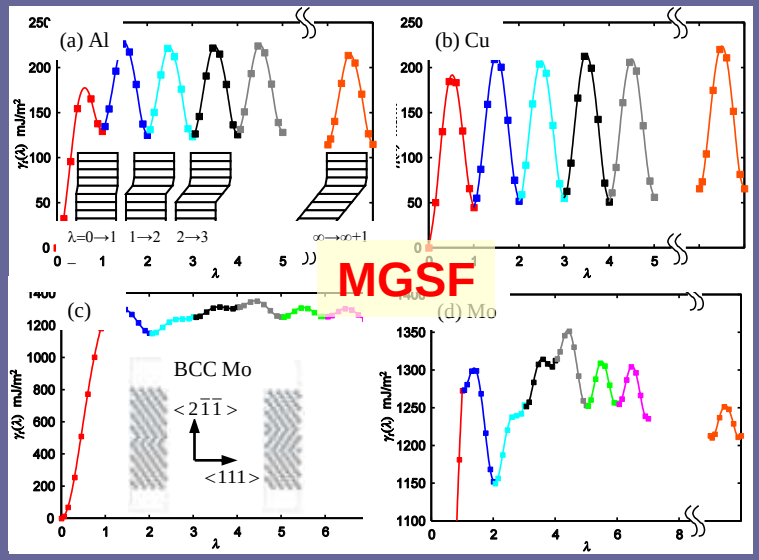

GSF energy for dislocation core structure/energy, peierls stress, nucleation barrier
MGSF energy for twin nucleation and growth

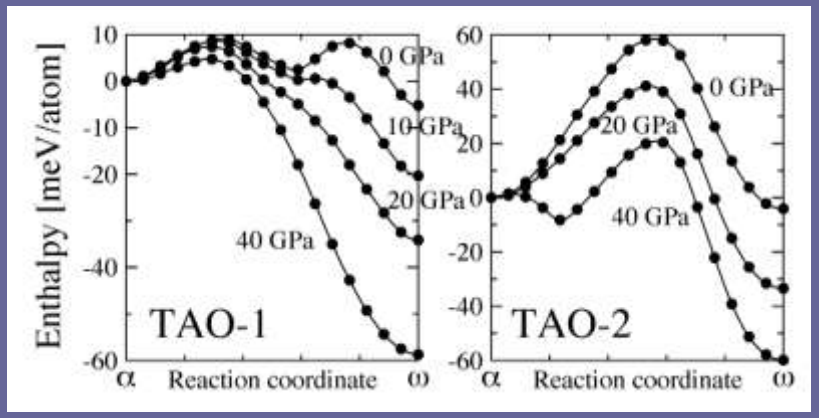

α→ w transformation in Ti

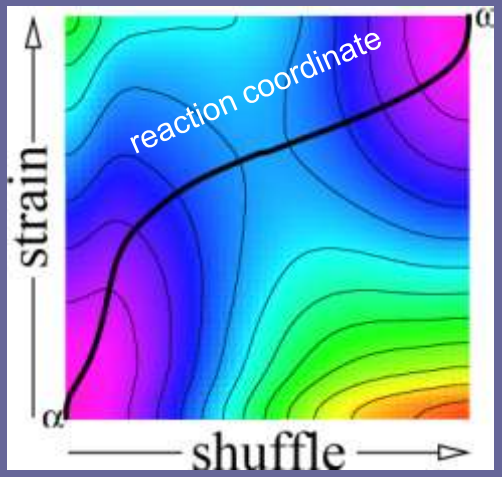

(Trinkle et. al. PRL 2003)

Landau free energy for martensitic transformation - "MGSF" energy for martensite nucleation and growth

Incorporation of activation energy into explicit nucleation algorithm in phase field

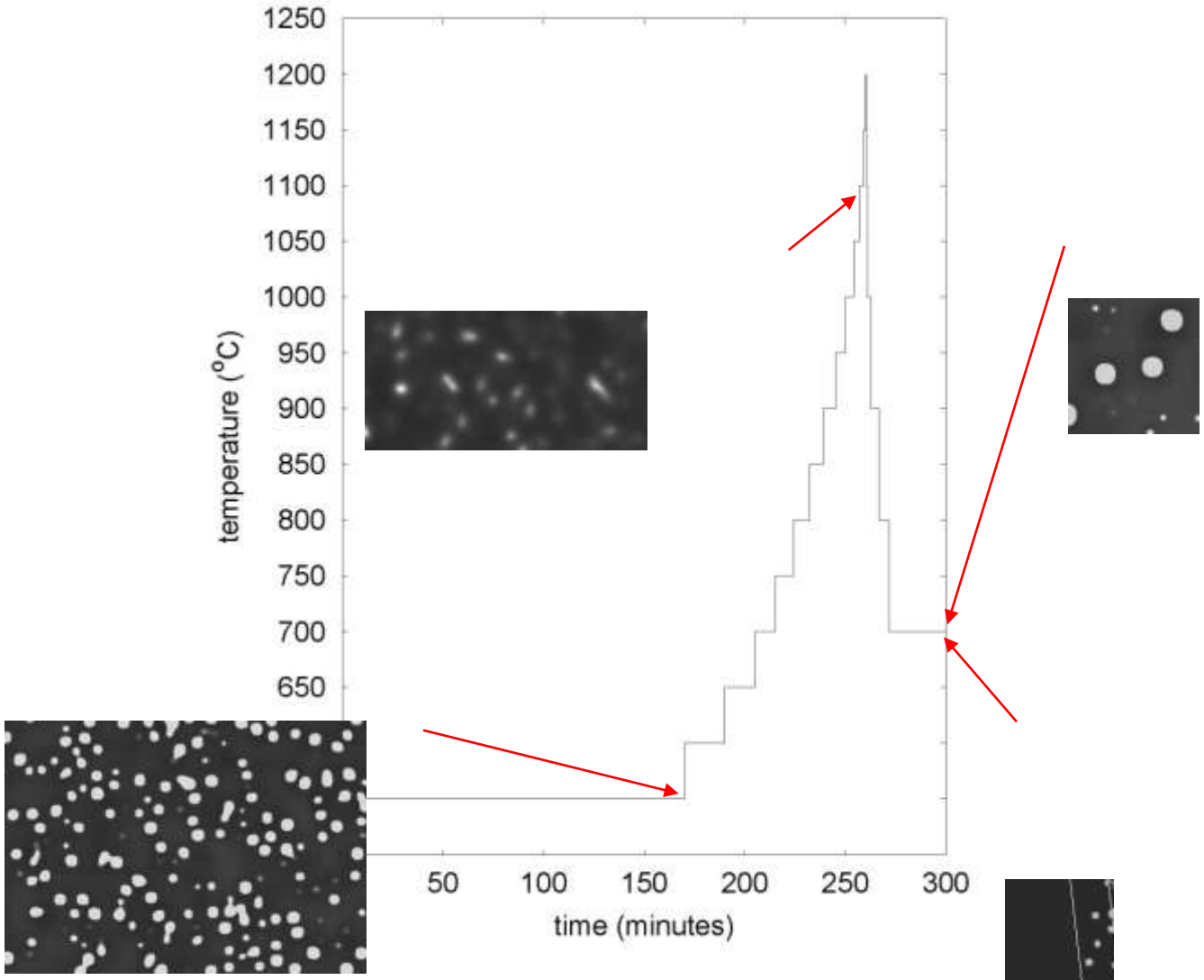

JP.Simmons et. al, *Scripta mater*. 2000; YH. Wen et al. Acta Mater. 2006

Example II. Langevin dynamics
Autocatalytic effect and collective nucleation

- Cubic to tetragonal transformation in 2D: - autocatalytic effect

- Cubic to tetragonal transformation in 3D:
  - collective nucleation
  - autocatalytic effect

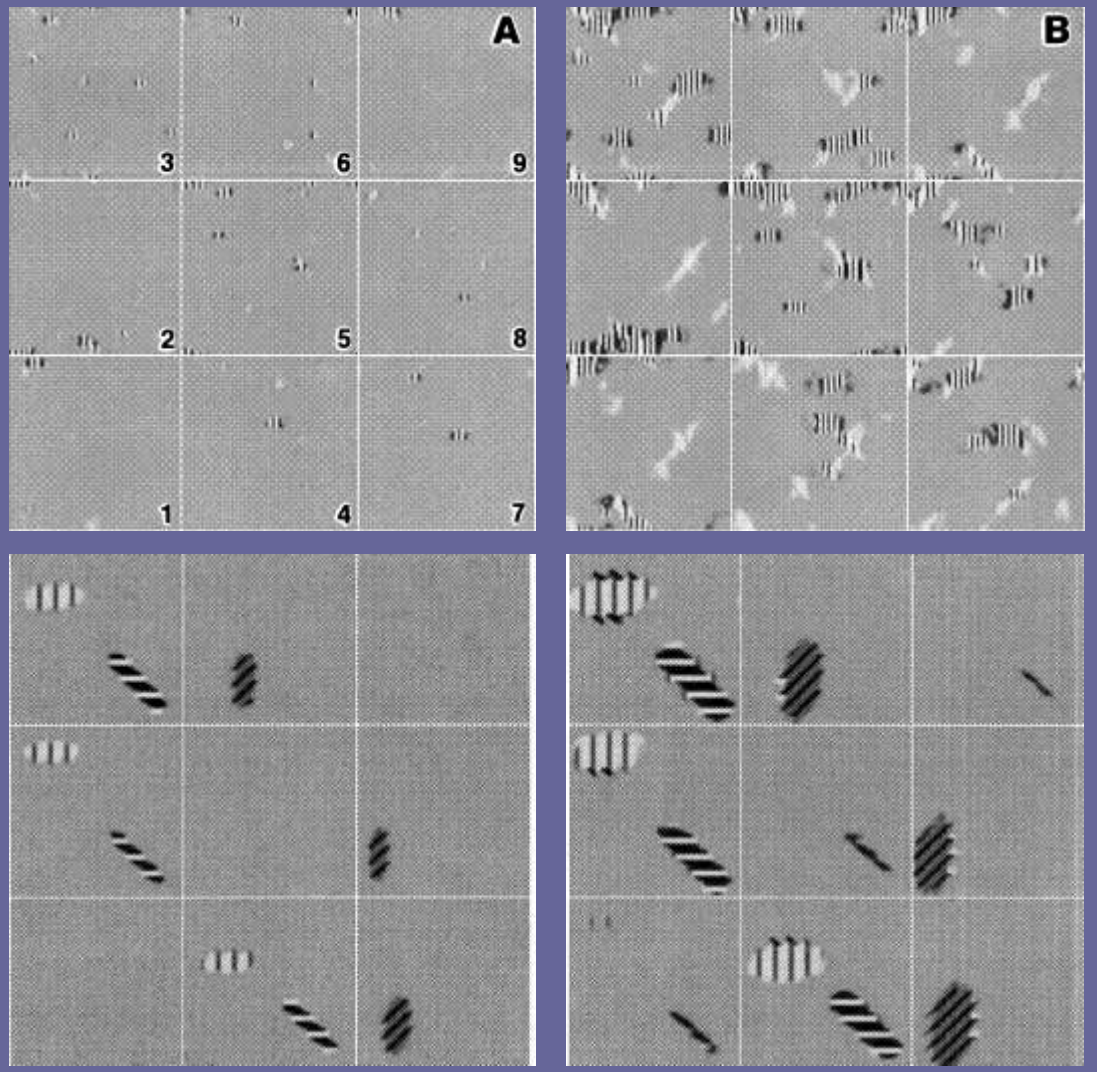

Quantitative Calculation

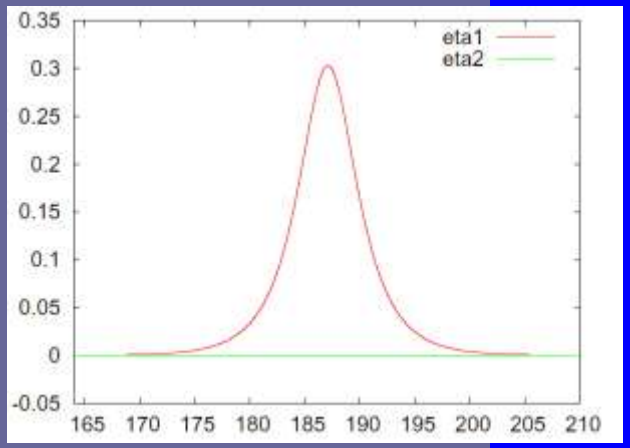

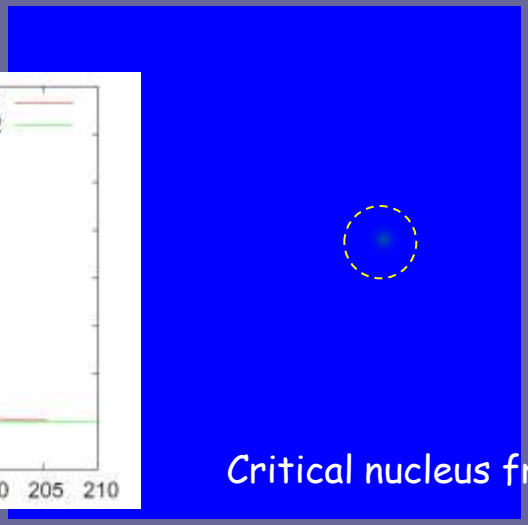

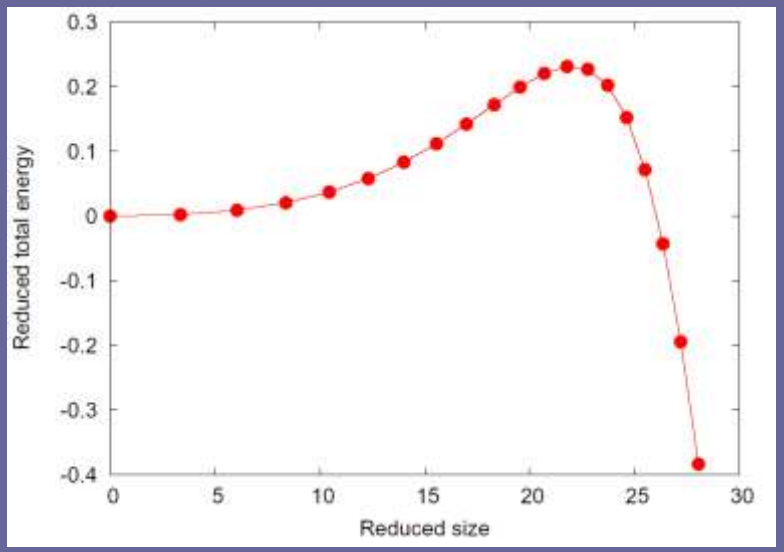

Critical nucleus from Nudged Elastic Band (NEB) calculation

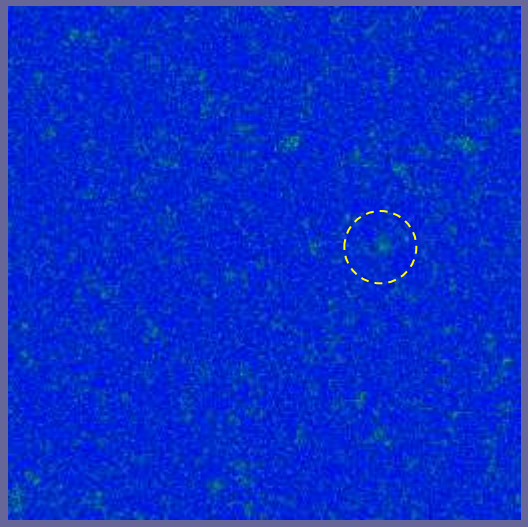

Near critical nucleus from Langevin dynamics

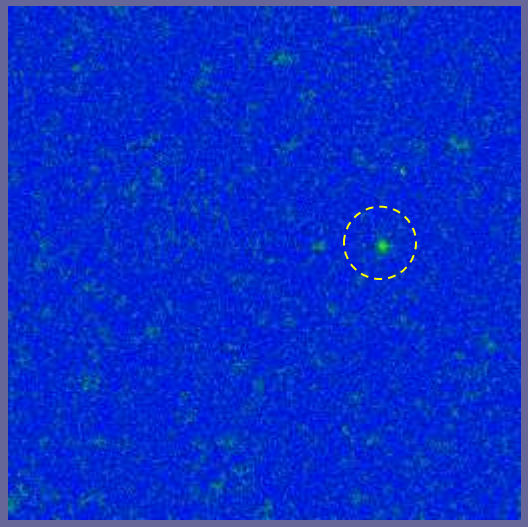

Super critical nucleus from Langevin dynamics

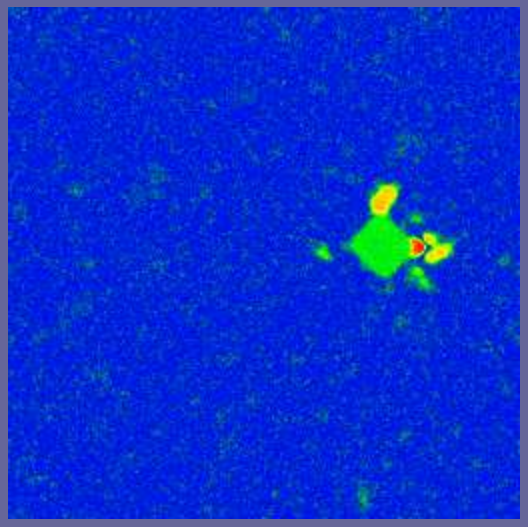

Grownup configuration from Langevin dynamics

Nucleation Movie

Formation of intersecting plates in Ti-64
Autocatalytic effect

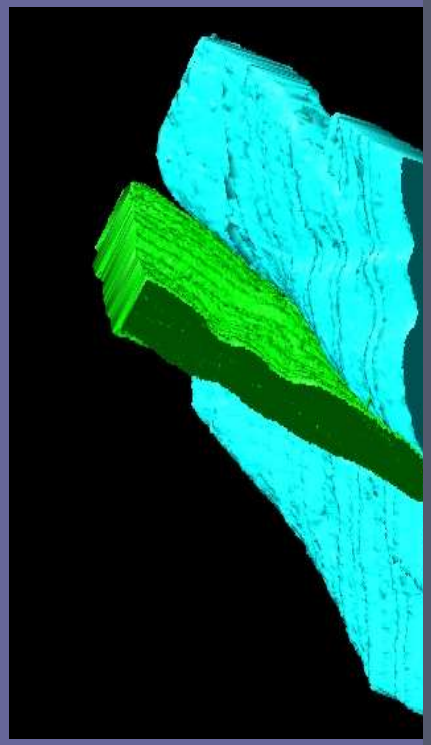

(Courtesy of HF.Fraser)

Movie

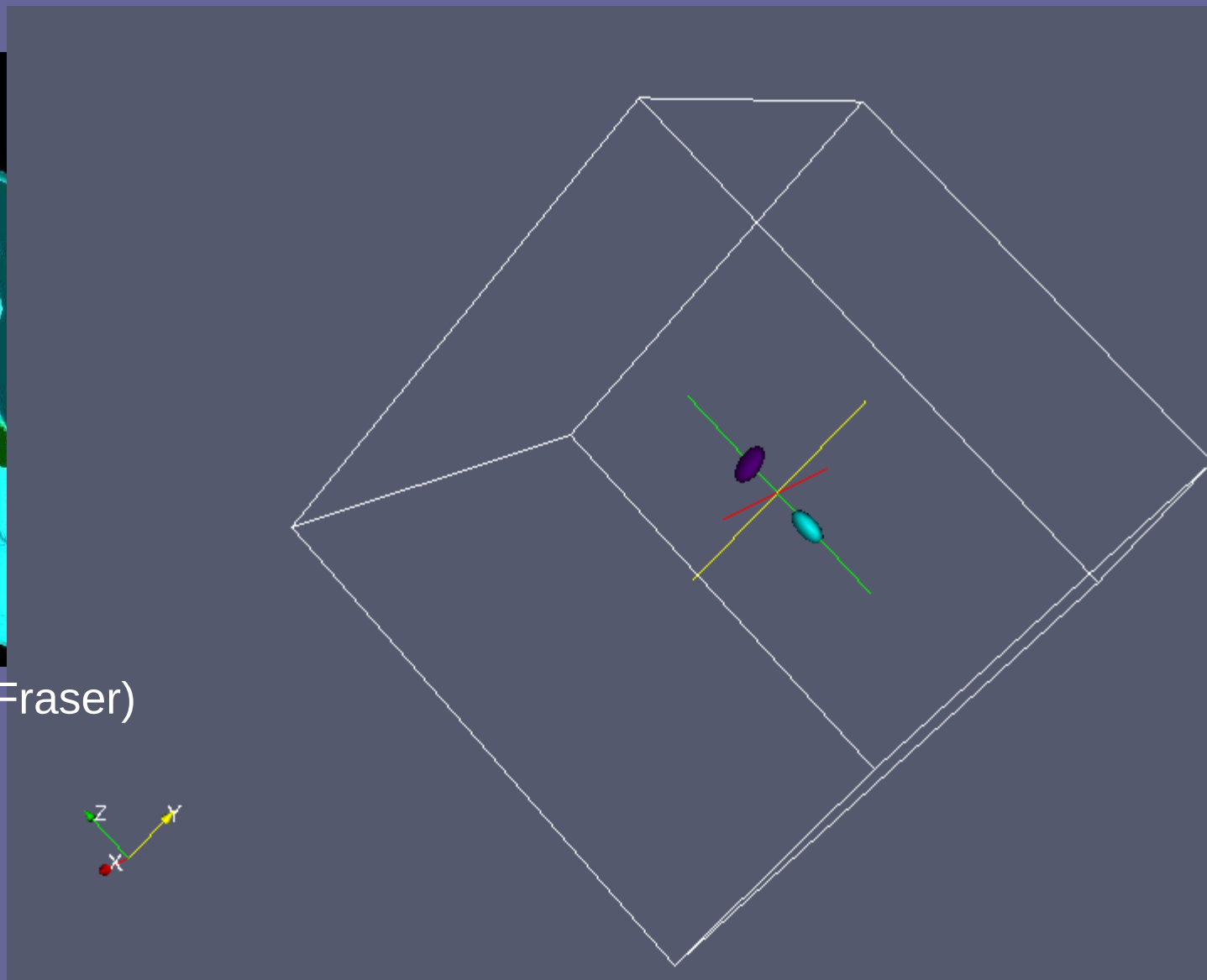

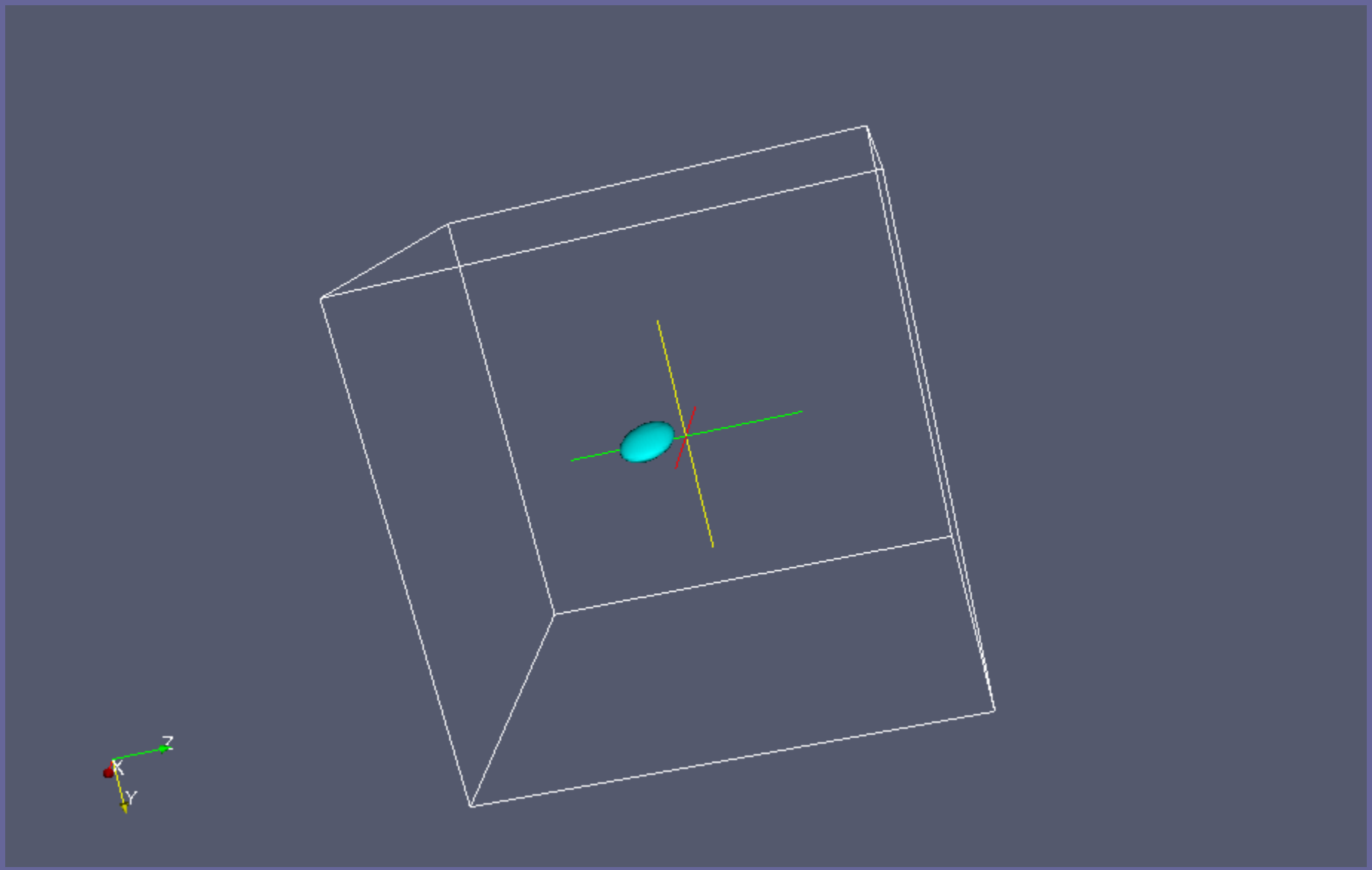
Z
X
Y

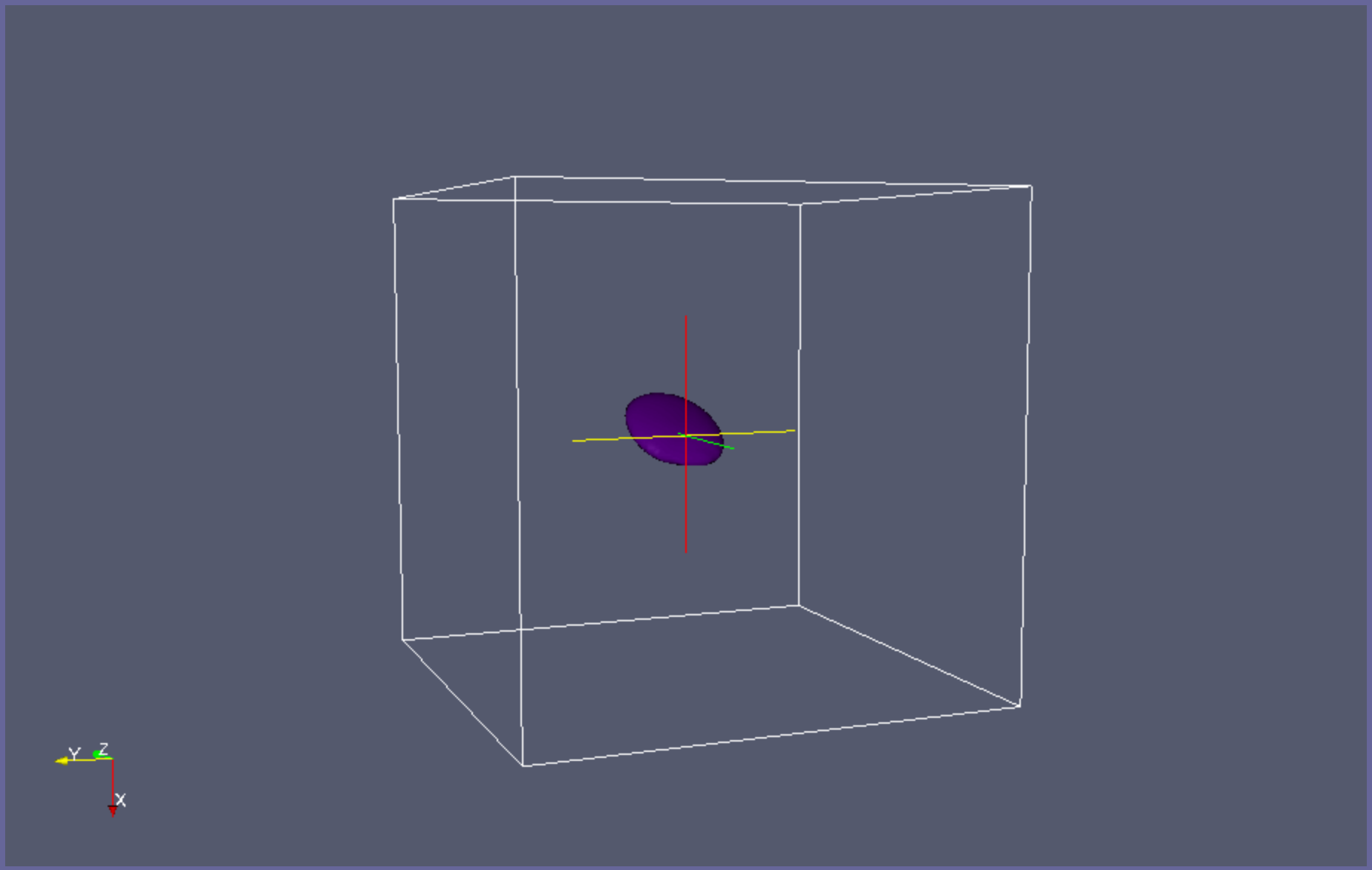
Y
Z
X

Contribution from elastic interaction

Interaction energy contour for variant 9 (- 4×10^7 J/m^3)

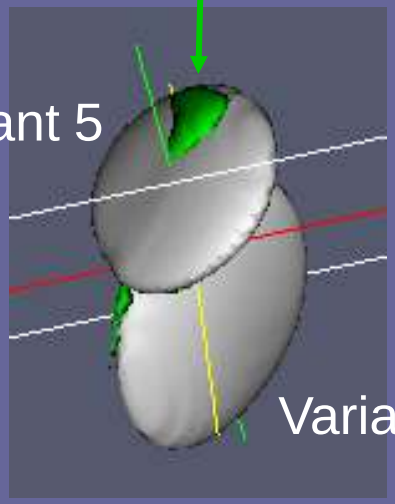

t=2.5s (right before the two plates touch each other)

Typical chemical driving force for nucleation: 4.32×10^7J/m^3, which is comparable to elastic interaction energy

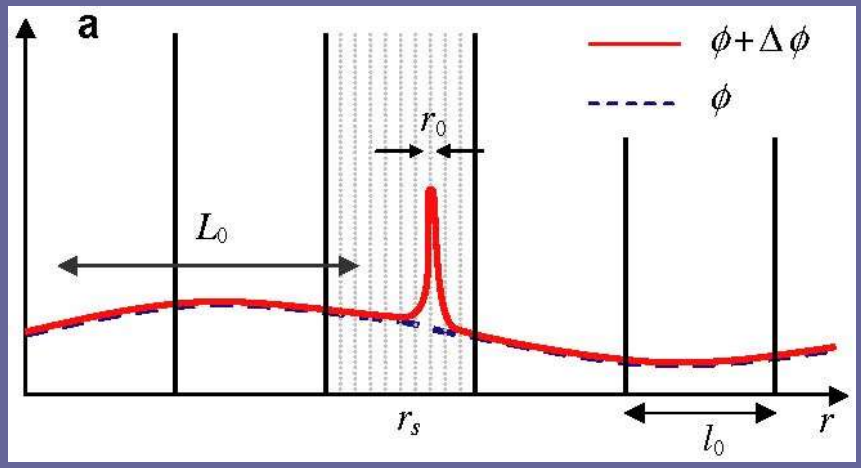

$$\Delta\Omega = -V_0\Delta f^{\mathrm{ch}} + A_0\gamma + \Delta E^{\mathrm{el}}$$

$$\Delta E^{\mathrm{el}} = E^{\mathrm{el},2} - E^{\mathrm{el},1}$$

$$\Delta E^{\mathrm{el}} = \Delta E^{\mathrm{el}}_{\mathrm{int}} + \Delta E^{\mathrm{el}}_{\mathrm{self}}$$

$$\Delta E^{\mathrm{el}}_{\mathrm{int}} = \sum_{p=1}^{N}\sum_{q=1}^{M}\int \frac{\mathbf{dg}}{(2\pi)^3} B'_{pq}(\mathbf{n})\tilde{\phi}_p(\mathbf{g})\Delta\tilde{\phi}^*_q(\mathbf{g})$$

$$\Delta E^{\mathrm{el}}_{\mathrm{self}} = \frac{1}{2}\sum_{p=1}^{M}\sum_{q=1}^{M}\int \frac{\mathbf{dg}}{(2\pi)^3} B'_{pq}(\mathbf{n})\Delta\tilde{\phi}_p(\mathbf{g})\Delta\tilde{\phi}^*_q(\mathbf{g})$$

Shen, Simmons and Wang, Acta Mater (2006), ibid, (2007).

Example III. Semi-quantitative calculations
a) Variant Selection: motivation

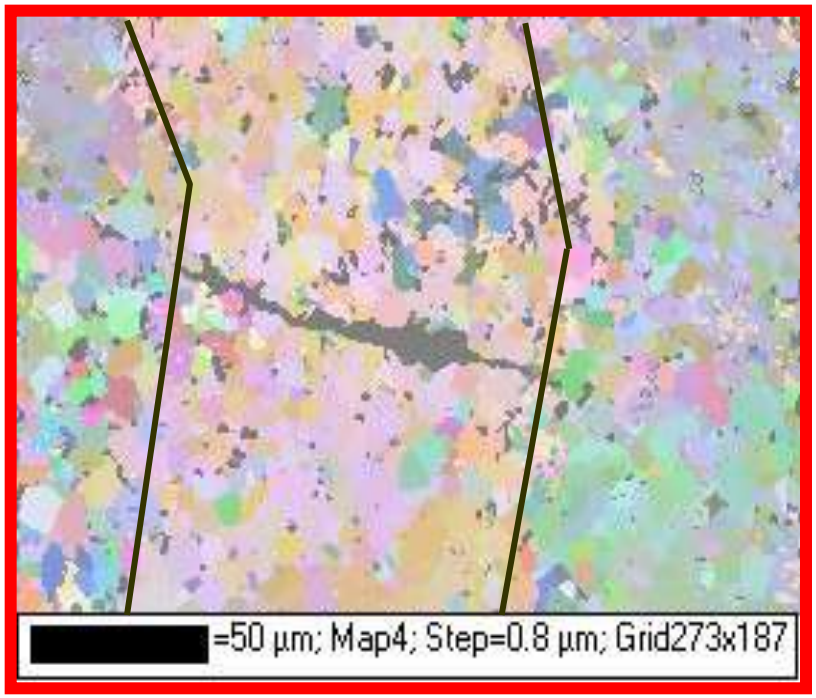

Fatigue crack growth in OIM image α/β forged Ti-6242 alloy in compressor rotor

JC. Williams and S. Ghosh (OSU)

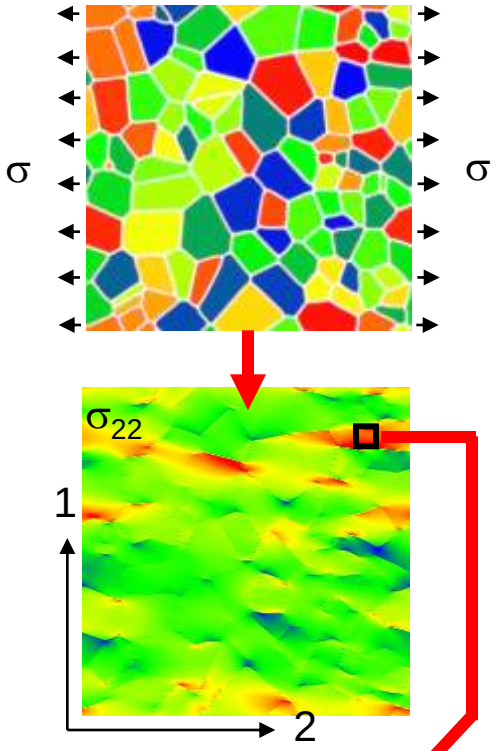

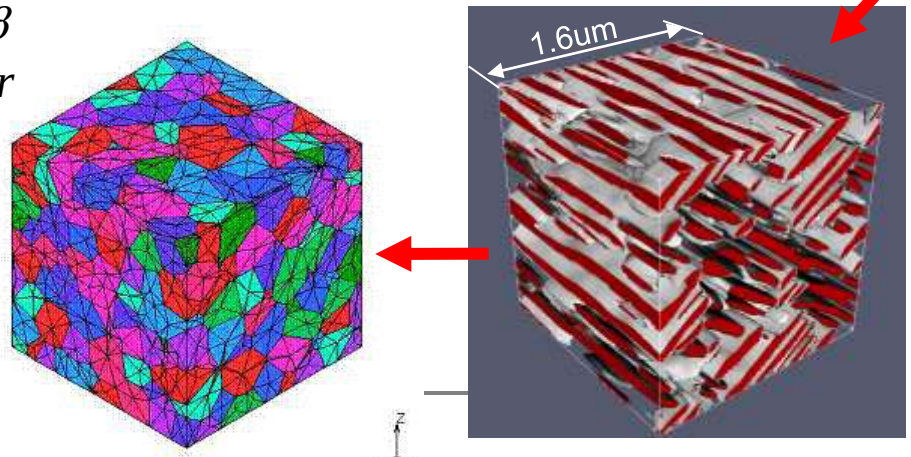

Challenges

- Interaction of local stress with elastically anisotropic polycrystalline microstructure

- Interaction of local stress with precipitation of coherent/semi-coherent α-phase particles

Interaction of local stress with evolving microstructures

{111}<110> γ-fiber Texture

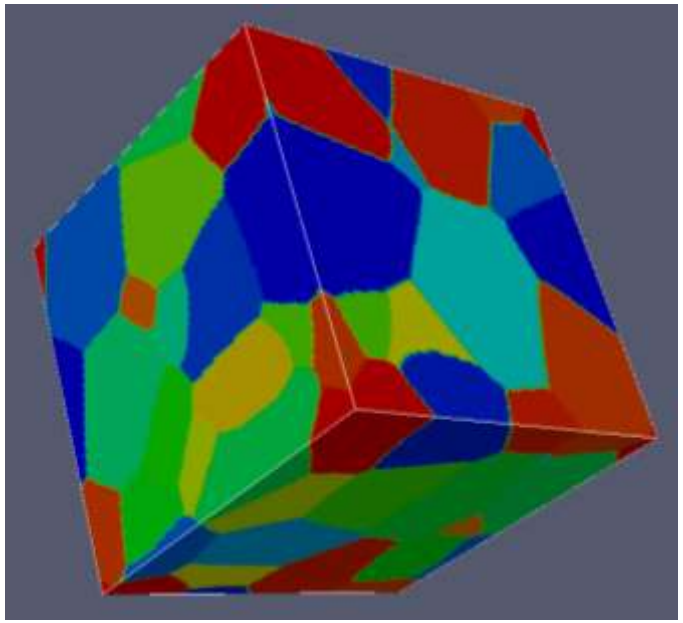

(a)

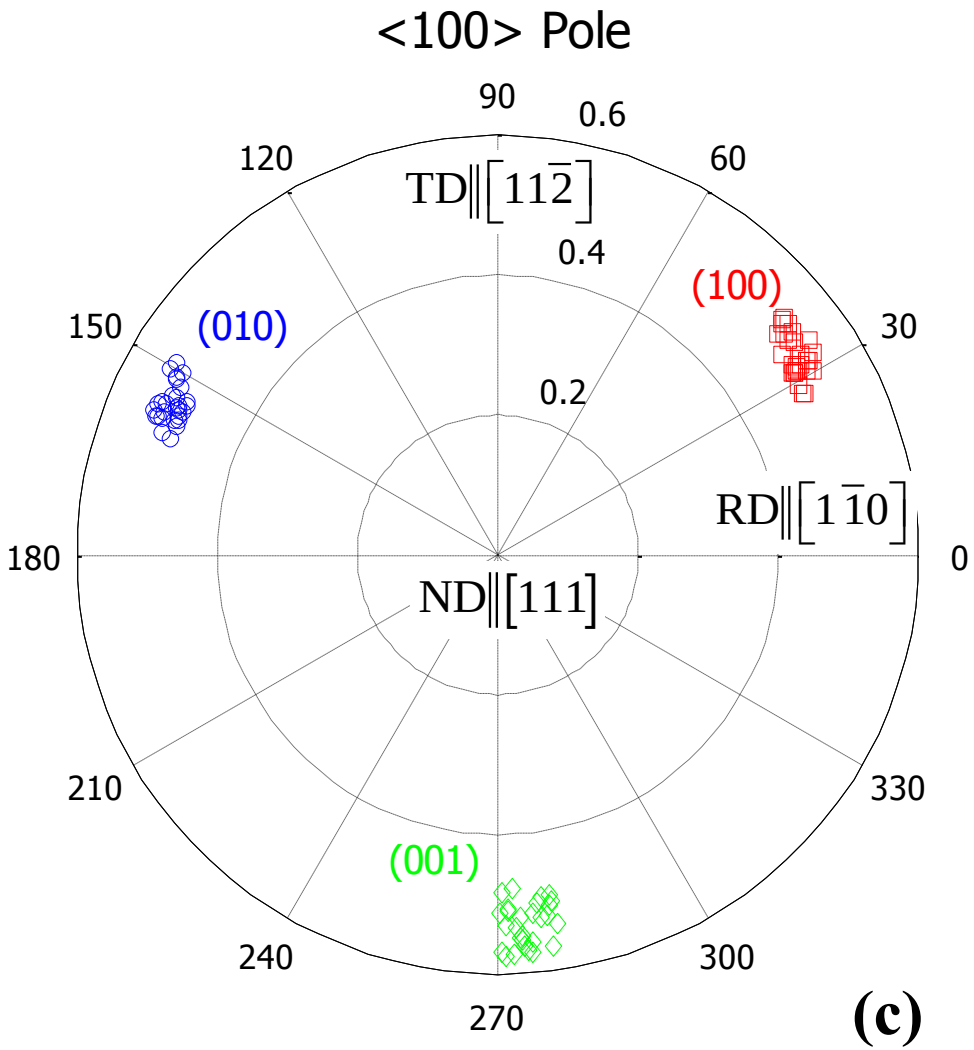

(c)

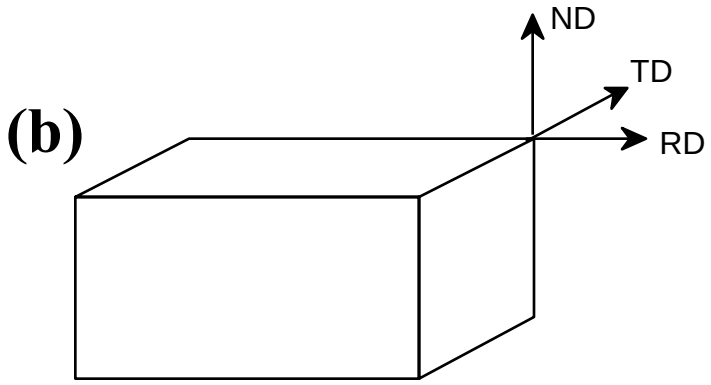

(b)

Stress Distribution

Applied stress: 98 MPa tensile along ND

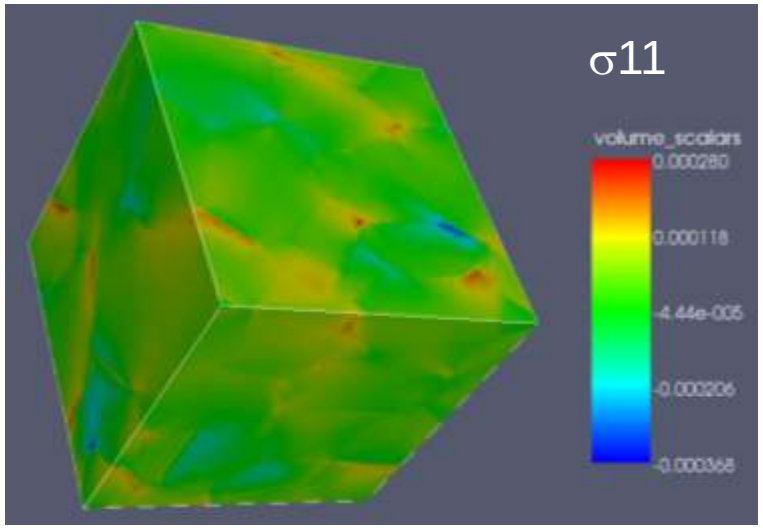

Max (Red) 28.0 MPa
Min (Blue) -35.4 MPa

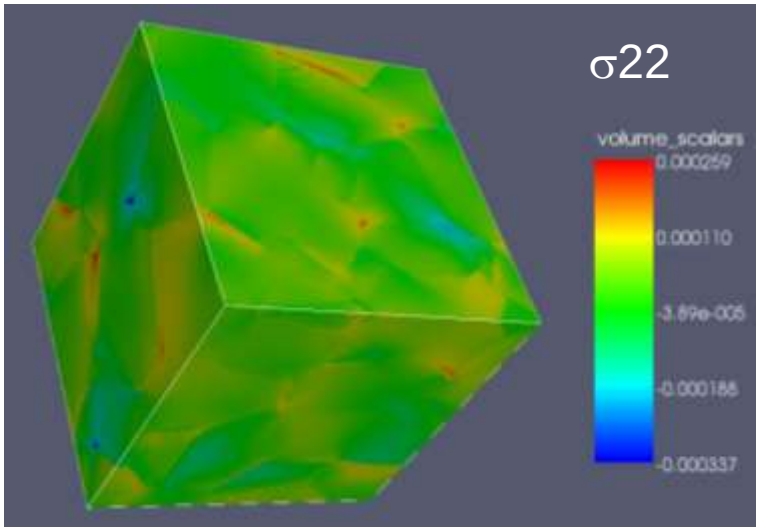

Max (Red) 28.3 MPa
Min (Blue) -35.1 MPa

Stress distribution in the polycrystalline sample under 98 MPa tension along ND.

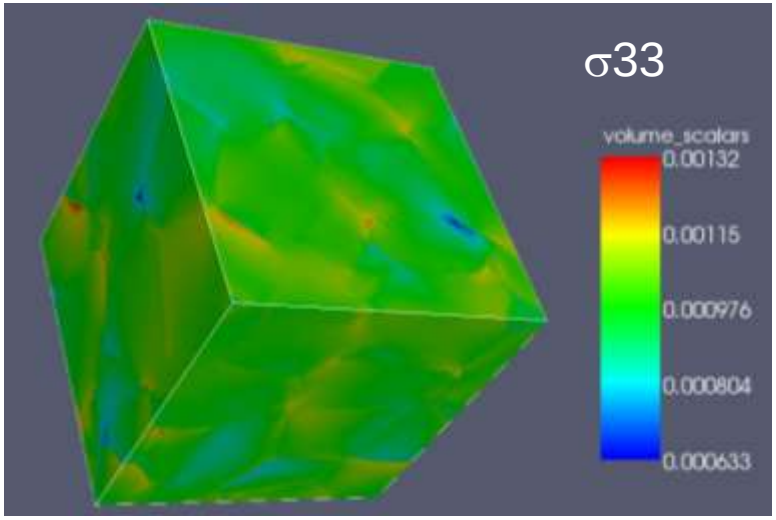

Max (Red) 132.0 MPa
Min (Blue) 62.6 MPa

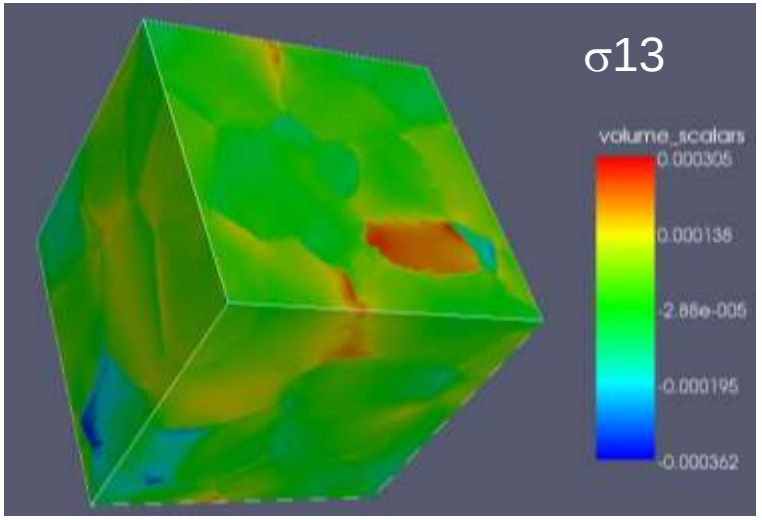

Max (Red) 29.0 MPa
Min (Blue) -34.8 MPa

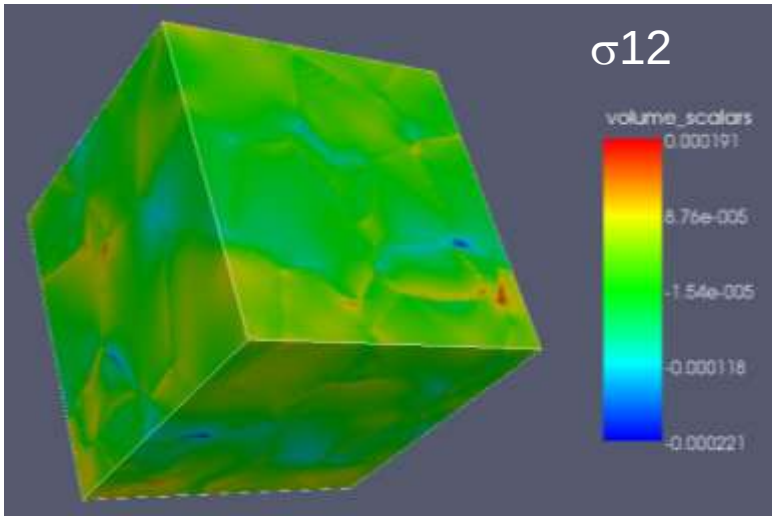

Max (Red) 18.9 MPa
Min (Blue) -20.7 MPa

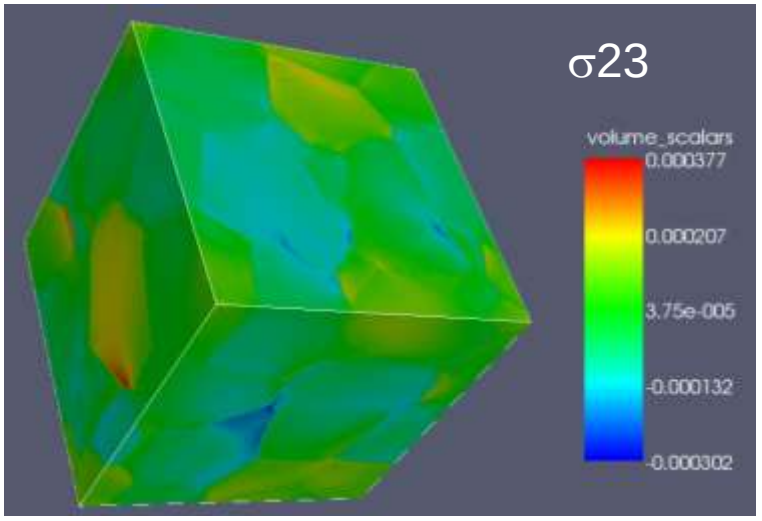

Max (Red) 38.4 MPa
Min (Blue) -29.6 MPa

BCC → HCP Transformation Mechanism

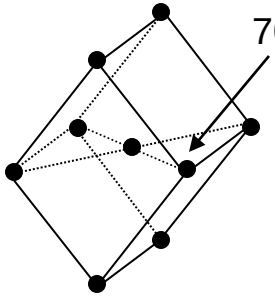

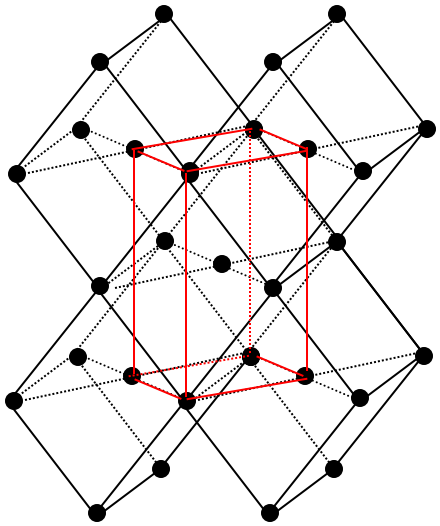

shear

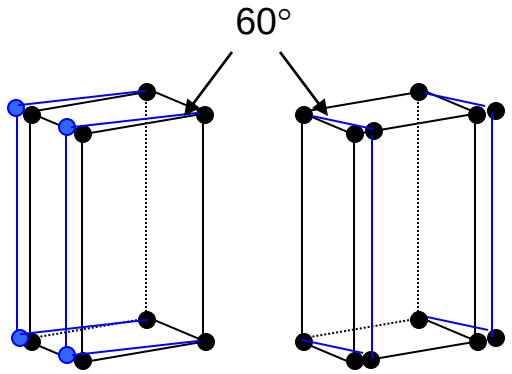

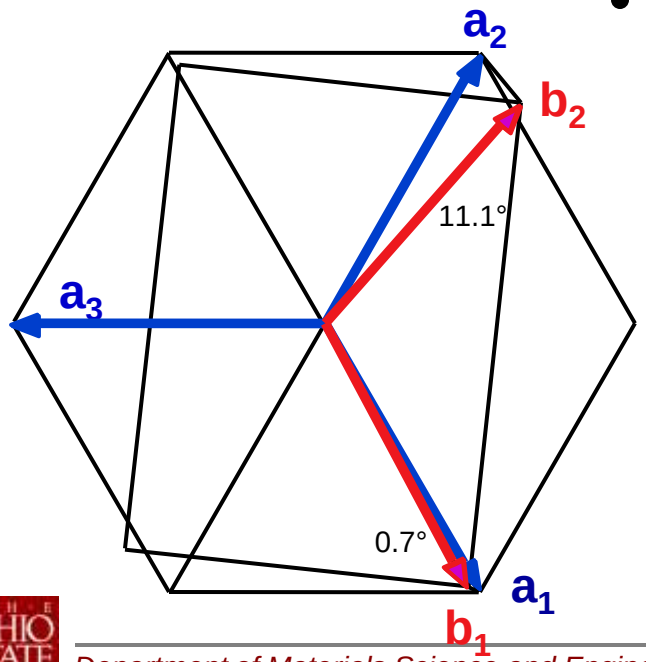

$$(101)_\beta \parallel (0001)_\alpha$$
$$[1\bar{1}\,\bar{1}]_\beta \parallel [2\bar{1}\,\bar{1}0]_\alpha$$

Burgers

$$\varepsilon = \begin{bmatrix} -0.117 & -2.65\times10^{-3} & \\ -2.65\times10^{-3} & 0.109 & \\ & & 0.035 \end{bmatrix}$$

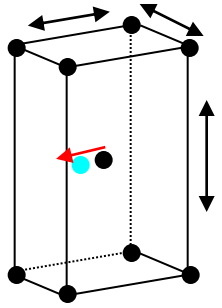

shuffle

W. G Burgers, Physica 1, 561 (1934)

Interface Dislocation Structure

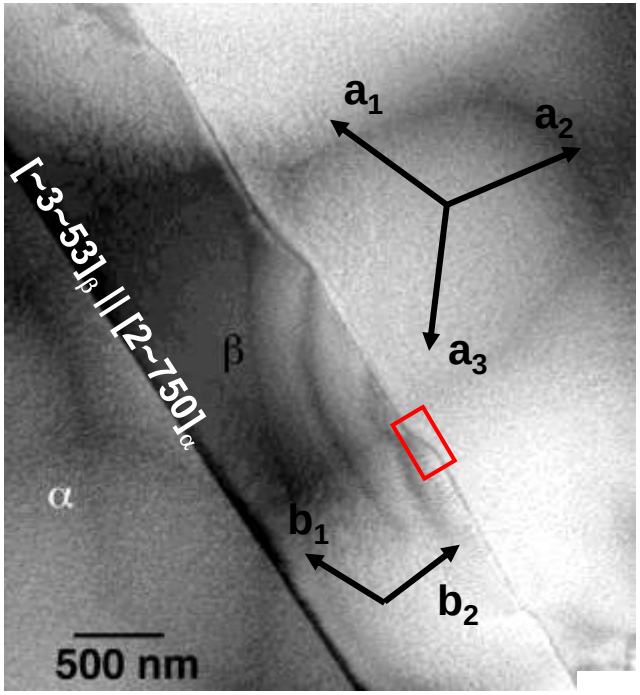

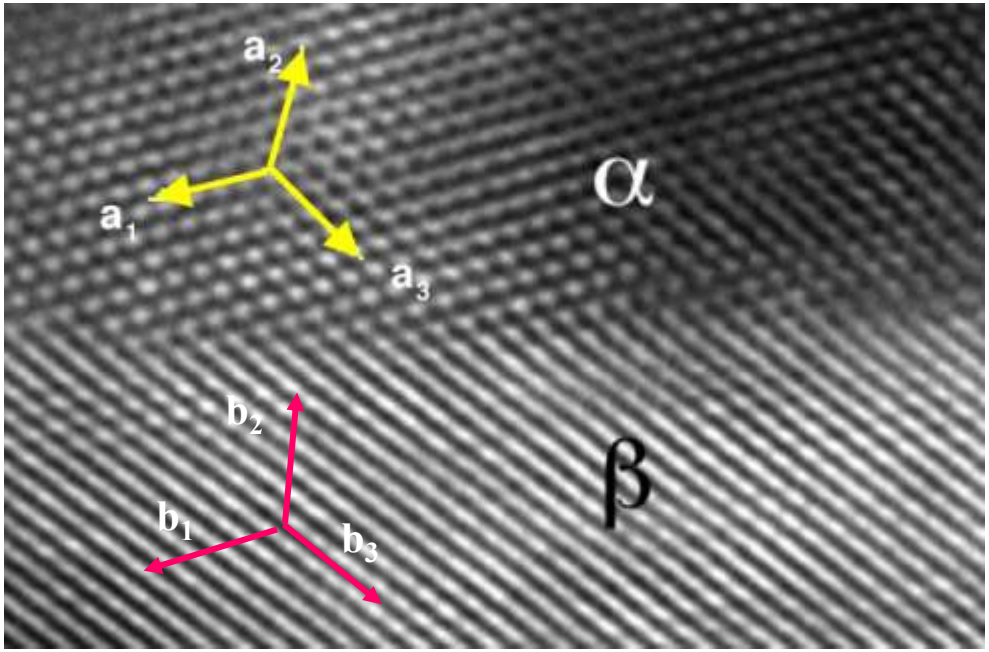

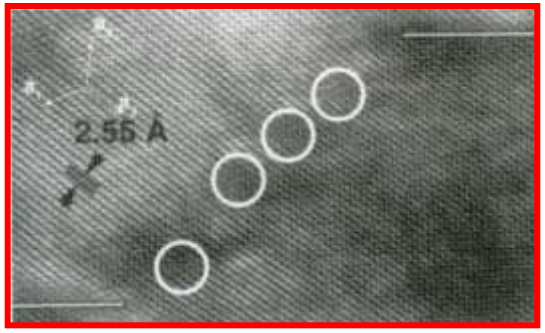

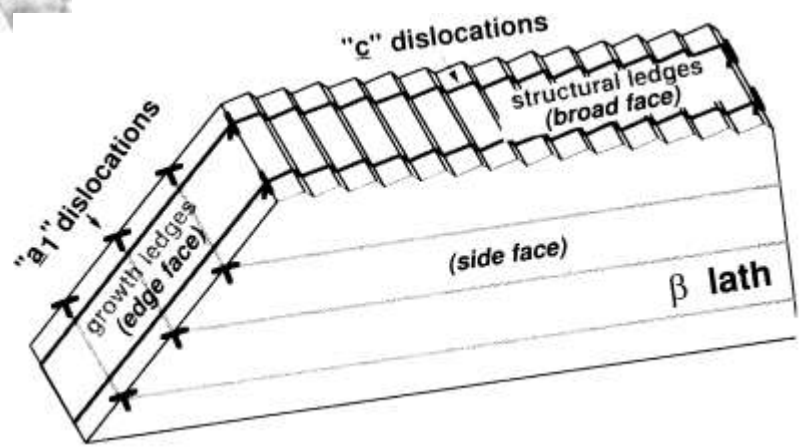

M. Savage and
M.J. Mills (OSU)

$[-11\ -13\ 11]_\beta$

$[-7250]_\alpha // [-353]_\beta$

$[0001]_\alpha // [101]_\beta$

Interfacial dislocation structure is important for both elastic energy and interfacial energy calculations

SFTS Calculation of Semi-coherent β Lath

1. dislocation-free (coherent)

$$F^0 = \begin{pmatrix} \frac{a_\alpha}{a_\beta} & & \\ & \frac{\sqrt{3}a_\alpha}{\sqrt{2}a_\beta} & \\ & & \frac{c}{\sqrt{2}a_\beta} \end{pmatrix} = \begin{pmatrix} 0.9208 & & \\ & 1.128 & \\ & & 1.0354 \end{pmatrix}$$

2. Displacement due to c-dislocations

$$F^c = \frac{-1}{30}\begin{pmatrix} 0 & & \\ & 0 & \\ & & 1 \end{pmatrix} + I = \begin{pmatrix} 1 & & \\ & 1 & \\ & & 0.9655 \end{pmatrix}$$

3. Shear accommodation due to a-dislocations

$$F^a = R\begin{pmatrix} 1 & -0.119 & \\ & 1 & \\ & & 1 \end{pmatrix}R^T = \begin{pmatrix} 1.078 & -0.055 & \\ 0.11 & 0.922 & \\ & & 1 \end{pmatrix}$$

a-dislocations (1 every 7) & [100] dislocations (1 every 25) on side face

a_1=1/3[-2110], b_1=1/2[-111]

c-dislocations (1 every 30 atomic planes) on broad face

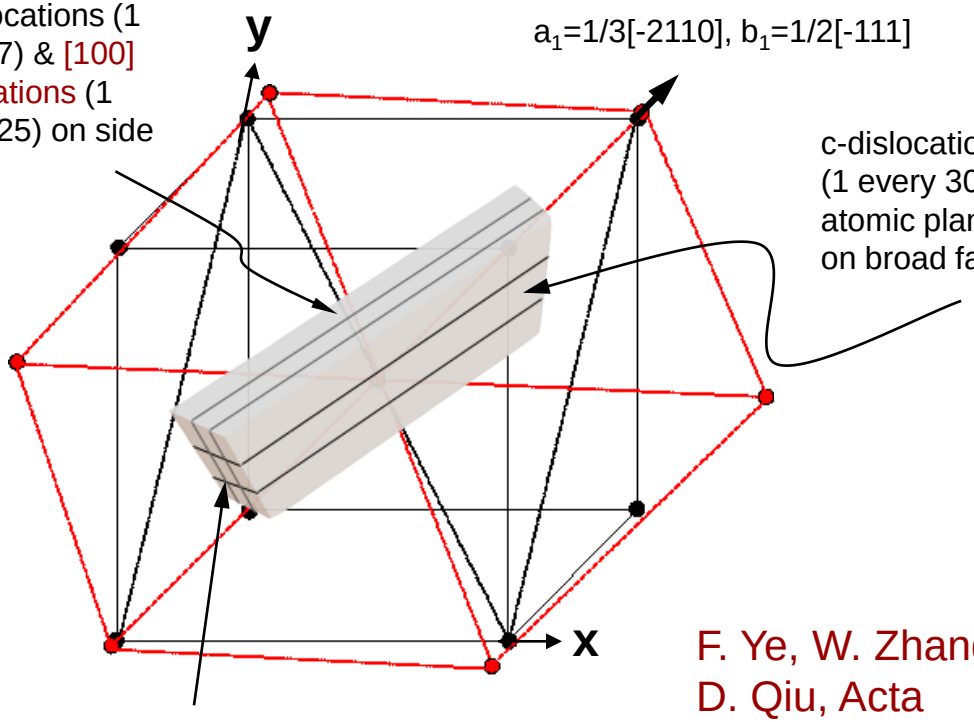

F. Ye, W. Zhang, D. Qiu, Acta Materialia, 54 (2006) 5377

4. Contribution due to [100] dislocation

$$F^{100} = \begin{pmatrix} 0.968 & -0.023 & \\ 0 & 1 & \\ & & 1 \end{pmatrix}$$

$$F_T = F^{100}F^aF^cF^0$$

5. Effective (semi-coherent) SFTS

$$\varepsilon = \frac{1}{2}\left(F_tF_t^T - I\right) = \begin{pmatrix} -0.049 & 0.023 & \\ 0.023 & 0.035 & \\ & & -2.998\times10^{-4} \end{pmatrix}$$

Interaction Energy $-\sigma_{ij}^{residual}\varepsilon_{ij}^{00}(p)$

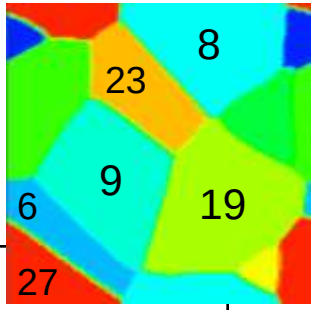

Grain ID / Variants	27	8	23	19	9	6
1	2.71259	0.89903	2.02104	2.08184	1.48684	1.01869
2	1.87571	0.88838	0.68961	1.37163	0.86486	0.37968
3	-0.64215	-0.06734	0.48023	-0.40484	0.17415	-0.02657
4	**2.90566**	**3.41058**	**4.01198**	**2.98381**	**3.2216**	**3.3507**
5	**-4.49931**	**-4.37091**	**-4.31057**	**-4.33573**	**-4.6636**	**-4.19092**
6	-1.11021	-1.08432	-0.90188	-1.10179	-1.75509	-0.9656
7	-0.66386	-2.39349	-1.35711	-1.14161	-1.41214	-2.19502
8	-1.03616	-2.62202	-1.56813	-1.46694	-1.68414	-2.40823
9	-0.98321	-0.28969	0.30907	-0.70342	-0.07474	-0.21775
10	**2.10003**	**3.40611**	**2.72041**	**2.30036**	**2.62273**	**2.73372**
11	-1.9285	-1.08286	-2.22398	-1.79573	-2.3635	-1.5942
12	**-4.8277**	**-4.5992**	**-4.4512**	**-4.62381**	**-4.90296**	**-4.3705**

Variant 5 and 12 are strongly favored by the applied stress

Variant 4 and 10 are strongly un-favored by the applied stress

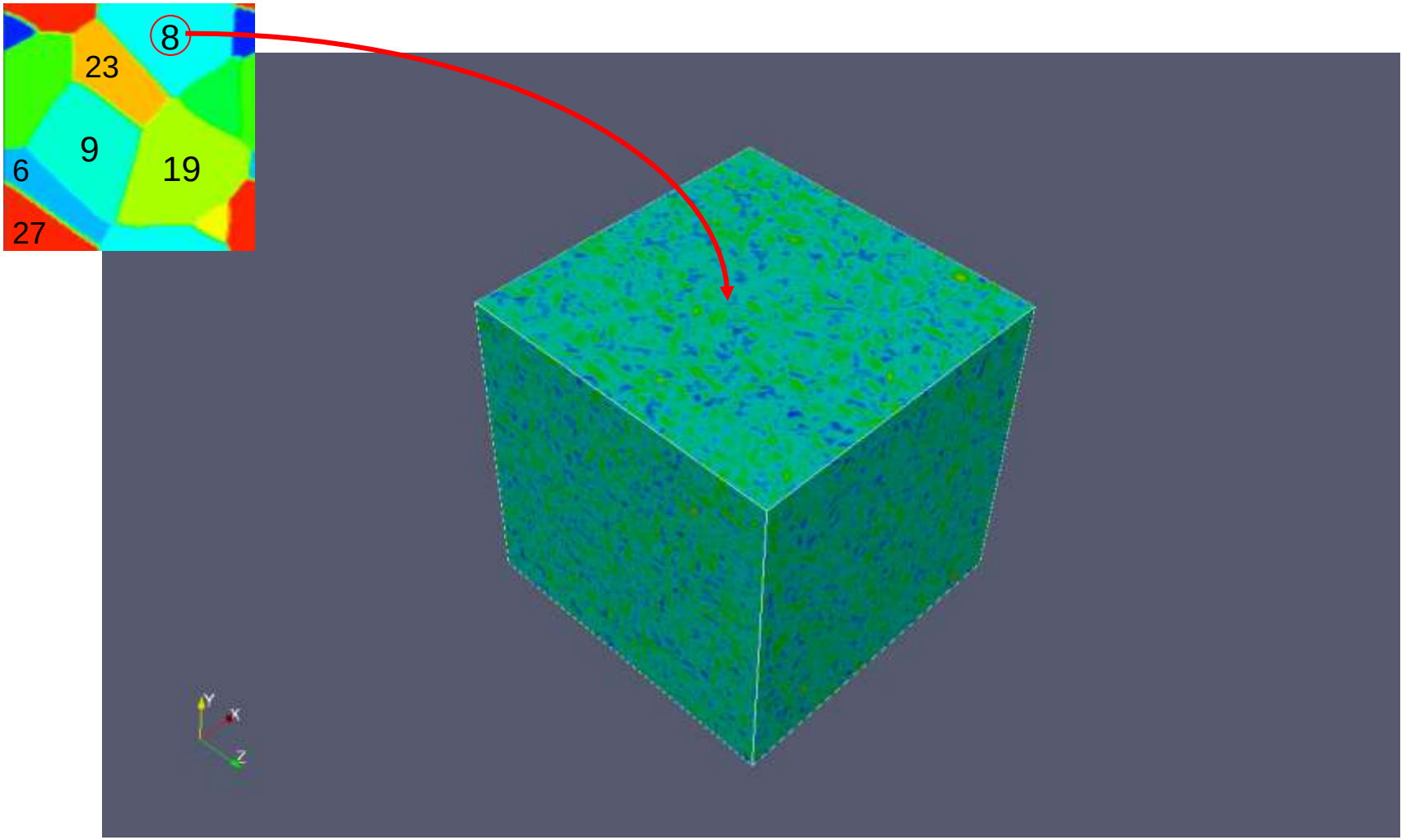

Ti-6Al-4V system: temperature=1073K, system size=6.4μm^3, interfacial energy anisotropy = 3:2:1 (edge:side:broad) with interfacial energy of edge face = 500mJ/m^2, total simulation time = 2.5s, volume fraction of α-phase = 0.4 and the equilibrium volume fraction is 0.86.

Variant Distribution

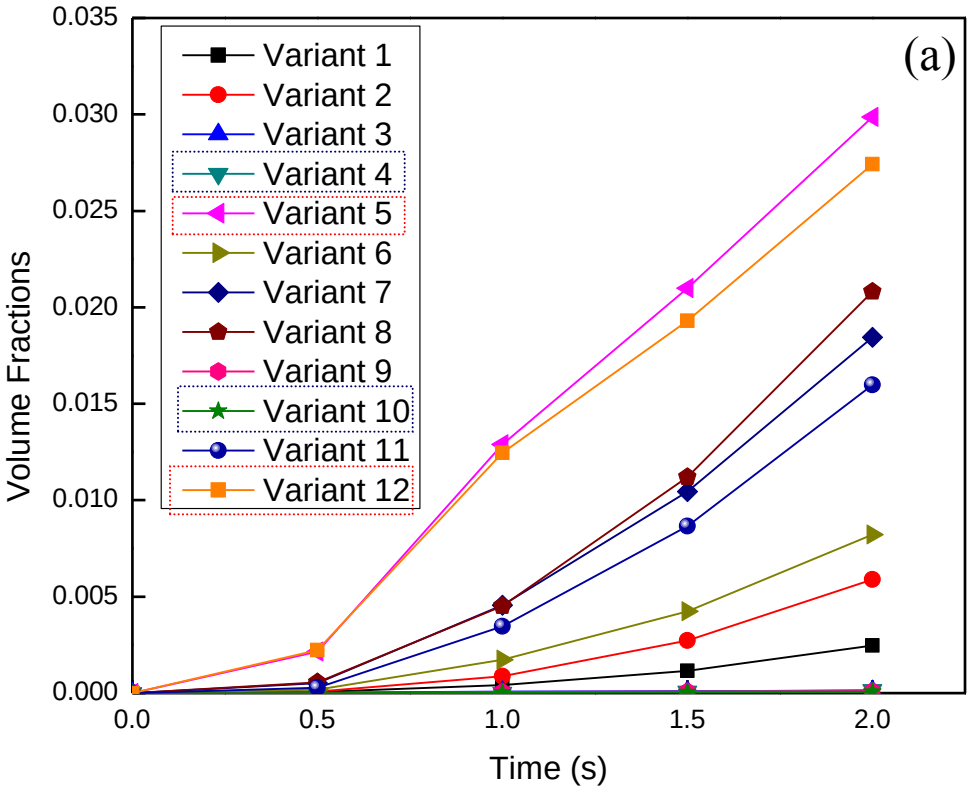

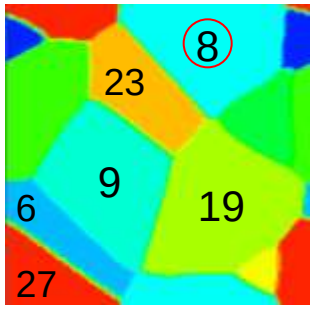

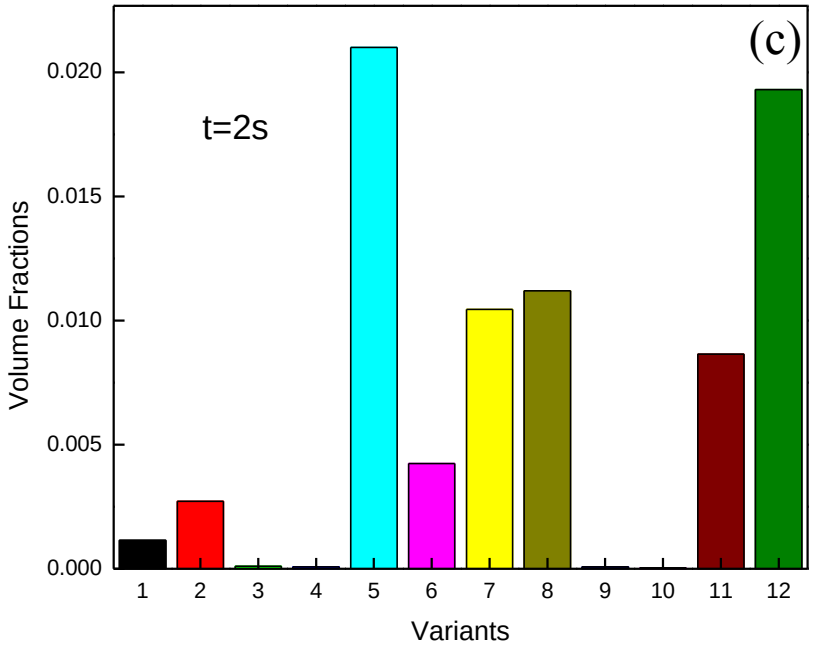

(a) Time evolution of different orientation variants during β → α transformation in Grain #8 (indicated in (b)). (c) Volume fraction of different variants at t = 2s.

Example III. Semi-quantitative calculations
b) nucleation at GB: motivation

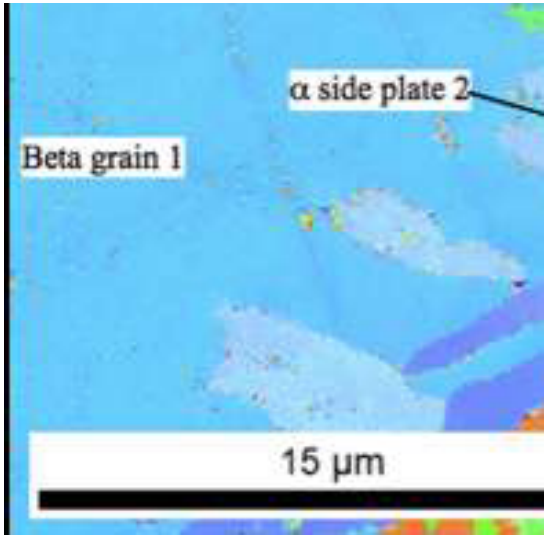

(courtesy of Hamish Fraser)

Fig. 1. An OIM Inverse pole figure map showing beta grains with grain boundary α and α sideplates

Heterogeneous nucleation at grain boundary

	No elastic Energy	HP//GB plane	HP ⊥ GB plane	45 degree
Habit plane and grain boundary plane orientation relationship		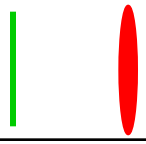		
Critical nucleus	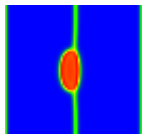	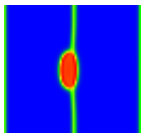	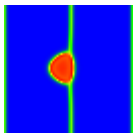	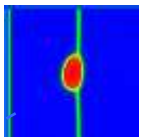
ΔG*	**13.633 K_BT**	**16.759 K_BT**	**16.090 K_BT**	**16.195 K_BT**

Grain boundary energy: 250mJ/m^2

Coherent interfacial energy: 121mJ/m^2

Incoherent interfacial energy: 319mJ/m^2

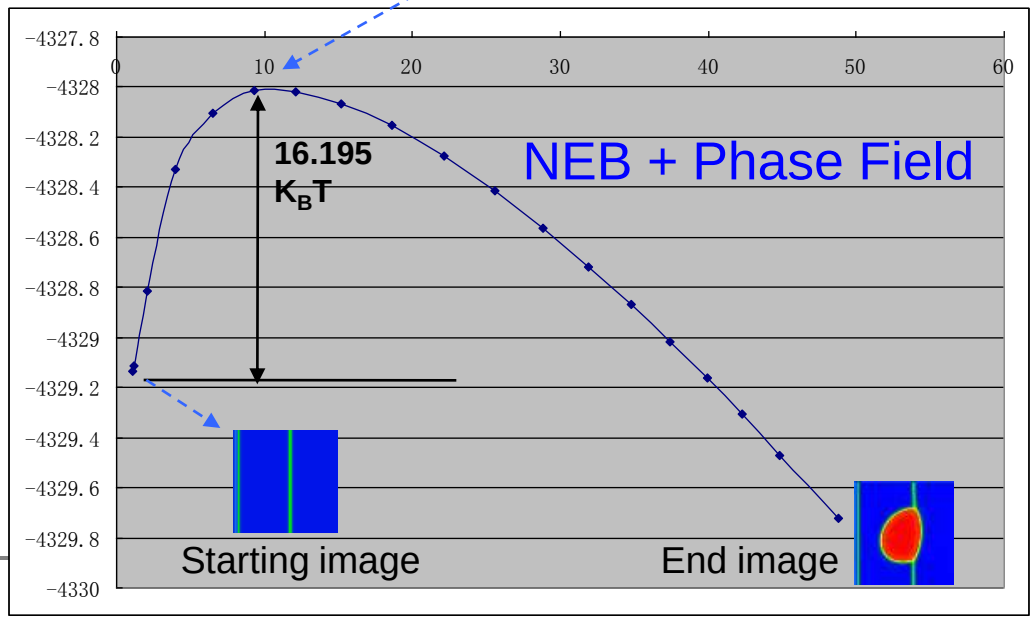

Summary

Phase field approach could be applied at several levels to develop fundamental understanding of nucleation behavior during solid state processes:

- At a **qualitative** level the Langevin dynamics could be applied to study effect of arbitrary chemical and structural non-uniformity in existing microstructure on nucleation. The examples given showed stress-induced collective and correlated nucleation, as well as autocatalytic effect. In particular, spatial distribution of different variants of the α phase was shown to correlate strongly with stress distribution in a polycrystalline sample. Under certain conditions, certain α variants may percolate through the entire sample.
- At a **semi-quantitative level**, the interaction energy calculation allows for systematic investigation of effect of stress fields associated with arbitrary existing microstructure on nucleation
- At **a quantitative level** the microscopic phase field model (in combination with NEB technique) could be applied to characterize activation energy and critical nucleus configuration. But this is energetic only. Need to put the activation energy into the framework of classical nucleation theory to predict nucleation (see next page for details)

THE OHIO STATE UNIVERSITY

Early Nucleation – Lessons Learned from the World of Semiconductors

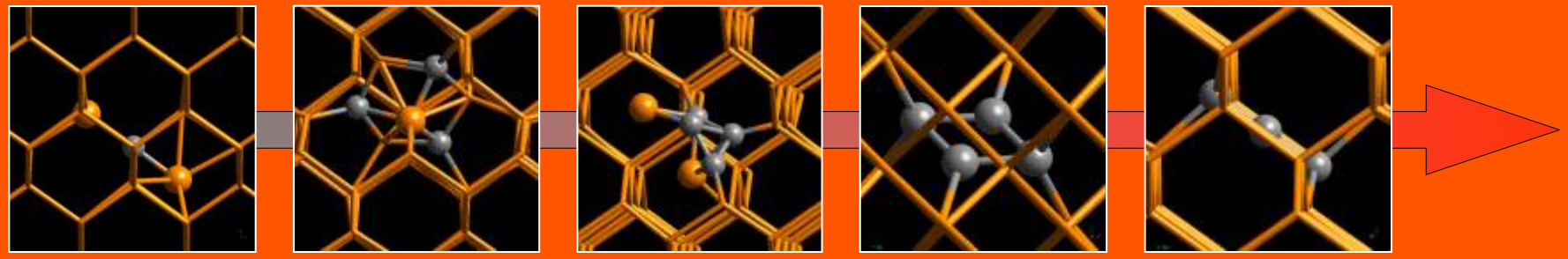

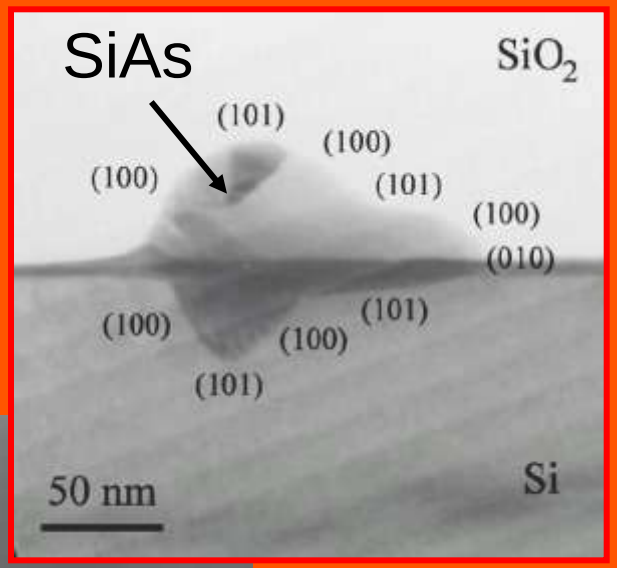

Wolfgang Windl

The Ohio State University

Columbus, OH, USA

Semiconductor Devices – MOSFET

Metal Oxide Semiconductor Field Effect Transistor

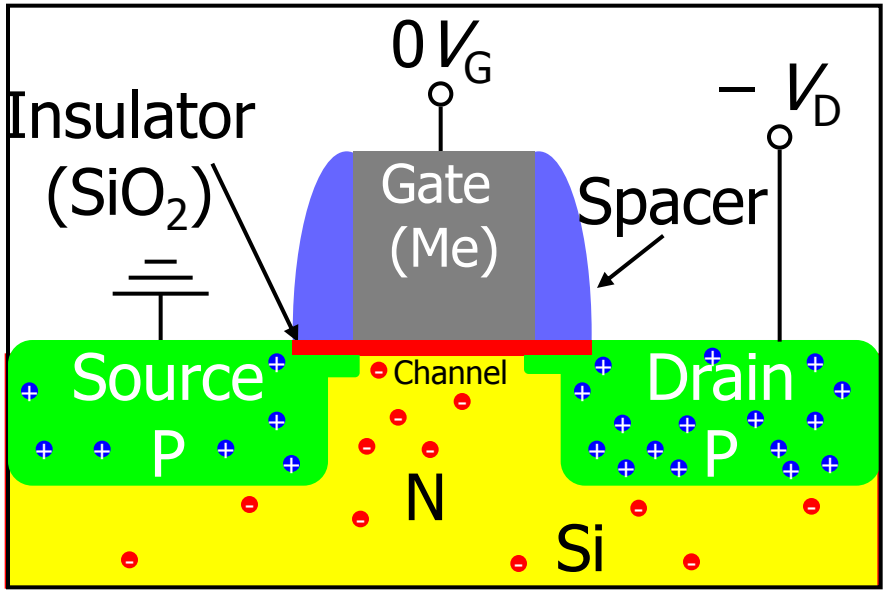

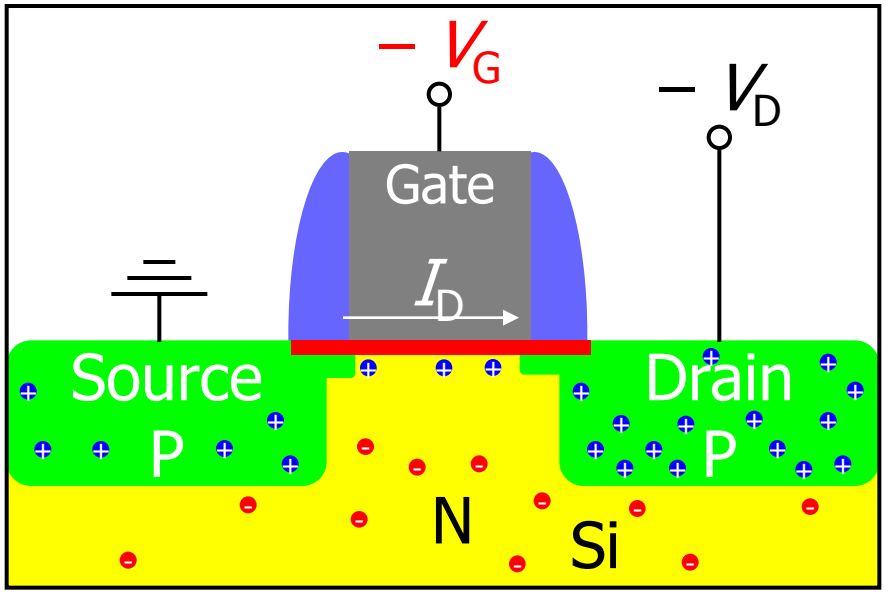

Doping:

N: e^-, e.g. As (Donor)

P: holes, e.g. B (Acceptor)

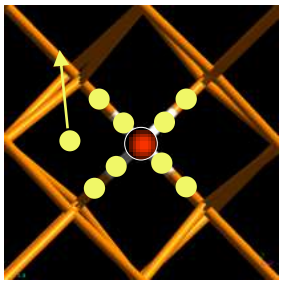

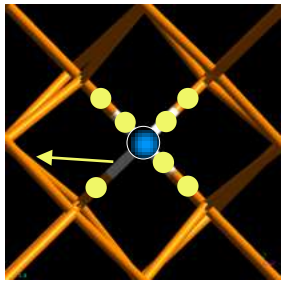

- Analog: Amplification
- Digital: Logic gates

Displacement Damage: Ion Implantation and Annealing

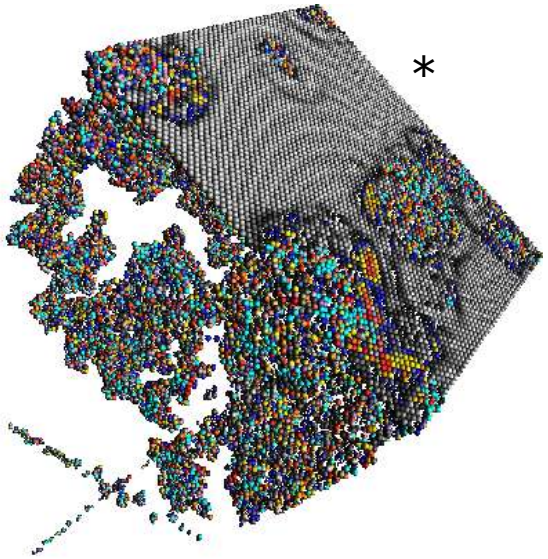

- Dopants inserted by ion implantation
  ⇒ damage
- Damage healed by annealing
- During annealing, dopants diffuse fast (assisted by defects)
  ⇒ important to optimize anneal

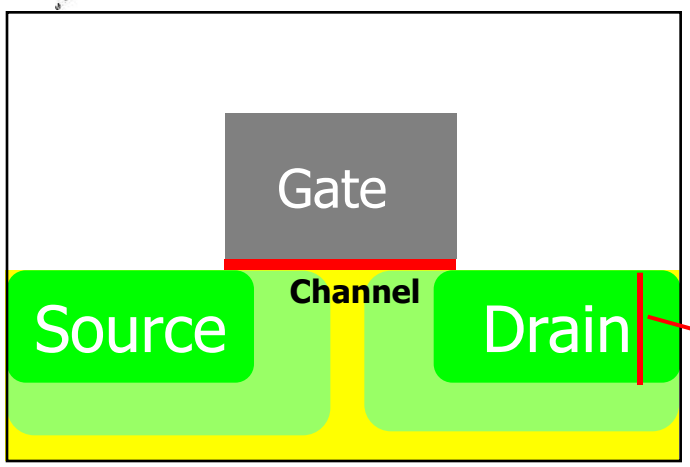

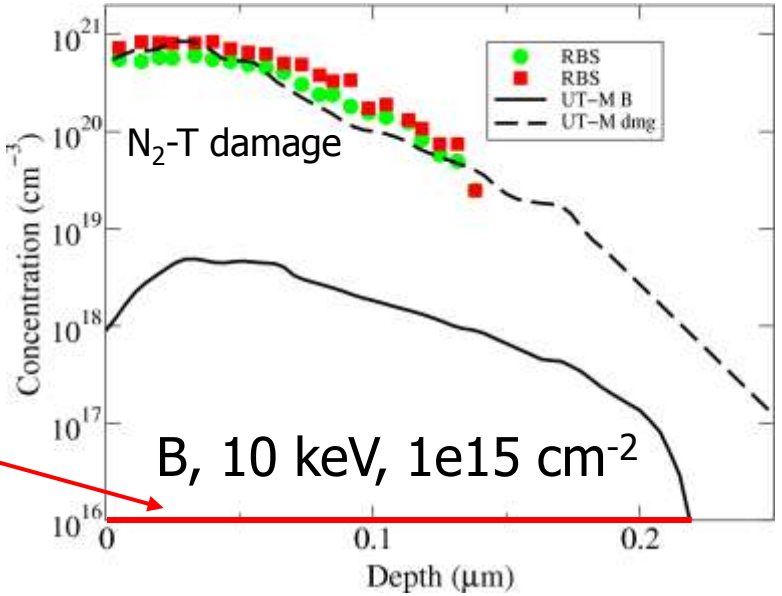

*Höchbauer
Nastasi
Windl

* K. Beardmore, S. Srinivasan

THE OHIO STATE UNIVERSITY

ITRS Requirements & Solubility Limit

Solid Solubility of Si Dopants

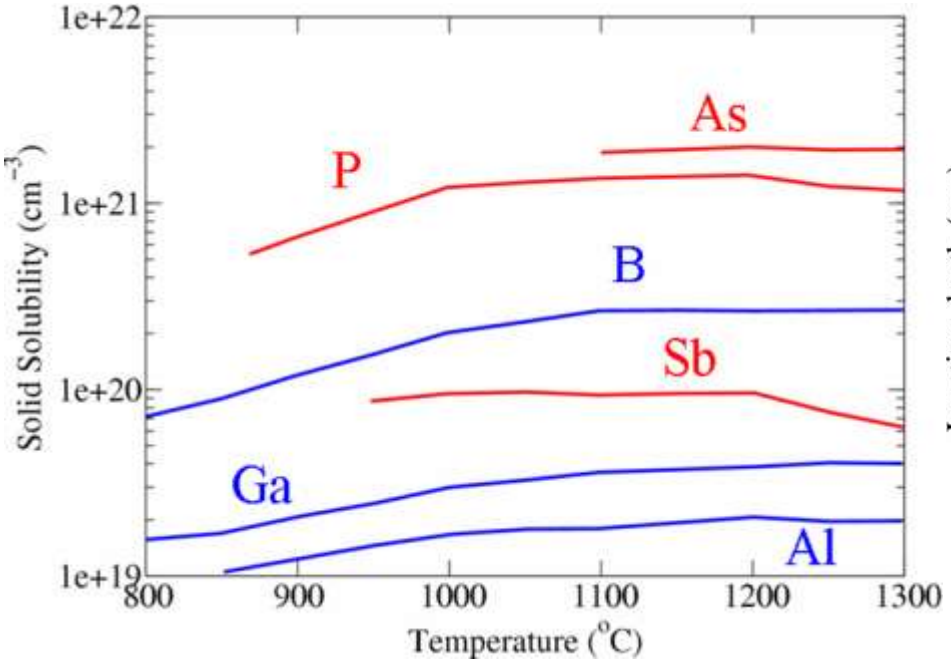

ITRS & Solubility Limit

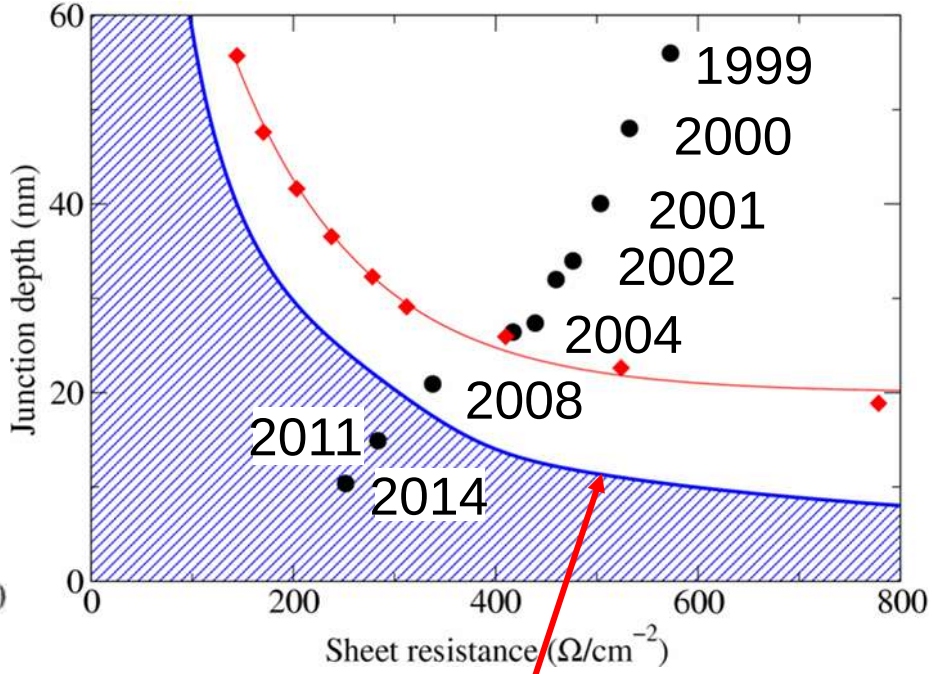

- Electrically active concentrations may be much lower
- "Practical" solubility ~ 2e20 cm^{-3}
- "Ideal profile": Box profile

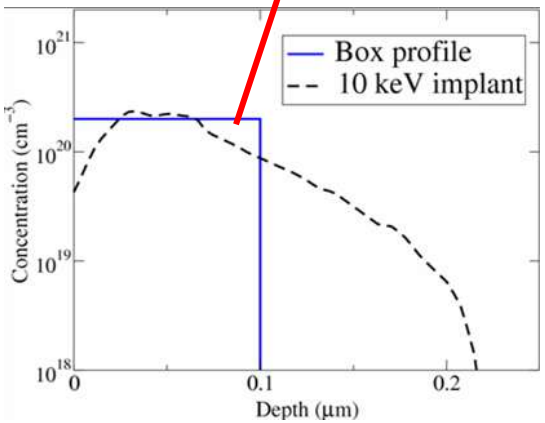

Example: Boron TED & Deactivation in Si

What you expect:
Intrinsic diffusion

$$\frac{dC_B}{dt} = \nabla\left(D_B \nabla C_B\right)$$

What you get:

- fast diffusion (TED)*
- immobile peak
- segregation & interface pile-up

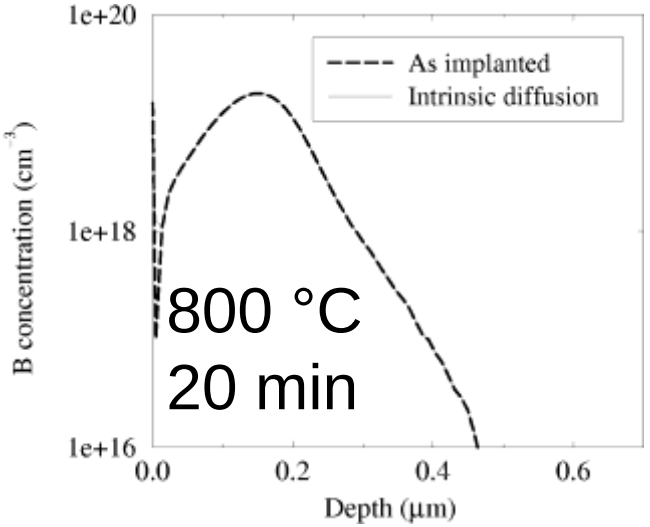

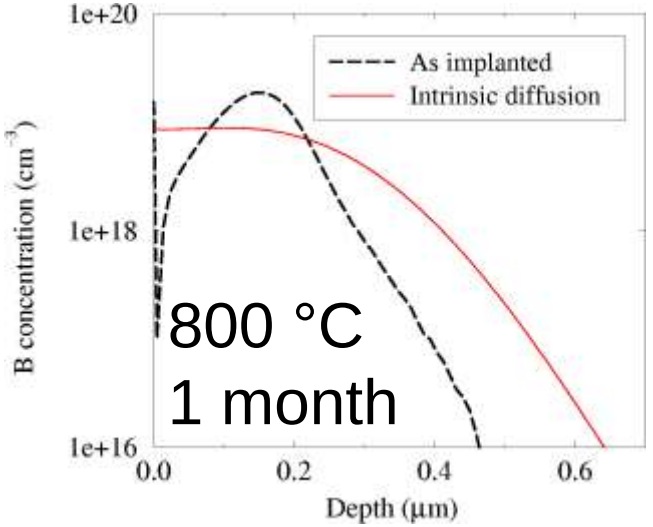

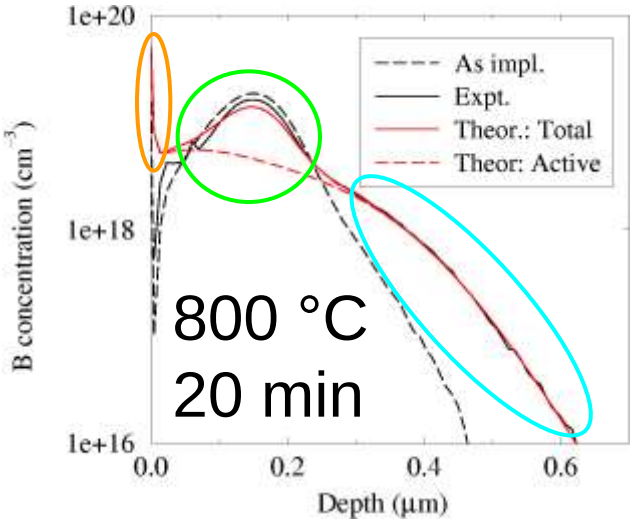

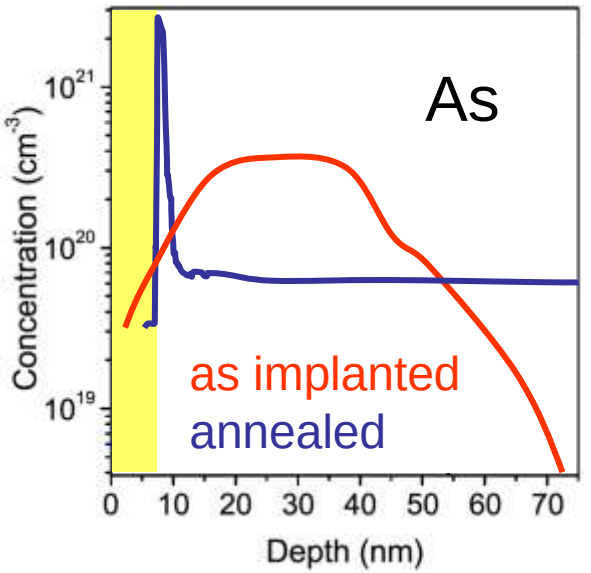

*W. Windl et al., PRL (99).

Bridging the Length Scales: Ab-Initio to Continuum

Point Defect Diffusion:

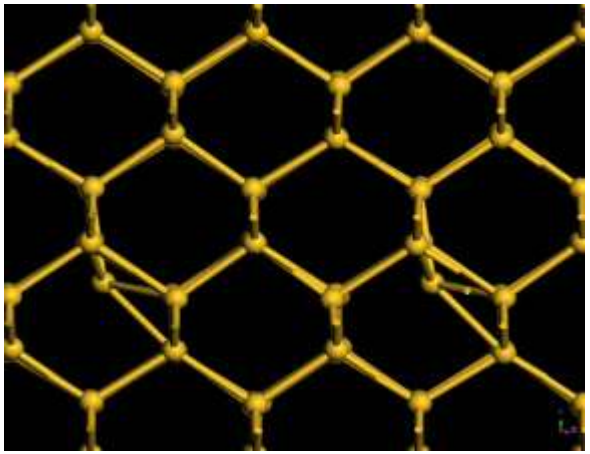

$$\frac{dC_I}{dt} = \nabla\left(D_I \nabla C_I\right)$$

$$D_I = D_I^0 \exp\left(-E_a/k\right)$$

Need to know:

- Diffusion prefactors [Uberuaga et al., PSS (02), Stoddard *et al.*, PRL (05)]
- Migration barriers [Windl *et al.*, PRL (99)]

Bridging the Length Scales: Ab-Initio to Continuum

Impurity Diffusion:

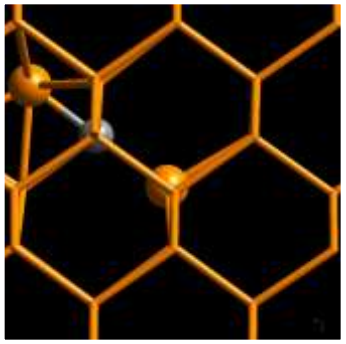

$$\frac{dC_B}{dt} = \nabla\left(D_B^{\text{eff}} \nabla C_B\right)$$

$$D_B^{\text{eff}} \sim D_B^0 \exp\left(-\frac{E_{\text{form}}^I - E_{\text{bind}}^{BI} + E_{\text{mig}}^{BI}}{k_B T}\right)$$

Need to know:

- Effective macro-D [Daw, Windl, PRB (01)]
- Binding free energies [previous papers]
- Previous quantities

Bridging the Length Scales: Ab-Initio to Continuum

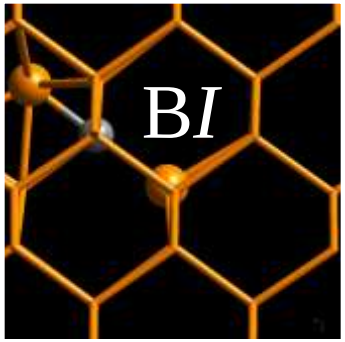

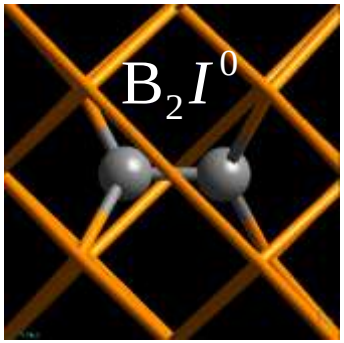

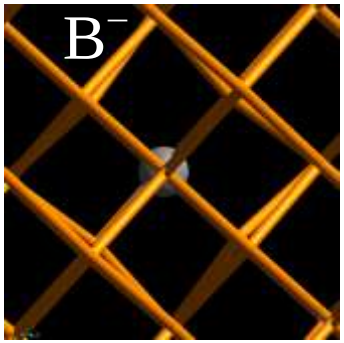

$$BI + B_s \rightarrow B_2 I$$

Reactions:

$$\frac{dC_{BI}}{dt} = \nabla\left(D_{BI}\nabla C_{BI}\right) - K^{f}_{BI_2} C_{BI} C_B + K^{r}_{BI_2} C_{BI_2} + \ldots$$

$$K^{r}_{I_2} \propto D_{BI}\, a_{BI_2} \exp - \left(E_b^{BI_2} / kT\right)$$

Need to know:
- Binding energies
- Capture radii

[Liu *et al.*, APL (00)]

[Beardmore *et al.*, Proc. ICCN (02)]

Transition State Theory (TST)

TST escape rate =
equilibrium flux through
dividing surface at $x = q$

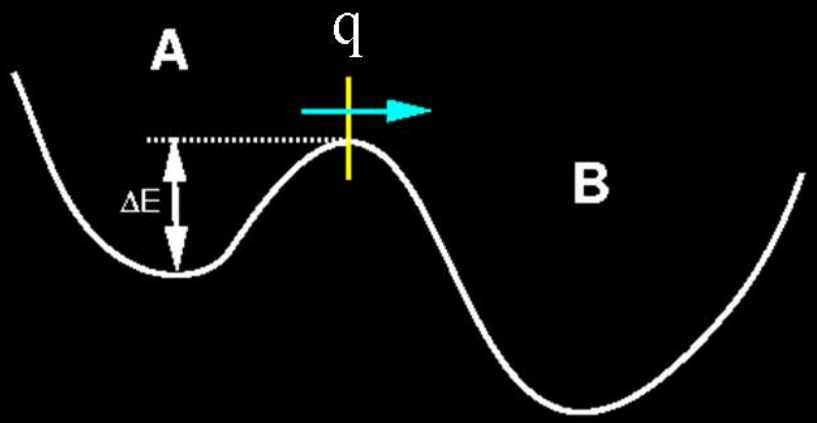

$$r_{A\to B}^{HTST} = \upsilon_0 \exp(-\Delta E / k_B T)$$

(harmonic approx.)

- classically exact rate if no recrossings or correlated events
- no dynamics required
- excellent approximation for materials diffusion
- can also exploit TST formalism to develop methods that do not require knowing in advance where the dividing surface is

Laidler, JPC (89).

How To Find Saddle Points

"Drag method": Guess final state & diffusion path (reaction coord.)

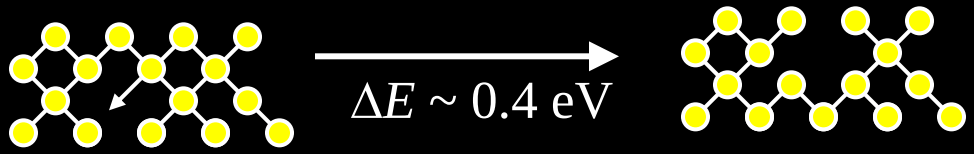

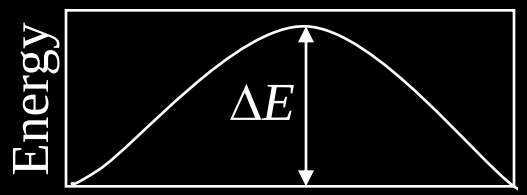

Reliable search for diffusion path: "Nudged elastic band method (Jónsson *et al.*).

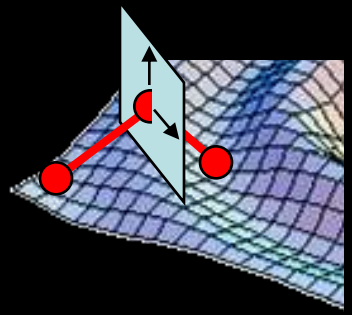

$$\mathbf{r}_{0.5} = 0.5\,(\mathbf{r}_i + \mathbf{r}_f)$$

Final state unknown ⇒ Dimer method, (accelerated) MD

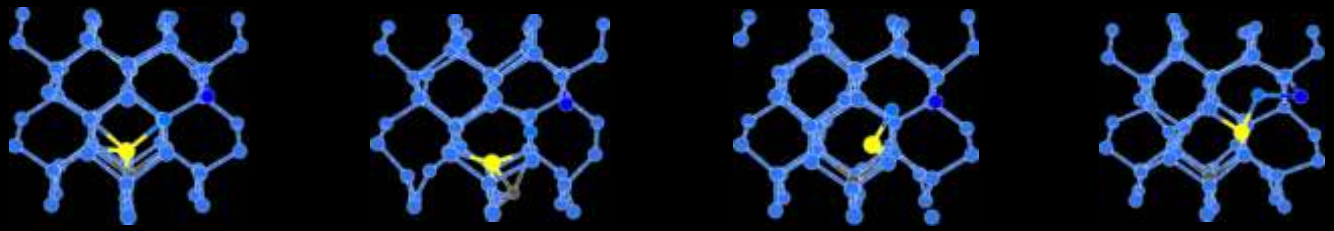

Prefactor

- **Necessary:** vibrational frequencies at minimum & saddle point (harmonic TST, Vineyard (1957))

$$D = \frac{p \cdot d^2}{12} \upsilon \exp\left(-\frac{\Delta S}{k_B}\right) \exp\left(-\frac{\Delta E}{k_B T}\right)$$

$$\upsilon = \frac{\prod_{j=1}^{N} \upsilon_j^{\mathbf{A}}}{\prod_{j=1}^{N-1} \upsilon_j^{\mathbf{S}}}$$

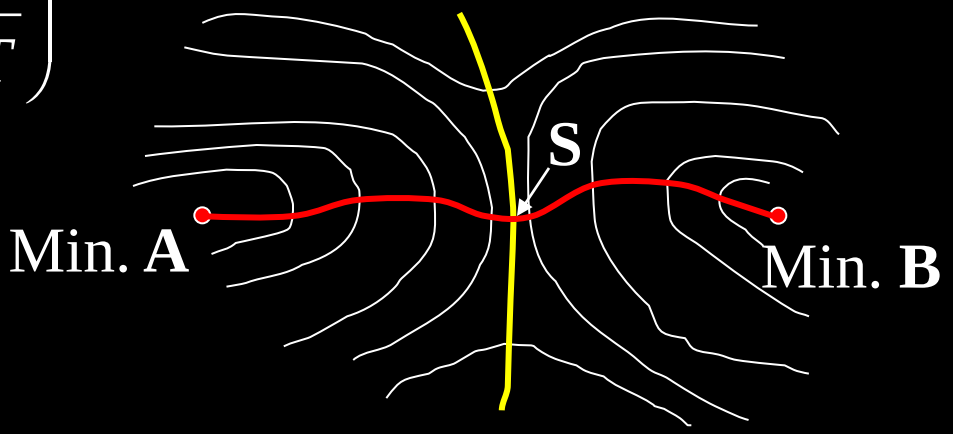

$$S = k_B \sum_{i=1}^{3N} \left\{ \frac{\hbar \upsilon_i}{2 k_B T} \coth\left(\frac{\hbar \upsilon_i}{2 k_B T}\right) - \ln\left[2 \sinh\left(\frac{\hbar \upsilon_i}{2 k_B T}\right)\right] \right\}$$

Uberuaga et al. PSS (02),
Stoddard et al, PRL (05).

Si Self Diffusion - Experiment

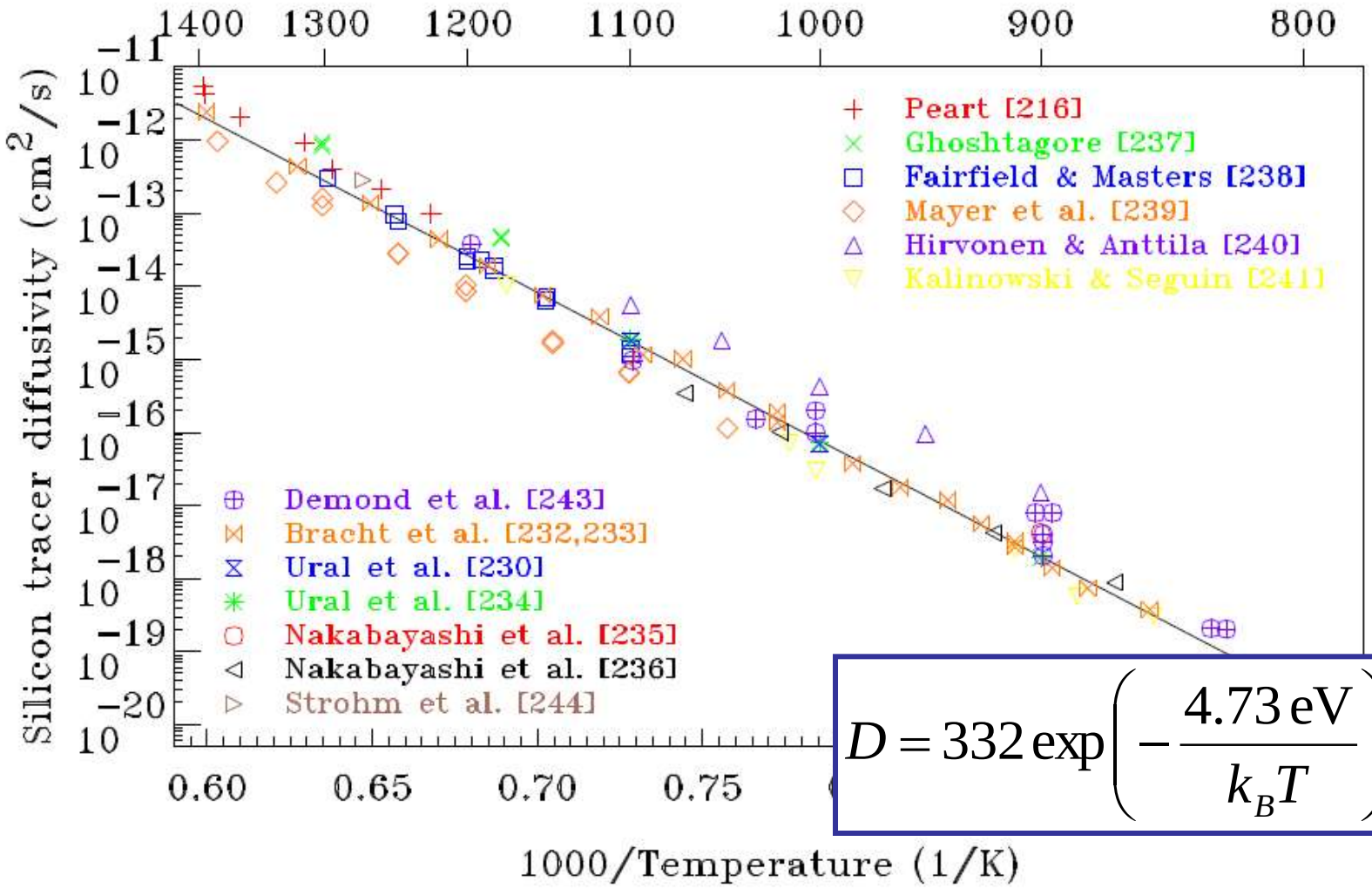

$$D = 332 \exp\left(-\frac{4.73\,\text{eV}}{k_B T}\right) \frac{\text{cm}^2}{\text{s}}$$

Figure: Pichler book

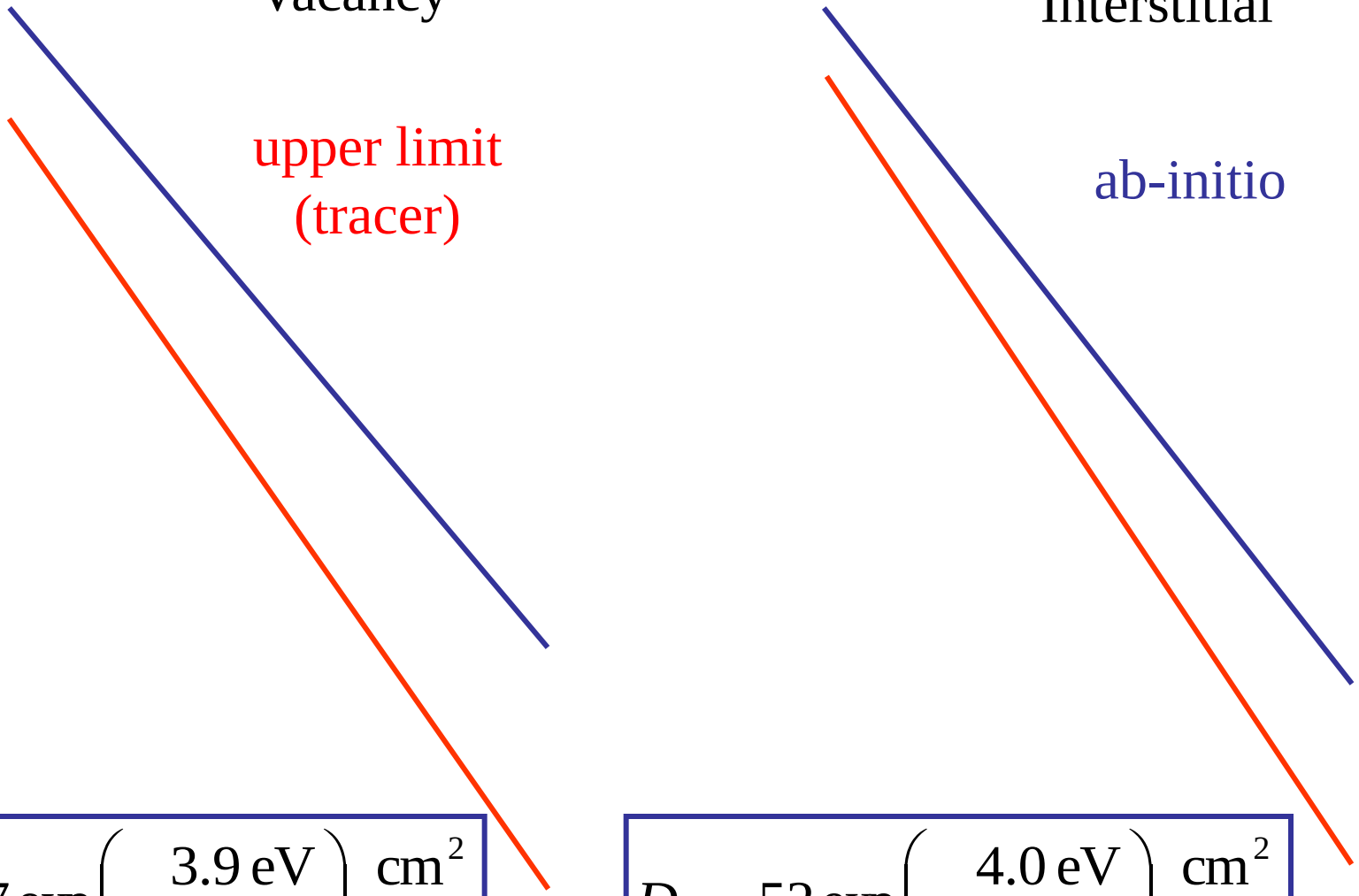

$$D_T = 437 \exp\left(-\frac{3.9\,\text{eV}}{k_B T}\right) \frac{\text{cm}^2}{\text{s}}$$

$$D_T = 52 \exp\left(-\frac{4.0\,\text{eV}}{k_B T}\right) \frac{\text{cm}^2}{\text{s}}$$

Theor: Uberuaga et al.,
Phys. Stat. Sol. B **233**, 24 (2002).

Nitrogen Pair Diffusion: Comparison

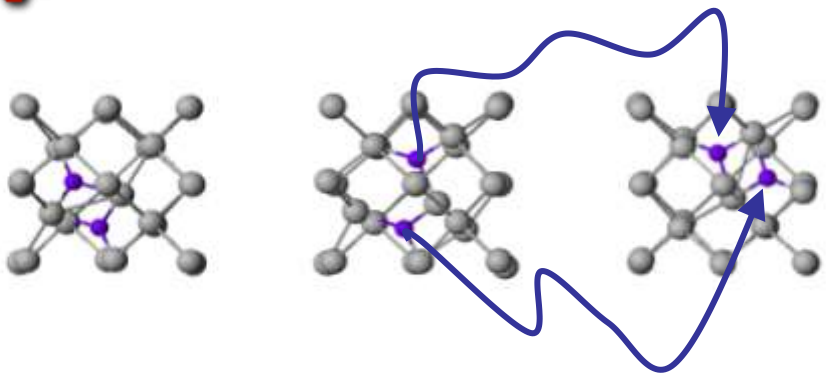

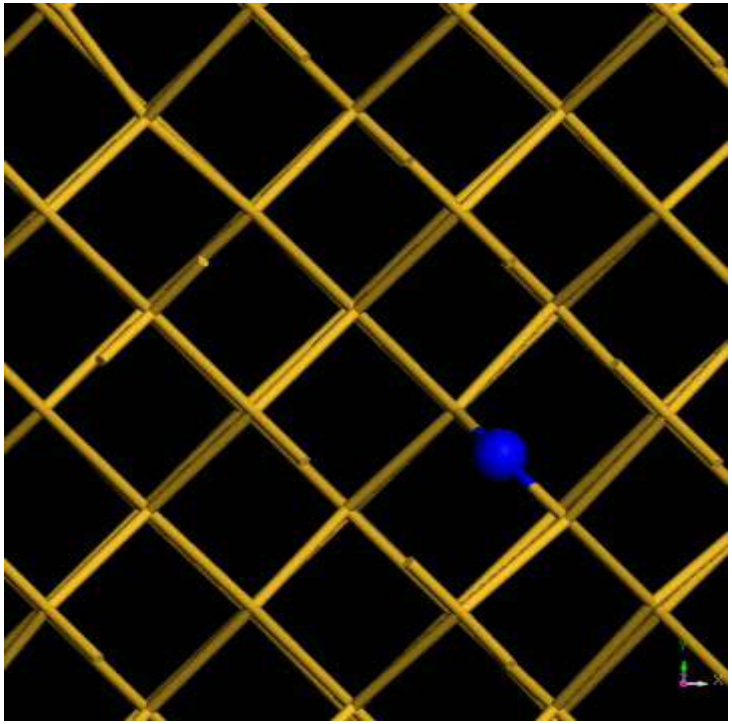

- Energy + prefactor

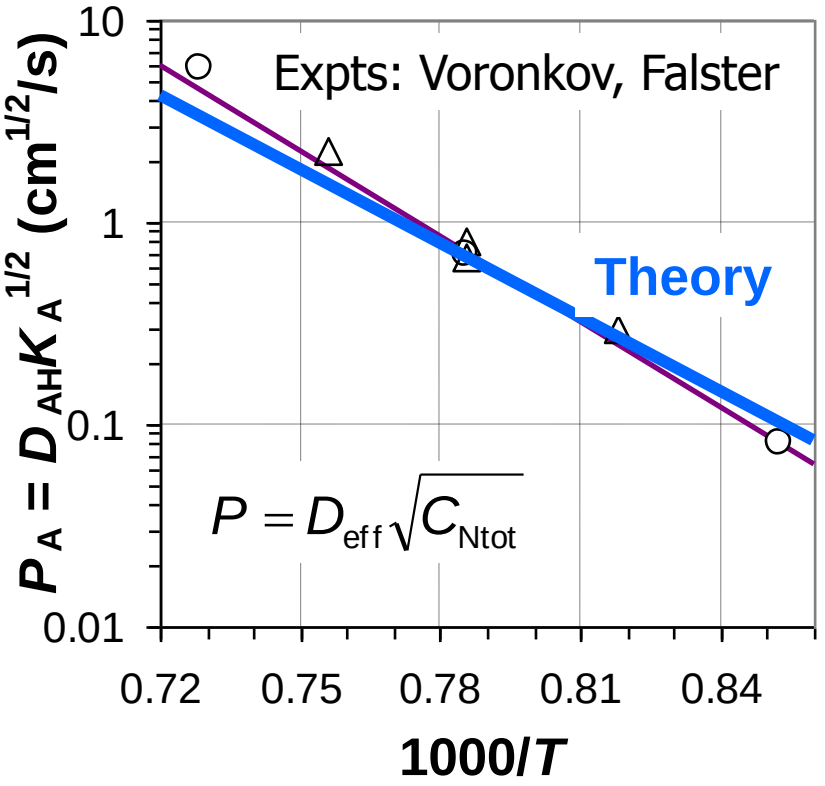

Equally good for other I-diffusers, e.g.:

- B (Windl et al, PRL 99)
- P (Liu et al., APL 03)

SiB_3 Nucleation – Expected Nucleus

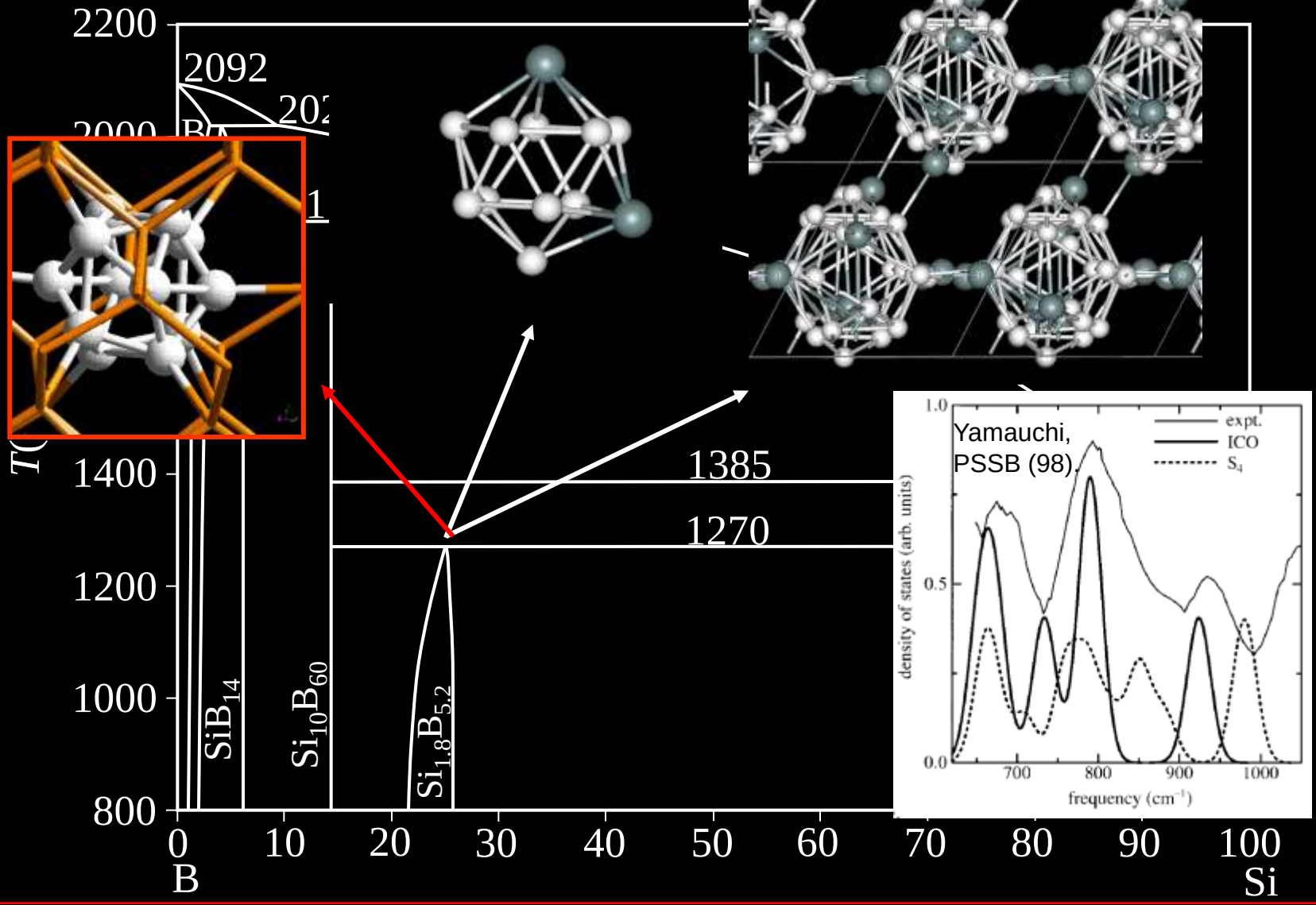

Sub-Microscopic Boron Clusters

Experimental situation:

- Structures too small to be seen in EM
  $\Rightarrow$ only "few" atoms
  - New phase wants to nucleate, but decays quickly
- Clustering dependent on B concentration and interstitial concentration
  $\Rightarrow$ formation of $B_m I_n$ clusters postulated;
  experimental estimate: m / n ~ 1.5*

$\Rightarrow$ *Approach*:

- Calculate clustering energies from first principles up to "max." m, n
- Build kinetic Monte Carlo / continuum model from it

*S. Solmi *et al.*, JAP **88**, 4547 (2000).

B-I Cluster Structures from *Ab Initio* Calculations

B_xI	BI^+		B_2I^0		B_3I^-	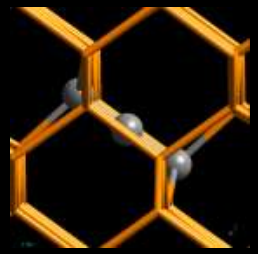	B_4I^{2-} 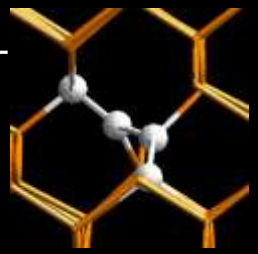
	LDA –0.5 GGA –0.4		–2.0 –1.2		–3.0 –2.2		–5.5 –4.3
B_xI_2	BI_2^0	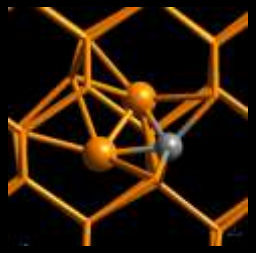	$B_2I_2^0$	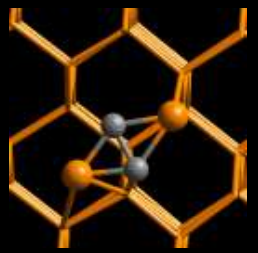	$B_3I_2^0$	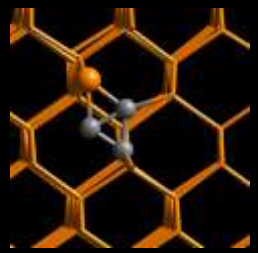	$B_4I_2^0$ 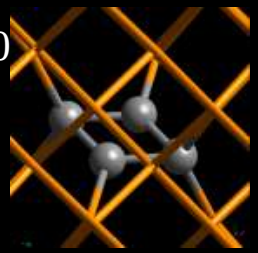
	–2.5 –2.3		–3.0 –2.4		–4.1 –2.6		–5.5 –4.3
B_xI_3	BI_3^+		$B_2I_3^0$		$B_3I_3^-$	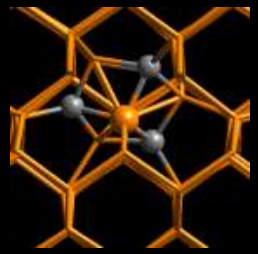	$B_4I_3^-$
	–4.8 –4.5		–6.0 –5.3		–6.6 –5.6		–7.0 –5.9
I>3	$B_4I_4^-$		$E_{\text{cluster}} = E_{B_nI_m} - n\left(E_{B^{-1}} - E_{Si}\right) - m\left(E_{I^0} - E_{Si}\right) - E_{Si}$				$B_{12}I_7^{2-}$
	–9.2 –7.8						–24.4 N/A

X.-Y. Liu, W. Windl, and M. P. Masquelier, APL **77**, 2018 (2000).

Activation and Clusters - GGA

30 min isochronal anneals

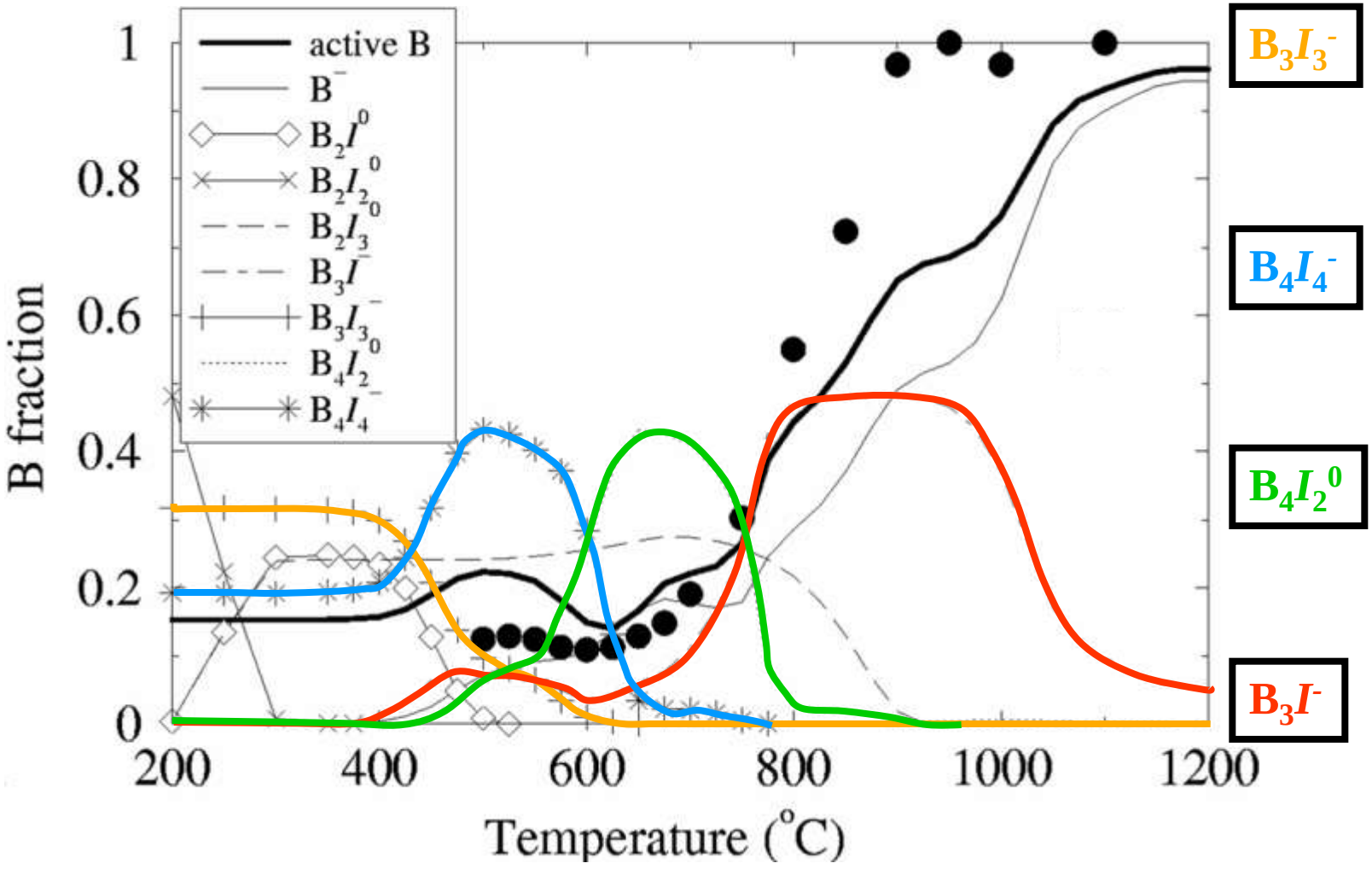

$B_3I_3^-$

$B_4I_4^-$

$B_4I_2^0$

B_3I^-

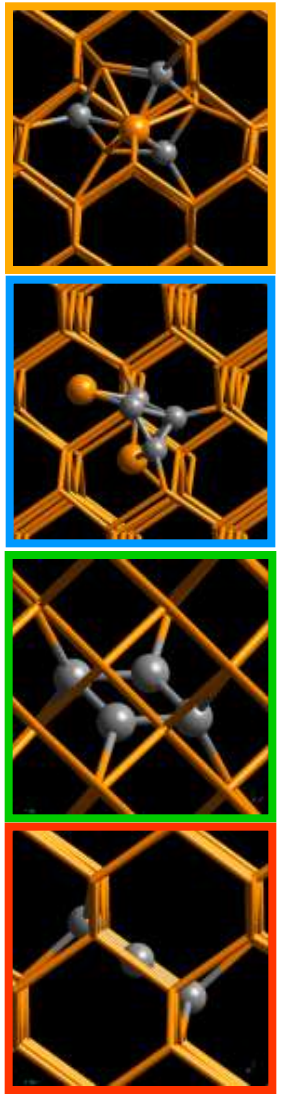

Expt: Mokhberi, Plummer

Activation and Clusters - “

30 min isochronal anneals

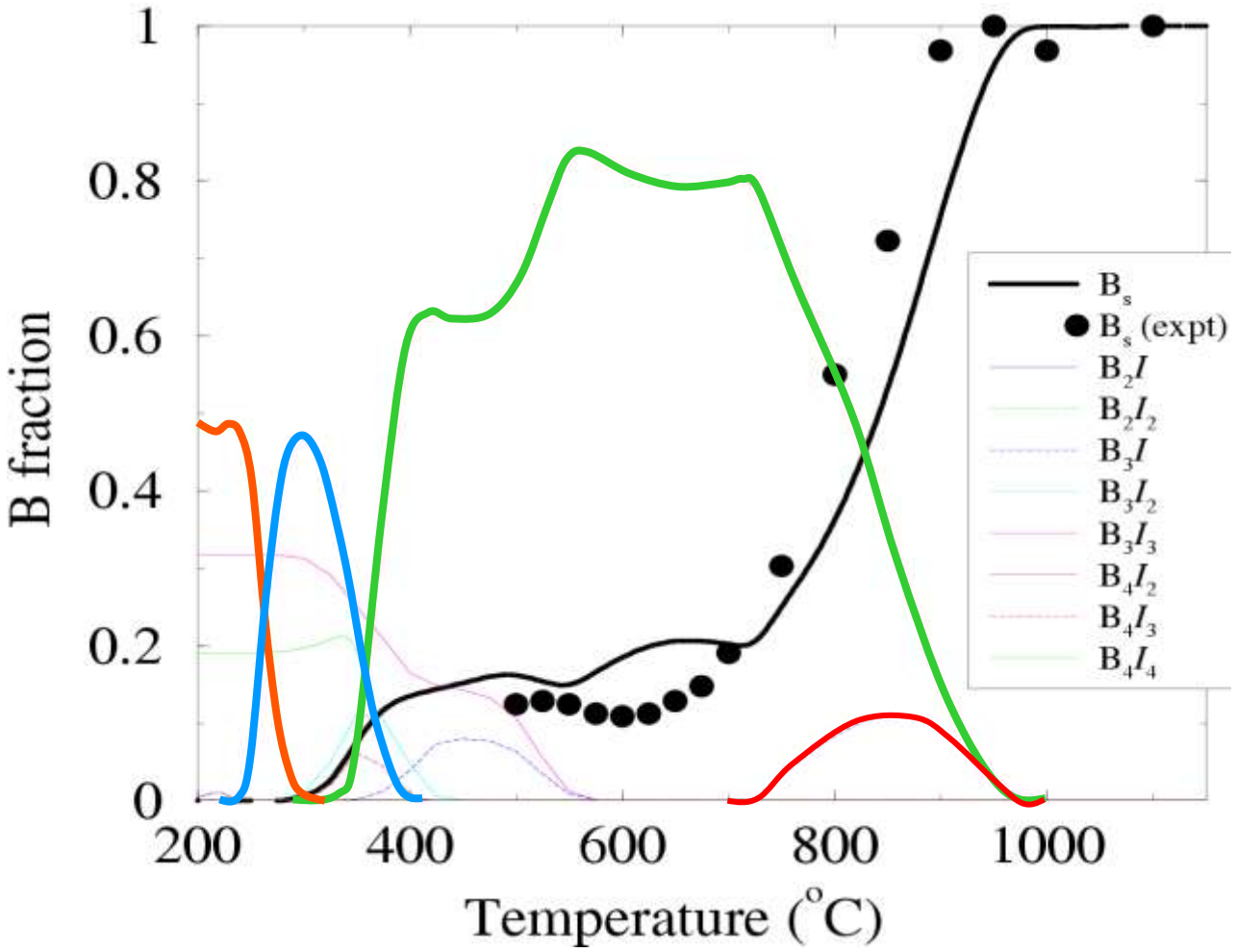

B_2I^0

$B_2I_2^0$

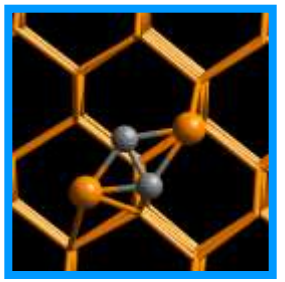

$B_4I_2^0$

B_3I^-

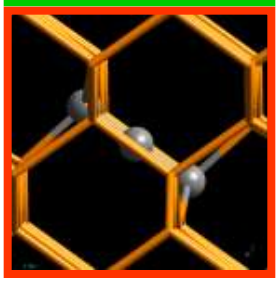

Expt: Mokhberi, Plummer

Which Path Is Right?

$B_4I_2^0$

B_3I^-

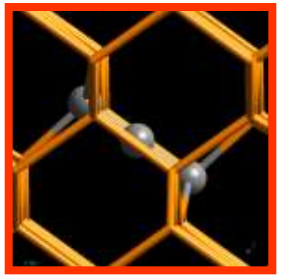

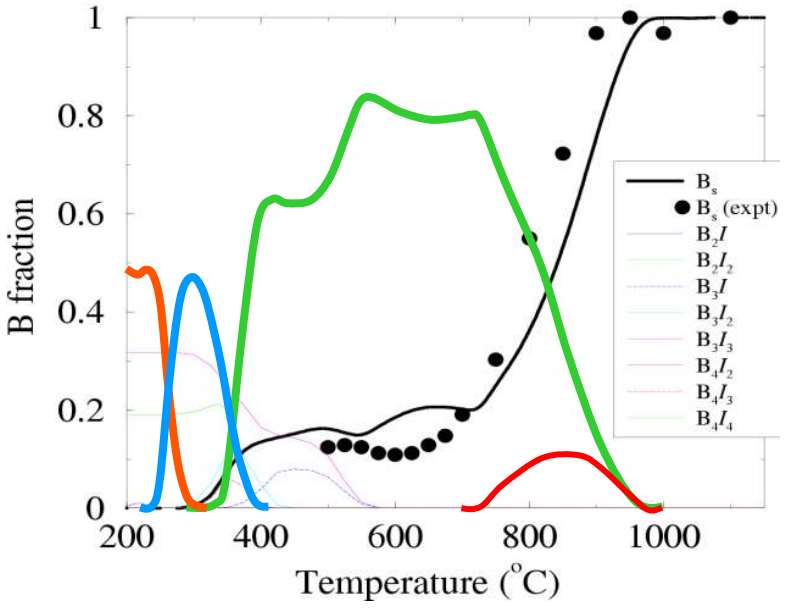

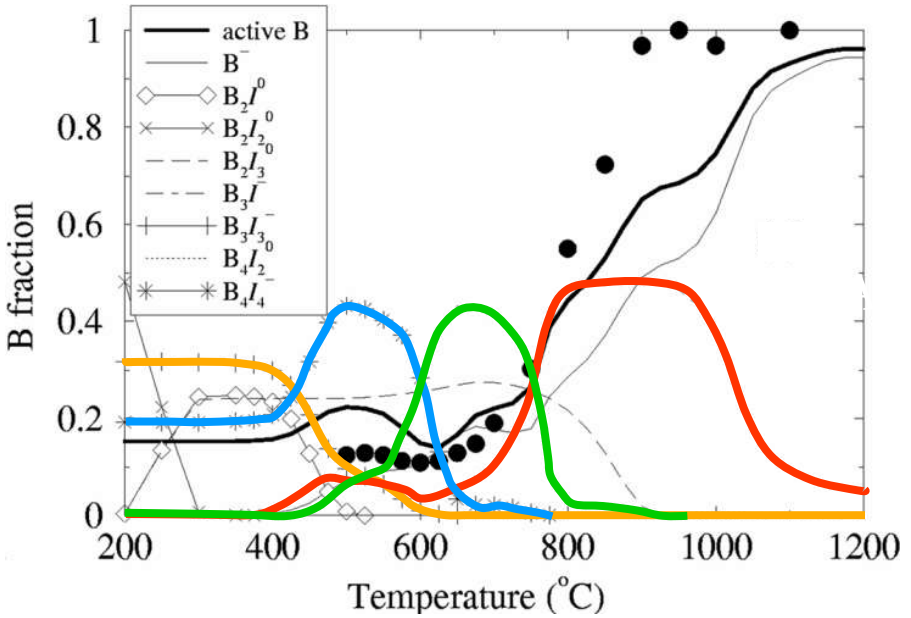

B3I$^-$ negatively charged, should insert hole concentration

Confirmed by Hall measurements

Summary

Semiconductors:

- Kinetic parameters from ab initio calculations today standard, including
  - charge effects
  - temperature effects (non-Arrhenius)
- Clustering/nucleation kinetics doable and helpful, demonstrated for
  - Pre-nucleation
  - Growth

Metals???

What Does It Take to Do Same Calculations for Metals?

- Start from different initial structure (e.g., fcc instead of diamond)
- Do not use pseudo-potential file for silicon, but for metal
- Do same

Example: Superdiffusers

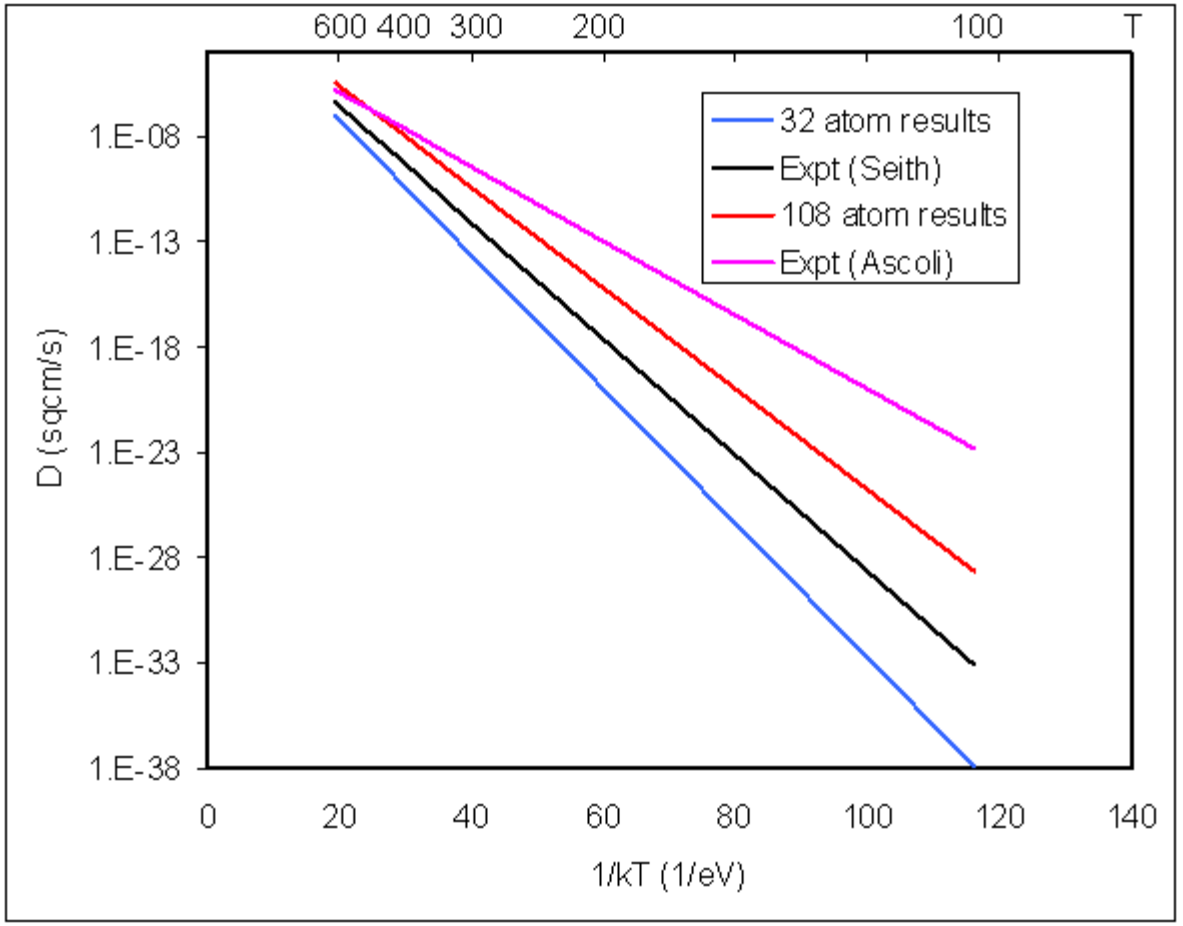

Explanation for superfast diffusion of Au in Pb: Interstitial mechanism

Windl and Rigney (under review)

Ab-Initio Lessons from Semiconductors!?

Energies, structures, Band Structures, "Bulk Modulus"	Kinetic Parameters, Free Energies	(Electronic) "Functional" Properties

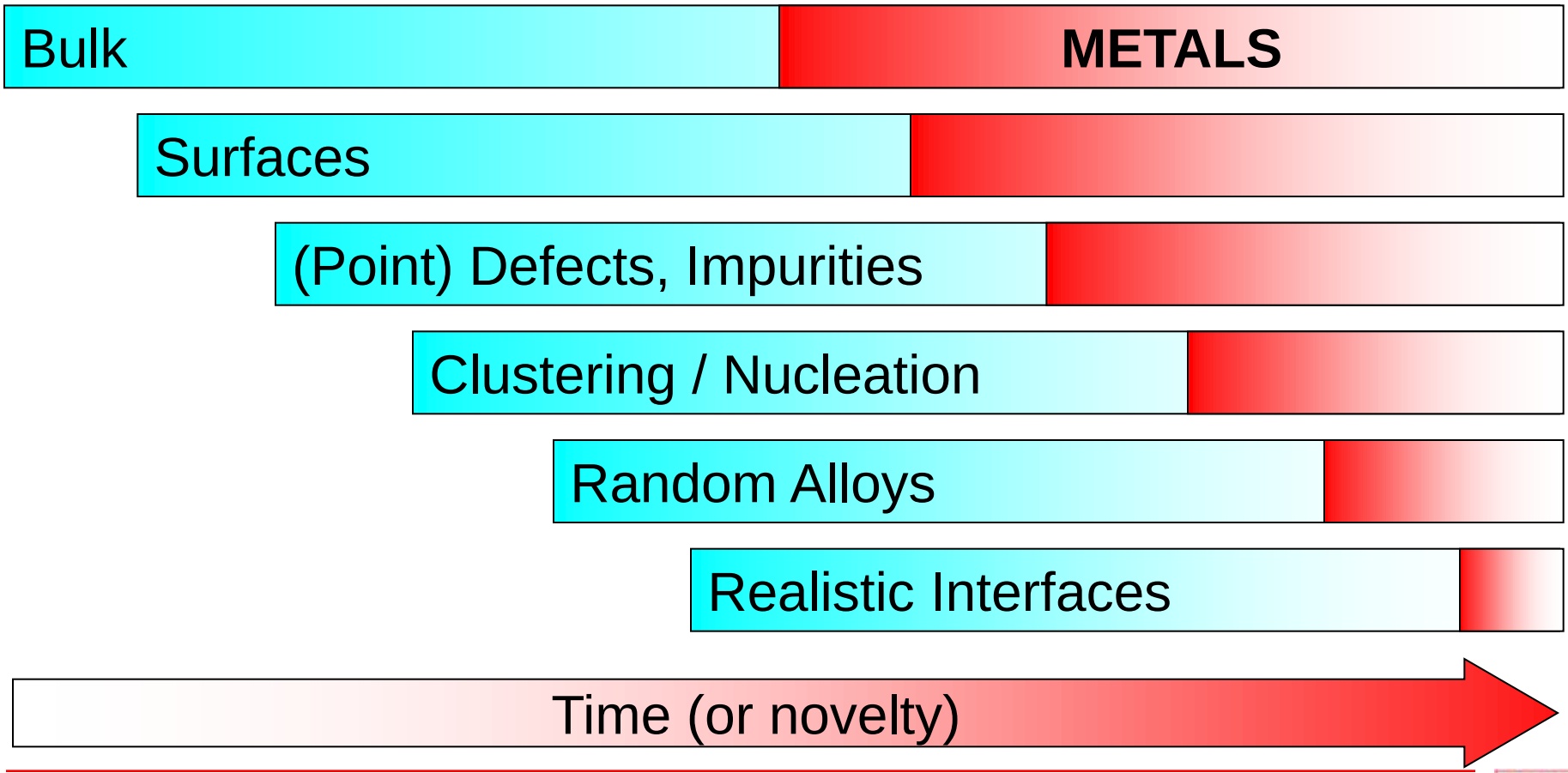

Example: Ab-Initio Diffusion Coefficients – Semiconductors ~2000…

phys. st

Example: Ab-Initio Diffusion Coefficients – Metals ~2008…

Available online at www.sciencedirect.com

ScienceDirect

Acta Materialia 57 (2009) 4102–4108

www.elsevier.com/locate/actamat

First principles impurity diffusion coefficients

M. Mantina [a,*], Y. Wang [a], L.Q. Chen [a], Z.K. Liu [a], C. Wolverton [b]

Dose Loss from Arsenic Pile-Up – Can We See The Clusters?

STEM
(HAADF,
EELS)

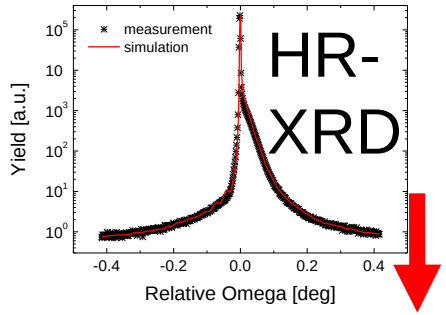

HR-XRD

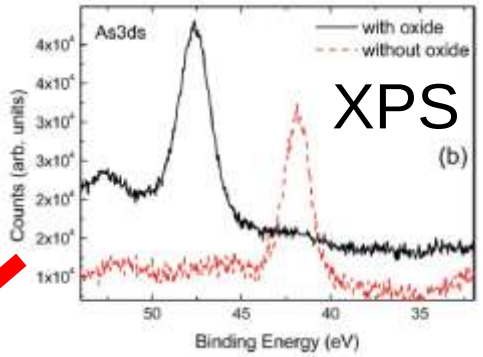

XPS

Modeling:

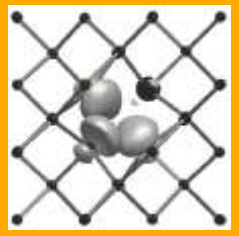

As_3V

Also:
- Four-point probe
- Hall
- Ellipsometry

GI-XRF

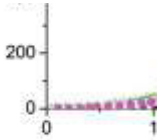

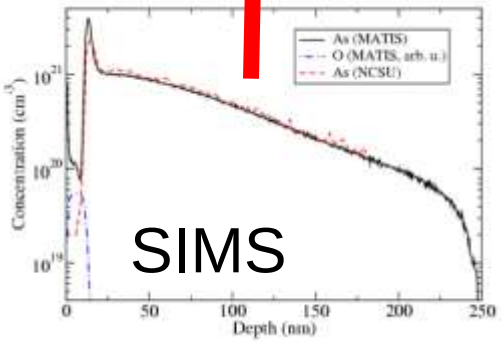

SIMS

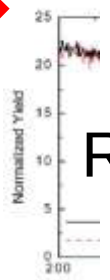

RBS

Pei, Duscher, Steen, Pichler, Ryssel, Napolitani, De Salvador, Severac, Cristiano, Ravichandran, Gupta and Windl.
Steen, Martinez-Limia, Pichler, Ryssel, Paul, Lerch, Pei, Duscher,Severac, Cristiano, and Windl. Both JAP 08.

SiAs: "Ugly" Precipitates – How Do They Fit and Grow?

- Monoclinic phase with incompatible lattice constants
- How does growth happen?

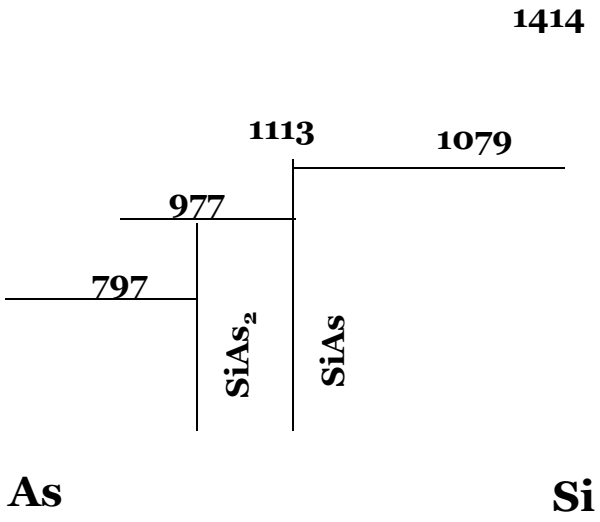

Phase diagram Si As

SiAs structure

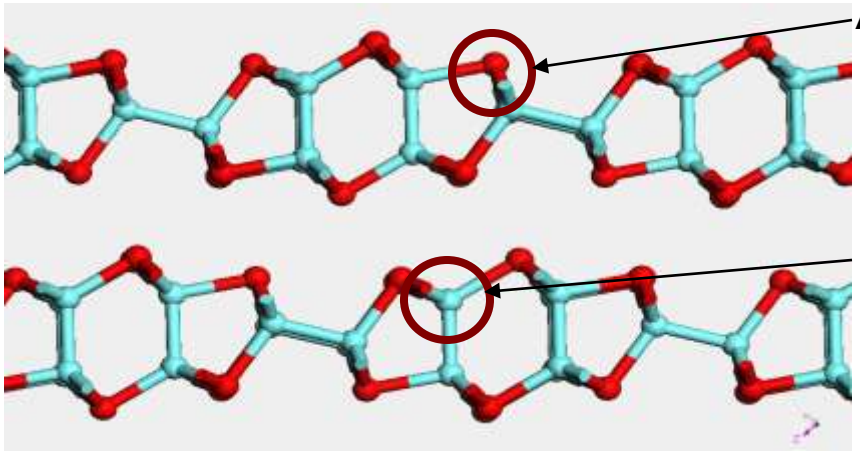

*Fabio Iacona *et. al*, Physical Review B, Vol 58, 10990 (1998)

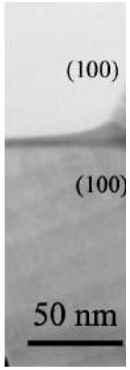

SiAs precipitate at Si/SiO_2 interface *

Final Summary

- Semicondutor research good guidance (e.g. irradiation to enhance supersaturation of solutes (“pre-amorphization implants”)
- Diffusion and rate constants from DFT doable
- Reliance on “knowledge” of processes (reaction paths) dangerous – need good initial data and sensible modeling tasks
- Complimentary experiments necessary
- Modeling essential for full interpretation of experiments

Thermodynamic Modeling of Multi-component Systems and Its Integration with Kinetic Simulation

Fan Zhang, W. Cao, K. Wu, S. Chen, Y. Yang, and Y. A. Chang
CompuTherm, LLC

Present at
Nucleation Workshop at Maui, Hawaii
May 5, 2010

Outline

- Introduction to the CALPHAD Approach
- Integration of Thermodynamic Calculation with Kinetic Models for the Simulation of Nucleation, Growth and Coarsening
- Are Those Gibbs Energies Developed by the CALPHAD Approach Trustworthy?

Why CALPHAD Approach?

Ni-Al binary

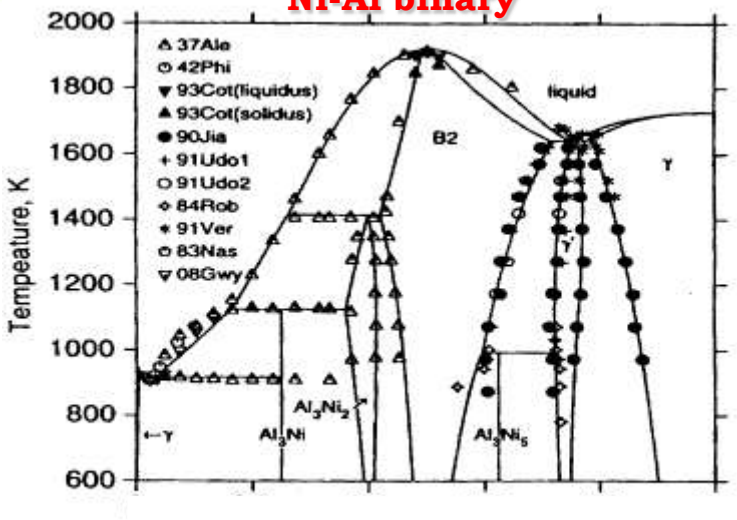

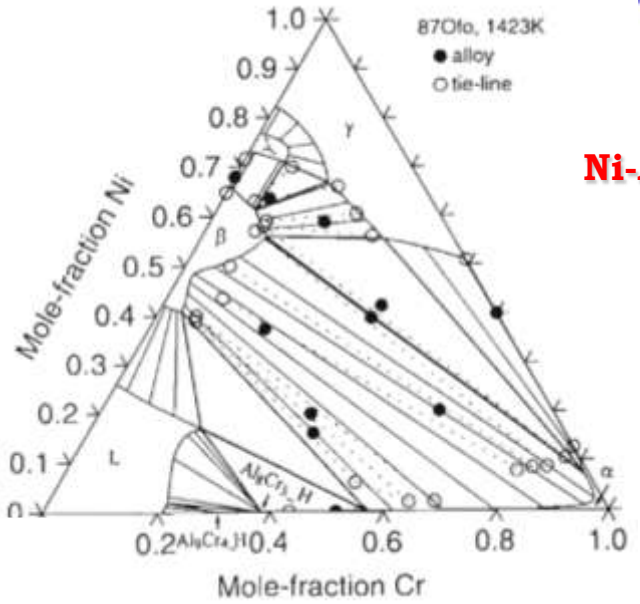

Ni-Al-Cr Ternary

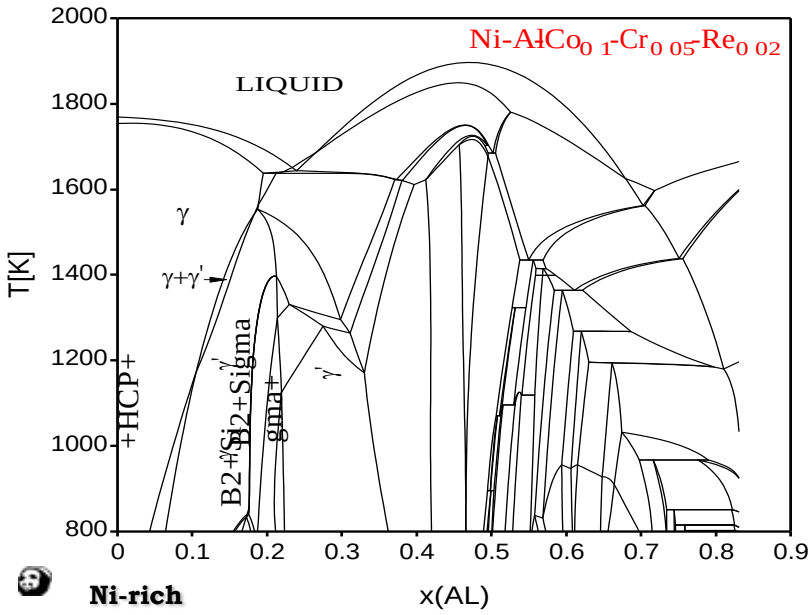

Ni-Al-10Co-5Cr-2Re (at%)

CALPHAD: CALculation of PHAse Diagram

CALPHAD Approach

Thermodynamic data of a binary or ternary

Phase equilibrium data of a binary or ternary

Self-consistent Gibbs energy functions for all the phases in the system (Thermodynamic Description)

Reproduce experimental diagrams and thermo-dynamic properties of the binaries and ternaries

More importantly – extrapolate the Gibbs energies of lower order systems to higher order systems to predict properties of higher order systems

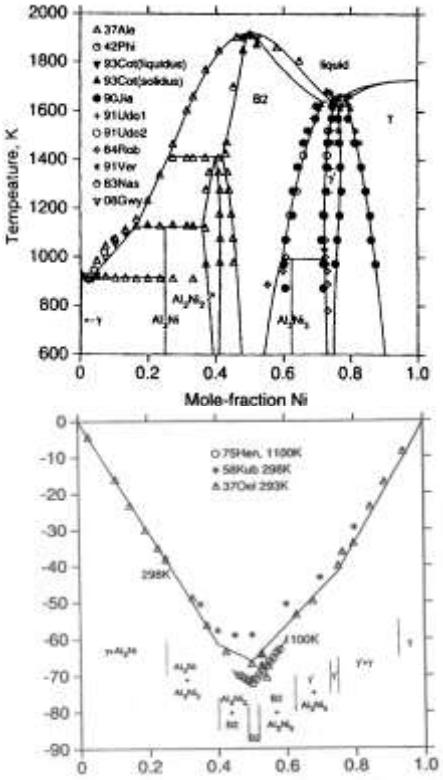

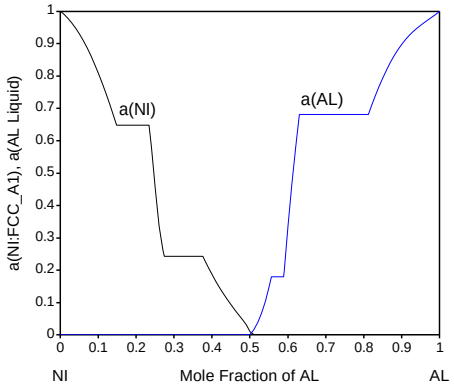

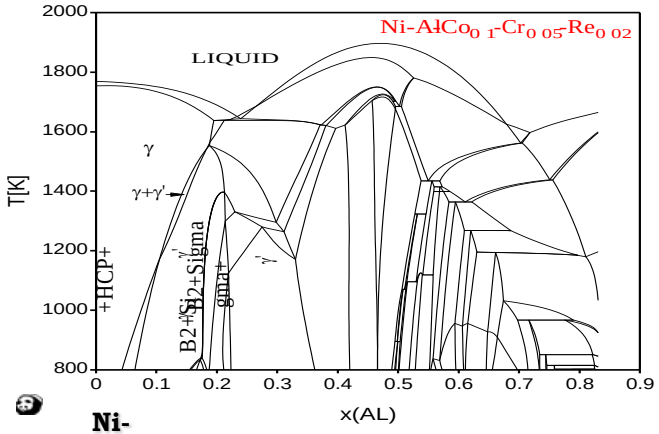

Ni-rich

Three Binaries To Form A Ternary

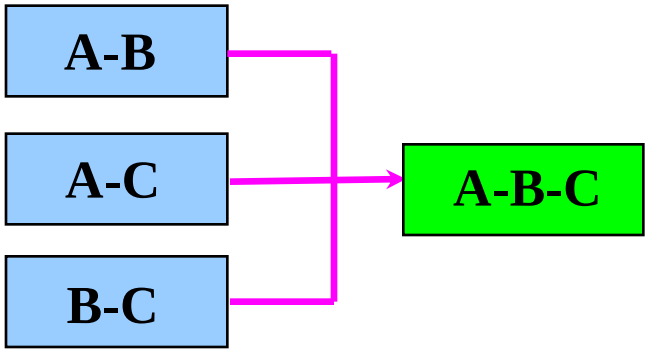

Muggianu Model:

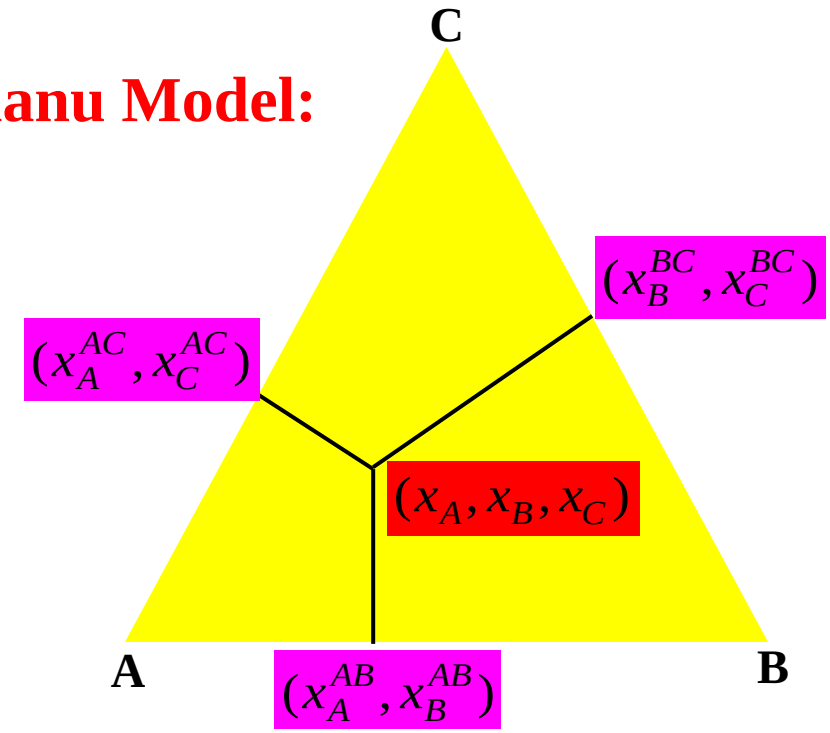

$$G(x_A, x_B, x_C) = \frac{x_A \cdot x_B}{x_A^{AB} \cdot x_B^{AB}} G^{AB}(x_A^{AB}, x_B^{AB}) + \frac{x_B \cdot x_C}{x_B^{BC} \cdot x_C^{BC}} G^{BC}(x_B^{BC}, x_C^{BC}) + \frac{x_A \cdot x_C}{x_A^{AC} \cdot x_C^{AC}} G^{AC}(x_A^{AC}, x_C^{AC})$$

How to Construct A Multicomponent Database

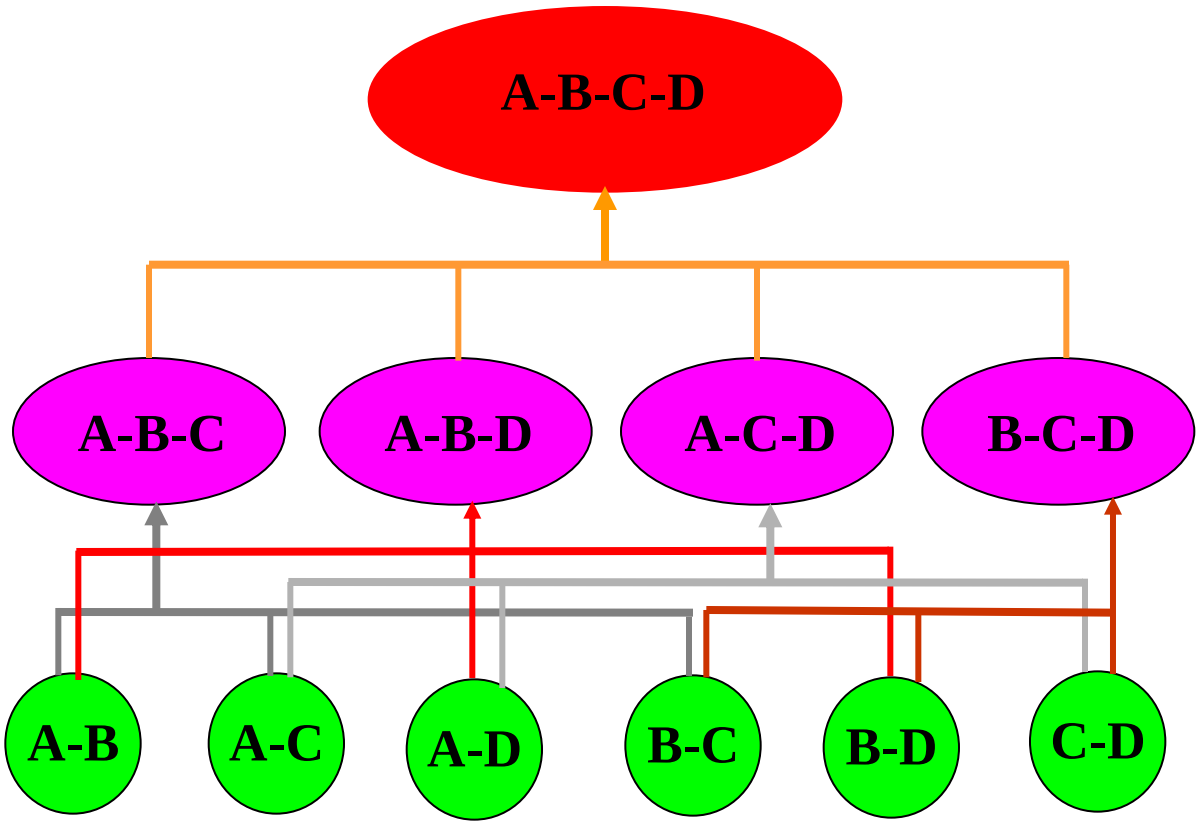

4 Ternary systems

6 Binary systems

Thermodynamic Databases of Multicomponent Systems

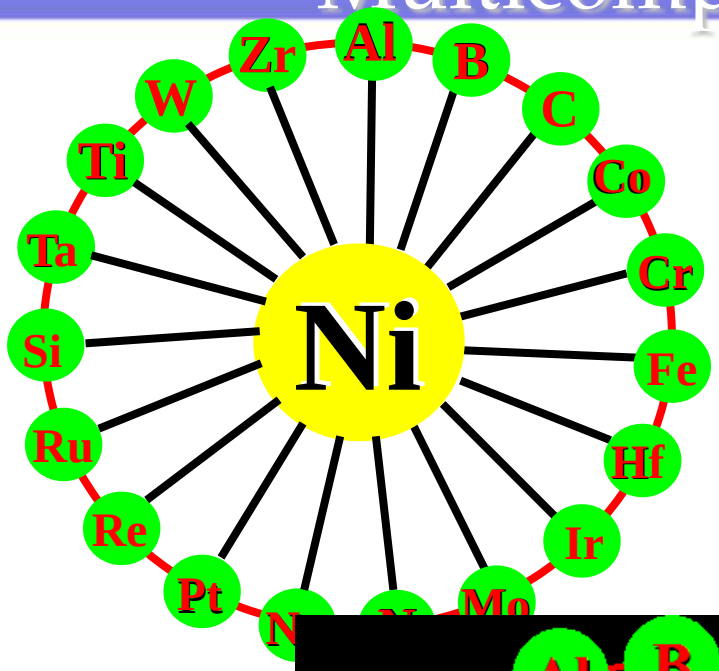

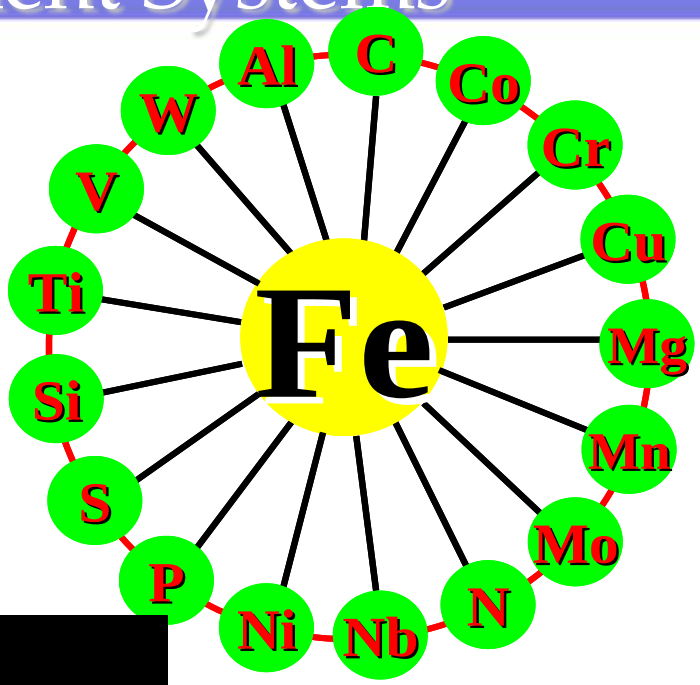

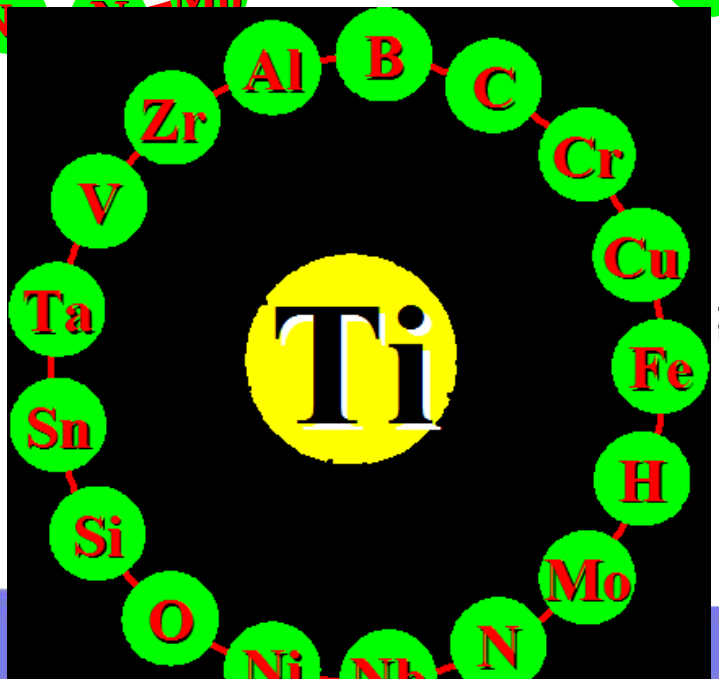

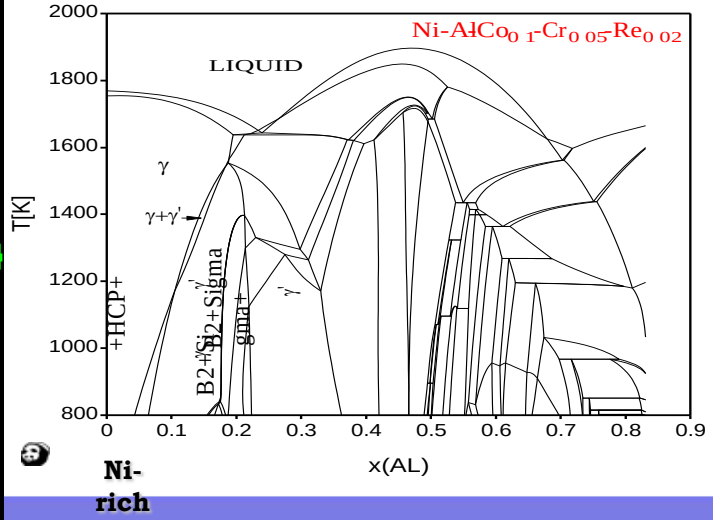

Outline

- Introduction to the CALPHAD Approach
- Integration of Thermodynamic Calculation with Kinetic Models for the Simulation of Nucleation, Growth and Coarsening
- Are Those Gibbs Energies Developed by the CALPHAD Approach Trustworthy?

Integration of Thermodynamic Calculation with Kinetic Simulation

Thermodynamic Database

Mobility Database
Other Kinetic
Parameters

Thermodynamic Calculation

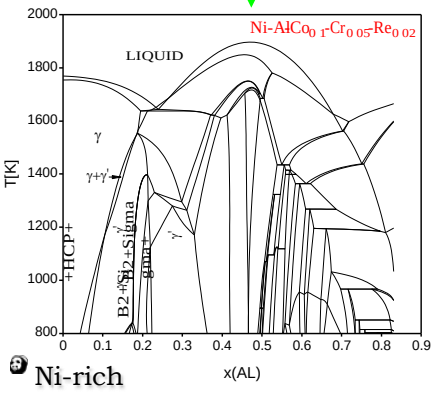

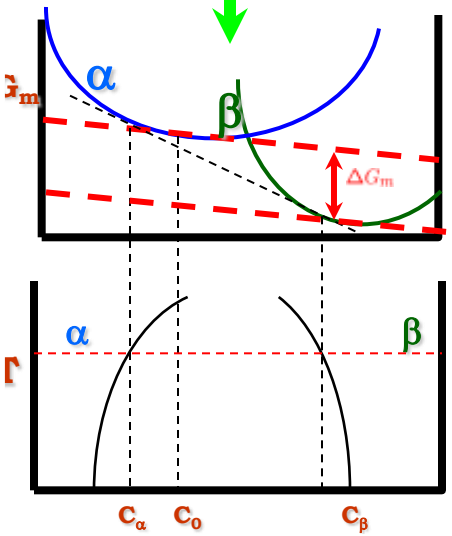

Kinetic Models

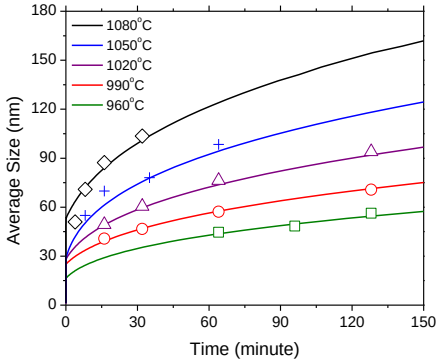

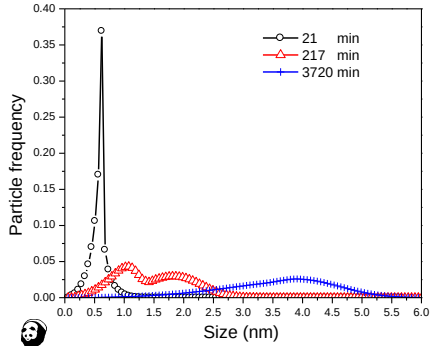

Microstructure Modeling: Fast-acting Model

The Fast-acting Model:

- Concurrent nucleation, growth and coarsening
- Evolution of average quantities: volume fraction, number density, particle size
- Average particle size change with time

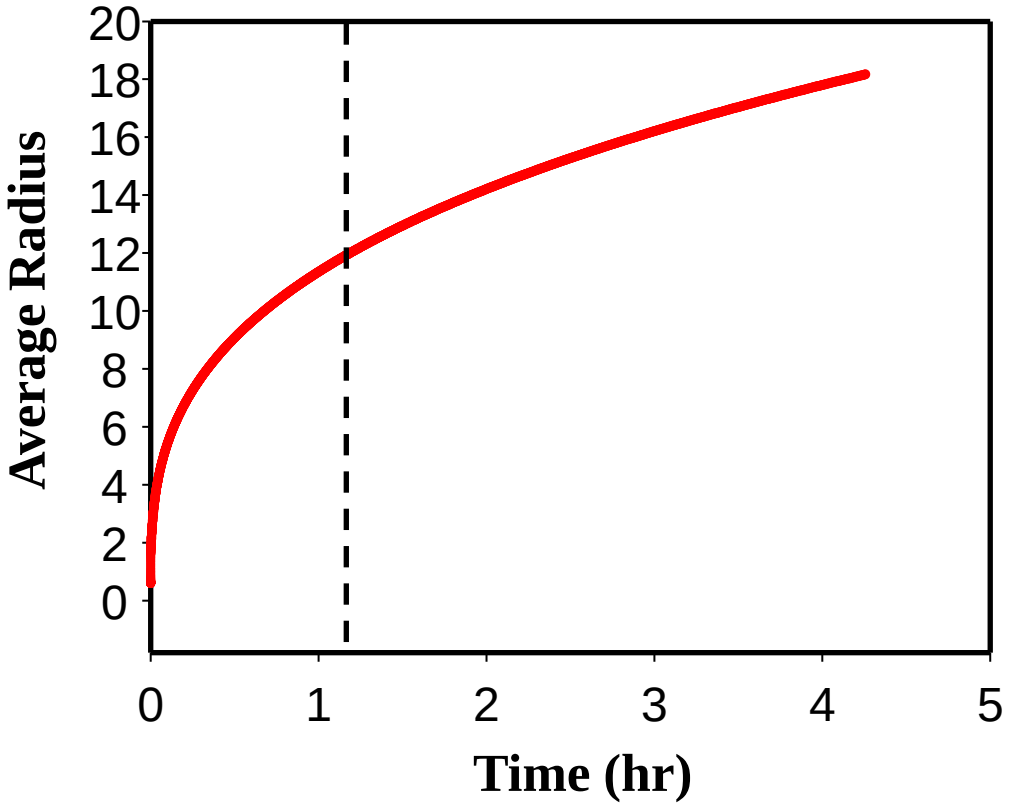

Microstructure Modeling: the KWN Model

The KWN (Kampmann-Wagner Numerical) Model:

- Concurrent nucleation, growth and coarsening
- Evolution of average quantities: volume fraction, number density, particle size
- Evolution of PSD: Particle Size Distribution
- Many size classes

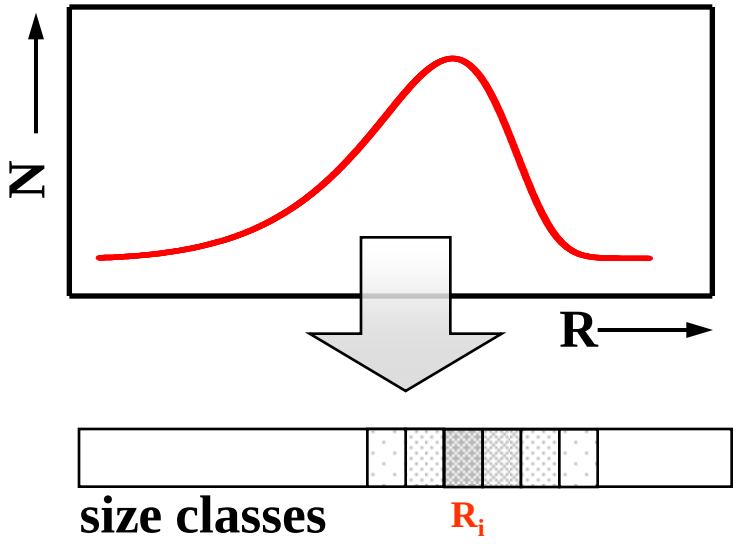

Nucleation Rate

Classical nucleation theory:

$$J = N_v Z \beta^* e^{-\frac{\Delta G^*}{kT}} e^{\frac{-\tau}{t}}$$

Nv : Number of nucleation sites per unit volume
Z : Zeldovich factor accounting for decay of supercritical particles
β^* : Rate of solute atoms joining the critical nucleus
τ : Incubation time
ΔG^*: Activation energy for nucleation

Growth Rate

Growth rate of multi-component alloys (small super-saturation)*

$$v = \frac{dR}{dt} = \frac{K}{R}\left(\frac{1}{R^*} - \frac{1}{R}\right)$$

ΔGm > 0, R < R* → Dissolution

ΔGm > 0, R > R* → Growth

R: particle radius **R*: critical nucleus radius**

$$K = \frac{2\sigma V_m}{\left(\Delta C^{\alpha\beta}\right]\left[M\right]^{-1}\left[\Delta C^{\alpha\beta}\right)}$$

kinetic parameter

($\Delta C^{\alpha\beta}$] : row vector of the solute concentration difference between α and β

[$\Delta C^{\alpha\beta}$) : column vector of the solute concentration difference between α and β

[M] : chemical mobility matrix

* Morral, J.E. and Purdy, G.R., Scripta Metallurgica et Materialia, 1994. **30**(7): p. 905-908

Coarsening Rate

Coarsening Rate of Multi-Component System

$$\bar{R}^3 - \bar{R}_0^3 = \frac{4}{9} Kt \quad \textbf{or} \quad \frac{d\bar{R}}{dt} = \frac{4}{27} \frac{Kt}{R^2}$$

$\bar{R}$: **average particle radius at time t**

$\bar{R}_0$: **average particle radius at the onset of coarsening**

K : **kinetic parameter**

13

Precipitation: Ni-14%Al

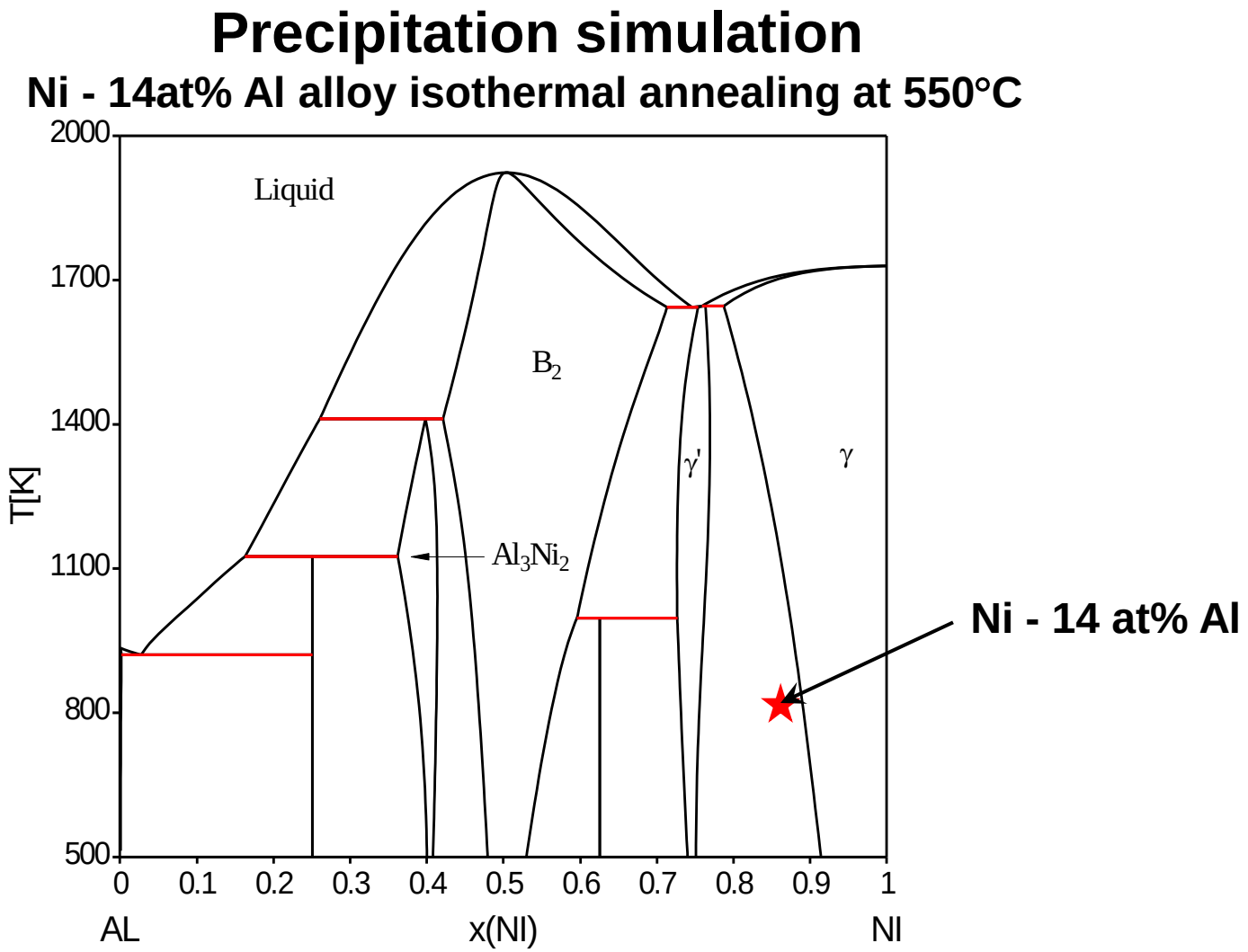

Precipitation: Ni-14%Al

Microstructure evolution in Ni - 14 at.% Al alloy at 550° C

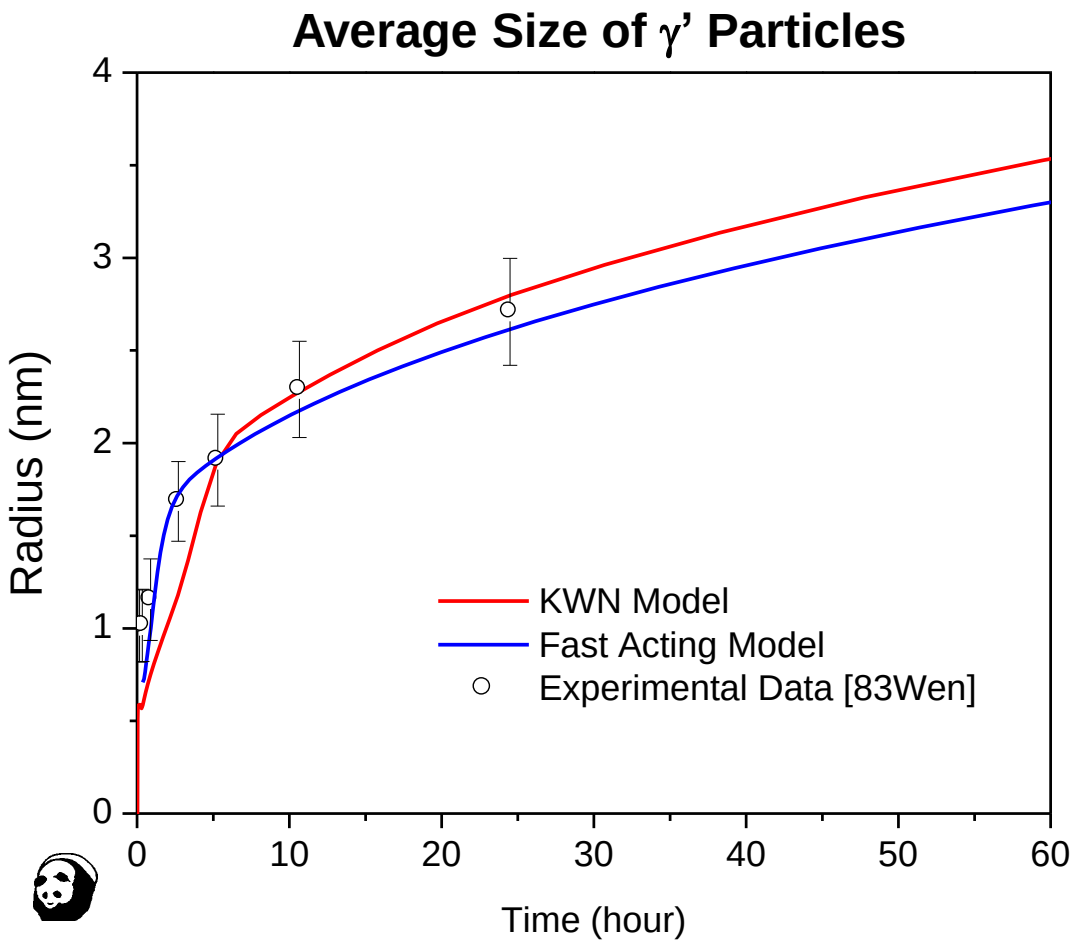

Precipitation: Ni-14%Al

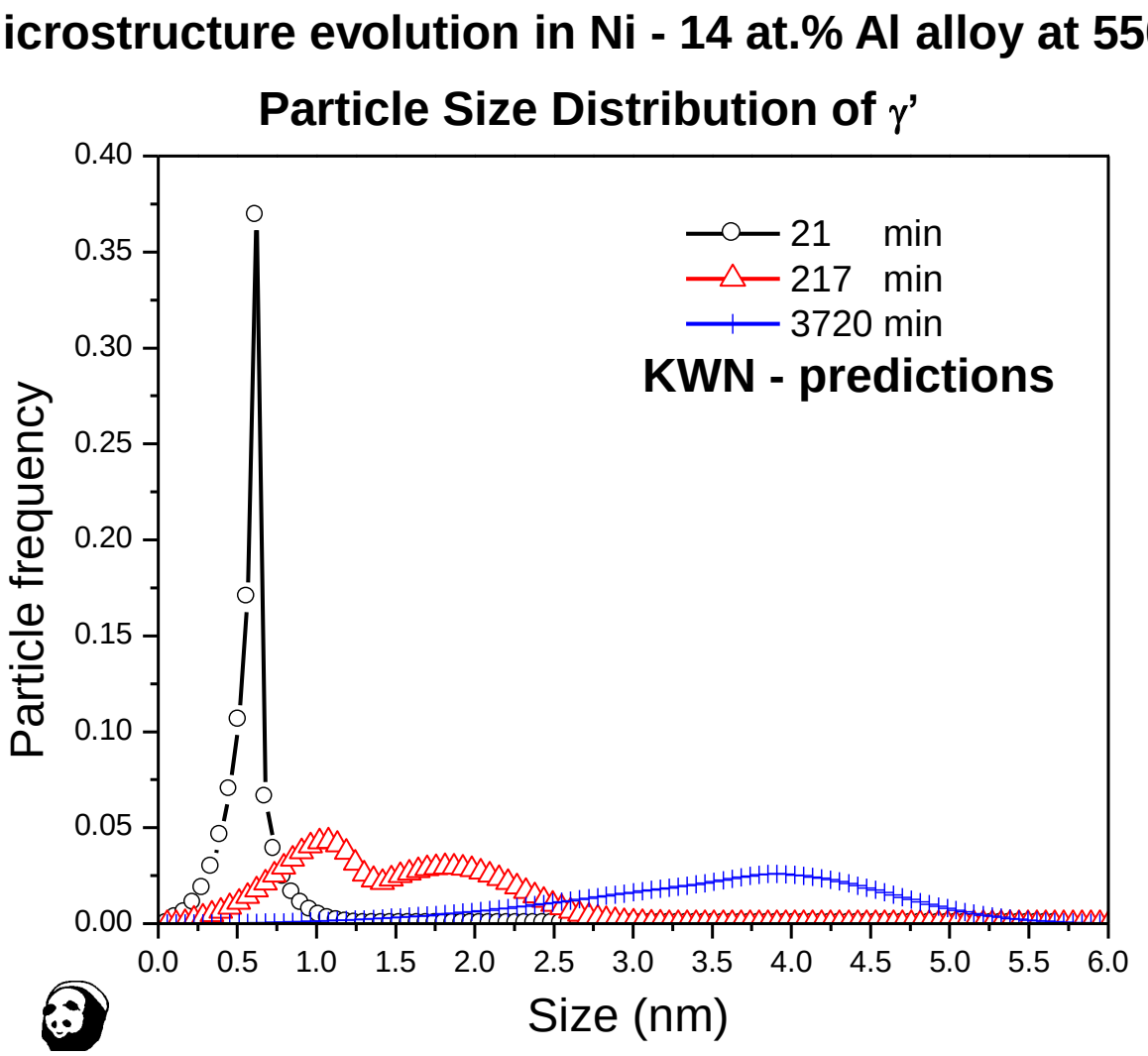

Precipitation: Ni-14%Al

Microstructure evolution in Ni - 14 at.% Al alloy at 550° C
KWN - predictions & experiment

γ' Particle Number Density

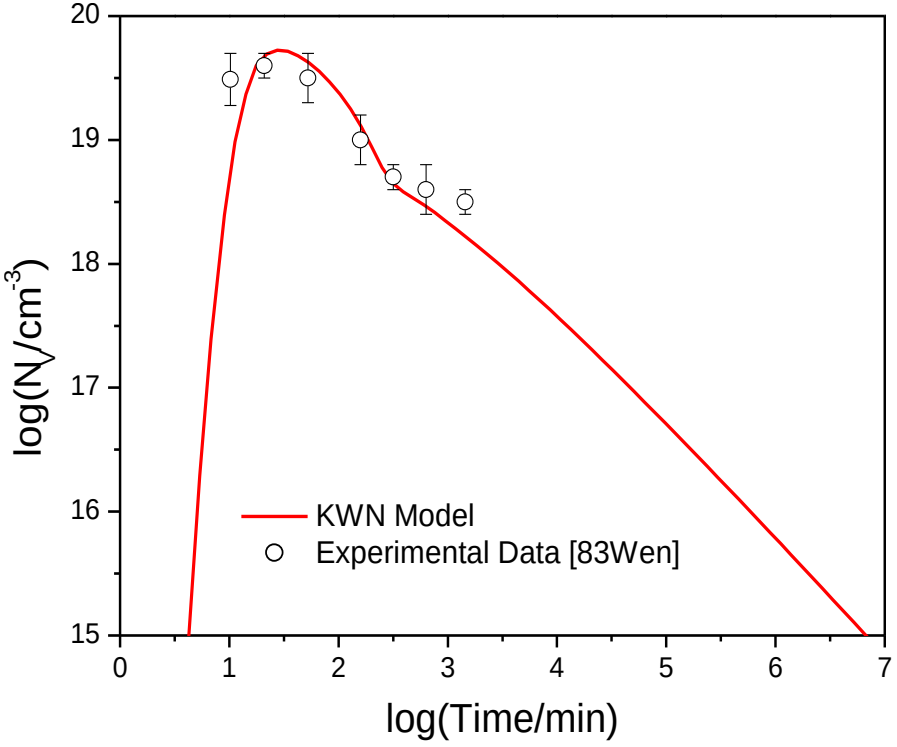

Supersaturation
of Al at the interface of γ - matrix

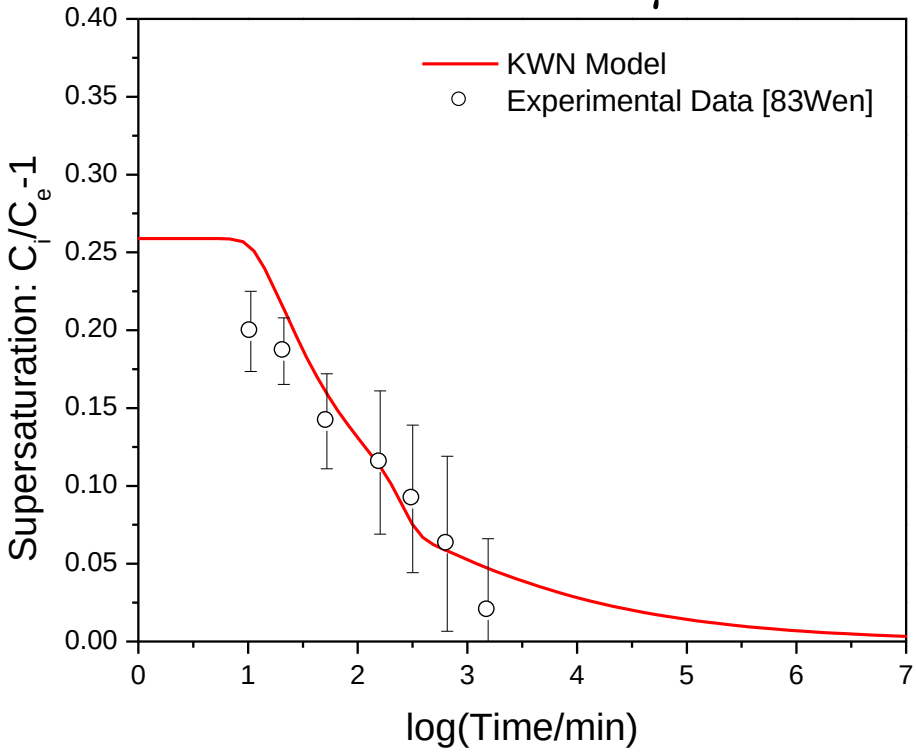

PanPrecipitation – Ni-5.2Al-14.2Cr at%

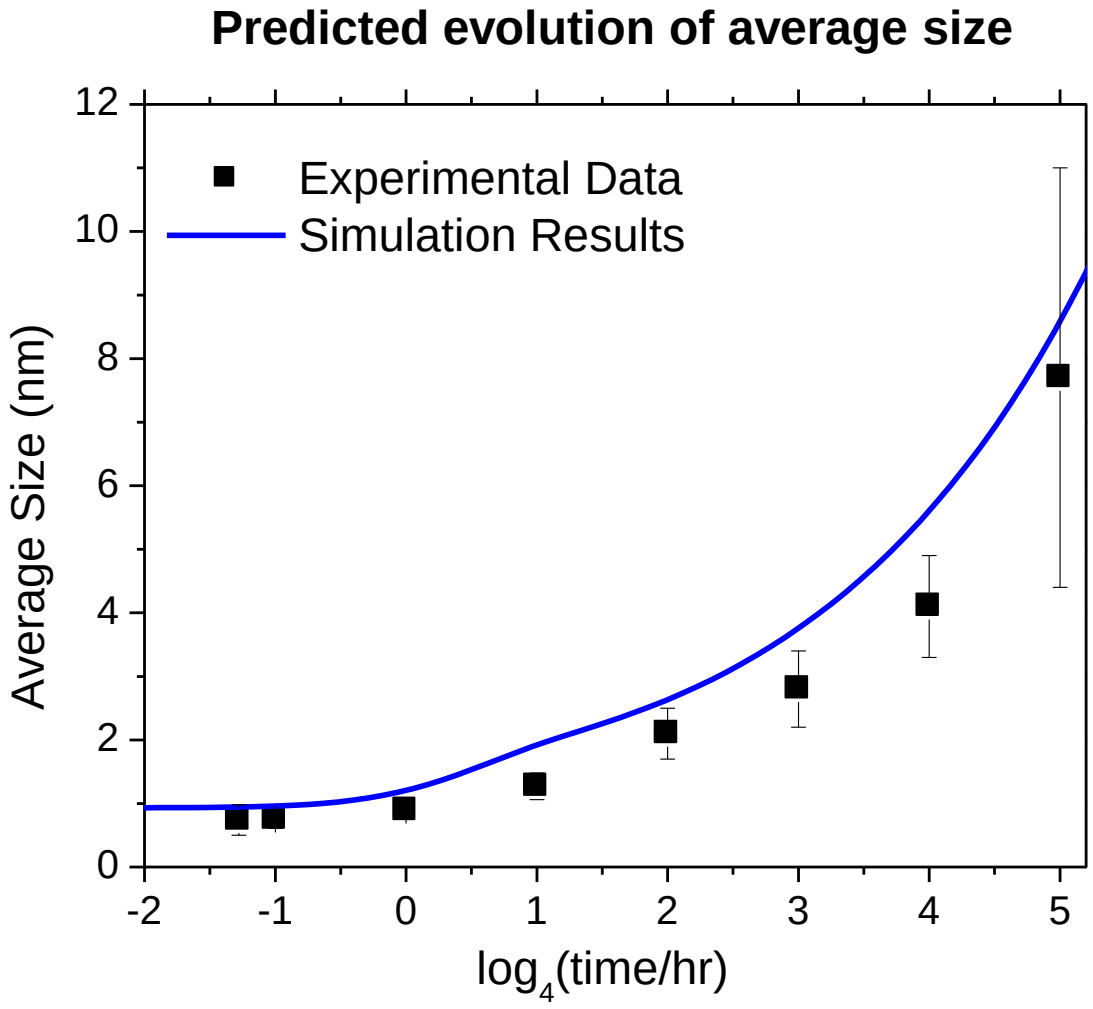

18

PanPrecipitation – Ni-5.2Al-14.2Cr at%

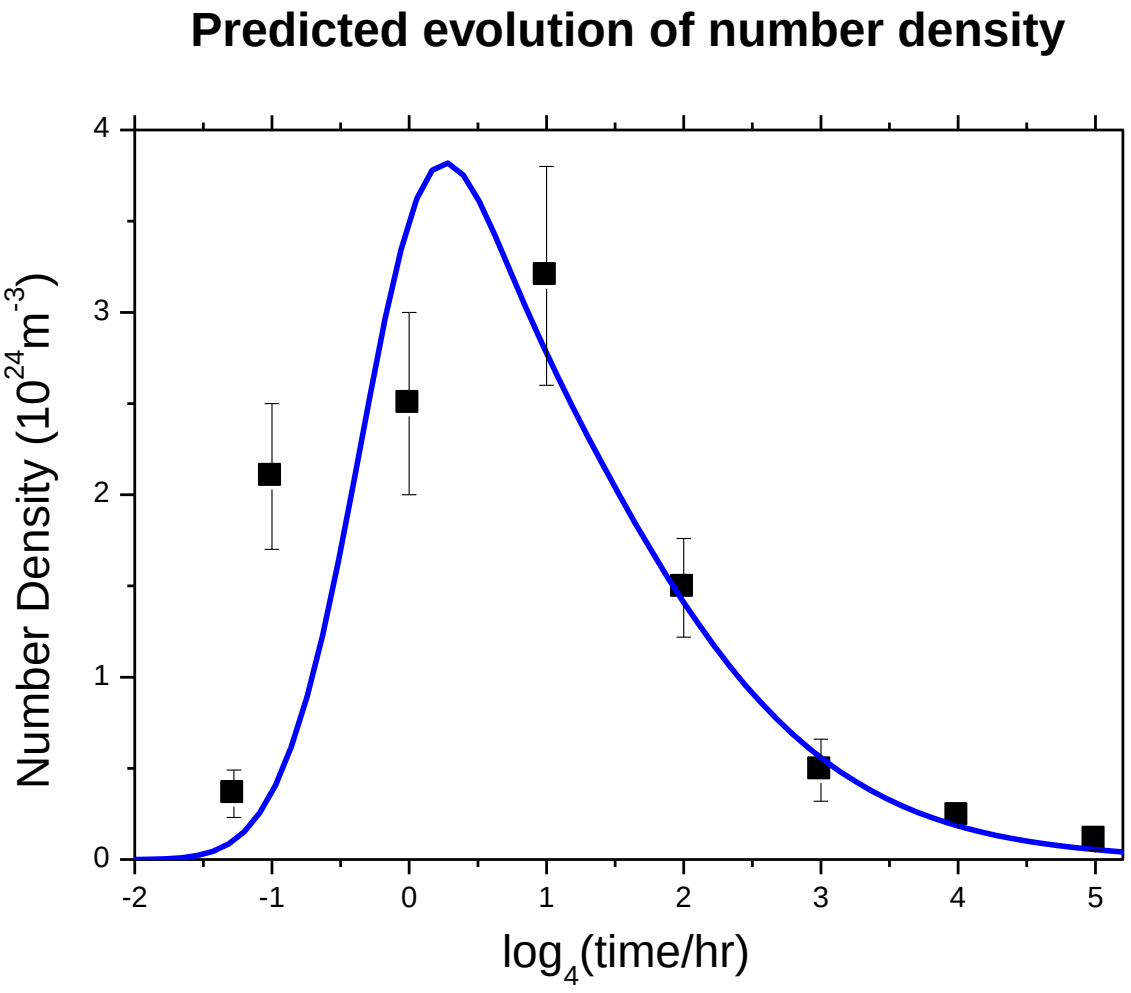

19

PanPrecipitation – Ni-5.2Al-14.2Cr at%

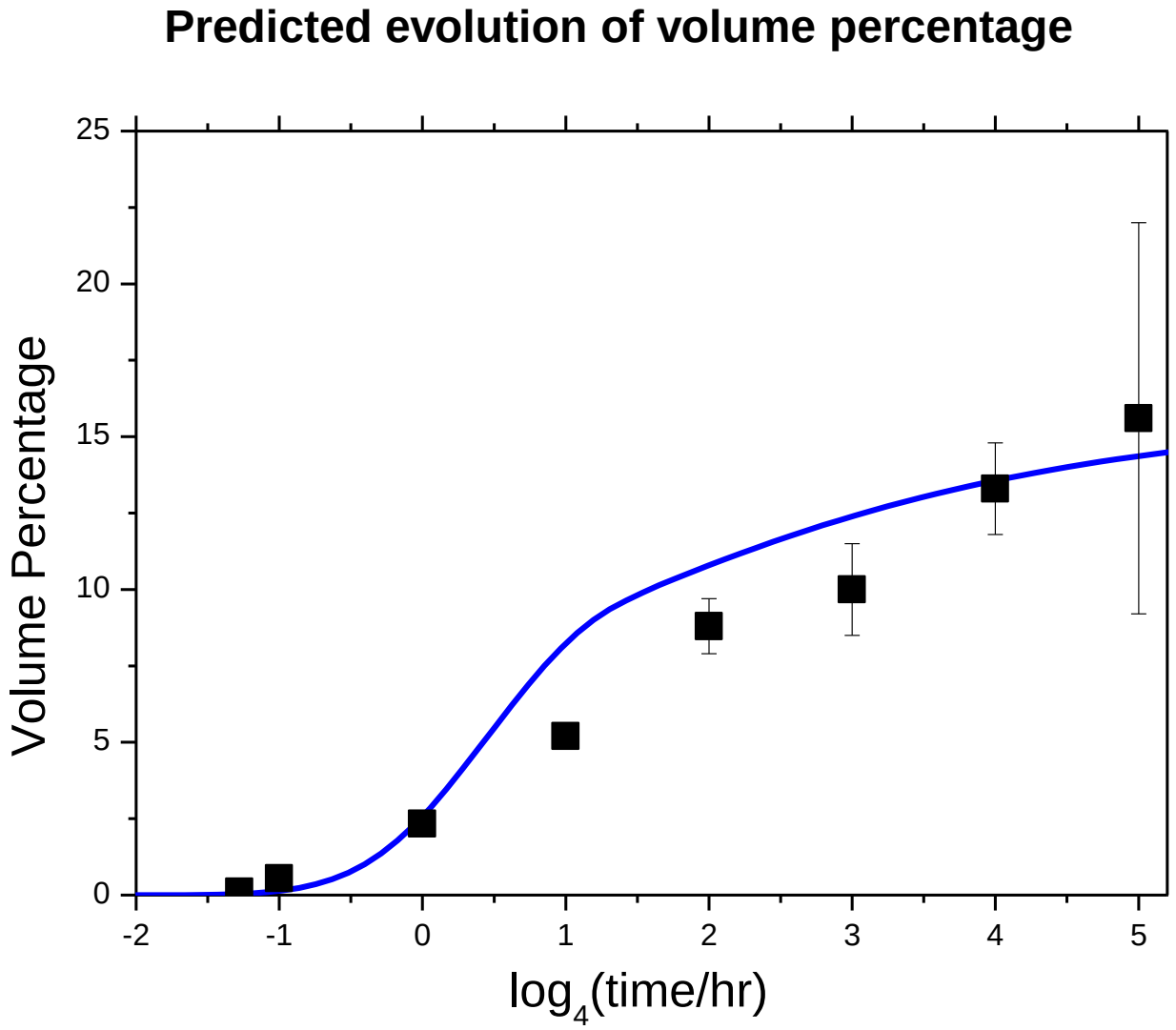

20

PanPrecipitation – Rene88DT

Predicted evolution of average size at different temperatures

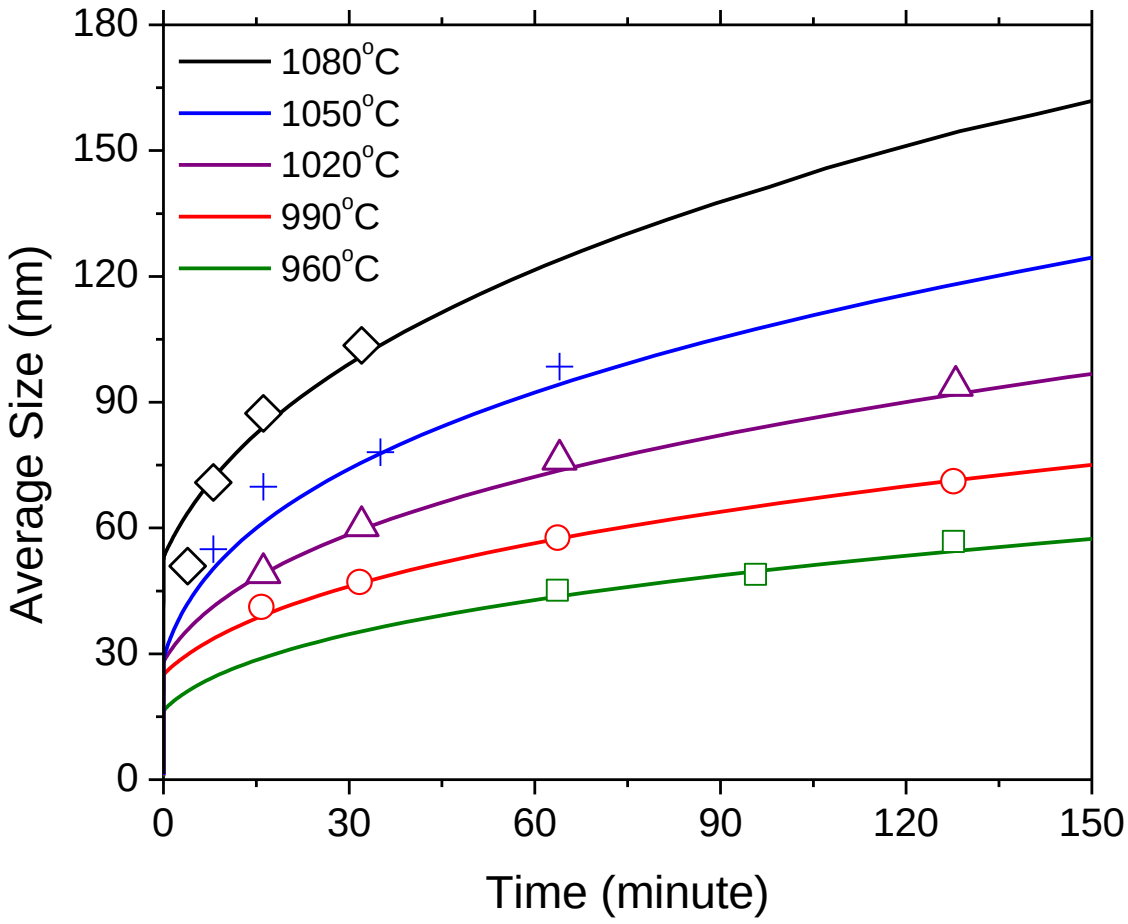

21

Integration of Thermodynamic Calculation with Microstructural Evolution Models

Thermodynamic Database

Mobility Database
Other Kinetic Parameters

Thermodynamic Calculation

Kinetic Models

Microstructural Evolution Models

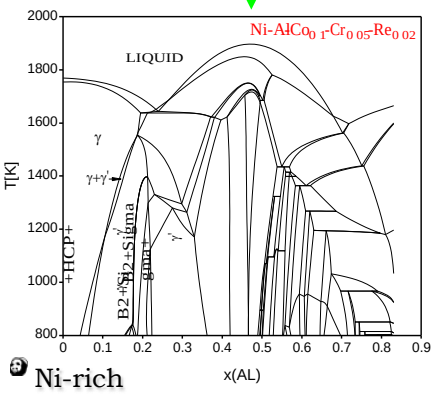

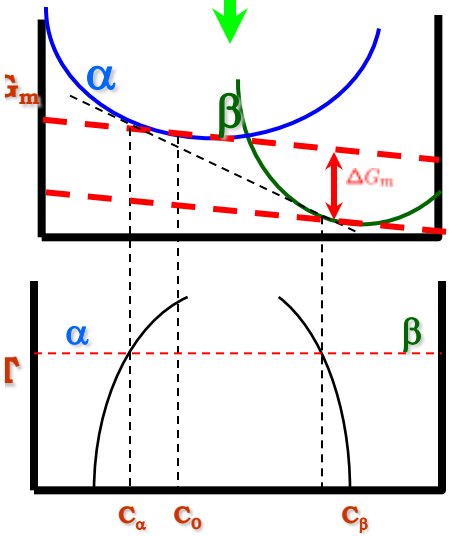

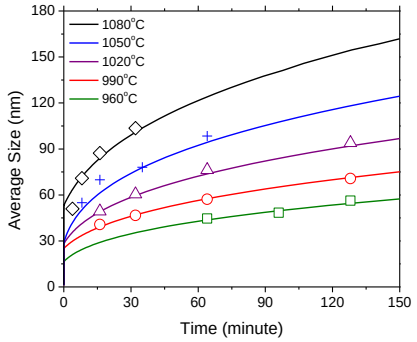

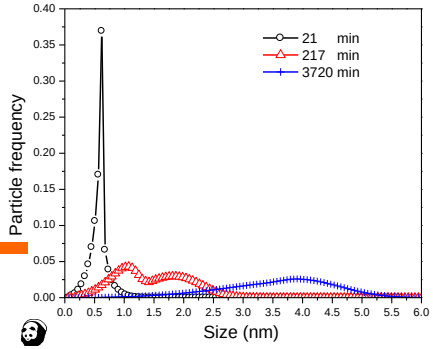

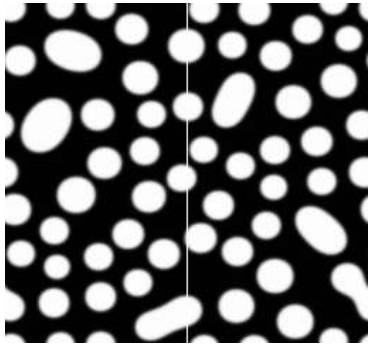

Integration of Thermodynamic Calculation, Kinetic Simulation with Mechanical Property Models

Thermodynamic Database

Mobility Database
Other Kinetic
Parameters

Thermodynamic Calculation

Kinetic Models

Mechanical
Property Models

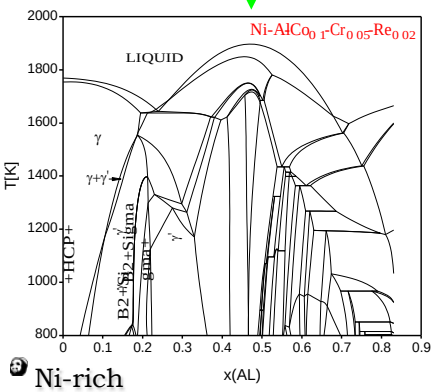

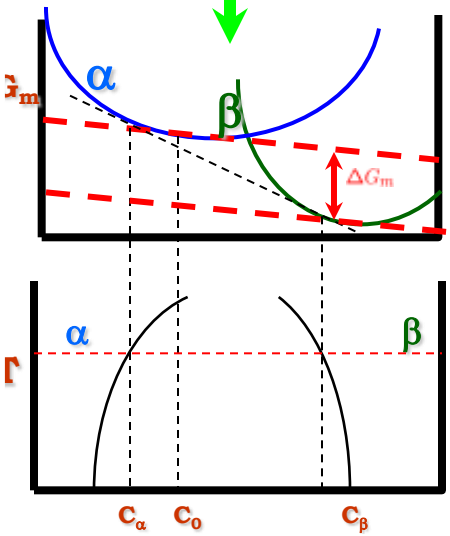

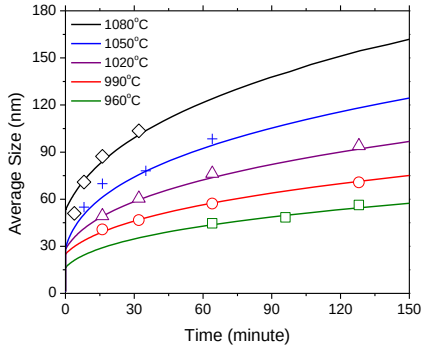

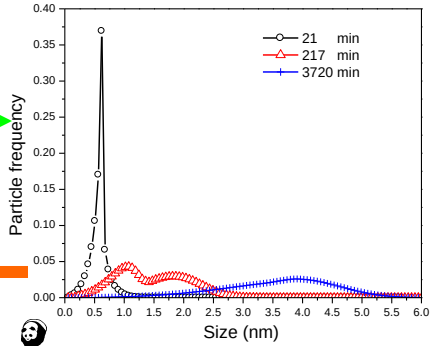

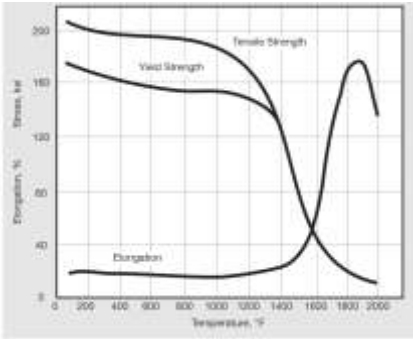

Aging Hardening of AL Alloys

Hardness: *HV* = 0.33σ + 16.0

$$\sigma_{SS} = \sum k_j C_j^{2/3}$$

Depends on the mean solute concentration of each alloying element

Yield Strength: $\sigma = \sigma_0 + \sigma_{SS} + \sigma_P$

Does not change during ageing process

- σ_I lattice resistance
- σ_{WH} work hardening
- σ_{GB} grain boundary hardening

Depends on the mean obstacle strength

$$\sigma_P = \frac{M}{bR}(2\beta G b^2)^{-1/2}\sqrt{\frac{3V_f}{2\pi}}\bar{F}^{3/2}$$

M is the Taylor factor
G is the shear modulus of the Al matrix
β Is a constant close to 0.5
b is the magnitude of the burgers vector
R is mean particle size; V_f is volume fraction
F is mean obstacle strength

$$F_i = \begin{cases} 2\beta G b^2 \dfrac{R_i}{R_C} & \text{if } R_i \le R_C \ (weak) \\ 2\beta G b^2 & \text{if } R_i \ge R_C \ (strong) \end{cases}$$

$$\bar{F} = \frac{\sum N_i F_i}{\sum N_i}$$

Age Hardening of an AA6005 Alloy

Comparison between measured and predicted response of an AA6005 Aluminum Alloy to artificial ageing at 185°C

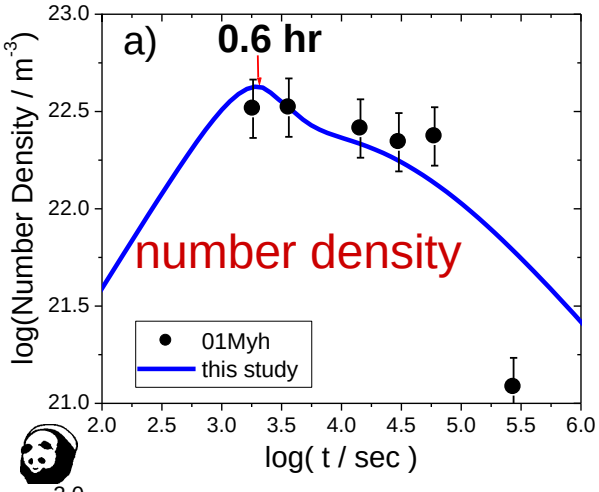

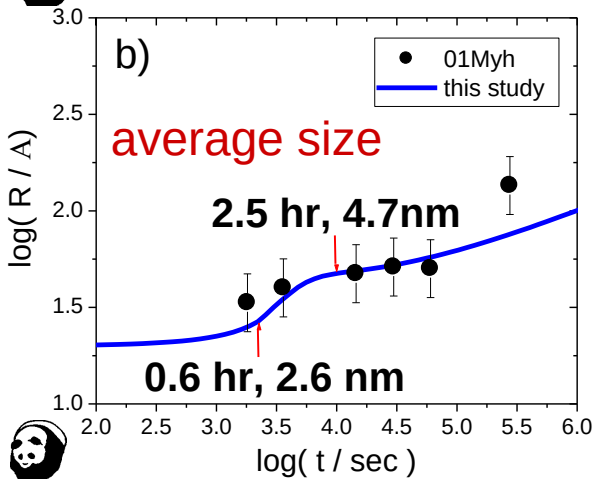

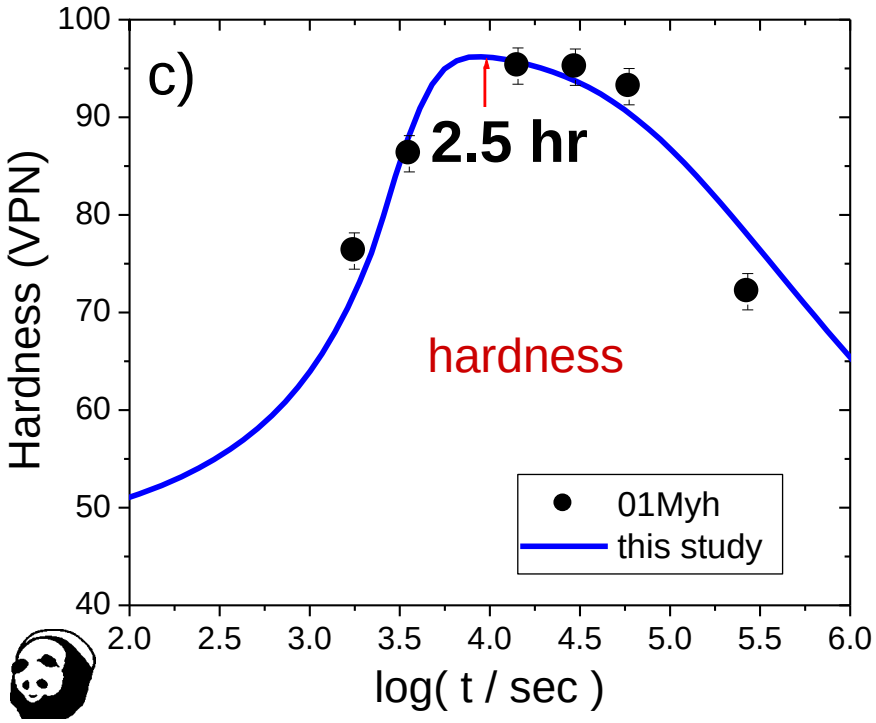

Alloy Composition: Al-0.55Mg-0.82Si-0.16Cu-0.2Fe-0.5Mn

Reference: Myhr, O.R., Grong, and Andersen, S.J., Acta Mater., 2001. 49(1): p. 65-75

Reheating of an AA6005 Alloy

Comparison between measured and predicted response of an AA6005 Aluminum Alloy to reheating at 350°C

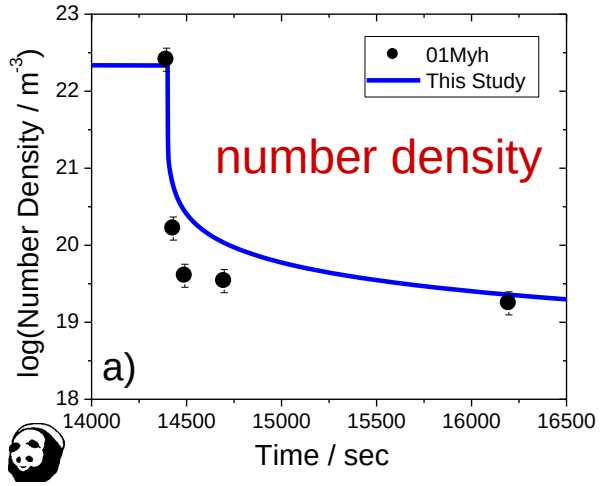

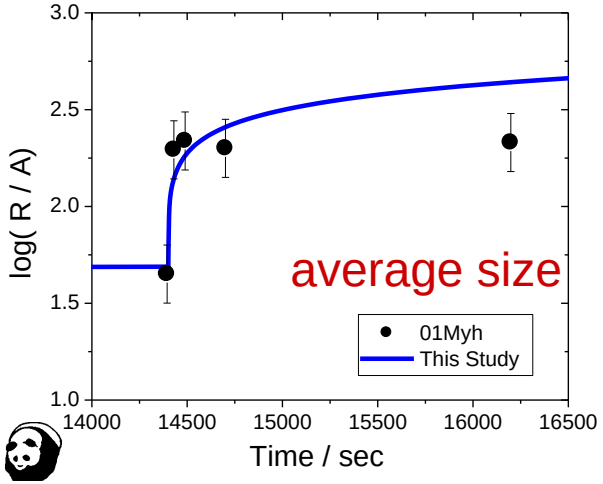

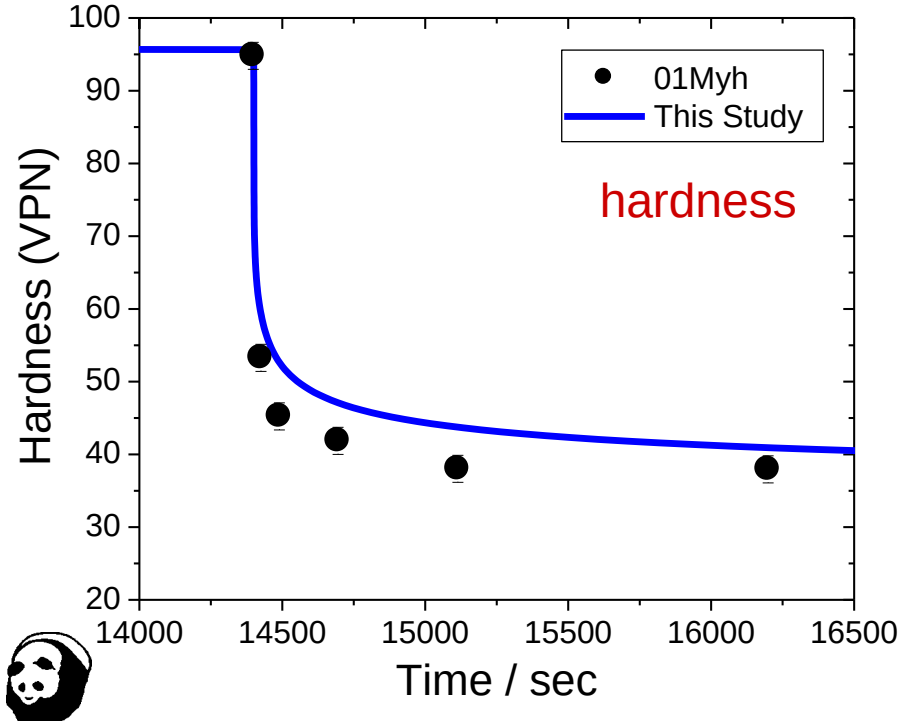

Alloy Composition: Al-0.55Mg-0.82Si-0.16Cu-0.2Fe-0.5Mn

Reference: Myhr, O.R., Grong, and Andersen, S.J., Acta Mater., 2001. 49(1): p. 65-75

AA6061: Response to Ageing and Reheating

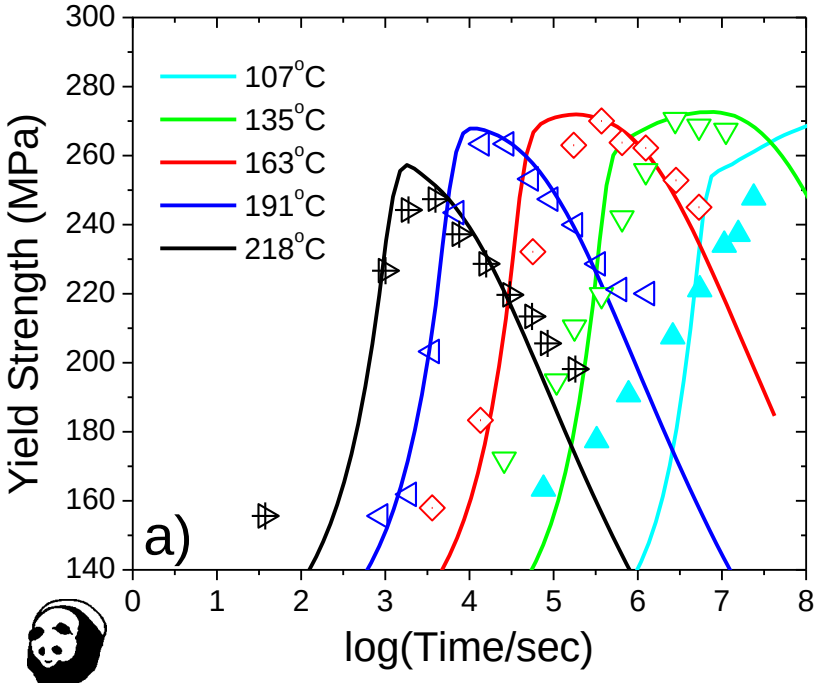

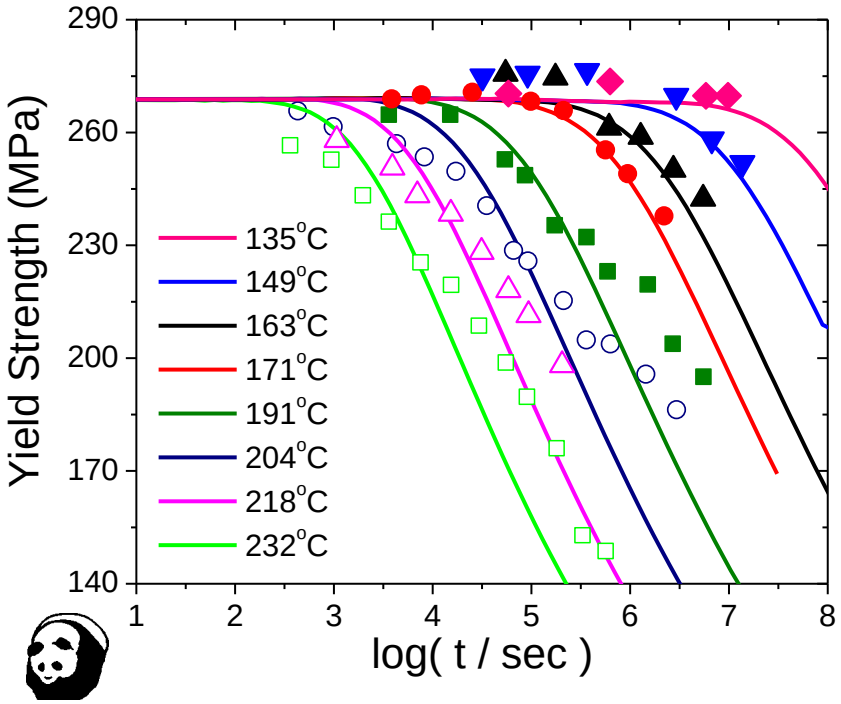

Experiment:

Anderson, W.A., *Precipitation from Solid Solution*. 1959, Metals Park, OH: American Society for Metals.

Outline

- Introduction to the CALPHAD Approach
- Integration of Thermodynamic Calculation with Kinetic Models for the Simulation of Nucleation, Growth and Coarsening
- Are Those Gibbs Energies Developed by the CALPHAD Approach Trustworthy?

How to Construct A Multicomponent Database

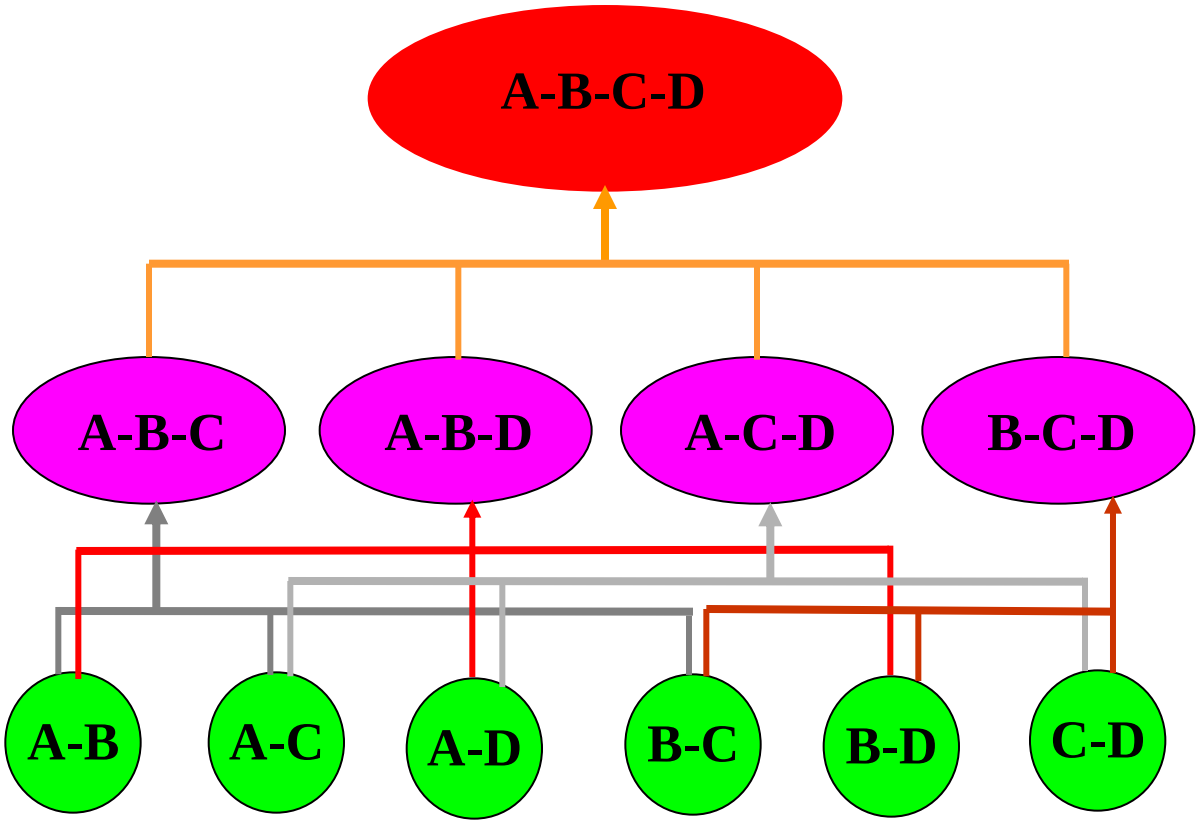

4 Ternary systems

6 Binary systems

A Complete Puzzle Picture

A Corner of a Puzzle Picture

Gibbs Energy-Outside the Stable Composition range

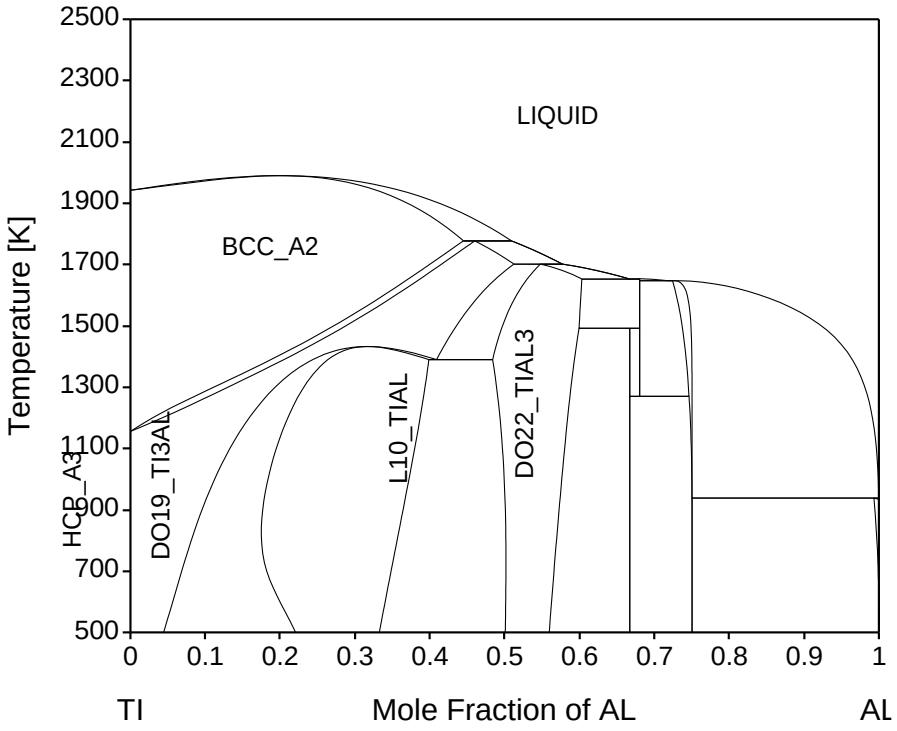

Ti-Al Phase Diagram

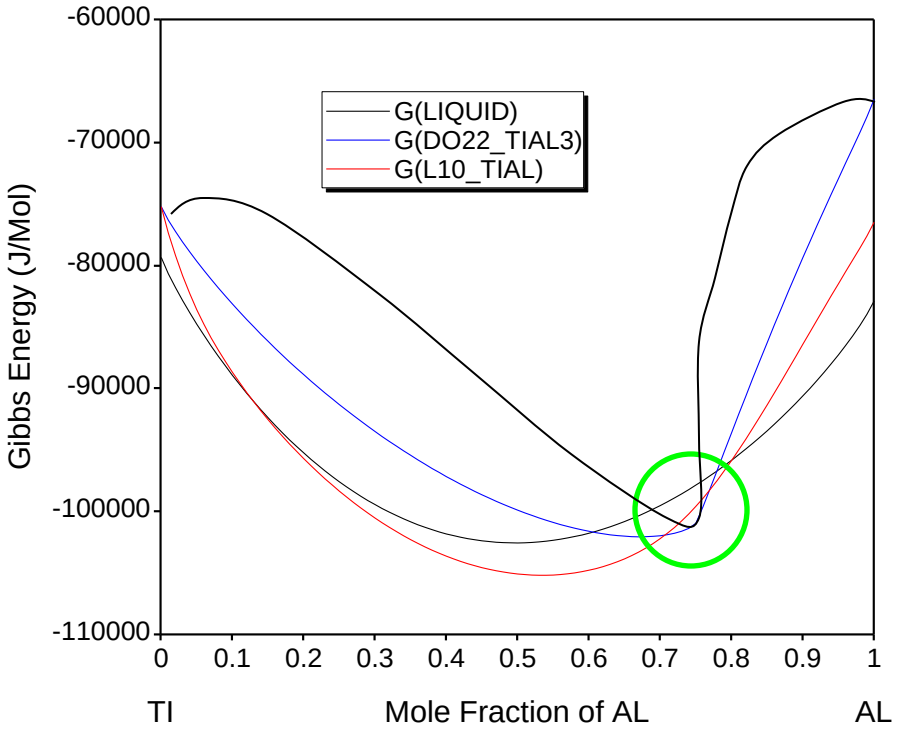

Gibbs Energy Curves at 1500K

Gibbs Energy-Outside the Stable Composition range

-

F. Zhang, S.-L. Chen, Y. A. Chang, W. A. Oates, *Intermetallics*, 9 (2001), 1079-1083.

Intrinsic Model Problems

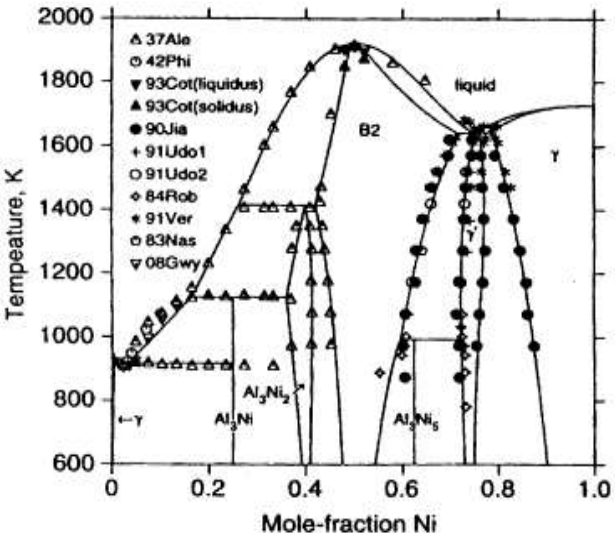

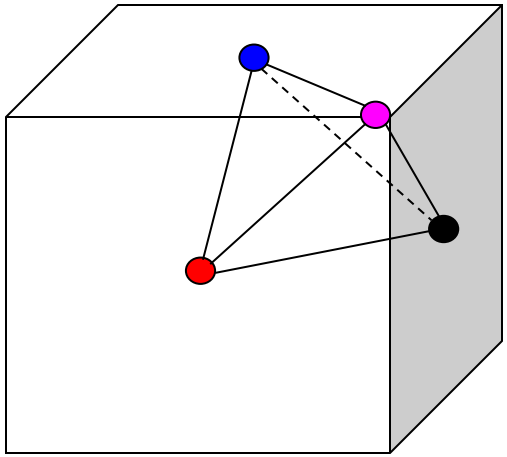

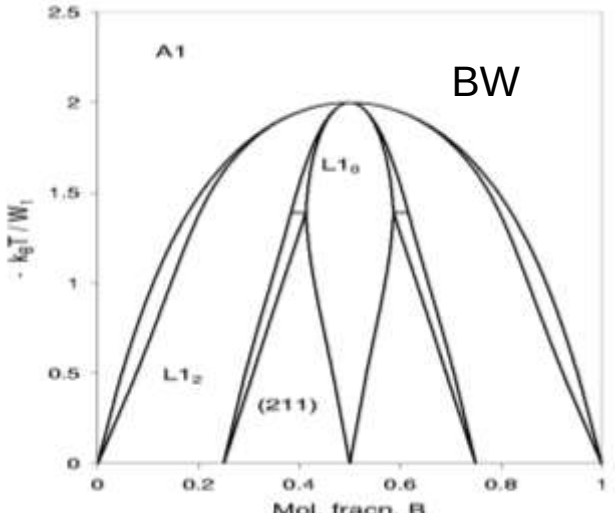

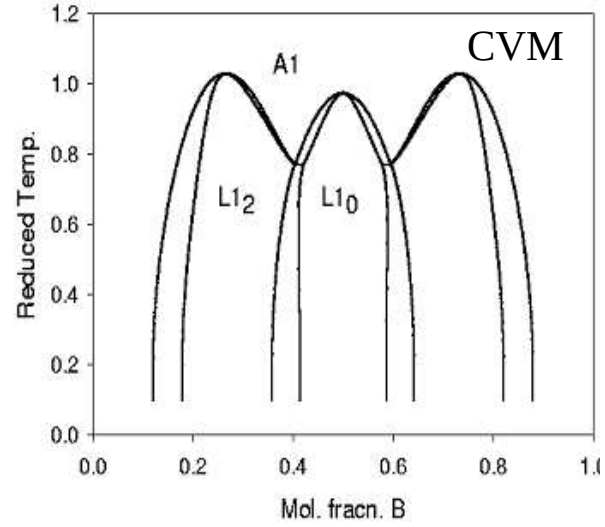

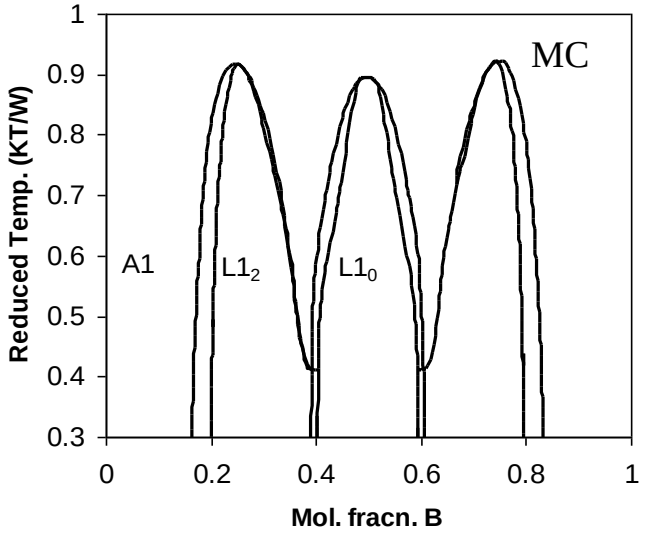

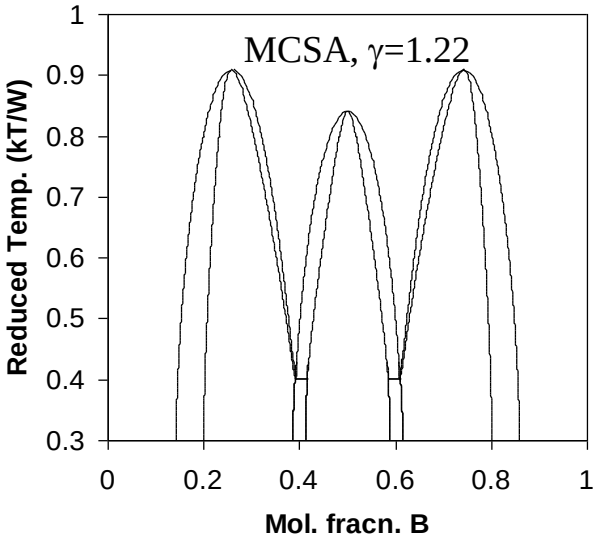

W. A. Oates, F. Zhang, S-L. Chen, and Y. A. Chang, *Physical Review B*, 59(17) (1999), 11221-11225.

F. Zhang, Y. A. Chang, Y. Du, S.-L. Chen, and W. A. Oates *Acta. Materialia*, 51(1) (2003), 207-216.

Conclusions

- **The CALPHAD approach has been applied to multi-component systems with some success**
- **Thermodynamic modeling can be integrated with kinetic models, microstructure models, mechanical property models for the simulation of materials properties**
- **Are there problems and concerns with the current CALPHAD approach? Yes**
- **Are there other better approaches for describing multi-component systems at this moment? No**
- **What can we do? Continue to improve this approach**

Acknowledgement

This work was financially supported by the USAF through SBIR, STTR and MAI projects

Thank You for Your Attention